

OFFICE OF THE CHIEF  
OF NAVAL RESEARCH  
Arlington, Virginia 22217-5000

GROUP 1, 2, 3, 4, 5, 6, 7



AD-A247 995



Reproduced From  
Best Available Copy

DTIC  
EFFECTIVE  
MAR 20 1992  
S D

North Atlantic  
(Informational)

ON  
DISSEMINATION

Portland, Oregon  
August 28 - September 1, 1988



This document has been approved  
for public release and sale; its  
distribution is unlimited.

VOLUME I

92 3 20 002

92-07200



Approved for public release; distribution is unlimited

# PROCEEDINGS Ninth Symposium (International) on Detonation

## VOLUME I

Sponsored by:

Office of Naval Research  
Air Force Armament Laboratory  
Army Armament Research, Development  
and Engineering Center  
Army Ballistic Research Laboratory  
Lawrence Livermore National Laboratory  
Los Alamos National Laboratory  
Naval Sea Systems Command  
Naval Surface Warfare Center  
Office of Naval Technology  
Sandia National Laboratories



Accession For	
NTIS	CRA&I <input checked="" type="checkbox"/>
DTIC	TAB <input type="checkbox"/>
Unannounced	<input type="checkbox"/>
Justification	
By	
Distribution /	
Availability Codes	
Dist	Avail. and/or Special
A-1	

August 28 - September 1, 1989

---

Red Lion Inn, Columbia River  
Portland, Oregon

---

Approved for public release; distribution is unlimited.



## FOREWORD

The Ninth Symposium (International) on Detonation was held at the Red Lion Inn, Columbia River, Portland, Oregon, from August 28 through September 1, 1989. The Symposium was one of a series started in 1951 as an Office of Naval Research sponsored "Conference on Detonation." Sponsorship has expanded over the years to include Army, Air Force, and Department of Energy Laboratories, as well as the Navy. The Symposia have been international since the fourth in 1965. The Symposium provided a forum for scientists from throughout the world to discuss special problems in the field of energetic materials, particularly detonation phenomena in solids and liquids.

There were 445 attendees at the Symposium; 122 were from countries outside of the United States. Fifteen countries submitted papers and sent authors to the Symposium, and a total of 20 countries participated in the meeting. Papers by scientists who were unable to attend were presented by other scientists. There were 17 exhibit booths by vendors specializing in equipment for the detonation research community.

Many conference participants and their families attended the Symposium banquet. Professor Claude Fauquignon of the Institut Franco-Allemand de Recherches de Saint-Louis served as the Master of Ceremonies. The guest speaker, Dr. Anthony Irving of the University of Washington's Geology Department, gave an interesting and educational presentation on the 1980 eruption of Mount St. Helen's.

To allow more papers to be presented at the Symposium, one and one half days were set aside for 16 Specialist Sessions, where as many as three papers were given simultaneously. Seventy-four papers were presented in the Specialist Sessions, forty nine in General Sessions, and thirty seven papers exhibiting research results were displayed in the Poster Session. Of the 160 presentations given at the Symposium, 156 papers are published in this book. Of the four that are not published, one was published in a journal that was distributed before this book was completed and three were not submitted to the editor in sufficient time to be included.

Volumes I and II of this book contain papers from the General, Specialist, and Poster Sessions, and also copies of poster displays if they were furnished by authors. With the exception of papers in the Poster Session, papers are grouped by subject and appear in the order in which they were presented at the Symposium. Poster Session papers appear in the order in which they were listed in the Technical Program, except the paper by S. Crane, et al., an index of the first through the eight symposia, which was placed at the end of Volume II. Copies of the poster displays that were provided by authors appear following the written version of the paper.

This book was composed on the Xerox 6085 word processing system which, in general, the editor feels is a good system for the presentation of technical work. However, readers should know that the gamma symbol ( $\gamma$ ) on this system looks very similar to the capital letter Y.

The Detonation Symposium Organizing Committee for the Ninth Symposium is gratified with the outstanding exchange of scientific information in the field of detonation phenomena in solids and liquids which took place at this meeting. The following are acknowledged for contributing to the success of the Symposium:

**SPONSORS:**

Office of Naval Research  
Air Force Armament Laboratory  
Army Armament Research, Development  
and Engineering Center  
Army Ballistic Research Laboratory  
Lawrence Livermore National Laboratory  
Los Alamos National Laboratory  
Naval Sea Systems Command  
Naval Surface Warfare Center  
Office of Naval Technology  
Sandia National Laboratories

**THE ORGANIZING COMMITTEE:**

**Edward L. Lee, Cochairman**  
Lawrence Livermore National Laboratory

**James M. Short, Cochairman**  
Naval Surface Warfare Center

Allan B. Anderson  
Los Alamos National Laboratory

William E. Deal  
Los Alamos National Laboratory

Joseph C. Foster  
Air Force Armament Laboratory

Robert B. Frey  
Army Ballistic Research Laboratory

Leona H. Hicks  
Lawrence Livermore National Laboratory

Pai Lu  
US Army Research, Development  
and Engineering Center

Dennis E. Mitchell  
Sandia National Laboratories

Wanda J. Morat  
Naval Surface Warfare Center

Alita M. Roach  
Los Alamos National Laboratory

Karen A. Spurlin  
Lawrence Livermore National Laboratory

Philip L. Stanton  
Sandia National Laboratories

**PORTLAND ARRANGEMENTS:**

Leona H. Hicks  
Lawrence Livermore National Laboratory

Edward L. Lee  
Lawrence Livermore National Laboratory

Karen A. Spurlin  
Lawrence Livermore National Laboratory

**REGISTRATION:**

Patricia C. Crawford  
Lawrence Livermore National Laboratory

Leona H. Hicks  
Lawrence Livermore National Laboratory

Mary Ann Lucero  
Los Alamos National Laboratory

Gay Maestas  
Lawrence Livermore National Laboratory

Beverly McCollough  
Lawrence Livermore National Laboratory

Wanda J. Morat  
Naval Surface Warfare Center

Alita M. Roach  
Los Alamos National Laboratory

Karen A. Spurlin  
Lawrence Livermore National Laboratory

**AUDIOVISUAL SERVICES:**

Matthew T. Dimercurio  
Lawrence Livermore National Laboratory

**PREPARATION OF PROCEEDINGS:**

Wanda J. Morat  
Naval Surface Warfare Center

Global Associates, Ltd.

Sandia National Laboratories is acknowledged for printing Volumes I and II of the preprints; Volume III was printed at the Naval Surface Warfare Center (NAVSWC) with funds provided by the Army Ballistic Research Laboratory.

This book was edited and produced by Wanda Morat of NAVSWC with the dedicated assistance of employees of Global Associates, Ltd., Alexandria, Virginia. Original plans were for the book to be assigned a NAVSWC publication number and reviewed for release by NAVSWC. However, publishing authority was subsequently requested and granted by the Office of the Chief of Naval Research (OCNR); therefore, it was necessary to assign the book an OCNR publication number. The Organizing Committee of the Symposium greatly appreciates the understanding of Richard Miller of OCNR concerning the importance of publishing this book, and the assistance of Judah Goldwasser and others from OCNR in the final publishing process.

Robert Frey, chairman of the Poster Session, is acknowledged for planning, organizing, and managing the Poster Session, and Alita Roach is acknowledged for planning and coordinating the displays by vendors.

The session chairmen, listed in the table of contents and on the section title pages, and others who assisted in the review process are acknowledged for assuring that the papers in this book were thoroughly reviewed.

The Organizing Committee would also like to thank Carol Lee, wife of Edward L. Lee, for organizing activities for companions of the attendees, and the staff of the Red Lion Inn, Columbia River, for their assistance before and during the Symposium.

Plans for the Tenth Symposium (International) on Detonation are under way. It will be held the week of July 11-16, 1993, at the Boston Park Plaza Hotel and Towers in Boston, Massachusetts.



**Edward L. Lee, Cochairman**  
Lawrence Livermore National Laboratory



**James M. Short, Cochairman**  
Naval Surface Warfare Center

# VOLUME I

## CONTENTS

### Page

#### SHOCK-TO-DETONATION TRANSITION

##### General Session

Cochairmen: Philip Howe and Mohammad Chaudhri

##### Combined Pressure Shear Ignition of Explosives

V. Boyle, R. Frey, and O. Blake ..... 3

##### Particular Aspect of the Explosive Particle Size Effect on Shock Sensitivity of Cast PBX Formulations

H. Moulard ..... 18

##### Particle Size Effects in the Initiation of Explosives Containing Reactive and Non-Reactive Continuous Phases

R. L. Simpson, F. H. Helm, P. C. Crawford, and J. W. Kury ..... 25

##### In-Situ Study of the Chemically Driven Flow Fields in Initiating Homogeneous and Heterogeneous Nitromethane Explosives

S. A. Sheffield, R. Engelke, and R. R. Alcon ..... 39

##### Decomposition of High Explosives in Shock and Detonation Waves

V. E. Fortov, G. I. Kanel, T. N. Fortova, S. I. Malyrenko, and A. V. Utkin ..... 50

##### Specialist Session

Cochairmen: Randall Simpson and Peter Haskins

##### Initiation of Explosive Crystals by Shock or Impact

C. S. Coffey ..... 58

##### Initiation Threshold of High Explosives in Small Flyer Plate Experiments

H. R. Kleinhanß, F. Lungenstraß, and H. Zöllner ..... 66

##### A Two-Dimensional Lagrangian Technique for Shock Initiation Diagnosis

Huan Shi and Ding Jing ..... 77

##### Influence of RDX Crystal Shape on the Shock Sensitivity of PBXs

A. C. van der Steen, H. J. Verbeek, and J. J. Meulenbrugge ..... 83

##### A Lagrange Gauge Study of the Shock Initiation Process in an Intermolecular Explosive EAK

M. Cowperthwaite, J. T. Rosenberg, and A. G. Taliancich ..... 89

## VOLUME I

### CONTENTS (Cont.)

Page

#### Specialist Session

Cochairmen: Jerry Wackerle and Robert Setchell

##### **Anomalous Shock Sensitivity/Density Relationship for Pressed Booster Explosives from a Small-Scale Gap Test**

R. J. Spear and V. Nanut ..... 98

##### **Shock Initiation of LX-17 as a Function of Its Initial Temperature**

P. A. Urtiew, L. M. Erickson, D. F. Aldis, and C. M. Tarver ..... 112

##### **Initiation and Detonation Properties of the Insensitive High Explosive TATB/Kel-F 800 95/5**

C. D. Hutchinson, G. C. W. Foan, H. R. Lawn, and A. G. Jones ..... 123

##### **Fabry Perot Velocimetry on Detonating LX-17 in Planar and Spherically Divergent Geometries**

K. L. Bahl, R. D. Breithaupt, C. M. Tarver, and W. G. Von Holle ..... 133

##### **Reaction Rates of PBH-9D Explosive**

Zhao Feng, Sun Chengwei, Chen Peiqi, and Ouyang Denghuan ..... 142

### TIME RESOLVED CHEMISTRY

#### General Session

Cochairmen: Anatolij Dremin and William Von Holle

##### **Pulsed-Laser-Excited Raman Spectra of Shock-Compressed Triaminotrinitrobenzene**

W. M. Trott and A. M. Renlund ..... 153

##### **Laser Ignition of Explosives: A Mass Spectroscopic Study of the Pre-ignition Reaction Zone**

H. Östmark and H. Nilsson ..... 162

##### **The Use of Time-Resolved Spectrometries in the Study of Initiation of Explosives at Molecular Level**

A. E. Delpuech ..... 172

##### **Vibrational Spectroscopic Investigations of Shock-Compressed Liquid Nitrogen and Shock-Compressed Liquid Nitromethane**

D. S. Moore and S. C. Schmidt ..... 180

##### **Absorption Spectroscopy of Shocked Benzene**

N. C. Holmes, G. Otani, P. McCandless, and S. F. Rice ..... 190

**VOLUME I**  
**CONTENTS (Cont.)**

Page

**INITIATION MODELING**

**General Session**

**Cochairmen: Pier Tang and John Field**

<b>Reaction Rates and the Charge Diameter Effect in Heterogeneous Explosives</b> G. A. Leiper and J. Cooper .....	197
<b>A Shock Initiation Model for Fine-Grained Hexanitrostilbene</b> M. E. Kipp and R. E. Setchell .....	209
<b>A Theoretical Picture of Shock-to-Detonation Transition in a Homogeneous Explosive</b> A. K. Kapila and J. W. Dold .....	219
<b>Chemical Phenomena Associated with the Initiation of Thermal Explosions</b> T. B. Brill and P. J. Brush .....	228

**Specialist Session**

**Cochairmen: Kibong Kim and Graeme Leiper**

<b>The Lattice Density of States Concept and its Role in Determining the Shock Sensitivity of PETN and Nitromethane</b> R. D. Bardo .....	235
<b>Unified Formulation of the Reactivity of Condensed Explosives</b> R. Cheret .....	246
<b>The Choice Problem of Equation Determining the Condensed Reacting Media Characteristics in Numerical Modeling of Shock Processes</b> V. S. Trofimov .....	250
<b>Global Calibration of Constitutive Relationships in Explosive Reaction Zone</b> Huan Shi and Ding Jing .....	252

**DEFLAGRATION-TO-DETONATION TRANSITION**

**General Session**

**Cochairmen: Richard Bernecker and Albert van der Steen**

<b>DDT - Determination of the Successive Phases of Phenomena</b> M. Samirant .....	259
---------------------------------------------------------------------------------------	-----

## VOLUME I

### CONTENTS (Cont.)

	<u>Page</u>
<b>Deflagration to Detonation in Granular HMX</b> J. M. McAfee, B. W. Asay, A. W. Campbell, and J. B. Ramsay .....	265
<b>Model Calculations and Experimental Measurements of the Response of HMX Porous Beds to Deflagration and Shock</b> D. F. Aldis, E. L. Lee, R. L. Simpson, and A. M. Weston .....	280
<b>Compressive Combustion of Granular Materials Induced by Low-Velocity Impact</b> M. R. Baer and J. W. Nunziato .....	293
<b>Compaction Wave Acceleration in Granular Energetic Material: Simulation with a Reactive Shock Wave Model</b> D. E. Kooker .....	306
<b>Specialist Session</b> <b>Cochairmen: Douglas Kooker and Henry Moulard</b>	
<b>Combined Experimental and Theoretical Investigations into the Deflagration-to-Detonation Transition</b> H. J. Verbeek and A. C. van der Steen .....	320
<b>Numerical Simulation of Deflagration-to-Detonation Transition for TS 3659 Propellants</b> T. Hsieh and K. Kim .....	329
<b>Dynamic Compaction and Compressive Reaction Studies for Single and Double-Base Ball Propellants</b> B. C. Glancy, H. W. Sandusky, P. J. Miller, and A. D. Krall .....	341
<b>DDT Studies of a High Energy Spherical Ball Propellant</b> R. R. Bernecker .....	354
<b>An Improved Model of the Deflagration-to-Detonation Transition in Porous Beds</b> C. F. Price, A. I. Atwood, and T. L. Boggs .....	363

### EQUATION OF STATE

**General Session**  
**Cochairmen: Claude Fauquignon and Milton S. Shaw**

<b>Shock Behavior of Explosives about the C-J Point</b> P. W. Cooper .....	379
-------------------------------------------------------------------------------	-----

**VOLUME I**  
**CONTENTS (Cont.)**

	<u>Page</u>
<b>Electrically Enhanced Detonation and Equations of State for Detonation Products</b>	
M. Cowperthwaite .....	388
<b>The Measurement of Electrical Conductivity in Detonating Condensed Explosives</b>	
D. G. Tasker and R. J. Lee .....	396
<b>Synthesis of Ultrafine Diamonds in Detonation Waves</b>	
V. M. Titov, V. F. Anisichkin, and I. Yu. Mal'kov .....	407
<b>Carbon in Detonations</b>	
J. D. Johnson .....	417
<b>Phase Changes in Carbon and Nitrogen Systems: Their Effects on the Detonation Properties of High Explosives</b>	
F. H. Ree and M. van Thiel .....	425
<b>Specialist Session</b> <b>Cochairmen: Francis Ree and Katsumi Tanaka</b>	
<b>The Detonation Parameters of New Powerful Explosive Compounds Predicted with a Revised VLW Equation of State</b>	
Wu Xiong, Sun Jian, and Xiao Lianjie .....	435
<b>Theoretical Model of Explosive Detonation Products: Tests and Sensitivity Studies</b>	
G. I. Kerley .....	443
<b>A New Simulation Method for the Efficient Calculation of Benchmarks for Detonation Products Equations of State</b>	
M. S. Shaw .....	452
<b>Calculations of Detonation Pressures for a Homologous Series of Polynitroaliphatic Explosives Using a Fluid Perturbation Equation of State and a New Chemical Equilibrium Computer Program</b>	
F. J. Zerilli and H. D. Jones .....	461
<b>Specialist Session</b> <b>Cochairmen: LeRoy Green and Manfred Held</b>	
<b>A Detonation Pressure Measurement System Employing High Resistance Manganin Foil Gauge</b>	
S. Y. Song and J. W. Lee .....	471



# VOLUME I

## CONTENTS (Cont.)

	<u>Page</u>
<b>Heat of Detonation, the Cylinder Test, and Performance in Munitions</b>	
I. B. Akst .....	478
<b>Theoretical Prediction of High Explosives Efficiency: Application to NTO</b>	
F. Bugaut, S. Bernard, and R. Chirat .....	489
<b>Determining JWL Equation of State Parameters Using the Gurney Equation Approximation</b>	
P. J. Miller and K. E. Alexander .....	498
<b>Specialist Session</b> <b>Cochairmen: Gerald Kerley and Douglas Tasker</b>	
<b>Studies about the Equations of State of the Detonation Products</b>	
N. Carion, J. Aveille, P. Andriot, F. Chaisse, G. Guri, M. T. Kerihuel, and M. Leroy .....	506
<b>Sensitivities of Adiabatic and Gruneisen Gammas to Errors in Molecular Properties of Detonation Products</b>	
W. Byers Brown and M. Braithwaite .....	513
<b>Reactive Flow Measurements and Calculations for ZrH<sub>2</sub>-Based Composite Explosives</b>	
M. J. Murphy, R. L. Simpson, R. D. Breithaupt, and C. M. Tarver .....	525

## COMPOSITES AND EMULSIONS

### General Session

#### Cochairmen: Ding Jing and Raymond McGuire

<b>Detonation Characteristics of Gun Propellants</b>	
B. W. Asay, A. W. Campbell, M. J. Ginsberg, and J. B. Ramsay .....	537
<b>Detonation Properties of Mixtures of HMX and Emulsion Explosives</b>	
J. D. Renick, P. A. Persson, and J. A. Sanchez .....	545
<b>The Prospects for Composite Explosive</b>	
Guo Yuxian .....	554
<b>Detonation Velocity and Pressure of the Non-Ideal Explosive Ammonium Nitrate</b>	
A. Miyake, A. C. van der Steen, and H. H. Kodde .....	560

**VOLUME I**  
**CONTENTS (Cont.)**

	<u>Page</u>
<b>Specialist Session</b> <b>Cochairmen: Herbert Richter and James Short</b>	
<b>Shock Sensitivities of Energetically Substituted Benzofuroxans</b>	
M. L. Chan, C. D. Lind, and P. Politzer .....	566
<b>Detonation and Shock Initiation Properties of Emulsion Explosives</b>	
J. Lee, F. W. Sandstrom, B. G. Craig, and P.-A. Persson .....	573
<b>Effect of Pressure on Shock Sensitivity of Emulsion Explosives</b>	
G. Om Reddy and F. P. Beitel, Jr. ....	585
<b>Development of a Model of Reaction Rates in Shocked Multicomponent Explosives</b>	
K. Kim .....	593
<b>A Model for the Initiation of Heterogeneous High Explosives</b>	
<b>Subject to General Compressive Loading</b>	
J. Starkenberg .....	604

**COMPOSITES AND EMULSIONS/UNDERWATER EXPLOSIVES**

<b>Specialist Session</b> <b>Cochairmen: Leslie Roslund and Algot Persson</b>	
<b>Calculation of Detonation Properties of Emulsion Explosives</b>	
K. Tanaka, M. Iida, Y. Nakayama, N. Ishiokawa, M. Yoshida, and S. Fujiwara .....	621
<b>Chemistry of Underwater Explosive Detonations</b>	
D. Carlson, R. Doherty, V. Ringbloom, J. S. Deiter, and G. B. Wilmot .....	626
<b>Estimation of Performance of Underwater Explosives</b>	
D. A. Cichra and R. M. Doherty .....	633
<b>Underwater Explosion of Emulsion Explosives</b>	
K. Hattori, Y. Kato, K. Tokita, Y. Fukatsu, N. Mori, and A. Torii .....	640
<b>The Fundamentals of Metal Combustion in Composite Explosives</b>	
<b>Revealed by High Speed Microphotography</b>	
W. C. Tao, A. M. Frank, R. E. Clements, and J. E. Shepherd .....	641

**VOLUME I**  
**CONTENTS (Cont.)**

Page

**REACTION ZONE**

**General Session**

**Cochairmen: William Davis and Joseph Foster**

<b>Detonation Reaction-Zone Structure for PBX 9502</b> W. L. Seitz, H. L. Stacy, R. Engelke, P. K. Tang, and J. Wackerle .....	657
<b>Reaction Zone Structure in Supracompressed Detonating Explosives</b> L. G. Green, C. M. Tarver, and D. J. Erskine .....	670
<b>Lagrangian Analysis of MIV Gauge Experiments on PBX 9502 Using the Mass-Displacement Moment Function</b> C. A. Forest, J. Wackerle, J. J. Dick, S. A. Sheffield, and D. R. Pettit .....	683
<b>The Heterogeneous Explosive Reaction Zone</b> C. L. Mader and J. D. Kershner .....	693
<b>Using Small Scale Tests to Estimate the Failure Diameter of a Propellant</b> C. M. Tarver and L. G. Green .....	701

**DETONATION WAVE PROPAGATION**

**General Session**

**Cochairmen: Roger Cheret and Michael Cowperthwaite**

<b>Molecular Dynamics Simulation of the Effect of Molecular Dissociation and Energy Absorption on Detonation Structure in Energetic Solids</b> S. G. Lambrakos, M. Peyrard, and E. S. Oran .....	713
<b>Multiprocess Detonation Model</b> A. N. Dremin, V. Yu. Klimenko, O. N. Davidova, and T. A. Zoludeva .....	724
<b>Detonation Shock Dynamics: A New Approach to Modeling Multi-Dimensional Detonation Waves</b> J. B. Bdzil, W. Fickett, and D. S. Stewart .....	730
<b>Nonequilibrium Effects of Slow Diffusion Controlled Reactions on the Properties of Explosives</b> M. van Thiel and F. H. Ree .....	743
<b>Computation of a Diverging Comp-B Detonation</b> B. G. Bukiet .....	751

## VOLUME I

### CONTENTS (Cont.)

	<u>Page</u>
<b>A Theoretical Analysis of the Sonic Point Properties in a Plane Detonation Wave</b> L. Brun and F. Chaisse .....	757
<b>Specialist Session</b> <b>Cochairmen: Craig Tarver and Patrick Gimenez</b>	
<b>Investigations of the Influence of Polymorphous Transformation on the Process of Detonation of Mixtures Containing HE and Substances Undergoing Transformation</b> E. Włodarczyk, R. Trebinski, W. Trzcinski, and W. Witkowski .....	766
<b>Examples of Detonation Shock Dynamics for Detonation Wave Spread Applications</b> D. S. Stewart and J. B. Bdzil .....	773
<b>Application of Whitham's Shock Dynamics Theory to the Propagation of Divergent Detonation Waves</b> B. D. Lambourn and D. C. Swift .....	784
<b>Propagation of Detonation Waves from an Impact Region</b> R. S. Lee, W. C. Tao, and L. D. Crouch .....	798
<b>Detonation Wave Propagation in PBXW-115</b> J. W. Forbes, E. R. Lemar, and R. N. Baker .....	806
<b>Specialist Session</b> <b>Cochairmen: Jerry Forbes and James Kennedy</b>	
<b>Non-Steady Flow in a Detonator</b> Jia Quansheng, Chen Fumei, and Wang Tinzhen .....	816
<b>Polysulfone SIP Gage for Flying Plate Explosive Components</b> T. W. Warren and R. R. Weinmaster .....	822
<b>The Effects of Inert Walls on the Velocity of Detonation in EDC35, an Insensitive High Explosive</b> G. Eden and R. A. Belcher .....	831
<b>Experimental and Numerical Study of Oblique Interactions of Detonation Waves with Explosive/Solid Material Interfaces</b> J. Aveillé, N. Carion, J. Vacellier, and J. M. Servas .....	842
<b>Experimental and Numerical Study of Corner-Turning Detonation</b> A. W. Gibb .....	853

## VOLUME II

### CONTENTS

Page

#### HOT SPOTS

##### General Session

**Cochairmen: Charles Coffey and Per-Anders Persson**

<b>The Initiation of Fast Decomposition in Solid Explosives by Fracture, Plastic Flow, Friction, and Collapsing Voids</b>	
M. M. Chaudhri .....	857
<b>Characterization of Defect Microstructure in High Explosives Single Crystals by Synchrotron X-Ray Tomography</b>	
W. C. Tao and J. H. Kinney .....	868
<b>Cavity Collapse in a Heterogeneous Commercial Explosive</b>	
N. K. Bourne and J. E. Field .....	869
<b>Response of Composite Propellants to Shock Loading</b>	
Bai Chunhua and Ding Jing .....	879
<b>Deformation and Explosive Properties of HMX Powders and Polymer Bonded Explosives</b>	
J. E. Field, M. A. Parry, S. J. P. Palmer, and J. M. Huntley .....	886

##### Specialist Session

**Cochairmen: Paul Cooper and Hyla Napadensky**

<b>Physical and Chemical Nature of Hot Spots in TATB and HMX</b>	
J. Sharma, B. C. Beard, J. Forbes, C. S. Coffey, and V. M. Boyle .....	897
<b>Hot Spot Formation in a Collapsing Void of Condensed-Phase, Energetic Material</b>	
P. B. Butler, J. Kang, and M. R. Baer .....	906
<b>Broad Bandwidth Study of the Topography of the Fracture Surfaces of Explosives</b>	
M. Y. D. Lanzerotti, J. J. Pinto, and A. Wolfe .....	918
<b>Effects of Microballoon Concentration on the Detonation Characteristics of Nitromethane-PMMA Mixtures</b>	
H. N. Presles, J. Campos, O. Heuzé, and P. Bauer .....	925

## VOLUME II

### CONTENTS (Cont.)

Page

#### DETONATION PRODUCTS

##### Specialist Session

Cochairmen: Anita Renlund and Gert Bjarnholt

<b>Detonation Characteristics of Dense Gaseous Explosive Mixtures</b> P. Bauer, M. Dunand, H. N. Presles, and O. Heuzé .....	933
<b>Detonation Temperature of Some Liquid and Solid Explosives</b> Y. Kato, N. Mori, H. Sakai, T. Sakurai, and T. Hikita .....	939
<b>The Studying of Detonation Temperatures of Solid High Explosives</b> Shi Huisheng, Han Chengbang, Kang Shufang, and Huang Lihong .....	947
<b>Free-Expansion Experiments and Modeling in Detonation: Chemistry and Hydrodynamics on a Laboratory Scale</b> N. R. Greiner and N. Blais .....	953
<b>Detonation Products of Less Sensitive High Explosives Formed Under Different Pressures of Argon and in Vacuum</b> F. Volk and F. Schedlbauer .....	962
<b>Explosive Potential of Carbohydrate-Metal Composites</b> A. J. Tulis, J. L. Austing, W. K. Sumida, D. E. Baker, and D. J. Hrdina .....	972

#### CHEMISTRY AND COMPOSITION

##### Specialist Session

Cochairmen: Tom Larson and Fritz Schedlbauer

<b>A Review of Paramagnetic Resonance Products in Condensed Phase Energetic Materials</b> M. D. Pace .....	987
<b>Properties of Bis(2,2,2-Trinitroethyl-N-Nitro) Ethylenediamine and Formulations Thereof</b> Dong Haishan .....	995
<b>NTO Development at Los Alamos</b> L. B. Chapman .....	1001
<b>Use of Oxynitrotriazole to Prepare an Insensitive High Explosive</b> A. Becuwe and A. Delclos .....	1008

## VOLUME II

### CONTENTS (Cont.)

#### Page

#### **Effects of Binder Concentration on the Properties of Plastic-Bonded Explosives**

R. D. Steele, L. A. Stretz, G. W. Taylor, and T. Rivera ..... 1014

#### **Specialist Session**

**Cochairmen: Horst Adolph and Fred Volk**

#### **Chemistry of Nitromethane at Very High Pressure**

S. F. Agnew, B. I. Swanson, J. Kenney, and I. Kenney ..... 1019

#### **Decomposition Mechanisms and Chemical Sensitization in Nitro, Nitramine, and Nitrate Explosives**

M. D. Cook and P. J. Haskins ..... 1027

#### **Decomposition of Energetic Materials on the Drop-Weight-Impact Machine**

G. A. Buntain, T. L. McKinney, T. Rivera, and G. W. Taylor ..... 1037

### **SPECIAL INITIATION**

#### **Specialist Session**

**Cochairmen: Pai Lu and Christopher Hutchinson**

#### **Behavior of an Unreacted Composite Explosive on Low Velocity Impact**

C. Loupias and A. Fanget ..... 1047

#### **Response of Rocket Propellants to Projectile Impact**

S. Y. Ho ..... 1052

#### **Characterization of Booster-Rocket Propellants and Their Simulants**

L. J. Weirick ..... 1060

#### **Experimental Study and Numerical Modeling of Thermal Initiation and Combustion of High Heterogeneous Explosives**

C. Castille, D. Bainville, P. Reynier, and R. Belmas ..... 1070

#### **Specialist Session**

**Cochairmen: Edward Lee and Krishna Mohan**

#### **Electrostatic Sensitivity Testing of Explosives at Los Alamos**

T. E. Larson, P. Dimas, and C. E. Hannaford ..... 1076

# VOLUME II

## CONTENTS (Cont.)

	<u>Page</u>
<b>Molecule-Surface Collision Induced Excitation and Dissociation: n,i-C<sub>3</sub>F<sub>7</sub>NO, C<sub>6</sub>F<sub>5</sub>NO, 2-Methyl, 5-Vinyl Tetrazole and C(NO<sub>2</sub>)<sub>4</sub> with MgO(100) Surfaces at E<sub>incident</sub> ≤ 7.5 eV</b>	
K. Kolodney, P. S. Powers, L. Iwata, H. Reisler, C. Wittig, I. B. Mishra, and C. Capellos .....	1084
<b>Initiation and Propagation in Primary Explosives</b>	
P. M. Dickson, M. A. Parry, and J. E. Field .....	1100
<b>Prompt Detonation of Secondary Explosives by Laser</b>	
D. L. Paisley .....	1110
<b>Laser Initiation of Secondary Explosives</b>	
A. M. Renlund, P. L. Stanton, and W. M. Trott .....	1118

## POSTER PAPERS

**Organizer and Chairman: Robert Frey**  
**Cochairmen: Harold Sandusky, John Kury, Philip Stanton,**  
**Allan Anderson, Michel Samirant, and Thomas Boggs**

<b>Intense Electron Beam Detonation of TATB Explosives</b>	
D. Demske, N. Brazell, W. E. Farley, S. Miller, and R. Warnes .....	1131
<b>Time-Resolved Mass Spectrometry Technique for Studying Fast Transient CHNO Explosive Decomposition Kinetics</b>	
R. D. Skocypec and K. L. Erickson .....	1140
<b>Laser Ignition of Explosives: Raman Spectroscopy of the Ignition Zone</b>	
H. Nilsson and H. Östmark .....	1151
<b>The Effect of the Pentafluorothio (SF<sub>5</sub>) Group on the Properties of Explosive Nitro Compounds: New SF<sub>5</sub> Explosives</b>	
M. E. Sitzmann and D. L. Ornellas .....	1162
<b>Chemistry of Detonation Soot: Diamonds, Graphite, and Volatiles</b>	
N. R. Greiner and R. Hermes .....	1170
<b>Molecular Models for Explosives: Applications to NTO</b>	
J. P. Ritchie and E. M. Kober .....	1185
<b>Reaction and Diffusion in Detonation</b>	
N. J. B. Green, M. J. Pilling, and S. H. Robertson .....	1193



# VOLUME II

## CONTENTS (Cont.)

	<u>Page</u>
<b>A Thermochemical Model for Shock-Induced Chemical Reactions in Porous Solids: Analogs and Contrasts to Detonation</b>	
M. B. Boslough .....	1199
<b>Reactive Modeling in Shock Initiation of Heterogeneous Explosives</b>	
M. Quidot and J. Groux .....	1217
<b>Reactive Flow Analysis and Its Applications</b>	
G. A. Leiper and D. L. Kennedy .....	1224
<b>Physical Evidence of Different Chemical Reactions in Explosives as a Function of Stress</b>	
T. P. Liddiard, J. W. Forbes, and D. Price .....	1235
<b>Towards Developing the Capability to Predict the Hazard Response of Energetic Materials Subjected to Impact</b>	
C. S. Coffey, D. F. DeVost, and D. L. Woody .....	1243
<b>"Frozen Hot Spots" in Shocked EDC35, an Insensitive High Explosive</b>	
G. Eden, R. A. Belcher, M. I. Andrew, and W. R. Marlow .....	1253
<b>Deformation and Shock Loading Studies on Single Crystals of Ammonium Perchlorate Relating to Hot Spots</b>	
H. W. Sandusky, B. C. Glancy, D. W. Carlson, W. L. Elban, and R. W. Armstrong .....	1260
<b>The Influence of Grain Morphology on the Behavior of Explosives</b>	
S. Dufort, H. Cherin, and P. Gohar .....	1271
<b>Role of Adiabatic Shear Bands in Initiation of Explosives by Drop-Weight Impact</b>	
V. Krishna Mohan, V. C. Jyothi Bhasu, and J. E. Field .....	1276
<b>Gap Tests as a Method of Discriminating Shock Sensitivity</b>	
S. A. Aubert, G. H. Parsons, J. G. Glenn, and J. L. Thoreen .....	1284
<b>Shock Sensitivity of Damaged Energetic Materials</b>	
H. P. Richter, L. R. Boyer, K. J. Graham, A. H. Lepie, and N. G. Zwierzchowski .....	1295
<b>Burning Rates of Two Cast Nitramine Explosives Using a Hybrid Closed Bomb-Strand Burner</b>	
W. C. Tao, M. S. Costantino, and D. L. Ornellas .....	1310
<b>Explosiveness and Shock-Induced Deflagration Studies of Large Confined Explosive Charges</b>	
P. J. Hubbard and R. Tomlinson .....	1322

**VOLUME II**  
**CONTENTS (Cont.)**

	<u>Page</u>
<b>Initiation and Detonation Measurements on Liquid Nitric Oxide</b> G. L. Schott, W. C. Davis, and W. C. Chiles .....	1335
<b>Mechanisms of Detonation and Failure in Weak Chemically Sensitized Mining Safety Explosives</b> M. Kennedy and I. D. Kerr .....	1351
<b>Experimental Studies on the Detonation of an Explosive by Multi-Point Initiation</b> Yu Jun, Fu Xinghai, and Zhang Guanren .....	1360
<b>Detonation Properties of Explosive Foams</b> C. J. Anderson, K. Von Rosen, A. W. Gibb, and I. O. Moen .....	1364
<b>F.P.I. Velocimetry Techniques Applied to Various Problems in Detonics</b> P. Gimenez, J. P. Bedoch, C. Saint-Martin, G. Baudin, and Y. de Longueville .....	1371
<b>Detonation Product Equation of State for Baratol</b> J. W. Kury and R. D. Breithaupt .....	1378
<b>Design and Development of Precision Linear Shaped Charges</b> M. G. Vigil .....	1385
<b>Jet Initiation Mechanisms and Sensitivities of Covered Explosives</b> M. Chick, T. J. Bussell, R. B. Frey, and A. Bines .....	1404
<b>Initiation Phenomena with Shaped Charge Jets</b> M. Held .....	1416
<b>Spherical Projectile Impact on Explosives</b> E. N. Ferm and J. B. Ramsay .....	1427
<b>Projectile Impact Initiation of Explosive Charges</b> M. D. Cook, P. J. Haskins, and H. R. James .....	1441
<b>Correlation of Explosive Sensitivity to Compressional Inputs</b> M. Kornhauser .....	1451
<b>Sensitivity of Several Explosives to Ignition in the Launch Environment</b> J. Starkenberg, D. L. McFadden, D. L. Pilarski, K. J. Benjamin, V. M. Boyle, and O. R. Lyman .....	1460
<b>Study of Explosive Shell Fillings with Defects in Simulated Gun Launch Conditions</b> C. Bélanger .....	1480

**VOLUME II**  
**CONTENTS (Cont.)**

	<u>Page</u>
<b>A Computational Assessment of the Role of Shielding in Preventing the Sympathetic Detonation of Munitions</b> J. Starkenberg, T. M. Dorsey, K. J. Benjamin, and A. L. Arbuckle .....	1489
<b>Output Measurements and Modeling of HNS Mild Detonating Fuse</b> R. G. Jungst and M. E. Kipp .....	1510
<b>Detonator Response Measurements with a Standardized Piezoelectric Polymer (PVDF) Gauge</b> L. M. Moore, R. A. Graham, and R. P. Reed, and L. M. Lee .....	1529
<b>Indexes for the Proceedings of the Symposia (International) on Detonation--1951 through 1985</b> S. L. Crane, W. E. Deal, J. B. Ramsay, and B. E. Takala .....	1543
<b>Author Index</b> .....	I-1

**SESSIONS ON**  
**SHOCK-TO-DETONATION TRANSITION**

**Cochairmen: Philip Howe**  
**Army Ballistic Research Laboratory**

**Mohammad Chaudhri**  
**University of Cambridge**

**and**

**Randall Simpson**  
**Lawrence Livermore National Laboratory**

**Peter Haskins**  
**Royal Armament Research and Development**  
**Establishment**

**and**

**Jerry Wackerle**  
**Los Alamos National Laboratory**

**Robert Setchell**  
**Sandia National Laboratories**

# COMBINED PRESSURE SHEAR IGNITION OF EXPLOSIVES

V. Boyle, R. Frey, and O. Blake  
USA Ballistic Research Laboratory  
Aberdeen Proving Ground, Maryland 21005-5066

*We have studied the ignition of several explosives by shear under conditions where the pressure and macroscopic shearing rate are controlled and independently varied within some constraints. We have analyzed the results in terms of a previously published, idealized model. The experiments have a relatively long duration of about one millisecond, a maximum pressure of about 1.0 GPa, and a maximum shearing velocity of about 80 m/sec. The experimental results and the model both show that the ignition threshold depends on both pressure and shear velocity. A relation derived from the model adequately describes the ignition threshold in terms of pressure and shear rate, but it requires a constant which cannot be predicted accurately by the model. The relative ordering of the sensitivity of the explosives to shear and to shock is vastly different. The least shear sensitive material studied was TNT; the most sensitive was a double base propellant. Surprisingly, small particle size and the presence of large amounts of plasticizer did not seem to have a desensitizing effect on the test.*

## INTRODUCTION

Shear is any mechanical deformation which does not result in any bulk compression (or decompression) of the material being deformed. During shear, materials may be heated by viscoplastic work. Shear plays a role in many situations where mechanical action leads to initiation of explosives, including drop weight tests,<sup>1,2,3</sup> friction tests, and (sometimes) shock tests.<sup>4,5</sup> Although shear is, or may be, involved in all of these tests, the local pressure (spherical component of stress) and local strain rate in the explosive vary greatly from point to point. Thus, in these tests, it is not possible to relate the conditions for ignition to local conditions of strain, strain rate, and pressure. In this paper we will discuss a test which allows shear ignition to be studied under conditions where the pressure and strain rate are controlled (from a macroscopic point of view), and independently varied within certain constraints. The pressure and strain rates considered are representative of low pressure initiation tests, such as drop weight tests, rather than of shock initiation tests (where

cavity collapse may cause very high shear rates in small regions). We have used this test to investigate the relative importance of pressure and strain rate in determining ignition thresholds, and to characterize the relative shear sensitivity of several explosives which vary in composition and particle size.

It may easily be demonstrated that some form of localization of the shear is normally required for shear ignition. The temperature which must be achieved to obtain ignition in an experiment of known duration may be estimated from the Frank-Kamenetski equation for thermal explosion and from published kinetic data.<sup>6,7</sup> To obtain ignition in TNT in a time of 300 microseconds (which is representative of the duration of a drop weight test), we estimate a temperature of about 530°C is required. The methods of Reference 8 can be used to calculate the strain necessary to heat a perfectly plastic solid to any temperature as a result of homogeneous adiabatic shear. If one uses a strength parameter corresponding to confined composition B,<sup>9</sup> one calculates that the sample length must be reduced by a factor

of about 28 to achieve a temperature rise of 100°C. In reality, viscous effects will contribute to the heat generated, but very large strains are clearly required to achieve the temperatures required for prompt ignition.

Localization of strain can occur as a result of the conditions of an experiment (i.e., pinch of the explosive or flow in the vicinity of collapsing micro cavities), or it can occur spontaneously in shear bands.<sup>2,3,10,11,12</sup> One of the authors published an analysis of spontaneously generated shear bands some time ago.<sup>13</sup> In this paper we compare the experimental critical pressure and shear rate for ignition with the theory. In the earlier paper, we considered how various factors affect the maximum temperature attainable in a shear band. Here, we also look at the time required for ignition, and the total energy dissipated in the vicinity of the shear band when ignition occurs.

## DESCRIPTION OF EXPERIMENT

The experiment was designed to pressurize an explosive sample, and to let it shear after it was pressurized. We used two different experimental arrangements. One was designed to test explosive sliding against a steel surface, and the other to test explosive shearing and sliding against itself. For brevity, we will refer to these arrangements as explosive on steel and explosive on explosive, respectively.

The first arrangement, explosive on steel, is shown in cross section in Figure 1. A short cylinder of explosive was placed within a steel confinement cylinder. A polyethylene buffer plug was butted against each face of the explosive sample, and then the transfer piston and velocity piston were slid into place, as shown. The purpose of the polyethylene buffer plugs was to prevent spurious ignition caused by steel on steel friction in the region adjacent to the explosive sample. Dimensions are given in Table 1.

For explosive on explosive shear, we used the arrangement shown in Figure 2. In this case, the explosive sample was clamped within steel sleeves, and a plug was sheared out of its center. End plates kept the sleeves from moving during the experiment. The end plates were hardened to 40 on the Rockwell C scale

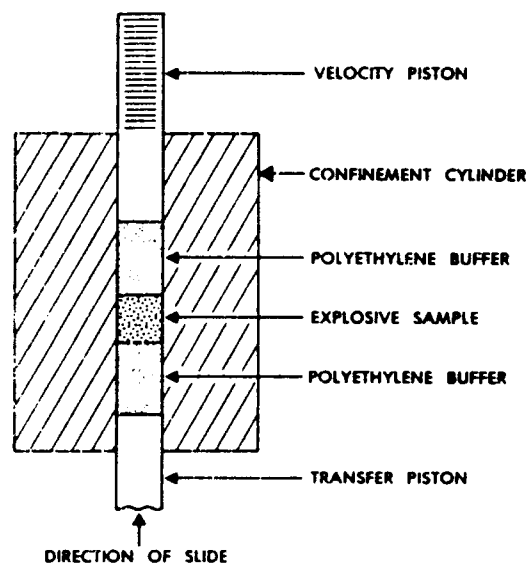


Figure 1. Test Arrangement for Explosive Sliding on Steel

Table 1. Test Sample Assembly for Explosive on Steel Shear

Component	Length (mm)	Diameter (mm)
Confinement Cylinder	82.6	63.5
Cylinder Bore	82.6	12.725 + .013 -0.000
Transfer Piston	69.9	12.700 + .013 - .013
Velocity Piston	57.2	12.700 + .013 - .013
Buffer Plugs	19.1	12.700 + .025 - .025
Explosive Sample	12.7	12.700 + .013 - .013

and fastened to the confinement cylinder with six 3/8-16 x 3/4 socket head cap screws. Other dimensions are given in Table 2. Either of these arrangements could be placed in the high pressure activator, as shown in Figure 3.

The high pressure activator, shown in Figure 3, was a modification of the one described in Reference 14. A heavier powder load was used in the breech in order to obtain higher pressures, and the breech was

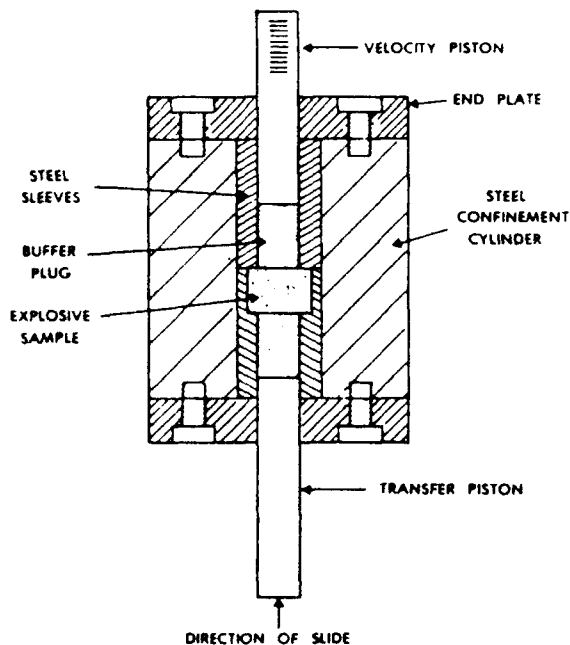


Figure 2 Test Arrangement for Explosive Shearing

Table 2. Test Sample Assembly for Explosive on Explosive Shear

Component	Length (mm)	Diameter (mm)
Confinement Cylinder	76.2	76.2
Confinement Cylinder Bore	76.2	25.4
Steel Sleeves	38.1	25.4 (Sliding Fit in Cylinder Bore)
Steel Sleeve Bore	25.4, 38.1	$12.725 + .013$ $-0.000$
Seat for Test Sample	$12.700 + .025$ $-0.000$	$19.075 + .013$ $-0.013$
Transfer Piston	69.9	$12.700 + .013$ $-0.013$
Velocity Piston	57.2	$12.700 + .013$ $-0.013$
Buffer Plugs	19.1	$12.700 + .025$ $-0.025$
Test Sample	$12.700 + .013$ $0.013$	$19.050 + .013$ $-0.013$
End Plates	12.7	76.2

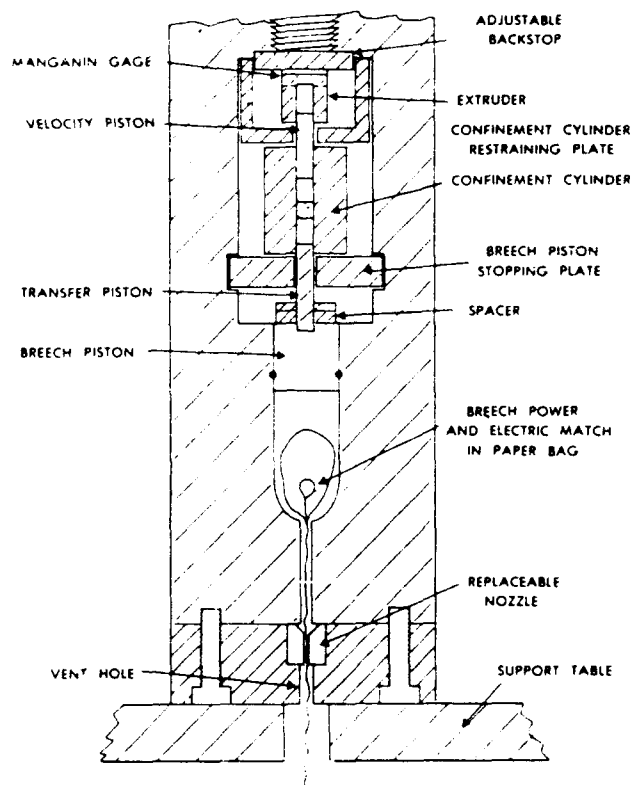


Figure 3. High Pressure Activator

continuously vented in order to decrease damage to the activator components. A manganin foil pressure gauge was used to measure pressure on the explosive sample, and a photodetection system was used to obtain sliding velocity. The activator was used in its contact mode (transfer piston in contact with the breech piston) in order to avoid shock formation which could occur if the breech piston impacted the transfer piston. M-9 propellant was used to pressurize the breech, because it left little residue and made clean-up easier. However, it has a high flame temperature and is, therefore, more erosive to the breech vent hole than a lower flame temperature propellant would be. For this reason, a replaceable nozzle of maraging steel was used, as shown in Figure 3. A confinement cylinder restraining plate, shown on Figure 3, was placed behind the confining cylinder to keep it from moving due to frictional force during the test. A breech piston stopping plate, also shown on Figure 3, was used to stop the motion of the breech piston before it hits the confinement cylinder.

The extruder, shown on Figure 3 between the sample confinement cylinder and the

backstop, is supposed to act as an elastic, perfectly plastic material. Its purpose is to resist piston motion until a predetermined pressure is reached and then to allow piston motion to proceed, and the explosive to shear, at a constant pressure. The device which we are currently using to approximate this behavior is shown in Figure 4. It consists of a steel cup filled with polyethylene. The cup is perforated with four orifices. The polyethylene resists piston motion until the pressure rises to a critical point; then, the polyethylene extrudes out the holes, and the piston moves while the pressure remains approximately constant. The pressure level at which the extrusion occurs is determined by the size of the orifices. The static yield pressure of the polyethylene filled extruder for various diameter holes was determined experimentally using a laboratory press. For orifices of 2.4 mm, 3.2 mm, and 4.8 mm, we measured static yield pressures of 0.35 GPa, 0.28 GPa, and 0.11 GPa. The dynamic yield pressure was generally 20 percent to 50 percent higher. The extruder body was 4340 steel hardened to 45 on the Rockwell C scale. The base of the extruder was ground flat.

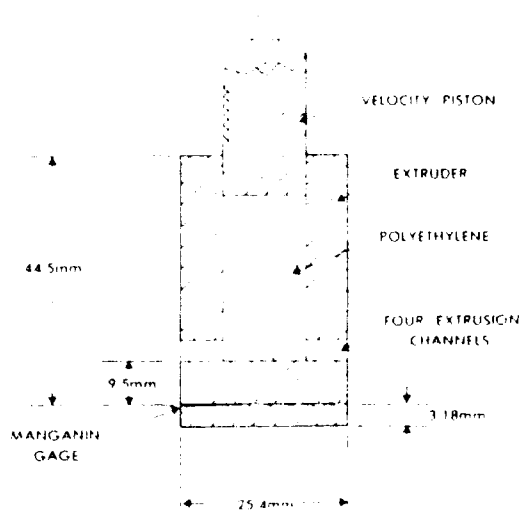


Figure 4 Design of the Failure Element Polyethylene is extruded through various diameter channels in order to obtain a range of pressures

The velocity piston was a standard steel piston which had been modified by machining 0.5 mm wide flats separated by 0.5 mm wide grooves near one end of the piston, as shown in Figure 4. These flats were polished to a final finish using .01 micron aluminum oxide powder. In order to measure the sliding velocity of the explosive sample, a one milliwatt helium-neon laser beam was reflected from the velocity piston through an interference filter, and into a 1P22 photomultiplier tube. The motion of the piston was measured by feeding the phototube output signal to a Data Precision Model 6000 waveform analyzer. As each reflecting flat on the velocity piston intercepted the laser beam, a voltage signal was generated. Knowing the distance between flats (1 mm center to center) and measuring the time between voltage peaks, we were able to calculate the sliding velocity.

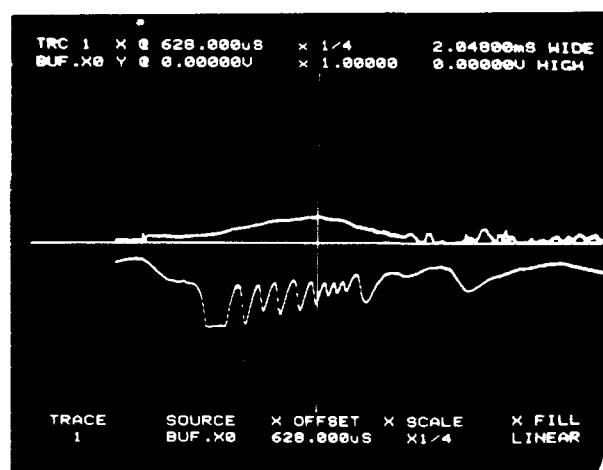


Figure 5. Test Records for TNT Shearing and Sliding Against TNT. No reaction. Upper trace shows manganin foil pressure gauge signal. Lower trace shows velocity piston displacement record from which sliding velocity is calculated.

The pressure on the explosive sample was measured by using a piezoresistive manganin foil pressure gauge sandwiched between two steel surfaces downstream from the explosive sample as shown in Figure 3. Since the activator is used in the contact mode, the pressure pulse measured at this point is probably a good representation of the pressure pulse on the



explosive sample. However, due to frictional force along the confinement cylinder bore, the downstream region may experience a somewhat lower pressure than the sample region. The piezoresistive manganin foil gage is sensitive to gage distortion. Great care was taken to support the gage on a flat surface, and to stress the gage and its support uniformly. In our current arrangement, the manganin gage is epoxied between two thin Mylar sheets, and this sandwich is epoxied between the ground surfaces of the pressure extruder and a 25.4 mm diameter steel plate. The gage was used in a standard Wheatstone bridge circuit, and the change in pressure was related to the resistance assuming a gage coefficient of 0.0023 ohms/ohm/kbar. The measured pressure at the gage was multiplied by the ratio of the area of the failure element to the area of the transfer piston to compute the pressure at the sample.

The explosive samples were sawed to a length of 12.7 mm. The sawed end was sanded using 600 grade emery paper under water. The sample was cleaned and then radiographed for possible voids or flaws. The explosive sample was positioned in the confinement cylinder bore, and the polyethylene buffer plugs were inserted as indicated in Figure 1. The purpose of the buffer plugs was to preserve the region of the bore adjacent to the explosive sample, free from high temperatures that could be generated by the steel piston rubbing against the bore surface. The bore had a reamed surface finish of 40 micron root mean square. A close-running fit of the sliding parts to the confinement cylinder bore was maintained in order to prevent or minimize extrusion of the explosive or buffer plugs when slid under pressure. Dimensions of the explosive on steel test assembly are shown in Table 1. The confinement cylinder was 1020 mild steel and the pistons were 4340 steel, heat treated to 40 on the Rockwell C scale.

Seven different explosives have been studied. A brief description of each follows:

1. Cast Composition B with a density of 1.69 g/cm<sup>3</sup>.
2. Cast TNT with a density of 1.60.
3. CMDB. This was a composite, modified, double base propellant containing

nitrocellulose, nitroglycerin, HMX (cyclotetramethylenetetranitramine), aluminum, and ammonium perchlorate.

4. Class A RDX/kraton. This was a 75/12.5/12.5 by weight mixture of class A RDX (cyclotrimethylenetrinitramine), kration rubber (a block copolymer made by the Shell Chemical Company), and tufflo oil (a hydrocarbon oil made by the Atlantic Richfield Company). It had a density of 1.43 g/cm<sup>3</sup>. The class A RDX had a mean particle size of about 150 microns.

5. FEM RDX/kraton. This was the same composition as above, but the RDX was run through a fluid energy mill to reduce its mean particle size to about 4 microns.

6. Detasheet. This is an explosive made by the Dupont Company and containing 63 percent by weight PETN, 8 percent nitrocellulose, and 29 percent acetyltributylcitrate. Its density was about 1.48 g/cm<sup>3</sup>.

7. RX-08-EL. This is an extrusion cast explosive made by the Lawrence Livermore National Laboratory which contains, by weight, 75.9 percent HMX, 22.2 percent FEFO (bis (2-fluoro-2,2-dinitroethyl) formal), and 1.9 percent of a polymer binder. Its density was 1.804.

## RESULTS

Typical pressure and shear displacement records are shown in Figures 5 to 8. Figure 5 illustrates the results obtained for TNT slid against itself without reaction. The upper trace represents the pressure sensed by the manganin foil gage, and the lower trace represents the displacement of the velocity piston; the horizontal time axis is 2.048 msec long. The vertical axis is located at the point of maximum deflection of the upper trace; the pressure on the TNT sample was calculated as explained previously. The average shear velocity occurring at this time is calculated by dividing the distance between the reflecting flats on the velocity piston (1 mm) by the time between adjacent peaks on the displacement trace. The data from these records indicate that TNT did not react when slid against itself at a pressure of 0.56 GPa and a velocity of 20 m/sec. As with most of our shots, the

Figure 6 represents TNT on TNT shear in which reaction occurred. The vertical axis is positioned at the estimated point where reaction occurred. This corresponds to a pressure of 1.08 GPa and a shear velocity of 33.3 m/sec. It can be seen that there is an increase in pressure and piston velocity at this point. There is an increase in pressure and piston velocity at an earlier time, but we attribute that to non-uniformities in the pressurization rate due, perhaps, to uneven burning of breech propellant or binding and subsequent releasing of pistons. We have obtained records showing increases in pressure and velocity where reaction did not occur. This figure illustrates the difficulty of picking a precise reaction point.

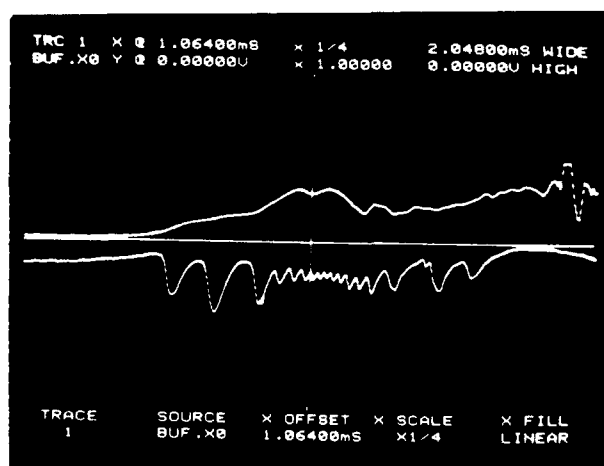
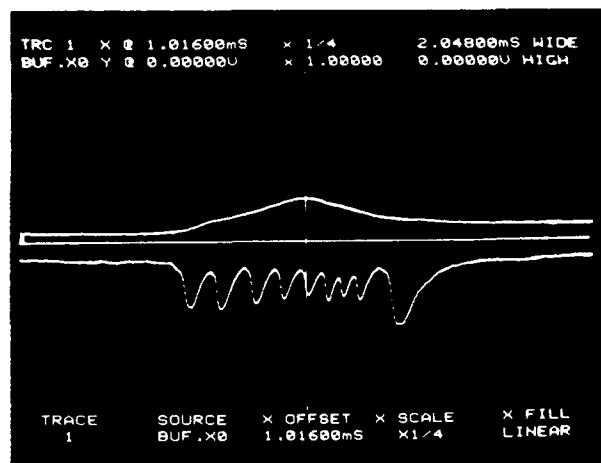
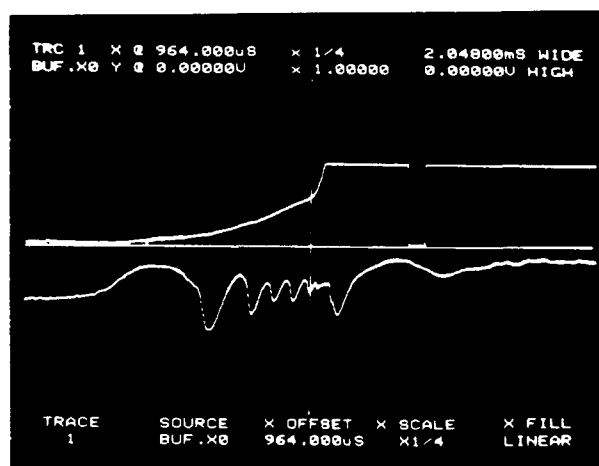


Figure 7 represents a non-reaction record when Comp B is slid on Comp B at a maximum pressure of 0.92 GPa and a shear velocity of 12.5 m/sec. Figure 8 shows Comp B reacting at a pressure of 1.07 GPa and a shear velocity of 26.3 m/sec. The reaction caused the piston velocity to increase to 100 m/sec within 50 microseconds. The pressure gage recorded 3.1 GPa before it broke.

The ignition data for TNT on steel are plotted in Figure 9 as sliding velocity vs peak pressure on the explosive sample. On most



**Figure 7. Comp B Shearing and Sliding Against Comp B. No reaction.**



shots, the peak pressure and maximum velocity were nearly simultaneous. The clear and filled symbols represent non-reaction and reaction, respectively. There is wide scatter in the data, some of which may be attributable to experimental problems. However, some of the pressures and velocities may have been increased due to explosive reaction. The shape of the solid line separating ignitions from no ignitions comes from the model which will be described later. The ignition data for Comp B on steel are shown in Figure 10. In this case, there is less overlap in the data, and it is more evident that there is an inverse relationship between the pressure and the velocity required for ignition.

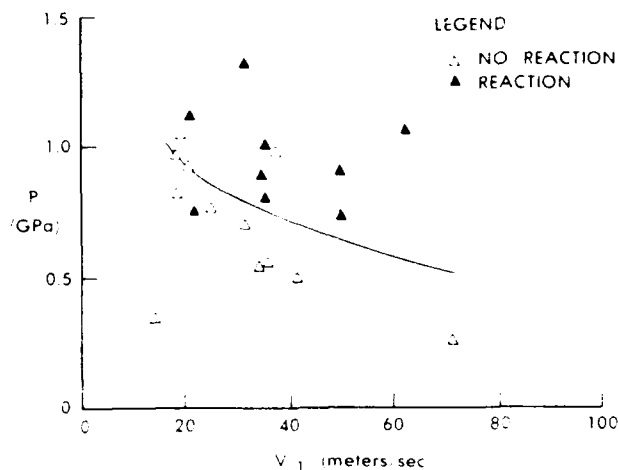


Figure 9. Data for TNT Sliding Against Steel. Open symbols indicate no reaction, and closed symbols indicate reaction. The solid curve represents the boundary between reaction and non-reaction.

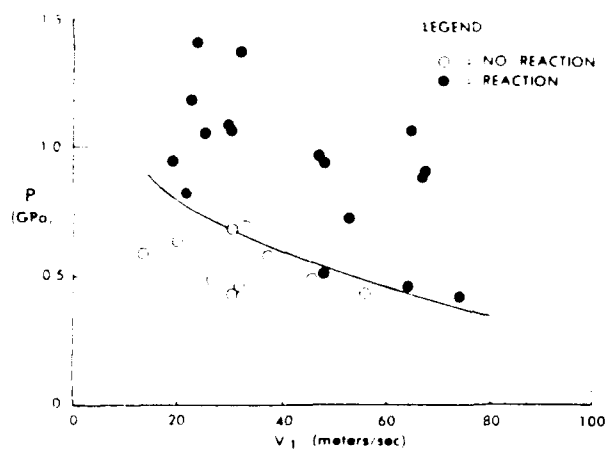


Figure 10. Data for Comp B Sliding Against Steel. The solid curve represents the boundary between reaction and non-reaction.

TNT and Comp B were also evaluated using the arrangement of Figure 2, where the explosive shears and slides on itself. The critical curves separating ignitions and no ignitions were indistinguishable from the case of explosive sliding on steel. We will suggest some reasons for this in the analysis section.

The other five explosives were all tested in the explosive on explosive mode (Figure 2). Figure 11 shows the pressure required for ignition as a function of sliding velocity for all seven explosives. The data for the two RDX/kraton

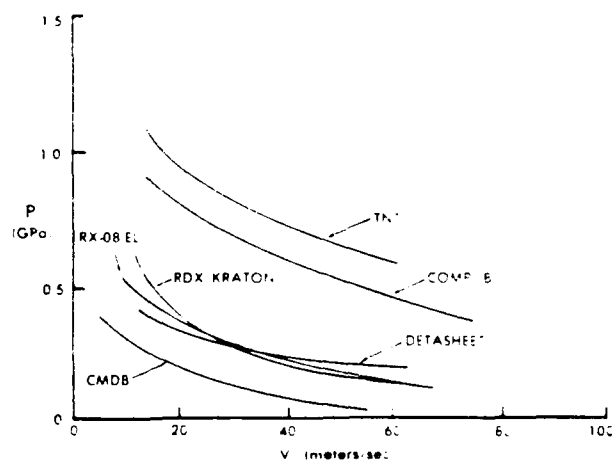


Figure 11. Summary Curves Showing How the Critical Pressure for Ignition Depends on Shear Velocity for the Six Explosives Considered

formulations was so close that only one curve is plotted for these two materials. Apparently, the particle size had little effect on the ignition threshold. TNT was, by far, the least sensitive material on this test. Composition B was the second least sensitive, and the CMDB was the most sensitive. The ordering of the shear sensitivity, as determined by this test, is vastly different from the ordering of the shock sensitivity of the materials. This is shown in Table 3, where we have listed the pressure required to get ignition at a sliding velocity of 30 m/sec, as determined from Figure 11, and the pressure required to get initiation in the NOL large scale gap test.

The primary purpose of these experiments was to determine the thresholds for shear ignition of the explosives. However, as a by product, we were also able to make some interesting observations regarding the explosiveness of the materials which were tested. With Composition B, any ignition usually resulted in complete combustion of the sample. Composition B is widely recognized to have high explosiveness. TNT often burned completely, but sometimes it burned only partially, leaving behind a central core and an annulus with charred surfaces. The tendency to burn only partially was particularly pronounced with the two RDX/kraton explosives and RX-08-EL. Both of these materials have large amounts of plasticizer and might be expected to show low explosiveness.

TABLE 3. Comparison of Shear and Shock Sensitivity. The minimum pressure for shear ignition at a sliding velocity of 30 m/sec is given under the column titled Shear. The pressure required for ignition at the end of the lucite gap in the NOL large scale gap test is given in the column titled Shock.

Critical Pressures (GPa)		
Explosives	Shear	Shock
TNT	0.82	4.4
Comp B	0.68	2.0
Detasheet	0.37	2.0*
RX-08-EL	0.28	1.0
FEM RDX/kraton	0.27	4.5**
CMDB	0.13	3.6

\* Rough estimate based on small scale gap test data

\*\* Rough estimate based on a 1.6 mm flyer plate impact test on the fine grained (FEM) formulation

## ANALYSIS

In a spontaneously generated shear band, strain localization occurs when thermal softening overwhelms the combined effects of strain hardening and strain rate hardening.<sup>10,11,12</sup> In this case, if one plane in a deforming block of material begins to shear faster than its neighbors, the extra heat generated by viscoplastic work will weaken that plane and cause still more of the deformation to be concentrated in the weak area. Extremely high strain rates can be achieved in narrow shear bands as a result. Very high temperatures can also be achieved in these bands, with the temperature being determined by a competition between heat conduction and viscoplastic work.

In a previous paper,<sup>13</sup> one of the authors computed the temperatures achieved in a spontaneously generated shear band in an explosive. In the model, an arbitrary shear velocity was imposed on an arbitrary thickness of material. The velocity gradient across the thickness (the strain rate) was initially assumed to be uniform, but a thin region was given a lower strength than the rest to stimulate the beginning of a

shear band. The thickness of the shearing block was varied in the range of 0.1 mm to 10 mm, and the thickness of the region which was initially weakened to stimulate the shear band was 0.1 to 10 microns. The development of the shear band was computed by numerically solving the one dimensional heat equation with source terms which represented viscoplastic work. The following assumptions were used in the calculations:

1. The shear stress in the explosive was the sum of an inviscid term and a viscous term:

$$\sigma_s = Y + \mu \frac{dv}{dx} \quad (1)$$

where,  $x$  is the distance coordinate which varies across the thickness of the shearing block,  $\sigma_s$  is the shear stress,  $Y$  is the inviscid yield stress,  $\mu$  is the viscosity, and  $v$  is the flow velocity in the  $y$  direction. In this paper, we will also consider a slightly more general relation:

$$\sigma_s = Y + \mu \frac{dv^n}{dx} \quad (2)$$

where  $n$  will be referred to as the strain rate exponent.

2. The inviscid yield strength decreased linearly to zero over a 25°C range of temperature below the melt point, and was zero above the melt point.

3. Changes in volume on melting were ignored. The heat of fusion was considered in one version of the model, but was ignored in the version which will be considered here. It had little effect on the predicted maximum temperatures in the shear bands.

4. The viscosity varied with temperature and pressure in accordance with Bridgeman's relation:

$$\mu = \mu_0 \exp\left(\frac{P}{P_0}\right) \exp\left(\frac{E}{T} - \frac{E}{T_0}\right) \quad (3)$$

where,  $P$  is the pressure,  $P_0$  is an empirical factor with the units of pressure,  $\mu_0$  is the viscosity at a reference temperature,  $T_0$  is the reference temperature, and  $E$  is an empirically

determined activation energy for viscous flow divided by the gas constant.

5. The shear stress was independent of  $x$ , but varied with time as the shear band developed. This assumption is a quasi steady state assumption which is true if the development of the shear band is slow when compared to the time for sound waves to propagate across the developing shear band. Since the original work was done, more complete calculations by Wright<sup>11,12</sup> have demonstrated that this is a reasonable assumption.

6. The melt point was assumed to increase by 20°C per kilobar. The constitutive relation defined by Equations (1) and (2), above, are at best a crude approximation of reality. Furthermore, the material parameters required are not known with any accuracy for any explosive at the pressures and strain rates of interest. Consequently, one can hope, at best, to reproduce qualitatively the results of real experiments. We attempted to choose parameters representative of TNT, and the values chosen are given in Reference 13; but we cannot claim to have described this explosive accurately.

Despite these limitations, the earlier work arrived at some interesting conclusions, some of which follow:

1. There was a maximum temperature which could be achieved at a shear band. The maximum temperature was achieved when the shear was entirely localized in a liquid layer at the center of the shearing block. After this happened, further shear caused the liquid layer (the shear band) to widen, but did not increase the temperature at the center of the band.

2. The maximum temperature did not depend on the thickness of the shearing block for a wide range of block thicknesses from 0.1 to 10 mm. This was a natural consequence of the fact that the thickness of the fully developed shear band (of the order of a micron) was always much smaller than the thickness of the shearing block. A corollary of this observation is that the temperature achievable in an experimentally localized shear band (for instance, one where the explosive is pinched or forced into a narrow aperture) may not be significantly different from the temperature achieved in a spontaneously localized shear

band, unless the experiment localizes the shear into a thickness which is less than the thickness of a fully developed, spontaneously generated shear band (circa one micron).

3. The thickness of the region which was weakened to stimulate shear band development also had no effect on the maximum temperature. However, both the thickness of the weakened region and the thickness of the whole block had a big effect on the time required for shear band development.

4. The maximum temperature depended on the pressure, the imposed shear velocity, and the viscosity. An increase in any of these parameters increased the maximum temperature.

5. Shear band development could be very fast. Maximum temperature could be obtained in times of one microsecond or less, although it varied greatly with circumstances.

In analyzing the results of the experiments in terms of this model, we observed that the model predicted a constant maximum temperature as long as the parameter  $Z$  remains constant, where  $Z$  is given by

$$Z = V^2 \exp\left(\frac{P}{P_0}\right) \quad (4)$$

This fact was actually derived by one of the authors (Boyle) on heuristic grounds, and then checked by computation using the model. Table 4 demonstrates the validity of this observation.

*Table 4. Effect of Pressure and Shear Velocity on Maximum Temperature*

Pressure (GPa)	Shear Velocity (km/sec)	$Z/10^{11}$ (km/sec) <sup>2</sup>	Computed Maximum Temperature (degrees C)
0.77	0.4	1.78	1101
1.00	0.2	1.78	1113
1.23	0.1	1.78	1118

We assumed that ignition would occur when a particular temperature was reached. Of course, in reality ignition depends on time

as well as temperature, but the duration of all of the experiments was about the same. We also assumed that the development of a shear band is very fast compared to the time scale of the experiment, so that the temperature achieved at any time in the experiment corresponds to the maximum possible temperature for that shear velocity and pressure. Since the calculations indicate that the shear bands form on a time scale of a few microseconds, this is probably a good assumption. If these assumptions are true, the curve defined by  $Z = \text{constant}$  should separate ignitions from non-ignitions. Although there was scatter in the data, this curve did seem to properly separate ignitions and non ignitions, as shown in Figures 9 and 10. Thus, both the data and the analysis support the idea that ignition thresholds depend on both shear rate and pressure. The only material parameter that enters into the calculation of  $Z$  is the viscosity parameter  $P_0$ .  $P_0$  depends on the complexity of the molecule<sup>15</sup> and other factors. For a range of molecules whose size is similar to simple explosive molecules,  $P_0$  is between 0.1 GPa and 0.2 GPa.<sup>15</sup> We let  $P_0$  have the value of 0.164 GPa for all of our explosives, and used a curve defined by  $Z = \text{constant}$  to define the boundary between ignitions and no ignitions in all cases. All of the solid curves drawn on Figures 9, 10, and 11 are based on  $Z = \text{constant}$ , and in all cases the curve seemed to appropriately separate ignitions and non ignitions.

While a curve defined by  $Z = \text{constant}$  seemed to correctly separate ignitions from no ignitions, the calculations could not correctly predict the appropriate value of  $Z$ . In fact, the calculations indicated that considerably greater pressures or shear velocities would be required for ignition than was in fact the case. For instance, in the experiments, a shear velocity of about 0.02 km/sec was required for ignition in TNT at 1.0 GPa. Based upon the available kinetic data,<sup>7</sup> a temperature of the order of 490°C would be required to produce ignition in the one millisecond time scale of these experiments. The model predicted that these conditions would produce a maximum temperature of only 378°C. However, the model is extremely sensitive to the viscosity and to the parameters  $P_0$  and  $E$ , which influence the viscosity. Decreasing  $P_0$  to 0.1 GPa

from 0.164 GPa increases the predicted temperature from 378°C to 894°C. Likewise, decreasing the activation energy for viscous flow ( $E$ ) from 3880°K to 2000°K raises the computed temperature from 378°C to 556°C.

A somewhat surprising result of the experiments was that the ignition threshold conditions for explosive sliding on steel were the same as for explosive shearing and sliding on itself. The model also predicted that these cases would be equivalent. A special version of the model was formulated which included a non-deforming block with a heat capacity and heat conductivity corresponding to steel. In this version of the model, the weakened layer of explosive which stimulated shear band formation was adjacent to the steel layer. The shear band developed more slowly in this case. Because of the cooling effect of the steel, the region of maximum temperature and highest shear rate moved away from the steel boundary and into the explosive. Eventually, the situation looked like a shear band within the interior of the explosive, and the maximum temperature approached that for the standard case with no steel present. Superficially, this result seems to be in conflict with the result of Randolph, et al.,<sup>16</sup> who saw an effect of the thermal conductivity of the target on ignition thresholds in the drop skid test. However, the duration of the drop skid test is very short compared to the duration of our test, and our calculations indicated that the presence of a steel layer greatly increased the time required to achieve maximum temperature.

In what has been said up to now we have assumed that ignition is controlled by the maximum obtainable temperature in the shear band. This seems to be a good assumption for our experiment, which has a relatively long duration and where the activator is capable of delivering very large amounts of energy to the explosive. In other situations, the time and/or energy required to reach a particular temperature may be more important than the maximum obtainable temperature. Although it is not directly germane to our experiment, it is of interest to consider cases where time or energy may be limiting factors. Therefore, we computed the total energy dissipated in the

shearing block in order to raise the temperature in the shear band to 700°C. The dissipated energy is given by the following relation:

$$w = \int \sigma_s V dt \quad (5)$$

where  $\sigma_s$  is the shear stress at any time, and  $v$  is the imposed shear velocity.

Figure 12 shows how the thickness of the shearing block affects the energy required to achieve 700°C. The calculation was carried out for a case with an applied pressure of 2.0 GPa, an imposed shear velocity of 0.2 km/sec, and a strain rate exponent of 0.8. The dissipated energy required to heat the shear band to 700°C increases rapidly with the thickness of block. This is primarily because the time required for shear band formation is longer

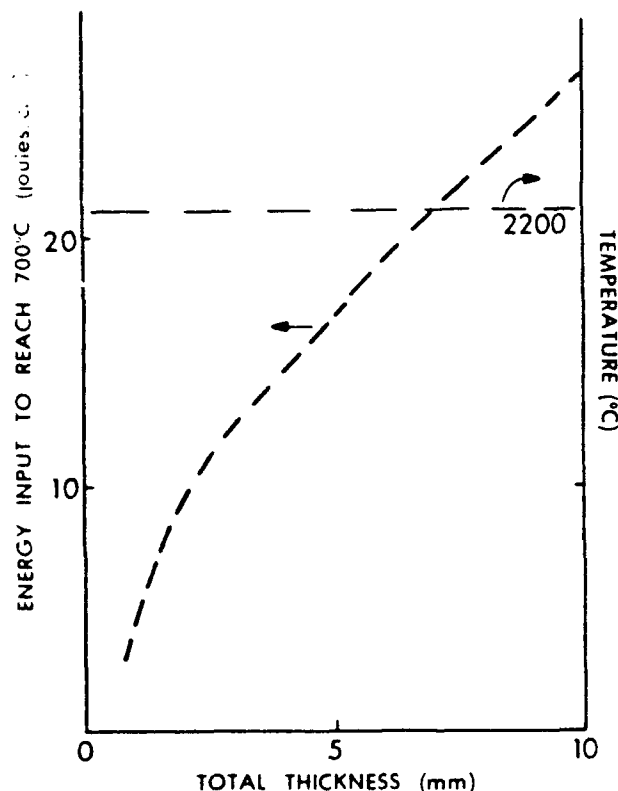


Figure 12 The Dissipated Energy Required to Heat a Shear Band to 700°C and the Maximum Obtainable Temperature in the Shear Band Plotted as a Function of the Thickness of the Shearing Region. The calculations are for a case where the pressure is 2.0 GPa, the shear velocity is 0.2 km/sec, and the strain rate exponent is 0.8. The reference viscosity is 0.14 poise.

when the shearing region is thicker. Figure 12 also shows the maximum temperature which can be achieved at the shear band under these conditions. As pointed out earlier, the maximum temperature is independent of the thickness of the shearing region. Imposing the shear over a narrow region can be considered as a representation of cases where localization is forced by the experiment, rather than by purely spontaneous shear band formation. For the range of thicknesses considered here, the maximum temperatures obtainable are the same for the two cases; but the experimentally localized case can reach the ignition temperature quicker and with less expended energy.

Figure 13 shows the maximum obtainable temperature, and also the energy required to achieve 700°C as a function of viscosity. The calculations were carried out with a pressure of 2.0 GPa, a shear velocity of 0.2 km/sec imposed over a region 10 mm thick, and with a strain

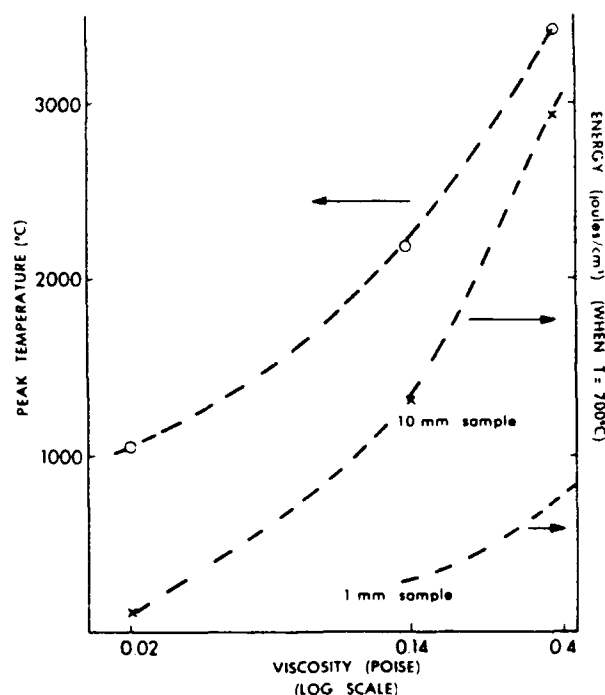


Figure 13. The Dissipated Energy Required to Heat a Shear Band to 700°C and the Maximum Obtainable Temperature Plotted as a Function of Viscosity. Conditions are as in Figure 12, except that the thickness of the shearing region is 10 mm or 1 mm.

rate exponent of 0.8. The abscissa gives the viscosity at the reference temperature and atmospheric pressure. The parameters  $E$  and  $P_0$  are constant for all cases. The maximum achievable temperature increases as viscosity increases, but the energy required to achieve 700°C also increases, primarily because the time required for shear band development is greater if the viscosity is greater. Thus, high viscosity could be either sensitizing or desensitizing, depending on circumstances. In our experiment, where the duration of the experiment is long and the activator is capable of delivering lots of energy, high viscosity is expected to be sensitizing.

Figure 14 shows how the maximum obtainable temperature varies with the strain rate exponent,  $n$ . The calculations were carried out with a pressure of 2.0 GPa and a shear velocity of 0.2 km/sec imposed over a region 10 mm thick. The computed temperature is very sensitive to the value of  $n$ , and higher values result in higher temperatures. Thus, in

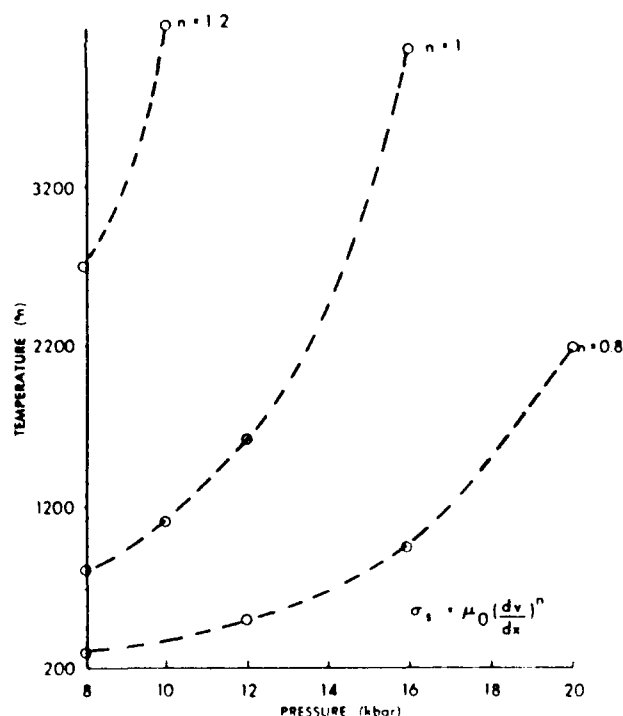


Figure 14 The Maximum Obtainable Temperature Plotted as a Function of the Pressure for Three Different Values of the Strain Rate Exponent. The shear velocity is 0.2 km/sec, and the thickness of the shearing region is 10 mm.

this sense, a high  $n$  value is sensitizing. Figure 15 shows the effect of  $n$  in a different way. Here the dissipated energy required to achieve 700°C in the shear band is plotted as a function of pressure for three different values of  $n$ . When the pressure is sufficiently great, the lower value of  $n$  permits the specified temperature to be achieved with less expenditure of energy. In this sense, a low value of  $n$  is sensitizing. This is because the lower value of  $n$  permits the shear band to develop more rapidly. However, if the pressure is too low (less than about 1.4 GPa in this example), the maximum obtainable temperature drops below 700°C for the case with the lower  $n$  value. In this case, ignition becomes impossible for the case with the lower  $n$  value, and the higher  $n$  value again looks to be more sensitive.

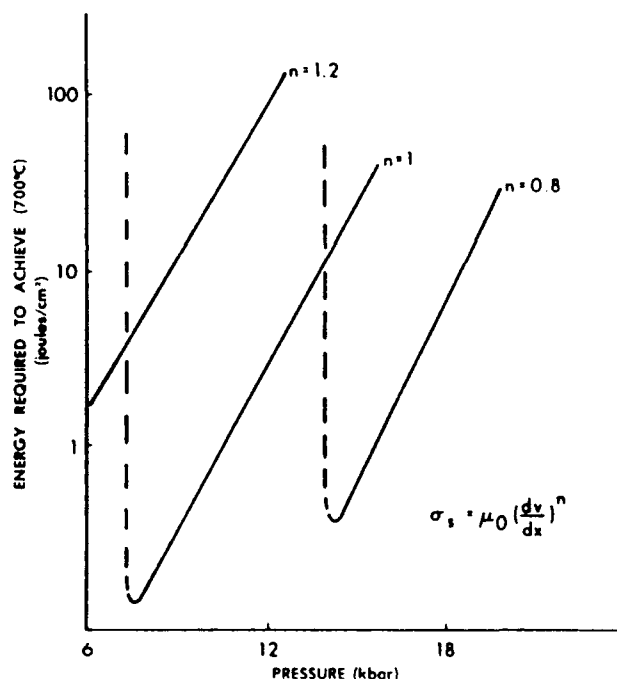


Figure 15. The Dissipated Energy Required to Achieve 700°C in the Shear Band Plotted as a Function of Pressure for Three Different Values of the Strain Rate Exponent. The shear velocity is 0.2 km/sec and was imposed over a region 10 mm thick.

These results demonstrate that it is not easy to say how variations in material properties will affect shear ignition. In long duration experiments, such as the one we have discussed in this paper, the maximum obtainable



temperature is probably controlling. In these cases, anything which increases the viscosity (pressure, increased strain rate exponent, increase  $P_0$ ) is probably sensitizing. In short duration experiments, the time required for shear band formation may be more important, and low viscosity may be sensitizing.

## DISCUSSION AND CONCLUSIONS

Our conclusions are summarized by the following comments:

1. Both pressure and shear velocity have a strong effect on ignition. This is confirmed by both theory and experiment.

2. The relation  $V^2 \exp(P/P_0) = \text{constant}$ , which was derived from the model, appeared to properly separate ignitions and no ignitions in our experiments.

3. The relative sensitivity of the explosives studied to shear, as measured on our test, and to shock, as measured on a large scale gap test, was very different. The shear sensitivity increased in the order  $\text{TNT} < \text{Comp B} < \text{RX 08 EL} = \text{Detasheet} = \text{RDX/kraton} < \text{CMDB}$ . Although the CMDB was by far the most shear sensitive, it was one of the least sensitive to shock.

4. Changing the particle size in the RDX/kraton formulation had no effect on the shear sensitivity. This may be a reflection of the fact that the fully developed shear bands are even smaller than the FEM RDX grains (circa 4 microns), and that the shear bands, therefore, cut through grains.

5. Shearing the explosive and allowing it to slide on steel produced similar results. The model predicted that the maximum temperature obtainable in these two cases would be the same, because the shear band would migrate into the interior of the explosive. Short duration tests would probably show different results.

6. Based upon the model, the way that material properties and experimental parameters affect the maximum obtainable temperature in a shear band and the way that they affect the energy required to achieve a specified temperature, can be different. Thus, it is difficult to specify in an unambiguous way how

a specific parameter may affect "sensitivity." We believe that the results of our long duration experiment are consistent with the idea that the results in this experiment are controlled by the maximum obtainable temperature.

7. The insensitivity of TNT in our test may be a reflection of its low melt point, and the fact that at any given temperature it very likely has a lower viscosity than the other materials. The high sensitivity of the CMDB material may be a reflection of the fact that the nitrocellulose has a high viscosity and does not melt.

8. We had expected that highly plasticized materials, such as RX-08-EL, might show low sensitivity on this test. This was not the case. We do not have a good understanding as to why it was not so. In the case of RX-08-EL, the plasticizer (FEFO) is energetic, and the shear may have localized and caused ignition in the FEFO phase. In the case of Detasheet, the plasticizer is not energetic, but Detasheet also contains nitrocellulose, which might explain its sensitivity.

## REFERENCES

1. Heavens, S. N. and Field, J. E., "The Ignition of a Thin Layer of Explosive by Impact," *Proceedings of the Royal Society of London*, A338, 1974, pp. 77-93.
2. Winter, R. and Field, J., "The Role of Localized Plastic Flow in the Impact Initiation of Explosives," *Proceedings of the Royal Society of London*, A343, 1975.
3. Coffey, C. S., "Hot Spot Production by Moving Dislocations in a Rapidly Deforming Crystalline Explosive," *Proceedings of the Eighth Symposium (International) on Detonation*, 1985.
4. Kipp, M., "Modeling Granular Explosive Detonations With Shear Band Concepts," *Proceeding of the Eighth Symposium (International) on Detonation*, 1985.
5. Frey, R. B., *Cavity Collapse in Energetic Materials*, BRL-TR-2748, U.S. Army Ballistic Research Laboratory, Aberdeen Proving Ground, MD, 1986.

6. Frank-Kamenetski, D. A., *Diffusion and Heat Transfer in Chemical Kinetics*, Princeton University Press, Princeton, NJ, 1955.
7. Rogers, R. N., "Thermochemistry of Explosives," *Thermochemica Acta*, Vol. 11, 1975.
8. Kachanov, L. M., *Foundations of the Theory of Plasticity*, North Holland Publishing Company, Amsterdam, The Netherlands, 1971.
9. Pinto, J.; Nicolaides, S.; and Weigand, D. A., *Dynamic and Quasi Static Mechanical Properties of Comp B and TNT*, Technical Report ARAED-TR-85004, U.S. Army Armament Research and Development Center, Picatinny Arsenal, NJ, 1985.
10. Recht, R. F., "Catastrophic Thermoplastic Shear," *Journal of Applied Mechanics*, Vol. 31, Series E, No. 2, 1964.
11. Wright, T. W. and Batra, R. C., *The Initiation and Growth of Adiabatic Shear Bands*, BRL-MR-3437, U.S. Army Ballistic Research Laboratory, Aberdeen Proving Ground, MD, 1985.
12. Wright, T. W. and Walter, J. W., "On Stress Collapse in Adiabatic Shear Bands," *Journal of Mechanics and Physics of Solids*, Vol. 35, No. 6, 1987.
13. Frey, R. B., "The Initiation of Explosive Charges by Rapid Shear," *Proceedings of the Seventh Symposium (International) on Detonation*, NSWC MP 82-334, Naval Surface Weapons Center, 1981.
14. Taylor, B. C. and Ervin, L. H., "Mode of Ignition in the Picatinny Arsenal Activator (Artillery Setback Simulator)," Special Publication ARLCD-SP-77004, *Proceedings of the Conference on the Standardization of Safety and Performance Tests for Energetic Materials - Vol. 1*, ARRADCOM, Dover, NJ, 1977.
15. Bridgeman, P. W., *The Physics of High Pressure*, Strangeways Press Ltd., Great Britain, 1931.
16. Randolph, A. D.; Hatler, L. E.; and Popolato, A., "Rapid Heating to Ignition

of High Explosives, I. Friction Heating," *Ind. Eng. Chem., Fundamentals*, Vol. 15, No. 1, 1976.

## DISCUSSION

**I. B. MISHRA**, Kanan Associates  
Churchville, MD

The following refers to comments made earlier.

(1) Observation that increased viscosity raises  $T$  implies that shear rate is increased.

(2) Measuring  $T$  in a nanosecond time frame with a thermocouple is absurd. Here you are at the limit of technology; the transient temperature has to be calculated.

## REPLY BY V. M. BOYLE

This comment is directed at another comment which is not being published with this paper. We agree that, for many reasons, thermocouples would not be likely to give good measurements of the temperature in the shear band in our experiment. The observation that increased viscosity increases the maximum computed temperature in the shear band does not necessarily mean that the shear rate in the band is increased. In fact, high viscosity tends to be delocalizing and, thus, reduces the strain rate at the center of the band, but it increases the heating rate associated with any given strain rate.

## DISCUSSION

**K. KIM**, Naval Surface Warfare Center  
Silver Spring, MD

Do you not have to worry about fractures in the analysis of shear? Do you assume that melting always occurs before fracture? Do you not see the opposite case sometimes? Would the analysis still hold in this case?

## REPLY BY V. M. BOYLE

Under compressive loading conditions in homogeneous materials, cracks and shear bands are essentially the same thing. When the material fails, the surfaces of adjacent blocks are held together by the imposed pressure, and viscous effects will cause the strain to

be spread out over a very narrow region, which is the shear band. When the pressure is removed, the band may appear as a crack. In composite materials where the constituents have very different mechanical properties, shear may cause some localized cracking (separation between particle and binder, for instance) while the material is still under compression. This could be occurring in the CMDDB, but probably not in the other materials considered here. In any case, complexities of this type are beyond the model which is discussed here. The model is intended only to provide some qualitative guidance into the factors which control the heating which occurs at shear bands

### DISCUSSION

C. D. HUTCHINSON, Atomic  
Weapons Establishment, England

It has been my understanding that manganin gages were not sensitive in the region of 0 - 2 GPa and that to function correctly a planar shock environment was necessary. Could you explain the choice of manganin gages for your experiments in which pressures  $< 1$  GPa are recorded in a non-planar shock environment?

### REPLY BY V. M. BOYLE

In our activator experiments, the manganin gage is sandwiched between two flat

steel surfaces and uniformly compressed for approximately one millisecond. The gage is encapsulated in plastic and the gage package has uniform thickness over the area of the steel pistons. At BRL, we have calibrated the manganin gages both statically and under compressive loading durations of 1 millisecond and find the piezoresistance coefficient to fall within the range .021 - .023 ohm/ohm/GPa. There also exist shock wave calibration data for manganin foil gages for pressures under 2.0 GPa. See, for example, "Calibration of Foil-Like Manganin Gages in Planar Shock Wave Experiments" by Rosenberg, Yaziv, and Parton, *Journal of Applied Physics*, Vol. 51, No. 7, July 1980.

### DISCUSSION

F. VOLK, Fraunhofer Institut  
Pfinztal, FRG

We can explain the high sensitivity of CMDDB to shear if we take into account the activation energies of nitric esters which are much lower than those of nitrocompounds and nitramines. Even by manufacturing of nitrocellulose (NC) containing pastes, we found a decrease of the molecular weight of NC, combined with a thermal decomposition producing nitric oxides and other products.

### REPLY BY V. M. BOYLE

We appreciate this comment.

# PARTICULAR ASPECT OF THE EXPLOSIVE PARTICLE SIZE EFFECT ON SHOCK SENSITIVITY OF CAST PBX FORMULATIONS

H. Moulard

Franco-German Research Institute (ISL)  
P.O. Box 301 - 68301 Saint-Louis, FRANCE

*Three monomodal (6  $\mu\text{m}$ , 134  $\mu\text{m}$ , 428  $\mu\text{m}$ ) and two bimodal formulations of a cast PBX (70 percent RDX, 30 percent polyurethane) are studied experimentally with well-defined sensitivity and detonation experiments. Our experimental results point out that the sensitivity classification does not vary linearly with the median particle size for the monomodal formulations. The sensitivity classification is strongly dependent on the shock pressure range. This could explain the discrepancy between opposite experimental observations, previously published, concerning the effect of RDX particle size on the shock sensitivity. Our work is not exhaustive, so an alternative interpretation of this experimental result is proposed based on either the morphology and the processing of RDX particles or a phenomenological explanation based on the fundamental mechanism of the shock detonation transition.*

## INTRODUCTION

The goal of our work is to study experimentally the effect of explosive particle size on the sensitivity and the detonability of cast plastic bonded explosives. There is, in fact, great practical interest in the relationship between the formulation parameters (particle size, load density, binder, etc.) and the reactive behavior of PBX.

For studying this particle size effect independently of other formulation parameters, the SNPE\* has specially prepared (Table 1) three monomodal (6  $\mu\text{m}$ , 134  $\mu\text{m}$ , 428  $\mu\text{m}$ ) and two bimodal formulations of a cast PBX, with the same weight composition (70 percent RDX, 30 percent polyurethane), with the same loading density (1.45 g/cm<sup>3</sup>, i.e.,  $\geq$  99.9 percent T.M.D.), and the only variation parameter is the choice of the RDX particle batch. The high content in inert binder is necessary to have a mixture viscosity compatible with the casting technique.

A small amount of micronized graphite particles (Table 1) is added to RDX batches for the safe handling of dry explosive particles.

Special attention has been taken to have a well defined particle size distribution (Table 2) with a negligible overlapping of the particle size in the three distinct RDX batches (6  $\mu\text{m}$ , 134  $\mu\text{m}$ , 428  $\mu\text{m}$ ). The fine (6  $\mu\text{m}$ ) and very coarse (428  $\mu\text{m}$ ) RDX batches are obtained directly by recrystallization in acetone and cyclohexanone, respectively. Then, the very coarse RDX particles are sieved to eliminate residual finer RDX particles to obtain the specified particle size distribution (Table 2). The coarse RDX batch (134  $\mu\text{m}$ ) is obtained by milling the very coarse RDX batch and sieving is applied to obtain the specified particle size distribution. Photomicrographs (Figure 1) show that recrystallization gives RDX particles with quasi-spherical shapes, whereas the milling process produces RDX particles with sharp edges.

First experimental results concerning the two monomodal formulations F and C (6  $\mu\text{m}$  and 134  $\mu\text{m}$ ) were previously presented at the

\*Work performed under contract from the Société Nationale des Poudres et Explosifs

Table 1. Monomodal and Bimodal Formulations

Formulation Identification	Components	Weight %	Volume %	Loading Density (g/cm <sup>3</sup> )	Median RDX Particle Size (μm)	Specific Surface Area BET (m <sup>2</sup> /g)
monomodal F	RDX M5 polyurethane graphite	70.00 29.30 0.70	55.75 43.80 0.45	1.45	6	1.53
bimodal F5	RDX M5 RDX 315 - 800 polyurethane graphite	50.00 20.00 29.40 0.60	39.80 15.90 43.90 0.40	1.45	127	
bimodal F2	RDX M5 RDX 315 - 800 polyurethane graphite	20.00 50.00 29.55 0.45	15.90 39.70 44.10 0.30	1.45	307	
monomodal C	RDX 100 - 200 polyurethane graphite	70.00 29.65 0.35	55.60 44.20 0.20	1.45	134	0.08
monomodal VC	RDX 315-800 polyurethane graphite	70.00 29.65 0.35	55.60 44.20 0.20	1.45	428	0.04

Table 2 RDX Particle Size Distribution

Fine RDX "F"		Coarse RDX "F"		Very Coarse RDX "VC"	
Particle Diameter (μm)	Weight (%)	Particle Diameter (μm)	Weight (%)	Particle Diameter (μm)	Weight (%)
< 1	1	< 26	2	0 - 100	1.0
1 - 2	1	26 - 41	2	100 - 200	0.4
2 - 3	3	41 - 65	3	200 - 250	0.6
3 - 4	7	65 - 103	8	250 - 315	7.1
4 - 5	13	103 - 130	30	315 - 400	31.2
5 - 6	19	130 - 164	43	400 - 500	34.2
6 - 8	23	164 - 206	11	500 - 560	16.7
8 - 10	19	> 206	1	560 - 630	5.8
10 - 12	8	---	---	630 - 710	1.2
> 12	6	---	---	710 - 800	1.8

last symposium.<sup>1</sup> Briefly, through our different shock sensitivity tests, the fine formulation was distinctly less sensitive than the coarse one. For instance, Figure 2 presents results of flyer plate test experiments where the critical energy fluence of the fine formulation is

measured twice as much as that of the coarse formulation.

But at the same time, opposite results were observed by other research workers,<sup>2</sup> with flyer-plate test experiments on several

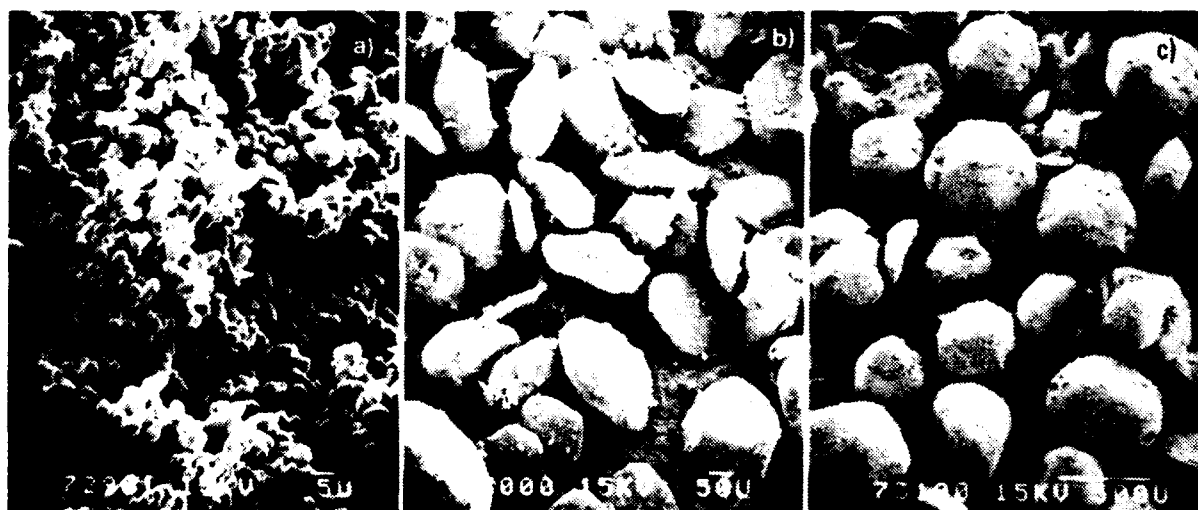


Figure 1. RDX Crystals: a) Fine; b) Coarse; c) Very Coarse

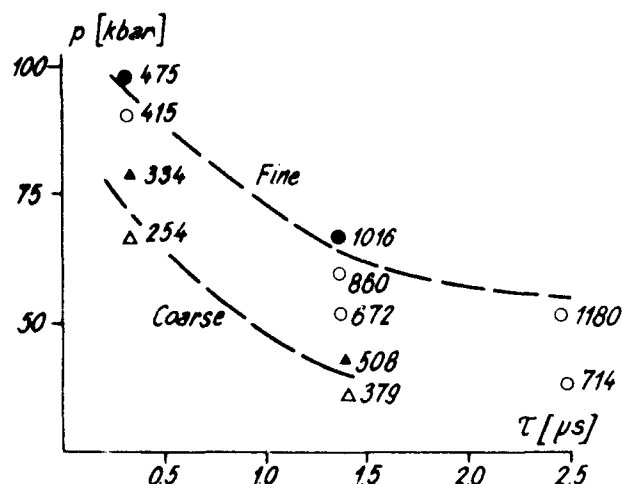


Figure 2. Input Pressure Vs. Pulse Duration for Fine and Coarse RDX Formulations. Numbers next to the points are critical energy fluence ( $p \cdot \tau$ ).

bimodal formulations of an industrial cast PBX also based on RDX; in their work, shock sensitivity is decreased by using coarser RDX particles. Our recent experimental work permits us now to better understand these opposite conclusions

## DETONABILITY EXPERIMENTS

Variation of the detonation velocity due to the diameter effect is measured with short-circuit pins on explosive cylinders with different

diameters; simultaneously, curvature of the detonation front is recorded with an electronic streak camera at the output of the explosive cylinder. Figure 3 shows the variation of the detonation velocity versus the inverse of the charge radius. The fine monomodal formulation is the most sensitive to detonation, having the smallest failure diameter. In monomodal formulations, the decrease of detonation velocity due to diameter effect is well controlled by the RDX median particle size. But, in the bimodal formulation F5, which has formally the same median RDX particle size as the coarse monomodal formulation C, the large amount of fine RDX particles increases strongly the detonation sensitivity of this bimodal formulation compared to that of the C formulation. So, in bimodal formulations, detonability is directly controlled by the actual values of the RDX particle size, and not by the median particle size which is in fact an excessive notion for bimodal formulations. Figure 4 shows streak camera records of the curvature of the detonation front at the output of 30 mm diameter charges, as a function of the content of fine RDX particles. The very coarse monomodal formulation exhibits high curvature of the detonation front. This is indicative of a long reaction zone. In adding  $6\mu\text{m}$  RDX to the formulation, the curvature is greatly reduced. In Figure 4, the measured detonation front curvatures are compared with that calculated assuming ideal "Huygens" propagation. In

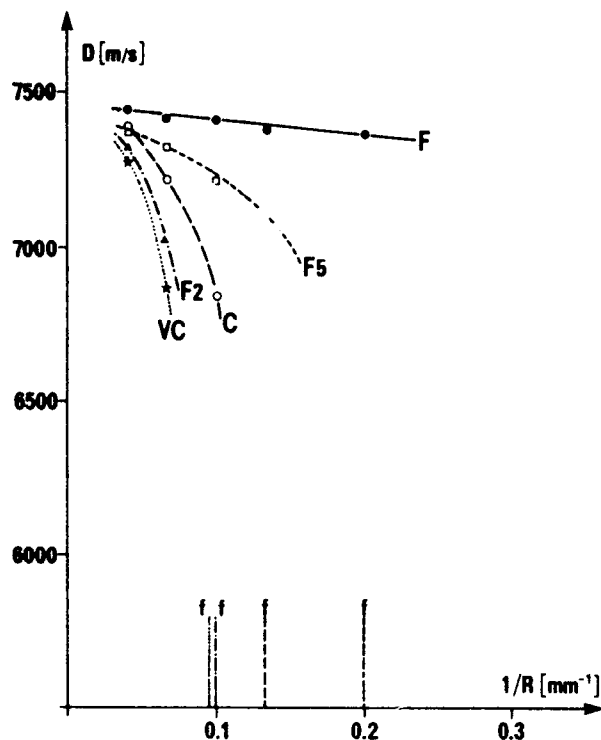


Figure 3. Detonation Velocity Vs. the Inverse of Explosive Cylinder Radius

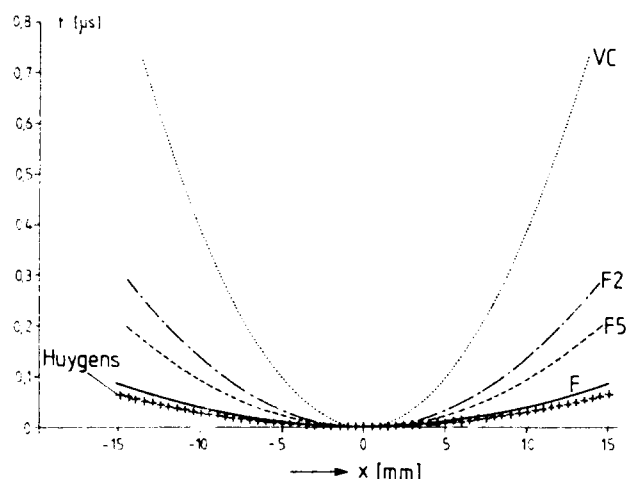


Figure 4. Experimental Curvature of Detonation Front

contrast to the extreme curvature shown by the very coarse monomodal formulation, the fine monomodal formulation has a detonation behavior very close to that of an ideal explosive.

## SENSITIVITY EXPERIMENTS

The different explosive formulations are submitted to sustained plane shock waves in Wedge-test experiments where a space-time diagram of the transition of initiation shock wave into detonation inside an explosive is recorded continuously by a streak camera and also by short-circuit pins. The impact velocity of 8 mm thick aluminum-alloy flyer plates has been varied from 1100 m/s to 2300 m/s. The Wedge-angle is 20°, except at the highest shock pressure where a 10° angle is used to increase spatial resolution. The Wedge-test technique with such rubber-like explosives requires special attention to be quantitative.

Figure 5 shows experimental space-time diagrams obtained in Wedge-test on the three monomodal formulations F, C, VC at four impact shock pressures:

- At 4.4 GPa, the lowest shock pressure studied, the very coarse monomodal formulation is distinctly more sensitive than the coarse monomodal formulation.
- At 5.4 GPa, the fine monomodal formulation is the least sensitive, but now, the coarse and very coarse formulations have a very close reactive behavior, the coarse formulation becoming slightly more sensitive than the very coarse formulation.
- At 6.6 GPa, the fine monomodal formulation is always the least sensitive, and the very coarse formulation has distinctly a sensitivity intermediate between the fine and the coarse formulation.
- At 12.0 GPa, the highest shock pressure studied, the most sensitive is now the fine formulation with a slight surdetonation close to the transition point. The very coarse formulation is the least sensitive, the coarse formulation having now the intermediate sensitivity order.

Figures 6 and 7, gathering the data of all our Wedge-test experiments, show the variation of the run distance to detonation and the time to detonation versus shock pressure. The

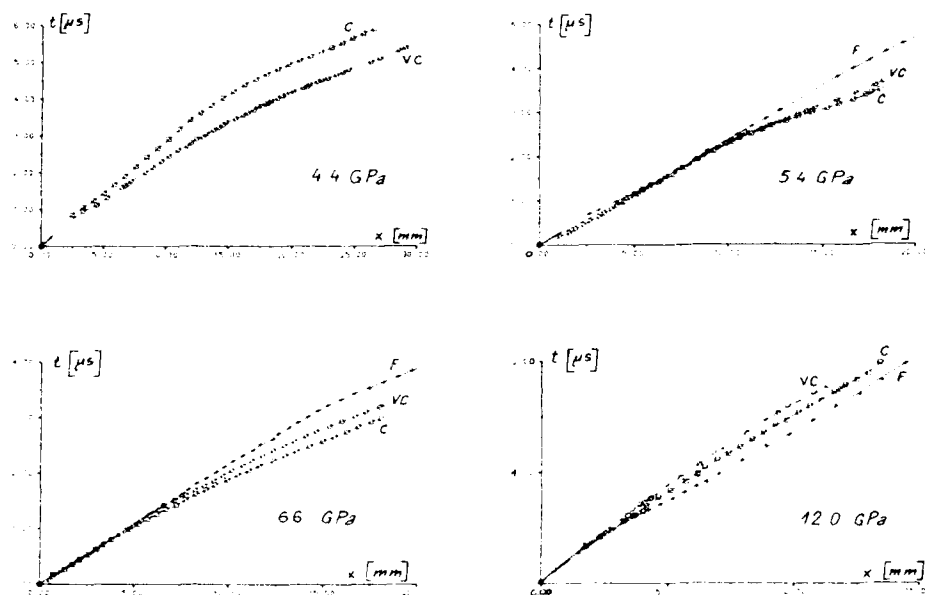


Figure 5. Wedge-Test Experiments on the Three Monomodal Formulations at Different Impact Shock Pressures

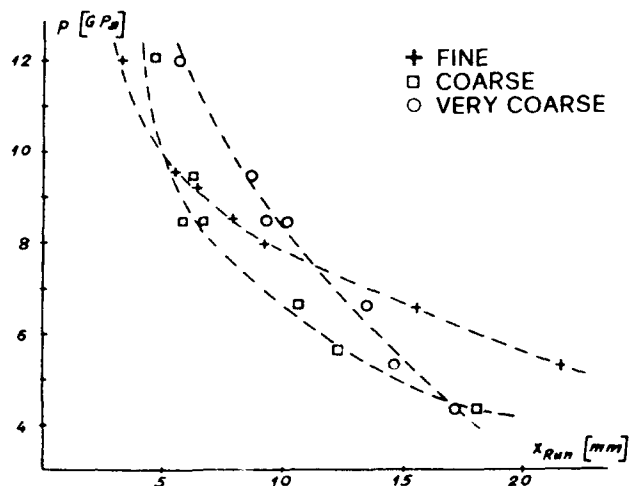


Figure 6. Run Distance to Detonation Vs. Impact Shock Pressure

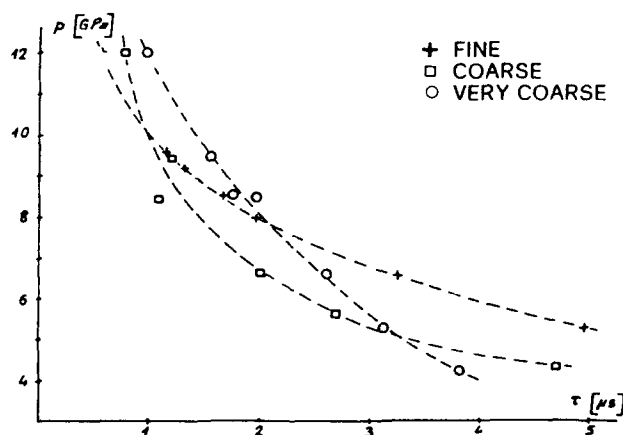


Figure 7. Time to Detonation Vs. Impact Shock Pressure

sensitivity classification of these three monomodal formulations depends strongly on the shock pressure level.

## INTERPRETATION AND DISCUSSION

At this time, to interpret such a result, we can merely invoke two hypotheses.

1. The complex sensitivity classification of monomodal formulations could be due to the morphology of RDX particles: coarse RDX batch is obtained by milling whereas the two

other RDX batches are obtained by direct recrystallization. Further work will be done to appreciate the exact weight of the differences in particle processing.

2. The second and more plausible explanation is based on the fundamental mechanism of the shock detonation transition. SDT is known as a two-step process: ignition of hot spots by the initiation shock wave and growth of the reaction by coalescence of the different burning front started at each hot spot in the ignition step.



Ideally, if we assume each RDX particle batch characterized by a unique hot spot size proportional to the median particle size, then the induction time for the thermal explosion of hot spots will be controlled by RDX particle size. So, for each RDX particle batch there will be a shock pressure threshold under which hot spot ignition cannot occur. Whereas at high shock pressures, the induction time for hot spot ignition is negligible compared to the duration of the growth step, then at high shock pressure there are the hot spot density and the higher specific surface area of the fine RDX batch which make it faster to attain completion of the decomposition reaction. This phenomenological interpretation permits us to draw qualitatively (Figure 8) curves of variation of run distances versus shock pressure for each monomodal formulation. At low shock pressures, SDT would be controlled by hot spot ignition where coarse RDX particles are more efficient. At high shock pressures, SDT would be controlled by the growth process where finer RDX particles are more efficient. At intermediate shock pressures, due to detailed balance between ignition and growth, crossover in the shock sensitivity is observed.

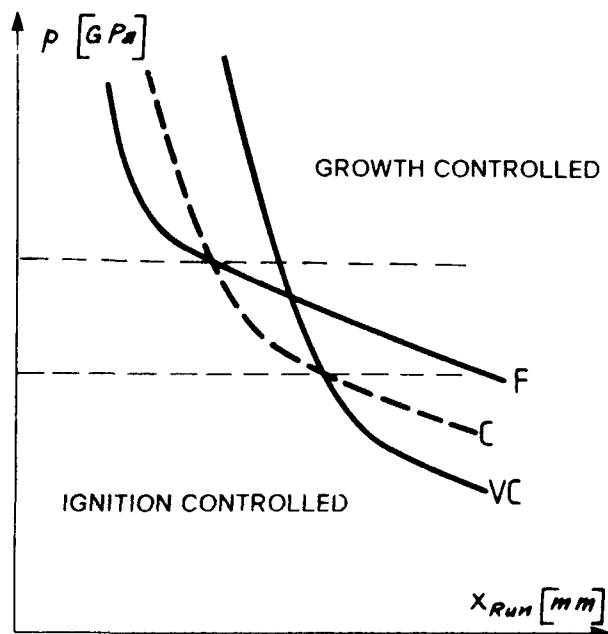


Figure 8. Pop-Plot Curves of the Three Mono-modal Formulations Predicted by the Assumed SDT Phenomenology

Very likely, reactive modeling<sup>3</sup> describing explicitly hot spot formation as a thermal explosion controlled process is more adapted physically to reconstitute our experimental results.

## CONCLUSION

Detonation and sensitivity experiments on three monomodal formulations of a cast PBX point out that the sensitivity classification is strongly dependent upon shock pressure and does not vary linearly with the median particle size. Further experiments and reactive modeling analysis are still necessary to better support the tentative phenomenological interpretation proposed here.

## REFERENCES

1. Moulard, H.; Kury, J. W.; and Delclos, A., "The Effect of RDX Particle Size on the Shock Sensitivity of Cast PBX Formulations," *Proceedings of the Eighth International Symposium on Detonation*, Albuquerque, NM, 15 Jul 1985, pp. 902-913.
2. Bélanger, C.; Pelletier, P.; and Drolet, J. F., "Shock Sensitivity Study of the Curable Plastic Bonded Explosives," *ibidem*, pp. 361-371.
3. Johnson, J. N.; Tang, P. K.; and Forest, C. A., "Shockwave Initiation of Heterogeneous Reactive Solids," *Journal of Applied Physics*, Vol. 7, No. 9, 1985, p. 4323.

## DISCUSSION

H. SCHUBERT, Director of I.C.T.  
Pfinztal, West Germany

We know that the shock sensitivity of PBX is dependent on the particle size of the explosive filler and also on the modal of elasticity. A higher modal increases the sensitivity. If you do not change the binder composition, than you will get with the smaller particles a higher modal of elasticity than with the larger ones. Therefore, you observe in reality two influences on the sensitivity working against each other.

## REPLY BY H. MOULARD

At high shock pressure and slow shock durations, it is not obvious that the great difference of mechanical behavior, statistically observed, would be so important. Very likely, the difference in local topography due to the various particle sizes can explain mainly the globally observed sensitivity behavior.

## DISCUSSION

A. C. VAN DER STEEN, TNO/PRL  
The Netherlands

You observed your PBX at a solid load of 70 percent weight. In these PBXs, the distances between the particles is relatively large. Do you expect that the same trends will be observed by varying the coarse/fine ratio in PBXs with a 25 percent solid load, where the distances between the particles are much smaller?

## REPLY BY H. MOULARD

The sensitivity behavior is not likely to be so distinct as observed with our 70 percent weight monomodal formulations. Experimentally, it certainly will be difficult to verify the result with 85 percent weight monomodal formulations based on the same particle size distributions due to the problem of obscurity with ultrafine explosive particles.

## DISCUSSION

DENNIS HAYES, Sandia National  
Laboratories, Albuquerque, NM

Your model of hot spot dominated and grain burning dominated regimes in shock initiation of cast PBXs has also been successfully used to interpret numerical simulations of the shock initiation process of porous HNS, in HDP-1978.

JULIUS ROTH, Consultant  
Portola Valley, CA

We also observed crossovers for coarse and fine RDX at about 85% TMD. Furthermore, the unreactive Hugoniot was about the same for coarse  $\sim 330 \mu\text{m}$  and fine  $\sim 8 \mu\text{m}$  RDX (*Proceedings of the 5th Symposium (International) on Detonation*, p. 219).

## REPLY BY H. MOULARD

It is effectively very important towards the understanding of the hot spots mechanism to point out that the pure granular explosive (HNS, RDX) with high porosity ( $\sim 85\%$  TMD) and the monomodal formulations of a cast PBX with essentially the porosity ( $\sim 99.9\%$  TMD) exhibit the same shock sensitivity behavior.

## DISCUSSION

ROGER CHÉRET  
Commissariat à l'Energie Atomique  
Paris, France

A unified model of the reactivity of condensed explosives has been recently developed (cf. Preprints Vol. I, p. 123). It is readable on the formulae that:

1. There is a strong coupling between the intensity of the ignition shock and the specific surface of the explosive charge;
2. A specific surface decrease may enhance the initial reactivity. This model already allows a fairly good interpretation of old Dremin and Shvedov experiments and, more recently, Setchell's experiments. Therefore, it may be reasonably hoped that this model might be a first step for the interpretation of your experimental results and for further predictions.

# PARTICLE SIZE EFFECTS IN THE INITIATION OF EXPLOSIVES CONTAINING REACTIVE AND NON-REACTIVE CONTINUOUS PHASES\*

R. L. Simpson, F. H. Helm, P. C. Crawford, and J. W. Kury  
Lawrence Livermore National Laboratory  
Chemistry and Materials Science Department  
Livermore, California 94550

*The shock sensitivity of HMX formulations has been determined using gun-driven wedge tests and multiple manganin pressure gauge tests. Mean HMX particle size was varied from 5 to 1700  $\mu\text{m}$ . Formulations with inert and reactive continuous fluid phases as well as extrusion cast formulations were tested. Both the HMX particle size and nature of the continuous phase were shown to affect the shock sensitivity. Radiometric experiments were also done to help verify the conclusions about reactivity drawn from the wedge and gauge experiments.*

## INTRODUCTION

The detonation shock sensitivity of explosives and high energy solid propellants is determined by the nature of the crystalline solids and binders used in such materials. In this paper we examine the effect of HMX<sup>1</sup> particle size on initiation in the presence of either an inert or an energetic continuous phase. The use of a continuous phase reduces the number of possible initiation mechanisms, such as, micro-jetting and viscous heating due to void collapse.

The formulations tested included HMX in water, HMX in FEFO<sup>2</sup> and HMX in extrusion castable binders containing FEFO (EXC formulations). Five different HMX particle sizes were tested in pinned wedge tests and in *in situ* pressure gauge experiments. The mean HMX particle sizes were 5, 60, 110, and 1700  $\mu\text{m}$ . Sustained shock pressures ranging from 2.5 to 8.3 GPa were generated with a 100-mm smooth bore gun.

As an independent check on the reactivity of HMX as a function of particle size, shock loaded samples of 5-, 60-, 110-, and 1700- $\mu\text{m}$  HMX in water were observed radiometrically. In addition, water mixtures with HMX sieve cuts in 10- $\mu\text{m}$  increments from less than 10  $\mu\text{m}$  to 60-70  $\mu\text{m}$  were tested for changes in emitted radiance at shock loadings of 6 and 8 GPa.

The details of this study are presented below. They show that both HMX particle size and the nature of the continuous phase significantly influence the shock sensitivity of formulations containing from 48 to 72 percent by volume HMX.

## EXPERIMENTAL

Three different experimental techniques were used to investigate the shock initiation behavior of the HMX formulations. Formulation characteristics and details of the experimental geometries, data measurement and reduction procedures and experimental results are presented in this section.

### HMX Formulations

The HMX used in the HMX/water and HMX/FEFO studies was taken from a single batch of high grade Holston Class 1 material.

\*Work performed under the auspices of the U.S. Department of Energy by the Lawrence Livermore National Laboratory under contract No. W-7405-ENG-48.

This material has an RDX<sup>3</sup> impurity level of 0.5 wt percent. The 60-, 110-, and 1700- $\mu$ m HMX were obtained as sieve cuts. A fluid energy mill was used to prepare the 5- $\mu$ m HMX. Figure 1 contains histograms of the HMX size distributions as determined by digital optical microscopy for the 1700- $\mu$ m material and with a Coulter counter for the others.

Loading the assemblies was accomplished in two fashions. In the fine grain size experiments the 5- $\mu$ m HMX/water was extrusion loaded as a paste. The three coarser materials were prepared by first loading the HMX and then injecting water containing the surfactant Aerosol-OT. For a given particle size distribution the final loading densities were essentially the same.

The HMX used in the extrusion cast formulation RX-08-EL is standard Holston I.X-04 grade with a broad distribution of sizes around a mean of 60  $\mu$ m. The 5- and 60- $\mu$ m

HMX used in RX-08-GB and RX-08-GG were from the same batch used in the HMX/water experiments. Table 1 lists the compositions used. Each of the assemblies was filled under vacuum using a deaerator loader. This process and the binding system are described in detail by Scribner et al.<sup>4</sup>

### Pinned Wedge Test<sup>5</sup>

In order to investigate these slurry and extrusion cast explosives, the traditional plane-wave lense wedge test<sup>6</sup> was modified as follows. Piezoelectric crystal pins were used to determine the shock arrival times in the explosive. Thirty of these pins were precisely arrayed at different depths in polymethyl methacrylate (PMMA) annuli which were used as containers for the explosives. Plates of 6061-T6 aluminum served both as container covers and as the projectile impact surface. The experimental configuration is shown in Figure 2.

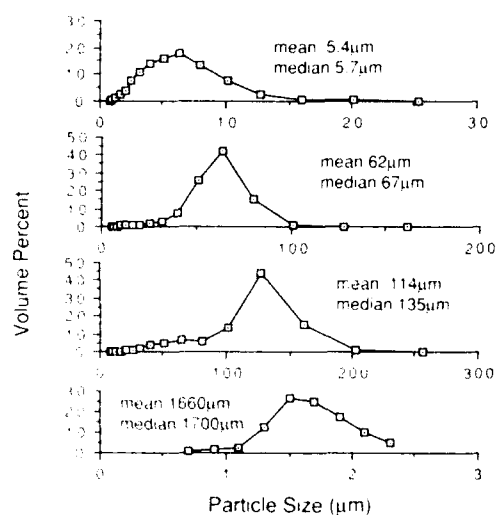


Figure 1. HMX Particle Size Distributions

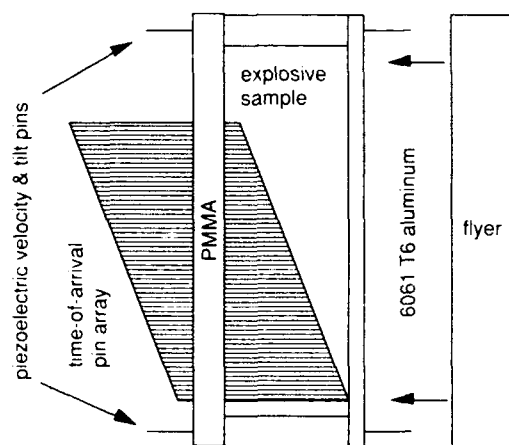


Figure 2. Pinned Wedge Test Configuration

Table 1. Compositions of the Extrusion Cast Explosives Used

	wt %		
	RX-08-EL	RX-08-GB	RX-08-GG
HMX 60 $\mu$ m	75.9		61.0
HMX 5 $\mu$ m		61.0	
FEFO	22.2	35.9	35.9
Urethane Binder	1.9	3.1	3.1

Planar shocks were generated in the samples by a flyer launched from a 100-mm smooth bore gun with tilt less than 5 mrad. Tilt pin data were used to correct the experimental results to within typical uncertainties of under 0.3 mrad in the tilt and 0.15 rad in the location of first contact.

The run distance vs. arrival time for experiment FH1 is presented in Figure 3. Initial shock velocity and final detonation velocity were obtained by least squares fit to early and late data respectively. Run distance to detonation was obtained from the intersection of the initial and late data fits. Initial input pressure was calculated from projectile velocity and Hugoniot data for the projectile and target array materials. Hugoniot data for the explosives tested are summarized in the Appendix.

Table 2 presents the experimental results for the HMX/water wedge tests. The data obtained for the HMX extrusion cast experiments are summarized in Table 3.

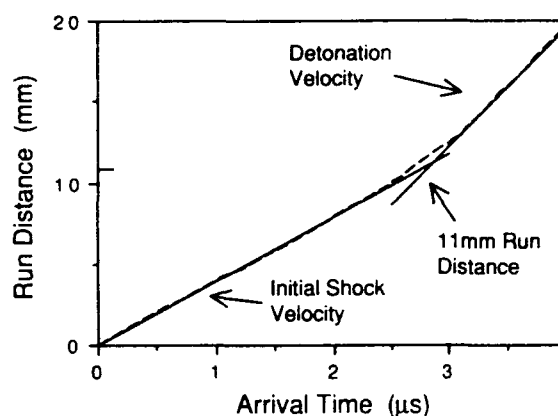


Figure 3. Wedge Test Result for 6- $\mu$ m HMX/Water with 6.0 GPa Input Pressure

### Multiple Manganin Gauge Experiments

Recently developed multiple manganin gauges were used to measure pressure *in situ* in shock loaded samples.<sup>7</sup> The gauges consist of several transducer elements placed at an angle to the oncoming flow so that each element is not only at a different depth within

Table 2. HMX/Water Pinned Wedge Test Data

Exp.	Mean Particle Size ( $\mu$ m)	HMX Vol%	Density (g/cc)	Flyer Velocity (mm/ $\mu$ s)	Pressure (GPa)	Initial Shock Velocity (mm/ $\mu$ s)	Detonation Velocity (mm/ $\mu$ s)	Run Distance (mm)
FH3	5	48	1.43	1.31	5.3	$3.69 \pm 0.01$	$6.92 \pm 0.09$	15
FH1	5	48	1.43	1.46	6.0	$3.87 \pm 0.01$	$7.09 \pm 0.04$	11
FH2	5	48	1.43	1.77	7.8	$4.40 \pm 0.02$	$7.17 \pm 0.07$	4.7
FH11	60	58	1.52	1.03	3.9	$3.67 \pm 0.02$	$7.67 \pm 0.11$	14
FH10	60	59	1.53	1.42	6.1	$4.19 \pm 0.03$	$7.77 \pm 0.01$	4.8
FH12	60	58	1.52	1.63	7.4	$4.61 \pm 0.01$	$8.10 \pm 0.02$	3.8
FH9	110	58	1.52	1.05	4.1	$3.60 \pm 0.01$	--	19
FH7	110	60	1.54	1.38	6.0	$4.06 \pm 0.02$	$7.74 \pm 0.02$	5.8
FH4	1700	61	1.55	1.03	4.0	$3.72 \pm 0.02$	$7.35 \pm 0.13$	14
FH6	1700	60	1.54	1.32	5.6	$4.01 \pm 0.06$	$8.12 \pm 0.04$	9.2
FH5	1700	60	1.54	1.74	8.3	$4.82 \pm 0.09$	$8.02 \pm 0.08$	6.0

Table 3. HMX-containing Extrusion Cast Explosives Pinned Wedge Test Data

Exp.	Explosive	Mean Particle Size ( $\mu\text{m}$ )	HMX Vol%	Density (g/cc)	Flyer Velocity (mm/ $\mu\text{s}$ )	Pressure (GPa)	Initial Shock Velocity (mm/ $\mu\text{s}$ )	Detonation Velocity (mm/ $\mu\text{s}$ )	Run Distance (mm)
EVH4	RX-08-GB	5	56	1.74	1.04	4.5	$3.78 \pm 0.05$	$8.31 \pm 0.15$	13
EVH5	RX-08-GB	5	56	1.74	1.33	6.2	$4.28 \pm 0.07$	$8.36 \pm 0.02$	5.6
EVH6	RX-08-GG	60	56	1.75	0.86	3.6	$3.59 \pm 0.05$	$8.25 \pm 0.18$	9.5
EVH7	RX-08-GG	60	56	1.75	1.18	5.3	$3.97 \pm 0.03$	$7.93 \pm 0.01$	4.0
EVH3	RX-08-EL	60	72	1.80	note 1	2.5	$3.37 \pm 0.02$	$8.68 \pm 0.02$	23
EVH2	RX-08-EL	60	72	1.80	1.14	5.4	$4.11 \pm 0.01$	$8.59 \pm 0.37$	4.4
EVH1	RX-08-EL	60	72	1.80	1.45	7.4	$4.72 \pm 0.06$	$8.96 \pm 0.01$	2.0

Note 1: Filter was polycarbonate at a velocity of 1.08 mm/ $\mu\text{s}$

the sample but it is also probing the original shock wave and the reactive flow behind it without disturbances from the proceeding gauge elements. The elements are piezoresistive. Absolute pressure is determined as variation in resistance which is measured using bridge circuitry and high speed transient recorders. The flow is generated by the impact of a flyer plate at the front surface of an assembly similar to that shown in Figure 2.

The pressure vs. time results at various depths for the water formulations with 5-, 60-, and 1700-HMX experiments are presented in Figures 4, 5, and 6, respectively. Similar results for FEFO formulations with 5- and

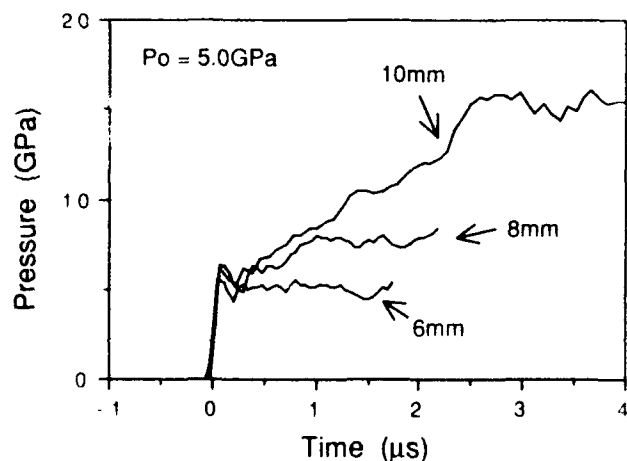


Figure 4. Pressure Buildup Curves for 5- $\mu\text{m}$  HMX/Water at Various Depths in the Explosives

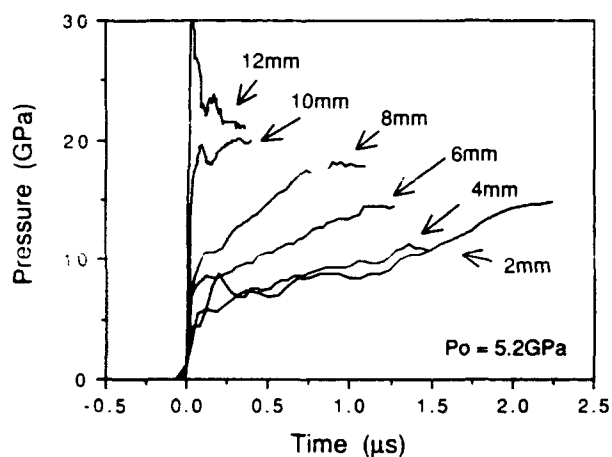


Figure 5. Pressure Buildup Curves for 60- $\mu\text{m}$  HMX/Water at Various Depths in the Explosive 1700- $\mu\text{m}$  HMX are shown in Figures 7 and 8.

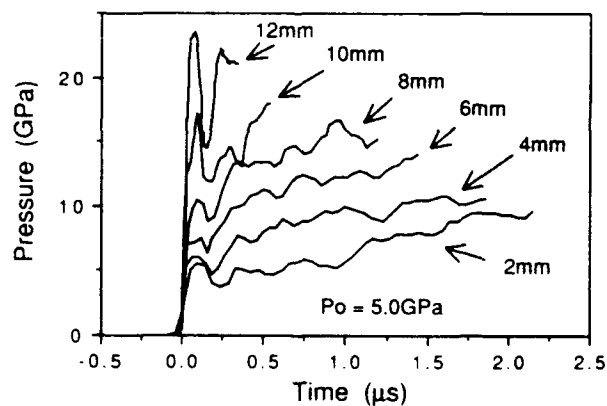


Figure 6. Pressure Buildup Curves for 1700- $\mu\text{m}$  HMX/Water at Various Depths in the Explosive

The pressure traces for the 5  $\mu\text{m}$  HMX/FEFO formulation at depths in the explosive greater than 4 mm are characteristic of detonation. The peak pressure, however, is about 8 GPa lower than would be expected for this energetic formulation. We are not able to explain the discrepancy at this time, nor are we able to ignore the experimental results.

### Radiometric Experiments

An electric gun<sup>8</sup> was used to shock HMX/water slurries monitored for thermal emission by a fiber optic, four channel, visible radiometer.<sup>9</sup> The experimental configuration used is shown in Figure 9. An electrically

exploded aluminum bridge-foil accelerated thick polycarbonate flyers into the samples. Pressure was supported in the samples for about 0.45  $\mu\text{s}$  with a 1.2-mm-thick flyer. Initial input pressure was controlled by modifying flyer velocity by varying the applied voltage across the bridge-foil. Calibration experiments have shown that this method of controlling velocity is accurate to 2-3 percent. Several piezoelectric crystal pins were used to relate shock position to the radiant emittance vs. time curves.

In these experiments only relative radiances (in arbitrary units) were compared. As an example, Figure 10 compares results

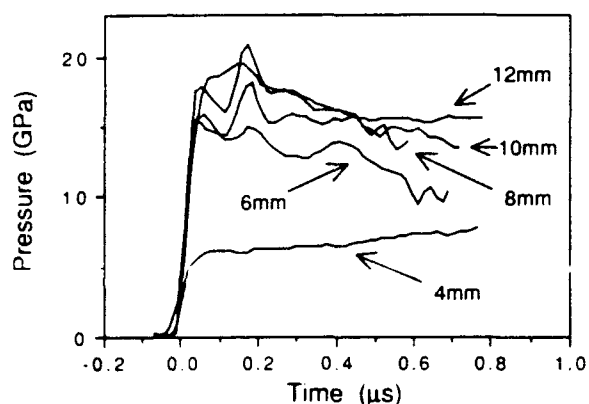


Figure 7. Pressure Buildup Curves for 5- $\mu\text{m}$  HMX/FEFO at Various Depths in the Explosive

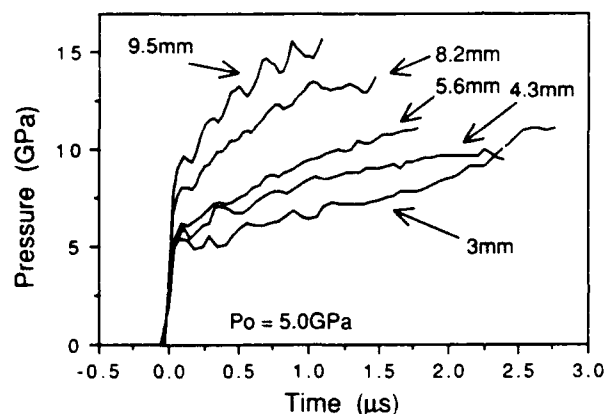


Figure 8. Pressure Buildup Curves for 1700- $\mu\text{m}$  HMX/FEFO at Various Depths in the Explosive

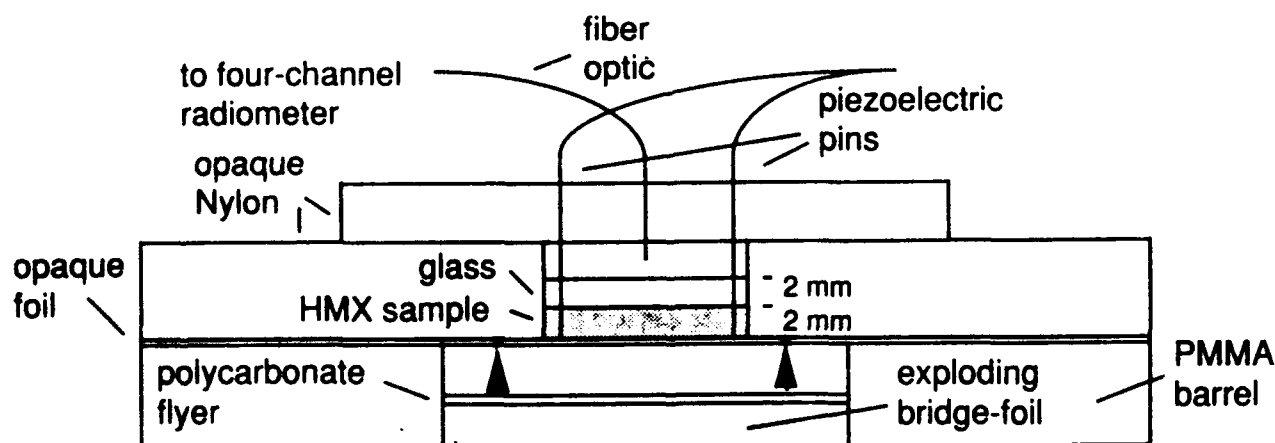


Figure 9. Diagram of Radiometry Experiments Showing Electric Gun Configuration

for 5- $\mu\text{m}$  HMX in water shocked to 4.0, 6.0, and 8.0 GPa. Figures 11 and 12 show the effect of HMX particle size on relative radiances for slurries shocked to 6.0 and 8.0 GPa, respectively.

## DISCUSSION

### Reaction at the Shock Front in the Wedge Test

In the usual interpretation of the wedge test, the early straight line distance-time data are assumed to represent the inert shock velocity. RDX data<sup>9</sup> showed this to be true for only very small particle size RDX at wedge test input pressures less than 6 GPa. The HMX/water data presented in this report indicate the same behavior.

The inert Hugoniot for HMX/water formulations presented in the Appendix accurately reproduced the initial shock velocity of the 5- $\mu\text{m}$  formulations shocked to 5.3 GPa and 6.0 GPa (Exps. FH3 & FH1). All the other experiments had initial shock velocities higher than that calculated with the inert Hugoniot indicating significant chemical reaction at or near the shock front. Radiometry experiments confirmed this interpretation.

Hydrodynamic calculations using Tarver's reactive model<sup>10</sup> and the equation of state data from the Appendix were done to estimate the amount of early reaction. The ignition term was used to limit the amount and time of reaction. Coefficients for the two growth terms

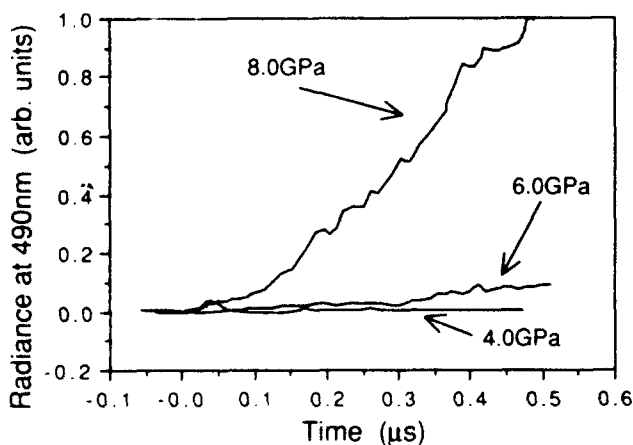


Figure 10. Radiant Emittance Traces of Shock Loaded 5- $\mu\text{m}$  HMX in Water

were set to zero in these calculations. Figure 13 summarizes the results for a series of such calculations for experiment FH2. The non-reactive Hugoniot predicts an initial shock velocity of 4.2 mm/ $\mu\text{s}$  vs. the measured velocity of 4.40 mm/ $\mu\text{s}$ . This is consistent with approximately 7 percent reaction in times equal to or less than 0.125  $\mu\text{s}$ .

Figure 14 compares the results of a series of calculations involving 0, 2, 5, 10, and 15 percent reaction at the shock front with actual measured results for the 60-, 110-, and 1700- $\mu\text{m}$  HMX/water formulations. The amount of early reaction is approximately the same for all the formulations and increases with pressure.

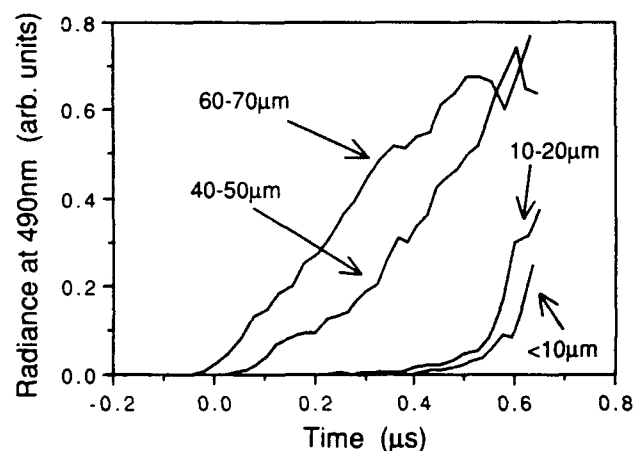


Figure 11. Radiant Emittance Traces for HMX in Water Shocked to 6.0 GPa

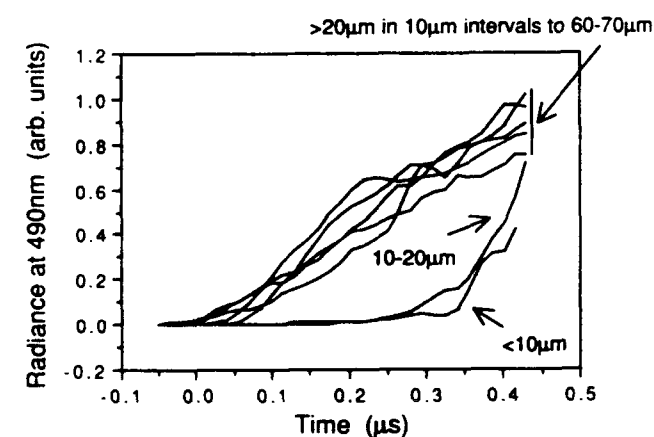


Figure 12. Radiant Emittance Traces for HMX in Water Shocked to 8.0 GPa



Table 4. Approximate Amount of Reaction Supporting the Shock Front

HMX Particle Size	Exp	Continuous Phase	Input Pressure	% Reaction Supporting Shock Front
5 $\mu\text{m}$	EVH4	FEFO	4.5	3
	FH3	H <sub>2</sub> O	5.3	<0.2
	FH1	H <sub>2</sub> O	6.0	<0.2
	EVH5	FEFO	6.2	6
	FH2	H <sub>2</sub> O	7.8	7
60 $\mu\text{m}$	EVH3	FEFO	2.5	1
	EVH6	FEFO	3.6	2
	FH11	H <sub>2</sub> O	3.9	4
	EVH7	FEFO	5.3	4
	EVH2	FEFO	5.4	4
	FH10	H <sub>2</sub> O	6.1	6
	FH12	H <sub>2</sub> O	7.4	9
	EVH2	FEFO	7.4	9
110 $\mu\text{m}$	FH9	H <sub>2</sub> O	4.1	2
	FH7	H <sub>2</sub> O	6.0	5
1700 $\mu\text{m}$	FH4	H <sub>2</sub> O	4.0	4
	FH6	H <sub>2</sub> O	5.6	5
	FH5	H <sub>2</sub> O	8.3	14

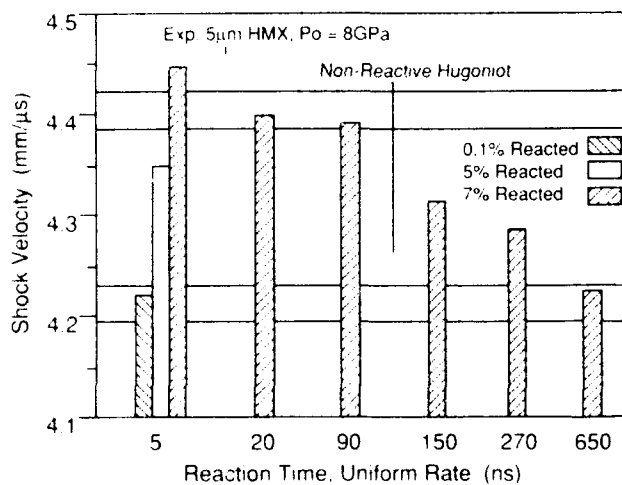


Figure 13. Initial Wedge Test Shock Velocity as a Function of Amount Reacted Near Shock Front

Similar calculations were done for the HMX/FEFO formulations. All the results are summarized in Table 4. In contrast to the water formulation results, the 5- $\mu\text{m}$  HMX/FEFO formulations showed significant reaction near the shock front even at pressures below 6 GPa.

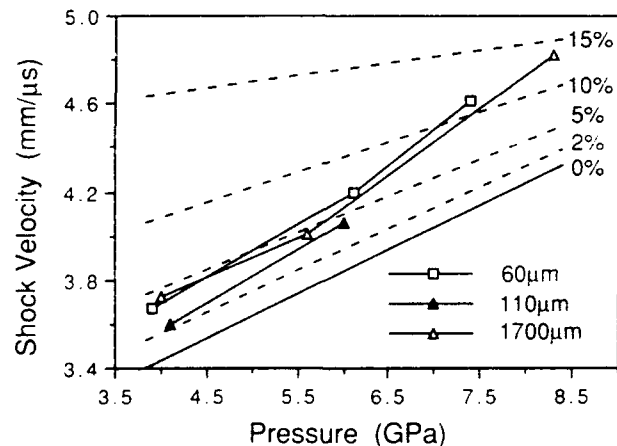


Figure 14. Initial Wedge Test Shock Velocities for HMX/Water Formulations. Dashed lines represent calculated effect on velocity due to reaction (errors in velocities < 0.05 mm/μs).

### Wedge Test Run Distances to Detonation

The run distances to detonation vs. input pressures for all the HMX/water and HMX/FEFO wedge tests are presented in Figure 15. Figures 16-18 present the distance-time data at approximately 4-, 6-, and 7.5-GPa input pressures.

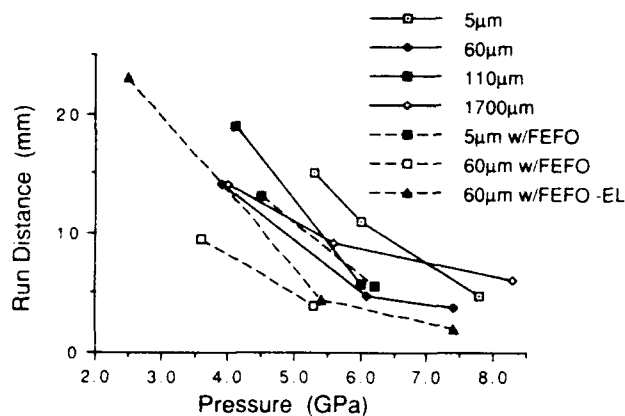


Figure 15. Run Distance vs. Pressure for HMX Formulations from Wedge Test Data

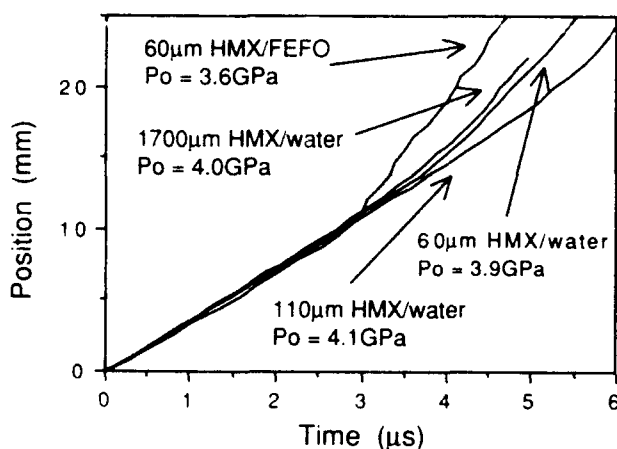


Figure 16. Effect of HMX Particle Size and Continuous Phase on Shock Sensitivity at Approximately 4-GPa Input Pressure

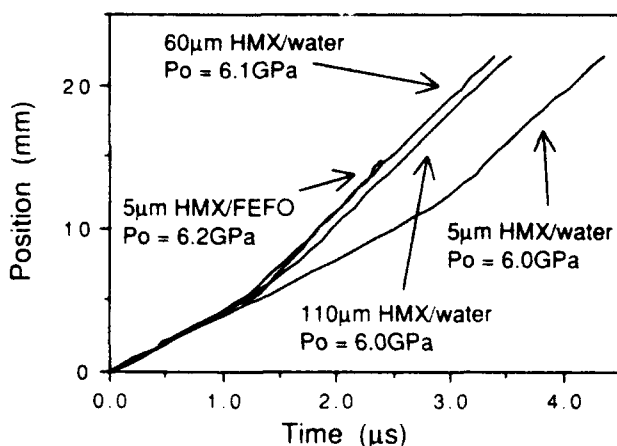


Figure 17. Effect of HMX Particle Size and Continuous Phase on Shock Sensitivity at Approximately 6-GPa Input Pressure

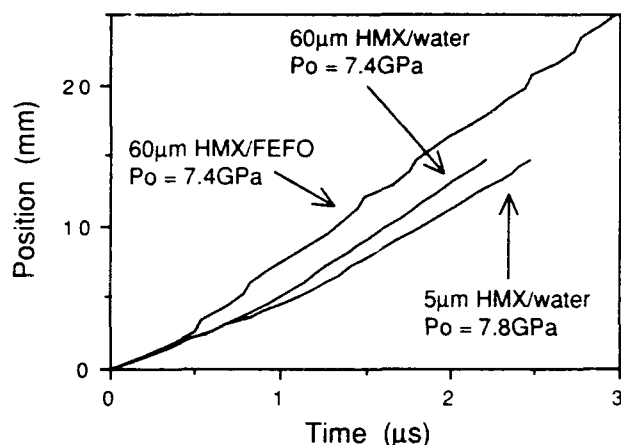


Figure 18. Effect of HMX Particle Size and Continuous Phase on Shock Sensitivity at Approximately 7.5-GPa Input Pressure

The data show that the 5- $\mu\text{m}$  HMX formulations are less shock sensitive than the larger particle size formulations for a given continuous phase. However, for a given HMX particle size, formulations containing the reactive FEFO were significantly more sensitive than those with the inert water phase.

The run distance vs. pressure curves for 5-, 60-, and 110- $\mu\text{m}$  HMX/water formulations have similar slopes. In the 4.0- to 8.0-GPa pressure range, however, the 60- $\mu\text{m}$  HMX exhibits shorter run distances than the 110- $\mu\text{m}$  HMX. Moreover, there is a major difference in behavior exhibited by the 1700- $\mu\text{m}$  HMX formulation. At 4 GPa its run distance is as short as the most sensitive 60- $\mu\text{m}$  HMX material. Whereas, at 8 GPa, its run distance is longer than the least sensitive 5- $\mu\text{m}$  HMX formulation.

The fact that these differences occur even though the amount ignited in the shock front is nearly independent of particle size suggests marked variation in reaction growth behavior as a function of particle size. Preliminary results, obtained by fitting the experimental wedge data using Tarver's reactive model, are consistent with this. Confirmation of these data, however, awaits the results of calculations now underway for the multiple manganin pressure gauge experiments described in this report.

## HMX Particle Size and Binder Effects on Pressure Buildup Profiles

Data from multiple manganin gauge experiments for 5-, 60-, and 1700- $\mu\text{m}$  HMX/water formulations are compared in Figures 19-21. The initial shock input pressures were approximately 5 GPa for all three materials. Impact flyer velocities were adjusted to account for small variations in sample impedance. The figures show that at 6, 8, and 10 mm into the explosive the 5  $\mu\text{m}$  HMX formulation has a much lower shock front pressure and pressure growth rate than the larger particle size formulations.

These data also confirm the relative shock sensitivity deduced from modeling the pinned wedge tests for 60 and 1700- $\mu\text{m}$  HMX/water formulations. That is, the 60- $\mu\text{m}$  HMX material has a shorter run distance to detonation due primarily to a larger reaction growth rate.

Figure 22 compares pressure profiles for 5- $\mu\text{m}$  HMX formulations containing either water or FEFO as the continuous phase. In spite of the somewhat lower shock input pressure (4.7 vs. 5.0 GPa) the FEFO formulation has a faster reaction growth rate and transitions to detonation much earlier. Again this is in agreement with the pinned wedge test data. These data not only showed earlier transition for the FEFO material, but also that a significant amount of material reacted at or near the shock front.

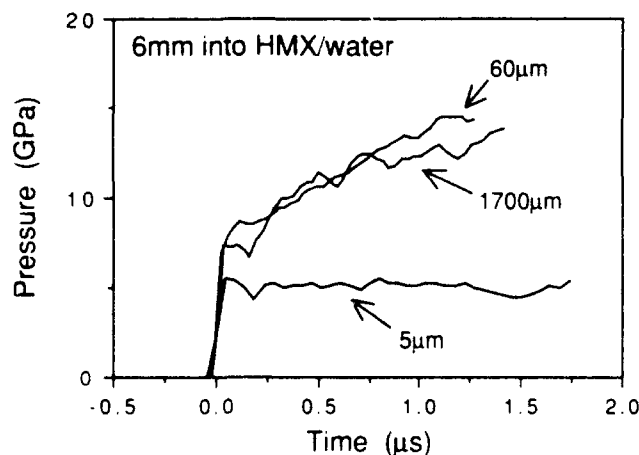


Figure 19. Effect of HMX Particle Size on Pressure Buildup 6 mm into the Flow with an Input Pressure of Approximately 5 GPa

## CONCLUSIONS

Wedge tests have shown that 5- $\mu\text{m}$  HMX formulations with either an inert (water) or a reactive (FEFO) continuous phase are less shock sensitive than formulations with HMX particle

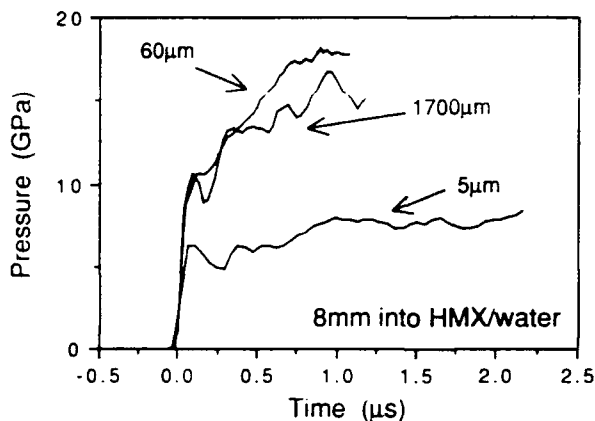


Figure 20. Effect of HMX Particle Size on Pressure Buildup 8 mm into the Flow with an Input Pressure of Approximately 5 GPa

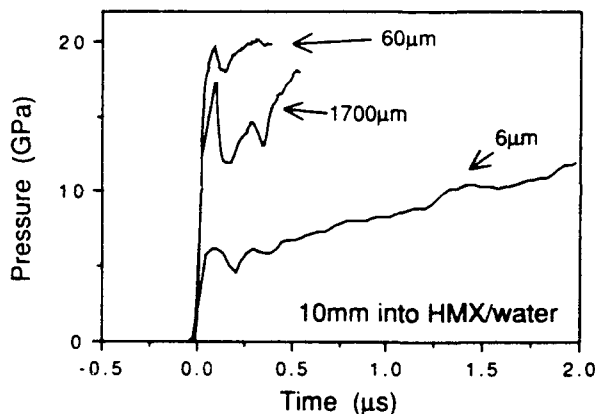


Figure 21. Effect of HMX Particle Size on Pressure Buildup 10 mm into the Flow with an Input Pressure of Approximately 5 GPa

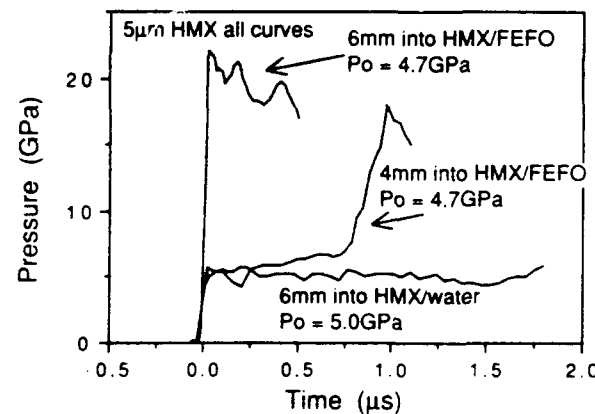


Figure 22. Effect of Continuous Phase on Pressure Buildup with an Input Pressure of Approximately 5 GPa

sizes of 60  $\mu\text{m}$  or greater. Radiometry experiments with HMX/water formulations have indicated that this decrease in sensitivity occurs when the HMX particle size is less than 20  $\mu\text{m}$ .

The shock sensitivity of 60- $\mu\text{m}$  HMX/water formulations is greater than that of either 110- or 1700- $\mu\text{m}$  HMX/water formulations. Since the amount reacted near the shock front for all three of these materials as a function of pressure is about the same, this difference results from growth rate changes. Both pressure gauge results and reactive modeling of the pinned wedge test data support this conclusion.

For 5- $\mu\text{m}$  HMX formulations, changing from an inert to a reactive continuous phase markedly increases the shock sensitivity. Wedge and gauge experiments show increases in both the amount reacted near the shock front and the reaction growth rate.

## APPENDIX

### Hugoniot and Detonation Product Equation Of State Data

Inert Hugoniot data is required to calculate the initial shock input pressures for the

HMX formulations described in this report. Where possible, published data were used covering the pressure region of interest (3 to 15 GPa). These included data for HMX,<sup>11</sup> water,<sup>12</sup> and FEFO.<sup>13</sup> Torrance's method<sup>14</sup> was used to estimate Hugoniot data for mixtures including the multicomponent ECX binder.

Table A1 presents the intercept and slope for the linear shock velocity - particle velocity curves. Table A2 presents the inert JWL equation of state constants for the slurry and ECX formulations used in the reactive model calculations.

Detonation product equations of state for the HMX/water mixtures were estimated from metal acceleration experiments.<sup>15</sup> The product equation of state for RX-08-EI was estimated from cylinder test experiments.<sup>4</sup> Product equations of state for HMX/FEFO slurries, RX-08-GG and RX-08-GB were estimated with the help of TIGER calculations.<sup>16</sup> The procedure involves comparing the energy release along the CJ isentrope for the new formulation with that for a well-characterized standard explosive. Table A3 lists the product equations of state parameters.

Table A1. Inert Hugoniot data

Material	Density (g/cc)	Intercept (mm/ $\mu\text{s}$ )	Slope
HMX	1.90	2.65	1.80
H <sub>2</sub> O	0.998	1.70	1.7
FEFO	1.61	1.70	1.76
ECX Binder	1.26	2.49	1.58
ECX/Binder/ FEFO (plasticized binder)	1.58	1.82	1.64
HMX/H <sub>2</sub> O (48 vol% HMX)	1.43	1.95	1.75
HMX/H <sub>2</sub> O (59 vol% HMX)	1.53	2.10	1.73
HMX/FEFO (48 vol% HMX)	1.75	2.09	1.74
HMX/FEFO (60 vol% HMX)	1.78	2.20	1.76
RX-08-GB & RX-08-GG (56 vol% HMX)	1.76	2.22	1.70
RX-08-EI (72 vol% HMX)	1.81	2.36	1.73

Table A2. Inert JWL Equations of State

Material	Density (g/cc)	A (GPa)	B (GPa)	R <sub>1</sub>	R <sub>2</sub>	ω	C <sub>v</sub> (GPa/K)	E (GPa-cc/cc)
HMX/H <sub>2</sub> O (48 vol% HMX)	1.43	2147	-3.901	8.22	1.174	1.253	1.682×10 <sup>-3</sup>	0.5011
HMX/H <sub>2</sub> O (59 vol% HMX)	1.53	2097	-4.652	7.96	1.137	1.419	1.797×10 <sup>-3</sup>	0.5357
HMX/FEFO (48 vol% HMX)	1.75	1630	-3.858	7.5	0.75	1.504	2.055×10 <sup>-3</sup>	0.6123
HMX/FEFO (60 vol% HMX)	1.78	1955	-4.261	7.6	0.76	1.634	2.091×10 <sup>-3</sup>	0.6231
RX-08-GB & RX-08-GG (56 vol% HMX)	1.76	1392	-4.197	7.2	0.72	1.629	2.086×10 <sup>-3</sup>	0.6161
RX-08-EL (72 vol% HMX)	1.81	1726	-4.801	7.3	0.73	1.812	2.125×10 <sup>-3</sup>	0.6334

Table A3. Product JWL Equations of State

Material	Density (g/cc)	D (mm/μs)	P <sub>CJ</sub> (GPa)	A (GPa)	B (GPa)	R <sub>1</sub>	R <sub>2</sub>	ω	C <sub>v</sub> (GPa/ K)	E <sub>0</sub> (GPa- cc/cc)
HMX/H <sub>2</sub> O (48 vol% HMX)	1.43	7.2	17.5	474.2	26.37	4.6	3.2	0.3	0.001	4.5
HMX/H <sub>2</sub> O (59 vol% HMX)	1.53	8.1	25.0	664.0	25.03	4.8	2.0	0.4	0.001	6.0
RX-08-GB & RX-08-GG (56 vol% HMX)	1.76	8.19	30.0	5678	137.8	9.05	2.55	0.46	0.001	9.5
RX-08-EL (72 vol% HMX)	1.81	8.51	33.5	2533	135.2	7.5	2.50	0.45	0.001	10

## ACKNOWLEDGMENTS

The authors would like to thank Drs. E. Lee and R. McGuire for their support of this research. We are also indebted to Dr. P. Urtiew, Mr. L. Erickson, and Mr. T. Cook for their assistance in carrying out the multiple gauge experiments.

## REFERENCES

1. HMX is octahydro-1,2,5,7-tetranitro-1,3,5,7-tetrazocine.
2. FEFO is 1,1-[methylenebis(oxy)]bis[2-fluoro-2,2-dinitroethane].
3. RDX is hexahydro-1,3,5-trinitro-1,3,5-triazine.
4. Scribner, K.; von Holtz, E. H.; and Simpson, R. L., "High Performance Extrusion Cast Explosives with Low Sensitivity," UCRL-53890, 1989. Lawrence Livermore National Laboratory, Livermore, CA.

5. Simpson, R. L.; Helm, F. H.; Crawford, P. C.; and Kury, J. W., "Shock Initiation Studies on Heterogeneous Explosives," Combustion and Detonation Phenomena, *Proceedings 19th International Annual ICT Conf.*, 29 Jun 1988, Vol. 98, pp. 1-11.
6. Campbell, A. W.; Davis, W. C.; Ramsay, J. B.; and Travis, J. R. "Shock Initiation of Solid Explosives," *Physics of Fluids*, Vol. 4, 1961, pp. 511-521.
7. Urtiew, P. A. and Erickson, L. M., "Multiple Gauges for *In Situ* Measurement of Pressure and Particle Velocity in Condensed Materials," UCRL-100106, 1989, Lawrence Livermore National Laboratory, Livermore, CA.
8. Chau, H. H.; Dittbenner, G.; Hofer, W. W.; Honodel, C. A.; Steinberg, D. J.; Stroud, J. R.; and Weingart, R. C., "The Electric Gun: A Versatile Tool for High-Pressure Shock-Wave Research," *Rev. Sci. Instrum.*, Vol. 51, No. 12, 1980, p. 1676.
9. Moulard, H.; Kury, J. W.; and Delclos, A., "The Effect of RDX Particle Size on the Shock Sensitivity of Cast PBX Formulations," *Eighth Symposium (International) on Detonation*, NSWC, MP 86-194, Albuquerque, NM, Jul 1985, pp. 902-913.
10. Tarver, C. M.; Hallquist, J. O.; and Erickson, L. M., "Modeling Short Pulse Duration Shock Initiation of Solid Explosives," *Eighth Symposium (International) on Detonation*, NSWC, MP 86-194, Albuquerque, NM, Jul 1985, pp. 951-971.
11. Simpson, R. L.; Helm, F. H.; and Kury, J. W., "Non-Reactive HMX Shock Hugoniot Data," Lawrence Livermore National Laboratory, *J. Propellants, Explosives and Pyrotechnics*, in press.
12. Marsh, S. P., Ed., *LASL Hugoniot Data*, University of California Press, Berkeley, CA, 1980, pp. 573-574, 595-596.
13. Simpson, R. L.; Helm, F. H.; von Holtz, E. H., "Shock Compression and Initiation Behavior of FEFO," UCID 21575, 1988, Lawrence Livermore National Laboratory, Livermore, CA.
14. Torvik, P. J., "A Simple Theory for Shock Propagation in Homogeneous Mixtures," Air Force Institute of Technology, AFIT-TR-70-3, May, 1970.
15. Private communication, R. Donald Breithaupt, Lawrence Livermore National Laboratory, Livermore, CA.
16. Cowperthwaite, M. and Zwisler, W. H., "TIGER Computer Program Documentation," Stanford Research Institute, SRI Publication Z106, 1973, Menlo Park, CA.

## DISCUSSION

**P. M. HOWE, Antiarmor Munitions  
Technology Office  
Aberdeen Proving Ground, MD**

Your paper provides a large number of interesting results and trends. I find especially interesting your conclusion that the sensitivity of the HMX/water systems you studied is controlled by a growth process rather than by an ignition process. It seems to me that your data require two growth processes to explain the trends. One reasonable assumption is that the growth processes arise from two kinds of ignition sources—intragranular and intergranular—which contribute to the initial reaction, serves as sources for additional grain burning reactions, and have different particle size dependencies. Thus, if the ignition sources are intergranular, one might assume an initial grain burning rate which is proportional to the initial granular surface area; i.e., the initial rate varies as  $nd/d$  or  $\%Vol/d$ , with a consequent reduced initial grain burning rate with increased particle size. For intragranular hotspots, the initial grain burning rate can be expected to increase with increasing imperfection of the crystals, which tends to increase with increased particle size. With both kinds of hotspots present and contributing, the buildup time, if controlled by grain burning, should go through a minimum as a function of particle size (see Figure 1).

The location of this minimum will be a function of the relative efficiencies of the two

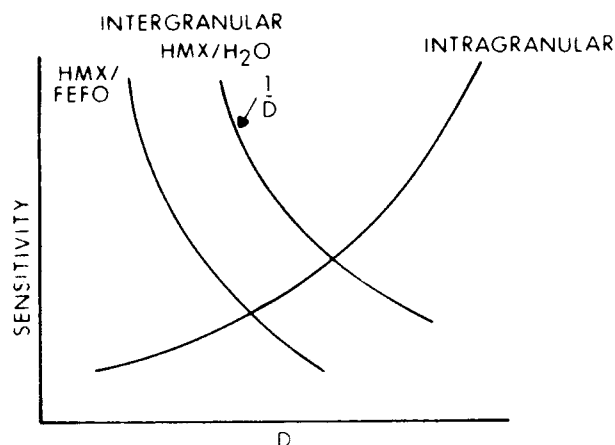


Figure 1. Schematic Showing Dependence of Inter- and Intra-granular Sites Upon Particle Size

kinds of hotspots. The liquid phase in your two component mixtures can affect sensitivity of the systems in several ways. I expect the energetic FEFO to augment the importance of intergranular hotspots to growth reactions. However, since HMX and FEFO have closer shock impedances than do HMX and water, the HMX/FEFO system will not be as efficient at forming these hotspots—i.e., lower nonreactive temperatures will be generated. There should be little or no effect of the liquids upon intra-granular sites.

If the above is correct, and since your results appear to be dominated by growth processes rather than ignition processes you should find the same trend of sensitivity versus particle size for HMX/FEFO systems as you did for HMX/water, except that the minimum will occur at a smaller particle size. In addition, since the FEFO can only contribute to the growth process through processes originating at intergranular sites, its effect should diminish with increasing HMX particle size. At large particle sizes, the HMX/FEFO and HMX/H<sub>2</sub>O formulations should behave similarly. Superposition of your results shown in Figures 6 and 8 (after making the scales comparable) supports this trend, but leads to a very interesting anomaly (See Figure 2 above). It is clear that the HMX/H<sub>2</sub>O and HMX/FEFO systems have comparable behavior at very small depths into the

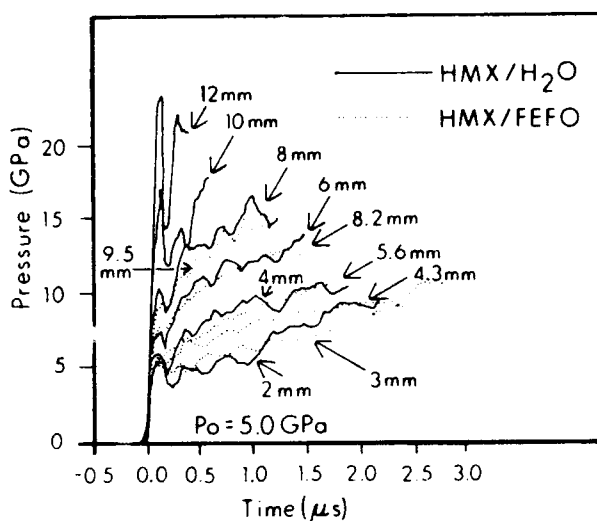


Figure 2. Pressure Buildup Curves for 1700- $\mu$ m IMX Systems. The HMX/H<sub>2</sub>O system appears to buildup to detonation more rapidly than the HMX/FEFO.

explosive. Thereafter, the HMX/H<sub>2</sub>O system is growing more rapidly to detonation than is the HMX/FEFO system. This may be due to experimental errors, but I don't think so, since the very early time data agree so well. The only explanation I have is that the differences in shock impedances are having an affect on both the intergranular and intra-granular sites.

I have provided what appears to me to be a very complicated (and, hence, dissatisfying) explanation for what may or may not be a very complicated process. I, therefore, solicit your thoughts as to what the correct explanation of these trends might be.

## DISCUSSION

ROGER CHERET, Commissariat à l'Energie Atomique  
Paris, FRANCE

A unified model of the reactivity of condensed explosives has been recently developed (cf. Preprints, Vol. I, p. 129). It is readable on the formula that:

- 1) There is a strong coupling between the intensity of the ignition shock and the specific surface of the explosive charge;

- 2) A specific surface decrease may enhance the initial reactivity. This model already allows a fairly good interpretation of 1976 Dremine and Shredov experiments, as well as of more recent Setchell's ones. Therefore it may reasonably be hoped that this model be a first step for the interpretation of your results and for further predictions.

## DISCUSSION

I. B. MISHRA, Kanan Associates, Inc.  
Churchville, MD

1. What is the rationale for finding 1700- $\mu\text{m}$  particles to be less sensitive than 60- $\mu\text{m}$  and 110- $\mu\text{m}$ ?
2. You stated on a slide about cavities in nitramines. Is 1700- $\mu\text{m}$  cavity-free? Did you check this? How did you check this?

## REPLY BY AUTHORS

1. Radiometric measurements and wedge tests indicate that there were similar amounts of material ignited near the shock front in all three particle size distributions. In the

1700- $\mu\text{m}$  case the growth rate to full detonation was significantly slower. Hence, the run distances, taken as the intersection of the linear regions in the pre- and post-transitions portions of the shock position vs. time plot, are longer than those which would be obtained with materials that have a slower growth rate after ignition. The differences in growth rate can be accounted for if different types of burning geometries were present. As these experiments are phenomenological in nature postulating the actual mechanism is not appropriate.

2. The 1700- $\mu\text{m}$  HMX is probably not entirely cavity-free. All particle sizes were examined with an electron microscope and in the case of the 1700- $\mu\text{m}$  material with an optical microscope. The 1700- $\mu\text{m}$  material appears to be an agglomeration of smaller particles with the possibility of reentrant cavities. Density studies were carried out on the HMX/fluid mixtures. From these measurements, the total void volume resulting from both intragranular cavities and any incomplete wetting was well below 0.3 percent in all experiments.



# IN-SITU STUDY OF THE CHEMICALLY DRIVEN FLOW FIELDS IN INITIATING HOMOGENEOUS AND HETEROGENEOUS NITROMETHANE EXPLOSIVES\*

Stephen A. Sheffield, Ray Engelke, and Robert R. Alcon  
Los Alamos National Laboratory  
Los Alamos, New Mexico 87545

*Electromagnetic gauging has been used to make in-situ measurements of particle velocity and impulse at five Lagrangian positions in nitromethane (NM) during gas-gun-driven, shock-to-detonation experiments. Homogeneous initiation experiments were conducted using NM that was chemically sensitized (using an organic base) and heterogeneous initiation experiments were done with physically sensitized NM (using silica particles). In the homogeneous initiation experiments, some of the features we observe are consistent with the classical homogeneous initiation model, however, our measurements show that the superdetonation does not form immediately after an induction time. Considerably behind the initial shock, reaction causes a wave to build up over a discernible length and this wave evolves into a superdetonation which catches the initial shock. In the heterogeneous initiation experiments, the waveforms indicate that wave growth occurs primarily in the shock front, similar to earlier observations in other heterogeneous explosives.*

## INTRODUCTION

The conclusions drawn in the classical studies of Campbell, Davis, Travis, and Ramsay<sup>1,2</sup> concerning the initiation process in homogeneous and heterogeneous explosives depend primarily on inferences drawn from shockwave trajectory measurements. Essentially all of our intuitions concerning the initiation of detonation in homogeneous condensed phase materials have their origin in such measurements; some of these ideas remain controversial. Although considerable in-situ measurements have been made on condensed-phase heterogeneous materials, little work has been done on heterogeneous materials in which the inhomogeneities are controllable. It is increased understanding of the wave evolution processes in homogeneous and controllable

heterogeneous explosives that this research addresses.

Classical homogeneous initiation can be illustrated using a time-distance diagram (first drawn by Chaiken<sup>3</sup> and later by Campbell, Davis and Travis<sup>1</sup>) as shown in Figure 1. The explosive is shocked and, after an induction period (which depends on the initial shock pressure), a thermal explosion occurs at the explosive/driver interface. After the explosion, a superdetonation runs forward into the precompressed explosive. Eventually, the superdetonation overtakes the initial shock and then decays to a steady ZND detonation. It seems reasonable that establishment of the superdetonation is more complex than this picture. Recently Kapila, et al.<sup>4,5</sup> have studied the homogeneous initiation process theoretically (in gaseous systems) and have obtained both analytical and numerical evidence of a more complex series of steps that lead to the superdetonation. Their ideas lead to modifications of the

\*Work performed under the auspices of the U.S. Department of Energy

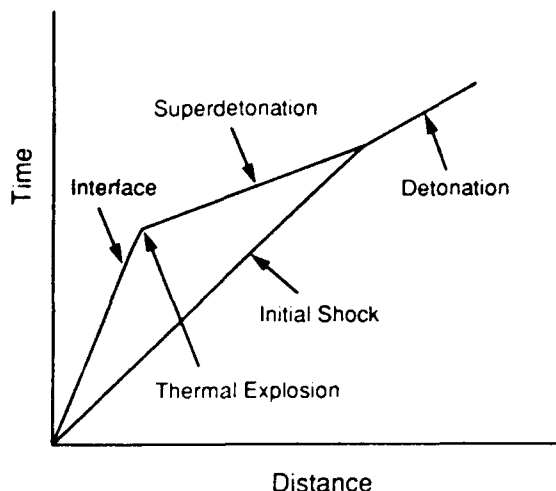


Figure 1. Time-Distance Diagram for the Classical Homogeneous Explosive Initiation Process

classical homogeneous model as shown in Figure 2. They have found an unsteady process in which the superdetonation develops from a weak detonation that, in turn, results from the thermal explosion at the input boundary. The weak detonation slows down and evolves into a superdetonation which then overtakes the initial shock. In this work we are looking for experimental evidence of how the superdetonation develops. This has been done by making in-situ measurements in a condensed-phase homogeneous nitromethane (NM) based explosive.

Studies of initiating NM have been conducted by a number of researchers in the past 30 years. Chaiken<sup>3</sup> (1957) studied shock-initiated NM and developed the time-distance diagram shown in Figure 1. Campbell, Davis, and Travis<sup>1</sup> (1961) produced considerable evidence that established the currently accepted homogeneous initiation model described above. Dremine, et al.<sup>6</sup> (1965) reported embedded electromagnetic gauge measurements that also support the ideas of the model; unfortunately, they were only able to make one measurement per experiment and because of inconsistencies in the explosive drivers, it was impossible to get a clear picture of the wave evolution process. Berke, et al.<sup>7</sup> (1970) studied NM, along with ten other liquid explosive materials, looking for clues as to the chemistry involved in the initiation process. Although there were definite clues, this

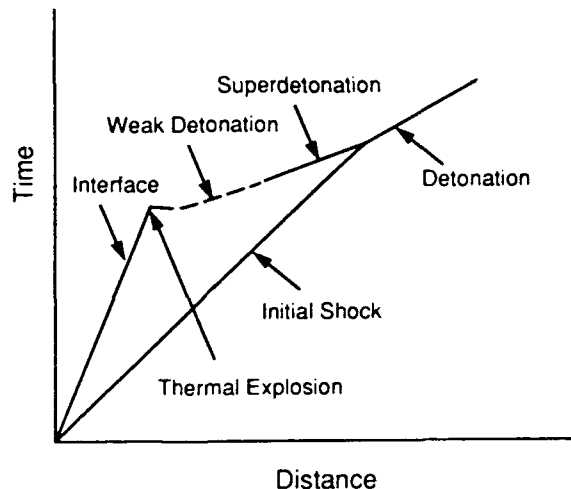


Figure 2. Time-Distance Diagram of Kapila, et al.<sup>5</sup> for Gaseous Explosive Initiation, Showing the Development of the Superdetonation

work was apparently stopped before in-depth understanding developed. Hardesty<sup>8</sup> (1976) reported gun-driven experiments in which a velocity interferometer system was used to measure the input boundary velocity and compare it to emitted light information obtained on the same experiments. Walker and Wasley<sup>9</sup> (1970) did very large scale experiments to study the initiation process at lower pressures than in the previous studies. Walker<sup>10</sup> (1979) also reported work in which initiation sensitivity was measured (at the same low input pressures) as a function of diethylenetriamine addition to the NM.

In all these studies, very few successful in-material measurements have been made to measure the evolutionary buildup process. Since all the experiments involve explosive driver systems (with the exception of those by Hardesty), the pressure inputs to the NM were not constant and sometimes ill-defined. The measurements usually made were time histories of shock trajectories, motion of boundaries, or emitted light--the latter being the most common. These studies all generally support the classical homogeneous initiation model, but details of the buildup process remain unknown. In addition, conflicts exist in superdetonation velocity measurements and in thermal-explosion-time data, depending on how the measurements were made and by whom. It was to clarify some of these conflicts and to

begin to understand the details of the buildup process that brought us to use a multiple, embedded particle velocity and impulse gauge technique to look again at this evolving reactive process.

A heterogeneous initiation process<sup>2</sup> is different from the homogeneous case in that wave growth occurs at the front, as well as behind the front. Such a wave has a relatively orderly growth to detonation, rather than the abrupt changes caused by a superdetonation. Little is known about the mechanisms that produce the wave growth other than that shock-induced hot spots develop at the inhomogeneities. This makes the explosive much more sensitive than it would be without the inhomogeneities. To date, the size and nature of the inhomogeneities have not been sufficiently controllable to allow detailed understanding.

Engelke<sup>11</sup> and Engelke and Bdzil<sup>12</sup> have made detailed studies on simple prototypical NM based condensed explosives concerning how chemical and physical sensitization of the NM affect steady two-dimensional detonation. It seems reasonable to expect corresponding sensitization effects in the initiation regime. We have studied the initiation process using these *same* materials. Our experiments are superior to earlier initiation work in two important respects: (1) the chemically driven flow fields were measured directly by use of in-situ, multiple electromagnetic gauges and (2) chemical reaction was induced in the test materials by use of gas-gun-driven projectiles allowing precise control of the initial fluid-dynamic state and following flow.

In this paper we describe the experimental setup, followed by a discussion of the homogeneous experiments and then a discussion of the heterogeneous experiments.

## EXPERIMENTAL SETUP

The liquid explosive NM was our homogeneous prototype; it was chemically sensitized to allow initiation with the available gas gun. (Chemically sensitized NM has long been known to be more sensitive to initiation than neat NM.<sup>13</sup>) The heterogeneous materials were produced from NM by

controlled addition of solid heterogeneities to gelled NM. Since the homogeneous and heterogeneous explosives are chemically similar, results obtained from the two cases help to separate the chemical from the physical effects. Addition of heterogeneities allows more rigorous control of hot-spot characteristics (e.g., size, spatial distribution, shape) than is feasible with standard (e.g., pressed) explosives.

The homogeneous, chemically sensitized NM was made by adding 5 wt% of the liquid organic base diethylenetriamine ( $\text{NH}_2(\text{CH}_2)_2\text{NH}(\text{CH}_2)_2\text{NH}_2$ --hereafter called DETA) to liquid commercial-grade NM to make a 95/5 wt% NM/DETA material. The heterogeneous material was made by gelling commercial-grade NM (with guar gum) to which silica beads had been added; the final composition was 92.75/6.0/1.25 wt% NM/silica/guar gum. For details concerning the materials and how they were prepared see References 11 and 12.

All the experiments were done using an 8-m long, 72-mm diameter bore single-stage gas gun capable of projectile velocities up to 1.43 mm/ $\mu\text{s}$ . An electromagnet was installed in the gun target chamber to provide the magnetic field ( $\approx 825$  gauss) for the magnetic gauging setup.

Electromagnetic gauging in shock experiments was first reported by Zaitsev, et al. in the Soviet Union in 1960.<sup>14</sup> The system that we are using was developed by Vorthman and Wackerle in the early 1980's.<sup>15</sup> The gauge package includes, in addition to particle velocity gauges, impulse gauges which were first reported by Young, Fowles, and Swift.<sup>16</sup> (We refer to this gauge package as an MIV gauge, for Magnetic Impulse and Velocity gauge.) The MIV gauge package is an  $\approx 60$   $\mu\text{m}$  thick membrane, which is suspended in the liquid so that a particle velocity and an impulse measurement are made at each Lagrangian position. The use of this gauging system is discussed in detail in Reference 15. In theory it is possible to measure particle velocity, impulse (pressure), and shock velocity in an unreactive material with the MIV gauge technique. In our experiments, reaction causes changes in the flow field from

one gauge to the next, so only average shock velocities are obtained. The impulse data are used primarily as an indicator of the pressure because of the difficulties encountered in numerical differentiation. The particle velocity data are the most reliable measured quantity and are the primary information obtained.

Since the NM materials were liquids, a 68.6-mm outside diameter cell made from Plexiglas (PMMA) was used to clamp the gauge package and contain the sample material. (Details of the gauge and cell construction are shown in Figure 3.) The cell fronts were either Kel-F or Plexiglas (depending on the pressure desired in the sample material) and were approximately 6 mm thick. The MIV gauge membrane was suspended in the cell at a 30 degree angle with the cell front, giving 5 particle velocity and 5 impulse gauge measurements in each experiment (one of each gauge type at a common axial position), with each of the 5 axial positions separated by approximately 1 mm. The inside of the cell, which comes in

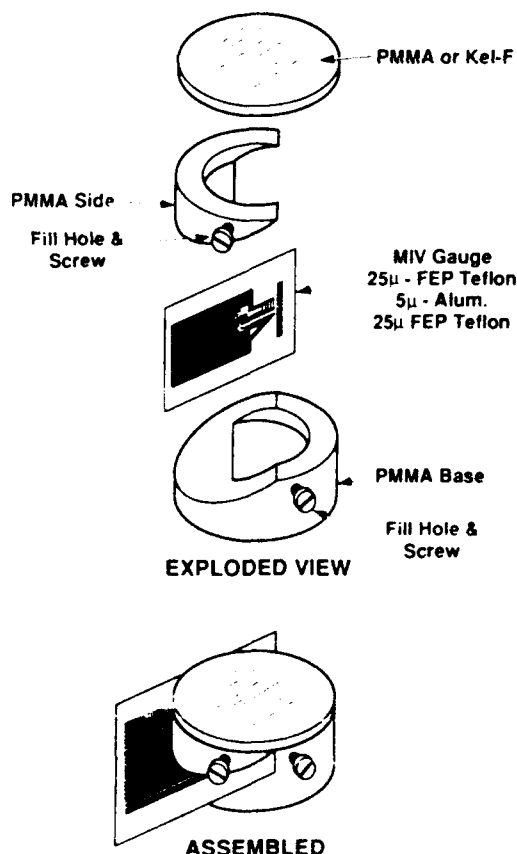


Figure 3. Cell and Gauge Construction Details

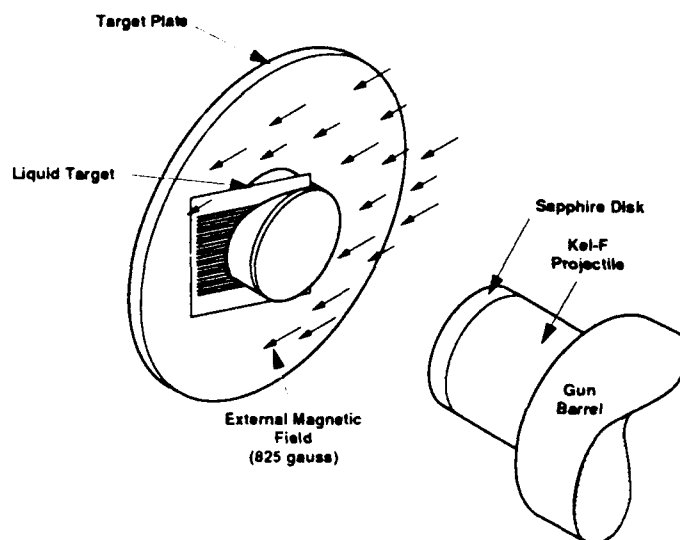


Figure 4. Projectile and Target Just Before Impact

contact with the NM, was lined with Teflon film to eliminate any NM attack on the PMMA. Before the cell front was attached, the positions of the gauges in the cavity were measured with a depth measuring microscope. After a cell was filled with explosive, care was taken to eliminate all the air bubbles in the explosive before sealing. In all cases, the shock initiation experiment was completed within 3 hours of filling.

Input to the NM was by a well-controlled gas-gun-driven Lexan projectile with a sapphire facing. Inputs ranged from 5.8 to 7 GPa (projectile velocities of 1.26 to 1.42 mm/μs). The target was positioned between the pole pieces of the electromagnet in a region where the magnetic field was uniform to within 1 percent. A schematic of the projectile and target is shown in Figure 4.

## RESULTS AND DISCUSSION

Shot data for each of the experiments are given in Table 1. Because Hugoniot for the two materials have not yet been measured, we used the "universal" liquid Hugoniot<sup>17</sup> for the shock velocity-particle velocity relationship, along with the appropriate densities, to obtain the input conditions by impedance matching. The input conditions are estimates with an accuracy of a few percent. These will be corrected later after the Hugoniot are measured.

Table 1. Nitromethane Shot Data

Impedance Match NM Input Conditions							
Shot No.	Impactor Mat'l	Cell Front Mat'l	Proj. Vel. mm/ $\mu$ s	Initial Density Mg/m <sup>3</sup>	Part. Vel. mm/ $\mu$ s	Stress GPa	Shock Vel. mm/ $\mu$ s
Homogeneous (95/5 wt% NM/DETA)							
747	Sapphire	Kel-F	1.41	1.11	1.48	6.8	4.12
755	Sapphire	Kel-F	1.26	1.11	1.34	5.8	3.89
Heterogeneous (92.75/6.0/1.25 wt% NM/silica/guar gum)							
748	Sapphire	Kel-F	1.42	1.17	1.47	7.0	4.10
754	Vistal	PMMA	1.42	1.17	1.33	6.0	3.88
756	Sapphire	Kel-F	1.39	1.17	1.44	6.8	4.06

### Homogeneous NM

Particle velocity profiles and the resulting time-distance (t-x) diagram from Shot 747 (a 95/5 wt% NM/DETA experiment with a NM input pressure of 6.8 GPa) are shown in Figure 5. (The third gauge record was noisy because the recording digitizer differential comparator was set incorrectly.) Notice the constant level initial shock, followed by changes in the waveform due to shock-induced reaction considerably behind the shock front. In this experiment transition to detonation occurred between the third and fourth gauges, as indicated by the changes in particle velocity waveform profiles. Times at both the start and the top of the growing wave (at each gauge position) were determined from the particle velocity waveforms, plotted on each gauge trajectory, and then joined to produce the wave paths shown in the t-x diagram. Notice they coalesce into a single shock.

This diagram indicates the detonation-wave evolution process occurs over a relatively long time and distance, with the wave starting out as a compressive wave and growing to form a shock. As shown, a superdetonation does not form immediately at the input boundary, but rather after a relatively long buildup process. In fact, we can only infer from our records that a superdetonation occurs just before overtake of the initial wave.

This inference is made because a wave of superdetonation velocity is required to link up the information from the particle velocity gauges into the consistent picture shown in Figure 5(b). In this figure, the dashed line with the shallow slope represents the locus of a superdetonation that would be required to agree with the initial shock overtake time observed from the waveforms, and indicates clearly that a relatively long induction time would be required when compared to our data. In previous studies, streak camera measurements of emitted light as the initiation progressed led to the model of the superdetonation being formed immediately after the thermal explosion at the input NM boundary. In our experiments, we do not yet know at what point light would begin to be emitted with an intensity that a streak camera could record.

A similar analysis was done for Shot 755, but since the wave did not completely grow to a detonation before the end of recording, it was only possible to estimate the condition where detonation would have been attained.

The evolving wave in this experiment achieved about the same wave shape at the position of the fifth gauge as was observed in the second gauge of Shot 747. The time-to-overtake data are tabulated in Table 2 for these two experiments.

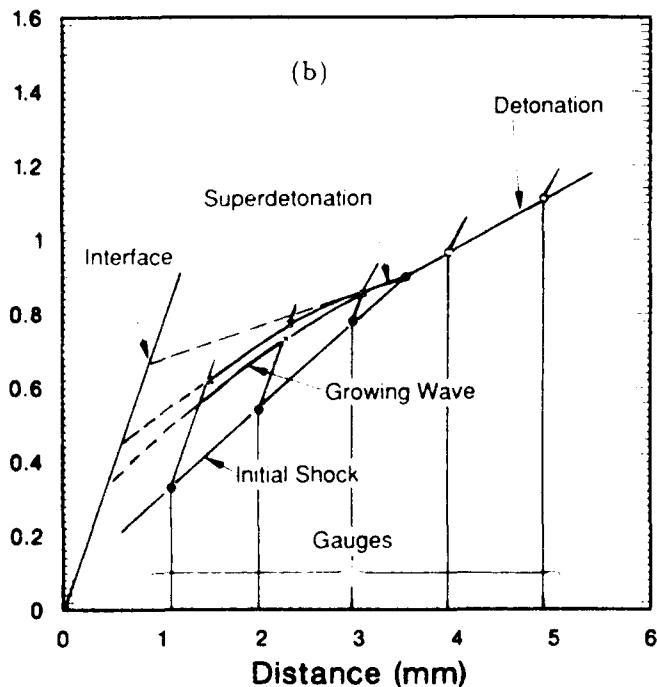
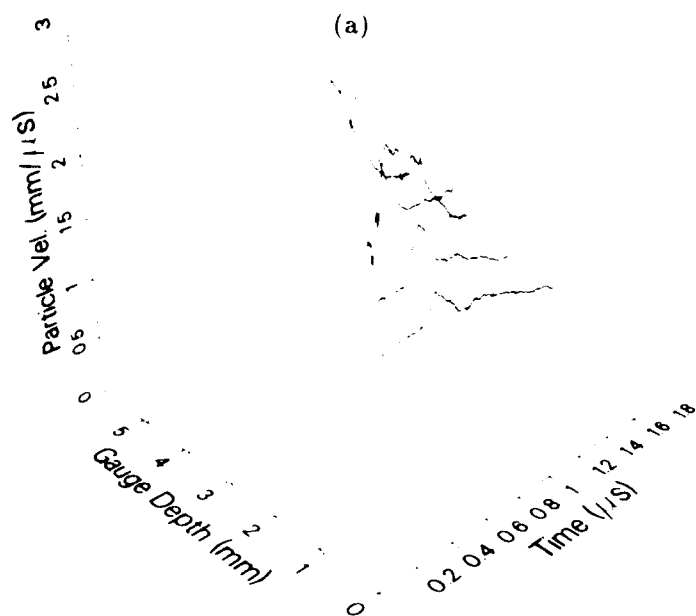


Figure 5 Particle Velocity Waveforms from Shot 747 are Shown in (a) and the Resulting Time-Distance Diagram in (b)

To give some idea of how our work fits with previous studies, we compare it to the work of Hardesty.<sup>8</sup> He reported a series of very nice powder gun driven experiments in which the NM input boundary particle velocity was measured using a VISAR velocity

interferometer system.<sup>18</sup> In the same experiments, the emitted light was measured with a streak camera in the same way that it had been done in several previous studies. These experiments were done on neat NM with pressures generated in the NM being between 7 and 9 GPa. Because the inputs were the result of projectile impact, a (known) constant state was developed in the NM after the initial shock. Hardesty observed that particle velocity decay at the input interface occurred considerably before any emitted light was visible on the streak camera record; in fact, the decay occurred in about 50 to 60 percent of the time to first light. He stated that using the emitted light to indicate the thermal explosion may lead to overestimates, by nearly a factor of two, in the induction time. He did not, however, indicate what effect this observation would have on the accepted homogeneous initiation model. It is obvious that decreasing the thermal explosion time by a factor of two, while leaving the time at which the superdetonation overtakes the initial wave the same, would lead to a low velocity superdetonation, too low to be physical.

If we fold our data into this picture, interpreting the information so that the reaction (i.e., the particle velocity relaxation) occurs earlier and the reactive wave does not give off sufficient light to record with the streak camera until it has built up to a strong compression wave, then our information agrees rather well with the observations of Hardesty. In this case it becomes necessary to modify the homogeneous initiation model to include these features. This new model is shown by the  $t$ - $x$  diagram of Figure 5(b). If the two models shown in Figures 1 and 2 are contrasted to our diagram, it is easy to identify considerable differences. In our model the superdetonation develops from a growing compression wave which starts from the runaway chemical reaction at the input interface, with the buildup occurring over a considerable time and distance. This sharply disagrees with the idea that the superdetonation forms immediately, giving off sufficient light to record, and indicates that emitted light is not a good measure of the induction time (time to runaway chemical reaction or a thermal explosion).

Table 2. Homogeneous NM Relaxation and Overtake Data

Calculated NM Input Conditions				From Gauge Meas.		Overtake Conditions	
Shot No.	Part. Vel. mm/ $\mu$ s	Pressure GPa	Shock Vel. mm/ $\mu$ s	Part. Vel. mm/ $\mu$ s	Pressure GPa	Distance mm	Time $\mu$ s
747	1.48	6.8	4.12	1.30	6.2	3.3	0.9
755	1.23	5.8	3.89	1.24→1.18	5.5→5.1	≈7.8	≈2.0

We are not yet prepared to guarantee that Figure 5(b) is the correct model for homogeneous NM initiation. Additional experiments will be required to eliminate the possibility of gauge perturbations and demonstrate that this model is correct. It should also be remembered that we are working with NM/DETA homogeneous explosive rather than neat NM, although the agreement between our data and Hardesty's neat NM data seems to indicate they have similar behavior. We also note that addition of 5 wt% of DETA to NM produces a small amount of the DETA/NM salt in suspension in the NM. We plan to eliminate this complication, in the future, by working with lower DETA concentrations.

Another interesting aspect of our measurements is that in each of the homogeneous NM experiments, the condition in the initial shock was somewhat different from that expected for the particular impact conditions and the estimated Hugoniot of the materials involved. The gauge measurements of the initial wave indicate a lower pressure (and also particle velocity) state than would be expected based on estimating the input NM conditions by impedance matching (by about 10% in both pressure and particle velocity). We feel this difference is more than the uncertainty in the Hugoniot for the NM, indicating that something (perhaps endothermic chemistry) may be happening in the initial wave. In fact, the particle velocity and impulse waveforms recorded on Shot 755 show a generally decreasing state from the first to the fifth gauge. To illustrate this difference, the expected input state and the measured state in the initial wave are

compared in Table 2 for the two homogeneous experiments.

Time-to-overtake values obtained from the t-x diagrams are also tabulated in Table 2. In Shot 747, overtake occurred between the third and fourth gauges and it appears that, to make all the times come out correctly, the reactive wave grew to a superdetonation prior to overtaking the initial wave. In the case of Shot 755, we extrapolated the measured wave behavior to where we thought the overtake would have occurred if a longer measurement were possible. These data have been plotted on a Pop-plot, along with some of the available neat NM data (taking some liberty in interpreting the data, because all the previous experimenters did not report the time-to-overtake). These are all shown in Figure 6. Data given in the figure are these: C,D,T are from Campbell, Davis, and Travis,<sup>1</sup> Hard. are

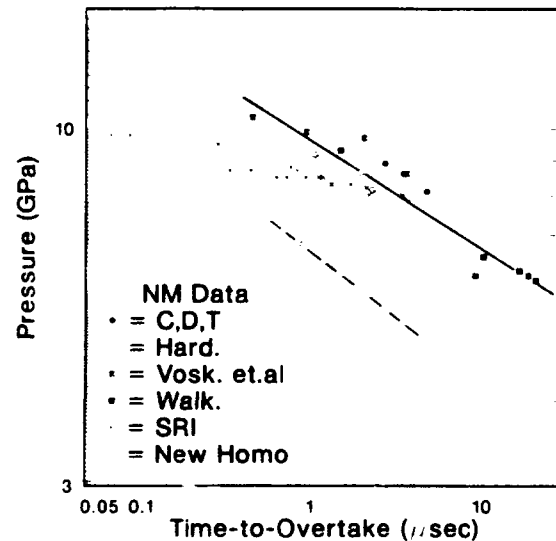


Figure 6. Pop-Plot of Our New Data for Sensitized NM and Some of the Available Data on Neat NM

Table 3. Heterogeneous NM Detonation Transition Conditions

Calculated NM Input Conditions				Transition Conditions	
Shot No.	Part. Vel. mm/ $\mu$ s	Pressure GPa	Shock Vel. mm/ $\mu$ s	Distance mm	Time $\mu$ s
748	1.47	7.0	4.10	3.2	0.72
754	1.33	6.0	3.88	4.57	0.93
756	1.44	6.8	4.06	3.27	0.74

from Hardesty,<sup>8</sup> Vosk. et al. are from the Soviet Union,<sup>19</sup> Walk. are from Walker and Wasley,<sup>9</sup> SRI are from Berke, et al.,<sup>7</sup> and New Homo are from this study. A line has been drawn through the neat NM data (without the benefit of a fitting routine) to give some idea of the slope of the data. A line has also been drawn through the two points of this study for the chemically sensitized NM (remembering that the lower pressure point is an estimate) and, while it is not the same slope as that of the neat NM, it is similar and much different than for the heterogeneous data, which will be shown later. It is interesting to note that adding the 5% DETA to the NM increases the sensitivity greatly; the line moves down in pressure by  $\approx 3$  GPa at an overtake time of 1  $\mu$ s.

### Heterogeneous NM

The buildup in the heterogeneous NM experiments was totally different from that observed in the homogeneous experiments. Figure 7 is a plot of the particle velocity waveforms measured in Shot 748 where the explosive was heterogeneous NM (92.75/6.0/1.25 wt% NM/silica/guar gum with an input pressure of 7.0 GPa). The gauge records indicate a wave that is growing both at the front and behind the front. Because of this growth in the front, it is impossible to estimate from the records what the input condition was. We have calculated this condition using impedance matching techniques, and the estimated input conditions are given in Table 1. Although the input conditions varied from 6 to 7 GPa, the wave forms from each experiment were similar. The t-x diagrams were plotted from the gauge data and the time and distance-to-detonation

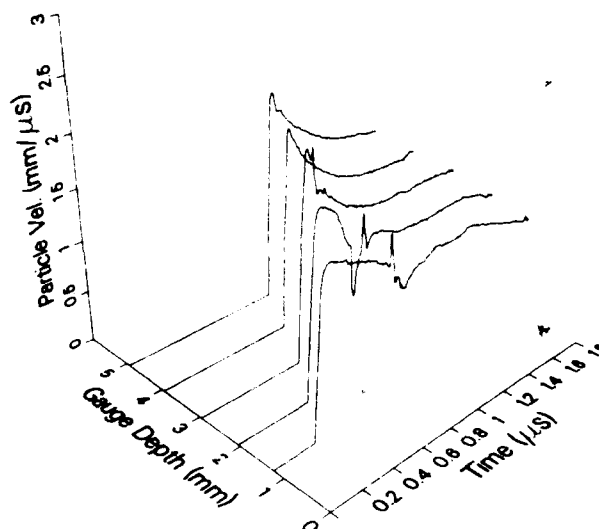


Figure 7. Particle Velocity Waveforms from Shot 748; Input 7.0 GPa

conditions were determined. These are tabulated, along with the estimated input conditions, in Table 3.

In all three heterogeneous experiments, an electrical burst occurred at about the same time that the apparent transition-to-detonation occurred. Evidence of this phenomenon can be seen in Figure 7 (in the form of noise on the particle velocity waveforms) indicating that the transition occurred between the third and fourth gauges. The source of this signal is unknown (it was not observed in the homogeneous experiments) although a similar phenomena was observed by Sheffield in shock-induced reacting carbon disulfide experiments done at Washington State University several years ago.<sup>20</sup> We used this electrical burst to pinpoint the transition-to-detonation when drawing the t-x diagrams.

The three time-to-detonation points for heterogeneous NM are plotted, along with



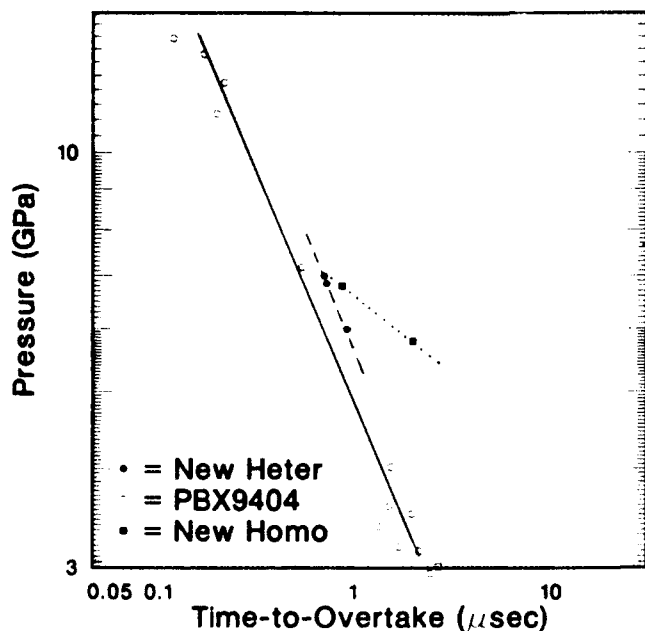


Figure 8. Pop-Plot for Heterogeneous NM, along with Other Materials for Comparison

the homogeneous data of this study and several data for PBX 9404,<sup>21</sup> in Figure 8. Lines have been drawn through all three sets of data to give some idea of the relationship between them. The heterogeneous NM is very close to the PBX 9404 data in both position and slope, showing that it is a relatively sensitive material. The slope of the chemically sensitized homogeneous NM is much different from the heterogeneous NM slope. It is interesting to note that one homogeneous datum and two heterogeneous data are nearly in the same position on the Pop-plot so that they achieved detonation in similar times and distances but the waveforms (and the initiation process) of Figures 3 and 7 are completely different.

Waveforms obtained in the heterogeneous experiments are consistent with earlier studies on solid, heterogeneous explosives, i.e., the wave grows at the front (as well as behind the front) into a detonation. However, we believe that a great deal can be learned about heterogeneous initiation by varying the size, number density, shape, and nature of the heterogeneities in the gelled NM. We conjecture that it will be possible to tailor initiation waveform profiles by changing the variables associated with the heterogeneities.

## SUMMARY AND CONCLUSIONS

In-situ multiple magnetic gauging experiments have been completed on homogeneous and heterogeneous NM. The homogeneous explosive was made by chemically sensitizing neat NM. This made it sensitive enough that it could be initiated with our gas gun, allowing a well-controlled input to the liquid explosive. We measured particle velocity profiles at discrete Lagrangian positions from initiation to detonation in a single experiment with multiple gauges. Based on our measurements, we have proposed important refinements to the classical homogeneous shock-to-detonation initiation model, including a relatively long reactive wave buildup which evolves into a superdetonation that overtakes the initial shock. This differs considerably from the classical model in which a thermal explosion occurs, immediately producing a superdetonation which travels a considerable distance in the precompressed NM before overtaking the initial shock. The chemically sensitized NM has a similar slope in the Pop-plot plane to neat NM but offset to lower pressures by  $\approx 3$  GPa.

Heterogeneous NM was produced by gelling the NM and suspending silica particles in it. Again we measured from initiation to detonation in a single experiment. Growth occurred both at and behind the front in a manner similar to that which has been measured in other heterogeneous materials. The sensitivity of this physically sensitized heterogeneous NM was similar to that of PBX 9404 ( $\rho_0 = 1.84 \text{ Mg/m}^3$ ) both in slope and position on a Pop-plot. We hope this is the first step in a program in which considerable understanding can be developed concerning the role of hot spots in heterogeneous initiation, as we can control the size, shape, number density, and impedance of the heterogeneities.

That these experiments could be done over the full detonation regime without gauge failure has been gratifying. This technique will almost certainly lead to a more detailed understanding of the buildup process in both homogeneous and heterogeneous systems. We are, however, concerned about gauge

perturbations and must check this possibility out carefully before making categorical statements. Much remains to be done to completely understand the processes observed in the waveforms we have already obtained. It will take a number of gun experiments on both the homogeneous and heterogeneous materials to rule out gauge perturbation effects and determine how the process varies with input conditions. At the present time, the consistency of our data, both between the experiments we have done and also with the earlier studies, suggests the perturbations are small.

## REFERENCES

1. Campbell, A. W.; Davis, W. C.; and Travis, J. R., *Phys. Fluids*, Vol. 4, 1961, p. 498.
2. Campbell, A. W.; Davis, W. C.; Ramsay, J. B.; and Travis, J. R., *Phys. Fluids*, Vol. 4, 1961, p. 511.
3. Chaiken, R. F., *The Kinetic Theory of Detonation of High Explosives*, M.S. Thesis, Polytechnic Institute of Brooklyn, (written June 1957, published 1958).
4. Kapila, A. K. and Jackson, T. L., "Dynamics of the Hot-Spot Evolution in a Reactive Compressible Flow," *Proceedings of the Workshop on Computational and Dynamics of Reactive Gas Flows*, Institute for Mathematics and its Application, University of Minnesota, Springer Verlag, 1988.
5. Kapila, A. K. and Dold, J. W., "A Theoretical Picture of Shock-to-Detonation Transition in a Homogeneous Explosive," *Proceedings of the Ninth Symposium (International) on Detonation*, Portland, OR, 28 Aug-2 Sep 1989.
6. Dremin, A. N.; Savrov, S. D.; and Andrievskii, A. N., *Comb. Expl. and Shock Waves*, Vol. 1, 1965, p. 1.
7. Berke, J. G.; Shaw, R.; Tegg, D.; and Seely, L. B., "Shock Initiation of Nitromethane, Methyl Nitrite, and Some Bis Difluoramino Alkanes," *Proceedings of the Fifth Symposium (International) on Detonation*, Office of Naval Research Report ACR-184, 1970, p. 237.
8. Hardesty, D. R., *Combustion and Flame*, Vol. 27, 1976, p. 229.
9. Walker, F. E., and Wasley, R. J., *Combustion and Flame*, Vol. 15, 1970, p. 233.
10. Walker, F. E., *Acta Astronautica*, Vol. 6, 1979, p. 807.
11. Engelke, R., *Phys. Fluids*, Vol. 22, 1979, p. 1623; Vol. 23, 1980, p. 875.
12. Engelke, R. and Bdzil, J. B., *Phys. Fluids*, Vol. 26, 1983, p. 1210.
13. Forshey, D. R.; Cooper, J. C.; and Doyak, W. J., *Explosivstoffe* No. 6, 1969, p. 125.
14. Zaitsev, V. M.; Pokhil, P. F.; and Shvedov, K. K., *Doklady Akademii Nauk. SSSR*, Vol. 132, 1960, p. 1339.
15. Vorthman, J. and Wackerle, J., "Multiple-Wave Effects on Explosives Decomposition Rates," *Proceedings 1983 APS Topical Conference on Shock Waves*, Published by North-Holland, Amsterdam, 1984, p. 613; Vorthman, J.; Andrews, G.; and Wackerle, J., "Reaction Rates from Electromagnetic Gauge Data," *Proceedings of the Eighth Symposium (International) on Detonation*, Albuquerque, NM, 15-19 Jul 1985, p. 99.
16. Young, C.; Fowles, R.; and Swift, R. P., in *Shock Waves and the Mechanical Properties of Solids*, Edited by Burke, J. J. and Weiss, V., Syracuse University Press, 1971, p. 203.
17. Woolfolk, R. W.; Cowperthwaite, M.; and Shaw, R., *Thermochimica Acta*, Vol. 5, 1973, p. 409.
18. Barker, L. M. and Hollenbach, R. E., *J. Appl. Phys.*, Vol. 43, 1972, p. 4669.
19. Voskoboinikov, I. M.; Bogomolov, V. M.; Margolin, A. D.; and Apin, A. Ya., *Doklady Akademii Nauk. SSSR*, Vol. 167, 1966, p. 610.
20. Sheffield, S. A., *Shock-Induced Reaction in Carbon Disulfide*, Ph.D. Dissertation, Washington State University, 1978.

21. Gibbs, T. R. and Popolato, A., Eds., *IASI Explosive Property Data*, University of California Press, Berkeley, CA, 1980, p. 359.

## DISCUSSION

LOUIS B'UN, CEA, France

How does your "new model" for initiation of detonation in nitromethane compare with the current model for initiation of PBX?

## REPLY BY S. A. SHEFFIELD

Our new model, which is a refinement of the model of Campbell-Davis-Travis-Chaiken, applies to homogeneous explosives. In general, PBX materials are considered to be heterogeneous in nature. Only when they are pressed to very nearly theoretical density or when the particle sizes of the explosive component of the PBX are very small (on the order of a few microns) do these materials start to have some of the features of homogeneous explosives. In the limit of solid explosives very near their theoretical maximum density (and for single crystals of pure explosives), it is likely that some or all of the features we have observed for liquid homogeneous materials also apply.

We expect the work we have done on heterogeneous nitromethane based explosives to have direct application to the initiation of PBX materials (which are clearly

heterogeneous in nature). Our work shows that the initiation behavior of these materials is very similar to the initiation behavior observed in other heterogeneous explosives, including PBX materials. The heterogeneous model described earlier by Campbell, Davis, Travis, and Ramsay applies. Although we have not yet done a large number of embedded gauge experiments on heterogenized nitromethane, we have not found any profound differences between our observation and those of earlier workers. We do feel, as stated in our paper, that by changing various parameters of the heterogenized nitromethane, such as the density, impedance, size, and number density of the heterogeneities, we should be able to tailor the nature of the initiation buildup process. While the conditions of having inert particles in an explosive matrix are not the same as those of experiments on solid explosive materials in which an explosive with a well defined particle size is embedded in an inert matrix (such as those described by Moulard in the previous paper), we feel that the initiation behavior should be similar. If this does indeed prove to be the case, our research in this area should lead to a much better understanding of the role of hotspots in heterogeneous explosive initiation. It is clear that we can control the nature of the hotspots much better than is the case when a material is pressed from an explosive powder.

# DECOMPOSITION OF HIGH EXPLOSIVES IN SHOCK AND DETONATION WAVES

V. E. Fortov and G. I. Kanel

Institute of High Temperature

USSR Academy of Sciences, Moscow, 127412, USSR  
and

T. N. Fortova, S. I. Malyrenko, and A. V. Utkin

Institute of Chemical Physics

USSR Academy of Sciences, Chernogolovka  
Moscow Region, 142432, USSR

*Cast and pressed TNT, RDX, and phlegmatized RDX have been investigated in series of experiments designed to provide information on macrokinetics of shock-wave decomposition of these high explosives. The shock-wave profiles of pressure were measured by manganin gauges in the pressure range of 2.5 - 15 GPa. The particle velocity history in detonation wave chemical spike was measured by VISAR and ORVIS interferometers. The particle velocity was measured at the interface between water window and aluminum foil that was in contact with high explosive sample. Computations have been conducted with received equations of state and macrokinetic for one-dimensional and two-dimensional geometries. Applicability of the kinetic in two-dimensional situation has been demonstrated by means of numerical simulation of the pressed TNT critical diameter.*

## INTRODUCTION

Information about the kinetics of high explosives (HE) decomposition in shock and detonation waves is needed for determining the operational safety, initiation, and explosion action computations. The process of shock initiation in solid explosives involves the nucleation of hot spots (i.e., localized regions of elevated thermal energy) behind the propagating shock front which act as ignition sites for a subsequent grain burning process that liberates energy by means of chemical reactions (e.g., References 1 and 2). At first, the greater part of the research on explosive initiation by shock waves concentrated on the experimental investigation of this phenomenon. Continuous measurement of flow parameters with the use of Lagrange gauges makes it possible to obtain information on explosive decomposition kinetics (e.g., References 3 and 4). But in this case there are many hard experiments to be carried

out. Also, in recent years more and more work is being done in the field of computer simulation of the detonation process.

While many recognize that models of HE burn should be based on first principles, there are numerous difficulties with this approach. Many authors studied such phenomena using various phenomenological models for simulating the chemical reactions (e.g., References 5, 6, and 7). Usually these models have some parameters that are often unknown and have to be measured in a limited number of experiments. The last method was used in this work to find the macrokinetic of shock wave decomposition of cast and pressed TNT, RDX, and phlegmatized RDX.

## EXPERIMENTAL RESULTS

The experimental schemes are shown in Figure 1. A high time resolution velocity

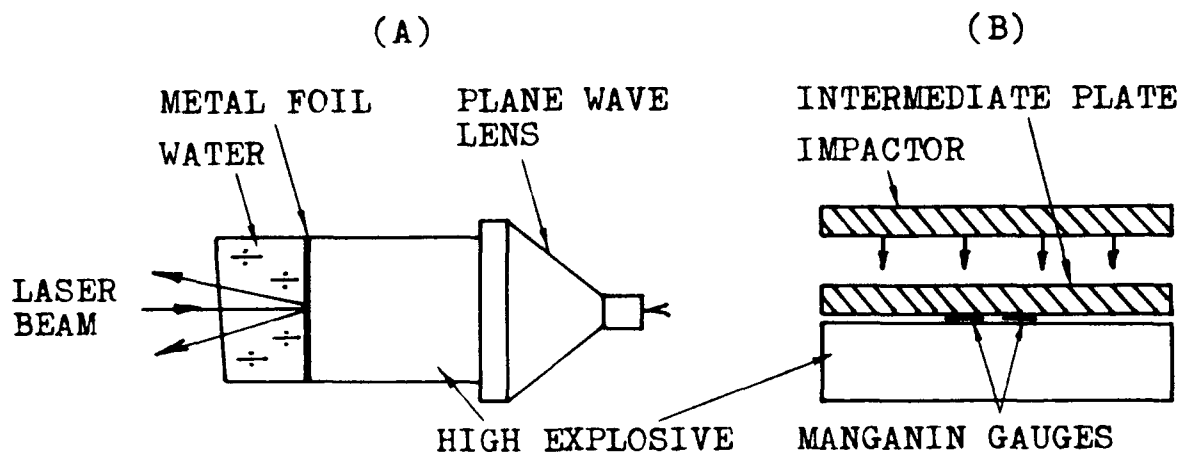


Figure 1. Experimental Schemes for Detonation Wave (A) and Shock-wave Profiles of Pressure (B) Measurements

systems ORVIS and VISAR were used for reaction zone structure recording of stationary detonation waves. Detonation fronts in HE have been examined through measurements of particle velocity histories resulting from the interaction of a detonation wave with a thin metal foil backed by a water window (Figure 1(A)) as is the case in Reference 10.

The shock wave profiles of pressure were measured by manganin gauges in the pressure range 2.5–15 GPa (Figure 1(B)). The pressure profiles were measured at the interface between the HE sample and intermediate plate. The shock waves with rectangular pressure profile were generated in the intermediate plate by high velocity impactor. The sample geometry afforded one dimensional situation.

The initial density of cast TNT was 1.60 g/cc, pressed TNT – 1.58 g/cc, RDX – 1.45 and 1.65 g/cc, phlegmatized RDX (contained 5 percent by weight phlegmatizer) – 1.41, 1.60, and 1.67 g/cc.

Measurements by manganin gauges of the profiles of pressure at the boundary between HE and inert plate are shown in Figure 2. The high explosive decomposition produces the pressure rise at the boundary. Maxima are formed on the profiles  $P(t)$ . These maxima are especially pronounced in dense charges. The final state on the boundary is determined by the condition that particle velocities and pressures in stationary detonation

products and inert plate are equal. Macrokinetic information about the HE Hugoniot and detonation products expansion isentrope through CJ point was found from these experiments.

One can see in Figure 2 that the initial pressure rise rate and maximum positions for

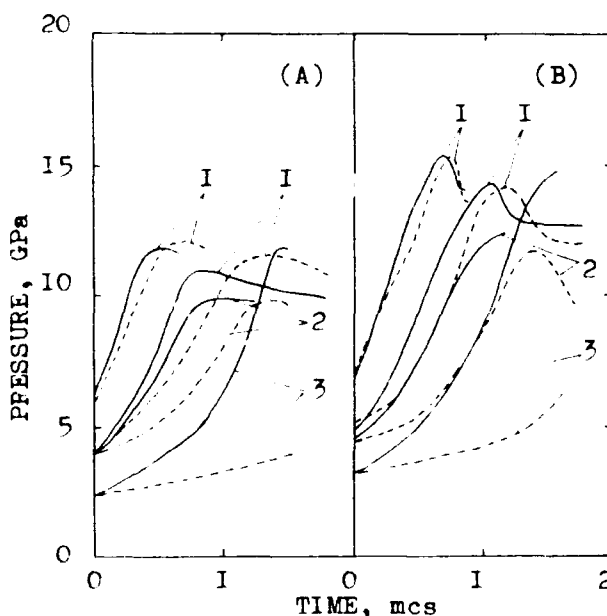


Figure 2. Experimental Profiles of Pressure Measured by Manganin Gauges for RDX (Solid Lines, (A) -  $g_0 = 1.45$  g/cc, (B) -  $g_0 = 1.65$  g/cc) and Phlegmatized RDX (Dashed Lines, (A) -  $g_0 = 1.41$  g/cc, (B) -  $g_0 = 1.60$  g/cc). The material of the intermediate plate: 1 - aluminum, 2 - PMMA, 3 - copper.

RDX and phlegmatized RDX differ, especially for densities 1.45 and 1.41 g/cc. That is phlegmatization lowers the HE sensitivity as well as decomposition rate. This agrees with hot spot forming mechanisms. The phlegmatizer coats the HE grain and, consequently, lowers the amount of potential ignition sites at low pressure, thus, decreasing the decomposition rate.

For example, in Figure 3 the particle-velocity histories of the aluminum foil/water interface for phlegmatized RDX of initial density 1.60 g/cc are presented. The interferometer system ORVIS was used in this case. The second jump of the velocity is caused by the shock reverberating between the high explosive/foil interface and the foil/water interface. The final velocity is determined by the intersection between the water Hugoniot and isentrope of the detonation products through CJ point. The foil thickness is shown in Figure 3. The reaction zone length of the RDX at the same density is not less. At the same time, the registered chemical spike amplitude in phlegmatized RDX (for equally foil thickness) is greater than it is in the RDX. It may be due to the following reasons: chemical spike amplitude in the RDX is less and/or initial reaction rate in the RDX is higher. According to the last circumstance, velocity spike will be quickly attenuated on passage through a foil. The VISAR was used

for registering the chemical spike in RDX with initial density 1.45 g/cc and phlegmatized RDX with initial density 1.41 g/cc.

Experimental results indicate that the reaction rate of pressed TNT is five times greater than cast TNT, both at detonation and the initiation threshold. The RDX decomposes faster than phlegmatized RDX during detonation initiation by plane shock wave. The change of phlegmatized RDX initial density from 1.41 to 1.67 g/cc decreases the reaction rate at the same pressure of initiation. A wide zone of chemical reaction for a detonation is decreased from 60 to 15 ns at CJ pressures, respectively.

## NUMERICAL SIMULATION

Experimental results were used to determine the empirical relationship of macrokinetic. For this purpose, we used a one-dimensional reactive hydrodynamic model of the process. Hydrodynamic calculations need an equation of state to describe the evolution of shock waves. The equation of states of the RDX and phlegmatized RDX are given by Mie - Grüneisen equation with the Birch's isotherm at O,K (Reference 11):

$$P_s = P_c(V_s) + G_s(E_s - E_c(V_s))/V_s$$

$$P_c = \frac{3}{2}B_0(y^7 - y^5)(1 - \frac{3}{4}(4 - B_1)(y^2 - 1)) \quad (1)$$

$$dE_c = -P_c dV_s, \quad y = 1/(g_m V_s)^{1/3}$$

where  $P_s$ ,  $V_s$ , and  $E_s$  = pressure, specific volume and internal energy for the solid phase,  $g_m$  = theoretical maximum density. Constants  $B_0$ ,  $B_1$  and  $G_s$  were found by approximating the HE Hugoniots for different densities. Figure 4 presents a comparison of experimental data and calculated Hugoniots for RDX and phlegmatized RDX. The constants used are presented in Table 1.

The product equation of state (gaseous phase) used for computer simulations was:<sup>12</sup>

$$P_g = P_l(V_g) + G_g(E_g - E_l(V_g))/V_g \quad (2)$$

$$P_l = Ae^{-aV} + B/V^n, \quad dE_l = -P_l dV_g$$

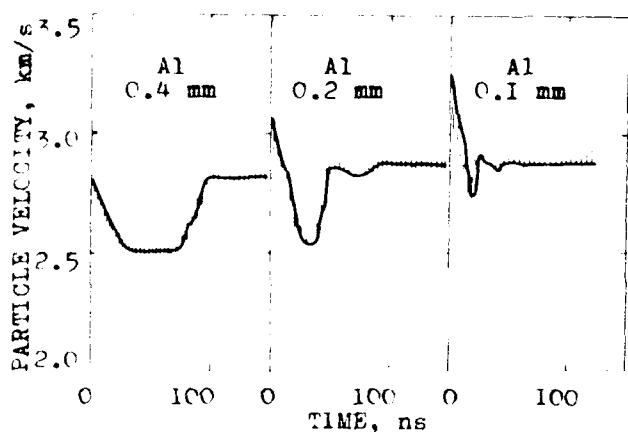


Figure 3 The Foil Surface Velocity vs Time for Phlegmatized RDX with Initial Density 1.60 g/cc. The dashed lines - experiments, solid lines - numerical simulation results

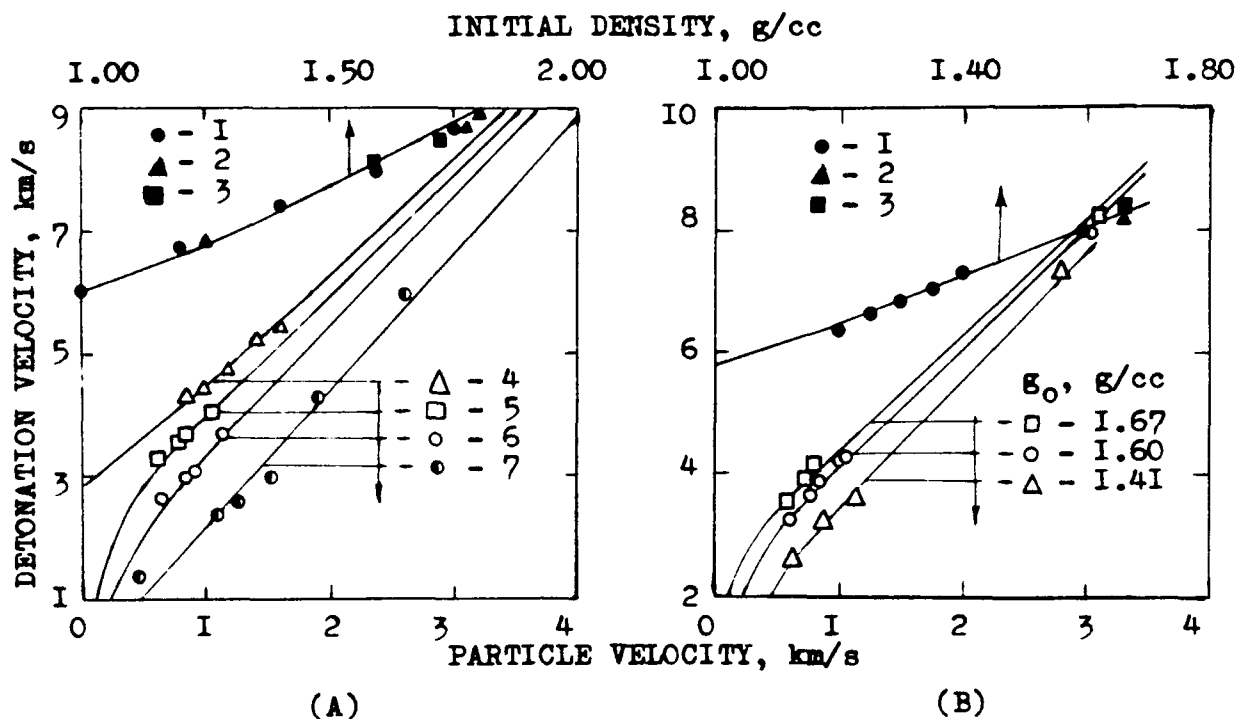


Figure 4. The Hugoniot of Porous HE (Shock-Wave Velocity  $D$  vs Particle Velocity) and Detonation Velocity  $D$  vs Initial HE Density. Solid lines are calculated, points - experimental data. (A) - RDX: 1 - Reference 20, 2 - Reference 21, 3 - Reference 22, 4 - Reference 23, 7 - Reference 20, 5 and 6 this work results. (B) - phlegmatized RDX: 1 - Reference 21, 2 - Reference 24, 3 - Reference 25,  $g_0 = 1.41, 1.60$ , and  $1.67$  g/cc - this work results.

Table 1 Equation of State Parameters for RDX (A) and Phlegmatized RDX (B)

	Unreacted HE				Reaction Products				
	$g_m$ , g/cc	$B_0$ , GPa	$B_1$	$G_s$	$A$ , GPa	$a$ , g/cc	$B$ , GPa	$n$	$G_g$
(A)	1.80	14.9	5.4	2.4	10922.7	16.35	4.73	2	0.3
(B)	1.72	13.2	6.4	2.4	896.2	10.11	3.98	2	0.3

Constants  $A$ ,  $B$ ,  $a$ ,  $n$  and  $G_g$  were found by approximating the final states in the manganese gauge experiments and experimental data for detonation velocity vs initial HE density. Figure 4 presents a comparison of experimental data and theoretical prediction for  $D(g_0)$  with constants from Table 1.

The Fortov's equation of state which describes original high explosive and detonation products uniformly have been used for cast and pressed TNT<sup>13</sup>. Equations of state for unreacted HE and reaction products joined with

some assumptions about mixture properties (e.g., Reference 14) allow the equation of state for the mixture to be found. This is required for reactive hydrodynamic model of the process with macrokinetic relationship. For numerical simulation of the experiments the phenomenological relationship have been used:<sup>15</sup>

$$C = K \cdot C^x \cdot (1 - C)^{1-x} \cdot (E_f - E_{to}) \cdot P \quad (3)$$

where  $C$  = mass fraction of detonation products;  $E_f$  = the specific energy for the shock

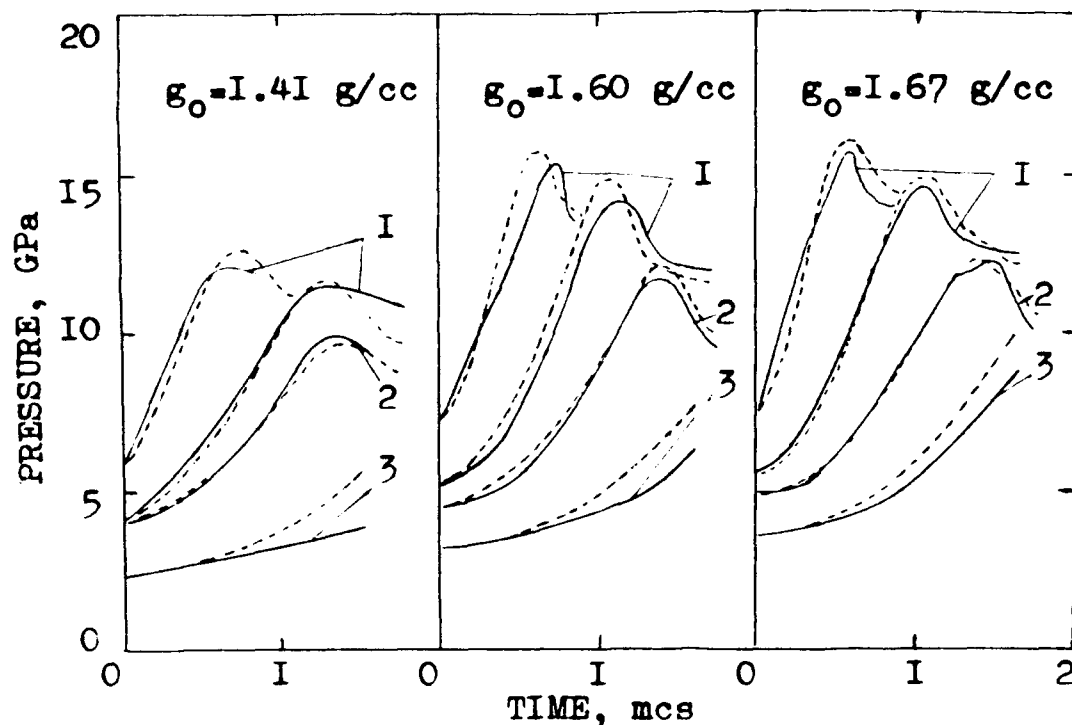


Figure 5 The Experimental Results (Solid Lines) and Numerical Simulation Results (Dashed Lines) for Phlegmatized RDX Detonation Initiation. The material of the intermediate plate: 1 - aluminum, 2 - PMMA, 3 - copper

wave passing through a particle,  $E_{t0}$  = the initiation threshold by shocks; and  $K$  and  $x$  = material parameters which depend on HE porosity. The equation form (3) was chosen by assuming that hot spots were generated, the reaction being initiated in them and extending over the hole volume as a combustion wave with a rate proportional to the pressure value. Unlike the hot spots initiation and growth model,<sup>7</sup> the number of activated hot spots is supposed to depend on the amplitude of the shock wave passed through the particle (being taken into account by  $(E_t/E_{t0})$  multiplier in Equation (3)) and not changing for the HE decomposition. The temperature is not included explicitly in the macrokinetic equation. This is due to the fact that different kinds of equations of state may be used without any phenomenological kinetic parameters correction. By this, as was shown in Reference 16, the calculation results agree within the experimental error. The multiplier in Equation (3) is responsible for the concentration that was chosen such that the decomposition rate at constant pressure had a maximum of  $C = x$ .

Figures 3 and 5 show the results of numerical simulation. It is clear that the macrokinetic relationship describes the experimental data with acceptable accuracy. In Table 2 the macrokinetic parameters are summarized. The higher initial decomposition rate of the RDX without phlegmatizator may be described successfully by decreasing the  $x$ -parameter, whose limiting value,  $x = 0$ , corresponds to the HE particle to be burned

Table 2. Macrokinetic Parameters for RDX (A), Phlegmatized RDX (B), Pressed TNT (C) and Cast TNT (D)

	$g_0$ , g/cc	$K \cdot 10^9$ , kb/(s·J·Pa)	$x$
(A)	1.45	0.5	0.0
	1.65	0.5	0.1
(B)	1.41	0.6	0.2
	1.60	0.8	0.3
	1.67	1.25	0.45
(C)	1.58	1.2	0.3
(D)	1.60	0.24	0.3



from its surface. According to the calculations, velocity spike decreases in RDX relative to one in phlegmatized RDX is caused by the greater initial reaction rate of the RDX chemical spike. Note that the cast and pressed TNT decomposition rates agree with detonation's critical diameters for these HE relations.<sup>17</sup> For phlegmatized RDX the dependence of the macrokinetic parameters upon the initial density may be expressed by the following equations:

$$K = 0.48(1 + 0.08/(1.72 - g_o)) \cdot 10^{-9} \text{ kg/(s} \cdot \text{J} \cdot \text{Pa)}$$

$$x = 0.13(1 + 0.20/(1.75 - g_o))$$

$$g_o = 1.41 - 1.67 \text{ g/cc.}$$

A limited number of the experimental data was used for numerical and physical experiment comparisons. Measurements carried out at the contact boundary allow the pressure range being investigated to be easily varied. The chemical spike structure data for steady detonation was also reproduced in the calculations.

Good agreement between numerical results and experimental data in the pressure range investigated provides a satisfactory description of the pressure pulse evolution through the HE sample. This conclusion is confirmed by showing in Figure 6 a comparison of the numerical pressure profiles and experimental data for cast TNT from Reference 18. In the experiments shock profiles in the intermediate plate were not perfectly rectangular. Taking into account the latter, the agreement may be recognized as acceptable regarding both qualitative wave profile evolution features and quantitative matter.

The calculation results based on empirical macrokinetic Equation (3) are in accordance with the experimental data in the one-dimensional flow and suggest utility for more general cases. Particularly, for numerical simulation of the detonation processes in finite size, HE samples close to critical, where the flow is not one dimensional, are interesting. According to experimental data from Reference 17, the pressed TNT critical diameter is nearly 3.2 mm. Therefore, the calculations

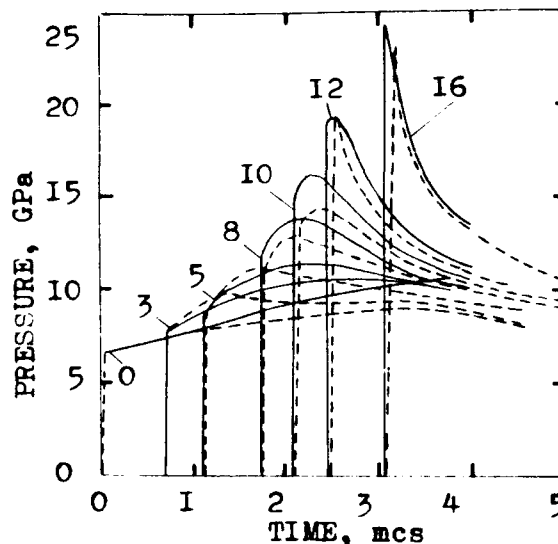


Figure 6. The Comparison of Experimental (Dashed Lines) Data and Calculated Profiles of the Pressure (Solid Lines) for Cast TNT. The distances from the intermediate plate (in mm) are denoted.

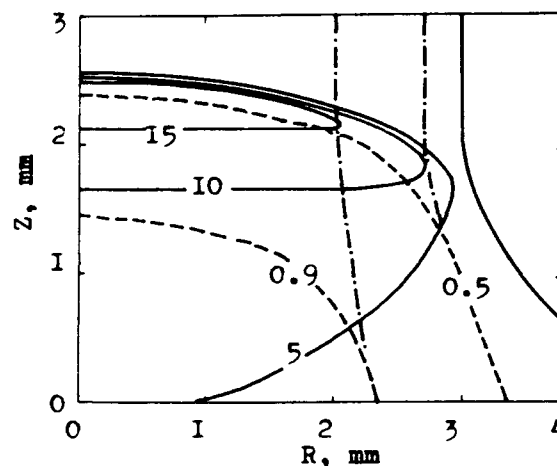


Figure 7. 2-D Simulation of Steady Detonation in Pressed TNT Results: Solid Lines - Isobars (the Pressures in GPa are Designated), Dashed Lines - the Constant Concentration Lines (the Values of  $x$  are Designated), Pointed Lines - Stream Lines.

were carried out for HE samples with diameters 6 and 3 mm, i.e., larger and slightly lesser than critical size.

Figure 7 shows calculated pressure and reaction product fields. The process in a cylindrical charge with diameter 6 mm being numerical simulated demonstrates the steady detonation establishment, which propagates with velocity being slightly lesser when ideal detonation one. Reference origin along  $Z$ -axis

in Figure 7 was chosen arbitrarily because the detonation wave passed the distance larger than several diameters, and initial values cannot influence the motion. As the detonation velocity and chemical spike pressure are lesser than ones in ideal one-dimensional process, the reaction zone extension along charge axis is 3-4 times larger. The chemical spike size at the charge axis (nearly 1 mm) is still noticeably smaller than the charge diameter, due to lateral release of the surface layer by the thickness nearly 1 mm being reacted only partly in the wave.

With the HE sample diameter decreasing up to 3 mm, the wave process alters significantly. The shock wave relaxation by lateral release dominates over the energy being received by shock wave front from the reaction zone. As a result, the detonation wave does not reach the stationary regime, and does relax quickly. In total accordance with Hariton's principle,<sup>19</sup> the material at the charge axis is dispersed before the energy release is accomplished completely.

## CONCLUSION

The results of this paper show that a limited number of experimental data joined with numerical simulation allow the empirical macrokinetic equation to be found. This is suitable for one dimensional, as well as more general situations.

## REFERENCES

1. Khasainov, B. A.; Borisov, A. A.; Ermolaev, B. S.; and Korotkov, A. L., "Two Phase Visco Plastic Model of Shock Initiation of Detonation on High Density Pressed Explosives," *Proceedings of the Seventh Symposium (International) on Detonation*, Naval Surface Weapons Center, NSWC MP 82 334, Jun 1981, pp. 435-447.
2. Howe, P.; Frey, R.; Taylor, B.; and Boyle, V., "Shock Initiation and the Critical Energy Concept," *Proceedings of the Sixth Symposium International on Detonation*, Office of Naval Research, ACR 211, Arlington, Virginia, 1976, pp. 11-15.
3. Cowperthwaite, M. and Rosenberg, J. T., "A Multiple Lagrange Gauge Study of the Shock Initiation Process in Cast TNT," *ibid*, pp. 786-793.
4. Wackerle, J.; Johnson, J. O.; and Halleck, P. M., "Shock Initiation of High Density PETN," *ibid*, pp. 20-28.
5. Utkin, A. V.; Kanel, G. I.; and Fortov, V. E., "Decomposition of High Explosives by Different Density in Shock and Detonation Waves," *Proceedings of the All-Union Symposium on Detonation*, Telavi, USSR, Nov 1988, pp. 103-109.
6. Lobanov, V. F.; Karakhanov, S. M.; and Bordsilovsky, S. A., "Study of Transient Processes at Shock Initiation of TNT," *Fizika Gorenija i Vzriva*, Vol. 18, No. 3, 1982, p. 90.
7. Lee, E. L. and Tarver, C. M., "Phenomenological Model of Shock Initiation in Heterogeneous Explosives," *Phys. Fluids*, Vol. 23, No. 12, 1980, p. 2362.
8. Barker, L. M. and Hollenbach, R. E., "Laser Interferometer for Measuring High Velocities of Any Reflecting Surface," *J. Appl. Phys.*, Vol. 43, No. 11, 1972, p. 4669.
9. Bloomquist, D. D. and Sheffield, S. A., *J. Appl. Phys.*, Vol. 54, No. 4, 1983, p. 1717.
10. Sheffield, S. A.; Bloomquist, D. D.; and Tarver, C. M., "Subnanosecond Measurements of Detonation Fronts in Solid High Explosives," *J. Chem. Phys.*, Vol. 80, No. 8, 1984, p. 3831.
11. Jarkov, V. N. and Kalinin, V. A., *Equations of State for Solids at High Pressure and Temperature*, Nauka, Moscow, 1970, p. 1932.
12. Evstigneev, A. A.; Jernokletov, M. V.; and Zubarev, V. N., *Fizika Gorenija i Vzriva*, Vol. 12, No. 5, 1976, p. 758.
13. Fortov, V. E. and Dremin, A. N., "Equation of State for TNT," *Dokl Akad. Nauk SSSR*, Vol. 222, No. 1, 1975, p. 162.
14. Johnson, J. N.; Tang, P. K.; and Forest, C. A., "Shock-Wave Initiation of Heteroge-

# INITIATION OF EXPLOSIVE CRYSTALS BY SHOCK OR IMPACT

C. S. Coffey

Naval Surface Warfare Center

White Oak Laboratory, Silver Spring, Maryland 20903-5000

*The formation of hot spots is an essential step in the process of initiating explosive crystals by shock or impact. Consequently, any attempt to understand the initiation of explosive crystals must first establish how the energy of the shock or impact is localized to form hot spots. More generally, it appears that energy localization occurs in all crystalline solids, both inert and energetic, when they are subjected to shock or impact induced plastic deformation. This paper examines the energy localization that occurs in the shear band and shear band-like structures that form in crystalline solids during shock or impact. These bands are the locus of plastic deformation and associated energy deposition during rapid deformation, and are the likely source of hot spots and ignition sites in energetic solids during shock or impact. The shear band width, growth rate, and energy density are obtained. The transition from a relatively slow heating and ignition during mild impact to a very rapid direct excitation and possible dissociation of the molecules is shown to occur as the input stimulus is increased from a mild impact to a high level shock.*

## INTRODUCTION

When crystalline solids undergo deformation at high rates due to shock or impact loading the deformation often occurs in very localized, band-like regions frequently referred to as shear bands. Associated with these regions of intense plastic deformation are high local concentrations of energy due to dissipation by the plastic flow. These localized energy concentrations can manifest themselves as heat; phase transitions including melting, internal molecular vibrational, and electronic excitations with the associated emission of optical photons; and the initiation of chemical reactions. The regions of the crystal outside of the shear bands experience little or no plastic deformation or energy increase. The time frame for this local deformation and associated energy dissipation/molecular excitation to occur has been observed to be of the order of 10 nanoseconds or less for very rapid shock loading. Spatially, the band-like regions can range from submicrons to several tens of microns in width, depending on the crystal

material and the amplitude and duration of the shock or impact. Depending on the orientation of the crystals, the bands have been observed to extend through many crystal grains in shocked or impacted metal targets. Often the bands have been observed to contain large numbers of dislocations.

On the basis of these observations that shear bands and similar band-like regions are formed during high rate deformation of crystals and that they can be regions of very high energy concentrations, we suggest that they form the hot spots in shocked or impacted explosive crystals from which ignition starts. This allows the ignition sensitivity of explosive crystals to shock or impact to be calculated by determining the shear band formation and dislocation density in the crystals due to the applied shock or impact. The energy concentration in the bands and band-like regions arises due to the energy dissipated by the moving dislocations that form these regions. This energy has been determined and shown to be sufficient to excite and cause ignition of the

molecules within the shear band regions. It has been shown that this is a quantum mechanical excitation process and is not describable by classical physics. Further, there occurs a very natural transition from the relatively slow, thermal-like ignition process associated with impacts, to a much more rapid molecular dissociation process associated with high amplitude shocks, which is similar to that which occurs in the transition from deflagration to detonation.

Shear banding and the associated heating in shocked or impact loaded steels was first reported by Zener and Holloman in 1941.<sup>1</sup> Since then numerous others have reported similar band-like structures in steels and in other metals that have experienced shock or impact loading.<sup>2,3,4</sup> Occasionally, these bands have been associated with metal failure or cracking.

Similar band-like structures have been observed in many non-metallic crystalline solids.<sup>5,6</sup> In single crystals of both quartz and lithium niobate shocked to 6.5 GPa and higher, the shear band-like structure has been observed emitting visible photons within nanoseconds after shock arrival.<sup>7,8,9</sup> In these materials, the emission of visible photons suggests that electronic excitation has occurred within the molecules in the shear bands.

In the study of the initiation of chemical reactions in explosive crystals during shock or impact, it has long been known (circa 1930) that some form of energy localization or "hot spot" formation must occur in order to account for the small amount of shock or impact energy required to ignite these materials.<sup>10,11</sup> Recent experiments on void free samples have shown that during impact, ignition always occurs in the regions of the sample undergoing the highest shear and shear rate deformation, and never in the regions of the sample experiencing the highest pressure.<sup>12</sup>

## **THE GENERATION OF SHEAR BANDS DURING RAPID DEFORMATION**

The microscopic mechanisms responsible for plastic deformation in crystalline solids are the creation and motion of dislocations. An examination of shear bands in many different materials shows them to be composed of large

numbers of dislocations. Because of a) the large numbers of dislocations that can exist in a crystal, up to  $10^{12}/\text{cm}^2$ , b) their extended two-dimensional structure, and c) their long range ( $1/r$ ) interaction potential, it would appear at first sight that a description of their behavior during shock or impact would be exceedingly difficult. However, the experimental observations of large numbers of dislocations clustered in the shear bands<sup>5,6</sup> suggests that this is not the case and that significant simplifications are possible. The concentrations of dislocations in the shear bands of shocked or impacted crystals indicates that most of the possible interactions between dislocations are overwhelmed by the shock or impact imposed shear stress. Since typically the amplitude of the stresses imposed on the crystal by the shock or impact are often several orders of magnitude greater than their yield stress, it is not surprising that it is these applied stresses that control the generation and motion of dislocations. Further, the formation of narrow, well defined, shear bands suggests that one or, at most, only a very few sources are responsible for generating the dislocations within any one shear band.

In the interest of simplicity, we will assume that the strength of the shock or impact induced applied shear stress is much greater than the strength of the interaction between dislocations. As suggested above, it will be assumed that the interactions between dislocations can, for the most part, be neglected, and that dislocation generation and motion are determined by the applied shear stress. Further, it will be assumed that for large applied shear stress the dislocations in a shear band are generated by a single source, and that once created, the dislocations are free to run along the active slip plane until they encounter some obstacle, whereupon they stop. This simplified picture allows a tractable model to be developed that can account for many of the features of shear band formation and energy dissipation in crystalline solids during high rate deformation due to shock or impact.

## **THE DISLOCATION SOURCE AND SHEAR BAND FORMATION**

Recently, we developed a model for dislocation source capable of creating dislocations at

rates sufficient to account for the dislocation number densities and generation rates observed in shear bands in shock or impact experiments.<sup>13</sup> Briefly, this is a generic model consisting of an oscillator-like source composed of a linear structure, such as a string of impurity atoms or molecules located within the crystal. The presence of this linear structure perturbs and distorts the local intercrystalline potential of the host lattice sufficiently so that, when a shear stress from a shock or impact is applied to the crystal across the impurity string, it is possible for local intermolecular or interatomic bonds to be broken. In this process a pair of oppositely oriented edge dislocations is created that, under the applied shear stress, are free to move away from the source region.

While they are still within the source region, the back stress from the newly created dislocation pair prevents the source from functioning again. The rate at which the source can function is determined, in part, by the time it takes the newly created dislocations to move a distance,  $L$ , from which they can no longer influence the source. Here, for simplicity, it will be assumed that  $L$  is independent of the applied shear stress. The other process controlling the operation of the source is the quantum mechanical probability,  $P(\tau)$ , that an intermolecular or an interatomic bond rupture can occur across the source string due to the applied shear stress,  $\tau$ . The rate of dislocation generation is given as

$$R(\tau) = 2 P(\tau) \frac{V}{L}, \quad (1)$$

where  $V$  is the dislocation velocity. The factor of 2 arises because of the pair of oppositely oriented dislocations that are created with each operation of the source. The dislocation velocity can be written as  $V = V_0 \exp(-\tau_0/\tau)$ , where  $V_0$  is nearly the shear wave speed and  $\tau_0$  is an effective shear stress related to the dissipation created by a moving dislocation.<sup>14,15</sup> The rate of dislocation generation now becomes

$$R(\tau) = 2 P(\tau) \frac{V_0}{L} e^{-\tau_0/\tau}. \quad (2)$$

For high level shocks or impacts  $P(\tau) \approx 1$  and  $\tau \gg \tau_0$ , so that

$$R(\tau) \approx 2 \frac{V_0}{L}. \quad (3)$$

Conservatively, it is unlikely that the source region will extend beyond 100  $b$ , where  $b$  is the length of the Berger's vector. For RDX, ( $b \approx 10^{-9}$  m and  $V_0 \approx 1.5 \times 10^3$  m/s), the dislocation generation rate is approximately  $R \approx .3 \times 10^{11}$  dislocation/s.

The width of the shear band can be estimated by observing that, once created, the dislocations are able to run along the slip plane until they encounter an obstacle such as a grain boundary, whereupon they stop and pile up behind the obstacle. Eventually, the number of dislocations in the pileup will increase to a level where it becomes energetically more favorable to transfer the newly created dislocations to an adjacent slip plane via the cross slip mechanism, rather than to expend the additional energy necessary to overcome the increasing back stress of the pileup, in order to continue to add dislocations to the original pileup. Obviously, a pileup will eventually form on this new slip plane, and once again it will become energetically favorable to transfer the newly created dislocations onto another nearby slip plane.

In this way a shear band can be built up by the accumulation of many slip planes. If  $N_0$  is the number of dislocations that can exist in a pileup before the transfer to a new slip plane occurs, and  $D$  is the average separation between slip planes, the rate of increase in the width of the shear band,  $\frac{dw}{dt}$ , is

$$\frac{dw}{dt} = \frac{RD}{N_0} \approx \frac{2 P(\tau) D V_0 e^{-\tau_0/\tau}}{N_0 L} \quad (4)$$

For a large applied shear stress,  $\tau \gg \tau_0$ , the maximum rate of increase in the shear band width is approximately

$$\frac{dw}{dt} \approx \frac{2 V_0 D}{N_0 L} \quad (5)$$

Typically  $D \approx b$  and for nominal 100 $\mu$  size crystal  $N_0 \approx 10^2$  to  $10^3$  so that  $\frac{dw}{dt} \approx .1$  to 1 m/s. For a shock of a few tens of microseconds duration, the width of the shear bands is about 10 microns. The number of dislocations in a pile-up,  $N_0$ , is determined<sup>16</sup> from a static, continuum calculation. Currently, we have no knowledge of how applicable these static calculations are to shock and impact situations.

## THE ENERGY DISSIPATION RATE

Attempts have been made to determine the energy dissipation rate by a moving dislocation.<sup>17,18</sup> Often these have been classical continuum calculations and appear to underestimate the energy dissipated by the moving dislocation. It is straightforward to show that the energy dissipated by a rapidly moving dislocation is a quantum mechanical problem, and that the classical continuum approach is inadequate. Consider a dislocation moving at a speed  $V$  through a crystal lattice; let  $d$  be the lattice interatomic or intermolecular spacing. To a first approximation, the lattice intercrystalline potential may be represented by the sinusoidal Peierls-Nabarro potential. As it moves through the lattice the dislocation encounters this potential at a rate of  $V/d$  times per second. To the moving dislocation and the surrounding atoms or molecules this represents a time varying perturbation at a radial frequency of  $\omega = 2\pi V/d$  rad/s. The maximum velocity at which a dislocation can move is nearly the shear wave speed,  $V \approx 2$  to  $3 \times 10^3$  m/s. For most explosive materials of interest, the interatomic or intermolecular spacing is typically  $10^{-9}$  m. The radial frequency of the lattice perturbation near the core of the dislocation for this simple lattice potential approaches  $10^{13}$  rad/s. For a more realistic intercrystalline potential appropriate for molecules with more complicated structure, the above frequency is just the center frequency of the perturbation frequency distribution that the molecules or atoms near the core of the dislocation experience. These maximum frequencies,  $\omega > 10^{13}$  rad/s, are sufficient to directly excite the internal molecular vibrational modes of most explosive molecules of interest, as will be shown shortly.

This direct molecular excitation process is not available in classical physics.

From an analytic approach, the perturbation of the lattice by the moving dislocations can be treated as a collection of phonons. It is possible to obtain an estimate of the phonon number density using the approximation

$$n\hbar\omega \approx \frac{1}{2} \rho (x\omega)^2$$

where  $\rho$  is a crystal density,  $x$  is the lattice displacement due to the moving dislocation, and  $n$  is the phonon number density. As a reasonable approximation, let the maximum lattice displacement due to the core of the dislocation be  $x = d/10$ ,  $\rho = 2$  gm/cm<sup>3</sup>, and  $\omega = 10^{13}$  rad/s. This gives  $n \approx 10^{23}$  phonons/cm<sup>3</sup> a phonon number density so large as to suggest that non-linear, higher order, quantum mechanical processes must occur.

The energy dissipation rate per moving dislocation has been calculated by determining the interaction between the moving edge dislocation and the lattice.<sup>19,20,21</sup> This can be written as

$$E = g\Gamma R^2 \sum_k (n_q + 1) N_k (N_{k-q} + 1) dq + \int \hbar\omega \sum_{f,u} \left| \sum_1 \frac{\langle f|H|1 \rangle \langle 1|H|u \rangle}{\omega_1 - \omega_u} \right|^2 dq dV,$$

where

$$\Gamma = \frac{1}{8(2\pi)^3 N m} \left( \frac{Gb}{1-\nu} \right)^2 \frac{1}{d^2 C}. \quad (6)$$

The first term above gives the dissipation rate for dislocations moving at velocities somewhat less than the shear wave speed. This is the appropriate term for determining the energy dissipation or lattice heating that occurs during mild impact. To illustrate this better, consider the Gilman relation for dislocation velocity as a function of applied shear stress  $\tau$ ,  $V = V_0 \exp(-\tau_0/\tau)$ . For mild impacts  $\tau$  is usually less than or slightly greater than the approximate yield stress  $\tau_0$  and, therefore,  $V < V_0$ .

For higher applied shear stress levels, typical of high amplitude shocks or impacts,  $\tau > \tau_0$ , the dislocation velocity will approach

the local shear wave speed of the compressed material within the shock wave,  $V \rightarrow V_0$ . More importantly, the frequency of the optical phonons generated by the moving dislocation approaches, and often equals, the internal molecular vibrational frequencies of many explosives' molecules,  $\approx 10^{13}$  rad/s. For example, as shown above, using the simple Peierls-Nabarro sinusoidal potential gives  $\omega = .9 \times 10^{13}$  rad/s. For these higher amplitude shocks, a transition begins to occur when the second and higher order terms in the dislocation energy dissipation rate become important, as their resonance conditions are approached.

For any real solid, and certainly for the solid explosives, the molecules are sufficiently complex that the simple Peierls-Nabarro sinusoidal potential is inadequate to describe the much more complicated intermolecular potential. A dislocation moving through the more complicated lattice with a velocity  $V$  will perturb the lattice and generate a spectrum of lattice vibrations or phonons. The center frequency of this spectrum will be  $\omega_c = 2\pi V/d$ . Within the band of phonons centered at  $\omega_c$  are frequencies that are likely to span nearly all of the possible internal molecular vibrational levels. This makes it possible to achieve resonant or near resonant excitation through most of these levels, including the virtual levels and on through to the quasi-continuum levels near the top of the internal molecular oscillator wells. For explosives, molecular dissociation can occur at the top of the potential well. For less reactive and non-reactive materials, electronic excitation may occur via the virtual levels between the potential wells of different electronic states.

It can be more informative if the probability of achieving a transition from an initial state  $i$  to an excited state  $f$  were written as

$$W = \sum_{j=1}^{\infty} P_{ij}^{(0)} + \sum_{j=1}^{\infty} \Pi_{i,e} P_{ie}^{(j)} \quad (7)$$

where  $P_{ij}^{(0)}$  is the non-resonant first order transition probability between states  $i$  and  $j$ , and  $P_{ie}^{(j)}$  is the higher order resonant transition probability between  $i$  and  $e$

$$P_{ie}^{(j)} = K \left| \frac{\langle j | H' | e \rangle \langle e | H' | i \rangle}{E_e - E_i - \hbar \omega} \right|^2 \quad (8)$$

where  $K = \text{constant}$ . The sums begin at an initial level  $i = i_0$  and extend to all possible levels. Generally, the selection rules will limit  $e$  to  $e = i \pm 1$ .

As the rate of plastic deformation of the crystal increases with increasing shock amplitude, the dislocation velocity increases and with it the phonon frequencies, so that eventually resonance is approached as  $\omega \rightarrow \omega_{ie} = (E_e - E_i)/\hbar$  and the denominator in  $P_{ie}^{(j)}$  becomes very small. Since  $P_{ie}^{(j)}$  is a probability, it approaches a limiting value of unity as the resonant condition is approached,  $P_{ie}^{(j)} \rightarrow 1$  as  $\omega \rightarrow \omega_{ie}$  (note that the perturbation approach to calculating the transition probabilities fails under the resonant condition, but more importantly, in this limit its value approaches unity). Further, if the width of the phonon spectrum generated by the moving dislocations is broad enough to resonantly excite many, if not most, of the transitions involved in exciting up the vibrational ladder, these probabilities will also approach unity. The probability of achieving a transition from a low lying state to a dissociative or an electronic excitation reduces to the product of just a few transition probabilities most likely to be associated with the more widely separated lower lying vibrational levels,

$$W \approx \sum_{j=i_0}^{\infty} \Pi_{i,e} P_{ie}^{(j)} \quad (9)$$

The first order terms associated with dislocation energy dissipation and lattice heating due to mild impact have been dropped here because they involve relatively slow overall excitation processes, in which all of the possible transitions must be non-resonantly excited when compared to the very rapid shock dissipation-lattice excitation processes. If it is assumed that all of the molecules initially reside in a low lying vibrational state  $i = i_0$  and only transitions to the level  $i = l$  are of interest because all of the transitions between higher levels are resonantly excited, then Equation (9) reduces to just

$$W \approx \Pi_{i=i_0}^l P_{i,i+1}^{(j)} \quad (10)$$

where  $l$  is a small number.

In analogy with the multiphoton absorption process, this shock induced multi-phonon excitation of the internal molecular vibrational modes will proceed very rapidly because transitions between only a few states are significant and, consequently, the transition time between the initial state of an explosive molecule and its dissociated state,  $W^{-1}$ , will be very short compared to the impact situation where all of the transitions between levels must contribute. This gives rise to a prediction of a significant increase in the reaction rate that must occur between the regime dominated by low rate crystal lattice deformation due to mild impact, and the regime dominated by very rapid lattice deformation due to high level shock. The ignition/molecular dissociation associated with rapid shock induced deformation must proceed much more rapidly than the ignition due to the much slower heating due to impact deformation. This prediction is very similar to the transition that occurs in the rate of reaction in explosives going from modest level impact to high amplitude shock loading. More generally, when the resonant absorption of the high energy phonons begins to occur the energy dissipation rate per moving dislocation will increase greatly, as does the corresponding internal molecular excitation rate. Such a process is in keeping with the rapid electronic excitation that is observed to occur within the shear bands of shocked quartz and lithium niobate.<sup>7,8,9</sup> The occurrence of electronic excitation suggests that shocked induced chemical reactions in non explosive substances could occur in this way. The transition from the slow rate impact induced dissociation processes, to the very rapid dissociation associated with detonation and shock waves, is suggestive of a deflagration driven deformation to detonation transition.

While we have not pursued it here, we have shown elsewhere that among other things, the first order terms contain a crystal particle size effect that the energy dissipation varies as  $\ell^{-1}$  where  $\ell$  is the particle size.<sup>20,21</sup> This is really no more than the classical Hall-Petch result from Material Science and has been confirmed for impacts on RDX.<sup>23,24</sup>

The possibility of rapid molecular excitation and dissociation by multiphonon processes in shock waves was studied earlier by this

author, but at the time the centrality of the shear band localization hot spot process was not fully appreciated.<sup>25</sup> Energy localization in shear band and shear band-like structures by rapidly moving dislocations is a much more efficient excitation process than bulk excitation of the molecules of the solid by shock or impact. Given the presence of shear bands and shear band-like structures in crystalline solids during rapid deformation, it is easy to understand how hot spots and the subsequent ignition occurs in shocked or impacted explosive crystals.

## CONCLUSIONS

Shear band-like formations frequently occur in shocked or impacted crystals, and they appear to be the sites of significant energy concentrations. This paper attempts to understand how this localization occurs because such a process must be similar, if not identical, to what happens in hot spot formation in crystalline solids during high rate deformation.

An analysis of the shear band formation process has been developed based on the rapid generation of dislocations during shock or impact. This analysis gives the size, rate of growth, and the dislocation number density of a typical shear band generated by an arbitrary shock or impact.

The energy dissipation by a moving dislocation has been determined and shown to be a quantum mechanical process not easily accessible to solution by classical means. The total energy dissipated is just the product of the number of moving dislocations times the energy dissipated per moving dislocation. For mild impacts, the energy dissipation takes place relatively slowly, in an almost thermal-like fashion, while with strong shocks the energy dissipated by a rapidly moving dislocation occurs very rapidly by direct pumping of the internal vibrational levels of the host molecules. With explosive materials the initiation of chemical reaction can be caused by either of these processes, however, there is a great difference in the rates at which this initial reaction occurs or is sustained if such sustaining requires that mechanical energy be continuously supplied by the shock or impact. It is shown that there is a transition in the reaction rate that



takes place at high rates of deformation, where the phonons generated by the rapidly moving dislocations approach the resonant frequency of the internal vibrational modes. At this point the slower impact induced molecular excitation shifts over to the very much faster shock driven dislocation induced multi-phonon excitation of the internal vibrational modes of the molecules of the host crystal.

## ACKNOWLEDGEMENTS

Support for this work was provided by the Office of Naval Research and NSWC IR funds. The author wishes to acknowledge the help and encouragement given by Drs. Charles Dickinson and Donald Liebenberg.

## REFERENCES

1. Zener, C. and Hollomon, J. H., *J. Applied Physics*, Vol. 15, 1944, p. 22.
2. Rogers, H. C. and Shastry, C. B., *Shock Waves and High Strain Rate Phenomena in Metals*, Edited by Meyers, M. A. and Murr, L. E., Plenum Press, New York, 1981, p. 285.
3. Winter, R. E. and Field, J. E., *Proc. Roy. Soc., A* Vol. 343, London, 1975, pp. 399-413.
4. Mebar, Y. and Shechtman, D., *Materials Science and Engineering*, Vol. 58, 1983, pp. 181-188.
5. Johnston, W. G. and Gilman, J. J., *J. Applied Physics*, Vol. 30, 1959, p. 129.
6. Herley, P. J., Jacobs, P. W. M., and Levy, P. W., *J. Chem. Soc.*, Vol. 3 (A), 1971, p. 434.
7. Brooks, W. P., *J. Applied Physics*, Vol. 36, 1965, p. 2788.
8. Brannon, P. J.; Konrad, C. H.; Morris, R. W.; Jones, E. D.; and Asay, J. R., *J. Applied Physics*, Vol. 54, 1983, p. 6374.
9. Brannon, P. J.; Morris, R. W., and Asay, J. R., *J. Applied Physics*, Vol. 57, 1985, p. 1676.
10. Kholevo, N. A. and Kazan, T., *Khim. Tech. Insu*, Vol. 10, 1946, p. 91.
11. Coffey, C. S.; DeVost, V. F.; and Woody, D. L., "Initiation of Explosive Crystals by Shock or Impact," *Ninth Symposium (International) on Detonation*, Portland, Oregon, 1989.
12. Coffey, C. S.; Frankel, M. J.; Liddiard, T. P.; and Jacobs, S. J., *Seventh Symposium (International) on Detonation*, NSWC MP 82-334, 1981, p. 970.
13. Coffey, C. S., *J. Applied Physics*, to appear 15 Aug 1989.
14. Gilman, J. J., *Aust. J. Phys.*, Vol. 13, 1960, p. 327.
15. Gilman, J. J. and Johnston, W. G., *Solid State Physics*, Edited by Seitz, F. and Tumbull, D., Academic Press, New York, Vol. 13, 1962, p. 147.
16. Hirth, J. P. and Lothe, J., *Theory of Dislocations*, McGraw-Hill, New York, 1968.
17. Eshelby, J. D. and Pratt, P. L., *Acta Metall.*, Vol. 4, 1956, p. 560.
18. Fredenthal, A. M. and Weiner, J. H., *J. Appl. Phys.*, Vol. 27, 1956, p. 44.
19. Coffey, C. S., *Phys. Rev. B* 24, Vol. 2, 1981, p. 6984.
20. Coffey, C. S., *Phys. Rev. B* 32, Vol. 8, 1985, p. 5335.
21. Coffey, C. S., *Phys. Rev. B* 34, Vol. 8, 1986, p. 5674.
22. Hall, E. O., *Proc. Phys. Soc., London, Sect. B*, Vol. 64, 1951, p. 747.
23. Petch, N. J., *J. Iron Steel Inst.*, Vol. 74, 1953, p. 25.
24. Armstrong, R. W.; Elban, W. L.; DeVost, V. F.; and Coffey, C. S., in preparation.
25. Coffey, C. S. and Toton, E. T., *J. Chem. Phys.*, Vol. 75, 1982, p. 949.

## DISCUSSION

P. C. CHOU, Dyna East Corporation  
Philadelphia, PA

To initiate your dislocation analysis of shear band formation, do you need particle

velocity gradient as input? If so, should the velocity distribution be calculated from a continuum hydrocode?

#### **REPLY BY C. S. COFFEY**

Yes, the applied shear stress on a crystal would, in most cases, be determined by a continuum hydrocode calculation. In general, I think that any attempt at a microscopic calculation of hot spot formation/ignition must

take inputs from continuum hydrocodes. Because of the time and expense, nobody will attempt a full calculation of all of the microscopic processes that occur in a full size charge (or even a small one). Rather, the microscopic processes will be used together with the appropriate macroscopic inputs to determine when and where hot spot-ignition occurs.

# INITIATION THRESHOLD OF HIGH EXPLOSIVES IN SMALL FLYER PLATE EXPERIMENTS

H. R. Kleinhanß, F. Lungenstraß, and H. Zöllner  
Institut für Experimentalphysik  
Universität Düsseldorf  
Universitätsstr.1  
D-4000 Düsseldorf, FRG

*The purpose of this study was to investigate the influence of the shock loading area on the initiation threshold and on the detonation buildup in shock initiation of high explosives. Contrary to projectile impact electrically driven thin flyer-plates were used to shock the explosive. Therefore, the shock duration is independent of the impact area and is essentially determined by the rear rarefaction wave. The investigations show that it is necessary to distinguish between a primary and a stable detonation in small shock loading initiation tests. The development of the detonation is strongly influenced by lateral release waves.*

## INTRODUCTION

Secondary high explosives are usually initiated by strong shock waves. While in one-dimensional shock initiation studies either the put- or the put-criterion<sup>1,2</sup> correlates the experimental data over a wide pressure range for many high explosives; these criterions fail in two dimensional projectile impact.<sup>3,4</sup> An increase of the threshold is observed when the impact area is decreased.

In order to explain this effect, there are successful theories by Moulard<sup>5</sup> and James.<sup>6</sup> These authors make suitable modifications to the one-dimensional put-criterion, and thus, they are able to transform this concept on the projectile impact. Although they presuppose different hypotheses to explain the influence of lateral release waves on the long duration projectile impact, both theories are identical in one aspect: there is no real increase in initiation threshold if the shock loading area is decreased, but the two-dimensional shock initiation is also ruled by the critical energy per unit area. Moulard and James can reconcile their experimental data with their models.

The purpose of this study was to investigate the influence of the shock loading area on

the initiation threshold, and on the detonation buildup in shock initiation of high explosives by using short pulses ( $t < 100$  ns) with a high magnitude ( $p > 10$  GPa) and a small impact area. Therefore, in the present impact test electrical driven thin flyer plates were used to initiate the high explosive. The flyer plate impact differs in two important aspects from the projectile impact. Firstly, the impact area remains nearly constant during shock transition, because the reduction by the lateral release wave can be neglected using the comparatively short pulse widths (30-100 ns). Secondly, the shock duration is independent of the impact area and is essentially determined by the rear rarefaction wave. In our opinion, the flyer plate impact is more suitable than the projectile method to investigate the role of shock loading area on the initiation threshold.

The investigations show that the result of this initiation threshold test is not only affected by the impact area, but also by the charge length. This charge length effect gives rise to distinguishing between the threshold for a primary initiation and for a stable detonation; especially when less sensitive explosive materials like Comp B are used.

## EXPERIMENTAL SETUP

A convenient device to accelerate small flyer plates is the Electric Gun, first introduced by Chau et al.<sup>7</sup> in 1980. This device consists of a capacitor bank and a thin metallic foil. The foil explodes by discharging the capacitor bank and the expanding plasma accelerates the thin flyer plate.

The flyer velocity is strongly affected by the foil explosion, demanding a high current with a short rise time. In order to comply with these requirements, the inductance of the circuit was reduced as far as possible. In the present design, the capacitor bank is connected to the shot assembly by a pair of flat conductors. The discharge is switched on by a detonator near the shot assembly. The electrical data of the Electric Gun are presented on the left hand side of Table 1.

*Table 1. Electrical and Impact Parameters of the Present Electric Gun Device (\* Calculated for the Impact Comp B<sup>9</sup> MYLAR<sup>8</sup>)*

Electrical Parameter		Impact Parameter	
Capacity	29 $\mu$ F	Flyer velocity	2.9 mm/ $\mu$ s
Inductance	30 nH	Barrel diameter	0.5-20 mm
Peak current	640 kA	Pressure*	10-70 GPa
Rise time	1.5 $\mu$ s	Pulse width*	30-100 ns

The foil flyer laminate consists of Aluminium and MYLAR with different thicknesses (20-50  $\mu$ m/100-250  $\mu$ m). The barrel diameter can be varied over the range of 0.5 to 20 mm and the maximum barrel length in use is 5 mm. The flyer velocity was measured by an optical device using fiber optics and an image converter camera. The flyer plates are accelerated up to 9 mm/ $\mu$ s producing an impact pressure of about 700 kbar with a typical cast high explosive (Table 1). The choice of distinct impact velocity for a given foil flyer laminate is made by changing either the charging voltage (5-25 kV) or the barrel length (2-5 mm). Figure 1 shows the flyer velocity as a function of the charging voltage for different

barrel lengths using a 50  $\mu$ m/Al-250  $\mu$ m/MYLAR-laminate.

In the first part of the studies, the initiation threshold was measured as a function of shock loading area. For that purpose, cylindrical high explosive pellets with fixed dimensions (length 20 mm, diameter 20 mm) were impacted by flyer plates varying their diameter, velocity, and thickness. The onset of a detonation was proved by a 3 mm copper plate placed at the end of the charge, as shown in Figure 2. A detonation was indicated by a circular hole punched out of the plate. Contrary, if initiation fails, only slight depressions were created in the contacting copper plate. In addition, the light output was detected by a photomultiplier using an optical fibre stuck through a hole at the copper plate. The optical signal gives the out-break of the detonation front at the face of the sample and, using cast explosives, also the impact of the flyer plate.

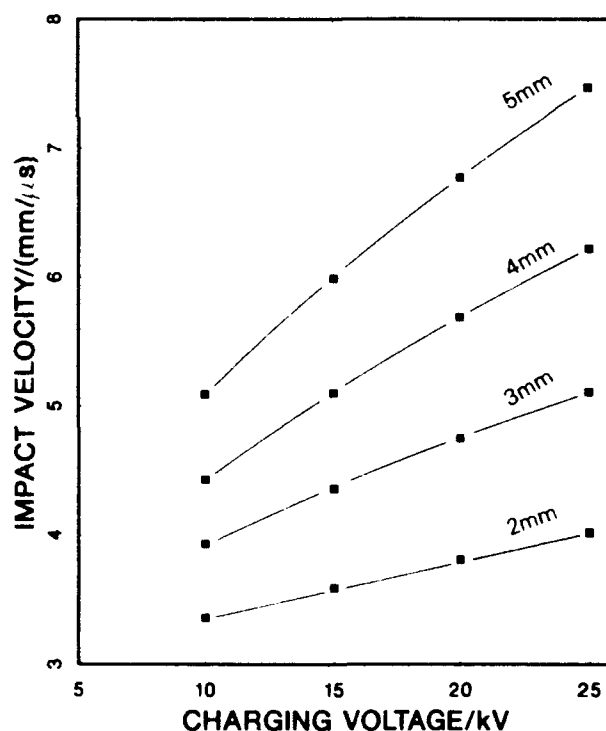


*Figure 1. Impact Velocity as a Function of Charging Voltage and Barrel Length; Flyer: MYLAR 0.25 mm Thick; Foil: Al 0.05x10x10 mm*

Optical diagnostics consisting of fibre optics, image converter camera, and photomultiplier were used to study the propagation of the detonation wave. Figure 2 shows the optical setup at the high explosive sample. Optical fibres are mounted at the rear and the side of the pellet; the remote ends are positioned in the streak plane of the image converter camera forming a streak slit. The arriving detonation front produces a short flash transmitted by the fibres. In order to get information about the detonation front at different times, the high explosive samples were varied in length from 40 mm down to 2 mm.

Routinely, the current was measured electromagnetically by a Faraday-probe and the current change was detected by an inductive probe. The foil explosion is marked by a sharp breakdown in the inductive trace. Measurement of current and burst time give the burst current density and, thus, the impact velocity can be checked by the Gurney equation<sup>10</sup>. The recordings of the inductive probe, the Faraday probe, and the optical device are presented in Figure 3 together with the streak camera record.

The happening of a single experiment can be illustrated by means of the photomultiplier trace. During acceleration of the flyer plate, the intense light of the metal vapor shines through the charge. The impact is determined by a short flash of the confined air between flyer and target. During the transit time of the shock/detonation wave through the sample, no light is observed. When the detonation front reaches the end of the high explosive, the fibre again transmits a short flash. The impact and the outbreak of the detonation front can also be recognized in streak camera record.

## EXPERIMENTAL RESULTS

The initiation threshold and the detonation development were studied as a function of the impact area for different types of explosives

pressed TNT, PBX N5  
cast Octol, Comp B, TNT

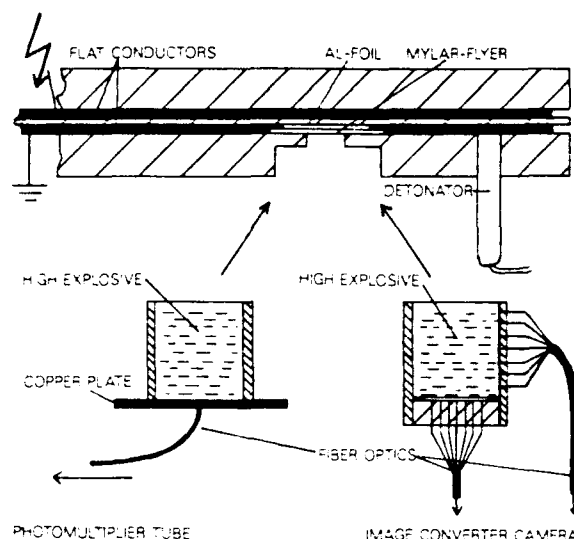


Figure 2. Experimental Setup of Initiation Threshold Test (Left) and Detonation Front Measurement (Right)

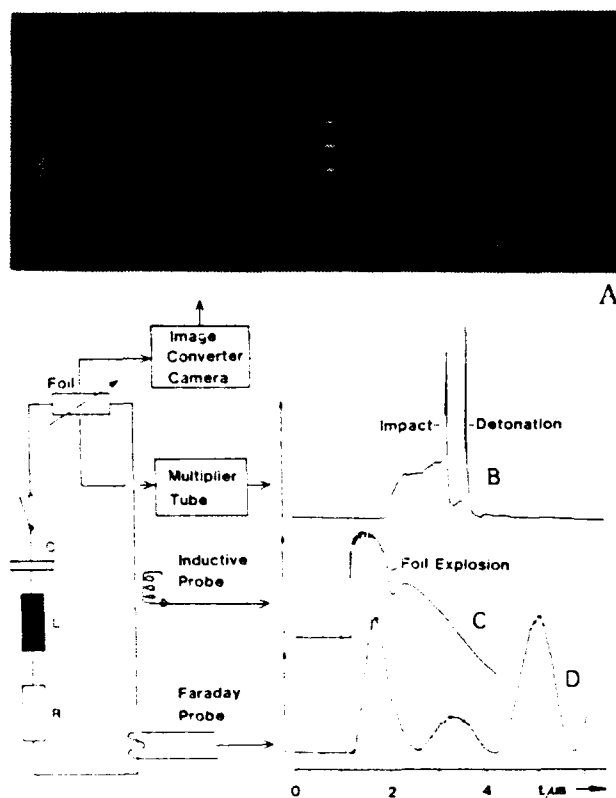


Figure 3. Diagnostics in Detonation Studies. Recordings by  
A Streak Camera → Detonation Front  
B Photomultiplier → Transit Time  
C Inductive Probe → Burst Time  
D Faraday-Probe → Current

The properties of the used explosive materials are listed in Table 2.

### Initiation Threshold

In the following initiation threshold test the charge length was routinely 20 mm. It is important to remark that the presented results are only valid for this fixed charge length. Performing the same experiments with another charge length may give differing initiation thresholds, as discussed later.

The results of about 100 experiments for Comp B are summarized in Figure 4. In this case, the so called critical energy is chosen to compare the initiation thresholds for different shock loading areas. The critical energy  $E_c$  is related to unit area, and specifies the minimum energy required for initiating the high explosive by a shock wave.<sup>1</sup> It is defined as

$$E_c = p \cdot u \cdot t$$

where  $p$  is the shock pressure,  $u$  the particle velocity, and  $t$  the usual pulse duration. In the present study the experiments were done with flyer plates, whose thickness-to-diameter-ratio  $l/\phi$  was generally much smaller than  $1/4$ . This value commonly represents the limit between flyer plate and projectile.<sup>11</sup> Thus, it is allowed to calculate the pulse duration  $t$  as

$$t = 2l/U$$

where  $U$  is the shock velocity. The energy delivered by the flyer to the explosive target during impact was calculated with the Hugoniot data of Comp B<sup>9</sup> and MYLAR.<sup>8</sup> One dot in the diagram summarizes many experiments using various flyer diameters, but same flyer energy. The transition detonation/no-detonation is typically observed by changing the shock loading diameter only by 1 mm in the critical region. The initiation threshold curve divides the  $E/\phi$  plane in the regions of detonation (above the curve) and no detonation (below the curve).

Comp B shows the expected rise of initiation threshold when decreasing the impact area. Additionally, there are three important conclusions deduced from the investigations

Table 2. Density and Composition of the Used Explosive Materials

Explosive	Density (g/cm <sup>3</sup> )	Explosive
Comp.B	1.74	64% RDX, 36% TNT, cast
Octol	1.81	75% HMX, 25% TNT, cast
PBX N5	1.79	95% HMX, 5% Viton-A pressed
TNT	1.59	pressed
TNT	1.59	cast

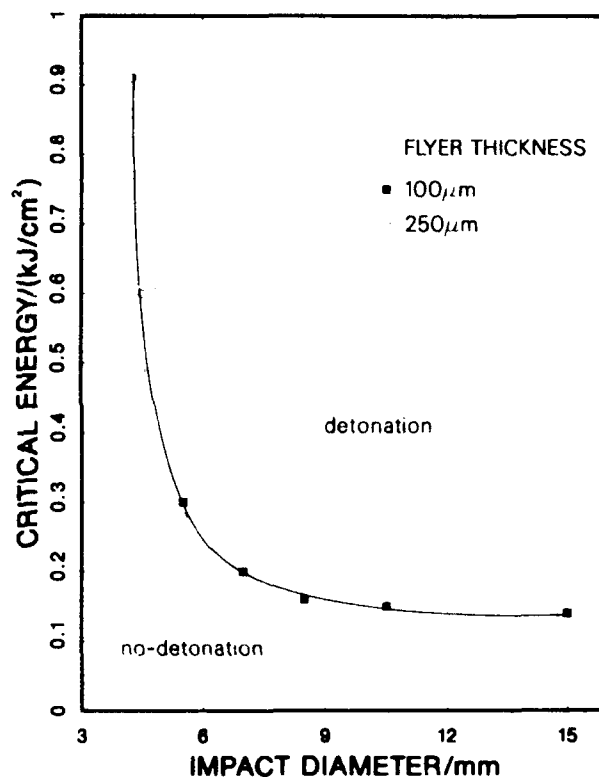


Figure 4. Initiation Threshold of Comp B Vs. Impact Diameter Using Two Types of Flyers

1. Using flyers with different thicknesses (which means various pulse widths) but same diameter, the same critical energy is measured. Obviously, the delivered energy per unit area controls the initiation process when small areas are used at least for short duration pulses ( $30 < t < 100$  ns)

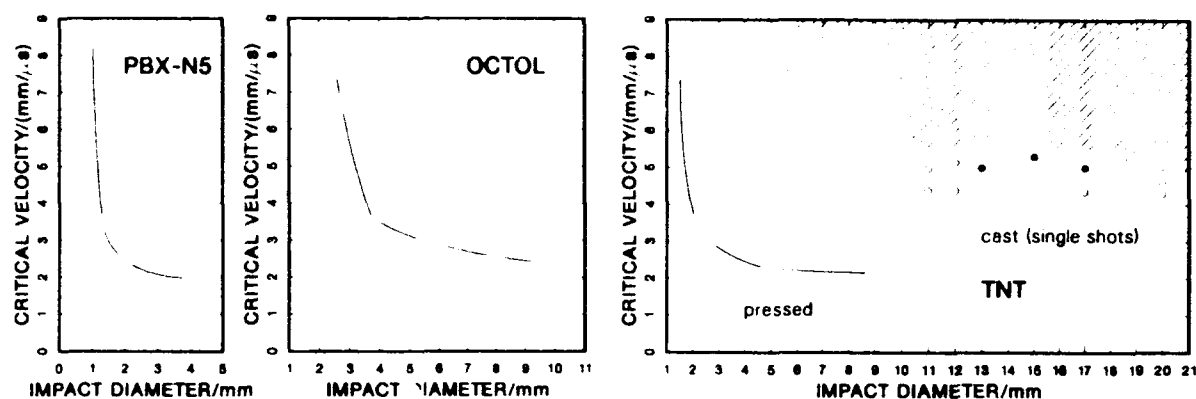


Figure 5. Initiation Threshold of Several High Explosives Vs. Impact Diameter. Each point results from a series of experiments except for cast TNT, where the single shots are noted (● Detonation; ○ No-Detonation).

Table 3 Experimental Results of the Initiation Studies.  
(\*Cast, α Pressed High Explosives)  $\phi_{min}$  is the Minimal Shock Loading Diameter

Explosive		Density (g/cm <sup>3</sup> )	D(mm/μs) lit. <sup>12</sup> exp.	E <sub>d</sub> (J/cm <sup>2</sup> ) lit. <sup>2</sup> exp.	$\phi_{min}$ /mm
Comp B	*	1.74	7.92 7.94	150 150	4
Octol	*	1.81	8.48 8.47	— 120	2.5
PBX N5	(α)	1.79	— 8.56	(109) 100	1.0
TNT	(α)	1.59	6.93 6.90	142 110	1.0
TNT	*	1.59	6.93 (6.5)	420 400	5-12

2. Increasing the shock loading area, the initiation threshold reaches a value of about 150 J/cm<sup>2</sup>. This result corresponds to the critical energy of Comp B for the plane detonation. The investigations show a continuous transition from one dimensional initiation described by the critical energy concept to two-dimensional shock initiation.

3 The onset of a stable detonation requires, even for the fastest flyer, a minimum shock loading diameter of about 4 mm. This result corresponds to the critical diameter due to the diameter effect.

The experimental results for PBX N5, Octol, and TNT are shown in Figure 5. Lacking precise Hugoniot data for these high explosives, the impact velocity is chosen as initiation threshold and the experiments are done with only one flyer thickness (250 μm). In principle, all explosives show the same

behavior: increasing initiation threshold by decreasing the shock loading area, and critical values for the impact diameter (similar to diameter effect) as well as for the impact velocity (in agreement with the one-dimensional put-criterion).

PBX-N5, the most sensitive explosive in this selection, shows a minimum impact diameter of 1 mm and a critical impact velocity of about 2 mm/μs. A high sensitivity is also observed for pressed TNT, featuring a minimal shock loading area of 1 mm in diameter and a critical impact velocity of about 2.2 mm/μs. The cast explosive Octol is less sensitive, with a flyer diameter of 2.5 mm and a critical velocity of 2.4 mm/μs. The most insensitive explosive is cast TNT. The experiments show a minimum velocity of 5.5 mm/μs. The critical impact diameter cannot be determined by means of the present electric gun. In Figure 5, the

shading marks the region of impact parameters not available by the gun. However, the minimal impact diameter is estimated with 12 mm.

Table 3 summarizes the results and compares the detonation velocity and the critical energy with data taken from other authors.<sup>2,12</sup>

The presented experiments, with fixed charge length of 20 mm, give an average detonation velocity calculated by the transit time taken from the multiplier trace. Comparing these velocities with the corresponding ideal detonation velocity, we found a remarkable difference between the less and the more sensitive explosives. In experiments using the pressed explosives and Octol, the average velocity agrees with the ideal detonation velocity if the impact conditions lie above the initiation threshold curve. For Comp B it makes a difference whether the impact conditions are near or far away from the initiation curve. In the second case, the measured transit-time gives the ideal detonation velocity. However, approaching the critical region near the initiation threshold curve, a significant increase of transit time is observed. This increase is an indication of run to detonation or transition effects. A similar behavior may be found for cast TNT, as indicated by the low average detonation velocity measured in our experiments.

### Detonation Velocity

In order to investigate the transition effects more precisely, the distance-time-development of the detonation front along the charge axis was measured by impacting samples with various charge lengths under the same impact conditions. The transit times were taken again from the multiplier trace. One may notice that the detonation propagates as a curved front. The transit times are detected on the charge axis, because it is here where the earliest outbreak of the detonation front is generally found.

The results for Comp B are presented in Figure 6. Three different flyer diameters are used. 14 mm is far away from the initiation threshold, 8 mm is near, and 4 mm is below the initiation threshold. For 14 mm impact diameter, the detonation wave is propagating with ideal detonation velocity  $D_{id}$ . Using 8 mm

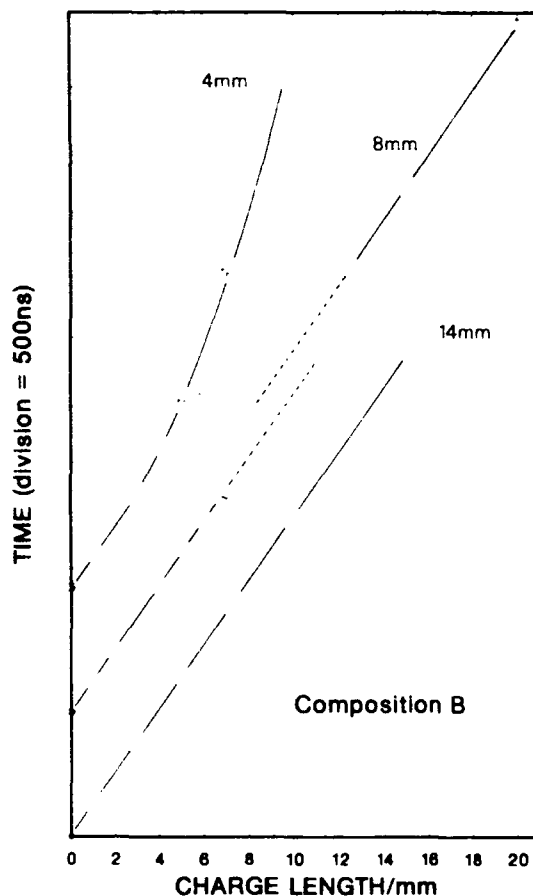


Figure 6. The Influence of the Impact Diameter on the Axial Propagation of Detonation for Comp B

diameter flyers, the detonation front starts again with  $D_{id}$ , but after 8 mm distance traversed the velocity is reduced to about 6 mm/ $\mu$ s. The transition phase of about 4 mm is followed by a stable detonation with  $D_{id}$ . At last, the 4 mm flyer plate leads to a dying detonation after a starting phase with  $D_{id}$ . Obviously, the lateral release waves are responsible for the phenomena observed beyond or near the critical energy level, and not a delayed start of the detonation. Further evidence for this assumption can be obtained from the experiments dealing with the detonation development presented in the next section.

The experimental results for the other explosives are shown in Figure 7. If a stable detonation occurs, the constant detonation velocity for the more sensitive explosives PBX-N5, Octol, and pressed TNT are independent of the used impact parameters. The relatively



insensitive cast TNT shows a slowly dying detonation; similar to Comp B impacted with 4 mm-diameter-flyer. Using charges shorter than 10 mm, we found ideal detonation velocity. For longer samples, the detonation velocity decreases, and above 30 mm, no detonation is observed. Obviously, the transmitted energy is greater than the one-dimensional critical energy. The reason for the failure of the stable detonation is the small charge diameter. Further experiments with 100 mm charges of cast TNT initiated by a Comp B-booster, showed the critical diameter due to diameter effect between 25 and 30 mm. Thus, the experiments with 20 mm charge diameter carried out with the Electric Gun, have to fail in the end.

### Detonation Development

Finding out the more or less strong influence of the lateral rarefaction waves for the onset of a stable detonation, the detonation development was studied with the described optical device. In this paper the results for Comp B, as an insensitive high explosive, and for PBX-N5, as a more sensitive explosive material, may be presented.

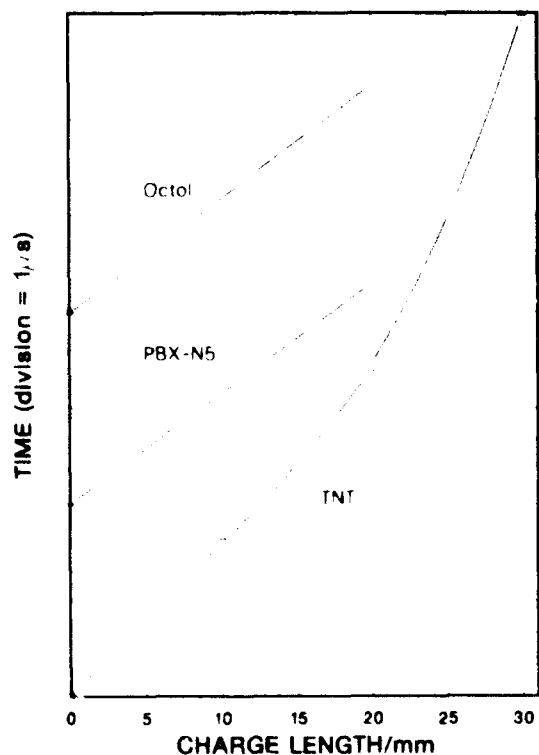


Figure 7. Propagation of Detonation on the Charge Axis for Different High Explosives

To calculate the detonation front from the experimental data, these data were at first combined in a three-dimensional-plot. An example is shown in Figure 8. Subsequently, one can find out the detonation front as the contour lines of the 3-dimensional-surface. The results for Comp B are presented in Figure 9. The impact parameters used here are the same as in the detonation velocity measurements discussed above.

One can easily find a correlation between the time-distance-development on the charge axis (Figure 6) and the changes in detonation front curvature. The developments and the correlations will be discussed in detail.

**Impact-diameter 14 mm:** In the beginning, the detonation front is flat according to the initiating shock wave. While propagating, lateral release waves are continuously decreasing the flat region, until at about 15 mm charge length, the release waves reach the charge

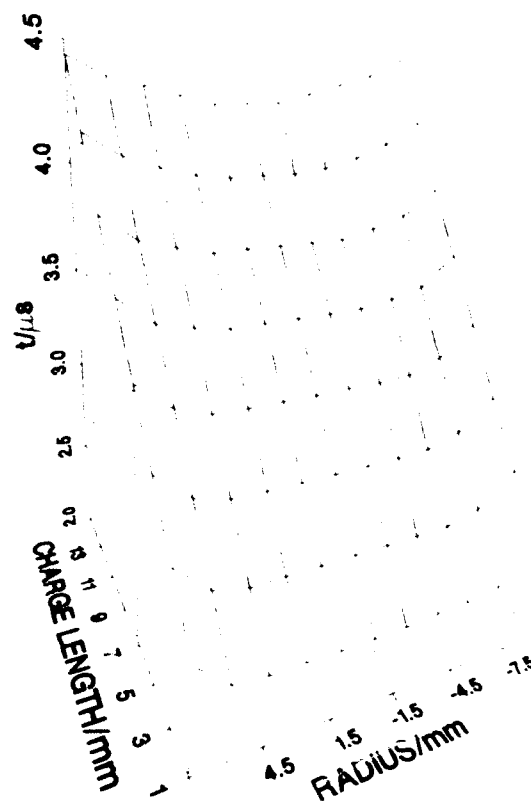


Figure 8. Three-Dimensional-Surface in a Radius-Length-Time-Plot Resulting from Comp B Experiments with the Same Impact Velocity and Diameter but Different Charge Lengths

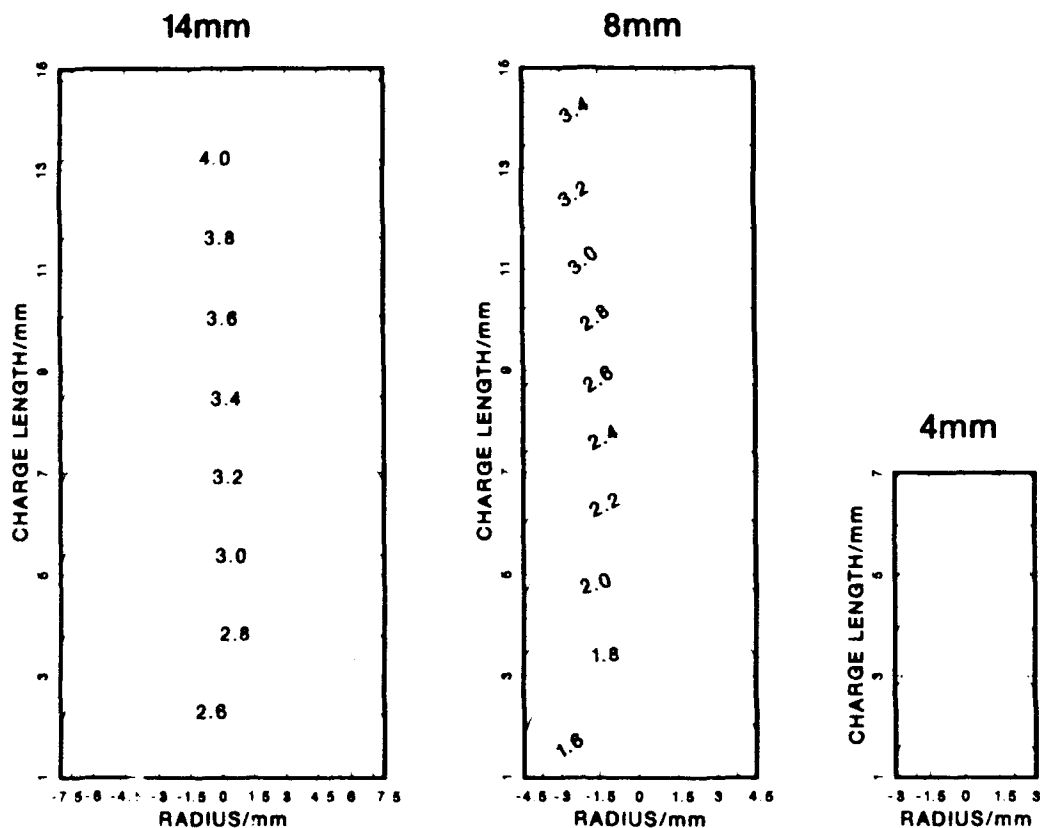


Figure 9. The Influence of Impact Diameter on the Development of the Detonation Front for Comp B. Charge diameter 20 mm, impact diameter 4/8/14 mm.

axis. From now on, the front curvature holds a constant value.

**Impact diameter 8 mm:** In this case, the release waves reach the axis at about 6 mm charge length. In the following process, the front curvature is increased to a maximum at 10 mm and becomes smaller for longer charge length. This maximum in front curvature correlates with the transition phase of the velocity measurement. Finally, the curvature becomes constant according to the ideal detonation velocity.

**Impact diameter 4 mm:** The first stage of the development agrees with the proceeding cases, except that the release waves reach the charge axis earlier, according to the smaller impact diameter. The front curvature reaches its maximum near 4 mm and, subsequently, the detonation dies.

Contrary to Comp B or cast TNT, where a stable detonation demands a minimal impact diameter of a few millimeters, an impact diameter of about 1 mm is sufficient to initiate

pressed TNT and PBX-N5 reliable. Especially for PBX-N5, with a critical diameter of 1 mm, the initiation can be regarded as nearly point-like. The detonation development after such a point-like shock initiation is presented in Figure 10. The calculation of the contour from the experimental data was done in two steps. First, it was proved using a side-on measurement of the phase velocity that the detonation velocity is independent of the direction. In the second step, the detonation front was calculated from the end-on measurement of the phase velocity with the help of the known initiation point. In addition to the experimental contours, Figure 10 also shows the theoretical detonation fronts with the assumption of an ideal spherical propagation.

For charge lengths greater than 8 mm, a good agreement between experimental and theoretical fronts exists in terms of the precision of test. On the basis of the end-on measurements, the detonation propagates at least in a generating angle of  $100^\circ$  with constant ideal detonation velocity. Deviations of

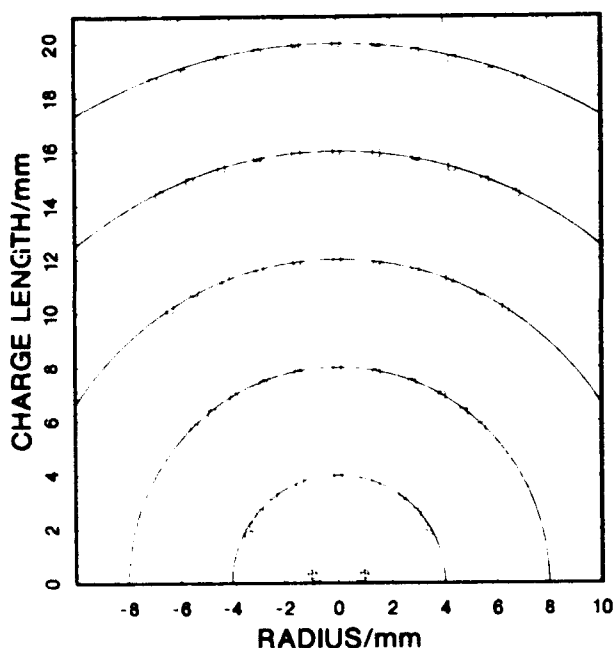


Figure 10. Detonation Front in PBX-N5. Charge diameter 20 mm, impact diameter 1 mm. The initiation occurs nearly point-like.

the lateral flanks of the front from the ideal development for short charge length are due to the disturbance of the propagation affected by the diagnostics

## DISCUSSION

At first sight, our results concerning the initiation threshold of high explosives having a fixed length are similar to the projectile studies. Although release waves should not be taken into account during the flyer impact, these investigations show a real increase of the initiation threshold with reference to the buildup of a stable detonation. In this case, a continuous transition from the one dimensional shock initiation described by the critical energy concept to two dimensional shock initiation effects is observed. However, in Comp B a modified put criterion is found in the case of the two dimensional flyer impact, using a fixed shock loading area but different flyer thicknesses, the critical energy to initiate a stable detonation is constant. Surely, this behavior has been proved only in a relatively small range of pulse width

Taking into account the experiments on the detonation buildup, the investigations show that the result of the initiation threshold test is not only affected by the impact area, but also by the charge length. It is necessary to distinguish between the threshold for a primary initiation and for a stable detonation.

An increase of the primary initiation threshold is not observed in the flyer plate experiments. This result is obtained by means of the detonation development on the charge axis for Comp B, shown in Figure 6. In all cases, a primary detonation was measured independently on the flyer diameter. Actually, an initial propagation with ideal detonation velocity is expected, at least until the lateral release wave reaches the axis of the charge for two reasons. Firstly, in this case, the provided energy per unit area of about  $360 \text{ J/cm}^2$  is much greater than the critical value of  $150 \text{ J/cm}^2$ . Secondly, the run-to-detonation is finished after less than 1 mm, because of the high impact pressure. From this point of view, an increase of the primary initiation threshold is not observed in the flyer plate experiments similar to the models of Moulard and James.

However, studies of detonation development show the buildup of a finally stable detonation being indeed affected by the shock loading area. In other words, the put-criterion is only veiled by the lateral release effects during the propagation of the detonation. Apparently, the higher threshold of a stable detonation is due to the losses of the lateral rarefaction wave. This shown difference between primary detonation and stable detonation raises the question of the comparability of initiation tests using small shock loading area. The results of such tests are strongly affected by the charge length, especially when less sensitive explosives such as Comp B or cast TNT are used.

In study of the detonation development, it is observed that the less sensitive the explosive material is, the stronger the buildup of the detonation is influenced by the lateral release wave. Using special impact conditions in experiments on Comp B transition phases from the primary initiation to a stable detonation, as well as dying detonation waves, were found.

The most sensitive high explosives in this study show no run-to-detonation effects. Furthermore, these materials can be initiated by very small flyers (diameter about 1 mm). In this case, the initiation can be regarded as nearly point-like, and the detonation front can be fitted by an ideal spherical propagation.

## ACKNOWLEDGEMENT

The authors wish to thank H. Scholles, Rheinmetall AG, for the preparation of the pressed high explosives.

## REFERENCES

1. Walker, F. E., et al., "Critical Energy for Shock Initiation of Heterogeneous Explosives," *Explosivstoffe*, Vol. 17, 1969, pp. 9-13.
2. Walker, F. E., et al., "A General Model for the Shock Initiation of Explosives," *Propellants, Explosives, Pyrotechnics*, Vol. 1, 1976, pp. 73-80.
3. Held, M., "Critical Area for the Initiation of High Explosive Charges" in Asay, J. R., et al., Ed., *Shock Waves in Condensed Matter-1983*, Elsevier Science Publishers B. V., 1984.
4. de Longueville, Y., et al., "Initiation of Several Condensed Explosives by a Given Duration Shock Wave" in *Proceedings of the Sixth Symposium on Detonation*, San Diego, CA 1976, ONR Report-ACR-221, pp. 16-24.
5. Moulard, H., "Critical Conditions for Shock Initiation of Detonation by Small Projectile Impact" *Proceedings of the Seventh Symposium on Detonation*, Annapolis, MD 1981, pp. 316-324.
6. James, H. R., "Critical Energy Criterion for the Shock Initiation of Explosives by Projectile Impact," *Propellants, Explosives, Pyrotechnics*, Vol. 13, 1988, pp. 35-41.
7. Chau, H. H., et al., "Electric Gun - A Versatile Tool for High-Pressure Shock Wave Research," *Rev. Sci. Instruments*, Vol. 51, 1980, pp. 1676-1681.

8. March, S. P., Ed., *LASL Shock Hugoniot Data*, University of California Press, Berkeley, 1980.
9. Hollenberg, K., et al., "Initiierung von Sprengstoffen durch Stoßwellen," *Verhandl. DPG (VI)*, Vol. 15, 1980, p. 634.
10. Tucker, T. J., et al., "Electrical Gurney Energy," Sandia Laboratories, Albuquerque, NM, 1975, Report-SAND-750244.
11. Howe, P. M., "On the Role of Shock and Shear Mechanism in the Initiation of Detonation by Fragment Impact," *Proceedings of the Eighth Symposium on Detonation*, Albuquerque, NM, 1985, pp. 1150-1159.
12. Dobratz, B. M., Ed., *LLNL Explosives Handbook*, Lawrence Livermore National Laboratories, 1981, Report-UCRL-52997.

## DISCUSSION

R. S. LEE, Lawrence Livermore National Laboratory, Livermore, CA

When you change flyer diameter, is the barrel always the same diameter as the width of the bridge?

## REPLY BY H. R. KLEINHANß

The width of the exploding foil was only changed to get higher impact velocities from small flyers and was always greater than the inner diameter of the barrel. The holder and the diameter of the explosives were constant in all experiments. If necessary, the direct shock wave was attenuated by a Pb-layer between holder and explosive.

## DISCUSSION

B. NEYER, EG&G Mound Applied Technology, Miamisburg, OH

We have noticed that the flyer velocity that corresponds to threshold is not constant but varies as a function of flyer distance, presumably due to curvature and/or pressure in the flyer. Thus, care must be used when talking about critical energy.

## REPLY BY H. R. KLEINHANß

It is necessary to take notice that the flyer distance has influence on both the flatness and velocity of the flyer. In our experiments care was taken for a flat impact and the change in velocity was considered. The mentioned effect was not observed.

## DISCUSSION

J. Roth, Consultant  
Portola Valley, CA

Since you appear to have agreed that the steep vertical rise in the critical velocity versus impact diameter plots (Figure 5) correlates with the critical diameter, I find it surprising that the "apparent" critical diameter of Octol is greater than that of pressed TNT.

## REPLY BY H. R. KLEINHANß

Regarding the influence of curvature on the propagation of the detonation front, a correlation between the critical diameter and the minimal impact diameter seems plausible. A difference between the two effects is that in our experiments the diameter of the high explosive is always greater than the impact diameter, while in the experiments investigating the critical diameter the explosive material is surrounded by an inert material. We found the high sensibility of pressed TNT surprising, too. We did not determine the critical diameter of the investigated pressed TNT but following the data of other authors the critical diameter of pressed TNT is indeed smaller than that of Octol (Campbell et al., 6th Symposium on Detonation).

# A TWO-DIMENSIONAL LAGRANGIAN TECHNIQUE FOR SHOCK INITIATION DIAGNOSIS

Huan Shi\* and Ding Jing\*\*  
Beijing Institute of Technology  
Department of Engineering Mechanics  
P.O. Box 327, Beijing 100081, PRC

*The one-dimensional Lagrangian measurement and analysis technique has been used successfully during the past decade in studying the shock initiation and detonation processes in energetic materials. However, many shock-to-detonation transitions and steady-state detonations are not really one-dimensional. The objective of this paper is to propose a two-dimensional (2-D) Lagrangian probe, a 2-D experimental system, and a quasi-one-dimensional Lagrange analysis. Advantages of this new technique are discussed. Using the proposed technique, some interesting results on the shock initiation of pressed TNT have been demonstrated.*

## INTRODUCTION

In the past decade, a one-dimensional (1-D) Lagrangian technique has been used successfully for shock initiation studies in heterogeneous explosives. Many positive results were obtained.<sup>1-3</sup> However, most shock initiation and steady-state detonation processes were not really 1-D. The two dimensional (2-D) effects on the shock initiation process have not been studied in detail. In this paper a 2-D Lagrangian technique is presented which includes a 2-D Lagrangian probe, a 2-D experimental system, and a quasi-1-D Lagrange analysis. The processes of 2-D shock initiation and shock wave attenuation in pressed TNT are measured simultaneously

## TWO-DIMENSIONAL LAGRANGIAN PROBE AND ITS CALIBRATION

Recently, G. Rosenberg et al.<sup>4</sup> modified the electromagnetic velocity gauge for

measuring the radial particle velocity in 2-D flow. A constantan radial velocity gauge has been developed by Z. Rosenberg et al.<sup>5</sup> to measure the radial displacement in axisymmetric impact configurations.

In the present work, a new probe is used to measure simultaneously the pressure  $p$  and the radial displacement  $(r - r_0)$  histories of particles at different Lagrangian positions, for axis-symmetric flow of condensed materials under shock loading. This new probe is called a 2-D Lagrangian Composite Manganin Constantan (CMC) ring probe (see Figure 1).<sup>6</sup>

The dynamic piezoresistance and tensile coefficients of the probe must be calibrated experimentally. The piezoresistance coefficient of manganin is obtained by a conventional 1-D method.

$$p(\text{GPa}) = 0.27 + 34.40 \left( \frac{\Delta R}{R_0} \right) \quad (1)$$

$$+ 1.07 \left( \frac{\Delta R}{R_0} \right)^2$$

$$2.2 < p < 46.0 \text{ GPa}$$

\* Present address: Changsha Institute of Technology, Department of Applied Physics, Changsha, Hunan, China

\*\* Currently on sabbatical leave at CETR, New Mexico Tech, Socorro, NM 87801

$$\frac{\Delta R}{R_0} = \left( \frac{\Delta R}{R_0} \right)_m - \frac{K_m}{K_c} \left( \frac{\Delta R}{R_0} \right)_c \quad (2)$$

$$r = r_0 \left| 1 + \frac{1}{K_c} \left( \frac{\Delta R}{R_0} \right)_c \right| \quad (3)$$

where  $\Delta R/R_0$  is the relative variation of the resistance,  $r_0$  the initial radius of the active element,  $R_0$  the initial resistance of the probe,  $K$  the tensile coefficient, subscripts  $m$  and  $c$  denote manganin and constantan, respectively.

The tensile coefficients of both manganin and constantan are about 2.0 in static calibration. However, the strain rate in shock loading could be up to  $10^3 - 10^6 s^{-1}$ . For this reason, an experimental system for dynamic calibration of these tensile coefficients<sup>7</sup> was designed. It was found:

$$K_c = \begin{cases} 2.141 & (\epsilon \leq 0.0466) \\ 4.178 - 90.30\epsilon + 999.7\epsilon^2 & (0.0466 < \epsilon \leq 0.09) \end{cases} \quad (4)$$

$$K_m = \begin{cases} 0.5205 + 0.8453\epsilon + 1771\epsilon^2 - 23215\epsilon^3 & (0.0046 < \epsilon \leq 0.0456) \\ 2.040 & (0.0456 < \epsilon \leq 0.171) \end{cases} \quad (5)$$

where strain  $\epsilon = \Delta r/r_0$ .

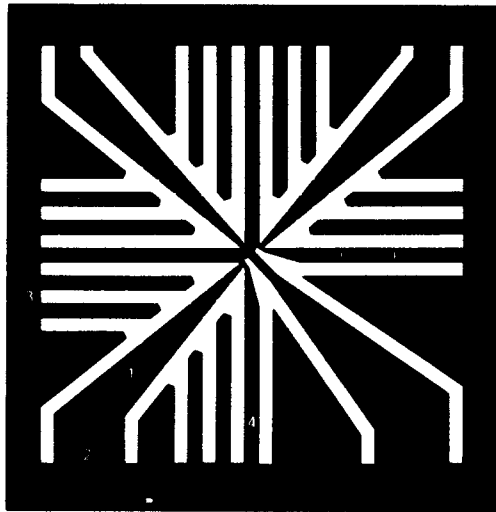


Figure 1. 2-D Lagrangian CMC Probe

- |                            |                           |
|----------------------------|---------------------------|
| 1. Active Elements         | 3. Leads (power terminal) |
| 2. Leads (signal terminal) | 4. Scale Mark             |

## 2-D SHOCK INITIATION EXPERIMENTS

In order to obtain the shock wave for initiating an explosive at a required amplitude, metal plates of different thicknesses are used. There are two devices with different diameters, which are simply called large (L) and small (S) devices, respectively (see Figure 2).

For each shot, four curves are recorded on two different Lagrangian positions ( $h, r_0$ ). In general, two of these are the records from the manganin parts, and the others are from the constantan parts. A four-channel constant current supply is used to power the probe, and to make the current impedance match at the probe terminals minimizing the influence of

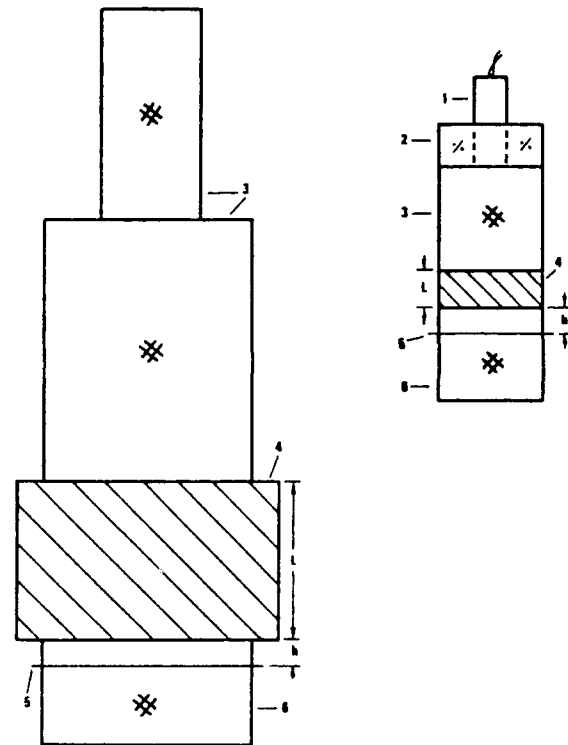


Figure 2. 2-D Shock Initiation Devices

1. Detonator
2. PMMA holder
3. Pressed TNT charges:
  - a -  $\phi 20.3 \times 39.6$  mm (1.577 g/cm<sup>3</sup>)
  - b -  $\phi 40.3 \times 49.7$  mm (1.594 g/cm<sup>3</sup>)
  - c -  $\phi 20.1 \times 19.8$  mm (1.594 g/cm<sup>3</sup>)
4. Metal Plate:
  - a - Aluminum,  $\phi 50.0$  mm
  - b - Copper,  $\phi 20.0$  mm
5. 2-D Lagrangian probe
6. Sample charge

leads resistance. Typical experimental records are shown in Figure 3.

In this work the 2-D axisymmetric shock initiation flow fields of pressed TNT ( $\rho_0 = 1.564\text{g/cm}^3$ ) were measured for three different initiation conditions. For the L device, the initial pressure at the center is about 4.1 GPa when the thickness of the aluminum gap  $L_{A1}$  is 43.01 mm (Figure 4). For the S device the pressures are about 4.3 and 3.2 GPa, respectively, for  $L_{Cu} = 7.02$  and 10.03 mm (Figure 5). The 2-D shock initiation processes under the first two conditions, and the shock failure process under the last condition for pressed TNT samples were studied. Results are shown in Figures 4, 5, and 6, respectively.

### QUASI-1-D LAGRANGIAN ANALYSIS

Near the axis of a 2-D axisymmetric flow, we have<sup>8</sup>

$$\rho \frac{\partial \rho}{\partial t} + \frac{\partial u}{\partial z} + \frac{2\omega}{r} = 0 \quad (6)$$

$$\rho + \frac{\partial u}{\partial t} + \frac{\partial p}{\partial z} = 0 \quad (7)$$

where  $\rho$  is density,  $u$  is the velocity component along the axis, and  $\omega$  is the velocity component perpendicular to the axis;  $z$ ,  $r$ ,  $t$  are space and time coordinates.

Transforming the above equations from the Eulerian form into the Lagrangian form, the following equations are obtained:

$$u = u_1 - \frac{1}{\rho_0} \int_{t_1}^t \left( \frac{r}{r_0} \right)^2 \quad (8)$$

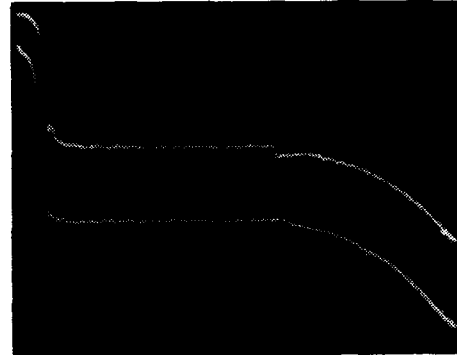
$$\left| \left( \frac{\partial p}{\partial h} \right)_j - \left( \frac{\partial p}{\partial t} \right)_h \left( \frac{\partial t}{\partial h} \right)_j \right| dt$$

$$V = V_1 + \left( \frac{r}{r_0} \right)^2 \int_{t_1}^t \quad (9)$$

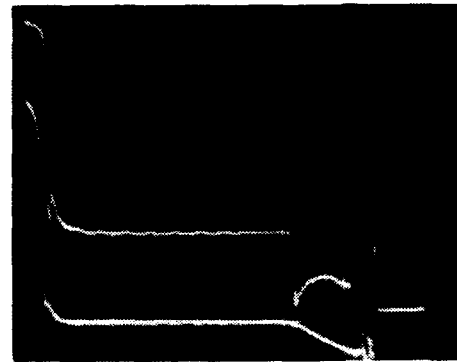
$$\left| \left( \frac{\partial u}{\partial h} \right)_j - \left( \frac{\partial u}{\partial t} \right)_h \left( \frac{\partial t}{\partial h} \right)_j \right| dt$$

where  $u$  is the particle velocity,  $V$  the specific volume,  $\rho_0$  the initial density, subscript 1 denotes the shock front,  $h$  denotes the partial differentiation along the particle path, and  $j$  along the  $j$ th pathline, respectively.

Comparing the quasi-1-D with the 1-D Lagrangian analysis, the only difference is that a factor  $(r/r_0)^2$  must be added in the former analysis. The particle velocity  $u$  can be obtained by using the quasi-1-D Lagrangian analysis code with  $p$  -  $r$  experimental data (as shown in Figures 4 and 5) for the input. The particle velocity and specific volume near the axis of symmetry can be obtained by solving Equations (8) and (9), respectively. The rest of the physical quantities, such as specific internal energy, reaction extent et al. can be obtained in a way similar to the 1-D Lagrangian analysis.<sup>3</sup> Figure 7 (a) and (b) show the experimental chemical reaction extent  $\lambda$  (dotted lines), compared with that calculated by the quasi-1-D Lagrangian method (solid lines).



(a)



(b)

Figure 3. Experimental Records (2  $\mu\text{s/div}$ )

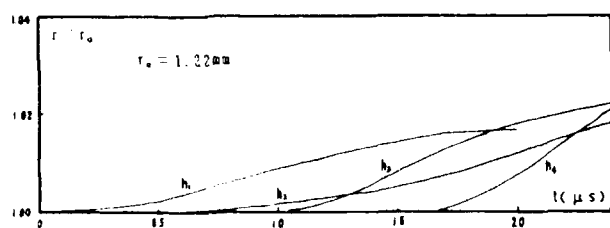


## DISCUSSION

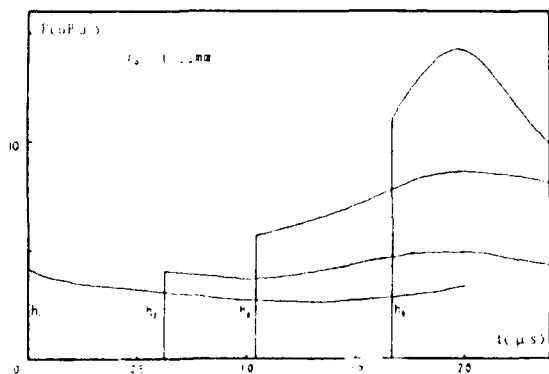
There are four obvious advantages with a 2-D Lagrangian experimental method. The first is a simplified loading device with small loading charge. The second is that the pressure of the initiating shock pulse can be adjusted continuously by changing gap thickness. The third is that no limitation is exerted on the length from the initiation point to the measuring point. This allows the study of the entire process of detonation failure or the transition from the initiation shock pulse to a steady state detonation wave. The fourth is the most important, that is, this method can be used to study the effects of lateral rarefaction in shock initiation and steady-state detonation processes.

The similarity between 1-D and 2-D shock initiation flow is that both have a pressure peak, that is a combustion wave peak,

which is moving toward the shock front. The difference is that the amplitude of the peak for a 2-D condition is lower than that in a 1-D condition. For a 1-D condition, the transition to detonation occurs very rapidly as the trailing pressure peak overtakes the shock front. However, this is not true for the 2-D condition. Even when the peak overtakes the shock front, the front pressure is still much lower than the C-J value, and should run about 2-3 mm to reach detonation. The shock initiation threshold of pressed TNT is in the range from 3.2 to 4.3 GPa under the 2-D small gap loading condition, but a shock of the same shock front pressure (3.2 GPa) could initiate this kind of TNT charge rapidly in a 1-D condition. All these differences provide evidence that the effects of the lateral rarefaction produce an energy loss which is an important factor for controlling the 2-D shock initiation process. They also suggest that the initiation



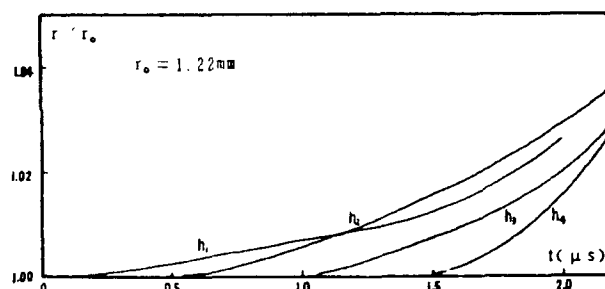
(a)



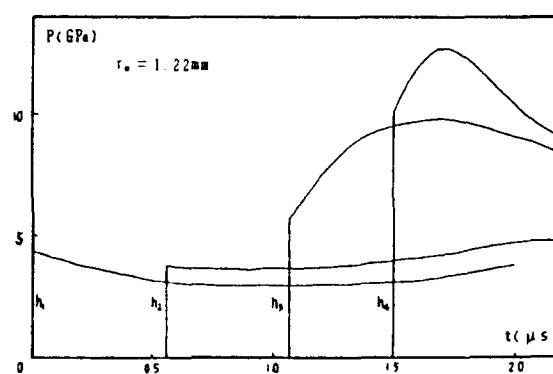
(b)

Figure 4. 2-D Shock Initiation (L device)

$$L_{A_1} = 43.01 \text{ mm} \quad h_1 = 0.00 \text{ mm} \quad h_3 = 4.00 \text{ mm} \\ r_0 = 1.22 \text{ mm} \quad h_2 = 2.34 \text{ mm} \quad h_4 = 7.00 \text{ mm}$$



(a)



(b)

Figure 5. 2-D Shock Initiation (S device)

$$L_{C_u} = 7.02 \text{ mm} \quad h_1 = 0.00 \text{ mm} \quad h_3 = 4.06 \text{ mm} \\ r_0 = 1.22 \text{ mm} \quad h_2 = 2.08 \text{ mm} \quad h_4 = 6.08 \text{ mm}$$

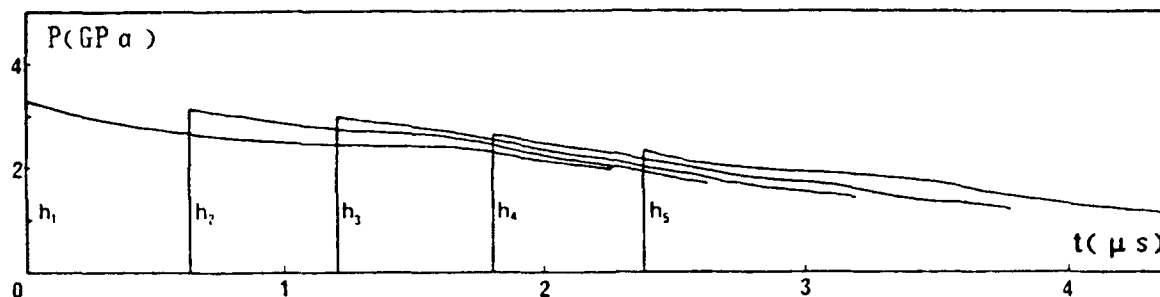


Figure 6. Shock Initiation Failure (S device)

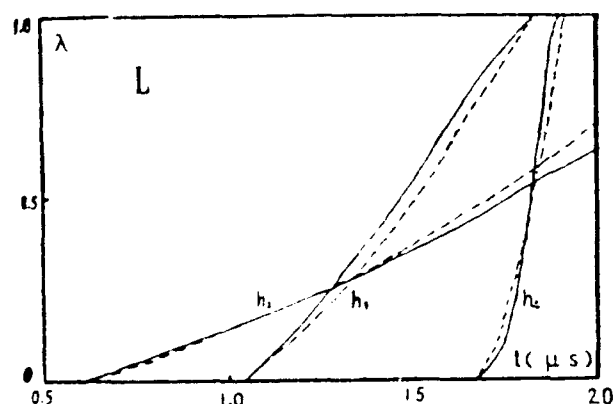
$$L_{cu} = 10.03 \text{ mm} \quad h_1 = 0.00 \text{ mm} \quad h_3 = 4.16 \text{ mm} \quad h_5 = 8.14 \text{ mm} \\ r_0 = 1.22 \text{ mm} \quad h_2 = 2.21 \text{ mm} \quad h_4 = 6.18 \text{ mm}$$

process is not only related to the shock front, but also related to the flow following the shock front.

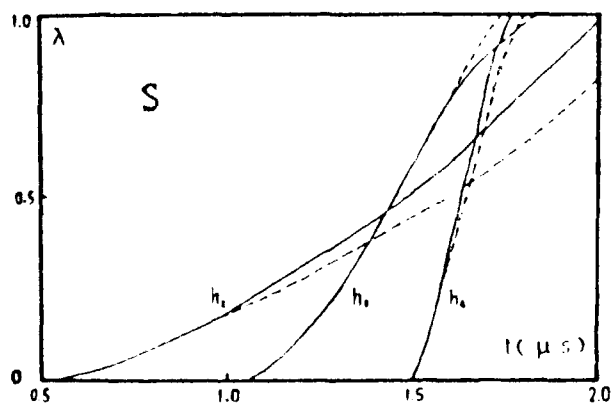
In a 2-D shock initiation flow field, the distribution of pressure is changed with the initial radius  $r_0$ . The farther from the axis the particle is, the lower are the pressures at the shock front and the combustion peak, the

faster the pressure decreases behind the shock front, and the larger is the radial component of the particle velocity. This trend becomes more pronounced as the charge diameter decreases.

The quasi-1-D Lagrangian analysis method can be applied to the flow fields near the axis of the 2-D axisymmetric flow to obtain many other physical quantities. Equations (8) and (9) show that the radial divergence, even near the axis, influences the flow field quadratically.



(a) L device



(b) S device

Figure 7. Reaction Extent Curves

## REFERENCES

1. Cowperthwaite, M. and Rosenberg, J. T., "A Multiple Lagrange Study of the Shock Initiation Process in Cast TNT," *Proceedings of the Sixth Symposium (International) on Detonation*, Coronado, CA 24 Aug 1976, pp. 786-793.
2. Vantine, H. C.; Rainsberger, R. B.; Curtis, W. D.; Lee, R. S.; Cowperthwaite, M.; and Rosenberg, J. T., "The Accuracy of Reaction Rates Inferred from Lagrangian Analysis and In-Situ Gauge Measurements," *Proceedings of the Seventh Symposium (International) on Detonation*, Annapolis, MD, 16 Jun 1981, pp. 466-478.
3. Huan, S.; Xue, H. L.; and Ding, J., "Lagrange Gauge Analysis for Evaluating Reaction Characteristics in Shocked Explosives," *Proceedings of the International Symposium on Intense Dynamic Loading and Its Effects*, Beijing, China, 3 Jun 1986, pp. 144-149.

4. Rosenberg, G.; Yaziv, D.; and Mayseless, M., "Electromagnetic Gauge for Measuring the Radial Particle Velocity in 2-D Flow," AIP Conference Proceedings No. 78, *Shock Waves in Condensed Matter-1981*, Menlo Park, CA, 23 Jun 1981, pp. 495-499.
5. Rosenberg, Z.; Mayseless, M.; and Rosenberg, G., "Measurement of Radial Displacement in 2-D Flow by Embedded Constantan Wires," Proceedings of APS Topical Conference, *Shock Waves in Condensed Matter-1983*, Sante Fe, NM, 18 Jul 1983, pp. 247-249.
6. Huan, S. and Ding, J., "Probe for Two-Dimensional Flow Field Measurement," Proceedings of APS Topical Conference, *Shock Waves in Condensed Matter-1987*, Monterey, CA, 20 Jul 1987, pp. 589-592.
7. Huan, S., Yang, W. B., and Ding, J., "Experimental Calibration for the Dynamic Tensile Coefficients of Metal Foils," presented at the APS Topical Conference, *Shock Compression of Condensed Matter-1989*, Aug 1989, Albuquerque, NM.
8. Chan, S. K., "A Theory to Predict the Velocity-Diameter Relation of Explosives," *Proceedings of the Seventh Symposium (International) on Detonation*, Annapolis, MD, 16 Jun 1981, pp. 589-601.

# INFLUENCE OF RDX CRYSTAL SHAPE ON THE SHOCK SENSITIVITY OF PBXs

A. C. van der Steen, H. J. Verbeek, and J. J. Meulenbrugge  
TNO Prins Maurits Laboratory  
P.O. Box 45  
2280 AA Rijswijk  
THE NETHERLANDS

*The shape of RDX crystals in HTPB-based PBXs has a very large influence on the shock sensitivity. For formulations with irregularly shaped RDX crystals, a critical pressure of 3.2 GPa is found with the NOL Large Scale Gap Test. Formulations with crystals which are more spherical and with smoother surfaces, are much less sensitive and possess a critical pressure of 3.9 GPa. Some possible mechanisms which could elucidate the interaction between crystal shape and shock sensitivity are discussed.*

## INTRODUCTION

One of the most frequently used techniques to obtain less-sensitive explosives is to embed the explosive crystals in a polymer matrix: plastic bonded explosives, PBXs. Generally, it is assumed that the polymer reduces the sensitivity of the explosive, however, the performance of the explosive is also reduced.

A great deal of research has been carried out to characterize the properties of the PBX in relation to the type of polymer used. For example, Swallowe and Field investigated the impact sensitivity of explosives in contact with different polymers, and found an enhanced or reduced sensitivity depending on the polymer. They ascribed these effects to the mechanical strength of the polymer under impact.<sup>1</sup>

Also, the particle size distribution of the explosive in relation to the sensitivity of the PBX has attracted a lot of attention. For conventional explosives, it is well known that the shock sensitivity decreases with a decrease of the particle size of the explosive crystals. For PBXs this is also demonstrated by Moulard et al., who compared the shock sensitivities of RDX-based PBXs with a solid load of 70 wt percent, and with RDX particles of 6  $\mu\text{m}$ , 134  $\mu\text{m}$ , and 428  $\mu\text{m}$ .<sup>2,3</sup> The initiation distances are considerably longer for the PBX with the

smallest particles, and a thinner reaction zone was also found. By comparing these results with theoretical simulations with the Lee-Tarver three term ignition and growth model, they found that the lower sensitivity has to be related to the amount of RDX ignited in the initial shock wave.

Surprisingly, the influence of the particle shape on the shock sensitivity did not receive much interest up to now while it could be expected that the shape, especially for the bimodal and trimodal mixtures used in PBXs, plays an important role in the mutual interaction between the crystals and in the bonding between the crystal and the surrounding polymer.

This paper describes the first results of an extensive research program at the TNO Prins Maurits Laboratory on the influence of particle shape on the sensitivity of explosives. This program is part of a project to process and characterize explosives which are less sensitive and have a lower vulnerability. HTPB-based PBXs with a solid load of 85 wt percent were investigated. To reach this high value for the solid load we used bimodal mixtures of RDX, a coarse fraction with an average size of about 300  $\mu\text{m}$  and a fine fraction of about 25  $\mu\text{m}$ . We started these investigations with

two, commercially available, coarse samples of RDX whose crystal shapes differed considerably. However, gaining more insight into the factors influencing the sensitivity, we also investigated the effect of RDX which was specially treated to increase the spherical shape of the crystals.

The shock sensitivity of an explosive is normally tested with a simple gap test, or with the wedge test to determine the distance to detonation. Besides the NOI gap test,<sup>4</sup> we used a rather simple test to determine the distance and time to detonation for different impact pressures. This test has shown to be highly reproducible and easy to perform so that many different samples could be tested.<sup>5</sup>

In an earlier paper, we reported on the detonation velocity and the detonation pressure of PBXs with an 85 percent solid load of RDX. They are 8.0 km/s and 26.5 GPa which are very close to theoretically predicted values.<sup>5</sup> The mechanical strength of the PBXs in relation to the particle shape and size and the effect of aging will be discussed elsewhere.

## EXPERIMENTAL

### Explosive

Three different samples of coarse RDX and two different samples of fine RDX have been used for the bimodal mixtures. Typical scanning electron micrographs are shown in Figure 1. The particle size distributions for the different samples are presented in Figure 2, and the characteristic values are summarized in Table 1.

The samples can be described as follows:

Coarse A: This sample contains very irregularly shaped particles. Spherical, oval, or particles with the crystal shape characteristic for RDX are not observed.

Coarse B: This RDX is from a different source than sample A, and contains more or less round particles. Most particles are broken and show cleavage planes and sharp edges. The average particle size is also larger, as compared to sample A.

Coarse C: The crystals of this sample have been physically and chemically treated,

*Table 1. Average Particle Size ( $D(0.5)$ ) and 10 Percent and 90 Percent Values of the Particle Size Distribution of the RDX Samples ( $\mu\text{m}$ )*

Sample	d(0.5)	d(0.1)	d(0.9)
A	285	185	430
B	460	350	625
C	370	235	530
D	17	5	50
E	52	28	80

resulting in more spherical and oval particles. Note that small cracks could be observed on the surface of the crystal.

Fine D: This sample of small and regularly shaped particles is used to form bimodal mixtures with sample A and B.

Fine E: This sample was treated in the same way as sample C. Unfortunately, it was not possible to reach the same particle size as sample D. The crystals do look the same as those of sample C.

PBXs containing the following bimodal mixtures were studied: AD, BD, and CE. The coarse/fine ratio was taken  $R=64/36$ . This ratio gives the highest tap density for mixtures AD and BD, viz. 1450 and 1400 kg/m<sup>3</sup> respectively. The maximum for mixture CE is shifted to a lower percentage of the fine fraction, which is probably due to the different particle size distribution. The same ratio as for the other mixtures is taken, with a tap density of 1410 kg/m<sup>3</sup>. Theoretically, a tap density of 1325 kg/m<sup>3</sup> would be enough to reach a solid load of 85 wt percent.

### PBX

A polyurethane binder (HTPB and IPDI) and an IDP plasticizer are the main ingredients of the polymer binder. Also, Dantocol was added to improve the bonding between the non-polar polymer and the polar explosive crystals. PBXs were cast under vacuum and after curing the density was found to be 1580 kg/m<sup>3</sup>, indicating that hardly any voids are present in the PBX. A more detailed description of the casting procedure can be

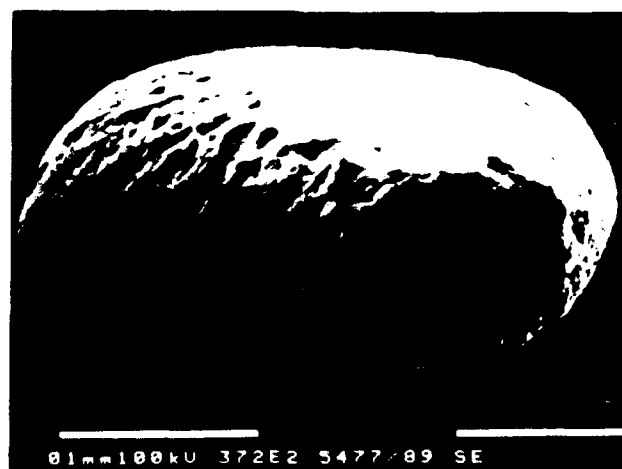
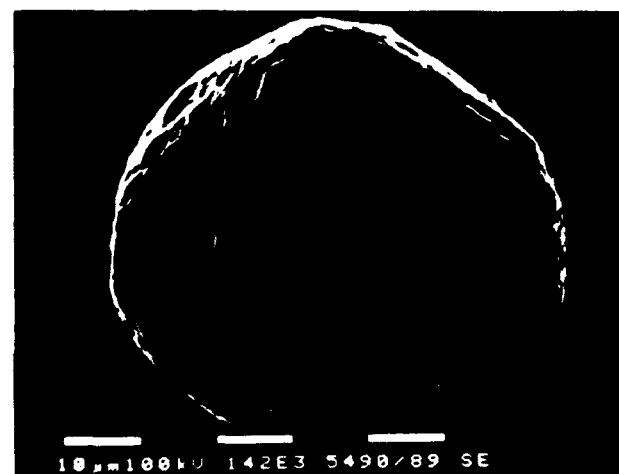


*Figure 1. Typical Scanning Electron Micrographs for the Coarse Samples A, B, and C (From Top to Bottom, Left Column) and the Fine Samples D and E (From Top to Bottom, Right Column)*

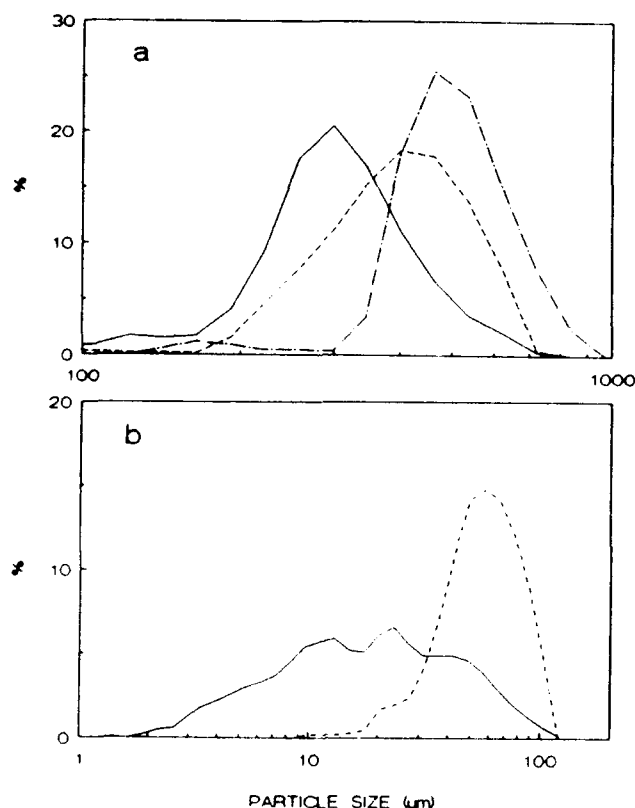


Figure 2. Particle Size Distributions of A: Coarse A (—), B (---), C (- · -), and D: Fine D (—), E (---) RDX Samples

found in Reference 5. Some samples were cast several times, to check the reproducibility of the casting procedure and the shock sensitivity test methods.

### Shock Sensitivity

The NOL Large Scale Gap Test is used to determine the critical pressure at which 50 percent of the experiments result in a detonation. It consists of a tetryl booster ( $l = 50$  mm,  $\phi = 50$  mm and  $\rho = 1510$  kg/m<sup>3</sup>) in combination with a plexiglass attenuator of the same diameter. The explosive is confined in a 140 mm long steel tube of 37 mm inner diameter and 48 mm outer diameter.

The same donor system is used to determine the time and distance to initiation of a bare PBX cylinder of 50 mm diameter, and without any confinement. A streak camera records the shock wave through the plexiglass

(back lighting) and the moment and position the shock wave enters the PBX. Also, the position and time the detonation wave emerges from the side surface of the PBX is recorded by the streak camera. The initiation distance and time are determined for different initiating pressures, i.e., lengths of the plexiglass attenuator.

In contrast with the wedge test, a spherical diverging shock wave is used to initiate the sample. Also, the distance to detonation is not determined on the central axis, but on the surface of the charge. However, from the streak recordings we learned that on arrival at the surface a detonation wave is propagating in the forward and backward direction. Since the velocities of both waves are about equal, they can probably be ascribed to the spherical extension of a detonation wave starting on the central axis of the charge. For this reason, it can be assumed that the results obtained with the present test will not differ considerably from wedge test results.

## RESULTS

The results obtained for the three different PBXs are presented in Figure 3. The solid lines represent the distances to detonation as a function of the pressure in the plexiglass at the plexiglass/PBX interface and the vertical dotted lines, the NOL measurements. The corresponding times to detonation show the same trend, and will be discussed elsewhere.

As could be expected, the trend observed for all formulations in Figure 3 is a steady decrease of the distance to detonation as the initiating pressure increases. At low pressures an asymptotic value is reached, below which the PBX cannot be initiated anymore. At very high pressures the distance to initiation seems to converge to a more or less constant value.

The PBX with bimodal mixture AD is the most sensitive, with initiation distances far below those of the other two formulations. The longest initiation distances are observed for formulation BD. The formulation with the spherical particles has a sensitivity which lies in between the other two. These results are confirmed by the NOL Large Scale Gap Test

results: the 50 percent pressures for which an initiation is obtained are 3.2, 3.7, and 3.9 GPa for formulation AD, CE, and BD respectively. The PBXs can be initiated at slightly lower pressures with the NOL LSGT because in this test the explosive is confined in a steel tube. Note that the correlation between NOL results and initiation distances can only be made if the same explosive is studied. This correlation fails if, for example, HMX-based PBXs and RDX-based PBXs are compared<sup>5</sup>

## DISCUSSION

The differences observed in Figure 3 could be ascribed to the particle size distribution, as well as to the particle shape of the samples tested. Although the coarse sample B does not have exactly the same particle size distribution as sample A, the much lower sensitivity of formulation BD is most likely caused by the more regular shape of the crystals in sample B. From other studies, we also know that such a drastic change in the sensitivity could not be ascribed to small changes in the particle size distribution.<sup>3</sup>

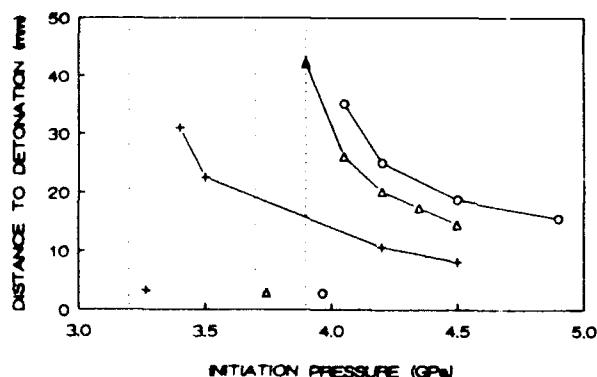


Figure 3. Distance to Detonation for Formulation AD (+), BD (O), and ED (Δ) as a Function of the Initial Shock Pressure. The horizontal lines indicate the critical NOL LSGT initiating pressures for these formulations

The influence of the crystal shape on the shock sensitivity could have different explanations. It is most likely that microscopic voids are formed on the surface of the crystals during casting, and it is much more difficult to create voids on the surface of the smoother and more regular shaped crystals of sample B, than on

the irregularly shaped crystals of sample A. It might also be possible that the difference in sensitivity is caused by the lower mechanical strength of the crystals of sample A. It is not clear, however, to what extent this plays a role at the very high pressures attained in a shock wave. A third possibility could be the effect of the bonding agent Dantocol on the sensitivity. To cover a crystal surface completely is more likely for sample B than for sample A. Any direct contact between the binder and the explosive might have caused an increase in the catalytic decomposition at the interface, as is also observed for AP in contact with different polymers.<sup>6</sup>

Because the crystals of sample B still show cleavage planes and sharp edges, we tried to make coarse as well as fine spherical crystals. Surprisingly, the resulting formulation is slightly more sensitive than formulation BD. This might be due to the effect of the fine fraction in this formulation, which is about twice the size of the fine fraction used for the other formulations. On the other hand, the very small cracks at the surface of the spherical crystals could also have caused the increased sensitivity. A study of a formulation with a bimodal mixture CD is presently under way.

## CONCLUSIONS

The study of these different PBX formulations has already revealed many aspects that could be used for the future development of less sensitive explosives:

First of all, these results show that the particle shape has a drastic influence on the shock sensitivity of the PBX. Shock sensitivities between those of RDX/wax compositions and Comp B are found. Also, the distances to detonation are doubled by using regularly shaped particles. The formulations we tested up to now have not been optimized for particle shape and size, and already we have a sensitivity nearly equal to Comp B. It is foreseen that an optimization of the particle shape and particle size distribution might reduce the sensitivity even more.

Secondly, from this study we also gained more information about the casting properties



of the different formulations. Formulations with 85 wt percent RDX were taken to have the possibility of casting all samples and are not restricted by a too high viscosity of the cast. The reduced sensitivity of a PBX has to be considered in relation to a high performance. For formulation BD, whose cast had a very low viscosity, an increase of the solid load to 88 or 89 wt percent RDX is certainly possible, maintaining good casting and shock sensitivity properties, and at the same time increasing the performance of the explosive considerably.

## ACKNOWLEDGEMENTS

Part of this research has been performed within the research program of the Anglo Norwegian Netherlands Committee. The authors wish to thank E. W. Koopmans, M. A. Schrader, and H. W. R. Sabel for their help with the experimental part of this study.

## REFERENCES

1. Swallowe, G. M. and Field, J. E., *Proc. R. Soc. Lond. A*, Vol. 379, 1982, p. 389.
2. Moulard, H.; Kury, J. W., and Dlechos, A., "The Effect of RDX Particle Size on the Shock Sensitivity of Cast PBX Formulations," *Proc. Eighth Symposium (International) on Detonation*, Albuquerque, NM, 1985, p. 902.
3. Moulard, H.; Dlechos, A.; and Kury, J. W., "The Effect of RDX Particle Size on the Shock Sensitivity of Cast PBX Formulations, II. Bimodal Compositions," *Proc. International Symposium of Pyrotechnics and Explosives*, Beijing, China, 1987, p. 304.
4. Price, D.; Clairmont, Jr., A. R.; and Erkman, J. O., *The NOL Large Scale Gap Test III. Compilation of Unclassified Data and Supplementary Information for Interpretation of Results*, Naval Ordnance Laboratory, NOLTR 74-40, 1974.
5. van der Steen, A. C. and Verbeek, H. J., "Initiation and Detonation of RDX and HMX HTPB-Based PBXs," *Proc. 19th International Conference of ICT on Combustion and Detonation Phenomena*, Karlsruhe, BRD, 1988; also to be published in *Propellants Explosives and Pyrotechnics*, 1989.
6. Schrader, M. A.; Leeuw, M. W.; and van der Steen, A. C., "The Heat Sensitivity of Solid Propellants," *AGARD Conference Proceedings No. 367, Hazard Studies for Solid Propellant Rocket Motors*, Lisse, The Netherlands, 1984, p. 19.

# A LAGRANGE GAUGE STUDY OF THE SHOCK INITIATION PROCESS IN AN INTERMOLECULAR EXPLOSIVE EAK

M. Cowperthwaite and J. T. Rosenberg\*  
SRI International  
Poulter Laboratory  
333 Ravenswood Avenue  
Menlo Park, California 94025

and

A. G. Taliancich\*\*  
AFATL/DLJE  
Eglin Air Force Base, Florida 32542

*Multiple Lagrange particle velocity gauge experiments were performed to investigate the shock to detonation transition (SDT) in baseline EAK. The particle velocity histories recorded in the initiating waves exhibited a spike region at the wave front connected to a region with a more gradual deceleration, with a discontinuity in deceleration at the point of connection. Such a two-region structure demonstrates that these flows are supported by global exothermic reactions with markedly different rates. The observation that the time between the shock front and the point of discontinuity is essentially independent of the gauge position in different experiments demonstrates that the rates of the faster reactions supporting the flow in the spike do not depend on the shocked state. The observation that the shock particle velocity histories recorded in different experiments are qualitatively different demonstrates that the distance to detonation concept is not valid for the SDT process in our baseline EAK.*

## INTRODUCTION

The use of physical synthesis<sup>1</sup> to improve the performance of intermolecular explosives containing ammonium nitrate (A)<sup>1,2</sup> led to the development of explosives based on EA, the eutectic of ethylenediamine dinitrate (E) and A. This paper presents a Lagrange gauge study of the shock initiation process in baseline EAK,<sup>3</sup> an EA based explosive containing

potassium nitrate (K). A series of multiple Lagrange gauge experiments were performed to obtain the particle velocity histories required to provide a better understanding of the shock initiation process in baseline EAK, and of shock-induced reactive flow in intermolecular explosives containing A. A similar series of multiple Lagrange gauge experiments, performed in a companion study of the detonation process in baseline EAK, were presented in a previous paper.<sup>4</sup>

## EXPERIMENTAL PROCEDURES

The SRI multiple Lagrange particle velocity gauge technique used in the present work has been described previously in some detail,<sup>4</sup>

\* Current Address: Lockheed Missiles and Space Company, P.O. Box 3504, Sunnyvale, CA 94088 3504.

\*\* Current Address: AI/RKPA, Edwards Air Force Base, CA 93523-5000.

and any reader requiring further information about this technique is referred to this paper.

The 10 inch diameter charges of baseline EAK used in the shock initiation experiments were cast around our standard gauge block<sup>3,4</sup> at the Los Alamos National Laboratory. The baseline EAK has a nominal composition 46/46/8 by weight E/A/K, and was creamed during the melt preparation operation to increase melt viscosity. Because no information about the density and microstructure of the targets was received from Los Alamos, we assumed that their average density was the same as the baseline EAK targets used previously in the detonation studies, i.e., 1.608 g/cm.<sup>3</sup>

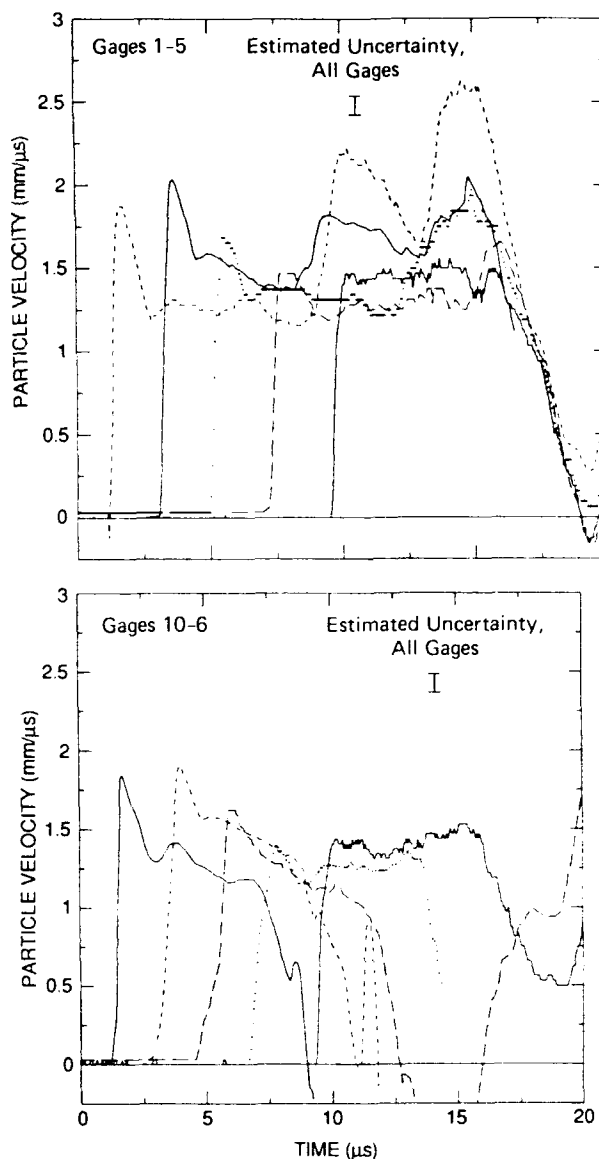
Our standard gauge block has 10 gauges numbered sequentially from one end of the block to the other. The gauges are made from aluminum strips nominally 0.15 mm thick by 3 mm wide, have an active element 25.4 mm long, and are arranged symmetrically so that pairs of gauges located at the same Lagrange position enter the flow in the order (1,10), (2,9), (3,8), (4,7), and (5,6). Adjacent gauges are separated by  $12.7 \pm 0.1$  mm in the propagation direction and by  $12.0 \pm 0.2$  mm, center-to-center, in the lateral position.

P-120 plane wave lenses and driver systems suggested by Dr. B. Craig,<sup>3</sup> were used to initiate the baseline EAK charges at the estimated pressures of 11.1, 13.4, and 15.3 GPa in Shots 10, 12, and 11. The sets of particle velocity histories recorded in these shots are presented below.

## PARTICLE VELOCITY HISTORIES RECORDED IN BASELINE EAK

### Gauge Records from Shot 10

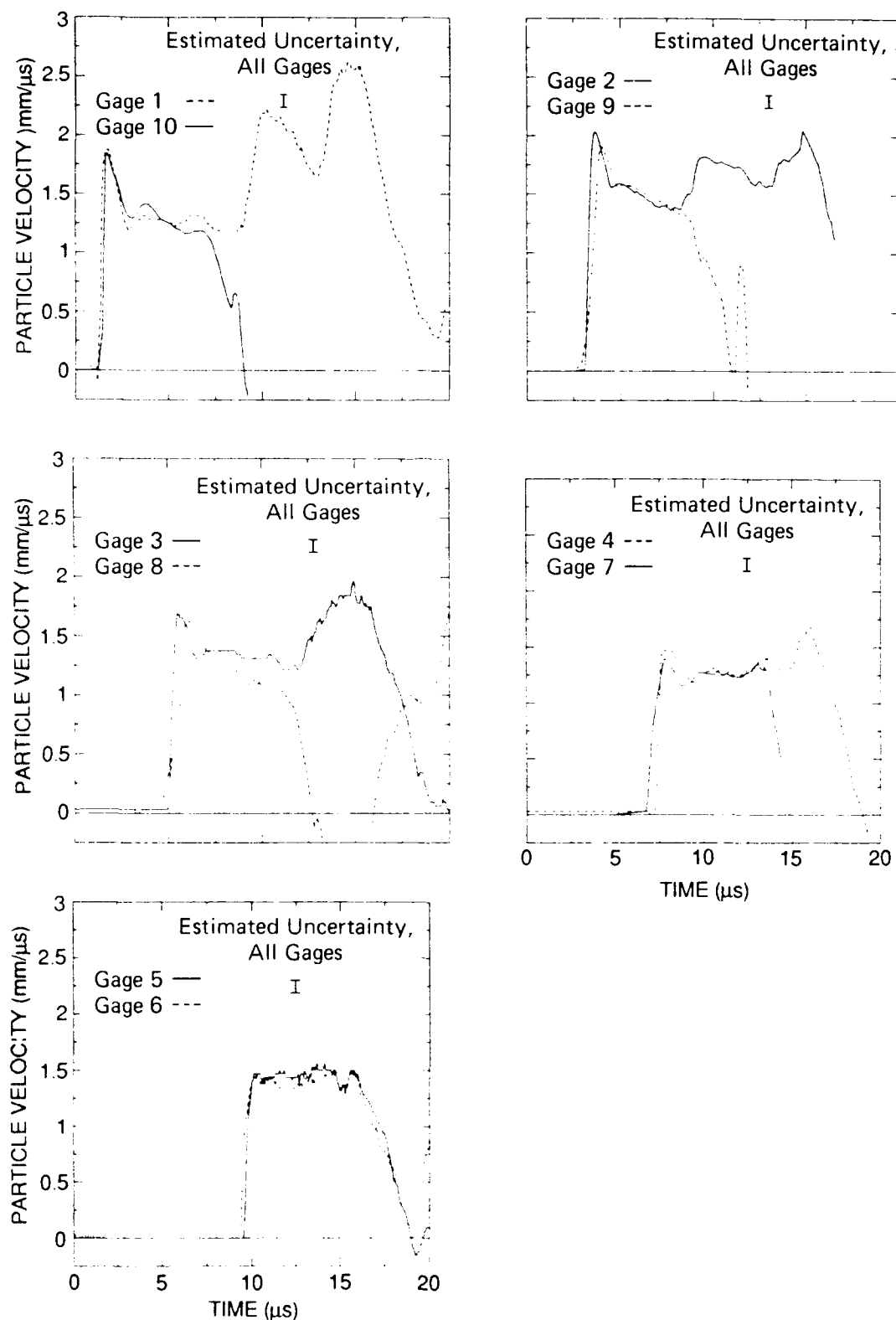
The particle velocity histories recorded in baseline EAK in the estimated 16.9 to 13 GPa region in Shot 10 are shown in Figures 1 and 2. The composite plots in Figure 1 show the evolution of the flow on both sides of the target; the comparison plots in Figure 2 show that the particle velocity histories recorded by the gauge-pairs at the five Lagrange positions are in relatively good agreement for about 6  $\mu$ s.



Lagrange Particle Velocity Histories, Gages 1-5 and 10-6.

Figure 1. Lagrange Particle Velocity Histories and Shock Trajectory for Shot 10

Examination of the composite plots in Figure 1 and the comparison plots in Figure 2, leads to the following description of the flow in baseline EAK initiated in Shot 10. Initially, the flow develops with a spike at the wave front. This spike decays as the shock attenuates between the second and fourth gauge positions and is not seen at the fifth and last gauge positions, where the particle velocity behind the shock is essentially constant for about 7  $\mu$ s. In the region between the fourth and fifth gauge positions, however, the shock



Lagrange Particle Velocity Histories from Gage Pairs at Each of Five Depths

**Figure 2. Lagrange Particle Velocity Histories and Shock Trajectory for Shot 10**

starts to accelerate as the spike decays and disappears.

Moreover, we believe that the shock will continue to accelerate beyond the last gauge position. This is because the particle velocity histories recorded by gauges 5 and 6 in Figure 2 show that the flow at the last gauge position exhibits essentially no pressure gradient and is, thus, reactive.

The shock-induced flow with the particle velocity histories shown in Figures 1 and 2 can be interpreted as follows. The spike in particle velocity history at the wave front recorded at the first gauge position shows that the initial shock is strong enough to initiate reaction in baseline EAK. As the flow develops, however, the chemical energy release rate is insufficient to overcome the hydrodynamic losses imposed by the rear-boundary conditions, because both the shock and the spike in the particle velocity histories decay in the region spanned by the second and fourth gauges. This situation is then reversed in the region between the fourth and fifth gauges, where the energy release rate becomes sufficient to (1) accelerate the shock as the particle velocity spike decays and disappears, and (2) produce a zero pressure gradient at the fifth gauge position. It is clear, although the flow at the fifth gauge position is reactive, that we are in no position to claim that the SDT process will occur in longer, 10 inch diameter charges of our baseline EAK subjected to initiating conditions similar to those used in Shot 10.

We conclude, following this interpretation of our shock-induced flow, that the initiating conditions produced in baseline EAK by our shock with an estimated initial pressure of 11.1 GPa are marginal as far as the SDT is concerned.

### Gauge Records from Shot 12

The particle velocity histories recorded in baseline EAK in the estimated 16.2 to 25.8 GPa region in Shot 12 are shown in Figures 3 and 4. The composite plot in Figure 3 shows the evolution of the flow recorded by gauges 6-10 on one side of the target. The comparison plots at the first four gauge planes in Figure 4 show that the differences between the particle velocity histories recorded at the

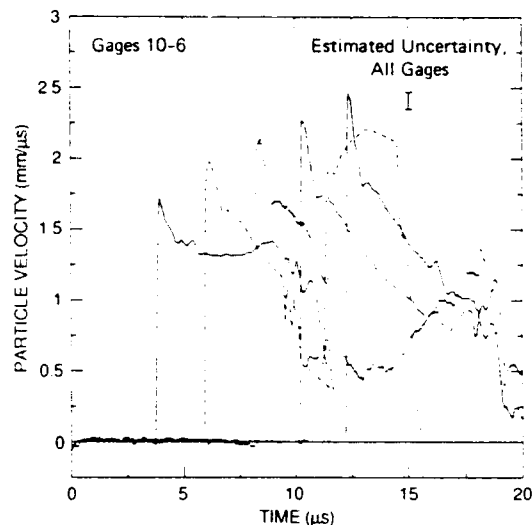
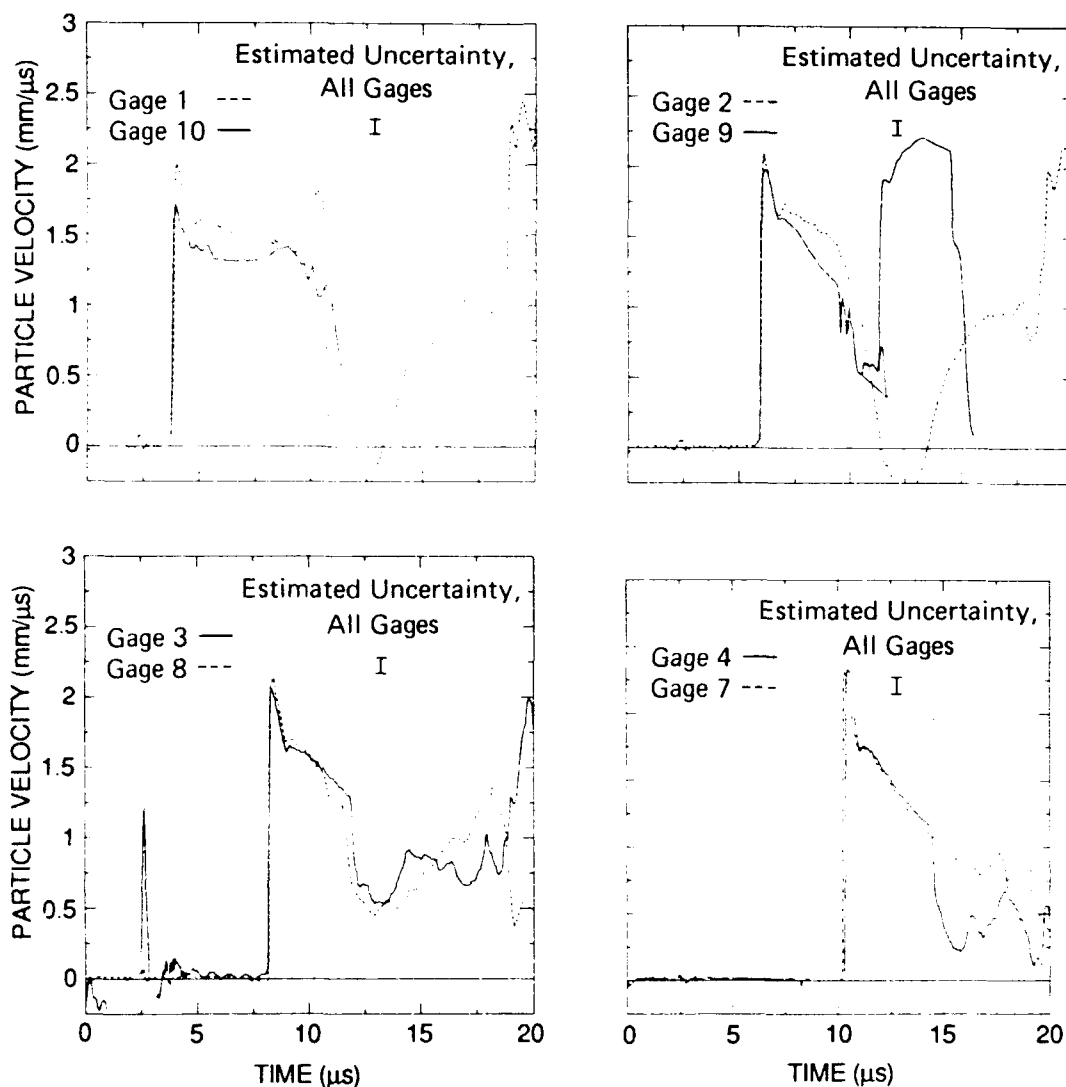


Figure 3. Lagrange Particle Velocity Histories and Shock Trajectory Recorded by Gauges 10-6 in Shot 12

same gauge plane diminish as the flow develops and are negligible beyond the first and second gauge planes.

Examination of the composite plot in Figure 3 and the comparison plots in Figure 4 leads to the following description of the flow in baseline EAK initiated in Shot 12. We first note that this flow, in contrast to that recorded in Shot 10, builds up continuously in the region spanned by the gauges. The shock amplitude increases linearly with time from  $\sim 1.75$  to  $\sim 2.5$  mm/ $\mu$ s, and the shock velocity increases smoothly from  $\sim 5.8$  to  $\sim 6.7$  mm/ $\mu$ s. Furthermore, the flow exhibits very unusual features in that the particle velocity histories at the last four gauge positions have a similar two-region structure: a spike region at the wave front connected to a region exhibiting a more gradual deceleration, with a discontinuity in the deceleration at the point of connection. As the shock accelerates, the particle velocity at the point of discontinuity increases and the spike grows in the sense that the difference in particle velocity between the shock front and the point of discontinuity increases. Superposition of the histories at the last four gauge positions also shows that:

- The time taken for a particle to travel from the shock front to the point of discontinuity is essentially the same at all four gauge positions.



Lagrange Particle Velocity Histories from Gage Pairs at Each of Four Depths

**Figure 4. Lagrange Particle Velocity Histories and Shock Trajectory for Shot 12**

- The region behind the spike has essentially the same structure at all four gage positions.

It follows from this description of these particle velocity histories, that the chemical energy release rate in our EAK initiated in Shot 12 is sufficient to overcome the hydrodynamic losses imposed by the rear-boundary conditions, and produce a growing self-similar type of flow. The existence of two particle velocity regions with markedly different decelerations suggests that the energy release rates in these regions are markedly different.

The fact that the time difference between the shock front and the point of discontinuity is essentially the same at four gauge positions indicates that an exothermic process induced in our EAK by shocks in the 16.2 to 25.8 GPa region proceeds at a rate which is independent of the shocked state.

#### Gauge Records from Shot 11

The particle velocity histories recorded in baseline EAK in the estimated pressure region of 24.3 to 32.8 GPa in Shot 11 are shown in Figures 5 and 6. The composite plot

in Figure 5 shows the evolution of the flow recorded by gauges 6-10 on one side of the target. The comparison plots in Figure 6 show that the particle velocity histories recorded by pairs of gauges at the same plane are in good agreement.

Examination of the composite plot in Figure 5 and the comparison plots in Figure 6, shows that the particle velocity histories recorded in Shot 11 have the same type of two-region structure as those recorded in Shot 12. Comparison of the composite plots in Figure 5 and 3, however, shows that the flow produced at the higher pressure in Shot 11 develops in a different manner than the flow produced in Shot 12.

At this stage, to provide a better description of the particle velocity histories recorded in Shot 11, as well as a better understanding of the SDT process in our baseline EAK, we will compare the particle velocity histories recorded in Shots 11 and 12 in more detail.

#### A Comparison of the Gauge Records from Shots 11 and 12

We first consider the shock trajectories recorded in Shots 12 and 11. Whereas the shock particle velocity in Shot 12 increases linearly with time from  $\sim 1.75$  to  $\sim 2.5$  mm/ $\mu$ s, it increases in Shot 11 in a stepwise fashion and has a value of  $\sim 2.3$  mm/ $\mu$ s at the first two gauge positions; a value of  $\sim 2.5$  mm/ $\mu$ s at the third and fourth gauge positions, and a value of  $\sim 2.8$  mm/ $\mu$ s at the fifth gauge position. This difference between the shock particle velocity histories recorded in Shots 11 and 12 shows that the SDT process in our baseline EAK depends strongly on the initial initiating conditions.

Superposition of the composite histories for Shots 12 and 11, shown respectively in Figures 3 and 5, shows other similarities and differences between these shock-induced flows. In both flows, the time taken for the particle velocity to drop from the shock front to the point of discontinuity is essentially the same at different gauge positions, and the particle velocity at the point of discontinuity increases with time. The spike and the adjoining region in the particle velocity histories, however, develop in

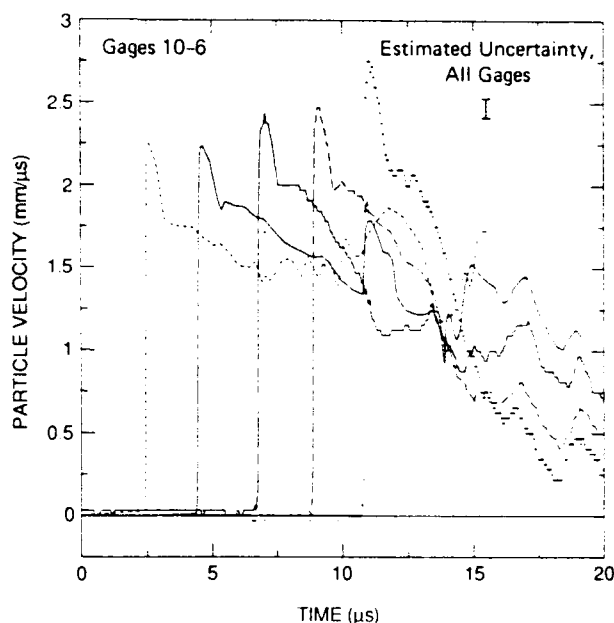


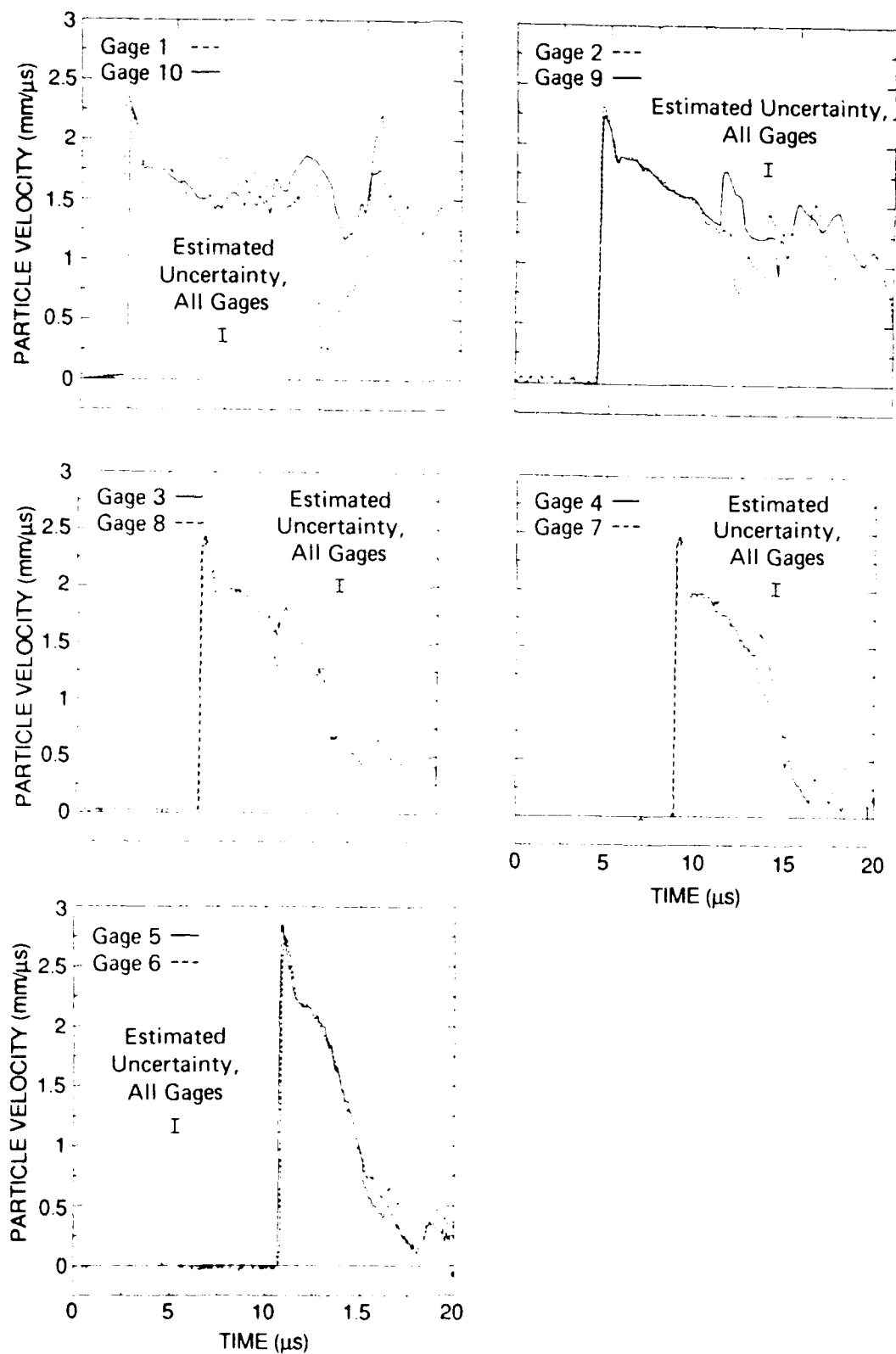
Figure 5. Lagrange Particle Velocity Histories and Shock Trajectory Recorded by Gauges 10-6 in Shot 11

different ways. The size of the spike does not increase with time in Shot 11 as it does in Shot 12 but decreases between the first and second gauges; is the same at the second, third, and fourth gauge positions; and then increases again between the fourth and fifth gauges. The flow behind the spike grows between the first two gauges in the same self-similar manner as the flow in Shot 12. It then steepens and forms a steady-state at the third and fourth gauge positions, and finally steepens again between the fourth and fifth gauges. Further examination of the composite plot for Shot 11 leads to the conclusion that the reaction along a particle path in the growing wave continues for about 5  $\mu$ s behind the shock front.

## CONCLUSIONS

The following conclusions about the SDT process in our baseline EAK follow from our interpretation of the multiple particle velocity histories recorded in our shock initiation experiments:

- SDT is marginal for input shocks with initial pressures in the 11 GPa region and pressure profiles similar to that



Lagrange Particle Velocity Histories from Gage Pairs at Each of Five Depths

Figure 6. Lagrange Particle Velocity Histories and Shock Trajectory for Shot 11



produced by the driver system used in Shot 10.

- SDT phenomenology for input shocks with initial pressures in the 13 to 15 GPa region and pressure profiles similar to those produced by the driver systems used in Shots 12 and 11, are governed by the formation and growth of both a reactive particle velocity spike at the wave front and an ensuing reactive rarefaction wave.
- The existence of the discontinuity in the deceleration, where the spike and the ensuing reactive, rarefaction wave are connected in the particle velocity profiles, indicates that the flow in the wave is supported by global exothermic reactions with significantly different energy release rates.<sup>5</sup>
- The observation that the time taken for the particle velocity to drop from its value at the shock front to its value at the point of discontinuity is essentially independent of gauge position and the same in Shots 12 and 11 indicates that the rate of the faster global exothermic reactions supporting the particle velocity spike at the wave front are independent of the shocked state.
- The observed differences between the multiple particle velocity histories recorded in Shots 12 and 11 demonstrate the dependence of the initiation process on the initial initiating conditions and indicate that the single shock curve buildup and distance to detonation concepts do not apply to the SDT process in our baseline EAK.

We finally conclude that the multiple particle velocity histories recorded in our shock initiation experiments should be subjected to a Lagrange analysis to provide a more quantitative description of the SDT process in our baseline EAK and the role of ammonium nitrate in shock-induced flow.

## ACKNOWLEDGEMENTS

Valuable contributions to this work were made by many people at SRI International.

We particularly acknowledge D. R. Henley for constructing the multiple Lagrange gauge assemblies, D. F. Walter and H. E. Hanna for assistance with the shock initiation experiments, and B. Y. Lew for help with data reduction.

We are especially indebted to A. P. Torres and J. A. Sanchez of Los Alamos National Laboratory for their cooperation in fabricating the baseline EAK targets used in these shock initiation experiments.

We also thank B. G. Craig for help in designing the driver systems for these shock initiation experiments.

This work was supported by Eglin Air Force Base under Contract F08635-88-K-0447.

## REFERENCES

1. Hershkowitz, J. and Akst, I. B., "Improvement of Performance of Composite Explosive Containing Ammonium Nitrate by Physical Synthesis," *Sixth Symposium (International) on Detonation*, ACR-221, 1976, pp. 439-449.
2. Akst, I. B., "Detonation in Intermolecular Explosives: Characteristics of Some Eutectic Formulations," *Seventh Symposium (International) on Detonation*, NSWC MP 82-334, 1982, pp. 548-558.
3. Cowperthwaite, M. and Rosenberg, J. T., "Lagrange Gauge Characterization of Intermolecular Explosives, Detonation and Initiation Studies of Some EA Based Explosives," SRI International Final Report, Project No. PYU-4941, 31 Oct 85.
4. Cowperthwaite, M. and Rosenberg, J. T., "Lagrange Gauge Studies of Detonation in Some Intermolecular EA Based Explosives," *Eighth Symposium (International) on Detonation*, NSWC MP 86-194, pp. 111-122.
5. Cowperthwaite, M., "Some Aspects of Nonideal Detonation in Composite Explosives," *Journal of Energetic Materials*, Vol. 1, 1983, pp. 141-175.

## **DISCUSSION**

**L. BRUN**  
**CEA, FRANCE**

If the concept of a reaction-zone length were to apply in your experiment, what would it be approximately in your opinion?

### **REPLY BY M. COWPERTHWAITE**

The reaction-zone length varies with Lagrange position in the initiation process, but is of the order of 7  $\mu$ sec.

## **DISCUSSION**

**JOHN KURY**  
**Lawrence Livermore National**  
**Laboratory, Livermore, California**

The driver systems used actually produce a large drop in pressure at the interface with

time. "Relatively flat top" is not applicable for these experiments.

### **REPLY BY M. COWPERTHWAITE**

I thank Dr. Kury for his information and have changed the first two conclusions in the paper, accordingly.

# ANOMALOUS SHOCK SENSITIVITY/DENSITY RELATIONSHIP FOR PRESSED BOOSTER EXPLOSIVES FROM A SMALL-SCALE GAP TEST

Robert J. Spear and Victor Nanut  
Defence Science and Technology Organisation,  
Materials Research Laboratory, Ascot Vale, Victoria, AUSTRALIA

*MRL SSGT results show a consistent and reproducible trend to decreased shock sensitivity as density (percent TMD) decreases for a series of pressed booster explosives over the range 96-80 percent TMD. This is the opposite of the generally accepted response pattern from gap testing. It was shown that this effect was not peculiar to the materials tested, and parameters such as decrease in particle size, disruption of surface coating, critical diameter, and run distance were not primary causes. Comparison with results for booster and main charge explosives from the NOL SSGT identified the effect to be derived from the unconfined acceptor. It is proposed that this leads to both ignition and buildup being important, unlike confined SSGTs which primarily measure ease of ignition under shock loading. Decreased shock sensitivity at lower percent TMD results from decreased ability to undergo buildup; results with the acceptor confined support this conclusion. Limitations for assessing data from gap (type) tests using unconfined acceptors are discussed.*

## INTRODUCTION

The shock sensitivity of pressed granular explosives is routinely measured by gap tests.<sup>1-6</sup> In these tests the shock from a standard explosive charge (the donor) is attenuated through an inert mechanical barrier (the gap) before interaction with the explosive under test (the acceptor). Go/no-go is normally judged by the physical damage to a witness plate placed at the end of the acceptor charge. The width of the gap is varied using a staircase go/no-go procedure<sup>7</sup> over a series of firings and the results analyzed statistically to yield a gap thickness at which there is a 50 percent probability of detonation ( $m_{50\%}$ ). In tests where the gap thickness has been calibrated to give shock pressure incident on the acceptor explosive, this is the result usually cited.

The most widely used gap tests are those that originated at Naval Ordnance Laboratories (now Naval Surface Warfare Center):

the small-scale gap test (NOL SSGT)<sup>2,8</sup> and large-scale gap test (NOL LSGT).<sup>2,9</sup> A large body of data from these and the related Los Alamos gap tests<sup>3</sup> have been published.<sup>2,3,5,8,9</sup> At MRL we use an SSGT based on a system originally developed at Atomic Weapons Research Establishment, Aldermaston (AWRE SSGT).<sup>6</sup> Full details have previously been published<sup>10</sup> and the experimental arrangement is shown in Figure 1. The donor consists of an exploding bridgewire (EBW) detonator, 5.57-mm i.d., filled with PETN, and the acceptor is two unconfined cylindrical pellets each 12.7-mm diameter x 12.7-mm high, i.e., total length 25.4 mm. The NOL SSGT (Figure 2) differs principally from the MRL SSGT in the use of PMMA for the attenuator (gap) and a smaller diameter, but very heavily confined acceptor.

The shock sensitivity within a range of explosives can vary widely depending on the gap test method used. Nevertheless, there

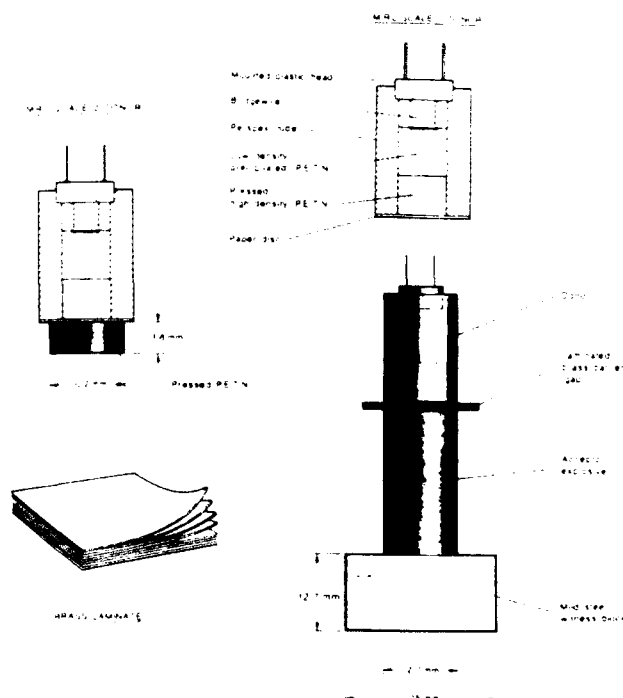


Figure 1. The MRL SSGT Assembly

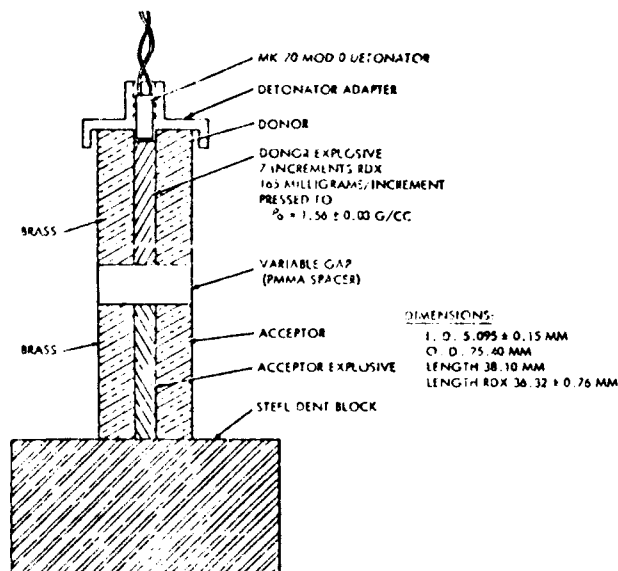


Figure 2. A Diagram of the NOL SSGT Assembly

seems to be universal agreement on the effect of one key variable: packing density. For example, Roth<sup>1</sup> states that, "without exception the shock sensitivity of any explosive increases as its (packing) density is decreased," while Price<sup>11</sup> states that, "the trends in critical

initiation pressure ( $P_g$ ) versus percent theoretical maximum density (TMD) are the same for all porous explosives. The higher the percent TMD, the higher  $P_g$  (hence smaller the gap in a gap test), which means the less sensitive the explosive. The more porous the explosive, the more sensitive it is."

In the mid-1970s, RDX grade B\*/polyethylene wax AC629 formulations were being studied at MRL as potential submunition fillings. It was observed that the shock sensitivity as measured by the MRL SSGT decreased with decreasing density over the range 96-89 percent TMD for the 92.3:7.7 and similar formulations.<sup>12</sup> This same trend was subsequently observed for RDX grade A\*/AC629 (91.9:8.1).<sup>13</sup> Although commented on in both reports,<sup>12,13</sup> this observation was not further investigated until the mid-1980s when we again observed shock sensitivity to decrease with decreasing density for RDX grade A/AC629 formulations with wax levels of 1.3-5.4 percent,<sup>14</sup> and also for RDX grade A/polyurethane/zinc stearate formulations.<sup>15</sup> Both formulation types were studied over an extended range: up to 96-80 percent TMD.

It is not the first time that this phenomenon has been observed. Both Seely<sup>16</sup> and Dinegar and Millican<sup>17</sup> observed reversals in shock sensitivity/density for tetryl; and Composition A-3 has been noted as increasing in shock sensitivity with density over the range 85-96 percent TMD using a wax gap test.<sup>18</sup>

The aim of the investigation reported here was to identify the cause of the anomalous shock sensitivity/density trends for results from the MRL SSGT.

## RESULTS

Some of the results from earlier MRL studies<sup>12-15</sup> noted in the Introduction are detailed in Table 1: a series of pressed RDX Grade A/AC629 polyethylene wax formulations; and in Table 2: RDX Grade B/AC629 (92.3:7.7), RDX Grade A/Impranil DLH dispersible polyurethane/zinc stearate (100.0:

\*RDX grades A and B correspond closely to US class A and B. RDX in all cases was type I (Woolwich).

Table 1. Shock Sensitivity (MRL SSGT) for RDX Grade A/AC629 Polyethylene Wax Formulations Pressed to Various Percent TMD

Composition	%TMD	m <sub>50%</sub> (mm)	σ (mm)
98.69:1.31	95.9	2.651	0.019
	91.0	2.593	0.020
97.94:2.06	96.1	2.614	0.042
	91.0	2.431	0.036
	85.8	1.880	0.027
	80.8	1.656	0.032
97.14:2.86	96.1	2.474	0.052
	90.9	2.276	0.048
95.31:4.69	95.9	2.126	0.022
	90.8	1.681	0.026
94.61:5.39	95.7	1.831	0.022
	90.8	1.288	0.019
91.9:8.1	96.48	1.744	0.050
	96.18	1.711	0.017
	95.46	1.659	0.042
	94.50	1.676	0.019
	93.91	1.563	0.015
	92.77	1.253	0.022
	91.94	0.953	0.022

Table 2. Shock Sensitivity (MRL SSGT) for Some Selected RDX Formulations and Tetryl Pressed to Various Percent TMD

Composition	%TMD	m <sub>50%</sub> (mm)	σ (mm)
RDX Grade B/ AC629 poly- ethylene wax (92.3:7.7)	95.97	1.770	0.014
	95.74	1.836	0.022
	95.41	1.676	0.053
	95.14	1.593	0.052
	94.67	1.649	0.030
	93.72	1.684	0.022
	92.60	1.532	0.014
	91.23	1.201	0.049
RDX Grade A/ Impranil DLH polyurethane/zinc stearate (100.00:2.00:1.03)	89.04	1.100	0.022
	95.11	2.616	0.036
	90.04	2.268	0.021
	85.03	1.814	0.028
CH-6	90.0	2.600	0.025
	85.0	2.352	0.022
Tetryl crystalline	90.0	2.814	0.021
	80.0	2.637	0.014
Tetryl granular	90.0	3.259	0.026
	83.5	2.814	0.056

2.00:1.03), CH-6 (RDX/polyisobutylene/calcium stearate/graphite 97.5:0.5:1.5:0.5) and crystalline and granular tetryl. Results are given in mm for the m<sub>50%</sub> gap width, together with standard deviations. The range of percent TMD is as wide as 80-96 percent in some cases, but typically covers more restricted limits. The lower limit of percent TMD (80 percent) is dictated by the necessity for the pellets to have sufficient mechanical strength for handling since the MRL SSGT uses unconfined acceptor pellets. Selected data from these tables are plotted in Figures 3-5.

Although our shock sensitivity data should desirably have been quoted in incident shock pressures rather than gap thicknesses, this was not possible because the MRL SSGT has not been calibrated for pressure output. However, Cachia and Whitbread calibrated peak pressure in the brass gap as a function of gap thickness in a similar gap test.<sup>19</sup> For the

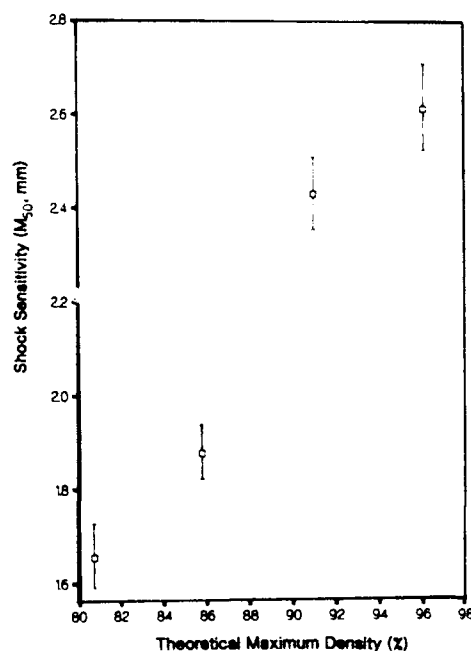


Figure 3. A Plot of Shock Sensitivity (m<sub>50%</sub>) from the MRL SSGT Versus Percent TMD for RDX/AC629 (97.94:2.06)

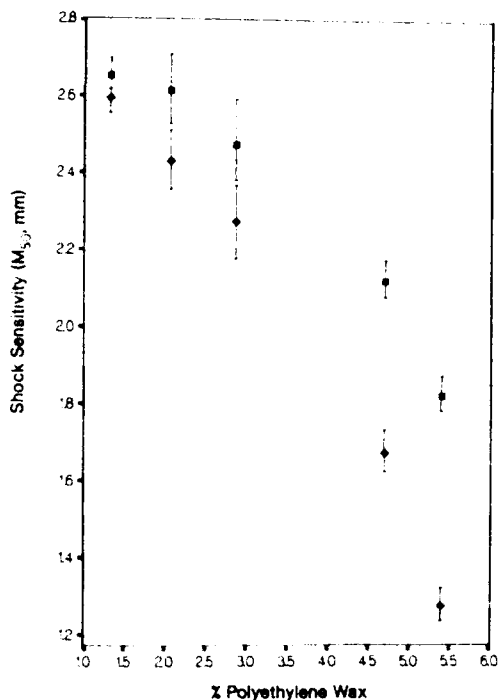


Figure 4. Shock Sensitivity ( $M_{50}$ ) Versus Wax Content (%) for Pressed RDX/AC629 Powders.

■ 95 %TMD, ◇ 90 %TMD.

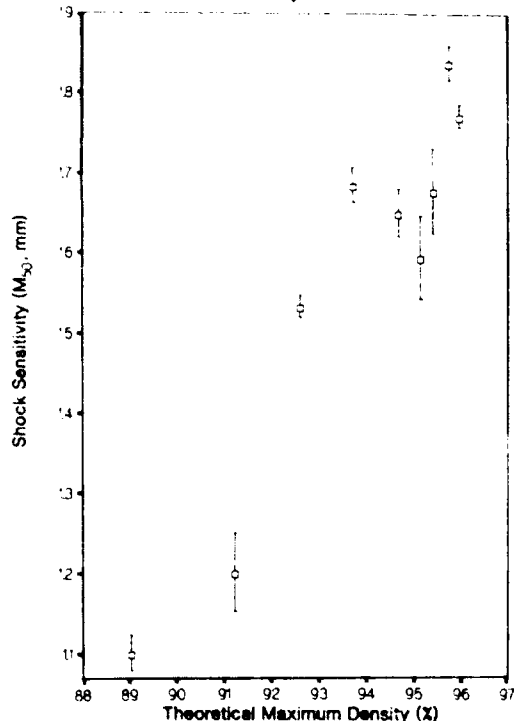


Figure 5. Shock Sensitivity of RDX Grade A/AC629 Polyethylene Wax (92.3:7.7) as a Function of Density

range of gap thicknesses covered by the results in Tables 1 and 2, the shock pressure was found to be approximately linearly related to gap

thickness, and to cover the relatively narrow range of 1.85-2.45 GPa (gap thickness 1.00-3.30 mm).<sup>19</sup>

## DISCUSSION

The reasons an apparent decrease is observed in shock sensitivity with decrease in density using the MRL SSGT could be due to a number of causes derived either from the explosives under test, or the test itself. Parameters investigated under these categories are discussed below.

### Materials Displaying the Observed Trend

All the earlier observations were for formulations based on RDX/AC629 wax at relatively high levels of AC629.<sup>12,13</sup> Although subsequently observed for much lower AC629 levels,<sup>14</sup> it was not until the polyurethane formulations were examined<sup>15</sup> that a different type of test material was examined.

Production grade tetryl crystalline (fine) and granular (coarse) were both tested at two densities and both displayed the same trends as the RDX formulations (Table 2). U.S. production grade CH-6 (RDX/polyisobutylene/calcium stearate/graphite 97.5:0.5:1.5:0.5) subsequently became available for another study, and shock sensitivity was determined at two densities (Table 2). Again the same trend is observed. Note, however, that CH-6 has been extensively characterized by the NOL SSGT<sup>2,8</sup> over the density range 1.48-1.78 Mg/m<sup>3</sup> and the results are unambiguous: shock sensitivity *increases* with decreasing percent TMD.

The above data shows conclusively that the results observed using the MRL SSGT are not peculiar to a limited range of explosive formulations, but are general for the test configuration. The obvious question is why such results have not been widely observed previously; the very similar AWRE SSGT has been in use in the UK for over 30 years and thousands of tests have been performed. The explanation is probably that over the first ten years virtually all tests at AWRE were carried out at near crystal density (98 + percent TMD).<sup>20</sup> It is likely that this trend has continued over the intervening years and the effect of changes in percent TMD has been overlooked.

Similarly the few reported studies<sup>9,21,22</sup> where confined and unconfined tests have been compared have not examined ranges of percent TMD; instead they covered a range of materials at similar percent TMD.

### **Reduction in Particle Size at Increasing Percent TMD**

Reduction in particle size at higher pressing loads (increased percent TMD) has been proposed by Price<sup>11,23</sup> as the major reason for the difference in shock sensitivity/density behavior between coarse and fine tetryl,<sup>16</sup> as well as a number of other examples.

Wilson<sup>13</sup> determined particle size for RDX Grade A/AC629 91.9:8.1 pressed to 94 percent TMD. The AC629 was extracted with carbon tetrachloride and the residual RDX showed a reduction, relative to the RDX from which the moulding powder was made, in weight average (227 to 200  $\mu\text{m}$ ), number average (89 to 50  $\mu\text{m}$ ) and median (236 to 227  $\mu\text{m}$ ) particle size as determined by sieve analysis. Extraction of the moulding powder as a control gave results identical, within experimental error, with the RDX used to prepare it. We extracted pressed pellets of 97.94:2.06 RDX Grade A/AC629 with toluene saturated with RDX, to remove the AC629, and determined particle size distribution on a Malvern particle size analyzer. The results for pellets pressed to 80.8, 85.8, 91.0, and 96.1 percent TMD are shown in Figure 6. We have made no attempt to quantify this data since each is derived from only a single pellet, but the clear trend is for an increased weight and number of fine particles ( $< 40 \mu\text{m}$ ) with increased percent TMD, indicative of the expected greater grain fracture at higher pressing loads.

However the effect of particle size on shock sensitivity is not entirely unambiguous. Perhaps the best summary is a statement by Kennedy and Stresau:<sup>24</sup> "fine-particle powders are often harder to ignite than coarse powders, but reactions in fine powders grow to detonation more rapidly once ignited." While thresholds for reaction are usually lower for coarser materials subjected to the sustained shocks used in gap testing, the more usually determined  $P_{50\%}$  is often lower ( $m_{50\%}$  higher)

for smaller grain materials, i.e., higher shock sensitivity.<sup>1</sup> We have recently observed increased shock sensitivity with decreasing particle size for a series of RDX Grade A sieve cuts using the MRL SSGT.<sup>25</sup>

Thus shock sensitivity could increase with increasing percent TMD, i.e., the decrease in particle size by grain fracture during pressing would more than compensate for the decrease in shock sensitivity from the decreased porosity. The major problem with such an argument is that CH-6, which should show increased grain fracture at increased percent TMD comparable with our RDX/AC629 formulations, exhibits a normal shock sensitivity/percent TMD relationship using the NOL SSGT as discussed in the previous section.

Since the results for CH-6 on the MRL SSGT are analogous to the results for our RDX formulations and tetryl, reduction in particle size could not be the answer, although it would contribute in a minor way. This must place some doubt on the arguments made by Price<sup>11,23</sup> based on particle size reduction to explain reversals in shock sensitivity/density behavior.

### **Disruption of Surface Coating**

A parallel effect to particle size reduction is disruption of surface coating for the RDX formulations. Crystal fracture exposes new (uncoated) RDX surface, but a more significant factor could be debonding of polymer coating by inter-crystalline friction during compaction. Eadie<sup>26</sup> demonstrated as early as 1965 that shock sensitivity was strongly dependent upon coating efficiency for pressed HMX moulding powders: at identical wax levels, the higher the surface coverage (least exposed HMX surface), the lower the shock sensitivity.

The proposal was therefore that pressing to higher percent TMD resulted in increased debonding of the AC629 or polyurethane from the RDX crystals. The increased area of exposed RDX surface would therefore lead to increased shock sensitivity which more than compensated for the decrease due to decrease in porosity. Although a good idea in principle, it would be very difficult experimentally to quantify this effect. Breakup of pellets to

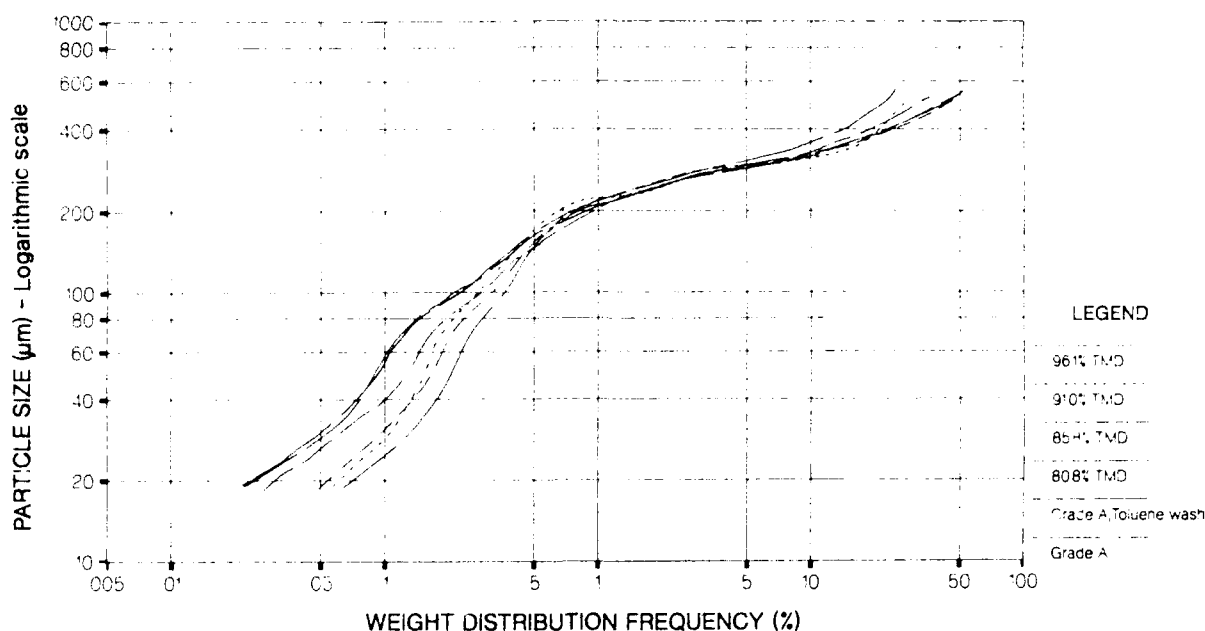


Figure 6. A Plot of Particle Size Distribution for RDX Grade A and RDX/AC629 97.94:2.06 Pressed to a Range of Percent TMD

examine the interior crystals would itself result in surface disruption, while although the pellet exteriors could be examined by scanning electron microscopy or FT IR, this would not necessarily yield reliable information about the pellet interior.

However, the fact that CH-6 exhibits the same behavior under MRL SSGT as the RDX/AC629 and polyurethane formulations rules this out as a cause; these polymers should show similar bonding properties to RDX crystals.

### Critical Diameter Effects

One suggestion for explaining our unusual results was that the shock from the donor in the MRL SSGT would be curved, and success/fail would depend critically on the width of the "flat" part of the shock front. Because the MRL SSGT uses an unconfined donor, this "flat" width may be so small as to be close to the critical diameter of the acceptor explosive. As the percent TMD decreased, the critical diameter would increase<sup>27</sup> and consequently a stronger incident shock would be necessary to overcome the problem of the flat

shock width being comparable to or below the critical diameter. This would oppose the increased shock sensitivity due to the greater porosity at lower percent TMD. Although the NOL SSGT donor has a smaller diameter, the acceptor is confined and this substantially decreases critical diameter.<sup>27</sup>

Hutchinson<sup>28</sup> has shown by ultra high speed photography that the shock output of a UK Mk 3 EBW donor\* is planar to within 15 ns over the central 3 mm. Although transmission through the brass gap may result in additional curvature, RDX/binder formulations with 15 percent or less binder typically have unconfined critical diameters of 1-2 mm,<sup>27</sup> RDX at density 1.0 Mg/m<sup>3</sup> (55.5 percent TMD) still has a critical diameter of only 1.1 mm.<sup>29</sup> The width of the central planar region of the

\*An MRL Scale 1 donor was used for the earlier results (pre-1985), then we changed to UK Mk 3 donor. The latter differs from the MRL Scale 1 (Figure 1) only in the geometry of the moulded plastic head and pins; the perspex barrel and explosive components are almost identical.



incident shock will therefore be greater than the critical diameter of all the explosives studied.

Additional experimental investigation as to whether donor shock width was the cause of the MRL trends was carried out by testing an RDX/AC629 95.0:5.0 formulation pressed at nominally 90 and 85 percent TMD using the MRL Scale 2 gap test. This differs from the Scale 1 test normally used in having a 10.2-mm diameter high density PETN pellet between the EBW donor and gap (Figure 1). The 95.0:5.0 formulation was chosen because it should have a critical diameter intermediate between the extremes of the compositions studied (Tables 1 and 2); stable detonation of 2-mm unconfined pellets at 90 percent TMD was observed by us using streak photography in another study, thus critical diameter will be below 2 mm.

Results are detailed in Table 3 for the Scale 2 MRL SSGT at 89.3 and 85.5 percent TMD, and for Scale 1 at 90.0 percent for comparison.

The  $m_{50\%}$  gap thicknesses are, as expected, substantially larger for Scale 2 than for Scale 1. However, the trends follow the Scale 1 results (Table 1). It can therefore be concluded that donor shock width/critical diameter cannot be the cause of the observed trends.

*Table 3. Comparison of Data for RDX/AC629 (95.0:5.0) Determined Using the MRL SSGT at Scale 1 and Scale 2*

MRL SSGT Type	%TMD	$m_{50\%}$ (mm)	$\sigma$ (mm)
Scale 1	90.0	1.433	0.037
Scale 2	89.3	4.018	0.063
	85.5	3.360	0.098

### Run Distance Effects

A shock wave from an explosive donor incident upon an explosive acceptor induces chemical reaction which may or may not build to detonation. The distance in the acceptor between the gap/donor interface and the point

at which detonation breaks out is the run distance. A plot of log (incident pressure) vs. log (run distance) is usually linear and known as a Pop plot.<sup>3</sup> Because the NOL SSGT has a longer acceptor (38.1 mm) than the MRL SSGT (25.4 mm), some tests for materials with long run distances at large gap/low incident pressure may not have built to detonation at the end of the acceptor in the MRL SSGT, but could have in the NOL SSGT. Since run distance usually increases with decreasing percent TMD, the sensitivity of lower percent TMD samples may therefore be underestimated by the MRL SSGT.

A large number of Pop plots are listed in Reference 3. In particular there is extensive data for tetryl over the range 75.1-98.2 percent TMD, and more limited data for the RDX formulations PBX 9407 (RDX/Exon 461 94:6) and PBX 9405 (RDX/NC/CEP 93.7:3.15:3.15). Taking the incident pressures at and below the 50 percent probability limit from NOL SSGT data,<sup>2,8</sup> run distances of at most 15 mm and typically below 10 mm would be expected for the booster formulations studied here. This is well short of the 25.4 mm length of the acceptor and strongly supports the conclusion that run distance is not a significant factor.

Run distances for RDX/AC629 (97.94:2.06) were determined at  $m_{50\%}$  for 85 percent and 90 percent TMD. Values obtained were approximately 6.5 and 5 mm, respectively. At gap  $m_{50\%} + 2\sigma$ , the run distance was still only 7 mm for the 85 percent TMD sample. Tasker<sup>22</sup> has previously shown rapid buildup for high RDX content explosives shocked above the burn threshold, further supporting our conclusions.

### General Comments on Density/Shock Sensitivity Dependence

Further insight into the observed results was obtained by consideration of some general factors which influence shock sensitivity, and then directly comparing results obtained using the MRL and NOL SSGTs; the latter was chosen because it is an extremely well-characterized<sup>2,8,11</sup> confined test.

Current models of shock to detonation separate the physical processes into two

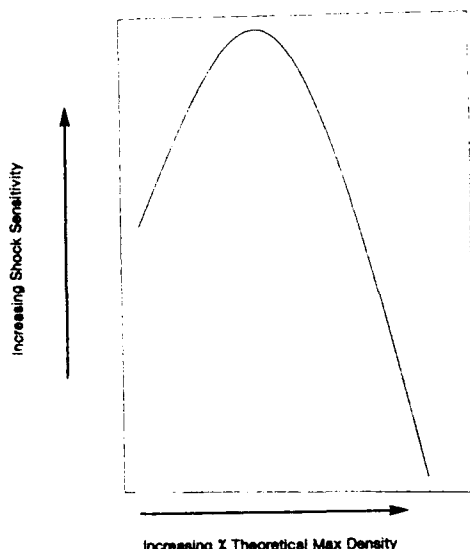


Figure 7. A "Normal" Shock Sensitivity/Percent TMD Relationship Expected From Gap Testing

distinct stages: ignition/initiation and buildup.<sup>30-33</sup> Their relative importance can be shown experimentally to depend primarily on the duration and pressure of the incident shock.

Gap testing characteristically uses relatively low pressure sustained shocks; most of the testing occurs around the marginal (50 percent) condition. Under these conditions a relatively small amount of explosive is ignited by the incident shock<sup>33</sup> and because the diameter of the acceptor is usually several times the critical diameter, conditions are very favorable for buildup once reaction has commenced. Gap tests such as the NOL SSGT are therefore regarded as principally a measure of the ease of ignition/initiation under shock loading.<sup>11</sup> Decrease in density (percent TMD) increases porosity—hence, the number and volume of inhomogeneities—and thus increases the probability of ignition. As a consequence shock sensitivity as measured by the NOL SSGT and similar tests is typically observed to increase with decreasing percent TMD.

In contrast, the short duration/relatively high pressure shocks delivered by flyer plates result in a large portion of the impacted explosive, perhaps as high as 50 percent, being ignited by the incident shock.<sup>33</sup> The key process governing success or failure to grow to

detonation is buildup which must be achieved in the very short time before rarefactions quench the induced reaction. One might envisage a more general picture for gap testing as depicted in Figure 7: as percent TMD decreases, a situation should be reached where buildup becomes the crucial factor (rather than ignition) due to increased difficulty for propagation between grains. The point of maximum shock sensitivity in Figure 7 will be outside the range of densities at which most military explosives are loaded. The only explosive for which such data has been reported is nitroguanidine (NQ), where the maximum shock sensitivity occurred at a density of  $0.45 \text{ Mg/m}^3$ .<sup>34</sup> This, of course, is below even the bulk density of most military explosives. NQ can exhibit unusual shock sensitivity behavior due to changes in critical diameter<sup>35</sup> and this result may not be general.

#### Comparison of Data from the MRL and NOL SSGTs: Ignition Versus Buildup

Further understanding of the results obtained using the MRL SSGT was carried out by directly comparing results for a series of booster and main charge explosives with data from the NOL SSGT. We were able to generate this data because we had recently carried out a comparative assessment of booster explosives qualified as replacements for tetryl using production samples supplied by NSWC White Oak.<sup>36</sup> NOL SSGT shock sensitivity data for all materials were readily available.<sup>2,8,37</sup> The MRL and NOL SSGT data, together with earlier data for TNT,<sup>10</sup> are detailed in Table 4 for  $m_{50\%}$  (MRL in mm) or  $P_{50\%}$  (NOL in GPa); these parameters change in the reverse order with higher shock sensitivity represented by larger gap or smaller shock pressure. Most of the data are for charges pressed to about 90 percent TMD.

Comparison of data from Table 4 at 90 percent TMD reveals the order shown below for sensitivity decreasing from left to right.

#### MRL SSGT:

HNS IIB > Tetryl crystalline > A-5 >  
CH-6 > HNS IB > PBXN-5 > PBXW-7  
> TNT > A-3

Table 4. Comparison of MRL SSGT and NOL SSGT Shock Sensitivities for Selected Explosives

Formulation	MRL SSGT		NOL SSGT <sup>2,8</sup>	
	%TMD	m <sub>50%</sub> (mm)	%TMD	P <sub>50%</sub> (GPa) <sup>a</sup>
A-5 (RDX/stearic acid 98.75:1.25)	90.0	2.642	89.7	1.03
CH-6 (RDX/polyisobutylene/calcium stearate/graphite 97.5:0.5:1.5:0.5)	90.0	2.600	90.0	1.21
	85.0	2.352	84.9	1.02
PBXN-5 (HMX/Viton A 95:5)	90.0	2.383	90.5	1.98
PBXW-7 Type II (RDX/TATB/Viton A 35:60:5)	90.0	1.415	90.5 <sup>b</sup>	2.16 <sup>b</sup>
HNS Type IB	90.1	2.438	89.4	2.49
HNS Type IIB	90.0	2.822	88.8	1.55
Tetryl crystalline	90.0	2.814	89.5	1.31
	80.0	2.637	82.4	0.97
TNT (pressed)	90.3	0.688	90.3	2.03
	92.1	1.219	93.6	2.22
A-3 (RDX/wax 91:9)	90.9	0.498	89.9	> 2 <sup>c</sup>

<sup>a</sup> Some data has been converted from Dbg to GPa using the conversion relationship.<sup>2</sup>

<sup>b</sup> Data for Type I (PTFE binder).<sup>36</sup>

<sup>c</sup> Data are only available for LSGT where P<sub>50%</sub> is 1.5 GPa.

#### NOL SSGT:

A-5 > CH-6 > Tetryl > HNS IIB > PBXN-5 > TNT > PBXW-7 > A-3 > HNS IB

Two key observations are apparent:

- (i) Both tests rank the wax/binder formulations in the same order, i.e., A-5 > CH-6 > PBXN-5 > PBXW-7 > A-3. All these materials are granular and consolidate to charges with good mechanical strength. The relative sensitivities vary somewhat, particularly PBXW-7 which is rated very much less sensitive than PBXN-5 in the MRL test, but only a little less sensitive in the NOL test.
- (ii) Pure crystalline explosives tend to be ranked as more sensitive by the MRL test than the NOL test. All these crystalline materials were of small particle size.

We suggest that the key result is for HNS IB. HNS IB is of very fine particle size (<10 μm)<sup>38</sup> and as such should be difficult to ignite under the sustained shock conditions of a gap test, but will build up to detonation very rapidly once suitably ignited.<sup>24</sup> One could equally argue that the pure crystalline explosives cited in (ii) above will more readily undergo buildup than the waxed/desensitized formulations; it is widely held that the principal effect of waxes/binders is to hinder propagation/buildup, not ignition.

The obvious conclusion is that the MRL SSGT appears to give significant rating to both ignition and buildup. As discussed previously, gap testing is usually considered to be principally an assessment of ease of ignition. In the NOL SSGT and related tests, the very heavy confinement of the acceptor means that energy losses from side rarefactions will be very much less important than in the MRL SSGT with its unconfined acceptor. Thus it is not surprising that buildup should be more

difficult in the MRL SSGT and, therefore, will become an important factor in determining success/failure.

We therefore propose that the principal reason that the MRL SSGT data show an apparent reduction in shock sensitivity with reduction in percent TMD over the range 80-96 percent TMD is the decreased ability to undergo buildup in the lower percent TMD charges which more than compensates for the greater ease of ignition.

### Effect of Confinement

Two experiments were carried out on the effect of confinement of the donor. In both cases the normal MRL SSGT configuration was used with the modification that the two acceptor pellets were fitted into a 25.4 mm o.d., 12.7 mm i.d. hollow brass cylinder such that the pellets were flush with the ends. A 97.94:2.06 RDX/AC629 formulation was pressed to 90.01 and 85.01 percent TMD and  $m_{50\%}$  and  $\sigma$  values determined. These results are detailed in Table 5 and compared with results for the same formulation obtained using the normal MRL SSGT configuration (from Table 1).

On the basis of arguments presented in the previous two sections, it was expected that the shock sensitivities would reverse, i.e., assume the normal relationship whereby the lower density compact was the most shock sensitive. However, it was observed that both test

materials had almost equal shock sensitivity with the higher density pellets still being more shock sensitive. The trends, nonetheless, were clearly in the expected directions.

It should be noted that Price<sup>9,21</sup> has compared results for the NOL LSGT in confined and unconfined configuration. For all the cast charges which were prepared,  $m_{50\%}$  increased with confinement (at the same percent TMD), as observed for our 85.01 percent TMD sample. However, our 90.01 percent TMD sample shows the reverse trend; Price<sup>21</sup> comments that pressed explosives show no consistent trend due to a difference in pressing techniques at different laboratories. Our results suggest that the observed effect will be derived principally from percent TMD of the samples, but further experimental results would be needed to clarify this.

### CONCLUSIONS

The MRL SSGT differs from most of the gap test configurations used to assess shock sensitivity in having an unconfined acceptor. A consistent and reproducible observation for pressed RDX-based formulations and tetryl is that shock sensitivity, as measured by  $m_{50\%}$ , decreases as percent TMD decreases. This is the opposite of the generally observed and accepted response pattern.<sup>1</sup>

A number of material parameters were investigated and shown not to be important, identifying this anomalous behavior as due to the test configuration. One such parameter was reduction in particle size upon sample compaction; this casts doubt on the use of this explanation previously for shock sensitivity/density reversals.<sup>11,23</sup> Critical diameter of the acceptor, and run distance to detonation were also not major factors; the former parameter would be important for relatively insensitive compositions with larger critical diameters.

Shock sensitivity was determined using the MRL SSGT for a series of pressed booster and main charge explosives and compared with results from the NOL SSGT, chosen as representative of a confined acceptor configuration. This showed that the principal difference between the two tests was that both ignition and buildup strongly influenced MRL SSGT

Table 5. A Comparison of Data for RDX/AC629 (97.94:2.06) Determined Using MRL SSGT in Normal Configuration and with Brass Confinement

MRL SSGT	Shock Sensitivity		
	%TMD	$m_{50\%}$ (mm)	$\sigma$ (mm)
Unconfined (normal) <sup>a</sup>	91.0	2.43	0.036
	85.8	1.88	0.027
Confined	90.01	2.23	0.026
	85.01	2.13	0.021

<sup>a</sup> Data repeated from Table 1.

results; the NOL SSGT has been shown previously to be principally a test of the ease of ignition under shock loading. The apparently lower shock sensitivities of lower density (percent TMD) samples as determined by the MRL SSGT therefore results from the decreased ability to undergo buildup being sufficient to overcome the increased ease of ignition.

Confining the acceptor charge in 25.4 mm o.d. brass raised the apparent shock sensitivity of RDX/AC629 98:2 at 85 percent TMD, but decreased that of the 90 percent TMD sample. However, the 90 percent TMD sample was still rated as more shock sensitive.

The unusual results observed by us have a number of important consequences for studies on shock sensitivity. Firstly, it should be noted that despite the widespread use of gap tests for over 30 years, only a few other isolated instances<sup>16-18</sup> of this phenomenon have been reported. This primarily results from almost universal use of confined acceptors, compounded by an insufficiently large range of percent TMD being studied where the acceptor explosives were unconfined. For example, the  $m_{50\%}$  value for cast explosives is greater when confined than unconfined.<sup>9,21</sup> However, this is not necessarily true for pressed explosives and this has been explained as being due to different pressing conditions.<sup>21</sup> Our results would suggest that the relative confined/unconfined  $m_{50\%}$  values will primarily derive from the sample percent TMD.

The MRL (and AWRE)<sup>6</sup> SSGTs have been excellent vehicles for comparative shock sensitivity data in the past, and will continue to be if used carefully. In particular, no conclusions should be drawn from results from different materials at different percent TMD, and materials with dissimilar particle size and/or physical form, such as waxed versus unwaxed, should be compared with caution. The sensitivity ranking of closely related formulations, such as the wax/binder materials studied here, are correctly predicted. Similarly, shock sensitivity of waxed formulations decreases with increasing wax content (see Figure 4) as expected; this should be the trend for decreased

ability to undergo buildup and thus would be expected to be correctly predicted.

Secondly, development of new gap test (type) configurations (such as LASI)<sup>22</sup> where the acceptor is unconfined, or where confined/unconfined configurations are alternatively used, have the potential to give misleading comparisons. These tests should be rigorously characterized by study of several types of explosives, e.g., waxed, pure crystalline, over an extended percent TMD range. Without this, effects of density, morphology, etc., may interact to produce anomalous results which may not be recognized by those using the tests.

## ACKNOWLEDGEMENTS

A number of people provided technical assistance to this project; Mr. R. Porteous, Mr. C. Louey, Mr. K. Lee, Mrs. J. Pinson, Mr. M. G. Wolfson, Mr. T. Kinsey, Mr. K. Shortland, and Mr. M. Lambrellis. Their assistance is gratefully acknowledged.

Several of our associates provided key insights to this project during extensive discussions; we would particularly like to express our thanks to Dr. J. Eadie, Mr. M. C. Chick, and Mr. J. R. Bentley. Lastly, discussions with Mr. M. Stosz and Dr. C. Bernstein during a visit by one of us (RJS) to NSWC were instrumental in extending our understanding of the problems encountered during this project.

## REFERENCES

1. Roth, J., "Shock Sensitivity of Explosives," in *Encyclopedia of Explosives and Related Items*, ed. S. M. Kaye, PATR 2700, Picatinny Arsenal, Dover, NJ, Vol. 9, 1980, p. S58.
2. Price, D. and Liddiard, T. P., Jr., "The Small Scale Gap Test: Calibration and Comparison with the Large Scale Gap Test," NOLTR 66-87, Naval Ordnance Labs., White Oak, MD, 1966.
3. Gibbs, T. R. and Popolato, A., *LASI Explosive Property Data*, University of California Press, Los Angeles, CA, 1980.

4. Peterson, R., *Susceptibility Index of Explosives to Accidental Initiation*, NWSY TR 81-6, Naval Weapons Station, Yorktown, VA, 1981.
5. Dobratz, B. M. and Crawford, P. C., *LLNL Explosives Handbook. Properties of Chemical Explosives and Explosive Simulants*, UCRL-52997, Change 2, Lawrence Livermore National Laboratory, Livermore, CA, 1985.
6. UK Sensitiveness Collaboration Committee, *Explosives Hazard Assessment, Manual of Tests*, SCC No. 3, 1980. Test No. 18/67, AWRE Small Scale Gap Test; Test No. 11/78, RARDE Small Scale Gap Test.
7. Culling, H. P., *Statistical Methods Appropriate for Evaluation of Fuze Explosive-Train Safety and Reliability*, NAVORD Report 2101, U.S. Naval Ordnance Labs., White Oak, MD, 1953.
8. Ayres, J. N.; Montesi, L. J.; and Bauer, R. J., *Small Scale Gap Test (SSGT) Data Compilation: 1959-1972. Vol. I, Unclassified Explosives*, NOLTR 73-132, Naval Ordnance Labs., White Oak, MD, 1973.
9. Price, D.; Clairmont, A. R.; and Erkman, J. O., *The NOL Large Scale Gap Test III. Compilation of Unclassified Data and Supplementary Information and Interpretation of Results*, NOLTR 74-40, Naval Ordnance Labs., White Oak, MD, 1974.
10. Wolfson, M. G., *The MRL Small Scale Gap Test for the Assessment of Shock Sensitivity of High Explosives*, MRL-R-896, Materials Research Lab., Maribyrnong, Vic., 1983.
11. Zerilli, F. J., *Notes from Lectures on Detonation Physics*, NSWC MP 81-399, Naval Surface Weapons Center, Silver Spring, MD, 1981. Lecture 9: *Critical Energy and Pressure for Initiation; Wedge and Gap Test*, by D. Price.
12. Wilson, W. S., *RDX/Polyethylene Wax Compositions as Pressed Explosives*, MRL R-722, Materials Research Lab., Maribyrnong, Vic., 1978.
13. Wilson, W. S., *Recrystallized RDX for RDX/Polyethylene Wax Compositions*, MRL-TN-436, Materials Research Lab., Maribyrnong, Vic., 1980.
14. Spear, R. J.; Nanut, V.; and Dagley, I. J., *RDX-Polyethylene Wax Formulations as Potential Replacements for Tetryl in Fuze Leads, Boosters and Magazines*, MRL-R-1015, Materials Research Lab., Maribyrnong, Vic., 1986.
15. Dagley, I. J.; Spear, R. J.; and Nanut, V., *High Explosive Moulding Powders from RDX and Polyurethane Dispersions*, MRL-R-1062, Materials Research Lab., Maribyrnong, Vic., 1987.
16. Seely, L. B., "A Proposed Mechanism for Shock Initiation of Low Density Granular Explosives," *Proceedings of the Electric Initiator Symposium*, Franklin Inst., Philadelphia, PA, Paper 27, 1963.
17. Dinegar, R. H. and Millican, M. S., "The Initiation of Tetryl by Small Charges of PETN," *Propellants Explos.*, Vol. 1, 1976, p. 111.
18. Engineering Design Handbook, Explosive Series, *Explosive Trains*, AMCP 706-179, US Army Materiel Command, Chapter 3, 1974, p. 35.
19. Cachia, G. P. and Whitbread, E. G., "The Initiation of Explosives by Shock," *Proc. Roy. Soc.*, A246, 1958, p. 268.
20. Chick, M. C., personal communication at MRL based on past experience at AWRE, 1988.
21. Price, D., "Gap Tests and How They Grow," *Proceedings of the Twenty-second DoD Safety Seminar*, Anaheim, CA, 26-28 Aug 1986, p. 365.
22. Tasker, D. G., "Shock Initiation and Subsequent Growth of Reaction in Explosives and Propellants: the Low Amplitude Shock Initiation Test, LASI," *Proceedings of the Seventh Symposium (International) on Detonation*, U.S. Naval Acad., Annapolis, MD, 1981, p. 285.

23. Price, D., *Effect of Particle Size on the Shock Sensitivity of Pure Porous HE*, NSWC TR 86-336, Naval Surface Weapons Center, White Oak, MD, 1986.
24. Stresau, R. H. and Kennedy, J. E., "Critical Conditions for Shock Initiation of Detonation in Real Systems," *Proceedings of the Sixth Symposium (International) on Detonation*, Coronada, CA, 1976, p. 68.
25. Spear, R. J. and Nanut, V., "Reversal of Particle Size/Shock Sensitivity Relationship at Small Particle Size for Pressed Heterogeneous Explosives under Sustained Shock Loading," *J. Energetic Mats.*, Vol. 6, 1989, in press.
26. Eadie, J., "The Effect of Wax on the Shock Sensitivity of Explosive Compacts," *Proceedings of the Fourth Symposium (International) on Detonation*, White Oak, MD, 1965, p. 399.
27. Reference 5, Section 8.5, and Reference 11, Lecture 6, *Factors which Affect Critical Parameters*, by D. Price.
28. Hutchinson, C. D., *The Response of Intermediate Explosives to Thermal and Shock Stimuli*, Ph.D. Thesis, University of Cambridge, UK, 1985, Chapter 8.
29. Price, D., "Contrasting Patterns in the Behaviour of High Explosives," *Proceedings of the Eleventh Symposium on Combustion*, Berkeley, CA, 1966, p. 693.
30. Taylor, B. C. and Erwin, L. W., "Separation of Ignition and Buildup to Detonation in Pressed TNT," *Proceedings of the Sixth Symposium (International) on Detonation*, Coronado, CA, 1976, p. 1.
31. Howe, P.; Frey, R.; Taylor, B.; and Boyle, V., "Shock Initiation and the Critical Energy Concept," *Proceedings of the Sixth Symposium (International) on Detonation*, Coronado, CA, 1976, p. 11.
32. Lee, E. L. and Tarver, C. M., "Phenomenological Model of Shock Initiation in Heterogeneous Explosives," *Phys. Fluids*, Vol. 23, 1980, p. 2362, and earlier references cited therein.
33. Tarver, C. M.; Hallquist, J. O.; and Erickson, L. M., "Modeling Short Pulse Duration Shock Initiation of Solid Explosives," *Proceedings of the Eighth Symposium (International) on Detonation*, Albuquerque, NM, 1985, Preprints, p. 884.
34. Savitt, J., Some Properties and Uses of Nitroguanidine, *Institut fur Chemie der Treib-und Explosivstoffe, ICT Int. Jahrestag*, Karlsruhe, Germ., 1985, Paper 38.
35. Price, D., *Factors Which Affect Critical Parameters*, Lecture 6 in Reference 11. See also Section 8.5 in Reference 5.
36. Spear, R. J. and Nanut, V., *A Comparative Assessment of US and UK Explosives Qualified as Replacements for Tetryl*, MRL-R-1094, Materials Research Lab., Maribyrnong, 1987.
37. Drimmer, B. E., *Navy Bank of Explosives Data (NAVBED) Volume III*, NSWC MP 83-230, Naval Surface Warfare Center, White Oak, MD, 1983.
38. US Department of the Navy, *Material Specification for HNS Explosive*, WS 5003J, 1981.

## DISCUSSION

JULIUS ROTH, Consultant  
Portola Valley, CA

It seems likely that your anomalous shock effect is an artifact of your experimental system. If the diameter and/or length of your acceptor is changed the effect may well disappear. Table 5 of your preprint (confinement) already suggests this. What you may be observing is the consequence of rarefactions which weaken the detonation before it gets to your witness plate. In the Fifth Detonation Symposium, we reported the results of a gap test on  $\frac{1}{4}$ -inch x  $\frac{1}{4}$ -inch circular pellets of RDX (as well as other explosives) of about ~75 to ~90 percent TMD unconfined. The former was definitely more shock sensitive. Incidentally, the almost universal observation is that "coarse" grained explosives are more shock

sensitive than "fine" grained explosives at threshold pressures. Also, the paper in this session (Hutchinson et al.) does not find a density effect reversal.

### REPLY BY ROBERT J. SPEAR

The MRL SSGT is based on, and very closely resembles, the AWRE SSGT. The paper by Hutchinson et al. in this session (Paper Number 5) shows results typical of the AWRE research on shock sensitivity carried out at near crystal density; shock sensitivity of EDC 35 over the very limited density range studied ( $1.893 - 1.905 \text{ Mg/m}^3$ ) is dominated by lot to lot variation and a density effect is consequently not apparent. Virtually all of the published AWRE data is for such very high densities.

We completed a study about two years ago (MRL-R-1077, 1987; *J. Energetic Mats.*, in press 1989) looking at the relationship between RDX particle size and shock sensitivity at 90 percent TMD using the MRL SSGT. It was found that the  $M_{50\%}$  values increased (shock sensitivity increased) as RDX particle size decreased from 250 to  $21.5 \mu\text{m}$  median particle size, then decreased for  $3.9 \mu\text{m}$

particle size. This was comparable to what you observed (Roth, Fifth Detonation Symposium) except that the change we observed from  $21.5$  to  $3.9 \mu\text{m}$  was less pronounced than that you observed for  $25$  to  $8 \mu\text{m}$ . As you noted, you observed a decrease in shock sensitivity as density increased from  $1.58$  to  $1.64 \text{ Mg/m}^3$ , whereas we would observe an increase. I agree with your other comments.

### DISCUSSION

BARRY T. NEYER  
EG&G Mound Applied Tech.  
Miamisburg, OH

This paper illustrates the importance of completely specifying all of the experimental conditions when reporting results. It also demonstrates the problem of comparing results of two different types of tests. The "shock sensitivity" of explosives is perhaps as strong a function of the test method as it is of the composition of the explosive.

### REPLY

No reply from the authors.



# SHOCK INITIATION OF LX-17 AS A FUNCTION OF ITS INITIAL TEMPERATURE\*

P. A. Urtiew, L. M. Erickson, D. F. Aldis, and C. M. Tarver  
High Explosives Technology  
Lawrence Livermore National Laboratory  
Livermore, California 94550

*The TATB-based pressed solid explosive LX-17 has been demonstrated to exhibit significant differences in shock sensitivity as its initial temperature is varied from  $-54^{\circ}\text{C}$  to  $+88^{\circ}\text{C}$ . In this combined experimental-computational study, embedded gauges were used to measure the particle velocity and pressure histories in reacting LX-17 at various initial shock pressures and time durations at three initial temperatures: cold ( $-54^{\circ}\text{C}$ ), ambient ( $25^{\circ}\text{C}$ ), and hot ( $88^{\circ}\text{C}$ ). The ignition and growth reactive flow computer model, which had previously been normalized to a great deal of embedded gauge and other shock initiation data for ambient temperature LX-17, was then used to determine the differences in chemical reaction rates which are required to calculate the cold and hot LX-17 data. The embedded gauge records clearly demonstrate that during shock compression at colder temperatures there are fewer ignition hot spots, and that the growth of reaction rates from these hot spots is also slower. At higher temperatures, the ignition is more vigorous and the growth of reaction rates is also faster. However, the transition to detonation occurs as rapidly in cold LX-17 as it does in ambient or hot LX-17. The changes in the three reaction rate terms of the ignition and growth model necessary for accurate simulations are consistent with these experimental observations.*

## INTRODUCTION

Triaminotrinitrobenzene (TATB)-based heterogeneous solid explosives have been experimentally demonstrated to exhibit important initial temperature effects on shock initiation, divergence of reaction, corner turning, and detonation failure.<sup>1-16</sup> To quantitatively determine the initial temperature effects on one dimensional, sustained shock pulse shock initiation of LX 17 1 (92.5 percent TATB plus 7.5 percent Kelf<sup>®</sup> pressed to  $1.90\text{ g/cm}^3$  or 98 percent TMD), three series of embedded gauge (both pressure and particle velocity) experiments were conducted in the 10-15 GPa

input shock pressure regime on cold ( $-54^{\circ}\text{C}$ ), ambient ( $25^{\circ}\text{C}$ ), and hot ( $88^{\circ}\text{C}$ ) LX-17.

This experimental data is simulated using the ignition and growth reactive flow computer model.<sup>17</sup> The model is based on three interconnected reaction rate laws: the ignition of hot spot reaction sites, the growth (or failure to grow) of these reaction sites in a high pressure deflagration-type process, and the rapid completion of reaction at very high pressures as the remaining unreacted explosive molecules decompose. The parameters for LX-17 at ambient temperature have accurately calculated a great deal of one- and two-dimensional shock initiation and detonation experimental data.<sup>18-21</sup> In this paper, calculations using these parameters are shown to agree with the new embedded gauge data, implying that modifications in the gauge packages have not

\*Work performed under the auspices of the U.S. Department of Energy by the Lawrence Livermore National Laboratory under Contract No. W 7405 ENG 48.

changed their response. The ignition and growth model parameters are varied in systematic ways to match the cold and hot LX-17 data. Implications of these numerical results, in terms of hot spot ignition and growth shock initiation theory, are discussed.

### Embedded Gauge Experiments

The embedded gauge experiments were carried out in our 4-inch gun test facility, where stationary targets placed in an evacuated test chamber are struck with a flying projectile fitted with a proper flyer material. By matching flyer and target material with the projectile velocity, one can achieve pressures in excess of 500 kilobars.

The experimental setup consists of the target assembly and the sabot containing the necessary flying plate. This setup is illustrated in Figure 1. The target assembly consists of several layers of the investigated material between which there are gauge stations. Each gauge station contains one or two pressure or particle velocity gauges, described elsewhere,<sup>22-28</sup> armored for protection with a 1 to 10 mils thick layer of Teflon on both sides of the gauge. Some target assemblies also contain a layer of buffer material to minimize the shock strain on the first gauge station, if it is to be placed on the front surface of the sample. The target assembly also contains six piezoelectric pins placed flush with the front surface to measure tilt of the oncoming flyer plate, and two more crystal pins extending a few mm in front of them to measure the projectile velocity. The latter is also measured with flash x-ray, catching the sabot in flight at two instances of time before it strikes the target.

In order to provide the hot or cold thermal environment, the target is placed into a metal container which is either heated with an electric heating pad or cooled with controlled flow of liquid nitrogen vapor through the hollow part of the target container.

A serious concern was given to the rate of heating or cooling of the target to maintain its integrity, and to prevent undesired stresses and strains due to different thermal expansion coefficients in various components of the gauge

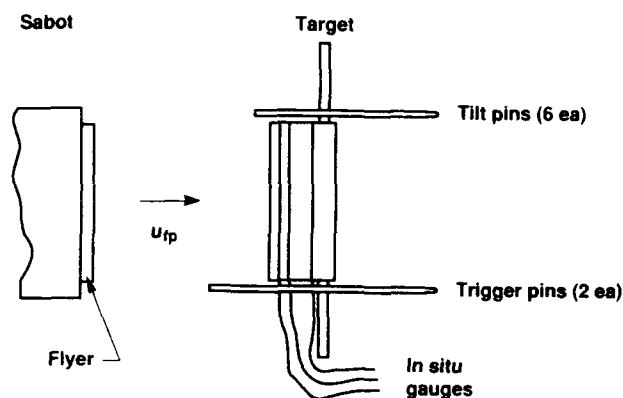


Figure 1. The 101 mm Gun Test Setup

package. During the heating or cooling process, the temperature was continuously monitored with several thermocouples strategically placed throughout the target. A printout of all temperature readings every 30 seconds provided a clear record of the temperature profile. Temperature throughout the target generally equilibrated to within  $\pm 3^\circ\text{C}$  of the desired final value. A reflective cover plate was used in front of the container to reduce thermal radiation effects on the front surface of the target. The cover plate was removed just prior to firing.

As is usually the case the experiments were designed with theoretical work in mind. Here, the demand from the modeling effort was to have the gauges survive longer and provide cleaner records, while the flow is still one-dimensional in the axial direction. At the same time, in order to combine pressure records with those of the particle velocity in the reactive medium for the Lagrange analysis, both types of these experiments should be conducted under identical impact conditions. These constraints required the flyer plate to be thicker (to delay release wave from the rear), denser, and faster (to provide higher impact pressure), and nonmetallic (to allow use of the magnetic field for particle velocity measurements). The combination of these constraints is rather severe but most difficult of all was to obtain identical impact conditions because a slight variation in flyer velocity results in a change of initial pressure and, thus, a different reaction rate.

The target assembly with six gauge stations containing particle velocity gauges and the flyer plate just prior to impact is shown in Figure 2. Also shown in this figure is the wave diagram resulting from the impact of the flyer striking the target at a velocity of 1.7 mm/ $\mu$ s. In this diagram, which is represented in the space-time plane, shock waves are represented as solid lines, particle streamlines as broken lines, and rarefaction waves as chain dotted lines. Numbers along these lines represent the slopes ( $\Delta x/\Delta t$ ) or the speeds (in mm/ $\mu$ s) at which these waves or particles propagate in the laboratory

coordinate system. Since each gauge station, once put into motion by the shock wave, will move along a particle path (Lagrangian path), its recorded response will correspond to the particle velocity profile along that same streamline. A typical set of particle velocity profiles is also included in Figure 2 to illustrate the correlation between the two planes. Thus, from the wave diagram, it follows that in the case at hand each gauge has slightly over 2  $\mu$ s of recording time during which the flow should be self-regulated by the reaction process before it is affected by the release wave coming from the rear.

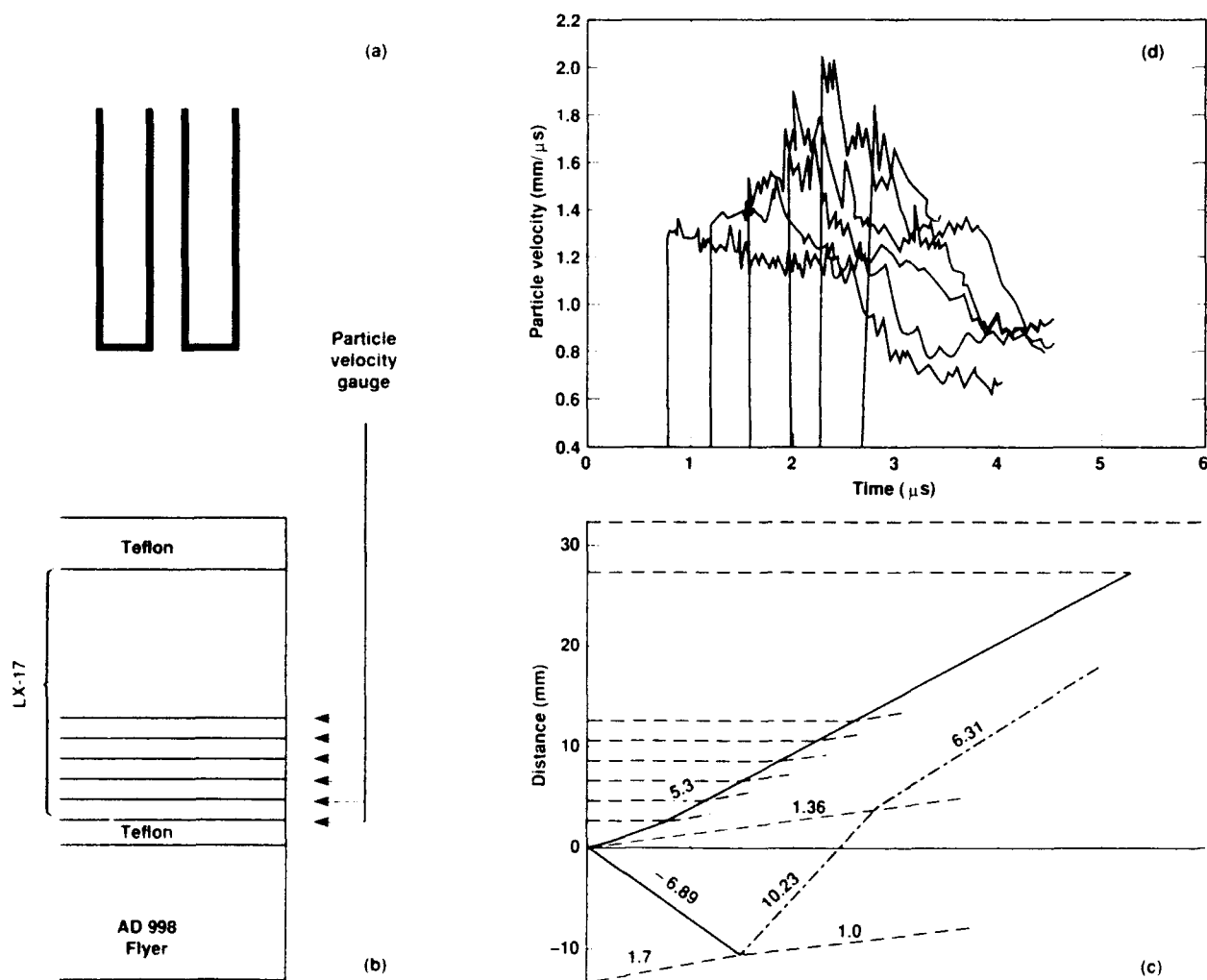


Figure 2. The Particle Velocity Experiment. (a) Particle velocity gauge. (b) Shot assembly showing the stack of target materials at the instant of flyer impact. (c) Distance-time plot of the wave train generated by the flyer impacting on the target. (Here solid lines represent shock waves, broken lines represent particle paths, and chained dotted lines represent rarefaction waves. Numbers along the lines represent velocities in mm/ $\mu$ s.) (d) Particle velocity profiles along the streamline of each interface with the gauge station.

The target assembly with two manganin gauge stations and its corresponding wave diagram in the space-time domain, together with a typical set of pressure profiles, is shown in Figure 3. Here again the pressure profiles show the corresponding changes in pressure along a given streamline, which are indicative of the chemical reaction that takes place in an explosive after being subjected to a dynamic loading.

To cover the desired region of interest, we fired 16 shots aiming for the same input conditions and searching for the best loading

state to ensure a good buildup before the reaction turns over into detonation. The spread of our shots is illustrated in Figure 4, where the loading states are plotted on the pressure-particle velocity plane for each initial temperature separately. Also included in that figure is the region of the turnover within our instrumented thickness of 10 mm, as determined from our records. It is clear that the hot samples turned over to detonation at a much lower loading pressure than the cold or even ambient samples.

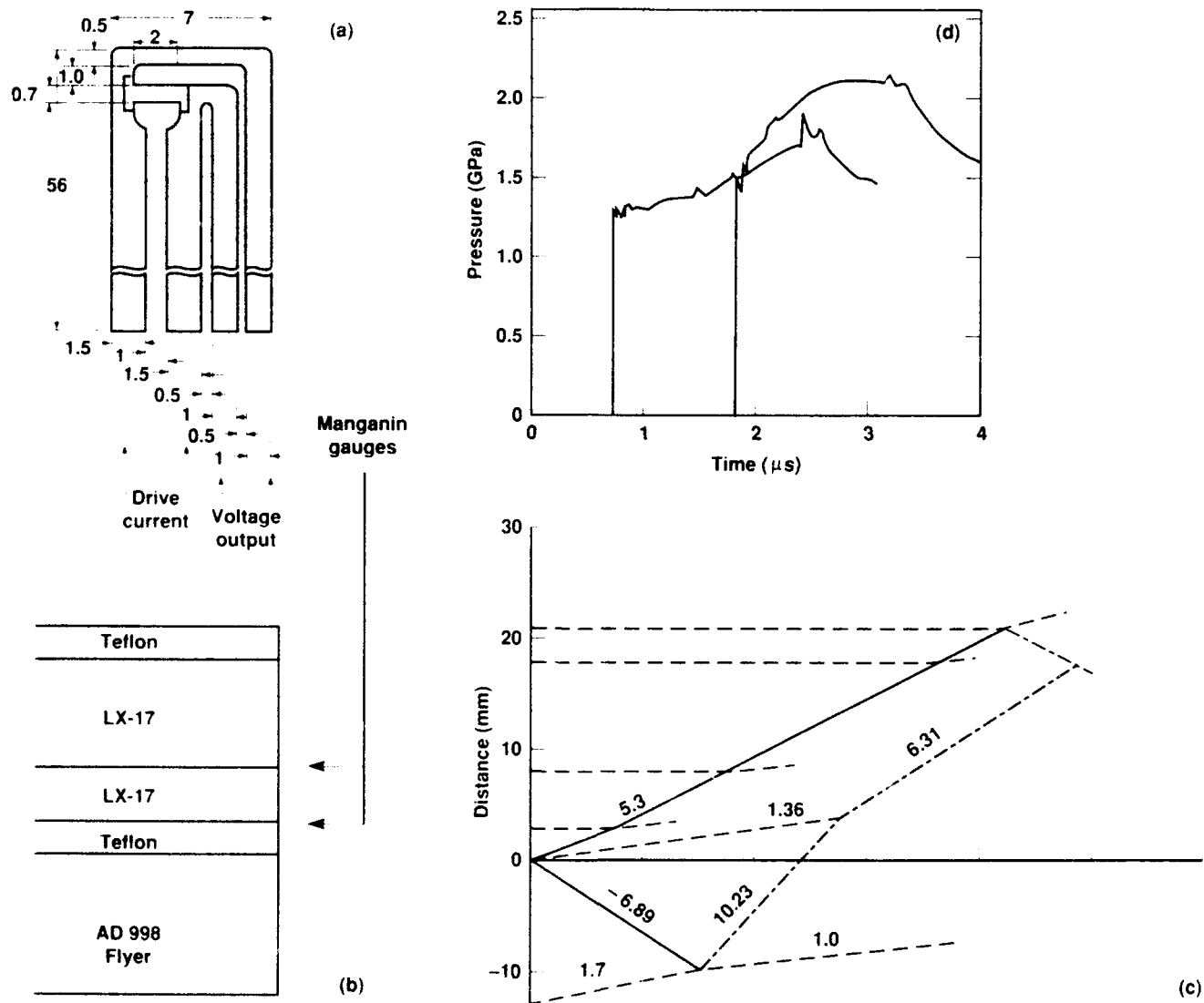


Figure 3. The Pressure Experiment. (a) Details of the manganin pressure gauges. (b) Shot assembly showing the stack of target materials at the instant of the flyer impact. (c) Distance-time plot of the wave train generated by the flyer impacting on the target. (Here solid lines represent shock waves, broken lines represent particle paths, and chain dotted lines represent rarefaction waves. Numbers along the lines represent velocities in mm/ $\mu$ s.) (d) Pressure profiles along the streamline of each interface with the gauge station.

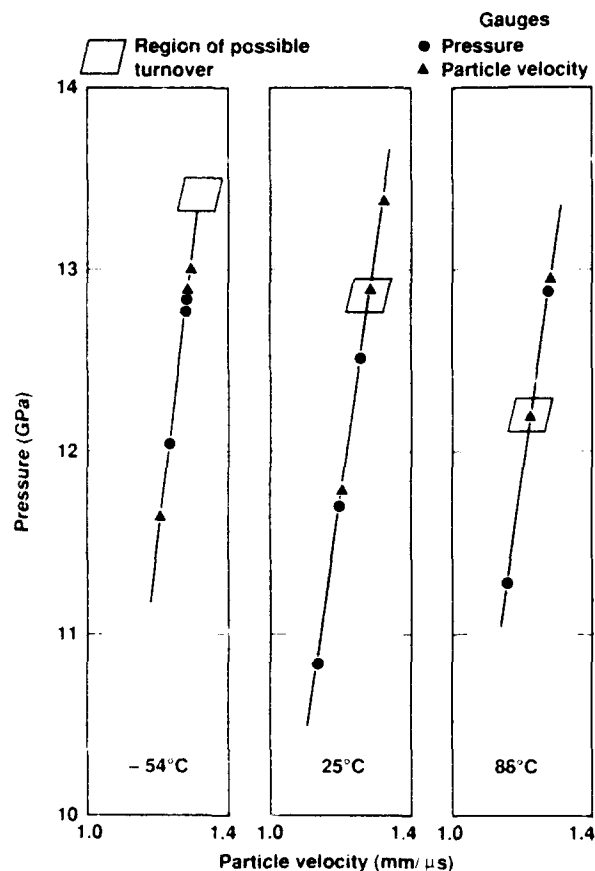


Figure 4. Pressure-Particle Velocity Plane with Points Indicating Experimental Runs and Shaded Areas Showing Possible Turnover to Detonation

Although this series was not aimed to obtain data on run distance to detonation, hot and ambient experiments were in the proper range of impact pressures and gauge depths to reveal some information on the subject. More appropriate tests for these data would be the wedge experiments with our newly developed multiple manganin and particle velocity gauges. These tests are planned for the near future. However, using the available information it is possible to make a reasonable estimate of the effect of initial temperature on the distance necessary to turn over to detonation. These estimates are indicated by broken lines on Figure 5, and agree with the classical data of Jackson et al.<sup>1</sup>

### Reactive Flow Modeling

The three term, ignition and growth model developed and used by Tarver, et al.<sup>17</sup> was used to simulate the shock initiation to detonation of

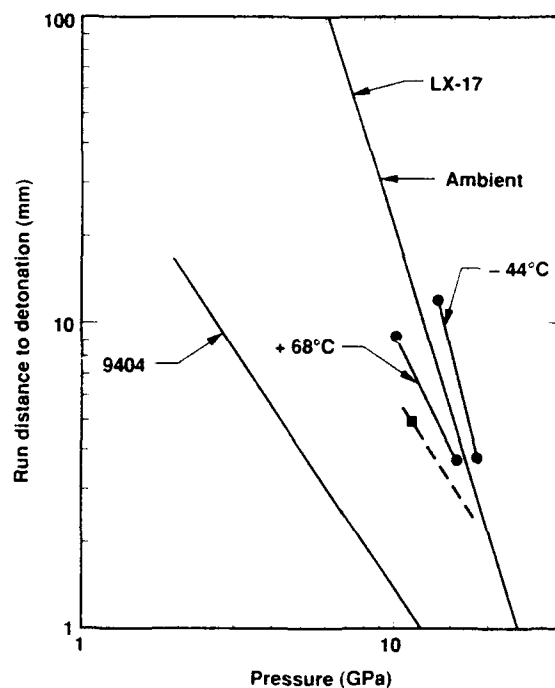


Figure 5. "Pop-Plot"-Run Distance to Detonation Vs. Pressure Showing Results of Earlier Wedge Tests

LX-17. The equation for the reaction rate law is given as

$$\frac{\partial F}{\partial t} = I(1-F)^b(\rho/\rho_0-1-a)^x + G_1(1-F)^c F^d p^y + G_2(1-F)^e F^g p^z$$

This model has been extensively used before to model shock initiation of several high explosives, including LX-17 at ambient conditions, that had been exposed to a wide variety of shock stimuli.<sup>17 21</sup>

In this present study, the initiation of LX-17 subjected to sustained shocks at three initial temperatures was simulated. A set of parameters was obtained for the LX-17 at each of the three temperatures. It may seem that the approach is somewhat inconsistent in that chemical reaction rates are functions of temperature and concentrations of the reactants. It has been previously shown, however, by Tarver and others that it is possible to predict explosive decomposition response with pressure dependent models. This present approach, of determining the overall pressure dependent rates as functions of the initial explosive temperature, is a small step in the direction of developing a temperature dependent rate model.

Several aspects of the temperature dependence of chemical kinetics can be qualitatively explored with the results of this study. A low initial temperature of the explosive causes it to both initially ignite more slowly than the ambient material, and to burn more slowly after it has become ignited. A high temperature causes the explosive to ignite more easily, and the burn rate is greater than the material at ambient temperature. The specific values used in the simulation are listed in Table 1. The values used for the simulation of the material at ambient conditions are also listed for comparison. The unreacted and the product equations of state of LX-17 were assumed to be the same at all three initial temperatures, and are taken from Tarver et al.<sup>17</sup>

To account for the observed differences in shock initiation of cold and hot LX-17, the numerical parameters that control these reaction rate laws were varied to obtain agreement with the gauge records at various initial

Table 1. Chemical Reaction Rate Parameters for LX-17

Parameter (Eq. 1)	Ambient (25°C)	Hot (88°C)	Cold (-54°C)
$I(\mu s^{-1})$	$4.0 \times 10^6$	$6.0 \times 10^6$	$2.8 \times 10^6$
b	0.667	0.667	0.667
a	0.22	0.22	0.22
x	7.0	7.0	7.0
$G_1(Mb^y \mu s^{-1})$	0.6	1.2	0.42
c	0.667	0.667	0.667
d	0.111	0.111	0.111
y	1.0	1.0	1.0
$G_2(Mb^z \mu s^{-1})$	400.0	400.0	160.0
e	0.333	0.333	0.333
g	1.0	1.0	1.0
z	3.0	3.0	3.0
$F_{igmax}$	0.5	0.5	0.5
$F_{G1max}$	0.5	0.5	0.5
$F_{G2min}$	0.0	0.0	0.0

pressures. One way to obtain fair agreement with the experiment is to simply increase (for hot LX-17) or decrease (for cold LX-17) the three ambient LX-17 reaction rate coefficients by the same factor (approximately 40 percent). However, detailed comparison shows that this technique does not accurately monitor the shock initiation behavior changes. Another method is to simply change the sustained pulse shock pressure at which LX-17 hot spots are ignited. Infrared and visible radiometry experiments on ambient LX-17 have clearly demonstrated that an input shock pressure of 6.5 GPa is necessary to establish ignition sites in ambient LX-17.<sup>29</sup> The ignition and growth model uses 6.5 GPa as the minimum pressure at which reaction can begin. A limited set of radiometry experiments have shown that ignition sites occur at lower pressures ( $\sim 5$  GPa) for hot LX-17 and higher pressures ( $\sim 8$  GPa) for cold LX-17.<sup>30</sup> Calculations made by adjusting the critical compression (or pressure) required for ignition to these values for cold and hot LX-17, while leaving the reaction rates constant, also result in fair agreement with experiment. Varying one or two reaction rate parameters at a time demonstrates that the critical compression, rate of ignition, and rate of growth of the hot spots all influence the cold and hot LX-17 shock initiation patterns. An independent study of the heat flow conditions in and around LX-17 hot spots also confirms these observations.<sup>31</sup> Sets of ignition and growth model parameters for cold LX-17 and hot LX-17 have been developed to match all of the experimental data in ways consistent with the observed experimental trends.

Two types of data are presented, material velocity measurements and pressure measurements, both versus time. The material velocities were measured at six positions: at the impact surface and at five depths in the sample—2, 4, 6, 8, and at 10 mm into the sample. The pressure measurements were made at two positions, at the surface and at a depth of 5 mm inside the sample. Each of the experiments was simulated with a separate calculation.

The experimental results, along with the theoretical predictions, are presented in Figures 6 through 15. The material velocity records for the ambient, cold, and hot are shown in Figures 6, 9, and 12, respectively. The pressure

measurements and predicted values are shown in Figures 7, 8, 10, 11, 13, and 14. Reasonable agreement exists between the experimental and the predicted values of pressure and material velocity versus time. The apparent growth of reaction seems to have been well-characterized by the ignition and growth model with the specific constants used.

The decrease in material velocity after the initial shock and the subsequent reaction effects is due to the rarefaction wave coming in from the unconfined end of the flyer plate. The arrival time of this wave is directly related to the equation of state used for the flyer plate. The principle used in the velocity measurement requires that a nonconductive flyer plate be used in this experiment. Aluminum oxide was selected because it is both nonconductive and it has a density of 3.998 gm/cc. One problem with aluminum oxide, is that its equation of state is not well-characterized.

The equation of state for this material was assumed to be similar to that for sapphire. Urtiew<sup>32</sup> and Graham<sup>33,34</sup> have reported that the shock velocity-material velocity curve for sapphire is not linear for the values of particle velocity used in this experiment. At velocities greater than approximately 0.42 mm/ $\mu$ s the shock velocity increases monotonically with increasing material velocity. For value of material velocity less than 0.42 mm/ $\mu$ s the shock velocity is greater than 10 mm/ $\mu$ s and has only a slight tendency to increase. In this earlier work, only five data points were reported for material velocities between 0 and 0.42 mm/ $\mu$ s, and the scatter in the data was large enough so that it did not appear that a significant relationship was present.

The effect of the inert equation of state was evaluated by repeating initiation calculations for the material velocity experiment at ambient temperature. For this calculation the shock velocity was assumed to be constant at 10.9 mm/ $\mu$ s. The results of this calculation are shown in Figure 15. Several differences are present between this calculation and the previous one shown in Figure 6. The initial velocity is slightly higher. This slight increase in material velocity also causes an increase in the initial shock pressure. The increased shock

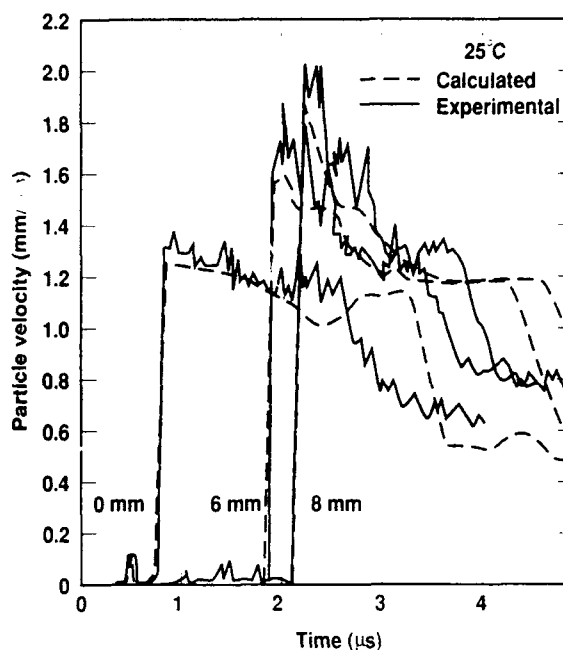


Figure 6. Comparison of Calculated and Experimental Particle Velocity Profiles in LX-17 Along the Streamlines of 0, 6, and 8 mm of the Explosive Initially at 25°C

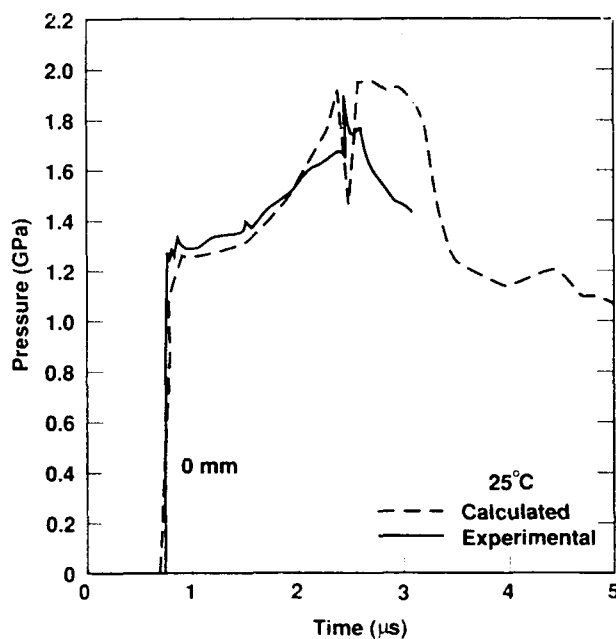


Figure 7. Comparison of Calculated and Experimental Pressure Profile in LX-17 Along the 0 mm Streamline of the Explosive Initially at 25°C

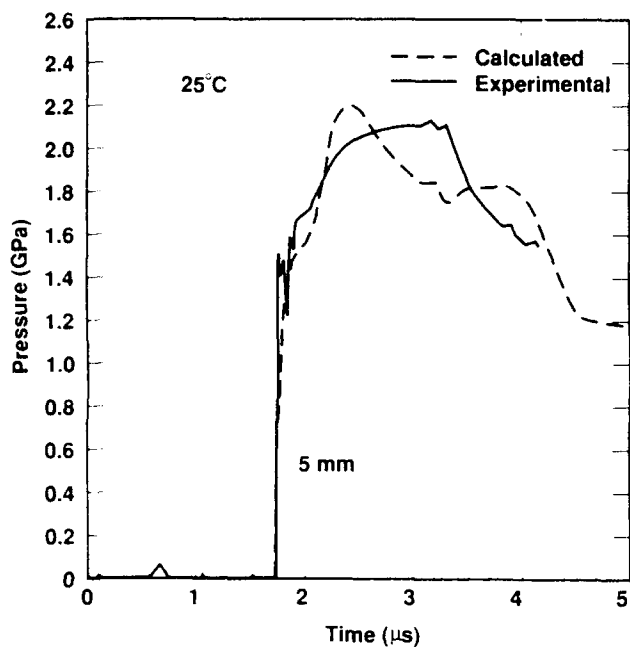


Figure 8. Comparison of Calculated and Experimental Pressure Profile in LX-17 Along the 5 mm Streamline of the Explosive Initially at 25°C

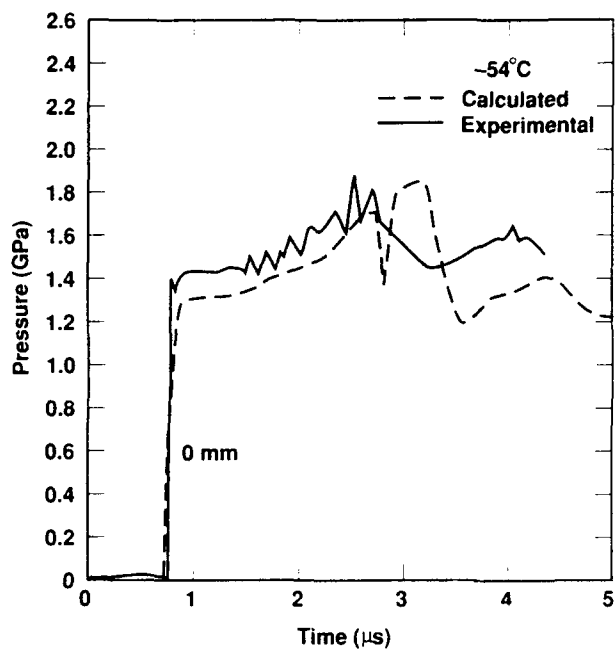


Figure 10. Comparison of Calculated and Experimental Pressure Profile in LX-17 Along the 0 mm Streamline of the Explosive Initially at -54°C

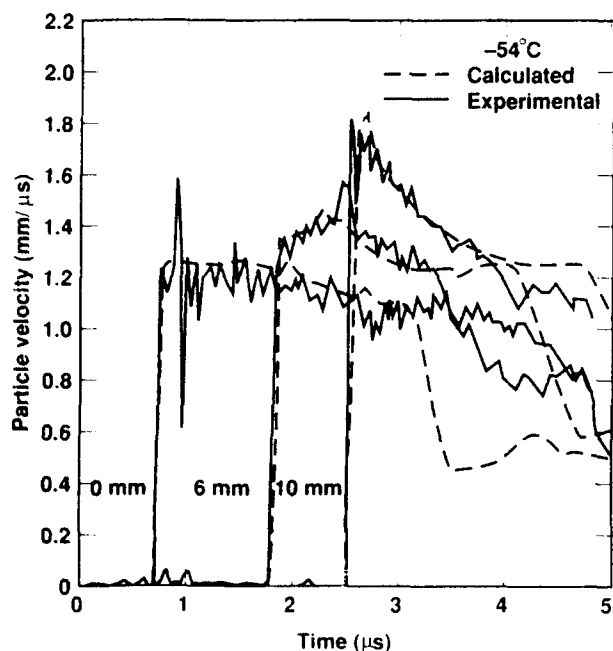


Figure 9. Comparison of Calculated and Experimental Particle Velocity Profile in LX-17 Along the Streamlines of 0, 6, and 10 mm of the Explosives Initially at -54°C

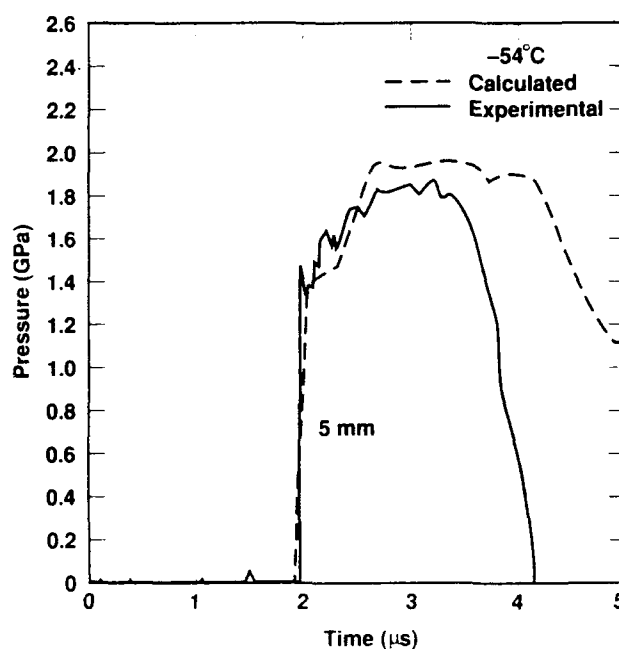


Figure 11. Comparison of Calculated and Experimental Pressure Profile in LX-17 Along the 5 mm Streamline of the Explosive Initially at -54°C



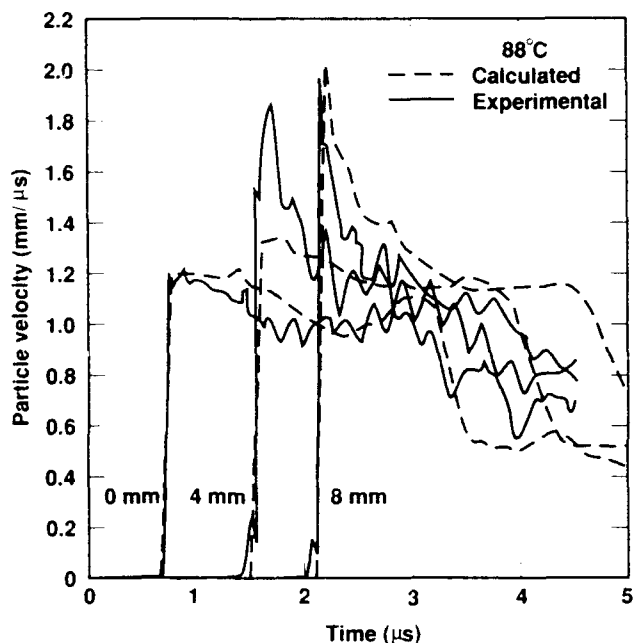


Figure 12. Comparison of Calculated and Experimental Particle Velocity Profile in LX-17 Along the Streamlines of 0, 4, and 8 mm of the Explosive Initially at +88°C

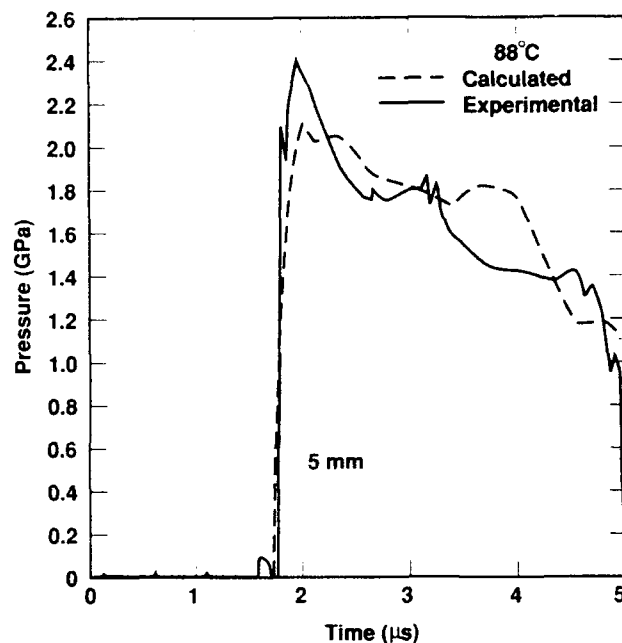


Figure 14. Comparison of Calculated and Experimental Pressure Profile in LX-17 Along the 5 mm Streamline of the Explosive Initially at +88°C

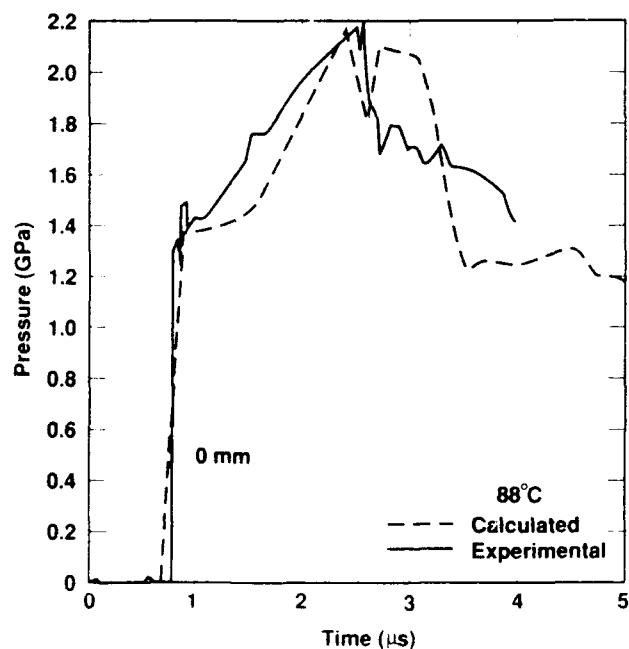


Figure 13. Comparison of Calculated and Experimental Pressure Profile in LX-17 Along the 0 mm Streamline of the Explosive Initially at +88°C

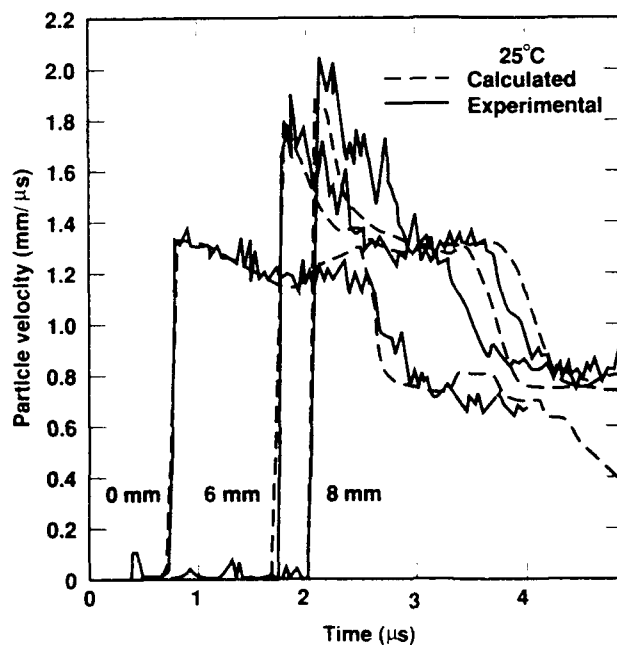


Figure 15. Comparison of Calculated and Experimental Particle Velocity Profiles in LX-17 Along the Streamlines of 0, 6, and 8 mm of the Explosive Initially at 25°C. Calculations were done with a shock velocity independent of the particle velocity, i.e.,  $U_s = 10.9 \text{ mm}/\mu\text{s}$ .

pressure causes the initiation of strong reaction to occur slightly sooner, as can be seen in the shape of the signal from the 6 mm gauge. Another interesting result is that the rarefaction coming in from the free back surface of the flyer plate is much closer to that measured experimentally. These effects, although interesting, cause only small variations in the overall response.

## RESULTS AND CONCLUSIONS

The shock initiation of LX 17 has been quantitatively studied experimentally and computationally at three initial temperatures. Analyzing the experimental embedded gauge records with the ignition and growth reactive flow model has clearly demonstrated that colder LX-17 exhibits a smaller fraction of explosive ignited in the hot spots created by shock compression. This results in a smaller increase in the shock velocity and pressure than those measured for hotter LX-17. The growth of hot spot reactions behind the shock front is also slower in cold LX-17. This results in a more gradual pressure rise behind the shock front than that measured for hotter LX-17. The colder temperature in the shocked LX 17 surrounding the hot spots is the most plausible cause of this decreased growth rate in the cold LX 17 experiments. Numerical modeling defines the magnitudes of these reaction rate effects. Comparison of the transitions to detonation in cold, ambient, and hot LX-17 indicate that this rapid completion of reaction and formation of the detonation wave front occur at approximately the same rate at all three initial temperatures. Sufficient heat has been transferred from the rapidly growing hot spots to the remaining unreacted molecules in this transition region, to overcome the 140°C initial temperature discrepancy.

This study will be extended to even more extreme temperatures and pressures and to more complex geometries. One must be careful not to violate the temperature regimes of the Kelf binder system. The ignition and growth model parameters will be tested on other initial temperature dependent TATB experimental data, such as the observed detonation wave front curvature and failure diameter data of Campbell.<sup>10</sup>

## REFERENCES

1. Jackson, R. K.; Green, L. G.; Barlett, R. H.; Hofer, W. W.; Kramer, P. E.; Lee, R. S.; Nidick, Jr., E. J.; Shaw, L. L.; and Weingart, R. C., *Sixth Symposium (International) on Detonation*, Office of Naval Research, ACR-221, Aug 1976, p. 755.
2. Davis, W. C., *ibid.*, p. 637.
3. Campbell, A. W. and Engelke, R., *ibid.*, p. 642.
4. Weingart, R. C.; Lee, R. S.; Jackson, R. K.; and Parker, N. L., *ibid.*, p. 653.
5. Honodel, C.; Humphrey, J.; Weingart, R.; Lee, R. S.; and Kramer, P., *Seventh Symposium (International) on Detonation*, Naval Surface Weapons Center, MP 82-334, Jun 1981, p. 425.
6. Anderson, A. B.; Ginsberg, M. J.; Seitz, W. L.; and Wackerle, J., *ibid.*, p. 385.
7. Davis, W. C. and Ramsay, J. B., *ibid.*, p. 531.
8. Cox, M. and Campbell, A. W., *ibid.*, p. 624.
9. Hayes, B. and Tarver, C. M., *ibid.*, p. 1029.
10. Campbell, A. W., *Propellants, Explosives and Pyrotechnics*, Vol. 9, 1984, p. 183.
11. Sheffield, S. A.; Bloomquist, D. D.; and Tarver, C. M., *J. Chem. Phys.*, Vol. 80, 1984, p. 3831.
12. Lee, R.; Bloom, G.; Von Holle, W.; Weingart, R.; Erickson, L.; Sanders, S.; Slettevold, C.; and McGuire, R., *Eighth Symposium (International) on Detonation*, Naval Surface Weapons Center, MP 86-194, Jul 1985, p. 3.
13. Seitz, W. L.; Stacy, H. L.; and Wackerle, J., *ibid.*, p. 123.
14. Ramsay, J. B., *ibid.*, p. 372.
15. Brief, D.; Ward, S. H.; and Cole, G. D., *ibid.*, p. 380.
16. Green, L.; Lee, E.; Mitchell, A.; and Tarver, C., *ibid.*, p. 587.
17. Tarver, C. M.; Hallquist, J. O.; and Erickson, L. M., *ibid.*, p. 951.

18. Bahl, K.; Bloom, G.; Erickson, L.; Lee, R.; Tarver, C.; Von Holle, W.; and Weingart, R., *ibid.*, p. 1045.
19. Cochran, S. G. and Tarver, C. M., *Shock Waves in Condensed Matter-1983*, J. R. Asay; R. A. Graham; and G. K. Straub, eds., Elsevier Science Publishers B. V., 1984, p. 593.
20. Tarver, C. M.; Breithaupt, R. D.; and Kury, J. W., *International Symposium on Pyrotechnics and Explosives*, Beijing, China, Oct 1987, p. 692.
21. Tarver, C. M., "Modeling Shock Initiation and Detonation Divergence Tests on TATB-Based Explosives," paper accepted for publication in *Propellants, Explosives, and Pyrotechnics*, 1989.
22. Weingart, R. C.; Barlett, R.; Cochran, S.; Erickson, L. M.; Chan, J.; Janzen, J.; Lee, R.; Logan, D.; and Rosenberg, J. T., *Proceedings of the Symposium on High Dynamic Pressures*, Paris, France, 1978, pp. 451-461.
23. Erickson, L.; Weingart, R.; Barlett, R.; Chan, J.; Elliott, G.; Janzen, J.; Vantine, H.; Lee, R.; and Rosenberg, J. T., *Tenth Symposium on Explosives and Pyrotechnics*, 21/1-7, San Francisco, CA, 1979.
24. Vantine, H.; Chan, J.; Erickson, L. M.; Janzen, J.; Lee, R.; and Weingart, R. C., *Rev. Sci. Instr.*, Vol. 51, 1980, p. 116.
25. Vantine, H. C.; Erickson, L. M.; Janzen, J. A., *J. Appl. Phys.*, Vol. 51, 1980, p. 1957.
26. Erickson, L. M.; Johnson, C. B.; Parker, N. L.; Vantine, H. C.; Weingart, R. C.; and Lee, R. S., *Seventh Symposium (International) on Detonation*, Naval Surface Weapons Center, MP 82-334, 1981, p. 1062.
27. Urtiew, P. A.; Erickson, L. M.; Hayes, B.; and Parker, N. L., *Combustion, Explosion and Shock Waves*, Vol. 22, 1986, p. 597.
28. Urtiew, P. A. and Erickson, L. M., "Techniques and Theory of Stress Measurements in Shock Wave Applications," *Proc. of the Summer ASME Meeting*, 1987, p. 29.
29. Von Holle, W. G., "Shock Waves in Condensed Matter," J. R. Asay, R. A. Graham, and G. K. Straub, eds., North Holland, New York, 1984, p. 283.
30. Von Holle, W. G., LLNL, private communication.
31. Tarver, C. M. and Nichols III, A. L., "The Growth or Decay Rates of Hot Spots in Shocked HMX- and TATB-Based Explosives," manuscript in preparation.
32. Urtiew, P. A., "Effect of Shock Loading on Transparency of Sapphire Crystals," *J. Appl. Phys.*, Vol. 45, 1974, p. 3490.
33. Graham, R. A. and Brooks, W. P., *J. Phys. Chem. Solids*, Vol. 32, 1971, p. 2311.
34. Graham, R. A., *J. Acoust. Soc. Am.*, Vol. 51, 1971, p. 1576.

## DISCUSSION

HAROLD GRYTING  
Gryting Energetics Sciences  
Company  
San Antonio, TX 78245

Compositions containing Estane may not age well unless the Estane used herein has been greatly improved. The manufacturer furnished me a sample probably over 20 years ago which I kept in the desk drawer for observation. This tensile sample became increasingly brittle and crumbly over a several year period. No physical measurements were taken however.

## REPLY BY THE AUTHORS

The authors appreciate this comment.

# INITIATION AND DETONATION PROPERTIES OF THE INSENSITIVE HIGH EXPLOSIVE TATB/Kel-F 800 95/5

C. D. Hutchinson, G. C. W. Foan, H. R. Lawn, and A. G. Jones  
Explosives Technology Branch, Atomic Weapons Establishment  
Aldermaston, Reading, RG7 4PR, Berks., UNITED KINGDOM

*TATB is the best insensitive high explosive available at present, and a common binder for the explosive moulding powder is Kel-F 800. This paper presents results from a number of firings carried out with the U.K. version of this explosive, known as EDC35 -- a TATB/Kel-F 800 95/5 formulation. The initiation and performance data presented include those relating to shock sensitivity, velocity of detonation as a function of both charge diameter and charge density, failure diameter, corner turning, and divergence. These results are published so that it may be possible to compare the U.K. material, EDC35, with similar U.S. formulations, namely PBX 9502 and LX-17.*

## INTRODUCTION

The discovery of the perfect explosive which combines high performance with high safety characteristics eludes synthetic chemists for the present, forcing us to accept a compromise solution -- an explosive based upon HMX when performance is paramount, or an explosive formulated with TATB when cost and performance are second to safety requirements. As discussed by Pruneda and von Holtz,<sup>1</sup> over the years priorities have changed and the demand for explosives offering "highest available energy with adequate safety" has now changed to "the safest explosive with adequate performance."

In the U.K., a considerable amount of work has been carried out to characterize the main TATB-based explosive in current use, known as EDC35 (Explosives Division Composition). This paper presents selected initiation and performance data which are available on this insensitive high explosive.

## EXPLOSIVE MANUFACTURE

TATB is synthesized by nitrating 1,3,5-trichlorobenzene to form 1,3,5-trichloro-2,4,6-trinitrobenzene, which is then dissolved in toluene and aminated with ammonia gas

under pressure. This process produces dry-aminated TATB.<sup>2</sup> If water is also present during the amination stage the product is known as wet-aminated TATB with typically 10 percent water being used. The former type of TATB is used in the U.S. explosive formulation PBX 9502, and the latter in the U.S. formulation LX-17-1.

In the U.K., about 2.5 percent water is used during the amination stage, and the damp-aminated TATB thus produced is known as Type A TATB. For some formulations, particularly the TATB/Kel-F 800 95/5 formulation designated EDC35, the Type A TATB is comminuted in a single pass through a micronizer, or fluid energy mill to form Type B TATB. The particle characteristics of both types of U.K. TATB are shown in Table 1.

EDC35 moulding powder is made using an aqueous solvent paste-mix process. A lacquer of Kel-F 800 in butanone is mixed with damp TATB, and water is sprayed onto the mixture while it is heated to drive off the solvent. Charge fabrication is then carried out either by die-pressing or, more usually, by isostatic pressing in order to achieve homogeneous, high density compacts. The normal specification range of densities for EDC35 charges is 1.897 to 1.912 Mg m<sup>-3</sup> [TMD = 1.942 Mg m<sup>-3</sup>].

**Table 1. Particle Size Characteristics of U.K. TATB**

Type A TATB. Cumulative wt % passing sieve of aperture:	250 $\mu\text{m}$	100%
	90 $\mu\text{m}$	85% minimum
	75 $\mu\text{m}$	75% minimum
	45 $\mu\text{m}$	65% minimum

Median particle diameter  $\sim 40 \mu\text{m}$ .

Specific surface area (by air permeametry)  
 $\sim 2000 \text{ cm}^2 \text{ g}^{-1}$ \*

Type B TATB. Cumulative wt % passing sieve of aperture:	75 $\mu\text{m}$	100%
	50 $\mu\text{m}$	90% minimum
	25 $\mu\text{m}$	60% minimum
	15 $\mu\text{m}$	40% minimum
	10 $\mu\text{m}$	25% minimum

Median particle diameter  $\sim 15 \mu\text{m}$ .

Specific surface area (by air permeametry)  
 $\sim 3000 - 4000 \text{ cm}^2 \text{ g}^{-1}$ \*

\* Not a very meaningful figure for TATB because of the porous nature of the crystals.

## SHOCK SENSITIVITY MEASUREMENTS

The standard AWE Scale I gap test cannot be used with EDC35 because at zero gap thickness the donor system will not initiate the acceptor. A new insensitive high explosive gap test was devised for EDC35. This is shown in Figure 1. The larger brass shim is always placed next to the acceptor charge and acts to prevent gas wash from the donor system from interfering with the response of the acceptor to the applied shock stimulus. Several series of firings were carried out to examine:

- normal density EDC35 from one Lot of moulding powder,
- normal density EDC35 from a second Lot of moulding powder,
- low density EDC35,
- high density EDC35,
- EDC35 which had undergone unconstrained thermal cycling, and
- moulding powder which had been made from wet aminated TATB.

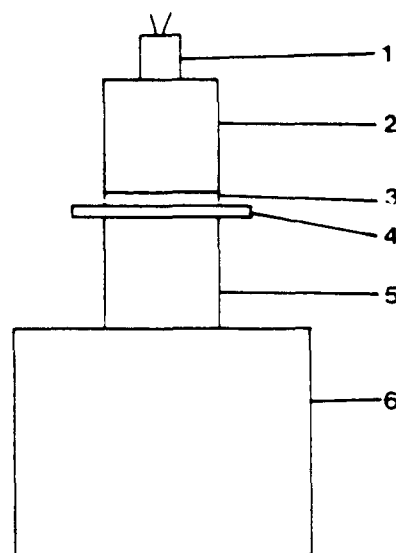


**Figure 1. HHE Gap Test Configuration.**

1. Detonator; 2. 25.4 mm diameter x 25.4 mm long HMX/Binder 95/5 donor charge ( $\rho = 1.77 \text{ Mg m}^{-3}$ ); 3. 25.4 mm x 25.4 mm square laminated brass shim; 4. 38.1 mm x 38.1 mm square laminated brass shim; 5. EDC35 acceptor charge, 25.4 mm diameter x 25.4 mm long; 6. Witness block.

It is known that when EDC35 is thermally cycled above the glass transition point of Kel-F 800,  $28^\circ\text{C}$ , the plastic bonded explosive (PBX) undergoes irreversible growth. The application of moderate pressure (e.g., 500 - 1000 kPa) can prevent this growth from taking place.<sup>3</sup> The experiments in series (e) above were designed to examine the shock sensitivity of EDC35 which had been subjected to 122 sinusoidal 12 hour temperature cycles from  $+25 \pm 1^\circ\text{C}$  to  $+101 \pm 1^\circ\text{C}$  and which resulted in a positive volume change in the samples of 0.74 percent.

The results of the shock sensitivity firings are given in Table 2. These data show that the gap test is sensitive to small changes of density in the acceptor material and, as such, it is a suitable test for EDC35. The increase in shock sensitivity of the thermally cycled samples [test series (e)] was larger than expected, and it took more charges than initially envisaged to achieve a "No Go." Consequently, insufficient charges remained to get an accurate 50 percent shim thickness result for this material. It is interesting to note, that these samples were

Table 2. Results from Shock Sensitivity Testing of EDC35

Explosive	Lot	Density/ Mg m <sup>-3</sup>	50% Shim Thickness/		No. Firings
			thou	[mm]	
(a) EDC35	40	1.905	49.4 ± 1.3	[1.255 ± 0.033]	24
(b) EDC35	66	1.904	51.7 ± 1.3	[1.313 ± 0.033]	24
(c) EDC35	66	1.890	74.2 ± 1.6	[1.885 ± 0.041]	20
(d) EDC35	66	1.915	38.2 ± 1.3	[0.970 ± 0.033]	24
(e) EDC35/TC	45	1.893	~102	~2.6	10
(f) Wet Aminated	1	1.903	55.2 ± 1.9	[1.402 ± 0.048]	10

more shock sensitive than the charges examined in test series (c) which had a lower density. It is possible that thermal cycling results in a charge with a more even distribution of voids compared with one which is initially pressed to a similar (low) density. This even distribution of voids would assist initiation and, hence, may account for the higher shock sensitivity of the thermally cycled samples compared with that from test series (c). From the short series of the experiments performed, it does not appear that the PBX manufactured from wet-aminated TATB differs much in shock sensitivity from normal EDC35. This view is supported by experiments discussed in the Divergence Testing section.

## VELOCITY OF DETONATION AND FAILURE DIAMETER

Velocity of detonation determinations on 280 mm long charges have been performed at different diameters at +20°C and -40°C. These firings were carried out with plane wave initiation systems and using foil ionization probes mounted in single or double pairs close to the centers of the charges at 25 mm, 152 mm, and 280 mm from the base of the plane wave shapers. The results are given in Table 3 and are plotted on a graph of velocity of detonation vs. reciprocal charge radius in Figure 2.

The shape of this plot is similar to that found for PBX 9502<sup>4</sup> and shows a double curve. The curves show a cross over point at 25.4 mm diameter, which contrasts with a figure of ~50 mm for PBX 9502.<sup>4</sup> This feature is attributed by Campbell to competition between the

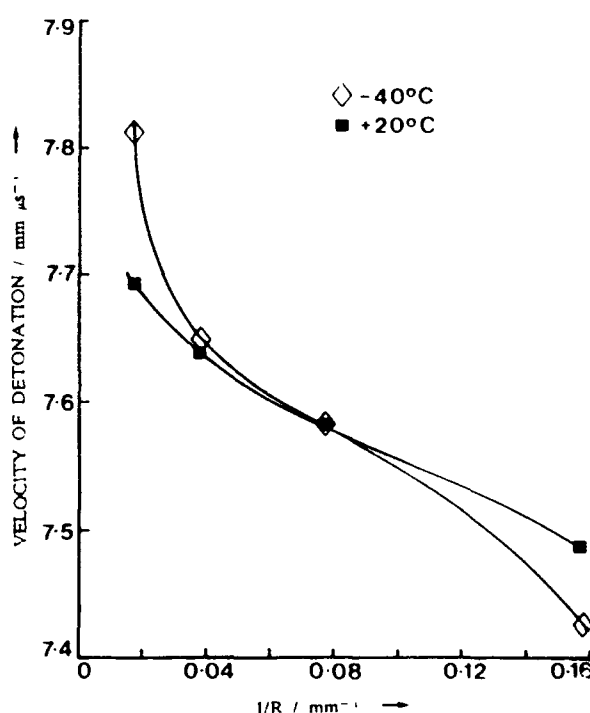


Figure 2. Velocity of Detonation Vs. Reciprocal Charge Radius Curves for EDC35 Fired at +20°C and -40°C

effect of temperature on density which dominates at large diameters, and the effect of temperature on reaction rates which dominates at small diameters. More sensitive high explosives, such as plastic-bonded HMX and RDX/TNT 60/40, show a single curve velocity of detonation vs. reciprocal charge radius plot and allow for extrapolation to infinite charge radius to obtain a value for  $D_{\infty}$ . Since the EDC35 plot is concave upwards at large charge radii, it is not possible to obtain an accurate value for  $D_{\infty}$ .

**Table 3. Results of Velocity of Detonation Firings**

Charge density =  $1.90 \text{ Mg m}^{-3}$ .

Temperature/ °C	Diameter/ mm	Velocity/ $\text{mm } \mu\text{s}^{-1}$
20	12.7	7.485
20	25.4	7.586
20	50.8	7.639
20	127.0	7.690
-40	12.7	7.423
-40	25.4	7.586
-40	50.8	7.648
-40	127.0	7.813

All data have a standard deviation of  $\sim 0.005 \text{ mm } \mu\text{s}^{-1}$ .

Approximate "by eye" straight line fits of the curves in Figure 2 produce values for  $D_x$  and the gradient of  $7.7 \text{ mm } \mu\text{s}^{-1}$  and  $-1.388 \text{ mm}^2 \mu\text{s}^{-1}$  at  $20^\circ\text{C}$  and  $7.8 \text{ mm } \mu\text{s}^{-1}$  and  $-2.439 \text{ mm}^2 \mu\text{s}^{-1}$  at  $-40^\circ\text{C}$ , respectively. Using the analysis of Campbell and Engelke<sup>5</sup> in which the Eyring et al,<sup>6</sup> and Wood and Kirkwood<sup>7</sup> studies on curved detonation fronts are combined with their own data on the radius of curvature of the detonation front as a function of charge radius for X 0219 (TATB/Kel F 800 90/10), values for the infinite-medium reaction zone thicknesses for EDC35 at  $+20^\circ\text{C}$  and  $-40^\circ\text{C}$  have been calculated as  $0.89 \text{ mm}$  and  $1.55 \text{ mm}$  respectively (assuming Campbell and Engelke's values of  $B$  and  $\alpha$  apply to EDC35). These values compare favorably with those quoted in Reference 5 as being good results and with more recent estimates, e.g., pure TATB (density =  $1.89 \text{ Mg m}^{-3}$ )  $>100 \text{ ns}$ <sup>8</sup> and LX-17  $1.3 \text{ mm}$ <sup>9</sup> and  $\sim 250 \text{ ns}$ .<sup>10</sup>

Additional experiments, using relatively short charges, have been carried out to determine the velocity of detonation in  $25.4 \text{ mm}$  diameter EDC35 charges pressed to different densities. The experimental arrangement is shown in Figure 3. The last quarter of each streak record was digitized and analyzed to produce the results presented in Table 4 and shown graphically in Figure 4. Because short

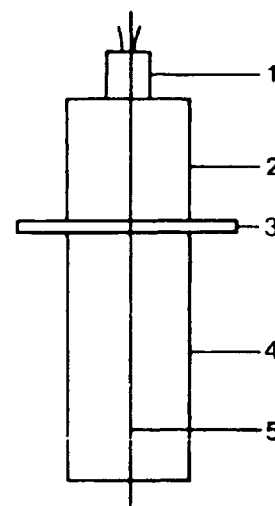


**Figure 3. Experimental Arrangement for Determining Velocity of Detonation as a Function of Charge Density.** 1. Detonator; 2.  $25.4 \text{ mm}$  diameter x  $25.4 \text{ mm}$  long HMX/Binder 97.5/2.5 donor charge ( $\rho = 1.81 \text{ Mg m}^{-3}$ ); 3. Magnesium shim; 4.  $25.4 \text{ mm}$  diameter x  $50.8 \text{ mm}$  long EDC35 charge; 5. Streak camera slit.

**Table 4. Velocity of Detonation Data as a Function of Density for  $25.4 \text{ mm}$  Diameter EDC35 Charges**

Density/ $\text{Mg m}^{-3}$	Velocity of Detonation/ $\text{mm } \mu\text{s}^{-1}$
1.873	7.67
1.910	7.74
1.923	7.91
1.926	7.95
1.930	7.83
1.932	7.77

All data have a standard deviation of  $\sim 0.01 \text{ mm } \mu\text{s}^{-1}$ .

charges were used, thin magnesium shim were placed between the powerful initiation system and the EDC35 to prevent excessive overdrive. Although it is acknowledged that the experimental arrangement is not ideal for accurate velocity of detonation studies, the results obtained show that for EDC35 the velocity of detonation at ambient temperatures reaches a

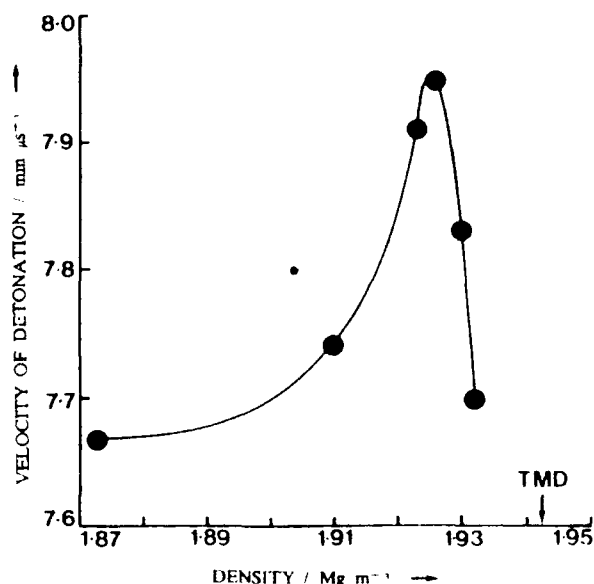


Figure 4. Graphical Representation of Velocity of Detonation as a Function of Charge Density for EDC35

maximum and then decreases as the density increases beyond  $\sim 1.926 \text{ Mg m}^{-3}$ ; a feature of Price's "Group 2" explosives<sup>11</sup> which has also been observed in hot-pressed TNT.<sup>12</sup> An apparent decrease in detonation velocity in PBX 9502 pressed to high density has also been found for charges made from micronized TATB which had 96 percent of particles smaller than  $20 \mu\text{m}$  in diameter; this is slightly finer than U.K. Type B TATB.<sup>13</sup> It would seem that there is a certain minimum percentage of voidage necessary in order that TATB can sustain a detonation wave above its normal critical diameter, and these experiments indicate that, for the diameter of charges examined, minimum percentage of voidage is rapidly being approached.

Two simple experiments were performed to determine the approximate failure diameter of EDC35 at ambient temperature pressed to a density of  $1.90 \text{ Mg m}^{-3}$ . Cylindrical charges with diameters ranging from 12.7 mm down to 2.54 mm, each 25.4 mm long, were stacked concentrically, and the largest diameter charge initiated with a 12.7 mm diameter HMX/Binder 95/5 booster charge. One test was performed in air and the other in water. The framing camera records of both experiments showed the detonation wave dying out in the 7.62 mm diameter test pieces. The failure diameter of EDC35 under these conditions is

taken to be about 8 mm and is consistent with data presented on PBX 9502 in Reference 4. Experiments to determine a more accurate value for EDC35 are in hand.

## CORNER TURNING

Simple corner turning experiments, using the arrangement shown in Figure 5, have been carried out on EDC35 charges. All charges had a density of  $1.906 \text{ Mg m}^{-3}$ , but those designated EDC35(DP) were die-pressed and isostatically repressed. Three donor charges were used, namely tetryl (density  $1.50 \text{ Mg m}^{-3}$ ), RDX/FPC461 94/6 (density  $1.66 \text{ Mg m}^{-3}$ ), and HMX/Polyurethane 95/5 (density  $1.77 \text{ Mg m}^{-3}$ ). All experiments were carried out at ambient temperature and the breakout patterns recorded on an Imacon 790 camera streaking at  $10 \text{ mm } \mu\text{s}^{-1}$ . The distance away from the donor/acceptor interface at which detonation broke out on the surface of the cylindrical acceptor charge, known as the breakout distance, was recorded by direct viewing with the streak camera, whereas the profile of the detonation front emerging from the base of the acceptor charge was recorded via a front-aluminized mirror placed at  $45^\circ$  beneath the acceptor explosive. The results are presented in Table 5.

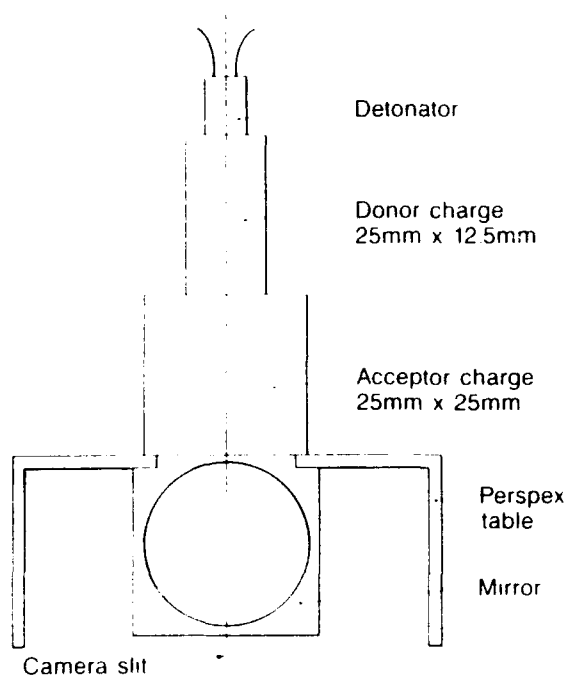


Figure 5. Experimental Arrangement for Corner Turning Firings



Table 5. Results from Corner Turning Experiments

Donor Explosive	Acceptor Explosive			
	EDC35		EDC35(DP)	
Tetryl	18.0		>25.4	
	19.4	18.5	>25.4	
RDX/FPC461 94/6	17.7		21.8	
	19.7	18.7	21.6	21.7
HMX/PU 95/5	20.0		21.2	
	20.8	20.4	23.3	22.2

Breakout distances in mm, accurate to  $\pm 1$  mm.

Donor Explosive	Acceptor Explosive			
	EDC35		EDC35(DP)	
	100 ns	200 ns	100 ns	200 ns
Tetryl	13.4	18.4	11.5	15.0
RDX/FPC461 94/6	14.2	18.9	13.3	18.0
	15.7	19.2	13.2	18.0
HMX/PU 95/5	13.9	18.9	12.9	17.4
	13.6	18.5	13.2	17.3

Base spread in mm after 100 ns and 200 ns from central breakout, accurate to  $\pm 0.5$  mm.

It is clear from the results that, within experimental error, the breakout distances for EDC35 and EDC35(DP) initiated by RDX/FPC and HMX/Polyurethane, together with EDC35 initiated by tetryl, are similar but significantly shorter than that for EDC35(DP) initiated by tetryl. This observation is confirmed by the base breakout profile measurements which again show a similarity for the first group, whereas the spreading distances for the EDC35(DP) charge initiated by tetryl are somewhat smaller at the same time of emergence.

Simplistically, we can say it is possible to distinguish the differing responses between isostatically pressed and machined EDC35 charges and die-pressed and isostatically repressed EDC35(DP) at the same density. On the basis of the experimental evidence presented here for mild initiating systems,

EDC35(DP) does not diverge as well as does EDC35. However, within the accuracy of the measurements we are not able to make any distinction when more powerful initiating systems are used. Although the difference highlighted here is not a serious problem and is probably caused by a combination of density gradients in the EDC35(DP) charges, skin effects in which binder material concentrates next to the drift during pressing and by the slight alignment of the plate-like TATB crystallites such that their {100} crystal faces lie to some extent preferentially perpendicular to the axis of maximum stress during compaction (but not to the extent that distinct lamellar texture is produced), it is one which should be realized and account taken of, especially if shock sensitivity testing is carried out on die-pressed samples.

With the experimental arrangement shown in Figure 5, it was not possible to measure detonation transit times through the acceptor charges. However, it was possible to judge whether large delays (e.g., hundreds of ns) occurred in the donor charge inducing detonation in the acceptor explosive from measurements on the streak record of the time between the detonation front on the surface of the donor charge reaching the end of this charge and the first appearance of light at the center of the base of the acceptor charge. True transit times could not be measured, because the time when the detonation front in the center of the donor charge reached the donor/acceptor interface was not recorded. Although this could have been measured with the aid of probes, none were inserted for fear of interfering with the flow. The times measured were, therefore, all shorter than the true transit times.

Comparing these times with the transit times calculated from the velocity of detonation of the acceptor explosive indicated that:

- there were no lost times greater than  $\sim 90$  ns recorded from charges initiated by either RDX/FPC461 or HMX/Polyurethane,
- the lost times from the tetryl donors were greater than those from the

RDX/FPC461 and HMX/Polyurethane donors by some 50-100 ns, and

- (c) with all donors there were no significant differences between the lost times when initiating either EDC35 or EDC35(DP).

[NB - the 'transit times' upon which these conclusions are based are not given here in case they be taken as real transit time measurements.]

## DIVERGENCE TESTING

Spherical divergence of detonation in EDC35 was monitored in a series of tests referred to as half peach experiments. These are identical in concept to the onion skin experiments described by other workers, and the hollow hemispherical explosive charge geometry used in these current tests has been previously reported by Hutchinson.<sup>14</sup> Figure 6 illustrates the experimental arrangement. HMX/Polyurethane 95/5 boosters with a density of  $1.787 \text{ Mg m}^{-3}$  were used, and had radii which varied from 10-15 mm. These were machined to accept exploding bridgewire detonators which would effectively produce point source initiation at the central point (origin) of the hemispherical charge. The detonators and booster charges were potted into their respective acceptor explosives with a low viscosity, slow curing silicone rubber, Sylgard 184, such that there was nominally zero potting material thickness between the detonator and booster, and a controlled thickness of potting from 0 to 0.1 mm thick at the pole of the booster/acceptor interface. A central section of the surface of each acceptor charge was spray coated with aluminum silicofluoride

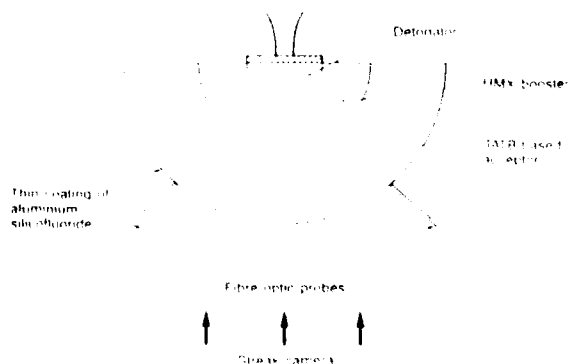


Figure 6. Half Peach Experimental Geometry

and two fiber optic probes, separated through the pole by  $90^\circ$ , were attached at the  $45^\circ$  position in the outer surface of each charge. These probes, in conjunction with the detonator current monitor traces, were used to determine the reaction transit times ( $I_{\text{burst}} - \text{End Event}$ ) through the half peach assemblies. These readings are considered to be accurate to  $\pm 20 \text{ ns}$ . The charges, which were fired both at ambient temperatures and at  $-40^\circ\text{C}$ , were monitored with an Imacon 790 camera operating in the streak mode at  $20 \text{ mm } \mu\text{s}^{-1}$ , aligned such that the optic axis of the camera coincided with the poles of the half peach assemblies, thereby affording a direct view of the reaction breakout. Digitization of the half peach records allowed the angular divergence of detonation on either side of the pole of the charge 50 ns after breakout of detonation at the pole to be measured, together with a time for the detonation front to spread to  $\pm 90^\circ$ .

Several series of experiments have been carried out using this geometry to examine different aspects of EDC35. These, which are similar to those discussed in Section 3, are:

- (a) Effect of charge density:  
ambient and  $-40^\circ\text{C}$  firings with 10 mm radius HMX/Polyurethane boosters. Densities of EDC35  $1.899$ ,  $1.904$ , and  $1.911 \text{ Mg m}^{-3}$ .
- (b) Effect of intercharge variability:  
15 mm radii HMX/Polyurethane boosters, Lot 40 EDC35 density  $1.904 \text{ Mg m}^{-3}$ , Lot 44 EDC35 density  $1.908 \text{ Mg m}^{-3}$ .
- (c) Effect of intra-charge variability:  
10 mm radii HMX/Polyurethane boosters, Lot 44 EDC35 density  $1.908 \text{ Mg m}^{-3}$ .
- (d) Effect of unconfined thermal cycling resulting in EDC35 which had undergone a volume increase of 0.85 percent ( $\rho = 1.891 \text{ Mg m}^{-3}$ ) fired at  $-40^\circ\text{C}$  with 10 mm radii HMX/Polyurethane boosters.
- (e) Effect of using wet-aminated TATB.  
10 mm radii HMX/Polyurethane boosters fired at  $-45^\circ\text{C}$ . Density of TATB-based charges  $1.903 \text{ Mg m}^{-3}$ .

The results of the eight firings at -40°C in series (c) above were taken as the base-line against which the results from the other firings were compared. These charges were assembled with 0.1 mm Sylgard 184 polar potting thicknesses between the 10 mm radii HMX/Polyurethane boosters and the EDC35 acceptor charges. These are the worst conditions considered which are known to permit acceptable initiation and divergence in EDC35. The results are presented in Table 6.

In the series (a) and (b), detonation wave divergence angles and  $I_{burst}$  - End Event times were good. The 50 ns spreading angles all exceeded  $\pm 50^\circ$ , and the detonation front spread to  $\pm 90^\circ$  in all firings. For a given set of conditions, i.e., booster size, temperature, and polar gap thickness between booster and acceptor, divergence and transit times showed little variability. Variability in charge density (within the range examined) does not significantly affect the initiation and divergence properties of EDC35.

Table 6 Results from Half Peach Divergence Firings

Effect of Charge Density: Half peach firings series (a)  
Booster radius 10 mm

Density/ Mg m <sup>-3</sup>	Booster-Acceptor Polar Gap / mm	50 ns Spread Angle / °	$I_{burst}$ - End Event / $\mu$ s	Time to Diverge to $\pm 90^\circ$ / ns
Ambient temperature firings				
1.899	0.040	79	4.63	140
1.899	0.050	72	4.67	160
1.904	0.025	76	4.63	210
1.904	0.050	72	4.65	160
1.911	0.090	79	4.71	190
-40°C firings				
1.904	0	62	4.80	560
1.904	0	72	4.84	400
1.911	0	64	4.76	470
1.911	0.075	62	4.81	670

Effect of Intercharge Variability: Half peach firings series (b)  
Booster radius 15 mm

Density/ Mg m <sup>-3</sup>	Booster-Acceptor Polar Gap / mm	50 ns Spread Angle / °	$I_{burst}$ - End Event / $\mu$ s	Time to Diverge to $\pm 90^\circ$ / ns
Ambient temperature firings				
Lot 40				
1.904	0	64 - 85	4.52 - 4.60	125 - 200 (4)
Lot 44				
1.908	0	70	4.55	100
-40°C firings				
Lot 40				
1.904	0 - 0.050	62 - 83	4.68 - 4.69	125 - 250 (3)
Lot 44				
1.908	0	55 - 76	4.62 - 4.72	150 - 225 (5)

Where a range of results is given, this refers to multiple firings, the number of which appears in brackets at the end of the line

Table 6. (Cont.)

Effect of Intra-Charge Variability: Half peach firings series (c)  
Booster radius 10 mm

Density/ Mg m <sup>3</sup>	Booster-Acceptor Polar Gap / mm	50 ns Spread Angle / °	I <sub>burst</sub> - End Event / μs	Time to Diverge to ± 90° / ns
Ambient temperature firings				
1.908	0.100	61	1.78	280
40°C firings				
1.908	0.100	52 - 61	4.80 - 4.87	580 - 720 (8)

Where a range of results is given, this refers to multiple firings, the number of which appears in brackets at the end of the line.

Effect of Unconfined Thermal Cycling: Half peach firings series (d)  
Booster radius 10 mm

Density/ Mg m <sup>3</sup>	Booster-Acceptor Polar Gap / mm	50 ns Spread Angle / °	I <sub>burst</sub> - End Event / μs	Time to Diverge to ± 90° / ns
40°C firings				
1.891	0.100	58 - 59	4.76 - 4.85	200 - 300 (2)

Where a range of results is given, this refers to multiple firings, the number of which appears in brackets at the end of the line.

Effect of Using Wet-Aminated TATB: Half peach firings series (e)  
Booster radius 10 mm

Density/ Mg m <sup>3</sup>	Booster-Acceptor Polar Gap / mm	50 ns Spread Angle / °	I <sub>burst</sub> - End Event / μs	Time to Diverge to ± 90° / ns
45°C firings				
1.903	0.060 - 0.110	52 - 63	4.73 - 4.95	500 - 625 (5)

Where a range of results is given, this refers to multiple firings, the number of which appears in brackets at the end of the line.

The divergence and I<sub>burst</sub> - End Event data from the firings in series (d) and (e) compare very favorably with the control set. The divergence angles after 50 ns breakout for both materials are generally equal or better than those produced from the control EDC35. A difference is readily apparent in the time to diverge to ± 90°, whereas the wet aminated material behaved like EDC35, the thermally cycled IHE showed a substantial reduction in divergence times. This improvement in

performance is probably linked with the lower density of these charges, but it is interesting to note that the divergence angles after 50 ns from breakout are not increased over those recorded from EDC35. A lower density is linked with an increase in shock sensitivity (see "Shock Sensitivity Measurements") which too will be linked to the divergence performance of the material, especially at high angles from the poles in half peach assemblies.

## CONCLUSIONS

At present, TATB is our best insensitive high explosive. There are a number of binder systems which are in use to allow it to be pressed into high density compacts. This paper has presented the results of firings carried out with the U.K. version of the Kel-F 800 bound TATB-based explosive, EDC35, in a number of selected experimental configurations. It has been known for some time that the U.K. composition differs in subtle ways from equivalent U.S. materials; it is hoped that the information supplied here will be of assistance to those who wish to carry out comparisons in greater depth. In being so insensitive, TATB brings with it problems not encountered in other high explosives but, with the continued study of the detonics of charges made under controlled conditions, we are gradually coming to understand it better. Our work continues.

## ACKNOWLEDGEMENTS

The authors would like to thank Mrs. I. M. Hutchinson and Mr. I. M. Findlay for performing some of the experiments reported here.

## REFERENCES

1. Pruneda, C. O. and von Holtz, E. H., "Formulating High Explosive Materials," *Energy and Technology Review*, Jan-Feb 1988, p. 23.
2. Honodel, C. A., et al., "Shock Initiation of TATB Formulations," *Seventh Symposium (International) on Detonation*, Annapolis, MD, 1981, p. 425.
3. Rizzo, H. F.; Humphrey, J. R.; and Kolb, J. R., "Growth of TATB II: Control of Growth by the Use of High  $T_g$  Polymeric Binders," *Propellants and Explosives*, Vol. 6, 1981, p. 57.
4. Campbell, A. W., "Diameter Effect and Failure Diameter of a TATB-Based Explosive," *Propellants, Explosives, Pyrotechnics*, Vol. 9, 1984, p. 183.
5. Campbell, A. W. and Engelke, R., "The Diameter Effect in High Density Heterogeneous Explosives," *Sixth Symposium (International) on Detonation*, Coronado, 1976, p. 642.
6. Eyring, H., et al., "The Stability of Detonation," *Chem. Rev.*, Vol. 45, 1949, p. 69.
7. Wood, W. W. and Kirkwood, J. G., "Diameter Effect in Condensed Explosives," *J. Chem. Phys.*, Vol. 22, No. 11, 1954, p. 1920.
8. Hayes, B. and Tarver, C. M., "Interpolation of Detonation Parameters from Experimental Particle Velocity Records," *Seventh Symposium (International) on Detonation*, Annapolis, 1981, p. 1029.
9. Bahl, K. L.; Lee, R. S.; and Weingart, R. C., "Velocity of Spherically-Diverging Detonation Waves in RX-26-AF, LX-17 and LX-10," *Shock Waves in Condensed Matter*, Santa Fe, 1983, p. 559.
10. Bahl, K., et al., "Initiation Studies on LX-17 Explosive," *Eighth Symposium (International) on Detonation*, Albuquerque, 1985, p. 1045.
11. Price, D., "Contrasting Patterns in the Behaviour of High Explosives," *Eleventh Symposium (International) on Combustion*, 1967, p. 693.
12. Price, D., "Shock Sensitivity, a Property of Many Aspects," *Fifth Symposium (International) on Detonation*, Pasadena, 1970, p. 207.
13. Akst, I. B.; Campbell, A. W.; and Ramsay, J. B., Unpublished Data, Los Alamos National Laboratory.
14. Hutchinson, C. D., "The Initiation of TATB-Based Insensitive High Explosives in Diverging Geometry," *Nineteenth International Conference (ICT)*, Karlsruhe, 1988, p. V38-1.
15. Controller HMSO, London, 1989.

# FABRY PEROT VELOCIMETRY ON DETONATING LX-17 IN PLANAR AND SPHERICALLY DIVERGENT GEOMETRIES\*

K. L. Bahl, R. D. Breithaupt,  
C. M. Tarver, and W. G. Von Holle  
Lawrence Livermore National Laboratory  
Livermore, California 94550

Fabry Perot velocimetry and hydrodynamic calculations are used to quantitatively determine the strengths of planar and spherically divergent detonation waves in LX-17 as functions of initial temperature, booster explosive and propagation direction. Cold LX-17 is shown to initiate more slowly than ambient temperature LX-17 but to eventually attain an equivalent detonation wave structure. LX-10 (HMX) boosters provide a greater initial momentum than do ultrafine TATB boosters, but the resulting LX-17 detonation waves are equivalent within 20 mm of propagation. No direction dependence is observed between 0° and 60° from the pole. Comparison of these experimental velocity histories to CJ and ignition and growth ZND reactive flow calculations demonstrate that well-defined LX-17 reaction zones with pressures well above Chapman-Jouguet (CJ) values are developed within one reaction zone length of propagation. After 20 to 30 mm of propagation, the LX-17 detonation waves approach steady state and the experimental records agree closely with the reactive flow calculations, whereas CJ calculations are 4-5 percent low in velocity.

## INTRODUCTION

The insensitivity of triaminotrinitrobenzene (TATB)-based explosives requires that large booster charges be used to shock initiate spherically diverging detonation waves in high density charges of LX-17 (92.5 percent TATB and 7.5 percent Kel F). Several such boosters have been developed and tested extensively at -54°C and ambient temperature (20°C).<sup>1-4</sup> Previous experiments have employed rotating-mirror streak cameras to record the breakouts of the detonation waves on the surfaces of LX-17 acceptor charges and layers of aluminum silicofluoride [Al<sub>2</sub>(SiF<sub>6</sub>)<sub>3</sub>]

which flashes brightly when struck by a well-developed LX-17 wave. In this study the shock initiation and detonation wave development is examined more quantitatively using a laser Fabry-Perot velocimeter system to measure the free surface velocity histories of 25 µm thick copper foils driven by various radii hemispherical charges of LX-17 initiated by either LX-10 (HMX) boosters or ultrafine TATB boosters. This Fabry-Perot system has been extensively used to study detonating solid explosives in planar geometries<sup>5</sup> and in cylinder test expansions.<sup>6</sup> The effects of booster type, initial temperature, angle along the hemisphere, and LX-17 acceptor thickness are discussed in this paper.

To assess the relative strength of the spherically diverging LX-17 detonation waves, the ignition and growth reactive flow hydrodynamic computer code model for LX-

\* Work performed under the auspices of the U.S. Department of Energy by the Lawrence Livermore National Laboratory under contract number W-7405-Eng-48.

17,<sup>7</sup> which has been normalized to a great deal of planar detonation wave Fabry-Perot data,<sup>8</sup> is compared to the various Fabry-Perot records of these spherically divergent reactive flows. Calculations assuming ideal Chapman-Jouguet (CJ) detonations are included for comparison.

## EXPERIMENTAL RESULTS

Figure 1 shows the two types of booster systems used in this study. The smaller LX-10 booster has an outer radius of 15.9 mm and is initiated by a 6.65 mm radius EBW detonator. The larger, ultrafine TATB (pressed to 1.80 g/cm<sup>3</sup>) booster has an outer radius of 25.4 mm and is initiated by a slapper type detonator. Hemispherical LX-17 acceptors of 2, 5, 10, 20, and 30 mm thickness are attached to the boosters and fired at -54°C or 20°C. Twenty-five  $\mu$ m thick copper disks are placed at the pole (0°) or at angles of 50 to 60 degrees from the pole, as shown in Figure 1. The Fabry-Perot laser is focused on the rear surface of the copper foil and its velocity history is recorded for several tenths of a microsecond. Figure 2 shows a comparison of the output of the two boosters measured by placing the copper foil directly on the booster explosive surface. Although the LX-10 booster has a smaller radius than the

ultrafine TATB booster, the higher Chapman-Jouguet (CJ) detonation pressure of LX-10 (approximately 37 GPa versus approximately 26.5 GPa for ultrafine TATB) causes the copper foil to be driven faster. Figure 3 shows the effect of spherical versus planar geometry. A planar LX-17 charge drives the copper foil

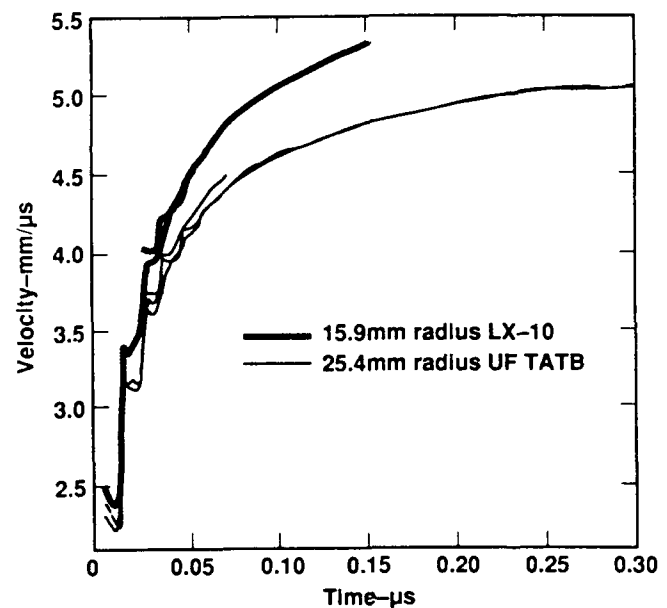


Figure 2. Comparison of Copper Foil Velocities Driven by Only the Boosters

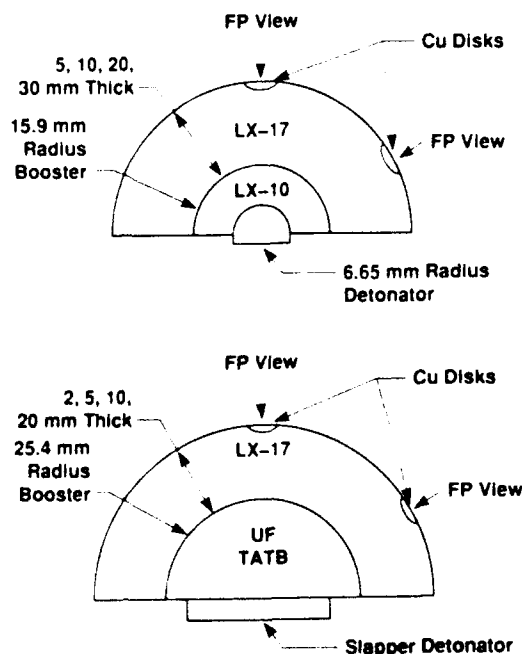


Figure 1. Experimental Geometries

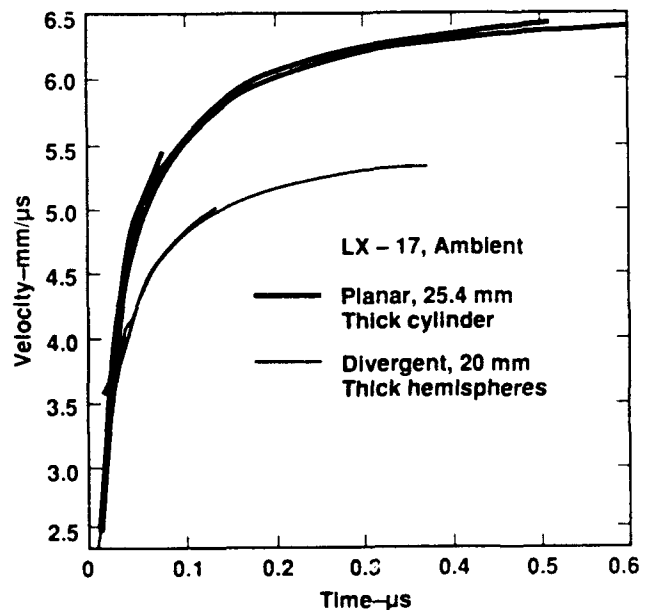


Figure 3. Copper Foil Velocities for Planar Versus Spherically Divergent Detonation

approximately 20 percent faster than a spherical LX-17 charge due to the momentum dissipated in spherical divergence of the wave front.

The first important comparison from this study is the copper foil acceleration as a function of angle. Figure 4 shows a typical angle comparison for 30 mm thick ambient temperature LX-17 hemispheres initiated by LX-10 boosters with copper foils at the pole ( $0^\circ$ ) and at an angle of  $50^\circ$ . For this and several other LX-17 thicknesses at ambient and cold temperatures, no angle dependence on the final copper foil velocity was observed up to  $60^\circ$ . It is well known<sup>1</sup> that there are regions of "weak" or no reaction in TATB-based explosives, especially at cold temperatures and with near critical size boosters. However, the spherical waves initiated by the boosters shown in Figure 1 were uniform over at least the  $0^\circ$  to  $60^\circ$  range.

Another important comparison is the relative buildup of ambient and cold LX-17. Figure 5 compares the copper foil velocities from 5 mm thick ambient and cold LX-17 hemispheres driven by LX-10 boosters. As expected, the ambient LX-17 reacts faster and delivers more momentum close to the booster.

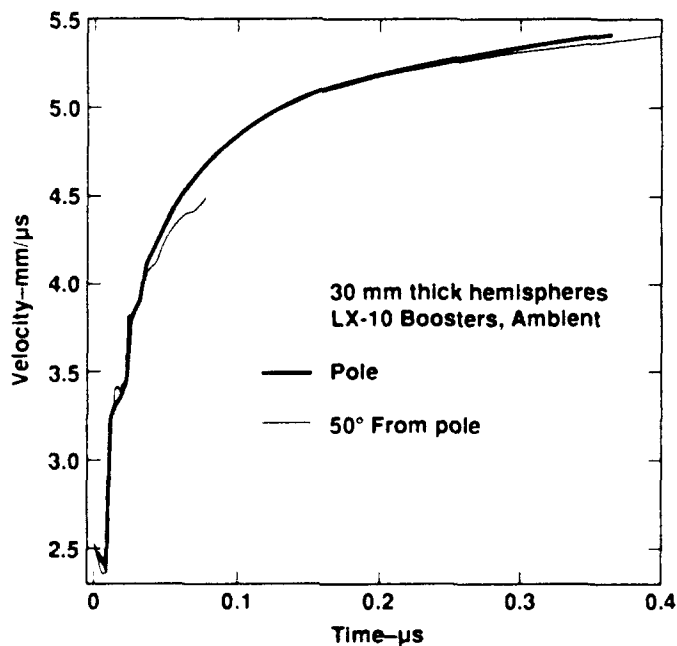


Figure 4. Angle Comparison in LX-17 Divergent Detonations

However, eventually the cold LX-17 detonation wave develops as fully as the ambient LX-17 wave, as shown in Figure 6, which demonstrates nearly identical waves from ambient and cold LX-17 after 30 mm of detonation propagation.

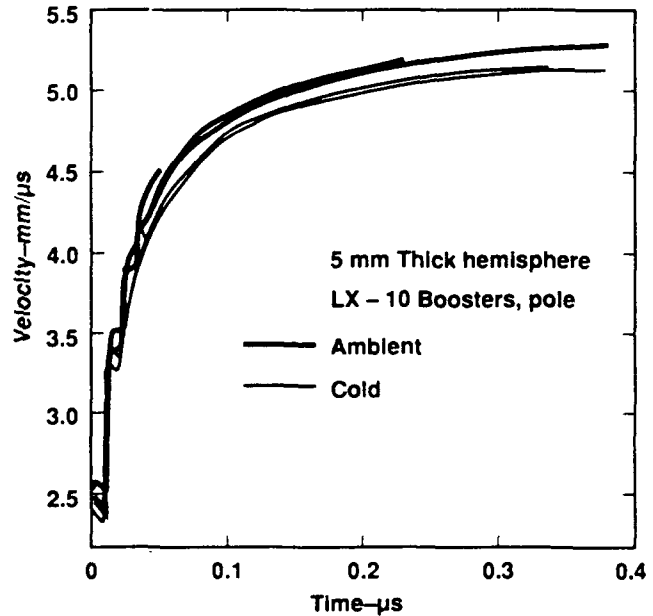


Figure 5. Ambient Versus Cold LX-17 Divergent Detonations

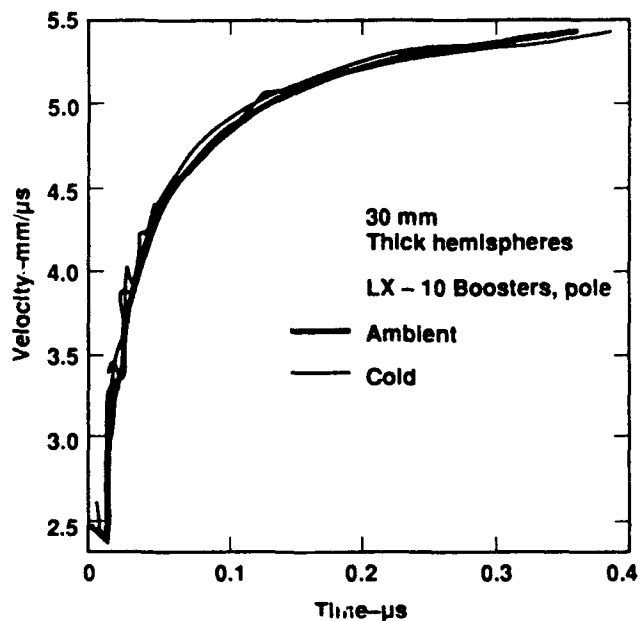


Figure 6. Ambient Versus Cold LX-17 Divergent Detonations at Large Radii



A final general comparison is the effect of the different booster output shown in Figure 2 on spherical LX 17 waves that have propagated several centimeters from the booster. Figure 7 shows that the detonation waves at 35 mm radius in ambient LX-17 hemispheres from LX 10 and ultrafine TATB boosters are essentially identical, as are those for 45 mm radius cold LX-17 hemispheres in Figure 8. Therefore, these LX-17 detonation waves, although initiated by different pressure histories, seem to approach CJ detonations after propagating 3-4 cm.

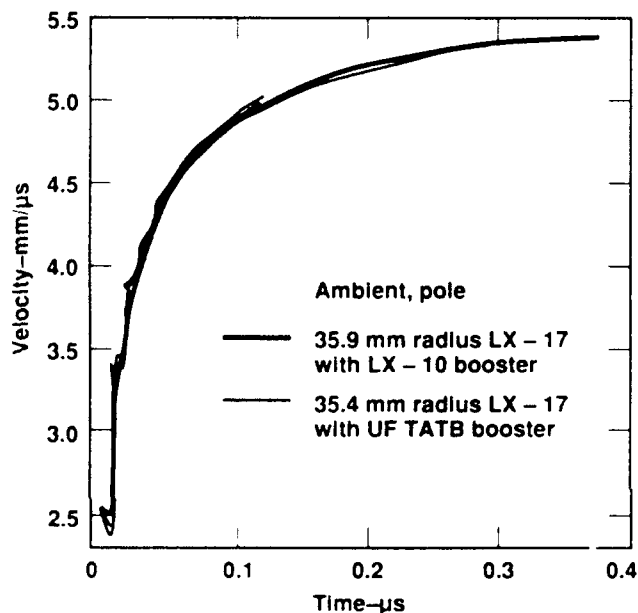


Figure 7. Comparison of Ambient LX-17 Initiation by Different Boosters

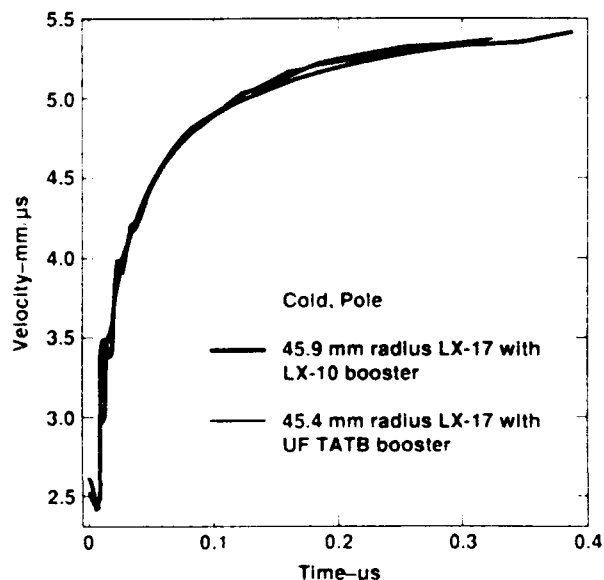


Figure 8. Comparison of Cold LX-17 Initiation by Different Boosters

## REACTIVE FLOW MODELING

To quantitatively determine how closely these spherically divergent LX-17 detonation waves approach steady state propagation, the Fabry-Perot experimental records are compared to hydrodynamic computer code simulations of the experiments. Two types of finely zoned (50 to 100 zones per millimeter) calculations are shown: CJ calculations in which the booster and LX-17 are assumed to detonate ideally at CJ velocity and pressures and their products then expand according to the Jones-Wilkins-Lee (JWL) equations of state, and Zeldovich-Von Neumann-Doring (ZND) reactive flow calculations in which the shock initiation and developing detonation reaction zone structures are modeled. The initial densities, CJ detonation velocities, CJ pressures and JWL reaction product equations of state of LX-10, ultrafine TATB and LX-17 required for CJ calculations are listed in Table 1. Also listed in Table 1 are the unreacted JWL equations of state and ignition and growth reaction rate parameters for detonating LX-10, ultrafine TATB and LX-17 determined in previous studies<sup>7-9</sup> using planar geometries. The ignition and growth model uses JWL equations of state for both the unreacted explosive and its reaction products of the form

$$p = Ae^{-R_1 V} + Be^{-R_2 V} + \frac{\omega C_v T}{V} \quad (1)$$

where  $p$  is pressure;  $V$  is relative volume;  $T$  is temperature; and  $A$ ,  $B$ ,  $R_1$ ,  $R_2$ ,  $\omega$  (the Grüneisen coefficient), and  $C_v$  (the average heat capacity) are constants. The ignition and growth reaction rate law is of form:

$$\begin{aligned} \frac{dF}{dt} = & I(1-F)^b (p/p_0 - 1 - a)^x \\ & + G_1(1-F)^c F^d p^y + G_2(1-F)^e F^g p^z \end{aligned} \quad (2)$$

where  $F$  is the fraction reacted;  $t$  is time;  $p_0$  is initial density;  $\rho$  is current density;  $p$  is pressure in Mbars; and  $I$ ,  $G_1$ ,  $G_2$ ,  $b$ ,  $x$ ,  $a$ ,  $c$ ,  $d$ ,  $y$ ,  $e$ ,  $g$ , and  $z$  are constants. The first term in Equation (2) controls the initial rate of reaction ignited during shock compression and

Table 1. Parameters for CJ and Ignition and Growth Calculations

Explosive	LX-10	Ultrafine TATB	LX-17
Unreacted Equations of State			
$\rho_o$ (g/cm <sup>3</sup> )	1.865	1.80	1.903
A (Mbars)	9522.0	1472.0	778.1
B (Mbars)	-0.05944	-0.04053	-0.05031
$R_1$	14.1	12.3	11.3
$R_2$	1.41	1.23	1.13
w	0.8867	0.5718	0.8938
$C_v$ (Mbars/K)	$2.7813 \times 10^{-5}$	$3.0202 \times 10^{-5}$	$2.48709 \times 10^{-5}$
$T_o$ (K)	298	298	298
Reaction Product Equations of State			
D (mm/ $\mu$ s)	8.82	7.472	7.596
$P_{CJ}$ (Mbars)	0.375	0.265	0.275
A (Mbars)	8.807	4.9775	6.5467
B (Mbars)	0.1836	0.05407	0.071236
$R_1$	4.62	4.2	4.45
$R_2$	1.32	1.2	1.2
$\omega$	0.38	0.40	0.35
$C_v$ (Mbars/K)	$1 \times 10^{-5}$	$1 \times 10^{-5}$	$1 \times 10^{-5}$
$E_o$ (Mbar-cm <sup>3</sup> /cm <sup>3</sup> g)	0.104	0.069	0.069
Reaction Rate Parameters			
I ( $\mu$ s <sup>-1</sup> )	$7.43 \times 10^{11}$	$4.0 \times 10^6$	$4.0 \times 10^6$
b	0.667	0.667	0.667
a	0.0	0.22	0.22
x	20.0	7.0	7.0
$G_1$ (Mbars <sup>-y</sup> $\mu$ s <sup>-1</sup> )	3.1	48.0	48.0
c	0.667	0.111	0.111
d	0.111	0.111	0.111
y	1.0	1.0	1.0
$G_2$ (Mbars <sup>-z</sup> $\mu$ s <sup>-1</sup> )	400.0	500.0	500.0
e	0.333	1.0	1.0
g	1.0	1.0	1.0
z	2.0	3.0	3.0
Figmax	0.3	0.0232	0.0232
$F_{GIMAX}$	0.5	0.85	0.85

is limited to fraction reacted  $F \leq \text{Figmax}$ . For detonation modeling, the second term in Equation (2) represents a relatively fast reaction following ignition up to its limiting value  $F \leq F_{GIMAX}$ . The third term is then used to simulate the slow (carbon coagulation) reaction.

Since the ignition and growth reactive flow model consists of a shock wave followed by

chemical reaction, the LX-17 model is initiated using an ignition and growth model for LX-10 or ultrafine TATB, rather than an idealized CJ detonation model in which the pressure is assumed to ramp up from zero to CJ over several zones. Therefore, totally reactive flow calculations and totally CJ detonation calculations are compared to the Fabry-Perot experiments in the next section.

## COMPARISON OF EXPERIMENT AND CALCULATION

The CJ and reactive flow calculations are first compared to the Fabry-Perot record of a 25  $\mu\text{m}$  copper foil driven in a planar experiment by 25.4 mm of detonating LX-17 in Figure 9. The ignition and growth calculation agrees much more closely to the experimental records than the CJ pressure which neglects the momentum delivered by the 2 mm thick reaction zone of detonating LX-17. After closely predicting the initial copper foil free surface velocity and the two subsequent shock reverberations, the reactive flow calculation lies slightly below the experimental records from 40 to 350 ns. This is most likely due to the influence on the LX-17 reaction rate of the rarefaction wave from the copper free surface after only 10 ns. The LX-17 adjacent to the copper is shocked first to its Von Neumann spike pressure of 33 GPa and then to 56 GPa by the shock reflected off the copper.

Although the LX-17 reaction rates have been calibrated at these pressures by supra-compression<sup>10</sup> and thicker copper and tantalum plate acceleration<sup>8</sup> experiments, this 25  $\mu\text{m}$  copper foil has only a 10 ns transit time for its first shock and rarefaction wave so the

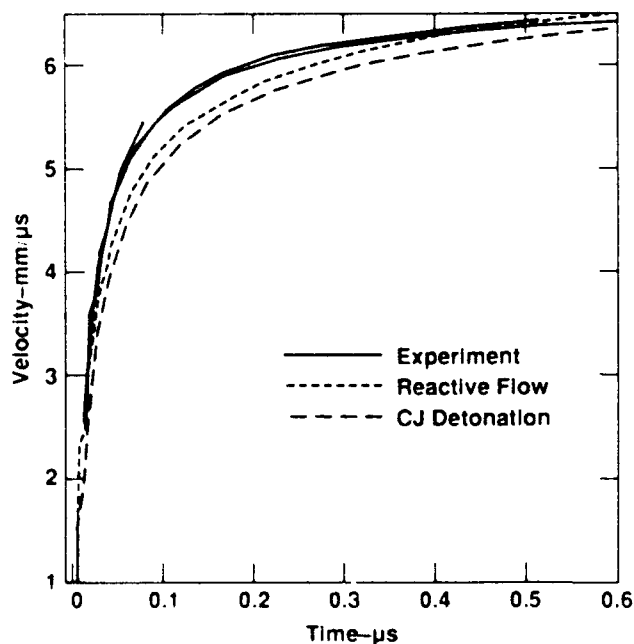


Figure 9 Comparison of Experimental and Calculated Copper Foil Velocity Histories for a 25.4 mm Long Planar LX-17 Detonation

high pressure in LX-17 is maintained for only 10 ns before dropping rapidly to less than CJ pressure (27.5 GPa) in this first rarefaction wave. The pressure-dependent LX-17 reaction rates decrease too rapidly in the first and subsequent rarefactions, as compared with experiment. However, the reactive flow in LX-17 does continue and by 350-400 ns the ignition and growth calculation agrees closely with the experiment in Figure 9.

Similar trends are noted in the remaining comparisons of experiment and calculations in Figures 10-14. Figure 10 shows the Fabry-Perot records from two experiments on 5 mm thick LX-17 initiated by LX-10 boosters. In this case, the reactive flow calculation is slightly low for the entire 0.45  $\mu\text{s}$  record but is much closer than the ideal CJ detonation. This implies that LX-17 develops an appreciable Von Neumann spike pressure in only 5 mm (2.5 reaction zones) of propagation. This may not be surprising because the LX-10 booster initially overdrives the LX-17 reaction rates. Figure 11 shows two Fabry-Perot records from an experiment using 20 mm of LX-17 driven by an LX-10 booster and the corresponding calculations. After 20 mm of propagation, the LX-17 detonation wave is approaching its steady

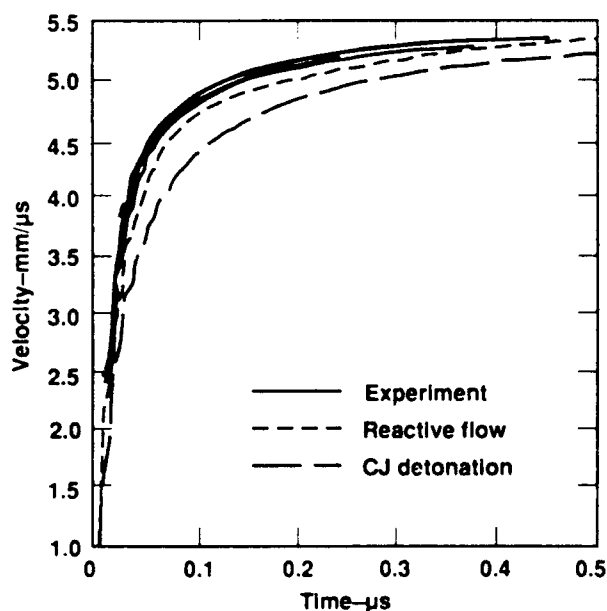


Figure 10. Copper Foil Velocities for Spherical LX-17 5 mm Thick Driven by an LX-10 Booster

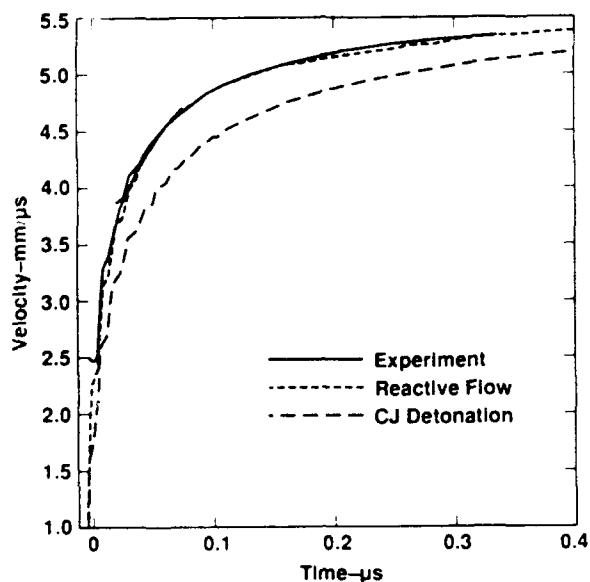


Figure 11. Copper Foil Velocities for Spherical LX-17 20 mm Thick Driven by an LX-10 Booster

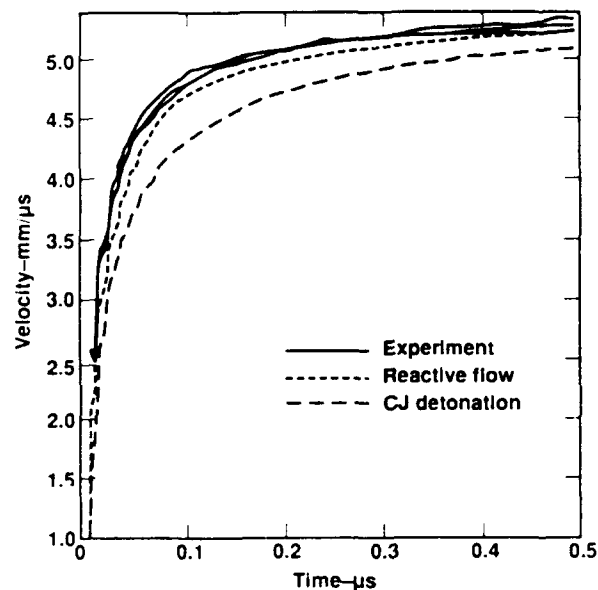


Figure 13. Copper Foil Velocities for Spherical LX-17 2 mm Thick Driven by an Ultrafine TATB Booster

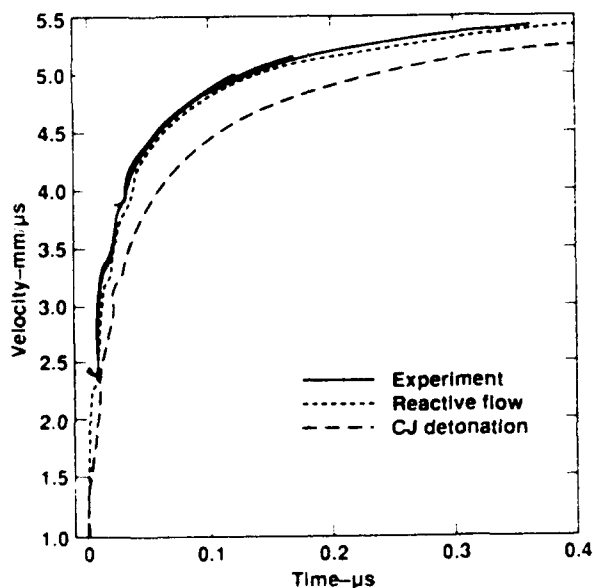


Figure 12. Copper Foil Velocities for Spherical LX-17 30 mm Thick Driven by an LX-10 Booster

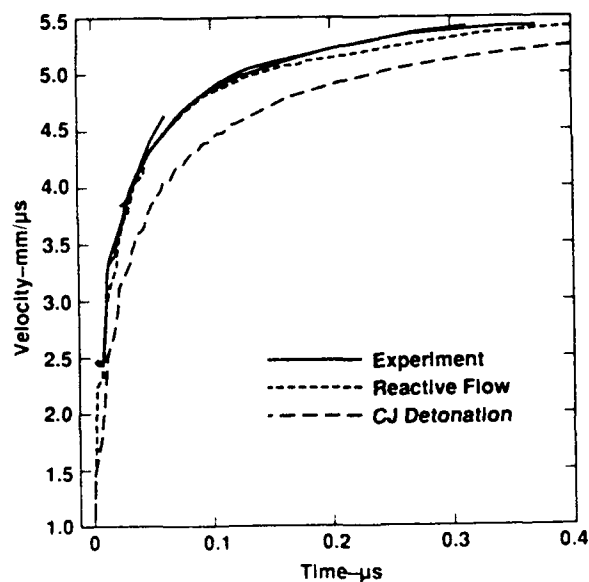


Figure 14. Copper Foil Velocities for Spherical LX-17 20 mm Thick Driven by an Ultrafine TATB Booster

state propagation structure experimentally and in the reactive flow calculations which agree very closely (generally within 1 percent) for the entire  $0.37 \mu\text{s}$  record. The CJ calculation is 4.5 percent lower than the experiment in Figure 11 because it does not account for the momentum contained in the LX-17 reaction zone. Very similar results are shown in Figure 12 for copper foils driven by 30 mm of LX-17 initiated by LX-10 boosters.

Figures 13 and 14 show the comparisons for 2 mm and 20 mm thick LX-17 respectively, initiated by ultrafine TATB boosters. The ultrafine TATB has a lower initial density and CJ pressure than LX-17 and thus "underdrives" the initial LX-17 shock waves. However, as shown in Figure 13, after only 2 mm (one reaction zone) of propagation, the LX-17 detonation wave has attained a ZND reaction zone structure which is well above the

idealized CJ detonation in Figure 13. It is also slightly above the reactive flow calculations in Figure 13. Initial ignition and growth modeling of high pressure, short pulse duration shock initiation of LX-17 from planar electric gun generated shock waves or spherically divergent booster shocks<sup>1</sup> predicted that the leading shock wave in LX-17 would initially decay to pressures below CJ before eventually building to the steady state Von Neumann spike value. However, these experimental records do not show a decay in lead shock pressure. The detonation model LX-17 parameters in Table 1 do not result in such a pressure decrease and therefore agree with the experimental records in Figure 13. Figure 14 compares the records for 20 mm of LX-17 initiated by an ultrafine TATB booster. The close agreement between the experimental records and the reactive flow calculation implies that the detonation wave is approaching its steady state flow. As for the LX-10 boosters, the CJ calculation for an ultrafine TATB booster is 4-5 percent lower than the experimental and reactive flow records.

## CONCLUSIONS

Fabry-Perot laser velocimeter measurements of spherically divergent LX-17 detonation waves have quantitatively demonstrated their initiation and growth from LX-10 and ultrafine boosters at ambient and cold initial temperatures. The cold LX-17 initiated more slowly but attained similar structures to ambient LX-17 within 30 mm of propagation. Both temperatures attained equivalent structures when strongly initiated by LX-10 boosters or weakly initiated by ultrafine TATB boosters within 20 mm of propagation. Velocity histories taken between 0 and 60 degrees were identical and thus no part of the LX-17 wave is weak or failing in this region. Regions of weak or no reaction are known to occur in the 75 to 90 degree region of certain LX-17 initiation systems. The extent of LX-17 energy release in such regions will be measured quantitatively in a future study.

The ignition and growth reactive flow model for detonating LX-17, developed from planar experiments, and an ideal CJ detonation model were used to calculate the

relative strength of these spherically diverging waves. Even when underinitiated by ultrafine TATB boosters, the LX-17 detonation waves exhibited finite thickness reaction zone structures with peak pressures well above CJ within 2 mm or one reaction zone propagation. The spherically divergent waves attained nearly steady state structures in close agreement with reactive flow predictions after 20-30 mm of propagation in ambient LX-17. The CJ calculations were uniformly 4-5 percent low in velocity, implying that this amount of momentum is contained in the 2 mm thick LX-17 reaction zone which decreases in pressure from the Von Neumann spike state (33 GPa) to the CJ state (27.5 GPa) in a fast reaction followed by a slower reaction process.<sup>8,10</sup> Therefore, the initiation and detonation development in hemispherical LX-17 charges in the region of strong reaction is now well-understood experimentally and calculationally. Reactive flow calculations of the regions of weak or no reaction will accompany the previously mentioned experiments in a future study.

## REFERENCES

1. Bahl, K.; Bloom, G.; Erickson, L.; Lee, R.; Tarver, C.; Von Holle, W.; and Weingart, R., *Eighth Symposium (International) on Detonation*, Naval Surface Weapons Center, NSWC MP 86-194, 1985, p. 1045.
2. Jackson, R. K.; Green, L. G.; Barlett, R. H.; Hofer, W. W.; Kramer, P. E.; Lee, R. S.; Nidick, Jr., E. J.; Shaw, L. L.; and Weingart, R. C., *Proc. of the Sixth Symp. (International) on Detonation*, Office of Naval Research, ACR-221 (U.S. Government Printing Office, Washington, D. C.), 1976, p. 755.
3. Weingart, R. C.; Lee, R. S.; Jackson, R. K.; and Parker, N. L., *ibid*, p. 653.
4. Bloom, G. H.; Chau, H.; Glaser, R.; Honodel, C.; Lee, R. S.; and Weingart, R. C., *Shock Waves in Condensed Matter*, 1983, Ed. Asay, J. R.; Graham, R. A.; and Straub, G. K., North-Holland, 1984, p. 535.
5. Murphy, M. J.; Simpson, R. L.; Breithaupt, R. D.; and Tarver, C. M., paper presented at this Symposium.

6. Lee, E.; Breithaupt, D.; McMillian, C.; Parker, N.; Kury, J.; Tarver, C.; Quirk, W.; and Walton, J., *Eighth Symposium (International) on Detonation*, Naval Surface Weapons Center, NSWC MP 86-194, 1985, p. 613.
7. Tarver, C. M.; Hallquist, J. O.; and Erickson, L. M., *Eighth Symposium (International) on Detonation*, Naval Surface Weapons Center, NSWC MP 86-194, 1985, p. 951.
8. Tarver, C. M.; Breithaupt, R. D.; and Kury, J. W., *International Symposium on Pyrotechnics and Explosives*, Beijing, China, 1987, p. 692.
9. Cochran, S. G. and Tarver, C. M., *Shock Waves in Condensed Matter*, 1983 (Asay, J. K.; Graham, R. A.; and Straub, G. K., editors), Elsevier Science Publishers B. V., 1984, p. 593.
10. Green, L. G.; Tarver, C. M.; and Erskine, D. J., paper presented at this Symposium.

# REACTION RATES OF PBH-9D EXPLOSIVE

Zhao Feng, Sun Chengwei,  
Chen Peiqi, and Ouyang Denghuan  
Southwest Institute of Fluid Physics  
P.O. Box 523, Chengdu, Sichuan, CHINA

*The reaction rates of PBH-9D explosive have been studied with Lagrange analysis and shock initiation data. The velocity histories at four Lagrange positions and the pressure history at one Lagrange position were measured for the explosive samples under a shock with increasing pressures from 3 to 9 GPa. With these input data the Lagrange analyses were performed and the histories of pressure, density and specific internal energy in the reactive flow have been obtained. The reaction degree and rate have been yielded by using the HOM, JWL as well as the  $\gamma$ -Law EOS of detonation products. Based on the calculated data, the coefficients in the Forest Fire and the ignition-growth rates were determined by the least square method. The rate fitted with the  $\gamma$ -Law EOS is apparently lower than those obtained with the JWL or HOM EOS. The results reproduced by the one-dimensional numerical simulation with the above rates are consistent with the experimental data.*

## INTRODUCTION

Because high explosives have been widely used in industry as well as for military purposes, detonation research is progressing rapidly. One of the basic problems about detonation is the mechanism and simulation of the reaction process in shocked explosives; i.e., the hydrodynamic problem coupled with the explosive chemical reaction. Up to now we knew little about the real reaction in condensed explosives; however, it is still possible to simulate the macroscopic effects of explosive reactions provided an inner variable  $\lambda$ , the reaction degree, is employed. The derivative of  $\lambda$  with respect to the time  $t$  is the reaction rate  $R$ .

In the 1940's, Von Neumann, Zel'dovich and other workers used a simple rate function  $d\lambda/dt = 2(1 - \lambda)^{1/2}$  which is easy to treat mathematically. Many authors employed Arrhenius' Law in chemical kinetics to numerically simulate the shock initiation in explosives.<sup>1</sup> Eyring et al.<sup>2</sup> investigated the

reaction rate and connected it with the curvature of detonation front propagating in the explosive charges with finite diameters. In 1976, Mader and Forest<sup>3</sup> put forward an empirical rate function Forest Fire that depends only on the pressure and is based on the experimental POP relations as well as the supposed reaction Hugoniot. The Forest Fire rate can reproduce many experiments on shock initiation. In recent years several phenomenological empirical rates have been suggested; for example, Cochran and Chan,<sup>4</sup> and Lee and Tarver<sup>1</sup> proposed a kind of rate function consisting of ignition and growth terms. The ignition term describes the set off of hydrodynamic hot spots and the growth term represents the explosive grain's burning. Obviously, the ignition-growth rates are potentially capable of reproducing the shock initiation process with a mechanism other than the simple multiplication of the hot spots. In 1985, Tarver et al.<sup>5</sup> suggested that the shock initiation in condensed explosives could be divided into three stages, accordingly

the reaction rate should consist of three terms in which the first term represents the hot spot's origins (such as void closure, viscous heating, shear banding, etc.), the second one describes the slow increasing of reaction in inward and/or outward "burning" of the isolated hot spots, and the third one denotes the rapid finishing of the reaction when the reacting hot spots begin to coalesce.

Since the 1970's the Lagrange analysis has been employed in shock initiation research; this analysis was established by Fowles and Williams.<sup>6</sup> Cowperthwaite<sup>7</sup> and Grady<sup>8</sup> employed Lagrange analysis for studying the constitutive relations in inert materials and explosives. The Lagrangian gauges embedded in tested explosive charges sense the evolution of reactive shock waves and give the records of pressure or particle velocity histories at some Lagrange positions. These records could be treated with the Lagrange analysis and offer the tabular data about the histories or profiles of the particle velocity, pressure, volume and internal energy in the reactive flow. Furthermore, the reaction degree and rate could be calculated as well, provided the EOS of partially reacted detonation products is given.

The reaction rates of PBH-9D explosive are obtained in this paper by using the experimental pressure and particle velocity histories and the Lagrange analysis. The constants in the empirical rate functions of Forest Fire and Cochran-Chan proposed ignition-growth form are fitted from the Lagrange analysis' results, where three equations of state for detonation products (JWL, HOM and  $\gamma$ -law) were used and compared. Finally, the numerical simulation using these fitted rates are performed to reproduce the experimental results, where we get better agreement between the calculated and experimental data at the Lagrange positions nearer to the shocked surface. The calculations show that the JWL and HOM EOS have small differences for fitting reaction rates; however, the results with the  $\gamma$ -law EOS are apparently lower than the previous ones.

## LAGRANGE ANALYSIS AND CALCULATIONS

### Conservation Equations and Integration

The Lagrange analysis is an unsteady numerical technique to treat the data resulting from the Lagrangian gauges (sensors) with the flow equations. In Lagrange coordinates the one-dimensional slab flow equations are:

$$\partial V / \partial t - \rho_0^{-1} \partial U / \partial h = 0 \quad (1)$$

$$\partial U / \partial t + \rho_0^{-1} \partial P / \partial h = 0 \quad (2)$$

$$\partial E / \partial t + P \rho_0^{-1} \partial U / \partial h = 0 \quad (3)$$

where  $\rho_0$ ,  $U$ ,  $V$ ,  $P$ ,  $E$ , and  $t$  are the particle's initial density, velocity, volume, pressure, specific internal energy, and time, respectively, and  $h$  is the particle's initial position or the Lagrange coordinate. The integration method of Equations (1)-(3) depends on the form of experimental data. We use the particle velocity histories at several Lagrange positions and the pressure history at some position as the original data, so we yield the integration form of Equations (1)-(3) as follows

$$P_2 = P_1 - \rho_0 \int_{h_1}^{h_2} (\partial U / \partial t)_h dh \quad (4)$$

$$V_2 = V_1 + \rho_0^{-1} \int_{t_1}^{t_2} [(\partial U / \partial h)_j - (\partial U / \partial t)_h (dt/dh)_j] dt \quad (5)$$

$$E_2 = E_1 - \rho_0^{-1} \int_{t_1}^{t_2} P [(\partial U / \partial h)_j - (\partial U / \partial t)_h (dt/dh)_j] dt \quad (6)$$

where  $( )_j$  denotes the derivative along the  $j$ th path line.<sup>8</sup> Subscripts 1 and 2 refer to the pressure values at different Lagrange positions for the same time or to the volume and internal energy values at the same position for different times.



## Reaction Degree $\lambda$ and Rate $R$

We assume the reaction in shocked explosives to be one-step, irreversible and exothermic, and the reactants and products are in local thermodynamic equilibrium. The explosive's reaction or burn can be characterized by the reaction degree or progress variable which is also the concentration of detonation products in the reaction mixture; so  $\lambda = 0, 1$  represents the states being unreacted and completely reacted, respectively. The reaction rate  $R = d\lambda/dt$  is a function of the reaction products' thermodynamic variables, including  $\lambda$ . Let the state of unreacted explosive be described by the solid HOM EOS. Meanwhile, there are three options for the EOS of detonation products: gas HOM, JWL, and  $\gamma$  law. Suppose that the state of reaction mixture could be calculated from the states of its two phases, solid (unreacted explosive) and gas (detonation products), according to the following mixing rule:

$$V = \lambda V^p + (1 - \lambda) V^x \quad (7)$$

$$E = \lambda E^p + (1 - \lambda) E^x \quad (8)$$

where the superscripts  $p$  and  $x$  denote the gas and solid, respectively. Meanwhile, it is assumed that the two phases are in equilibrium of pressure and temperature,

$$P^p = P^x = P \quad (9)$$

$$T^p = T^x = T \quad (10)$$

where the variables  $P, V, E$  of the mixture should be calculated by the flow Equations (1)-(3), and those with the superscripts  $p$  or  $x$  should satisfy the corresponding EOS for gas or solid. Then we can get the rate  $R$  as well as the reaction degree  $\lambda$  by an iterative solution to Equations (7)-(10). Consequently,  $\lambda$  as well as  $R$  depends on the EOS, especially that for detonation products. The comparison of results from different EOS will be given later in detail.

After the tabular thermodynamic variables are obtained, the nonlinear, least square fitting with generalized orthogonal polynomials will be performed to get the constants in two empirical rate functions.

## EXPERIMENTS

The experimental assembly is shown in Figure 1. The PBH-9D explosive sample, an HMX-based plastic bonded explosive, had an initial density  $\rho_0 = 1.846 \pm 0.003 \text{ g/cm}^3$  and a diameter of 10 cm. It was initiated by the attenuated shock wave propagating from the PMMA plate. An explosive planar wave lens was placed above the 1 cm thick PMMA plate by an air separation of 1 cm, so that the plate would be impacted by the flying detonation products from the explosive lens. The EM particle velocity gauges were fixed at the positions of  $h = 0, 3, 6, 9 \text{ mm}$ , where  $h$  was the distance from the explosive's shocked surface. The magnetic field was generated with a pair of Helmholtz coils 40 cm in diameter and 20 cm in spacing. With a magnetizing current of 1 kA the intensity of the central uniform magnetic field is 0.1 Tesla. The pressure history at the surface ( $h = 0$ ) was measured with a manganin piezoresistance gauge of type F4/203A<sup>9</sup>. The smoothed particle velocity histories measured by the EM gauges are shown in Figure 2. It must be noted that the loading pressure profile looks like a ramp wave rather than a square wave (see the  $h = 0$  curve shown in Figure 3), because of the design of the experimental assembly.

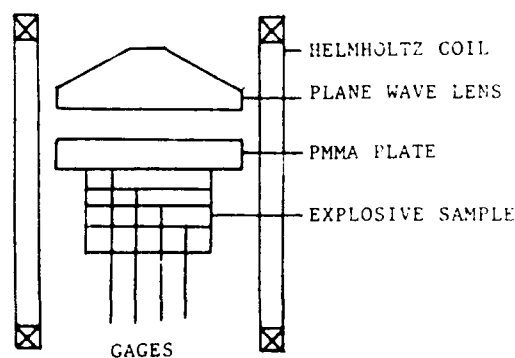


Figure 1. Experimental Assembly

## FLOW AND REACTION VARIABLES CALCULATED WITH THE LAGRANGE ANALYSIS

The input data for the Lagrange analysis are the experimental histories in Figure 2

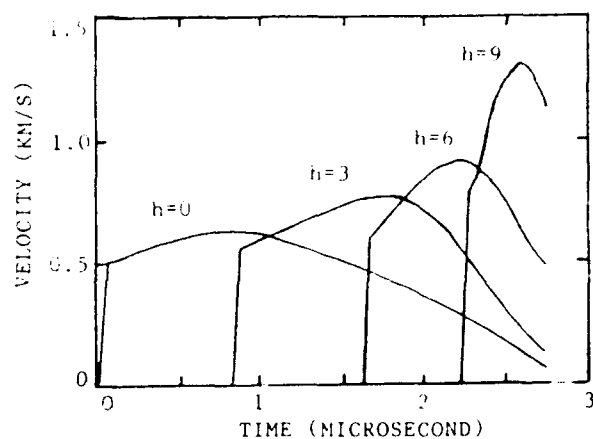


Figure 2. Measured Particle Velocity Histories at Lagrange Positions of  $h = 0, 3, 6, 9$  mm

and that of  $h = 0$  in Figure 3. The calculated histories for pressure, density and specific internal energy at the four positions are shown in Figures 3, 4, and 5, respectively.

The reaction degree histories calculated with the HOM EOS of detonation products for the four positions are shown in Figure 6. The histories at  $h = 6$  but with different EOS are compared in Figure 7. Differentiating  $\lambda$  histories with respect to time we have the reaction rate  $R$  directly. From Figure 7 it can be concluded that  $\lambda$  histories are basically the same for the JWL and HOM EOS; however, the history with the  $\gamma$  law EOS is lower. During the buildup to detonation the reactive shock wave accelerates; therefore, the entropy production increases considerably. In this situation the constant  $\gamma$  law EOS may behave worse than the other two equations of state.

## FITTING OF CONSTANTS IN EMPIRICAL RATE FUNCTIONS

The rate function is one of the keys to performing successful numerical simulation of detonation, particularly for shock initiation, since the behavior of initiation process basically depends on the reaction rate under the same loading conditions. People show great interest in seeking a suitable form for rate functions according to different initiation models or mechanisms, from pure phenomenological descriptions to the molecular dynamics technique. The Forest Fire and the

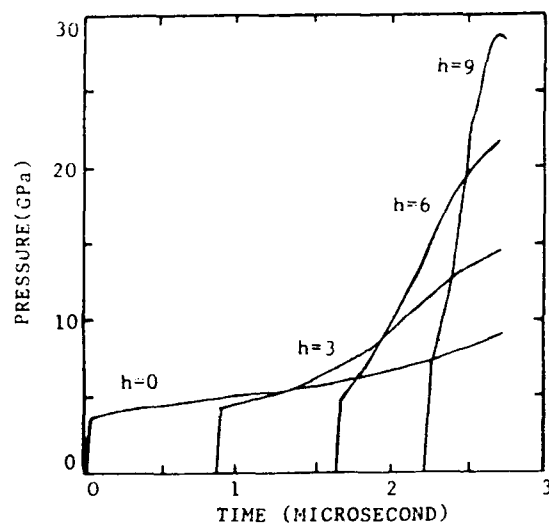


Figure 3. Measured ( $h = 0$ ) and Calculated ( $h = 3, 6, 9$  mm) Pressure Histories

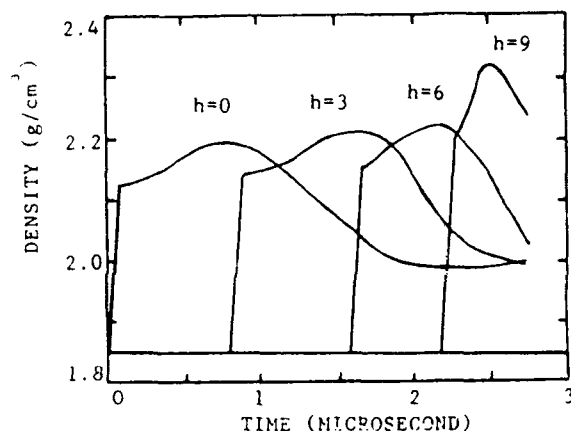


Figure 4. Calculated Density Histories

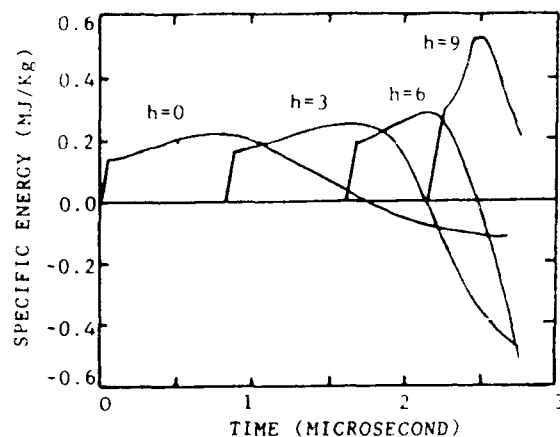


Figure 5. Calculated Specific Internal Energy Histories

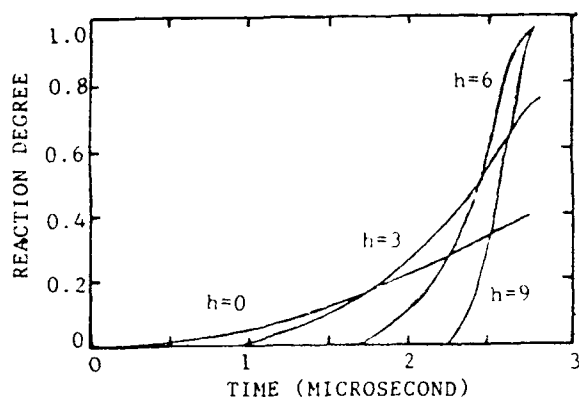


Figure 6. Reaction Degree Histories with HOM EOS of Detonation Products

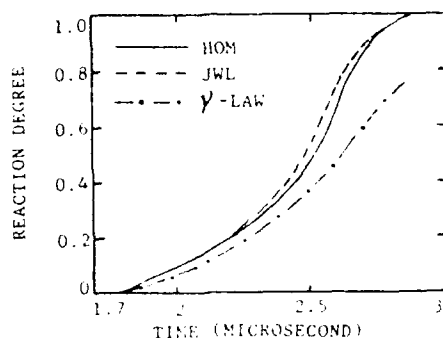


Figure 7. Reaction Degree Histories at Position of  $h = 6\text{mm}$  with the JWL, HOM and  $\gamma$ -law EOS for detonation products.

ignition growth form are very useful in practice, not only for their simplicity but also for their success in many numerical simulations of shock initiation in heterogeneous explosives. The Forest Fire proposed by Mader and Forest<sup>3</sup> is derived from the single curve hypothesis during the buildup to detonation and the experimental POP relations, it concludes that the reaction rate depends only on pressure, i.e., on the effects of hydrodynamic hot spots. The function of Forest Fire can be written as

$$(1-\lambda)^{-1} d\lambda/dt = \exp(a_0 + a_1 P + a_2 P^2 + \dots + a_n P^n) \quad (11)$$

where  $a_i$  ( $i = 0, 1, \dots, n$ ) are constants to be fitted. The ignition growth form of a rate function was first proposed by the scientists at LLNL; they considered that the ignition term plays the main role in the early stage of initiation, during the hydrodynamic formation

of hot spots. However, the growth term turns out to be the dominant one for the later stage, during grain burning, and the rate is approximately proportional to the pressure. Several practical forms of the ignition-growth rate function have been suggested; here only the form proposed by Cochran and Chan<sup>4</sup> will be calculated:

$$(1-\lambda)^{-1} d\lambda/dt = \omega_1 P^n + \omega_2 \lambda P^m \quad (12)$$

where  $\omega_1$ ,  $\omega_2$ , and  $n$  are constants to be fitted, and  $m$  usually is set to 1. The first term in the RHS of Equation (12) represents ignition, and the second one denotes growth. Using the above two rate functions we could well reproduce the experimental variable histories at positions with lower  $h$ , and no considerable difference between them has been observed (see Figures 9 and 10).

### Forest Fire Constants

The Forest Fire constants were fitted by using standard generalized orthogonal polynomial techniques, and the results are listed in Table 1. The curves of  $(1-\lambda)^{-1} d\lambda/dt$  vs pressure are plotted in Figure 8 along with those of PBX-9404 and Comp B explosives,<sup>10</sup> as well as that of PBH-9D explosive obtained by Sun<sup>11</sup> using an approximation method. It has been shown that the curves calculated with the JWL and HOM EOS are close to each other within a certain pressure range, and between the curves for explosives PBX-9404 and Comp B. It means the PBH-9D explosive is less sensitive to shock initiation than PBX-9404, but more sensitive than Comp B. We think this result is reasonable since the PBH-9D explosive is compounded on the base of a sensitive explosive. The curves in Figure 8 are not very smooth; this may be due to the data treatment procedure without multi-smoothing and the fact that there were no empirical relations (such as the POP relation) used.

### Cochran-Chan Proposed Rate Constants

These constants in the Cochran-Chan proposed rate function are fitted by using nonlinear optimization technique, and the results are listed in Table 2.

Table 1. Forest Fire Constants of PBH-9D Explosive

EOS for Detonation Products	n	$a_0, a_1, a_2, \dots, a_n$		
HOM	10	1.5016841E+01, 4.4811070E+06, 5.7215222E+09, -1.1735394E+11,	-2.833713E+03, 7.6094592E+07, -2.5882972E+10, 8.1658839E+10,	1.5732775E+05, -8.1882163E+08, 7.3136603E+10,
JWL	9	0.25690365E+00, -1.4284010E+06, 1.1896018E+09, -6.5322680E+09,	-8.9675342E+02, 2.1953328E+07, -4.1522092E+09,	5.3004965E+04, -2.0549970E+08, 8.0006676E+09,
$\gamma$ LAW ( $\gamma = 2.96$ )	8	-1.2000313E+01, 1.2036025E+05, 1.5902000E+07,	5.0082788E+02, -5.6149600E+05, -5.5780176E+07,	-1.0705477E+04, -5.9020400E+05, 6.3588816E+07,

## COMPARISON OF ONE-DIMENSIONAL NUMERICAL SIMULATION WITH EXPERIMENTAL DATA

The particle velocity histories and other variables were numerically simulated with the one-dimensional computer hydrocode SSS for reactive media<sup>12</sup>, where the rate functions were taken from the above fitted ones. Figures 9 and 10 show the comparisons between calculated and experimental data for the Forest Fire and Cochran-Chan proposed rate, respectively. It can be noted that for the particle velocity histories at positions of  $h = 0$  and 3 mm they agree well with each other, however, for those of  $h = 6$  and 9 mm the calculated ones are apparently higher than the experimental ones. No considerable difference appears between the two rate functions.

The results calculated with the Forest Fire constants given by Sun<sup>11</sup> are also shown in Figure 9; these are closer to the experimental data since this rate vs pressure curve is a bit lower than that of this paper (See Figure 8). The spacing of EM particle velocity gauges in our experiments might be too large, so that the numerical interpolation and differentiation brings about larger errors, especially at the deeper positions where the process more rapidly approaches to the complete reaction. The response and calibration of the Lagrangian gauges are worse under this circumstance.

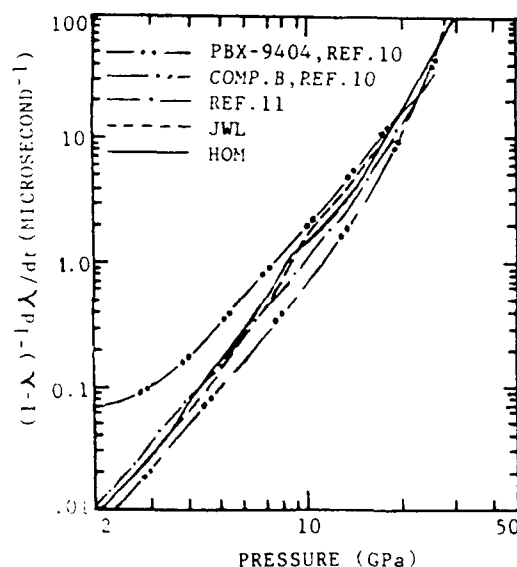


Figure 8.  $(1-\lambda)^{-1} d\lambda/dt$  VS  $P$  from the Fitted Forest Fire Rate Functions

Table 2. Cochran-Chan Proposed Rate Constants of PBH-9D Explosive

EOS for Detonation Products	$\omega_1$	$\omega_2$	n
HOM	1195	25	3,105
JWL	3990	22	3,940
$\gamma$ -LAW ( $\gamma = 2.96$ )	1200	20	3,806

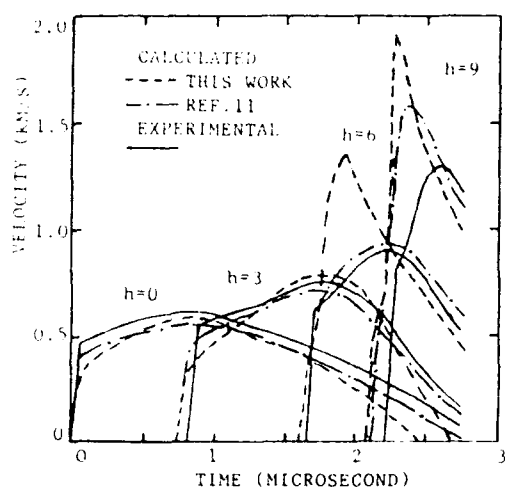


Figure 9. Comparison of Calculated Particle Velocity Histories with Experimental Data for the Forest Fire Rate Function

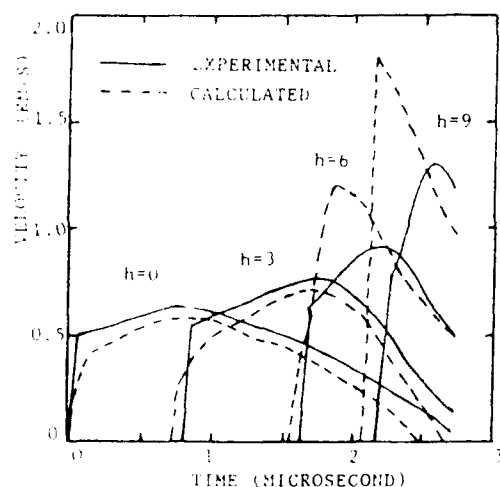


Figure 10. Comparison of Calculated Particle Velocity Histories with Experimental Data for the Cochran-Chan Proposed Rate Function

## CONCLUSIONS

Using the Lagrange analysis and fitting techniques we have obtained empirical rate function constants from the experimental pressure history at one position and particle velocity histories at several positions. In order to get good results it is necessary to measure the flow variables precisely in experiments, (a relative error less than 2 percent, as pointed out by Vantine)<sup>13</sup>

With these rate function constants fitted according to the procedure described in this paper, the experimental data could be reproduced by one-dimensional numerical simulation. Good agreement is yielded, especially for the histories at positions close to the shocked surface.

By comparing the Forest Fire rates for three explosives under lower shock pressures, we conclude that PBH-9D explosive is less or more sensitive to shock initiation than PBX-9404 or Comp B, respectively.

The equation of state for detonation products affects the fitted rate constants to some extent. For the situation considered in this paper the JWL and HOM EOS show no considerable difference; however, the rate fitted with the  $\gamma$ -law EOS is apparently lower than the above ones. It seems that the  $\gamma$ -law EOS of detonation products behave worse in numerical simulations of shock initiation.

## ACKNOWLEDGMENTS

The authors are indebted to Prof. Wei Yuzhang, and Engineer Wang Cuilian for their helpful discussions and contributions in the experiments.

## REFERENCES

1. Lee, E. L. and Tarver, C. M., *Phys. of Fluids*, Vol. 23, No. 12, 1980, p. 2362.
2. Eyring, H. et al, *Chem. Rev.*, Vol. 45, 1949, p. 69.
3. Mader, C. L. and Forest, C. A., *LA-6259*, 1976.
4. Cochran, S. G. and Chan, J., *UCID-18024*, 1979.
5. Tarver, C. M., et al, *Proc. of 8th Inter. Symp. on Detonation*, 1985, p. 884.
6. Fowles, R. and Williams, R. F., *J. Appl. Phys.*, Vol. 41, No. 1, 1970, p. 360.
7. Cowperthwaite, M., and Williams, R. F., *J. Appl. Phys.*, Vol. 42, No. 1, 1971, p. 456.
8. Grady, D. E., *J. Geophys. Res.*, Vol. 78, No. 8, 1973, p. 1299.

9. Chi Jiachun and Wu Guodong, *Explosion and Shock Waves*, Vol. 3, No. 3, 1983, p. 75.
10. Mader, C. L., *Numerical Modeling of Detonations*, Univ. of California Press, 1979, Chapter 4.
11. Sun Chengwei, *Numerical Fitting of Empirical Rate Constants for Explosives* (to be published).
12. Sun Chengwei, *Computation Physics*, Vol. 3, No. 2, 1986, p. 142.
13. Vantine, H. C. and Rainsberger, R. B., et al., *Proc. of 7th Inter. Symp. on Detonation*, 1981, p. 593.

## DISCUSSION

DR. C. D. HUTCHINSON  
Atomic Weapons Establishment  
United Kingdom

Could the author please give the formulation of PBH-9D?

## REPLY BY ZHAO FENG

The formulation of PBH-9D is 90 percent HMX and 10 percent binder. The details on this formulation can be found in the classified literature.

**SESSION ON**  
**TIME RESOLVED CHEMISTRY**

**Cochairmen:**   **Anatolij Dremin**  
                          **Institute of Chemical Physics**

**William Von Holle**  
                          **Lawrence Livermore National Laboratory**

# PULSED-LASER-EXCITED RAMAN SPECTRA OF SHOCK-COMPRESSED TRIAMINOTRINITROBENZENE

Wayne M. Trott and Anita M. Renlund  
Sandia National Laboratories  
Albuquerque, New Mexico 87185

*Pulsed-laser-excited Raman scattering methods have been used to examine sustained shock compression of 1,3,5-triamino-2,4,6-trinitrobenzene (TATB) at an optical window interface. Records of vibrational frequency shifts and line shape changes have been obtained under variable and well-controlled shock loading, using a 63-mm-diameter compressed gas gun to provide a planar impact geometry. To facilitate interpretation of the shock data, Raman spectra of TATB samples at elevated temperatures and ambient pressure have also been acquired. Raman modes identified with the nitro and amino groups in TATB exhibit complex behavior arising from interactions associated with the extensive intra- and intermolecular hydrogen bonding network in this material. The distinct (and frequently competing) effects of pressure and temperature on these modes are discussed in relation to the known insensitivity of TATB to shock initiation.*

## INTRODUCTION

In order to acquire detailed understanding of the relevant physical and chemical processes leading to initiation and sustained detonation of secondary explosives, real-time optical spectroscopic measurements are needed to supplement the information available from studies of bulk properties under shock compression (e.g., pressure and particle velocity). Various optical methods have been used to probe shocked and detonating energetic materials, including emission and absorption spectroscopy, as well as spontaneous and nonlinear Raman scattering techniques.<sup>1</sup> We have shown that pulsed-laser-excited spontaneous Raman scattering is a useful tool for studying many heterogeneous (i.e., compressed polycrystalline) explosive materials.<sup>2-4</sup> Recently, we reported single-pulse Raman measurements of vibrational frequency shifts and line shape changes in 1,3,5-triamino-2,4,6-trinitrobenzene (TATB) upon sustained shock loading at a fused silica window interface.<sup>4</sup> These measurements were obtained under complex, time-dependent shock conditions due to the use of an explosive driver for dynamic loading. As

a result, analysis of particle velocity-time records (in parallel experiments) was required in order to correlate the Raman spectra with reliable estimates of shock pressure. In this paper, we discuss the behavior of TATB Raman modes under the fully supported and well-controlled shock compression provided by a compressed gas-gun driver. As in the previous study, measurements have been made at a window interface. To facilitate interpretation of the shock data, we have also examined changes in the Raman modes of TATB as a function of temperature alone.

In addition to the fact that TATB is a well-known insensitive high explosive, this compound is an interesting subject for pulsed-laser-excited Raman studies for several reasons. In spite of its susceptibility to long-term photolytic degradation at ambient pressure, the Raman spectrum of TATB is readily obtained via single-pulse methods. Moreover, TATB displays excellent stability under high temperature and high static pressure.<sup>5</sup> The former property permits Raman measurements of the parent species at temperatures as high as 575K. Finally, TATB contains many



unusual structural features, including an extensive intra- and intermolecular hydrogen bonding network, very long C-C bonds in the benzene ring, and very short C-NH<sub>2</sub> bonds.<sup>6</sup> The strong intermolecular hydrogen bonds result in a graphite-like layered crystal structure. Vibrational spectroscopy provides an ideal probe of the effects of shock compression on these structural features. In the present study, we have focused on the Raman modes associated with the nitro and amino groups in the molecule. These modes are strongly affected by the hydrogen bonding network. Shock-induced changes in these modes are discussed in relation to TATB's insensitivity to shock initiation.

## EXPERIMENTAL

A schematic diagram of the experimental arrangement for the shock compression studies is shown in Figure 1. The TATB samples (3-4 mm thick) were prepared from loose

powder pressed to a density of 1.876 g/cm<sup>3</sup> and confined in an annular (15.9 mm ID) PMMA fixture. The surfaces were machined flat and parallel and one side was confined by an optical window. Care was taken to ensure good contact between the TATB and the window. Sustained shocks were introduced into the TATB using projectiles driven by a 63 mm diameter light gas gun. Measurements at the initial shock state are nearly impossible due to the limited probe depth in single-pulse Raman scattering from polycrystalline samples (i.e., timing the laser pulse to occur precisely as the shock arrives at the interface is extremely difficult). Therefore, shocks were allowed to run into the window and spectra were acquired after the TATB near the window was reshocked. Low-amplitude initial shocks (1.0-1.1 GPa) were obtained using PMMA impactors (9.5 mm thick) and projectile velocities near 0.5 km/s. Higher shock pressures were generated with aluminum impactors (13 mm thick) and projectile velocities of 0.49-

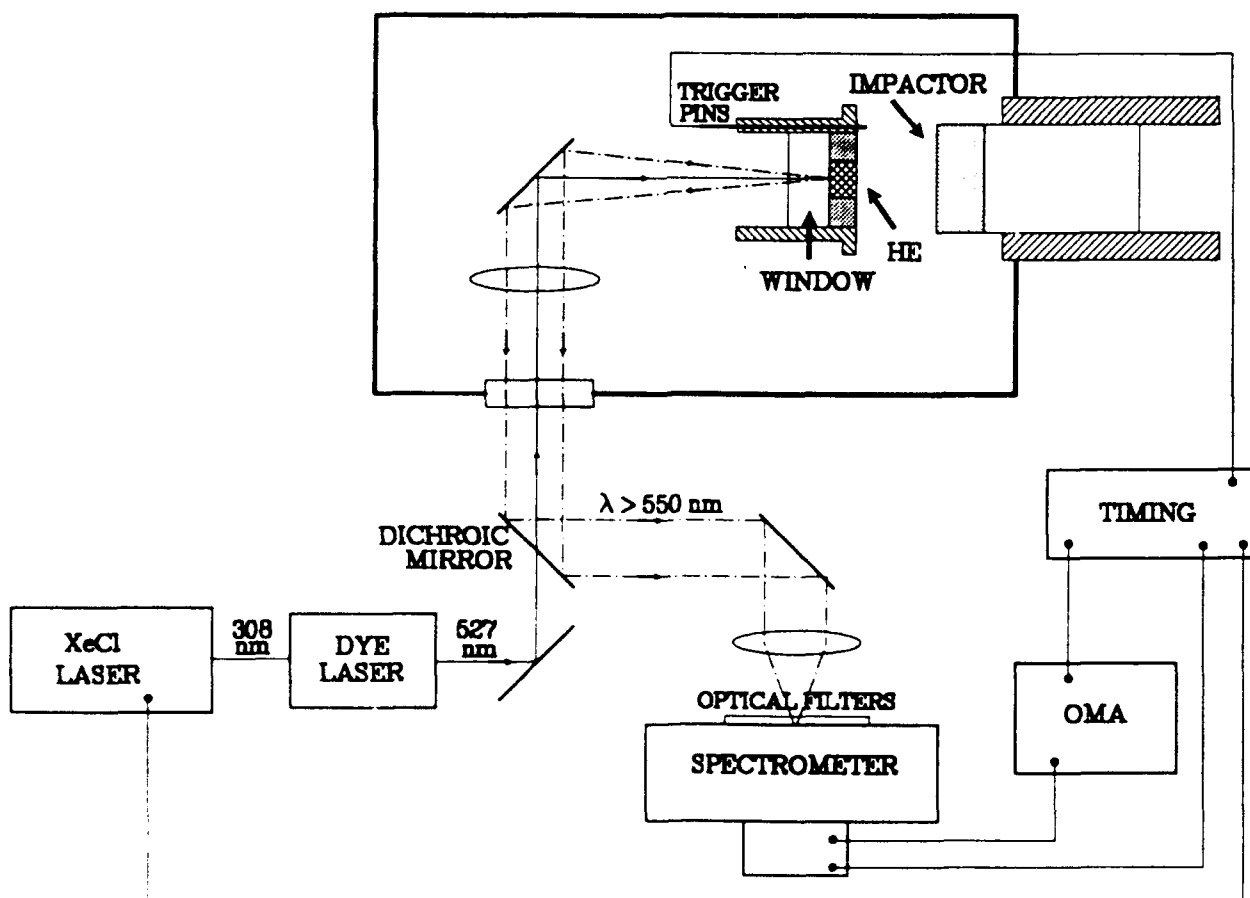


Figure 1 Schematic Diagram of Experimental Arrangement

0.88 km/s. Three different window materials were used in this study. Fused silica was suitable for tests at pressures < 5 GPa. In other tests, sapphire and LiF windows were used to generate higher reshock pressures in TATB (up to 7.5 GPa) and also to maintain satisfactory optical transmission under the shock conditions. Shock pressures were calculated using published Hugoniot data for 1.876 g/cm<sup>3</sup> TATB and for the impactor and window materials.<sup>7,8</sup>

An excimer-laser-pumped dye laser (Lambda Physik FL-2002) was used to generate Raman spectra at the TATB/window interface. For each shot, the laser output (20 ns FWHM) was focused in front of the target/window assembly so that the diverging beam was approximately 1 mm in diameter at the interface. Frequency-shifted radiation due to spontaneous Raman scattering from the shock-compressed TATB was separated from the scattered 527 nm laser light using a dichroic mirror. The spontaneous Raman light was focused into the entrance slit of a 0.8 m double spectrometer and the dispersed spectrum was viewed by an intensified diode array detector. The signal was processed by an optical multichannel analyzer (Tracor Northern, TN-1710A). The detector was gated on by a voltage pulse that was triggered ahead of the laser pulse using digital delay

generators. A 500 ns gate width avoided signal loss due to timing jitter and provided adequate discrimination against background emission. Digital delay generators were also used to set the required temporal delay for the laser/detection system in relation to the impact time (determined by time-of-arrival pins). The laser output was programmed to occur several hundred nanoseconds after shock arrival at the TATB/window interface. Spectra were thus obtained before axial and transverse rarefactions reached the optical axis at the interface. The spectral resolution in these experiments was typically 0.05 nm (~1.5 cm<sup>-1</sup> at 570 nm). Wavelength calibration was accomplished using known line positions in the emission spectra of Hg, Kr and Ar discharge lamps.

We used a very similar laser and detection system arrangement for studies of unshocked TATB at elevated temperatures. In this case, 100 mg pellets of TATB were placed in a small fixture containing an electric button heater and an iron-constantan thermocouple. The TATB samples were heated in an evacuated (<0.01 Torr) explosive test chamber to minimize heat loss to the surrounding atmosphere. Whenever the sample temperature was changed, Raman spectra were obtained only after 15-30 minutes elapsed in order to ensure adequate thermal equilibration

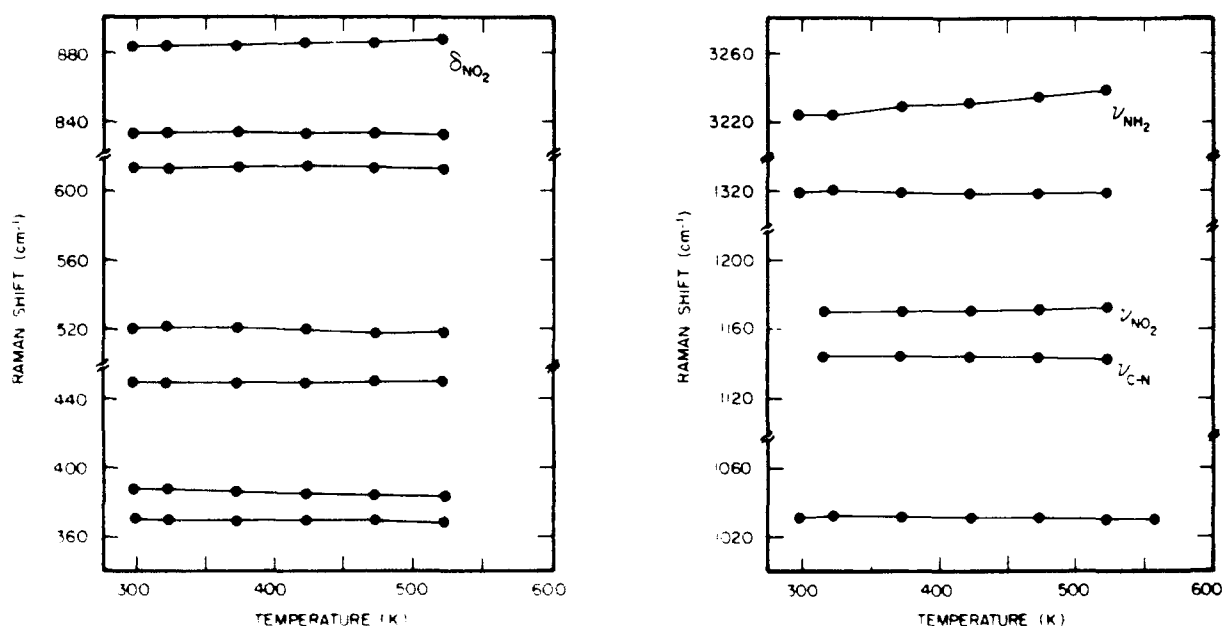


Figure 2. Raman Shifts as a Function of Temperature for Twelve Different Modes in TATB

between the TATB and the thermocouple junction. In these experiments, signal averaging was feasible and up to 32 shots were taken to acquire a spectrum.

## RESULTS AND DISCUSSION

### Temperature Behavior

The effects of increased temperature on the peak positions of twelve of the vibrational modes in TATB are illustrated in Figure 2. A detailed discussion of temperature-induced vibrational frequency shifts and line shape changes in TATB will be presented elsewhere. For the purposes of the present discussion, it is sufficient to note the unusual behavior of some strong modes associated with the nitro and amino groups in the molecule. Increased temperature generally causes a Raman line to broaden and shift to lower frequency<sup>9</sup> and most of the features in TATB experienced either no change or a small negative shift (i.e., to lower frequency) under these conditions. In contrast, the totally symmetric  $\text{NH}_2$  stretching mode (near  $3220\text{ cm}^{-1}$ ) displayed a substantial positive shift with increased temperature. The totally symmetric  $\text{NO}_2$  stretching mode (near  $1170\text{ cm}^{-1}$ ) and the in-plane  $\text{NO}_2$  deformation mode ( $884\text{ cm}^{-1}$ ) also exhibited positive shifts; however, the changes were much smaller. In addition, the line widths of all these modes were significantly more temperature sensitive (i.e., broadened more) than average. These effects arise from the strong hydrogen bonding network in TATB and the strong coupling between the  $\text{NO}_2$  and  $\text{NH}_2$  group motions that occurs: a result of this bonding structure

Since the extensive hydrogen bonding network in TATB probably plays a very important role in its remarkable stability at high static pressures<sup>5</sup> and also its relative insensitivity to shock initiation,<sup>10</sup> the behavior of the aforementioned  $\text{NO}_2$  and  $\text{NH}_2$  modes under shock compression is of interest. Shock-induced effects on these three modes, as well as the C- $\text{NO}_2$  stretching mode (near  $1145\text{ cm}^{-1}$ ) are considered in the following sections.

### C- $\text{NO}_2$ and Totally Symmetric $\text{NO}_2$ Stretching Modes

The anomalous pressure-dependent behavior of the C- $\text{NO}_2$  ( $\nu_{\text{C-N}}$ ) and totally

symmetric  $\text{NO}_2$  ( $\nu_{\text{NO}_2}$ ) stretching modes was first observed in static high pressure measurements by Satija and Swanson.<sup>5</sup> Briefly, the observed effects are as follows: (1) the C- $\text{NO}_2$  mode frequency increases in the usual manner as a function of pressure and the line width remains constant, (2) the  $\text{NO}_2$  mode frequency is nearly invariant up to 6 GPa while the line width increases from  $3.5\text{ cm}^{-1}$  at ambient pressure to a maximum of  $15\text{-}20\text{ cm}^{-1}$  near 5 GPa and then decreases as the pressure is raised further, (3) a dramatic reversal in the intensities of the two modes occurs at pressures of 4-6 GPa. These effects were attributed to pressure-enhanced coupling between  $\text{NO}_2$  and  $\text{NH}_2$  group motions, resulting in the nearly constant  $\text{NO}_2$  stretching mode frequency (i.e., the expected frequency increase in  $\text{NO}_2$  is canceled by increased  $\text{NO}_2/\text{NH}_2$  coupling that acts to drive the frequency lower). This phenomenon leads, in turn, to mixing of the  $\text{NO}_2$  and C- $\text{NO}_2$  modes as increased pressure draws the two frequencies closer together. Both the intensity reversal and the line width behavior of the  $\text{NO}_2$  mode are consistent with this explanation.

We observed similar effects in our earlier dynamic pressure study; however, the shock compression data indicated consistently larger shifts in the  $\text{NO}_2$  mode as a function of pressure and also less efficient mixing of  $\nu_{\text{C-N}}$  and  $\nu_{\text{NO}_2}$ .<sup>4</sup> Differences in the spectra seen under dynamic and static high-pressure conditions are consistent with inhibited  $\text{NO}_2/\text{NH}_2$  coupling due to the increased temperature under shock loading. This explanation is supported by the data acquired in the present study. Figure 3 shows Raman spectra in the  $1140\text{--}1220\text{ cm}^{-1}$  region under fully supported shock compression to pressures as high as 7.5 GPa. The subtly different mode behavior under dynamic vs. static high pressure conditions is again evident in these spectra. In particular, the less efficient mixing of the  $\text{NO}_2$  and C- $\text{NO}_2$  modes is reflected in the much narrower  $\text{NO}_2$  feature observed at 4.3 GPa ( $11\text{ cm}^{-1}$  vs.  $18\text{ cm}^{-1}$  for static high pressure).

The effects of elevated temperature alone are shown in Figure 4. A temperature increase drives the  $\text{NO}_2$  stretching mode to higher frequency (in agreement with the shock data)

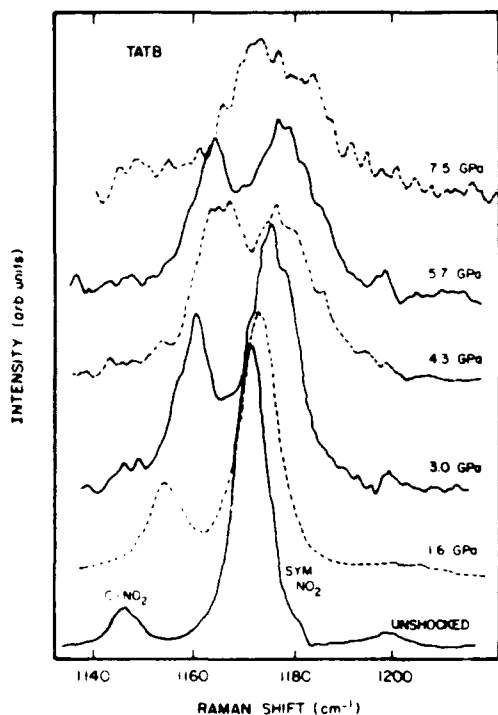


Figure 3. Raman Spectra (1140-1220  $\text{cm}^{-1}$  Region) of Shock-Compressed TATB. A spectrum of unshocked sample is shown for comparison.

while the C-NO<sub>2</sub> mode shifts slightly to lower frequency. Although the temperature-induced increase in separation between the modes is fairly small ( $\sim 3 \text{ cm}^{-1}$  at 500 K, cf. Figure 2), it is apparently sufficient to inhibit the pressure-enhanced mixing. In the shock compression data (Figure 3), the two features do appear to coalesce at pressure  $>6 \text{ GPa}$ . This phenomenon may reflect growing structural disorder in the molecule or possibly arises from a crossing or avoided crossing of  $\nu_{\text{C-N}}$  and  $\nu_{\text{NO}_2}$ . This effect in the TATB Raman spectrum was not evident in our earlier study.<sup>4</sup>

### NO<sub>2</sub> Deformation Mode

The effects of shock compression on the  $884 \text{ cm}^{-1}$  NO<sub>2</sub> deformation mode are illustrated in Figure 5. Observed changes in line width as a function of temperature alone are also shown in this figure. The negative Raman shift with increasing pressure is consistent with the static high pressure results of Satija and Swanson.<sup>5</sup> Opposite effects are seen, however, in the line width. Under static compression,

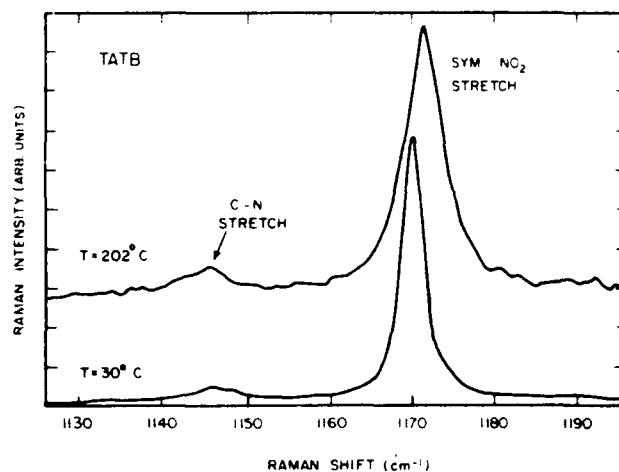


Figure 4. Raman Spectra (1130-1190  $\text{cm}^{-1}$  Region) of Unshocked TATB at Two Different Temperatures

the line width of this mode decreases by a factor of two as pressure increases to 8 GPa. The shock compression data indicate a substantial increase in the line width up to 5 GPa. The same trend is observed as a function of temperature alone. This correspondence suggests that temperature effects largely dominate the response of this mode to shock loading. This behavior possibly reflects changes in NH<sub>2</sub> group motions to which the NO<sub>2</sub> deformation mode is coupled. Studies of deuterated TATB under shock compression could resolve this issue.

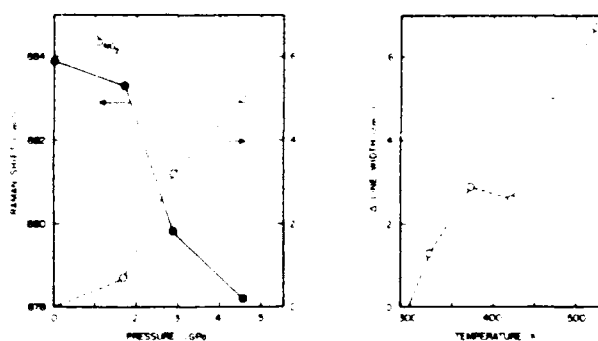


Figure 5. NO<sub>2</sub> Deformation Mode Properties as a Function of Shock Pressure (Left) and Temperature (Right). Raman shifts are shown as solid dots. Changes in line width are represented by open circles.

## NH<sub>2</sub> Stretching Mode

The frequency, band width and structure of a XH (X=O,N,...) stretching mode can provide much useful information about a hydrogen bonded system.<sup>11</sup> Unfortunately, the intensity of the XH stretch fundamental is generally very weak in the Raman spectrum. The NH<sub>2</sub> stretching mode in TATB is no exception to this rule and, as yet, we have not characterized the behavior of this mode using gas-gun driven shock compression. However, we have examined the response of the NH<sub>2</sub> stretch fundamental to elevated temperatures and we have obtained preliminary shock data using explosive drivers.

Figure 6 illustrates the effects of increased temperature on the NH<sub>2</sub> mode. Signal averaging was used to obtain these spectra from unshocked samples. The NH<sub>2</sub> band in the room-temperature spectrum is fairly broad (~37 cm<sup>-1</sup> FWHM) and is shifted >100 cm<sup>-1</sup> below the comparable mode for a simple amine. These effects are direct results of the extensive hydrogen bonding network in TATB. Empirical relationships between the stretching frequency and the hydrogen bond distance in crystals have been established<sup>12,13</sup> and the peak band intensity near 3220 cm<sup>-1</sup> implies a hydrogen bond length near 2.96 Å. This predicted bond length is in good agreement with the known range of inter-molecular N-H...O lengths (2.93-2.995 Å) in the crystal structure.<sup>6</sup> The fairly wide range of hydrogen bond lengths undoubtedly contributes to the broad band width of the NH<sub>2</sub> mode. Increasing temperature leads to a large positive Raman shift (>15 cm<sup>-1</sup> at 550 K) and pronounced broadening (to ~60 cm<sup>-1</sup> at 550 K). Clearly, a primary effect of elevated temperature is a weakening of the hydrogen bonding network in TATB. Using the simple frequency-bond distance relationship derived by Bellamy and Owens,<sup>13</sup> a shift of 15 cm<sup>-1</sup> implies an increase in the N-H...O bond distance of approximately 0.02 Å. Considering the large number of individual N-H...O bonds in TATB, an average increase of this amount may appreciably diminish the stabilizing influence of the network. The pronounced broadening at high temperatures likely indicates rapidly increasing structural disorder.

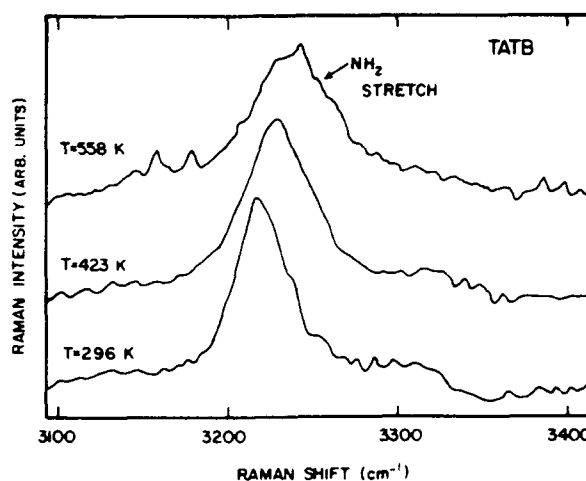


Figure 6. Raman Spectra (3100-3400 cm<sup>-1</sup> Region) of Unshocked TATB at Three Different Temperatures

An alternative method of examining the NH<sub>2</sub> mode is to use infrared (IR) absorption spectroscopy. The NH<sub>2</sub> stretch fundamental is very strong in the IR spectrum. Using time-resolved infrared spectral photography (TRISP),<sup>14,15</sup> we have obtained IR absorption spectra for thin-film (~2 µm) samples of TATB.<sup>16</sup> The response of the symmetric and antisymmetric NH<sub>2</sub> modes to elevated temperature is shown in Figure 7. As expected, the observed trends are essentially identical to those seen using Raman spectroscopy.

As Figure 8 shows, the behavior of the NH<sub>2</sub> mode under low-amplitude shock compression is very different. Modest shock pressures lead to a negative Raman shift, indicating a pressure-induced enhancement of the hydrogen bonding network. As pressure increases to 3 GPa, the negative shift in this mode appears to "stall." This may indicate that temperature is beginning to play an important role and drive the mode to higher frequency. In shots above 3 GPa, we were unable to distinguish the NH<sub>2</sub> mode from the background.

Overall, the shock-compression and high-temperature results suggest that pressure and temperature act as opposing forces with respect to the hydrogen bonding network. In analyzing these effects, it is difficult to characterize adequately temperatures in our

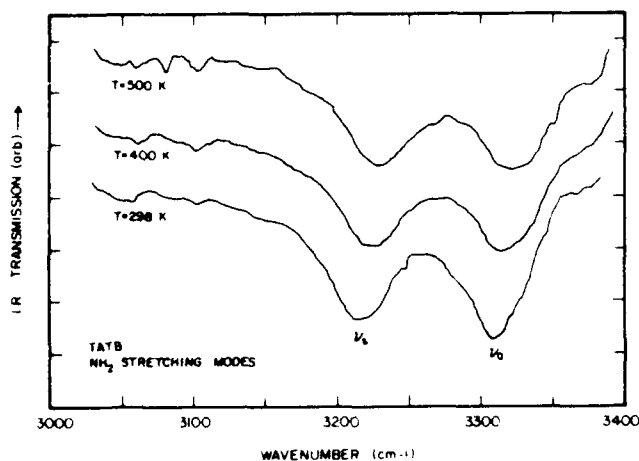


Figure 7. TRISP Spectra (3025-3400  $\text{cm}^{-1}$  Region) of Unshocked TATB at Three Different Temperatures. For visual clarity, the baselines are shifted vertically along an arbitrary axis.

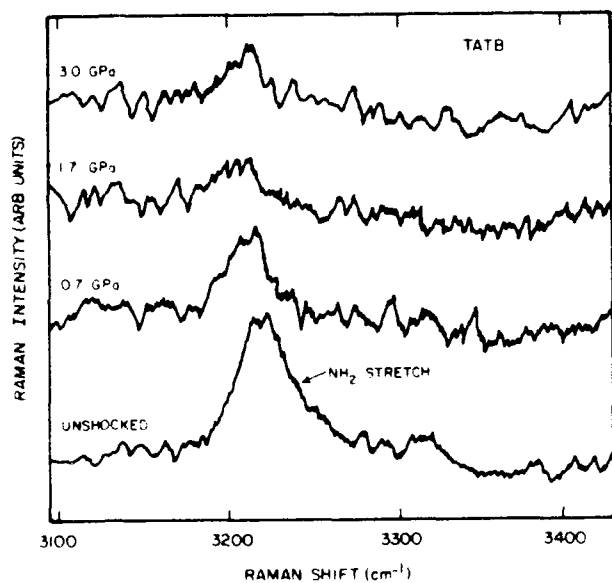


Figure 8. Raman Spectra (3100-3400  $\text{cm}^{-1}$  Region) of Shock-Compressed TATB. A spectrum of unshocked sample is shown for comparison. For these data, shocks were generated by an explosive driver/buffer and pressures estimated from particle velocity measurements in parallel experiments.

experimental system. Since the dynamic pressures achieved in our experiments are the result of two-step shock loading, the temperatures will be lower than in a single-step

process. Moreover, temperature calculations based on a homogeneous shock-compressed state do not account for effects of local heating that occur in porous samples. Nevertheless, it is instructive to consider the expected pressure-temperature relationship in TATB subjected to a single shock. Figure 9 shows calculated temperatures for TATB of various densities as a function of shock pressure. This plot compares temperatures calculated from the equation-of-state formulation of Pastine and Bernecker<sup>17</sup> with calculations based on a formulation for the Helmholtz free energy of solid TATB similar to that used by Sheffield et al.<sup>18</sup> for HNS. Both sets of calculations show that the temperature rise in the bulk material corresponding to shock pressures up to 3-4 GPa is likely to be fairly modest. The  $\text{NH}_2$  band behavior indicates that the combination of moderate shock pressures and relatively low temperatures may actually stabilize the molecule against decomposition; however, larger temperature increases corresponding to higher shock pressures (Figure 9) will weaken the

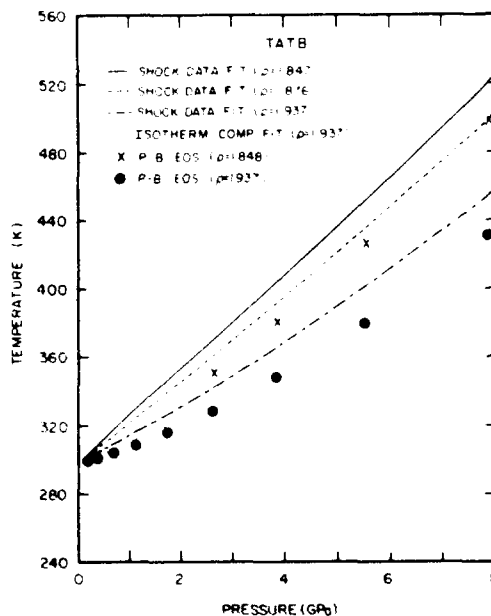


Figure 9. Calculated Temperatures for TATB of Various Densities as a Function of Shock Pressure. Solid dots and X's are taken from Reference 17. Broken and solid lines show calculated temperatures using methods similar to those described in Reference 18. Equation of state parameters were derived from isothermal compression and shock data.<sup>19,20</sup>

hydrogen bonding network and promote reaction. In this manner, the competing effects of pressure and temperature may dictate the shock initiation threshold for TATB.

## SUMMARY

Using pulsed-laser-excited Raman spectroscopy, we have obtained records of vibrational frequency shifts and line shape changes under fully supported and well controlled shock compression of TATB at a window interface. These results have been compared to complementary data for unshocked TATB at elevated temperatures. Several modes associated with the nitro and amino groups in TATB exhibit anomalous behavior under shock compression which can be largely resolved into competing pressure and temperature effects. In particular, studies of the  $\text{NH}_2$  stretching mode show that hydrogen bonding in TATB is enhanced at modest dynamic pressures; however, elevated temperature promotes the opposite trend. These effects correlate directly with the relative insensitivity of TATB to shock initiation. Techniques that can improve our understanding of these phenomena include careful examination of low-frequency modes, spectroscopic studies of homologous compounds (i.e., trinitrobenzene, monoaminotrinitrobenzene, etc.) and studies utilizing isotopic substitution. Data from these studies should provide significant input for models of molecular energetics and dynamics under shock compression.

## ACKNOWLEDGMENTS

This work was performed at Sandia National Laboratories supported by the U. S. Department of Energy under Contract DE-AC04-76DP00789. The authors gratefully acknowledge the fine technical assistance of H. C. Richardson and J. C. Miller. Special thanks are extended to Dr. Basil Swanson of Los Alamos National Laboratory for sharing the results of the static high pressure study of TATB.

## REFERENCES

1. Schmidt, S. C.; Moore, D. S.; and Shaner, J. W., "Diagnostics for Determining Phenomenology of Condensed-Phase Shock-Compressed Molecular Systems," *Los Alamos National Laboratory Report*, LA-UR 83-901, March 1983.
2. Trott, W. M. and Renlund, A. M., "Single-Pulse Raman Scattering Studies of Heterogeneous Explosive Materials," *Appl. Optics*, Vol. 24, 1985, p. 1520.
3. Renlund, A. M. and Trott, W. M., "Spectroscopic Studies of Shocked and Detonating Explosives," *Proc. 5th Am. Phys. Soc. Topical Conf. on Shock Waves in Condensed Matter*, S. C. Schmidt and N. C. Holmes, Eds., North Holland, Amsterdam, 1988, p. 547.
4. Trott, W. M. and Renlund, A. M., "Single-Pulse Raman Scattering Study of Triaminotrinitrobenzene (TATB) Under Shock Compression," *J. Phys. Chem.*, Vol. 92, 1988, p. 5921.
5. Satija, S. K. and Swanson, B. I., *J. Phys. Chem.*, in press.
6. Cady, H. H. and Larson, A. C., *Acta Cryst.*, Vol. 18, 1965, p. 485.
7. Marsh, S. P., Ed., "LASL Shock Hugoniot Data," U. California Press, Berkeley, CA, 1980.
8. Wise, J. L. and Chhabildas, L. C., "Laser Interferometer Measurements of Refractive Index in Shock-Compressed Materials," *Proc. 4th Am. Phys. Soc. Topical Conf. on Shock Waves in Condensed Matter*, Y. M. Gupta, Ed., Plenum Press, New York, 1986, p. 441.
9. Krishnan, R. S., in *The Raman Effect*, Volume 1, Anderson, A., Ed., Marcel Dekker, Inc., New York, 1971, pp. 30-31. Sherman, W. F. and Wilkinson, G. R., *Advances in Infrared and Raman Spectroscopy*, Vol. 6, Heyden and Son, Philadelphia, PA, 1980, pp. 158, 200-205.
10. Rogers, J. W., Jr.; Peebles, H. C.; Rye, R. R.; Houston, J. E.; and Binkley, J. S., "A Carbon Auger Lineshape Study of Nitroaromatic Explosives," *J. Chem. Phys.*, Vol. 80, 1984, p. 4513. Ayres, J. N., Montesi, L. J., Bauer, R. J., Naval Ordnance Laboratory Report, NOLTR 73-132, White Oak, Silver Spring, MD, 1973.

11. Hadzi, D. and Bratos, S., "Vibrational Spectroscopy of the Hydrogen Bond," *The Hydrogen Bond*, P. Schuster, G. Zundel and C. Sandorfy, Eds., North Holland, Amsterdam, 1976, p. 567.
12. Nakamoto, K.; Margoshes, M.; and Rundle, R. E., "Stretching Frequencies as a Function of Distances in Hydrogen Bonds," *J. Amer. Chem. Soc.*, Vol. 77, 1955, p. 6480.
13. Bellamy, L. J. and Owen, A. J., "A Simple Relationship Between the Infrared Stretching Frequencies and the Hydrogen Bond Distances in Crystals," *Spectrochimica Acta*, Vol. 25A, 1969, p. 329.
14. Avouris, Ph.; Bethune, D. S.; Lankard, J. R.; Ors, J. A.; and Sorokin, P. P., "Time-Resolved Infrared Spectral Photography: Study of Laser-Initiated Explosions in  $\text{HN}_3$ ," *J. Chem. Phys.*, Vol. 74, 1981, p. 2304.
15. Renlund, A. M.; Sheffield, S. A.; and Trott, W. M., "Time-Resolved Infrared Spectral Photography Studies of Shock-Induced Chemistry in  $\text{CS}_2$ ," *Proc. 4<sup>th</sup> Am. Phys. Soc. Topical Conf. on Shock Waves in Condensed Matter*, Y. M. Gupta, Ed., Plenum Press, New York, 1986, p. 237.
16. Skocypec, R. D. and Erickson, K. L., "Time Resolved Mass Spectrometry Technique for Studying Fast Transient CHNO Explosive Decomposition Kinetics," *Proc. 9th Symp. (International) on Detonation*, in press.
17. Pastine, D. J., and Bernecker, R. R., "P,v,E,T Equation of State for 1,3,5-triamino-2,4,6-trinitrobenzene," *J. Appl. Phys.*, Vol. 45, 1974, p. 4458.
18. Sheffield, S. A.; Mitchell, D. E.; and Hayes, D. B., "The Equation of State and Chemical Kinetics for Hexanitro-stilbene (HNS) Explosive," *Proc. 6th Symp. (International) on Detonation*, Office of Naval Research ACR-221, Arlington, VA, 1976, p. 748.
19. J. R. Kolb and H. F. Rizzo, "Growth of 1, 3,5-triamino-2,4,6-trinitrobenzene," *Propellants and Explosives*, Vol. 4, 1979, p. 10.
20. Gibbs, T. R. and Popolato, A., Eds., *LASL Explosive Property Data*, U. California Press, Berkeley, CA, 1980, p. 152.

## DISCUSSION

**HAROLD J. GRYTING**  
Gryting Energetics Sciences Co.  
San Antonio, TX

What role does hyperconjugation play (i.e., the tendency for hydrogen attached to an element such as carbon or nitrogen which is attached to a benzene ring or other conjugated system to lose electrons to the conjugated system—thus enhancing the conjugative behavior and stability of the TATB)?

## REPLY BY W. M. TROTT

The role of amino groups as electron donors in TATB has been examined in detail by Rogers, et al. (cf. Reference 10). The important effects are (1) destabilization of ring bonding due to overpopulation of the pi levels in the ring and (2) polarization of the molecule which leads to formation of the strong intra- and intermolecular hydrogen bonding network. The latter effect appears to be dominant in terms of the sensitivity of TATB to shock initiation. Shock- or temperature-induced changes in the strength of the H-bonding network are reflected in the vibrational spectrum of TATB, as shown in the present study.



# LASER IGNITION OF EXPLOSIVES: A MASS SPECTROSCOPIC STUDY OF THE PRE-IGNITION REACTION ZONE

H. Östmark and H. Nilsson  
Swedish Defence Research Establishment  
S-102 54 Stockholm, SWEDEN

*By combining a laser ignition technique with mass spectroscopic analysis, we have developed a way of rapid determination of some of the molecules which are involved in the thermal ignition process of a high explosive. This technique enables the study of how parameters such as initial gas pressure (0.1 - 2.5 MPa), laser pulse width (1 ms - 1 s), and laser power (0 - 250 W) influence the major decomposition products ( $N_2O$ ,  $HCN$ ,  $NO_2$ ,  $H_2CO$ ,  $CO_2$ ) in the reaction zone. It also enables the detection of some of the larger molecule fragments involved in the ignition process. The results in this paper are mainly for RDX, but some results are presented also for HNS, PETN, TNT, and Tetryl. For RDX we have shown that the ignition process is a multi-phase reaction.*

## INTRODUCTION

Earlier studies of laser ignition have shown that this is a very useful method for studying the ignition parameters for pyrotechnic mixtures.<sup>1,2</sup> This method applied to high explosives (HE) showed that the ignition energy is highly pressure-dependent.<sup>1,3</sup> Similar results have been demonstrated for propellants<sup>4</sup> and for pyrotechnics.<sup>5</sup> Results for laser initiation of detonations in PETN have shown a strong gas phase influence.<sup>6</sup> This indicates that the ignition process is a multi-phase problem. Present work shows how mass spectroscopy (MS) and capillary gas chromatography (GC) combined with the laser ignition method can be used to study the pre ignition reaction zone, and how it is possible to follow the transition from slow thermal decomposition to a self sustaining deflagration. This method alone cannot give a very detailed description, due to the limited time and spatial resolution of the ignition process. It will, however, with relative ease, give some of the molecular fragments that are involved in the process. These can then be studied with other spectroscopic methods with better time resolution, e.g., Laser Raman Spectroscopy,<sup>7</sup> LIF, or CARS spectroscopy. The combined method will also give a clue to the ignition process on a

molecular scale, due to the fact that it allows the study of how the concentration of certain molecules varies with different parameters (e.g., gas pressure, pulse width, and laser power).

Figure 1 shows how the ignition energy depends on the gas pressure and the type of gas (from Reference 3). The figure clearly demonstrates why it is necessary to have the possibility to study the ignition at pressures of up to at least 4 MPa.

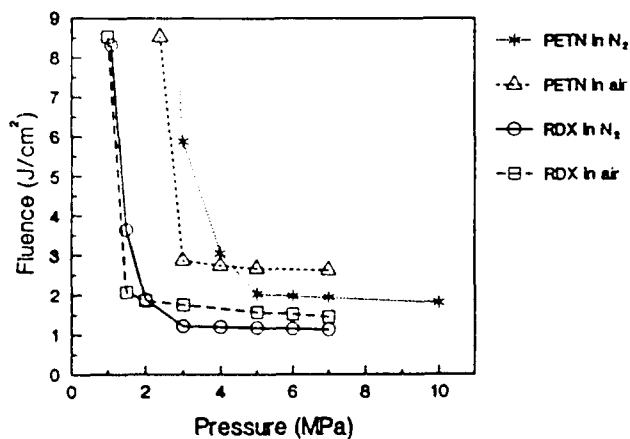


Figure 1. Ignition Energy as a Function of Pressure (from Reference 3)

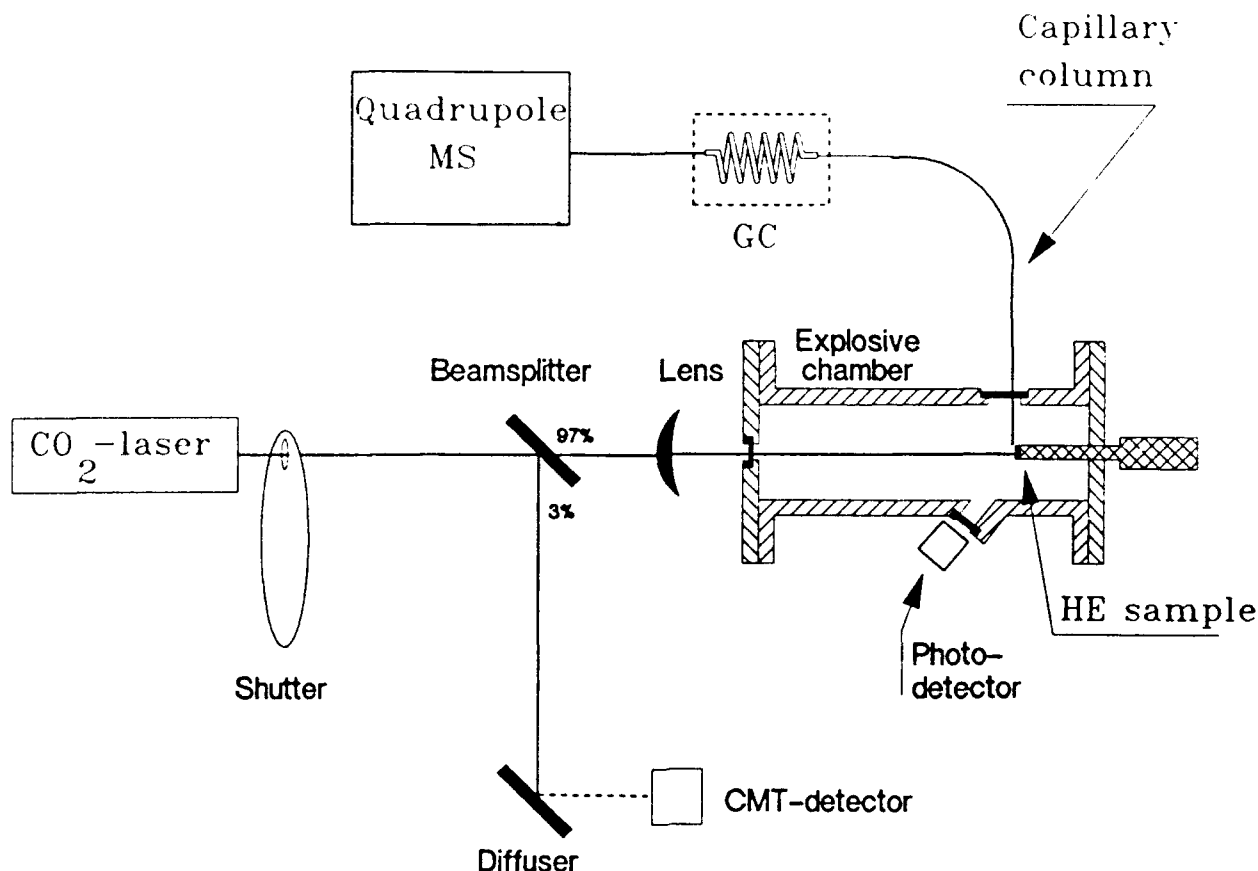


Figure 2. Experimental Setup

## EXPERIMENTAL

The laser ignition method is fully described in earlier work.<sup>1-3</sup> The experimental setup for LI/MS (Laser Ignition/Mass Spectrometry) is shown in Figure 2. It consists mainly of a 300W cw CO<sub>2</sub> laser (Coherent CR41) and a gas chromatograph/mass spectrometer (Finnigan 1020). About 300 mg of HE (technical quality) was pressed to a pellet with a diameter of 10 mm and a thickness of 2 mm. The density of the pellet was 95 percent of TMD. The pellet was glued onto a sample holder in the explosive chamber. The sample holder was rotated for each laser pulse so that unreacted explosive was exposed to the laser beam. The capillary was connected to the explosive chamber by a capillary feed through and put in position by a fixture. The position of the capillary in the reaction zone had a large influence on the result. If the capillary was slightly "out of focus" the number of counts decreased rapidly and the distribution of

counts between the different mass peaks changed. During experiments where self-sustained deflagration occurred, it proved necessary to move the capillary to a distance of c. 2 mm from the focus and from the sample surface since the capillary otherwise melted. The interface between the reaction zone and the mass spectrometer was a deactivated (and therefore "nearly" chemically inert) fused silica capillary ( $\phi = 0.1 - 0.25$  mm) which was 3 - 30 m long.

The use of a capillary column enabled us to use pressures of up to 2.5 MPa in the explosive chamber and thereby study the influence of the pressure on the chemical reaction. Most of the experiments were carried out in a helium atmosphere. Helium is a mono atomic gas and thus does not react with radicals. That gives us a greater possibility to observe them. The use of helium also minimizes the background in the mass spectrometer. By varying the laser power, and the laser pulse width acting on the

HE, it was possible to control the degree of reaction from a very weak decomposition to a strong deflagration. By connecting a capillary GC between the reaction zone and the mass spectrometer, it proved possible, to some degree, to separate the decomposition/deflagration products, especially those with the same mass numbers (e.g., NO/H<sub>2</sub>CO). The other main advantage of using a capillary column before the mass spectrometer is that it becomes possible to study the ignition process at a pressure which is relevant to normal ignition conditions. The mass spectrometer has a maximum sweep speed of 1600 amu/s which gives a possibility to obtain real time measurements of the ignition process. (The real time measurements are to some degree corrupted by the fact that even a chemically deactivated column has different retention times for some molecules.) The time resolution when acquiring full scans (100 - 200 amu) is 0.1 s. By using the technique of selective ion monitoring, it was possible to get down to a time resolution of below 10 ms.

## RESULTS

The results given in this paper mainly derive from studies of RDX, but the following high explosives have been tested: HMX, Tetryl, PETN, TNT, and HNS. Figure 3 shows a typical RIC (Reconstructed Ion Chromatogram) curve from the reaction zone. The measurement parameters for obtaining this curve were: HE RDX; laser power 60 W on 0.5 mm<sup>2</sup>; pulse width 2 ms; capillary column (0.2 mm x 6 m); pressure 0.25 MPa; and a mass range from 10 - 90 amu in 0.1 s. In this case, two peaks may be seen, but one to five peaks have been found, dependent on the HE and the measurement conditions.

By plotting the intensities of some of the most interesting masses time resolved, see Figure 4 (same shot as in Figure 3), some interesting observations can be made. Peak group one consists of at least 2 different peaks. In this case, it proved to be due to different retention times in the column. Peak group two consists mainly of the two mass peaks, m/e 42 and m/e 46, and derives probably from a molecule with mass 88.<sup>8</sup> This indicates that part of the decomposition occurs in the gas phase as a ring opening process. The mass peak

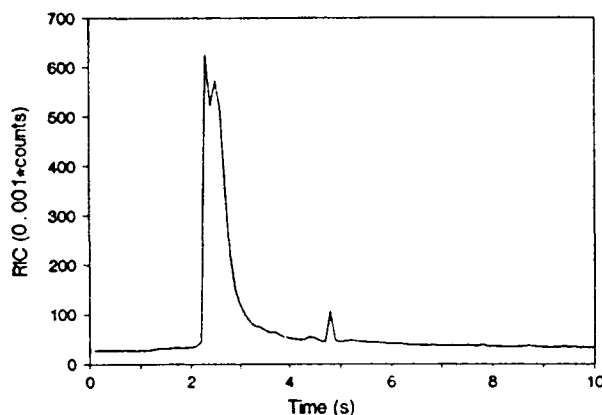


Figure 3. RIC Spectra for RDX (Pre-Ignition Reaction)

m/e 81 (which is determined by the simultaneous occurrence of mass peak m/e 54) could be identified as 1,3,5-Triazin. The formation of triazine implies that the reaction to some extent occurs in the solid or the liquid phase as a loss of side groups with the ring remaining intact.<sup>8</sup>

In order to assign the detected mass peaks to different molecules, different approaches were used. By varying the column length, some of the molecules could be separated by different retention times. We were mainly interested in shortening the column, in order to try for also relatively short-lived molecules. This approach worked best for larger molecules with a mass over 50. For the main decomposition products (N<sub>2</sub>O, NO, NO<sub>2</sub>, N<sub>2</sub>, CO<sub>2</sub>, HCN, and CO) we used the fragmentation pattern of the molecules, which is caused by the ionization in the mass spectrometer, to identify these (Table 1).

Table 1. Reference Mass Spectra for the Main Decomposition Products (from Reference 9)

Substance	Main Mass Peaks (Mass Number/Abundances)					
NO	30/100	14/7.5	15/2.4	16/1.5		
NO <sub>2</sub>	30/100	46/37	16/22.3	14/9.6		
CO <sub>2</sub>	44/100	28/6.6	16/6.2	12/2.5		
CO	28/100	12/4.7	16/1.7	29/1.2		
H <sub>2</sub> CO	29/100	30/88.5	28/30.9	14/4.4	13/4.3	12/3.3
N <sub>2</sub> O	44/100	30/31.3	14/12.9	28/10.8	16/5.0	
HCN	27/100	26/16.8	25/4.2			

By varying the laser power and recording the variation in intensity of the mass peaks of the decomposition products, it was possible to study the change in the products from the decomposition to a self-sustained deflagration. In Figure 4, the intensity for selected mass peaks is shown as a function of the laser power. The measurement conditions were: column length 15 m; column diameter 0.1 mm; pressure 0.6 MPa; pulse width 2.5 ms; and a radiated surface of 0.5 mm<sup>2</sup>. Some interesting conclusions can be drawn from this figure: The N<sub>2</sub>O (which is recognized by mass peaks 30 and 44 in the ratio 1 to 3, see Table 1) increases approximately linearly for powers of up to 80 - 90 W and is the main product (of the molecules detectable with this column length) over the interval. Above this power level increasing amounts of HCN (mass peaks 26 and 27) and CO<sub>2</sub> (mass peak 44) are generated. Along with data shown in the figure, one interesting observation was made: the concentration of H<sub>2</sub>CO (determined by m/e 29, cf. Table 1) is very low (c. 1000 counts) at power levels below 100 W.

Table 2 is a compilation of the total collected information on products in the pre-ignition reaction zone of RDX. The total data volume were 15 Mb. The table is divided into four parts: mass number (m/e), possible assignment, strength (in a scale from 1 to 4, where 1 is very strong and 4 is just above the background), and comments. Substances that could be identified are shown with the masses they were identified by as one row. Observe especially the strong peak with m/e 70.

Rauch and Fanelli<sup>10</sup> and Bradley et al.,<sup>8</sup> have shown that NO<sub>2</sub> mainly derives from a gas phase decomposition and that H<sub>2</sub>CO and N<sub>2</sub>O arise from a liquid phase decomposition. From this, from the data in Figures 4 and 5, and from the observation that the amount of H<sub>2</sub>CO increases and the amount of NO<sub>2</sub> decreases as the laser pulse width (or possibly the energy) increases, we can draw the conclusion that the ignition of RDX is a multi-phase reaction. The gradual transition of the reaction from gas to condensed phase, indicated by the

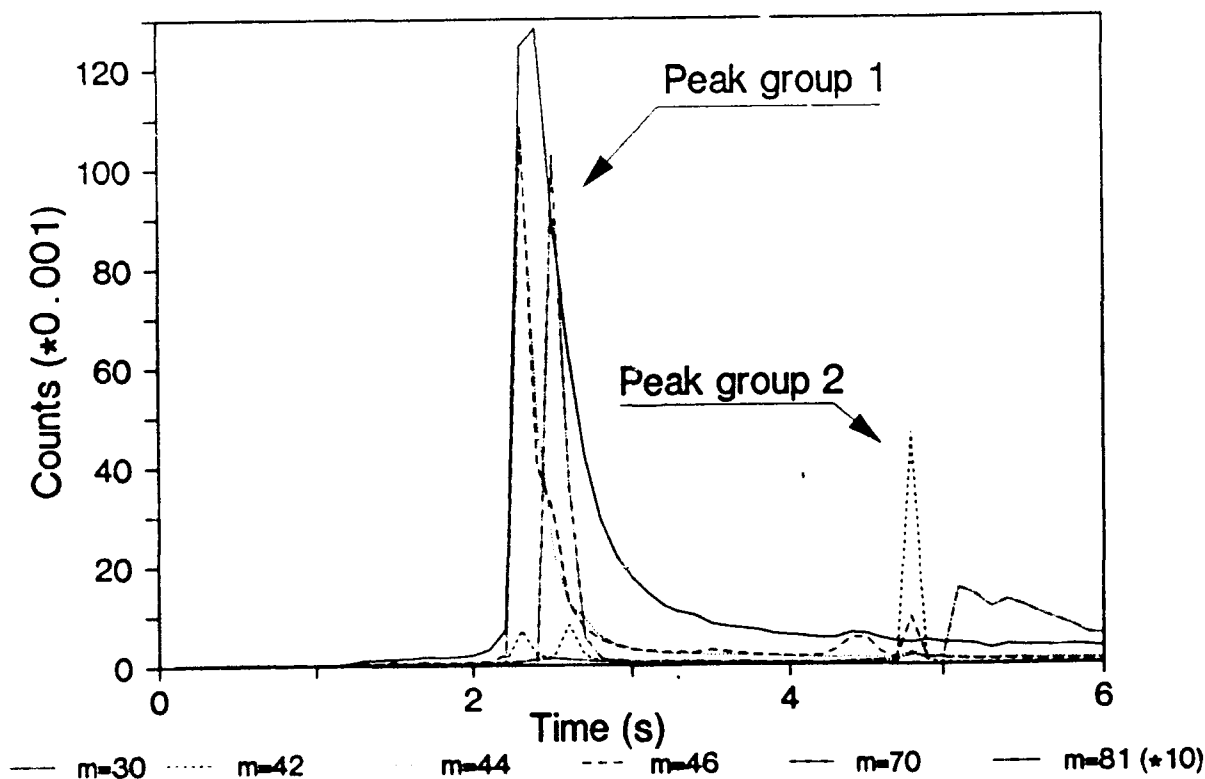
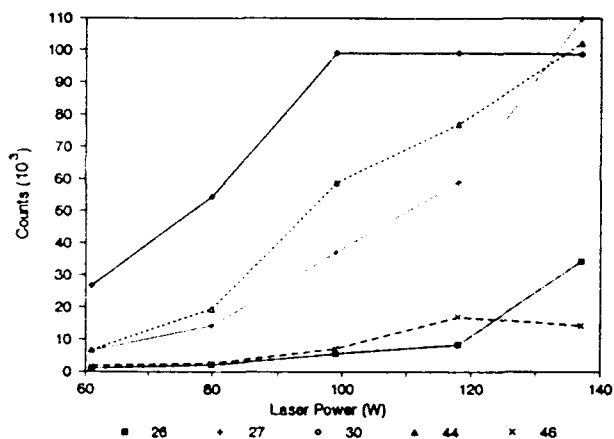


Figure 4. Time Resolved Mass Spectra for RDX Decomposition (Selected Masses)

**Table 2. Products in the Pre-Ignition Reaction Zone for RDX**

Mass Number	Assignment	Strength	Comments
17/18	H <sub>2</sub> O	1	
26	CN	2	
26/27	HCN	1	Cf. Fig. 5
27		1	
28	N <sub>2</sub> , CO	1	
29	HCO	1	
29/30	H <sub>2</sub> CO	1-3	Increases strongly with laser energy!
30	(NO)	1	See Table 1
31		3	
40		2	
41		2	
42	N(CH <sub>2</sub> )N, (CH <sub>2</sub> ) <sub>2</sub> N	2	
42/46	(CH <sub>2</sub> ) <sub>2</sub> NNO <sub>2</sub>	2	Indicates ring opening in gas phase!
43		1	
44	N <sub>2</sub> O, CO <sub>2</sub>	1	Cf. Fig. 5 and Table 1
46	NO <sub>2</sub> , (HCOOH)	1	
52		2	
54/81	C <sub>3</sub> N <sub>3</sub> H <sub>3</sub> (1,3,5-Triazine)	3	Solid phase decomposition reaction
61/60/46/45	CH <sub>3</sub> NO <sub>2</sub> (Nitromethane)	2	
61		3	
64/91/119	C <sub>6</sub> H <sub>5</sub> N <sub>3</sub> (Azidobenzene)	4	Occurs only at pressures above 0.5 MPa
70	Oxadiazole	1	Heaviest of the stronger peaks
76		3	
91		4	
95		4	

increase of H<sub>2</sub>CO and the decrease of NO<sub>2</sub> as the laser pulse width (or possibly the energy) increases, together with the facts stated above, tells us that the gas phase reactions play an important part in the ignition process, at least at pressures below 2 MPa. It is necessary to examine these reactions at pressures above



**Figure 5. Peak Intensity as a Function of Laser Power (Selected Mass Peaks)**

3 MPa, where a break in the curve for ignition energy occurs (see Figure 1), in order to get a complete understanding of the processes involved. Figure 1 is for a laser pulse width of 1.2 ms.

Figure 6 shows the time resolved mass spectra for some of the most interesting masses in the reaction zone of Tetryl. In these spectra, one can distinguish at least five peaks. The spectra are interpreted as follows: The first peak is for the main decomposition products which consist of relatively small molecules with short retention times. The second to fifth peaks are for larger molecules with longer retention times. These molecules are probably the important ones, as they can tell us which is the first step of the reaction. The mass spectra for peaks one and four are given in Figures 7 and 8. The measurement parameters for obtaining these spectra were: laser power 60 W on 0.5 mm<sup>2</sup>; pulse width 2 ms; capillary column (0.2 mm x 6 m); pressure 0.4 MPa; and a mass range of 12 - 300 amu in 0.2 s.

The decomposition of HNS gave rise to only two detectable peaks in the time resolved spectra (see Figure 9) and very few mass peaks (namely 28, 30, and 44) in the first peak (main decomposition products). Mass spectra for the two peaks are shown in Figures 10 and 11. The measurement parameters for obtaining these spectra were: laser power 60 W on 0.5 mm<sup>2</sup>; pulse width 2 ms; capillary column (0.2 mm x 6 m); and a mass range from 12 - 300 amu in 0.2 s.

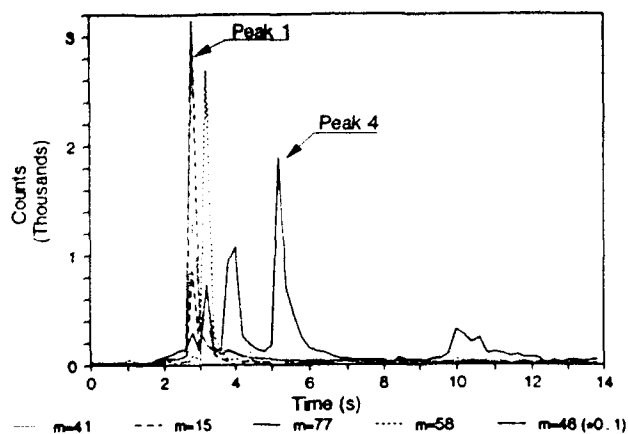


Figure 6. Time Resolved Mass Spectra for Decomposition of Tetryl

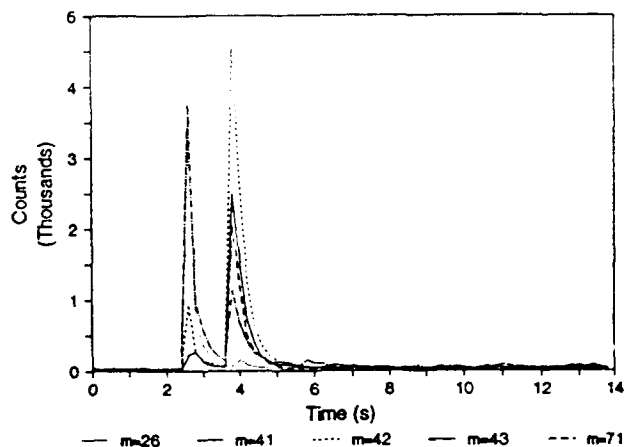


Figure 9. Time Resolved Mass Spectra for HNS Decomposition (Selected Masses)

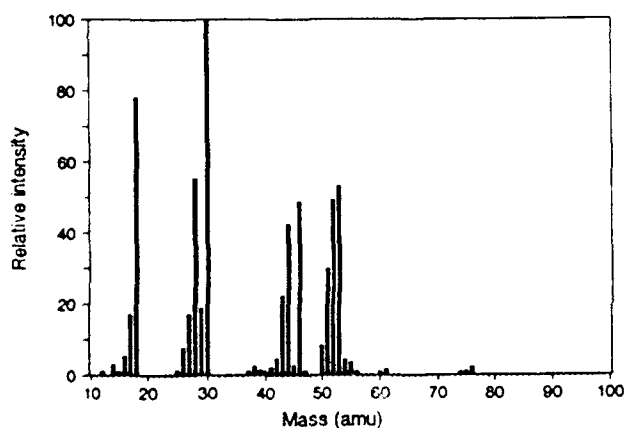


Figure 7. Mass spectrum for Tetryl: Peak One

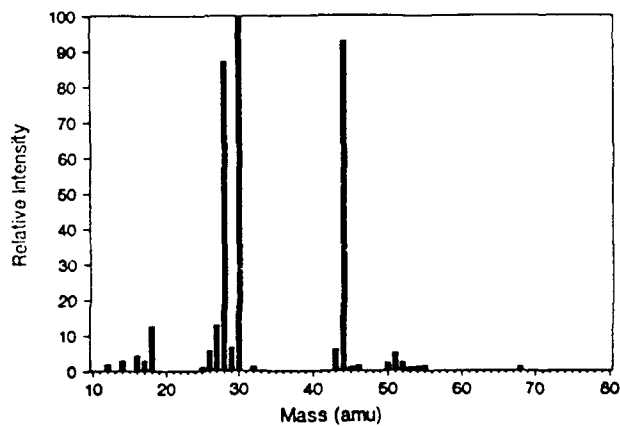


Figure 10. Mass Spectrum for HNS: Peak One

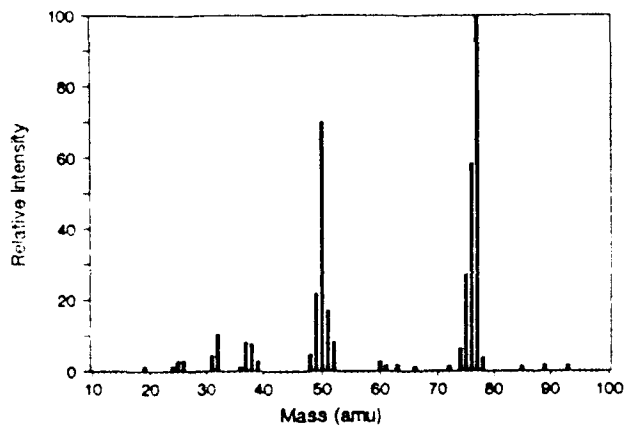


Figure 8. Mass Spectrum for Tetryl: Peak Four

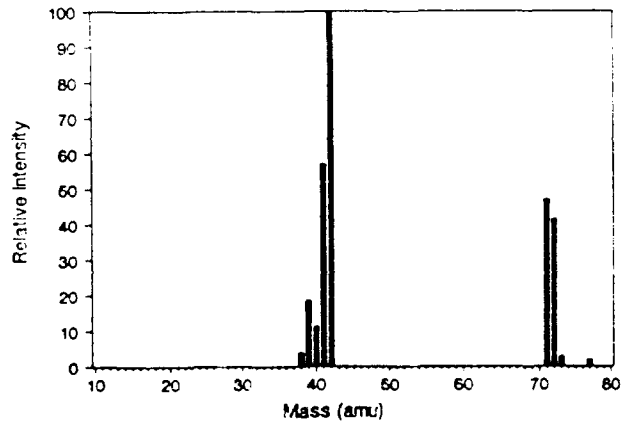


Figure 11. Mass Spectrum for HNS: Peak Two

The decomposition of PETN gave rise to three peaks in the time resolved spectra (see Figure 12). Mass spectra for the first and third peak are shown in Figures 13 and 14. The measurement parameters for obtaining these spectra were: laser power 60 W on 0.5 mm<sup>2</sup>; pulse width 2 ms; capillary column (0.2 mm x 6 m); and a mass range from 12 - 250 au in 0.1 s.

In the pre-ignition reaction zone of TNT a lot of gas phase TNT could be observed in conjunction with the main decomposition products.

The spectra for HMX were very much like those for RDX with one notable difference: a large mass peak at 26 (CN!?) was found which could not arise from HCN (no mass peak at 27).

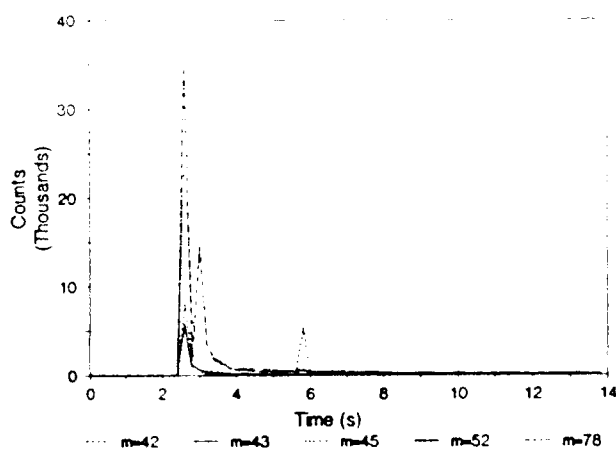


Figure 12. Time Resolved Mass Spectra for PETN Decomposition

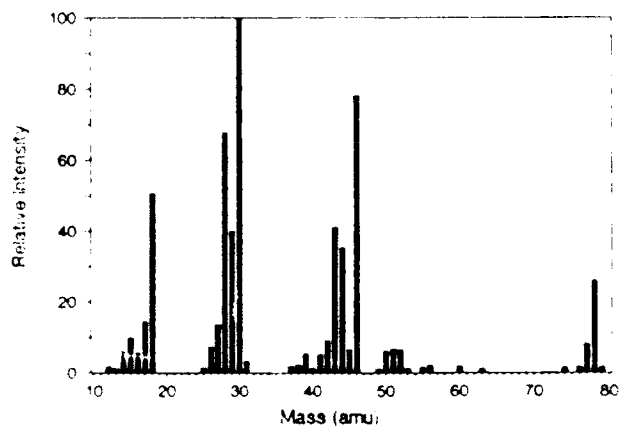


Figure 13. Mass Spectrum for PETN Peak One

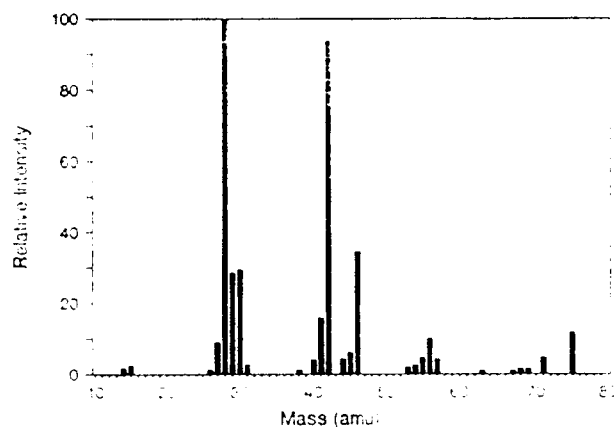


Figure 14. Mass Spectrum for PETN: Peak Three

## DISCUSSION

The combined laser ignition/mass spectroscopy method gives advantages over the pyrolysis/MS studies in other works<sup>11,12</sup> because it enables us to follow the transition from a slow thermal decomposition to a self-sustained deflagration. Thus, we get a better understanding of the ignition process and may also be able to model it mathematically. The method alone cannot reveal the whole truth about the ignition processes, but it can give some clues to it. In particular, it gives, in a relatively easy way, some of the molecule fragments involved in the ignition process. These may then be studied with other techniques, e.g., laser spectroscopic methods, with a better resolution in time and space. The molecule fragments must have a lifetime greater than the transition time in the capillary in order to be detected. The most interesting results were obtained with the shortest column, most mass peaks were detected here. But in order to start a self-sustained reaction, a very long column was necessary due to the need for high initial pressures.

The laser ignition method itself offers a way to a purely thermal start of a reaction (hereby getting rid of any mechanical and chemical disturbance of the reaction and the measurement of the processes). This does not, however, mean that the ignition process is the same for a laser ignition as for an ignition occurring in a fire, for instance; but they are probably very closely related, so that one can

use the results obtained with this method to draw conclusions valid at least for cases with the same time scale (1 ms - 1 s), i.e., all thermal ignition in practice.

The combined LI/MS method has two drawbacks, which also affect the results and conclusions of this work: The time resolution is limited (10 - 100 ms in this paper) and so is the mass number resolution (here 1 amu). Both of these factors could preferably be improved on.

We have had difficulties in separating the delay of the occurrence of molecules in the reaction zone from the delay caused by the retention time of the capillary. Other difficulties involve the separation of the fragmentation incurred by the decomposition process from the fragmentation taking place in the mass spectrometer.

## CONCLUSIONS

This paper is mainly a description of the combined method, LI/MS, but we also report some interesting results obtained with it.

- The ignition of RDX is a multi-phase reaction (gas phase and condensed phases).
- HCN and H<sub>2</sub>CO play important parts in the ignition process of RDX. The relative amounts of these molecules increase with increasing energy/power.
- The LI/MS method is useful for parametric studies of the ignition process.
- It is possible to detect and record mass spectra for large molecules or molecule fragments ( $m/e > 60$ ) found in the pre-ignition reaction zones of RDX, HMX, Tetryl, HNS, and PETN.

## COMMENT

There is no scientific agreement concerning the decomposition reactions occurring in the solid and liquid phase of RDX. We, therefore, present some additional results supporting the existence of a condensed phase reaction in the pre-ignition reaction zone.

In Figure 15, the time delay (i.e., time between the first peak,  $m/z$  28, and peak  $m/z$  70) for mass peak 70 is shown as a function of the laser pulse width. These measurements were made under otherwise constant conditions which implies that we have here a time-dependent process which gives the  $m/z$  70 fragment. The time is of an order of magnitude that could only arise from a condensed phase reaction. The  $m/z$  70 peak is probably an oxadiazole.

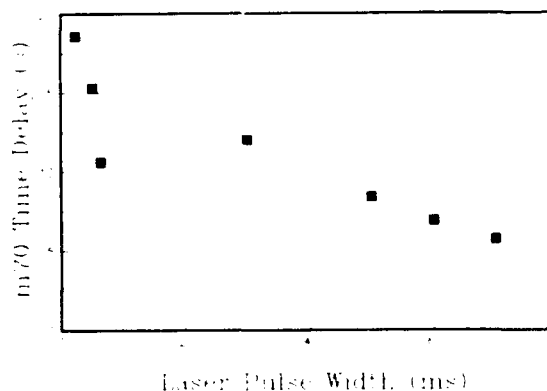


Figure 15. Time Delay for Mass Peak 70 Vs. Laser Pulse Width

## REFERENCES

1. Östmark, H., "Laser as a Tool in Sensitivity Testing of Explosives," *Proceedings of the Eighth Symposium (International) on Detonation*, Albuquerque, NM, 15-19 Jul 1985, pp. 473-484.
2. Östmark, H., "Laser Ignition of Explosives: Ignition Energy Dependence on Particle Size," *3e Congrès International de Pyrotechnie du Groupe de Travail de Pyrotechnie Spatial and 12th International Pyrotechnics Seminar*, Juan-les-Pins, France, Jun 1987, pp. 241-245.
3. Östmark, H. and Gräns, R., "Laser Ignition of Explosives: Effects of Gas Pressure on the Threshold Ignition Energy," submitted to *J. Energ. Mat.*
4. Soufe, T. and Iwama, A., "Ignition of Composite Propellant at Subatmospheric Pressures by Means of Carbon Dioxide Laser," *Propellants and Explosives*, 4, 1979, pp. 98-106.



5. Holy, J. A., "Laser Initiation of  $\text{TiH}_x/\text{KClO}_4$ ," *Proceedings of the Eleventh International Pyrotechnics Seminar*, Vail, CO, 7-11 Jul 1986, pp. 313-325.
6. Chernai, A. V., "Initiation of a Chemical Reaction in PETN by Light Radiation," *Fizika Goreniya i Vzryva*, Vol. 18, No. 6, 1982, pp. 48-53.
7. Nilsson, H. and Östmark, H., "Laser Ignition of Explosives: Raman Spectroscopy of the Ignition Zone," *Ninth Symposium (International) on Detonation*, Aug 1989.
8. Bradley, J. N.; Butler, A. K.; Capey, W. D.; and Gilbert, J. R., "Mass Spectrometric Study of the Thermal Decomposition of 1,3,5-Trinitrohexahydro-1,3,5-triazine (RDX)," *J. Chem. Soc. Trans. Faraday I.*, 73, 1977, pp. 1789-1795.
9. Cournu, A. and Massot, R., *Compilation of Mass Spectral Data*, Second Edition, Heyden & Son Ltd., London, 1979.
10. Rauch, F. C. and Fanelli, A. J., "The Thermal Decomposition Kinetics of Heaxahydro-1,3,5-trinitro-s-triazine above the Melting Point: Evidence for Both a Gas and Liquid Phase Decomposition," *J. Phys. Chem.*, 73, 1969, pp. 1604-1608.
11. Liebman, S. A.; Snyder, A. P.; Kremer, J. H.; Reutter, D. J.; Schroeder, M. A.; and Fifer, R. A., "Time-Resolved Analytical Pyrolysis Studies of Nitramine Decomposition with a Triple Quadrupole Mass Spectrometer System," *J. Anal. Appl. Pyrolysis*, 12, 1987, pp. 83-95.
12. Tang, B. T.; Chaudhri, M. M.; Rees, C. S.; and Mullock, S. J., "Decomposition of Solid Explosives by Laser Irradiation: A Mass Spectroscopic Study," *J. Mater. Sci.*, 22, 1987, pp. 1037-1044.

## DISCUSSION

**J. C. CUMMINGS**, Sandia National Laboratories, Albuquerque, NM

In order to model the experiments you have described, it is critical to know the amount of  $\text{CO}_2$  laser energy that is actually absorbed by the sample and the depth of

absorption. Have you measured these quantities for your samples? In addition, have you measured or calculated the temperature in your sample as a function of time?

## REPLY BY H. ÖSTMARK

In my paper at the Eighth Detonation Symposium, I described methods for measuring these parameters. I have not measured them for RDX, but the reflection coefficient for RDX has been measured by others<sup>1</sup> and is 0.71. The absorption coefficient can be estimated by IR spectroscopy measurements.

## COMMENT

**J. C. CUMMINGS**, Sandia National Laboratories, Albuquerque, NM

Detailed knowledge of this kind seems critical to advancing our understanding of the physics and chemistry occurring in your sample as you vary experimental parameters.

## REPLY BY H. ÖSTMARK

I agree. A model for calculating the temperature, based on these parameters as well as the gas phase reaction interactions, is under way.

## DISCUSSION

**F. VOLK**, Fraunhofer Institut 7507 Pfinztal, FRG

The ion masses 44 and 46 consist of different gases, such as  $\text{N}_2\text{O} + \text{CO}_2$  and  $\text{NO}_2 + \text{HCOOH}$ , etc. Were you able to separate these ions quantitatively using a GC/MS Quadropole system? You know that GC columns absorb  $\text{NO}_2$  very strongly.

## REPLY BY H. ÖSTMARK

It was possible, at least to some degree, to separate these ions by using the fragmentation patterns. We were not, however, able to do quantitative measurements, because of the problems you discuss. Neither was this our aim. We sought to obtain a method for detecting the molecules or molecule fragments occurring in the ignition zone and to study the influence of

pressure, laser pulse width, and laser power on the ignition process. The main reason for having a long capillary column was to reduce the pressure in the MS. In our second paper at the Ninth Detonation Symposium, "Laser Ignition of Explosives: Raman Spectroscopy of the Ignition Zone," we present an alternative method for measuring the molecules in the reaction zone. This Raman method is believed to be better for quantitative measurements,

but unfortunately it is also much more time consuming.

## REFERENCES TO DISCUSSION

1. Strakovskij, L. G.; Uljakov, P. I.; and Frolov, E. I., *Khim. Fiz. Protessov. Gorenija: Gorenje Kondens. Sist.*, 1977, p. 8.

# THE USE OF TIME-RESOLVED SPECTROMETRIES IN THE STUDY OF INITIATION OF EXPLOSIVES AT MOLECULAR LEVEL

Alain E. Delpuech  
Commissariat à l'Energie Atomique  
CER - BP n°16 - 37260 MONTS, FRANCE

*A theoretical approach, using quantum chemistry techniques, led us to the conclusion that the origin of explosive decomposition lies in the brutal modifications of the electronic structure of the molecules. In this paper we present the three experimental techniques which have had to be conceived and developed in order to verify the various predictions of the model:*

- *Ultra Fast Raman spectrometry, developed with the objective of revealing the structural modifications of the molecules behind the shock front;*
- *Initiation by shock-light coupling, developed in an attempt to determine the influence of the molecular structure modifications on the speed of decomposition of the explosive;*
- *Laser probe mass spectrography, used to study energy transfer between molecules.*

## INTRODUCTION

In an earlier series of papers,<sup>1</sup> we showed the influence of the molecular electronic structure on the conditions of initiation of secondary explosives under shock. We proposed a single mechanism of response at the molecular level applicable to all explosives subjected to external solicitation. This mechanism implies, during the first step of molecular decomposition, increased occupation of excited electronic energy levels due to a shock process analogous to that observed under irradiation.<sup>2</sup> The model considers the molecular population behind the shock wave to be the sum of three populations:

$$P(M) = P(M') + M(M^*_{ND}) + P(M^*_{D})$$

Where  $P(M')$  is the population in the ground state,  $P(M^*_{ND})$  is the population in non dissociative excited state  $i$ .

$$P(M^*_{ND}) = \sum_i P(M^*_{ND}^i)$$

$P(M^*_{D})$  is the population in an excited state  $j$  leading to molecular dissociation.

$$P(M^*_{D}) = \sum_j P_j(M^*_{D})$$

This breakdown leads us to the hypothesis that the first phase of initiation may be characterized by the existence in certain parts of the crystal of zones where, following modifications of molecular electronic structure:

- The intermolecular energy transfer properties are significantly modified owing to the existence of the population  $P(M^*_{ND})$ . In the proposed model these properties cause the nitrated bonds to play an important role; the deactivation process is envisaged via photons in the crystal structure.

- Simultaneously, certain molecules decompose following excitation into a dissociative state,  $P(M^*_D)$ .

Given the characteristics of these two populations:

- The parameters associated with the population  $P(M^*_D)$  determine the properties of the substance directly related to the conditions of molecular decomposition. We have shown that this is the case regarding shock sensitivity.<sup>3</sup>
- The parameters associated with the population  $P(M^*_{ND})$  influence the conditions of birth of the detonation phase, requiring the establishment of a cooperative mode. The characteristics of this population depend on the temperature and pressure conditions and of the lifetime of the excited energy levels.

We propose to present in this paper the three experimental techniques which we have developed in order to verify the various predictions of the model.

- Existence of the populations  $P(M^*_{ND})$  and  $P(M^*_D)$  behind the shock front
- Effect of the molecular electronic changes on the decomposition of the explosive
- The privileged role of the  $NO_2$  groups.

## THE MOLECULAR POPULATION BEHIND THE SHOCK FRONT

In order to visualize the structural modifications of the explosive molecule—just behind the shock front and before decomposition—we developed an ultra-rapid technique making use of Raman scattering of the light. This technique is, in fact, the only experimental method of obtaining sufficiently quickly information on molecular structure at a precise point. The principle of the experiment is to compare the Raman spectra emitted by a crystal of explosive with that emitted by the same zone of the same crystal immediately after the passage of the shock front. The shock pressure is of about 100 kbars; the zone observed is located 1 mm from the face of entry

of the shock in the monocrystal. The phenomenon is observed during 10 ns in a time interval of several tens of nanoseconds after that shock wave has passed through the observed area.

The experimental set-up has been described elsewhere.<sup>4</sup> We present here the main results, obtained for RDX and PETN.<sup>5</sup>

1. The decomposition of the whole molecule is not immediately behind the shock front; indeed, we observe that during several tens of nanoseconds behind shock front, the spectrum is characteristic of the molecule and presents the same lines as those registered at rest.
2. All the observations agree with the hypothesis of the existence behind the shock front, before explosive decomposition, of a molecular population whose only structural modification is a reorganization of the electronic structure. This is the population  $P(M^*_{ND})$ . The observations reveal large intensity variations in the spectrum lines without change in frequency ( $5\text{ cm}^{-1}$ ). In these conditions this can be explained only by changes in the number and characteristics of the occupied excited levels (electronic and vibrational); these variations depend on pressure and temperature conditions, and the lifetime of the concerned levels.
3. On the other hand, it has not been possible to prove the existence during this period of the population  $P(M^*_D)$ , the molecules in the course of decomposition. The fact that we did not observe the spectra corresponding to  $NO_2$  or  $MNO_2$  may be explained, however, by the small proportion of decomposed molecules and the instability of the fragments formed.<sup>6</sup>

## CHANGES OF MOLECULAR ELECTRONIC STRUCTURE AND THE DECOMPOSITION MODE

In order to define a model describing the birth of the detonation mode, close attention must be given to the population  $P(M^*_{ND})$  of

excited but non-decomposed molecules. Indeed it is within this population that energy and transfer phenomena leading to a cooperative decomposition process can develop. It is to be expected that such a process will depend heavily on the concentration  $P(M^*_{ND})/V$  of these molecules and on their lifetime in the considered excited state.

In order to verify experimentally this proposition, we have considered artificially creating, behind the shock front, a population of excited and non decomposed molecules. If our hypotheses are correct, this modification of  $P(M^*_{ND})/V$  should affect the decomposition parameters.

### Experimental Set-up

The experimental set-up is shown in Figure 1.

**Choice of Explosive.** HMX was chosen since it displays non-dissociative states which can be populated by excitation using an excimer laser emitting at 249 nm (corresponding to an energy of about 5 eV per photon). Furthermore, a pyrotechnical chain of modest dimensions is capable of detonating a monocrystal.

**Shock Generator.** The shock generation system must allow variation of the energy transmitted to the HMX crystal. The pyrotechnical set up is inspired by gap test type experiments. It comprises a PETN detonator which ignites a booster. The pressure induced in the explosive crystal lies between 80 and 330 kbars depending on the thickness of the AU 4G barrier placed between the crystal and the booster. It is determined by Doppler-laser interferometry.

**Light Source.** The light source is an excimer laser whose wavelength is that associated with the dissociation of krypton fluoride (KrF); this lies in the ultraviolet at 249 nm. The maximum available energy output per pulse is 1 J. The maximum repetition frequency is 10 Hz. The pulse half width is 20 ns. Allowing for the absorption in the optical focusing apparatus and the passage of the beam in ambient air, the energy delivered at

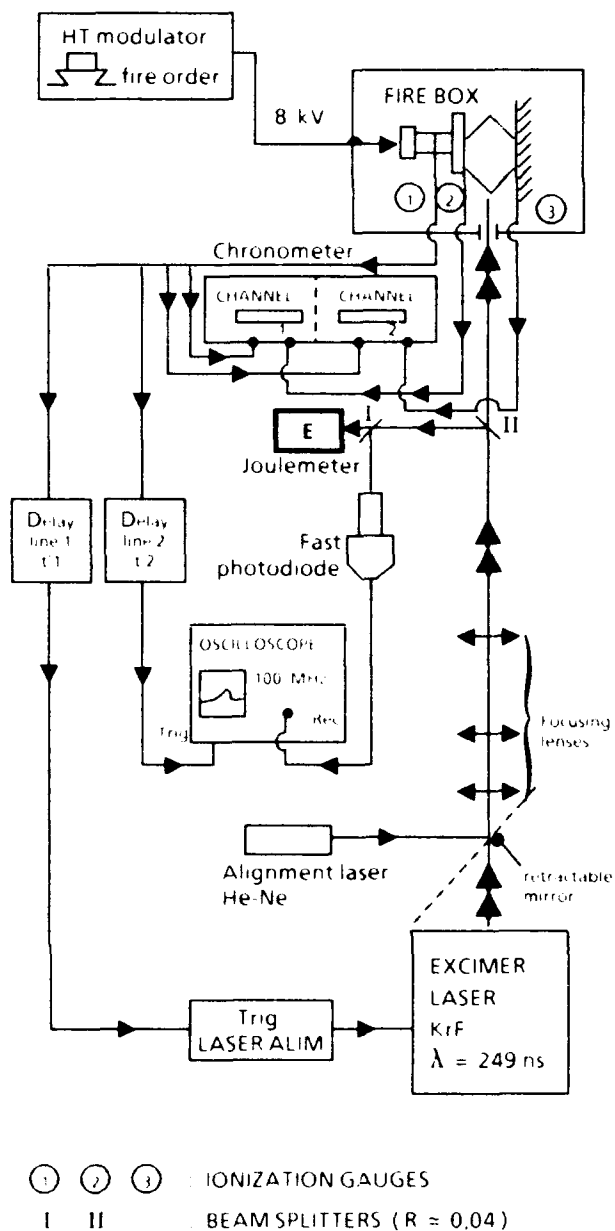


Figure 1. Experimental Setup for Shock-Light Coupling

the focus is 300 mJ. The dimension of the focus is 6 x 6 mm.

For each laser pulse, the laser operation is checked by simultaneous measurement of the pulse energy and the variation of the luminous intensity as a function of time.

The alignment of the optical system is assured using a helium-neon continuous emission laser.

**Shock-light Synchronization.** The monocrystal is irradiated perpendicularly to the shock front. The synchronization between the propagation of the shock in the monocrystal and its excitation by the laser was adjusted such that it is unaffected by the lifetime of the excited states created. For this reason the illumination by the laser starts only when the shock wave has penetrated about 0.6 mm into the crystal.

## Results

In order to study the effect of the shock-light coupling, we compared the values of the speed of decomposition of the explosive measured for three different shock pressures (160, 210, and 290 kbars) in the cases:

- Shock wave alone (speed  $v_1$ ),
- Shock coupled with the irradiation of the explosive by the laser beam (speed  $v_2$ )

Examination of the changes and dispersion of the measured decomposition speeds in the two cases above leads us to conclude<sup>7</sup>:

- For pressures of 160 and 210 kbars, the dispersion of the speeds in the case of shock light coupling is much less than for shock alone. Furthermore, the values of  $v_2$  are grouped in the area of maximal values of  $v_1$ .
- For a pressure of 290 kbars, the intervals of dispersion of  $v_1$  and  $v_2$  coincide.

Table 1 summarizes the average values obtained from 8 shots at each pressure

We observe that the average speed of decomposition determined for shock light coupling at 160 kbars is equal to the average value at 210 kbars in the case of shock alone. In other words, the difference in pressure (50 kbars) generated in the crystal is compensated by the effect of the laser.

The first conclusion of these experiments is that the results confirm the theory. It appears that the increased occupation of excited states behind the shock wave provoked by the UV light leads to a change in the speed of decomposition of the monocrystal of HMX.

*Table 1. Evolution of the Speed of Decomposition of the Monocrystal of HMX as a Function of Shock Pressure*

P (Kbars)	Speed of decomposition Shock only $v_1$ (mm/ $\mu$ s)	Speed of decomposition Shock + laser $v_2$ (mm/ $\mu$ s)	$v = v_2 - v_1$ (mm/ $\mu$ s)
290	5.92	5.92	0
210	5.60	5.73	0.13
160	5.45	5.61	0.16

In addition, the effect of the shock light coupling appears to be even greater when the decomposition regime is far from the detonation mode.

## Study of a Counter-Example

It appeared to be necessary to perform a counter test, using an explosive non-absorbant around this excitation wavelength, in order to eliminate any effect due to the laser beam. The explosive used was PETN ( $\epsilon_{249\text{ nm}} = 0$ ). In this case, the measured average decomposition rates under the influence of shock alone ( $v_1$ ) and shock-light coupling ( $v_2$ ) should be essentially the same.

The results of 5 shots at 3 pressures (45, 110 and 270 kbars) are shown in Table 2.

*Table 2. Evolution of the Speed of Decomposition of the Monocrystal of PETN as a Function of Shock Pressure*

P (Kbars)	Speed of decomposition Shock only $v_1$ (mm/ $\mu$ s)	Speed of decomposition Shock + laser $v_2$ (mm/ $\mu$ s)
270	8.09	8.03
110	6.69	6.63
45	4.27	4.30

To within experimental uncertainty, the  $v_1$  and  $v_2$  values are identical at all pressures. These results therefore support the conclusions regarding HMX and confirm the predominant role played by excited non-dissociative states

in the establishment of the decomposition regime of an explosive.

## ROLE OF THE NITRATED GROUPS

So as to analyze and confirm the special role of the  $\text{NO}_2$  groups in the mechanism of molecular excitation, we decided to study the photon-phonon interactions in secondary nitrated explosives.

The first difficulty was the choice of an experimental technique capable of providing information on decomposition fragments and on the mechanisms involved. The only technique available fulfilling this requirement is laser probe mass spectrography.<sup>8</sup>

We present below the results obtained using this technique on monocrystals of RDX and HMX.

These results are then analyzed in a non-linear model of laser-explosive interaction.

### Experimental Technique

**Description of the L.P.M.S. - 2S Probe.**<sup>9</sup> The vaporization and ionization of the explosive single crystal are induced by bombardment of one of its faces with a YAG pulsed laser beam tripled in frequency ( $\lambda = 0.355 \mu\text{m}$ ). The total energy of the laser impulse is between 10 and 30  $\mu\text{J}$  and focused on a surface of about  $400 \mu\text{m}^2$  with Gaussian spatio-temporal profiles. The laser time duration is 3-4 ns and the shot repetition rate is 1 Hz.

The so-created laser micro-plasma is released in an equipotential expansion box without electric and magnetic fields. The positive ionic species are then extracted and accelerated by an electrostatic field corresponding to a difference of potential of 8 kV. These ions are analyzed by a spatio-temporal mass-separator combining both magnetic field action and time of flight separation. They are detected by an electro-optic panoramic device and their masses identified by time of flight measurements.

The instrument is equipped with a sample viewing system which provides a high power observation ( $G : 300 - 420 \times$ ). The

diagram of this apparatus is presented in Figure 2.

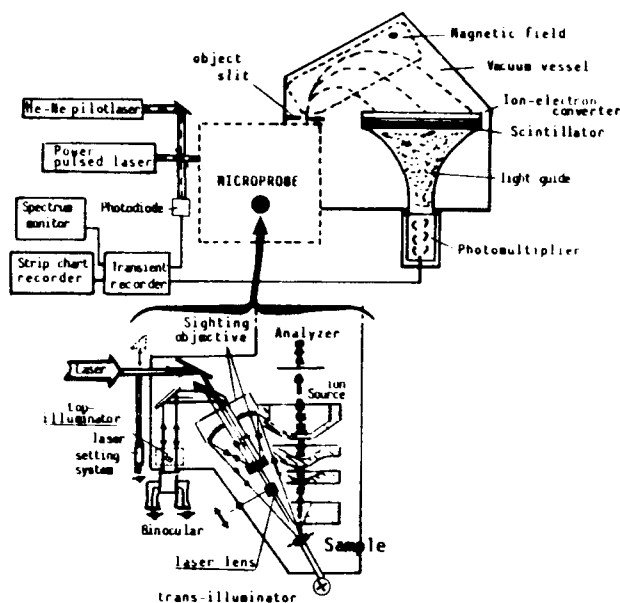


Figure 2. Laser Probe Mass Spectrograph (LPMS)

**Characterization of the Ions.** The different ionic species are identified by their time of flight. The times of flight in the expansion box of plasma and in the ionic optic source depend on the ion mass. The time of flight ( $t_1$ ) in the spatio-temporal mass separator is inversely proportional to the square root of the initial kinetic energy of the ions.

With the measurements of  $t_1$ , we consequently intended to study different parameters of initial ionic energy as a function of (laser energy, crystal orientation of the RDX sample face, etc.).

### Results

**Characteristic Behavior of the Explosive.** The spectra obtained fall into three categories (Figure 3):

**Type 1:** a group of 3 peaks corresponding to the masses 28 ( $\text{CO}^+$ ), 29 ( $\text{COH}^+$ ), and 30 ( $\text{NO}^+$ ), with  $\text{NO}^+$  as a major peak (laser pyrolysis mass spectrum).

**Type 2:** a group of 3 peaks 12 ( $\text{C}^+$ ), 14 ( $\text{N}^+$ ) and 16 ( $\text{O}^+$ ) situated between 1.9 and 2.1  $\mu\text{s}$ ; and a group of 3 peaks

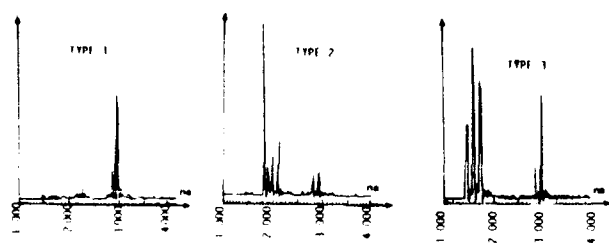


Figure 3. Different Types of Time of Flight Mass Spectra

identical to the type 1 spectra except for their weaker intensity. The electronic temperatures and densities of the plasma ( $T_e = 10,000$  K,  $N_e = 10^{17}$  e $^-$ /cm $^3$ ) are close to those obtained by laser pyrolysis in the case of "classic" organic substances.<sup>10</sup>

**Type 3:** a group of 3 peaks 12, 14, and 16 displaced towards the lower TOFs (1.3 to 1.6  $\mu$ s) and another group identical to the type 1 spectra but displaced towards higher TOFs. In this case the temperature and densities of the plasma are much higher ( $T_e = 20$  to  $25,000$  K,  $N_e = 10^{10}$  e $^-$ /cm $^3$ ).

The study of the behavior of the RDX and HMX therefore reveal the appearance of slow ions and fast ions. The former (spectral types 1 and 2) correspond to classical fragmentation of organic compounds by laser pyrolysis. On the other hand, the RDX and HMX appear to display type 3 spectra, distinguished by ions of very high energy and very high plasma temperature and density. It is probable that such spectra are related to the "explosive" nature of these compounds.

**Influence of the Incident Laser Energy and the Orientation of the Crystal.** The RDX single crystal was irradiated on faces (1.1.1.) and (2.1.0.). We observe that the threshold of laser energy necessary to provoke type 3 spectra depends on the face irradiated: it is 18  $\mu$ J for face (2.1.0.) and 13  $\mu$ J for face (1.1.1.). The spectra obtained at higher energies are similar. Although the ions are more energetic in the case of face (2.1.0.). These results suggest a nonlinear mechanism governing the laser-explosive interaction.

**Analysis of the Cratering.** A study of the cratering by optical microscopy (binocular) shows that the laser-explosive interaction is not limited to the area of the focus (diameter 10  $\mu$ m). The laser induces physical transformations of the crystal up to distances varying from 30 to 30  $\mu$ m. In the case of RDX this phenomenon is more pronounced on the face (2.1.0.). Examination of the craters by scanning electron microscopy reveals:

- Formation of macroscopic defects (cracks) at large distances from the crater (50  $\mu$ m) following collapse of the structure;
- The truncated shape of the craters, which is characteristic of a brutal vaporization initialized "in volume."

We shall now examine the phenomena which might explain both the non-linear interaction and the creation of the white area (diameter 30 to 80  $\mu$ m) in the vicinity of the crater.

#### Proposal of a Model for the Laser-Explosive Interaction

Taking only the phonons (created by the laser beam in surface and in volume) into account is insufficient to explain our experimental results. The energy carried by the phonons is insufficient to generate the observed craterization effect and the appearance of the "white zone" supposes a speed of propagation for the particles twice the speed of phonons. In fact, a non-negligible probability of interaction exists between photons and phonons in the crystalline medium. These interactions generate a process of "chain reaction." Each center of interaction becomes the spot where an energy liberation can produce dislocation and energetic chain reactions by bond breakings. In this case the laser decomposition is initiated in volume (and not in surface) in opposition to the general case of organic and metallic materials.

The coupling of the vibration waves (or phonons) of the lattice with an electromagnetic wave causes a polarization wave (or polariton) to appear. This P wave propagates itself in the material and induces the application of a force



on the bond dipole. This force will be all the stronger as the dipolar moment is strong. In the case of RDX, the N-NO<sub>2</sub> groups will be the more strongly activated.

Three facts are in keeping with the model proposed:

- The initiation of the laser decomposition by such a process leads to a large proportion of NO<sup>+</sup> ions. Our mass spectra reveal systematically this effect;
- The middle extinction curve of polarization wave (P-wave) is compatible with the size of the sensitive "white zone;"
- The observation of an interaction especially efficient with the crystalline axis which offers a higher density of nitrated bonds.

## CONCLUSION

These difficult experiments, which have been developed over a number of years, were designed to verify, a posteriori, the main results predicted by the theoretical model of explosive decomposition at molecular level.

The results obtained provide experimental confirmation of the main theoretical predictions, in particular:

- The existence behind the shock front of a population of molecules, whose only modification is a reorganization of the electronic structure, is confirmed;
- The effect of these electronic modifications on the rate of decomposition of the explosive is confirmed and quantified;
- The fundamental role played by the nitrated bonds in the initiation mechanism of the explosive decomposition is confirmed and analyzed.

Finally, it might be mentioned that the results obtained from this double approach— theoretical and experimental—have already been applied in research of new explosives. Their sensitivity to shock can be predicted, a

priori, from their structure before they are synthesized.

## REFERENCES

1. Delpuech, A.; Cherville, J.; and Michaud, C., *The Seventh Symposium on Detonation*, Annapolis, MD, 1981, p. 65.
2. Delpuech, A., Thèse Doctorat ès Sciences, n° 656, Université de Bordeaux 1, 1980.
3. Delpuech, A. and Cherville, J., *Propellants and Explosives*, Vol. 3, 1978, Chapter 6, p. 169; Vol. 4, 1979, Chapter 2, p. 61; Vol. 4, 1979, Chapter 6, p. 121.  
Delpuech, A. and Cherville, J., *Symposium International sur le comportement des milieux denses sous hautes pressions dynamiques*, Paris, 1978, p. 21.
4. Boisard, F.; Linares, B.; Delpuech, A.; and Cherville, J., *Symposium International sur le comportement des milieux denses sous hautes pressions dynamiques*, Paris, 1978, p. 33.
5. Tailleur, M. H., Thèse spécialité, Université Bordeaux 1, 1980.
6. Darnez, C., *Int. J. Radiat. Phys. Chem.*, Vol. 4, 1972, p. 11.
7. Dufort, S. and Delpuech, A., *The Eighth Symposium on Detonation*, Albuquerque, NM, 1985, p. 847.
8. Eloy, J. F. and Delpuech, A., *Shock Waves in Condensed Matter*, 1987, Schmidt, S. C. and Holmes, N. C. (Editors), p. 557.
9. Chamel, A. and Eloy, J. F., *Scanning Electron Microsc.*, Vol. II, 1983, p. 841.

## DISCUSSION

ANDRZEJ W. MIZIOLEK  
Ballistic Research Laboratory  
Aberdeen Proving Ground, MD

1. What are the typical values for the incident pulse energies for the KrF laser used in the Raman experiments?
2. Have possible photochemical effects due to the short wavelength of the Raman

laser (248 nm) been taken into account in the data analysis?

### REPLY BY A. DELPUECH

1. The KrF laser was not used for Raman experiments, but for shock/light coupling purposes. Its typical output reaches 1 J during 20 ns.
2. The role of the KrF laser is to increase the population of non-dissociative electronic excited states in HMX single crystals by an absorption process. We have never observed photochemical induced decomposition of the crystal with the chosen operating conditions.

### DISCUSSION

**WILLIAM VON HOLLE**  
Lawrence Livermore National  
Laboratory  
Livermore, CA

1. Why is it not possible to explain your results on the "shock/light" coupling and the Raman spectrum of shocked RDX crystals in some other ways? For example, a small percentage change in the shock velocity through the crystal of irradiated RDX could simply be the result of a temperature effect upon absorption of the u.v. radiation.
2. In the case of the Raman spectra, I do not understand how a small shift in frequency and a change in intensity indicates excited electronic states. I would expect a 100 kb pressure to induce a fairly large frequency shift (based on other papers in this symposium, i.e., Moore and Schmidt, and Renlund and Trott), and

shocked crystal band intensities could change for other reasons.

3. Also, how do the observations of focussed laser irradiation of RDX and HMX, resulting in physical and chemical change, "verify" the theoretical predication of your model?

### REPLY BY A. DELPUECH

1. In the case of Raman spectrometry results, we do not assign the frequency shift to the population of an excited state. We state that, taking into account this slight shift, the molecular structure is not strongly altered. The only significant modification relates to a modification of bands intensities. This modification of the intensities implies a modification of the molecular wave function and, by this way, of the electronic distribution on the different bonds and atoms. That is what we call an electronic excited state.
2. In the case of shock/light coupling applied to HMX, we increase the population of the "interesting" excited states; in the case of PETN, we populate "non-interesting" excited states, on the level of our model. From the temperature elevation point of view, the results are identical; however, from the shock velocity through the crystal point of view, the effects are different.
3. The observations of focussed laser irradiation of RDX and HMX can be explained by the creation of a polarization wave interacting preferentially with the NO<sub>2</sub> bonds. It is the show off of this preferential interaction that verifies our theoretical predictions.

# VIBRATIONAL SPECTROSCOPIC INVESTIGATIONS OF SHOCK-COMPRESSED LIQUID NITROGEN AND SHOCK-COMPRESSED LIQUID NITROMETHANE\*

D. S. Moore and S. C. Schmidt  
Los Alamos National Laboratory  
Los Alamos, New Mexico 87545

*Vibrational spectra of liquid nitrogen and liquid nitromethane shock compressed to several high pressure/high temperature states were recorded using single-pulse multiplex coherent anti-Stokes Raman scattering. Vibrational frequencies were extracted from the data by computer spectral simulation techniques. Vibrational frequencies of liquid nitrogen were found to increase monotonically up to  $\approx 17.5$  GPa single shock and  $\approx 30$  GPa double shock, and then to decrease with further increases in pressure. The consequence of the decrease in vibrational frequency on the Grüneisen mode gamma and its effect on the  $N_2$  equation-of-state is discussed. A model is developed that includes the thermally-excited vibrational state transitions in the synthesized spectral fits of the nitromethane CARS data. The adequacy of the model of interpretation of CARS spectra in both ambient and shock-compressed nitromethane is discussed.*

## INTRODUCTION

Nitrogen is a relatively simple and stable diatomic molecule that has been studied over a wide range of pressure and temperature. Presently, there is renewed interest in this material, especially in the planetary sciences and in chemical explosives technology, because of the unusual effect high pressure and temperature have on its physical and chemical properties. Equation-of-state and thermodynamic data have been obtained for nitrogen at pressures up to 130 GPa, and temperatures to beyond 10,000 K using both static<sup>1-6</sup> and dynamic<sup>7-11</sup> compression techniques. These measurements have been complemented by calculations for both the solid<sup>12-14</sup> and fluid<sup>11,15-21</sup> phases. The shock Hugoniot of liquid nitrogen exhibits an increase in compressibility above 30 GPa and 7000 K that has been attributed to a dissociative phase transition.<sup>10,16,18,22,23</sup> Much recent experimental work has attempted to observe such a phase

transition directly,<sup>24,25</sup> or to provide further bulk property or molecular level evidence for such a phase transition.<sup>26</sup> The investigation reported on here<sup>27</sup> extends the pressure and temperature range of the measured fluid nitrogen vibrational frequency closer to the transition region in order to provide molecular level details about the behavior of this interesting material. Nitromethane is a prototypical homogeneous high explosive. As such, it has received considerable attention from a variety of researchers. Some recent progress has been made in the elucidation of the initiation mechanism,<sup>28,29</sup> but much is still unknown. We also report here the results of an investigation into the behavior of the CN-stretching-mode vibrational frequency in shock-compressed liquid nitromethane.

## EXPERIMENTAL METHODS

The high pressure/high temperature states investigated here were produced by dynamic compression techniques, and the vibrational spectra were recorded using coherent anti-Stokes Raman spectroscopy

\* Work performed under the auspices of the U. S. Department of Energy

(CARS). The experimental apparatus has been described in detail previously.<sup>27</sup> Briefly, a projectile launched by a two-stage light-gas gun dynamically compressed a sample in a target designed to reflect the CARS signal back out an optical aperture. The cryogenic target assembly used to condense and hold liquid N<sub>2</sub> for these experiments has been described elsewhere,<sup>9</sup> but was modified to include a highly polished 304 stainless steel target plate at the front and a 6.3 mm diameter quartz or lithium fluoride window at the rear. The room temperature targets used for nitromethane contained a similar sample chamber in a simple 150 mm diameter, 12 mm thick aluminum cylinder. Impactor and target plate thicknesses were chosen, and electrical time-of-arrival pin assemblies were installed in the liquid sample, so as to ensure that rarefaction waves would not compromise the one-dimensional character of the compression in the region observed optically.

Pressures, densities, and temperatures for the singly- and doubly-shocked regions of N<sub>2</sub> were calculated using an effective spherical potential that has been shown to accurately reproduce both nonspherical molecular dynamics simulations and experimental Hugoniot and brightness temperature data.<sup>17-19</sup> Doubly-shocked states were inferred from impedance matching of the N<sub>2</sub> shock, at the measured shock velocity, reflecting off the known window material assuming the theoretical equation of state for nitrogen. The equation-of-state parameters for the quartz and lithium fluoride windows are from published data.<sup>30</sup> The shock pressures in CH<sub>3</sub>NO<sub>2</sub> were inferred using standard data reduction techniques<sup>31</sup> and published shock-velocity/particle-velocity data.<sup>30</sup>

CARS<sup>32</sup> is a parametric process in which three waves, two at a pump frequency,  $\omega_p$ , and one at a Stokes frequency,  $\omega_s$ , are mixed in a sample to produce a coherent beam at the anti-Stokes frequency,  $\omega_{as} = 2\omega_p - \omega_s$ . The efficiency of this mixing is greatly enhanced if the frequency difference  $\omega_p - \omega_s$  coincides with the frequency  $\omega_j$  of a Raman active mode of the sample. The intensity of the beam at  $\omega_{as}$  is given by

$$I_{as} \propto \sum_i \frac{\omega_{as}^2 \Gamma_i^2 |N_i L_i|^2 \left( \frac{n_{as}^2 + 2}{3} \right)^2 \left( \frac{n_s^2 + 2}{3} \right)^2 \left( \frac{n_p^2 + 2}{3} \right)^4}{n_p^2 n_s^2 n_{as}^2} \times \left[ \left( \sum_j \frac{\Gamma_j \chi_j^{pk} (\omega_j - \omega_p + \omega_s)}{(\omega_j - \omega_p + \omega_s)^2 + \Gamma_j^2} + \chi^{nr} \right)^2 + \left( \sum_j \frac{\Gamma_j^2 \chi_j^{pk}}{(\omega_j - \omega_p + \omega_s)^2 + \Gamma_j^2} \right)^2 \right] \quad (1)$$

where  $I_p$  and  $I_s$  are the incident intensities of the pump and Stokes beams, respectively, and  $n_{as}$ ,  $n_s$ , and  $n_p$  are the refractive indices at  $\omega_{as}$ ,  $\omega_s$ , and  $\omega_p$ , respectively.  $N_i L_i$  corresponds to the Lagrangian density of the  $i$ th layer, and the sum is over noninterfering layers.  $\chi^{nr}$  is the nonresonant susceptibility,  $\chi_j^{pk}$  is the peak third-order susceptibility, and  $\Gamma_j$  is the half-width at half-maximum (HWHM) line-width. The sum on  $j$  is over transitions. This equation only holds in the case of no electronic resonance enhancement.<sup>32</sup>

The pump frequency in the CARS process was obtained by using approximately 40 percent of the 6 ns-long frequency-doubled output of a Nd:YAG laser (Quanta-Ray DCR-1A) to pump a narrow-band dye laser (Quanta-Ray PDL-1) at near 557 nm for the nitrogen data, and near 605 nm for the nitromethane data. A broad range of Stokes frequencies was produced using a home-built broadband dye laser, utilizing the laser dye DCM (Exciton, lasing region 627 to 645 nm) pumped by the remaining Nd:YAG output. Some of the nitromethane data was obtained using the frequency-doubled Nd:YAG laser for the pump frequency and Rhodamine 590 (Exciton) in the broadband dye laser for the Stokes frequencies. The CARS signals produced in the sample were directed through a 6 nm-bandwidth filter monochromator and then dispersed by a 1 m spectrometer. Multi-channel detection of the CARS signals was done using an intensified photodiode array (Tracor Northern 6132) and analyzer (Tracor Northern 6500). In addition, the broadband dye laser spectral profile was measured in each experiment using another 1 m spectrometer and an intensified photodiode array (Princeton Instruments IRY-512G) and analyzer (Princeton Instruments ST-100).

Phase matching was experimentally optimized in the ambient sample for the focusing conditions used. The dispersion in the sample was assumed to linearly scale with the increase in refractive index due to volume compression<sup>33</sup>. Linear scaling of the dispersion results in the same phase-matching angle at all compressions. The scaled refractive indices were also used in the local field correction terms of Equation (1).

Vibrational frequencies were all calibrated ( $\pm 1 \text{ cm}^{-1}$ ) using vacuum wavenumbers of atomic emission lines obtained from standard calibration lamps. The spectral instrument function of the CARS spectrometer/photodiode array was measured using either an atomic emission line or by extraction from the ambient liquid nitrogen transition. The later method has the advantage of including the spectral profile of the pump laser. The measured instrument function was then convoluted with the synthesized CARS spectra to give spectra that could be directly compared with the experimental data.

## RESULTS AND DISCUSSIONS FOR NITROGEN

We have obtained CARS spectra of fluid  $\text{N}_2$  at many shock pressures and temperatures up to 21.3 GPa and 5020 K (single shock), and 40.8 GPa and 5160 K (reflected shock). Because of initial projectile velocity uncertainty and projectile tilt, the arrival time of the shock wave at the center of the target rear window (the location of the laser beam waists and the center of the rear time-of-arrival pin pattern) could only be predicted to  $\pm 30 \text{ ns}$ . For experiments where the shock wave had not reached the window, spectra corresponding to the solid curve in Figure 1a were obtained. The large peak at  $2328.1 \text{ cm}^{-1}$  is the CARS signal from unshocked nitrogen, and the remaining progression of lines are the fundamental transition and hot bands from the singly-shocked fluid. Because unshocked liquid  $\text{N}_2$  has a very narrow linewidth ( $0.029 \text{ cm}^{-1}$  IWHM<sup>34</sup>) compared to a width of several wavenumbers for the shock-compressed fluid, two difficulties were found. At the laser

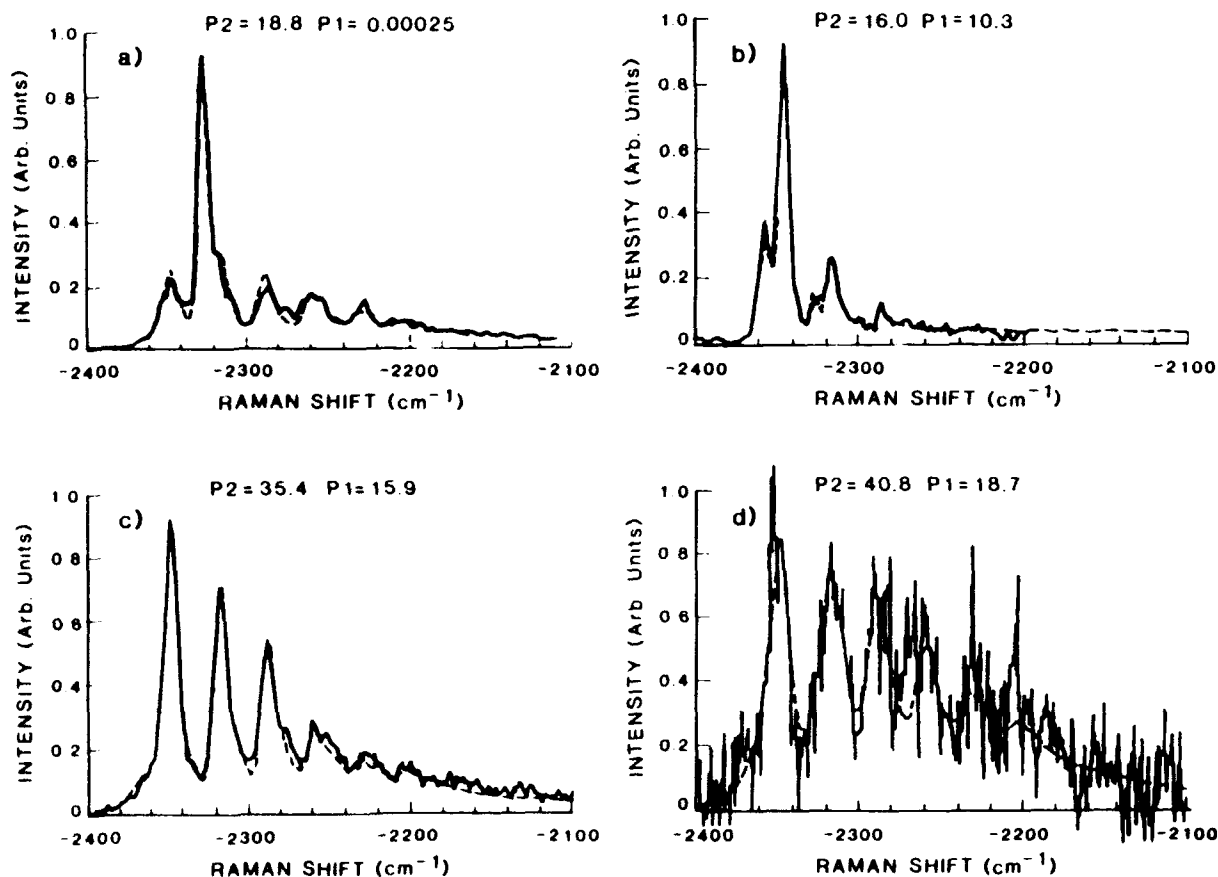


Figure 1 Representative CARS Spectra of Shock-Compressed  $\text{N}_2$

intensities used to produce CARS in the shock-compressed  $N_2$ , the CARS process either could be easily saturated<sup>35</sup> leading to an increase in the apparent linewidth of the ambient  $N_2$ , or could result in large enough signals from the ambient  $N_2$  to locally saturate the detector.

If the shock wave reached and reflected from the rear window, both the singly- and doubly-shocked regions in the sample were interrogated by the incident laser beams. The resultant spectra, similar to those depicted by solid curves in Figures 1b, 1c, and 1d, consisted of two partially overlapped progressions of transitions arising from the two interrogated regions. Figure 1b illustrates the case for which the lines have not broadened sufficiently to obscure the individual peaks of the two progressions. At higher shock pressures and temperatures, the lines broaden considerably (Figure 1c) and it is difficult to distinguish the two progressions without a spectral simulation. Figure 1d is similar to the case of Figure 1c, except with a much poorer signal-to-noise ratio. The results of the spectral simulations using Equation (1) are shown in Figure 1 by the dashed curves. The simulations assume that the linewidths of the fundamental and hot bands are the same for a given shock pressure.

At the highest pressures investigated, the sample appeared to be a grey-body emitter. In the experiments near 21 GPa, photomultipliers monitoring the emission of the samples at 630 nm and at 520 nm recorded rise-times of the emission of several tens of ns. Significantly higher single-shock pressures resulted in much faster rise times. In addition, CARS signals became very difficult to observe at the higher pressures. The difficulty became especially acute after the shock had reached the window. By adjusting the timing to intentionally leave the shock short of the window when the CARS spectra were taken, data were successfully recorded near 21 GPa. Attempts to record CARS spectra above 22 GPa (single shock) have not yet been successful.

Figure 2 shows the Raman shifts extracted from the CARS spectra [using Equation (1)] of shock-compressed  $N_2$  versus reduced density for the fundamental and observed hot band transitions. In the singly-shocked material,

there is a monotonic increase of the vibrational frequency with increasing density or pressure up to a compression of 2.23 (or a pressure of 17.5 GPa). Above this density the frequency no longer increases, and appears to begin to decrease. The vibrational frequency in the doubly-shocked material (whose temperature is lower than singly-shocked material of the same density) shows similar behavior, but the reversal occurs at higher densities or pressures. It is interesting to note the effect of temperature in these data. When the fluid is singly or doubly shocked to the same density, the difference in measured Raman shift is due to the effects of temperature on the potential and on the portion of the potential sampled on average. Within the precision of the data, the anharmonicity of the intramolecular potential appears to be constant for all pressures and is the same as that expected from gas-phase data.

Static high pressure measurements of vibrational frequencies in solid nitrogen<sup>24,25</sup> and solid hydrogen<sup>25</sup> show a similar reversal

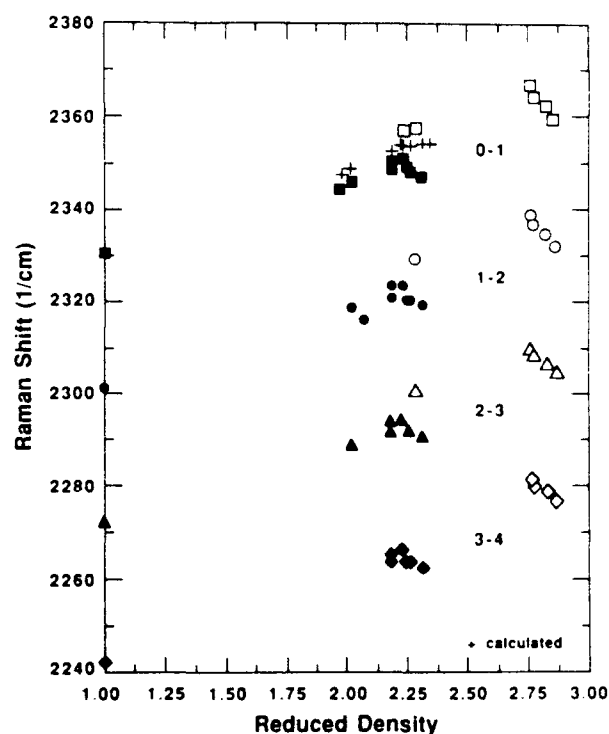


Figure 2. The Measured  $N_2$  Raman Shifts of the Fundamental and Several Hot Band Transitions Plotted Against Reduced Density. The solid and open symbols represent single- and double-shock data, respectively.

in the dependence of Raman shift with increasing pressure. Initial explanations of this effect invoked a change in the molecular electronic structure at the highest densities.<sup>25</sup> Recent isotopic mixture studies indicate that the reversal in the frequency shift in the molecular solids at high density is most likely due to resonant interactions (i.e., dynamic couplings between molecules).<sup>36</sup> Although in these experiments the sample remains a fluid, similar dynamic couplings may exist and may explain the reversal. Nevertheless, there still may be a temperature and density dependent alteration of the electronic structure in the fluid at the conditions encountered here. Alternatively, the ionization/dissociation mechanism proposed to explain the softening of the Hugoniot<sup>10,26</sup> may be producing a sufficient density of charged species to affect the forces that influence the nitrogen vibrational frequency. Further progress towards identification of the operative mechanism might be gained using isotopic mixture studies.

Also plotted in Figure 2 are the vibrational frequencies predicted by the pressure/temperature fit to the Monte Carlo simulation results.<sup>21</sup> The published fit was adjusted, in the linear term only, so that the fit and the measured frequency agreed at our initial conditions. The simulation results show the correct trend with density up to  $\rho/\rho_0 = 2.23$ , where they level off with shock pressure rather than following the data as it appears to decrease. The simulations may be inadequate at these pressures and temperatures, however, for several reasons. For example, the nitrogen may be dissociating, which is not taken into account in the simulation. Additionally, ionization would introduce charges into the material that are not accounted for by the simulation.

The vibrational frequency data also allow the direct determination of single mode Grüneisen parameters,  $\gamma_i = -d\ln\omega_i/d\ln V$ , for the vibrational modes. The  $\gamma_i$  for the fundamental transition was calculated from a smooth curve drawn through the measured Raman shifts and is presented in Figure 3 for the single shock data. Note that this  $\gamma_i$  initially increases with decreasing volume (increasing pressure), then decreases rapidly

and changes sign as the frequencies begin to decrease upon further decreases in reduced volume below 0.47 (pressures above  $\approx 15$  GPa). The magnitude of the single mode  $\gamma_i$ , even at the maximum, is only a small fraction ( $\approx 1$  percent) of the total Grüneisen gamma for the fluid  $N_2$ .<sup>21</sup> Consequently, this interesting behavior of the vibrational mode gamma is not reflected in the  $N_2$  equation of state. It may be said that this behavior of the vibrational modes has little consequence for the bulk behavior of this material. Conversely, it may be pointed out that this behavior provides further evidence that measurement of bulk properties provides very little information about molecular level details, which may be of larger importance in other materials, especially in chemically reactive systems.

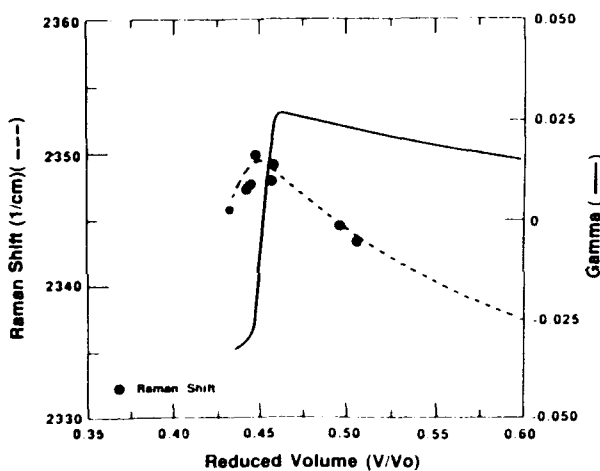


Figure 3. The Fundamental Vibrational Mode Grüneisen Gamma (Line) Calculated from the Smooth Curve (Dashed Line) Drawn Through the Measured Raman Shift Plotted Versus Reduced Volume

## RESULTS AND DISCUSSION FOR NITROMETHANE

For a polyatomic molecule such as nitromethane, the vibrational spectroscopy is considerably more complicated than that discussed above for the diatomic molecule  $N_2$ . At low temperatures, only the vibrational fundamentals need be considered, leading to much simplification in the spectra. In the case of nitromethane, there are 15 possible vibrational normal modes, one of which is the nearly

free rotation of the methyl group around the CN bond. If the molecule is assumed to possess  $C_{2v}$  symmetry when factoring the secular equation, the normal modes divide into 5 totally symmetric ( $A_1$ ) modes, 5 modes parallel to the plan of the  $NO_2$  ( $B_1$ ), and 4 modes perpendicular to the  $NO_2$  plane ( $B_2$ ), with the torsion around CN being  $A_2$ . Table 1 lists the literature frequencies of these vibrations obtained from Raman spectroscopy of the liquid.<sup>37,38</sup> As temperature is increased, even just to room temperature, the low frequency modes start to become thermally populated to a measurable extent. The measured band contour is not just a collisionally broadened single vibrational frequency, but contains contributions from hot bands, not only from the thermal population of the level being probed, but also from the combination bands of the probed transition with all other thermally populated levels. This situation would still be completely tractable if all the anharmonicity constants,  $X_{jk}$ , were known. In the case of nitromethane, however, we could find only one reliable anharmonicity constant involving the vibration of interest in this work, namely the CN stretching mode,  $\nu_4$ .<sup>37</sup>

In order to interpret the CARS spectra of shock compressed nitromethane correctly, a model of the vibrational band contour was developed that includes the contributions of the hot bands. The relationship between CARS intensities and the spontaneous Raman cross section and vibrational-level populations can be approximated by:<sup>32</sup>

Table 1. Frequencies, Assignments, Degeneracies, and Calculated Anharmonic Coefficients of the Vibrational Modes of Nitromethane

$\omega_j$ (cm <sup>-1</sup> )	Assignment			g	$X_{4k}$ (cm <sup>-1</sup> )
480	$\nu_8$	$b_1$	$r(NO_2)$	1	3.1
607	$\nu_6$	$b_2$	$w(NO_2)$	1	4.0
655	$\nu_5$	$a_1$	$\delta(NO_2)$	1	4.3
917	$\nu_4$	$a_1$	$\nu(CN)$	1	3
1096	$\nu_{11}$	$b_1, b_2$	$r(CH_3)$	2	7.2
1379	$\nu_7$	$a_1$	$\delta_s(CH_3)$	1	9.0
1402	$\nu_2$	$a_1$	$\nu_s(NO_2)$	1	9.2
1426	$\nu_{10}$	$b_1, b_2$	$\delta_a(CH_3)$	2	9.3
1561	$\nu_3$	$b_1$	$\nu_t(NO_2)$	1	10.2

$$\Gamma_j X_j^{pk} \frac{h}{2\pi c^4} \omega_p \omega_s^3 = \left( \frac{d\sigma}{d\Omega} \right)_j (\rho_j - \rho_k) \quad (2)$$

where  $h$  is Planck's constant,  $c$  is the speed of light,  $(d\sigma/d\Omega)_j$  is the spontaneous Raman cross-section of the  $j$  to  $k$  vibrational transition, and  $\rho_j$  and  $\rho_k$  are the number densities in vibrational levels  $j$  and  $k$ , respectively. For the CN-stretching mode transition in nitromethane discussed here, the  $j$  to  $k$  transitions all have  $\Delta\nu_4 = 1$ , and the  $\rho_j$  and  $\rho_k$  are all calculated assuming a Boltzmann population distribution among all the vibrational levels. A similar treatment was found to work well for shock-compressed liquid nitrogen.<sup>27</sup> The model then assumes that the  $\nu_4$  mode Raman cross section depends on  $\nu_4$  as prescribed for a harmonic oscillator, i.e.,  $(d\sigma/d\Omega)\nu_4 \propto (\nu_4 + 1)$ . The cross section is further assumed to be independent of initial state  $\nu_j$  when  $j \neq 4$ .

The final step in the model is the determination of the frequencies of the possible hot bands that contribute to the contour of the CN stretching mode Raman spectrum. In the model proposed here, the prescription of previous work is used,<sup>39</sup> wherein the anharmonic shift for a given vibrational band is proportional to the amount of vibrational energy in the lower state. That is,

$$X_{44} = \frac{1}{2} A \omega_4 \quad (3)$$

$$X_{4j} = A \omega_j \quad j \neq 4,$$

where  $\omega_j$  is the frequency of mode  $j$ . The parameter  $A$  is set from the measured position of the first overtone of  $\nu_4$ .<sup>40</sup> The anharmonicity coefficients calculated using Equation (3) are listed in Table 1. The frequency of a transition originating from the state  $|\nu_j\rangle$  is given by

$$\omega[\nu_j] = \omega[0] + 2X_{44}V_4 + \sum_{k \neq 4} X_{4k}V_k \quad (4)$$

where  $\omega[0]$  is the frequency of the  $\Delta\nu_4 = 1$  transition originating from the vibrational ground state, and is given by



$$\omega[0] = \omega_4[0] + X_{44} + \frac{1}{2} \sum_{k \neq 4} X_{4j} g_k \quad (5)$$

where  $\omega_4[0]$  is the fundamental frequency of the  $\nu_4$  mode, and  $g_k$  is the degeneracy of mode  $k$ .

This model was used to calculate the positions and intensities of the hot bands of the CN stretching mode for ambient nitromethane and several shock-compressed pressure and temperature states of nitromethane. The first observation of note is the improved fit of the synthetic CARS spectrum to the ambient nitromethane CARS spectrum when using the above model, as is shown in Figure 4. For this spectrum, the measured (using high resolution spontaneous Raman) linewidth of the  $\nu_4$  mode of  $17 \pm 0.2 \text{ cm}^{-1}$ ,<sup>41</sup> was convoluted with the measured  $2.7 \text{ cm}^{-1}$  triangular instrument function. The low frequency side of the peak is not satisfactorily fit without inclusion of the available hot bands. For the CARS spectra of shock-compressed nitromethane, the vibrational levels change with pressure. CARS spectra of

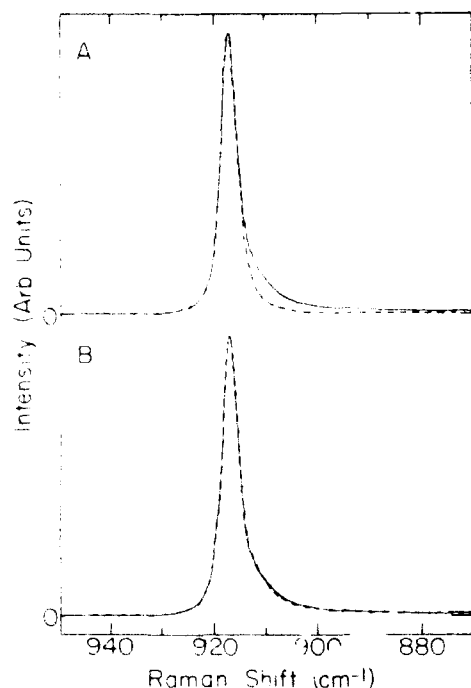


Figure 4. CARS Spectrum of Ambient Nitromethane CN-Stretching Mode. (a) Synthetic spectrum (dashed) includes no hot bands (b) Synthetic spectrum (dashed) includes all possible hot bands

the  $\nu_4$  mode at several pressures in shock-compressed nitromethane have been previously reported,<sup>42-44</sup> as has a preliminary estimate of the  $\nu_4$  vibrational frequency versus shock pressure.<sup>44</sup> Since not all the vibrational frequencies were measured in the shocked material, the other frequencies were assumed to shift according to the available static high pressure results.<sup>45</sup> However, since the measured frequency shifts of the  $\nu_4$  mode in the shock-compressed liquid are slightly smaller than those measured in the static high pressure solid, the other high pressure solid vibrational frequencies were assumed to scale proportionally. The spectral fit of the shock-compressed nitromethane CARS spectrum in Figure 5a is that given by the above model with the assumption that the anharmonic coefficients do not change with pressure. The linewidth of the transition was the only variable adjusted for the fit shown. The shock temperature was taken from the Lysne/Hardesty equation of state.<sup>46</sup> There is something obviously wrong with this model, which works well for the ambient liquid

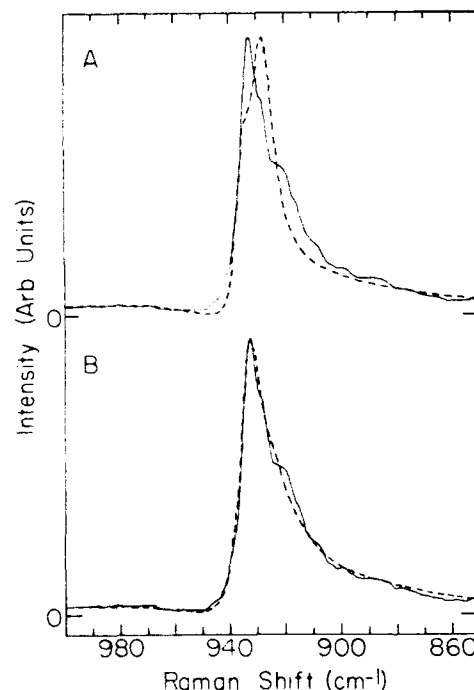


Figure 5. CARS Spectrum of Shock-Compressed Liquid Nitromethane CN-Stretching Mode. (a) Synthetic spectrum (dashed) with all hot bands and using model. (b) Synthetic spectrum (dashed) with all non-diagonal anharmonic coefficients set to zero.

nitromethane CARS spectrum, when it is applied to the shock-compressed material, even at modest pressures and temperatures. The weakest approximation in the model is that of the values of the anharmonicity coefficients, and the assumption that they do not change with pressure. Since the  $\nu_4$  vibrational frequency increases with pressure, indicating a stiffening of the potential for that motion, it might also become more resilient to the presence of other thermally populated vibrational motions. The consequence of this picture would be that the off-diagonal anharmonic coefficients would become small compared to  $X_{44}$ . Figure 5b shows a synthetic CARS spectrum assuming  $X_{4j} = 0$ , for  $j \neq 4$ , and only  $X_{44}$  and  $\Gamma$  are varied for the best fit. The quality of the fit in Figure 5b is clearly better than that of 5a. The value of  $X_{44}$  used for 5b is only slightly larger than that used for the ambient spectrum. The increase may be indicative of some softening of the upper portion of the potential well with pressure. This behavior is somewhat different from that observed in nitrogen,<sup>27</sup> but may be due to the different depths of the wells or the different nature of diatomic molecules versus polyatomic molecules.

The apparent failure of the simple model presented here to satisfactorily represent the vibrational spectra of shock-compressed nitromethane suggests that intermolecular interactions can affect intramolecular potentials in sometimes surprising ways. Much further experimental work and substantial theoretical guidance will be necessary before these effects are fully understood.

## ACKNOWLEDGEMENTS

We are indebted to John Chavez, John Chacon, Rick Eavenson, James Esparza, Concepcion Gomez, Vivian Gurele, Werner Haufchild, J. D. Johnson, Robert Livingston, David O'Dell, George Pittel, Dennis Price, Terry Rust, Dennis Shampine, and M. S. Shaw for their invaluable work in obtaining the results presented here. We appreciate the use of Josephs Fritz's MACRAME code that was used to calculate shock states, and Robert Caird's Fourier smoothing routines that were used in our data analysis. We are grateful to

J. L. Lyman, R. S. McDowell, and D. J. Taylor for enlightening discussions about polyatomic vibrational spectra. Finally, we are especially grateful to J. W. Shaner for his encouragement and support of this work.

## REFERENCES

1. Schuch, A. F. and Mills, R. L., *J. Chem. Phys.*, Vol. 52, 1970, p. 6000.
2. Mills, R. L.; Liebenberg, D. H.; and Bronson, J. C., *J. Chem. Phys.*, Vol. 63, 1975, p. 4026.
3. Schiferl, D.; Cromer, D. T.; and Mills, R. L., *High Temp. High Pressures*, Vol. 10, 1978, p. 493.
4. Schiferl, D.; Buchsbaum, S.; and Mills, R. L., *J. Phys. Chem.*, Vol. 89, 1985, p. 2324.
5. Young, D. A.; Zha, C.-S.; Boehler, R.; Yen, J.; Nicol, M.; Zinn, A. S.; Schiferl, D.; Kinkead, S.; Hanson, R. C.; and Pinnick, D. A., *Phys. Rev. B*, Vol. 35, 1987, p. 5353.
6. Zinn, A. S.; Schiferl, D.; and Nicol, M. F., *J. Chem. Phys.*, Vol. 87, 1987, p. 1267.
7. Zubarev, V. N. and Telegin, G. S., *Soviet Physics - Doklady*, Vol. 7, 1962, p. 34.
8. Dick, R. D., *J. Chem. Phys.*, Vol. 52, 1970, p. 6021.
9. Nellis, W. J. and Mitchell, A. C., *J. Chem. Phys.*, Vol. 73, 1980, p. 6137.
10. Nellis, W. J.; Holmes, N. C.; Mitchell, A. C.; and van Thiel, M., *Phys. Rev. Lett.*, Vol. 53, 1984, p. 1661.
11. Schott, G. L.; Shaw, M. S.; and Johnson, J. D., *J. Chem. Phys.*, Vol. 82, 1985, p. 4264.
12. Nosé, S. and Klein, M. L., *Phys. Rev. Lett.*, Vol. 50, 1983, p. 1207.
13. LeSar, R., *J. Chem. Phys.*, Vol. 81, 1984, p. 5104.
14. McMahan, A. K. and LeSar, R., *Phys. Rev. Lett.*, Vol. 54, 1985, p. 1929.
15. Ree, F. H. and Winter, N. W., *J. Chem. Phys.*, Vol. 73, 1980, p. 322.

16. Ross, M. and Ree, F. H., *J. Chem. Phys.*, Vol. 73, 1980, p. 6146.
17. Shaw, M. S.; Johnson, J. D.; and Holian, B. L., *Phys. Rev. Lett.*, Vol. 50, 1983, p. 1141.
18. Johnson, J. D.; Shaw, M. S.; and Holian, B. L., *J. Chem. Phys.*, Vol. 80, 1984, p. 1279.
19. Shaw, M. S.; Johnson, J. D.; and Ramshaw, J. D., *J. Chem. Phys.*, Vol. 84, 1986, p. 3479.
20. Lesar, R. and Shaw, M. S., *J. Chem. Phys.*, Vol. 84, 1986, p. 5479.
21. Belak, J.; Etters, R. D.; and Lesar, R., *J. Chem. Phys.*, to be published 1988.
22. Ross, M., in *Shock Waves in Condensed Matter - 1987*, edited by S. C. Schmidt and N. C. Holmes, North-Holland, Amsterdam, 1988, p. 95.
23. Hamilton, D. C. and Ree, F. H., *J. Chem. Phys.*, to be published 1989.
24. Reichlin, R.; Schiferl, D.; Martin, S.; Vanderborgh, C.; and Mills, R. L., *Phys. Rev. Lett.*, Vol. 55, 1985, p. 1464.
25. Bell, P. M.; Mao, H. K.; and Hemley, R. J., *Physica*, Vols. 139-140B, 1986, p. 16.
26. Radousky, H. B.; Nellis, W. J.; Ross, M.; Hamilton, D. C.; and Mitchell, A. C., *Phys. Rev. Lett.*, Vol. 57, 1986, p. 2419.
27. Moore, D. S.; Schmidt, S. C.; Shaw, M. S.; and Johnson, J. D., *J. Chem. Phys.*, to be published 1989.
28. Engelke, R., *Phys. Fluids*, Vol. 23, 1980, p. 875.
29. Engelke, R.; Schiferl, D.; Storm, C. B.; and Earl, W. L., *J. Amer. Chem. Soc.*, to be published 1988.
30. Marsh, S. P., *LASL Shock Hugoniot Data*, University of California Press, Berkeley, CA, 1980, p. 599.
31. Rice, M. H.; McQueen, R. G.; and Walsh, J. M., *Solid State Physics 6*, Academic Press, NY, 1958, p. 1.
32. Druet, S. A. J. and Taran, J. -P. E., *Appl. Phys. Lett.*, Vol. 29, 1976, p. 174.
33. Vedam, K., in *Critical Reviews in Solid State and Materials Sciences*, edited by D. E. Schuele and R. W. Hoffman, CRC, Boca Raton, FL, 1983, p. 1.
34. Akhmanov, S. A.; Gadjiev, F. N.; Koroteev, N. I.; Orlov, R. Yu.; and Shumay, I. L., *Appl. Opt.*, Vol. 19, 1980, p. 859.
35. Shumay, I. L.; Zadkov, V. N.; Heinzen, D. J.; Kash, M. M.; and Feld, M. S., *Optics Lett.*, Vol. 11, 1986, p. 233.
36. Yu, Z. H.; Strachan, D.; and Daniels, W. B., Private Communication.
37. McKean, D. C. and Watt, R. A., *J. Mol. Spectrosc.*, Vol. 61, 1976, p. 184.
38. Malewski, G.; Pfeiffer, M.; and Reich, P., *J. Mol. Structure*, Vol. 3, 1969, p. 419.
39. Nowak, A. V. and Lyman, J. L., *J. Quant. Spectrosc. Radiat. Transfer*, Vol. 15, 1975, p. 945.
40. Arndt, R. and Yarwood, J., *Chem. Phys. Lett.*, Vol. 45, 1977, p. 155.
41. Hill, J. R.; Moore, D. S.; Schmidt, S. C.; and Storm, C. A., "Raman, Infrared, and Coherent Anti-Stokes Raman Spectroscopies of the Mixed Deuterium Isotopomers of Nitromethane," to be published.
42. Schmidt, S. C.; Moore, D. S.; Shaner, J. W.; Shampine, D. L.; and Holt, W. T., "Coherent Anti-Stokes Raman Scattering in Benzene and Nitromethane Shock-Compressed to 10 GPa," *Physica*, Vol. 139 & 140B, 1986, p. 587.
43. Moore, D. S.; Schmidt, S. C.; Shaner, J. W.; Shampine, D. L.; and Holt, W. T., "Coherent Anti-Stokes Raman Scattering in Benzene and Nitromethane Shock-Compressed to 11 GPa," *Shock Waves in Condensed Matter - 1985*, Gupta, Y. M., Ed. (Plenum Publishing, NY, 1986), p. 207.

44. Schmidt, S. C.; Moore, D. S.; Schiferl, D.; Châtelet, M.; Turner, T. P.; Shaner, J. W.; Champine, D. L.; and Holt, W. T., "Coherent and Spontaneous Raman Spectroscopy in Shocked and Unshocked Liquids," in *Advances in Chemical Reaction Dynamics*, Rentzepis, R. M. and Capellos, C., Eds. (D. Reidel Publishing, NY, 1986) p. 425.
45. Cromer, D.; Ryan, R. R.; and Schiferl, D., *J. Phys. Chem.*, Vol. 89, 1985, p. 2315.
46. Lysne, P. C. and Hardesty, D. R., *J. Chem. Phys.*, Vol. 59, 1973, p. 6512.

# ABSORPTION SPECTROSCOPY OF SHOCKED BENZENE

N. C. Holmes, G. Otani, P. McCandless, and S. F. Rice  
University of California, Lawrence Livermore National Laboratory  
Livermore, California 94550

*We have used absorption spectroscopy to observe the formation of carbon particles as a separated phase during the passage of strong shock waves in samples of liquid benzene ( $C_6H_6$ ). The use of a two-stage light-gas gun allows the study of this phenomenon as a function of shock pressure near the reaction threshold at about 13 GPa. Time resolved measurements of sample opacity were performed along with absorption spectra obtained during a 60 ns interval during shock passage. The rate of formation of the particles is rather slow, but is strongly dependent on the final pressure and temperature achieved in the shock loading process.*

## INTRODUCTION

Chemical equilibrium calculations have indicated that hydrocarbon compounds should form a separated graphitic or diamond-like phase after decomposition at high pressures and temperatures.<sup>1</sup> This is expected to be a common process, and is expected to occur in simple organic fluids as well as high explosives. The rates of formation of such particulates are crucial to understanding the reaction process and detonation behavior of energetic materials. If the process is slow, then the reaction zone behind a shock or detonation front may be extended in time and space, and it becomes difficult to precisely determine the Chapman-Jouget point, for example. It also means that equilibrium calculations may be insufficient to describe the behavior of energetic materials at early times after reaction or detonation.

In these experiments, we have attempted to determine the presence of particulates in the samples, and their rate of formation, by observing Mie scattering<sup>2,3</sup> from the particles. The scattering cross-section for this process varies as the inverse fourth power of the wavelength, so we expect to see strong scattering at short wavelengths with a distinctive power-law behavior. This process was previously observed qualitatively in several organic

liquids, but with low spectral and time resolution.<sup>4</sup>

We chose benzene ( $C_6H_6$ ) as a sample for several reasons: it has a well-determined equation of state with a well-defined reaction threshold,<sup>5</sup> it is initially transparent to visible wavelengths, and it is easily handled. A two-stage light-gas gun was used to generate shock waves in the samples. This has several important advantages for these studies. The shock loading is uniform over a relatively large diameter (25 mm), and is uniform in time. The shock pressure can be varied in small steps by varying the projectile velocity. The final shock state can be very precisely determined using the projectile velocity,<sup>6</sup> the initial state and equation of state of the sample, and simple conservation relations. These characteristics make it possible to carefully map out the behavior of the sample over a narrow range of pressures near the anticipated reaction threshold.

## EXPERIMENTAL METHODS

We developed a double-beam, double-pass method for measurements of scattering in shocked samples as shown in Figure 1. It features a gateable, dual, linear, diode-array detector to record spectra of the incident light on the sample, and the transmission spectrum

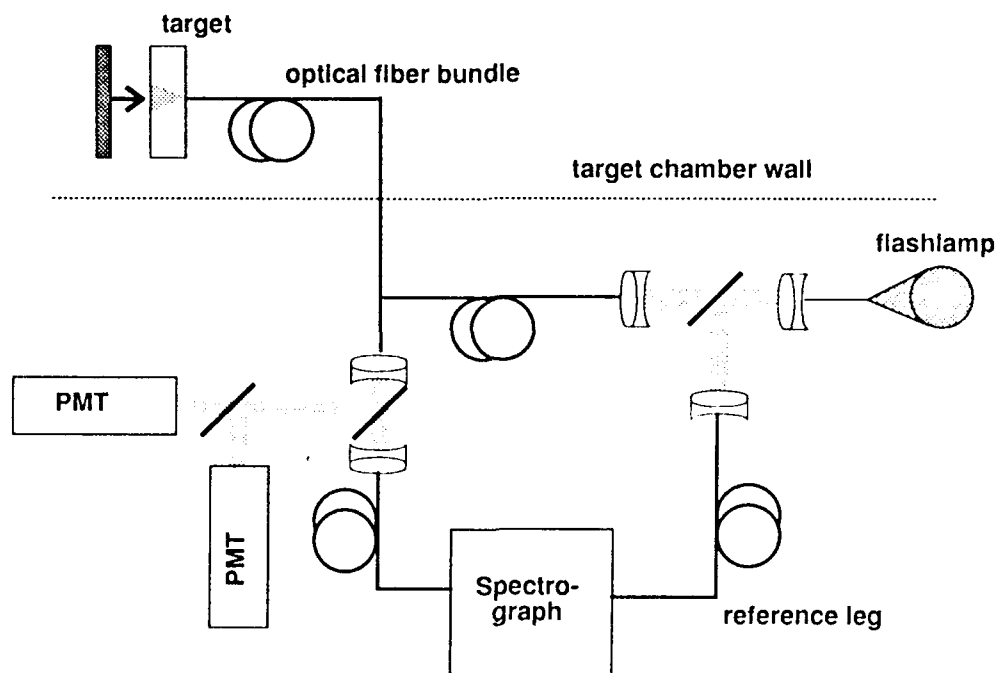


Figure 1. Schematic Representation of the Absorption Experiment

of the sample during shock passage through the sample. An intense argon flash-lamp is used to illuminate the sample. A portion of the flashlamp light is coupled to the spectrograph with a fiber bundle. Light from the flashlamp illuminates the sample using the center fiber of a 7-fiber bundle. This light passes through the sample, reflects from a diamond-turned Al baseplate, traverses the sample again, and the return light is collected with 6 fibers arranged in a circle around the center fiber. The thickness of the sample cavity is 5 mm. The optical fibers were silica with a diameter of 400  $\mu\text{m}$ . The inter-fiber spacing was 500  $\mu\text{m}$  between centers. The six output fibers are combined into a single bundle. Its output is then imaged onto another bundle which is used to illuminate the second array detector in the spectrograph. A portion of the output light is also split to two photomultiplier tubes, providing time-resolved detection in two wavelength bands centered at 600 nm and 450 nm. However, for the experiments described here, we had electronic difficulties with the double-array detector. We found that the light source was reproducible within about 2 percent in intensity and spectral shape; that made it possible to use a single, 1024-element, array detector. The system was calibrated

with a flash spectrum obtained with a sample of benzene in the target just prior to the shock experiment. This allows us to correct for the transmission characteristics of the entire optical system. Wavelength calibration was obtained using a low-pressure Hg discharge lamp. For most of the experiments, the wavelength range covered by the spectrograph was 370-630 nm. The gate width of the diode-array detector was set to about 60 ns.

Benzene samples were reagent grade. We removed dissolved gas using a sequence of three cycles in which the benzene container was frozen in liquid nitrogen, evacuated to about 10  $\mu\text{m}$  Hg pressure, and then warmed to room temperature to release trapped gasses. The sample was introduced into the sample cavity using a small positive pressure of He to flow the fluid through the target. The target was pumped out to about 10  $\mu\text{m}$  Hg pressure before filling. This procedure was used to minimize any chance of bubble formation in the sample.

To test the response of this system, we measured the absorption of water at 13 GPa, where it is known to be transparent. The ratio between the pre-shock and shocked spectra (Figure 2a) shows no absorption, and the ratio

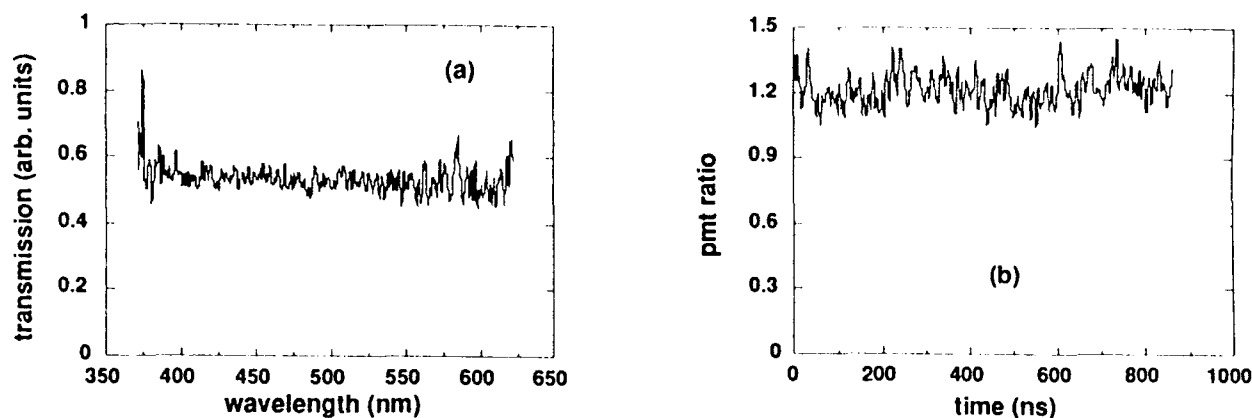


Figure 2. Transmission Data for Water Shocked to 13.0 GPa. In (a), we show the ratio between the dryrun spectrum with water in the sample chamber, and the spectrum acquired 300 ns after shock entry into the water sample chamber. The flat overall spectrum indicates that no absorption exists in the wavelength interval shown. The average value is less than 1 because the reflecting baseplate is less reflective after shock arrival in the sample. In (b) we show the time-resolved ratio between the red (600 nm) and blue (450 nm) photomultiplier records. The constant ratio also indicates that the sample remains transparent throughout the transit of the shock across the sample.

of the time-resolved photomultiplier records shows no significant time dependence (Figure 2b). The time dependence of the records is shown in Figure 3 for the 450 nm channel. The arrival of the shock in the sample is clearly marked by a decrease in reflected intensity as the baseplate of the sample becomes rougher. The increasing intensity after this initial decrease arises from the collection geometry, since the reflecting surface is moving closer to the collection fibers.

## EXPERIMENTAL RESULTS

Four benzene samples were shocked to pressures between 12.4 and 13.8 GPa using Al impactors. The sample bodies were Al also, and the projectile velocity varied between 3.19 and 3.42 km/s. These experiments were completed just a few days prior to the submission deadline for this report, so only a preliminary analysis of the data is available.

All of the experiments showed a decrease of intensity in the blue channel with time, indicating blue scattering. At the highest pressure studied, both photomultiplier channels became effectively opaque after several hundred nanoseconds. This provides a measure of the rate of particle formation. In

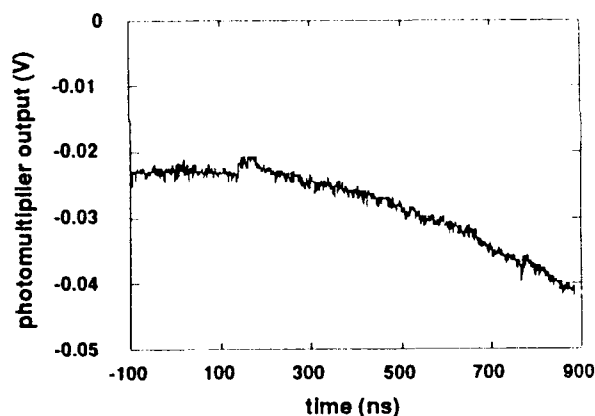


Figure 3. Photomultiplier Record for the Water Absorption Experiment at 13.0 GPa at 450 nm

Figure 4, we show the photomultiplier data for benzene shocked to 130 kbar, the same pressure observed by Yakusheva et al.<sup>4</sup> The response in the red channel at 600 nm (Figure 4a) is very similar to that observed for water, but the record for the blue channel (Figure 4b) shows a monotonic decrease in transmitted light up to the time at which the shock reaches the fibers at about 930 ns. Similar behavior was obtained for the other experiments.

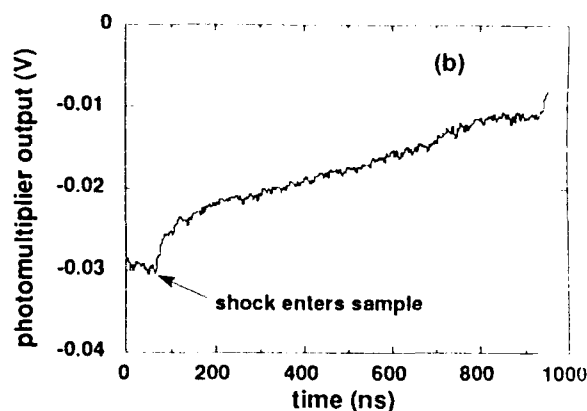
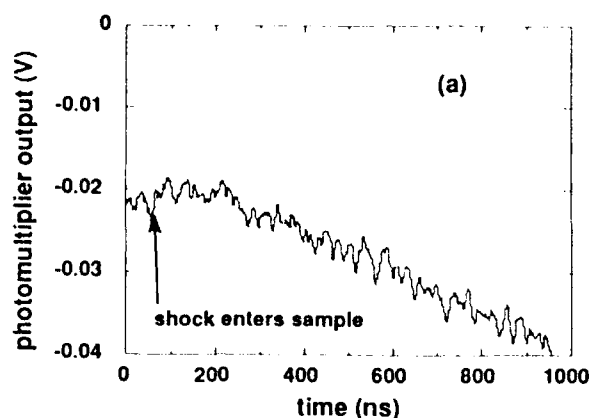


Figure 4. Photomultiplier Data for Absorption of Benzene at 13.0 GPa. In (a), recorded at 600 nm, note that the overall response is very similar to Figure 3, indicating very little absorption. In the 450 nm Channel (b), the transmission decreases steadily after shock arrival in the sample.

By taking the ratio between the blue and red channels, we can get an indication of the normalized time-resolved transmission characteristics, with the effects of target light-collection geometry removed. In Figure 5, we show these ratios for four shock experiments. The reaction rate appears to increase monotonically as the pressure is increased from 12.4 GPa to 13.8 GPa. At the highest pressure, the sample becomes nearly opaque in the blue region after about 500 ns. We do not observe, in this case, a sharp onset of the reaction as has been observed in other fluids.<sup>4</sup> Spectroscopic evidence also indicates that some backscatter from carbon particles may be present at the highest pressure.

## SUMMARY

We have used a double-pass absorption technique to measure the time-dependent transmission of benzene shocked from 12.4–13.8 GPa. Blue light is strongly attenuated in these samples, and the strength of the attenuation increases monotonically with time and shock pressure in the range studied. We believe that the apparent absorption of the blue light is due to Mie scattering from solid carbon particles. These particles form as a result of phase separation after chemical decomposition by the high pressures and temperatures behind the shock front. Further analysis of the photomultiplier data and the

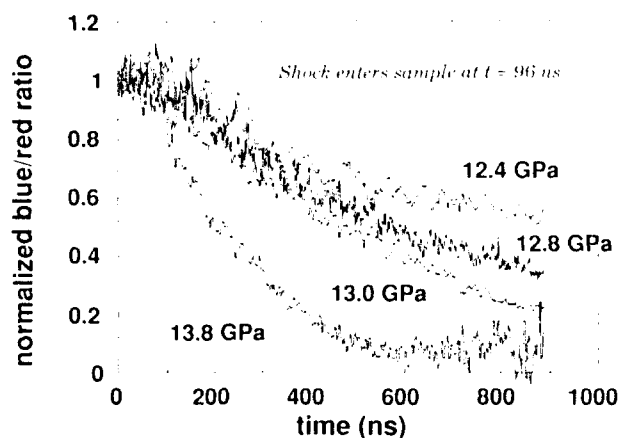


Figure 5. The Ratio of the 450 nm to 600 nm Photomultiplier Data for Benzene Shocked to Pressures from 12.4 GPa to 13.8 GPa

spectroscopic data will be required to confirm this conjecture.

## ACKNOWLEDGEMENTS

We are pleased to acknowledge the assistance of L. Oswald, K. Pederson, and R. Schuldheisz for gun operations. The flashlamp power supply was kindly furnished by L. Steinmetz, and the technical assistance provided by S. Mueldner and A. Rivera is greatly appreciated. We also gratefully acknowledge the encouragement and support of W. J. Nellis, M. Ross, E. Lee, and R. McGuire.



This work was performed under the auspices of the U. S. Department of Energy (DOE) under contract No. W-7405-Eng-48.

## REFERENCES

1. Ree, F. H., *J. Chem. Phys.*, Vol. 81, 1984, p. 1251.
2. Mie, G., *Ann. d. Physik (4)*, Vol. 25, 1908, p. 377.
3. Born, M. and Wolf, E., *Principles of Optics*, fifth edition, Pergamon Press, Oxford, 1975, pp. 633-664.
4. Yakusheva, O. B.; Yakushev, V. V.; and Dremin, A. N., *High Temp.-High Press.* Vol. 3, 1971, p. 261.
5. Dick, R. D., *J. Chem. Phys.*, Vol. 52, 1970, p. 6021.
6. Mitchell, A. C. and Nellis, W. J., *Rev. Sci. Instrum.*, Vol. 52, 1981, p. 347.

## DISCUSSION

FRED VOLK  
Fraunhofer Institut  
Pfinztal, FRG

What do you think about shocking acetylene?

Did you look for the carbon formed by the shocking of benzene?

## REPLY BY N. C. HOLMES

I have considered experiments on the alkanes, to investigate systems which have their electronic absorption in the far UV. I believe that acetylene will also qualify on these grounds. The alkanes have been better characterized with respect to their EOS.

The second question, I believe, aims at whether carbon is found in the recovered decomposition products of shocked benzene. The answer is obviously, yes, but the yield of diamond is strongly dependent on the overall pressure-temperature history undergone by the sample. This means that sample geometry is very important. In our few attempts, we have not tried to achieve a quench after a single shock, so it is not surprising that the residue found is graphitic in nature. Our spectroscopic data strongly indicate that diamond-like carbon is formed initially in shocked benzene near the 13 GPa reaction threshold on the principal Hugoniot.

**SESSIONS ON  
INITIATION MODELING**

**Cochairmen: Pier Tang  
Los Alamos National Laboratory**

**John Field  
University of Cambridge**

**and**

**Kibong Kim  
Naval Surface Warfare Center**

**Graeme Leiper  
ICI Explosives**

# REACTION RATES AND THE CHARGE DIAMETER EFFECT IN HETEROGENEOUS EXPLOSIVES

G. A. Leiper

Nobel's Explosives Company, Ltd.  
Stevenston, KA20 3LN, UNITED KINGDOM

and

J. Cooper

Explosives Group Technical Centre  
ICI PLC, Stevenston, KA20 3LN, UNITED KINGDOM

*The relationship between the rate of release of chemical energy during detonation in condensed heterogeneous explosives, and the effect of charge diameter on the steady unconfined detonation velocity of such explosives, have been investigated. An axisymmetric detonation model based on slightly divergent flow theory and a multi-phase multi-component chemical reaction rate law, has been used to demonstrate that the functional form of the diameter effect curve varies from strongly downwards convex to strongly downwards concave in the detonation velocity inverse diameter plane, depending on the nature of the chemical heat release function. Experimental measurements on the diameter effect in a variety of explosives have been carried out and analyzed with the detonation model in support of the hypothesis. A development of the model has been used to analyze diameter effect curves to yield chemical reaction rate data without an a priori choice of reaction rate function. The effect of increasing heterogeneity on the reaction rate function has been illustrated. Finally, the relationship between the lower branch of the charge diameter effect and initiation has been used to discuss discontinuous diameter effect curves.*

## INTRODUCTION

The behavior of condensed phase explosives has been studied intensively for over 50 years. During that time, many means have been found for categorizing the various types of detonation behavior that have been seen, such that a series of logical classes could be constructed. One of the most successful of those schemes was that proposed by Price et al.,<sup>1</sup> who suggested that the detonics of the explosive, as characterized by the variation in critical diameter and detonation velocity - charge diameter effect, VoD(d), with voidage, provided a unique classification. Price demonstrated the existence of at least two classes, Group I and Group II

explosives, and related the classification scheme to the chemical and physical nature of the explosive. Group I explosives were intramolecular systems with the fuel and oxidant species in the same molecule, and Group II explosives were intermolecular compositions with the fuel and oxidizers intimately, but not atomically, mixed. The importance of this classification was in formalizing a relationship between the chemical and physical nature of explosives and detonation performance.

Hino and Hasegawa,<sup>2</sup> using a modified Eyring model, also established such a link by analyzing the VoD(d) behavior of various commercial dynamites to derive the shape of

the chemical heat release function within the reaction zone of the explosives. Paterson<sup>3</sup> carried out similar calculations with a model based on the work of Jones.

Since these publications, detonation theory has been significantly refined, with both analytic<sup>4</sup> and numerical models<sup>5</sup> being used to investigate fundamental aspects of explosive behavior. The types of explosives in use have also greatly increased, and the distinction between military and commercial compositions diminished, as common goals of low sensitiveness, high reliability, and optimal performance have been achieved. In this paper the relationship between the physical and chemical composition of explosives, the chemical reaction rate of explosives, and the detonation velocity-charge diameter effect--have been further examined.

Initially, a small divergent detonation model, valid for steady state axisymmetric flows, was used to demonstrate the functional relationship between the rate of release of chemical energy within the detonation and the shape of the VoD(d) function. The model was then used with a multi-phase, multi-component reaction rate function to interpret experimentally determined VoD(d) relationships for a variety of explosives ranging from cast Composition B 3, to a high voidage "permitted" ("permissible") nitroglycerine sensitized powder. From these, the chemical reaction rate of the explosive was calculated as a function of shock pressure and extent of reaction. An explicit picture of the relationship between the functional form of the chemical reaction rate and the VoD(d) behavior was developed. An extension of the flow theory, capable of interpreting the VoD(d) function without recourse to a predetermined reaction rate function was used to elucidate the effect of voidage level, heterogeneity, and chemical sensitization of the reaction rate behavior of various commercial and military explosives. Finally, the flow theory was used to comment on the behavior of the initiation branch of the VoD(d) curve, and the high/low velocity regimes of nitroglycerine sensitized explosives in particular.

## FLOW THEORY

The model used in this analysis was derived from the Wood-Kirkwood<sup>8</sup> theory, after the work of Chan.<sup>9</sup> It has been fully reported elsewhere,<sup>6</sup> and only a brief outline will be given. The model is one of a steady state detonation wave propagating in a cylindrical charge of finite radial dimension. The solution is specialized onto the charge axis, the radial terms becoming a perturbation on the one-dimensional ZND model. A consequence of these terms is the occurrence of a second CJ condition representing a balance between the rate of chemical energy deposition in the flow and the rate of energy loss due to lateral expansion. The detonation velocity becomes an eigenvalue of the equation set and is dependent on the radial flow field, i.e., the charge diameter and confinement, and on the chemical reaction rate of the explosive. A knowledge of either the kinetic behavior or the VoD(d) relationship can, by use of the model, be used to determine the other. The CPEX model, as developed along these lines by Kirby and Leiper,<sup>6</sup> was used in this work. It has been extensively tested, and has been found to be reliable when used in either a predictive<sup>10</sup> or interpretive manner.<sup>11</sup>

A key aspect to successful use of the model is the functional form chosen to represent the chemical reaction rate of the composition under shock conditions. The latest generation of military explosives and all commercial explosives are multi-phase, multi-component mixtures that require a complex rate law in which reaction of any one component or phase may depend upon the reaction of any other. A rate law based on Gaussian functions has been proposed previously,<sup>6</sup> which successfully modelled several types of explosives using only four adjustable parameters. The form of the law was

$$\beta = (1 - \beta) \left( \frac{a_h (p - p_h)^{b_h}}{t_h} + \frac{a_l p^{b_l}}{t_l} + \frac{a_s p^{b_s}}{t_s} \right) \quad (1)$$

where  $\beta$  was the degree of reaction;  $\bullet$  denoted time differentiation; and the subscripts h, l,

and  $s$  referred to hot-spot, matrix, and included solid phases within the explosive. The  $a_i$  ( $i = h, l, s$ ) were form functions, dependent only on the initial formulation and degree of reaction of the explosive. The  $b_i$  pressure exponents were normally set to unity and the  $t_i$  were time constants used as fitting parameters. A critical pressure for the hot-spot  $p_h$  was used to represent the criticality condition of the hot-spot, and provided a fourth fitting parameter. The strength of the model was the ability of the functional form of the  $a_i(\beta)$  terms to reproduce the complex reaction rate behavior of the explosive. The above relationship was used throughout the following analyses.

## REACTION RATES AND THE VoD(d) RELATIONSHIP

### General Principles

The VoD(d) relationship could be characterized in terms of the position of the critical point, i.e., the critical diameter and the velocity decrement at failure, and the shape of the function between the ideal and critical states, e.g., downward convex, linear, downward concave, and discontinuous.

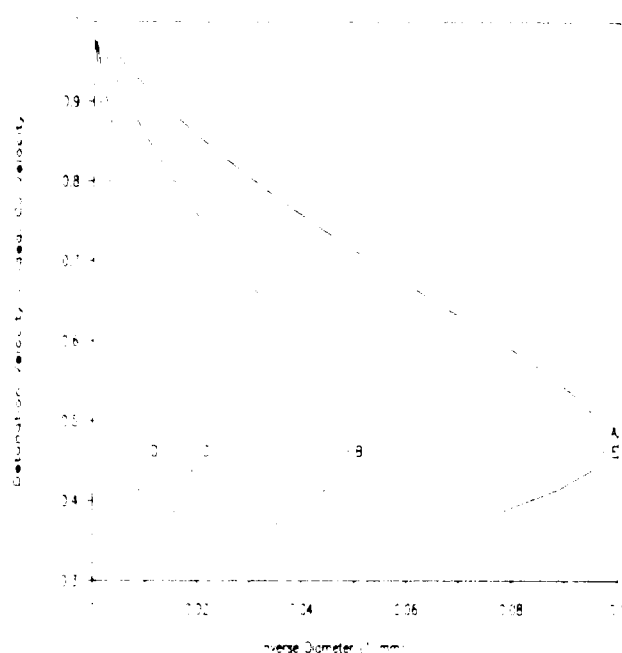


Figure 1. Effect of Absolute Reaction Rate on VoD(d)

The critical diameter was found to scale with absolute chemical reaction rate; fast reactions in general giving small critical diameters and vice versa. This was demonstrated qualitatively by modeling the behavior of a standard composition with CPEX, then modifying the rate parameters by increasing the reaction times, Figure 1. For curves B, C, and D the reaction was slowed, compared to curve A, by factors of 2, 5, and 10, respectively. Curves B, C, and D were then scaled according to their critical diameters, and the scaled lines, curve E, lay on top of curve A.

The velocity decrement at failure could be taken as a measure of the sensitivity of the reaction rate to the local thermodynamic state variables. For explosives with reaction schemes in which key steps were critically affected by the local temperature and pressure, small changes in shock velocity (pressure, temperature) might cause the reaction to cease. There would, therefore, be a small velocity decrement at failure. For schemes which were robust to fluctuations in the local environment, the decrement at failure would be large. Modifying the reaction rate parameters of the standard composition by increasing

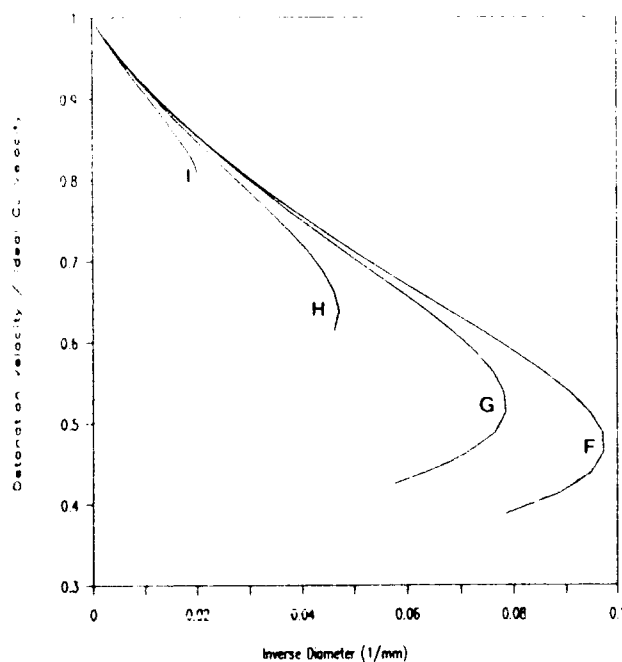


Figure 2. Effect of Rate Sensitivity on VoD(d)

the critical pressure illustrated this effect (Figure 2). With increasing critical pressure the failure velocity increased from 45 percent to 80 percent of the ideal value; see curves F to I.

The factors controlling the functional form of the VoD(d) relationship were investigated. A hypothesis was constructed that the VoD(d) behavior curve could be controlled either by hydrodynamic, or chemical reaction rate effects. If chemical reaction was complete, or if the reaction profile was such that there were significant periods of slow reactivity in the system, hydrodynamic control predominated. If the reaction profile was rapidly varying in the region of the CJ plane, then the control would be chemical in nature. Moreover, for multi phase, multi component systems each component or phase might exert control over particular regions of VoD(d). Detailed experimental evidence of the hypothesis is given below; however, a general example of the effect has been constructed

A standard explosive was analyzed with the flow model, assuming that there were three phases (hot spot, bulk 1, bulk 2). A reaction dependency was invoked such that bulk 2 was ignited by bulk 1, which was ignited by the hot spot phase. The reaction time constants of each phase were varied from 100:1 to 1:100,

and the VoD(d) behavior predicted (Figure 3). The constant pressure reaction rate was also calculated at a reference pressure of 5 GPa and plotted in the reaction coordinate - reaction rate plane,  $\beta(\beta)$ , Figure 4. A family of VoD(d) curves were calculated, ranging from downward convex to downward concave. The shape of the curves correlated with the shape of the  $\beta(\beta)$  functions. Those relationships that showed "thermal explosion" behavior, a very low initial rate followed by a sharp peak, gave downward convex VoD(d), Curve A;  $\beta(\beta)$  that showed more heterogeneous behavior, high initial rates followed by flat or slowly varying functions, gave downward convex VoD(d), Curve C.

The regions of hydrodynamic and chemical control in the VoD(d) relationships differed markedly in the two cases. Complete chemical reaction within the CJ zone was attained in diameters close to critical for "thermal explosion" type behavior, but only in diameters far from critical for heterogeneous-type reactions. Hydrodynamic control was, therefore, the dominant effect in the former, but chemical control in the latter. "Thermal explosion" behavior is that normally seen in monomolecular and mixed monomolecular military explosives,<sup>12</sup> and heterogeneous that normally associated with the VoD(d) of blasting agents.<sup>13</sup>

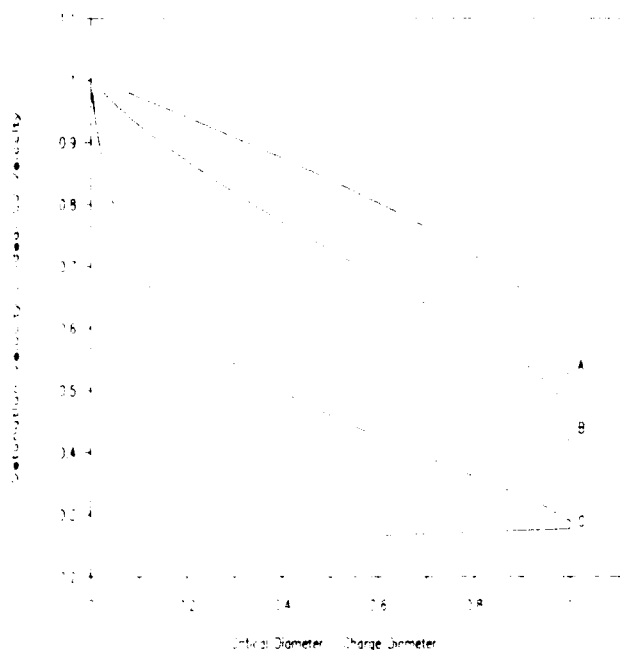


Figure 3. Effect of Rate Form on VoD(d)

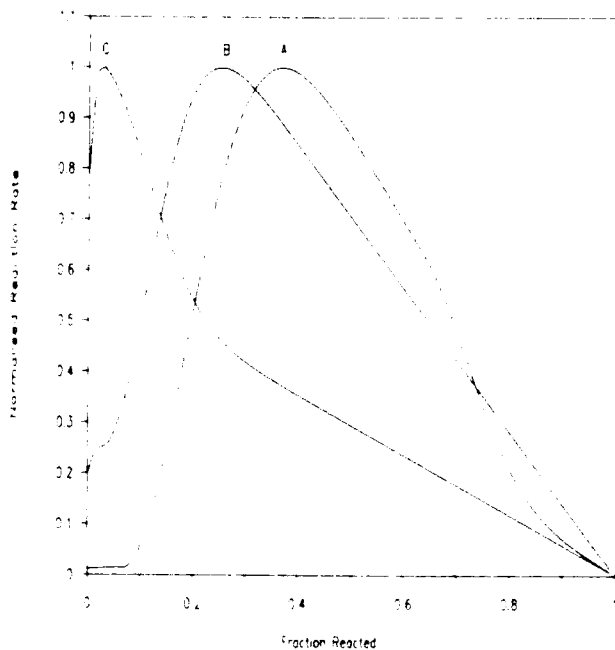


Figure 4. Reaction Rate Forms

## Experimental Evidence

The VoD(d) relationships for a variety of real explosives were either measured or taken from the literature, and analyzed with the flow theory using the multi component, multi-phase reaction rate. The explosives examined were Composition B-3, an air sensitized all liquid emulsion, an air/paint grade aluminum sensitized slurry with both solid oxidizer and metallic fuel phases, and a nitroglycerine sensitized powder. These corresponded to an increasingly heterogeneous and non-ideal sequence of compositions.

For all but the Composition B-3, where sufficient data was available in the literature,<sup>14</sup> detonation velocities were measured on right cylindrical rate sticks cartridged in manila paper. The velocity measurement was made by a time of flight technique over a distance of 200 mm, using either collapse pin probes or capped fiber optic flash gaps. The detonation was initiated by a strong detonator or small primer, such that it was initially overdriven. The wave was allowed to run at least six charge diameters before any measurement was made. Critical diameters were measured in an independent series of experiments without probes, as these perturbed the flow sufficiently to cause the detonation wave to fail prematurely.

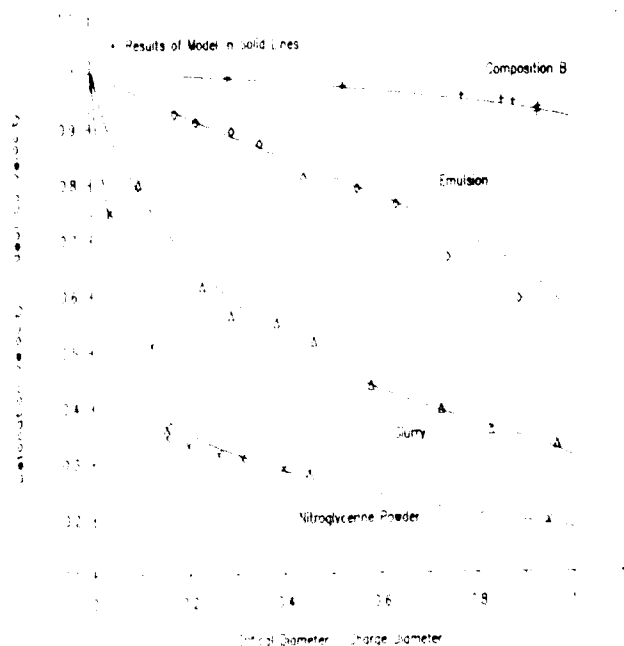


Figure 5. Experimental Diameter Effect Curves and CPEX Fits

The flow model was fitted to the experimental data, using the time constants and critical pressure in Equation (1) as parameters. A modified line search method was used to first fit the theory to the critical state. This was followed by a constrained minimization, optimizing the fit over all the data, while ensuring that the calculated critical state lay at smaller diameter and lower detonation velocity than the experimental value. In very difficult cases, the minimization technique was not robust, and a line search method was used throughout the procedure. The experimental VoD(d) data and the fits from the theory are shown below (Figure 5).

The absolute values of the fitting parameters in the reaction rate were of little significance. The functional form of the rate was, however, of interest, and the parameterized equation was used to predict the reaction rate profile,  $\beta(\beta)$ , at constant pressure (Figure 6). The profiles were plotted in a reduced coordinate system to facilitate comparison; the reaction rate being normalized by the maximum algebraic value of the function. The pressure at which the reaction rate profile was calculated depended upon the performance of the explosive. A pressure corresponding to the shock pressure at the mid point between ideal and failure velocities was chosen.

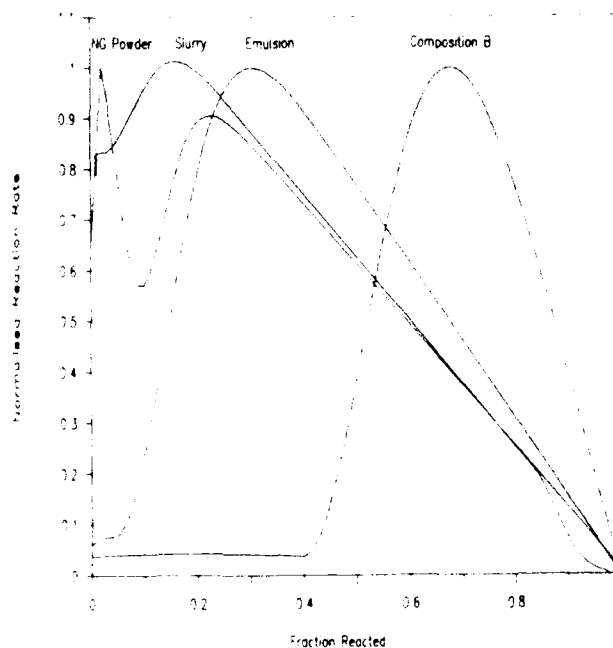


Figure 6. Reaction Rate Functions Based on VoD(d) Fits

Interpretation of the experimental VoD(d) data with the flow theory gave results in good agreement with the principles derived from the general cases derived above. Composition B 3, which displayed a downwards convex VoD(d), was best fitted by a rate law of the "thermal explosion" class. As the degree of heterogeneity increased from the emulsion to the slurry and NG powder, the  $\beta(\beta)$  function became more gently varying, with the absolute range of reaction rate within the function being much reduced, and the range of reaction coordinate over which the rate significantly varied being much wider.

Further comment on possible gross reaction mechanisms in heterogeneous explosives is required before more detailed analysis of the rate functions is attempted. A shock passing through the explosive would cause both a bulk temperature rise, and the creation of hot spots at the sites of density discontinuities. The simplest explosive, therefore, would be composed of hot spot and bulk phases. Two types of reaction could be initiated: thermal explosion or combustion. In either case, the first event would be consumption of the hot spot, and the propagation of a flame front into the bulk.

Consider first the behavior of the bulk and of components within the bulk which are capable of self reaction. If the thermal explosion process in the bulk was fast, then reaction would have occurred before the flame front could propagate a significant distance from the hot spot, and the reaction profile would be controlled by the sequential thermal explosions. If thermal explosion in the bulk was slow, then the reaction would be controlled by the flame velocity and by the geometry of the flame front as it expanded from the hot spot, resulting in a gently varying form for the  $\beta(\beta)$  relationship. Such behavior was demonstrated on comparing Composition B 3, where thermal explosion was possible in both phases, to emulsion, where thermal explosion of the bulk was not possible at typical shock induced temperature rises, and grain burning of the matrix had to occur (Figure 6).

If the explosive contained ingredients incapable of self combustion, e.g., metallic fuels, the reaction rate function should be smoothed out. The combustion of these

ingredients would only occur after ignition by reaction of surrounding material; the rate function would be a summation of the reaction rates of all the different phases present, staggered in time by the ignition process. Late time diffusion effects would enhance this smoothing for multi-component systems. The effect of reaction interdependency was proven by comparing single component emulsion to a multi component slurry, which displayed a much broader  $\beta(\beta)$  curve. The dependency of one reaction on another was seen in the NG powder; an initially high reaction rate was found to decline and then accelerate, as the hot-spot reacted and ignited the other components.

## EXPLICIT CHEMICO-PHYSICAL EFFECTS

A major disadvantage of the analysis up to this juncture has been that the reaction rate derived from the VoD(d) relationship was constrained to be a function represented by the rate law given in Equation (1). This was not a significant drawback in obtaining a general appreciation of the underlying physics, nor in commenting on the overall reaction processes in various explosives. However, it could be a major problem if more detailed comment was to be made on the relationship between the reaction profile and the physical and chemical composition of the explosive. In such cases, assuming a form for the rate law presupposed the nature of the reaction in the explosive.

A variant on small divergent flow theory has been used previously<sup>7</sup> to derive reaction profiles from VoD(d) data, with a minimum number of assumptions on the form of the rate law. The basis of the theory was that the VoD(d) data could be interpreted directly to give the locus of  $(\beta, \beta, t)_{CJ}$  as a function of charge diameter. The  $(\beta, \beta, t)_{CJ}$  triplets could then be combined to synthesis  $\beta(\beta)$  for the explosive, provided a method was known to correct for the effect of the different CJ pressures of each triplet set in the locus. The only disadvantage in this approach was the lack of data on the reaction profile below the critical point, i.e., at low degrees of reaction.

Leiper and Kirby<sup>7</sup> have shown that this technique, used with a simple  $ap^b$  scaling law with an exponent of unity, could provide



sufficiently accurate data to calculate the correct run to detonation in emulsion explosives. Their approach was followed in this work.

### Effect of Voidage

The effect of voidage on the reaction rate of an air sensitized emulsion explosive was examined. An all liquid emulsion explosive, comprising a continuous organic fuel phase and 83 percent ammonium nitrate solution oxidizer phase, was sensitized by the addition of various levels of thin walled hollow glass microspheres of size distribution between +75 -90 microns. The VoD(d) relationship was measured as a function of the microsphere concentration, and therefore, the voidage of the explosive (Figure 7).

The reaction profiles obtained from the VoD(d) data using the modified analysis (Figure 8), were interpreted in terms of the reaction process in the material. Consider both the fraction reacted at the critical point, corresponding to the starting point of each curve, and the reaction rate from that point upward. As voidage increased, the fraction reacting at the critical point increased from 40 percent at 10 percent voidage to 75 percent at 25 percent voidage. The relationship

between the degree of reaction at the critical point and the voidage was not linear, which inferred the presence of cooperative processes during hot spot formation, giving rise to a relatively greater volume of hot spot material at higher voidage. Subsequent reaction from the hot spot through the bulk was found to be accelerated by greater degrees of voidage. This was attributed purely to a decrease in the web thickness of the material, with increasing number density of hot spot sites.

### Effect of Chemical Sensitization

An emulsion was manufactured in which one half of the ammonium nitrate was replaced with hydrazine mono-nitrate, a self-explosive material. The detonation properties of the system were radically altered: the failure diameter was reduced by a factor of 3 and the failure velocity to one third of the ideal value (Figure 7). The gross sensitization reaction was investigated from the calculated reaction profile (Figure 8). The results showed the detonation at the critical state was supported by 15 percent reaction, and that the reaction profile, when compared with a similarly aerated standard emulsion, was only slightly accelerated. From these findings, it was

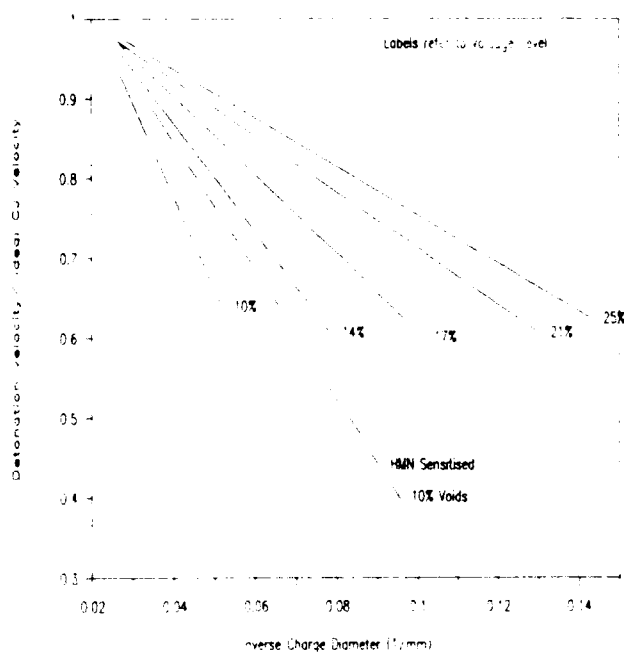


Figure 7. VoD(d) for Emulsion Explosive at Various Voidages

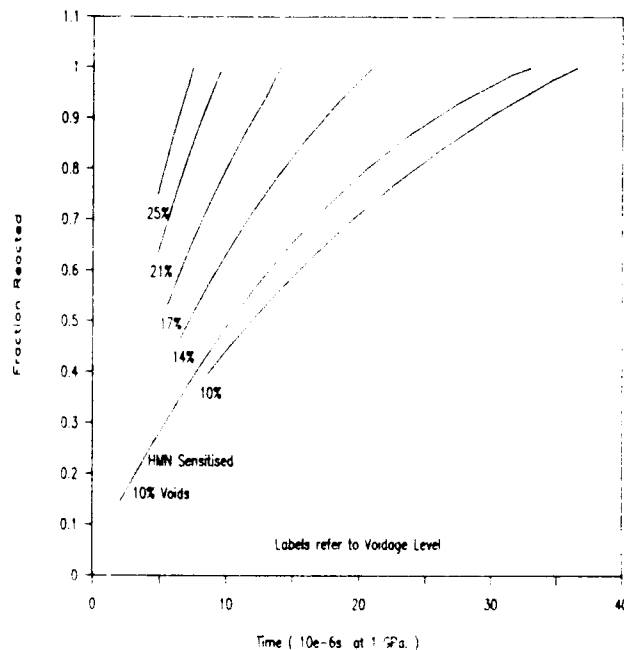


Figure 8. Emulsion Reaction Profiles at Various Voidages

inferred that the sensitizer operated by enhancing the hot spot chemistry, allowing reaction at very low shock stimuli, but not significantly affecting the velocity of the reaction emanating from the reacted hot spot volume.

### Very Heterogeneous Systems

In highly heterogeneous systems, the reactions which control the way performance varies with charge diameter might be those of the slower reacting energizing ingredients: solid oxidizers and fuels. The effect of such constituents on performance has been studied by comparing the performance of three explosives: cast Amatol, a paint grade aluminized slurry, and a NG sensitized powder explosive (Figures 9 and 10).

Amatol displayed a classic reaction profile, starting at 67 percent reaction corresponding to complete consumption of the TNT at the critical state, and progressing with a gently lessening slope to complete reaction. Assuming that this slope reflected the combustion of the ammonium nitrate by a grain burning process, and that the surface area initially available for combustion was that given by the outer surface of the particles,

the profile was used to calculate the surface erosion velocity of the ammonium nitrate at the detonation pressures in Amatol, which was found to be in good agreement with other combustion data published by Leiper.<sup>15</sup>

The nitroglycerine powder provided a more heterogeneous system which included a sensitizing phase, two solid energizers, and a large degree of voidage. The reaction profile clearly demonstrated a multi-phase, multi-component nature. At the critical point, the 15 percent reaction corresponded to complete consumption of the nitroglycerine sensitizer; there were then two separate consecutive phases to the reaction, a fast burn to 30 percent reaction followed by a grain burning profile to completion.

Finally, a three phase slurry was examined. The reaction profile was found to have several regions, reflecting the reaction of the various phases in the composition. At the critical state 15 percent has reacted, corresponding to hot-spot reaction of the flake grade aluminum sensitizer, and a fraction of the aqueous ammonium nitrate continuous phase. The reaction profile then underwent a number of stages: a region of steady reaction, comprising consumption of the residual matrix by a

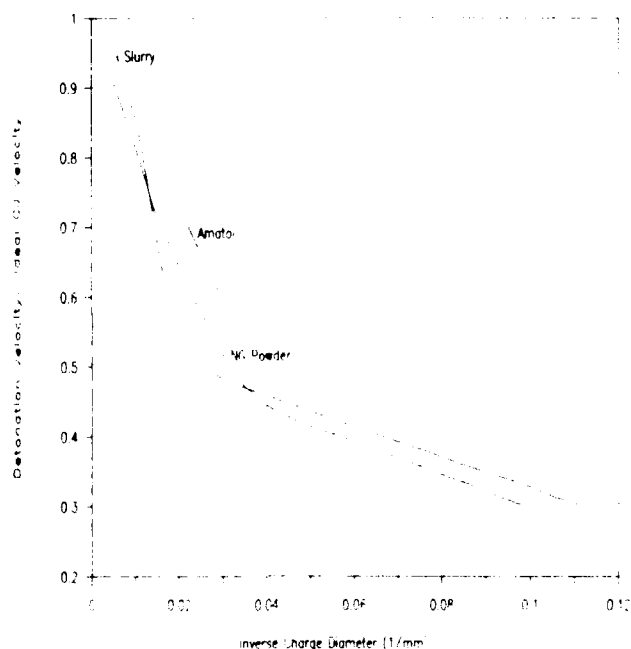


Figure 9. VoD(d) for Very Heterogeneous Systems

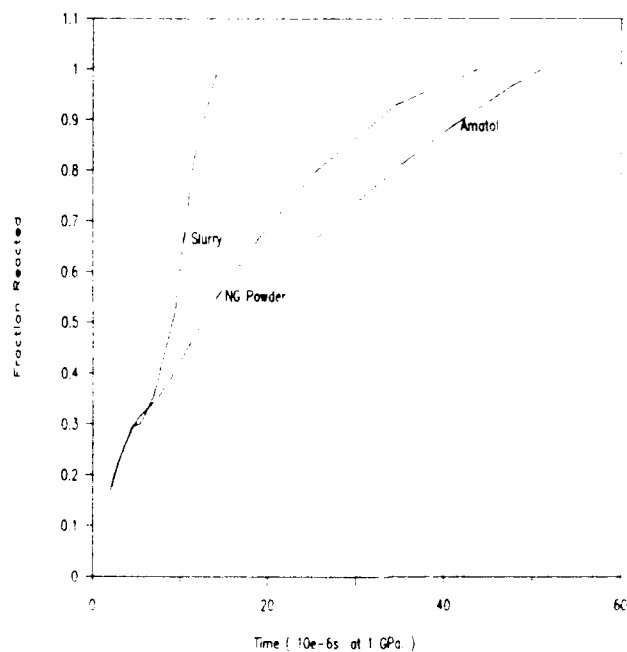


Figure 10. Effect of Energizers on VoD(d)

flame initiated at the hot spot; a region of almost no reaction, the crystalline ammonium nitrate self-combusting; and a region of accelerating reaction caused by ignition of the fuel grade aluminum, releasing fuel and energy to accelerate the ammonium nitrate combustion and completing reaction. The relationship between degree of reaction at the CJ plane and the charge diameter showed an extended flat area in the region between 1.5 and 4.5 times the critical diameter. In this zone, corresponding to the very slow region in the reaction profile at  $\beta = 0.3$ , the variation of detonation velocity with charge diameter was hydrodynamically as opposed to kinetically controlled, even though the reaction was far from completion.

## INITIATION BEHAVIOR

Conventionally, the VoD(d) relationship would be defined between the critical state and the ideal state, with detonation velocity rising with increasing charge diameter. In slightly divergent flow theory the locus of states is extended below the critical velocity, with detonation velocity falling with increasing charge diameter. It was suggested that this lower branch corresponded to a critical initiation locus for the explosive.<sup>6,16</sup> Slightly divergent flow theory could then be used to give an indication of the response of the explosive to various initiation stimuli: if conditions were created within the explosive, that lay within the area bounded by the VoD(d) curve and the ordinate, the shock would be accelerated; if conditions were such that the shock state fell outside that region, the shock would be retarded. A necessary requirement of a primer in establishing detonation in a charge would be, therefore, that a shock was generated which had a path in VoD(d) space that intersected the bounded region; for the shock was then accelerated to the stable point on the upper branch.

Using this hypothesis, and several of the calculations made above (Figures 1, 2, and 3), it was inferred that explosives based on "thermal explosion" type reaction profiles and concomitant high failure velocities, would be more difficult to initiate than those relying on hot spot/grain burning mechanisms, all other

aspects being equal. It was clear that an explosive which could detonate by either mechanism might display a VoD(d) relationship, which had a discontinuity at the diameter in which the change from mass "thermal explosion" to hot spot and burning occurred.

A tentative explanation of the phenomena of high and low velocity detonation was derived by considering the VoD(d) behavior of an explosive which might behave in such a fashion (Figure 11). The VoD(d) relationships (Curve 1 for the case of mass explosion in both the hot spot and the bulk phases, and Curve 2 for explosion in the hot spot phase but grain burning in the bulk) showed stable high and low velocity regimes, and a forbidden transition region. The explosive would detonate stably at low velocity on Curve 2 for all diameters below the critical diameter of Curve 1. For diameters greater than the intersection point of Curves 1 and 2, the stable state would lie at high velocity on Curve 1, as Curve 2 lay within the acceleration region of Curve 1 and was, therefore, not a stable solution point. In the region between the intersection point and the critical diameter of Curve 1 there would be two allowed solutions. If the explosive was detonating on Curve 1, then it would always remain on Curve 1, as any downward deviation would lead into an acceleration zone. If the explosive was detonating on Curve 2, then a

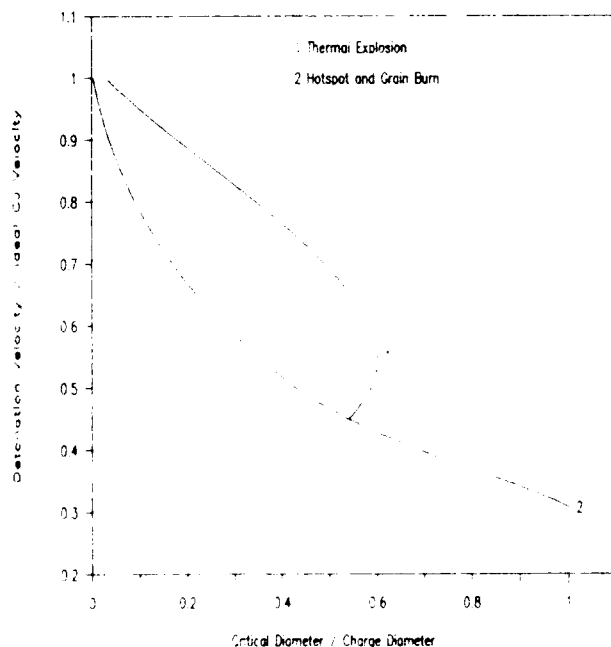


Figure 11. High and Low Order Behaviors

explosive was detonating on Curve 2, then a small perturbation might move the state point off Curve 2, through the deceleration region between the curves, into the acceleration region of Curve 1 and, hence, to stable high velocity. Thus, low order detonations could become high order, but not vice versa. Moreover, as the magnitude of the stimulus required to cause the switch would depend on the line shape of Curves 1 and 2, and more precisely on the length of the deceleration region that would have to be traversed between the curves, the magnitude of the stimulus would be a function of charge diameter and explosive type. In certain cases the transition might not be possible, and an extended region of high/low order behavior might be found. Substantial literature evidence has been found to support the above arguments, both in nitroester and nitramine sensitized explosives,<sup>17,18,19,20</sup> and on the effect of reaction behavior on the VoD(d) relationship.<sup>21</sup>

## CONCLUSION

A strong link has been found between the reaction mechanism of heterogeneous explosives, and the shape of the detonation velocity charge diameter function. Two typical behaviors of multi phase, multi-component systems have been examined: thermal explosion of all phases, and thermal explosion of the hot spot followed by grain burning. The former behavior has been shown to give downward convex VoD(d) functions and high failure velocities, the latter downward concave VoD(d) functions and low failure velocities. Critical diameter has been shown to be a function of the absolute reaction rate, and critical velocity a function of the sensitivity of the reaction rate to the local thermodynamic state variables. Specific examples of these effects have been given.

The reaction behavior of various explosives have been examined in detail, and a qualitative link between the reaction behavior and the formulation has been demonstrated. The effect of voidage and heterogeneity on the reaction behavior has been elucidated.

A tentative proposal has been made to explain the phenomenon of high and low order detonation in condensed heterogeneous explosives, which is qualitatively consistent with the known characteristics of such behavior.

## ACKNOWLEDGEMENTS

The authors wish to thank M. Logan and M. Harding for the careful determination of many of the experimental detonation velocities in this paper. Some of the numerical fitting of the flow theory to experiment was executed by Dr. M. P. duPlessis. Discussions with Dr. I. J. Kirby aided both the authors in crystallizing the ideas reported herein. The permission of Nobels Explosives Company and ICI allowing publication of this work, is gratefully acknowledged.

## REFERENCES

1. Price, D., "Contracting Patterns in the Behavior of High Explosives," *Proceedings of the 11th Symposium on Combustion*, 1966, pp. 693-702.
2. Hino, K. and Hasegawa, S., "The Theory of Variable Reaction Zones in the Detonation of Industrial Explosives," *J. Industrial Explosive Society of Japan*, 20(1), 1959, p. 2.
3. Paterson, S., Internal ICI Report.
4. Fickett, W. and Davis, W. C., "Detonation," Univ. California, Berkeley, 1979.
5. Mader, C. L., "Numerical Modeling of Detonation," Univ. California, Berkeley, 1979.
6. Kirby, I. J. and Leiper, G. A., "A Small Divergent Detonation Theory for Inter-molecular Explosives," *Proceedings of the 8th Symposium (International) on Detonation*, Albuquerque, NM, 1985, p. 176.
7. Leiper, G. A. and Kirby, I. J., "A Method of Parameterising Hydrocode Kinetic Models for Non-Ideal Explosives Based on the Variation of Detonation Velocity with Charge Diameter," *Proceedings of the 4th APS Topical Conference on Shockwaves*, Spokane, WA, 1981, p. 917.
8. Wood, W. W. and Kirkwood, J. G., "Diameter Effect in Condensed Explosives. The Relationship Between Velocity and Radius of Curvature of the Detonation Wave," *J. Chem. Phys.*, 22(11), 1954, p. 1920.

9. Chan, S. K., "A Theory to Predict the Velocity-Diameter Relation of Explosives," *Proceedings of the 7th Symposium (International) on Detonation*, Annapolis, MD, 1981, p. 589.
10. Leiper, G. A.; Kirby, I. J.; and Hackett, A., "Determination of Reaction Rates in Intermolecular Explosives Using the Electromagnetic Particle Velocity Gauge Technique," *Proceedings of the 8th Symposium on Detonation*, Albuquerque, NM, 1985, p. 186.
11. Leiper, G. A.; Kennedy, M.; and Kerr, I. D., "Calculations and Measurements of the Flow in Unconfined Detonations," *J. Ener. Mater.*, in press.
12. Campbell, A. W. and Engelke, R., "The Diameter Effect in High Density Heterogeneous Explosives," *Proceedings of the 6th Symposium (International) on Detonation*, Coronado, 1976, p. 642.
13. Johanson, C. H. and Persson, P. A., "Detonics of High Explosives," Academic, London, 1970.
14. Malin, M. E., "Particle-Size Effects in Explosives at Finite and Infinite Diameters," *J. App. Phys.*, Vol. 28, No. 1, 1957, p. 63.
15. Leiper, G. A., "The Behavior of Non-Ideal Explosives in the Ballistic Mortar," *J. Energetic Mater.*, in press.
16. Leiper, G. A. and Cooper, J., "The Effect of Charge Diameter and Porosity on the Initiation of Commercial Explosives," *Proceedings of the 9th Congress International de Pyrotechnique Spatiale*, Juan-Les-Pins, 1987, p. 371.
17. Paterson, S., "Maximum Velocity of Commercial Explosives," ICI Internal Report, 1948.
18. Taylor, J., "Detonation in Condensed Explosives," Clarendon, London, 1952.
19. Kusakabe, M. and Fujiwara, S., "Explosive Behavior of Methylnitrate and its Mixtures with Liquid Diluents," *Proceedings of the 5th Symposium (International) on Detonation*, Pasadena, CA, 1970, p. 267.
20. Jones, E. and Mitchell, D., "Spread of Detonation in High Explosives," *Nature*, 161, Jan 1948, p. 98.
21. Engelke, R. and Bdzil, J., "A Study on the Steady State Reaction Zone Structure of a Homogeneous and a Heterogeneous Explosive," *Physics Fluids*, Vol. 26, No. 5, 1983, p. 1210.

## DISCUSSION

**J. BDZIL**

Los Alamos National Laboratory  
Los Alamos, NM

In your presentation you mentioned that you had done a stability analysis of the diameter effect curve. This analysis revealed that of the two branches of the curve, the upper branch was stable and the lower branch was unstable. Can you comment on the nature of the analysis that you conducted?

I have done a hydrodynamic stability analysis of disturbances on a curved two-dimensional detonation shock. That analysis shows instability of shocks that correspond to points on the upper branch, but near the knee of the diameter effect curve. It is a catastrophic instability, occurring when  $dDn/dK > 0$  (where  $Dn \equiv$  normal shock speed,  $K \equiv$  shock curvature). The  $dDn/dK > 0$  condition always occurs before the knee of the diameter effect curve is reached.

## REPLY BY G. A. LEIPER AND J. COOPER

The stability analysis referred to in the paper was reported by Kirby and Leiper, Reference 6. The analysis was based on considering the effect of small accelerations on the slightly divergent flow equation set used to describe unconfined axisymmetric detonations. The time dependent terms were then generated from one dimensional flow theory. We believe the approximations used in the approach gave qualitatively correct results. The theory at that time was, and still is, not quantitative. The results of the analysis indicated that at any point on the diameter effect curve, solutions to the left of the point in inverse

diameter space accelerated, and those to the right decelerated.

We have not examined the stability of the solution close to the critical diameter in more detail. We note that there exists a singularity in the analysis at the steady-state critical point, which would correspond to catastrophic failure of the accelerated detonation before the knee of the accelerated diameter effect curve could be reached.

The existence of catastrophic failure conditions close to the knee in the diameter

effect curve does not alter the arguments on high and low order detonation. It is sufficient that for some explosives, the kinetics admit two independent solutions for the diameter effect, and that over some part of inverse diameter space, the stable region of one lies within the acceleration region of the other. Transition from one solution to the other must occur in this region, giving rise to an apparent discontinuity in the measured diameter effect data.

# A SHOCK INITIATION MODEL FOR FINE-GRAINED HEXANITROSTILBENE

M. E. Kipp and R. E. Setchell  
Sandia National Laboratories  
Albuquerque, New Mexico 87185

*An established body of data indicates that very fine-grained hexanitrostilbene (HNS), when pressed to 92 percent of crystal density, exhibits shock initiation characteristics unlike those typical of porous, granular explosives. That is, a progressive buildup towards detonation from an initial shock by hot spot formation and growth processes is not observed. Instead, this particular HNS exhibits shock initiation characteristics normally associated with homogeneous explosives (e.g., the formation of a superdetonation wave after an initial shock has been introduced). In the present work, a comprehensive effort has been made to develop a predictive model for shock initiation in this material. This model is based on a theory of homogeneous reactive mixtures, and includes a refined equation of state for porous HNS reactant and a JWL equation of state for gaseous reaction products. The model has been incorporated into wave propagation codes, and comparisons with available initiation data are made.*

## INTRODUCTION

Very fine grained hexanitrostilbene (HNS) has been recognized as an attractive acceptor explosive for slapper detonators.<sup>1</sup> An established body of data indicates that this particular HNS (grain size 1-2  $\mu\text{m}$ , specific surface area  $\sim 8 \text{ m}^2/\text{g}$ ), when pressed to 92 percent of crystal density ( $1600 \text{ kg/m}^3$ ), exhibits shock initiation characteristics normally associated with homogeneous explosives. Unlike a typical granular, porous explosive, this material does not show a progressive buildup towards detonation from an initial shocked state resulting from hot spot formation and growth processes. Instead, there is evidence for the formation of a super-detonation wave in this material after an initial shock has been introduced.<sup>2,3</sup> Hence, an opportunity exists for developing a much-simplified reactive model based on earlier studies of homogeneous explosives, where the reactant is uniformly shock heated and reacts by thermal explosion. This work represents a comprehensive effort to generate such a predictive model for shock initiation in this material. This model is based on a theory of

homogeneous reactive mixtures, and includes a refined equation of state for porous HNS reactant and a JWL equation of state for gaseous reaction products. The model has been incorporated into wave propagation codes, and comparisons with available initiation data are made (plate impact and small-diameter slapper impact).

A fundamental issue in the present study is how a granular explosive with 8 percent initial porosity can behave like a homogeneous explosive. Normally, in an explosive with a granular structure, heterogeneous heating would be expected to occur behind a shock, typically by void collapse.<sup>4-7</sup> However, if the density is held constant, decreasing the grain size results in a higher number density of smaller voids, and we expect the amplitude of temperature variations caused by heterogeneous heating to become smaller. Two complementary mechanisms contribute to this trend: first, void collapse is less effective in creating local hot spots as the voids decrease in size;<sup>8</sup> second, thermal transport is more effective at equilibrating spatial variations in

temperature as the ratio of surface area to volume of hot spots increases. This view of the thermal state of granular explosives after being shock loaded is supported by visible emission data.<sup>2,9</sup> Both particle velocity and emission intensity were measured simultaneously in a series of planar impacts on HNS samples of three different grain size distributions. The strong influence that grain size has on shock wave growth to detonation was shown most sensitively by the emission intensity records. In particular, very fine-grained HNS showed essentially no energy release for a considerable time following the initial shock, consistent with a thermal explosion process in a homogeneous explosive.

The next section contains the description of each aspect of the model, including equations of state and reaction kinetics. The constitutive model has been included in both one- and two-dimensional Lagrangian finite difference wave propagation codes (WONDY<sup>10</sup> and ARTOO<sup>11</sup>), in the manner described by Nunziato and Kipp,<sup>12</sup> and the subsequent section is devoted to results of numerical calculations using this homogeneous kinetics model for HNS.

## CONTINUUM MIXTURE MODEL

A continuum mixture model for homogeneous explosives was previously constructed for the liquid explosive nitromethane.<sup>12</sup> The consequence of the arguments for behavior of this very fine-grained HNS being similar to that of a homogeneous explosive is that only solid reactant and reaction product gases are required as phases in the model. In the current formulation, these two phases coexist at the same spatial point, and are assumed to be in thermal equilibrium. Although the phases share a common density, the reactant and reaction products may each have distinct pressures and internal energies. The extent of reaction (the time integral of the reaction rate) is used in a linear mixing rule to calculate a pressure for the mixture and equivalent moduli for the mixture. The reaction rate for chemical energy release, based on Arrhenius kinetics, includes a simple depletion factor. Parameters for the equations are listed in the appendix.

## Solid Phase

An accurate characterization of the dynamic response of the unreacted explosive is required in order to establish the thermodynamic states induced by mechanical loading. Since the reaction rates are driven by temperature, the parameters determined for the kinetics are coupled to thermal states calculated in the explosive. Recent experimental studies of the static compaction of HNS powders have led to an improved isothermal compressibility description of this material. This description, together with recent values for thermophysical constants, has been used to revise a previously formulated equation of state for unreacted HNS.<sup>13</sup> The Helmholtz free energy of solid, unreacted HNS was proposed by Sheffield, et al.<sup>14</sup> to take the following form:

$$\begin{aligned}
 F(T, V) = & F(T_0, V_0) + P_0(V_0 - V) - S_0(T - T_0) \\
 & + C_{vs}(T - T_0) \left[ 1 + \frac{\gamma}{V}(V_0 - V) \right] \\
 & + C_{vs} T_0 \ln \left( \frac{T_0}{T} \right) + \frac{B_{T_0} V_0}{N(N-1)} \cdot \\
 & \left[ \left( \frac{V}{V_0} \right)^{1-N} - (N-1) \left( 1 - \frac{V}{V_0} \right) - 1 \right] \quad (1)
 \end{aligned}$$

where  $T$  is temperature,  $V$  is specific volume,  $C_{vs}$  is the specific heat at constant volume,  $\gamma$  is the Gruneisen coefficient, and  $B_{T_0}$  is the isothermal bulk modulus. A zero subscript represents reference conditions. The derivation of this formulation is based on four assumptions: (1) the internal energy is the sum of two components, where one component is a function only of temperature, and a second component is a function only of specific volume; (2) the specific heat at constant volume,  $C_{vs}$ , is constant; (3) the ratio  $\gamma/V$  is constant; and (4) the isothermal compression of the solid is described by the compressibility of a Murnaghan solid.

In order to determine the values of these material parameters for the fine-grained HNS,



mechanical and thermo-mechanical data are required. Isothermal compressibility data for HNS powders were acquired in static experiments that were performed under conditions of uniaxial strain compression.<sup>13</sup> The measurements showed that grain size distribution influenced the compressibility of the HNS only below 0.8 GPa (Figure 1). It is assumed that within the stress range 0.8 - 2.0 GPa the material response is that of isothermal compression of solid HNS under hydrostatic loading

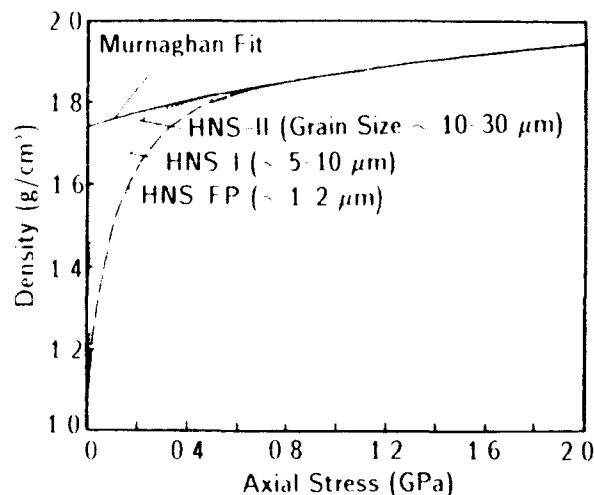


Figure 1. HNS Sample Density as a Function of Applied Axial Stress for Three Grain Sizes, and the Murnaghan Solid Fit to the Hydrostatic Data

In this range, then, the experimental curves are fit with the relation for the isothermal compression of a Murnaghan solid (Figure 1),

$$P = P_0 + \frac{B_{T_0}}{N} \left[ \left( \frac{V}{V_0} \right)^{-N} - 1 \right], \quad (2)$$

hence determining the parameters  $B_{T_0}$  and  $N$ . Recent experiments have determined the value of the specific heat at constant pressure,<sup>15</sup>  $C_p$ , resulting in refined values of  $\gamma/V$  and  $C_{vs}$ . A summary of these parameters is given in the appendix

Application of this equation of state to the fine grained HNS requires that porosity be

treated, since HNS samples are pressed from powders to less than crystal density. If it is assumed that porosity persists through some range of pressure, then the porosity must be retained as a variable in the equation of state. A convenient measure for the porosity is given by  $\alpha = V/V_s$ , where  $V_s$  is the specific volume of the solid (non-porous) material at the same temperature and pressure. Then, if the original equation of state for the solid was defined as

$$P_s = f(E, V_s), \quad (3)$$

the pressure,  $P$ , in the porous material can be represented by<sup>16</sup>

$$P = f(E, V/\alpha)/\alpha. \quad (4)$$

Modification of the equation of state in this way permits us to account for the porosity that exists at low pressures so that the porous material pressure can be written in terms of density,  $\rho$ ; reference (crystal) solid density,  $\rho_R$ ; distension,  $\alpha$ ; and temperature,  $T$ ,

$$P = [C_{vs} \gamma_0 \rho_R (T - T_0) + B_{T_0} \cdot ((\rho\alpha/\rho_R)^N - 1)/N] / \alpha. \quad (5)$$

The distension in the HNS is defined with a quadratic  $P$ - $\alpha$  relationship,<sup>13</sup> assumed to hold below the crush pressure,  $P_c$ ,

$$\alpha = 1 + (\alpha_0 - 1)(1 - P/P_c)^2, \quad (6)$$

which enables consistent values of  $\alpha$  and  $P$  to be determined for a given density and temperature.

Compaction goes to completion ( $\alpha = 1$ ) when the pressure reaches  $P_c$ . The value of this compaction pressure depends on the assumed compaction form (quadratic in this case), and whether isothermal or adiabatic compression is used as a constraint in the evaluation (adiabatic, for the dynamic compression appropriate to the present case). With this equation of state, wholly constructed from low pressure data, predicted Hugoniot states (solid curve in Figure 2) agree closely with the results from reverse-impact experiments to shock pressures as high as 8.5 GPa,<sup>13</sup> as well as with results

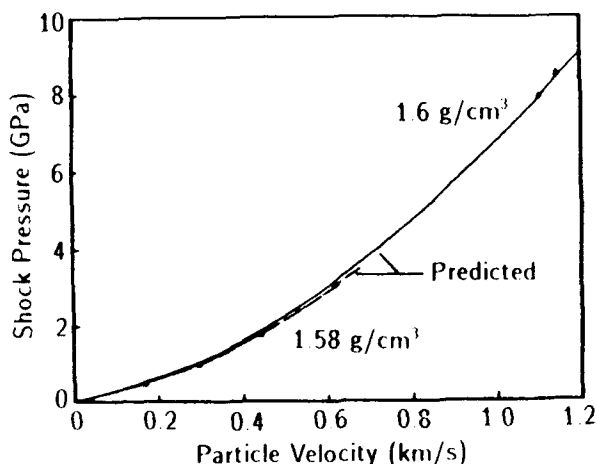


Figure 2. Comparison of Shock Hugoniot Data and Hugoniot States Predicted With the Present Equation of State (Pressure Vs. Particle Velocity)

from experiments that utilized variable ramp-wave loading to systematically inhibit the onset of reaction (upper data points in Figure 2).

### Product Gas Phase

$$P_g = Ae^{-R_1 \rho_0 / \rho} + Be^{-R_2 \rho_0 / \rho}$$

The JWL equation of state is used to describe the reaction product gases. In its original form,<sup>17</sup> JWL employs density and internal energy as state variables. However, within our model, temperature is an explicit state variable, being used in the reaction kinetics and the solid equation of state. Procedures to modify the energy dependence in JWL have been described by Baer and Nunziato<sup>18</sup> and Thompson.<sup>19</sup> With some additional tailoring of their free energy functions to our purposes, the pressure of the reaction products can be written as

$$+ C_j \rho^{\omega+1} + \omega C_{vg} \rho T, \quad (7)$$

and the internal energy of the reaction products takes the form

$$e_g = \frac{A}{R_1 \rho_0} e^{-R_1 \rho_0 / \rho} + \frac{B}{R_2 \rho_0} e^{-R_2 \rho_0 / \rho} + C_j \omega \rho^{\omega} + C_{vg} T. \quad (8)$$

The advantage of this form is that the JWL parameters ( $A$ ,  $B$ ,  $R_1$ ,  $R_2$ , and  $\omega$ ) determined for HNS<sup>17</sup> can be used without modification. In these equations for the explosive,  $\rho_0$  is the initial explosive density, and  $C_{vg}$  is the specific heat. The additional parameter,  $C_j$ , is determined by evaluating the pressure at the Chapman-Jouguet (C-J) state. The temperature at that state is obtained from the TIGER code.<sup>20</sup> The heat of detonation is defined to be the gas product internal energy evaluated at the C-J state minus the shock energy to the C-J state from the reference solid conditions

$$H_{DET} = e_g(V_{CJ}, T_{CJ}) - \frac{1}{2} P_{CJ}(V_0 - V_{CJ}). \quad (9)$$

### Kinetics

This formulation was first evaluated by comparing with measurements obtained in wedge tests.<sup>3</sup> These data are shown in Figure 3 as uncertainty boxes for run distance and time to detonation. The data cover a regime of sustained shock pressure from about 3.5 to 7 GPa (calculated shock temperatures from 455 K to 578 K, respectively). The geometry defined to obtain sustained shock loading in WONDY calculations for run distance and run time to detonation was a kapton flyer impacting an HNS target, with sufficient thicknesses of flyer and target so that release waves would not influence the results. Calculations using single-step Arrhenius kinetics, with an activation temperature  $\theta_1$ , frequency factor  $\Lambda_1$ , and simple depletion factor,

$$\lambda = \Lambda_1 (1 - \lambda) e^{-\theta_1 / T} \quad (10)$$

result in a straight line fit to this data (solid line in log-log space, Figure 3). However, the data at pressures below 4.5 GPa indicate deviations from linearity in the form of larger run distances and longer run times. The reasons for the delayed reaction at lower pressures are not clear, but the delay can be accommodated with a two-step reaction<sup>21</sup> having two activation temperatures and two frequency factors,

$$\dot{\lambda} = A_1(1 - \lambda)\eta e^{-\theta_1/T} \quad (11)$$

$$\dot{\eta} = A_2(1 - \eta)e^{-\theta_2/T} \quad (12)$$

The intermediate reaction,  $\eta$ , serves to retard the primary kinetics at low shock temperatures. With this more complex reaction, similar to an autocatalytic process, the calculations (circles with dashed line) provide a very close fit to the data (Figure 3).

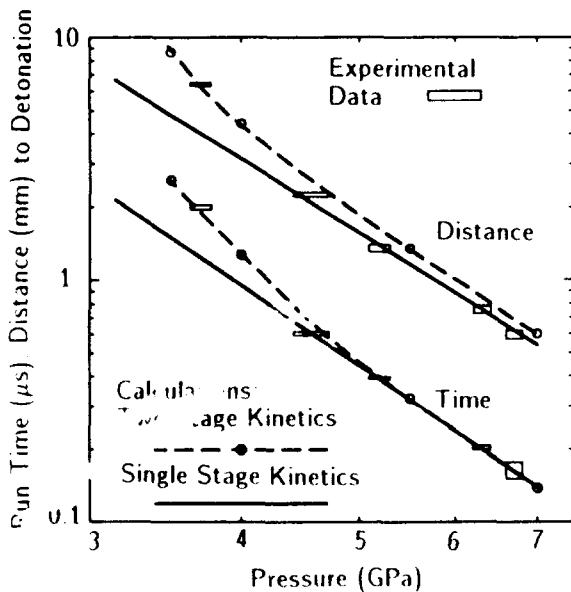


Figure 3. Sustained Shock Initiation in Very Fine-Grained HNS

In calculations at lower pressures, we observe that the reaction begins at the interface where the HNS has been at the shock temperature the longest time. A superdetonation wave forms, with shock pressures as large as 4 GPa, and overtakes the initial shock (Figure 4). Run distance and time to detonation are assumed to occur at the point of overtaking. On the other hand, at initial pressures on the order of 7 GPa, a superdetonation wave never has time to form. Instead, interactions between the shock front, the reaction, and the impact interface rapidly increase the amplitude of the initial shock until a steady detonation is formed (Figure 5). In this case, detonation is assumed to have been reached

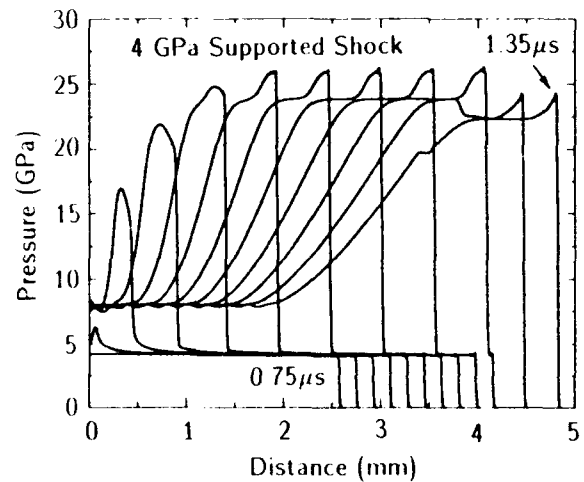


Figure 4. Growth to Steady Detonation From an Initial Supported 4 GPa Shock

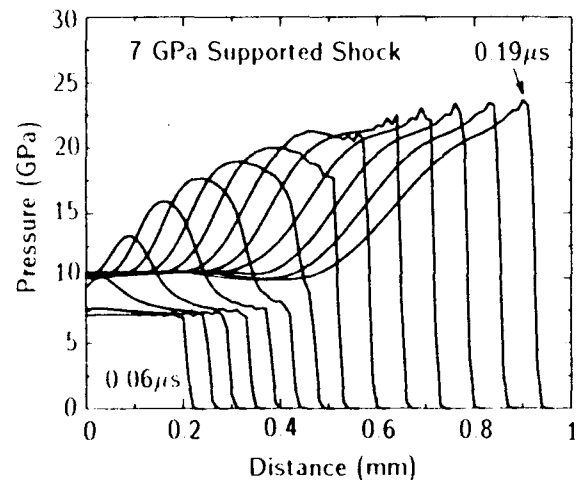


Figure 5. Growth to Steady Detonation From an Initial Supported 7 GPa Shock

when the C-J pressure has been attained (about 20 GPa), at which point the shock front is propagating at the detonation velocity.

## RESULTS

An important application of this model is to simulate slapper initiation of HNS. Some relevant data exist for the case of thin-pulse shock loading of very fine-grained HNS<sup>1,22</sup> at a density of 1600 kg/m<sup>3</sup>, generated by impacting

samples of the explosive with small diameter, thin disks of kapton. Our corresponding calculations are one-dimensional uniaxial strain, using parameters for the HNS determined from the sustained shock data discussed above. The two cases for which data are published are for kapton flyers of 1 mil (0.025 mm) and 3 mil (0.076 mm) thicknesses, with corresponding diameters of 15 mil (0.38 mm) and 40 mil (1 mm) respectively

For the 1 mil flyer, the pressure below which no detonation results is calculated to be 10 GPa, corresponding to an impact velocity of 2.70 km/s. The experimental value<sup>22</sup> is about 11 GPa. As the impact velocity of the 1 mil flyer is increased, we observe that the run distance to detonation decreases (Figure 6), approaching the sustained shock run distances. Note that when run time to detonation is comparable to the double transit time of the flyer, the pulse generated at impact appears to the HNS target as a sustained shock. Similar behavior is observed in the calculations for the 3 mil flyer (Figure 6), where the longer pulse reduces the detonation threshold pressure to 7 GPa, corresponding to an impact velocity of 2.15 km/s. The experimental value is about 6.7 GPa<sup>1</sup>. Again, as the impact velocity is increased, the run distances approach the calculated sustained shock values. The absence of lateral release waves in these one dimensional calculations should cause initiation at impact velocities no greater than observed experimentally. This is indeed the case in the calculations for the 1 mil flyer, but the 3 mil flyer calculations show a threshold pressure ~5 percent higher than the data. The experimental studies did not establish whether or not the observed thresholds were elevated due to finite diameter effects

The kapton flyer impact velocity that separates successful initiation from failure in the HNS appears as a very sharp transition. Computationally, a 3 percent change in impact velocity for the 3 mil flyer is sufficient to discriminate between initiation or failure. Experimentally, a 5 percent velocity variation is sufficient to lead from no initiation to successful initiation<sup>1</sup>. This sharp transition is one of the features that make this HNS material attractive as an acceptor explosive in a

slapper detonator. At the lowest impact velocity at which initiation is established, the run distance to detonation is large because reactions start and fail several times before build-up to detonation is accomplished (Figure 7).

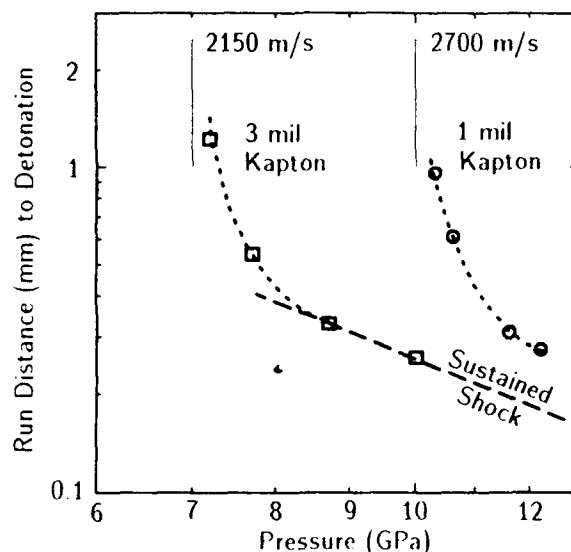


Figure 6. Calculations and Data for Slapper Initiation of HNS

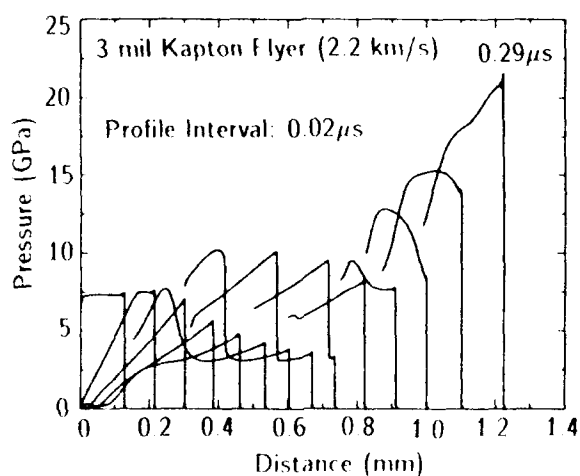


Figure 7. Unsteady Buildup to Detonation from a Thin Pulse

The results of these one-dimensional calculations with a homogeneous model for HNS are very encouraging, and provide strong motivation for extending the model to multiple dimensions. To date, we have incorporated the model in ARTOO,<sup>11</sup> a two-dimensional Lagrangian finite difference wave propagation code. Calculations of detonation waves propagating in thick-walled cylinders have been made, in which the influence of the wall impedance is very pronounced. The detonation properties of HNS contained in cylinders of PMMA and aluminum (wall thickness 0.2 mm, inner diameter 0.6 mm) have been compared, using the same HNS reactive model and parameters as in the one-dimensional code. The detonation velocity in PMMA confinement is clearly slower than that which is sustained in aluminum confinement (Figure 8). In addition, the lower impedance of the PMMA supports a lower pressure than in the aluminum, causing the reaction front to lag at the wall. As a consequence, the reaction front in the PMMA displays much more pronounced curvature than in the aluminum case.

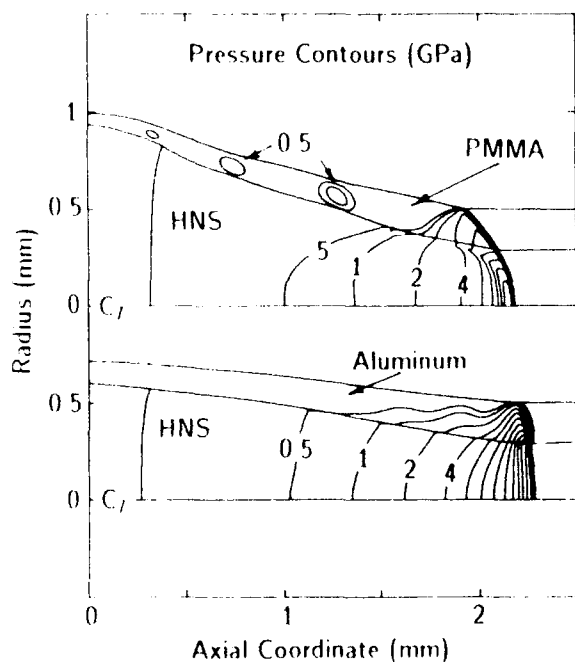


Figure 8. Calculations Showing the Influence of Confinement Impedence on a Detonating Cylinder of HNS

We are optimistic that the multi-dimensional capability can be extended to determine the roles slapper disk diameter or disk curvature have in the ignition process. Additional attention might also profitably be directed to the kinetics processes; our two-step reaction can be modified to account for the energy release associated with multiple steps, in which the first can be endothermic.<sup>21</sup>

## ACKNOWLEDGMENT

The authors are grateful to R. Rabie and M. Baer for their helpful comments regarding the reaction kinetics. This work performed at Sandia National Laboratories supported by the U.S. DOE under contract #DE-AC04-76DP00789.

## REFERENCES

1. Schwarz, A. C., "Shock Initiation Sensitivity of Hexanitrostilbene (HNS)," *Proceedings of the Seventh Symposium (International) on Detonation*, 1981, pp. 1024-1028.
2. Setchell, R. E., "Experimental Studies of Chemical Reactivity During Shock Initiation of Hexanitrostilbene," *Proceedings of the Eighth Symposium (International) on Detonation*, 1985, pp. 15-25.
3. Kramer, P. E., *HNS Wedge Tests*, Mason and Hanger-Silas Mason Report MHSM-83-46, Dec 1983.
3. Lee, E. L. and Tarver, C. M., "Phenomenological Model of Shock Initiation in Heterogeneous Explosives," *Phys. Fluids*, Vol. 23, 1980, pp. 2362-2372.
5. Kipp, M. E.; Nunziato, J. W.; Setchell, R. E.; and Walsh, E. K., "Hot Spot Initiation of Heterogeneous Explosives," *Proceedings of the Seventh Symposium (International) on Detonation*, 1981, pp. 394-406.
6. Hayes, D. B.; Kipp, M. E.; and Nunziato, J. W., "Application of Mixture Theory to Shock Initiation of Porous HNS Explosive," *Shock Waves in Condensed Matter - 1983*, Elsevier, 1983, pp. 589-592.

7. Johnson, J. N.; Tang, P. K.; and Forest, C. A., "Shock-Wave Initiation of Heterogeneous Reactive Solids," *J. Appl. Phys.*, Vol. 57, 1985, pp. 4323-4334.
8. Setchell, R. E. and Taylor, P. A., "The Effects of Grain Size on Shock Initiation Mechanisms in Hexanitrostilbene (HNS) Explosive," *Dynamics of Shock Waves, Explosions, and Detonations*, J. R. Bowen, N. Manson, A. K. Oppenheim, and R. I. Soloukhin, Eds., Progress in Aeronautics and Astronautics, Vol. 94, AIAA, New York, 1985, 350-368.
9. Setchell, R. E., "Visible Emission from Granular Explosives During Shock Initiation," *Shock Waves in Condensed Matter*, S. C. Schmidt and N. C. Holmes, Eds., 1988, pp. 553-556.
10. Kipp, M. E. and Lawrence, R. J., *WONDY V - A One-Dimensional Finite-Difference Wave Propagation Code*, Sandia National Laboratories Report SAND81-0930, Jun 1982.
11. Swegle, J. W., *ARTOO - An Automatically Rezoning Two-Dimensional Lagrangian Finite Difference Wavecode*, Sandia National Laboratories Report SAND81-2235, Dec 1981.
12. Nunziato, J. W. and Kipp, M. E., "Numerical Simulation of Detonation Failure in Nitromethane," *Proceedings of the Seventh Symposium (International) on Detonation*, 1981, pp. 608-619.
13. Setchell, R. E. and Taylor, P. A., "An Improved Equation of State for Unreacted Hexanitrostilbene," *J. Ener. Mat.*, Vol. 6, 1989, p. 157.
14. Sheffield, S. A.; Mitchell, D. E.; and Hayes, D. B., "The Equation of State and Chemical Kinetics for Hexanitrostilbene (HNS) Explosive," *Proceedings of the Sixth Symposium (International) on Detonation*, 1976, pp. 748-754.
15. Roth, E. P., Sandia National Laboratories, private communication, 1987.
16. Carroll, M. M. and Holt, A. C., "Static and Dynamic Pore-Collapse Relations for Ductile Porous Materials," *J. Appl. Phys.*, Vol. 43, 1972, pp. 1626-1636.
17. Lee, E. L.; Walton, J. R.; and Kramer, P. E., *Equation of State for the Various Products of Hexanitrostilbene at Various Charge Densities*, Lawrence Livermore National Laboratory Report UCID-17134, May 1976.
18. Baer, M. R. and Nunziato, J. W., "A Two-Phase Mixture Theory for the Deflagration-to-Detonation Transition (DDT) in Reactive Granular Materials," *Int. J. Multiphase Flow*, Vol. 12, 1986, pp. 861-889.
19. Thompson, S. L., *Improvements in the CHART D Energy Flow - Hydrodynamic Code V: 1972/1972 Modifications*, Sandia National Laboratories Report SLA-73-0477, Oct 1973.
20. Cowperthwaite, M. and Zwisler, W. H., *TIGER Computer Program Documentation*, Stanford Research Institute Publication No. Z106, Jan 1973.
21. McGuire, R. R. and Tarver, C. M., "Chemical Decomposition Models for the Thermal Explosion of Confined HMX, TATB, RDX, and TNT Explosives," *Proceedings of the Seventh Symposium (International) on Detonation*, 1981, pp. 56-64.
22. Klassen, S. E. and Jungst, R. G., *Production and Characterization of Fine Particle Hexanitrostilbene Explosive for Slapper Detonator Applications*, Sandia National Laboratories Report SAND85-1471, Aug 1985.

## APPENDIX

### HNS Equations of State Parameters:

#### Solid Phase

$\rho_R = 1740 \text{ kg/m}^3$	Reference Crystal Density
$C_{vs} = 889 \text{ m}^2/\text{s}^2 \cdot \text{K}$	Specific Heat
$B_{T_0} = 9.1065 \text{ GPa}$	Modulus
$N = 10.973$	Exponent
$T_0 = 298 \text{ K}$	Reference Temperature
$\gamma_0 \rho_R = 2828 \text{ kg/m}^3$	Gamma-Rho (Constant)
$\rho_0 = 1600 \text{ kg/m}^3$	Initial Mixture Density
$\alpha_0 = 1.0875$	Reference Distension
$P_c = 1.43 \text{ GPa}$	Crush Pressure

#### Gas Products

$A = 460.6 \text{ GPa}$	JWL Coefficient
$B = 7.262 \text{ GPa}$	JWL Coefficient
$R_1 = 4.60$	JWL Exponent
$R_2 = 1.30$	JWL Exponent
$\omega = 0.35$	JWL Exponent
$C_{vg} = 2527 \text{ m}^2/\text{s}^2 \cdot \text{K}$	Specific Heat
$C_J = -1.278 \text{ GPa}$	Coefficient
$H_{DET} = 4.436 \text{ MJ/kg}$	Heat of Detonation

$C_J$  and  $H_{DET}$  are calculated from the Chapman-Jouguet condition ( $\rho_0 = 1600 \text{ kg/m}^3$ )

$P_{CJ} = 20 \text{ GPa}$	C-J Pressure
$T_{CJ} = 2942 \text{ K}$	C-J Temperature
$D = 6950 \text{ m/s}$	Detonation Velocity

#### Kinetics Parameters:

##### Single Stage Kinetics

$A_1 = 6.7(10^9) \text{ s}^{-1}$	Frequency Factor
$\theta_1 = 6000 \text{ K}$	Activation Temperature

##### Two Stage Kinetics

$A_1 = 3.7(10^9) \text{ s}^{-1}$	Frequency Factor 1
----------------------------------	--------------------

$\theta_1 = 7000 \text{ K}$	Activation Temperature 1
$A_2 = 5.8(10^{17}) \text{ s}^{-1}$	Frequency Factor 2
$\theta_2 = 15000 \text{ K}$	Activation Temperature 2

#### Kapton (Hydrodynamic Mie-Gruneisen)

$\rho_0 = 1414 \text{ kg/m}^3$	Initial Density
$C_0 = 2660 \text{ m/s}$	Initial Sound Speed
$s = 1.48$	Slope of Linear $U_S$ , $U_P$
$\Gamma = 1.4$	Gamma (Constant)

## DISCUSSION

**JULIUS ROTH, Consultant**  
Portola Valley, CA

For moderately fine HNS II ( $\sim 18 \mu\text{m}$ ) wedge test geometry, we saw little if any acceleration of the input shock (20-30 kbar) before detonation, in room temperature tests, or for HNS pre-heated to  $260^\circ\text{C}$  (Fifth International Symposium on Detonation). This appears to be in accord with your observation of the near homogenous behavior of fine HNS.

## REPLY BY M. E. KIPP

Thank you for bringing this data to our attention.

## DISCUSSION

**JULIUS W. ENIG**  
Enig Associates, Inc.  
Silver Spring, MD

Your assumption that two phases (solid reactant and reactant product gases) can exist at the same spatial point and have the same temperature but different pressures is incorrect. Pressure equilibrium must occur first; temperature equilibrium may or may not occur, depending on how rapidly the heat conduction between the two phases is assumed to occur. Despite the fact that heat conduction in the "large" is assumed to satisfy a parabolic partial differential equation, in the "small," temperature signals derived from heat conduction move with acoustic-like speeds.

## REPLY M. E. KIPP

More complete continuum mixture models have been constructed in which each phase has a unique density, temperature, and pressure satisfying an appropriate equation of state, and applied to heterogeneous granular explosives (e.g., Kipp, et al., Seventh Symposium (International) on Detonation, 1981, p. 394). The current formulation for homogeneous explosives represents one particular numerically efficient, application of that more general approach. We have assumed that the reactant and product phases coexist at the same spatial point (i.e., no internal structure), and have a common temperature and density, consistent with thermal decomposition of the homogeneous explosive. These assumptions result in a distinct pressure and internal energy for each phase to satisfy the respective equations of state. Other approaches (enforcing pressure equilibrium, for example) are quite readily effected; we do not know at this time to what extent alternate formulations would influence the shock response of the explosive.

## DISCUSSION

HAROLD J. GRYTING, Ph.D  
Gryting Energetics Sciences Co.  
San Antonio, TX

Please explain the significance of the two grossly different frequency factors for hexanitrostilbene (HNS); can you relate these frequency factors to the chemical decomposition of the HNS in terms of molecular species?

## REPLY BY M. E. KIPP

We have not at this time attached any significance to the magnitudes of the frequency factors. We have noted that they are not in accordance with published values from thermal decomposition studies. Rather, they are best fits to the particular data available for this very fine-grained HNS.



# A THEORETICAL PICTURE OF SHOCK-TO-DETONATION TRANSITION IN A HOMOGENEOUS EXPLOSIVE

A. K. Kapila

Department of Mathematical Sciences  
Rensselaer Polytechnic Institute  
Troy, New York 12180-3590

and

J. W. Dold

Laboratoire de Recherche en Combustion  
Universite de Provence, Centre Saint Jerome  
Boite 252, Marseille Cedex 13, FRANCE

*The shock-initiation of a homogeneous explosive has long been thought to occur in the following way. The explosive is preconditioned by the passage of the initial shock that raises its temperature. After an induction time, a thermal explosion occurs at the piston/explosive interface. This explosion then transforms into a detonation via a series of unexplained steps. The present work is concerned with giving a complete mathematical description of the entire sequence of events that occurs prior to the emergence of a fully developed ZND detonation.*

## INTRODUCTION

When a steadily moving piston of sufficient velocity strikes a homogeneous explosive, the resulting shock wave can raise the pressure and temperature of the compressed material to a level at which chemical reaction becomes important. It is well-recognized that if the reaction rate is strong enough, the shock and reaction can evolve into a detonation. However, the true nature of the evolutionary process which culminates in the establishment of a detonation has not yet been fully described. It is the purpose of the present study to provide such a description, based upon an asymptotic and numerical study of the problem in the framework of a polytropic fluid, capable of undergoing a one-step, unimolecular reaction of the Arrhenius type.

Hitherto, the transition sequence has been thought to consist of the following steps, illustrated in Figure 1: A) after the constant-volume induction time for the explosive has elapsed, a reaction runaway event occurs close

to the piston-explosive interface, producing high pressures and temperatures; B) this causes a ZND detonation to propagate forward at the Chapman-Jouguet (CJ) velocity appropriate to the state behind the precursor shock wave (super detonation); C) once this detonation catches up with and overtakes the precursor shock, a ZND detonation is formed which propagates at the slower CJ-velocity appropriate to the state of the mixture ahead of the initial shock wave. This picture, originally put forth by Campbell, Davis, and Travis<sup>1</sup> on the basis of their experiments with liquid nitromethane, has been supported by the experimental studies of Hardesty,<sup>2</sup> and in fact, has served as the model for the interpretation of much of the experimental data on homogeneous explosive initiation.

Our theoretical study refines this scenario in two essential aspects. First, it finds that weak chemico-acoustic interactions in the induction stage delay thermal runaway at the explosive interface. As a result, the actual time-to-runaway is not the constant-volume

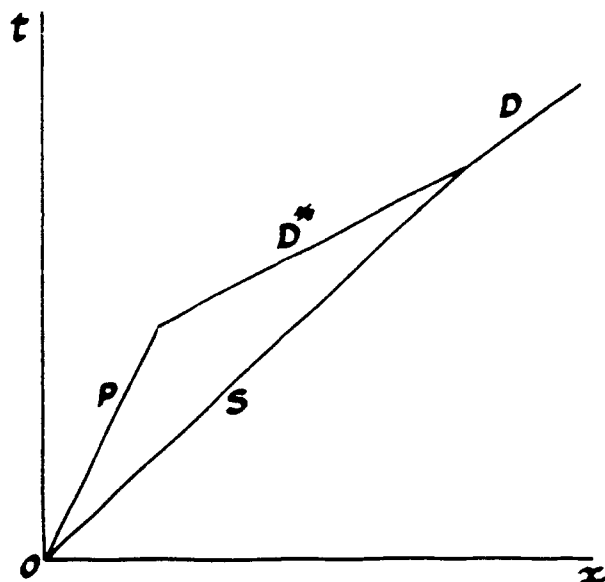


Figure 1. Conventional Picture of Shock Initiation. The piston path is represented by  $P$ , shock path by  $S$ , the CJ detonation in the precompressed material by  $D^*$ , and the CJ detonation in the uncompressed material by  $D$ .

induction time; rather, it is an intermediate value between the constant-volume and the constant-pressure induction times and, indeed, is close to the arithmetic mean of the two. Second, the analysis demonstrates that prior to the emergence of the superdetonation in the shocked medium, three distinct events occur. These are: (1) a localized thermal explosion in a thin core of inertially-confined material at the explosive interface, leading to (2) the propagation of a quasisteady, *weak* detonation into the explosive at a steadily decreasing velocity until the CJ-velocity has been reached, at which point (3) a weak shock wave is born at the rear of the reaction wave, which strengthens and rapidly advances to the front of the zone, thereby producing the ZND structure.

## MODEL

The explosive is modeled as a polytropic reactive fluid subject to compression by a constant-velocity piston, and the configuration is assumed to be plane and one-dimensional. The reactive Euler equations govern the flow, and assume the following

dimensionless form in a piston-attached, density-weighted Lagrangian coordinate frame:

$$\begin{aligned} v_t - u_h &= 0, \\ u_t + \frac{1}{\gamma} p_h &= 0, \\ T_t - \frac{\gamma-1}{\gamma} v p_t + \beta Y_t &= 0, \\ T &= p v, \\ Y_t &= -\Omega \equiv -\frac{1}{\beta \theta} e^{\theta - \theta T}. \end{aligned} \quad (1)$$

Here,  $p$ ,  $T$ ,  $v$ , and  $Y$  are, respectively, the pressure, temperature, specific volume, and reactant mass fraction, referred to the uniform shocked state that would result if the reaction were absent. The particle velocity relative to the piston,  $u$ , is measured in units of the frozen sound speed, and time in units of the spatially homogeneous induction time at the reference state. The dimensionless parameters appearing in the equations are the polytropic exponent  $\gamma$ , the heat-release parameter  $\beta$ , and the activation energy  $\theta$ . The piston velocity,  $V_0$ , in the laboratory frame is presumed known. The appropriate boundary conditions are  $u(0,t) = 0$ , and the Rankine-Hugoniot jump conditions across the shock locus, which itself is affected by the reaction and is, therefore, to be determined. We seek an asymptotic solution to the above problem in the limit

$$\varepsilon = 1/\theta \ll 1.$$

To be sure, the results of the analysis pertain only to the kinetic model under consideration. It should be recognized, however, that large activation energy kinetics does embody a universal characteristic of explosives, namely, the large sensitivity of their reaction rates to changes in state.

## ANALYSIS

For the sake of brevity, we have chosen to emphasize the results of the analysis rather than the mathematical details; the latter can

be found in, References 3-6. The sequence of events can be examined in the following stages.

### The Induction Stage

During the induction stage, the state of the shocked gas is but a small perturbation of the reference state, i.e.,

$$u \sim u_1, \quad \psi \sim 1 + \psi_1, \quad (2)$$

for  $\psi = p, T, v$ , and  $Y$ , where the perturbations satisfy

$$u_{1t} + \frac{1}{\gamma} p_{1h} = 0,$$

$$\frac{1}{\gamma} p_{1t} + u_{1h} = e^{T_1}, \quad (3a)$$

$$T_{1t} - \frac{\gamma-1}{\gamma} p_{1t} = e^{T_1},$$

and

$$T_1 = p_1 + v_1, \quad Y_{1t} = -\frac{1}{\beta} e^{T_1}. \quad (3b)$$

The primary connection is between linearized acoustics and weak but nonlinear chemical heating. The appropriate boundary conditions are  $u_1 = 0$  at the piston position,  $h = 0$ , and linearized jump conditions at the undisturbed shock location. This problem has been solved in References 3 and 7. The solution exhibits thermal runaway, characterized by the appearance of logarithmic singularities in  $p_1$  and  $T_1$ , and therefore  $Y_1$ , first at the piston face at a definite time  $t_e$ , where  $t_e$  depends upon  $\gamma$  and  $V_0$ . Typical profiles of  $T_1(x, t)$  for various values of  $t \leq t_e$  are displayed in Figure 2, which shows the emergence of a shrinking boundary layer near  $h = 0$  within which the solution grows rapidly. Reference 7 computes  $t_e$  for various values of  $\gamma$  and  $V_0$ , and shows that  $t_e$  is nearly the arithmetic mean of  $1/\gamma$ , the constant-volume induction time, and  $1$ , the constant-pressure induction time. The structure of the runaway singularity is analyzed further in Reference 4.

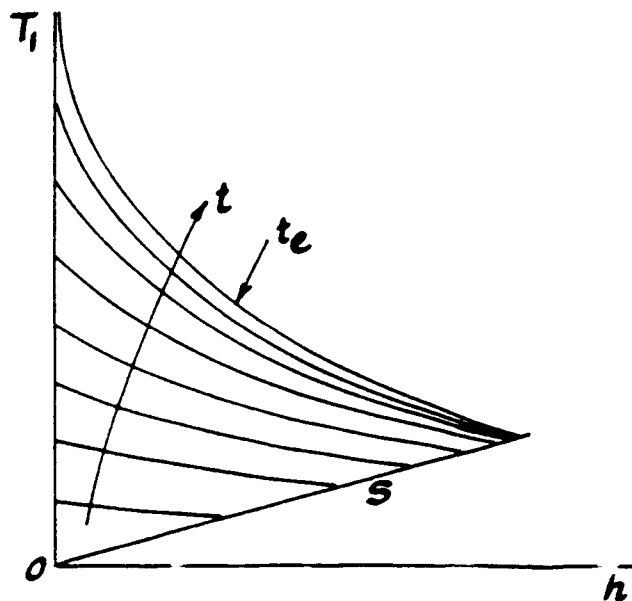


Figure 2. Evolution of Temperature Perturbation  $T_1$  up to Runaway Time  $t_e$ .  $S$  represents the shock locus.

### The Localized Thermal Explosion

Induction is followed by explosion, characterized by exponentially rapid depletion of reactant in the boundary layer at the piston-explusive interface. In this layer, the characteristic chemical time plunges dramatically because of the exponential chemical sensitivity of the rate. The corresponding acoustic time drops as well, but not nearly by as much, so that growth of the layer is dominated by chemical heating. There is little time for expansion, with the result that pressure and temperature rise together within the layer while changes in particle velocity are negligible. Since the explosion phase is of utmost brevity, the state of the explosive away from the boundary is practically frozen during this period, which ends when pressure and temperature within the layer have peaked. Their peak values,  $1 + \beta\gamma$ , are the same to leading order as in a spatially homogeneous constant-volume explosion.

The essential features of the localized explosion can be summarized in a simple way by giving only the leading-order results in the explosion stage; for details the reader is

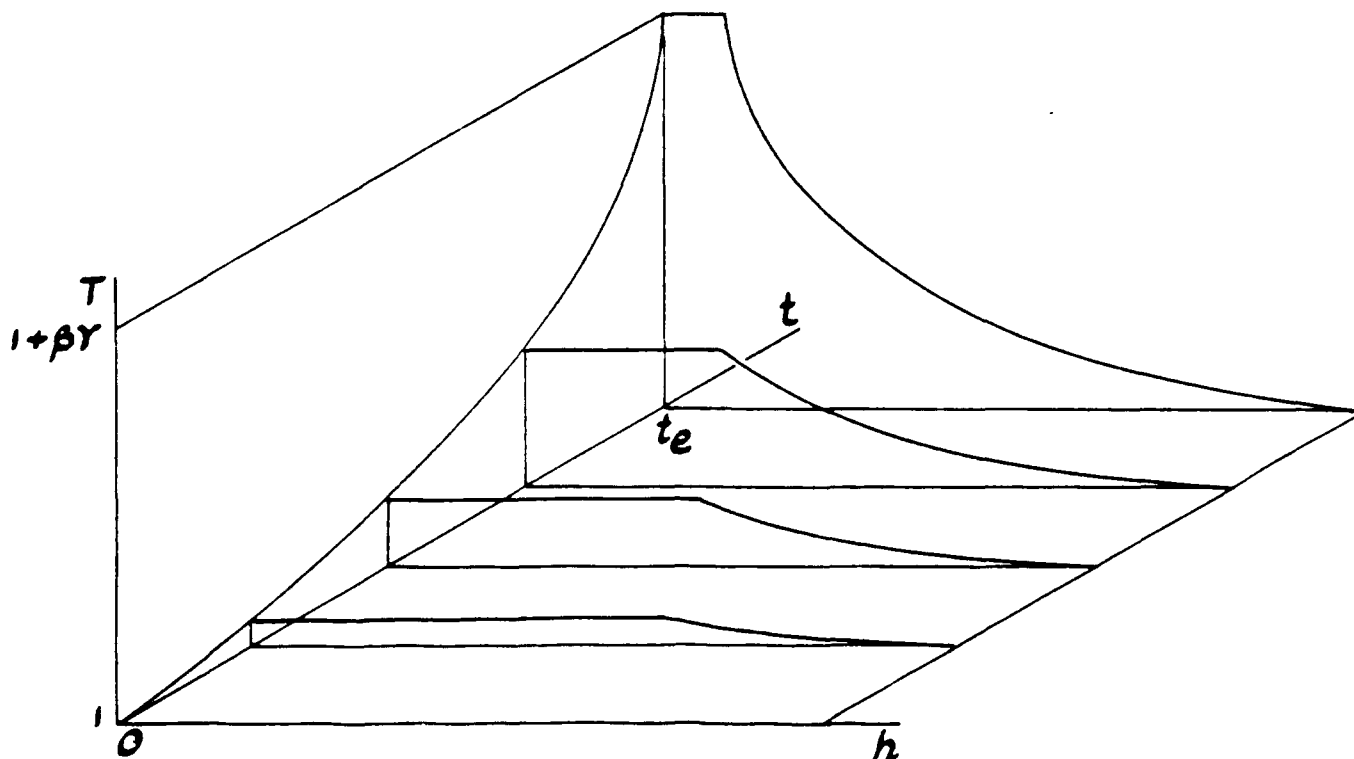


Figure 3. Evolution of Temperature  $T$  During the Explosion Phase Near the Piston Face, According to Equations (4). Temperature increases rapidly and nearly uniformly (in space) in a shrinking layer, leaving a sharp gradient of temperature (and hence induction times) outside.

referred to the asymptotic study in Reference 4. For  $h \rightarrow 0$  and  $t \rightarrow t_e$ , the explosion is described to a first approximation by the formulas

$$T, p \sim \frac{1}{1 + \varepsilon \log(t_e - t)}, \quad v \sim 1, \quad u \sim 0, \\ \text{for } 0 < h < (t_e - t)^{\gamma/(2\gamma-1)}, \quad (4a)$$

and

$$T, p \sim \frac{1}{1 + \frac{\varepsilon \log h}{\gamma(2\gamma-1)}}, \quad v \sim 1, \quad u \sim 0, \\ \text{for } h > (t_e - t)^{\gamma/(2\gamma-1)}, \quad (4b)$$

while

$$e^{-\beta\gamma\varepsilon/(1+\beta\gamma)} < t_e - t \ll 1. \quad (4c)$$

A sketch of the evolution of temperature according to these formulas is shown in Figure 3. Note that at the culmination of the

localized explosion, the high-temperature boundary layer at a nearly uniform temperature is followed by a thin transition region of large temperature gradient, or equivalently, a large gradient in induction times. This region is, therefore, ripe for a series of successive inertially-confined local thermal explosions, generating thereby a high-speed reaction wave which propagates into the explosive. This wave decelerates as it crosses the induction time gradient, and when it reaches the edge of the transition region, inertial confinement ends and gasdynamic effects are reinstated, because the lowered temperatures have brought the chemical and acoustic times back into balance. Further evolution of the reaction wave, which is still supersonic relative to the following flow, will then be governed by the induction Equations (3).

### The Quasisteady Reaction Wave

We have already seen that the induction solution becomes singular at the piston face at  $t = t_e$ . For  $t > t_e$ , one can continue to compute

the induction solution, but the singularity now moves into the interior of the domain (Figure 4). The singularity locus  $t = t(h)$  is characterized by  $T_1(h, t(h)) = \infty$ , while  $T_1(h, t) < \infty$  for  $t < t(h)$ . Furthermore, the singularity locus is supersonic, i.e.,  $dt/dh < 1$ , although its speed diminishes as it advances toward the precursor shock. (The requirement of supersonic motion of the singularity follows from the observation that a characteristic triangle emanating backwards from a point just below the singularity locus must be contained entirely in the region where the solution is bounded.)

As already demonstrated in the explosion stage, the reaction proceeds with extreme rapidity subsequent to thermal runaway. Therefore, the locus of the runaway singularity describes to an excellent approximation the path of the reaction wave into the explosive. The singularity path must, of course, be computed numerically from the induction equations, but once this computation has been completed and the wave speed,

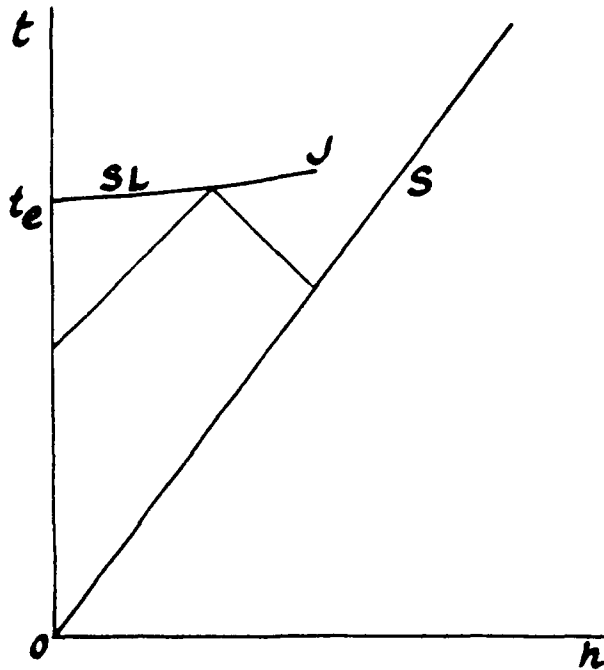


Figure 4. Propagation of the Induction Singularity (SL) Away from the Interface. S represents the shock locus. Also shown are the typical acoustic characteristics.

$$D(h) = [\hat{dt}(h)/dh]^{-1}, \quad (5)$$

ascertained, it is a simple matter to determine the wave structure.

First, let us define a new coordinate,  $s = t - \hat{t}(h)$ , which measures the time remaining before the wave arrives at the location  $h$ . In the  $(h, s)$  system, the full Equations (1) take the form

$$p_s - \gamma Du_s = Dp_h,$$

$$p_s + \gamma D^2 v_s = D(p_h + \gamma Du_h),$$

$$T_s - \frac{\gamma - 1}{\gamma} v p_s + \beta Y_s = 0, \quad (6)$$

$$T = pv,$$

$$Y_s = -\frac{1}{\beta \theta} Y e^{\theta - \theta T},$$

while the induction Equations (3) transform into

$$p_{1s} - \gamma Du_{1s} = Dp_{1h},$$

$$p_{1s} + \gamma D^2 v_{1s} = D(p_{1h} + \gamma Du_{1h}), \quad (7a)$$

$$T_{1s} - \frac{\gamma - 1}{\gamma} p_{1s} + \beta Y_{1s} = 0,$$

and

$$T_1 = p_1 + v_1, \quad Y_{1s} = -\frac{1}{\beta} e^{T_1}. \quad (7b)$$

Now, the wave structure consists of a region of thermal runaway near the wavehead, in which expansions (Equation (2)) hold and reactant depletion is weak, followed by an explosion region of swift, nearly completed reaction. The structure of thermal runaway can be deduced by observing that as the wavehead, or singularity locus, is approached, i.e., as  $s \rightarrow 0-$ , the  $s$ -derivatives dominate the  $h$ -derivatives in the induction Equations (3). To leading order, therefore, the latter become quasisteady, and can then be integrated to yield the asymptotic relations

$$T_1 \sim -\log\left(-\frac{\gamma D^2 - 1}{D^2 - 1}s\right),$$

$$u_1 \sim \frac{p_1 - a_1}{\gamma D}, \quad v_1 \sim \frac{b_1 - p_1}{\gamma D^2}, \quad (8)$$

$$p_1 \sim \frac{\gamma D^2 T_1 - b_1}{\gamma D^2 - 1}, \quad \beta Y_1 \sim \frac{\gamma D^2 c_1 - (D^2 - 1)p_1}{\gamma D^2}.$$

Here,  $a_1(h)$ ,  $b_1(h)$ , and  $c_1(h)$  are determined numerically. The notion of quasisteadiness applies, in fact, just as well to the full Equations (6), the first three of which can be integrated to yield

$$p_0 - \gamma D_0 = A_0, \quad p_0 + \gamma D^2 v_0 = B_0,$$

$$T_0 + \frac{\gamma - 1}{2} \left( u_0 - \frac{B_0 - A_0}{\gamma D} \right)^2 + \beta Y_0 = C_0, \quad (9)$$

where the functions of integration  $A_0$ ,  $B_0$ , and  $C_0$ , depend upon  $h$  and  $\theta$  and have the asymptotic forms

$$A_0 \sim 1 + \epsilon a_1, \quad B_0 \sim \gamma D^2 + 1 + \epsilon b_1,$$

$$C_0 \sim 1 + \beta + \frac{\gamma - 1}{2} D^2 + \epsilon \left( \frac{\gamma - 1}{\gamma} b_1 + c_1 + 1 \right). \quad (10)$$

Elimination of  $u_0$ ,  $v_0$ , and  $T_0$  from Equations (9) leads to a quadratic equation for  $p_0$  whose solutions are

$$p_0 = \frac{B_0 \pm \gamma R}{\gamma + 1} \quad (11)$$

where

$$R = (\delta^2 + 2\beta(\gamma + 1)D^2 Y_0)^{1/2} \quad (12)$$

with

$$\delta^2 \equiv B_0^2 - 2(\gamma + 1)C_0 D^2.$$

It can be shown that

$$\delta^2 = (D^2 - D_1^2)(D^2 - D_2^2), \quad (13)$$

where

$$D_1 = D_{10} + O(\epsilon), \quad D_2 = D_{20} + O(\epsilon),$$

$D_{10}$  and  $D_{20}$  being, respectively, the CJ detonation speed and the DJ deflagration speed at the reference state.

For supersonic flow through the wave, the proper sign in Equation (11) is the lower one, so that

$$p_0 = \frac{B_0 - \gamma R}{\gamma + 1}.$$

Then, Equations (9) yield the following expressions for the remaining state variables:

$$u_0 = \frac{1}{(\gamma + 1)D} \left( \frac{B_0 - (\gamma + 1)A_0}{\gamma} - R \right),$$

$$v_0 = \frac{B_0 + R}{(\gamma + 1)D^2},$$

$$T_0 = \frac{(B_0 - \gamma R)(B_0 + R)}{(\gamma + 1)^2 D^2}.$$

also, from Equation (12),

$$Y_0 = \frac{R^2 - \delta^2}{2\beta(\gamma + 1)D^2}. \quad (14)$$

All the variables through the reaction zone are now known in terms of  $R$ . One can also obtain an expression for the sonic parameter  $M^2 - 1$ , where  $M$  is the local Mach number. At leading order, it is found that

$$M_0^2 - 1 = \frac{(\gamma + 1)R}{B_0 - \gamma R}.$$

We observe that the sonic parameter approaches zero with  $R$ . Note also, from Equations (12) and (13), that

$$R > 0 \text{ for } D > D_1 \text{ and } Y_0 > 0, \quad (15)$$

so that the flow becomes locally sonic first when  $D \rightarrow D_1$  and  $Y_0 \rightarrow 0$ , i.e., when the wave velocity approaches the CJ value and the reaction reaches completion.

In order to complete the description of the reaction-zone structure, it remains to determine the variation of  $R$  with  $s$ . The relevant equation, obtained from the last of Equation (6) by way of Equation (14), is just the rate equation

$$\frac{\partial(R^2)}{\partial s} = -\frac{R^2 - \delta^2}{\beta\theta} \cdot \exp\left(\theta - \theta \frac{(\gamma + 1)^2 D^2}{(B_0 - \gamma R)(B_0 + R)}\right).$$

At fixed  $h$ , this equation shows that  $R$  decreases monotonically from  $[\delta^2 + 2\beta(\gamma + 1)D^2]^{\frac{1}{2}}$  to  $\delta$  as  $s$  increases through the wave. The problem for  $R$  is essentially the thermal-explosion problem, and its solution is readily obtainable, especially in the limit of  $\theta$  large. The solution will consist of an explosion region, in which  $R - \delta = O(1)$ , and a tail in which  $R - \delta = O(\epsilon)$ . These regions correspond to  $Y = O(1)$  and  $Y = O(\epsilon)$ , respectively. With  $R$  thus determined, the quasisteady wave structure is completely known at leading order. The structure is shockless and corresponds to a weak detonation.

### The Near-CJ Structure

The quasisteady structure described above breaks down when the wave velocity falls to the CJ value. Mathematically, the breakdown is associated with the fact that in Equations (6) the  $h$ -derivatives, neglected in obtaining the quasisteady solution, must now be reinstated. The physical reason for the breakdown is the appearance of a subsonic region in the flow. In fact, the nonuniformity appears when  $R$  first vanishes (see Equation (15)), and that happens at the CJ point in the tail of the reaction zone. A new unsteady solution must, therefore, be constructed in this inner region.

Suppose that the quasisteady wave arrives at the CJ point at  $h = h_1$ . Then a detailed analysis, available in Reference 6, shows that the appropriate independent variables for the inner region are  $\eta$  and  $\xi$ , defined by

$$\eta = \frac{h - h_1}{b\Delta^{2/3}}, \quad \text{and} \quad \xi = \frac{s + (2/3)\Delta(\log\Delta - \xi_0)}{\Delta}$$

where  $b$  and  $\xi_0$  are certain positive  $O(1)$  constants and  $\Delta$ , defined by

$$\Delta = \beta\theta e^{-\theta + \theta/T_c},$$

is exponentially small for  $\theta$  large,  $T_c$  being the temperature at the CJ state in the shocked material. It can also be shown that in the inner region the primary dependent variable is  $P$ , the deviation of pressure from the CJ value  $p_c$  measured on the  $\Delta^{1/3}$  scale, i.e.,

$$P = \frac{p - p_c}{\alpha\Delta^{1/3}},$$

where  $\alpha$  is another positive,  $O(1)$  constant. It turns out that  $P < 0$  corresponds to supersonic flow and  $P > 0$  to subsonic flow, and that  $P$  is the solution to the problem

$$P_\eta - PP_\xi - \frac{1}{2}e^{-\xi} = 0,$$

$$P \rightarrow -e^{-\xi/2} + \frac{1}{2}e^{\xi/2}(\eta - 2e^{\xi/2}) \text{ as } \xi \rightarrow -\infty.$$

The hyperbolic PDE in the problem above represents an interaction between a nonlinear unidirectional wave operator and the chemical heat release. Note that the initial data for the PDE represents supersonic flow, which corresponds to characteristics leading into the inner region from the wavehead. As a result of interaction with the chemical term, some of these characteristics reverse direction and the collision produces a shock. These observations can be confirmed by examining the solution

$$P = -\sqrt{\phi} \cot[\sqrt{\phi}(\eta - \phi)/2],$$

$$\phi e^\xi = \sin^2[\sqrt{\phi}(\eta - \phi)/2].$$

The first of these equations gives  $P$  in terms of the characteristic parameter  $\phi$ , which itself is defined by the second equation. Note that the argument  $q = [\sqrt{\phi}(\eta - \phi)/2]$  appearing above has the range

$$0 < q < \pi/2 \text{ for supersonic flow,}$$

$$\pi/2 < q < \pi \text{ for subsonic flow,}$$

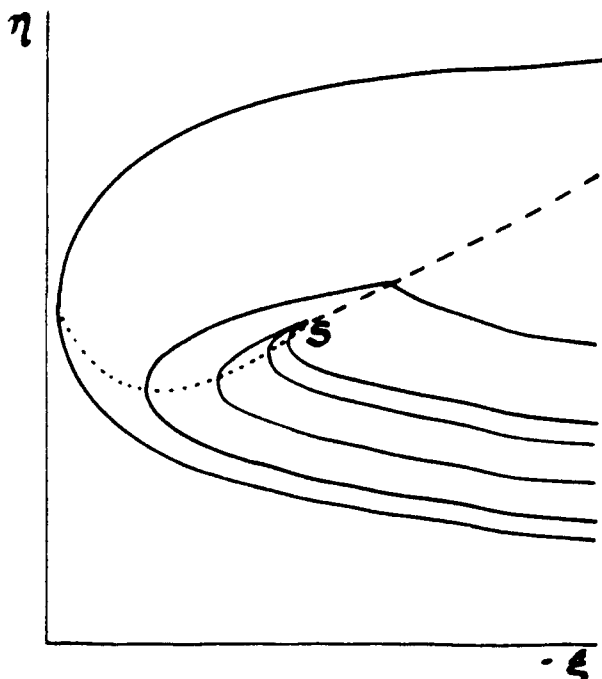


Figure 5. The Characteristic Diagram for the Inner Problem. The dotted line is the sonic locus (supersonic below) and the dashed line the shock.  $S$  denotes the point of the shock birth.

with  $q = 1/2$  on the sonic locus. Figure 5 is a schematic diagram of the  $\xi\eta$ -plane, displaying the characteristic paths, the sonic locus, and shock formation. The birth of the shock and its tendency to strengthen as it propagates can also be seen in Figure 6, which is a plot of the scaled pressure  $P$  for a number of equally spaced values of  $\eta$ .

Once the shock leaves the inner region, it progressively moves forward to positions of less complete reaction. The corresponding flow again acquires a quasisteady structure, much in the manner of the weak detonation already described. When it reaches positions at which the reaction has progressed little from its state immediately behind the precursor shock, the nearly steady super-detonation found in the scenario of Figure 1 is finally produced.

## FINAL REMARKS

The entire evolutionary process described above can be represented rather picturesquely on the Hugoniot diagram of Figure 7. The precursor shock connects the inert states  $U$  and  $C$ . The constant-volume explosion on the piston face occurs along the vertical line  $CW_1$ .

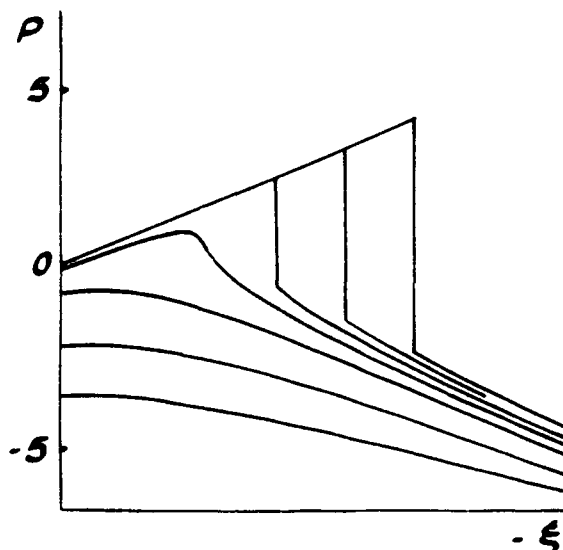


Figure 6. Evolution of  $P$  According to the Inner Problem.  $P$  is negative for supersonic flow; positive for subsonic.

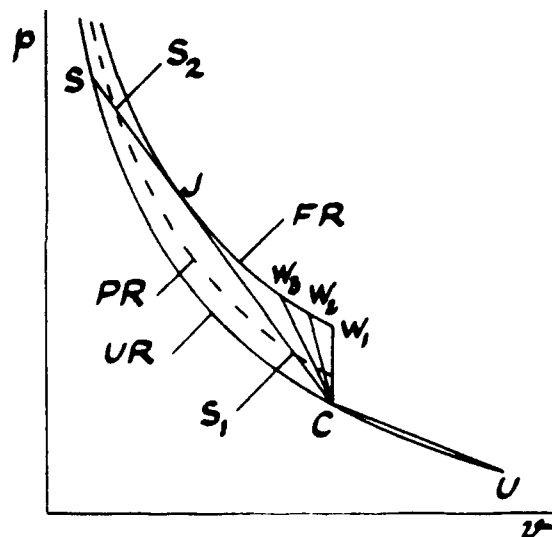


Figure 7. Evolution Towards  $D^*$  on the Hugoniot Diagram.  $FR$  denotes fully reacted,  $PR$  Partially reacted, and  $UR$  unreacted Hugoniot curves.

The subsequent progress of the weak detonation towards the CJ point is illustrated, at selected times, by the sequence of Rayleigh lines  $CW_2$ ,  $CW_3$ , and  $CJ$ . The swift transformation near the CJ point, from the weak detonation structure ( $CJ$ ) to the ZND structure ( $CSJ$ ) occurs through a succession of intermediate stages (such as  $CS_1S_2J$ ) as the shock strengthens.



## ACKNOWLEDGEMENTS

A. K. Kapila is grateful to J. B. Bdzil for strong and continued encouragement, and for useful discussions. J. W. Dold was supported in this work by the British Science and Engineering Research Council as well as by the Universite de Provence (while on leave from the School of Mathematics, University of Bristol, Bristol BS8 1TW, U.K.). A. K. Kapila was supported by the U.S. Army Research Office and by the Los Alamos National Laboratory under Contract DOE-LANL-9XG9-4906Y1. Cooperation between the authors was facilitated by a NATO collaborative research grant.

## REFERENCES

1. Campbell, A. W.; Davis, W. C.; and Travis, J. R., "Shock Initiation of Detonation in Liquid Explosives," *Physics of Fluids*, Vol. 4, 1961, p. 498.
2. Hardesty, D. R., "An Investigation of the Shock Initiation of Liquid Nitromethane," *Combustion and Flame*, Vol. 27, 1976, p. 229.
3. Jackson, T. L. and Kapila, A. K., "Shock Induced Thermal Runaway," *SIAM J. Appl. Math.*, Vol. 45, 1985, p. 130.
4. Jackson, T. L.; Kapila, A. K.; and Stewart, D. S., "Evolution of a Reaction Center in an Explosive Material," *SIAM J. Appl. Math.*, Vol. 49, 1989, p. 432.
5. Bdzil, J. B. and Kapila, A. K., "Shock-to-Detonation Transition, A Model Problem," *Physics of Fluids*, 1989, to appear.
6. Dold, J. W. and Kapila, A. K., "Asymptotic Analysis of Detonation Initiation," 1989, submitted for publication.
7. Clarke, J. F. and Cant, R. S., "Non-steady Gasdynamic Effects in the Induction Domain Behind a Strong Shock Wave," *Progress in Aeronautics and Astronautics*, Vol. 95, 1984, p. 142.

## DISCUSSION

JULIUS ROTH, Consultant  
Portola Valley, CA 94028

You showed calculations for a constant-volume thermal explosion for which the temperature rise for most of the induction period was very small and thermal explosion occurred almost instantaneously with almost no volume change. I believe we observed exactly these conditions for  $\text{PbN}_6$  initiated with high intensity light (*J. Chem. Phys.*, Vol. 41, No. 7, 1964, p. 1929). To explain our observations we had to invoke an activation energy of 30 to 40 Kcal/mole and we showed that thermal explosion occurred within  $1\mu\text{m}$  of the irradiated  $\text{PbN}_6$  face.

## REPLY BY A. K. KAPILA

The authors are grateful to Dr. Roth for acquainting them with an experimental result which appears to be in accord with the theory presented in this paper.

# CHEMICAL PHENOMENA ASSOCIATED WITH THE INITIATION OF THERMAL EXPLOSIONS\*

T. B. Brill and P. J. Brush  
Department of Chemistry  
University of Delaware  
Newark, Delaware 19716

*A microscale experiment is described to study the initiation of thermal explosions by simultaneously measuring the time-to-exotherm with thermocouples and the gas products evolved from the sample by FTIR spectroscopy. Time-to-exotherm data are given for N-NO<sub>2</sub>, C-NO<sub>2</sub>, and O-NO<sub>2</sub> compounds, an azide, a tetrazole, and NH<sub>4</sub>ClO<sub>4</sub> in the time range of 1-10 seconds. Heat flow dominates the apparent activation energy in this range. The gas products from HMX show that N<sub>2</sub>O and NO<sub>2</sub> are evolved before CH<sub>2</sub>O. All three of these gases appear before the exotherm. The concentrations of NO and HCN increase at the exotherm. The final gas product concentrations from HMX heated to 310°C and 420°C are similar indicating that the overall decomposition mechanism is the same at these two conditions.*

## INTRODUCTION

Chemical and physical phenomena associated with the initiation of thermal explosions continue to be frontier areas of energetic materials research. Examples of tests that measure the time-to-explosion (or time-to-exotherm) as a function of temperature are described by Henkin,<sup>1</sup> Wenograd,<sup>2</sup> Lee et al.,<sup>3</sup> Rogers,<sup>4</sup> and McGuire and Tarver<sup>5</sup> for various sample configurations, temperatures, and pressures. None of these tests are designed to study chemical events at the same time. Our interest in this subject was stimulated by the opportunity to investigate some of the chemical processes associated with the time to exotherm by using rapid scan Fourier transform infrared spectroscopy (FTIR)/temperature profiling.<sup>6</sup> This technique was developed to study the thermolysis mechanisms of energetic materials heated at rates exceeding 70°C/sec. Near real time observation of the gas

products evolved can be made simultaneously with the measurement of the temperature of the condensed phase when minute quantities of material are heated rapidly. In effect, the technique can be viewed as a spectroscopically instrumented thermal explosion test. For this type of study, the method of heating was modified so as to heat the sample rapidly to a chosen temperature and then hold the temperature constant while waiting for the exotherm (explosion). It was hoped that this procedure would minimize lower temperature "cooking" reactions that could complicate the interpretation of the chemistry.

Described here are the first results from this ongoing study to characterize the times-to-exotherm of energetic materials at relatively high temperatures in terms of the apparent activation energy and the gas products measured in near real time.

## EXPERIMENTAL

Figure 1 shows the main features of the cell used for this work. Except for the addition of a sample port to the top and the modification

\*This paper is number 38 in our series "Thermal Decomposition of Energetic Materials."

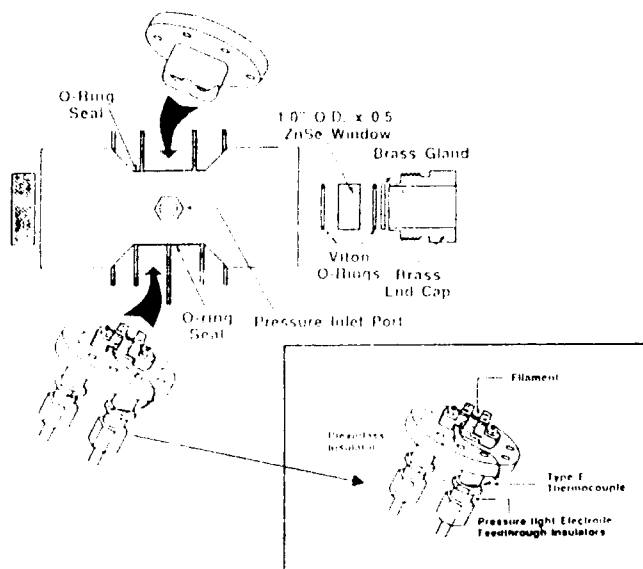


**Figure 1.** A Sketch of the Filament System and Cell Used for FTIR/Temperature Profiling Studies of Time-to-Exotherm

in the filament, the overall design is the same as that described previously.<sup>6,7</sup> The windows consist of 0.5 inch thick, anti-reflection coated ZnSe so that the cell can be safely pressurized to 1000 psi Ar, if desired. In place of the larger nichrome IV filament used for other work,<sup>6,7</sup> a 5.0 mm x 1.17 mm x 0.02 mm nichrome IV ribbon filament bridged the modified electrode posts shown in Figure 1.<sup>8</sup> A 0.005 inch diameter type E thermocouple was spot-welded to the underside of the filament and its output passed through a Metrabyte DAS-16 AD converter to an IBM-PC.<sup>6</sup> The heating circuit has been described.<sup>6</sup> The filament was found to reach a highly uniform temperature in the center third portion. 200-300  $\mu$ g of polycrystalline, powdered sample was thinly spread over this area to a nominal thickness of about 0.5 mm. Since most of the compounds studied melt before the decomposition gases are detected, decomposition occurs from a liquid layer about 0.2 mm thick. The existence of a liquid actually enhances the heat transfer between the filament and sample. The decomposition gases evolve into the cooler Ar atmosphere above the filament and are detected with the IR beam of the spectrometer focussed several mm above the filament. The gases were quantified as described before.<sup>6,7</sup> H<sub>2</sub>O was not quantified because the rotation-

vibration fine structure makes this difficult; no IR intensities for HNCO are known; and IR-inactive gases are not detected.

Plans are underway to develop a heating method that allows an even lower temperature region to be covered in the experiment described above. The current device works most effectively at higher temperatures.

## TIME-TO-EXOTHERM STUDIES

The efficiency of heat transfer between the filament and the sample, along with any temperature gradients, could affect the time-to-explosion data, especially at high temperature and fast heating rates. Therefore, the experiment was designed for the smallest possible sample size and the maximum contact between the sample and filament. The temperature variations through the sample are expected to be small compared to the uncertainty in the temperature ( $\pm 5^\circ\text{C}$ ). The rapid rate of heating of the sample to an isothermal or near-isothermal temperature was intended to reduce the effect of any sidelight "cooking" reactions that might occur while the sample heats to the temperature range of interest. It is possible that a very thin layer of gas separates the sample from the filament during the decomposition phase making both heat and mass transfer important. The heat capacity of this region might be expected to vary somewhat from compound to compound depending on the gas products present. Modeling of this experiment is needed (and is planned) to address these issues. The most important observations and conclusions obtained so far will be described here.

It was desirable to measure time-to-exotherm data on a variety of compounds. Data have been obtained on primary and secondary nitramines, azides, C-NO<sub>2</sub> compounds, O-NO<sub>2</sub> compounds, a tetrazole, and a salt (NH<sub>4</sub>ClO<sub>4</sub>). Figure 2 shows selected, but representative, time-to-exotherm data for HMX as a function of the filament temperature. A slight endothermic deflection is detected in the vicinity of 270-280°C corresponding to melting. All of the compounds studied that melt before decomposition display this endotherm. In order to minimize evaporation of the parent compound, several of the compounds

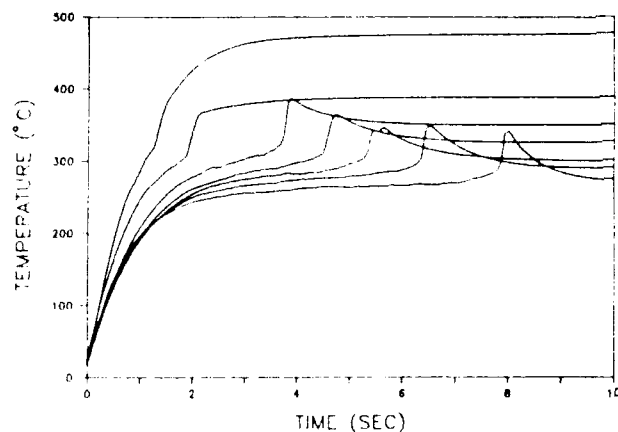


Figure 2. Selected Temperature Traces Showing the Time-to-Exotherm for 250 µg Samples of HMX Under 15 psi Ar

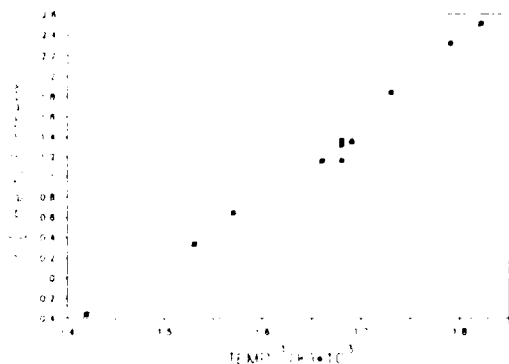


Figure 3. Apparent Activation Energy Plot of the Time-to-Exotherm of HMX at 15 psi Ar Showing the Slope Break

were investigated with an Ar pressure in the 15 200 psi range. A study of HMX as a function of pressure in this range indicated that the pressure differences caused a negligible change in the position of the exotherm, but did affect the gas product distribution, as is well known.<sup>9</sup> Much higher pressures would greatly affect the exotherm.<sup>10</sup>

As in all other thermal explosion experiments,<sup>1,5</sup> the time to explosion decreases with increasing temperature. The lowest temperatures studied in this work corresponds to the highest temperatures used in ODTX experiments<sup>5</sup> and, therefore, the data extend the range of the ODTX test

Most time to explosion data are plotted as  $\ln(t_{\text{exo}})$  vs.  $1/T$  to obtain an apparent activation energy.<sup>1,2,5</sup> Figures 3, 4, and 5 show such plots for HMX, RDX, and PETN. Each data point was obtained in a separate experiment with a fresh sample. As indicated in Table 1 and

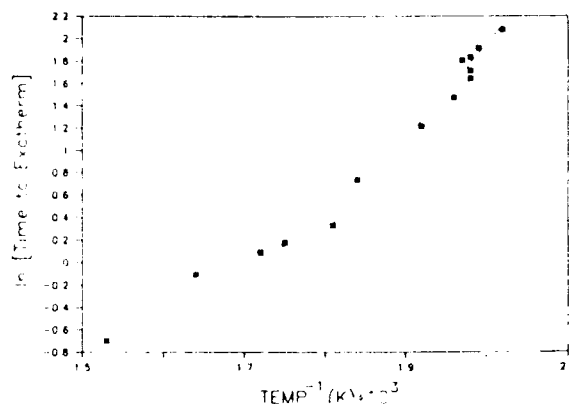


Figure 4. Apparent Activation Energy Plot of the Time-to-Exotherm of RDX Under 40 psi Ar Showing a Slope Break

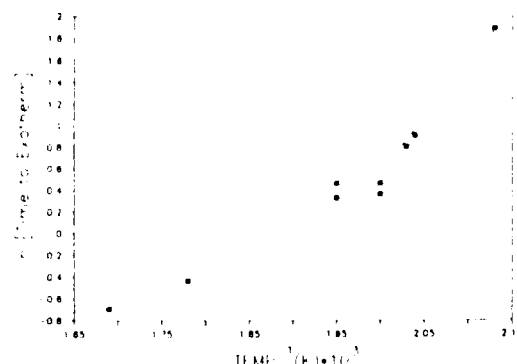


Figure 5. Apparent Activation Energy Plot of the Time-to-Exotherm of PETN Under 200 psi Ar Showing a Slope Break

these figures, all of the compounds studied to date display a slope break somewhere in the temperature range studied. The temperature of this slope break varies with the sample and, therefore, is probably not an experimental artifact. As a result, two apparent activation energies are reported. The highest value is associated with the lowest temperature range. We hope to learn more about the characteristics of these slope breaks (and whether they are device dependent) with a redesigned heating method under construction at the moment.

It has been recognized since the earliest efforts in this area<sup>2,11</sup> that the apparent activation energy ( $E_a$ ) calculated from time-to-explosion data does not necessarily reflect an isolated chemical process. Rather the apparent  $E_a$  probably represents a mixture of chemical and thermophysical processes. To us, its value is to indicate which of the many contributing factors dominates the time-to-exotherm in a given temperature range. The apparent  $E_a$

values in Table 1 are small compared to the global activation energy for thermal decomposition of these compounds (40-55 Kcal/mol). Consideration was given to the possibility that the apparent  $E_a$  values represent self-diffusion in the condensed phase to produce defects associated with hot-spot formation.  $E_a$  for self-diffusion in the solid state is approximately  $2(\Delta H_{\text{sub}})$ .<sup>12</sup> Since the heats of sublimation of HMX and RDX are about 40 and 30 Kcal/mol,<sup>13</sup> respectively, self-diffusion is unlikely to be the controlling influence. Moreover, all of the compounds, except AP, are molten before the exotherm.

The apparent  $E_a$  values can be interpreted in terms of an extension of the ODTX model. McGuire and Tarver<sup>5</sup> measured the time-to-explosion of HMX containing explosives (LX-10, OCTOL) and RDX from lower temperatures up to about the lowest temperature shown in Figures 3 and 4. A somewhat convex downward curvature occurs when  $\ln(t_{\text{exo}})$  vs  $1/T$  is plotted. Dividing the lower and higher temperature regions of these HMX data into two parts gives an apparent  $E_a$  of 52 Kcal/mol in the lower temperature range and 34 Kcal/mol in the higher temperature range. 52 Kcal/mol resembles the global  $E_a$  for condensed phase decomposition of HMX.<sup>14</sup>

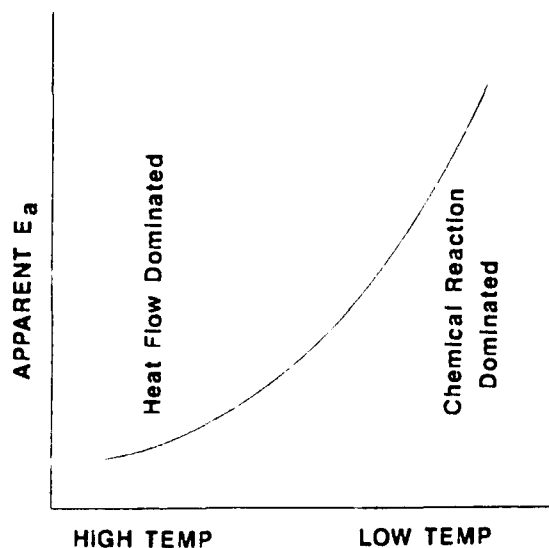


Figure 6. The General Pattern of the Apparent Activation Energies for Time-to-Exotherm Over a Wide Temperature and Time Range

The value of 34 Kcal/mol was ascribed to the overall  $E_a$  of gas phase reactions. However, it is well-known that heat flow and chemical activation energies are balanced forces in time-to-explosion data.<sup>5,15-17</sup> At lower temperatures  $E_a$  of chemical reactions dominate the heat flow effects, while at higher temperatures, heat flow can dominate despite the fact that chemical reactions are occurring. This general pattern provides a plausible explanation for the small apparent  $E_a$  values given in Table 1. Preliminary calculations by Tarver on the HMX data shown in Figure 3 bear this out.<sup>18</sup> Figure 6 gives a pictorial view of this notion for all compounds studied to date. The larger apparent  $E_a$  values at lower temperature are dominated by chemical processes while the smaller  $E_a$  values at higher temperature are small because they are dominated by the rate of heat flow.

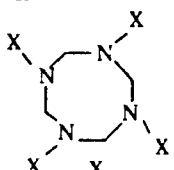
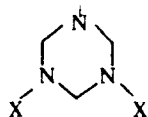
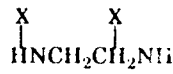
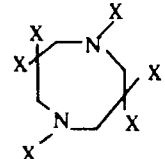
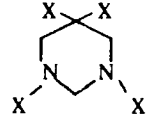
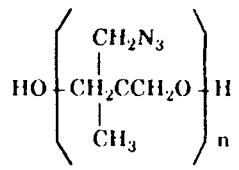
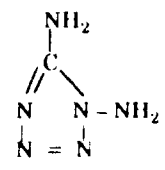
The apparent  $E_a$  values for  $\text{NH}_4\text{ClO}_4$  differ somewhat from the other compounds and merit mention.  $\text{NH}_4\text{ClO}_4$  exhibits an exotherm at a higher temperature than the other compounds studied. Thus, the apparent  $E_a$  value at the lower temperatures reflects mostly chemical processes just as it does in the ODTX data. The small apparent  $E_a$  value at higher temperature reflects the dominance of heat flow as described above.

In summary, the apparent activation energies in Table 1 (when coupled with ODTX data at lower temperatures) are useful for visualizing how chemical processes blend with the thermophysical component to initiate a thermal explosion. Heat transfer dominates at the higher temperature limit while chemical processes are reflected at lower temperature. Work aimed at modeling this pattern is planned.

## CHEMICAL PROCESSES

An important question is why the data in Table 1 differ from compound to compound if the heat flow dominates. Some of the chemical and physical characteristics of the individual materials are apparently retained. A unique feature of the experiment described here, that may help answer this question, is the ability to interrogate the near-surface, IR-active gas products in near real-time simultaneously

Table 1. Apparent Activation Energies for Times-to-Exotherm

	Compound <sup>a</sup>	Pressure, psi Ar	Apparent Activation Energy, Kcal/mol	
			Low temperature <sup>b</sup>	High temperature <sup>b</sup>
HMX		15	15.1 (276-317)	10.4 (318-431)
RDX		40	15.2 (222-280)	7.2 (281-381)
EDNA		50	13.9 (175-267)	5.0 (268-348)
HNDZ		40	18.3 (265-318)	14.8 (319-422)
DNNC		50	25.2 (209-237)	10.0 (238-314)
PETN	$C(CH_2Y)_4$	200	18.1 (196-231)	7.8 (232-317)
AMMO		15	22.7 (265-297)	6.7 (298-479)
TZL4		15	14.6 (248-347)	2.8 (348-431)
AP	$NH_4ClO_4$	50	47.5 (468-491)	14.8 (492-554)

<sup>a</sup> X = NO<sub>2</sub>; Y = ONO<sub>2</sub>

<sup>b</sup> Parenthetical numbers are the temperature range in °C.

with the time-to-exotherm measurement. In effect, the experiment is a spectroscopically instrumented time-to-explosion device. Work on the chemical aspects of time-to-explosion is in its infancy in our laboratory. Therefore, only one result will be described.

Figure 7 shows the gas products quantified in relative percent composition under two different heating conditions from HMX. Data were obtained at other temperatures, but are

not shown for clarity. The sequence in which these gases appear and their relative concentrations provide information about the thermal decomposition process. Gases are first detected from HMX decomposition in the 290-310°C range under these fast-heating conditions. N<sub>2</sub>O and NO<sub>2</sub> are the first detected gas products and consistently appear before CH<sub>2</sub>O is detected. All three gases dominate before the exotherm. The fact that N<sub>2</sub>O and CH<sub>2</sub>O do not appear at the same time suggests that either

they are not formed in the same reaction or that the evolution of  $\text{CH}_2\text{O}$  is physically retarded. It is interesting to note that Behrens<sup>19</sup> also found a delay in  $\text{CH}_2\text{O}$  evolution compared to  $\text{N}_2\text{O}$  when HMX was thermally decomposed at lower heating rates.

The exotherm is associated with a sharp rise in HCN and NO. After the exotherm the relative gas concentrations are not markedly different for the two heating conditions shown implying that the decomposition mechanism has not changed. Note especially that the ratio  $\text{NO}_2$  to  $\text{N}_2\text{O}$  is similar after the exotherm. These two products form by fundamentally different processes,<sup>20</sup> yet the branching ratio is essentially the same with these two heating conditions.

Work is continuing to define the gas product distributions of many other energetic materials in these time-to-exotherm experiments. Attempts will be made to connect the results to models of the apparent activation energies of these compounds. With a modification of the heating method we hope to be able to investigate somewhat lower temperatures and longer times to exotherm so that the full range phenomena depicted by Figure 6 can be studied in the same experiment.

## ACKNOWLEDGEMENTS

We are grateful to the Air Force Office of Scientific Research for support of this work on AFOSR-87-0033.

## REFERENCES

1. Henkin, H. and McGill, R., *Indust. Eng. Chem.*, Vol. 44, 1952, p. 1391.
2. Wenograd, J., *Trans. Farad. Soc.*, Vol. 57, 1961, p. 1612.
3. Lee, E. L., Sanborn, R. H.; and Stromberg, H. D., *Proceedings of the Fifth Symposium (International) on Detonation*, ACR-184, ONR, Arlington, VA, 1975, p. 131.
4. Rogers, R. N., *Thermochim. Acta*, Vol. 11, 1975, p. 131.
5. McGuire, R. R. and Tarver, C. M., *Proceedings of the Seventh Symposium*

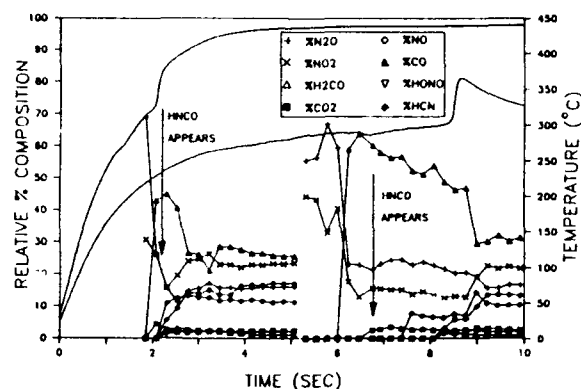


Figure 7. The Relative Percent Composition of the Quantified Gas Products From HMX Superimposed on the Thermal Trace of the Sample Heated to 310°C and 420°C

(International) on Detonation, US Naval Academy, Annapolis, MD, 1981, p. 56.

6. Cronin, J. T. and Brill, T. B., *Appl. Spectrosc.*, Vol. 41, 1987, p. 1141; *Appl. Spectrosc.*, Vol. 43, 1989, p. 650.
7. Oyumi, Y. and Brill, T. B., *Combust. Flame*, Vol. 62, 1985, p. 213.
8. Cronin, J. T., Ph.D. Dissertation, University of Delaware, Dec 1988.
9. Oyumi, Y. and Brill, T. B., *Combust. Flame*, Vol. 68, 1987, p. 209.
10. Shaw, R.; DeCarli, P. S.; Ross, D. S.; Lee, E. L.; and Stromberg, H. D., *Combust. Flame*, Vol. 35, 1979, p. 37.
11. Kaye, S. M., *Encyclopedia of Explosives and Related Items*, Vol. 9, USARDEC Dover, NJ, 1980, pp. T173-T188.
12. Flynn, C. P., *Point Defects and Diffusion*, Clarendon Press, Oxford, 1972, pp. 509-544.
13. Federoff, B. T., *Encyclopedia of Explosives and Related Items*, Vol. 7, Picatinny Arsenal, Dover, NJ, 1975, p. H44.
14. Schroeder, M. A., CPIA Publ. 308, *Proceedings of 16th JANNAF Combustion Meeting*, Monterey, CA, Vol. II, Sep 1979, pp. 17-34.

15. Frank-Kamenetskii, D. A., *Acta Phys. Chem. USSR*, Vol. 10, 1939, p. 365.
16. Chambre', P. L., *J. Chem. Phys.*, Vol. 20, 1952, p. 1075.
17. Zinn, J. and Mader, C. L., *J. Appl. Phys.*, Vol. 31, 1960, p. 323.
18. Tarver, C. M., LLNL, personal communication, Dec 1988.
19. Behrens, R., CPIA Publ. 476, *Proceedings of 24th JANNAF Combustion Meeting*, Monterey, CA, Vol. 1, Oct 1987, pp. 333-432.
20. Melius, C. F., *J. Phys.*, Vol. 48, 1987, p. C4-341.

### DISCUSSION

**ALBERT VAN DER STEEN**  
TML-TNO, Netherlands

What is the relevance of the small  $\Delta E$  values in the high temperature region? Because the heat source has not yet reached a constant temperature, Frank-Kamenetskii theory cannot be applied.

When the heating time of the heat source is very short, a constant activation energy will be found for most explosives. This is shown by

Schrader, Leeuw, and Van der Steen in Proc. 9th Int. Pyr. Seminar, Colorado Springs, 1984.

### REPLY BY T. B. BRILL

Because we are not at the steady state condition  $\partial T/\partial t = 0$ , we believe that the heat flow term,  $\lambda \nabla^2 T$ , increasingly dominates the chemical reaction terms when the heating rate and temperature are very high. The small apparent activation energy at high temperature probably results from this fact.

### DISCUSSION

**JULIUS ROTH**, Consultant  
Portola Valley, California

In further study of the Wenograd test (SRI report contract 65-0283-d, 1966), we also observed breaks in  $\log t_{\text{exp}}$  vs.  $1/T$  plots for liquid explosives. Our lowest temperature corresponded to your highest temperature, but our plots in that region were much steeper than yours. Indeed, our apparent activation energies were of the same order as the ones you found for HMX at 200 psi in your low temperature region.

### REPLY BY T. B. BRILL

Thank you for calling my attention to this report.



# THE LATTICE DENSITY OF STATES CONCEPT AND ITS ROLE IN DETERMINING THE SHOCK SENSITIVITY OF PETN AND NITROMETHANE

Richard D. Bardo  
Naval Surface Warfare Center  
10901 New Hampshire Avenue  
Detonation Physics Branch  
Silver Spring, Maryland 20903-5000

*A theory of shock ignition for single crystals, which was introduced previously to describe the interrelationship among bimolecular chemical reactions and processes for energy transfer between the nitromethane lattice and its molecules, is expanded to include other nitroexplosives such as PETN. An expression for the total rate coefficient is derived which includes the lattice densities of states for both acoustic and optical phonon modes. The acoustic modes are needed to describe slip while the optical modes are required for initiation of reaction. For nitromethane, application of this expression gives (1) the gradual change from "Arrhenius" to "non-Arrhenius" kinetics over the shock pressure range of 50 to 80 kbar, (2) approximate times which may pertain to periods of "induction" and "superdetonation," and (3) an approximate relationship between amplitudes of initiating shock and delay time to detonation. From a new expression for the combined density of states of acoustic and optical modes, calculation of energy transfer times suggests that slip plays a greater role in the initiation of PETN than it does in the initiation of nitromethane.*

## INTRODUCTION

The nature of shock initiation in homogeneous explosives continues to be of experimental and theoretical interest. Recently, the electromagnetic gauge studies of Sheffield et al.<sup>1</sup> have helped to clarify certain details of the initiation process, including placement of the formation of superdetonation relative to the initial shock. Confirmation is made of previous studies which showed that the initiation processes are entirely different for homogeneous and heterogeneous materials, even for similar input pressures and times to detonation. These experiments indicate that the way initiation proceeds in the different materials is determined to a large extent by the ignition process which, for homogeneous explosives, is characterized by the induction time,  $t_{ind}$ . Since the shock insensitivity of many homogeneous

explosives may be traced to a relatively long  $t_{ind}$ , and since a major thrust of the detonation community is to minimize shock sensitivity while maximizing performance, a basic understanding of the origination of  $t_{ind}$  is deemed essential. While the performance of explosives has been satisfactorily dealt with by the macroscopic (continuum), steady-state picture, it has become increasingly evident that the difficult problem of shock sensitivity must be interpreted in terms of concepts based on the microscopic point of view.

Calculations of  $t_{ind}$  by Campbell et al.,<sup>2</sup> Enig and Petrone,<sup>3</sup> and Mader<sup>4</sup> have employed Arrhenius reaction kinetics and thermal explosion theory to show that, for liquid nitromethane, liquid TNT, and single crystal PETN, their values are consistent with those of experiment. This consistency is remarkable

and, in fact, may be fortuitous since the half-lives for the assumed kinetics may be shown to be larger than  $10^{-4}$  seconds, which exceeds by  $10^2$  the arrival of rarefactions in the geometries considered. In addition to these studies, past quantum mechanical calculations of  $t_{ind}$  for nitromethane<sup>5</sup> have been made with complex methods which have hindered the study of more complicated systems. These latter calculations, while ignoring chemistry, did show a possible connection between the induction time and energy transfer processes.

In Reference 6, a theory of shock ignition was introduced and shown to contain appropriate physical and chemical concepts as a possible basis for the prediction of shock sensitivity. From quantum and statistical mechanical calculations of rates of vibrational energy transfer and chemical reaction for nitromethane, the results showed that it may now be possible to identify some of the critical microscopic quantities required for the formulation of a comprehensive theory of sensitivity for condensed explosives. One of these quantities was shown to be the lattice vibrational density of states for the optical modes, which give rise to bimolecular reactions. In the past, these modes had been incorrectly called "acoustic." With the optical modes, it was possible to show the existence of a relationship between chemistry in the bulk and the mechanics of the lattice.

The purpose of the present paper is to show how the theory of Reference 6 may be expanded and applied to nitroexplosives other than nitromethane. The expanded theory includes (1) the acoustic modes which, in addition to determining the speed of sound in the crystal, are needed to describe slip in nitromethane and PETN, and (2) a total rate which determines more clearly the evolution of "Arrhenius" to "non-Arrhenius" kinetics as shock pressures are increased in nitromethane. The rates of energy transfer and reaction introduced previously<sup>6</sup> are reviewed in the following section. In the "Total Rate for Energy Transfer and Reaction" section, an equation is derived for the total rate coefficient, which is shown to be useful in approximating periods of "induction" and "superdetonation." In the "Rates of Energy

Transfer for Crystalline PETN" section, the combined density of states for acoustic and optical modes is estimated for different crystallographic directions in PETN, and is shown to provide a possible theoretical basis for a description of the observed directional sensitivity of single crystals of PETN.<sup>7</sup>

## REVIEW OF RATES OF ENERGY TRANSFER AND REACTION

According to the theory of Reference 6, the ignition of homogeneous explosives over wide ranges of shock pressure may be understood in terms of a relatively small number of critical elements, which are the lattice vibrational density of states for optical phonon modes  $\rho$ , the numbers of excited optical phonons  $n$  and molecular vibrational quanta or vibrons, and the entropy, volume, and energy of activation parameters  $S_a$ ,  $V_a$ , and  $E_a$  for bimolecular chemical reaction. As shown in Reference 6, these quantities determine (1) the rate of flow of shock energy into the molecule from the lattice prior to reaction, (2) the rate of energy flow back into the lattice from the molecule also prior to reaction, and (3) the reaction rate, which is determined from the activation parameters and the absolute reaction rate or Arrhenius-like formulae. The corresponding characteristic times are given by Equations (1), (2), and (3) for the above rates (1), (2), and (3), respectively:

$$t_{pv} = \hbar \rho, \quad (1)$$

$$t_{vp} = t_{pv}/2n, \quad (2)$$

and

$$- \ln t(\frac{1}{2}) = \ln \frac{k_B T}{h} + \frac{S_a}{k_B} - \frac{PV_a}{k_B T} - \frac{E_a}{k_B T}. \quad (3)$$

The subscripts  $pv$  and  $vp$  in Equations (1) and (2) refer to phonon-to-vibron and vibron-to-phonon energy transfer, respectively. The time  $t(\frac{1}{2})$  denotes a reaction half-life. The symbol  $k_B$  is the Boltzmann constant. The inverse of each characteristic time is a rate coefficient. These times are used to determine the evolution of the explosive during initiation before

significant reaction beyond the first step has occurred. If several reactions were to occur in parallel, for example, Equation (3) would apply to the fastest one, which, in the case of competition between bimolecular and unimolecular reactions at high pressure, would usually be bimolecular. This was shown to be the case for nitromethane in Reference 6. Otherwise, Equation (3) would represent a net rate coefficient.

Bimolecular reaction occurs as a natural consequence of the optical mode lattice vibrations, which represent back-and-forth (fixed center-of-mass) motions of molecules within each unit cell. On the other hand, acoustic mode vibrations, which correspond only to center-of-mass motion within a unit cell, are coupled much less strongly to the vibron modes and, as a consequence, generate little reaction. It is important to note in this regard that no optical modes, numbering  $3N(p-1)$  where  $N$  is the number of unit cells and  $p$  is the number of molecules per unit cell, exist for molecular crystals with  $p = 1$ . In that case, detonation is unlikely to occur when  $p$  remains unchanged under shock. Intermolecular-to-intramolecular energy transfer, which must precede chemical reaction, is directly caused, then, by optical phonon vibron coupling. It will be shown in the two following sections that an expansion of the theory of Reference 6 does require, however, consideration of the available acoustic vibrational states into which optical and vibron energy is dissipated, decreasing the probability of initiation.

The three different processes pertaining to Equations (1) - (3) may be visualized from the energy level diagram of Figure 1, which gives a kind of pictorial representation of the formalism developed in Reference 6. In Figure 1, each intramolecular vibrational or vibron level has associated with it a series of lower-frequency intermolecular vibrational or phonon states. As depicted, these states are not evenly spaced since most or all of the available phonon modes may be excited by shock. A formal statement of this condition is expressed as the compound or lattice density of states,  $\rho \equiv \rho(\omega)$ ,

$$\rho(\omega) = \int d\epsilon_1 d\epsilon_2 \dots \int d\epsilon_N \cdot \rho_1(\omega - \epsilon_1) \rho_2(\epsilon_1 - \epsilon_2) \dots \rho_N(\epsilon_{N-1}) \quad (4)$$

where  $N$  is the number of sets of phonon states, each set having a density of states  $\rho_i$ , and where  $\omega$  is a frequency corresponding to the energy that is transferred. For clarity in Figure 1, these states are shown for one vibron level, and the excited vibron levels are displaced to the right. These levels may be

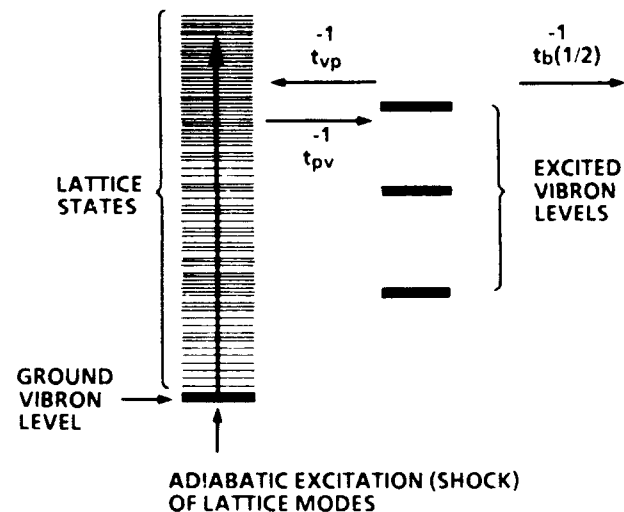


Figure 1. *Vibrational Energy Level Diagram Associated With Shock Excitation and the Resulting Steps for Phonon-to-Vibron (pv) and Vibron-to-Phonon (vp) Energy Transfer and Bimolecular Reaction*

associated with the lowest frequency modes of the molecule which usually belong to the  $\text{NO}_2$  groups. If the shock strength is sufficient, the high-lying excited vibron levels are reached by multiphonon excitation. In Figure 1, the shock strength determines the length of the vertical arrow which is a measure of the maximum energy deposited in the lattice. The verticality of the arrow is a consequence of the adiabatic shock process, during which little energy is communicated between the molecules, and in which only the lattice modes corresponding to a limited region of the crystal are excited. In a cylinder of explosive, for example, this region could be a given cross-section with a width, say, on the order of the shock front, and a diameter equal to that of the cylinder. As long as the shock pressure is sustained, the arrow maintains its length, and the distribution of excited phonons is preserved.

The degree of excitation of a molecule is determined by the number of available phonons corresponding to a distribution

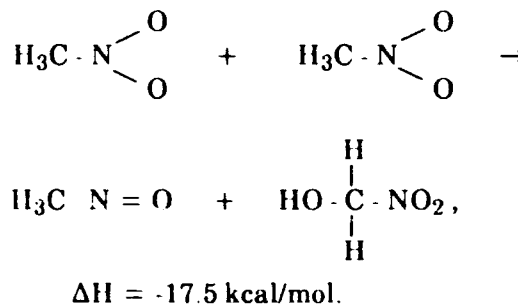
derived from the shock process. According to perturbation theory,<sup>8</sup> the square of the Fourier transform of a time-dependent energy deposition profile is the number of excited phonons. It may be shown that, if the rate of energy deposition is sufficiently slow, the resulting distribution of phonons is Boltzmann-like. If, on the other hand, the rate is extremely rapid, as in a shock, the distribution is a truncated Lorentzian.

The truncated Lorentzian is due to the quantized nature of the problem. For example, in crystalline nitromethane, the most energetic phonon at 80 kbar is nearly  $200\text{ cm}^{-1}$ .<sup>6,9</sup> In this case, if all of the thermal energy of 10 kcal/mol, as determined from the energy jump condition and the molecular repulsion energy,<sup>6</sup> is initially deposited in the lattice modes, and if only the  $200\text{ cm}^{-1}$  phonons are excited, approximately 20 such phonons per molecule are needed to bridge the gap between the ground vibron level and the level in the vicinity of 10 kcal/mol. Actually, as shown in Reference 6 for nitromethane, seven of the nine available optical degrees of freedom per unit cell are needed, since only four optical phonons per mode may be excited at 80 kbar. This restriction in the number of quanta per mode eliminates the long "tail" that exists in Maxwell-Boltzmann statistics for unrestricted molecular motion. This means, of course, that chemical reaction in a solid begins in a different way than in a gas where high velocity collisions are important for initiation of reaction. In the solid, shock activation of high-lying internal molecular modes depends on the excitation of all of the available lattice modes and, as such, is strictly "non-monochromatic." It is interesting to note in this regard that Equations (1) and (2) will still apply to good approximation in the limit of a phase change to a gas, where  $p$  becomes the density of states of the translational degrees of freedom of the gas. This would be the statistical limit where Maxwell-Boltzmann statistics apply.

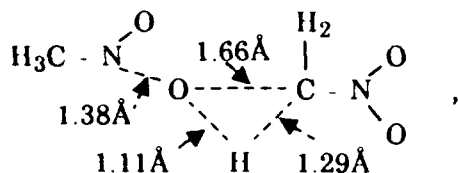
In the vicinity of the shock front, lattice vibrational energy begins to flow between the lattice states and vibron levels as a consequence of phonon-vibron coupling. In Figure 1, the horizontal arrow pointing to the right

denotes flow into the vibron level. The accumulated energy in that level also flows back into the lattice, as indicated by the left-pointing arrow. The latter process is often called non-radiative since no infrared photons are emitted. According to Equations (1) and (2), the rate coefficient  $t_{vp}^{-1}$  for this step is larger than  $t_{pv}^{-1}$ , so that  $t_{pv} > t_{vp}$ , which is a direct consequence of the fact that the density of states of the lattice is usually larger than the vibron level density. In the case of nitromethane, the above inequality is seen from Figure 2, where the results of calculations<sup>6</sup> are plotted against shock pressure. Over the indicated pressure range of  $10 \leq P_s \leq 80\text{ kbar}$ , the ratio of times lies in the range  $32 \geq t_{pv}/t_{vp} \geq 21$ . As indicated in Reference 6, these times pertain to the exchange of shock energy between the lattice and vibron levels of the lowest frequency  $\text{NO}_2$  rocking mode where  $0.3 \leq E_s \leq 10\text{ kcal/mol}$  for the above pressure range.

From the discussion above, it may appear that all of the shock energy must be deposited in the molecules for reaction to occur. This is unnecessary and, in fact, is not required by the theory of Reference 6. There it is shown that the most likely vibron excitations are the lowest-order energy transfer processes involving the smallest number of phonons which can activate the most probable reactions under the given shock conditions. For the initial reaction discussed in Reference 10, the average activation energy per monomer of 11 kcal/mol, which may be utilized to surmount the activation barrier of 22.5 kcal/mol at 80 kbar, is distributed over the optical phonon modes and vibron modes. That head-to-tail bimolecular reaction, which involves the formation of nitrosomethane and nitromethanol as intermediates, is expressed as



Here, the formation of the activated complex,



arises in large part from the simultaneous reduction of the distance between centers-of-mass of neighboring monomers and their  $\text{CH}_3$  and  $\text{NO}_2$  groups, and the stretching of N-O and C-H bonds, the latter occurring during energy transfer.

In the gas phase, the kinetics of the above reaction would be given completely by Equation (3), which contains the temperature  $T$  of the intramolecular vibrations. In a shocked crystal, however, that description in terms of a set of thermalized vibrons is incomplete over shock initiation pressures of interest, as will be demonstrated more clearly in the next section.

It is of interest to note the similarity of Figure 1 to energy level diagrams used to describe electronic excitation and radiationless transitions in solids. Figure 1, however, applies to the ground electronic state of each molecule and to the lowest-lying band in the solid. It is important, moreover, to emphasize here, in connection with the previous comments on lower-order phonon processes, that much higher-order multiphonon excitation would be needed to reach electronic states, than is already available to excite vibron levels associated with single electronic state. For the usual shock strengths, electronic excitation is not likely in the early stages of initiation where, for example, along the nitromethane Hugoniot centered at 244K,  $\Delta E$  is only 10 kcal/mol (15 kcal/mol) at 50 kbar (80 kbar).

## TOTAL RATE FOR ENERGY TRANSFER AND REACTION

### Derivation of Total Rate Coefficient

In Figure 2, the intersections of the curves for  $t_{pv}$  and  $t_b$  may suggest that the rate-determining or slow step changes abruptly at  $P_s \approx 50$  kbar. When measurements of rates are made, however, the total rate is the one usually determined. It reflects a more gradual

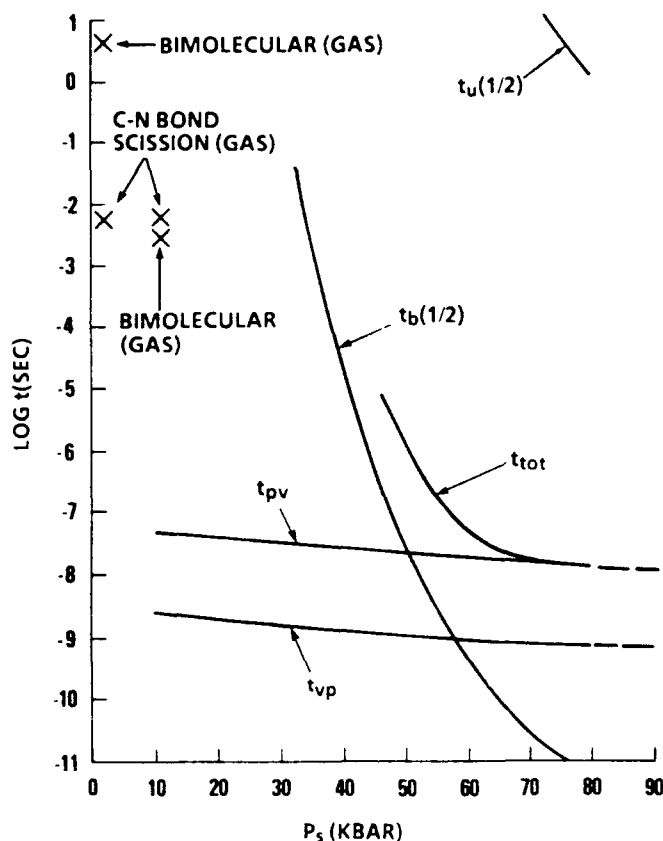
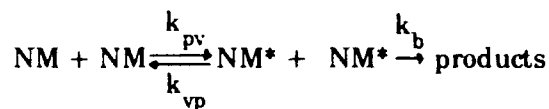


Figure 2. Shock Pressure Dependence of Energy Transfer Times  $t_{pv}$  and  $t_{vp}$ , Reaction Half-Lives  $t_b(\frac{1}{2})$  and  $t_u(\frac{1}{2})$  for Bimolecular and Unimolecular (C-N) Reactions, and Total Time  $t_{tot}$  for Nitromethane. Solid lines pertain to the single crystal. Data denoted by X pertain to the gas phase undergoing thermal decomposition at  $T = 1000\text{K}$  with the same activation parameters used for  $t_b$  and  $t_u$ .

change over a larger pressure range, as is seen from the curve for  $t_{tot}$  in Figure 2. An expression for the total rate coefficient  $k_{tot}$  is now derived.

The combined steps of energy transfer and reaction may be represented by



where NM and  $\text{NM}^*$  denote a normal nitromonomer and an energized monomer, respectively, and  $k_{pv}$ ,  $k_{vp}$ , and  $k_b$  are inverses of Equations (1) through (3). It should be noted that  $\text{NM}^*$  is not an activated complex for reaction. If the rates of energy transfer are  $k_{pv}f^2$  and  $k_{vp}f^{*2}$ , where  $f$  and  $f^*$  are mole

fractions, and the rate of bimolecular reaction is  $k_b f^{*2}$ , the rates of formation of  $NM^*$  and of disappearance of  $NM$  are

$$\frac{df^*}{dt} = k_{pv} f^2 - k_{vp} f^{*2} - k_b f^{*2} \quad (5)$$

and

$$-\frac{df}{dt} = k_{pv} f^2 - k_{vp} f^{*2} \quad (6)$$

Now, it is a good approximation to assume that, for times following passage of the shock front,  $f^*$  is small compared to  $f$ , so that

$$\frac{df^*}{dt} \approx 0 \quad (7)$$

As a result, solution of Equation (5) for  $f^{*2}$  gives

$$f^{*2} = \frac{k_{pv} f^2}{k_{vp} + k_b} \quad (8)$$

Substitution of this equation into Equation (6) gives, then,

$$-\frac{df}{dt} = \frac{k_{pv} k_b}{k_{vp} + k_b} f^2, \quad (9)$$

where  $k_{tot}$  is defined as

$$k_{tot} = \frac{k_{pv} k_b}{k_{vp} + k_b} \quad (10)$$

Also, from  $k_{tot}^{-1} = t_{tot}$ ,

$$t_{tot} = \frac{t_{pv} (t_{vp} + t_b)}{t_{vp}} \quad (11)$$

### Significance of The Total Rate

The derivation of Equation (9) represents a generalization of the Lindemann theory<sup>11</sup> which shows how activation by collision of molecules in a gas results in a change from second-order to first-order kinetics as the pressure increases. His theory applies to unimolecular reactions where only one excited  $NM^*$

species is formed. In the present approach for a shocked solid, the kinetics remain second-order over the pressure range. This result is to be expected on the basis of the effects of high  $P$  on  $k_b$  in Equation (3), and also from the magnitude of the unimolecular rate coefficient

$$k_u = t_u^{-1}$$

calculated in Reference 6 for nitromethane and plotted in Figure 2. As a comparison, the gas phase points, identified with an X in Figure 2, were obtained from Equation (3) with the same activation parameters used to generate the  $t_b$  and  $t_u$  curves for the solid. These results show that, in contrast to the shocked solid, the higher temperatures,  $T > 1000K$ , generated by much smaller shocks in a gas can lead to competition between unimolecular and bimolecular reactions at certain pressures. For  $P < 5$  kbar, C-N bond scission dominates the competition with the bimolecular reaction which confirms the known kinetics for thermal decomposition at ambient pressure.

Since  $t_{pv}/t_{vp}$  is slowly varying over the pressure range of Figure 2, Equation (11) shows that  $t_{tot}$  depends on the relative magnitudes of  $t_{vp}$  and  $t_b$ . If  $t_b \gg t_{vp}$ ,

$$t_{tot} = \frac{t_{pv}}{t_{vp}} t_b \quad (12)$$

so that the reaction appears to occur in accordance with the absolute reaction rate of Equation (3), but modified by a factor of order 20. It may be recalled that Equation (3) is valid if equilibration of the vibron levels is instantaneous so that a temperature  $T$  exists throughout the solid. Initiation can occur only when  $t_{tot}$  from Equation (12) is shorter than the arrival time of rarefactions. From Figure 2,  $P_s = 50$  kbar is the absolute lower limit for initiation of high-velocity detonation in homogeneous nitromethane.

If, on the other hand,  $t_b < t_{vp}$ ,

$$t_{tot} = t_{pv}, \quad (13)$$

where the total rate is determined by the slow step of  $pv$ . The reaction appears to proceed in violation of Equation (3), since thermalization of the vibrons is not achieved sufficiently rapidly. Here, then, the temperature of the solid is ill-defined for  $P_s > 60$  kbar. Moreover,

the above inequality indicates that reaction becomes so fast after vibron excitation, that energy can be released and localized during times of order  $t_b$ . As indicated in the "Review of Rates of Energy Transfer and Reaction" section, the amount of energy in the initial exothermic bimolecular reaction for nitromethane is 17.5 kcal/mol. If  $t_{vp}$  is also taken to be a measure of the time for this energy to be dissipated by the vibrationally-excited products to the lattice, then the localized energy represents a microscopic hot spot. It is interesting to note in this regard that, since the speed of sound  $c$  is  $c \geq 2.6 \times 10^5$  cm/sec for  $P_s \geq 60$  kbar,  $ct_{vp} < 0.007$  mm. This satisfies the communication criterion of Nunziato, et al.<sup>12</sup> who show that, for superdetonation to occur,  $ct_{pv} \ll \delta$ , where  $\delta$  is the propagation distance of the initiating shock. These results indicate the possibility of reaction occurring immediately behind a new shock front, and the formation of a small reaction zone.

The shape of the curve for  $t_{tot}$  in Figure 2 approximates the relationship between the amplitude of an initiating shock and the variation of delay time to steady-state detonation. Thus far, this complete relationship has not been empirically determined for nitromethane. From Figure 2, high-velocity detonation in homogeneous nitromethane is not possible for  $P_s < 50$  kbar, which is consistent with initiation experiments. For  $P_s < 50$  kbar,  $t_{tot} > 1$   $\mu$ sec, which can exceed the arrival time of rarefaction waves in the usual geometries. For pressures on and above the curve, and for  $t_{tot} < 1$   $\mu$ sec, initiation may occur. Since the curve for  $t_{tot}$  more closely approximates the induction time as a function of pressure, it does not include contributions from reactions subsequent to the one described above and, as such, can apply at later times only if that reaction continues to dominate the mechanism.

It is important to note that a direct comparison of  $t_{tot}$  in Figure 2 with experimental induction times is not possible, since no such measurements appear to have been made for solid nitromethane, but only for liquids initially near room temperature.<sup>13</sup> Moreover, the curve for  $t_b$  in Figure 2 was obtained in Reference 6 from temperatures calculated along a

Hugoniot centered at the melting point of 244.6K. It is expected from Equation (1), however, that induction times will decrease from the liquid to the solid phase since, as a general rule, the density of states decreases as the denser local modes of liquids evolve continuously into lattice modes in the absence of slip planes. Additional comments are made about modes in liquids in the next section, and about the effects of slip in connection with PETN in "Rates of Energy Transfer for Crystalline PETN."

### Role of the Acoustic Modes

Thus far, the total rate has been described in terms of  $t_{pv}$  and  $t_{vp}$  as functions of only the density of states for optical modes. As emphasized in the "Review of Rates of Energy Transfer and Reaction" section, the optical, not acoustic, phonons couple strongly to the vibrons, since the acoustic modes involve translational motion of the centers-of-mass of all molecules comprising the unit cell and, as a result, determine the speed of sound in the crystal and provide for the transport of energy. However, excitation and de-excitation of optical (o) and acoustic (a) phonons exist according to the selection rule,  $a + a \Rightarrow 0$ ,<sup>14</sup> so that the acoustic modes serve as a reservoir which can significantly affect the total rate. It will now be shown that, to a good approximation, Figure 2 is still applicable to nitromethane, and that the rates for initiation are determined by  $\rho$  for the optical phonons. For crystals of PETN, on the other hand, where slippage is known to be important, the acoustic modes are essential, as will be shown in the following section.

The joint density of states  $\bar{\rho}$  is the geometric mean of  $\rho_a$  for the acoustic modes and  $\rho_o$  for the optical modes,

$$\bar{\rho} = \sqrt{\rho_a \rho_o} \quad (14a)$$

The time  $t_{pv}$  is then redefined as

$$\bar{t}_{pv} = \hbar \bar{\rho} \quad (14b)$$

Since the acoustic modes arise from translational motion within a unit cell, the density of states for a particle in a box of the size of the unit cell with periodic boundary conditions may be used here, so that

$$\rho_a = \frac{M^{3/2} E^{1/2} V}{2^{1/2} n^2 h^3} \quad (15)$$

where  $M$  pertains to the center-of-mass,  $E$  is the unit cell energy derived from the shock energy discussed in the "Review of Rates of Energy Transfer and Reaction" section, and  $V$  is the volume of the unit cell.

Equation (15) shows more clearly the effects of  $E$  and  $V$  on the density of states than does the expression for  $\rho$  given in Reference 6. There,  $\rho$  is given by

$$\rho = \left( \frac{2}{nn} \right)^{1/2} \frac{(1 - 1/12n)\lambda}{h <v> (1 + \eta)} \left| \left( 1 + \frac{\eta}{2} \right) \right. \\ \left. \times \left( 1 + \frac{2}{\eta} \right)^{\eta/2} \right|^n \left| 1 - \frac{1}{(1 + \eta)^2} \right|^{\beta_0} \quad (16a)$$

where  $n$  is the number of vibrational degrees of freedom,  $<v>$  is the average of the  $n$  frequencies  $v_i$ , and  $\lambda$ ,  $\beta_0$ , and  $\eta$  are defined by the equations

$$\lambda^{-1} = 11(v_i / \langle v \rangle), \quad (16b)$$

$$\beta_0 = [(n-1)(n-2)\alpha_2 - n^2]/6n, \quad (16c)$$

$$\alpha_2 = \langle v^2 \rangle / \langle v \rangle^2, \quad (16d)$$

$$\eta = E/E_0. \quad (16e)$$

In Equation (16e),  $E$  is the internal energy interval and  $E_0$  is the zero-point energy. While Equations (15) and (16a) are both applicable to the acoustic modes, only Equation (16a) applies to the optical modes.

For shocked nitromethane,  $M = 4.05 \times 10^{-22}$  g, since there are assumed to be four molecules per unit cell and, from the Hugoniot centered at  $T_0 = 244.6$  K,  $8.33 \times 10^{-14} \leq E \leq 1.51 \times 10^{-12}$  erg,  $2.43 \times 10^{-22} \geq V \geq 2.19 \times 10^{-22}$  cm<sup>3</sup> for  $10 \leq P_s \leq 80$  kbar. Substitution of these values into Equation (15) gives  $1.60 \times 10^{20} \geq \rho_a \geq 1.51 \times 10^{20}$  erg<sup>-1</sup>. In utilizing the frequencies from Reference 6, calculation of  $\rho_0$  from Equations (16a) through (16e) gives the range  $5.52 \times 10^{19} \geq \rho_0 \geq 1.50 \times 10^{19}$  erg<sup>-1</sup>. Calculation of  $\bar{\rho}$  and  $t_{pv}$  from Equations (14a) and (14b) then give the curve labeled NM in Figure 3. These times are seen to be somewhat longer than  $t_{pv}$  shown in Figure 2. Here,  $\rho_0 < \rho_a$  over the entire pressure range.

The times  $t_{pv}$  are still shorter than the known induction times  $t_{ind}$  for liquid nitromethane at  $P_s > 75$  kbar<sup>13</sup> where, for example, at  $P_s = 75$  kbar and  $T_0 = 297$  K,  $t_{ind} \approx 1.8$   $\mu$ sec. These longer empirical times may result from larger densities of states for liquids, and from the use of unsustained shocks. As indicated in Figure 3, a falloff in pressure increases  $\bar{\rho}$ .

## RATES OF ENERGY TRANSFER FOR CRYSTALLINE PETN

For initiation in single crystals of PETN, the dependency of the time and run distance on crystal direction has been observed by Dick.<sup>7</sup> He suggested that this effect could be understood in terms of the available slip planes affected by the uniaxial strain associated with planar shock compression. Shocks of 8.6 GPa and 12.4 GPa were found to yield initiation in the  $\langle 110 \rangle$  and  $\langle 001 \rangle$  directions. From a study of the crystallography of PETN, he indicated that the strong interleaving or overlap of the NO<sub>2</sub> groups across the  $\{100\}$  plane would cause the molecules to be the most sterically hindered for slippage, so that  $\langle 110 \rangle$  shocks would yield the shortest times and run distances.

A fundamental explanation of this behavior is directly related to the ability of PETN molecules to undergo reaction as a consequence of the strength of phonon-vibron coupling. As in the case of nitromethane, this ability is measured by the time  $t_{pv}$  required to "pump" the vibron modes to a sufficient level for reaction to occur. The time to initiation of detonation is then proportional to  $t_{pv}$  and, from Equation (14b), to  $\bar{\rho}$ . As indicated previously, the strongest coupling occurs between the vibrons of the NO<sub>2</sub> groups and the lattice.

Along the directions of easiest slip and low molecular disruption, the shock energy may be assumed to be concentrated in the acoustic modes, with a lower probability of excitation of the optical vibrations required for reaction. From the Hugoniot data for single crystals of PETN,<sup>15</sup> the ranges of average energy  $E$  and volume  $V$  are calculated to be  $1.1 \times 10^{-12} \leq E \leq 4.6 \times 10^{-12}$  erg and  $5.2 \times 10^{-22} \geq V \geq 4.6 \times 10^{-22}$  cm<sup>3</sup> for  $10 \leq P_s \leq 80$  kbar, so that from Equation (15),  $1.1 \times 10^{22} \geq \rho_a \geq 2.0 \times 10^{21}$ /erg.



Then, letting  $t_{pv} = \hbar \rho_a$ ,  $-4.93 \geq \log t_{pv} \geq -5.67$ . These times give the upper curve for PETN in Figure 3 which is labeled  $\langle 100 \rangle$ . This direction will yield a low probability of initiation if rarefaction waves arrive at times of the order of 1  $\mu$ second.

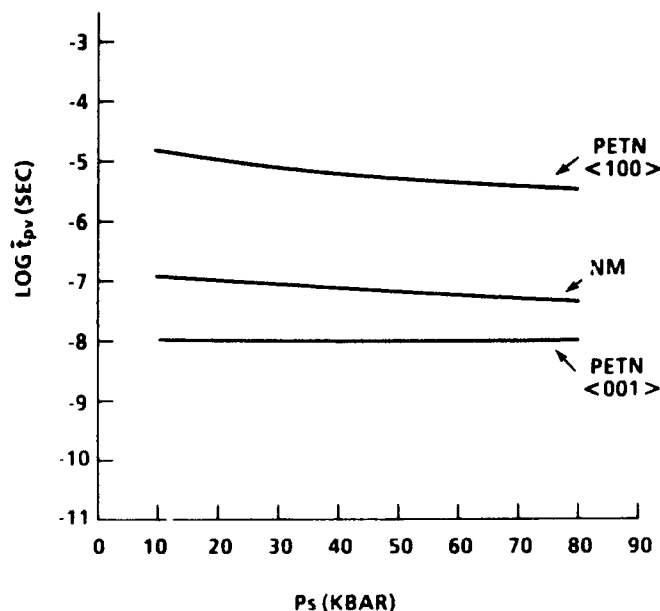


Figure 3. Shock Pressure Dependence of  $t_{pv}$  for Acoustic and Optical Modes of Nitromethane (NM) and Crystal Direction  $\langle 001 \rangle$  in PETN, and for Acoustic Modes Only in PETN Direction  $\langle 100 \rangle$

The optical mode frequencies for PETN have not been determined experimentally. However, a good approximation to  $p$  may be made by first observing that Equation (16a) depends more strongly on the number of molecules per unit cell  $p$  and on  $n = 3p-3$ , the number of optical degrees of freedom per unit cell, than on the magnitudes of the largest frequencies. These frequencies, in general, belong to the modes having the largest phonon-vibron coupling. Second, it may be assumed in Equation (16a) that, for shocks,  $n$  remains unchanged from its  $n = 3$  ( $p = 2$ ) value at ambient pressure. This assumption will be valid when local ordering is maintained, as may happen in solid-liquid phase changes. To a good approximation, then,  $\rho_0$  may be evaluated from the three largest ambient pressure optical mode frequencies 114.0, 99.5, and 95.5  $\text{cm}^{-1}$  for nitromethane. As in the case of

nitromethane,<sup>6</sup> these frequencies may also be scaled by factors of 1.3 to 1.8 over the pressure range of  $10 \leq P_s \leq 80$  kbar for PETN. Substitution of the scaled frequencies and energies  $E$  into Equations (16a) through (16e) gives, then,  $2.1 \times 10^{16} \leq \rho_0 \leq 6.2 \times 10^{16} \text{ erg}^{-1}$ . From Equation (1),  $2.2 \times 10^{-11} \leq t_{pv} \leq 6.6 \times 10^{-11}$  seconds.

Some slip is also expected to occur along the crystal directions for which ignition more readily occurs. For these directions, Equations (14a) and (14b) must be used. Substitution of the above values for  $\rho_a$  and  $\rho_0$  into Equation (14a) gives  $1.0 \times 10^{19} \leq \bar{p} \leq 1.1 \times 10^{19} \text{ erg}$ . In Figure 3, the lower line for PETN, which may be labeled as either  $\langle 001 \rangle$  or  $\langle 110 \rangle$ , is then obtained from Equation (14b).

In spite of the fact that average energies from the Hugoniot data of Reference 15 were used to generate the two curves for PETN in Figure 3, the existence of an orientational dependency of  $t_{pv}$  is clearly shown. The identification of  $t_{pv}$  with  $t_{tot}$  would, of course, require the kinetics of the initial reaction of PETN which, as yet, has not been determined from either theory or experiment. However, one may reasonably expect that a change of rate-determining step also exists for PETN, so that  $t_{tot} = t_{pv}$  at sufficiently high  $P_s$ . Thus, even in the absence of detailed reaction rate information, the placement of the curves in Figure 3 is consistent with the observations of Dick.<sup>7</sup> The relative placement of the curves is maintained at pressures higher than 80 kbar.

A comparison of the curves for NM and  $\langle 001 \rangle$  for PETN in Figure 3 may suggest that the shock sensitivities of the single crystals are not significantly different. If, however, slip could be somehow inhibited by proper confinement of a PETN crystal, the effect of  $\rho_a$  would be less and the times  $t_{tot} = t_{pv}$  shorter, approaching

$$t_{pv} \approx 10^{-11}$$

seconds for the optical modes. Such confinement may exist, for example, in polycrystalline PETN, which is known to be much more shock-sensitive than NM. These considerations for polycrystalline materials are dependent on other factors such as particle size.

In the preceding discussion of the sensitivities of PETN and nitromethane, the times  $t_{vp}$  were not considered. For nitro explosives such as PETN which contain only two molecules per unit cell, the ratio  $t_{pv}/t_{vp}$  approaches unity for the following reason. As shown in Reference 6, the number of phonons  $n$  in Equation (2) is given by  $p\gamma$ , where  $\gamma$  is the half-width of the probability distribution for a vibron level immersed in a denser set of phonon states (Figure 1). As the density of phonon states approaches the density of vibron levels for reduced numbers of molecules per unit cell,  $2n$  in Equation (2) approaches unity. From Equation (11),  $t_{pv}/t_{vp}$  becomes less important for  $t_{tot}$ , which then approximates  $t_{pv}$  when  $t_{vp} \gg t_b$ . In the case of the  $\text{NO}_2$  vibron modes (405, 609, and  $663 \text{ cm}^{-1}$ ), which have the largest vibron-phonon coupling of all the intramolecular modes,<sup>6</sup> the ratio  $\rho_{\text{phonon}}/\rho_{\text{vibron}}$  at 80 kbar, say, can be shown from Equation (16a) to be  $10^6$  and  $\sim 1$  for NM and PETN, respectively. The four  $\text{NO}_2$  groups contribute to the larger value of  $\rho_{\text{vibron}}$  for PETN.

## CONCLUSIONS

The theory that has been described makes it possible to interpret the sensitivity properties of single crystals of explosives in a way that has not been previously possible. While past studies of crystalline nitromethane have suggested that energy transfer between a lattice and its molecules may be important in shock initiation, the results of the present detailed calculations in connection with the observed directional sensitivity in PETN indicate that energy transfer and its relation to the lattice density of states play an even greater role than had been expected. The introduction of the total rate coefficient for reaction and energy transfer shows how it may be possible to utilize microscopic concepts to establish a rigorous foundation for heretofore, imprecise ideas of "induction" and "superdetonation" which have arisen from relationships between measured times and the varying behavior of initiating homogeneous explosives.

The lattice density of states, as the most important component of the foundation, was shown to consist of contributions from the

acoustic and optical lattice modes. The latter modes were seen to give rise to chemical reaction, while the former were shown to provide a reservoir for deposition of shock energy and to reduce the probability of reaction. The utility of the density of states was seen to lie in its ease of calculation for the different crystal structures of nitromethane and PETN. The much shorter times for pumping the internal modes of PETN molecules, as compared to nitromethane, were seen to arise as a consequence of the smaller number of molecules in the PETN unit cell, with the assumption that the higher lattice frequencies were similar for both crystals.

The conceptual and computational power of methods based on the quantization of the lattice is well-known in the field of solid state physics. The inherent statistical character of the nonideal gas of bosons (phonons and vibrons) makes the lattice density of states an indispensable tool for energy transfer calculations within the shocked solid, as borne out by the results for PETN and nitromethane. The reasonableness of the estimates of the times pertaining to the behavior of shocked explosives should not, perhaps, have been unexpected, since the density of states is known to provide a natural bridge between microscopic and macroscopic phenomena, enabling the calculation of entropy and the isentropes.

## ACKNOWLEDGMENTS

This work was supported by the NSWC Independent Research Program. Special thanks are extended to Drs. C. S. Coffey and R. Armstrong for helpful discussions.

## REFERENCES

1. Sheffield, S. A. and Engelke, R., "In-situ Study of the Chemically Driven Flow Fields in Initiating Homogeneous and Heterogeneous Nitromethane Explosives," in preprints of the *Ninth Symposium (International) on Detonation*, Portland, OR, 28 Aug - 1 Sep 1989.
2. Campbell, A. W.; Davis, W. C.; and Travis, J. R., "Shock Initiation of Detonation in Liquid Explosives," *Phys. Fluids*, 4, 1961, p. 498.

3. Enig, J. W. and Petrone, F.J., "Equations of State and Derived Shock Initiation Criticality Conditions for Liquid Explosives," *Phys. Fluids*, 9, 1966, p. 398.
4. Mader, C. L., *Numerical Modeling of Detonation*, University of California Press, Berkeley, 1979, pp. 158-159.
5. Zerilli, F. J. and Toton, E. T., "Shock-Induced Molecular Excitation in Solids," *Phys. Rev.*, B29, 1984, p. 5891.
6. Bardo, R. D., "Theoretical Calculations of Rate-Determining Steps for Ignition of Shocked Condensed Nitromethane," *Int. J. Quantum Chem.*, S20, 1986, p. 455.
7. Dick, J. J., "Effect of Crystal Orientation on Shock Ignition Sensitivity of PETN Explosive," *Appl. Phys. Lett.*, 44, 1984, p. 859.
8. Schiff, L. I., *Quantum Mechanics, Second Edition*, McGraw-Hill Book Co., Inc., New York, 1955, pp. 197-198. See also Coffey, C. S. and Toton, E. T., "A Microscopic Theory of Compressive Wave-Induced Reactions in Solid Explosives," *J. Chem. Phys.*, 76, 1982, p. 949.
9. Cromer, D. T.; Ryan, R. R.; and Schiferl, D., "The Structure of Nitromethane at Pressures of 0.3 to 6.0 GPa," *J. Phys. Chem.*, 89, 1985, p. 2315.
10. Bardo, R. D., "Calculated Reaction Pathways for Nitromethane and Their Role in the Shock Initiation Process," *Proceedings of the Eighth Symposium (International) on Detonation*, NSWC, MP 86-194, 15-19 Jul 1985, p. 855.
11. Laidler, K. J., *Chemical Kinetics, Second Edition*, McGraw-Hill Book Co., Inc., New York, 1965, pp. 144-147.
12. Nunziato, J. W.; Kennedy, J. E.; and Hardesty, D. R., "Modes of Shock Wave Growth in the Initiation of Explosives," *Proceedings of the Sixth Symposium (International) on Detonation*, Office of Naval Research, ACR-221, 24-27 Aug 1976, p. 47.
13. Hardesty, D. R., "An Investigation of the Shock Initiation of Liquid Nitromethane," *Comb. and Flame*, 27, 1976, p. 229.
14. Ziman, J. M., *Electrons and Phonons*, Oxford University Press, Oxford, 1960, p. 144.
15. Campbell, A. W. and Travis, J. R., "The Shock Desensitization of PBX-9404 and Composition B-3," *Proceedings of the Eighth Symposium (International) on Detonation*, NSWC, MP 86-194, 15-19 Aug 1985, p. 1057.

## DISCUSSION

I. B. MISHRA, Kanan Associates, Inc.  
Churchville, MD

Thank you for a brilliant paper attempting to explain shock sensitivity. I could not understand how  $n = 3$  for PETN and 9 for nitromethane. Will you kindly explain that?

## REPLY BY R. D. BARDO

The optical lattice modes leave the molecular center-of-mass (CM) stationary in each unit cell. These "collisional" modes make, by far, the largest contribution to the pumping of the vibron(molecular) modes. Since there are 3 degrees of freedom for the CM in each unit cell, the number of optical modes  $n$  is  $3p-3$ , where  $p$  is the number of molecules per unit cell. For PETN,  $p = 2$  so that  $n = 3$ . For nitromethane (NM),  $p = 4$  so that  $n = 9$ . These values pertain to the low-pressure, low-temperature crystal. However, D. T. Cromer, et al., in the *J. Phys. Chem.* 89, 2315(1985), have shown that, for hydrostatic pressures up to 60 kbar in NM, the space group and packing arrangement are unchanged. Since initiation in "homogeneous" PETN and NM takes place in a near hydrostatic environment away from the initiating shock front, those values are likely to be unchanged.

# UNIFIED FORMULATION OF THE REACTIVITY OF CONDENSED EXPLOSIVES

R. Cheret  
Commissariat à l'Energie Atomique  
33, rue de la Fédération, 75015 Paris  
FRANCE

*One deals with the reactivity of explosives, assuming a zeroth-order reaction scheme. A formulation is brought forward, which includes homogeneous as well as inhomogeneous substances, where the parameters belong to the molecular, submacroscopic, and macroscopic levels. This formulation allows the interpretation of old as well as recent detonation experiments and enlarges the physical basis of the related numerical simulations.*

## INTRODUCTION

Since the famous work of Paul Vieille<sup>1</sup> in 1899 and 1900, it is well established that detonation is the transformation that occurs in a so called explosive substance when acted upon by a shock (named ignition shock) in appropriate conditions. Moreover, it is commonly accepted that most features of the detonation phenomenon are not dependent on the detailed reaction scheme, and may, therefore, be modeled while assuming the transformation to be (a)→(b), where (a) is the explosive substance and (b) is another substance consisting of new species in chemical equilibrium (referred to as detonation products). Thus, within the frame of a continuous description of a flow associated with detonation, it is sufficient to add

- (i) to the usual dependent variables, one more variable: the mass fraction  $m$  of (b),
- (ii) to the usual  $\tilde{u}$  equations, one more equation which shows the local reactivity  $dm/(m)dt$  as a function  $S$  of the local thermodynamic state

For homogeneous explosive substances, Arrhenius law

$$S = Z \exp(-T^*/\tilde{T}) \quad (1)$$

( $Z$  is the frequency factor,  $T^*$  is the activation temperature,  $\tilde{T}$  is the shock temperature) is

unanimously accepted. On the other hand, for inhomogeneous explosive substances, the existing formulations show a large variety. Some are based on a volume reactivity and heterotherm assumption, others on surface reactivity and the homotherm assumption; the most recent discern an ignition term and a growth term, in the frame of an additive process<sup>2</sup> or a multiplicative process,<sup>3,4</sup> or even a coupled process.<sup>5,6,7</sup> Within each school, the complexity and the number of adjustable parameters increases as the number and precision of experimental results increases. Each of them score successes where it is difficult to discriminate what comes from the selection of experiments, from the achieved adjustments, and from the physical relevance of the law itself.

The present work aims at building a unified formulation which would apply to all explosive substances, homogeneous as well as inhomogeneous. That requirement has two consequences. It leads to uniformly assuming that the (a, b) mixture is homobar homotherm, as is obvious in the homogeneous case. It leads also, as Partom<sup>8</sup> already noticed, to looking for  $S$  as a sum

$$S = S^* + S^+ \quad (2)$$

of a molecular reactivity  $S^*$  term and an aggregative reactivity  $S^+$  term.

## THE INGREDIENTS OF THE AGGREGATIVE REACTIVITY

Let us notice first, that the contribution of  $S''$  to the total reactivity should increase in the inverse ratio of the time needed by the ignition shock to travel (with  $\hat{U}$  velocity) across the characteristic length  $\hat{L}$  of the aggregate; this argument urges one to consider  $S''$  as proportional to  $U/\hat{L}$ . Let us note then that, when  $m = 0$ ,  $S''$  ought to actually depend on the temperature  $\hat{T}$  which is reached at the boundary of explosive domains, according to an  $\exp(-T^x/\hat{T})$  Arrhenius law. Let us notice finally, that  $(1-m)S''$  has to be an increasing function of  $m$  in the vicinity of  $m = +0$  (geometric growth of the flame front which originates at each hot spot) and decreasing function of  $m$  in the vicinity  $m = 1.0$  (coalescence of flame fronts).

The simplest expression which meets with these requirements is:

$$S'' = \frac{\hat{U}}{\hat{L}} \frac{1 - 2m_1 + m}{(1 - m_1)^2} \quad (3)$$

where  $m_1$  is defined within the  $[0, 1/2]$  interval by

$$\frac{1 - 2m_1}{(1 - m_1)^2} = \exp\left(-\frac{T^x}{\hat{T}}\right) \quad (4)$$

In order to get Equation (3) completely written in terms which would be compatible with a continuous description, there remains the problem of formulating  $\hat{L}$  and  $\hat{T}$  as functions of the parameters of the aggregative state and those of the shock.

As for  $\hat{L}$ , one would first think of the mean dimension of the grains which serve as a basis of the aggregate. However, due to the practical ambiguousness which occurs when trying to estimate that dimension, one should rather call on the specific surface  $\sigma_0$  of the powder and set

$$\hat{L} = U/p_0 \sigma_0 \quad (5)$$

As for  $\hat{T}$ , let us proceed to a submacroscopic analysis of the flow around a connected explosive domain  $D$  (whose boundary is  $\partial D$ , and external normal vector is  $n$ ), at a time

when it is lying in the near downstream of the ignition shock  $\hat{\Sigma}$ . The temperature which prevails on  $\partial D$ , results from thermal exchanges between the hot interstitial medium and the explosive domain itself. Taking into account the well-known experimental fact, i.e., the relative velocity  $W$  and the stresses remain stationary in the near downstream of  $\hat{\Sigma}$ , as long as the decomposition remains hardly perceptible, and neglecting the tangential components of  $\text{grad } T$  compared to that along  $n$ , one may within each medium write the conservation of energy within the flow relative to  $\hat{\Sigma}$  in the form:

$$\rho(W \cdot n) c_p \frac{dT}{d\zeta} = -\lambda \frac{d^2 T}{d\zeta^2} \quad (6)$$

Let us scale the vicinity of  $\partial D$  with a length  $\hat{L}$ , which will be defined later, and let us introduce the reduced distance  $\bar{\zeta} = \zeta/\hat{L}$ , and the corresponding Péclet numbers,  $\hat{P}_e$  and  $\hat{P}'_e$ , related to the downstream state of the explosive medium and of the interstitial medium, respectively; then Equation (6) may be written

$$P_e \frac{dT}{d\bar{\zeta}} = -\frac{d^2 T}{d\bar{\zeta}^2}, \quad P_e = \hat{P}_e \text{ or } \hat{P}'_e \quad (7)$$

which, within  $P_e = \text{cte}$  approximation, may be integrated in each medium in the form:

$$\frac{T(\bar{\zeta}) - T(0)}{T(0)} = \frac{1}{P_e} [1 - \exp(-P_e \bar{\zeta})],$$

$$P_e = \hat{P}_e \text{ or } \hat{P}'_e \quad (8)$$

There remains to be seen how to define  $\hat{L}$ .

The simplest situation would be obtained by identifying  $\hat{L}$  and  $\hat{L}'$ ; that would be erroneous, as one is easily convinced when going through the shock-induced comminution effects.<sup>10</sup> A contrario, one realizes that  $\hat{L}$  must follow from the specific surface  $\hat{\sigma} \gg \sigma_0$ , which is achieved downstream of the ignition shock. Moreover, from the evanescence of  $\hat{L}$  for homogeneous initial states follows the proportionality of  $\hat{L}$ , and the initial porosity  $n_0$  defined as:

$$n_0 = 1 - Y_0 \alpha_0$$

( $Y_0$  is the mass fraction of the explosive in the aggregate;  $\alpha_0$  is the ratio of actual density  $\rho_0$  to the maximum theoretical density of the aggregate).

Therefore,

$$\hat{L} = u_0/\rho_0 \hat{\sigma}, \quad (9)$$

which may be interpreted by saying that  $\hat{L}$  represents the mean thickness of the interstitial medium in the near downstream of the shock. From which it follows that:

- (i) everything goes on as if a hot heat source  $\hat{T}$  were located in the interstitial medium at infinitely large distances  $\bar{\zeta}$  from  $\partial D$ ,
- (ii) the extra temperature  $\hat{T} - \hat{T}$  in the explosive medium were affecting the unit thickness layer  $-1 < \bar{\zeta} < 0$

Then integral (8) yields.

$$\begin{aligned} \hat{P}_e(\hat{T} - \hat{T}) &= \hat{T}(0)[1 - \exp \hat{P}_e] \\ \hat{P}_e(\hat{T} - \hat{T}) &= \hat{T}'(0) \end{aligned} \quad (10)$$

whereas the continuity of the normal component of the heat flux vector on  $\partial D$  yields:

$$\hat{\lambda} \hat{T}'(0) = \hat{\lambda}' \hat{T}'(0) \quad (11)$$

Moreover, one may take advantage from the continuity of the normal mass flux through  $\hat{\Sigma}$  and from the uniformly still state upstream of  $\Sigma$ , and write:

$$(\hat{\rho} \hat{W}) - (\hat{\rho} \hat{W})' = \rho_0 U N \quad (12)$$

where  $N$  is the unit normal to  $\Sigma$  directed from upstream towards downstream. From Equation (12) follows the equality:

$$\hat{\lambda}' \hat{P}_e / \hat{\lambda} \hat{P}_e = \hat{c}_p' / \hat{c}_p = 1 \quad (13)$$

When averaged over all positions of  $n$ , Equations (9) to (13) yield

$$\frac{\hat{T}}{\hat{T}} = 1 + [1 - \exp(-\hat{P}_e)] \left| \frac{\hat{T}}{\hat{T}} - 1 \right| \quad (14)$$

$$\hat{P}_e = \frac{u_0 U \hat{c}_p}{\hat{\sigma} \hat{\lambda}} (n \cdot N)$$

## TOTAL REACTIVITY

Equations (1) to (4) and (14) make up a unified formulation of the total reactivity of an explosive substance, which arouses four comments.

a) Thirteen parameters are involved explicitly:

- two related to the explosive molecule:  $Z$  and  $T^\infty$ ,
- six related to the submacroscopic structure:  $\alpha_0, Y_0, \alpha_0 \hat{\sigma}, \hat{T}, \langle n \cdot N \rangle$ ,
- five related to the macroscopic state:  $\rho_0, \hat{U}, \hat{T}, c_p, \hat{\lambda}$ .

Within the usual frame, where the explosive substance is assumed to behave -- as regards the ignition shock -- as a Navier-Fourier fluid, the initial state ( $\rho_0, T_0$ ) and the shock velocity  $U$  fix unambiguously the temperature  $\hat{T}$ , as well as the thermodynamic coefficients  $\hat{c}_p$  and  $\hat{\lambda}$ , so that eleven only (out of thirteen) are independent. In another connection, one may expect that

$$\frac{\hat{T}}{\hat{T}} = 1.5, \quad \hat{\sigma} = 10 \sigma_0, \quad \text{and } \langle n \cdot N \rangle = 2/u,$$

so that at last eight ( $Z, T^\infty, \alpha_0, Y_0, \alpha_0 T_0, \rho_0, U$ ) may be considered as measurable, and the three others ( $\hat{\sigma}, \hat{T}, \langle n \cdot N \rangle$ ) as adjustable.

b) Owing to the usual values of  $Z$  ( $10^{11}$  to  $10^{19} \text{ s}^{-1}$ ) and of  $\rho_0 \alpha_0 U$  ( $10^9$  to  $10^{11} \text{ s}^{-1}$ ), the unified formulation shows that a remarkable value of  $U$  generally exists, for which the initial values of the two components of the reactivity are equal. Ipso facto, the unified formulation enables the interpretation of old experiments by Dremin and Shvedov<sup>11</sup> on TNT, RDX, Teteryl, PETN,  $\text{NO}_3\text{NH}_4$ , etc.

c) Hexanitrostilbene (HNS) does not follow the general case mentioned above: the value of  $Z$  ( $1.53 \cdot 10^9 \text{ s}^{-1}$ )<sup>12</sup> is lower than the values of  $\rho_0 \alpha_0 U$  entailing ignition. Thus, the initial value of the aggregative reactivity is always higher than that of the molecular reactivity. In that case too, the unified formulation enables the interpretation of a series of recent experiments by Setchell<sup>13</sup> on pressed HNS ( $\rho_0 = 1.60 \text{ g/cm}^3$ ;  $\alpha_0 = 0.92$ ;  $Y_0$

= 1;  $n_0 = 0.008$ ) with three values of  $\sigma_0$  (8.1; 3.9; 0.94 m<sup>2</sup>/g), and tested under three shock amplitudes ( $P = 25, 30, 34$  kbar). (Cf detailed discussion in Reference 15.)

d) Although the two previous cases are already significant examples of the scope of the unified formulation, all aspects of this modeling of reactivity are to be recognized only through a numerical study of the coupling between decomposition and flow, which lies beyond the frame of this paper.

## NOTICE

The content of this paper originates from Reference 14

## REFERENCES

1. Vieille, P., *C.R. Acad. Sci. Paris*, 130, 1 900, p. 413.
2. Lee, E. L. and Tarver, C. M., *Phys. Fluids*, 23, 1980, p. 2362.
3. Wackerle, J., et al., *Proceedings of H.D.P. Symposium*, Paris, France, Aug 1978, pp. 127-138.
4. Anderson, A. B., et al., *Proceedings of the Seventh Symposium (International) on Detonation*, Annapolis, MD, Jun 1981, pp. 385-393.
5. Tang, P. K., et al., *Proceedings of the Eighth Symposium (International) on Detonation*, Albuquerque, NM, Jul 1985, pp. 52-61.
6. Nunziato, J. W., et al., *Proceedings of H.D.P. Symposium*, Paris, France, Aug 1978, pp. 139-148.
7. Kipp, M. E., et al., *Proceedings of the Seventh Symposium (International) on Detonation*, Annapolis, MD, Jun 1981, pp. 394-406.
8. Partom, Y., Characteristics Code for Shock Initiation, LANL Report No. 10, 1986, p. 773.
9. de Longueville, Y., et al., *Proceedings of the Sixth Symposium (International) on Detonation*, Coronado, CA, Aug 1976, pp. 105-114.
10. Graham, R. A., *Proceedings A.P.S. Shock Wave Meeting*, Menlo Park, CA, 1981, pp. 4-13.
11. Dremin, A. N. and Shvedov, K. K., *Proceedings of the Sixth Symposium (International) on Detonation*, Coronado, CA, Aug 1976, pp. 29-35.
12. Mader, C. L., *Numerical Modeling of Detonation*, University of California Press, 1979, p. 146.
13. Setchell, R. E., *Proceedings of the Symposium on Pyrotechnics and Explosives*, Beijing, China, 1987, pp. 635-643.
14. Chéret, R., *C.R. Acad. Sci.*, Paris, 306, Série II, 1988, pp. 863-866.
15. Chéret, R., *La Detonation des Explosifs Condenses*, Masson, Editor, Paris, 1989.

# THE CHOICE PROBLEM OF EQUATION DETERMINING THE CONDENSED REACTING MEDIA CHARACTERISTICS IN NUMERICAL MODELING OF SHOCK PROCESSES

V. S. Trofimov

Institute of Structural Macrokinetics

USSR Academy of Sciences

Moscow Region, Chernogolovka, USSR, 142432

*A new system of equations to determine the condensed reacting media characteristics is proposed. The system includes experimentally measurable variables only.*

## INTRODUCTION

The present calculations of shock processes in condensed reacting media (e.g., Reference 1) are based on the following general assumptions:

- a) transfer effects may be neglected,
- b) stress tensor is isotropic,
- c) the physical chemical transformation depth of media may be accurately described by only one scalar variable.

Different authors use various additional specific assumptions to construct the equations that determine the media characteristics. These equations should be included in a system of complete hydrodynamic equations.

The following equations determining the media characteristics are generally used

$$V = V(P, T, \alpha), \quad (1)$$

$$E = E(P, T, \alpha), \quad (2)$$

$$\frac{d\alpha}{dt} = f\left(P, T, \alpha, \frac{dV}{dt}\right), \quad (3)$$

where  $V$  is the specific volume,  $P$  is the pressure,  $T$  is the temperature,  $\alpha$  is the depth of physical chemical transformation of media,  $E$  is the specific internal energy (as defined in classical thermodynamics), and  $d/dt$  is the Lagrangian time derivative. This system permits the calculation of the fields of  $V$ ,  $P$ ,  $E$ ,

$\alpha$ ,  $T$ , and particle velocity vector  $U$ , if initial and boundary conditions are given.

Excluding  $T$  out of Equations (1)-(3), we come to another system determining the media characteristics:

$$E = E(P, V, \alpha), \quad (4)$$

$$\frac{d\alpha}{dt} = f\left(P, V, \alpha, \frac{dV}{dt}\right) \quad (5)$$

This system permits the calculation of the fields of  $V$ ,  $P$ ,  $E$ ,  $\alpha$ , and  $U$ , if corresponding initial and boundary conditions are given. In addition, the system may be used when  $T$  is not determined.

Using the first law of thermodynamics combined with assumption (a)

$$\frac{dE}{dt} - P \frac{dV}{dt} = 0, \quad (6)$$

the expression for square of frozen sound velocity

$$C^2 = V^2 \frac{\left(\frac{\partial E}{\partial V}\right)_{P, \alpha} + P}{\left(\frac{\partial E}{\partial P}\right)_{V, \alpha}}, \quad (7)$$

and also using the expression for generalized kinetic characteristic of media (according to Reference 2)



$$-\dot{P}^* = \frac{d\alpha}{dt} \frac{\left(\frac{\partial E}{\partial \alpha}\right)_{P,V}}{\left(\frac{\partial E}{\partial P}\right)_{V,\alpha}}; \quad (8)$$

we may eliminate  $\alpha$  from Equations (4)-(5). Finally, we come to one more system determining the media characteristics.

$$\frac{dP}{dt} = -\frac{C^2}{V^2} \frac{dV}{dt} + \dot{P}^*, \quad (9)$$

$$C = C(P, V, E), \quad (10)$$

$$\dot{P}^* = f\left(P, V, E, \frac{dV}{dt}\right). \quad (11)$$

This system permits us to calculate the fields of  $V$ ,  $P$ ,  $E$ , and  $U$ , if corresponding initial and boundary conditions are given.

Inverse deduction--Equations (4)-(5) from Equations (9)-(11) and Equations (1)-(3) from Equations (4)-(5)--is impossible, in consequence of the fact that a countless variety of Equations (4)-(5), correspond to Equations (9)-(11). Also, countless variety of Equations (1)-(3), correspond to Equations (4)-(5). These statements are based on the fact that the variables  $T$ ,  $\alpha$  can be represented as functions of  $P$ ,  $V$ , and some other variables  $T'$ ,  $\alpha'$ . Thus, each next system describes more general properties of the media under discussion than the previous one does. Hence, it is apparent that at present it is most convenient to carry out calculations using the system, Equations (9)-(11).

Indeed, the present shock wave technique permits us to find from experiment only Equations (9)-(11) (see References 3,4). For determination of Equations (1)-(3) and Equations (4)-(5), methods for measuring current meanings of  $\alpha$ ,  $T$  are necessary. But there are no such methods. Therefore, when Equations (1)-(3) and Equations (4)-(5) are used in calculations, they are constructed on the basis of specific assumptions, which imply that certain constants are to be introduced and then adjusted to experimental data for fields of  $V$ ,  $P$ ,  $E$ , and  $U$ . It is not difficult to show that in this way one may derive only formal

systems like Equations (1)-(3), (4)-(5). At best, they make it possible to calculate the fields of  $V$ ,  $P$ ,  $E$ , and  $U$ , but lead to distorted results on the fields of  $\alpha$ ,  $T$ . Accidental coincidence of calculated and real fields of  $\alpha$ ,  $T$  could not happen because of incorrect specific assumptions. For example, in most works the reaction heat  $Q_{P,V} = -(\partial E / \partial \alpha)_{P,V}$  is assumed equal to another reaction heat  $Q_{cal} = -(\partial E / \partial \alpha)_{P,T}$  determined by calorimeter. But this is possible only for ideal gases. Thus, variables  $\alpha$ ,  $T$  in Equations (1)-(3), (4)-(5) are always formal.

Equations (9)-(11) are not yet determined for any media. Nevertheless, the fact of its existence may be successfully used in analysis of experimental data. For example, we have succeeded in showing that cast TNT is able to decompose considerably in shock fronts, and the rate of its postfront decomposition depends on  $dV/dt$  (see details in Reference 5). That is why additional variable  $dV/dt$  has been introduced in kinetic Equations (3), (5), and (11).

## REFERENCES

1. Mader, C. L., *Numerical Modeling of Detonations*, University of California Press, Berkeley, Los Angeles, London, 1979.
2. Dremin, A. N. and Trofimov, V. S., "Oprirade kriticheskogo diametra detonacii condensirovannich vzrivicatich veschestv," *Fizika gorenija i vsriva*, Vol. 5, No. 3, 1969, pp. 304-311.
3. Adadurov, G. A.; Trofimov, V. S.; and Jakovleva, V. A., "Opredelenie parametrov nestacionarnoj volni ssatija," *Fizika gorenija i vsriva*, Vol. 4, No. 3, 1968, pp. 397-399.
4. Trofimov, V. S., "Dinamiceskij metod issledovanija relaksacionnich processov," *Fizika gorenija i vsriva*, Vol. 17, No. 5, 1981, pp. 93-101.
5. Trofimov V. S. and Trofimova, G. P., "O vosmosnosti razlosenija litogo TNT v udarnom skachke," *Fizika gorenija i vsriva*, Vol. 16, No. 2, 1980, pp. 92-99.

# GLOBAL CALIBRATION OF CONSTITUTIVE RELATIONSHIPS IN EXPLOSIVE REACTION ZONE

Huan Shi\* and Ding Jing\*\*

Beijing Institute of Technology

Department of Engineering Mechanics

P.O. Box 327, Beijing 100081, PEOPLES' REPUBLIC OF CHINA

*For calculating the reaction characteristics in Lagrangian gauge studies of shocked explosives, constitutive relationships for the reacting explosive are required. In this paper, a global procedure is suggested for the calibration of constitutive relationships. This method has been tested in numerical simulation for five explosives. Results obtained are promising.*

## INTRODUCTION

The constitutive relationships for describing the properties in an explosive reaction zone are composed of the chemical reaction equation, equations of state of explosive, and products and their mixing law. It has not been verified whether it is effective to use an assumed mixing law and a phenomenological reaction rate equation together with the equations of state of explosive and product to describe the chemical nonequilibrium state with high pressure and high temperature in reaction zone. No guarantee has been given on the consistency or compatibility for these equations. Therefore, some coefficients of constitutive equations must be readjusted in numerical simulations to make the calculation in correspondence with the experimental results. In fact, this is the process of building consistency among these equations which constitute the constitutive relationships in reaction zone.

## METHOD

In this paper, a global method is proposed for calibrating the constitutive relationships in

the explosive reaction zone. Taking the histories of pressure  $P$  and the records of the one-dimensional Lagrange test as the input of a Lagrangian analysis code, one can obtain the histories<sup>1</sup> of particle velocity  $u$ , specific volume  $V$ , and specific internal energy  $E$ . If the EOSs of explosive and products are given and their mixing law is assumed, the histories of chemical reaction extent  $\lambda$  and other reaction characteristics can also be obtained.<sup>2</sup> These  $\lambda$  curves are used to calibrate the reaction rate equation as below:

$$\frac{\partial \lambda}{\partial t} = \begin{cases} a_1(a_2\eta^{a_3} + \lambda)^{a_4}(a_5 - \lambda)^{a_6} P^{a_7} & \lambda \leq \min(1, a_5) \\ 0 & \lambda > \min(1, a_5) \end{cases}$$

where  $\eta = 1/V_1 - 1$  and  $V_1$  is the specific volume on shock front,  $a_i$  ( $i = 1, 2, \dots, 7$ ) are constants with following physical significance:

- $a_1$ : the average ratio of the surface area to the volume of explosive particles.<sup>3</sup>
- $a_2$ : the effective hot spot coefficient which is related to the size of explosive particles.
- $a_3$ : a constant related to the mechanism of hot spot formation.
- $a_4$ : a geometrical constant for the growth of hot spots.
- $a_5$ : a constant related to the reaction rate at the end of a reaction.
- $a_6$ : a constant related to the position of maximum of the reaction rate.

\* Present address: Changsha Institute of Technology, Department of Applied Physics, Changsha, Hunan, China

\*\* Currently on sabbatical leave at CETR, New Mexico Tech, Socorro, New Mexico 87801

a7: a constant related to the laminar burn rate.

As the two equations of the state of explosive and reaction products and the equation of mixing law have been used in the calculation process to get the  $\lambda$  curves, the reaction rate equation calibrated by using these curves must be consistent with the above mentioned three equations. The  $\lambda$  curves could be varied with the change of the equations of state or their mixing law (see Figure 1). Since the calibrated rate equation is certainly related with the equations of state and the mixing law, these four become a complete set of consistent constitutive relationships. In this sense, the method is called a global calibration of constitutive relationship.

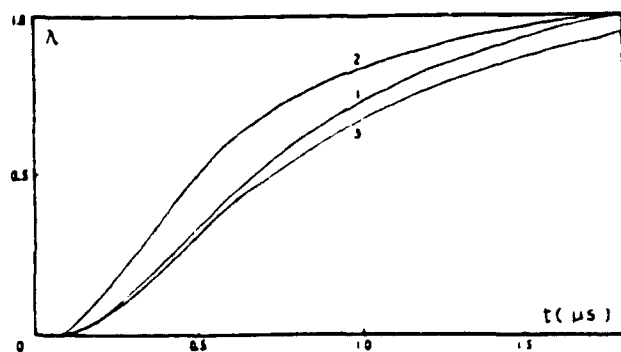
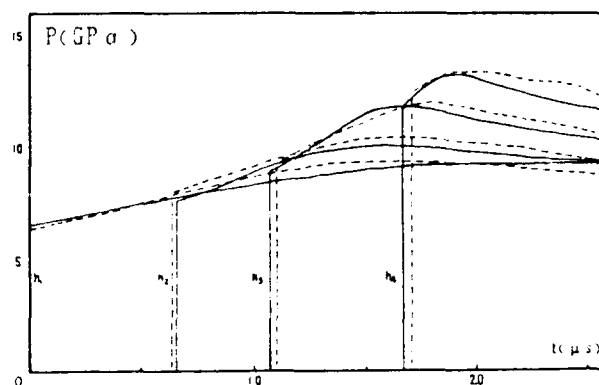


Figure 1. The Change of Reaction Extent History  $\lambda$ - $t$  for Cast TNT of Density  $1.61 \text{ g/cm}^3$  (Curve 1) Caused by Changing the Mixed Law (Curve 2) and the EOS of Reaction Products (Curve 3)

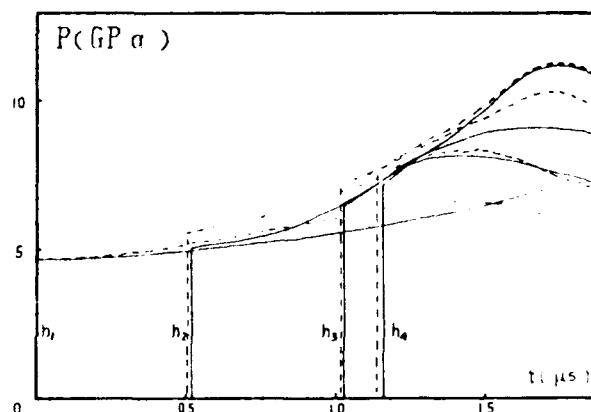
## EXAMPLES

In order to show the importance of the completeness of the constitutive relationships and the effectiveness of the global calibration method, we calibrated the constitutive relationships for five condensed explosives. They were used directly in one dimensional numerical simulations, and fairly well simulated the results of one dimensional Lagrangian tests and wedge tests (Figures 2 and 3). These relationships have also been used to calculate a two dimensional steady state detonation reaction zone,<sup>4</sup> and will be used in two dimensional numerical simulations



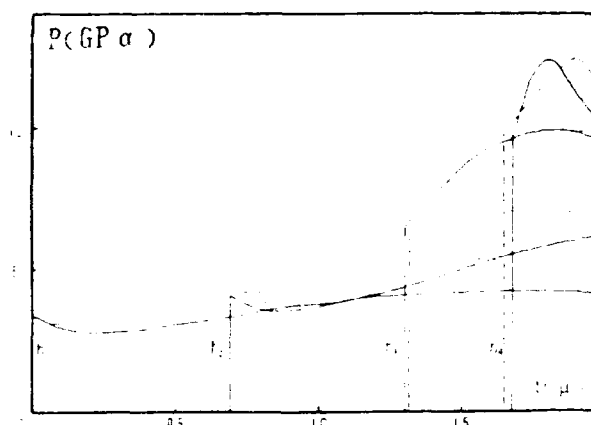
a. Cast TNT ( $\rho_0 = 1.61 \text{ g/cm}^3$ )

$$\begin{aligned} h_1 &= 0.0 \text{ mm} & h_3 &= 5.0 \text{ mm} \\ h_2 &= 3.0 \text{ mm} & h_4 &= 8.0 \text{ mm} \end{aligned}$$



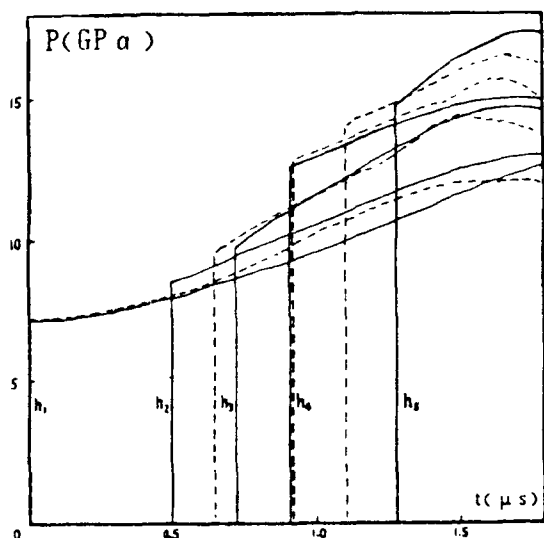
b. Pressed TNT ( $\rho_0 = 1.60 \text{ g/cm}^3$ )

$$\begin{aligned} h_1 &= 0.00 \text{ mm} & h_3 &= 4.15 \text{ mm} \\ h_2 &= 2.07 \text{ mm} & h_4 &= 4.72 \text{ mm} \end{aligned}$$



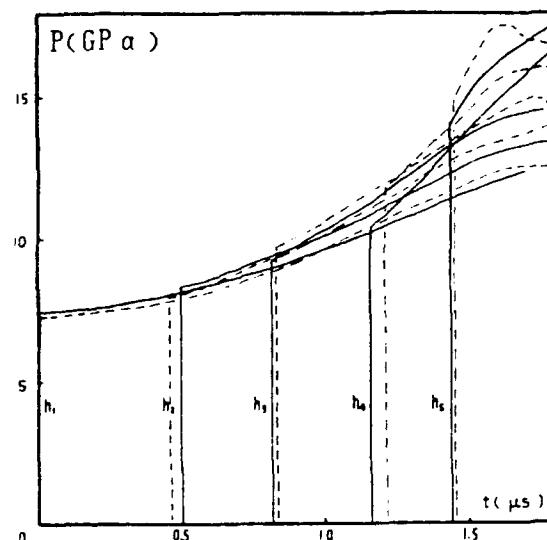
c. Pressed TNT ( $\rho_0 = 1.564 \text{ g/cm}^3$ )

$$\begin{aligned} h_1 &= 0.0 \text{ mm} & h_3 &= 4.9 \text{ mm} \\ h_2 &= 2.5 \text{ mm} & h_4 &= 6.6 \text{ mm} \end{aligned}$$



d. Standard grind TATB ( $\rho_0 = 1.8 \text{ g/cm}^3$ )

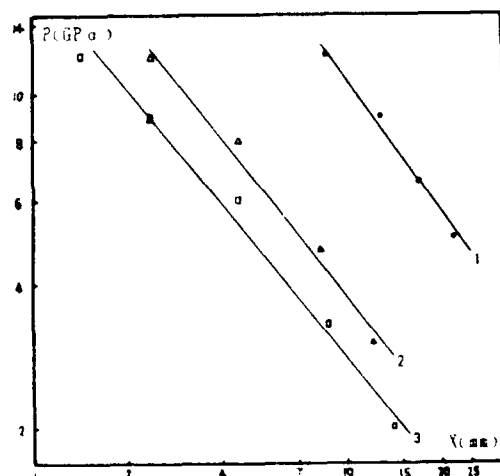
$h_1 = 0.000 \text{ mm}$        $h_5 = 6.275 \text{ mm}$   
 $h_2 = 2.275 \text{ mm}$        $h_4 = 4.275 \text{ mm}$   
 $h_3 = 3.275 \text{ mm}$



e. Super fine TATB ( $\rho_0 = 1.8 \text{ g/cm}^3$ )

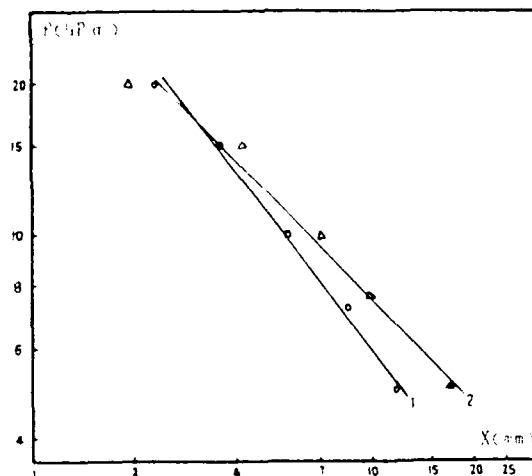
$h_1 = 0.00 \text{ mm}$      $h_3 = 3.72 \text{ mm}$      $h_5 = 6.69 \text{ mm}$   
 $h_2 = 2.28 \text{ mm}$      $h_4 = 5.27 \text{ mm}$

Figure 2. Results of One-dimensional Lagrangian Experiments (Real Lines) and One-dimensional Numerical Simulations (Dotted Lines)



(a)

1. Cast TNT ( $\rho_0 = 1.610 \text{ g/cm}^3$ )  
 2. Pressed TNT ( $\rho_0 = 1.600 \text{ g/cm}^3$ )  
 3. Pressed TNT ( $\rho_0 = 1.564 \text{ g/cm}^3$ )



(b)

1. Standard TATB ( $\rho_0 = 1.8 \text{ g/cm}^3$ )  
 2. Super fine TATB ( $\rho_0 = 1.8 \text{ g/cm}^3$ )

Figure 3 Run Distance to Detonation Versus Shock Pressure for TNT and TATB

## REFERENCES

1. Huan Shi and Xue Honglu, "Method of Langrange Analysis for Shock Initiation of Explosives," *J. Explosion and Shock Waves*, China, Vol. 5, No. 3, 1985, pp. 20-26.
2. Huan Shi, Xue Honglu, and Ding Jing, "Langrange Gauge Analysis for Evaluating Reaction Characteristics in Shocked Explosives," *Proceedings of the International Symposium on Intense Dynamic Loading and Its Effects*, Beijing, China, 3-7 Jun 1986, pp. 144-149.
3. Lee, E. L. and Tarver, C. M., "Phenomenological Model of Shock Initiation in Heterogeneous Explosives," *Phys. Fluids*, Vol. 23, No. 12, 1980, pp. 2362-2372.
4. Huan Shi and Ding Jing, "Sonic Surface and Flow Field in Two-Dimensional Reaction Zone," *Proceedings of the International Symposium on Pyrotechnics and Explosives*, Beijing, China, 12-15 Oct 1987, pp. 525-535.

## DISCUSSION

G. A. LEIPER  
ICI Explosives  
NEC, Stevenston, UK

Can you describe in more detail the changes made to the mixing law which resulted in the changes in reaction rate you described in your paper?

## REPLY BY DING JING

In Figure 1, the curve 2 is the reaction extent history ( $\lambda - t$ ) obtained by changing the mixing law of specific volume to that of partial pressure.

## DISCUSSION

M. COWPERTHWAIT  
SRI International  
Menlo Park, California

Rate laws calibrated with gauge records and pop-plot data have to be modified or extended to reproduce the experimental velocity histories observed in plate push experiments.

## REPLY BY DING JING

In this paper, the rate law was calibrated with the data from one-dimensional Lagrangian measurement and analysis. We have not used this rate equation so far to reproduce the results observed in plate push experiments.

**SESSIONS ON**  
**DEFLAGRATION-TO-DETONATION TRANSITION**

**Cochairmen: Richard Bernecker**  
**Naval Surface Warfare Center**

**Albert van der Steen**  
**TNO Prins Maurits Laboratory**

**and**

**Douglas Kooker**  
**Army Ballistic Research Laboratory**

**Henry Moulard**  
**Institut Saint-Louis (ISL)**

# DDT - DETERMINATION OF THE SUCCESSIVE PHASES OF PHENOMENA\*

M. Samirant

Franco-German Research Institute (ISL)  
P.O. Box 301 - 68301 Saint-Louis, FRANCE

*Depending upon the porous medium mechanical behavior, two DDT modes were determined: progressive or with a deflagration and a sudden transition to detonation. By varying both the nature and the density of the hot spots we can shift from one mode to the other. With an array of different types of gages we determine the different waves propagating in the reacting medium.*

## INTRODUCTION

This presentation concerns the continuation of a long-term study of DDT phenomenology in highly confined porous beds. We will first summarize former results and present new data achieved in varying both the nature and the density of the hot spots in the reactive porous bed.

## EXPERIMENTAL SETUP

We choose a classical setup in order to make use of the important number of data published on this topic.<sup>1,2,3</sup> Figure 1 shows a schematic of the setup. It is a thick walled steel tube (16 mm I.D., 50 mm O.D., 390 mm length) with heavy end closures. Two kinds of gages are distributed along the tube: ionization pins, and shock probe needles set in PMMA block and in contact with the tube outer face. The initial isolation is achieved by a 10  $\mu$ m Mylar sheet. When the displacement of the tube wall is slow the whole block moves and there is no contact, only a sharp increase in velocity can ensure the short circuit. The igniter is a thick (0.3 mm) wire reinforced by 50 mg of a mixture of potassium nitrate with zirconium and titanium.

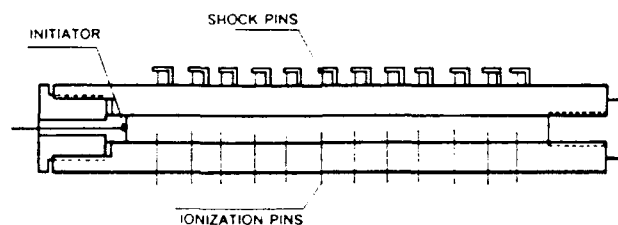


Figure 1. Experimental Setup

## TWO MODES OF TRANSITION FROM COMBUSTION TO DETONATION

At the Seventh Symposium on Detonation, we reported<sup>4</sup> on two different modes of transition to detonation in highly confined media. The first mode was observed in ball powder. The second mode was observed in porous RDX.

- Figure 2 shows the trajectories of the combustion and shock-waves obtained with a low diameter double-based ball powder (diameter 0.3 mm) and with a loading density of 1.07 g/cm<sup>3</sup>. The acceleration of the combustion wave being continuous, the location of the

\*Work performed partly under contract from the DRET.

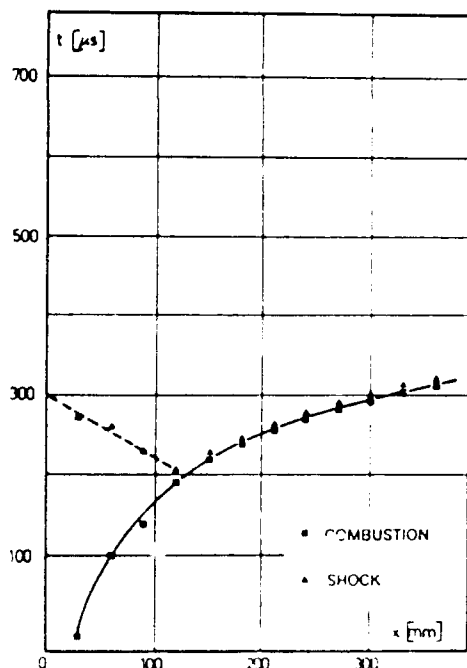


Figure 2 Combustion and Shock Front Path in Ball Powder

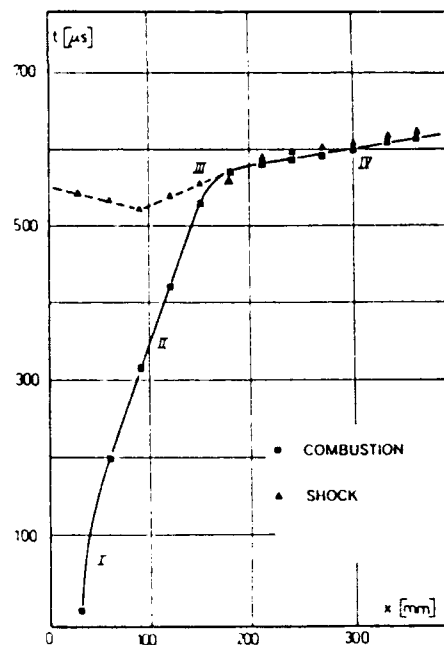


Figure 3. Combustion and Shock Front Path in RDX-Wax

transition cannot be determined precisely. The velocity of the stationary detonation is  $5240 \text{ ms}^{-1}$ .

- Figure 3 shows the results obtained with RDX-wax (95/5) with a grain size of  $150-200 \mu\text{m}$  and a loading density of  $1.3 \text{ g/cm}^3$ . We can observe

- I an accelerated combustion
- II a stationary deflagration
- III a rapid transition at a well defined location
- IV a stationary detonation of  $D = 6650 \text{ ms}^{-1}$

## INFLUENCE OF THE MECHANICAL PROPERTIES OF THE POROUS BED

At the Eighth Symposium on Detonation<sup>5</sup> the transition mode was shown to be not related to the chemical composition of the reactive bed, but to be related to the mechanical properties of the grains. If there is an elastic propagation of the mechanical compaction energy in the porous bed, the combustion zone has a limited volume, the energy flow is limited, and a constant velocity deflagration is achieved. If

there is plastic deformation of the grains, the density of hot spots is not limited and the energy flow causes velocity to increase up to detonation.<sup>6,7</sup> This hypothesis was confirmed by varying the mechanical properties of the porous bed of constant composition.<sup>8</sup>

It is the purpose of the present paper to report on the results achieved in varying both the nature and the density of the hot spots in the reactive porous bed.

## MODIFICATION OF HOT SPOT DENSITIES

Due to the elastic behavior of the medium in the porous RDX, there are few hot spots localized at the contact area between the grains and in the voids. In the voids the adiabatic compression of the air by the pressure waves generates ignition sites. The low density of these hot spots behind the low-level elastic compression waves is responsible for the slow quasi stationary deflagration.<sup>9,10,11</sup>

The plastic behavior of the ball powder bed under compression leads to large shear effects in all the grains, thus setting free a large amount of thermal energy. This creates



a large density of internal hot spots in the grains which do not depend at first approximation on the interfaces and confined gases.

In order to verify the influence of the density of hot spots on the transition mode, we have done a test series under well-controlled conditions.

### INCREASING THE HOT SPOT DENSITIES AT THE CONTACT AREA BETWEEN THE GRAINS

To increase the number of hot spots with mechanical origin in the RDX bed the test tube was loaded with the mixture (RDX 150 + 200  $\mu\text{m}$  + 5 percent wax) + 5 percent silica of 200  $\mu\text{m}$  grain size.

The pressing and assembly of such mixtures being particularly dangerous, the porous bed has been made up from pellets of reduced mass (5 g) pressed under protection from remote.

The results of the transition test are shown on Figure 4. We can well observe the change in the transition mode which has a progressive character similar to the ball powder transition. This corresponds to the high density of hot spots avoiding the dynamic

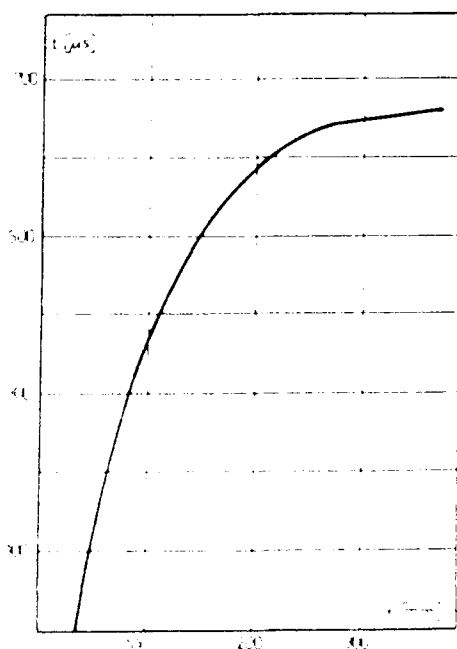


Figure 4. Combustion Front Path in RDX-Wax with Granular Silica

equilibrium which controls the stationary deflagration.

### MODIFICATION OF THE GAS CONTAINED IN THE VOIDS OF THE POROUS BED

To determine the role of the adiabatic compression of the air as a source of hot spots initiating the transition, we have run tests under vacuum and with another gas with different thermodynamical properties.

At the downstream end of the tube we have introduced a pipe leading to a primary-vacuum rotary pump. We first control the quality of the vacuum by inserting a pressure gage at the other tube end, at the normal igniter location, and define in this way the pumping process and duration. During the firing sequence only one reference gage was placed on the vacuum piping. Immediately before the run the residual pressure in the porous bed was 100 Pa for RDX and 1000 Pa in ball powder. This last value is due to the permanent evaporation of nitroglycerine contained in the propellant. In this case we reduce as much as possible the pumping duration to avoid high nitroglycerine losses.

Figure 5 shows the results of the tests under these conditions. The propagation of the combustion wave in the ball powder initiated by hot spots in the grains is not modified. The RDX shows a longer combustion and deflagration phase duration followed by a progressive transition due to a very low hot spot density.

By introducing a bypass valve in the preceding setup, we can fill the porous bed with argon under normal pressure.

The results are shown in Figure 6. As we expected, the ball powder behavior is not modified, however, due to the highest energy released at each adiabatic compression site, the reactions in the RDX are faster, the deflagration rapidly gets a high velocity, accelerating after 90 mm propagation and leads to a transition after 350  $\mu\text{s}$ .

We observed that the RDX maintains its typical transition mode which is very different from that achieved by increasing the number

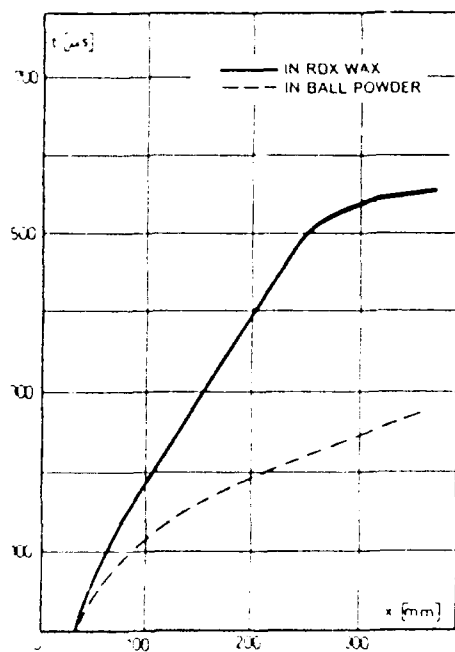


Figure 5. Combustion Front Path Under Vacuum

of mechanical hot spots (Figure 4) but with a reduced overall reaction time.

## DATA OBTAINED WITH DIFFERENT REACTION SENSITIVE SPECIFIC GAGES

### Different Types of Gages

The two types of hot spots which are supposed to explain the two transition modes can be distinguished by use of appropriate gages.

The ionization gages we normally use are very sensitive to hot gases created by the adiabatic compression in the initiation area.

If we use optical fibers, we do not see the hot spots but we record the light from the zone of intense combustion. We designed several specific gages:

- classical ionization pins
- needle pins to detect the shocks
- coaxial ionization pins, the extremity of which is protected by a lacquer: they do not respond to ionized gas but only to a high combustion.

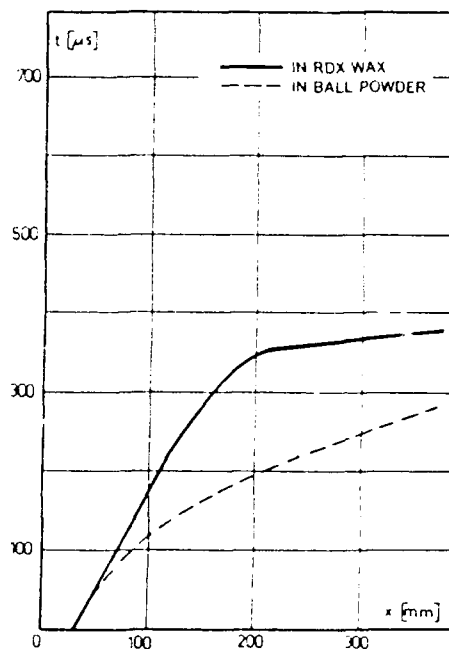


Figure 6. Combustion Front Path in the Presence of Argon

- optical fiber gages - The fiber protected by a steel tube is introduced through the confinement wall, they are flush mounted to avoid destruction by the mechanical waves. The light collected by the fibers is recorded by a photomultiplier;
- manganin gages protected by an inert buffer and located on the axis of the porous bed register pressure profiles.

## RESULTS

Based on the time reference delivered by the ionization gages, we can picture the propagation of the different phenomena yielded by each gage type.

With the ball powder (Figure 7) all the data are obtained during a short time and space interval. If we take for example a point located at 100 mm from the igniter, the porous bed has first undergone a rapid compression creating the hot spots by grain shearing. After 20  $\mu$ s the combustion is intense as it can be seen from the quasisimultaneous responses of the ionization pins of the coaxial gages and the optical fibers.

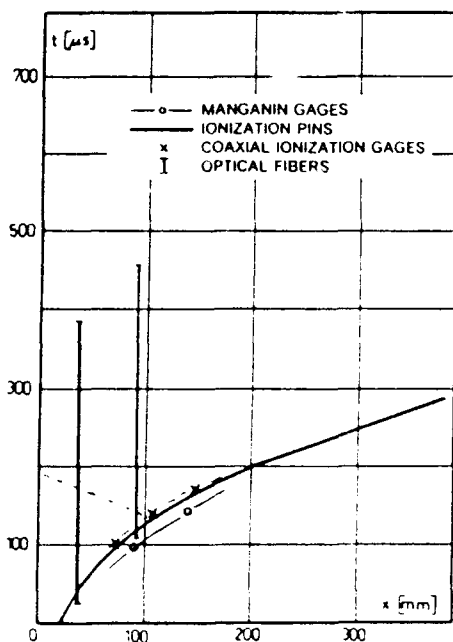


Figure 7 Waves Propagation in Ball Powder

With RDX wax, at the same location, (Figure 8) we observe an initiation of the grains detected by the ionization pins which is due to the gas compression that is followed 90  $\mu$ s later by the plastic pressure wave. 250  $\mu$ s after initiation the coaxial gages and the optical fibers show an intense combustion. In the transition zone this high velocity com-

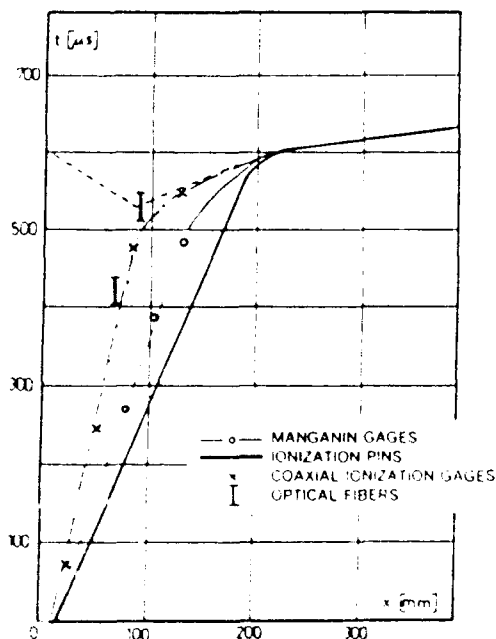


Figure 8 Waves Propagation in RDX-Wax

bustion wave is simultaneous with the shock that leads to the transition.

If we take into consideration only the high velocity combustion waves, there is a great similarity between the propagation in both types of transition which only differs by the velocities and the total duration of the reaction.

## CONCLUSIONS

From the complete experimental results presented in these studies, we get a good phenomenological representation of the DDT for porous nitramines. As has been shown by McAfee,<sup>12,13</sup> the acceleration of the reactions leading to the sudden transition to detonation must be imputed to a highly compressed and pulverized zone in the porous bed resulting in a great increase of the combustion surface of the medium.

We are now studying the density of the hot spots and the energy released during the initiation phase in the nitramines as a function of the porous bed structure and of the binder amount.

## REFERENCES

1. Bernecker, R. R. and Price, D., "Transitional Characteristics and Mechanisms Observed in 91/9, RDX/Wax," *Combustion Flame*, No. 22, 1974, pp. 119-129.
2. Bernecker, R. R. and Price, D., "Proposed Mechanisms for Transition and Comparison with Other Proposals in the Literature," *Combustion Flame*, No. 22, 1974, pp. 161-170.
3. Bernecker, R. R.; Sandusky, H. W.; and Clairmont, A. R., "Deflagration to Detonation Transition Studies of Porous Explosive Charges in Plastic Tubes," *Proceedings of the Seventh Symposium on Detonation*, Annapolis, MD, 16-19 Jun 1981, pp. 119-138.
4. Samirant, M., "Deflagration to Detonation Transition in Waxed RDX," *Proceedings of the Seventh Symposium (International) on Detonation*, Annapolis, MD, 16-19 Jun 1981, pp. 139-142.

5. Samirant, M., "DDT in RDX and Ball Powder: Behavior of the Porous Bed," *Proceedings of the Eighth Symposium (International) on Detonation*, Albuquerque, NM, 15-19 Jul 1985, pp. 972-976.
6. Akhatov, S. and Vainshtein, P. B., "Transition of Porous Explosive Combustion into Detonation," *Combustion Explosion Shock Waves (English Translation)*, Vol. 20, No. 1, 1984, pp. 63-69.
7. Nigmatulin, R. I.; Vainshtein, P. B.; and Akhatov, S., "Transition of Powdered Explosive Convective Combustion into Detonation," *Combustion, Explosion, and Shock Waves (English Translation)*, Vol. 19, No. 5, 1983, pp. 618-621.
8. Samirant, M. and Lichtenberger, A., Propriétés mécaniques des poudres et explosifs pulvérulents et mode de transition déflagration → détonation, *Propellants, Explosives, Pyrotechnics*, No. 11, 1986, pp. 176-183.
9. Frey, R. B., "Some Aspects of the Micro-mechanics of Hot Spot Formation in Energetic Materials," *AGARD Conference Proceedings*, Hazard Studies for Solid Propellant Rocket Motors, No. 367, 21-30 May 1984, p. 11.
10. Kumar, M. and Kuo, K. K., "Ignition Phenomena Near the Closed End of a Solid Propellant Crack," *AIAA/SAE/ASME 15th Joint Propulsion Conference*, Las Vegas, NV, 18-20 Jun 1979.
11. Boggs, T. L.; Price, C. F.; and Derr, R. L., "Transient Combustion: An Important Consideration in Deflagration to Detonation Transition," *AGARD Conference Proceedings*, Hazard Studies for Solid Propellant Rocket Motors, No. 367, 28-30 May 1984, p. 12.
12. McAfee, J. M.; Campbell, A. W.; and Asay, B. W., "Deflagration to Detonation in HMX Under High Confinement," *DEA Conference*, Schrodenshausen, FRG, 1 Jul 1987.
13. McAfee, J. M.; Asay, B. W.; Campbell, A. W.; and Ramsay, J. B., "Deflagration to Detonation in Granular HMX," *Preprints of Papers to be Presented at the Ninth Symposium (International) on Detonation*, Portland, OR, 28 Aug - 1 Sep 1989, pp. 144-154.

## DISCUSSION

**J. G. GLENN**  
Air Force Armament Lab  
Eglin AFB, FL

Where is the manganin gauge? Is it embedded?

## REPLY BY M. SAMIRANT

Due to survivability problems and because we need a very long recording duration ( $> 100 \mu s$ ), the manganin gauges are embedded into an inert material which presents the same density, grain size, and dynamical behavior as the explosive.

# DEFLAGRATION TO DETONATION IN GRANULAR HMX

John M. McAfee, Blaine W. Asay, A. Wayne Campbell,  
and John B. Ramsay

Los Alamos National Laboratory  
Los Alamos, New Mexico 87545

*The deflagration-to-detonation transition (DDT) of granular HMX, confined in steel tubes, was studied by means of x-radiography, light emission, a stress gauge, and various pin techniques. Simplification and consistency of results were obtained by igniting the HMX with a piston (initially at rest and in contact with the HMX) driven into the bed. A gasless igniter is used to start the burning of the piston propellant (low-density HMX), providing the piston with a smooth initial motion. Analysis of the data gives a detailed picture of the DDT process under these conditions. The qualitative and quantitative experimental results show the transition from burning to detonation is discontinuous. The results are discussed in terms of a descriptive model.*

## INTRODUCTION

The early study of deflagration to detonation transition (DDT) was strongly influenced by the views of Kistiakowsky.<sup>1</sup> His basic idea, that convective burning could accelerate to detonation velocities, formed the framework of many studies. There has been much speculation on how shock waves are formed by the burning explosive. Macek<sup>2</sup> and Gipson and Macek<sup>3</sup> hypothesized the reinforcement of pressure waves that results from coalescence of the  $u + c$  characteristics in cast explosives. Taylor<sup>4</sup> suggested that convective burning plays a central role in bridging the gap between conductive burning and the transition to detonation.

The transition from deflagration to detonation in porous beds of explosive and propellant has received considerable attention both experimentally<sup>5-11</sup> and theoretically.<sup>12-17</sup> In many cases,<sup>5,6,9</sup> the use of hot gas producing igniter complicates the interpretation and subsequent modeling of experiments because considerable effort is required to account for the effect of the igniter gases on the granular bed. Hot wire ignition<sup>7,8</sup> is less intrusive; however, the ignition front is not planar. Thus, the early events in these experiments cannot be approximated as one dimensional.

Because of the complex nature of the early burning, we simplify the process of igniting the bed by pushing a combustion-driven piston into the lightly tamped HMX bed. HMX above the piston is ignited by the shear of and friction between particles after compaction by the piston. This ignition technique separates the early effects of igniter gas and conductive and convective burning that produce a weak compaction wave<sup>5</sup> in the bed from those processes at higher pressures that produce a more substantial compaction of the granulated bed. Our method of initiation also starts all processes in a single plane at one end of the tube. At later times, expansion of the tube walls adds some two-dimensional character to the experiments. Piston-driven experiments in Lexan tubes were also done by Sandusky.<sup>19</sup>

The hypothesis given by Campbell<sup>10</sup> for the steps of DDT is similar to that proposed in this work. However, the mechanism described here is based on more extensive experimental observation and is more detailed than that of Reference 10. Because the description of the DDT process is complex and requires considerable nomenclature, the deduced mechanism is presented before the experimental evidence is detailed.

## NOMENCLATURE

To establish the nomenclature used in this description, a schematic chronology of a typical DDT experiment is shown in Figure 1. The initial conditions (Figure 1a) are the piston at rest, in contact with the HMX bed, confined in a steel tube. The piston starts and its velocity increases until the stress of the bed compaction approximately equals the driving pressure. The velocity settles to about 100 m/s after the piston travels a very short distance. The motion of the piston  $p$  generates a compaction wave  $c$  (Figure 1b) with a velocity near 400 m/s and a density near 90 percent of theoretical maximum density (TMD). Throughout this dynamic compaction of the bed, shear of and friction between the granules provide energy to start decomposition in the compacted material. The bed, compacted by the piston, is not readily permeated by combustion product gases. The start of significant burning (ignition) progresses up the tube as a well-defined wave  $b$  (Figure 1c).

As more material is burned, the pressure rises and the ignition wave accelerates. With each incremental acceleration, stress waves propagate from the burning region.<sup>18</sup> These stress waves ( $\sigma_i$ ) are represented schematically in the distance vs time plot in Figure 2. At some distance up the tube from the ignition front, the stress waves coalesce. When the resultant stress exceeds the strength of the 90% TMD HMX, the bed will further compact to near 100% TMD (Figure 1d). Sometime after formation, the lower boundary of this region is analogous to a piston supporting the

shock  $S$ , the upper boundary. Thus we name this interface the virtual piston,  $vp$ . The shock  $S$  accelerates slowly until the ignition wave intersects the virtual piston. Then the pressure driving the virtual piston rises rapidly, increasing its acceleration. This dense region between the virtual piston and the shock is designated the "plug."<sup>10</sup> Mass conservation arguments show the velocity of the shock  $U_s$  is several times that of the virtual piston  $u_{vp}$  and the actual mechanical piston  $u_p$  (details are given in the discussion). The transition to detonation occurs when the shock pressure is sufficient for initiation of the 90 percent compact (Figure 1f). This is a shock-to-detonation transition. The run to detonation, commonly denoted by  $x^*$ , is analogous with, but not exactly equal to, the plug thickness. The detonation propagates at a velocity characteristic of the 90% TMD HMX ( $D_1$  in Figure 2) until it overtakes the original compaction wave  $c$ , where the detonation slows to the characteristic velocity of the original bed ( $D_2$  in Figure 2). The evidence for this scenario is the subject of the balance of this paper.

## EXPERIMENTAL PROCEDURES

A schematic of the experimental arrangement is given in Figure 3. A maraging steel (Vascomax 250) tube (usually 12.7-mm i.d. and 23.8-mm o.d.) is hand packed with 8-mm increments of Class A or LX-04 grade HMX (mean particle diameters of about 170  $\mu\text{m}$  and  $\leq 60 \mu\text{m}$ ) initial densities of 1.22 g/cm<sup>3</sup>

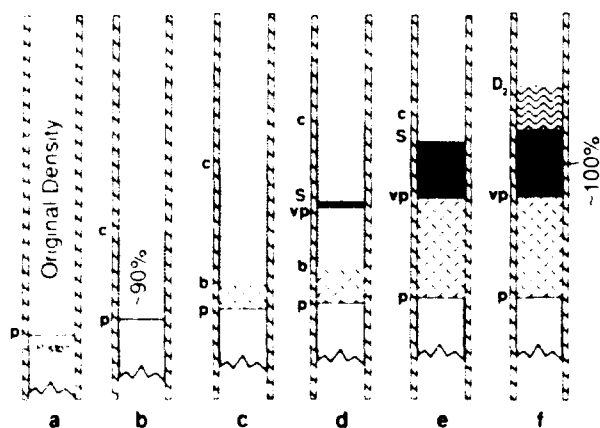


Figure 1. Schematic of the Deflagration-to-Detonation Transition in Granular HMX

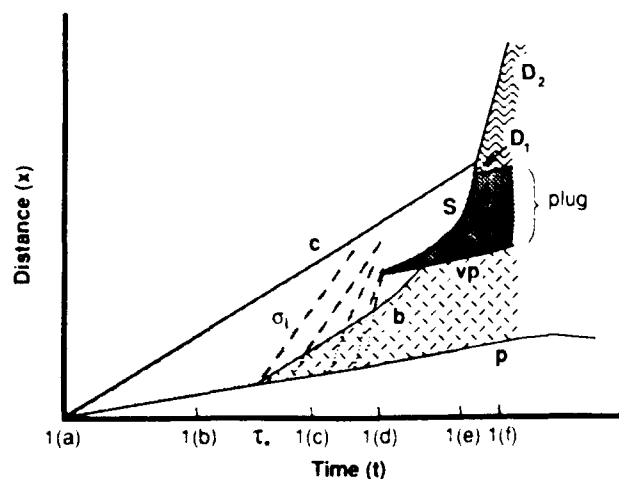


Figure 2. Distance-Time Representation of the Simple DDT Process (Time Axis Marks Refer to Figure 1)

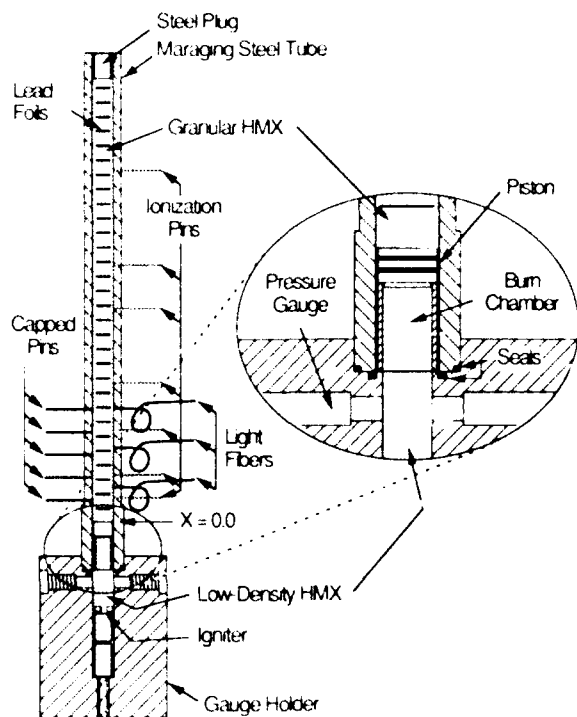


Figure 3. Schematic of DDT Tube Experiments

(65% TMD) and  $1.42 \text{ g/cm}^3$  (75% TMD), respectively. A 0.13-mm thick lead foil is placed between each increment of HMX as a radiographic marker. The O-ring sealed piston at the bottom of the tube is driven into the HMX bed by igniting the low density ( $\leq 0.5 \text{ g/cm}^3$ ) HMX in the burn chamber with a combination of a PYROFUSE<sup>®</sup> and 20 mg of stoichiometric mixture of titanium and boron. The first current from the Capacitor Discharge Unit (CDU) to the PYROFUSE<sup>®</sup> is the zero of laboratory time. All time measurements are made relative to this zero by means of time-interval meters accurate to  $\pm 3 \text{ ns}$ . The pressure in the burn chamber is measured with a transducer in the gauge holder. The response of the HMX bed is measured with a combination of diagnostics—self shorting (capped) pins measure the trajectory of low pressure waves (2 to 7 MPa or 50 to 70 MPa closing pressure, depending on the cap-to-electrode distance), coaxial ionization pins measure the onset of conductivity, optical fibers and detectors measure light emission and reflectivity, a strain compensated Manganin gauge measures the stress history of a particular region, and x radiographs are used to measure the position of the lead foils

All pins and optical fibers were placed flush with the inner-tube surface by insertion through minimum-clearance holes. Each was supported by epoxy applied from outside the tube. The emitted light transmitted by the optical fibers was converted to voltage using Optelecom Series 3200R Analog Fiber Optic Receivers. The active area of the Manganin gauge was placed perpendicular to the tube axis. The leads were at right angles to the gauge, along the inner bore and exited the tube at the top next to the steel plug (see Figure 3).

The apparatus used to measure a change in reflectivity of the bed is diagrammed in Figure 4. A 5-mW helium-neon laser was focused into a 0.2-mm diameter light fiber through a polarizing filter. The cleaved end of the fiber was placed flush with the steel-wall/HMX interface. The signal returned from the fiber and analyzed with a crossed polarizing filter is a measure of the reflectance of the granular bed.

The x-radiographs were analyzed by measuring the position of the piston and all the foils to  $\pm 0.08 \text{ mm}$  with a scanning microdensitometer. Magnification and reference points were obtained from the know pin positions. The average density between foils was calculated using the ratio of static-to-dynamic spacing and tube diameter measurements. Propagation of the uncertainties in the density calculation indicates a  $\pm 2\%$  TMD standard deviation in the density measurements. In cases where a leading wave was between two foils at the time of the radiograph, the average

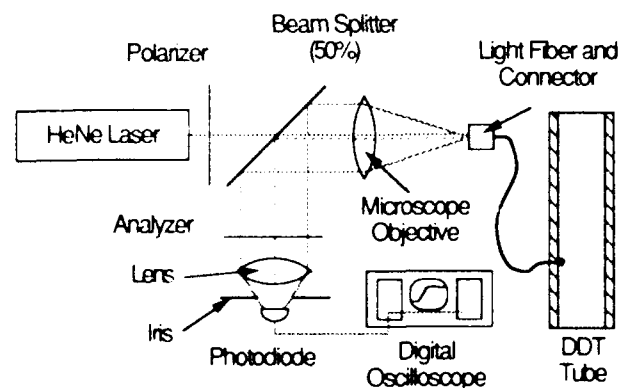


Figure 4. Diagram of Reflectance Change Apparatus

density could be decomposed into two densities. This was done using the position of the wave determined from interpolating pin signals from this wave and the undisturbed bed density.

## RESULTS

The inherent difficulty in interpreting numerous diagnostics of a complex process in different experiments leads necessarily to parallel and overlapping lines of evidence. Therefore, the following exposition of experimental results is by nature cumbersome, at best, and occasionally obtuse. We have sorted the experimental results into an order based on our description of the DDT process. For every observation, we have confirmatory evidence from other experiments that we do not report here. Frequent reference to Figures 1 and 2 is recommended.

### The Compaction Wave

The trajectory of the compaction wave was most often measured by low-pressure capped pins (2- to 7-MPa closing pressure). Velocities between 290 and 420 m/s were measured for various tests depending on the loading of the burn chamber. After a few millimeters of run, the compaction wave had constant velocity in a given test. The temporal profile was measured by two independent methods on Shot No. C 5947. The first method detected the change of reflectivity of the HMX bed at a given position. Compaction changed the amount of light reflected. The temporal profile of this signal (Figure 5) is thus a measure of the compaction wave profile.

Five millimeters above the reflectance light fiber, we placed the Manganin gauge in the HMX bed, perpendicular to the tube axis. The pressure\* obtained by analysis of the gauge record is also given in Figure 5. The good agreement between the two records' temporal profiles indicates a valid measurement of the compaction wave. The thickness of the wave is approximately 1.5 mm.

\*The pressures reported on the abscissa around 1 kbar are quite uncertain owing to the elastic plastic transition in Manganin at about 1 kbar.

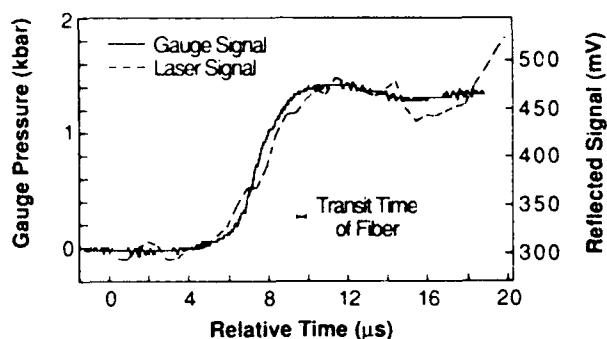


Figure 5. Manganin Gauge Pressure and Laser Light Reflected from the Compaction Wave for Shot No. C-5947

Radiographs of seven experiments at times corresponding to Figure 2b show that the density of the bed behind the compaction wave varies from 86% to 92% TMD for the Class-A HMX depending on the piston velocity. We quote % TMD in reference to the neat HMX density of 1.89 g/cm<sup>3</sup>. The complete stress gauge signal in the compact region, given in Figure 6(b),\*\* shows that the pressure level remains relatively constant behind the compaction wave until other phenomena occur. Figure 7 shows the estimated trajectory of the stress gauge, relative to the other diagnostics for Shot No. C-5947. The other features in this record are discussed below.

### The Ignition Wave

In Shot No. E 5586, three light fibers were added to the usual pins and radiographs. The signals recorded from the three fibers, along with their positions relative to the piston's starting position, are shown in Figure 8. Radiographs show that the third fiber was positioned in the plug region (between S and vp in Figures 1 and 2), and the others were below the virtual piston. Therefore, the third fiber is observing an entirely different region and gave a qualitatively distinct signal.

\*\* Record (b) was recorded at a higher gain than records (a) and (c), thus it shows the detail of the pressure variations in the compacted region without the loss of accuracy owing to the digital resolution of the recording device.



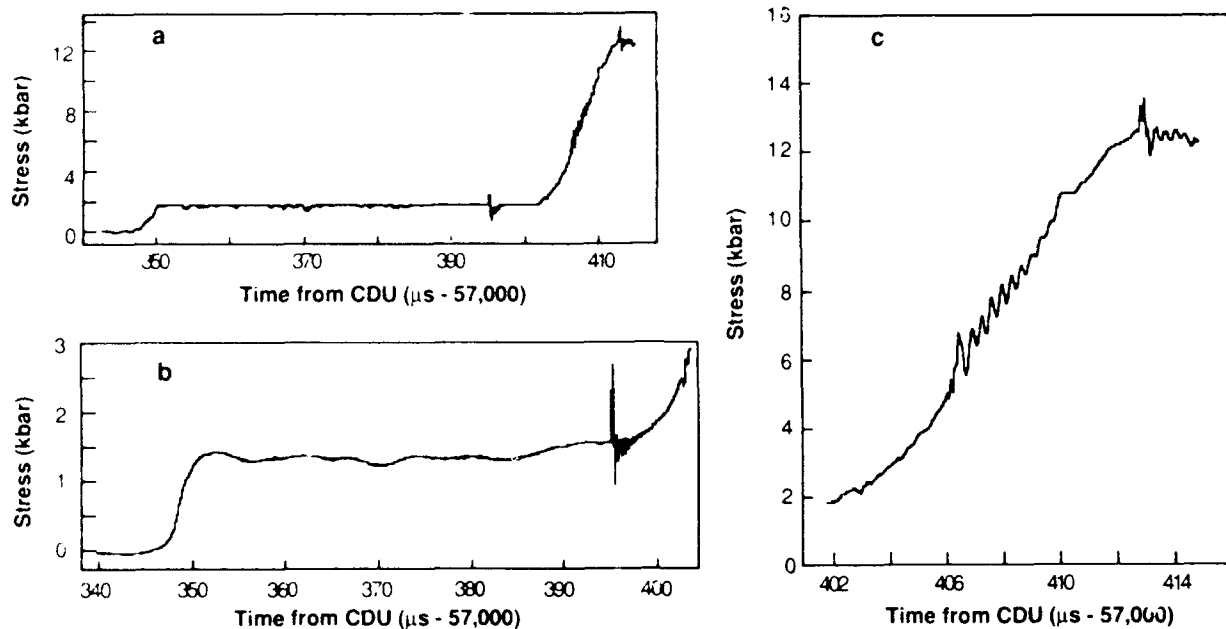


Figure 6. Manganin Gauge Stress Measurements of the Compaction Wave and the Plug Region for Shot No. C-5947. The time of detonation is approximately 57,415  $\mu$ s from CDU.

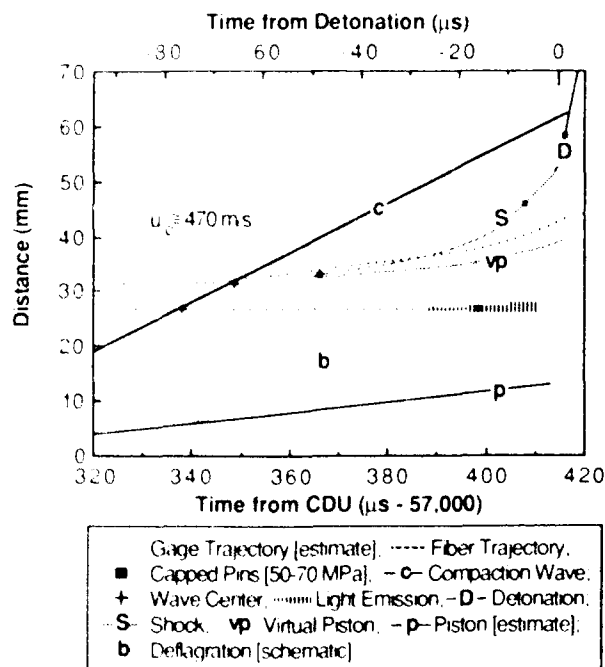


Figure 7. Distance-Time Summary for Shot No. C-5947

The salient features of the first two fibers ( $x = 23.5$  and  $33.0$  mm) are the fast rise and the "spike" of the initial edge, and the constant signal level until times after transition to detonation (about  $230 \mu$ s). Upon close inspection of the data, the rise time of the signal from  $x = 33$  mm fiber is significantly greater than that from  $x = 23.5$  mm fiber (not

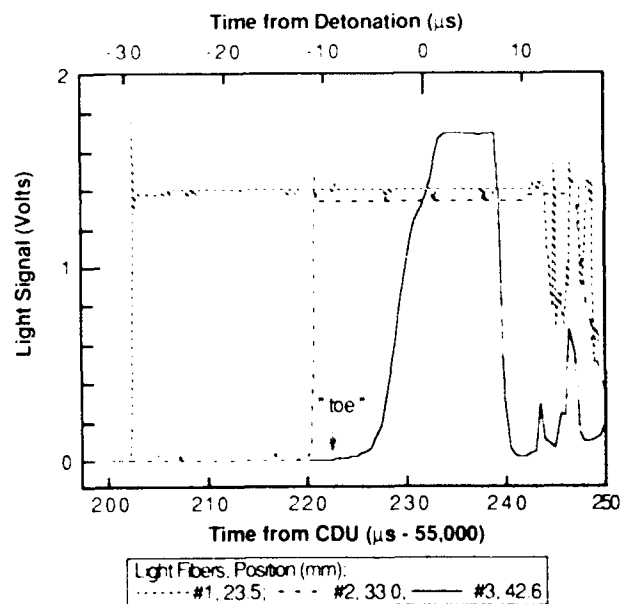


Figure 8. Signals from Light Fibers for Shot No. E-5586

evident from Figure 8, as presented). The data from the first two fibers are taken as evidence of an ignition front b (shown schematically in Figures 2 and 3) with nearly constant temperature conditions behind. The increasing rise time as a function of position may indicate the edge of the ignition front is becoming somewhat more diffuse as it progresses through the

90% TMD bed. The ignition wave velocity from the two signals is 520 m/s.

The third signal ( $x = 42.6$  mm) is characterized by a low-level "toe" (starting at 222  $\mu$ s), a more slowly rising signal to a point of inflection (231-232  $\mu$ s), and a final signal level 0.3 V higher than the signals from the first two fibers. Because this signal originates in the plug region, it will be discussed in the next section.

### The "Plug"

The radiographs are typified by those shown in Figure 9 for Shot No. B-9153. The figure consists of radiographs taken at four different times. The first (static) is an exposure showing the position of the equally spaced lead foils before the HMX in the burn chamber is lit. The first radiograph shows the piston moving into the tube and the change in spacing of foils 1-3, which is due to the compaction wave. The second radiograph was taken after the transition to detonation. The detonation wave is between foils 8 and 9. Foils 3-6 are closely spaced, and the tube wall is expanded less in this region. The third radiograph shows

the same features, except the detonation front is between foils 11 and 12.

Quantitative analysis of the foil positions and the tube expansion yields a measure of the average material density between adjacent foils. Typical analyses are shown in Figure 10, where the results of Shot No. B-9026 are interleaved with those of Shot No. B-9153. The features of these density-vs.-position plots are readily correlated with the schematic in Figure 1. Figure 10(a) shows the 90% TMD compaction wave as the only feature. This is the situation in Figure 1(b). Figure 10(b) shows a 100% TMD plug between about 33 and 50 mm, with a region of lower density (higher temperature) from the piston to about 30 mm indicating burning. This corresponds to Figure 1(e). The situation represented in Figure 10(c-e) occurs after the transition to detonation, corresponding to Figure 1(f). The detonation wave is at positions of about 65, 83, and 92 mm, successively.

The salient feature in these "density snapshots" in Figure 10 is the region of TMD, the plug. The radiograph for Figure 10(b) was taken 1.1  $\mu$ s before the transition to detonation.



Figure 9 Radiographs of Shot No. B-9153

It clearly shows the shock at 50 mm, the shocked material from 33 to 50 mm, and the burning region from the piston face at 12 mm to 33 mm. Figures 10(c-e) show the detonation progressing through the tube, whereas the plug region remains mostly intact in its original position. The low-density burning region continues to increase in temperature, as deduced from the decrease in density.

Additional evidence for this scenario comes from a compilation of the ionization-pin, capped pin, light fiber, and radiographic data for Shot No. E-5586. These data are projected in the  $x-t$  plane in Figure 11. The temporal extent of the light signals (Figure 8) is represented by textured lines with symbols at each end. The 42.6-mm signal has three symbols on the line noting the leading edge of the "toe," the point of inflection, and the cessation of the signal. The extent of the plug on the distance axis is indicated. In Figure 11, the two ionization pins at about 202 and 232  $\mu$ s are connected by line segments to the "toe" of the third light

signal. This is a reasonable assumption because the ionization pins report at the first appearance of conductivity, and the first light emission indicates the presence of reaction, which should also be accompanied by conductivity. This trajectory is the shock S, as in Figure 2. Note that the plug forms some 20  $\mu$ s before the ignition wave intersects the virtual piston.

The front edges of the light signals from the first two fibers are schematically connected by a line that is extrapolated to shorter times. The previously discussed temporal profile of these light signals is the evidence for a well-defined ignition front. We postulate that the time the ignition front intersects with the virtual piston is important in the deflagration-to-detonation transition. After this time, the plug is subjected to the full pressure of the burning HIMX without any layer of unburned material to reduce the stress. This interface, the virtual piston, behaves like an accelerating piston, and the resultant shock S is driven at an ever-increasing velocity into the compacted bed. When the velocity of the shock and the pressure generated are high enough, the HIMX bed will transit to detonation in a manner analogous to the mechanism of heterogeneous initiation.<sup>20</sup>

The stress gauge record for Shot No. C-5947 (Figure 6) gives the pressure history along the particle trajectory indicated in Figure 7. The first hint of increasing stress in the

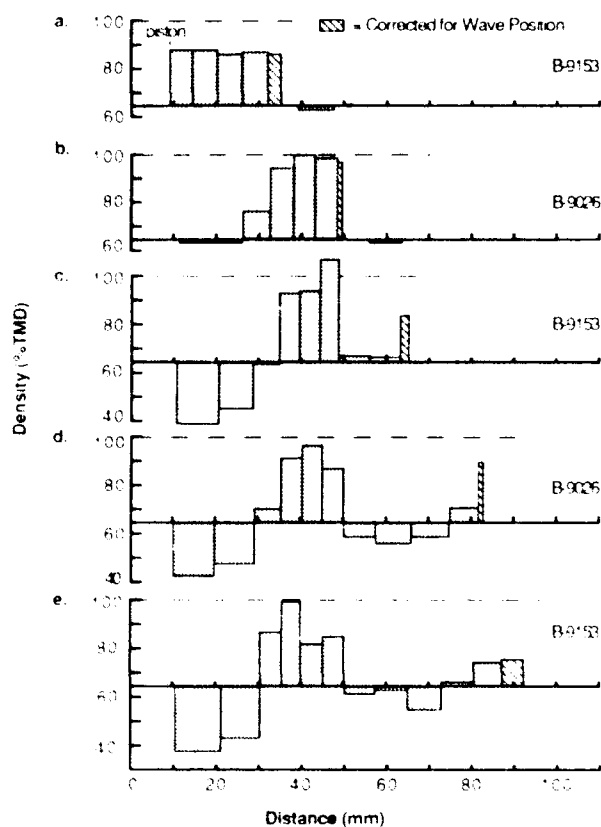


Figure 10. Density Vs. Position from Radiographs for Shot Nos. B-9153 and B-9026

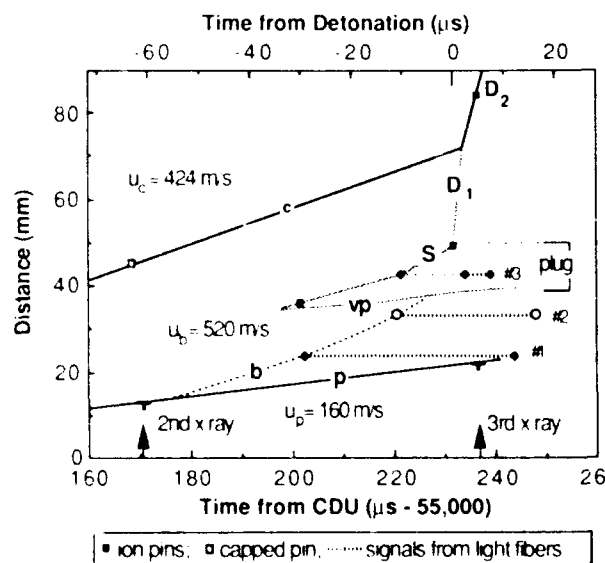


Figure 11. Pin and Light Signals for Shot No. E-5586

compact (i.e., the leading edge of the plug) is the small increase shown in Figure 6(b) at 385  $\mu$ s, 30  $\mu$ s before detonation. The collapse to near TMD may be sudden, although the evidence is tenuous. The indication for this is the ringing of the stress gauge signal at 395  $\mu$ s, followed by the rapid increase in pressure. As the pressure rises to about 12 Kbar at 413  $\mu$ s, there is a long-period ringing that may be associated with stress waves in the plug. The disturbance evident at 413  $\mu$ s may presage the transition to detonation that occurred at 415  $\mu$ s.

## Detonation

The exact position of the transition to detonation is a function of shock strength and the initiation characteristics of the compacted bed. Transition will occur after the formation of a shock of sufficient strength. The clearest observation of detonation in the compacted region is given by the combination of capped and ionization pin data for Shot No. B-9036 in Figure 12. These data show conclusive evidence for detonation in compacted material. In Figure 12(a), the combination of capped and ionization pins shows the compaction wave (313 m/s), an accelerating wave in compacted material (the ignition front), and the detonation wave. The burn chamber pressure is also plotted. The piston positions measured from the radiographs are also shown, along with an extrapolation. Figure 12(b) is an expanded plot of the ionization pin responses that shows

these data more clearly. The three ionization pins at 99, 125, and 150 mm measure a wave with velocity of 8.19 km/s. This is the detonation velocity in 93% TMD HMX.<sup>21</sup> After the compaction wave is overtaken, the wave slows to the detonation velocity of the original density bed (6.36 km/s). The trajectories shown in Figure 12 are labeled according to the nomenclature in Figure 2.

## Multiple Shocks

All the experiments performed in this study have not behaved as simply as those discussed in the preceding sections. Figure 13 reproduces the radiographs from Shot No. F-5408 (LX-04 Grade HMX, initial density 1.42 g/cm<sup>3</sup> = 75% TMD, tube-wall thickness = 3.12 mm). In the second dynamic radiograph are two regions of closely spaced foils indicating the formation of two shocked, but undetonated regions (plugs). Analyses of the dynamic radiographs are given in Figure 14. The first radiograph shows a low density (burning) region from the piston to about 48 mm, followed by a 100% TMD plug from 48 to 68 mm, followed by another 96% TMD region to about 88 mm. The second radiograph, taken after transition to detonation, shows the residuals of two separate plugs with lower boundaries near 57 mm and 83 mm and upper boundaries near 72 and 108 mm. The piston has moved backward, out of the radiograph.

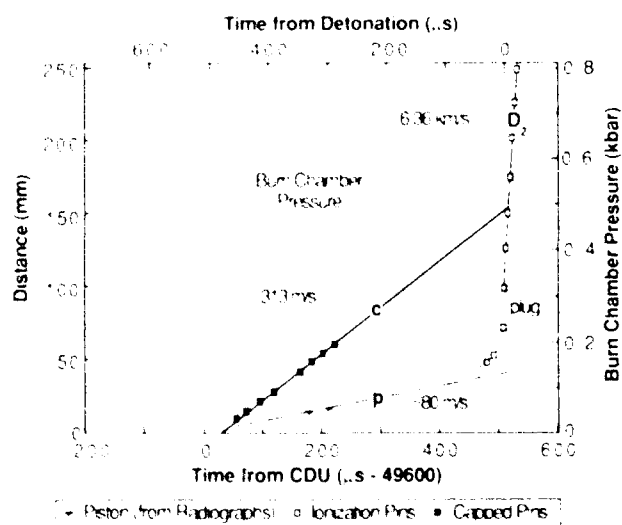


Figure 12(a). Capped and Ionization Pin Data for Shot No. B-9036

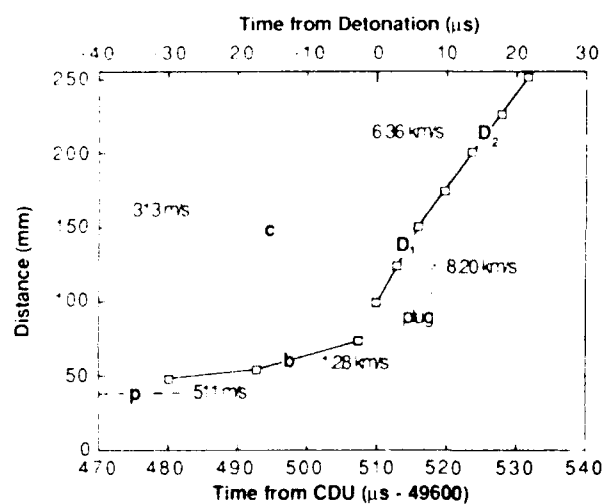


Figure 12(b). Ionization Pin Data for Shot No. B-9036

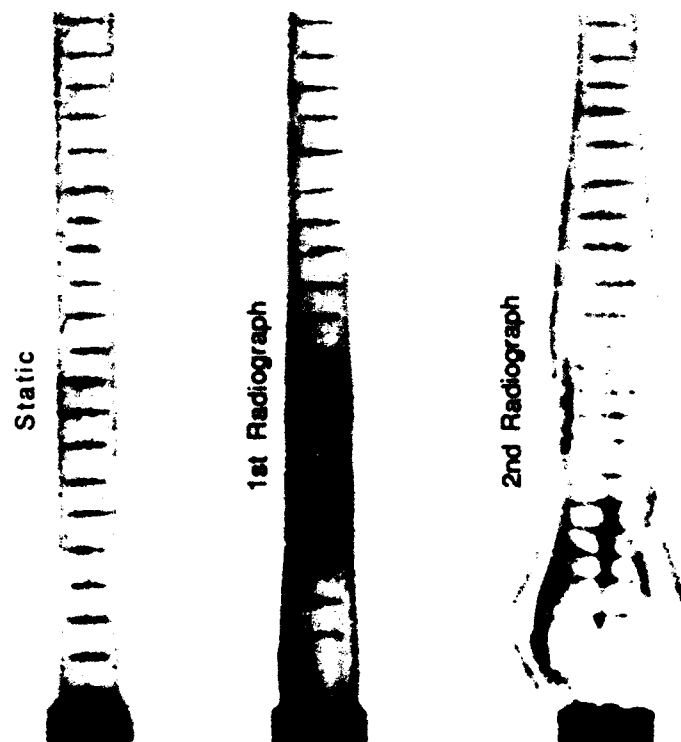


Figure 13. Radiographs of Shot No. F-5408

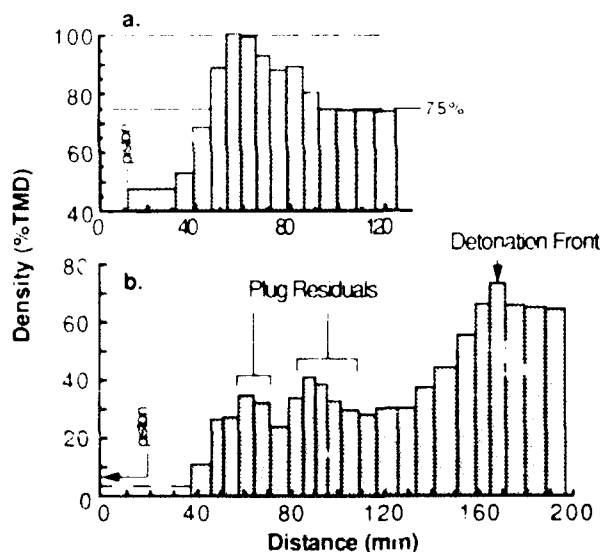


Figure 14. Density Vs. Distance for Radiographs of Shot No. F-5408

In this experiment detonation failed to occur after formation of the first shoe, but did occur after the second. An  $x-t$  schematic for this scenario is presented in Figure 15. The details of the various wave interactions are analogous to those presented in Figure 2, except that the first shock fails to initiate detonation (probably because of the drop in burn region pressure which is due to the confinement failure). When  $S_1$  overtakes the first compaction wave  $c_1$ , shock

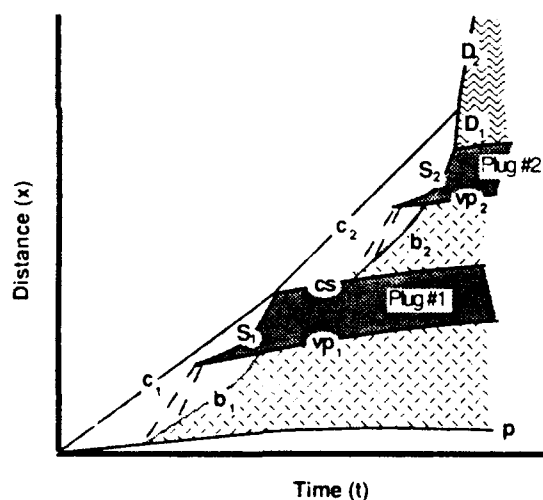


Figure 15. Distance-Time Representation of Consecutive Plug Formation in DDT Process

matching with Hugoniot curves derived from quasi-static compaction data<sup>22</sup> via the P-alpha model of Herrmann<sup>23</sup> shows the wave velocity (and the shock pressure) in the original density bed (75% TMD) will drop by about a factor of two. The slowed shock in the 75% TMD material becomes a second compaction wave  $c_2$  because the pressure conditions for shock initiation of detonation are not met. The contact surface  $cs$  (the boundary between the

100% TMD material of the first plug and the compacted 75% TMD material) acts as another piston. The events from ignition front development to shock formation are then repeated further up the tube. If pressure along  $S_2$  is sufficiently high, transition to detonation will occur. Figure 16 is a compilation of the pin and radiograph data for Shot No. F 5408 showing the formation of two plugs. The methods used to estimate some of the wave velocities are indicated in the figure.

There is no *a priori* reason for detonation to occur after the second plug. Situations where burn confinement fails before transition to detonation are easily envisioned. Consecutive plug formation could continue indefinitely. Indeed, the radiographs of Shot No. B-9088 (not shown here) show three, and possibly four plugs. The acceleration, velocity, and pressure behind a shock are a direct function of the virtual piston trajectory. This trajectory is controlled by the pressure in the burn region. In a one dimensional system, the burn pressure will increase until burning is complete. However, in our experimental arrangement, the lateral confinement eventually fails to some extent (see radiographs in Figures 9 and 13), thus reducing the pressure driving the virtual piston. Clearly, this provides a mechanism for reducing pressure and slowing shocks.

## DISCUSSION

Although other workers<sup>5,7,10,11</sup> have described the gross phenomenology of the DDT process in general terms, a complete, detailed synthesis and connection of the various steps has been lacking. In this discussion we will follow the chronology of the experimental results section while we compare our findings and speculations to those of others in an attempt to provide this synthesis.

Before diving headlong into the tangle of observation and analysis, we must answer the fundamental question of whether starting the DDT process with a physical piston is equivalent to igniting it with a flame. Campbell,<sup>10</sup> in his early studies, showed conclusively that barriers to convective flow did not affect the run-to-detonation in HMX beds. Bernecker<sup>5</sup> and Butcher<sup>24</sup> both show that the hot gas produced by an igniter and the initial burning of the bed

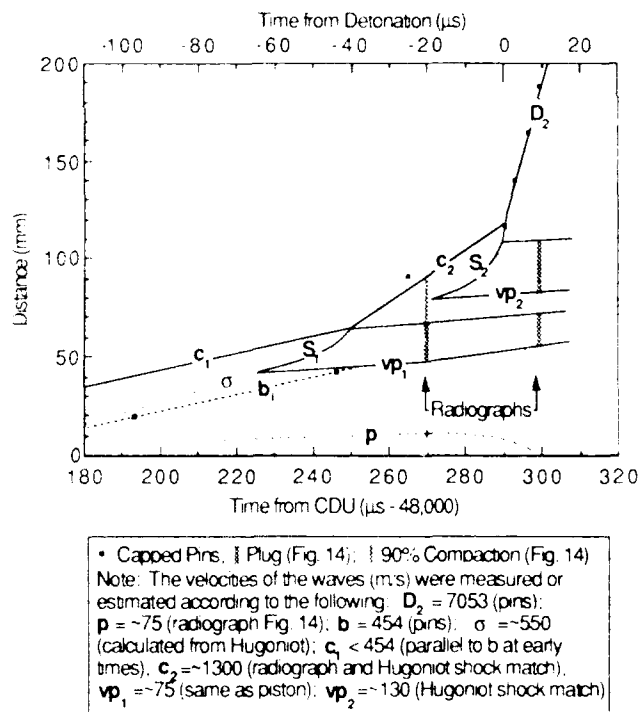


Figure 16. Capped Pin and Radiograph Data for Shot No. F-5408

causes a compaction of the bed downstream of the burning region. The compacted region is not permeated by the initial combustion gases. The main events leading to detonation all occur as a result of the action of this compacted region (which propagates as a wave) on the bed further along the tube. Therefore, by starting our experiments with a piston that forms this compaction wave immediately, we have removed only the uncertain and difficult-to-reproduce effects of initial bed ignition by a gas producing igniter. In fact, our use of a piston provides this bed compaction in a more controlled and consistent manner.

Piston driven compaction waves in granular energetic material have been studied experimentally by Sandusky<sup>25</sup> and theoretically by Kooker<sup>12</sup> and Baer.<sup>26</sup> The extent of reaction and specific mechanical history of the material behind the wave are a function of the piston velocity and the specific material properties. An unreactive compaction wave velocity  $u_c$  can be determined by the shock jump-mass balance relations,

$$u_c = u_p \rho_o / (\rho_c - \rho_o), \quad (1)$$

where  $u_p$  is the piston velocity,  $\rho_0$  is the initial density, and  $\rho_c$  is the compact density. The modeling of bed reaction and gas pressure growth are discussed in detail in References 17, 26, and 27.

The thermal decomposition of HMX is kinetically autocatalytic.<sup>28</sup> Therefore the rate of reaction is proportional to the concentration of both reactant and product (Rate =  $k[\text{HMX}][\text{Product}]$ , where  $k$  may be a function of pressure). An important feature of autocatalytic kinetic is the induction period between the first appearance of products (possibly from pyrolysis at grain contact points)<sup>17</sup> and rapid, pressure-dependent burning. The induction period is that length of time when the reaction rate is low and directly proportional to time. When product concentrations increase, the reaction rate accelerates rapidly and is proportional to an exponential in time. The transition between the two regions is abrupt and is often associated with ignition or thermal explosion.<sup>29</sup> Consideration of particle histories behind the ignition front shows that the *initial* trajectory of the ignition front must be parallel to the compaction wave but displaced in time by an induction period  $t_0$  (see Figure 2). Our data show that the ignition of rapid burning occurs approximately 100 microseconds after the HMX is compacted.<sup>\*\*\*</sup> This ignition spreads up the tube (downstream) as a well-defined front. The induction period would remain constant were the conditions behind the compaction front to remain unchanged. However, with the advent of the ignition wave, the increasing pressure in the voids upstream of the ignition will propagate stress waves of ever-increasing strength into the compact. These stress waves move at the local sound speed of the compact (on the order of 500-600 m/s<sup>†</sup> plus the particle velocity) and affect the intergranular properties. Because of this

change, the induction period of the autocatalytic decomposition will be shortened owing to an increase in the concentration of decomposition products. Thus the ignition wave will accelerate and propagate stress waves of increasing strength at increasing velocity. The length of the constant-velocity portion of the ignition trajectory is not known from these experiments. The schematic distance-time plots (Figures 3, 7, and 15) are drawn to accentuate our description of the process, and are not necessarily quantitative.

Sandusky<sup>19</sup> has done piston-driven, Lexan-confined experiments. He found a weak luminosity starting at the piston, behind the compaction front. However, his initial velocities were greater than the compaction wave velocity, and the ignition front did not accelerate, but ran at constant velocity. We agree with his statement that his observations are suspect due to loss of confinement by tube expansion.

Our data show (Figures 6, 7, and 11) a further collapse of the 90% TMD bed occurs behind the compaction wave and ahead of the ignition wave. We postulate the origin of this plug is a coalescence of the stress waves that originated at the ignition front. The exact nature of the plug at early times is unclear. It is not a classic shock at first. The upstream and downstream boundaries are probably not sharply defined. It is a region of higher density than the compact. We named the upstream limit of this discontinuity the virtual piston because of its function at later times, when the shock wave in the compact material is well formed.

The discontinuity at the virtual piston is a contact surface between the burning region and the shocked region. Thus the transition from burning to detonation is not a continuous process with one stage moving smoothly to another. It requires the interaction of an accelerating burn with a previously formed boundary. When the ignition wave intersects this higher-density region (near 100% TMD), the burning rate slows down dramatically (to as little as 1/25 of its original value).<sup>30</sup> For simplicity of description, we assume that between the time the ignition wave intersects the virtual piston and the initiation of a full

\*\*\* The induction time is a function of the strength of the compaction wave, hence the piston velocity. Note a long delay ( $\sim 300 \mu\text{s}$ ) for Shot No. B-9036 in Figure 12(a).

† The bulk sound speed for various bed densities was calculated from the slope of the Hugoniot generated from the P-alpha model and quasi-static compaction data.

detonation (about 20-30  $\mu$ s), the ignition wave does not ignite any of the material downstream of the virtual piston. During this time, the virtual piston is exposed to the continuously increasing pressure of the burning region and is thus accelerated.

The efficiency of this mechanism in forming a strong shock above the virtual piston can be estimated by considering the mass-balance jump relations across the shock, and the details of the upstream bed structure. The result is expressed as the ratio of the shock velocity  $U_s$  to the virtual piston velocity  $u_{vp}$ .

$$U_s / u_{vp} = [\rho_s - (u_p / u_{vp}) \rho_c] / [\rho_s - \rho_c], \quad (2)$$

where  $\rho_s$  is the density of the shocked material (about 100% TMD),  $u_p$  is the velocity of the mechanical piston (near 100 m/s), and  $\rho_c$  is the density of the compacted region (about 90% TMD). If we assume a modest virtual piston velocity of three times the mechanical piston velocity,  $U_s$  is about 2.1 km/s. This translates to a shock pressure of about 11 kbar (1.1 GPa). With Equation (2) as a guide, even moderate conditions can easily lead to shock pressures high enough to shock initiate HMX. We need not invoke high-velocity convective burning or low-velocity detonation to reach the velocities necessary for transit to detonation.

As an analytical tool, we have constructed a simple shock initiation model based on Equation (2) and Pop-plot data for HMX.<sup>31</sup> The trajectory and velocity of the virtual piston are calculated using the gas pressure generated by burning the HMX upstream of the virtual piston. The effects of wall friction and bed strength are also approximated. The distance and time to detonation are calculated, relative to the shock trajectory, using the pressure calculated at the shock front and the Pop plot. As the shock pressure increases, the position of the transition to detonation reaches a minimum in laboratory coordinates. This minimum is assumed to be the start of full detonation in the tube.

The calculation predicts maximum plug thickness (the distance between the virtual piston and the point of full detonation) of 30 to 35-mm. This calculated thickness is reasonably insensitive ( $\pm 15$  percent) to mechanical

piston velocity, wall friction coefficient, bed stress, gas temperature, and Pop-plot data. Our radiographic data shows plugs about 20-25 mm thick. The actual transition to detonation is governed by the same properties as any shock-to-detonation transition (SDT). Quantitatively, the major difference between the classic SDT<sup>20,32</sup> and this mechanism is that the shock in the DDT process is supported and accelerating rather than decaying in amplitude with a sharp, following rarefaction. We would thus expect a shorter run to detonation for a given strength shock than that predicted by the model using Pop-plot data.

Although this model of the transition to detonation is rudimentary, it calculates plug thickness (distance to detonation) reasonably, without much sensitivity to the parameter values. Therefore, our basic description of the physical process of shock formation, separate from flame propagation, is consistent with the experimental data. The exact position of plug formation in the bed is not addressed by this model. It is certainly a function of the material properties of the bed (original density, particle size distribution, confinement, material strength, and reactivity, to name a few).

Our observations of multiple-shock formation before transition to detonation reiterates the fact that the DDT process is complex and discontinuous. These results also indicate the necessity of using multiple diagnostic techniques on experiments of this type. Coarse spacing of pins or other sensors can easily lead to the conclusion that the process being observed is continuous and smooth, whereas the reality is quite different. Without being exhaustive or going into analytical detail here, we can show that DDT tube data published by others<sup>5,7,8,11</sup> is reasonably interpreted in terms of our described mechanism.

## CONCLUSIONS

Our observations of several piston-ignited granular-HMX-filled tubes with multiple diagnostic techniques have given a detailed description of the transition from simple burning to high-order detonation. Unique to our findings is the early time of formation (relative to the ignition front) of a near-100% TMD region (Figure 11). The lower boundary of this "plug"



of material provides a material and mechanistic separation between the deflagrating HMX and the shock that initiates detonation. The interaction of the burning region with this lower boundary provides a simple mechanism for shock acceleration using only moderate particle velocities.

In some of the experiments, released confinement of the burning region led to the formation of multiple shocks before transition to detonation. An example of this behavior is described by Smith<sup>33</sup> for RDX-filled-aluminum-sheathed detonating cord. His Figure 2 shows a piece of detonating cord with 13 confinement failures at approximately equal spacing. The transition to full detonation was not reached in this case. Consideration of this multiple-shock formation process may also be useful in the analysis of accident scenarios involving very large partial detonations.

## REFERENCES

1. Kistiakowsky, G. B., "Initiation of Detonation of Explosives," *Symposium on Combustion, Flame, and Explosion Phenomena*, University of Wisconsin, Madison, WI, 1948, pp. 560-565.
2. Macek, A., "Transition from Deflagration to Detonation," *J. Chem. Phys.*, Vol. 31, 1959, pp. 162-167.
3. Gipson, R. W. and Macek, A., "Flame Fronts and Compression Waves During Transition from Deflagration to Detonation," *Eighth Symposium (International) on Combustion*, Baltimore, MD, 1962, pp. 847-854.
4. Taylor, J. W., "The Burning of Secondary Explosive Powders by a Convective Mechanism," *Trans. Faraday Soc.*, Vol. 58, 1962, pp. 561-568.
5. Bernecker, R. R.; Sandusky, H. W.; and Clairmont, A. R., Jr., "Deflagration-to-Detonation Transition: Studies of Porous Charges in Plastic Tubes," *Seventh Symposium (International) on Detonation*, Annapolis, MD, 1981, pp. 119-138.
6. Bernecker, R. R.; Sandusky, H. W.; and Clairmont, A. R., Jr., "Deflagration-to-Detonation Transition of a Double-Base Propellant," *Eighth Symposium (International) on Detonation*, Albuquerque, NM, 1985, pp. 658-668.
7. Samirant, M., "Deflagration to Detonation Transition in Waxed RDX," *Seventh Symposium (International) on Detonation*, Annapolis, MD, 1981, pp. 139-142.
8. Samirant, M., "DDT in RDX and Ball Powder," *Eighth Symposium (International) on Detonation*, Albuquerque, NM, 1985, pp. 972-976.
9. Bernecker, R. R.; Price, D.; Erkman, J. O.; and Clairmont, A. R., Jr., "Deflagration-to-Detonation Transition Behavior of Tetryl," *Sixth Symposium (International) on Detonation*, Coronado, CA, 1976, pp. 426-435.
10. Campbell, A. W., "Deflagration-to-Detonation Transition in Granular HMX," *1980 JANNAF Propulsion Systems Hazards Subcommittee Meeting*, Monterey, CA, 1980, pp. 105-130; or Los Alamos National Laboratory document, LA-UR-80-2016, 1980.
11. Verbeek, H. J. and van der Steen, A. C., "Linking Experimental and Theoretical Results on the Deflagration to Detonation Transition," *Nineteenth International Conference of ICT on Combustion and Detonation*, Karlsruhe, FRG, 1988, preprint.
12. Butler, P. B. and Krier, H., "Analysis of Deflagration to Detonation Transition in High-Energy Solid Propellants," *Combustion and Flame*, Vol. 63, 1986, pp. 31-48.
13. Baer, M. R. and Nunziato, J. W., "A Two-Phase Mixture Theory for the Deflagration-to-Detonation Transition (DDT) in Reactive Granular Materials," *Int. J. Multiphase Flow*, Vol. 12, No. 6, 1986, pp. 861-889.
14. Nigmatulin, R. I.; Vainshtein, P. B.; and Akhatov, I. Sh., "Transition of Powdered Explosive, Convective Combustion into Detonation," *Combust. Explos. and Shock Waves*, U.S.S.R., Vol. 19, No. 5, 1983, pp. 618-621.

15. Akhatov, I. Sh. and Vainshtein, P. B., "Nonstationary Combustion Regimes in Porous Powders," *Combust. Explos. and Shock Waves*, U.S.S.R., Vol. 19, No. 3, 1983, pp. 297-304.
16. Akhatov, I. Sh. and Vainshtein, P. B., "Transition of Porous Explosive Combustion into Detonation," *Combust. Explos. and Shock Waves*, U.S.S.R., Vol. 20, No. 1, 1984, pp. 63-69.
17. Kooker, D. E., "A Reactive Shock Wave Model for Compaction Waves in Granular Energetic Material," Army Ballistic Research Laboratory report BLR-TR-2945, Nov 1988.
18. Bernecker, R. R. and Price, D., "Studies in the Transition from Deflagration to Detonation in Granular Explosives-II. Transitional Characteristics and Mechanisms Observed in 91/9 RDX/Wax," *Combustion and Flame*, Vol. 22, 1974, pp. 119-129.
19. Sandusky, H. W., "Compressive Ignition and Burning in Porous Beds of Energetic Materials," 1983 JANNAF Propulsion Systems Hazards Subcommittee Meeting, Los Alamos, NM, 1983, pp. 249-257.
20. Campbell, A. W.; Davis, W. C.; Ramsay, J. B.; and Travis, J. R., "Shock Initiation of Solid Explosives," *Phys. of Fluids*, Vol. 4, No. 4, 1961, pp. 511-521.
21. Gibbs, T. R. and Popolato, A., *LASL Explosive Property Data*, University of California Press, Berkeley, CA, 1980, p. 148.
22. Elban, W. L. and Chiarito, W. A., "Quasi-Static Compaction Study of Coarse HMX Explosive," *Powder Technol.*, Vol. 46, 1986, pp. 181-193.
23. Herrmann, W., "Constitutive Equation for the Dynamic Compaction of Ductile Porous Materials," *J. Appl. Phys.*, Vol. 40, No. 6, 1969, pp. 2490-2499.
24. Butcher, A. G.; Keefe, R. L.; Robinson, N. J.; and Beckstead, M. W., "Effects of Igniter and Compaction on DDT Run Up in Plastic Pipes," *Seventh Symposium (International) on Detonation*, Annapolis, MD, 1981, pp. 143-150.
25. Sandusky, H. W.; Glancy, B. C.; Campbell, R. L.; Krall, A. D.; Elban, W. L.; and Coyne, P. J., "Compaction and Compressive Reaction Studies for a Spherical Double-Base Ball Propellant," *Twenty-fifth JANNAF Combustion Meeting*, Huntsville, AL, 1988, preprint.
26. Baer, M. R., "Numerical Studies of Dynamic Compaction of Inert and Energetic Granular Materials," *J. Appl. Mech.*, Vol. 55, 1988, pp. 36-43.
27. Atwood, A. I.; Price, C. F.; Boggs, T. L.; and Richter, H. P., "Transient Combustion Analysis of Energetic Materials," *Nineteenth International Conference of ICT on Combustion and Detonation*, Karlsruhe, FRG, 1988, pp. 1-1 and 1-14.
28. Rogers, R. N. and Janney, J. L., "Thermochemical Evaluation of Zero-Order Processes Involving Explosives," *Proceedings of the Seventh International Conference on Thermal Analysis*, Vol. II, Chichester, GB, 1981, p. 1434.
29. Kondratiev, V. N., "Chain Reactions," *Comprehensive Chemical Kinetics*, Vol. 2, Banford, C. H. and Tipper, C. F. H., Ed., Elsevier Publ. Co., New York, NY, 1969, pp. 88-90.
30. Fifer, R. A. and Cole, J. E., "Transition from Laminar Burning for Porous Crystalline Explosives," *Seventh Symposium (International) on Detonation*, Annapolis, MD, 1981, pp. 164-174.
31. Dick, J. J., "Measurement of the Shock Initiation Sensitivity of Low Density HMX," *Combustion and Flame*, Vol. 54, 1983, pp. 121-129.
32. Ramsay, J. B. and Popolato, A., "Analysis of Shock Wave and Initiation Data for Solid Explosives," *Fourth Symposium (International) on Detonation*, White Oak, MD, 1965, pp. 233-238.
33. Smith, A. H., "Low Velocity Detonation in 2.5 Gr/Ft RDX Aluminum Detonating Cord," *Proceedings of the Eighth Symposium on Explosives and Pyrotechnics*, The Franklin Institute, Philadelphia, PA, 1974, pp. 11-1 and 11-7.

## DISCUSSION

JACQUES BOILEAU  
SNPE  
Paris, France

Is it possible with your apparatus to observe and to study the possible influences of the defects of HMX crystals, e.g., brittleness, depending for instance on the crystallization solvent of HMX?

### REPLY BY JOHN M. MCAFEE AND BLAINE ASAY

We have not examined the effects of crystal defects or morphology in our present studies. However, if defects influence distance to detonation or compaction behavior we should be able to measure these effects. Particularly, crystal defects could change the temporal shape of the compaction wave as measured by stress gauges or reflectometry.

## DISCUSSION

JULIUS ROTH  
308 Canyon Drive  
Portola Valley, CA 94028

In the First Detonation Symposium (1951) we presented streak camera records that showed many of the characteristics discussed in your paper, even though our observations were for lightly confined, low density, non-planar initiated material. Our best records were obtained for EC Blank Fire (an uncolloided single base NC smokeless powder) or for very lightly confined mercury fulminate.

### REPLY BY JOHN M. MCAFEE AND BLAINE ASAY

Even though we have studied only HMX in detail, we have no reason to believe that the observed behavior is material specific. We would expect the transition-to-detonation in many granular materials with autocatalytic-decomposition kinetics to proceed according to the mechanism presented.

# MODEL CALCULATIONS AND EXPERIMENTAL MEASUREMENTS OF THE RESPONSE OF HMX POROUS BEDS TO DEFLAGRATION AND SHOCK\*

D. F. Aldis, E. L. Lee, and R. L. Simpson  
High Explosives Technology  
Lawrence Livermore National Laboratory  
Livermore, California 94550

and

A. M. Weston  
KMI Energy Services, Project 90  
Division of Kirk-Mayer, Inc.  
Livermore, California 94550

*The experimental research on the response of porous beds of HMX has yielded a body of evidence which includes accurate measurements of gas flow, compaction ratio, detonation transit distance, and time. As the experimental research has progressed, we have developed a one-dimensional numerical model (1DUCT) to describe this response in a special hydrodynamic code in which the gas phase is allowed to flow through a solid phase. Gas phase relative velocity is limited to be subsonic. In addition, we have developed special constitutive and fluid EOS models (2DUCT) for use with the two-dimensional Lagrange hydrocode, DYNA2D, in which there is no cell-to-cell gas phase mass transfer.*

*Our study strategy was to analyze several, very different experiments to derive values of phenomenological parameters in the model. These experiments include squib ignited events where relative gas flow is important and compression ignition tests where it is not.*

## INTRODUCTION

Deflagration to detonation transition (DDT) and shock to detonation transition (SDT) have been studied for many years. However, only within the last ten years has the true nature of this phenomena been revealed experimentally.<sup>1-4</sup> In this paper, we will refer to the phenomena under study as DDT/SDT since in several tests it might more properly be described as SDT in porous beds of

HMX. It now appears that the DDT/SDT processes in a confined cylinder of granulated material happen in at least two steps. The first step consists of the formation of a high density plug. Due to high pressure combustion products compacting material downstream, the void fraction and the permeability of the plug to gas flow are both reduced to low values. In the second step of the process, the plug is further accelerated by the combustion process and produces a shock with sufficient strength to cause a detonation. In HMX, as in most reactive materials, the combustion rate is a function of the local gas pressure. As the pressure builds, the combustion rate increases. Additional surface area is created by fracture

\*Work performed under the auspices of the U.S. Department of Energy by the Lawrence Livermore National Laboratory Under Contract W-7405-ENG 48.

in the compaction process. The net increase in the combustion rate leads to a detonation. Several modeling efforts have made significant contributions to understanding the SDT/DDT phenomena.<sup>5-9</sup> The principle difference between the 1DUCT model and other approaches is the treatment of the bed as a sequence of porous elements corresponding to the grain size of the material in the bed. The motion of the solid bed is described using a Lagrangian coordinate system through which the gas moves relative to the solid.

We will describe an experimental study on the response of porous HMX to a shock, using an inclined, multiple gauge pressure sensor and computational models of the SDT/DDT process. The first model is a one-dimensional, two-phase model called 1DUCT. The second is a two-dimensional, single phase model called 2DUCT. 2DUCT is a single-phase model in the sense that a single velocity is used to describe the motion of the solid and the gases in a computational cell. However, two phases are considered with respect to the equation of state. For example, the total stress within a computational cell is a combination of the stress in the solid and gaseous phases, as is also done in 1DUCT.

## FLYER PLATE EXPERIMENTAL MEASUREMENTS

A multiple manganin gauge package, recently developed by Urtiew and Erickson<sup>10</sup> was used to make in situ pressure measurements in a porous bed of HMX. The gauge

package consisted of six individual  $60 \times 10^{-3}$  ohm, four lead piezoresistive manganin gauges. During an experiment, a current level of 50A was maintained across the elements and the variation in resistance was measured using a bridge circuit.

The gauge package had 25- $\mu$ m thick elements and leads bonded between two 250- $\mu$ m thick Teflon sheets. The positioning of the elements in the HMX bed was done by mounting the package at a precise angle in a target assembly, diagramed in Figure 1. Element to element spacing was 8 mm. A gauge angle of  $14.5^\circ$  was used, resulting in 2 mm separation between each gauge element in the hydrodynamic flow. The first gauge was located 2 mm into the HMX bed. An additional gauge was placed at the buffer plate/HE interface.

Shock loading was accomplished using a 100-mm smooth bore gun with a polycarbonate flyer. The Hugoniot data of the aluminum buffer plate and the flyer are listed in Table 1. Flyer velocity was measured at 0.656 mm/ $\mu$ s using piezoelectric pins and flash radiography. The flyer tilt was measured at  $0.3^\circ$  and the tilt orientation was determined to within  $5^\circ$ . These values were used to correct the pressure data time base for the shock tilt plane.

Sieved Class A HMX with a median particle size of 170  $\mu$ m was used. The target assembly was carefully loaded to a density of 1.03 gm/cm<sup>3</sup>. Prior to firing, the HMX bed was evacuated to  $10^{-4}$  Torr.

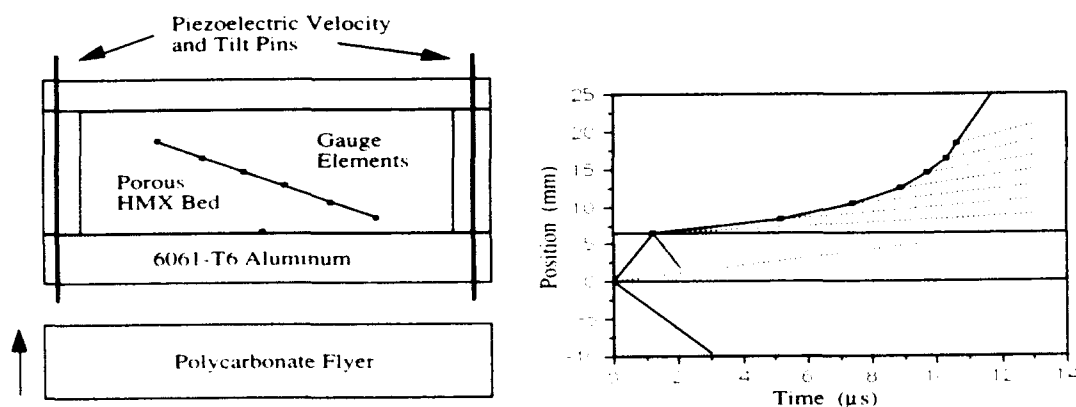


Figure 1. Experimental Configuration, and Shock and Particle Position Histories

Table 1. Shock Hugoniot Data

Material	$\rho_0$ (g/cc)	$C_0$ (mm/ $\mu$ s)	$S_0$	$g$
6061-T6 aluminum	2.703	5.24	1.4	1.97
polycarbonate	1.196	1.933	3.49	0.61

The data is shown in Figure 2. Measurements were made during the 10  $\mu$ s in which the reaction supported wave front transitioned to full detonation. The peaks at the leading edge of each pressure trace are due to the impedance mismatch between the HMX bed and the gauge package. The small local pressure maximum in the first gauge trace at 4.77  $\mu$ s is the result of shock reverberations in the aluminum buffer plate.

## 1DUCT MODEL

The 1DUCT code performs one-dimensional, two-phase (solid and gas) DDT calculations in a solid phase Lagrange coordinate system. The gas phase can pass through the structural solid phase cells. The solid phase hydrodynamic calculation is conventional as described by Wilkins.<sup>11</sup>

Explicit scaling is required to handle the gas phase with regard to flow relative to the solid phase, heat transfer, grain burning, and

gas production in a compaction front where porosity is rapidly changing. The scaling factor,  $R_s$ , is the ratio between the initial computational cell width,  $\Lambda_0$ , and a smaller mean characteristic dimension,  $S$ , that represents the grain dimension distribution of the simulated porous bed.

## Relative Gas Flow and Heat Transfer

Gas flow is predicted by using an equation derived from low pressure gradient permeability data for the explosive PETN.<sup>12-15</sup> This fit is then combined with the turbulent flow permeability correlation developed by Jones and Krier.<sup>16</sup> The convective portion of the heat transfer coefficient used in 1DUCT is based on Denton's correlation.<sup>17</sup> Denton's correlation uses a characteristic grain size in its definition of a Reynold's Number which is the reciprocal surface to volume ratio multiplied by porosity. The 1DUCT code calculates a surface to volume ratio for consolidated grains which approaches zero as porosity approaches zero. This calculated surface to volume ratio is used in the Denton correlation directly.

Heat conduction into the solid in a cell is controlled by a one-dimensional spherical conduction equation. Thermal difference equations are derived for equal mass thermal zones. The initial grain mass for heat transfer is equal to that of the computation cell divided by the cube of the scaling factor,  $R_s$ . When a grain is burning, zones at the surface are discarded as the solid is converted into gas. For the simulations in this paper, we use forty thermal zones in each cell.

## Grain Burning Modes

Grain burning is a combination of three modes, i.e., compaction front gas production; a growth mechanism which is a function of burn fraction and pressure; and regression rate burning which is only a function of gas pressure. Regression rate burning and growth do not occur simultaneously; the 1DUCT code chooses the largest incremental value and ignores the other. Regression rate burning begins after a time delay based upon a fit to one-dimensional thermal explosion (ODTX) data.<sup>9,18</sup>

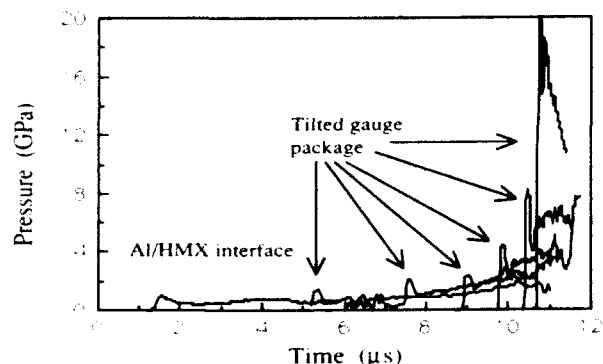


Figure 2. Pressure Versus Time Plot From Seven In Situ Manganin Gauges, Initial Positions at 0, 2, 4, 6, 8, 10, and 12 mm

## Fracture

Typical calculated values for grain surface to volume ratio are illustrated in Figure 3 for two types of HMX: a large #20 sieve cut HMX and Class A HMX which has a much smaller mean grain size. The computational algorithm assumes that individual grains will fracture into a given number of fragments and that the fraction of fragmented grains increases as porosity is reduced. We determined from the photomicrographs presented by Elban<sup>21</sup> of unconsolidated grains and grain fragments after different levels of compaction that the #20 grain breaks into 10 pieces and the smaller Class A grain breaks into 3 pieces. The algorithm also includes the effects of burning so that the surface to volume ratio is a function of both porosity and burn fraction.

## Compaction

The compaction model has been described earlier by Weston and Lee.<sup>9</sup> However, the constitutive model, based on the notion of closing a spherical pore, has been replaced by an empirical equation based on quasi-static data.<sup>19-21</sup> Figure 4 illustrates results on Class A HMX from hydrostatic and

one-dimensional plane strain, tube tester, experiments. The data for #20 sieve cut, Class D HMX in the one-dimensional plane strain test is also shown.

## 1DUCT SIMULATION OF EXPERIMENTS

We have used 1DUCT to model three kinds of compression ignition experiments and one squib ignition experiment, all using porous HMX. The HMX used in the flyer plate experiment described in the experimental section was sieved, and that used in the explosive lens experiments was neat Class A HMX. The particle size distribution for each is illustrated in Figure 5. For both experiments, we assumed compaction was similar to that observed by Costantino<sup>23</sup> with a hydrostatic device. The permeability of the sieved HMX is probably greater than that for the neat HMX due to a more uniform grain size.

McAfee and Campbell<sup>24</sup> performed experiments in which a gas generator driven piston compacted a porous bed of neat Class A HMX inside a steel tube. We assumed in this case that compaction constitutive behavior was like that observed by Campbell.<sup>20</sup> For

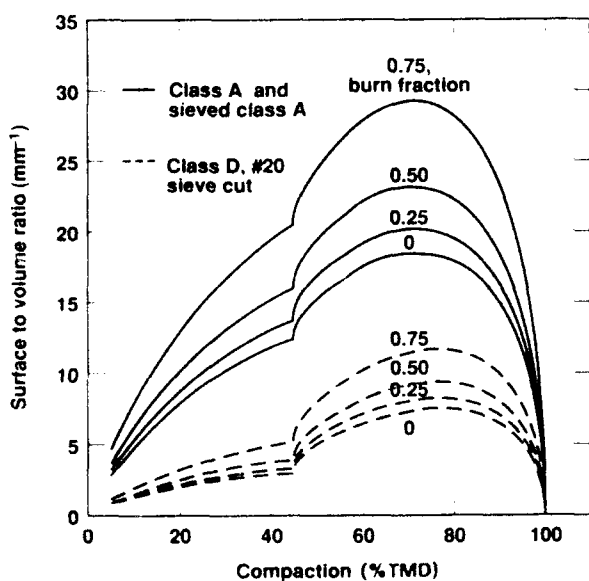


Figure 3. Surface to Volume Ratio for Two HMX Granulations

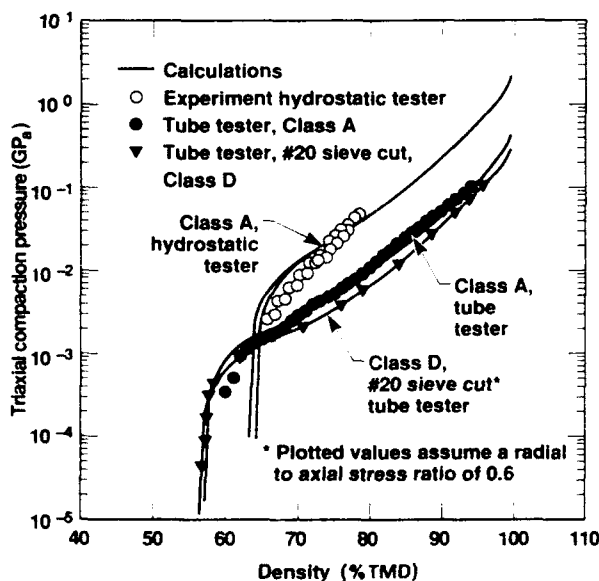


Figure 4. Quasi-static Compaction Pressure for HMX

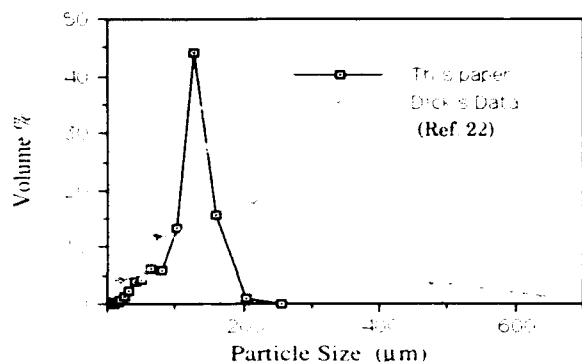


Figure 5. Particle Size Distribution for the HMX Used in the Flyer Plate Experiment (This Paper) on the Explosive Lens Experiment

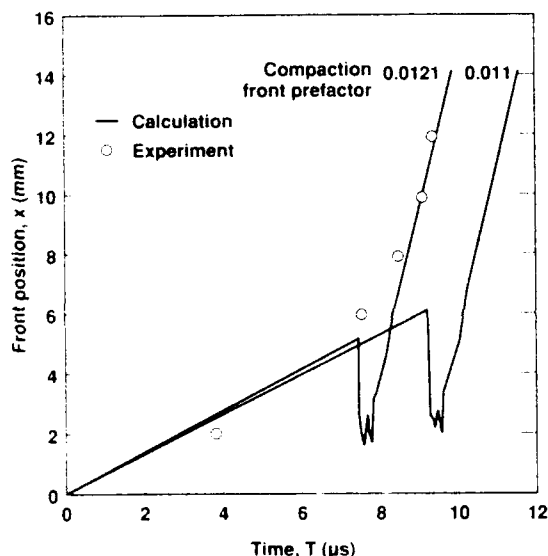


Figure 6. Calculated and Experimental Front Position Versus Time for Flyer Plate Experiment

modeling permeability and burn surface area, we assumed a precompacted grain size of 174 microns to represent both neat and sieved Class A material.

The squib driven DDT tube experiment on #20 sieve cut HMX reported by R. Bernecker<sup>1</sup> also was modeled. For this simulation, we assumed a characteristic grain dimension of 882  $\mu\text{m}$  and one dimensional plane strain compaction behavior as observed by Elban.<sup>21</sup>

## Flyer Plate Experiment

The flyer plate experiments are described in the experimental section above. In Figure 6, the manganin gauge arrival times are compared to computed arrival times using compaction front prefactors of 0.011 and 0.0121. We used the value 0.011 to model the transit time measurements of the explosive lens fragments. The computed  $x-t$  curves are plots of the maximum artificial viscosity in the computational layer versus time. The maximum artificial viscosity occurs at the location of maximum strain rate.

In Figure 7, the experimental and calculated pressures are compared. A value of 0.0121 was used for the compaction front gas production prefactor for this calculation. It can be seen that when detonation occurs, the computed turnover process is more rapid than that indicated by the manganin gauge records. The simulation was repeated using permeability parameters for #20 sieve cut HMX. The results, shown in Figure 8, are similar to those in Figure 7, except that the fit is improved.

To model this experiment, we imposed a particle velocity of 0.2 mm/ $\mu\text{s}$  on the first computational cell. Thus, we obtain estimates of the arrival times at the 2-mm and 4-mm gauge positions consistent with those observed experimentally. This velocity is consistent with a free surface velocity of the aluminum cover of 0.29 mm/ $\mu\text{s}$  impacting an empty sabot.

## Explosive Lens Experiments<sup>22</sup>

In this series of experiments, an explosive lens was used to propel a polymethylmethacrylate flyer into porous Class A HMX which had a mean density of 1.24 g (approximately 65% TMD). Transit times across the target layer were observed optically. There were two series of shots with several target layer thicknesses included in each series. The first series was conducted over a high pressure range (approximately 20 kb), and the second at a low pressure range (approximately 8 kb). The effect of the flyer was simulated by imposing a particle velocity on the first computational cell. In Figure 9, a comparison is shown



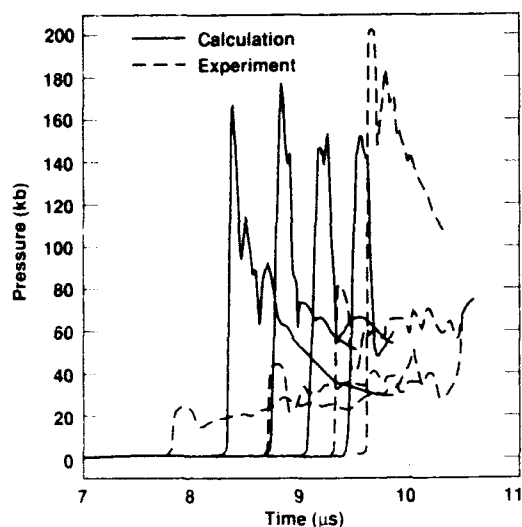


Figure 7. Calculated Arrays of Pressure Versus Time Using Permeability Parameters for Class A HMX Versus Lagrange Gauge Records for Flyer Plate Experiment

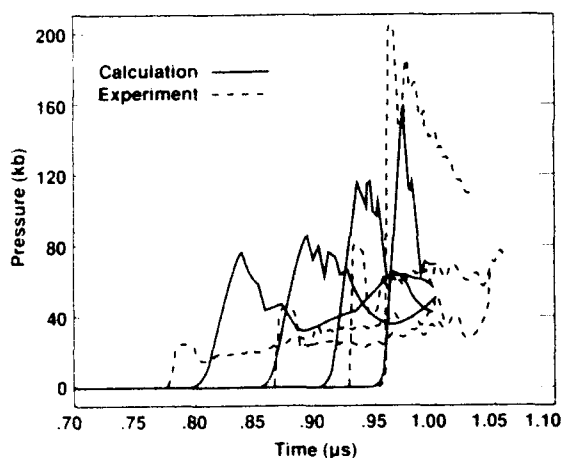


Figure 8. Calculated Arrays of Pressure Versus Time Using #20 Sieve Cut Class D Permeability Parameters Versus Lagrangian Gauge Records for the Filter Plate Experiments

between the experimental and predicted arrival times for both the high pressure and the lower pressure.

To match both arrival times and density, it was necessary to use the hydrostatic compaction data rather than the tube tester compaction data. The hydrostatic compaction data is associated with a much higher pressure

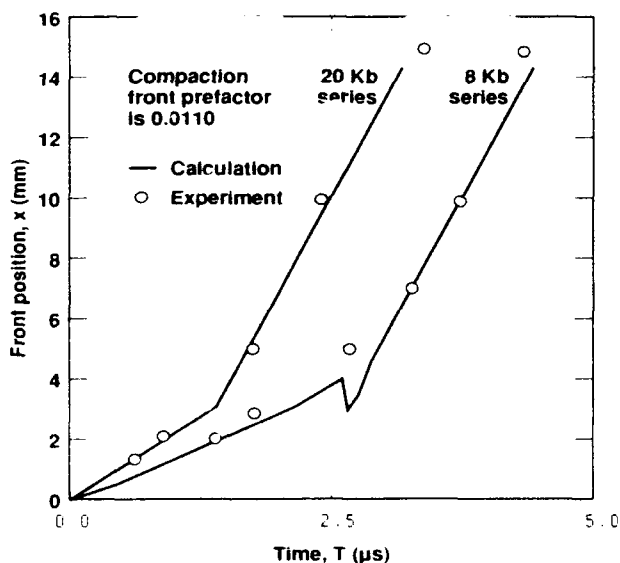


Figure 9. Calculated and Experimental Front Position Versus Time for Explosive Lens Experiments

for a given level of compaction. In our simulation of these experiments, we calculated a "no reaction" pressure of 7 kb for the 8 kb test series and 17 kb for the 20 kb series.

#### Piston Driven, Steel Tube Experiment<sup>24</sup>

In this experiment, labeled B-9153, low density HMX was used as a gas generator to drive a piston into the test bed of porous Class A HMX located inside a merging steel tube. The HMX had a mean density of 1.22 g/cc. A steady piston velocity of 0.077 mm/μs was achieved after an initial low pressure acceleration phase. In our modeling, we simulated the acceleration by imposing a velocity on the piston. The shape of the imposed velocity/time curve was a quarter cycle sinusoid that went from 0.0 to 0.077 mm/μs in 24 μs. This choice of rise time strongly influences the early time compaction front gas production and also affects the calculated time for turnover. The chosen value results in a simulation that correctly predicts the timing between the first radiograph density profile and the time of turnover.

In contrast to the explosive lens experiments, we were unable to model both timing

and density for the piston driven compaction experiment if we used hydrostatic tester compaction data.<sup>23</sup> It was necessary to use the tube tester compaction data.<sup>20</sup>

Figure 10 illustrates both the experimental and the calculated arrival time curves. In Figure 11, the radiographically measured and computed density profiles are shown at a time of approximately 30  $\mu$ s prior to turnover. In Figure 12, the density profiles are shown after turnover.

### Squib Driven DDT Experiment<sup>1</sup>

The squib driven DDT experiments began when a BKNO<sub>3</sub> squib was ignited. The gas generated by the squib caused an 80% TMD (1.54 g/cc) compaction wave to pass through a bed of porous #20 sieve cut, Class D HMX. The bed of HMX was initially composed of large uniform grains, at a density of 64.1% TMD (1.22 g/cc). After 300  $\mu$ s, a wave with a density of nearly 1.903 gm/cc formed at the end of the tube where the squib was ignited. It traveled over the 80% TMD compaction wave and formed a detonation at about 423  $\mu$ s.

Our model of the squib driven DDT experiment includes a simulation of the squib

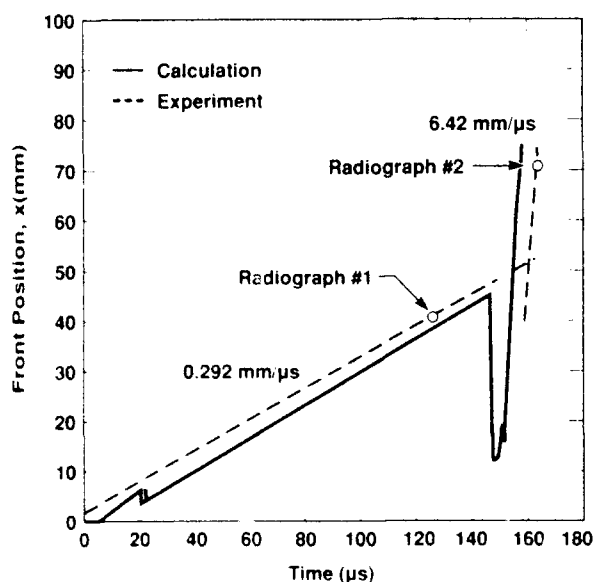


Figure 10 Calculated and Experimental Front Position Versus Time for Piston Driven, Steel Tube Experiment B-9153

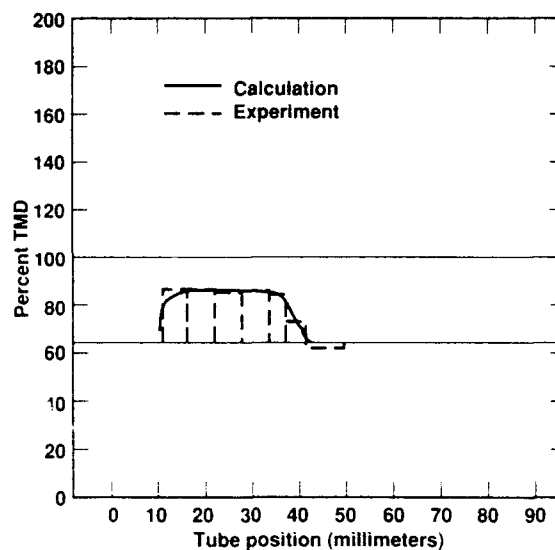


Figure 11. Calculated and Experimental Density Profiles for First Dynamic Radiograph

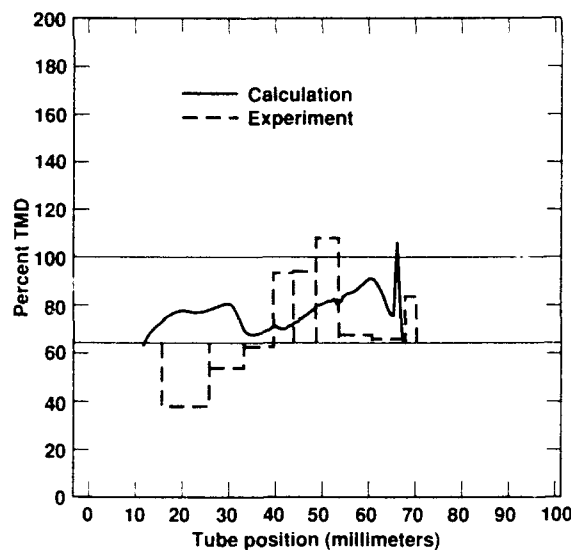


Figure 12. Calculated and Experimental Density Profiles for Second Dynamic Experiment

combustion which drives hot, high pressure gas into the porous bed and leads to an 80% TMD compaction wave. The pressure rise time at the front of the bed was about 50  $\mu$ s. At 20  $\mu$ s, regression rate burning is started in the first cell. Thereafter, the ODTX thermal

criterion is used to begin regression rate burning in all other cells. The squib induced compaction wave front was not sharp enough to produce gas. At about 340  $\mu$ s, the regression rate burning started in the first cell is sufficiently intense to start plug formation. The density gradient at the front of the plug then becomes steep enough to produce gas and start the turnover process.

Figure 13 illustrates the experimental streak camera record, the experimental location of the squib compaction front, and the computed arrival time plot. Note that the computed x-t plot lags the experimental record before plug formation. This is to be expected since the squib induced compaction front is quite broad. In Figure 14, experimental and computed displacement profiles are compared at about 300  $\mu$ s before plug formation begins and at 400  $\mu$ s just before turnover occurs.

We were able to model all the compression ignition experiments on Class A HMX with a single set of parameters for compaction front gas production and the growth combustion mechanism. To model the squib induced DDT on #20 sieve cut HMX, the growth premultiplier constants had to be

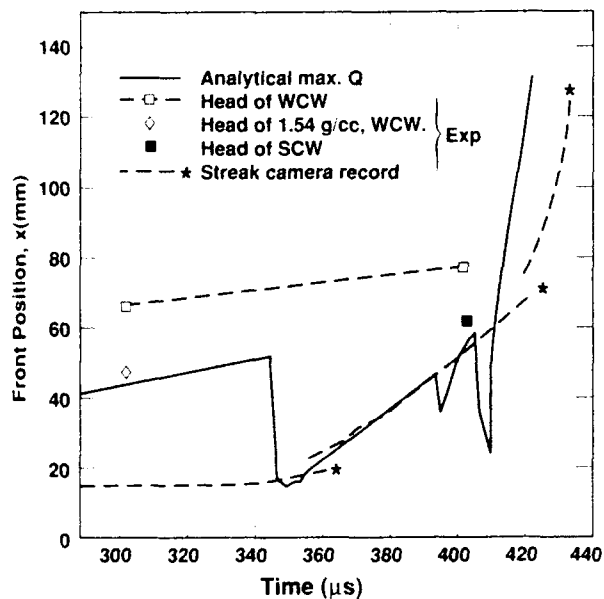


Figure 13. Calculated Front Position Versus Experimental Measurements of the Front Position

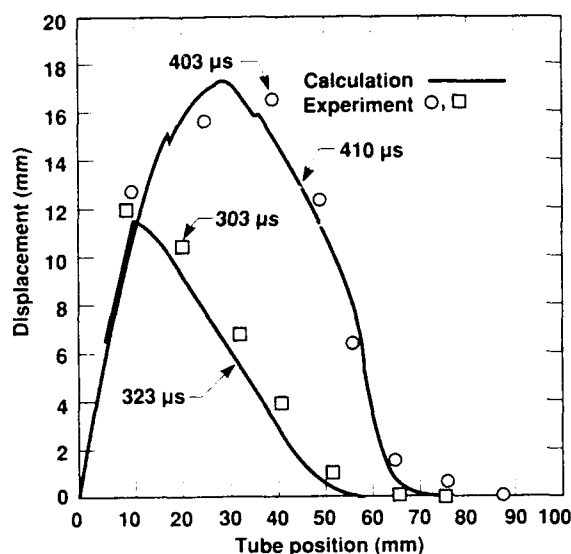


Figure 14. Calculated and Experimental Displacement Profiles for the Squib Driven DDT Experiment

reduced by 50 percent and the parameters that control gas production had to be modified to obtain 50 percent turn-on at a compaction of 90% TMD. The parameters previously used caused a 50 percent turn-on at a compaction of 70% TMD.

## 2DUCT MODEL

In order to determine how multi-dimensional aspects affect the results of the more detailed one-dimensional analysis, the most significant features of 1DUCT have been implemented into 2DUCT. These features include the structural aspects of the granular bed, the equation of state of the reactive material, and the surface area, pressure dependent reaction growth model.

2DUCT was implemented into the Lagrangian hydrocode DYNA2D, into the subroutines in which the pressure equalization between the reactant and the product had been previously performed. In 2DUCT, pressure equalization between the reactants and the products is not assumed. As in 1DUCT, a solid stress, consistent with the pure solid and the compaction stress measured by Elban, was combined with the pressure predicted by the gaseous of state equation for the products. The JWL equation used by

1DUCT for the gaseous product was also used in 2DUCT. The solid reaction equation used in 2DUCT was the ignition and growth model developed by Lee and Tarver.<sup>25</sup> The ignition and growth model can be thought of as being composed of three terms—an ignition term, a first growth term, and a final growth term. The values used for the constants in the ignition and growth model are the values listed for PBX 9404 in the DYNA2D manual,<sup>26</sup> except for the constant in the first growth term and the exponent of the compression term.

The 2DUCT model does not treat relative phase motion, interphase energy exchange, or the time to explosion ignition scheme.

The interphase energy exchange rate was strongly dependent on the convective heat transfer coefficient, a strong function of the local gas velocity relative to the solid, i.e., the relative phase motion. The time to explosion ignition scheme is a strong function of the solid temperature, which is, in turn, a function of the heat transfer coefficient or the interphase energy transfer rate.

In order to evaluate the implementation of 1DUCT model into 2DUCT, two experiments, previously performed by McAfee,<sup>24</sup> were simulated. The experimental apparatus used for these experiments consisted of three parts, a confinement tube, a bed of granulated reactive material, and a piston. X-Ray radiographs taken during the experiments indicated the piston location, the local mixture density, and the tube wall deformation. The experiment began as the piston moved into the tube against the granulated Type A, HMX. By using the radiographs, bed compaction sensors, and detonation or reaction sensors, it was possible to develop a clear experimental interpretation of the experiment.

## 2DUCT MODEL SIMULATION RESULTS

The difference between the two McAfee experiments<sup>2,24</sup> that were simulated was the effective piston velocity. The velocity of the piston in experiment B-9153 was 77 m/s and the velocity in experiment B-9130 was 100 m/s. The first growth constant and the exponent of the compression term in the ignition and growth model were adjusted to obtain a strong

reaction turnover at approximately the time observed for experiment B-9153. A value of 4.0 was used for the exponent of the compression term. A value of the growth constant of 1.15 caused turnover at approximately 130  $\mu$ s and a value of 1.1 caused a turnover at approximately 135  $\mu$ s. A value of 1.15 was used for all subsequent calculations.

A comparison between the experimental and simulated front position vs. time, ( $x$  vs.  $t$ ), is shown in Figure 15. The experimental time zero is about 10  $\mu$ s before the extrapolated first motion of the piston. The simulated starting time is the time of first piston motion. This difference in time zero is indicated in the offset in the compaction velocity part of the  $x,t$  curve. In the simulation, a granulated bed length of only 7 cm is simulated rather than the full 25 cm bed. In the experiment, the strong reaction front formed at a time of about 130  $\mu$ s. The simulation predicted that the strong reaction front formed at between 130 and 135  $\mu$ s. Unfortunately, this occurred as the compaction front hit the end of the simulated bed. A steady detonation was not predicted, but the turnover appeared to be well under way.

The simulation of the second experiment, B-9130, correctly predicted a strong reaction turnover at a position of about 5 cm at a time of about 100  $\mu$ s, as shown in Figure 16. A front velocity of approximately 5 mm/ $\mu$ s occurred as the wave hit the end of the simulated tube. The pressure-distance plot, shown in Figure 17, indicates the presence of both a detonation and a retonation. The detonation in experiment B-9130 had a velocity of 6 mm/ $\mu$ s.

A question of interest in the two-dimensional analysis was whether or not the strong reaction turnover was seriously affected by the tube wall expansion in the time and distance domain of the detonation process. The effect of the tube wall expansion was simulated by rerunning the simulation of experiment B-9130 with a tube wall that had a yield strength of 20 kbar. The time of turnover occurred at approximately 100  $\mu$ s—similar to the simulation with the stronger tube. In Figure 18, the extent of the tube deformation can be seen. The tube wall radius has expanded by about 1.7 mm as the wave hit the simulated end wall of the tube. In this simulation,

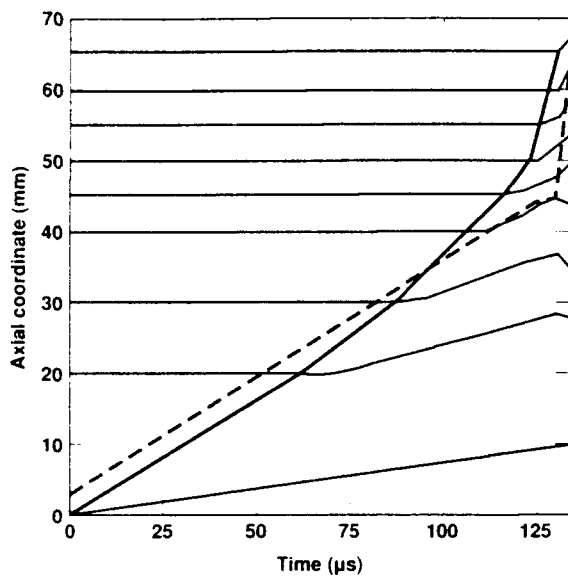


Figure 15. Calculated (—) and Experimental (---) Front Position for the Piston Driven Steel Tube Experiment with a Piston Velocity of 77 m/s

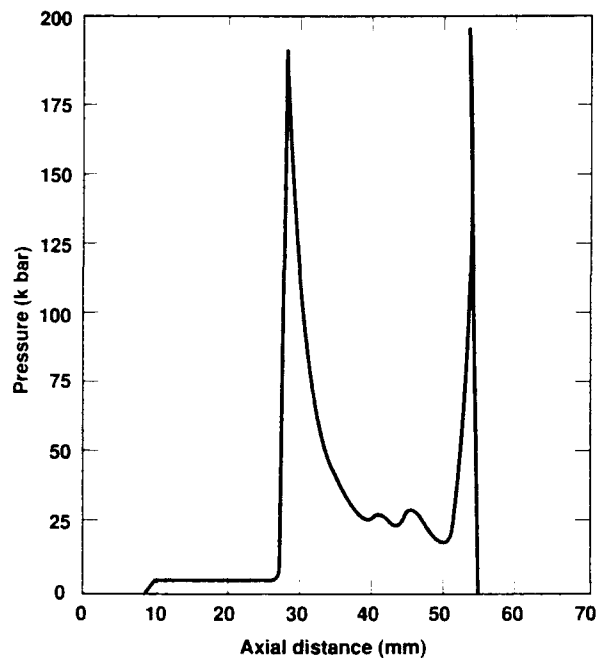


Figure 17. Calculated Pressure Along Center Line for Piston Driven Steel Tube Experiment with a Piston Velocity of 100 m/s

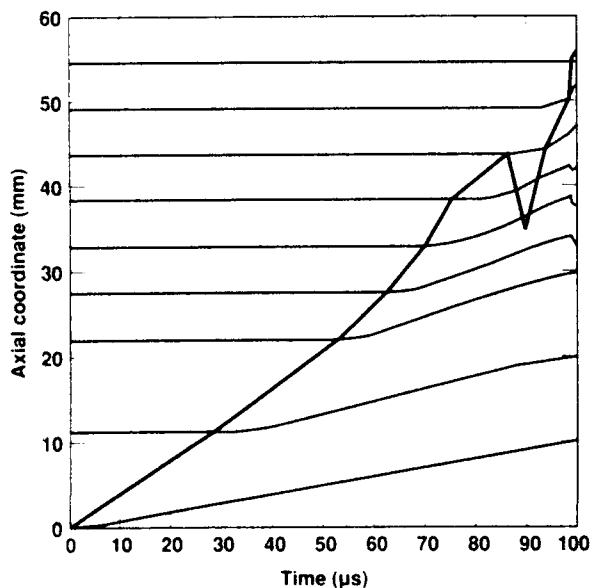


Figure 16. Calculated Front Position for the Piston Driven Steel Tube Experiment with a Piston Velocity of 100 m/s

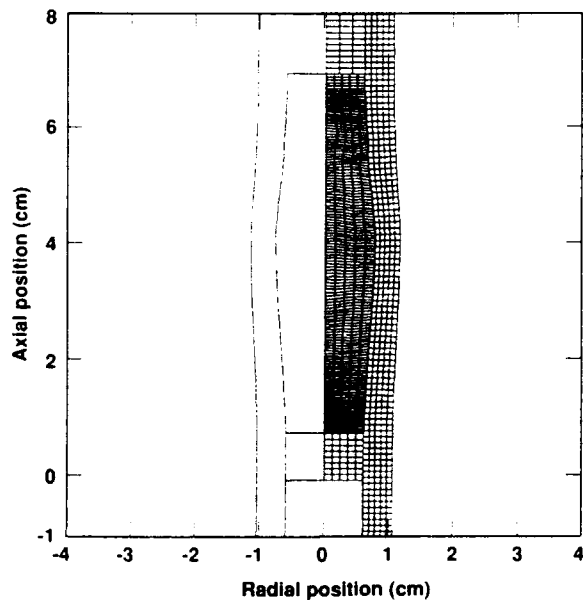


Figure 18. Calculated Lagrangian Grid Location for the Piston Driven Steel Tube Experiment with Piston Velocity of 100 m/s and Tube Wall Yield Strength of 20 kbars at 100  $\mu$ s

the strong reaction turnover occurred before the tube wall expansion interacted with the tube end cap. The effect of the tube wall expansion does not seem to affect the reaction turnover process and the one-dimensional approximation seems to be a reasonable approximation for these experiments.

## CONCLUSIONS

Granular beds of HMX appear to compact differently in different environments. When modeling experiments in tubes, the results were best described using the hydrostatic compaction pressure data obtained from compaction experiments performed in tubes. When modeling the explosive lens and the flyer plate experiments, compaction data obtained in a hydrostatic apparatus gave a better description. Having taken into account this variation in the compaction behavior, we then successfully modeled the remaining features of the compression ignition, detonation turnover experiments over a wide variation in stimulus and response on Class A HMX with a single set of parameters.

The two-dimensional simulations of the piston compaction experiments correctly predicted the influence of the piston velocity. We found that the effect of the tube wall expansion on the time to detonation predicted by the two dimensional simulation was small. The assumptions made, therefore, that allow the more detailed one-dimensional simulations of the two-dimensional piston compaction experiments appear to be justified.

## REFERENCES

1. Bernecker, R. R.; Sandusky, H. W.; and Clairmont, Jr., A. R., *Seventh Symposium (International) on Detonation*, Naval Surface Weapons Center MP82-334, Jun 1981, p. 119.
2. McAfee, J. M. and Campbell, A. W., "An Experimental Study of the Deflagration to Detonation Transition in Heavily Confined HMX," 1986 JANNAF Propulsion Systems Hazards Subcommittee Meeting, Chemical Propulsion Information Agency, Laurel, MD, 1986.
3. Bernecker, R. R., *AIAA Journal*, Vol. 24, 1986, p. 82.
4. Glancy, B. and Sandusky, H. W., "Dynamic Compaction and Compressive Reaction Studies for a Single-Base Ball Propellant," 1989 JANNAF Propulsion Systems Hazards Subcommittee Meeting, Chemical Propulsion Information Agency, Laurel, MD, 1989.
5. Price, C. F.; Atwood, A. I.; Richter, H. P.; and Boggs, T. B., "Modeling the Behavior of Mechanically Stimulated Porous Beds," 1989 JANNAF Propulsion Systems Hazards Subcommittee Meeting, Chemical Propulsion Information Agency, Laurel, MD, 1989.
6. Baer, M. R. and Nunziato, J. W., "A Multiphase Model for the Compressive Combustion of Ball Propellants," 1989 JANNAF Propulsion Systems Hazards Subcommittee Meeting, Chemical Propulsion Information Agency, Laurel, MD, 1989.
7. Kooker, D. F., "Modeling of the Piston Driven Compaction Experiment: Results Before and After Release of the Experimental Data," 1989 JANNAF Propulsion Systems Hazards Subcommittee Meeting, Chemical Propulsion Information Agency, Laurel, MD, 1989.
8. Hsieh, T. and Kim, K., "Numerical Simulation of Piston Driven Compaction Experiments for TS-3659 and WC-140 Propellants," 1989 JANNAF Propulsion Systems Hazards Subcommittee Meeting, Chemical Propulsion Information Agency, Laurel, MD, 1989.
9. Weston, A. M. and Lee, E. L., "Modeling one-dimensional Deflagration to Detonation Transition (DDT) in Porous Explosive," *Proceedings of the Eighth Symposium (International) on Detonation*, Albuquerque Convention Center, Albuquerque, NM, Jul 1985, p. 258.
10. Urtiew, P. and Erickson, L., "Multiple Gauges for *In Situ* Measurements of Pressure and Particle Velocity," *12th International Colloquium on Dynamics of*

*Explosions and Reactive Systems*, University of Michigan, Ann Arbor.

11. Wilkins, M. L., "Calculation of Elastic-plastic Flow," UCRL-7322 Rev. 1, Lawrence Livermore National Laboratory, Jan 1969.
12. Bernecker, R. R., Personnel Communication.
13. Andreev, K. K. and Gorbunov, V. V., "Transition of the Burning of Explosives into an Explosion. II. Stability of the Normal Burning of Powered Explosives," *Russian Journal of Physical Chemistry*, Sep 1963, pp. 1061-1065.
14. Andreev, K. K. and Chuiko, S. V., "Transition of the Burning of Explosives into an Explosion. I. Burning of Powdered Explosives at Constant High Pressure," *Russian Journal of Physical Chemistry*, Jun 1963, pp. 695-699.
15. Belyaev, A. F.; Korotkov, A. I.; and Sulimov, A. A., "Breakdown of Surface Burning of Gas-Permeable Porous Systems," *Combustion, Explosions, and Shock Waves*, 1966, pp. 28-34.
16. Jones, D. P. and Krier, H., "Gas Flow Resistance Measurements Through Packed Beds at High Reynolds Numbers," *Journal of Fluids Engineering*, Vol. 105, Jun 1983, pp. 168-173.
17. Denton, W. H., "The Heat Transfer and Flow Resistance for Fluid Flow Through Randomly Packed Spheres," *General Discussion on Heat Transfer*, Institute of Mech. Eng. and ASME, London, 1951, pp. 370-373.
18. Tarver, C. M.; McGuire, R. R.; Lee, E. L.; Wrenn, E. W.; and Brein, K. R., "The Thermal Decomposition of Explosives with Full Containment in One Dimension Geometries," *Seventh Combustion Symposium*, Leeds, U.K., Combustion Institute, Aug 1978.
19. Coyne, Jr., P. J. and Elban, W. L., "A Strain Rate Sensitivity Prediction for Porous Bed Compaction," Poster Presentation at Third American Physical Society Topical Conference on Shock Waves in Condensed Matter, Santa Fe, NM, Jul 1983.
20. Campbell, R. L.; Elban, W. L.; and Coyne, Jr., P. J., "Sidewall Pressure Measurements in Quasi-static Compaction of Porous Beds of HMX Powders and ABL 2523 Casting Powder," The 1988 JANNAF Propulsion Systems Hazards Meeting, Aerospace Corp., Los Angeles, CA, Mar 1988.
21. Elban, W. L. and Chiarito, M. A., "Quasi-static Compaction Study of Course HMX Explosive," *Powder Technology*, Vol. 46, 1986, pp. 181-193.
22. Dick, J., "Measurement of the Shock Initiation Sensitivity of Low Density HMX," *Combustion and Flame*, Vol. 54, 1983, pp. 121-129.
23. Costantino, M. and Tao, W., "Compaction of Non-Consolidated HMX Beds," University of California, Lawrence Livermore National Laboratory, Rept. UCRL-95861, 1987.
24. McAfee, J. M.; Assay, B. W.; Campbell, A. W.; and Ramsey, J. B., "Deflagration to Detonation in Granular HMX," *Preprints of The Ninth Symposium (International) on Detonation*, 1989, p. 144.
25. Lee, E. L. and Tarver, C. M., "A Phenomenological Model of Shock Initiation in Heterogeneous Explosives," University of California, Lawrence Livermore National Laboratory, Report UCRL-83618, 1979.
26. Halquist, J., "Users Manual for Dyna2d, An Explicit Two-dimensional Hydrodynamic Finite Element Code with Interactive Rezoning and Graphical Display," Revision 3, University of California, Lawrence Livermore National Laboratory, Report UCID-18756, 1980, p. 58.

## DISCUSSION

**JOHN C. CUMMINGS**  
Sandia National Laboratories  
Albuquerque, NM 87185

Please explain the nature of your wave front versus time curves for 1DUCT in those cases where the calculations appear to be discontinuous. You mentioned that you were plotting "Q" in an artificial viscosity parameter. What does this really mean when comparing to experimental data?

### REPLY BY D. F. ALDIS

The wave position versus time curves for the 1DUCT results are a plot of the maximum value of the artificial viscosity,  $Q$ . The maximum value of  $Q$  occurs, in a hydrodynamic calculation, at the position in the computational region which is experiencing the maximum rate of volumetric deformation. For the motion of a simple shock wave, this will occur at the leading edge of the shock, where the originally uncompressed

material is compressed. Experimentally, this position will correspond to the location in the region at which the pressure increases from the original undisturbed pressure to the pressure behind the shock.

The systems being modeled in this paper are more complicated than the motion of a simple shock wave. Several shocks are observed within the computational region being investigated at the same time. Since several shocks of similar magnitude are occurring simultaneously, the position of the single maximum value of  $Q$  may occur at more than one location from one computational time step to the next. The maximum value of  $Q$  has been plotted as connected points, which switch between each shock in the flow. The result of this switching appears as discontinuities in the curves.

If it were possible to experimentally record the pressure at every position in a flow, such as those modeled in this paper, more than one pressure wave would be observed. The position of each wave would correspond to one of the regions of maximum  $Q$ .



# COMPRESSIVE COMBUSTION OF GRANULAR MATERIALS INDUCED BY LOW-VELOCITY IMPACT

M. R. Baer and J. W. Nunziato  
Sandia National Laboratories  
Fluid and Thermal Sciences Department  
Albuquerque, New Mexico 87185

*A reactive multiphase mixture model is used to describe the initiation and compressive combustion of granular energetic materials induced by dynamic compaction. Incorporated in this description is a two-step combustion model whereby compressive reaction is initiated by dynamic compaction. Subsequent energy release from the reaction gases evolved during compaction is delayed following an induction rate law based on time-to-reaction experimental data. Given conditions of sufficient energy release and heat transfer, grain burning is initiated when granular surface temperatures exceed decomposition conditions. Model parameters are formulated for the granular explosive HMX and for nitrocellulose-based ball propellants. This model is used to simulate the low-velocity impact experiments of Sandusky and co-workers. Numerical calculations compare well with experimental observations. Details of compaction and combustion behavior are illustrated near the threshold of deflagration-to-detonation transition (DDT).*

## INTRODUCTION

The modes of flame spread and the transition from deflagration to detonation (DDT) in gas-permeable reactive granular materials are known to involve a variety of complex thermal/mechanical/chemical processes. To gain a fundamental understanding of these processes, several experimental studies have focused on various aspects of a DDT event. Bernecker et al.<sup>1,2</sup> studied accelerated combustion in confined columns of granular explosives and propellants, and proposed mechanisms for DDT based on wave trajectory information, flash radiographic observations, and pressure-time measurements. Most importantly, it has been shown that compaction of the granular reactant plays a major role in the combustion process. In view of this result, a number of subsequent studies investigated the nature of mechanically induced ignition and reaction using low level impact experiments. The projectile impact studies of

Green et al.<sup>3</sup> demonstrated that compaction, by itself, triggers a combustion event that readily accelerates to detonation provided that a certain level of porosity exists. In similar studies, Sandusky and coworkers<sup>4,5</sup> showed that rapid distortion of the granular material at a compaction front induces compressive reaction with a delay in energy release. Reaction product gases assist the mechanical loading of the granular material and strengthen the compaction wave.<sup>6</sup> McAfee and Campbell<sup>7</sup> conducted piston impact experiments that revealed multiple compaction fronts that form as a result of the interaction of combustion and the loss of lateral wall confinement. In all of these studies, low-velocity impact produces low amplitude compressive waves that are insufficient to cause direct shock initiation, and yet, DDT is observed. It is now recognized that 'hot-spot' reaction during compaction is the key that links the combustion modes of convective burning and detonation.

Much progress has been made toward the development of reactive multiphase mixture models describing deflagration-to-detonation transition in granular materials. A review and survey of the various modeling approaches is beyond the scope of this work and the interested reader is referred to the works of Baer and Nunziato,<sup>8</sup> Butler and Krier,<sup>9</sup> Kooker and Anderson,<sup>10</sup> Kim,<sup>11</sup> and the various works on DDT which appeared in the Eighth Symposium (International) on Detonation.<sup>12</sup> Much effort has been devoted to the determination of appropriate constitutive models and in providing verification data for modeling. Indeed, the interactive use of numerical models and experimental data calibrates modeling quantitatively and assists in elucidating the operative mechanisms in experiments.

Although existing models are well-founded from a thermodynamic and mechanical point of view and the concept of 'hot-spot' formation is well accepted, little progress has been made in defining the precise microscopic physical mechanisms that control nucleation, growth, and coalescence of 'hot-spots'. Moreover, chemical mechanisms and rates are not well-defined for conditions of high dynamic pressure. Given limited experimental time-to-reaction data relevant at the conditions of high strain rate deformation, a phenomenological combustion description for 'hot-spot' decomposition and grain burning is used in this study.

In the sections that follow, we review the multiphase mixture model for energetic granular materials with emphasis on the combustion description. Appropriate model inputs are defined and numerical calculations are carried out to model the low-velocity impact experiments conducted by Sandusky et al.<sup>4,5</sup> investigating Class D HMX and nitrocellulose-based ball propellants. These reactants are well-characterized and experimental data exist to construct appropriate constitutive models for compaction and combustion. Additionally, the ball propellants are ideally suited for modeling since these materials consist of uniform spherical particles that deform plastically

during compaction, whereas HMX crystals fracture during loading.

## REACTIVE MULTIPHASE MIXTURE MODEL

In this model, chemically reacting mixtures are assumed to consist of two phases: the solid granular reactant ( $a=s$ ) and the interstitial gas products ( $a=g$ ). Associated with each phase is a set of state variables: phase velocity  $v_a$ , material density  $\rho_a$ , pressure  $p_a$ , total energy

$$E_a = e_a + v_a^2/2,$$

internal energy  $e_a$ , and volume fraction  $\phi_a$ . In one dimension, the reactive multiphase equations are written in conservation form as:<sup>8</sup>

Conservation of Mass

$$\frac{\partial}{\partial t}(\phi_a \rho_a) + \frac{\partial}{\partial x}(\phi_a \rho_a v_a) = c_a^+, \quad (1)$$

Conservation of Momentum

$$\frac{\partial}{\partial t}(\phi_a \rho_a v_a) + \frac{\partial}{\partial x}(\phi_a \rho_a v_a^2 + \phi_a p_a) = m_a^+, \quad (2)$$

Conservation of Energy

$$\frac{\partial}{\partial t}(\phi_a \rho_a E_a) + \frac{\partial}{\partial x}((\phi_a \rho_a E_a + \phi_a p_a) v_a) = e_a^+, \quad (3)$$

Compaction Equation

$$\frac{\partial \phi_s}{\partial t} + v_s \frac{\partial \phi_s}{\partial x} = \frac{\phi_s \phi_g}{\mu_c} (p_s - p_g - \beta_s) + \frac{c_s^+}{\rho_s}, \quad (4)$$

where  $c_a^+$ ,  $m_a^+$  and  $e_a^+$  represent phase interactions of mass, momentum, and energy, respectively. These phase interaction terms account for the chemical reactions, the interphase drag, and the interphase heat transfer. Constitutive equations for the interphase drag and heat transfer are given elsewhere.<sup>8</sup>

In this description, independent equations of state for each phase are used given in the form:

$$p_a = p_a(p_a, e_a). \quad (5)$$

For the gas phase, the Jones-Wilkins-Lee equation of state<sup>13</sup> is used and for the solid phase a thermoelastic state relationship<sup>14</sup> is fit to available shock Hugoniot data.<sup>15,16</sup>

Volume fraction changes are described by the compaction Equation (4) and the phases occupy all of the total volume, thus:

$$\phi_s + \phi_g = 1. \quad (6)$$

Notice that compaction is rate-dependent and is driven by pressure differences. The intragranular stress is denoted as  $\beta_s$  and reflects distortion of the solid granular reactant. The compaction viscosity  $\mu_c$  controls the rate at which the volume fraction adjusts toward pressure equilibrium. Quasi-static<sup>17,18</sup> and dynamic compaction data<sup>19</sup> are used with compaction shock jump conditions defining the intragranular stress and the compacted solid volume fraction. In this work, wall friction effects and granular shear stresses are neglected.

In terms of multiphase mixtures, the reaction rate includes the effect of compressive reaction in the mass exchange  $c_a^+$ . Thus, the mass exchange combines the effects of compaction-induced 'hot-spot' combustion and grain burning:

$$c_s^+ = -c_g^+ = -\frac{\rho_s(\phi_s - \phi_s^0)}{\tau_H} - \rho_s \left\langle \frac{S}{V} \right\rangle a p_g^n H(T_i - T^*), \quad (7)$$

where  $\phi_s^0$  is the undisturbed solid volume fraction,  $\tau_H$  is a 'hot spot' reaction time characterizing compaction induced combustion,  $\langle S/V \rangle$  is the specific surface area of the granular reactant, and  $a p_g^n$  is the pressure-dependent surface burn rate<sup>20,21</sup> which is activated by the Heaviside function,  $H(T_i - T^*)$ . The Heaviside function has a value of one when the granular surface temperature,  $T_i$ , exceeds a critical 'ignition' temperature,  $T^*$  (corresponding to rapid thermal decomposition<sup>22</sup>), otherwise it is zero.

The first term of this expression applies only to compacted reactant (i.e.,  $\phi_s > \phi_s^0$ ) and reflects the effect of compaction-induced combustion. Following experimental observation<sup>4</sup> the reaction time,  $\tau_H$ , is scaled to the inverse of the square of mixture pressure:

$$\tau_H^{-1} = b p_m^2. \quad (8)$$

The coefficient  $b$  is a model parameter determined for each reactant calibrated to replicate the reactive wave characteristics for a specified loading condition. At other impact conditions, this combustion parameter remains fixed.

The second term of Equation (7) represents grain burning and incorporates strand data.<sup>20,21</sup> The specific surface area of the granular reactant is modified by particle burning and by the reduced surface area of pore-collapse during compaction:

$$\left\langle \frac{S}{V} \right\rangle = \frac{6\phi_s}{d_p} \left( \frac{\phi_s^0}{\phi_s} \right)^{\frac{1}{3}} \left( \frac{1 - \phi_s}{1 - \phi_s^0} \right)^{\frac{2}{3}}, \quad (9)$$

where  $d_p$  is the unreacted surface mean particle diameter.

Motivated by experimental observations,<sup>4</sup> the delay of energy release in the 'hot-spot' decomposition gas products is included in the model using a normalized induction time,  $I$ . This is mathematically expressed as an evolutionary equation:

$$\frac{\partial I}{\partial t} + v_g \frac{\partial I}{\partial x} = c p_m^2. \quad (10)$$

The heat release in the gas phase,  $\Delta E$ , is then given by:

$$\Delta E = Q^* + (\Delta E_R - Q^*) H(I - 1), \quad (11)$$

where  $Q^*$  is the energy release during compaction-induced combustion due to 'hot spots' and  $\Delta E_R$  is the heat of explosion of the reactant. The  $Q^*$  is estimated based on the condensed-phase (subsurface reaction) energy release given by Fifer.<sup>23</sup> The parameter  $c$  is determined based on experimental time-to-reaction data.<sup>4</sup>

During convective burning, the surface layers of the granular reactant are first ignited. The grain surface temperature,  $T_i$ , is determined using a relationship which approximates the heat conduction within particles subjected to convective heat transfer from the hot reaction product gases.<sup>24</sup> The resulting thermal fields are defined by an evolutionary equation, in terms of a surface temperature function  $\zeta$ :

$$\frac{\partial \zeta}{\partial t} + v_s \frac{\partial \zeta}{\partial x} = \frac{4\alpha_s B_i}{d_p^2} (T_g - T_i), \quad (12)$$

where  $T_g$  is the local bulk gas temperature,  $\alpha_s$  is the solid thermal diffusivity, and  $B_i$  is the Biot modulus (based on the local gas film coefficient  $h_g$ , solid thermal conductivity  $k_s$ , and the particle diameter  $d_p$ ):

$$B_i = \frac{h_g d_p}{2k_s}. \quad (13)$$

The granular surface temperature is defined as:

$$T_i = \frac{5(3\zeta + T_s) + B_i T_g}{(5 + B_i)(1 + B_i)} + \frac{B_i(T_s + \sqrt{(B_i \zeta)^2 + 2\zeta B_i(T_g - T_s) - B_i \zeta})}{(1 + B_i)} \quad (14)$$

where  $T_s$  is the bulk temperature of the solid phase.

## NUMERICAL METHOD

Typical of reactive flow models, the coupling of multiphase transport of mass, momentum, and energy with the effects of phase interaction leads to descriptions exhibiting disparate length and time scales. Furthermore, accelerated combustion involves processes that have dominant influences at different times and these processes occur in regions of high gradients or shocks. Thus, an appropriate numerical solution of reactive multiphase flow must recognize and address mathematical stiffness.<sup>25,26</sup> Explicit shock-capture methods, which employ excessive

numerical viscosity, can exhibit adequate numerical stability; however, it is usually at the price of accuracy in resolving the combustion physics. Unfortunately, the mathematical structure of multiphase formulations has not been adequately studied for the development of a characteristic-based numerical method.<sup>27</sup> Alternatively, we use a high quality numerical method, extensively studied for this class of reactive flows,<sup>25</sup> that resolves Eulerian multiphase equations with accuracy in time and space.

In this work, one-dimensional numerical solutions of the multiphase flow equations are obtained using an adaptive finite element technique. In this shock-capture method, spatial derivatives are evaluated at Gauss quadrature points and the resulting ordinary differential equations are solved using well-developed ODE software that resolves a large set of highly stiff equations. To incorporate a piston boundary condition, a coordinate transformation is introduced that maps the computational domain to a fixed space.<sup>28</sup> Boundary motion appears explicitly in the conservation equations as grid convective terms. Unphysical numerical dispersion in the hydrodynamic calculations is prevented using a minimal amount of numerical viscosity incorporated such that numerical truncation and smearing are greatly reduced with grid refinement. An adaptive gridding scheme enhances the accuracy of the numerical solutions by placing fine meshes in regions of extreme gradients. With the adaptive meshing, 50 to 200 computational nodes with eight levels of refinement (each level producing finer meshing) is sufficient for numerical accuracy.

## LOW VELOCITY IMPACT OF GRANULAR ENERGETIC MATERIALS

In this section, we use our multiphase reactive flow model to analyze the piston-impact experiments of Sandusky and co-workers.<sup>4,5</sup> Low amplitude impact conditions, similar to those experienced during a DDT event, were investigated using flash X-rays of embedded tracers and probed with high-speed photography, ionization and self-shortening

Table 1. Thermophysical and Material Property Data

Variable [cgs units]	TS3659	WC140	HMX
$d_p[\mu\text{m}]$	434	411	150
$\phi_s^0$	0.60	0.60	0.73
$\rho_s^0[\text{g}/\text{cm}^3]$	1.62	1.65	1.90
$c_v^s[\text{erg}/\text{g}^\circ\text{K}]$	$1.0 \times 10^7$	$1.0 \times 10^7$	$1.5 \times 10^7$
$\mu_c[\text{g}/\text{cm}^3\text{s}]$	$5.0 \times 10^2$	$5.0 \times 10^2$	$1.0 \times 10^3$
$T^*[\text{K}]$	460.0	460.0	550.0
$k_s[\text{erg}/\text{g}^\circ\text{K}]$	$1.0 \times 10^4$	$1.0 \times 10^4$	$2.3 \times 10^4$
$n$	0.86	0.74	1.0
$a[\text{cm}/\text{s MPa}^n]$	0.247	0.306	0.123
$b[\text{s}^{-1}\text{MPa}^{-2}]$	0.012	0.022	0.018
$\Delta E_R[\text{erg}/\text{g}]$	$4.62 \times 10^{10}$	$3.84 \times 10^{10}$	$7.91 \times 10^{10}$
$Q^*[\text{erg}/\text{g}]$	$0.4 \times 10^{10}$	$0.4 \times 10^{10}$	$0.4 \times 10^{10}$

probes, piezoelectric transducers, and microwave interferometry. Determination of compaction particle velocities, wave characteristics, and wall pressure histories at several locations provide detailed information about the convective and compressive combustion of several confined granular materials; Class D HMX (unstressed average particle diameter  $\sim 870 \mu\text{m}$ ), and ball propellants TS3659 (79.9 percent NC/21.6 percent NG), WC231 (74.8 percent NC/25.2 percent NG) and WC140 (98 percent NC). Listed in Table 1 are the material properties and combustion parameters for these materials (all transport data are given in Reference 8).

As observed, low-velocity impact produces reaction due to the generation of 'hot spots' during compaction; however, there is a delay time between impact and the detection of intense reaction. After the onset of reaction, the observed growth varied significantly depending on the impact velocity, the confinement, and the run distance. In the first

comparison of calculation and experimental observation, granular HMX is examined. In quasi-static loading measurements of Class D HMX, widespread particle fracture is known to occur<sup>17</sup> and unpressed particle size (nominally having a 700-800  $\mu\text{m}$  mean particle diameter) is not an appropriate material characterization of dynamically compacted HMX. Therefore, we use a modified HMX particle diameter of  $\sim 150 \mu\text{m}$  in the reactive flow calculations. Figure 1 displays the observed compaction and burn front trajectories for an impact velocity of 98 m/s in 73 percent dense Class D HMX. Calculation of this loading condition is shown in Figure 2 as time and distance profiles of solid phase pressure. After impact, a shock-like compaction wave forms that travels into the granular bed at a speed of 430 m/s. After a delay of  $\sim 100 \mu\text{s}$ , chemical energy is released in the reaction gases produced by the 'hot-spots.' A secondary combustion front then forms and a  $\sim 3$  kbar shock travels at 760 m/s toward the primary compaction front. When this pressure wave reaches the compaction front, its

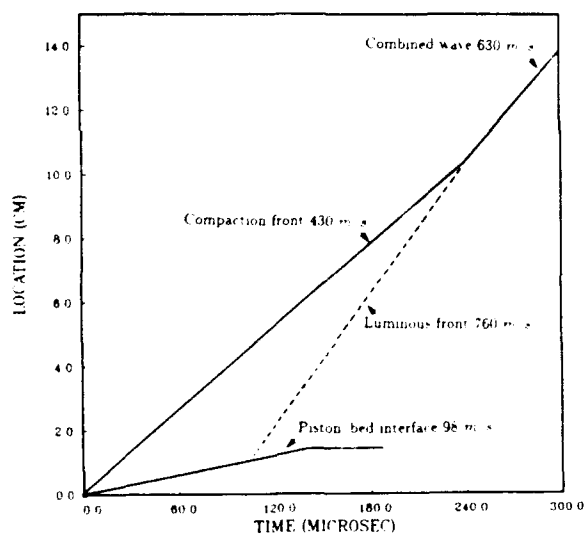


Figure 1. Distance-Time Experimental Data for an Impact of 98 m/s on 73 Percent TMD HMX

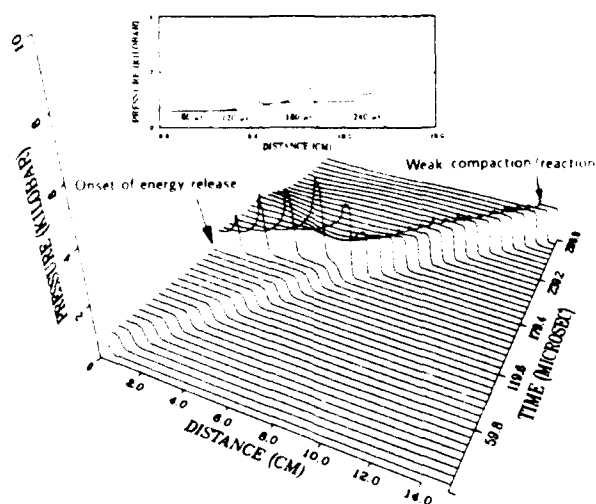


Figure 2. Calculated Solid Phase Pressure Profiles After Impact at 98 m/s

amplitude rapidly decays due to the loss of the gas phase pressurization in the compacted mixture (the loss of pressurization is due to the venting into undisturbed material). After these waves coalesce, a steady low velocity combustion wave propagates the remaining length of the granular bed at a speed of  $\sim 600$  m/s. Solid volume fraction wave profiles are shown in Figure 3. Compaction waves with finite wave front thickness of  $\sim 2$  mm are supported by a small amount of solid-phase

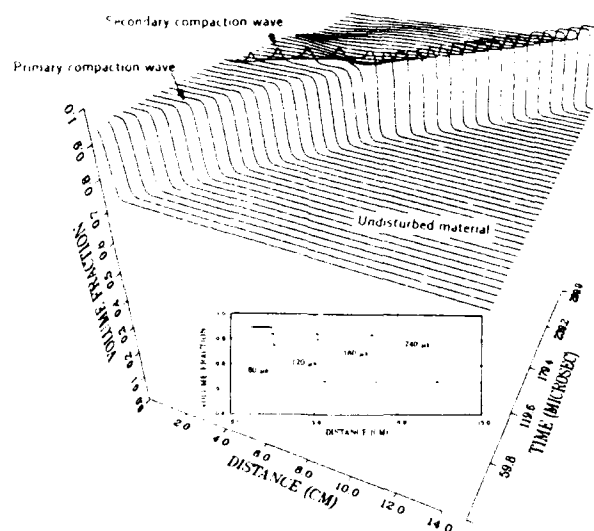


Figure 3. Solid Phase Volume Fraction Profiles after Impact at 98 m/s

decomposition. Grain surface temperatures are calculated to be below the temperature needed to initiate grain burning.

At an impact velocity of 160 m/s, the compaction front is luminous, indicating the presence of 'hot-spot' decomposition very near the front as shown in Figure 4. Figure 5 displays the transient pressure wave profiles calculated for this impact condition. 'Hot-spot' initiation occurs quickly after impact and the ignition locus follows the compaction wave front. Initially, combustion assists the piston to produce a compaction wave with a speed of  $\sim 800$  m/s and, after 20  $\mu$ s, grain surface temperatures indicate that grain burning is underway. Consistent with the experimental observation,<sup>4</sup> grain burning occurs for a duration of  $\sim 10$   $\mu$ s, whereupon at a distance of 5 cm the transition to detonation takes place.

In the series of experiments investigating dynamic compaction of nitrocellulose-based ball propellants, the reactive wave fields are probed using microwave interferometry. Wall pressure gauges provide additional information on the structure of the compaction and reactive pressure waves. In the calculations, wall pressures are estimated using the radial mixture stress defined by

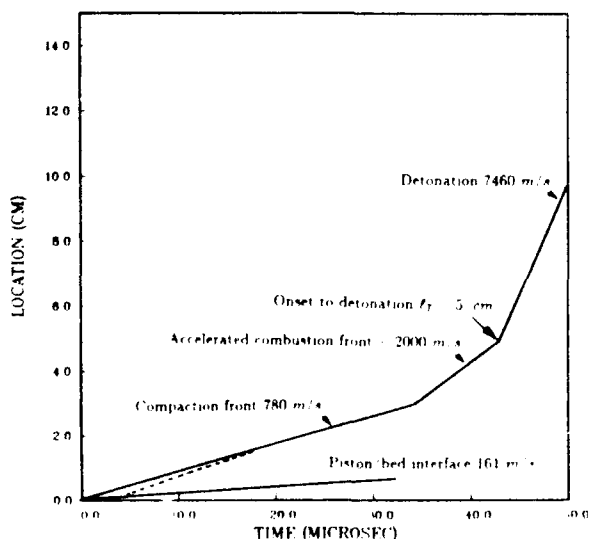


Figure 4. Distance-Time Experimental Data for an Impact of 161 m/s on 73 Percent TMD HMX

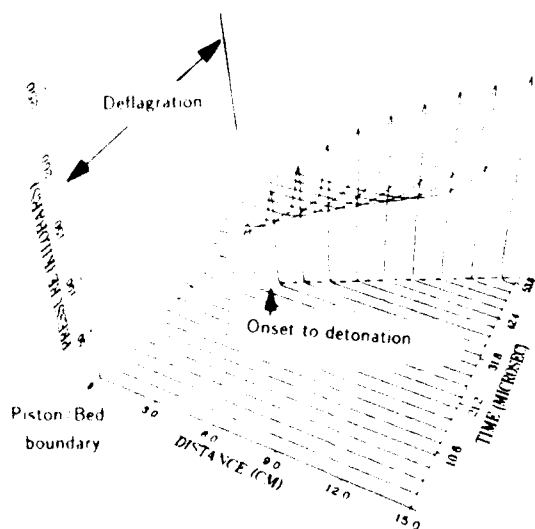


Figure 5. Solid Phase Pressure Profiles After Impact of 161 m/s

Kooker<sup>29</sup> incorporating the quasi-static axial and radial stress measurements of Campbell, et al.<sup>30</sup> Shown in Figure 6 are the distance-time trajectories of the waves induced by 192 m/s impact on 60 percent TMD TS3659. The compaction wave trajectory, measured by ionization pins,<sup>5</sup> is superimposed over the adaptive nodal meshing. In the adaptive calculations, closely-spaced node clusters indicate regions of high gradients, hence, the

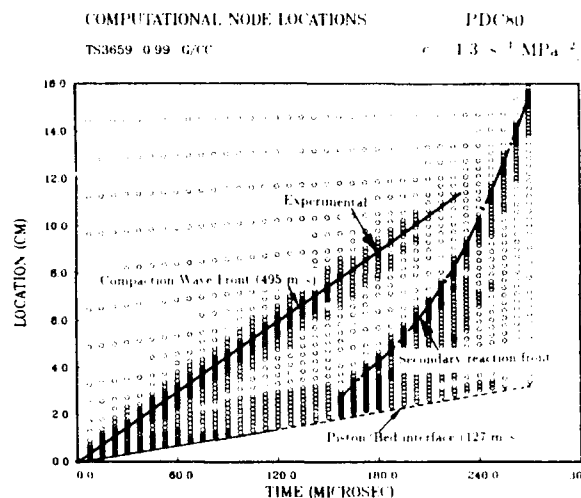


Figure 6. Transient Variation of the Computational Nodes that Follow Compaction and Reaction Wave Fronts. Overlaid is the observed compaction wave front for test PDC80.

compaction and reactive waves can be clearly identified. As observed, piston impact produces a compaction wave that travels in the bed at 495 m/s. Following a delay of  $\sim 150 \mu\text{s}$ , energy release in the 'hot-spot' reaction products within the 80 percent TMD compacted material supports a secondary wave that further compresses the reactant to total pore closure. Rapid heat transfer initiates grain burning and the two-phase combustion wave accelerates toward the primary compaction wave. Coalescence of the waves produces an abrupt change in the flame speed to  $\sim 2000 \text{ m/s}$ . (In this experiment, the length of confinement was 10 cm so the merging of the reactive and compaction waves could not be elucidated.) Included in these experiments are wall pressure gauges located at 3.81 and 7.62 cm from initial impact. Figure 7 shows a comparison of experimental and calculated wall pressures during dynamic compaction and combustion. As seen in this figure, predicted wall pressures are in reasonable agreement with experimental measurement. The slight drop in observed pressure following compaction is apparently due to the deceleration of the impacted piston.

Test PDC81 examines a higher impact condition on the double-based ball propellant

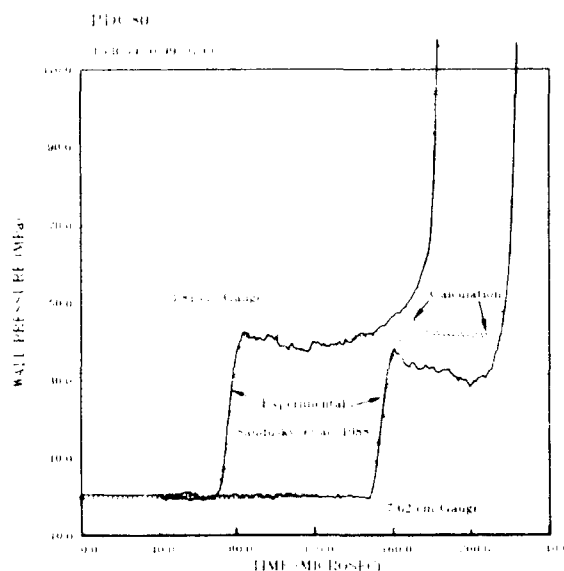


Figure 7. Comparison of Calculated and Measured Wall Pressures at 3.81 cm and 7.62 cm from Impact in Test PDC80

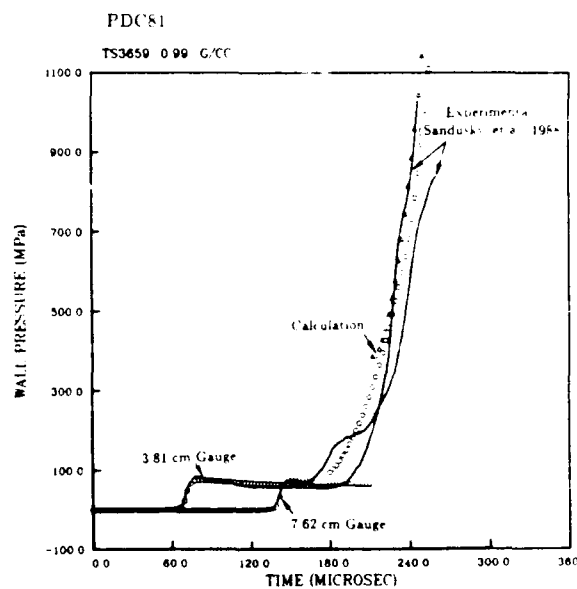


Figure 9. Comparison of Calculated and Measured Wall Pressures in Test PDC81

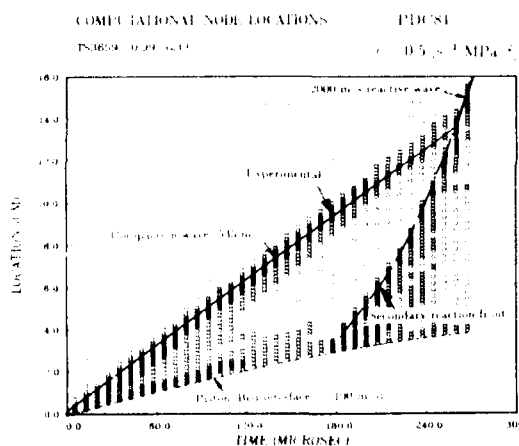


Figure 8. Wave Trajectories Followed by the Adaptive Nodes. Microwave interferometric data is overlaid for comparison. Note the abrupt change in wave speed at time of  $\sim 240 \mu s$ .

TS3659 held in a steel confinement. Measurement of the transient piston velocity indicates significant piston deceleration after impact. The calculated and experimental wave trajectories are displayed in the adaptive node plot of Figure 8. For this case, impact produces a primary compaction wave with a speed of 535 m/s and after 180  $\mu s$ , energy release triggers the secondary wave within the 90 percent TMD compacted material. When

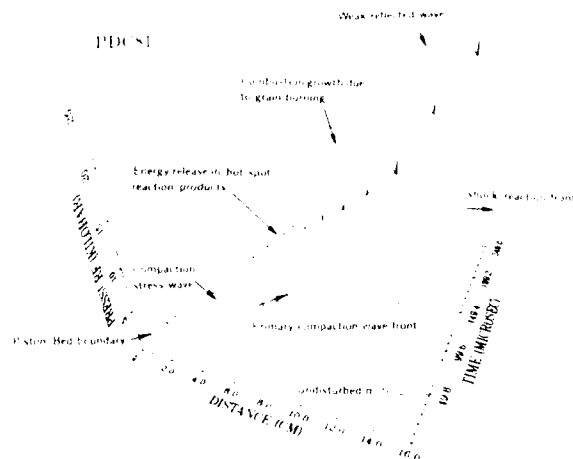


Figure 10. Calculated Mixture Pressure Profiles after Impact in TS3659 Ball Propellant in Test PDC81

these waves coalesce, the reactive wave speed changes to  $\sim 2000$  m/s consistent with the microwave interferometric data. Figure 9 shows a comparison of calculated and measured wall stress. After 180  $\mu s$ , rapid pressure growth occurs due to total pore closure ahead of the burn front. Figures 10 and 11 display the time and space evolution of mixture pressure and solid volume fraction for this loading condition. All wave features can be clearly identified.



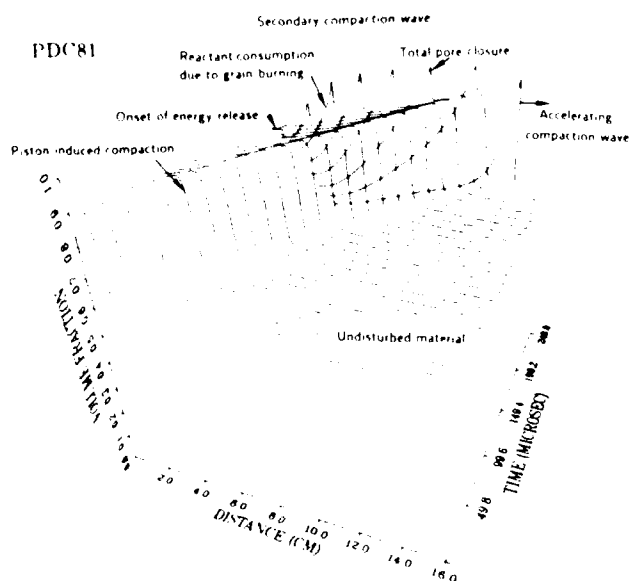


Figure 11. Calculated Solid Phase Volume Fraction Profiles after Impact in Test PDC81. Note the development of the secondary compaction wave that produces total pore closure.

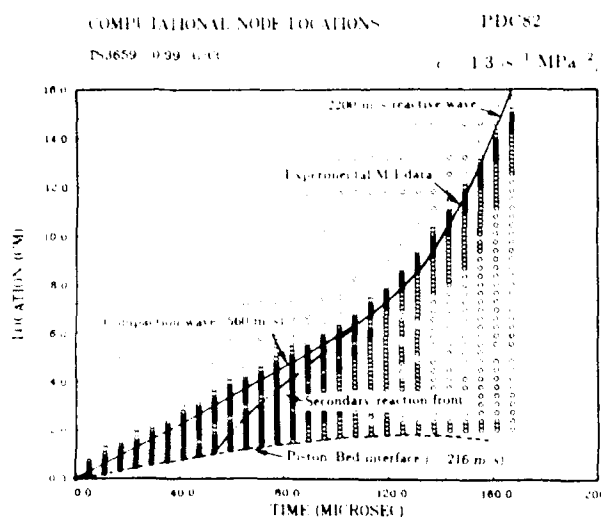


Figure 12. Wave Trajectories Followed by the Adaptive Nodes in Test PDC82. Microwave interferometric data is superimposed.

At a higher impact velocity of 216 m/s in test PDC82, piston impact produces compaction to 95 percent TMD and a deflagration front is promptly initiated leading to accelerated burning. Figure 12 displays the calculated and experimental wave trajectories. As experimentally observed, delayed reaction

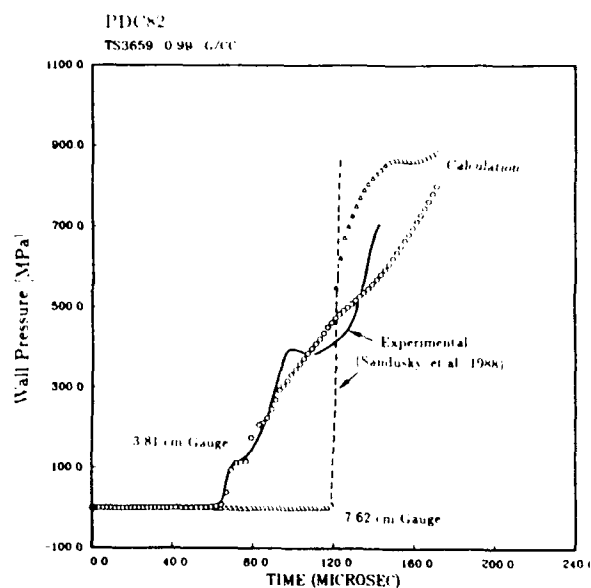


Figure 13. Comparison of Calculated and Measured Wall Pressures in Test PDC82

occurs 60  $\mu$ s after impact and an accelerated combustion wave coalesces with the primary compaction wave at a distance 7 cm from initial impact at a time of  $\sim 120 \mu$ s. The radial stress measurements and calculations are compared in Figure 13. Calculations indicate that energy release in the 'hot spot' decomposition products requires additional heat up time before the onset of grain burning seen as a 'plateau' in the pressure history of the 3.81 cm gauge 100  $\mu$ s after impact.

In a piston impact experiment on 50 percent WC231, only wave trajectory information was obtained. All combustion and material property data were assumed to be equivalent to TS3659 with modification of particle size to  $d_p = 790 \mu$ m. Figure 14 shows the experimental waves observed for a 183 m/s impact condition. Calculation of this impact condition is shown in Figure 15 displaying the transient pressure wave profiles. For this case, a 85 percent TMD compaction wave evolves after impact and delayed energy release after  $\sim 120 \mu$ s leads to a combustion event similar to that observed for TS3659. Merging of the waves produces a reactive shock wave that travels at a speed of 1300 m/s.

Finally, impact of the single-based ball propellant WC140, designated as test M30, is

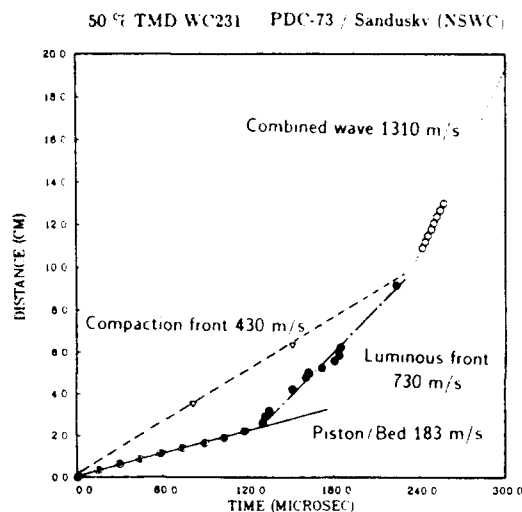


Figure 14. Distance-Time Trajectories of Impact at 183 m/s on 50 Percent TMD WC231

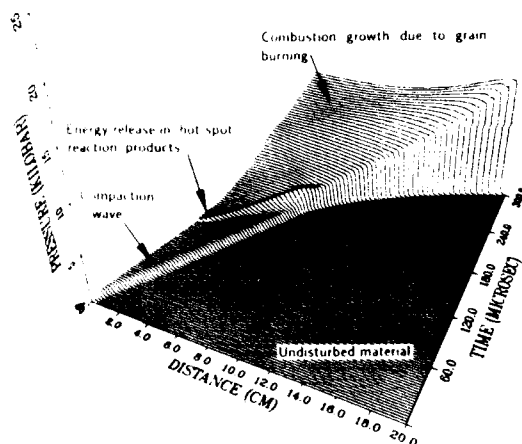


Figure 15. Calculated Mixture Pressure Profiles for a 183 m/s Impact on WC231

considered. The first 100  $\mu$ s of piston velocity were measured and piston deceleration was observed. The wave trajectories are shown in the adaptive node plot of Figure 16. After 240  $\mu$ s, a secondary compaction/reaction wave appears and the microwave interferometry, monitoring the delayed wave, confirms a wave speed of  $\sim 1100$  m/s consistent with that calculated.<sup>31</sup> The wall pressure comparisons are shown in Figure 17. For this low impact condition, significant decay in wall

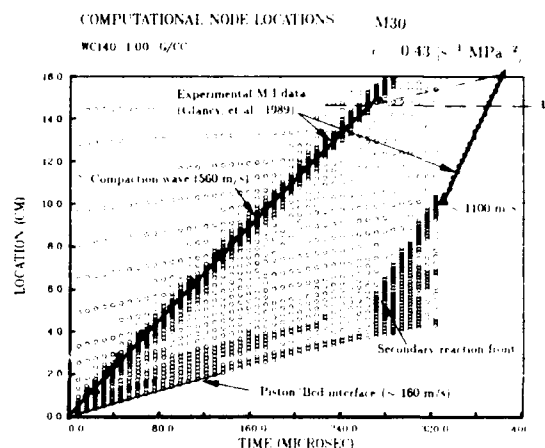


Figure 16. Wave Trajectories Followed by the Adaptive Nodes and the Microwave Interferometric Data for Impact on WC140. Note that the calculated secondary wave is consistent with experimental observation.

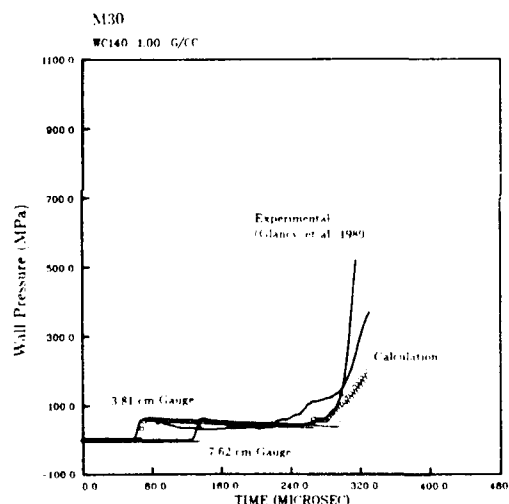


Figure 17. Comparison of Calculated and Measured Wall Pressures for a 160 m/s Impact on WC140

pressure following compaction was observed prior to the onset of energy release. Although rarefaction is a result of deceleration of the piston, the unloading of the pressure within the compaction wave is greater than calculated. This behavior may be due to hysteresis of the loading vs. unloading intra-granular stress that is not treated in the calculations. The reduced pressures during compaction appears to support the less reactive nature of WC140.

## SUMMARY

This study has applied a multiphase flow description to treat the initiation and reactive growth of dynamically compacted granulated energetic materials. The multiphase reactive flow is described by a non-equilibrium continuum theory of mixtures formulated to include the compressibility of all phases and compaction behavior. A phenomenological model has been formulated within the context of the model to describe the 'hot-spot' thermal decomposition and grain burning.

As a general feature of the theoretical calculations, piston impact produces a shock-like compaction wave and a small fraction of the compacted reactant decomposes near the front. Subsequent energy release by the 'hot-spot' decomposition products triggers a pressure disturbance that supports a secondary compaction wave. Additional pore-collapse takes place (sometimes to total pore closure) and rapid pressurization occurs due to the inertial confinement of the compacted reactant. With sufficient energy release and heat transfer, grain burning takes place within the compacted region whereupon high specific surface area of the granular reactant leads to rapid burning and the formation of additional compressive waves within the compacted reactant. A delayed reactive wave overtakes the primary compaction wave and combustion spreads rapidly into undisturbed material, provided that inertial confinement of the unreacted material is sufficient to sustain accelerated combustion. Similar reaction/compaction wave behavior is described by Kooker's shock-wave model.<sup>32</sup>

Although the presented multiphase combustion model is sufficient to replicate the experimental data, this model is far from complete due to the complex nature of the processes involved. More fundamental micro-mechanical and combustion models<sup>33</sup> are warranted. Clearly, better experimental insights into 'hot-spot' temperatures, number density distributions, and volumes are required for detailed models of the compressive reaction induced by compaction.

## ACKNOWLEDGEMENT

This work was performed at Sandia National Laboratories and was supported by the U. S. Department of Energy under contract number DE-AC04-76DP00789.

## REFERENCES

1. Bernecker, R. R.; Sandusky, H. W.; and Clairmont, A. R., "Deflagration-to-Detonation Transition Studies of Porous Explosive Charges in Plastic Tubes," *Seventh Symposium (International) on Detonation*, NSWC MP 82-334, 1981, pp. 119-138.
2. Bernecker, R. R.; Sandusky, H. W.; and Clairmont, A. R., "Deflagration-to-Detonation Transition (DDT) Studies of a Double-Based Propellant," *Eighth Symposium (International) on Detonation*, NSWC MP 86-194, 1985, pp. 658-668.
3. Green, L. G.; James, E.; Lee, E. L.; Chambers, E. S.; Tarver, C. M.; Westmoreland, C.; Weston, A.; and Brown, B., "Delayed Detonation in Propellants from Low Velocity Impact," *Seventh Symposium (International) on Detonation*, NSWC MP 82-334, 1981, pp. 256-264.
4. Sandusky, H. W. and Bernecker, R. R., "Compressive Reaction in Porous Beds of Energetic Materials," *Eighth Symposium (International) on Detonation*, NSWC MP 86-194, 1985, pp. 881-891.
5. Sandusky, H. W.; Glancy, B. C.; Campbell, R. L.; Krall, A. D.; Elban, W. L.; and Coyne, P. J., "Compaction and Compressive Reaction Studies for a Spherical, Double-Base Ball Propellant," 1988 JANNAF Combustion Meeting, Huntsville, AL, Oct 1988.
6. Kooker, D. E., "A Reactive Shock Wave Model for Compaction Waves in Granular Energetic Materials," BRL-TR-2945, U.S. Army Ballistic Research Laboratory, Nov 1988.
7. McAfee, J. M. and Campbell, A. W., "An Experimental Study of the Deflagration to Detonation Transition in Heavily Confined HMX," 1986 JANNAF

- Propulsion Systems Meeting, CPIA Pub. 446, Vol. 1, 1986, pp. 163-186.
8. Baer, M. R. and Nunziato, J. W., "A Two-Phase Mixture Theory for Deflagration-to-Detonation Transition in Reactive Granular Materials," *International J. Multiphase Flow*, Vol. 12, 1986, pp. 861-889.
  9. Butler, P. B. and Krier, H., "Analysis of Deflagration-to-Detonation Transition in High-Energy Propellants," *Combustion and Flame*, Vol. 63, 1986, pp. 31-48.
  10. Kooker, D. E. and Anderson, R. D., "A Mechanism for the Burning Rate of High Density, Porous Energetic Materials," *Seventh Symposium (International) on Detonation*, NSWC MP 82-334, 1981, pp. 198-215.
  11. Kim, K., "Numerical Simulation of Convective Combustion of Ball Powders in Strong Confinement," *AIAA J.*, Vol. 22, No. 6, 1984, pp. 793-796.
  12. *Eighth Symposium (International) on Detonation*, NSWC MP 86-194, 1985, see papers by Weston and Lee, Price and Boggs, and Verbeek.
  13. Lee, E.; Hornig, H. C.; and Kury, J. W., "Adiabatic Expansion of High Explosive Detonation Products," LLNL UCRL-50422, Lawrence Livermore National Laboratory, 1968.
  14. Sheffield, S. A.; Mitchell, D. E.; and Hayes, D. B., "An Equation of State and Chemical Kinetics for Hexanitrostilbene (HNS) Explosive," *Sixth Symposium (International) on Detonation*, ACR-221, 1977, pp. 748-754.
  15. Olinger, B.; Roof, B.; and Cady, H., "The Linear and Volume Compression of  $\beta$ -HMX and RDX to 9 GPa," LA-UR-78-1424, Los Alamos National Laboratory, 1978.
  16. Verentennikov, V. A.; Dremin, A. N.; and Shvedov, K. K., "Shock Compressibility of NB Powder in the Porous and Non-porous States," *Fizika Goreniya i Vzryva*, Vol. 5, No. 4, 1969, pp. 499-505.
  17. Elban, W. L. and Chiarito, M. A., "Quasi-Static Compaction Study of Coarse HMX Explosive," *Powder Technology*, Vol. 46, 1986, pp. 181-193.
  18. Elban, W. L., "Quasi-Static Compaction Studies for DDT Investigations, Ball Propellants," *Propellants, Explosives & Pyrotechnics*, Vol. 9, 1984, pp. 119-129.
  19. Sandusky, H. W. and Liddiard, T. P., "Dynamic Compaction of Porous Beds," NSWC TR-83-246, Naval Surface Weapons Center, 1985.
  20. Boggs, T. L., "The Thermal Behavior of Cyclotrimethylenetrinitramine (RDX) and Cyclotetramethylenetetranitramine (HMX)," *Fundamentals of Solid-Propellant Combustion*, ed. K. Kou and M. Summerfield, Progress in Astronautics and Aeronautics, Vol. 90, 1984, pp. 121-175.
  21. Kooker, D. E., "A Workshop Summary of Model Predictions of the Piston-Driven-Compaction Experiment," 1989 JANNAF Propulsion Systems Hazards Meeting, San Antonio, TX, Feb 1989 (and references therein).
  22. Dobratz, B. M., "LLNL Explosives Handbook: Properties of Chemical Explosives and Chemical Simulants," UCRL-52997, 1981.
  23. Fifer, R. A., "Chemistry of Nitrate Ester and Nitramine Propellants," *Fundamentals of Solid-Propellant Combustion*, ed. K. Kou and M. Summerfield, Progress in Astronautics and Aeronautics, Vol. 90, 1984, pp. 177-237.
  24. Baer, M. R., "A Model for Interface Temperature Induced by Convective Heat Transfer in Porous Materials," SAND88-1073, Sandia National Laboratories, 1989.
  25. Baer M. R.; Benner, R. E.; Gross, R. J.; and Nunziato, J. W., "Modeling and Computation of Deflagration-to-Detonation Transition (DDT) in Reactive Granular Materials," *Lectures in Applied Mathematics*, American Mathematical Society, Vol. 24, 1986, pp. 479-498.
  26. Verbeek, H. J., "Modelling of DDT in Granular Explosives," *Eighth*

*Symposium (International) on Detonation*, NSWC MP 86-194, 1985, pp. 669-677.

27. Embid, P. F. and Baer, M. R., "Mathematical Analysis of a Two-Phase Model for Reactive Granular Material," SAND88-3302, Sandia National Laboratories, 1989.
28. Baer, M. R., "Numerical Studies of Dynamic Compaction of Inert and Energetic Granular Materials," *J. of Applied Mechanics*, Vol. 55, 1988, pp. 36-43.
29. Kooker, D. E., "Predictions for the Piston-Driven Compaction Experiment Based on a Transient Shock Wave Model," 1989 JANNAF Propulsion Systems Hazards Meeting, San Antonio, TX, Feb 1989.
30. Campbell, R. L.; Elban, W. L.; and Coyne, P. J., "Side-Wall Pressure Measurements in Quasi-static Compaction of Porous Beds of HMX Powders and ABL 2523 Casting Powder," *Proceedings of 1988 Propulsion System Hazards Subcommittee Meeting*, CPIA Publ. 477, Vol. I, 1988.
31. Glancy, B. C.; Sandusky, H. W.; and Miller, P. J., "Dynamic Compaction and Compressive Reaction Studies for Single and Double-based Ball Propellants," *Ninth Symposium (International) on Detonation*, Portland, OR, 1989.
32. Kooker, D. E., "Collision of Reactive Compaction/Shock Waves in Granular Energetic Materials," *Proceeding of 1988 JANNAF Propulsion Systems Hazards Meeting*, CPIA 477, Vol. I, 1988, pp. 17-36.
33. Nunziato, J. W. and Baer, M. R., "A Microscopic Approach to the Initiation and Detonation of Condensed-Phase Energetic Mixtures," *Journal de Physique*, Colloque C4, No. 9, Tome 48, Sep 1987, pp. 67-83.

## DISCUSSION

A. VAN DER STEEN,  
Prins Maurits Laboratory TNO  
Rijswijk, The Netherlands

In your evaluations, you use an average particle size of 150  $\mu\text{m}$  for HMX. Spear and

Nanut show, in a different presentation at this Symposium, that the particle size distribution is hardly affected by compressing the explosive to different densities. Could you please comment on this?

## REPLY BY M. R. BAER AND J. W. NUNZIATO

Elban and Chiarito (Reference 17) have provided photographic evidence that widespread fracture occurs during quasi-static compaction of coarse HMX—even at applied stresses as low as  $\sim 1$  MPa. Furthermore, low density coarse material (unpressed particle size  $\sim 900$   $\mu\text{m}$ ) is observed to break into fine particles during compaction until the density is pressed to  $\sim 85$  percent TMD whereupon material agglomeration appears to suppress continued fracture. Spear and Nanut (this symposium) examine pressed materials that are above  $\sim 85$  percent TMD, thus material fracture (and subsequent modified particle size distribution) is expected to be a minor effect consistent with Elban and Chiarito's observations.

The stresses supported by the granular material during dynamic compaction far exceed the 1 MPa threshold and sliding/tumbling motions during dynamic compaction are likely to enhance breakage of the granular HMX. Thus, for low density granular HMX and other brittle granular materials unpressed particle size is not an appropriate material characterization. In our modeling of the HMX impact experiments, one of the most important influences of particle size is linked to grain burning. To simulate the 160 m/s impact condition, a particle size of  $\sim 150$   $\mu\text{m}$  is necessary to produce the onset and growth of combustion consistent with that observed. Since grain burning does not appear to occur at the 100 m/s impact condition, the reduced particle size has a minor effect. Clearly, mechanically and thermally-induced material fracture remains a DDT model uncertainty and continued studies are warranted.

# COMPACTION WAVE ACCELERATION IN GRANULAR ENERGETIC MATERIAL: SIMULATION WITH A REACTIVE SHOCK WAVE MODEL

Douglas E. Kooker  
U.S. Army Ballistic Research Laboratory  
Aberdeen Proving Ground, Maryland 21005-5066

*In studies of granular material, data from both the piston-driven-compaction (PDC) experiment and the closed-pipe deflagration-to-detonation transition (DDT) experiments displayed in distance-time plots appear to show abrupt changes in propagation speed of the luminous front as the wave accelerates to a reactive shock wave (1-3 km/s) and then to a detonation wave. In addition, Sandusky's (NSWC) PDC data on time to onset of compressive reaction includes the observation that the first appearance of flame usually occurs in material adjacent to the projectile face. Vigorous combustion in this region will generate and support a stress wave system which must propagate into material already compressed by the initial compaction front. It is suggested that collision of these two waves may "trigger" an increase in reactivity. A simple quasi-steady analysis which represents compaction fronts as reactive shock waves demonstrates that modest increases in reactivity induced by the collision could produce an altered wave pattern similar to those seen in the experiments.*

## INTRODUCTION

The transition to detonation in confined granular energetic material involves a complicated sequence of events which are influenced by strength of confinement, shock sensitivity, particle size, permeability, and energy release rate during combustion. Special laboratory experiments on a number of different materials have provided many important observations about this complex process. The deflagration-to-detonation transition (DDT) studies of Bernecker and Price,<sup>1-3</sup> Price and Bernecker,<sup>4</sup> and Bernecker et al.,<sup>5-8</sup> the combustion-driven-piston experiments of Campbell,<sup>9</sup> McAfee and Campbell,<sup>10</sup> McAfee et al.,<sup>11</sup> and the shock-to-detonation transition (SDT) or impact studies of Sandusky et al.,<sup>12-15</sup> Green et al.,<sup>16</sup> and Dick<sup>17,18</sup> have all contributed to our understanding of the behavior. The data seem to suggest that the latter stages of the transition are essentially independent of the initial stimulus, whether from impact or from hot gas

ignition. Successful transition to detonation appears to require formation and maintenance of a strong compressive wave which ignites unburned material in its path. The present theoretical study is directed toward an interpretation of this wave, before full detonation has been established.

It is common practice to display data from the piston-driven-compaction (PDC) experiment (Sandusky/NSWC), the DDT experiments (e.g., Bernecker/NSWC) and the combustion-driven piston experiment (McAfee / LANL) in "distance-time" plots. In many cases, these X-T plots appear to show abrupt changes in propagation speed as the compaction wave accelerates to a reactive shock wave (speeds in the range of 1-3 km/s) and then to a detonation wave. Furthermore, Bernecker's<sup>8</sup> DDT experiment with TS-3659 double-base ball propellant shows the presence of a rearward propagating compressive wave, i.e., a wave which propagates back into material which is already burning.

The origin of this wave seems to be in the vicinity of an increase in speed of a strong compaction wave.

With the PDC experiment, Sandusky<sup>12,14</sup> has observed that the time to the onset of compressive reaction correlates as " $t^2\Delta t = \text{constant}$ ," where  $t$  is a measure of the stress state in the solid phase and  $\Delta t$  is the time interval after impact. Sandusky notes that the first appearance of "flame" usually occurs in material adjacent to the projectile face. Vigorous combustion in this region will generate and support a stress wave system which must propagate into material already compressed by the initial compaction wave. The objective of the present work is to determine if collision of this wave system with the leading compaction front could produce an altered wave pattern responsible for the abrupt change in speed during acceleration.

## MODEL DEVELOPMENT

The intention here is to deliberately pose the simplest possible model which might identify controlling mechanisms. Such an attempt is always haunted by the prospect of neglecting an important part of the physics and thus fatally distorting the predictions. Although the results should be interpreted with due caution, simplicity sometimes provides important insight.

### Compaction Waves

The Reactive Shock Wave Model<sup>19</sup> of compaction waves in confined granular energetic material evolved from this philosophy. The analysis intentionally neglects all "loss" mechanisms as well as rate-dependent material processes. Resistance to porosity change is assumed vanishingly small, i.e., the compressed aggregate instantaneously adjusts to its "equilibrium" stress state. It is assumed that both phases travel at the same velocity in the compressed aggregate, which eliminates gas/particle drag. Inter phase heat transfer is also neglected, although the two phases may exist at different temperatures. The heat transfer problem is addressed separately in Reference 19, and this artificial decoupling is removed in Reference 20. In the present analysis, combustion occurs only within the wave

front itself. Friction between the compressed aggregate and the lateral confining boundary is ignored. Removing all rate-dependent processes form the general equation system<sup>21</sup> means that compaction waves in granular material are represented as infinitesimally thin shock waves. Note that constant-velocity impact generates only steady wave propagation; there are no transients.

Compaction waves (shock waves) in the present model are not necessarily inert. The mechanism responsible for wave-induced reaction of some portion of the solid material is undoubtedly related to mechanical work done at high strain rate. In a granular aggregate, a description of this process involves extremely complex physics and is presently unavailable. Of course, a shock wave model (zero thickness, and infinite strain rate) could not predict the strain-rate history imposed on material which passes through the compaction wave. To circumvent this problem, the analysis assumes that a prescribed fraction of the solid material reacts within the shock front to form gaseous combustion products immediately downstream. Outside the shock front, reaction ceases. In reality, reaction probably does fail when the system is near the limiting condition. For those systems which exceed this limit, it is more likely that reaction "falters" during an induction period and then resumes.

Predictions from this model have been compared in Reference 19 to Sandusky's<sup>12,14</sup> data from the PDC and CGC experiments. A majority of experimental compaction wave speeds are greater than the model predictions for an inert compaction shock wave. Since loss mechanisms have been ignored, something has to be "driving" these waves. In principle, rate-dependent resistance to dynamic compaction of the granular aggregate could create an increased stress state which would support the higher speed; however, rate-dependent compaction models<sup>21,22</sup> suggest that the magnitude of relaxation time required to maintain this condition would produce excessively thick compaction waves (not indicated by the experiment). The other possibility is wave-induced reaction involving a small fraction of solid material (also postulated in Dick<sup>18</sup>). Since the aggregate is simultaneously being

compressed the newly created combustion gases released into the available porosity of the aggregate are trapped and will exert a pressure. This gas pressure increases the "stiffness" of the two-phase aggregate, which in turn supports an increased compaction wave speed. Computations show that wave-induced reaction (which releases the total heat of reaction) of a *few tenths of one percent* of the solid phase creates enough gas pressure to stiffen the aggregate and enable it to support the compaction wave speeds measured in the experiments.

### Collision of Compaction Waves

Simulation of the collision between two compaction/shock waves of the same family (the weaker wave is overtaken from behind) employs the reactive equilibrium shock wave model discussed above. The collision model follows from a simple idea. To begin, consider a piston in contact with a quiescent inert rate-independent medium as sketched in Figure 1. At time zero, the piston assumes a constant velocity. A plot of this event in "Distance-Time" plane shows a constant velocity shock wave running ahead of the piston path.

Note the direct analogy of this wave diagram with the flow field produced by steady two-dimensional supersonic flow over a wedge

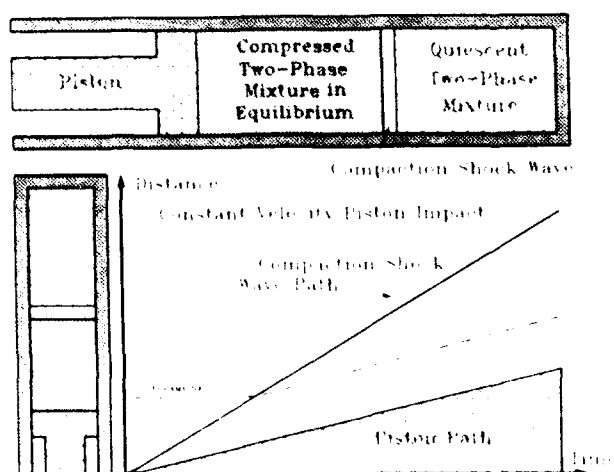


Figure 1. Distance-Time Plot of Constant-Velocity-Piston Impact on a Quiescent Inert Rate-Independent Medium. Note analogy with steady two-dimensional supersonic flow over a wedge.

(i.e., the piston path). Focusing on the analogy with supersonic flow for a moment, imagine that the single wedge is replaced with a double wedge, i.e., the body has a second abrupt change in slope (see shaded region in Figure 2). Of course, this new slope change will create a second shock wave which eventually must collide with the leading shock wave. As illustrated in Figure 2 for a nonreacting medium, the collision produces a combined shock wave whose strength is intermediate between the strengths of the two waves attached to the body. A centered simple wave system (expansion fan) anchored at the collision point will attempt to equilibrate this pressure difference.

Of course, steady supersonic flow over a double wedge is not the problem of interest. However, application of this wave diagram to one-dimensional wave propagation requires an interpretation of the second increase in piston velocity. Once the projectile impacts the granular bed in the PDC experiment, it does not suddenly accelerate to an increased speed after a certain time interval. On the contrary, its velocity may begin to decrease. However, the onset of combustion of material adjacent to the piston face might generate a sudden increase in stress level which would have the same effect as an increase in piston velocity. Thus, the present model will employ an increase in

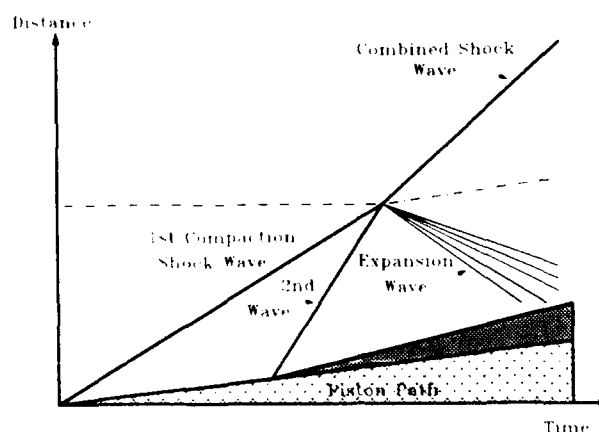


Figure 2. Distance-Time Plot of Double Impact of Piston (Two Abrupt Changes to Constant Velocity) on Quiescent Inert Rate-Independent Medium. Note analogy with steady two-dimensional supersonic flow over a double wedge.



piston velocity to *simulate* the effect of vigorous combustion which begins at the piston face, after a suitable delay time, and then propagates away from the piston into the compressed aggregate. Note that the combustion process which "begins" at the piston face is the onset of substantial burning in the aggregate, since in the Reactive Shock Wave Theory,<sup>19</sup> a small amount of the solid material could have already reacted within the initial compaction wave.

The wave diagram for a double impact shown in Figure 2 applies to an inert medium. If, however, the medium is reactive and shock waves are capable of inducing energy release, the wave pattern can easily be altered. In particular, if the combined shock wave induces a nominal increase in reactivity compared to the initial shock wave, this will raise the downstream mixture pressure (or stress level) enough to wipe out any expansion wave. Any further increase in reactivity will raise the mixture pressure such that a rearward propagating shock wave will appear in the location of the original expansion wave system, as illustrated in Figure 3. The dividing streamline (chain-dot line) which passes through the collision point becomes a contact discontinuity between the regions downstream of shock waves (3) and (4) (see Figure 3). A contact discontinuity separates two regions with different density and temperature, but particle velocity and mixture pressure must be equal. The physical meaning is the following. All the material lying above the contact discontinuity [closest to shock wave (4)] has been influenced only by shock wave (4); all the material lying below has been subjected to shock waves (1), (2), and (3). This contact discontinuity plays an important role in the examples to follow.

### Governing Equations

The problem to be solved is that posed in Figure 3. Both piston velocities are assumed constant. Since all rate processes have been removed from the equation system, each shock wave is quasi steady and travels at a constant velocity. Thus the solution can be found from a system of coupled "jump condition" equations. The model equations are based on the following assumptions.

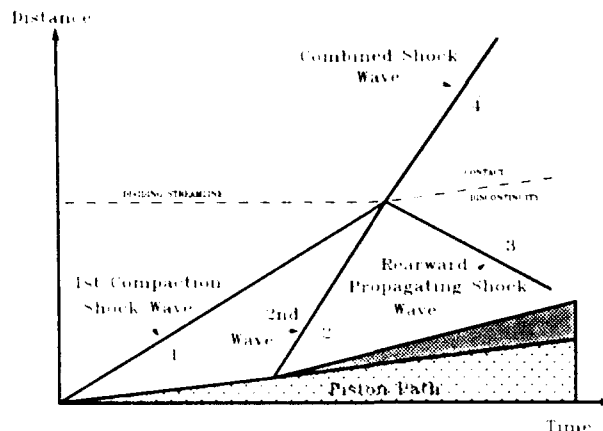


Figure 3. Possible Distance-Time Plot of Double Piston Impact on Quiescent Rate-Independent Reactive Medium

(a) The stress tensor of the compressed aggregate can be described as a pressure (deviator components are ignored).

(b) The two-phase mixture instantaneously adjusts to its equilibrium stress state (defined below).

(c) Wall friction between the compressed aggregate and the confining boundary is negligible.

(d) Behind the compaction shock wave, both phases travel at the same velocity. In addition, heat transfer between the phases as well as combustion is neglected.

(e) A specified fraction,  $\eta$ , of the granular solid material can react and form gas-phase combustion products (with a given energy release) during passage of the shock wave, i.e., shock induced reaction.

Although the eventual goal is to be able to predict the value of the important parameter  $\eta$ , at present its value must be specified. Thus the current analysis will be used to interpret experimental wave patterns, as opposed to predicting them. In several examples discussed here, the shock wave induced reaction releases the total heat of reaction of the energetic solid. However, in single- and double-base propellants, the available evidence suggests that

only a fraction of the total energy is released in this reaction (see Reference 20 and discussion below).

Define the variables:

- $\rho_s$  = density of solid = solid mass / solid volume
- $\rho_g$  = density of gas = gas mass / gas volume
- $\epsilon_s$  = solid volume fraction = solid volume / total volume
- $\epsilon_g$  = gas porosity =  $1 - \epsilon_s$
- $e_s$  = solid-phase internal energy per unit mass
- $e_g$  = gas phase internal energy per unit mass
- $P_s$  = pressure of the solid phase
- $P_g$  = pressure of the gas phase
- $v$  = velocity (by assumption, gas = solid velocity)
- $V_s$  = shock wave velocity
- $V_p$  = piston velocity
- $\eta$  = fraction of solid-phase mass flux entering the shock wave which is converted to gaseous combustion products.

The subscripts "u" and "d" represent -

- ( )<sub>u</sub> = properties upstream (in front) of the shock wave
  - ( )<sub>d</sub> = properties downstream of (behind) the shock wave
- and
- ( )<sub>i</sub> = pertains to the "i" shock wave

#### Balance of Mass / Solid Phase

$$\rho_{s_d} \epsilon_{s_d} (v_d - V_{s_i}) - (1 - \eta_i) \rho_{s_u} \epsilon_{s_u} (v_u - V_{s_i}) = 0 \quad (1)$$

#### Balance of Mass / Gas Phase

$$\rho_{g_d} (1 - \epsilon_{s_d}) (v_d - V_{s_i}) - \left[ \rho_{g_u} (1 - \epsilon_{s_u}) + \eta_i \rho_{s_u} \epsilon_{s_u} \right] (v_u - V_{s_i}) = 0 \quad (2)$$

#### Balance of Momentum / Mixture

$$P_{m_d} + \rho_{m_d} v_d (v_d - V_{s_i}) - P_{m_u} - \rho_{m_u} v_u (v_u - V_{s_i}) = 0 \quad (3)$$

where

$$P_m \equiv \epsilon_s P_s + (1 - \epsilon_s) P_g$$

$$\rho_m \equiv \epsilon_s \rho_s + (1 - \epsilon_s) \rho_g$$

#### Balance of Energy / Solid Phase

$$\begin{aligned} & \rho_{s_d} \epsilon_{s_d} (v_d - V_{s_i}) E_{s_d} + \epsilon_{s_d} P_{s_d} v_d \\ & - \rho_{s_u} \epsilon_{s_u} (v_u - V_{s_i}) E_{s_u} - \epsilon_{s_u} P_{s_u} v_u \\ & = -\eta_i \rho_{s_u} \epsilon_{s_u} (v_u - V_{s_i}) e_{s_u} \end{aligned} \quad (4)$$

#### Balance of Energy / Gas Phase

$$\begin{aligned} & \rho_{g_d} (1 - \epsilon_{s_d}) (v_d - V_{s_i}) E_{g_d} + (1 - \epsilon_{s_d}) P_{g_d} v_d \\ & - \rho_{g_u} (1 - \epsilon_{s_u}) (v_u - V_{s_i}) E_{g_u} - (1 - \epsilon_{s_u}) P_{g_u} v_u \\ & = \eta_i \rho_{s_u} \epsilon_{s_u} (v_u - V_{s_i}) e_{s_u} \end{aligned} \quad (5)$$

where

$$E_s \equiv e_s + (1/2) v^2$$

$$E_g \equiv e_g + (1/2) v^2$$

These equations are applied to the various shock waves in the following manner:

Wave	"u" / upstream	"d" / downstream	Constraint
1	quiescent (known)	1	$v_d = V_{p1}$
2	1 (as computed)	2	$v_d = V_{p2}$
4	quiescent (known)	4	$P_{m3} = P_{m4}$
3	2 (as computed)	3	$v_{d3} = v_{d4}$

where  $P_m$  is the mixture pressure defined in Equation (3). The solution procedure begins by specifying the piston speed at initial contact,  $V_{p1}$ , the time delay before the second impact, and the piston speed at the second impact,  $V_{p2}$ . Values of reactivity in both compaction/shock waves,  $\eta_1$  and  $\eta_2$ , must also be specified. The solution is then obtained sequentially in stages, as outlined in Reference 23. Computation time is less than one second on the Cray-2.

### Equilibrium Stress State

The model assumes that the state of stress in the compacted aggregate can be described as hydrostatic, i.e., deviator stress components are neglected. This mixture pressure,  $P_m$  [see Equation (3)], is a strong function of porosity (or solid volume fraction). Constitutive theory must supply prescriptions for  $P_s$  and  $P_g$ , as well as a methods to compute  $\epsilon_s$ . Thus the equation system must be supplemented by a phenomenological model of pore collapse or some other concept of porosity change in the aggregate. The present analysis employs a rate-independent expression which is a modified version of the radial force balance originally presented by Carroll and Holt<sup>24</sup> under quasi-static conditions. This equilibrium constraint on solid volume fraction is given by,

$$P_s(\rho_s, \epsilon_s) - P_g(\rho_g, \epsilon_g) = \beta_s(\epsilon_s) \quad (6)$$

where  $\beta_s$  is defined in Equation (9), and the root of Equation (6) determines the equilibrium value of solid volume fraction  $\epsilon_s$ . Under conditions of vigorous reaction when  $P_g$  attempts to exceed  $P_s$ ,  $\beta_s$  is set to zero and the mixture "unloads" to a fluidized bed.

Compressibility of the solid phase at TMD (theoretical maximum density) is predicted on the basis of an assumed linear path in the shock velocity/particle velocity plane. If the Hugoniot of the TMD solid is represented as

$$V_s = a_{sh} + A_{sh} u_s \quad (7)$$

the solid phase equation of state can be written<sup>25</sup>

$$\begin{aligned} P_s(\rho_s, \epsilon_s) = & \rho_{s_0} \Gamma_0 \left[ (\epsilon_s - \epsilon_{s_0}) / (R + 1) \right] \\ & + P_{s_0} [1 + \Gamma_0 R / (R + 1)] \\ & - (\rho_{s_0} a_{sh}^2 / 2) [2 + \Gamma_0 R / (R + 1)] R / (1 + A_{sh} R)^2 \end{aligned} \quad (8)$$

where

$$R \equiv (\rho_{s_0} / \rho_s) - 1$$

A constant co-volume equation of state is used to describe the gas phase combustion products. This simple representation only approximates the real gas behavior, but it is adequate for most of the examples except near detonation conditions.

The quasi-static compaction behavior of a given granular mixture is built into the term,  $\beta_s$ . A strong function of porosity,  $\beta_s$  is a measure of the "strength" of the aggregate which must be exceeded to further increase the solid volume fraction. It is represented as

$$\beta_s(\epsilon_s) = \tau_1 \left[ 1 - \zeta^{p_1} + B_2 (\zeta^{-p_2} - 1) \right] \ln(1 / \epsilon_g) \quad (9)$$

where

$$\zeta \equiv (\epsilon_g / \epsilon_{g_0})$$

and  $\tau_1$ ,  $B_2$ ,  $p_1$ , and  $p_2$  are constants to be determined by comparison to experimental data.  $\tau_1$  has units of stress, but the others are nondimensional. For values of these parameters representing various granular materials, see Kooker.<sup>19,23</sup> There is an important distinction between the equilibrium stress state and the quasi-static stress state. The equilibrium stress state is calibrated with data from the quasi-static compaction experiment<sup>26,27</sup> under conditions where the contribution from gas-phase pressure is essentially negligible. However, the equilibrium stress state follows directly from the root of Equation (6) which is indeed sensitive to value of  $P_g$ . Combustion-generated gas pressure can lead to an equilibrium stress state different than the quasi-static state for equivalent values of mixture density.

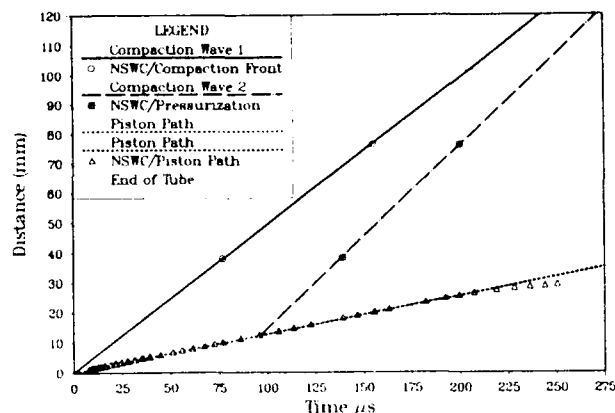
## DISCUSSION OF RESULTS

The above analysis will be used to interpret data from Sandusky's<sup>15</sup> PDC experiment, a combustion-driven piston experiment of McAfee,<sup>11</sup> and a DDT experiment reported by Bernecker.<sup>8</sup> Granular materials include two double-base ball propellants (WC-231 and TS-3659) as well as Class A and D HMX. Values of the modeling parameters used to define the quasi-static stress state, total energy release, properties of the gas-phase combustion products, etc. for these materials can be found in References 19 and 23.

### PDC-80 / 60.2% TMD TS-3659 Ball Propellant

TS 3659 is a double-base ball propellant (nominally 21.6 percent NG in NC) with essentially spherical grains (434  $\mu\text{m}$  diameter). The PDC experiment<sup>15</sup> denoted PDC-80 involved a 160 m/s impact on 60.2% TMD propellant confined in the aluminum tube, 101.7 mm long. Although later runs in this series made use of microwave interferometry to track motion of the strong compaction front, PDC-80 relied on two wall-mounted pressure transducers located at 38.1 and 76.2 mm from the impacted end. The time at which the compaction front passes the gage location is determined as the midpoint of the initial pressure rise. From each transducer record, Sandusky also estimates the time for the "onset" of significant pressurization, which is somewhat subjective but not unreasonable. These data appear in Figure 4 along with the location of the projectile face after impact; particle velocity is nearly constant at 127 m/s before a deceleration begins beyond 200  $\mu\text{s}$  (presumably due to vigorous combustion). By this time, however, the leading compaction front has reached the downstream end of the tube. Although the tube eventually ruptured, there was no transition to detonation.

Predictions from the model are compared to the PDC data in Figure 4. There are two observations here which seem to have general applicability. The first concerns the under-prediction of propagation speed of the leading compaction front. The PDC data imply a wave speed of 494 m/s, but present theory predicts



Partial Energy Release (304 cal/g)

Shock	$\eta(\%)$	$v_s$ (mm/ $\mu\text{s}$ )	$P_m$ (MPa)	$P_g$ (MPa)	$v_s$	$\rho_m$ (g/cc)	$\rho_m/\rho_{m0}$
quiescent	0.0	0.0	0.10	0.10	0.00	9844	1.0
1	1.32	0.4947	61.93	36.82	0.787	1.324	1.345
2	0.0	0.613	62.57	37.22	0.7887	1.327	1.348

Figure 4. Distance-Time Data for PDC-80; 160 m/s Impact on 60.2% TMD TS-3659. Data from Reference 15. Tabular values are model predictions downstream of indicated wave.

385 m/s for an *inert* wave in which the aggregate maintains the equilibrium stress state. If, however, this compaction wave induces reaction accompanied by full heat release (1104 cal/g for TS-3659), then conversion of only 0.44 percent of the solid would create enough gas pressure to stiffen the aggregate and allow it to support the wave speed of 494 m/s. The magnitude of gas pressure required to support the increased wave speed is nearly independent of an important ambiguity concerning the amount of energy released in the wave-induced reaction. Reaction-generated gas pressure is essentially a function of the product of the energy released and the amount of solid converted to gaseous products. Little evidence is available to determine the amount of energy release accompanying this reaction. However, liberation of the full heat of combustion of the solid phase means that the product gases trapped in the porosity of the aggregate will be near the equilibrium flame temperature (except for minute amounts of

reaction). Unless the aggregate has been compressed above 90% TMD, confined gases at these temperatures should produce visible radiation which could be seen by a high-speed camera looking through a Lexan tube confinement. For TS-3659 propellant, Glancy et al.<sup>15</sup> attempted three such runs at impact speeds up to 290 m/s and failed to see any evidence of light on the camera records, although the tube ruptured. This observation implies that wave-induced reaction in TS-3659 releases only a fraction of the total energy and this fraction is less than the value which would produce gas-phase temperatures of say 1500 K. As an example, the computational results in Figure 4 show that a compaction wave speed of 494 m/s could be supported by reaction of 1.32 percent releasing only 304 cal/g (27.5 percent of the total) which leads to a gas temperature of 1243 K.

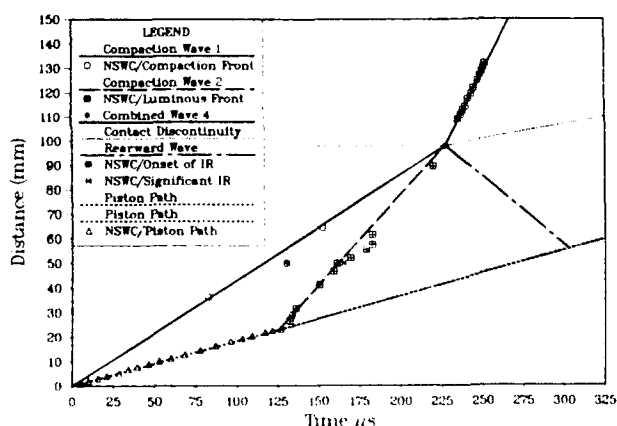
The second observation concerns the implied propagation speed and strength of the second compression wave. Differencing the two data points determined from the transducer records as the "onset" of significant pressurization (see Figure 4) produces a wave speed of 624 m/s. If, in the model, the piston velocity is assumed to increase by 1 m/s at 95  $\mu$ s, this anchors a very weak "shock" wave which propagates into the aggregate at 613 m/s, virtually passing through the data points. The implication is that the leading edge of the pressurization wave propagates near the local sound speed in the compressed material. Since the transducers testify to a rapidly rising pressure field downstream of wave (2), the quasi-steady assumption in the model breaks down in this important region. Thus, the single weak wave (2) shown in Figure 4 does not properly represent the influence of vigorous combustion which begins near the piston face. Successive pressure increases generated by transient combustion behind wave (2) will propagate at increasing speeds toward the collision point, and their coalescence may influence the "trigger" mechanism.

#### PDC-73 / 49.4% TMD WC-231 Ball Propellant

The material WC 231 is a double-base ball propellant (nominally 25 percent NG in

NC) whose grains are shaped like "fat pancakes" (spheres which have been rolled) with an average diameter of 790  $\mu$ m. In the PDC run designated PDC-73,<sup>15</sup> 49.4% TMD WC-231 is confined in a Lexan tube and impacted at a projectile speed of 220 m/s. Transition to detonation did not occur within the experimental tube length (146 mm).

A simulation is shown in Figure 5 along with the PDC data.<sup>15</sup> If the piston velocity is equated to the measured particle velocity of 183 m/s, the model predicts the leading compaction front (if inert) would propagate at 390 m/s; the PDC data imply approximately 430 m/s. If wave-induced reaction releases the full heat of combustion (1150 cal/g, assumed), then reaction of only 0.22 percent of the solid would support the observed wave speed. The luminosity data suggest that vigorous reaction begins near the piston face at approximately 125  $\mu$ s. Assuming a 1 m/s increase in piston velocity at this time generates a weak shock



Shock	$\eta$ (%)	$x_c$ (mm $\mu$ s)	$P_m$ (MPa)	$P_g$ (MPa)	$\lambda_s$	$\rho_m$ (g/cc)	$\rho_m/\rho_m$
quiescent	0.0	0.0	0.10	0.10	0.50	8204	1.0
1	0.22	0.4309	64.79	33.97	0.859	1.426	1.738
2	0.0	0.735	65.58	34.42	0.8604	1.429	1.741
4	5.2	1.309	131.1	131.0	0.5095	9049	1.103
3	0.0	0.557	131.1	77.46	0.9288	1.559	1.900
Partial Energy Release (250 cal/g)							
1	0.80	0.4113	64.85	35.32	0.853	1.425	1.737
2	0.0	0.738	65.65	35.79	0.855	1.428	1.740

Figure 5. Distance-Time Data for PDC-73; 220 m/s Impact on 49.4% TMD WC-231. Data from Reference 15. Tabular values are model predictions downstream of indicated wave.

wave propagating at 736 m/s which forms a boundary for the leading edge of luminosity. Although overly simplistic, if collision of the second shock wave with the leading compaction front were to trigger about 5 percent reaction, the combined shock wave would propagate at 1.31 km/s and pass through the experimental data representing strong luminosity. The predicted magnitude of reaction to drive the combined shock wave is plausible, but it is unlikely that collision of the postulated weak second shock wave with the leading wave could be the sole trigger for the increase in reactivity; transient combustion behind the second wave must play a role.

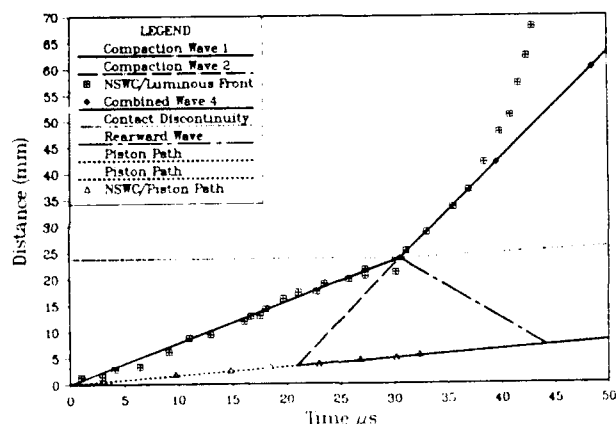
The fact that luminosity was not observed directly behind the leading front again suggests partial energy release in the wave-induced reaction. If it is assumed that only 250 cal/g are liberated by reaction of 0.8 percent of the solid, the wave pattern in Figure 5 is unchanged except that the temperature of the trapped gases reaches only 1205 K. In both simulations of PDC-73, the leading edge of luminosity propagates at the local sound speed in the aggregate just as the onset of pressurization did in PDC-80.

Partial confirmation of the reactive wave assumption in the present model may be provided by an experimental measurement<sup>15</sup> unique to PDC 73. This run included two infrared detectors which observed the aggregate through a NaCl window apperture (50 mm from the impacted end) in the wall of the Lexan tube. Although the IR signals were not calibrated for absolute temperature, their ratio indicates relative temperature.<sup>15</sup> First response from the two detectors occurred at 121 and 127  $\mu$ s, while the maximum ratio (maximum temperature) occurred at 130  $\mu$ s; arrival time of the leading compaction wave is predicted to be 117  $\mu$ s. This strongly suggests that the compaction wave itself initiated reaction. Just behind the wave representing the leading edge of luminosity, the IR signals indicate a broad based participation in reaction but temperatures remain below the previous maximum until after the appearance of the brightly luminous front which coincides with the combined shock wave in the present model

## PDC-27/73% TMD Class D HMX

Simulations of impact on Class D HMX are clouded by the influence of particle size distribution, which introduced a variability in quasi-static compaction behavior<sup>27</sup> and, hence, wave propagation speed in the present study. But a simulation of one of Sandusky's PDC runs will be used here to illustrate some consequences of the multiple wave structure.

PDC-27<sup>14</sup> involved Class D HMX loaded at 73% TMD into a 147 mm long Lexan tube and impacted at 267 m/s; a transition to detonation *did* take place, as indicated in Figure 6. Since luminosity is coincident with the leading compaction front, the simulation of wave-induced reaction assumed total energy release and found that reaction of approximately 0.5 percent is required to support the observed wave speed of 778 m/s. If collision

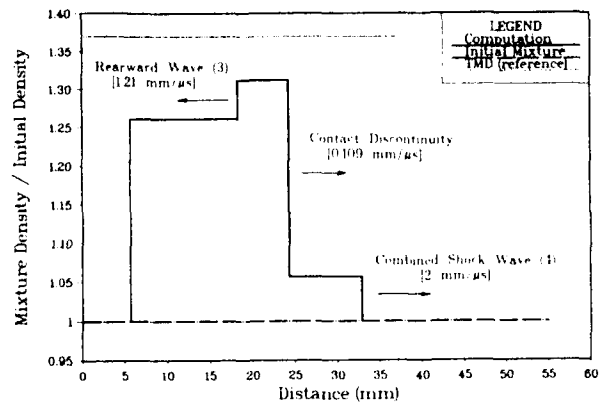


Shock	$t_{\text{GTD}}$	$x_s$ (mm, $\mu$ s)	$P_{\text{in}}$ (MPa)	$P_{\text{g}}$ (MPa)	$\lambda_s$	$\rho_{\text{in}}$ (g/cc)	$\rho_{\text{in}}/\rho_{\text{in}_0}$
quiescent	0.0	0.0	0.10	0.10	0.73	1.389	1.0
1	0.16	0.7786	174.2	143.1	0.9067	1.752	1.261
2	0.009	2.143	177.7	146.5	0.9068	1.753	1.261
4	3.2	2.019	305.6	305.5	0.7327	1.469	1.057
3	0.0	1.213	305.6	237.7	0.9364	1.823	1.312
Altered PDC 27							
4	5.87	6.01	477.3	477.3	0.6737	1.407	1.009
3	0.0	1.469	47.3	358.1	0.9533	1.873	1.348

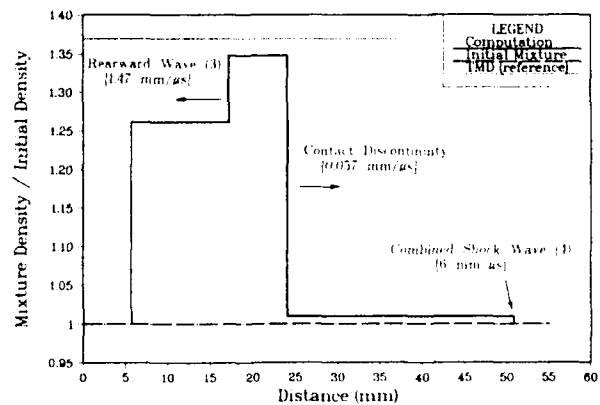
Figure 6. Distance-Time Data for PDC-27; 267 m/s Impact on 73% TMD Class D HMX. Data from Reference 14. Tabular values are model predictions downstream of noted wave.

triggers reaction of 3.2 percent, the combined shock wave will be driven at 2 km/s and pass through the next four data points for strong luminosity. In this run, the wave continues to accelerate and quickly achieves the detonation velocity of 7.46 km/s.

Up to this point, the role played by the rearward propagating shock wave (3) and the contact discontinuity between waves (3) and (4) has been rather obscure. This study would contend, however, that the density differences bounded by these waves should be clearly discernable in a radiograph. Figure 7A is a plot of the spatial distribution of mixture density (ratioed to initial mixture density) at 35  $\mu$ s, derived from the computed flow field for PDC-27 shown in Figure 6. It simulates what a flash radiograph would record if triggered (at 35  $\mu$ s) shortly after the collision. There are several interesting features here. Density of the reacting mixture directly behind the combined shock wave (4) traveling at 2 km/s is not much greater than the quiescent value. Even though this reacting mixture is supporting a stress of 300 MPa, the solid volume fraction is virtually unchanged because the high pressure gas-phase combustion products can carry the same "load" as the solid material. The high density region ("plug") is material trapped behind the slow moving contact discontinuity. The highest density represents material which has been compressed by shock waves (1), (2) and (3). The "reverse step" in density is created by shock wave (3), which is propagating rearward into material already subjected to (1) and (2). This density pattern is accentuated when the collision triggers an increased level of reaction in the combined shock wave (4). For demonstration purposes, the flow field for PDC-27 was altered by increasing the amount of reaction assumed to be triggered by the collision. Although shock waves (1) and (2) remain unchanged, the case labeled ALTERED PDC-27 (see table under Figure 6) predicts a combined shock wave (4) propagating at 6 km/s. The corresponding simulated radiograph at 35  $\mu$ s is shown in Figure 7B. Note that mixture density behind shock wave (4) is now virtually equal to the quiescent value. The highest density in the "plug" has increased, and the reverse step is



(A) PDC-27 / Data from Figure 6

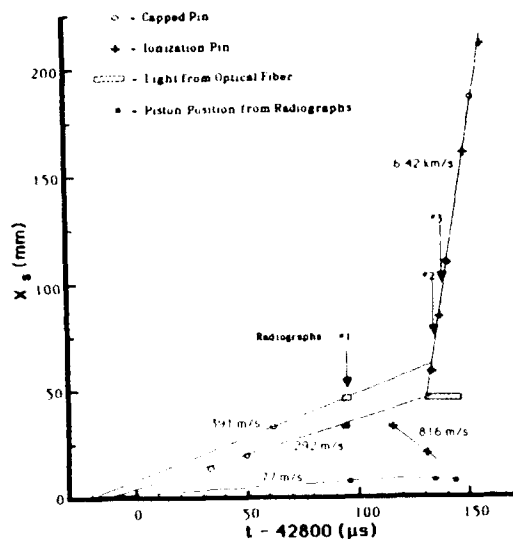


(B) Altered PDC-27 / See Figure 6

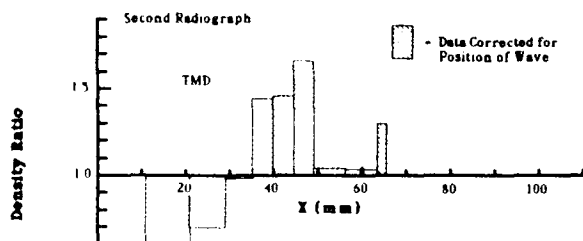
Figure 7. Simulated Radiographs at 35  $\mu$ s From Model Predictions Listed in Figure 6

more pronounced because the rearward propagating shock wave (3) is stronger.

PDC-27 did not happen to include flash radiography, but it may be appropriate to compare the above prediction to a result obtained by McAfee<sup>10,11</sup> in 64% TMD Class A HMX. In McAfee's experiment, combustion of ignitor material at one end in a closed tube creates a rising pressure field against a steel cylinder or "piston" which is then driven into the confined Class A HMX. Confinement is a fairly thin-walled maraging steel tube which allows flash radiography to record the position of tracer foils seeded into the original bed; diagnostics also include capped and ionization pins. The X-T plot of McAfee's run B-9153 reproduced here as Figure 8A shows that a transition to detonation (6.42 km/s) did occur.



(A) Distance-Time Data / Run B-9153



(B) Radiograph #2 / Run B-9153

Figure 8. Data From Combustion-Driven Piston Experiment<sup>10</sup> on 64% TMD Class A IMX. Figures courtesy of McAfee/LANL.

Radiograph #2 was taken just after the transition, and the results are reproduced in Figure 8B. Some striking similarities are evident when comparing this experimental result with the simulated radiograph in Figure 7B for the 6 km/s combined shock wave (4). If it can be assumed, in McAfee's experiment, that a shock wave collision triggered an abrupt increase in wave-induced reaction, then the present model would appear to be compatible with the LANL results.

#### DDT Shot A266 / 59.8% TMD TS-3659

At the present time, none of the impact experiments have produced pressure transducer records which offer conclusive evidence for the

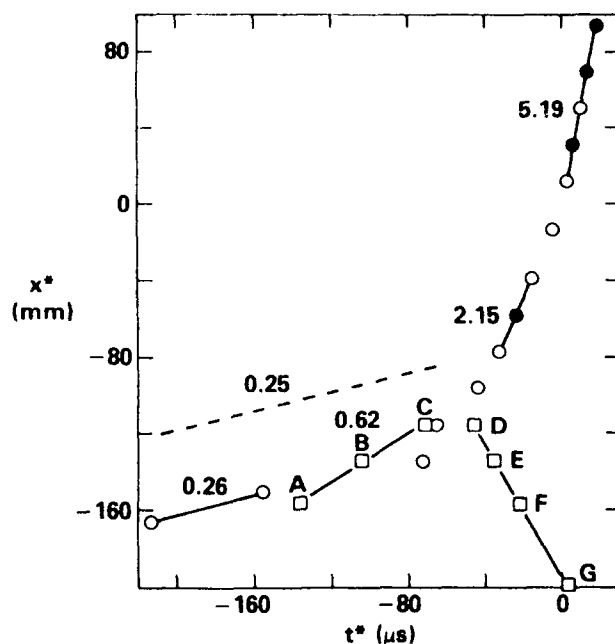


Figure 9. Relative Distance-Time Data From Bernecker's<sup>8</sup> DDT Shot A266; 59.8% TMD TS-3659. (Circles = probe response, squares = transducer excursion; velocity in mm/μs.)

presence of the rearward propagating wave. Such evidence is provided by a DDT experiment. Bernecker<sup>8</sup> has reported results for 59.8% TMD TS-3659 confined in the thick wall steel tube which was instrumented with a series of ionization pins as well as several wall-mounted pressure transducers.<sup>8</sup> The arrival time of the strong reaction front can be extracted from the pin data, but the transducers continue to record a time-history after the front has passed. The results<sup>8</sup> from Shot A266 are reproduced here in Figure 9, in terms of  $x^*$  and  $t^*$  which are distance and time referenced to the onset of detonation. The acceleration of the strong compaction front from 620 m/s to 2.15 km/s is accompanied by a rearward propagating compression wave (speed of  $\sim 1.7$  km/s) as indicated by the transducer excursions at symbols D, E, F and G.

The present theory based on simple motion of a piston driver is ill-equipped to simulate a DDT experiment which begins with ignitor combustion. In particular, no experimental value of particle velocity is available to determine the motion of a hypothetical "piston." A simulation was based on a 230 m/s particle velocity and 0.29 percent reaction to create the strong compaction front at 630 m/s, a 45  $\mu$ s time delay, and then a 1 m/s increase in



particle velocity to anchor the second wave. Although clearly not unique, this wave structure predicts that a collision which triggers ~10 percent reaction would produce a combined shock wave (4) traveling at 2.15 km/s. Furthermore, a rearward propagating shock wave (3) will travel at 1.72 km/s if it induces an additional 0.72 percent reaction in the already burning material compressed by waves (1) and (2). The path of both these waves lies parallel to the experimental data. Comparison of the transducer time-history to the predicted pressure level of 350 MPa behind shock wave (3) indicates that theory is low by approximately a factor of two, which may not be surprising when considering the assumptions which have been made. Although the analysis suggests that the rearward wave was triggered by a collision, this computational example does not constitute proof.

## SUMMARY

Various laboratory experiments on SDT and DDT in granular energetic material have observed abrupt increases in the speed of propagation of compaction waves and the leading edge of luminosity. The DDT experiment, in at least one case, has evidence of a strong rearward propagating wave. A possible explanation is provided by a simple quasi-steady model which envisions an increase in reactivity triggered by the collision of two reactive compaction/shock waves. Simulation of experimental data shows that:

(a) The leading compaction wave created by modest impact on confined granular energetic material is not necessarily inert. The experimental propagation speeds which exceed the predicted inert wave speed could be supported by wave-induced reaction of a few tenths of one percent of the solid material, if the reaction releases the total heat of reaction. If wave-induced reaction is accompanied by partial heat release (highly probable for single- and double-base propellants), then the magnitude of reactivity is near one percent.

(b) After a time delay, the onset of vigorous combustion of material adjacent to the piston face will drive a second compressive wave system into the aggregate which has been formed

by the initial compaction wave. The leading edge of this second wave system propagates at a speed near the local sound velocity.

(c) The analysis predicts that the abrupt increases in propagation speed observed experimentally would require the collision to induce reaction in the range of 2 to 10 percent. Transient combustion (neglected in this model) behind the leading edge of the secondary wave system must play a role in the "trigger" mechanism.

(d) The wave pattern produced by the collision includes both a combined compaction/shock wave exhibiting an abrupt increase in speed, and a rearward wave which propagates back into material compressed by the first two waves. A simulated radiograph taken shortly after the collision predicts:

(1) The density behind the combined shock wave may appear nearly equal to the quiescent value. Wave-induced reaction generates enough gas pressure to counteract (resist) the normal occurrence of bed compaction caused by a large value of mixture stress.

(2) A high density ("plug") region is trapped behind the slow-moving contact discontinuity.

(3) The spatial distribution of the high density region will exhibit a "reverse step" as a direct result of the rearward propagating shock wave.

It appears from these simulations that the appearance of a rearward propagating wave may be a direct indicator that a "trigger" mechanism is responsible for the abrupt increase in wave speed. The lack of any rearward propagating wave may signify that the transition mechanism is controlled by nearly complete combustion which "drives" from behind until it catches the leading compaction front.

## ACKNOWLEDGEMENTS

The author is indebted to H. W. Sandusky (NSWC), R. R. Bernecker (NSWC), M. R. Baer (SNIA), and J. M. McAfee (LANL) for many stimulating discussions.

## REFERENCES

1. Bernecker, R. R. and Price, D., "Studies in the Transition from Deflagration to Detonation in Granular Explosives - I. Experimental Arrangement and Behavior of Explosives Which Fail to Exhibit Detonation," *Combustion & Flame*, Vol. 22, 1974, pp. 111-117.
2. Bernecker, R. R. and Price, D., "Studies in the Transition from Deflagration to Detonation in Granular Explosives - II. Transitional Characteristics and Mechanisms Observed in 91/9 RDX/Wax," *Combustion & Flame*, Vol. 22, 1974, pp. 119-129.
3. Bernecker, R. R. and Price, D., "Studies in the Transition from Deflagration to Detonation in Granular Explosives - III. Proposed Mechanisms for Transition and Comparison with Other Proposals in the Literature," *Combustion & Flame*, Vol. 22, 1974, pp. 161-170.
4. Price, D. and Bernecker, R. R., "DDT Behavior of Porous Columns of Simple Propellant Models and Commercial Propellants," *Combustion & Flame*, Vol. 42, 1981, pp. 307-319.
5. Bernecker, R. R., "The Deflagration-to-Detonation Transition for High Energy Propellants - A Review," *AIAA Journal*, Vol. 24, No. 1, 1986, pp. 82-91.
6. Bernecker, R. R.; Sandusky, H. W.; and Clairmont, Jr., A. R., "Deflagration-to-Detonation Transition Studies of Porous Explosive Charges in Plastic Tubes," *Seventh Symposium (International) on Detonation*, NSWC MP 82-334, Jun 1981, pp. 119-138.
7. Bernecker, R. R., Sandusky, H. W. and Clairmont, Jr., A. R., "Deflagration-to-Detonation Transition (DDT) Studies of a Double-Base Propellant," *Eighth Symposium (International) on Detonation*, NSWC MP 86-194, Jul 1985, pp. 658-668.
8. Bernecker, R. R., "DDT Studies of a Spherical, Double-Base Ball Propellant," 1987 JANNAF Propulsion Systems Hazards Meeting, CPIA Publication 464, Vol. I, Mar 1987, pp. 1-11.
9. Campbell, A. W., "Deflagration-to-Detonation Transition in Granular HMX," 1980 JANNAF Propulsion Systems Hazards Meeting, CPIA Publication 330, 1980, pp. 105-130.
10. McAfee, J. M. and Campbell, A. W., "An Experimental Study of the Deflagration to Detonation Transition in Heavily Confined HMX," 1986 JANNAF Propulsion Systems Hazards Meeting, CPIA Publication 446, Vol. I, Mar 1986, pp. 163-186.
11. McAfee, J. M.; Asay, B. W.; Campbell, A. W.; and Ramsay, J. B., "Deflagration to Detonation in Granular HMX," *Ninth Symposium (International) on Detonation*, Portland, Oregon, 28 Aug - 1 Sep 1989.
12. Sandusky, H. W., "Compressive Ignition and Burning in Porous Beds of Energetic Materials," 1983 JANNAF Propulsion Systems Hazards Meeting, CPIA Publication 381, Vol. I, Sep 1983, pp. 249-258.
13. Sandusky, H. W. and Liddiard, T. P., *Dynamic Compaction of Porous Beds*, NSWC TR 83-246, 26 Dec 1985, NSWC, White Oak.
14. Sandusky, H. W. and Bernecker, R. R., "Compressive Reaction in Porous Beds of Energetic Materials," *Eighth Symposium (International) on Detonation*, NSWC MP 86-194, July 1985, pp. 881-891.
15. Glancy, B. C.; Sandusky, H. W.; Miller, P. J.; and Krall, A. D., "Dynamic Compaction and Compressive Reaction Studies for Single and Double-Base Ball Propellants," *Ninth Symposium (International) on Detonation*, Portland, Oregon, 28 Aug - 1 Sep 1989.
16. Green, L. G.; James, E.; Lee, E. L.; Chambers, E. S.; Tarver, C. M.; Westmoreland, C.; Weston, A. M.; and Brown, B., "Delayed Detonation in Propellants From Low Velocity Impact," *Seventh Symposium (International) on Detonation*, NSWC MP 82-334, Jun 1981, pp. 256-264.
17. Dick, J. J., "Measurement of the Shock Initiation Sensitivity of Low Density

- HMX," *Combustion & Flame*, Vol. 54, 1983, pp. 121-129.
18. Dick, J. J., "Stress-Time Profiles in Low Density HMX," *Combustion & Flame*, Vol. 69, 1987, pp. 257-262.
  19. Kooker, D. E., "A Reactive Shock Wave Model for Compaction Waves in Granular Energetic Material," 1987 JANNAF Propulsion Systems Hazards Meeting, CPIA Publication 464, Vol. I, Mar 1987, pp. 39-59. [also see BRL-TR 2945, Nov 1988, U.S. Army Ballistic Research Laboratory]
  20. Kooker, D. E., "Predictions for the Piston-Driven Compaction Experiment Based on A Transient Shock Wave Model," CPIA Publication 509, Vol. I, 1989 JANNAF Propulsion Systems Hazards Meeting, San Antonio, TX, 20-24 Feb 1989, pp. 47-72.
  21. Kooker, D. E., "A Numerical Study of Compaction Waves in Class D HMX," 1986 JANNAF Propulsion Systems Hazards Meeting, CPIA Publication 446, Vol. I, March 1986, pp. 213-238.
  22. Baer, M. R. and Nunziato, J. W., "A Two-Phase Mixture Theory for the Deflagration-to-Detonation Transition (DDT) in Reactive Granular Mixtures," *Int. J. of Multiphase Flow*, Vol. 12, No. 6, 1986, pp. 861-889.
  23. Kooker, D. E., "Collision of Reactive Compaction/Shock Waves in Granular Energetic Material," 1988 JANNAF Propulsion Systems Hazards Meeting, CPIA Publication 477, Vol. I, Mar 1988, pp. 17-36 (see also BRL TR-2949, Dec 1988, U.S. Army Ballistic Research Laboratory).
  24. Carroll, M. M. and Holt, A. C., "Static and Dynamic Pore-Collapse Relations for Ductile Porous Materials," *Journal of Applied Physics*, Vol. 43, No. 4, 1972, pp. 1627-1636.
  25. Kooker, D. E. and Anderson, R. D., "A Mechanism for the Burning Rate of High-Density, Porous, Energetic Materials," *Seventh Symposium (International) on Detonation*, NSWC MP 82-334, Jun 1981, pp. 198-215.
  26. Elban, W. L., "Quasi-Static Compaction Studies for DDT Investigations. Ball Propellants," *Propellants, Explosives, Pyrotechnics*, Vol. 9, 1984, pp. 119-129.
  27. Elban, W. L. and Chiarito, M. A., "Quasi-Static Study of Coarse HMX Explosive," *Powder Technology*, Vol. 46, 1986, pp. 181-193.

# COMBINED EXPERIMENTAL AND THEORETICAL INVESTIGATIONS INTO THE DEFLAGRATION TO DETONATION TRANSITION

H. J. Verbeek and A. C. van der Steen  
Prins Maurits Laboratory TNO  
P. O. Box 45  
2280 AA Rijswijk  
THE NETHERLANDS

*The results of a DDT tube test have been compared with the outcome of a numerical model. The interaction between the two research methods leads to a better understanding of the DDT phenomenon than either method separately. The emphasis of the research at PML has been put on the early stages of the DDT process, i.e., the ignition process and the convective and compressive burning stages. For the situation tested, the particle diameter appeared to be the parameter with the largest influence on the progress of the DDT process.*

## INTRODUCTION

At the Prins Maurits Laboratory TNO, a research project is being undertaken on the deflagration to detonation transition (DDT). This project consists of both an experimental part in which DDT tube tests are performed, and a theoretical part where a computer model has been developed. In the DDT project, fundamental research is carried out which is aimed at gaining a better insight into the DDT phenomenon from the combination of these two approaches, so that eventually a better understanding can be reached of DDT hazards in practical situations. The DDT work at PML is similar to earlier DDT work performed in other institutes (see, for example, the experimental work performed at NSWC<sup>1</sup> and ISL,<sup>2</sup> and the modelling work carried out at the University of Illinois at Urbana-Champaign<sup>3</sup>). In the PML effort, the research of the early stages of the DDT process is emphasized, i.e., the ignition process and the convective and compressive burning stages. Considerable effort is being expended on achieving a well-defined and reproducible ignition of the explosive. It is also considered important to reach a strong interaction between the experimental and the modelling work.

The computer model is a one-dimensional computer simulation of the actual tube tests where the explosive system is treated as a fluid mixture of two components--the explosive, and the reaction products. Although the discrepancy between such a description and the real situation is considerable, the model can, nevertheless, be very useful in the study of DDT, probably not as a means of precisely predicting the occurrence and progress of a DDT, but certainly as a way to reach a better understanding of the process and to examine the behavior of the explosive system by means of parameter variations.

In parallel with the modelling work, a DDT tube test has been developed. Usually DDT experiments are performed in heavily confined steel tubes. To study the influence of the confinement, we used tubes with various sizes of both the inner and outer diameter. Another important parameter in our test is the strength of the igniter system. To obtain reproducible results in a DDT test, it is essential that the igniter system gives a well-defined ignition. To study the effect of the amount of gas produced by the igniter, we tested various pyrotechnic mixtures. In the tubes, several types of RDX/wax compositions

have been tested which mainly differed in the particle size distribution.

A description of the model, preliminary results of the tests, and the simulations have been presented earlier.<sup>4,5</sup> In this paper, a more extensive survey of the results of both the tests and the simulations is given. First, descriptions of the model and the test setup are given. Next, the experimental results and the results of the calculations are presented with the attention focused on the way the explosive is ignited and on the type of RDX/wax composition used. Finally, the outcome of the experiments and the calculations is compared, and the implications for our view of the DDT process are discussed.

## THE THEORETICAL MODEL

A detailed description of the model has been given at the Eighth Symposium on Detonation.<sup>4</sup> The model gives a simplified description of the complex physical and chemical processes occurring in a DDT by treating the explosive system as a fluid mixture of two separate components, the solid (unreacted) explosive and the gaseous reaction products. For this system, a set of differential equations was composed consisting of the conservation laws of mass, momentum and energy for each phase, and completed with a number of constitutive equations such as the equations of state, the burning-rate law, the heat-exchange law between the two phases, etc. To describe the static and dynamic compaction, a particle stress term is used, based on the modification by Frey of the Carroll-Holt pore collapse model.<sup>9</sup> The set of equations is solved numerically by a finite difference procedure.

Compared to Reference 4, some adjustments have been made to the code. The main differences are not in the set of equations, but in the finite-difference procedure. In the flux corrected transport method used (FCT),<sup>6</sup> the effective numerical diffusion has been further minimized in order to avoid unphysical propagation of pressure and temperature waves. Also, the semi-implicit procedure that is used to handle the stiff terms in the equations has been adjusted in order to obtain a better approximation of the real solution.

An extensive discussion of the numerical methods used will be given in a future article.

In the model, a great number of simplifications with respect to the physical reality necessarily had to be made. One of them that is particularly relevant to the current paper is the description of the ignition of the particles. In the model, the solid particles are assumed to start decomposing only after a certain temperature has been reached. The reaction rate is then given by the burning-rate law. Another simplification is the absence in the model of a shock initiation mechanism, as, for example, a description of shear processes. Therefore, a temperature rise and ignition of the solid particle can only be caused by heat exchange with the gas or by compression. As a consequence, the model is only capable of describing convective burning and compressive burning processes.

How important these and other simplified descriptions are for a good description of the DDT process must be decided by comparison of the numerical and the experimental results.

## THE EXPERIMENTAL SETUP

A schematical representation of the setup is given in Figure 1. Up to now, most of the DDT experiments have been performed in a steel tube (7) (to be called tube I) of i.d. = 15.9 mm, o.d. = 33.5 mm, and  $l = 200$  mm, closed at both ends with screw caps (4). The granular explosive (8) is pressed into the tube up to 10 mm from the end. The last 10 mm is used for the igniter system, which is supported by a copper plate (3). Also, some experiments have been performed in a larger tube of i.d. = 36.2 mm, o.d. = 65 mm, and  $l = 300$  mm (to be called tube II). Tubes with still other dimensions will be used in future tests.

The igniter consists of a PVC cylinder (5) with a central hole for a resistance wire (2) to ignite the pyrotechnic mixture and an optical fiber (1) to register the moment the mixture is ignited. The remaining space in the hole is filled up afterwards with glue. At the explosive side, a cavity (6) is made for the pyrotechnic mixture. Note that with this type of igniter system, ignition of the explosive



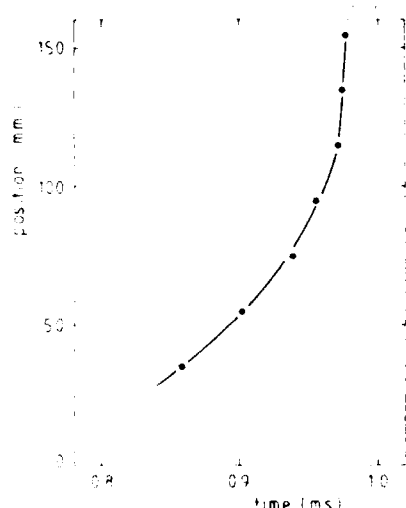


**Figure 2.** The Position of the Flame Front as a Function of Time for Composition I Ignited with Igniter I

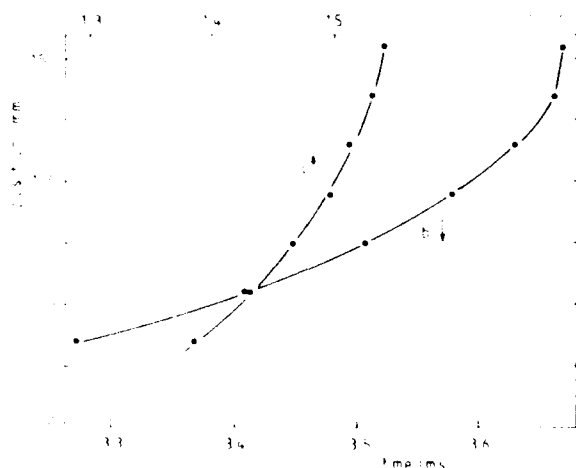


**Figure 3.** The Position of the Flame Front as a Function of Time for Explosive Composition IIa and Ignited with Igniter I (a) and Igniter II (b)

the moment the pyrotechnic mixture ignites and the position is relative to the igniter/explosive interface. In Figure 3, the results for composition IIa are presented for ignition with igniter I(a) and igniter II(b).

The curves presented in Figures 2 and 3 are typical for the given experimental conditions. If igniter I is used, the experiments are reproducible to within 100  $\mu$ s (Figures 2 and 3a). The main difference between different experiments is the moment the first probe is triggered. The differences in the rate of

acceleration of the flame front are much smaller. If igniter II is used, however, the reproducibility of the trigger time of the first probe is much worse. It varies from 1 ms to several tens of milliseconds. On the other hand, the shape of the distance versus time plot of the flame front shows only minimal variations for the various experiments. Ionization probes at distances shorter than 35 mm were not used because they are not triggered or triggered too late. Also, in many experiments with composition IIa and IIb, the first probe is triggered later than the second or even the third one.

The acceleration of the flame front as shown in Figure 2 is typical for DDT and has been explained by many authors (e.g., see Reference 1). The ignition of the pyrotechnic mixture generates a very slow convective burning and, therefore, it takes about 850  $\mu$ s before the flame front reaches the first probe at 35 mm. Next, the speed of the convective combustion increases from about 500 m/s between 35 mm and 75 mm to 2 km/s around 100 mm; at this point, the burning wave propagates by means of the process of compressive burning; finally, within the next 10 to 20 mm, a detonation wave with a speed of 6.67 km/s is generated. This result is confirmed by the fragmentation of the DDT tube.

The slow burning of the RDX/wax mixture over the first part of the tube is demonstrated even more clearly in Figure 3 for composition IIa, where the effect of different pyrotechnic mixtures is demonstrated. Igniter I causes the first probe to be triggered after about 1.3 ms which is about 0.5 ms later than for composition I. The flame front also accelerates for this composition, but to a much lesser degree than for composition I, and it also has not reached the detonation velocity after 160 mm. The velocity changes from 0.4 to 2 km/s over the last 20 mm, indicating that the process is still in the stage of compressive burning, and this result is confirmed by the fragmentation of the tubes. Most striking is the effect of the different igniters on composition IIa. Where igniter I cannot initiate a detonation within 155 mm, igniter II can. In this case, the acceleration of the convective burning process is initially

much slower. The velocity changes from 0.3 to 0.6 mm/ $\mu$ s at about 130 mm from the igniter. At that point, however, a sudden steep acceleration is seen (to about 3 mm/ $\mu$ s) and, judging from the remaining fragments of the tube, a full detonation is reached at the very end of the tube.

Figure 4 shows the effect of an increase in the tube diameter (tube II). In this tube measurements were performed with composition II, both sieved (IIa, Figure 4a) and unsieved (IIb, Figure 4b). The results of the sieved composition (Figure 4a) are in reasonable agreement with the corresponding results with the smaller tube (Figure 3a). In this case, however, the process does reach the detonation velocity, but only at a distance of 150 mm from the igniter, which is almost as long as the length of the small tube. The shape of curve 4a, however, more resembles that of curve 3b than that of curve 3a. The experiments with the unsieved composition (Figure 4b) show a much longer burning stage with a gradual acceleration from 0.4 to 0.7 mm/ $\mu$ s and the transition to detonation only takes place at a distance of 210 to 240 mm from the igniter, shortly before the end of the tube.

## THEORETICAL CALCULATIONS

Several calculations were performed to simulate the influence of the igniter and the explosive composition. The effect of the igniter is simulated in the model by filling the

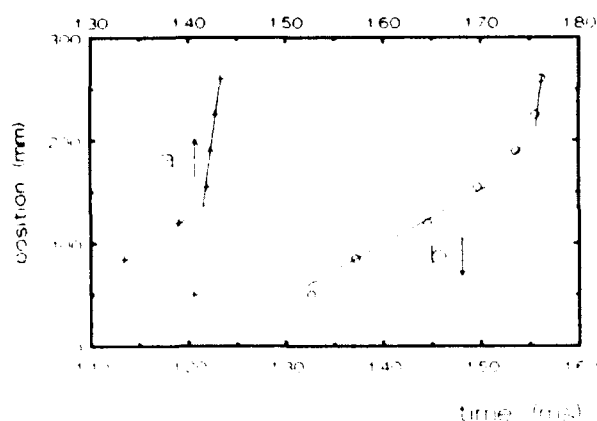


Figure 4. The Position of the Flame Front as a Function of Time in Tube II for Explosive Composition IIa (a) and IIb (b), Ignited with Igniter I

first zone (i.e. the explosive layer pressed against the pyrotechnic mixture) with a gas of a specified density and temperature, and adding a heat source in that layer to simulate the presence of hot solid particles. The explosive particles are assumed to be ignited when the particle temperature surpasses a threshold value of 301 K. The combustion of the particles is then described by a simple burning-rate law, in which the burning rate is proportional to the particle density and the 0.9th power of the pressure and inversely proportional to the particle diameter. For the KNO<sub>3</sub>/Zr igniter (igniter I), the values for the initial gas temperature and density are set at 1000 K and 68 kg/m<sup>3</sup>, respectively, while for the Pb304/tetrazene/B mixture (igniter II) the values are set at 900 K and 10 kg/m<sup>3</sup>, respectively. These values have been obtained from thermocouple measurements of the reaction temperature of the igniter and from calculations with the TIGER code.<sup>7</sup> The final values of temperature and density are calculated from these by estimating the effects of the expansion of the gaseous reaction products into the first explosive layer, using TIGER. The two igniters especially differ in the gas density reached, because the Pb304/tetrazene/B mixture produces many fewer gaseous reaction products than the KNO<sub>3</sub>/Zr mixture.

Figure 5 shows the results of two simulations, assuming a particle size of 200  $\mu$ m. Curves 5a and 5b correspond to igniter I and

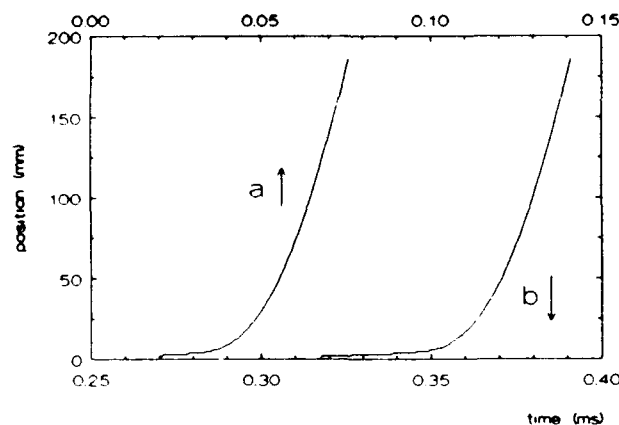


Figure 5. The Calculated Position of the Flame Front as a Function of Time for a Particle Size of 200  $\mu$ m and for Igniter I (a) and II (b)



igniter II, respectively. The results show that for these conditions first a convective combustion is generated which soon passes into a rapidly accelerating compressive combustion. At the end of the tube, the front is still slowly accelerating and has reached a velocity of over 8 mm/ $\mu$ s, higher than the detonation velocity for this composition (6.7 mm/ $\mu$ s). The two curves are very similar, the only differences being the time that the explosive starts burning and the somewhat longer stage of slow convective burning in curve 5b. The type of igniter used does not have any influence on the subsequent acceleration to detonation in the simulation.

Figure 6 shows simulations for a particle size of 600  $\mu$ m again for igniter I (6a) and II (6b). In this case, a quite different behavior is observed. After ignition, first a slow convective burning stage is seen, which lasts much longer than for the 200  $\mu$ m simulation. Then the reaction front suddenly makes a jump of about 20 mm, while at the same time its velocity increases from about 0.3 mm/ $\mu$ s to 2 mm/ $\mu$ s. After the jump, the front keeps accelerating, but at the end of the bed it still has not reached the detonation velocity, but instead a velocity of about 5 mm/ $\mu$ s. The type of igniter used again only influences the time the reaction starts.

A closer analysis of the modelling results reveals the reason for the sudden jump. It appears that in the 600  $\mu$ m case the initial phase of slow convective burning, which

generates pressure waves extending into the bed, is able to strongly compress a part of the unburned fraction of the bed. This plug impedes a further penetration of the gaseous reaction products into the bed and, therefore, forms a strong obstruction for the convective burning process. Such a plug has recently been observed experimentally by McAfee et al.<sup>8</sup> As the pressure at the igniter end of the plug rises, the plug is slowly accelerated forward, while it also increases in length. This process continues for a considerable length of time until the pressure drop at the front of the plug has become so high that the grains are ignited at that point by the compression heat of the shock wave. Then, a compressive burning wave is initiated that propagates towards the end of the bed with a gradually increasing speed. In Figure 7, the location and shape of the plug is shown at a point of time just prior to the jump of the reaction front. An analysis of the 200  $\mu$ m simulation shows that in that case no plug can be formed during the period that the velocity of the convective burning front is still low, due to the lower compressibility of the smaller particles. The convective burning stage can, therefore, seamlessly pass into a compressive burning in that simulation.

Finally, Figure 8 shows the results of a simulation for a particle size of 800  $\mu$ m, using igniter I and a bed length of 300 mm. The shape of the curve resembles that of the curves in Figure 6, but the convective burning stage is even longer, giving the opportunity to form

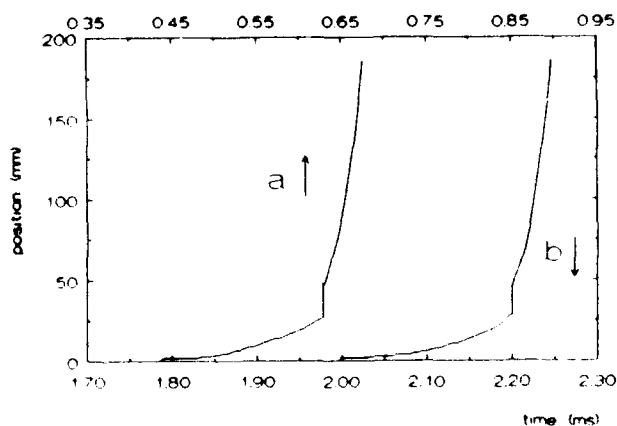


Figure 6. The Calculated Position of the Flame Front as a Function of Time for a Particle Size of 600  $\mu$ m and for Igniter I (a) and II (b)

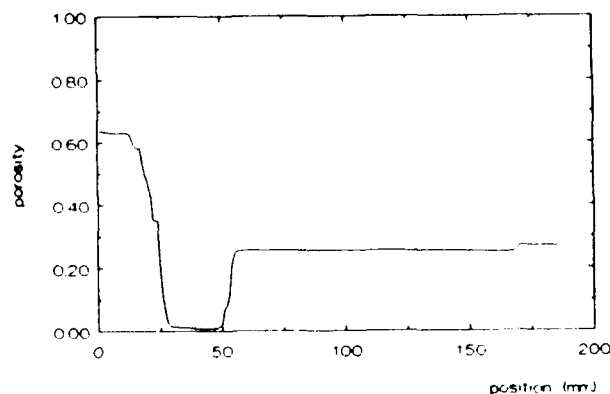
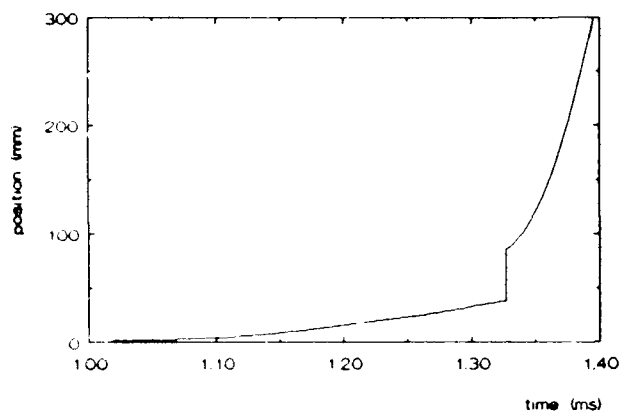


Figure 7. The Porosity as a Function of Distance, Just Before the Generation of a Compressive Burning Wave



*Figure 8. The Calculated Position of the Flame Front as a Function of Time for a Particle Size of 800  $\mu\text{m}$*

a plug of more than 50 mm length before the compressive burning wave is generated. The acceleration of this compressive front is even slower than for the 600  $\mu\text{m}$  data and the end velocity reached is only 5 mm/ $\mu\text{s}$ , in spite of the greater length of the tube.

## DISCUSSION

One of the most conspicuous aspects of the experimental results is the difference in DDT behavior between the fine-particle composition and the coarse-particle composition, i.e., a fast and smooth transition to detonation versus a long, slow burning phase followed by a sudden, rapid transition to detonation. This different behavior is clarified to a great extent by the results of the simulations, especially the fact that plug forming can occur in one case while it cannot in the other. The formation of a plug explains the long, and only slowly accelerating convective burning stage observed for composition II. It might also explain the fact that for this composition the first probe often responds later than expected. The location of this probe coincides with the location of the plug as predicted by the model. On the other hand, the longer response time might also be caused by a low ionization level in the slow convective combustion stage.

The agreement between model and experiments is much less in the following stages of the transition to detonation. While the simulations predict that the compressive

burning phase sets in before a distance of 90 mm from the igniter, the experiments show that a convective burning stage can be maintained over a distance of even 240 mm for composition IIb. Explanations for this discrepancy might be the occurrence of a radial expansion of the tube (since the model is one-dimensional it can only describe an infinitely high confinement), the formation of a second or even third plug (as was observed by McAfee et al.<sup>8</sup>), or the inadequate description of the particle ignition in the model. The final sudden transition to detonation observed in the experiments is never reproduced in the simulations, but this is to be expected in view of the absence of a shock-initiation model in the code.

Also, the influence of the type of igniter used could not be explained by the model. In the simulations, the igniter only influences the time the explosive composition is ignited and, to a minor extent, the initial speed of the convective burning stage. An explanation must probably again be looked for in the factors mentioned above or a combination of them. Further, it is noteworthy that curve 4a shows more resemblance to curve 3b than to curve 3a while the opposite should be the case. More research will be needed to clarify these observations.

The prediction by the model of the time of ignition of the explosive shows large discrepancies with the experiments. This is not at all surprising, however, for several reasons. In the first place, the experiments are also not sufficiently reproducible in this respect. A slight variation in the ignition parameters has a large impact on the ignition time. Another reason is that in the simulation, the ignition time is strongly influenced by the ignition parameters which are not precisely known and are only estimated. Further, the description of the ignition in the model is very simple. Work is going on at PML to further improve the control of the igniter in the experiments and, on the other hand, to obtain more precise values of the ignition parameters. Further, a more sophisticated ignition description will be incorporated into the model. At the same time, the experiments will be extended to tubes of other dimensions, and the number,

type, and location of the measuring probes will also be varied.

## CONCLUSIONS

The experimental results clearly show the large influence of the particle size on the DDT process, especially since it determines whether or not a plug can be formed. The type of igniter also appears to have a large influence. From the modelling results it appears to be possible to explain some, but not all, aspects of the experiments. The inability to completely describe the experiments can be ascribed, on one hand, to the uncertainty in the values of several experimental parameters and, on the other hand, to an inadequate description of certain aspects in the DDT process, e.g., the description of particle ignition.

From the comparison with the theoretical results, it is possible to reach a better understanding of the experimental results. On the other hand, from the results of the experiments we can obtain a clear indication of areas in which the model should be improved. Combined experimental and theoretical research can lead to a better understanding of the DDT phenomenon than could be achieved using each research method separately.

## REFERENCES

1. Bernecker, R. R. and Price, D., "Studies in the Transition from Deflagration to Detonation in Granular Explosives," *Comb. and Flame*, Vol. 22, 1974, pp. 111-118, 119-129, and 161-170.
2. Samirant, M., "DDT in RDX and Ball Powder: Behavior of the Porous Bed," *Proceedings of the Eighth Symposium (International) on Detonation*, 1985, pp. 972-976.
3. Butler, P. B. and Krier, H., "Analysis of Deflagration to Detonation Transition in High-Energy Solid Propellants," *Comb. and Flame*, Vol. 63, 1986, pp. 31-48.
4. Verbeek, H. J., "Modelling of DDT in Granular Explosives," *Proceedings of the*

*Eighth Symposium (International) on Detonation*, 1985, pp. 669-677.

5. Verbeek, H. J. and van der Steen, A. C., "Linking Experimental and Theoretical Results on the Deflagration to Detonation Transition," *Proceedings of the 19th International Annual Conference of ICT on Combustion and Detonation Phenomena*, Karlsruhe, BRD, Jun 29-Jul 1, 1988; also to be published in *Prop. Explos. and Pyrotechn.*, Vol. 15, 1989.
6. Boris, J. P. and Book, D. L., "Flux-Corrected Transport III: Minimal-Error FCT Algorithms," *J. of Comp. Phys.*, Vol. 20, 1976, pp. 397-431.
7. Cowperthwaite, M. and Zwisler, W. H., "Tiger Computer Program Documentation," SRI Publ. No. Z106, Stanford Research Institute, Jan 1973.
8. McAfee, J. M.; Campbell, A. W.; and Asay, B.W., "Deflagration-to-Detonation in HMX under High Confinement," *Report LA-UR-87-3170*, Los Alamos National Laboratory.
9. Howe, P. M. and Frey, R. B., *Proc. AGARD Conf. No. 367*, Lisse, The Netherlands, May 1984.

## DISCUSSION

D. E. KOOKER, U.S. Army  
Ballistic Research Laboratory  
Aberdeen Proving Ground, MD

Your theoretical predictions of transition are strongly influenced by collapse of the aggregate to something close to TMD (denoted a "plug"). The computations show that a "plug" does form in an aggregate composed of 600  $\mu\text{m}$  grains, but it does not form in an aggregate composed of 200  $\mu\text{m}$  grains. This behavior would be a consequence of the mechanical properties assigned to the aggregate.

1. How does your constitutive model of the aggregate account for grain diameter?

2. Have you compared predictions from your constitutive model of the aggregate to quasi-static compaction data for an RDX/wax mixture? Presumably, any rate-dependent

effects would make the aggregate more difficult to compact.

3. As you mentioned, the LANL group [see McAfee et al., Proceedings of the Ninth Symposium (International) on Detonation] has observed "plug" formation during the transition to detonation in Class A HMX. Since Class A has a particle size closer to 200  $\mu\text{m}$  than 600  $\mu\text{m}$ , is there an inconsistency here or would RDX/wax be expected to behave in a different manner?

#### **REPLY BY H. J. VERBEEK AND A. C. VANDER STEEN**

1. Our compaction model is a complicated function of the porosity, the grain diameter, and their time derivatives. Essentially, the compressibility is higher for larger grain sizes.

2. The compaction model has not been compared with experimental data since such

data were not available. The parameters in the model have been estimated. Indeed, the rate-dependent effects make the aggregate more difficult to compact.

3. In our calculations, it appears that plug formation starts at a particle diameter of about 300  $\mu\text{m}$  and becomes more pronounced at larger diameters. The absolute values obtained from the model, however, should not be taken too literally. The model must mainly be seen as a qualitative means to examine the influence of various parameters on the DDT process. It cannot be used as a means to give an accurate quantitative prediction of experimental results, since too many parameters are unknown and since many important effects are not incorporated into the model, such as, e.g., the effect of the particle size distribution and fracture effects. Regarding the LANL experiments, it would be very interesting if they could present results about the influence of the particle size on the plug formation.

# NUMERICAL SIMULATION OF DEFLAGRATION-TO-DETONATION TRANSITION FOR TS 3659 PROPELLANTS

T. Hsieh and K. Kim  
Naval Surface Warfare Center  
Silver Spring, Maryland 20903-5000

*Numerical simulation and comparison with experimental data have been conducted for the deflagration-to-detonation transition process of TS 3659 propellant in a steel tube. In addition to the criteria used to specify the initiation of pyrolysis and compressive reaction, it was found necessary to introduce a particle breakup model in order to achieve the high pressure observed in experiments. A simple particle breakup model based on modification of surface burning area has been shown to serve the purpose. Detailed results are presented for pressure-time histories, distance-time history, distributions of gas pressure, solid stress, concentration of the intermediate product gas, and the final product gas.*

## INTRODUCTION

Experiment and theoretical/numerical modeling of the deflagration-to-detonation transition (DDT) process for porous energetic materials have been the subject of research for decades. Recently at NSWC, a series of experimental studies on DDT process in porous energetic materials in plastic or steel tubes has been carried out.<sup>1-3</sup> These experiments provide valuable information such as pressure-time histories at various locations along the tube wall, propagation of weak and strong shock waves, etc. This information, in turn, not only elucidates the mechanism of DDT but can also be used as guidance in development of theoretical or numerical models. Currently, there is a considerable amount of work on DDT modeling based on a two-phase flow theory with different degrees of sophistication in their constitutive equations.<sup>4-8</sup> The efforts to simulate numerically the DDT process in a tube have also been conducted at NSWC.<sup>9-12</sup> In References 9 and 10 the ignitor characteristics and convective combustion (CC), which is the early phase of DDT, had been numerically simulated for porous beds of HMX particles and WC 231 ball powder. The ignitor used in all of the above experiments was the same and,

therefore, is kept the same for all numerical simulations. The results of the simulation of convective combustion described in References 9 and 10 have compared favorably against experimental observation. However, because of the lack of a compressive combustion model in References 9 and 10, a precipitous rise of pressure near the end of the CC process was not predicted. In References 11 and 12 the empirical Forest Fire model was introduced and modified to give a single reaction rate expression as a function of pressure for both the surface and compressive reaction. It was found that the predicted pressure-time history and most flowfield features compared well with experimental observations. The success of References 11 and 12 encouraged us to attempt to simulate the experiment reported in Reference 3.

In Reference 3, Bernecker performed a DDT experiment with a porous bed of TS 3659 ball propellants. The ball propellants have a nearly spherical shape, which is a desirable feature in numerical simulation. The TS 3659 particles of nominal diameter of 432  $\mu\text{m}$  are packed at 59.8 percent of theoretical maximum density (TMD) (TMD of 1.65 g/cc) into a steel tube 305 mm long. The inner diameter of the

tube is 25.4 mm and the outer diameter is 76.2 mm. Both ends of the tube are closed and a small amount of ignitor mixture (which is made of 0.8 g of B/KNO<sub>3</sub> with a particle size of 140  $\mu$ m and has a density of 51.2% TMD) is located at one end. Events after the ignition of the ignitor are recorded by piezoelectric (PE) pressure transducers, located along the tube up to a predetonation column length and mounted flush to the wall. The output from a transducer was sent to both a high sensitivity recording channel ( $\sim 30$  MPa) and to a low sensitivity recording channel ( $\sim 1000$  MPa) of a digital oscilloscope. The transducers have a maximum pressure limit of 860 MPa. A total of four tests have been conducted and pressure-time histories at four locations along the tube will be used to compare with the numerical simulation to be presented in this paper.

## NUMERICAL SIMULATION

The present numerical simulation is based on the DETOVA code which was a minor modification of the XNOVAK<sup>13</sup> Code originally developed to simulate the transient flowfield in guns by numerical integration of a set of quasi-one-dimensional equations of unsteady, heterogeneous, reacting two-phase flows. The numerical method used was the explicit two-step predictor/corrector finite difference algorithm of MacCormack.<sup>14</sup> In this

paper the following assumptions are made: (1) the wall is rigid; (2) an equilibrium stress-strain (porosity) relationship taken from quasi-static compaction data is valid; (3) a correction for the solid phase compressibility based on the linearized Mie-Gruneisen equation of state as described in Reference 11 is valid at high pressures after the chemical reaction is initiated; (4) the flow resistance law of Jones and Krier<sup>15,11</sup> is valid; and (5) a global two-step chemical reaction from solid to the intermediate product gas, and from the intermediate product gas (TS 3569I) to the final product gas (TS 3659F) is valid.

The compaction law, which is a curve fit of the experimental quasi-static compaction data,<sup>16</sup> is expressed as follows:

$$\ln \sigma = a - b\varepsilon + c\varepsilon^2 + d/\varepsilon^2 \quad (1)$$

where  $\sigma$  is solid stress in psi,  $\varepsilon$  is porosity and  $a = -52.03$ ,  $b = -360.7$ ,  $c = 549.2$ , and  $d = 0$  for  $0.4 > \varepsilon > 0.35$  and  $a = 9.23$ ,  $b = 1.962$ ,  $c = -13.26$ , and  $d = 0.0002$  for  $0.35 > \varepsilon > 0.005$ . When  $\varepsilon$  is less than 0.005, it is set to 0.005 in computing  $\sigma$ . Figure 1 shows the experimental data and curve fit of Equation (1).

The ignitor modeled in the simulation occupies a small volume of a disk at one end of the tube. The thickness of the disk is 1.73 mm

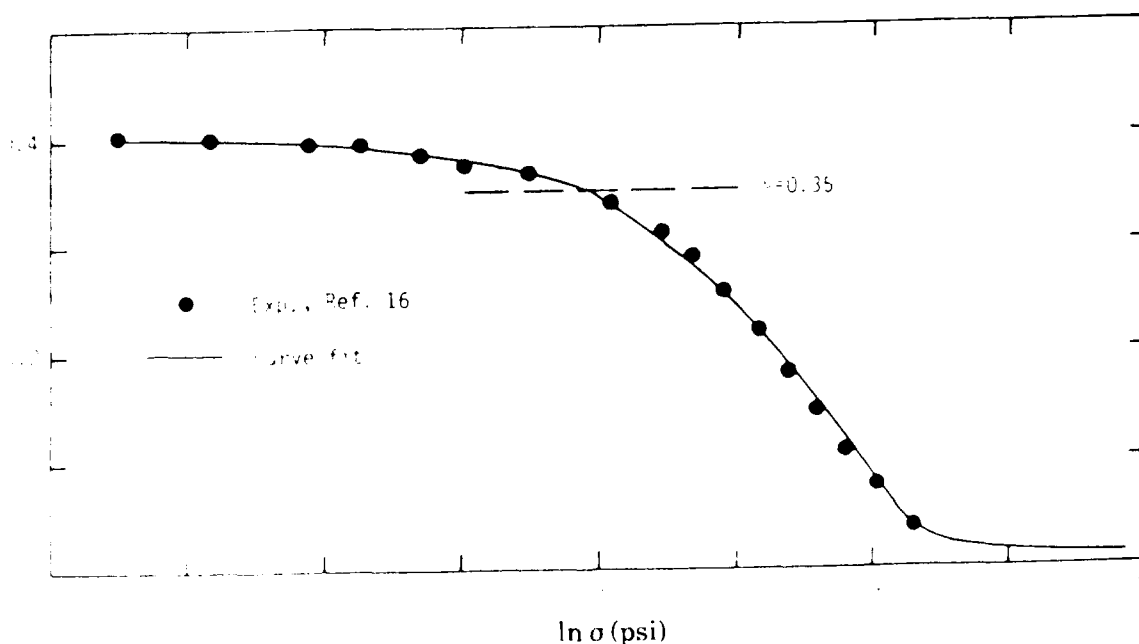


Figure 1. Curve Fit for the Compaction Law

and is assumed to have been ignited at the start of the simulation. In addition, a small ignitor gas source is assumed to exist with a prescribed discharge rate as shown in Table 1. Table 1 was used in Reference 6, but a shift of the time origin has been made with a very small increase (0.002 g/mm/ms) to the gas rate in order to match the experimental data of Reference 3 in this paper.

The first pyrolysis reaction from the solid propellant (TS 3659) to produce a pyrolysis product gas is initiated by an ignition temperature, which was set at 555°K. Once the reaction is initiated, it is assumed to progress according to a surface burning mode. The surface regression rate has been data-fitted by Kooker:

$$\dot{r} \text{ (mm/s)} = 2.44 p^{0.857} \text{ (MPa)} \quad (2)$$

Experimental data used in obtaining Equation (2) cover the pressure range from 7 to 200 MPa. In this paper, Equation (2) is assumed to be valid for all pressure ranges. The reaction rate from the pyrolysis gas, TS 3659I, to the final product gas, TS 3659F, is governed by the Arrhenius law; and the values of pre-exponential factor and activation energy are given as input data. A set of input parameters for TS 3659 for the experiment of Reference 3 is given in Table 2.

The criterion for the initiation of compressive reaction is the critical solid stress,  $\sigma^*$ . In each computational cell, once the solid stress has reached the value of  $\sigma^*$ , the compressive reaction begins. In this paper,  $\sigma^*$  is set to be 20.7 MPa (3000 psi). Once the compressive reaction is started, it is assumed to progress under the surface burning mode. The burning rate equation, Equation (2), is applied to the available surface area in the computation of the reaction rate. It should be noted that as soon as the compressive reaction is initiated, the pressure  $p$  in Equation (2) should be a newly-established mixture equilibrium stress (rather than the gas pressure calculated up to this point) between the gas pressure and the solid stress. This argument is based on the assumption that the initiation of the compressive reaction is fast and generates additional gas products. However, in the current modeling this sudden increase of gas pressure is not included, nor is the mixture equilibrium stress accurately calculated as the compressive reaction progresses. An approximate method that would work well in the simulation is to use  $p$  in Equation (2) as the larger of the gas pressure or the solid stress.

The rate of gas generation is dictated by the burning rate and the local available burning surface area of these particles. In Reference 18, it was found that the modified model of Kim for the burning surface area,

Table 1. Extra Ignitor Gas Source Description

$t^{**} \text{ (}\mu\text{s)}$ \diagdown $x^* \text{ (mm)}$	0.0	1.9	4.4	12.7
0.0	0.0***	0.0	0.0	0.0
135.0	0.002	0.002	0.0	0.0
215.0	0.054	0.054	0.0	0.0
235.0	0.134	0.134	0.0	0.0
255.0	0.339	0.339	0.0	0.0
415.0	0.303	0.303	0.0	0.0
425.0	0.0	0.0	0.0	0.0
1000.0	0.0	0.0	0.0	0.0

\*  $x$  is measured from the base of the tube

\*\*  $t$  in the simulation is shifted by 600  $\mu\text{s}$  from the reference time (detonation time) used in Reference 3

\*\*\* values at all intermediate points are linearly interpolated, unit is g/mm/ms

Table 2. Input Parameters

Length of the DDT tube	228.6 mm
Number of computational grids	241
Initial ambient gas	
Temperature	21°C
Pressure	0.2 MPa
Molecular weight	29.0
Ratio of specific heats	1.4
Ignitor	
Material	B/KNO <sub>3</sub>
Gas generation rate	See Table 1
Burning rate	2.67 p <sup>0.107</sup> cm/s with same erosive burning effect as TS 3659
Gas phase thermochemistry	
Heat of reaction	2.05 x 10 <sup>3</sup> Joule/g
Molecular weight	58.24 g/mole
Ratio of specific heats	1.1165
Covolume	0.36 cm <sup>3</sup> /g
TS 3659 solid	
Initial temperature	21°C
Material and initial density	59.8% TMD ball propellant powder
Initial grain diameter	432 μm
Ignition temperature for pyrolysis	555°K
Pyrolysis rate	2.44 p <sup>0.857</sup> cm/s with erosive burning effect
Erosive burning preexponential factor	3.76 cm <sup>3</sup> °K/Joule
Erosive burning exponential factor	105
Thermal conductivity	1.0 x 10 <sup>-3</sup> cal/cm/s/°K
Thermal diffusivity	0.2 x 10 <sup>-2</sup> cm <sup>2</sup> /s
TS 3659 pyrolysis product gas	
Heat of reaction	1.59 x 10 <sup>3</sup> Joule/g
Molecular weight	50.0 g/mole
Ratio of specific heats	1.15
Covolume	0.36 cm <sup>3</sup> /g
Reaction rate (to final product gas)	
Preexponential factor	0.554 x 10 <sup>8</sup> g/cm <sup>3</sup> s
Activation energy	2.62 x 10 <sup>10</sup> cm <sup>2</sup> /s <sup>2</sup>
TS 3659 final product gas	
Heat of reaction	2.98 x 10 <sup>3</sup> Joule/g
Molecular weight	24.78 g/mole
Ratio of specific heats	1.227
Covolume	0.36 cm <sup>3</sup> /g



which takes into consideration the available burning surface area under compaction of spherical particles, is adequate. The rate of generation of gas phase per unit volume, according to Kim's model, can be expressed by

$$\dot{m} = -\rho_s \phi_s \left( \frac{S}{V} \right) \left( \frac{1 - \phi_s}{\phi_s} \right)^{2/3} \dot{r}, \phi_s > 0.5 \quad (3)$$

where  $\rho_s$  is the solid density,  $\phi_s$  is the solid volume fraction,  $S$  and  $V$  are the surface area and the volume of each solid particle and  $\dot{r}$  is given by Equation (2). Equation (3) was used in this paper. It is noted that Equation (3) differs from that of Gough<sup>8</sup> by the factor  $F_a = [(1 - \phi_s) / \phi_s]^{2/3}$ . When  $\phi_s$  is less than 0.5,  $F_a$  is greater than 1, which is nonphysical. Therefore, when  $\phi_s < 0.5$ ,  $F_a$  is set to 1.0.

In Reference 6, it was found that the rate of reaction has a rapid increase around the pressure of 20 MPa. This phenomenon was attributed to the breakup of particles. It is known that TS 3659 ball propellant is hard to break at low to medium (static) pressure. However, it was found that it is still necessary to have a particle breakup model (at medium to high pressures) which rapidly increases the burning surface area and therefore increases reaction rate in order to match the measured pressure rise over the entire tube. It may be possible that particles break up in dynamic situations more easily than in static situations. A simple model to account for the particle breakup was developed. The idea is that when particles break up, a sudden increase of burning surface area must occur. Therefore, one must specify a particle-breakup pressure  $p_b$  and a factor for the increase of burning surface area,  $f_b$  (greater than 1). For TS 3659,<sup>3</sup> it was found that  $p_b \sim 35$  to 50 MPa with  $f_b \sim 2.0$  to 2.5 works well as described in the next section. It must be pointed out that the suggested particle breakup model requires further experimental investigation to justify its validity.

With a proper description of the boundary conditions and the initial conditions, the problem is ready for numerical simulation. At both ends of the tube, the boundary conditions require both the gas and solid particle velocity to be zero. An initial condition specified in the

simulation was that everywhere in the tube the temperature and pressure for the air and solid particles are given, their velocities are zero and the porosity is specified also.

In the simulation a total of 240 computational cells were evenly distributed over the entire tube length of 228.6 mm. All computations were performed using a CRAY-XMP computer and the CPU time was 0.00075 s/cell/step. Normally a case took about 5500 steps to complete.

## RESULTS AND DISCUSSIONS

In Reference 3 five tests were conducted with TS 3659 in steel tubes. It was found that events appeared reasonably consistent between each test when measured from the onset of detonation (both temporally and spatially). In the numerical simulation, because of the lack of high pressure data base for the surface burning rate, the compaction law, and a possibility of tube deformation, the accuracy of simulation at the high pressure range is always in question. Therefore, from the simulation point of view, one would like to see a good comparison with experiment in the low pressure range, which covers the convective combustion range, before extending the calculations toward the high pressure regime. This is the approach used in this paper.

In the numerical simulation, the pressure-time history at  $x = 3.2$  mm was selected as the primary guideline data. Figure 2 shows the comparison of pressure-time data between the numerical computation and the experiments (only two sets of experimental data are used, denoted as A266 and A268, because they are the most complete) for times up to 400  $\mu$ s. The agreement is satisfactory. One is, therefore, reasonably confident that the early phase of DDT process, or the convective combustion, has been correctly simulated.

For  $t > 400$   $\mu$ s, as seen in Figure 3, the experimental data indicate a rapid increase of pressure up to about 150 MPa, point B, then the rate of pressure increase slows down somewhat between 150 and 230 MPa. For  $230 < p < 580$  MPa, the curves become nearly a straight line and it is later followed by another straight line with greater slope. In the

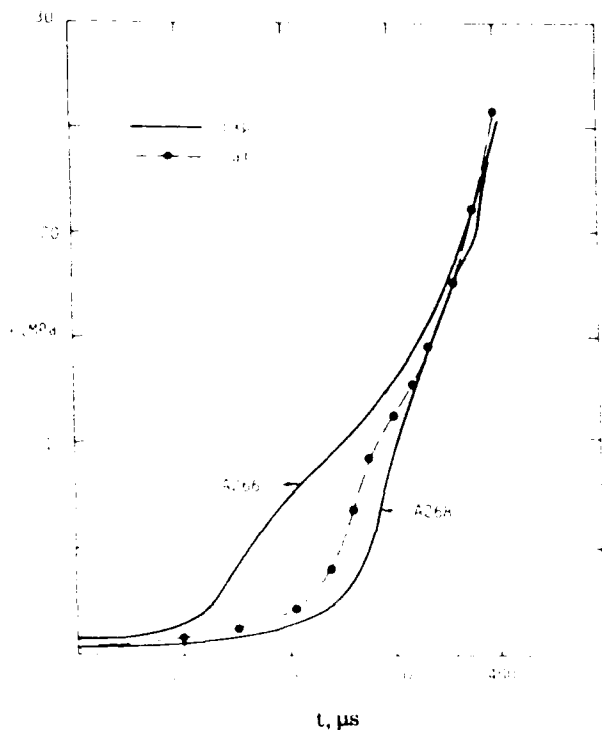


Figure 2. Comparison of Pressure-time History Between Experiment and Computation at  $x = 3.2$  mm in Low Pressure Range

numerical simulation, one could not simulate all the fine details of the  $p - t$  history. It was first found that without the particle breakup model as described in the previous section, the rise of the pressure is very slow as shown by the dashed line. The breakup model is very helpful in that it brings the pressure up to match the measured pressure, up to 600 MPa. The agreement between computation and experiment shown in Figure 3 is generally quite good except in the pressure range beyond 600 MPa, where another enhancement of the reaction rate is suspected.

The comparisons of pressure-time histories at  $x = 44.2$ , 66.2, and 85.2 mm between the computation and the experiment are shown in Figure 4. The agreement is good for  $x = 44.2$  mm until the pressure reaches 600 MPa where the computation starts to slow down (Figure 4a). Again it is suspected that there is an additional enhancement of the

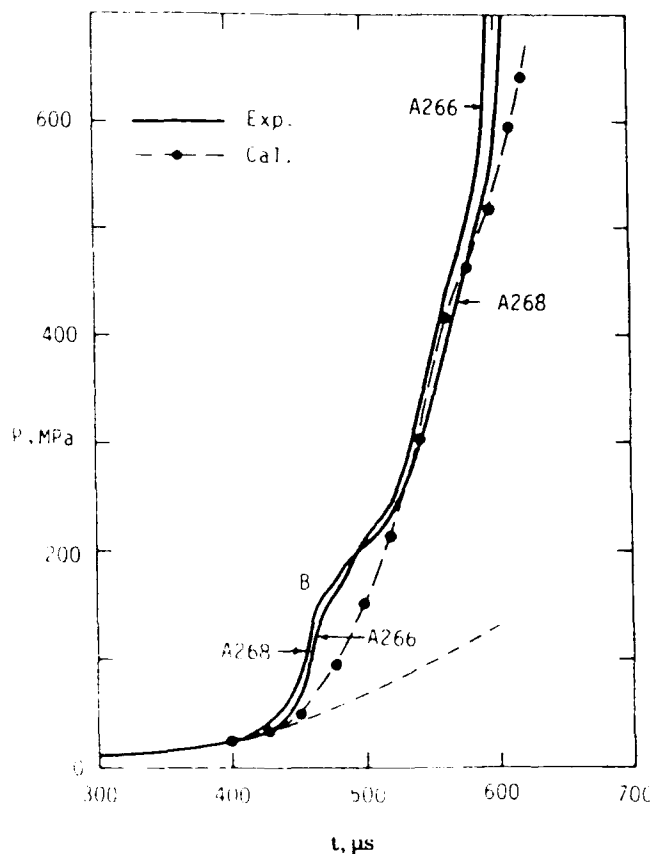
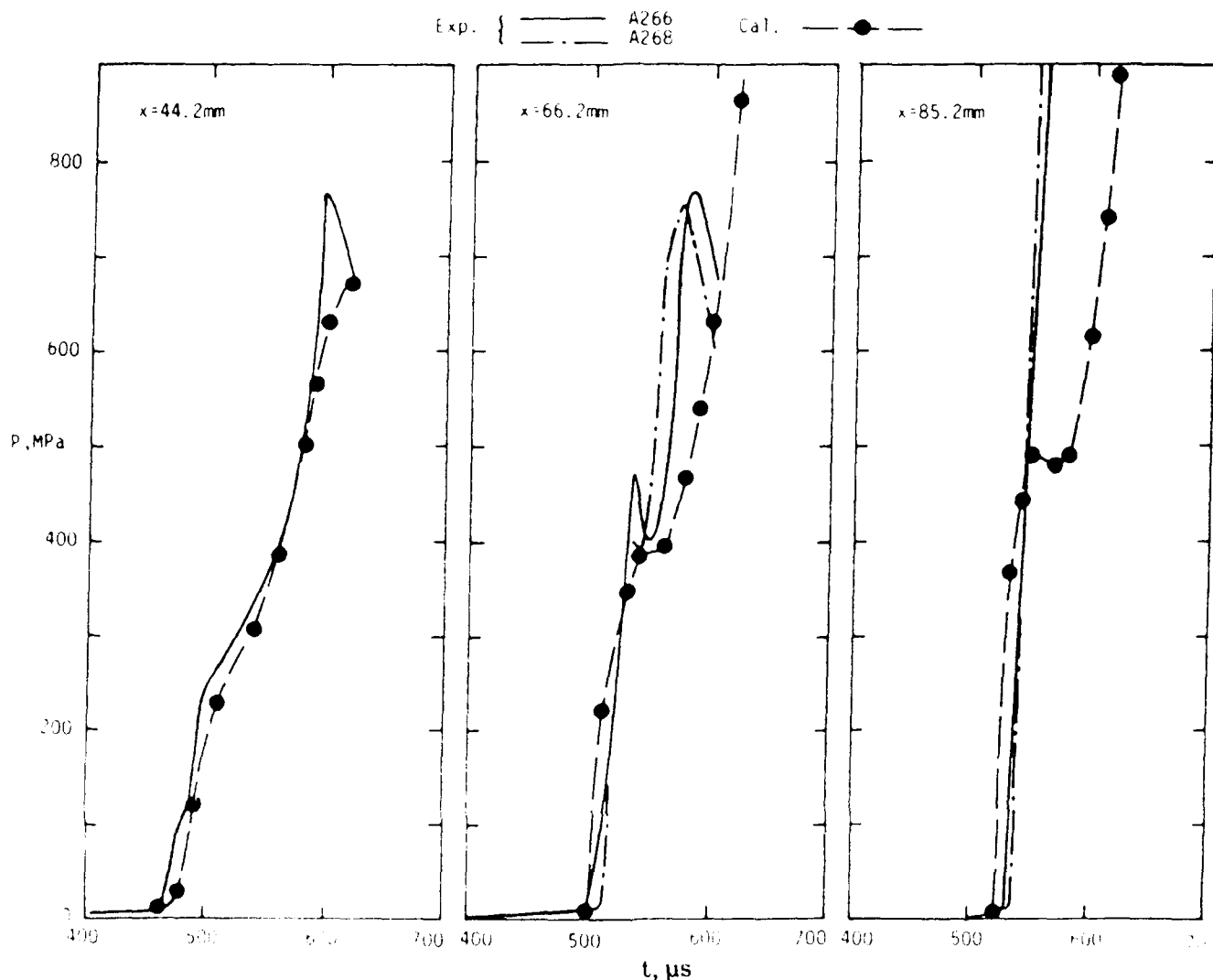


Figure 3. Comparison of Pressure-time History Between Experiment and Computation at  $x = 3.2$  mm in High Pressure Range

reaction rate at high pressures. At the locations of  $x = 66.2$  mm (Figure 4b) and 85.2 mm (Figure 4c), the agreements are good for pressure less than 400 MPa and 500 MPa, respectively. The wiggle of the experimental curve at  $t \sim 540$   $\mu$ s in Figure 4b, to some degree, also appears in the simulation. Such wiggles in  $p - t$  curves continue to exist in the computation as shown in Figure 4c, whereas in the experimental curves it disappears. As a result, in the computation the pressure rise in Figures 4b and 4c are delayed.

In Figure 5, a comparison of the relative distance-time data between computation and experiment is presented. For  $t < 530$   $\mu$ s, the experimental data between A266 and A268 differ from each other somewhat, but become very close for  $t > 530$   $\mu$ s. According to Reference 3, four regions can be identified from the distance-time plot: the weak compaction wave (WCW, velocity of 0.26-0.27 mm/ $\mu$ s), the



**Figure 4. Comparison of Pressure-time Histories Between Experiment and Computation at Various Locations**

strong compaction wave (SCW, velocity of 0.62-0.7 mm/ $\mu$ s) the reactive shock wave (RSW, velocity of 2.15 mm/ $\mu$ s) and detonation wave (DW, velocity of 5.17-5.19 mm/ $\mu$ s). In the numerical simulation, the picture is somewhat different. At  $t < 475 \mu$ s, one can identify two wave fronts: the compaction wave front of the solid and the shock wave front of the gas. These two fronts can be seen more clearly in Figure 6a where plots of the distribution of solid stress and gas pressure along the tube at different times are shown. The solid compaction wave front (associated with the introduction of compressive reaction) has a velocity of

0.23 mm/ $\mu$ s, which is close to the measure velocity of WCW; the velocity of gas shock wave front is about 0.15 mm/ $\mu$ s at this stage. Near  $t \sim 475 \mu$ s, after the introduction of particle breakup model described in the previous section, the propagating velocity increases rapidly to 0.89 which is close to the measured velocity of SCW and soon the gas shock wave front catches up with the solid compaction wave front to form a reacting shock wave. The velocity of RSW is about 1.3 at  $t \sim 520 \mu$ s and gradually increases to 1.7 mm/ $\mu$ s at  $t \sim 620 \mu$ s. It was not possible to obtain the measured detonation velocity of 5.19 mm/ $\mu$ s after extensive

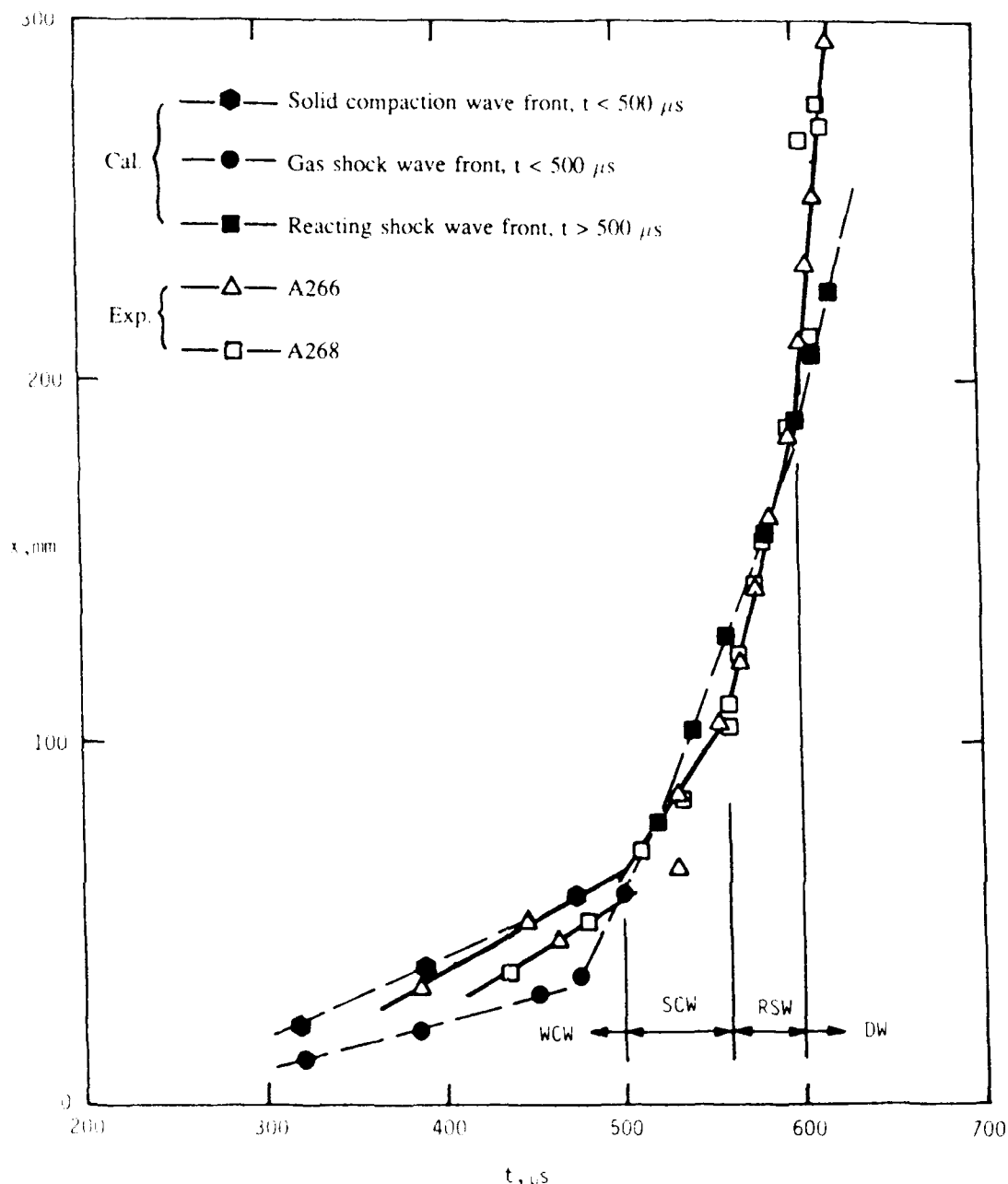


Figure 5. Comparison of Distance-time Data Between Computation and Experiment

effort to adjust the particle breakup model by using high values of  $f_b$ . This indicates that the present modeling is inadequate at the very high pressure range. Factors attributable to the inadequacy may be the following: (a) the surface regression rate, Equation (2), may be inadequate at the high pressure; (b) the particle breakup model used here is not adequate; and (c) the possibility of multidimensional effects such as the plastic deformation of the tube.

Figures 6a and 6b show the distribution of solid stress and gas pressure along the tube at various times. Before  $t \sim 300 \mu s$ , the formation of the solid compaction front and the gas shock wave front are not clear and, hence, were not plotted. In Figure 6a, one can see that the propagation of the solid compaction wave is faster than that of the gas shock wave. The rapid increase of the propagation velocity of the gas shock wave occurs after  $t \sim 452 \mu s$ . In Figure 6b, the solid stress plots were not shown

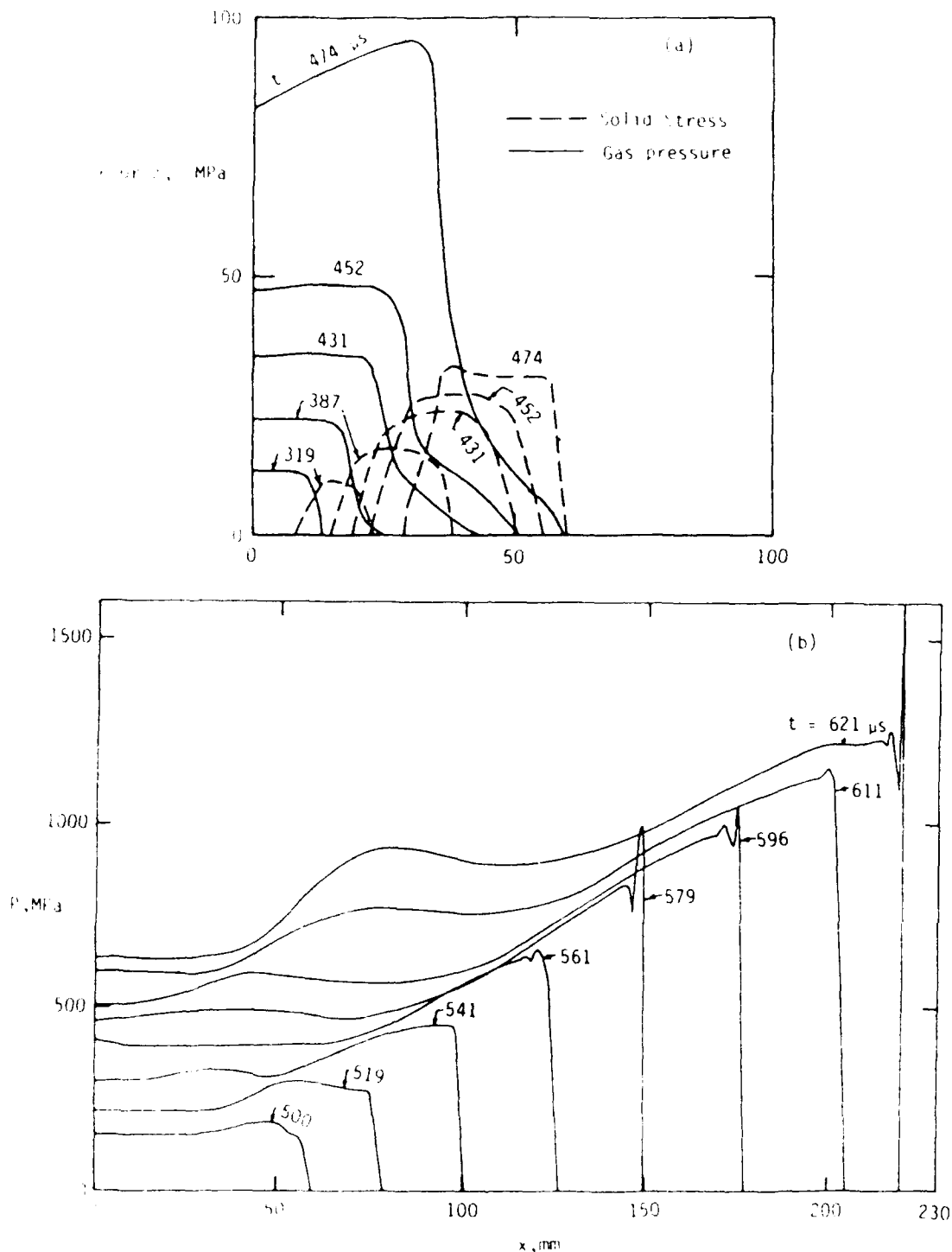


Figure 6. The Computed Distribution of Solid-Stress and Gas Pressure at Various Times

after the gas shock wave catches and merges with the solid compaction wave front at  $t \sim 500 \mu s$ . The DETOVA code, for the sake of simplicity, calculates only the gas pressure correctly (but not the solid stress) when the gas shock wave takes over the solid stress wave.

The computed concentrations of TS 3659I and of TS 3659F within the bed are shown in Figure 7 for various times. The close double humps of TS 3659I at  $t = 414 \mu s$  come from two different reactions: the pyrolysis produces the first hump and compressive burning produces

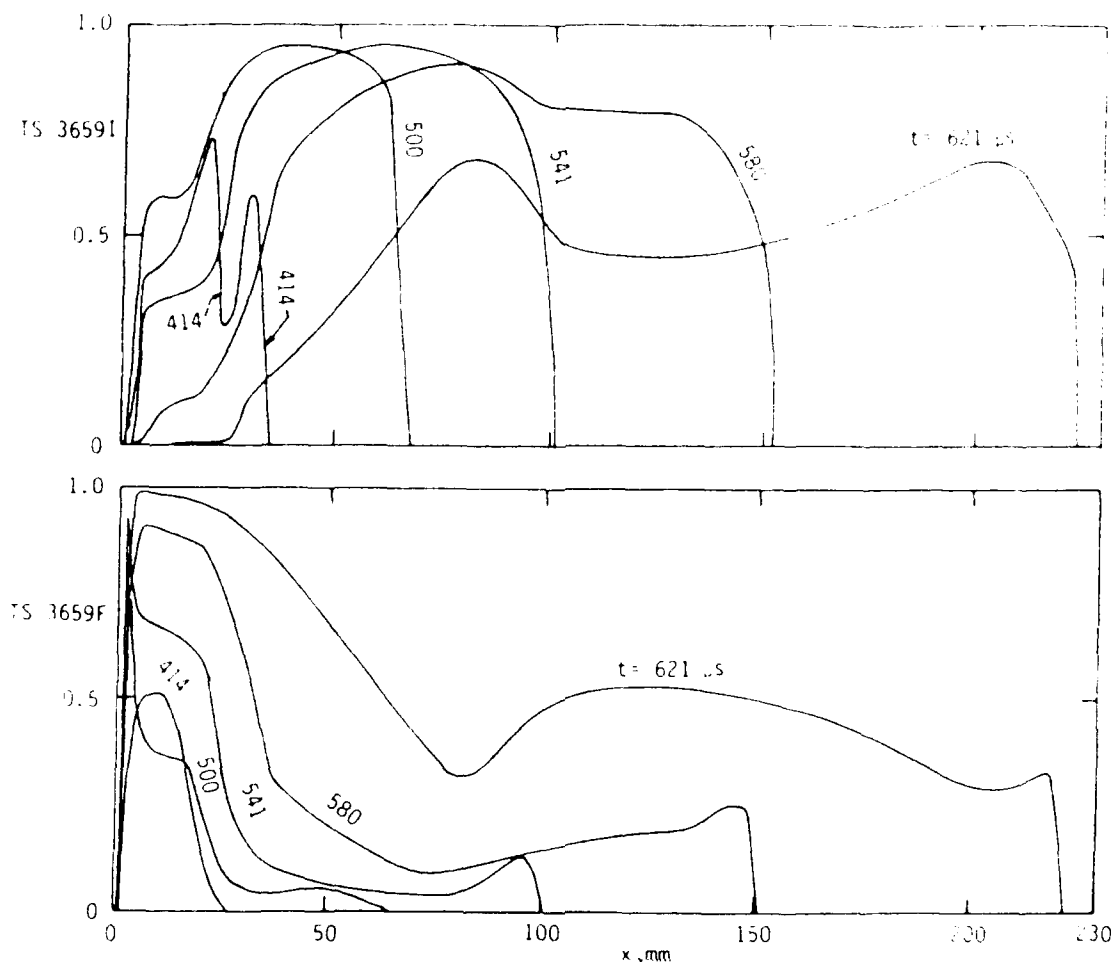


Figure 7. The Computed Concentrations of TS 3659I and TS 3659F at Various Times

the second hump. After the merge of the solid compaction wave front and the gas shock wave front near  $t \sim 500 \mu s$ , the distribution curve for TS 3659I becomes almost a single plateau. However at a later stage ( $t = 621 \mu s$ ) the curve becomes double-humped again with a large distance between the humps. It is also noted from Figure 7 that not until near the end, most energy release comes from the surface burning mode, which generate the TS 3659I. In other words, the reaction from TS 3659I to TS 3659F is relatively slow.

## SUMMARY

A numerical simulation of the deflagration-to-detonation transition process of TS 3659 propellant has been conducted and compared with experiments. The numerical simulation utilized the DETOVA code, which solves the conservation equations of quasi-one-

dimensional, unsteady, heterogeneous, reacting two-phase flows. Empirical equations for the flow resistance law, the solid compaction law, and the surface regression rate were used. A global two-step reaction scheme, from solid to intermediate product gas (TS 3659I) and from TS 3659I to the final product gas (TS 3659F) was employed. An ignition temperature was used to initiate the pyrolysis reaction and a critical solid stress was specified to initiate the compressive reaction. A modified surface burning model of Kim was used to describe the rate of gas generation after the initiation of both pyrolysis and compressive reactions. The results of the numerical simulation and comparison with experiment can be summarized as follows:

1. At low pressure range ( $p < 25 \text{ MPa}$ ) or in the convective combustion stage, the computed pressure-time histories near

the ignitor end compare well with the experiments.

2. At pressures beyond 20 MPa, the compressive reaction based on the original surface regression rate was found insufficient to simulate the experimental data. A simple particle breakup model, which modifies the surface area of burning, has been introduced and found to give better comparison with experiments.
3. For pressures less than 400 MPa, the pressure-time histories at four locations of the tube compare well with the experimental data. However, this is not true for  $p > 400$  MPa, where the computed pressure lags the experiment.
4. The four experimentally observed wave fronts, (i.e., weak compaction wave, strong compaction wave, reacting shock wave, and detonation wave) can only be roughly identified in the numerical results. Instead, the simulation offers a slightly different explanation.
5. The computed distributions (along the bed) of gas pressure, solid stress, and concentration of TS 3659I and TS 3659F are presented for various times.

## ACKNOWLEDGEMENT

The CRAY-XMP computer support of NASA ARC under the cooperative program with NSWC is gratefully acknowledged.

## REFERENCES

1. Bernecker, R. R.; Sandusky, H. W.; and Clairmont, Jr., A. R., "Deflagration-to-Detonation Transition Studies of Porous Explosive Charges in Plastic Tubes," *Proceedings of Seventh Symposium (International) on Detonation*, 1982, pp. 119-138.
2. Bernecker, R. R.; Sandusky, H. W.; and Clairmont, Jr., A. R., "Deflagration-to-Detonation Transition Studies of a Double Based Propellant," *Proceedings of Eighth Symposium (International) on Detonation*, 1985, pp. 658-668.
3. Bernecker, R. R., "DDT Studies of a Spherical, Double-Based Ball Propellant," *Proceedings of 1987 JANNAF PSHS Meeting*, CPIA Pub. 464, Vol. 1, 1987, pp. 1-11.
4. Baer, M. R. and Nunziato, J. W., "A Two-Phase Mixture Theory for the Deflagration-to-Detonation Transition (DDT) in Reactive Granular Materials," *Int. J. Multiphase Flow*, Vol. 12, No. 6, 1986, pp. 861-889.
5. Price, C. and Boggs, T. L., "Modeling the Deflagration-to-Detonation Transition in Porous Beds of Propellant," *Proceedings of Eighth Symposium (International) on Detonation*, NSWC MP 86-194, 15-19 Jul 1985, pp. 934-942.
6. Weston, A. M. and Lee, E. L., "Modeling 1-D Deflagration-to-Detonation Transition (DDT) in Porous Explosives," *Proceedings of Eighth Symposium (International) on Detonation*, NSWC MP 86-194, 15-19 Jul 1985, pp. 914-925.
7. Butler, P. B. and Krier, H., "Analysis of Deflagration-to-Detonation Transition in High Energy Transition Propellants," *Combustion and Flame*, Vol. 63, 1986, pp. 31-48.
8. Krier, H. and Keizerle, J. A., "A Separated Two-Phase Flow Analysis to Study Deflagration-to-Detonation (DDT) in Granulated Propellant," *Proceedings of Seventh Symposium (International) on Combustion*, The Combustion Institute, 1978, pp. 23-33.
9. Kim, K. and Glancy, B., "Numerical Simulation of Convective Combustion in Porous Beds of HMX Particles Using Two-Step Chemical Reactions," *Proceedings of 1987 JANNAF Propulsion Systems Hazards Meeting*, CPIA Publication 464, Vol. 1, 1987, pp. 29-38.
10. Hsieh, T. and Kim, K., "Numerical Simulation of Convective Combustion in Porous Beds of WC 231 Ball Powder," *Proceedings of 1988 JANNAF Propulsion Systems Hazards Meeting*, CPIA Publication 477, Vol. I, Mar 1988, pp. 37-46.

11. Hsieh, T. and Kim, K., "Numerical Simulation of Complete Deflagration-to-Detonation Transition Process in Porous Beds of HMX Particles," presented at the 19th International Annual Conference on Combustion and Detonation Phenomena, Karlsruhe, West Germany, Paper No. 100, 1988.
12. Hsieh, T. and Kim, K., "Flowfield in a Porous Bed of HMX Particles During a Complete Deflagration-to-Detonation Transition Process," Proceedings of the 3rd International High Dynamic Pressure Symposium, La Grande Motte, France, 5-9 Jun 1989.
13. Gough, P. S., "Theoretical Modeling of Navy Propelling Charges," Paul Gough Associates, Inc., Report PGA-TR-84-1, Portsmouth, NH, 1984.
14. MacCormack, R. W., "The Effect of Viscosity in Hypervelocity Impact Cratering," AIAA Paper 69-354, 1969.
15. Jones, D. P. and Krier, H., "Gas Flow Resistance Measurements Through Packed Beds at High Reynolds Numbers," *J. of Fluid Engineering*, Vol. 105, 1983, pp. 168-173.
16. Sandusky, H. W.; Glancy, B. C.; Campbell, R. L.; Krall, A. D.; Elban, W. L.; and Coyne, Jr., P. J., "Compaction and Compressive Reaction Studies for Spherical, Double-Base Ball Propellant," *Proceedings of 25th Combustion Meeting*, NASA Marshall Space Flight Center, Oct 1988.
17. Kooker, D. E., "Predictions for the Piston-Driven-Compaction Experiment Based on Transient Reactive Shock Wave Model," JANNAF PSHS Meeting, 15-26 Oct 1988, Huntsville, AL.
18. Hsieh, T. and Kim, K., "Numerical Simulation of Piston-Driven-Compaction Experiment for TS 3659 Propellant," JANNAF PSHS Meeting, at Brooks Air Force Base, San Antonio, TX, 21-24 Feb 1989.

## DISCUSSION

**BARRY BUTLER**  
University of Iowa  
Iowa City, IA

(a) You use a particle breakup mechanism in your DDT model. First, is particle breakup observed in quasi-static compaction experiments of your material?

(b) Second, do you treat the effect of particle breakup on other processes during DDT (e.g., permeability changes, heat transfer changes, etc.)?

## REPLY BY K. KIM AND T. HSIEH

(a) No, we do not observe particle breakup in quasi-static compaction; however, there is no experimental observation on dynamic compaction. In dynamic compaction where the compaction rate is very fast as is the case of DDT in our paper, different particle breakup behavior may be expected. Another possibility is an increased surface regression rate at high pressure.

(b) No, we do not need to treat the effect of particle breakup. Other physical parameters/processes such as gas permeability and heat transfer are no longer important in the high pressure burning region of our consideration.



# DYNAMIC COMPACTION AND COMPRESSIVE REACTION STUDIES FOR SINGLE AND DOUBLE-BASE BALL PROPELLANTS

B. C. Glancy, H. W. Sandusky, and P. J. Miller  
Naval Surface Warfare Center  
White Oak Laboratory  
Silver Spring, Maryland 20903-5000

and

A. D. Krall  
Advanced Technology and Research, Inc.  
14900 Sweitzer Lane, Suite 104  
Laurel, Maryland 20707

*Dynamic compaction and compressive reaction were examined in detail for radially confined porous beds of three ball propellants that were impacted on one end by a long plastic rod (velocities of 75 to 300 m/s). The data are required for numerically modeling the final stages of deflagration-to-detonation transition (DDT). High-speed photography, flash radiography, ionization and self-shorting probes, piezoelectric transducers, microwave interferometry, and IR radiometry were used, depending on the tube confining the porous bed, to measure impactor velocity after impact, to locate reaction sites, to resolve temporally and spatially the compaction/reaction waves, as well as to obtain their pressure profiles. A comparison of dynamic compaction data with previously obtained quasi-static data indicates that ball propellants are substantially more difficult to compact dynamically than quasi-statically, especially in the middle of the compaction range. Observations are made concerning the creation of hot spots by dynamic compaction and the compressive reaction initiated at those sites. Marginal reaction was obtained in the single-base material, versus vigorous reaction in the double-base materials. The sensitivity to compressive reaction for these propellants correlates with their propensity to undergo DDT.*

## INTRODUCTION

The rapid growth of reaction that occurs in the final stages of DDT in porous materials is initiated by high strain rate deformation ( $\sim 10^5 \text{ s}^{-1}$ ) within a strong compressive wave (SCW). This process was studied by driving a single, well-defined SCW with the impact of a piston, thus avoiding the complications of a DDT experiment in which compressive waves are generated by conductive/convective burning near the ignitor and coalesce into a SCW

further downstream.<sup>1</sup> Using the piston impact approach, the thresholds for first detection of "compressive" reaction, the onset of rapid growth of reaction, and the transition to detonation were obtained as a function of impact pressure for a variety of materials. Observations reported in Reference 1 were primarily deduced from high-speed photography of beds confined by plastic tubes or from the responses of ionization probes in beds confined by steel tubes, thus few details of the onset and growth of compressive reaction were obtained.

This paper provides both pressure measurements and front locations during compressive reaction for some "simple" energetic materials so that the experiments can be modeled numerically. These "simple" materials are the Olin ball propellants WC 140 and TS 3659. The TS 3659 particles are spherical while the WC 140 particles are mostly spherical with some "jelly beans".<sup>2</sup> The particles of both materials are nearly uniform in size (411  $\mu\text{m}$  for WC 140 and 434  $\mu\text{m}$  for TS 3659), which permits the particles and the packed beds they form, to be easily described. WC 140 is a single-base material of nitrocellulose (NC) with a theoretical maximum density (TMD) of 1.65 g/cc. TS 3659 has a TMD of 1.64 g/cc and is a double-base propellant consisting of NC with 21.6 percent nitroglycerin (NG). Ball propellants deform in a predictable manner under load, rather than fracturing into uncertain sizes and numbers of particles; bed compaction can be described by fundamental analyses.<sup>3</sup> These analyses utilized quasi-static compaction measurements for both TS 3659<sup>4</sup> and WC 140.<sup>2</sup> Both of these materials have also been evaluated in steel DDT tube tests; TS 3659 transits to detonation,<sup>5,6</sup> whereas WC 140 does not.<sup>5</sup>

Another Olin material that has been studied previously, WC 231 reloading powder, was reexamined in an experiment that included IR radiometry measurements. The temperature and total luminescence provided by those measurements were correlated with simultaneous high-speed photographic and flash radiographic observations. WC 231 is NC with 25.2 percent NG, about the same composition as TS 3659 but is a rolled material with pancake-like particles containing large cracks.<sup>2</sup> This material is more shock sensitive than other ball powders studied at the Center,<sup>5</sup> and will undergo DDT in both plastic and steel tubes.<sup>5,7</sup>

## EXPERIMENTAL ARRANGEMENTS AND INSTRUMENTATION

The experimental apparatus<sup>1</sup> (Figure 1) consists of a powder gun for propelling a polycarbonate (Lexan) rod into a tube which confines a porous bed of the material under

investigation. Various tubes have been used which offer differing confinement and possibilities for instrumentation. Optically clear tubes of Lexan are often used in initial experiments on an energetic material because these tubes permit observations by both high-speed photography and flash radiography. However, the low confinement of Lexan tubes is sometimes insufficient for any growth of compressive reaction, and compaction measurements must be corrected for tube expansion.<sup>8,9</sup> Compaction measurements not requiring correction have been obtained by flash radiography in intermediate confinement, which utilizes either 1) a supported thin-wall aluminum tube where the x-rays are directed between the supports<sup>9</sup> or 2) a thick-wall aluminum tube with the wall thinned in the zones requiring x-ray penetration.<sup>4</sup> Most of the compressive reaction experiments to be discussed were conducted in the high confinement of thick-wall (25.4 mm) steel tubes. These tubes had ionization and/or self-shortening probes, mounted every 12.7 mm through the tube wall, with their sensing end flush with the inner wall; piezoelectric pressure transducers (PCB 109A02) with an upper limit of 0.86 GPa were similarly mounted at two locations, generally  $\sim 38$  and  $\sim 76$  mm from the upstream end of the tube. The disadvantage of not having high-speed photographic and flash radiographic observations of the bed were in part overcome by inclusion of a microwave interferometer (MI).<sup>10</sup>

The MI was primarily used as a non-intrusive, continuous monitor of the first front in the bed, but responds to any microwave reflector. The interferometer circuit is much like that used in a previous DDT study.<sup>11</sup> The microwaves are directed into the downstream end of the tube shown in Figure 1. Before reaction begins, the microwaves are partially reflected by the change in dielectric constant associated with the change in bed density at the compaction front; the remainder of the microwaves are reflected by the foil-faced piston. Once "hot spot" reaction begins at the front, additional reflection occurs from the ionization associated with the reaction. The reflected signals return to an interferometer circuit where they are mixed with a reference signal. A beat occurs every time the first front

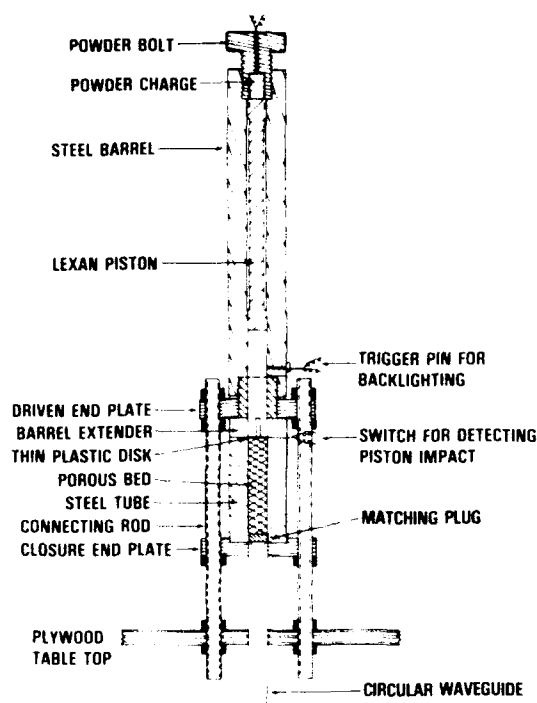


Figure 1. Schematic of Apparatus for Dynamic Loading Experiments

moves one half of the microwave wavelength in the original bed packing (the wavelength was independently measured for these porous beds using a cavity resonance method). When examining the quadrature output signals for only peaks and valleys, the resolution for locating the downstream front is one eighth of the wavelength, which in these experiments results in a resolution of  $\sim 3$  mm.

## EXPERIMENTAL DATA

A summary of initial conditions and results for all experiments is listed in Table 1. Some piston velocities prior to impact ( $v_p$ ) are listed as approximate because they are based on a calibration of the gun. Otherwise, a streak camera was used in measuring both  $v_p$  and  $u$ , the piston velocity after impact, and hence the particle velocity as listed in Table 1. In the experiments with WC 140 confined by an aluminum tube, both the particle and compaction front velocities were from flash radiography data; the three sets of data for each experiment are arranged in the order of the radiographic exposures. In the other

experiments in which compaction front velocity ( $U$ ) is reported, its measurement was usually verified by more than one method, as will be shown. The measured values of  $u$  and  $U$  were used in jump condition calculations to obtain extent of compaction,

$$\%TMD = \%TMD_0 / (1 - u/U), \quad (1)$$

and axial bed pressure,

$$p(\text{MPa}) = p_0 + \%TMD_0 \cdot TMD \cdot U \cdot u \cdot 10^{-5}, \quad (2)$$

where  $\%TMD_0$  is the initial bed packing,  $p_0 = 0.1$  MPa, and both  $u$  and  $U$  are in units of m/s.

The listings in Table 1 of "time for first detection of reaction" ( $\Delta t$ ) and "COMMENTS" indicate the ease of igniting and then obtaining growth of compressive reaction. The values for  $\Delta t$  were obtained in a different manner from that used in Reference 1, and may not correspond to the same level of reaction. For example, while "first light" on the camera film in a Lexan tube experiment was usually associated with  $\Delta t$  in Reference 1, no luminous reaction was observed during the Lexan tube experiments on TS 3659 (Shots PDC-76, 77, 78). The reported  $\Delta t$  in Table 1 for Shot PDC-78 corresponds to a noticeable decrease in backlighting through the piston, presumably from optically opaque reaction products flowing between the inner wall and the piston.

## HIGH CONFINEMENT EXPERIMENTS ON WC 140

Prompt compressive reaction did not occur in any of the WC 140 experiments. Hence, observations concerning compaction front (CF) propagation, onset and growth of compressive reaction, and formation of a strong compressive wave (SCW) by the pressure buildup from reaction could be clearly distinguished. The first high confinement experiment (Shot PDC-71) was instrumented with only self-shortening probes; the SCW overtook the CF 152 mm down the bed,<sup>12</sup> but the time frame for development of the SCW and the pressures associated with it are unknown. These questions were addressed in subsequent experiments (Shots M-30, 31) which were instrumented with self-shortening and ionization probes, pressure transducers,

Table 1. Summary of Dynamic Loading Experiments

Initial Conditions						Results					
Matl.	Shot	%TMD <sub>0</sub>	L (mm)	Tube	v <sub>p</sub> (m/s)	u (m/s)	U (m/s)	%TMD	p (MPa)	Δt (μs)	Comments
WC 140	PDC-62A	60.4	101	Alum.	~75	57	455	69.0	25.9	—	Tube intact
						56	448	69.0	25.1		
						54	453	68.5	24.50		
	PDC-62B	60.5	101	Alum.	~161	100	503	75.5	50.3	—	Tube intact
						102	548	74.3	55.9		
						95	512	74.3	48.6		
	PDC-64	60.5	126	Alum.	~200	156	594	82.0	92.6	—	Tube ruptured by late reaction
						146	552	82.2	80.5		
						145	559	81.7	81.0		
	PDC-71	60.5	191	Steel	180	134	558	79.8	74.7	<200	Late ignition
	M-30	60.5	146	Steel	210	161	563	84.7	90.6	119	Late ignition with slow growth of reaction
	M-31	60.5	146	Steel	300	204	574	93.9	117	~133	Late ignition with slow growth of reaction
TS 3659	PDC-76	60.2	146	Lexan	~150	207	—	—	—	83	Tube intact
	PDC-77	60.2	146	Lexan	~200						Tubes ruptured but no luminous reaction seen (for both Shots 77 and 78)
	PDC-78	60.2	146	Lexan	291						
	PDC-80	60.2	102	Alum.	160						Delayed reaction
	PDC-81	60.1	147	Steel	237						Delayed reaction
	PDC-82	60.1	147	Steel	300						Vigorous reaction
WC 231	PDC-73	49.4	127	Lexan	220	183	405	90.1	60.1	119	Luminous reaction

% TMD<sub>0</sub> = Initial bed density

% TMD = Jump condition calculation for bed compaction, %TMD<sub>0</sub>·U/(U-u)

L = Bed length including driven end disk (~0.8 mm)

v<sub>p</sub> = Velocity of Lexan piston just prior to bed impact

u = Particle velocity of bed (Piston velocity<sub>z</sub> after bed impact)

U = Compaction front velocity

p = Jump condition calculation for compaction pressure (see text)

Δt = Time between bed impact and detection of reaction

and the MI. The 210 and 300 m/s impacts in Shots M-30 and M-31, respectively, resulted in very similar events; it is data from Shot M-30 that will be presented in detail.

For Shot M-30, the low range of pressure data from transducers at 38.4 mm (P<sub>1</sub>) and

76.4 mm (P<sub>2</sub>) are shown in Figure 2a and distance-time data are plotted in Figure 2b. Several observations, which also apply to other experiments, can be made about the response of the transducers to the CF in Figure 2a (note that the observed pressures are radial pressures on the inner wall, not the axial

pressure driving the CF). The risetime of the front pressures (10.0  $\mu$ s for  $P_1$  and 9.5  $\mu$ s for  $P_2$ ) correspond to a maximum thickness for the CF of 5.6 mm; however, the actual thickness may be less considering that the piezoelectric sensing area is 4.0 mm in diameter. The peak pressures for the CF, 65.9 MPa at  $P_1$  and 61.1 MPa at  $P_2$ , declined slightly as the front propagated from  $P_1$  to  $P_2$ ; therefore, reaction pressure was not yet compensating for loss of piston momentum and wall friction. Following each peak there was a rapid decline in pressure; by the time the CF reached  $P_2$ , the  $P_1$  pressure was only about half of the peak CF pressure at  $P_2$ , indicating that the decline may not be a true indication of axial pressures. The end of the rapid decline in pressure behind the CF, indicated by the points "E", forms a line parallel to the CF in Figure 2b. A similar pressure decline behind the CF was also observed in WC 140 Shot M-31 and TS 3659 Shot PDC-81, which had about the same impact velocity as Shot M-30. For the lower velocity impact (160 m/s) in TS 3659 Shot PDC-80, there was very little pressure decline after passage of the CF.<sup>4</sup>

The first detection of reaction is associated with the minimum pressure behind the CF, and is designated by the symbol "M" on the traces in Figure 2a. Extrapolating these points back to the piston face, where first reaction is expected to occur, yields a time of 119  $\mu$ s. There was no significant growth of reaction at that time; the symbol "R" in Figure 2a is used to show the first appearance of reaction growth and is still early relative to the rapid rise seen at  $\sim 300 \mu$ s on  $P_2$ . As evidenced by the constant CF velocity, the SCW never caught the CF before it reached the end of the bed; in Shot PDC-71 with the somewhat longer bed it did catch the CF. The rapid rise in pressure at  $P_2$  corresponds well with the "late reaction" detected by the MI; however, MI data after the CF reaches the end of the bed cannot be interpreted exactly.

## HIGH CONFINEMENT EXPERIMENTS ON TS 3659

The initial response of TS 3659 to a 237 m/s impact (Shot PDC-81) was much the same as in the WC 140 experiments, except

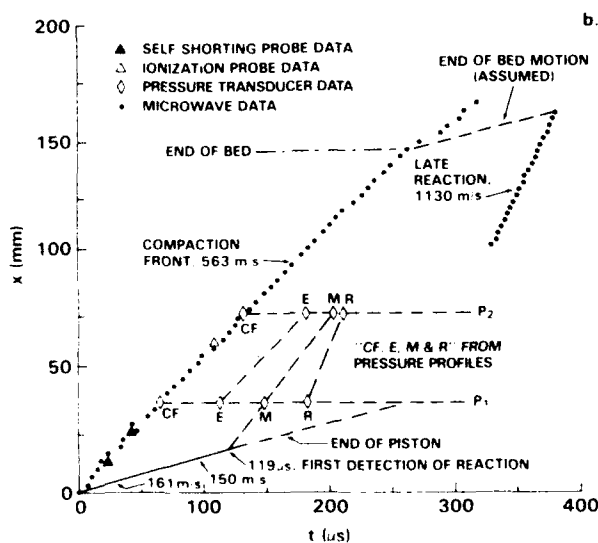
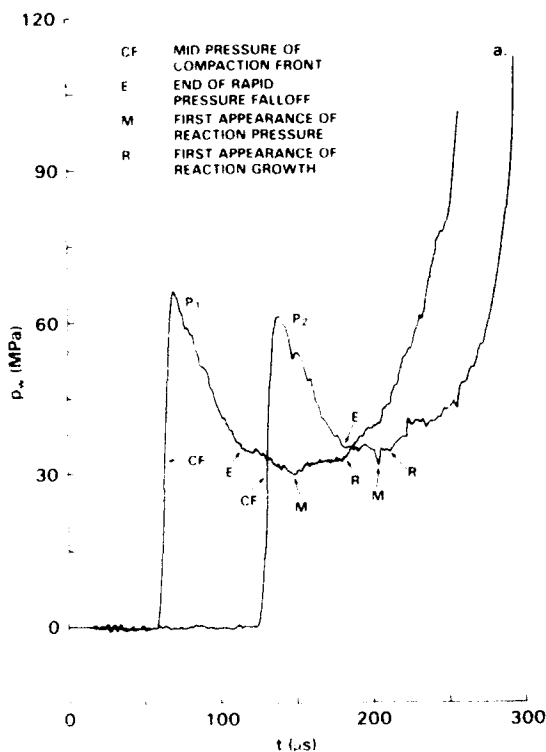


Figure 2. Data from a 210 m/s Impact of 60.5 Percent TMD WC 140 (Shot M-30): a. Low Range of Inner Wall Pressure at 38.4 mm ( $P_1$ ) and 76.4 mm ( $P_2$ ); b. Summary of Distance-Time Data

that compressive reaction occurred somewhat sooner and the growth of reaction was more rapid. The high range of pressure data in Figure 3a for Shot PDC-81 show reaction pressures near or exceeding the 0.86 GPa limit of the transducers. The distance-time data in Figure 3b indicate that weak compressive waves, driven by the onset of reaction growth (symbol "R"), reached the CF prior to its abrupt transition to a velocity of 1800 m/s. Note that the compaction front velocity, which is a relatively insensitive measure of pressure, does not appear to increase until the abrupt change  $\sim 13$  mm before the end of the bed; however, triggering of ionization probes just prior to the transition also indicate that the CF pressure was increasing. The rapid rises in pressure at  $\sim 200$   $\mu$ s, seen in Figure 3a, apparently drove a SCW which caused the abrupt transition in the CF velocity.

In a 300 m/s impact on TS 3659 (Shot PDC-82) much greater growth of reaction occurred with little delay. The transducer outputs in Figure 4a show that rapid growth of reaction was just behind the compaction front as it passed  $P_1$  and that the first arrival at  $P_2$  was a strong shock. The pressure behind the front did not actually decline as the transducer indicates, rather the decline is due to

transducer failure. The 300 m/s impact resulted in such violent and prompt reaction that the 305 mm long Lexan impactor had stopped and was reversing direction by the time the first front had propagated 80 mm into the TS 3659 (Figure 4b).

The MI fringe data provided additional insight into these experiments beyond tracking the position of the first front. The fringe data in Figure 5a from Shot PDC-81 were, in large part, very similar to those obtained for an inert compaction wave.<sup>10</sup> The relatively weak, high frequency signal from the compaction front was superimposed onto the lower frequency signal from the conductively faced piston, which reflected all of the signal reaching it. After the SCW overtook the front, the reactive front reflected considerably more of the signal. This larger signal could only be partially attributed to a change in dielectric constant from increased compaction.<sup>10</sup> Therefore, ionization from hot spots created at the front was the most probable cause of the increased reflection of microwaves. Interestingly, the MI output neither outlined nor was affected by the propagation of the SCW until it overtook the compaction front. This indicates that the SCW was itself not initiating new hot spot reaction (until it overtook the

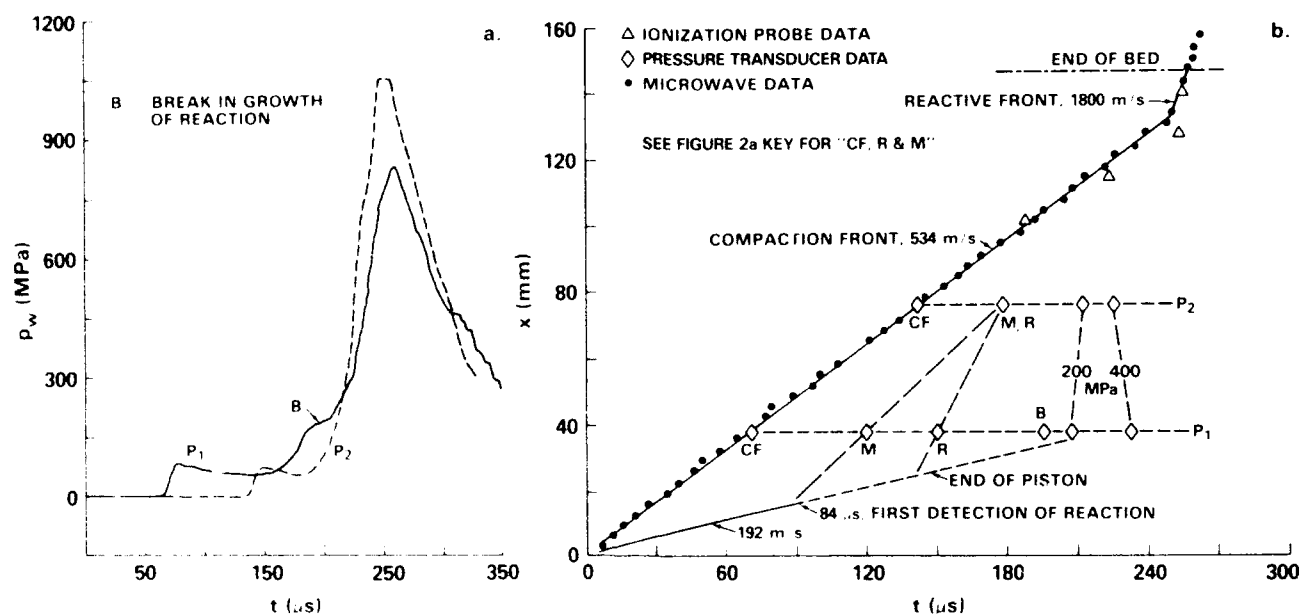


Figure 3 Data from a 237 m/s Impact of 60.1 percent TMD TS 3659 (Shot PDC-81): a. Inner Wall Pressures at 38.1 mm ( $P_1$ ) and 76.2 mm ( $P_2$ ), b. Summary of Distance-Time Data

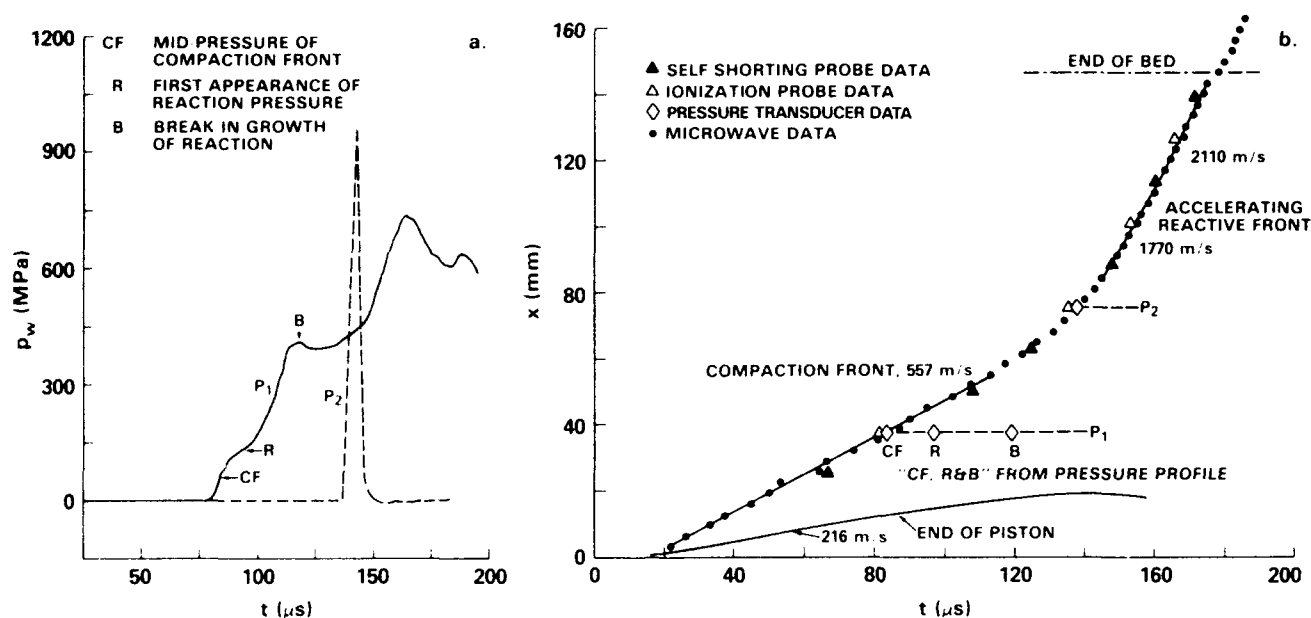


Figure 4. Data from a 300 m/s Impact of 60.1 Percent TMD TS 3659 (Shot PDC-82): a. Inner Wall Pressure at 38.1 mm ( $P_1$ ) and 76.2 mm ( $P_2$ ); b. Summary of Distance-Time Data

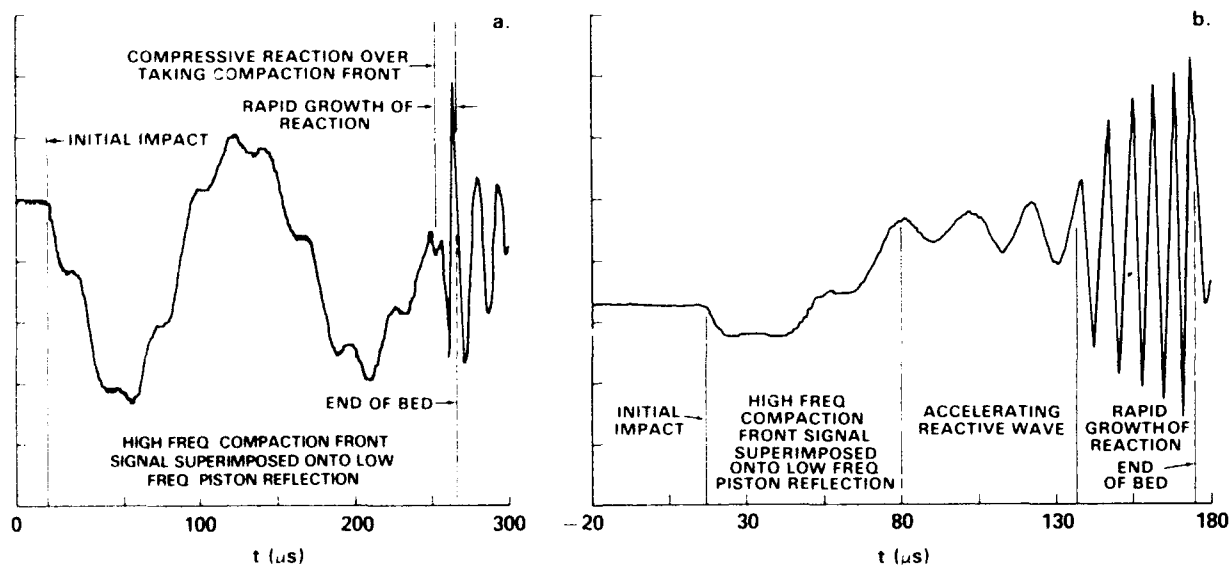


Figure 5. Microwave Interferometer Outputs from (a) Shot PDC-81 and (b) Shot PDC-82

compaction front) and that there was little ionization in the reaction zone behind the SCW despite pressures in the GPa range.

The MI data in Figure 5b from Shot PDC-82 impact show only a brief period of "inert" compaction followed by an accelerating reactive front, whose microwave signal

increased in both frequency and amplitude with time. The amplitude of the first front signal began to increase at  $\sim 80 \mu$ s without any detectable frequency increase for another  $30 \mu$ s. The interpretation is that the first front was becoming stronger without a measurable change in velocity; the  $x-t$  data in Figure 4b also indicate that first front pressure was

increasing before the velocity change was observed. As the amplitude of the first front signal began to increase at  $\sim 80 \mu\text{s}$ , the signal from the piston face in Figure 5b disappeared entirely. Whatever signal was not reflected from the first front (not all of it was since the amplitude continued to increase) was absorbed by the reaction behind the front. This reaction zone is different from the one which transmitted microwaves as it drove the SCW toward the CF in Shot PDC-81. Thus, the amplitudes of the various MI signals provide some information about reaction processes.

## LOW CONFINEMENT EXPERIMENT ON WC 231

IR radiometry signals from both compaction and compressive reaction were observed following a 220 m/s impact on WC 231 (Shot PDC-73). The IR emissions from the bed were transmitted through a flush mounted NaCl window in the wall of the Lexan tube at  $x = 50.8 \text{ mm}$ , directed to a beam splitter, and then entered two detectors. The indium antimonide (InSb) detector responded to wavelengths of 1.5 to 5  $\mu\text{m}$ ; the mercury cadmium telluride (HgCdTe) detector responded to wavelengths of 5.5 to 9  $\mu\text{m}$ . No effort was made to calibrate the detectors with a known radiating source within the confining tube; damage to the NaCl window by compaction and reaction of the bed would have invalidated any calibration during the experiment. The IR signals in Figure 6a are inverted from each other for ease of viewing; the two sharp spikes on those signals are from the generation of x-rays for radiographs. However, a qualitative assessment of temperatures, using the ratio of the two signals, will be discussed.

The various fronts and piston path are summarized on the distance-time plot in Figure 6b. The streak camera recorded the onset of luminous reaction ( $\Delta t$ ) beginning near the piston at 119  $\mu\text{s}$ ; from there a weakly luminous front propagated down the bed. Radiographs, which were taken both before and after  $\Delta t$  (82.6  $\mu\text{s}$  and 152.1  $\mu\text{s}$  respectively), mapped the progress of the CF and provided the compaction behind that front. Between the two radiographs, the compaction increased from 86.8 to 93.5% TMD; the

compaction observed on the second radiograph was uniform without any indication of reaction from the luminous front which was in that section of the bed. When the weakly luminous front caught the CF further downstream, a brightly luminous front with a 1300 m/s velocity resulted. As shown in Figure 6b, the NaCl window was between the two CF locations found on the radiographs.

The IR signals from Figure 6a are also summarized on the distance-time plot. The initial response of the IR detectors was just behind the CF; although the signals were small, the maximum short/long wavelength signal ratio occurred then. This indicates that the highest temperatures were associated with the hot spots formed by the CF. Between the passage of the CF and the weakly luminous front, the short wavelength signal remained relatively small while the longer wavelength signal continued to increase, indicating temperature decline. As the weakly luminous front passed the NaCl window, the amplitude of both signals increased; however, the short/long wavelength ratio, and thus the temperature, continued to decline until after the CF had become brightly luminous at  $\sim 225 \mu\text{s}$ . Therefore, both the IR signals and the radiographs indicated that very few or no new hot spots were initiated by the weakly luminous front. The pressure buildup from reaction in that zone was probably slow; otherwise, the Lexan tube would have ruptured before the first front reached the far end of the bed.

## DISCUSSION

### Dynamic Compaction

The dynamic compaction data from all the experiments listed in Table 1, except Shot PDC-73 which was affected by both tube expansion and early reaction of the WC 231, are shown in Figure 7. (Dynamic compaction data for WC 231 and additional compaction data for WC 140 at lower pressures have been reported previously.<sup>8,9</sup>) Compared with the dynamic data in Figure 7 are lattice compaction model fits (WC 140<sup>12</sup>, TS 3659<sup>4</sup>, WC 231<sup>3</sup>) of quasi-static measurements. The comparison shows that the two spherical



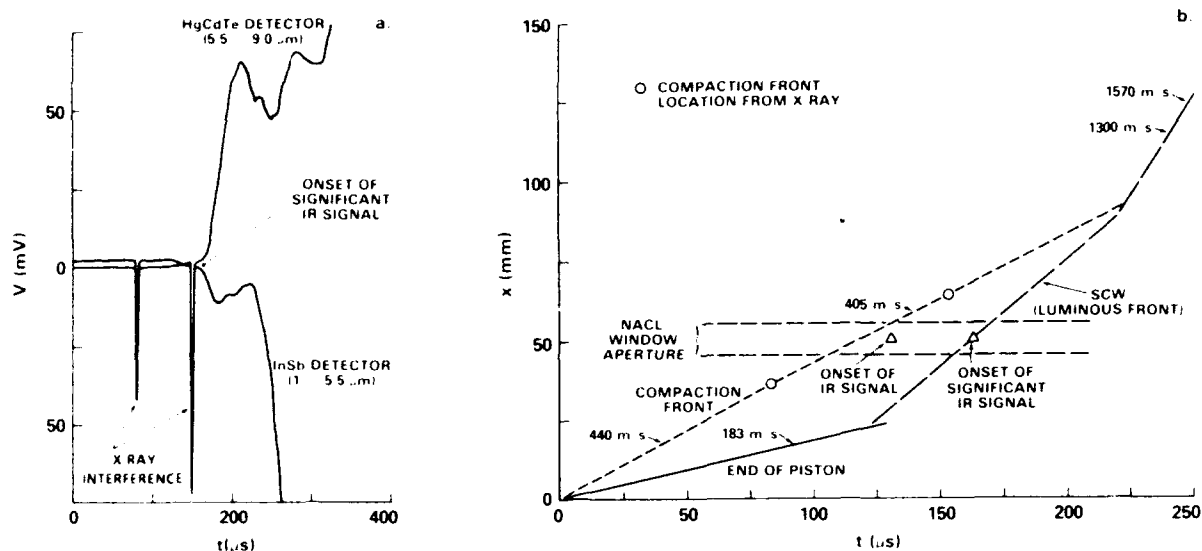


Figure 6. Data from a 220 m/s Impact of 49.4 Percent TMD WC 231 in Low Confinement (Shot PDC-73): a. IR Radiometry Signals; b. Summary of Distance-Time Data

powders (WC 140 and TS 3659) are more difficult to compact dynamically than quasi-statically, as had been observed earlier for ball propellants.<sup>8,9</sup> Also shown is that WC 140 is only slightly more difficult to compact dynamically than TS 3659, whereas there are much larger differences between the two powders during quasi-static compaction.

The largest range of dynamic compaction data (69 to 94% TMD) obtained to date in studies at this Center was for WC 140 because of the long delays before growth of compressive reaction contributed to the CF pressure. As seen in Figure 7, the greatest differences between dynamic and quasi-static data occur in the middle of range. This is where significant plastic deformation occurs at particle-to-particle contacts without the neighboring contact surfaces impinging on each other. With the onset of this significant plastic deformation, both compressive reaction and strain rate effects could be contributing to the difference in dynamic versus quasi-static compaction. However, if the observed effect had been caused by compressive reaction, the differences between dynamic and quasi-static data should increase as the bed density approaches TMD, because 1) more reaction should be occurring while 2) less porosity remains to accommodate

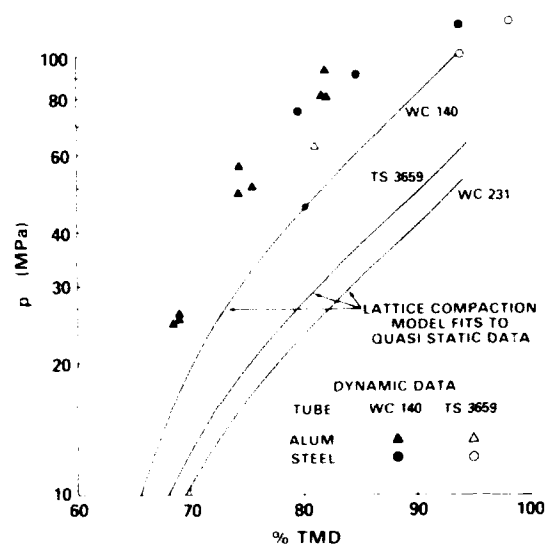


Figure 7. Dynamic and Fitted Quasi-Static Compaction Data

gaseous reaction products. Since these data did not diverge as higher % TMDs were approached, strain rate effects similar to those also observed from compaction tests on Teflon 7C powder<sup>13</sup> were probably responsible.

The pressure transducers provided some new information about compaction, as well as

verified some earlier observations.<sup>9</sup> They showed that the CF steadily propagated with little decline in peak pressure. This was previously thought to be the case based on steady CF velocity, but front velocity is an insensitive measure of pressure. Also, previous flash radiography data indicated the thickness of the CF was no more than 6 mm, which was the separation between x-ray tracers. This is only somewhat improved; the maximum ~5 mm thickness determined in this study is limited by the 4 mm diameter sensing area of the transducers. The transducers showed a rapid fall off in pressure behind the CF (Figure 2a) that has not been understood. Possibilities for the effect include a changing stress deviator as the compacted bed begins to slide across the transducer, or continued compaction near the wall since that portion of the bed is less tightly packed than the core of the bed. Since a similar rapid fall off in pressure behind the CF occurred in Teflon 7C<sup>12</sup>, an inert material, it appears that the effect is unrelated to reaction.

### Compressive Reaction

As in previous experiments, the first detection of reaction occurred near the piston face, which is the zone of the bed which had been compacted for the longest time. In Reference 1,  $\Delta t$  was usually based on the first appearance of luminosity on a camera film. Similar experiments for TS 3659 in the present study did not show any reaction light, and because of that, no attempt was made to conduct a camera study on the less reactive WC 140. However,  $\Delta t$  measurements were obtained from the pressure transducers that were mounted in the wall of the confining tube. The previously reported correlation<sup>1</sup> between  $\Delta t$  and the square of the average solid stress (p% TMD) applies also for the TS 3659 data in Table 1, but not for WC 140. Initiating compressive reaction in WC 140 was so marginal that  $\Delta t$  did not decrease when increasing the impact velocity from 210 to 300 m/s (Shots M-30,31).

The high confinement TS 3659 experiments exhibited growth of compressive reaction much as in the final stages of DDT. The transducer records from Shot PDC-82 in Figure 4a are quite similar to those from transducers located 133 and 89 mm before the onset

of detonation in DDT Shot A268 on TS 3659.<sup>6</sup> For several reasons, a transition to detonation did not occur in the present study, whereas it had in the steel tube DDT experiments. One reason is that the steel ignitor plate in the DDT experiment offers more confinement than the Lexan piston. In Shot PDC-82, the loss of confinement as the piston was being pushed from the tube probably contributed to the failure of the reactive wave to develop into a shock of sufficient strength for SDT. Also, in the DDT experiments on TS 3659,<sup>6</sup> at least 100 mm of run length existed between the formation of a strong reactive front and the transition to detonation. As shown in Figure 4b, a similar run length was not available; therefore, a longer tube may have permitted detonation.

Although TS 3659 initiates in a time frame consistent with WC 231, the growth of reaction between the two is dramatically different. Growth of reaction is so rapid in WC 231 that it has transitioned to detonation in both Lexan tube PDC and DDT experiments, whereas TS 3659 requires high confinement. Since the major difference between the two propellants is the rolling of the WC 231 grains, material damage and increased surface area from rolling must enhance growth of reaction.

The microwave interferometry and the IR radiometry data have provided additional insight into compressive reaction. Even as the pressure rises near the impacted end of the bed to ~1 GPa from compressive reaction, the transmission of microwaves is not interrupted and the IR radiometry indicates a declining temperature; apparently no new hot spots are being created in that zone of the bed. Once the strong compressive wave from the pressure buildup overtakes the compaction front, the amplitude of the reflected microwave signal from the front rapidly increases as an accelerating front develops. The most obvious explanation is the increased number and size of hot spots, which are reflecting the microwaves. The above is also suggested by camera film records in other materials such as WC 231 and HMX. The strong compressive wave is weakly luminous as it propagates through the compacted bed, but becomes brightly luminous

and accelerates upon overtaking the compaction front.

## SUMMARY

Dynamic compaction and compressive reaction were investigated for three NC/NG propellants: WC 140, TS 3659 and WC 231. Compaction fronts had a maximum thickness of ~5 mm and steadily propagated prior to compressive reaction. The beds were more difficult to compact dynamically than quasi-statically, especially in the middle of the %TMD range where extensive plastic deformation occurs at particle-to-particle contacts without the neighboring contact surfaces impinging. Compressive reaction was most difficult to initiate in the pure NC propellant WC 140 and was marginal even at the highest compaction pressure (>100 MPa). First detection of reaction in WC 140 occurred at times approximately twice those for the NG containing propellants, TS 3659 and WC 231, at comparable compaction pressures. Even though both TS 3659 and WC 231 contained a similar amount of NG, 20 to 25 percent, the spherical TS 3659 powder exhibited less growth of reaction than the rolled WC 231 powder, probably because of the damage and increased surface area caused by rolling. The sensitivity to compressive reaction for these three propellants correlates with their propensity to undergo DDT.

## ACKNOWLEDGEMENTS

The authors appreciate the initial guidance of Dr. Richard Bernecker, the encouragement of Dr. Doug Kooker (BRL) while pursuing the study, and the review of the manuscript by Dr. Donna Price. The experiments were conducted with the assistance of Carl Groves and Patrick Femiano.

## REFERENCES

1. Sandusky, H. W. and Bernecker, R. R., "Compressive Reactions in Porous Beds of Energetic Materials," *Eighth Symposium (International) on Detonation*, NSWC MP 86-194, Naval Surface Warfare Center, Silver Spring, MD, 1986, pp. 881-891.
2. Elban, W. L., "Quasi-Static Compaction Studies for DDT Investigations. Ball Propellants," *Propellants, Explosives, Pyrotechnics*, Vol. 9, No. 4, 1984, pp. 119-129.
3. Jacobs, S. J. and Sandusky, H. W., "Modeling of Porous Bed Compaction with Deformed Spheres in a Regular Lattice," *Proceedings of 1986 JANNAF Propulsion Systems Hazards Subcommittee Meeting*, Chemical Propulsion Information Agency (CPIA) Publ. 446, Vol. 1, 1986, pp. 149-162.
4. Sandusky, H. W.; Glancy, B. C.; Campbell, R. L.; Krall, A. D.; Elban, W. L.; and Coyne, P. J., Jr., "Compaction and Compressive Reaction Studies for a Spherical, Double-Base Ball Propellant," *Proceedings of the 25th JANNAF Combustion Meeting*, CPIA Publ. 498, Oct 1988, Vol 1, pp. 83-94.
5. Bernecker, R. R., "The Deflagration-to-Detonation Transition Process for High-Energy Propellants - A Review," *AIAA Journal*, Vol. 24, No. 1, Jan 1986, pp. 82-91.
6. Bernecker, R. R., "DDT Studies of a High Energy Spherical Ball Propellant," this Symposium.
7. Bernecker, R. R.; Sandusky, H. W.; and Clairmont, A. R., Jr., "Deflagration-to-Detonation Transition (DDT) Studies of a Double-Base Propellant," *Eighth Symposium (International) on Detonation*, NSWC MP 86-194, 1986, pp. 658-668.
8. Sandusky, H. W.; Elban, W. L.; and Liddiard, T. P., "Compaction of Porous Beds," *Shock Waves in Condensed Matter - 1983*, Elsevier Science Publishers B. V., 1984, pp. 567-570.
9. Sandusky, H. W., and Liddiard, T. P., "Dynamic Compaction of Porous Beds," NSWC TR 83-246, Naval Surface Warfare Center, Dec 1985.
10. Glancy, B. C.; Krall, A. D.; and Sandusky, H. W., "Microwave Interferometric

Applications in SDT/DDT Studies," *Shock Waves in Condensed Matter 1987*, Elsevier Science Publishers B. V., 1988, pp. 711-714.

11. Stanton, P. L.; Venturini, E. L.; and Dietzel, R. W., "Microwave Interferometer Techniques for Detonation Study," *Eighth Symposium (International) on Detonation*, NSWC MP 86-194, 1986, pp. 485-498.
12. Glancy, B. C.; Sandusky, H. W.; and Krall, A. D., "Dynamic Compaction and Compressive Reaction Studies for a Single-Base Ball Propellant," *Proceedings of 1989 JANNAF Propulsion Systems Hazards Subcommittee Meeting*, CPIA Publ. 509, Vol. I, pp. 37-46.
13. Coyne, P. J., Jr., and Elban, W. L., "A Strain Rate Sensitivity Prediction for Porous Bed Compaction," *Shock Waves in Condensed Matter - 1983*, Elsevier Science Publishers B. V., 1984, pp. 147-150.

## DISCUSSION

**BARRY BUTLER**  
University of Iowa  
Iowa City, IA

Would you please explain how a wall-mounted pressure transducer responds to a gas/grain mixture. That is, what stress are you reading?

## REPLY BY B. C. GLANCY

The pressure transducer responds to the radial mixture stress of the porous bed at the wall of the tube. The mixture stress combines gas pressure within the voids and particle contact pressure, in proportion to the areas of gas and solid. This stress is an average of many voids and contacts since the 4 mm sensor diameter of the transducer is more than 10 times larger than the particle size. Kooker, and more recently Baer, have successfully used the mixture concept in modeling transducer measurements. One must realize, though, that this is not the axial pressure that drives the compaction front.

## DISCUSSION

**DOUGLAS E. KOOKER, U.S. Army**  
Ballistic Research Laboratory  
Aberdeen Proving Ground, MD

Your experiments are providing the modeling community with invaluable information about the transition to detonation in granular energetic material. A successful model should be able to predict the motion of the strong compaction front which is clearly outlined by your microwave interferometry data. An equally important test would be to reproduce the time-history from the wall-mounted transducers. My question concerns the data from the transducers. For the run displayed in Figure 2a, both transducer records show a pronounced decay from the initial report value, before the onset of runaway. I believe you mentioned that this decline in value may not be a true indication of axial pressure or stress. Is there an explanation for this behavior?

As background to this question, several modelers (see Reference 1 below) attempted to predict the results from this experiment before the data were released. None of the one-dimensional models (at that time) predicted a time-dependent decay of mixture stress once the compaction front passed the transducer location. In an effort to explain the decay, one area of speculation is rate-dependent stress relaxation in the compressed aggregate. The model of Baer and Nunziato (this Symposium) does account for a rate effect in the mixture stress tensor. However, with their parameter values, the rate effect vanishes behind the compaction front and the initial gage report value is predicted with the radial component of the "equilibrium" mixture stress tensor [see Figure 7 of Baer and Nunziato]. Thus, this stress component cannot relax to a lower value. Another possibility might be the influence of rarefaction waves generated by substantial (and unmonitored) deformation of the front face of the projectile.

## REFERENCE

1. Kooker, D. E., "A Workshop Summary of 'Model Predictions of the Piston-Driven-Compaction Experiment,'" BRL-TR-3029, U.S.

Army Ballistic Research Laboratory, Aug 1989.

### REPLY BY B. C. GLANCY

The main purpose of the radially-mounted pressure transducers was to record the growth of compressive reaction, at which time differences in gas and solid pressures and differences in radial and axial stresses should be diminished. Prior to compressive reaction though, there may be a number of effects contributing to the pressure decay following

the abrupt pressure rise due to compaction front passage at each transducer location. The long Lexan rod for impacting the bed was designed to maintain a constant compaction pressure for the duration of the experiment, but the rod does gradually slow and at the higher velocities will also deform. Both the continual slowing and deformation of the rod will result in rarefaction waves. Also, as soon as the compacted bed begins sliding past a slightly recessed transducer, the radial stress may not be accurately recorded.

# DDT STUDIES OF A HIGH ENERGY SPHERICAL BALL PROPELLANT

Richard R. Bernecker  
Naval Surface Warfare Center  
10901 New Hampshire Avenue  
Silver Spring, Maryland 20903-5000

*DDT studies have been conducted with very porous samples (60% TMD) of a special ball propellant, TS 3659, confined in thickwalled steel tubes. Diagnostic instrumentation consisted of ionization probes and piezoelectric (PE) pressure transducers. Replicate experiments were run in which the PE transducers were placed at various locations along the predetonation column such that data from at least two experiments could be compared for a given location. Events are reasonably consistent between experiments when measured from the onset of detonation (both temporally and spatially). The pressure-time ( $p$ - $t$ ) data outline the propagation of various compressive fronts: that arising from the action of the ignitor, that (the strong compressive wave, SCW) associated with the convective burning process; and the evolving shock wave. In addition, the  $p$ - $t$  data outline the presence of a rearward compressive wave whose origin is the "event" which causes the SCW to evolve into the shock wave. The shock reactivity of TS 3659 is deduced to be less than that of another granular propellant (WC 231) of comparable nitroglycerin (NG) content.*

## INTRODUCTION

Theoretical/numerical models of the total DDT process have been developed in recent years. However, these modeling efforts have not been completely successful because of factors such as incomplete formulation and description of compressive reaction and the evolving reactive shock wave. In an earlier paper,<sup>1</sup> we provided new observations concerning the onset of compressive reaction, resultant from convective combustion, using piezoelectric transducers mounted in thickwalled steel tubes. In the present work, we wish to extend the observation of the pressure-time ( $p$ - $t$ ) histories along the predetonation column in high confinement (steel) tubes to another granular double base propellant and to correlate these  $p$ - $t$  data with the various stages of the DDT process. In particular, we are interested in convective combustion, compressive reaction and the shock regime. It is of interest to compare the DDT characteristics for

the spherical ball powder, TS 3659 (21.5 percent NG), with those characteristics obtained previously<sup>1</sup> for the ammunition propellant, WC 231 (~25 percent NG), which is disk-like in shape. It is hoped that these experimental observations will contribute to the development of physical models (of the various stages of the DDT process) for use in the numerical modeling efforts.

As in the WC 231 study, we have found it very informative to assess the statistical nature of the DDT process, as reflected in replicate experiments, by referencing all events relative to the location ( $\ell$ ) and time ( $t_d$ ) of the onset of detonation. Thus, distances are measured relative to the ignitor/propellant interface ( $x = 0$ ), as well as relative to point of onset of detonation ( $x = \ell$ ); the latter is designated  $x^*$ , where  $x^* = x - \ell$ . Time ( $t$ ) is relative to the response of an optical/photodetector at the ignitor interface while  $t^*$  is relative to the onset of detonation;  $t^* = t - t_d$ .

This procedure, of referencing events to the onset of detonation, essentially eliminates variability in the burning of our B/KNO<sub>3</sub> ignitor. However, we have conducted some supplemental experiments to characterize the pressure-time loading provided by our ignitor at the ignitor/propellant interface. These experiments utilized a porous column of glass beads in place of the porous column of propellant. Pressure time data (obtained just beyond this interface) from the glass bead columns are compared with the corresponding data from TS 3659 in order to provide some estimate of the time at which reaction of the propellant can first be detected.

## EXPERIMENTAL ARRANGEMENTS

The steel tube arrangement, shown in Figure 1, has been described elsewhere;<sup>1</sup> it is called a modified steel tube arrangement in order to differentiate it from our earlier steel tube arrangement.<sup>2</sup> Piezoelectric (PE) pressure transducers were located along the predetonation column length and mounted flush to the wall. The output from a transducer was sent to a high sensitivity recording channel (30 MPa maximum output) and to a low sensitivity recording channel (1000 MPa maximum output) of a digital oscilloscope. The transducers' sensitivity factor reported by the manufacturer was typically 0.09 mv/psi (13 mv/MPa); the transducers have a maximum pressure limit of about 860 MPa. In this paper, only our regular ignition system was used (i.e., with the ignitor in intimate contact with the end of the propellant column).

The propellant used in this study, TS 3659, was one of four specially ordered ball powders.<sup>3</sup> It was nearly spherical in shape, was undeterred, and has a fairly narrow particle size distribution; its average particle size was taken to be 0.43 mm.<sup>4</sup> It was packed into a steel tube in 12.7 mm increments to give a "stable" pour density (0.987 g/cc) which corresponds to 60.2% TMD (TMD being taken as 1.64 g/cc).

## EXPERIMENTAL RESULTS

Five experiments were conducted with TS 3659 in the modified steel tube

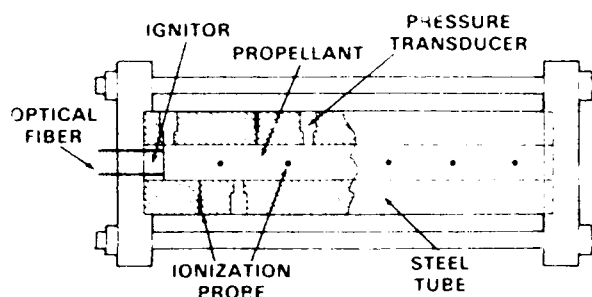


Figure 1. Modified Steel DDT Tube Arrangement

Table 1. Steel Tube Data for 60.2% TMD TS 3659 Ball Propellant

SHOT	TRANSDUCER LOCATION (mm)		$\ell$ (mm)	$(t_d)$ ( $\mu$ s)	DET. VEL. (mm/ $\mu$ s)
	x	x*			
A12	-	-	200	391.2	5.36
A172	3.2	-190.8	194	148.2	5.23
	83.0	-111.6			
	142.9	-51.1			
A266	3.3	-197.7	201	313.4	5.19
	45.1	-155.9			
	66.8	-134.2			
	85.9	-115.1			
A267	3.3	-195.7	199	370.2	5.27
	45.2	-153.8*			
	66.9	-132.1			
	86.0	-113.0			
A268	3.2	-196.8	200	263.4	5.17
	66.7	-133.3			
	85.7	-114.3			
	111.3	-88.7			

\*Bad transducer circuit

arrangement and our regular ignitor system; a summary of initial conditions is included in Table 1. The first experiment (A12) only used ionization/conductivity probes as the diagnostic instrumentation. The object was to determine the distance and time to detonation with a minimum of probe or transducer openings in the steel wall. Subsequent experiments utilized PE transducers located along the predetonation column length. Based upon the ionization probe (IP) and transducer data from Shots A12 and A172, the IP and transducer

locations for subsequent experiments were selected such that they would be at similar locations in replicate experiments. Using the IP response times from Shot A12 as typical of the first two experiments, three different regimes were identified: a regime with a response rate of 0.3 mm/ $\mu$ s, a regime with a response rate of about 2 mm/ $\mu$ s (the shock region), and the detonation region. The output from the transducer at  $x^*$  of -51 mm (located in the shock region) in Shot A172 indicated that the more useful pressure-time data would be obtained in the first regime. Hence, in the last three experiments the transducers were primarily located at  $x^*$  locations less than -110 mm. It is the utilization of these pressure-time data which allows us to associate the responses in this portion of the predetonation column with the various stages of the DDT process.

## SHOT A266

The low pressure data from Shot A266 are shown in Figure 2 for the time ( $t^*$ ) regime of -400 to -50  $\mu$ s. The transducers from -156 to -115 mm show the onset of a more rapid  $dp/dt$  "event," as identified by the symbols A, B, and C. This event is the passage of the strong compressive wave (velocity of 0.62 mm/ $\mu$ s)

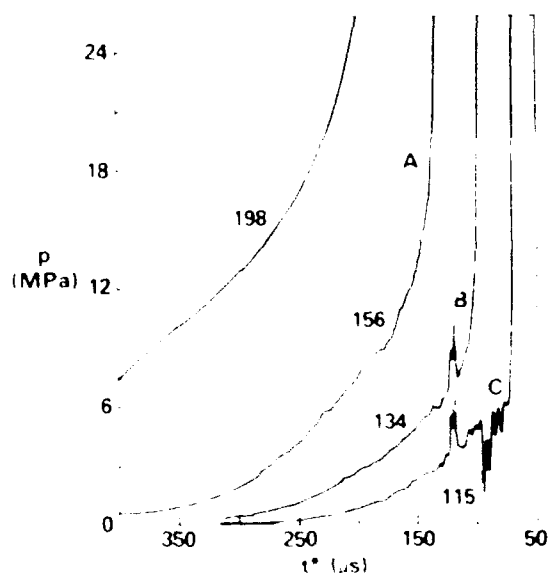


Figure 2 Pressure - Time Data (0-26 MPa) for Shot A266. (Numbers represent transducer locations.)

which originated near the ignitor end of the burning propellant column; this is evident when these times (symbols) are plotted in the distance-time ( $x^*-t^*$ ) plane of Figure 3. The low pressure data in Figure 2 were also used to determine the times at which 1 MPa of pressure was attained at all four transducer locations. The resultant isobar is the dashed line shown in Figure 3 and has a slope of 0.25 mm/ $\mu$ s (parallel curves were also found at 2 and 3 MPa pressure levels). This curve is associated with the weak compressive wave (WCW), identified in flash radiographic studies,<sup>1,5</sup> which results from the arrival of the B/ $\text{KNO}_3$  burning process at the ignitor/propellant interface. The response times of the -166 and -151 mm IPs (a rate of 0.26 mm/ $\mu$ s) thus appear to be associated with the propagation of this WCW. The velocity of this WCW is consistent with compaction front velocities found for other ball powders in the pressure range of 5 to 10 MPa.<sup>6</sup>

The high pressure data from Shot A266 (shown in Figure 4) confirm that the 0.62 mm/ $\mu$ s wave is the strong compressive wave (SCW) seen in the earlier studies—WC 231 propellant<sup>1</sup> and explosives such as HMX.<sup>5</sup> Moreover, the data in Figure 4 show a feature which previously could only be seen, in

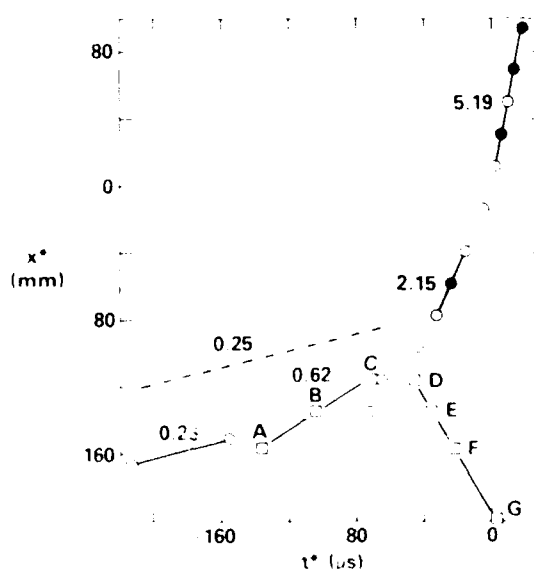


Figure 3 Relative Distance - Time Data for Shot A266. (○, ● Probe response; □ transducer excursion; number is velocity in mm/ $\mu$ s.)



our earlier work, from strain gage data for materials<sup>7</sup> which exhibited weak convective combustion—namely a rearward wave which arises from the conversion of the SCW into a developing, reactive shock wave. (In this experiment, the 2.15 mm/ $\mu$ s IP response rate in Figure 3 is associated with the shock wave which ultimately drives the system to detonation.) The symbols D, E, F, and G in Figures 3 and 4 show the propagation path of this rearward compressive wave (1.8 mm/ $\mu$ s). This wave is a compressive wave since it has a finite risetime of about 50 MPa/ $\mu$ s.

## SHOT A268

The IP responses are shown in the  $x^* t^*$  plane of Figure 5. Four regimes have been identified: the WCW regime, the SCW regime, the shock wave region, and the detonation region. A comparison of Figures 3 and 5 shows very reproducible response rates in corresponding regions. Moreover, the IP data at -133 and -114 mm outline the propagation path of the SCW (response rate of 0.72 mm/ $\mu$ s). The arrival times of the SCW at transducer locations of 133 and -114 mm (points A and B) were taken from the low pressure transducer data shown in Figure 6 and yield a SCW velocity of 0.70 mm/ $\mu$ s.

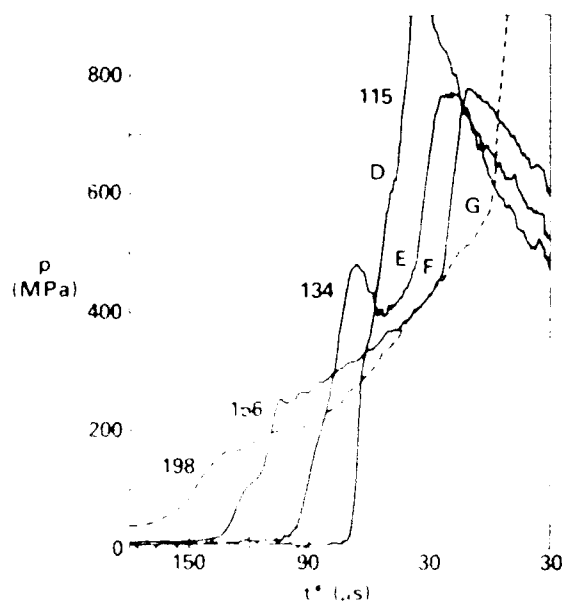


Figure 4. Pressure - Time Data (0-900 MPa) for Shot A266. (Numbers represent transducer locations.)

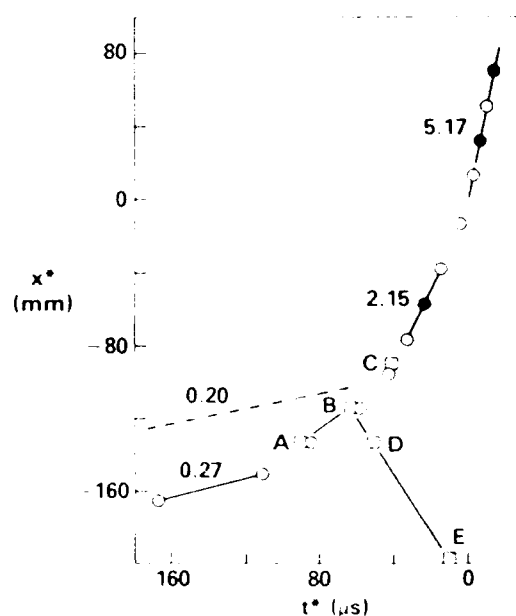


Figure 5. Relative Distance - Time Data for Shot A268. (○, ● Probe response; □ transducer excursion; number is velocity in mm/ $\mu$ s.)

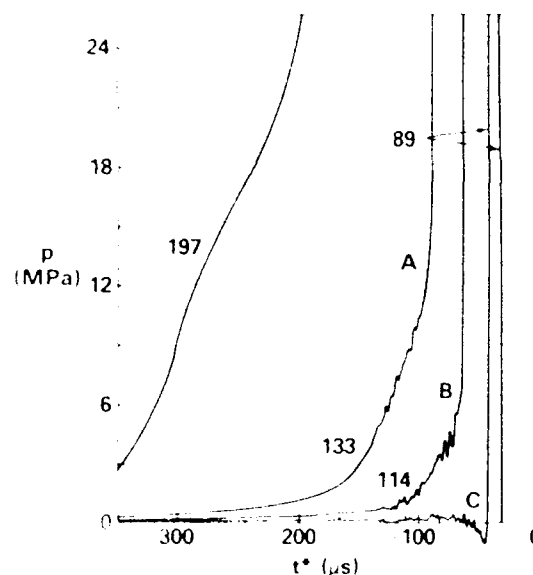


Figure 6. Pressure - Time Data (0-26 MPa) for Shot A268. (Numbers represent transducer locations.)

The low pressure data in Figure 6 include data for a location 89 mm upstream from where detonation started. At this location only a fraction of a MPA of pressure is detected before the reactive shock wave reaches that location. Also, in accordance with earlier observations and discussions,<sup>1,2</sup> a negative excursion is seen to precede the arrival of the

shock wave. This has been found to be the case when PE transducers or strain gages are used to monitor pressure. Finally, the magnitude of the shock wave is unknown since the PE transducers were not designed to operate in shock loading environments.

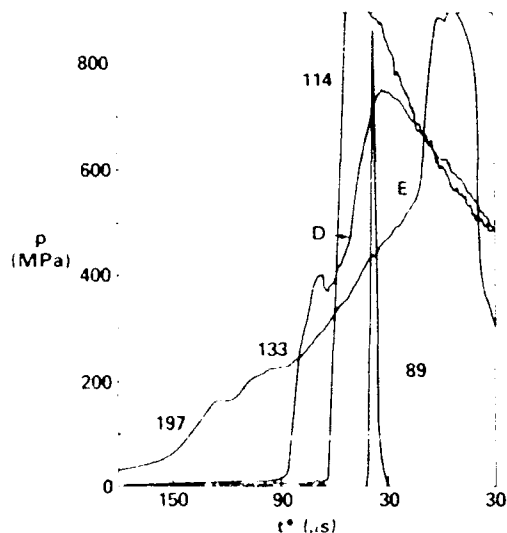


Figure 7. Pressure - Time Data (0-900 MPa) for Shot A268. (Numbers represent transducer locations.)

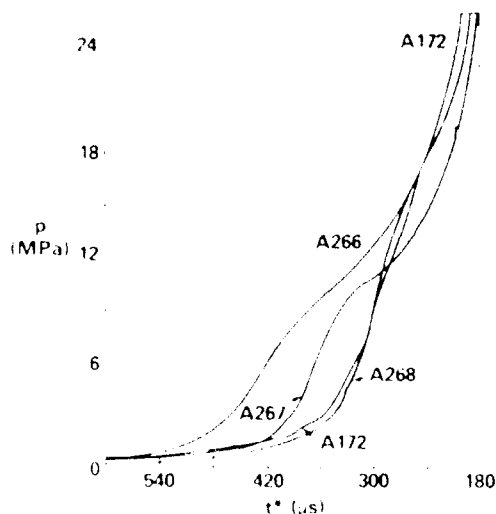


Figure 8. Pressure - Time Data at  $x^*$  Location of -195 mm

## DISCUSSION

### Pressure-Time Histories

The pressure-time data have provided significant information concerning the various stages of the DDT process. However, one

question that arises is the reproducibility of events in the  $x^* - t^*$  plane for the various replicate experiments. The selection of the transducer locations (see the  $x^*$  column in Table 1) allows some comparisons to be made among the various experiments; this is possible for both low ( $< 27$  MPa) and high ( $< 900$  MPa) pressure data. In this paper, we will concentrate on the low pressure data while both pressure regimes will be discussed in Reference 8. For the  $x^*$  location of about -195 mm (the ignitor transducer location), low pressure data from all but Shot A12 are compared in Figure 8. Data for  $x^*$  of about -133 mm (Shots A266, A267, and A268) are shown in Figure 9. In Figure 10, data are shown for  $x^*$  of approximately -113 mm.

The data from the ignition region (Figure 8) show two different groupings of characteristics which reflect the action of the ignitor. Shots A266 and A267 illustrate an initial ramping of pressure up to about 10 MPa followed by a slower pressurization rate until the rate increases dramatically (suggestive of propellant ignition) at about -220  $\mu$ s. On the other hand, data from Shots A172 and A268 show a relatively more monotonous increase in pressure until the -220  $\mu$ s period. However, the observation that all four data sets show the same dramatic increase in pressure at roughly the same time suggests that the initial pressurization rate does not really influence the "time to ignition."

The downstream transducer location which was used the most frequently is the -113 mm location (see Figure 10). The four traces show reasonably consistent characteristics. If one considers the arrival time of the SCW at this location, then there is excellent agreement between Shots A172, A267, and A268 while in Shot A266 the SCW arrives 8  $\mu$ s earlier. Moreover, the pressure level when the SCW arrives at -113 mm is consistent with the initial pressurization rates and pressure levels seen at the ignitor/propellant interface at about -350  $\mu$ s (see above discussion and Figure 8). That is, the pressure level (in Figure 10) when the SCW arrives at -113 mm is lower for A172 and A268 than for A266 and A267. This is merely a manifestation of the p-t history at the ignitor/propellant

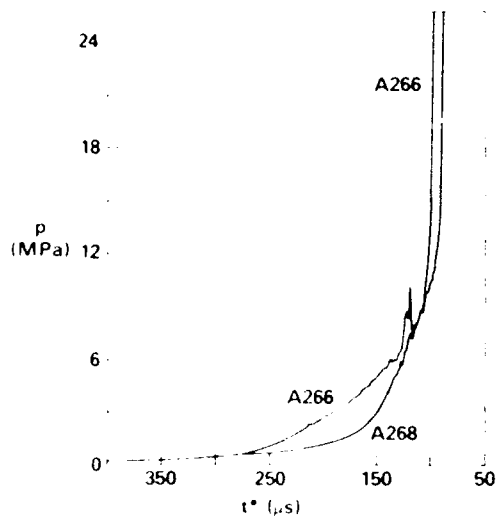


Figure 9. Pressure - Time Data at  $x^*$  Location of -133 mm

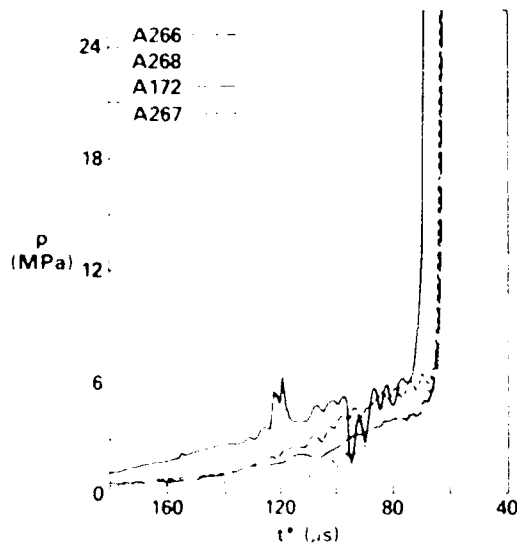


Figure 10. Pressure - Time Data at  $x^*$  Location of -113 mm

interface. Other interesting but, as of now, not well understood features are the continuous oscillations observed some 80  $\mu$ s before the arrival of the SCW. Currently, we hypothesize that they are associated with the combustion processes at the ignitor end of the compacted column.

Nearly all the above comments for the 113 mm location are also seen at the 133 mm location as shown in Figure 9. In addition, the high pressure data in Figures 4 and 7 show that at 133 mm the pressure history associated with the SCW (maximum pressure of 400 to 500 MPa) exhibit an overshoot

phenomenon. It is speculated that this overshoot is associated with a relaxation process following the passage of the SCW. The relaxation process appears to be, at least in part, associated with the difference in pressure level between that of the compressive wave and the pressure level at which the inner wall of the tube begins to yield plastically.

## DDT Mechanism

Seven stages have been identified and discussed earlier for the DDT process in porous systems;<sup>1,5</sup> they are listed in Table 2. A comparison of the DDT characteristics of TS 3659 ball powder ("spherical" particles and 21.6 percent NG) and those of WC 231 reloading powder ("disk-like" particles and 25.2 percent NG) point out one major difference—an apparently large difference in compressive burning (shock reactivity) in the hot spot process—Stage 6.

This difference is evident when the  $x^*-t^*$  data in either Figure 3 or 5 are compared to the  $x^*-t^*$  data in Figure 6 of Reference 1. In the latter, the presence of the developing shock wave (as outlined by IP responses) is noted only downstream of about -40 mm. This contrasts with the detection here of the evolving shock wave at about -100 mm for TS 3659. Thus, it appears that the hot spot (compressive) reaction induced by the shock wave is slower in developing in TS 3659. This was checked and confirmed in a preliminary manner in some exploratory shock initiation experiments.<sup>3</sup> Other DDT studies<sup>9</sup> with these special spherical ball powders lead to the speculation that this decrease in shock reactivity is, in part, associated with the spherical shape of the special ball powders and

Table 2. Stages of DDT Mechanism for Porous Charges

- |                                     |       |
|-------------------------------------|-------|
| 1. Pre-ignition                     |       |
| 2. Ignition/Conductive Burning      |       |
| 3. Convective (Reaction) Burning    |       |
| 4. Compressive ("Hot Spot") Burning |       |
| 5. Shock Formation                  |       |
| 6. Compressive Burning              | } SDT |
| 7. Detonation                       |       |

its influence on the hot spot process. That is, the spherical ball powders have been observed to deform plastically under stress loading<sup>4</sup> which WC 231 appeared to fracture under stress loading. Consequently, the apparently slower hot spot process for TS 3659 would lead to the hypothesis that in double-base materials the fracture process is more effective in generating faster reaction (higher temperatures ?) than plastic deformation. Finally, it should be noted that a reduced reactivity of TS 3659 may be apparent in Stage 4 (compressive burning) as well. This is based upon the consideration that a) while data for WC 231 in Reference 1 has been interpreted to show compressive reaction behind the SCW, no compressive reaction behind the SCW has been seen in the current work, and b) the relative reactivity found in Stage 6 should pertain to Stage 4 as well. If compressive reaction had been present for TS 3659, then the rearward propagating wave would have been more difficult to resolve and detect.

In this study, the transducer data have been used to locate where the SCW essentially evolves into a shock wave. (The identification of this location is dependent upon the ability to outline the path of the rearward propagating compressive wave.) For TS 3659, this location appears to lie between 110 and 100 mm. The data in Figure 3 suggest that the rearward compressive wave (velocity of 1.8 mm/ $\mu$ s between 156 and 115 mm) does not originate at the location where the SCW enters unconfined propellant (density of 0.987 g/cc). (It is interesting to note that the apparent amplitude of the rearward wave is essentially constant at a value of 400 to 500 MPa.) Instead, the rearward wave appears to originate in material which has been slightly consolidated by the WCW. The event which gives rise to both the shock wave and the rearward traveling compressive wave was first thought to be a thermal explosion<sup>10</sup>. The high pressure data shown in Figure 4 provide some evidence that a second compressive wave follows the SCW (see 156 mm data after about 110  $\mu$ s) and may cause a thermal explosion near 110 mm, in previously compressed material. Recently, Kooker<sup>11</sup> has shown in theoretical/numerical modeling of compressive reaction in ball powders that a wave pattern

similar to that seen in Figures 3 and 5 (SCW, shock wave and rearward wave) arises as a natural consequence from the collision of two (slightly reactive) compressive waves. Thus, the SCW and a following wave, as discussed above for the 156 mm location in Figure 4, would lead to the observed wave pattern.<sup>11</sup>

The p-t data have also been used to confirm the propagation paths of the WCW and SCW; for the latter, a technique was used which was similar to that in earlier studies where strain gages monitored pressure.<sup>2</sup> To outline the propagation path of the WCW, the very low pressure data were used. The velocity of the WCW is consistent with the response rates of the IPs and data from other sources (see Reference 6, for example).

From the very low pressure data, it has also been found in four of the experiments that there is a reasonably consistent time when the ignitor pressure transducer reaches 25-30 MPa. At earlier times, the p-t data vary from experiment to experiment. To obtain more information on the burning characteristics of our B/KNO<sub>3</sub> ignitor, we have recently<sup>9</sup> monitored the pressure at the x location of 3 mm (the x\* location of 195 mm in this TS 3659 work) for experiments in which the porous propellant column was replaced by a column of glass beads. Preliminary data have been obtained for columns composed of either 1.1 mm glass beads or 0.16 mm glass beads. In both cases, the pressure-time data at the 3 mm location had the characteristics of Shots A172 and A268 as seen in Figure 8. The average maximum pressure for the 1.1 mm beads was 17 MPa (from four experiments) while dp/dt at half the maximum pressure was 80 MPa/ $\mu$ s. The corresponding data (from two experiments) for the 0.16 mm beads were 24 MPa and 112 MPa/ $\mu$ s, respectively. Consequently, it would appear that any pressure rise above approximately 20 MPa, as seen in Figure 8, would be associated with the pyrolysis/burning of the ball powder.

Although the pressurization (dp/dt) associated with the burning of the ignitor varies from experiment to experiment (as seen in Figure 8), it is quite obvious that those p-t characteristics do not influence the transition to detonation for the given configuration of

the ignition system. It is the time at which the SCW is formed that determines the formation of the shock wave and a transition to detonation. It appears that for our regular ignitor, the p-t history at -195 mm does not effect the time at which the SCW is formed. Hence, it is suggested that an exact description of the burning of the B/KNO<sub>3</sub> is not necessary as long as the calculated p-t history for the ignitor fits the band of data below 20 MPa in Figure 8.

## CONCLUSIONS

Pressure time data from piezoelectric transducers have been used to confirm and extend earlier observations concerning the DDT process in very porous columns of double-base propellants. Correlations pertaining to nearly every stage of the DDT mechanism have been deduced from the p-t data. One of the most important observations is the fact that when the SCW evolves into a shock wave, a rearward compressive wave is simultaneously formed. (This wave pattern suggests the possibility that the model of Kooker<sup>11</sup> may represent the events occurring after the formation of the SCW.) The p-t data were also used to provide information concerning the propagation path of the WCW which, until now, has only definitively been outlined in studies using flash radiography. The combined data indicate that the pressure-time loading history from the ignitor plays a very minor role in influencing the time and location where a transition to detonation may occur. Finally, it must be noted that our pressure transducers record events next to the steel wall—not on axis. This feature affects the absolute value of the pressure level to be considered when comparisons are being made to one dimensional modeling studies.

## ACKNOWLEDGEMENTS

The author is indebted to Carl Groves for the assembly of the DDT tubes and the low pressure calibration of the transducers.

## REFERENCES

1. Bernecker, R. R., Sandusky, H. W., and Clairmont, A. R., Jr., "Deflagration to

Detonation Transition (DDT) Studies of a Double-base Propellant," *Proceedings of the Eighth Symposium (International) on Detonation*, NSWC, Silver Spring, MD, Jul 1985, pp. 658-668.

2. Bernecker, R. R. and Price, D., "Studies in the Transition from Deflagration-to-Detonation in Granular Explosives II. Transitional Characteristics and Mechanisms Observed in 91/9 RDX/wax," *Combustion and Flame*, Vol. 22, 1974, p. 119.
3. Bernecker, R. R., "The Deflagration-to-Detonation Transition Process for High Energy Propellants—a Review," *AIAA Journal*, Vol. 24, 1986, p. 82.
4. Elban, W. L., "Quasi-static Compaction Studies for DDT Investigations: Ball Propellants," *Propellants, Explosives, and Pyrotechnics*, Vol. 9, 1984, p. 119.
5. Bernecker, R. R.; Sandusky, H. W.; and Clairmont, A. R., Jr., "Deflagration-to-Detonation Transition Studies of Porous Charges in Plastic Tubes," *Proceedings of the Seventh Symposium (International) on Detonation*, NSWC, Silver Spring, MD, 1982, pp. 119-138.
6. Sandusky, H. W. and Liddiard, T., *Dynamic Compaction of Porous Beds*, NSWC TR 83-246, NSWC, Dec 1985.
7. Bernecker, R. R.; Price, D.; Erkman, J. O.; and Clairmont, A. R., Jr., "Deflagration to Detonation Transition Behavior of Tetryl," *Proceedings of the Sixth Symposium (International) on Detonation*, Office of Naval Research, Arlington, VA, Rept. ACR 221, 1976, pp. 426-435.
8. Bernecker, R. R., "DDT Studies of a Spherical, Double base Ball Propellant," NSWC TR 87-52 (to be published).
9. Bernecker, R. R., unpublished data.
10. Bernecker, R. R., "DDT Study of a Spherical, Double Base Ball Propellant," *1987 JANNAF Propulsion Systems Hazards Subcommittee Meeting*, CPIA Publication 464, Vol. 1, Mar 1987, pp. 1-11.

11. Kooker, D. E., "Compaction Wave Acceleration in Granular Energetic Material: Simulation with a Reactive Shock Wave Model," *Proceedings of the Ninth Symposium (International) on Detonation*, Portland, OR, 28 Aug-1 Sep 1989.

spaces between the grains, the run to detonation distance in our grounded powder is about a half of the run to detonation distance in the original ball powder.

## DISCUSSION

M. M. SAMIRANT  
French German Research Institute  
(ISL), St. Louis, France

As confirmation of the influence on combustion of the particles projected in the

# AN IMPROVED MODEL OF THE DEFLAGRATION-TO-DETONATION TRANSITION IN POROUS BEDS

C. F. Price, A. I. Atwood, and T. L. Boggs  
Engineering Sciences Division  
Naval Weapons Center  
China Lake, California 93555-6001

*The purpose of this paper, the third in a series, is to describe the additions and improvements made to the model since 1985 and to show their importance. A most significant change in the model is in the treatment of the chemical reactions controlling the energy-release rates. A more complex reaction scheme has been substituted, embodying two competing gasification reactions, followed by two parallel supporting gas-phase reactions which lead to the final products.*

*Of nearly equal import is the behavior of the bed as it is compacted. For materials which deform as they compact (plastics), there is a formality to express the change of shape as it affects drag and heat transfer. For those materials which compact by fracture (crystals) there is a heuristic functionality to express the reduced effective particle diameter. These constitutive relations and their verification are discussed.*

*The fixed boundary condition at one end has been relaxed so that mechanically-stimulated experiments may be modeled. Calculated results are shown for several experimental conditions, to demonstrate the effect of the new features. Both deforming and fracturing materials are treated, and the results of a thermally-stimulated (ignitor) simulation are shown, as well as those of a mechanically-stimulated (piston) simulation.*

## INTRODUCTION

When a propellant or explosive exhibits a large surface to volume ratio either through manufacture, as is the case of some gun propellants, or through damage, as in the case of some missile propellants, the possibility of a deflagration-to-detonation transition exists. When the porous material is stimulated, either mechanically or thermally, the stress wave passing through the material increases in amplitude due to the product gases of burning particles. Eventually, the wave will become strong enough to compact the porous material, this action will prevent the flow of convective gases ahead of the wave. The wave magnitude increases to

that of a shock, which initiates a detonation reaction.

Considerable research has been directed towards understanding the mechanisms involved in the Deflagration-to-Detonation (DDT) process, and in the development of numerical models that can be used to describe the DDT event. The modeling process of the entire DDT event is not a trivial problem; it requires the input of numerous constitutive relationships. A previous paper, "Modeling the Deflagration to Detonation Transition in Porous Beds of Propellant," Eighth Symposium (International) on Detonation,<sup>1</sup> describes the fundamental relationships found in the analytical model. A feature of this model is

analytical model. A feature of this model is that wherever possible, experimental observations are utilized as input parameters. Indeed, the analysis and experiment are mutually dependent, each guiding the other towards an increased understanding of the DDT process

## DESCRIPTION OF MODEL

The model, as described in Reference 1, is a modification of that used by Pilcher, Beckstead, et al.<sup>2</sup> It includes the effects of confinement, as well as gas flow and pressure buildup due to burning. The model is a composite of conservation equations, auxiliary relationships, and several submodels. The basic elements are:

1) Gas phase conservation equations, one dimensional.

Mass

$$\frac{d}{dt}(\rho_g \epsilon A) + \frac{d}{dx}(\rho_g \epsilon U_g A) = \epsilon A \Gamma_g$$

In addition, there are four species conservation equations, so that ignitor, pyrolysis, and final product gases may be tracked.

Momentum

$$\rho_g \left( \frac{dU_g}{dt} + U_g \frac{dU_g}{dx} \right) = - \frac{dP}{dx} + (U_p - U_g) \Gamma_g - D_{gp}$$

Energy

$$\rho_g \left( \frac{d\epsilon}{dt} + U_g \frac{d\epsilon}{dx} \right) =$$

$$\begin{aligned} & - \left( \frac{P_g}{\epsilon A} \right) \left\{ \frac{d}{dx} [\epsilon U_g + (1-\epsilon) U_p] A + \frac{dA}{dt} \right\} \\ & + (U_g - U_p) \Gamma_g + (U_g - U_p) D_{gp} \\ & - \dot{q}_{gp} \left[ \frac{(1-\epsilon)}{\epsilon} \right] \left[ \left( \frac{s_p}{V_p} \right) + \sum RR_g \Delta H_{rg} \right] \end{aligned}$$

2) Condensed phase particle conservation equations, quasi one dimensional

Mass

$$\frac{d}{dt}[(1-\epsilon)A] + \frac{d}{dx}[(1-\epsilon)U_p A] = \frac{-\epsilon A \Gamma_g}{\rho_s}$$

Momentum

$$\rho_s \left( \frac{dU_p}{dt} + U_p \frac{dU_p}{dx} \right) =$$

$$- \frac{dP}{dx} - \left( \frac{1}{1-\epsilon} \right) \frac{d\sigma}{dx} + D_{gp}$$

The condensed-phase energy conservation is accomplished through the inter-phase relations, rather than through an energy conservation equation.

3) Porous-bed drag (permeability) equations of Jones and Krier,<sup>3</sup> modified by the use of an effective diameter to account for non-spherical and deformed particles.

$$F_v = \frac{\Delta P}{L} \frac{D^2}{\mu U} \left( \frac{\epsilon}{1-\epsilon} \right)^2 = 150 + 3.89(Re')^{0.87}$$

4) Denton's correlation for heat transfer to the bed.<sup>4</sup>

$$h_{px} = 0.41 \lambda_g (s_p/V_p)$$

$$\left[ \left( \frac{\rho_g |U_g - U_p|}{\mu} \right) \left( \frac{\epsilon}{s_p/V_p} \right) \right]^{0.7} (Pr)^{1/3}$$

5) Particle to particle stress (compaction) relationship of Carroll and Holt,<sup>5</sup> as modified by Kooker and Anderson.<sup>6</sup>

Mode 1 (elastic)  $\epsilon_0 > \epsilon > \epsilon_1$

$$\sigma = \frac{4G(1-\epsilon)[(1-\epsilon)/(1-\epsilon_0) - 1]}{3\epsilon}$$

Mode 2 (elastic plastic)  $\epsilon_1 > \epsilon > \epsilon_2$

$$\begin{aligned} \sigma = \frac{2}{3} Y \left\{ 1 - \frac{2G[(1-\epsilon)/(1-\epsilon_0) - 1]}{Y} \right. \\ \left. + \ln \left\{ \frac{2G[(1-\epsilon)/(1-\epsilon_0)]}{\epsilon Y} \right\} \right\} \end{aligned}$$



Mode 3 (plastic)  $\varepsilon_2 > \varepsilon > 0$

$$\sigma = \frac{2}{3} Y \ln\left(\frac{1}{\varepsilon}\right)$$

where

$$G = G_0 e^{5\varepsilon}$$

$$Y = Y_0 [(1 - \varepsilon)/(1 + \varepsilon)]^2$$

$$\varepsilon_1 = \varepsilon_0 [1 + (1 - \varepsilon_0) \frac{Y}{2G}]$$

$$\varepsilon_2 = \varepsilon_0 - (1 - \varepsilon_0) \frac{Y}{2G}$$

6) Igniter description that considers individual ingredients, their pressure-dependent combustion behavior, and their individual thermochemical description.

7) Confinement of the bed by the tube walls is accomplished by coupling the model to a finite element material code, HONDO.<sup>7</sup>

## CODE MODIFICATIONS

Modification and refinement of the analytical code has continued since the last Symposium, and it is our purpose to describe these changes, the ancillary laboratory work supporting them, and their effects on calculated results.

The model of Reference 1 was probably the first to separate the mass addition and energy addition terms in describing the "gasification" of the solid particles. The attempt to model the transition process as a continuous one without recourse to switches to proceed from one combustion "phase" to another represented a significant improvement in such analysis. Since that time, a more complicated combustion model has been developed at the Naval Weapons Center (NWC), involving competing condensed phase decomposition reactions in the solid particles and supporting second order gas phase reactions to the final product state.

### NWC Combustion Model

If we neglect molecular diffusion, the conservation equations for species and energy as written in partial derivative form are

Species:

$$\rho \frac{dY_i}{dt} = \pm RR_i + \rho v \frac{\partial Y_i}{\partial x}$$

Energy:

$$\rho \frac{dh}{dt} = \frac{\partial}{\partial x} \left( \frac{\lambda}{C_p} \frac{\partial h}{\partial x} \right) + \rho v \frac{\partial h}{\partial x} - \sum_{i=1,n} \mp RR_i \Delta H_i$$

The convective terms, involving the spatial gradient, serve to describe the flow process in the gas phase, and the effect of the moving boundary at the interface between condensed and gas phase. If we limit our present analysis to isobaric processes, and both the steady state burn rate and the ignition process are isobaric, then there is no pressure gradient in time, and we can safely ignore the pressure gradient in distance (as do most burn rate models), and thus obviate the need to write an equation for the conservation of momentum.

The reactions in the condensed phase are classically described in first order Arrhenius form.

$$RR_i = \rho_s A_i \left( 1.0 - \sum_{j=1,n} Y_j \right) e^{-E_i/RT}$$

In the gas phase, a general nth order rate equation is employed, in terms of the molar concentration of the reactants.

$$RR_i = \frac{A_i}{MW} (\rho Y_j)^n e^{-E_i/RT}$$

There are a large number of reactions to be considered for even a simple monopropellant such as HMX.<sup>8</sup> In some quarters there is still a disagreement about the reactions themselves, and there is insufficient accuracy in many of the rate values which have been published. In addition to this real difficulty is the desire to simplify the reaction sequence to conserve computer resources.

An overall reaction concept (or global kinetics) has been investigated by Coffee, Kotlar, and Miller.<sup>9</sup> They compared the flame properties for a premixed, laminar steady-

steady-state flame as obtained through the solution of an exhaustive set of reactions, to those calculated by a single overall reaction. They indicate that quite reasonable agreement can be obtained, and point the way to the utilization of such a concept for other systems. In our application, the global kinetic values are derived from the data obtained by both steady-state regression and ignition experiments.

There was a temptation to lump the total condensed phase reactive behavior into one "global" reaction. This was the approach taken in many of the earlier regression rate models (Reference 10, for instance), where the single reaction was considered as a "surface" (condensed gas interface) phenomenon, much like an inert ablation process.

Some time ago,<sup>11</sup> we became convinced that certain materials (most notably the nitramines) could not be adequately described by a single path gasification process. Accordingly, our model deals with two decomposition reactions in the condensed phase leading to gasification. In the case of the nitramines, one path is exothermic, the other endothermic. A difference in the activation energies of the two reactions provides the leverage to augment one reaction at the expense of the other, as the experimental conditions of pressure and/or initial temperature change. This variation in the composition of the gasified products at the interface is vital to the understanding of the pressure and temperature sensitivity of HMX at low pressures.

The NWC model utilizes two decomposition reactions, in each of which one mol of solid becomes two mols of gas, regardless of the reaction path. Recent experimental work by many researchers has shown this to be a fairly accurate description of nitramine decomposition. Thus, the gasification process leads to two different bi molecular compositions, each of which must react to the final product composition in the gas phase. This bi molecular character leads to our use of second order gas phase reactions to change the decomposition products into the final equilibrium products. Thus the general solution proceeds from a set of six partial derivatives in distance and time, four expressing the conservation of species, and two for the enthalpy.

External heating effects (radiative and/or convective) are introduced at the "surface" position, and integration proceeds from the initial and cold condensed-phase boundary conditions to the final (equilibrium) steady-state solution. This is the set of equations for a radiant ignition condition.

The steady-state regression condition is represented by a reduced form in which the time dependent terms are set to equal zero. This leads to a set of six ordinary, non-linear, differential equations in distance.

In attempting to solve the partial derivative set, it rapidly becomes apparent that the evaluation of the spatial derivatives in the gas phase is a difficult task as compared to the well behaved gradients which build up in the condensed phase.

The scenario which develops (particularly with radiative heating) is as follows. As the condensed phase is heated, a thermal profile is established in the condensed phase, the sample begins to react and to gasify. The gases leave the surface with a velocity sufficient to satisfy the conservation of mass, and they begin to react as they flow away from the surface. Initially these gas-phase reactions are quite slow, as the temperature is that of the surface. However, the heating of the gases, due to the exothermic reaction to final products, causes a conduction of heat back to the surface. Thus, the gases leaving the "surface" an instant later flow into a higher temperature region, leading to faster reactions. This "bootstrapping" action continues until, rather suddenly, the reaction zone snaps back toward the surface and a steady state profile is established.

Under steady-state conditions, the total reaction zone thickness is measured in micrometers, whereas the intermediate transient condition may involve partial reactions occurring several centimeters from the "surface." The task of evaluating spatial derivatives becomes extremely difficult as the extended (centimeter scale) reaction zone collapses to the steady-state (micron scale) reaction zone in at most a few microseconds.

The spatial (geometric) effects were cast as a reaction distance (standoff) in the manner of the Beckstead-Derr-Price model,<sup>10</sup> while the

time dependent effects (fraction of completion of reaction, temperature at flame sheet position) were solved as ordinary differential equations. Thus evolved the model in use today at NWC.

The reaction distance (standoff) relations which are normally derived by integration of the spatial derivatives in the gas phase<sup>10</sup> are as follows:

$$x^* = \frac{\rho_s r}{\Lambda_f e^{-E_f/RT} p^n}$$

$$Z = \frac{C_p \rho_s r x^*}{\lambda_g} \quad (\text{dimensionless})$$

$$\left| \lambda_s \frac{dT}{dx} \right|_s = \rho_s r \Delta H_e^{-Z} \quad (\text{flame feedback})$$

These are, of course, for the steady-state, fully reacted case. We have chosen to modify the relations to reflect the developing character of the reaction profile with time by introducing a fractional reaction term,  $F$ , which represents the fractional completion of the reactions along a given path.

Thus, our modified relations become

$$x^* = \frac{\rho_s r}{\Lambda_g \rho_g / MW F_1^2 e^{-E_g/RT_1}}$$

$$\left| \lambda_s \frac{dT}{dx} \right|_s = \rho_s r \sum_{i=1,n} \Delta H_i e^{-Z_i}$$

If we define the average fraction complete and the average gas temperature as

$$\overline{F}_1 = (1.0 - F_1/2)$$

$$T_1 = \frac{F_1}{2.0} \left( \frac{\Delta H_1}{C_p g} - T_s \right) + T_s$$

and the time dependent relation for the fraction of reaction completed is defined as

$$\frac{dF_1}{dt} = \left( 1.0 - F_1 \right) \Lambda_g / MW \rho_g \overline{F}_1^2 e^{-E_g/RT_1}$$

we now have written a set of equations which utilize one set of kinetic parameters to describe both spatial and temporal effects. The regression rate is approximated by

$$r = A e_s^{-E_s/RT_s} \sum_{i=1,n} Y_i$$

for the early phases of the radiant ignition process where the decomposition reactions are not yet complete at the surface.

This leads to a working set of equations used for the NWC combustion model, described as follows:

For steady state:

- 3 Ordinary differential equations for the condensed phase
- 2 Flame standoff equations for heat feedback

For transient (ignition):

- 3 Partial derivatives  $f(x,t)$  for the condensed phase
- 2 Ordinary differential equations for fraction reacted, gas phase
- 2 Flame standoff equations,  $f(t)$ , for heat feedback

The development of this model and the laboratory experiments leading to the kinetic parameters are described in some detail in References 11 and 12. Radiative ignition and steady state combustion rate measurements are utilized to generate global kinetic and energetic parameters for a given material. These parameters are then used in the porous bed code to describe the transient response of the energetic material under study. The application of this more complex combustion scheme to the porous bed model and the results of calculations with it are given in References 12 and 13.

### Porous Bed Model

The porous bed model of Reference 1 has been further improved in the manner in which the solid particles are described during the transient process. Particles, which in the referenced model were compacted without change in size or shape, are now allowed to deform and/or fracture. This change in effective size (shape factors may be treated as effective diameters)

has marked effect on several interphase relationships. The rate of convective heat transfer is increased, as it is influenced by the reciprocal of the diameter of the particle. The inter phase drag (or bed permeability) is also heavily influenced by the effective diameter of the particle. In addition, the rate of mass addition is greatly affected by the surface-to-volume ratio, which is proportional to the reciprocal diameter. The effect of a change of diameter was known; the degree of change during a compaction process and a way to mathematically represent it were not. The remainder of this paper will be devoted to our solution of this problem.

## EXPERIMENTAL INVESTIGATION

A conventional apparatus designed to measure the pressure drop across a porous bed of given length as a function of gas flow rate was modified so that after the initial pressure drop measurements on the uncompacted material, a ram could be inserted to compact the material, leading to a bed of reduced porosity. After removing the ram, the pressure drop measurements were repeated on the *in situ* compacted material. This process was repeated several times to increasingly lower porosities.

The test section of the apparatus was nominal 1 inch inside diameter tubing, and bed lengths from one to four inches were investigated. A family of three gas flowmeters were employed to measure the flow, thus expanding the experimental range. The bed length was measured at each level of compaction. Two classes of materials were investigated, those that compact by particle deformation, and those that compact by particle fracture. Ball propellants (primarily nitrocellulose) are an example of those which deform, and several ball propellants of differing plasticizer content were evaluated in our facility. The diameters of the materials were in the 400-600 micron range and initial (tap) densities were typically 59-61 percent of theoretical. Representative data for such a material containing 12 percent plasticizer, compacted to three higher loading densities, is shown in Figure 1. The curves are calculated from the Jones-Krier correlation used in the porous bed code, neglecting the

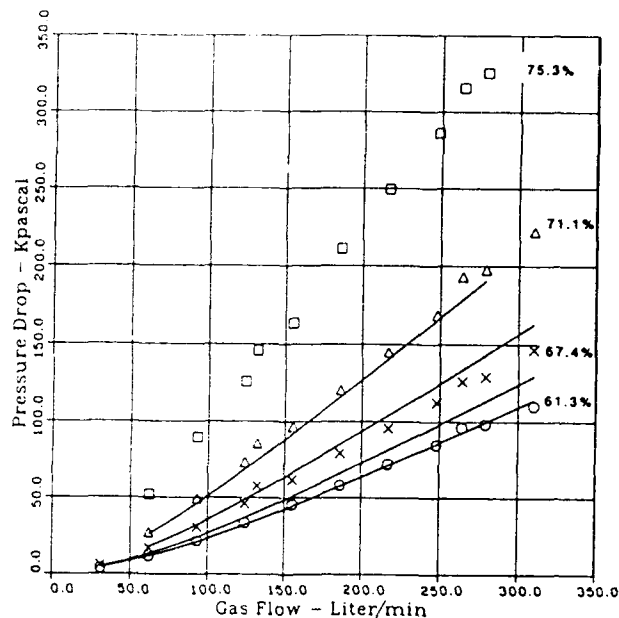


Figure 1. Experimental and Calculated Data for Deforming Ball Propellant at Four Porosity Levels—Changes in Particle Shape Neglected

effect of particle deformation. The changes in porosity and bed length associated with the compaction have been included. It is obvious that the bed pressure drop is underestimated at the lower porosities.

The particle-to-particle stress relationship of Carroll-Holt was utilized to correlate the deformed shape (increased or decreased surface area) in terms of the elastic and plastic regimes of the compaction. A proportionality constant was introduced to relate the stress in the plastic regime with the deformation.

$$SR_1 = 1 - \frac{\sigma}{4Y(1 - \epsilon)}, \quad \epsilon > \epsilon_1$$

$$SR_{2,3} = \left| 1 - \frac{\sigma}{4Y(1 - \epsilon)} \right| \left| 1 + \frac{2/3bY}{\rho \ln(\epsilon_1/\epsilon)} \right|$$

By utilizing such a scheme to provide an "effective" diameter at each compaction level, the correlation of bed pressure drop is markedly improved, as shown in Figure 2. This formality seems to allow a good representation of the permeability of a deforming material over a range of porosity

The compaction of materials which compact by fracture seems to lack such a

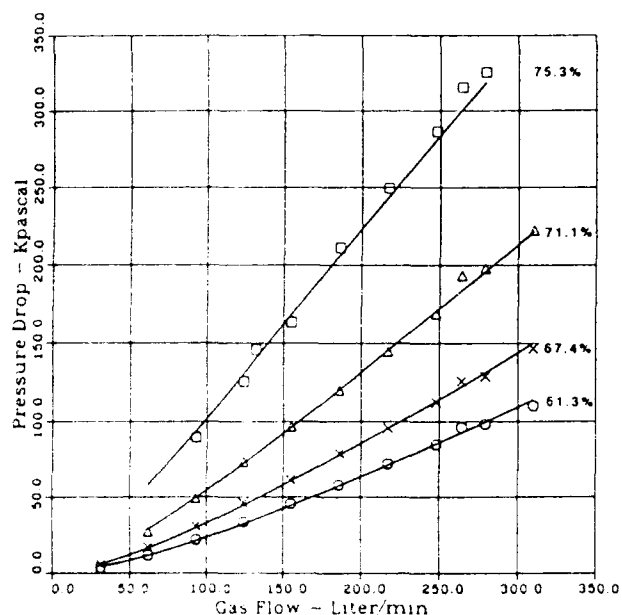


Figure 2. Experimental and Calculated Data for Deforming Ball Propellant at Four Porosity Levels—Changes in Particle Shape Considered

mathematical form. The problem is complicated by the fact that unimodal samples become polymodal during compaction. One approach to the evaluation of an "effective" diameter for such a mixture is based on the summation of the effects of each weight fraction, divided by its diameter.

$$D_{eff} = 1.0 / \sum (Frac / Diam)$$

$D_{eff}$  = "Effective" Diameter  
 $Frac$  = Weight Fraction  
 $Diam$  = Diameter of Fraction

One method of evaluation would entail the determination of a size distribution curve at each compaction level employed, followed by the calculation of an "effective" diameter. As an alternative, the Jones Krier correlation was used to find the "effective" diameter which best fitted the experimental bed pressure drops at each degree of compaction. A well defined sample of HMX (500-590 micron) was chosen as an example of a material which compacts by fracture. It was incrementally compacted to a total porosity decrease of 29 percent. Bed pressure drop measurements were made at several different porosity levels, and subjected to analysis.

The correlation shown in Figure 3 is the result of ignoring the size reduction associated with the compaction process. Again a marked

under-prediction of bed pressure drop is noted. If the diameters are allowed to change to optimize the correlation, a marked improvement can be noted, as shown in Figure 4. Each level of porosity now has its own "effective" diameter due to fracture, as before each level had its own deformation, or roughness. The "effective" diameters obtained by the analysis

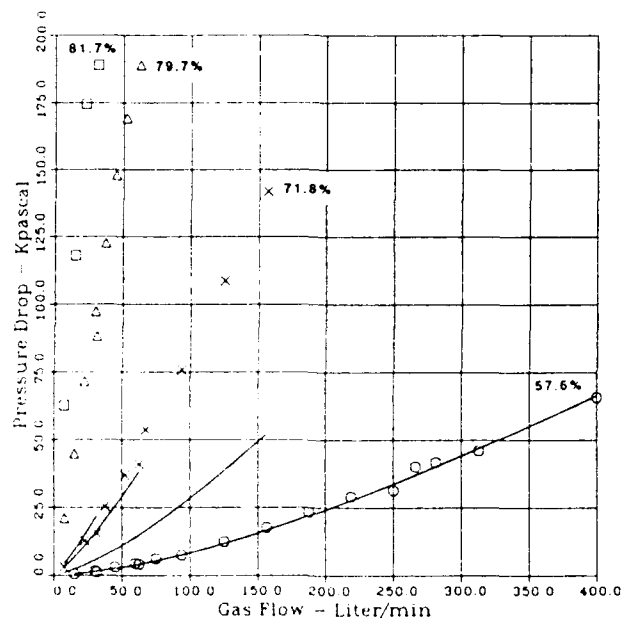


Figure 3. Experimental and Calculated Data for Fracturing HMX at Four Porosity Levels—Change in Diameter Neglected

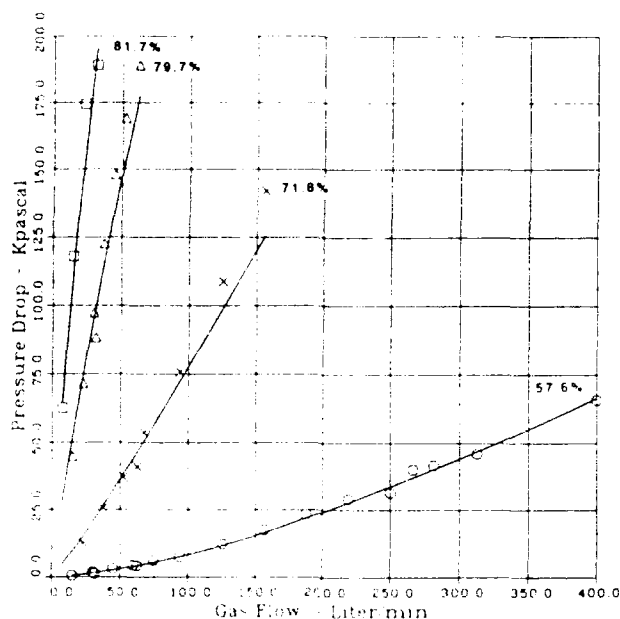


Figure 4. Experimental and Calculated Data for Fracturing HMX at Four Porosity Levels—Change in Diameter Considered

of a representative experiment are shown in Figure 5

In order to include this effect in the porous bed (DDT) code, a simple polynomial expression was utilized to relate "effective" diameter to degree of compaction. Perhaps in the future a form more related to the physics may become available.

## APPLICATION TO THE POROUS BED MODEL

In order to demonstrate the importance of a proper particle description during the complete calculation, several representative experiments have been modelled, carrying out the calculations with and without a changed description of the particles. A ball propellant was chosen as representative of a deforming material, and HMX as a fracturing material.

Both of these materials had been subjected to quasi-static compaction experiments, both had been studied in the NWC permeability/drag apparatus, and the kinetics and energetics of each had been derived from the analysis of steady state burn rate behavior and radiant ignition data, utilizing the NWC combustion model. Each material has been

utilized in porous bed experiments under conditions quite comparable to those used in the present modeling

## THERMAL STIMULATION

A typical DDT configuration was chosen, with an igniter similar to those referred to in Reference 14. The steel tube had an inner diameter of 25.4 mm, a wall thickness of 25.4 mm, and lengths of 250 to 300 mm. The tube wall was allowed to respond in accordance to the internal loading, and the calculations were stopped when the strain at the worst location reached 60 percent.

As an example of a fracturing material, a case was chosen with unimodal 1000 micron HMX, at 62 percent initial loading density. The curves of Figure 6 show how the compaction profiles develop in time. The front locations (represented by the circles) may be plotted to yield a map of front location versus time. This has been done in Figure 7, along with similar data derived from the particle ignition profiles. "Ignition" is defined as the time when a particle reaches self-sustaining burning due to the development of the gas-phase reactions associated with the particle. These data may be compared to those reported by Bernecker, et al., as shown in Figure 8, which were obtained from a nearly identical experiment. The agreement of shape, timing, and velocity is quite good. The pressure profile

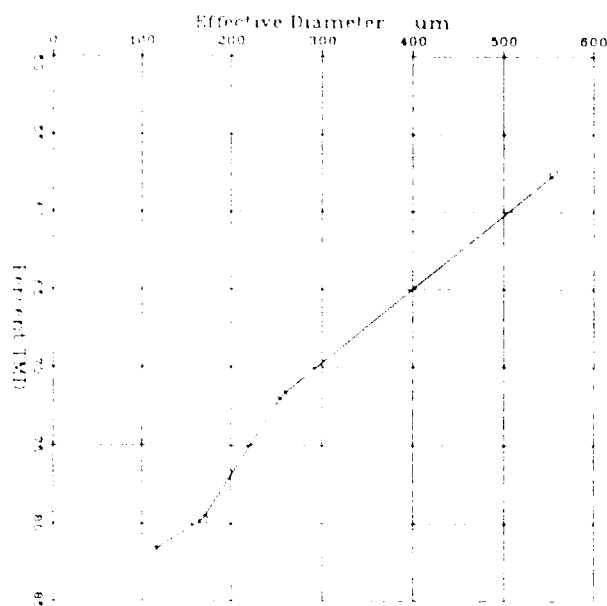


Figure 5. Calculated "Effective" Diameters for Fracturing HMX as a Function of Percent TMD (from Data in Figure 4)

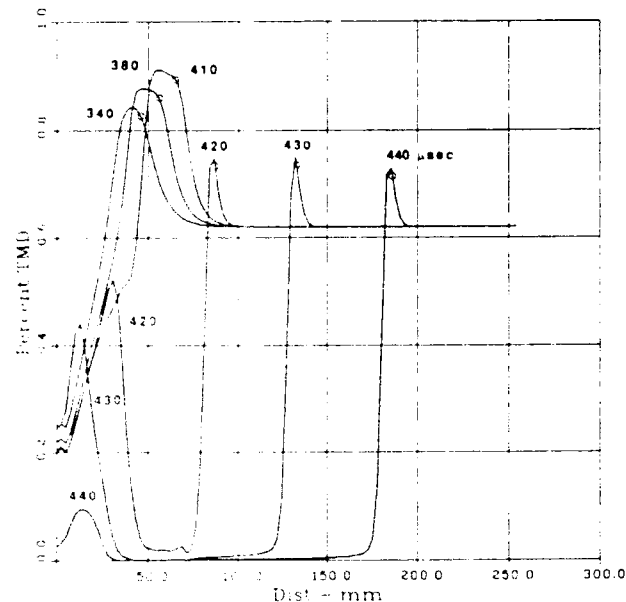


Figure 6. Compaction Profiles at Selected Times for Unimodal HMX, with Fracture

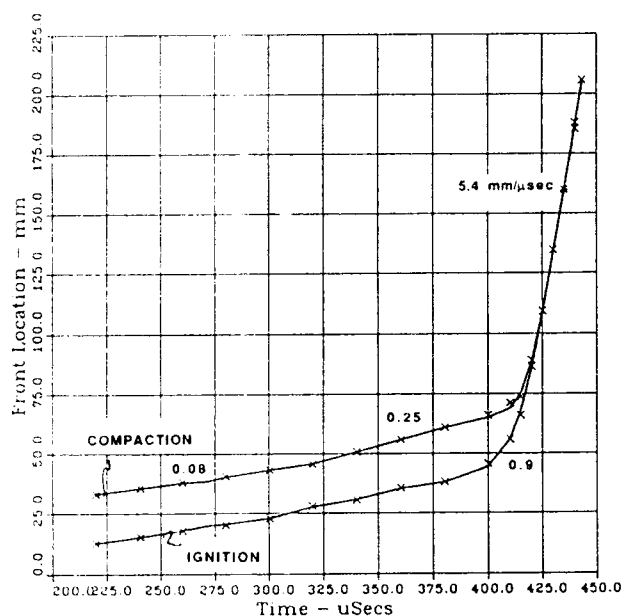


Figure 7. Calculated Compaction and Ignition Front Locations as a Function of Time Unimodal HMX, with Fracture

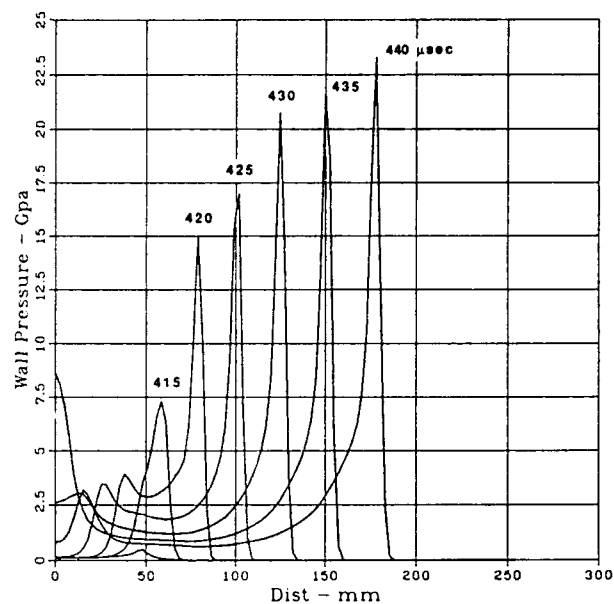


Figure 9. Calculated Wall Pressure Profiles at Selected Times for Unimodal HMX, with Fracture

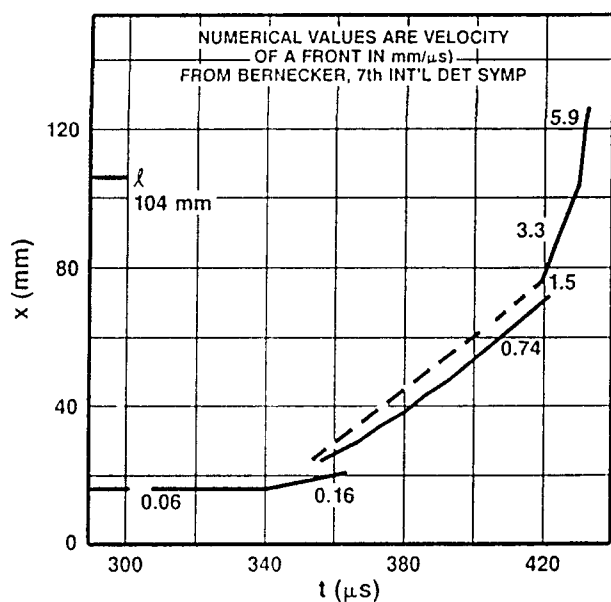


Figure 8. Experimentally Determined Velocities and Locations Reported by Bernecker, et al., Reference 14

data of Figure 9 show pressures in the 200-225 kilobar range, which are quite consistent with the velocities noted in Figure 7.

The curves of Figure 10 compare the calculated "wave" behavior of the same material

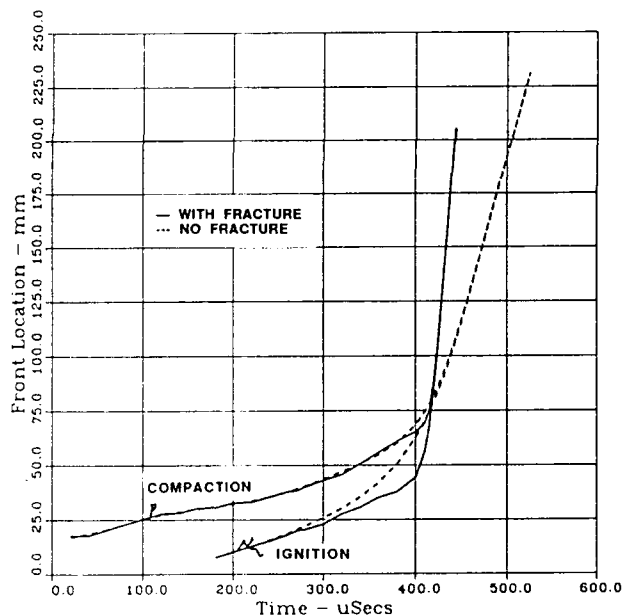


Figure 10. Calculated "Wave" Behavior for Unimodal HMX With and Without Consideration of Particle Fracture

with and without fracture. The upper curves show the location of the leading edge of the advancing compaction front, while the lower curves track the progress of the "ignition" front through the material. The solid and dotted

curves represent the results with fracturing and non-fracturing particles. There seems to be little effect until the "ignition" front for the non-fracturing material begins to accelerate at about 300 microseconds. The compaction process has caused fracture of the compacted material, leading to a greatly increased surface to absorb the igniter energy. The lower surface area and lower drag associated with the larger particles allows better penetration of the igniter gases, leading to quicker "ignition."

The "ignition" front accelerates more markedly (though later) through the fractured material, and exhibits an even greater difference in wave velocity after the "ignition" front catches the compaction front. The fractured material shows a velocity of about 5.4 mm/microsecond compared to 1.5 mm/microsecond for the non-fracturing material. The fractured material has a significantly higher surface-to-volume ratio, leading to the greatly amplified pressures shown in the profile plots of Figure 11.

The curves of Figure 12 demonstrate the calculated "wave" behavior for a ball propellant at initial 60 percent loading density, which was chosen as a deforming material. Again, the upper curves are for compaction, the lower for ignition. It can be seen that there

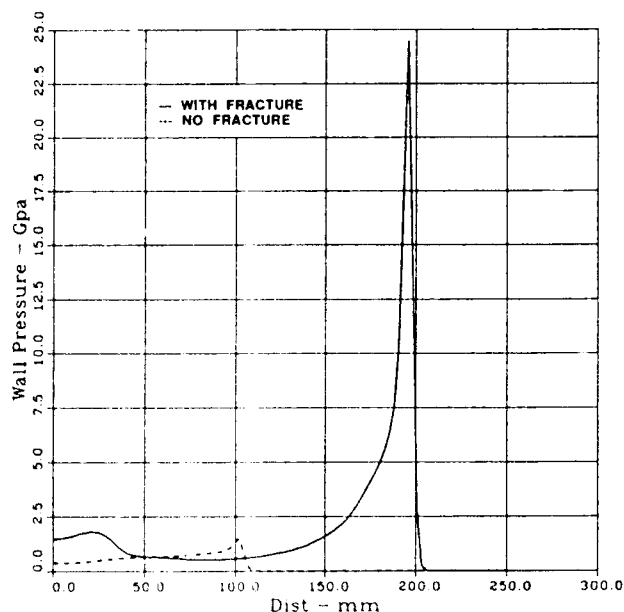


Figure 11. Calculated Wall Pressures at 440 microseconds, With and Without Consideration of Fracture of Unimodal HMX

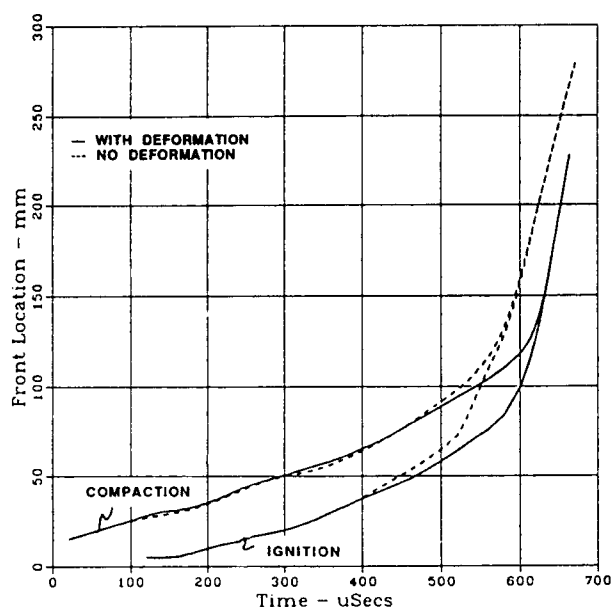


Figure 12. Calculated "Wave" Behavior for Ball Propellant With and Without Consideration of Particle Deformation

is very little effect of deformation until about 400 microseconds. At that time the "ignition" front for the undeformed material begins to accelerate. This is probably due to the lower drag (pressure drop) associated with the spherical particles, which allows better penetration of the hot gases from the igniter, coupled with the lower particle surface to be heated.

However, as the "ignition" front in both cases catches up with the compaction front, a marked difference in slope may be noted. The velocities are about 2.5 mm/microsecond as opposed to 1.7 mm/microsecond. The calculated response of pressure gauges located in the wall at 50, 100, and 150 mm from the igniter end is shown in Figure 13. The much more violent reaction of the deformed material can be clearly seen in the curves of Figure 14, which show the pressure profiles at 660 microseconds after start.

## MECHANICAL STIMULATION

The porous-bed code has been modified to allow simulation of mechanically stimulated materials in experiments such as the piston driven compaction tests described by Sandusky in Reference 15. The normally immovable



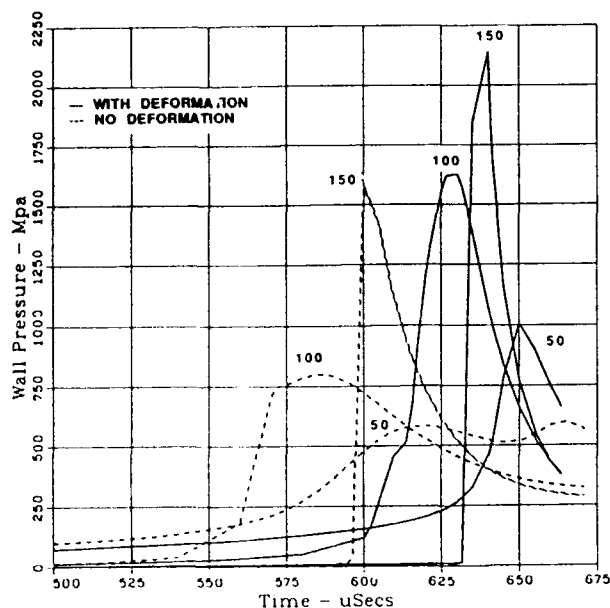


Figure 13. Calculated Pressure Gauge Responses at 50, 100, and 150 mm from Igniter, Ball Propellant With and Without Deformation

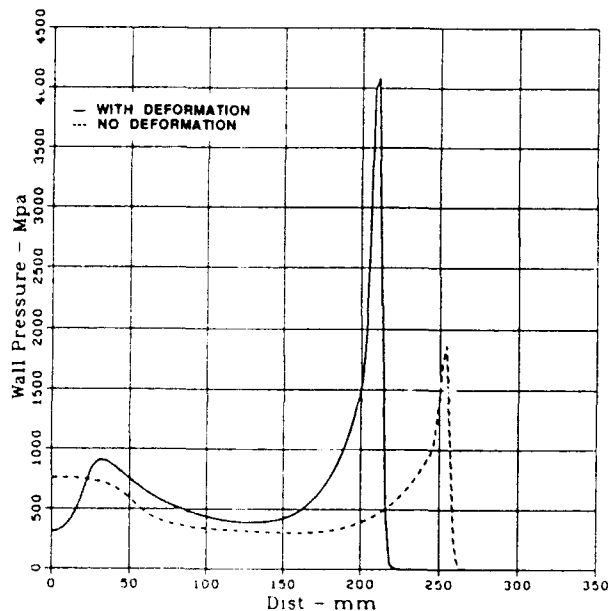


Figure 14. Pressure Profiles at 660 Microseconds After Igniter Stimulus, Ball Propellant With and Without Deformation

igniter end boundary has been replaced by one which moves, controlled either by a programmed velocity-time history or by conservation of momentum at the interface, treating the piston as a lumped parameter.

The same ball propellant at an initial loading density of 60 percent was impacted by

a piston which imparted a constant interface velocity of 185 meters/second. The confining tube was steel of the same diameter as above, but with a length of 150 mm. The calculated wave behavior is shown in Figure 15. The "ignition" front, although its appearance is delayed in time, is never very far from the compaction front. This relates to the location of maximum mechanical work due to compaction at the leading edge, which is the primary source of heating. As in the DDT case, the difference in slope is very pronounced after the "ignition" front accelerates, with velocities of 2.3 and 1.7 mm/microsecond for the deforming and non-deforming materials, respectively.

The calculated response of pressure gauges, located at 25, 50, and 75 mm from the original piston boundary, are shown in Figure 16. Again, the higher pressures resulting from the deformed material are evident, as well as a more highly transient character.

It should be iterated that the kinetic/energetic parameters used to describe the material for this simulation were identical to those used for the thermally-stimulated case. No new rates were required to describe a "compressive reaction," nor was it necessary to derive an "ignition" parameter peculiar to a mechanically-stimulated bed. The kinetics

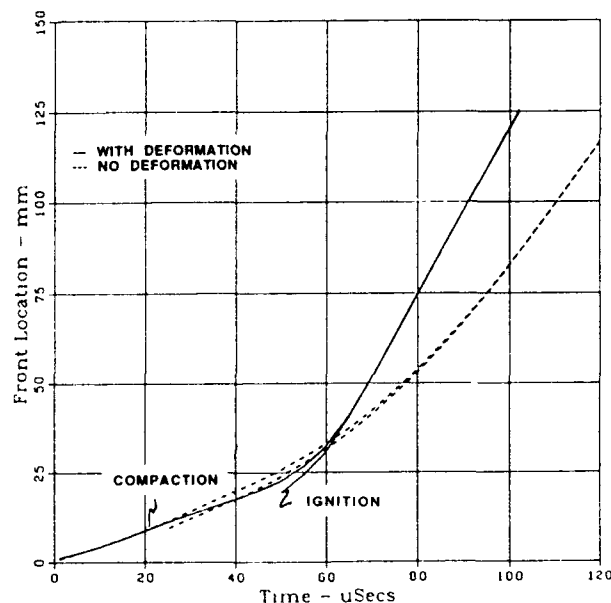


Figure 15. Calculated "Wave" Behavior for Ball Propellant, Mechanical Stimulation, With and Without Deformation, 185 Meters Per Second Piston Velocity

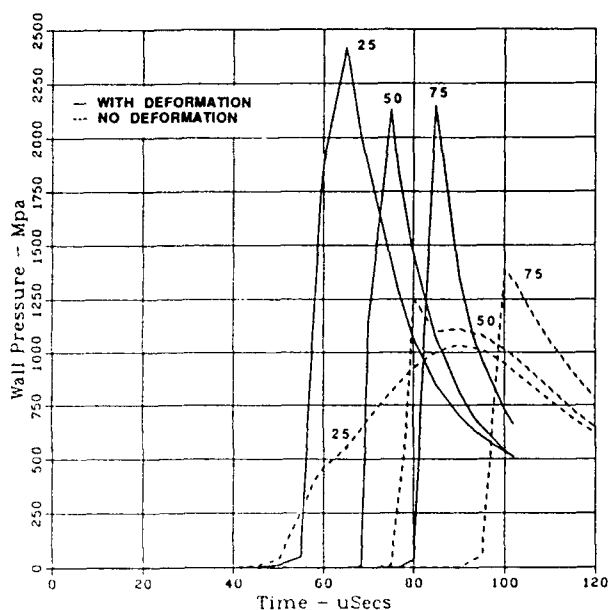


Figure 16. Calculated Pressure Gauge Responses at 20, 40, and 60 mm from Original Interface --Mechanical Stimulation, 185 Meters Per Second Piston Velocity

and energetics were derived from steady-state burn rate and radiant ignition measurements, and are applied without change to either igniter or piston-driven transient-combustion experiments.

For the mechanically-stimulated experiment, it is necessary to assume some concentration of the mechanical work (hot spots), which is physically realistic in light of the manner of deformation. The deformation is not uniform, beginning with dents, followed by flattening and "cubing" of the material. Our localized heating treatment is somewhat arbitrary at this time, relating the hot spot fraction to the degree of compaction.

## CONCLUSIONS

The modifications to the NWC porous-bed code have been described and related to the supporting laboratory work. Although we have chosen in this paper to concentrate on the effects of particle behavior during compaction, the modified combustion sub-model is of at least equal importance. The proper evaluation of the condensed-phase reaction behavior is of particular importance in the study of mechanically-stimulated beds.

We have shown how the behavior of both deforming and fracturing particles may be evaluated through the laboratory determination of bed pressure drop (permeability), and how this behavior may be introduced into the porous-bed code.

The importance of this behavior on the calculated response of a porous bed to both thermal and mechanical stimulation has been demonstrated for two representative materials. As a single parameter, it can affect the onset, as well as the severity of the ensuing response. It most certainly should not be ignored.

## REFERENCES

1. Price, C. F. and Boggs, T. L., "Modeling the Deflagration to Detonation Transition in Porous Beds of Propellant," *Eighth Symposium (International) on Detonation*, Preprint Vol. 2, 1985, pp. 650-657.
2. Pilcher, D. T.; Beckstead, M. W.; Christensen, L. W.; and King, A. J., "A Comparison of Model Predictions and Experimental Results of DDT Tests," *Sixth Symposium (International) on Detonation*, 1976, pp. 258-266.
3. Jones, D. P. and Krier, H., "Gas Flow Resistance Measurements Through Packed Beds at High Reynolds Numbers," *Journal of Fluids Engineering*, Vol. 105, Jun 1983, pp. 168-173.
4. Denton, W. H., "The Heat Transfer and Flow Resistance for Fluid Flow Through Randomly Packed Spheres," *General Discussion on Heat Transfer, Institute of Mechanical Engineering and ASME*, London, 1951, pp. 370-373.
5. Carroll, M. M. and Holt, A. C., "Static and Dynamic Pore-Collapse Relations for Ductile Porous Materials," *Journal of Applied Physics*, Vol. 43, Apr 1972, pp. 1626-1636.
6. Kooker, D. E. and Anderson, R. D., "A Mechanism for the Burning Rate of High Density, Porous, Energetic Materials," *Seventh Symposium (International) on Detonation*, pp. 198-215.

7. Key, S. W., "HONDO—A Finite Element Computer Program for the Large Deformation Response of Axisymmetric Solids," *SLA-74-0039, Sandia Laboratories*, Albuquerque, NM, Apr 1974.
8. Melius, C. F., "Theoretical Studies of the Chemical Reactions Involved in the Ignition of Nitramines," *24th JANNAF Combustion Meeting*, Monterey, CA, Oct 1987.
9. Coffee, T. P.; Kotlar, A. J.; and Miller, M. S., "The Overall Reaction Concept in Premixed, Laminar, Steady-State Flames," *Technical Report ARBRL-TR-02528*, U.S. Army Ballistic Research Laboratory, Aberdeen Proving Ground, MD, Oct 1983.
10. Beckstead, M. W.; Derr, R. L.; and Price, C. F., "The Combustion of Solid Monopropellants and Composite Propellants," *Thirteenth Symposium (International) on Combustion*, The Combustion Institute, Pittsburgh, PA, 1971, pp. 1047-1056.
11. Price, C. F. and Boggs, T. L., "A Simultaneous Mathematical Treatment of Deflagration and Ignition Phenomena," *Proceedings of the 22nd JANNAF Combustion Meeting*, Volume 1, CPIA Publication 432, Oct 1985, pp. 505-513.
12. Price, C. F. and Boggs, T. L., "Transient Combustion: An Important Aspect of Deflagration-to Detonation Transition," *Nonsteady Burning and Combustion Stability of Solid Propellants (The AIAA Progress Series)*, New York, American Institute of Aeronautics and Astronautics (in progress).
13. Atwood, A. L.; Price, C. F.; Boggs, T. L.; and Richter, H. P., "Transient Combustion Analysis of Energetic Materials," *Combustion and Detonation Phenomena*, 19th International Annual Conference of ICT, Karlsruhe, Federal Republic of Germany, 1988.
14. Bernecker, R. R.; Sandusky, H. W.; and Clairmont, A. R., Jr., "Deflagration-to-Detonation Transition Studies of Porous Explosive Charges in Plastic Tubes," *Seventh Symposium (International) on Detonation*, 1982, pp. 119-138.
15. Sandusky, H. W. and Bernecker, R. R., "Compressive Reaction in Porous Beds of Energetic Materials," *Eighth Symposium (International) on Detonation*, Preprint Vol. 2, 1985, pp. 631-640.

## NOMENCLATURE

A	=	Area
$A_i$	=	Reaction prefactor
$A_f$	=	Arrhenius prefactor
$A_{gi}$	=	Second order prefactor, reaction i
$A_s$	=	Surface rate prefactor
b	=	Proportionality factor
$C_p$	=	Mass average specific heat
$C_{pg}$	=	Specific heat of gas
D	=	Particle diameter
$D_{gp}$	=	Interphase drag
$E_i$	=	Activation energy
$E_f$	=	Arrhenius activation energy
$E_{gi}$	=	Activation energy, reaction i
$E_s$	=	Surface rate activation energy
$E_g$	=	Total specific gas phase energy
$\bar{F}_i$	=	Average fraction complete, reaction i
$F_v$	=	Drag force
$G_0$	=	Shear Modulus
h	=	Specific enthalpy
L	=	Bed length
MW	=	Molecular weight of reacting species
$MW_j$	=	Molecular weight of species j
n	=	Reaction order, most normally taken as 2
P	=	Pressure
$q_{gp}$	=	Interphase heat flux
R	=	Universal gas constant
$Re'$	=	Reynolds number
$RR_g$	=	Rate of reaction, gas phase
$RR_i$	=	Rate of reaction, species i
r	=	Regression rate
$s_p$	=	Particle surface area
SR	=	Effective surface area ratio
T	=	Temperature, $f(t,x)$

$T_i$	=	Average gas temperature, reaction i	$v$	=	Mass average velocity
$T_s$	=	Temperature at condensed-gas interface	$\epsilon$	=	Bed porosity
$U_g$	=	Gas phase velocity	$\epsilon_0$	=	Critical porosity
$U_p$	=	Condensed phase velocity	$\rho$	=	Mass density
$V_p$	=	Particle volume	$\rho_g$	=	Average gas phase density
$x^*$	=	Flame standoff distance	$\rho_s$	=	Condensed phase density
$x_i^*$	=	Flame standoff distance, reaction i	$\sigma$	=	Bed stress
$Y_i$	=	Mass fraction of species i	$\Delta H$	=	Heat of reaction to final products
$Y_j$	=	Mass fraction of gasified reactant species j, which reacts to species i	$\Delta H_i$	=	Heat of reaction, species i
$Y_o$	=	Yield stress	$\Delta H_{rg}$	=	Heat of reaction, gas phase
$Z$	=	Flame standoff ratio	$\lambda$	=	Thermal conductivity
$\frac{\partial h}{\partial x}$	=	Spatial gradient of enthalpy	$\lambda_g$	=	Thermal conductivity of gas
$\frac{\partial Y_i}{\partial x}$	=	Mass fraction spatial gradient of species i	$\Gamma_g$	=	Interphase mass flux
			$\mu$	=	Gas phase viscosity

**SESSIONS ON**  
**EQUATION OF STATE**

**Cochairmen: Claude Fauquignon**  
**Institut Saint-Louis (ISL)**

**Milton S. Shaw**  
**Lawrence Livermore National Laboratory**

**and**

**Francis Ree**  
**Lawrence Livermore National Laboratory**

**Katsumi Tanaka**  
**National Chemical Laboratory for Industry**

# SHOCK BEHAVIOR OF EXPLOSIVES ABOUT THE C-J POINT

Paul W. Cooper  
Sandia National Laboratories  
Albuquerque, New Mexico 87185

*Experimental data for pressure and particle velocity along the Hugoniot of detonation reaction products for a number of explosives are correlated in a reduced parameter form  $P/P_{cj}$  versus  $u/u_{cj}$ . Two correlations are found:  $P/P_{cj} = a + b(u/u_{cj}) + c(u/u_{cj})^2$  when  $P/P_{cj} > 0.08$ , and  $P/P_{cj} = m(u/u_{cj})^n$  when  $P/P_{cj} < 0.08$ . The correlations yield results that agree reasonably with code calculations.*

## INTRODUCTION

In explosives engineering calculations, there is often a need to know the properties of detonation reaction products at the shock states created when an explosive detonates in contact with another material. If the adjacent material has a shock impedance greater than that of the detonation reaction products at the Chapman-Jouguet (CJ) state, then the resulting pressure at the interface is greater than the CJ pressure. These pressures lie along the shock adiabat of the detonation reaction products. Conversely, if the adjacent material has a shock impedance lower than that of the detonation reaction products at the CJ state, then the resulting pressure at the interface will be lower than the CJ pressure. These pressures lie along the expansion isentrope of the detonation reaction products. Although only the adiabat is usually called the Hugoniot, for the purpose of this paper, the Hugoniot is the combination of these two regimes, joined at the CJ state.

This Hugoniot can be estimated by computer codes that utilize estimated product composition equilibria along with nonlinear empirical equations of state (EOS) for the gases. While these codes are quite good at estimating the values along the Hugoniot, they are not readily available to most engineers, nor are the large computers that are required to run them.

Some experimental data is available in the open literature, but is limited to relatively

few explosives and only to a few initial densities of those explosives. Therefore, a simple means is needed to estimate the values along the Hugoniot for any explosive and at any density, based only upon easily obtained or estimated parameters. This paper will develop one such method, which is based upon a simple correlation of existing experimental data.

## EXPERIMENTAL METHODS

Three different experimental methods are used to determine the pressure and particle velocity created at the interface of a detonating explosive and an adjacent material. In the first, the free surface velocity of the target material is measured for various thicknesses of the target, using either optical techniques or electrical pin switches. The free surface velocity is twice the particle velocity, and the data of particle velocity versus target thickness is extrapolated back to zero thickness. The particle velocity thus obtained at the interface is then used with the known Hugoniot of the target material and the Rankine-Hugoniot equations for mass and momentum to calculate the interface pressure.

The second method is to measure the shock velocity in the target material at various distances from the interface and extrapolate back to the interface. This method is usually employed for optically transparent targets where high speed streak photography can be used. Again, these data are used in the known Hugoniot or EOS of the target material to

obtain the desired interface pressure and particle velocity.

The third method determines the interface state from target pressure measurements obtained using various gauge techniques.

When these experiments are conducted for a given explosive with a variety of targets spanning the range from low- to high-target shock impedance, the Hugoniot of the detonation reaction products of that particular explosive can be constructed. One such Hugoniot is shown in Figure 1 for a plastic bonded explosive consisting of TATB and a binder.<sup>1</sup> The target materials used in these experiments were copper, aluminum, magnesium, transacryl (a polymer), water, and argon gas at various initial pressures ranging from 5 to 705 bar.

## SCOPE OF EXPERIMENTAL DATA

Past proceedings of the Detonation Symposium (International) were examined and a body of data was obtained representing a varied group of explosives. Besides purely CHNO types, explosives containing aluminum, barium (as barium nitrate), and tungsten are

included. Densities ranged from 1.13 to 7.47 g/cm<sup>3</sup>. One liquid explosive, nitromethane, is included. These data are shown in Table 1.

Where CJ parameters were not measured or calculated in the reference, they were obtained from Reference 11. Where the data were not transposed to pressure/particle velocity values, they were calculated using material Hugoniot values from Reference 12.

## CORRELATION OF DATA

A common engineering practice is to correlate sets of data by reducing the various parameters to some shared reference state. This was done to the data in Table 1 where the reference states were the CJ pressure and CJ particle velocity. This formed two nondimensional or reduced parameters,  $P/P_{cj}$  and  $u/u_{cj}$ . When these parameters were plotted against each other, they fell into a narrow band that could be approximated by a simple correlation, shown in Figure 2, where  $P/P_{cj}$  is plotted versus  $u/u_{cj}$  on log axes.

The plotted data falls into two regions. For reduced pressure above 0.08, the data is correlated by

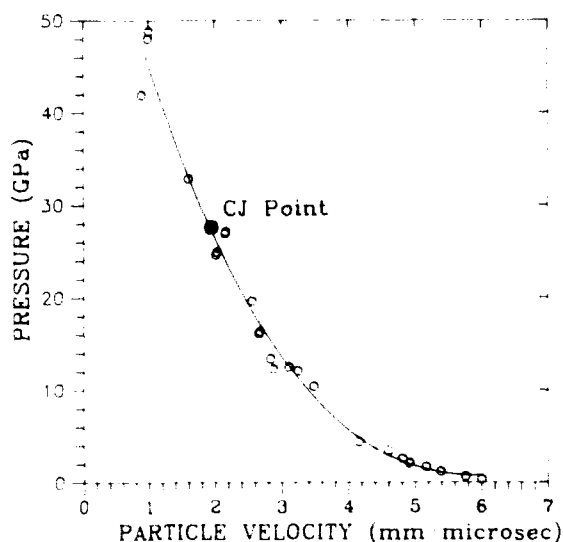


Figure 1.  $P$ - $u$  Hugoniot of TATB/T2<sup>1</sup> Developed from Experimental Data

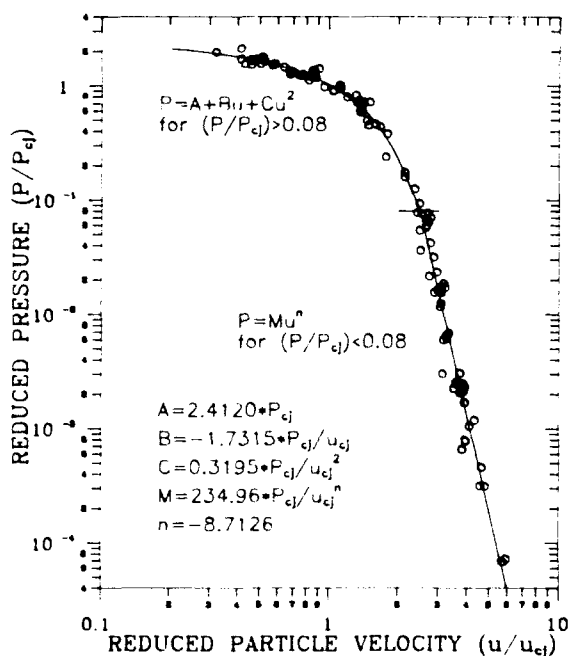


Figure 2. Reduced Pressure Versus Reduced Particle Velocity for Experimental Data in Table 1

Table 1. Experimental Values for Pressure and Particle Velocity

Explosive	Target Material	Interface Pressure (GPa)	Interface Part. Vel. (mm/ $\mu$ s)	P/P <sub>cj</sub>	u/u <sub>cj</sub>	Reference
TATB/T2 $\rho = 1.855$	Copper	48.8	1.00	1.77	0.516	1
	Copper	41.9	0.889	1.52	0.458	1
	Copper	48.0	0.991	1.74	0.511	1
	Al (1100)	32.8	1.61	1.19	0.827	1
	Magnesium	27.1	2.16	0.982	1.11	1
	Magnesium	24.9	2.03	0.902	1.05	1
	Magnesium	24.6	2.01	0.891	1.04	1
	Magnesium	26.9	2.15	0.975	1.11	1
	Transacryl	19.6	2.56	0.710	1.32	1
	Water	16.1	2.66	0.583	1.37	1
	Water	16.3	2.68	0.591	1.38	1
	Argon (705 bar)	13.4	2.83	0.485	1.46	1
	Argon (588 bar)	12.2	2.87	0.443	1.48	1
	Argon (493 bar)	12.4	3.10	0.450	1.60	1
	Argon (415 bar)	12.0	3.24	0.435	1.67	1
	Argon (297 bar)	10.3	3.48	0.374	1.79	1
	Argon (100 bar)	4.34	4.17	0.157	2.15	1
	Argon (70 bar)	3.42	4.61	0.124	2.38	1
	Argon (50 bar)	2.55	4.81	0.0924	2.48	1
	Argon (40 bar)	2.08	4.91	0.0754	2.53	1
	Argon (30 bar)	1.64	5.16	0.0594	2.66	1
	Argon (20 bar)	1.15	5.38	0.0417	2.78	1
	Argon (10 bar)	0.64	5.76	0.0232	2.97	1
	Argon (5 bar)	0.34	6.0	0.0123	3.09	1
	Water	6.78	1.51	0.235	1.77	2
HMX/Tungsten (13.2/85.5 %wt) $\rho = 7.47$						
Composition B $\rho = 1.73$	Dural	36.8	1.74	1.40	0.907	3
Composition B (cast) $\rho = 1.671$	Uranium	55.4	0.79	2.11	0.413	3
Composition B (cast) $\rho = 1.733$	Aluminum	32.0	1.55	1.25	0.773	4
Composition B (pressed) $\rho = 1.703$	Water	19.1	2.96	0.638	1.37	6
Composition B-3 $\rho = 1.72$	Aluminum	32.8	1.58	1.22	0.768	4
Composition B (Overdriven) $\rho = 1.65$	Al (6061)	37.8	1.8	1.32	0.851	5
	Al (6061)	38.6	1.83	1.35	0.865	5
	Al (2024)	38.4	1.80	1.34	0.849	5
	W-alloy	81.8	0.97	1.95	0.320	8
	Nickel	71.6	1.25	1.71	0.413	8
	Brass	68.9	1.41	1.64	0.465	8
	Titanium	60.4	1.94	1.44	0.640	8
	Dural	52.2	2.31	1.24	0.762	8
	Magnesium	40.7	2.88	0.969	0.950	8
	Perspex	33.2	3.62	0.790	1.20	8
	Air (1 bar)	0.126	9.5	0.0030	3.14	8
	Air (.7972 bar)	0.0655	7.97	0.00233	3.89	10
	Air (.7972 bar)	0.0660	7.99	0.00235	3.90	10
	Air (.810 bar)	0.0649	7.97	0.00231	3.89	10



Table 1. Experimental Values for Pressure and Particle Velocity (Continued)

Explosive	Target Material	Interface Pressure (GPa)	Interface Part. Vel. (mm/ $\mu$ s)	P/P <sub>cj</sub>	u/u <sub>cj</sub>	Reference
NM $\rho = 1.133$	Dural	20.6	1.09	1.53	0.580	3
	Dural	20.1	1.07	1.50	0.570	5
	Dural	20.7	1.10	1.54	0.583	5
PBX 9502	Dural	35.9	1.7	1.24	0.859	3
Baratol $\rho = 2.452$	Aluminum	18.4	0.988	1.20	0.790	4
HMX/Inert $\rho = 1.776$	Aluminum	35.9	1.69	1.11	0.812	4
HBX-1 $\rho = 1.624$	Brass	33.8	0.8	1.53	0.431	7
	Aluminum	27.0	1.37	1.23	0.737	7
	Plexiglas	18.1	2.43	0.821	1.31	7
	Water	15.6	2.62	0.710	1.41	7
	Polyurethane	3.79	3.99	0.172	2.15	7
	Argon (40 bar)	1.69	4.5	0.0767	2.42	7
	Argon (27 bar)	1.18	4.62	0.0535	2.49	7
	Argon (17.9 bar)	0.792	4.66	0.0359	2.51	7
	Argon (9 bar)	0.470	5.1	0.0213	2.75	7
	Argon (6 bar)	0.339	5.37	0.0154	2.89	7
	Air (6 bar)	0.254	5.7	0.0115	3.07	7
	Air (3 bar)	0.141	6.02	0.00640	3.24	7
	Air (3 bar)	0.146	6.13	0.00662	3.30	7
	Air (3 bar)	0.130	5.87	0.00590	3.16	7
	Air (1 bar)	0.067	6.97	0.00304	3.75	7
	Air (1 bar)	0.067	6.92	0.00304	3.72	7
	Air (.7 bar)	0.051	7.28	0.00231	3.92	7
	Air (.5 bar)	0.037	7.27	0.00168	3.91	7
	Air (.5 bar)	0.037	7.3	0.00168	3.93	7
	Air (.3 bar)	0.026	8.05	0.00118	4.33	7
	Air (.3 bar)	0.023	7.64	0.00104	4.11	7
	Air (.1 bar)	0.0101	8.6	0.000458	4.63	7
	Air (.1 bar)	0.0101	8.6	0.000458	4.63	7
	Air (.07 bar)	0.0069	8.48	0.000313	4.56	7
	Air (.07 bar)	0.0069	8.9	0.000313	4.79	7
	Air (.01 bar)	0.0015	10.5	0.000068	5.67	7
	Air (.01 bar)	0.0015	10.7	0.000068	5.76	7
	Air (.01 bar)	0.0016	11.0	0.000072	5.94	7
PBX-9404 $\rho = 1.846$	Water	22.0	3.20	0.586	1.39	6
Pentolite(50/50)	Water	17.9	2.85	0.712	1.40	6
LX-04 $\rho = 1.867$	Water	20.1	3.04	0.581	1.38	6
Cyclotol(75/25) $\rho = 1.76$	Water	19.1	2.95	0.603	1.36	6
HMX/TNT/Inert (68/30/2) $\rho = 1.776$	Nickel	51.8	0.974	1.66	0.456	9
	Nickel	51.9	0.985	1.67	0.461	9
	Brass	48.1	1.08	1.54	0.505	9
	Brass	50.7	1.12	1.63	0.525	9
	Titanium	41.4	1.44	1.33	0.674	9
	Titanium	41.6	1.45	1.34	0.676	9

Table 1. Experimental Values for Pressure and Particle Velocity (Continued)

Explosive	Target Material	Interface Pressure (GPa)	Interface Part. Vel. (mm/ $\mu$ s)	P/P <sub>cj</sub>	u/u <sub>cj</sub>	Reference
HMX/Inert (95/5) $\rho = 1.781$	Aluminum	38.0	1.8	1.22	0.843	9
	Dural	37.2	1.81	1.19	0.845	9
	Magnesium	30.9	2.37	0.993	1.11	9
	Magnesium	31.1	2.38	0.998	1.12	9
	Perspex	22.4	2.86	0.720	1.34	9
	Perspex	23.0	2.90	0.739	1.36	9
	Water	22.0	3.21	0.707	1.50	9
	Air (.256 bar)	0.0241	8.43	0.000773	3.95	9
	Air (.26 bar)	0.0247	8.38	0.000792	3.92	9
	Air (.99 bar)	0.0777	7.68	0.00249	3.60	9
	Air (.99 bar)	0.0765	7.63	0.00246	3.57	9
	Air (1.001 bar)	0.080	7.77	0.00257	3.64	9
	Air (2.98 bar)	0.189	6.98	0.00607	3.27	9
	Air (3.15 bar)	0.212	7.13	0.00681	3.34	9
	Air (8.91 bar)	0.499	6.39	0.0161	2.99	9
	Air (9.05 bar)	0.536	6.64	0.0172	3.11	9
	Air (9.08 bar)	0.510	6.5	0.0164	3.04	9
	Argon (6.4 bar)	0.575	6.79	0.0185	3.18	9
	Argon (30.7 bar)	2.18	5.93	0.0700	2.78	9
	Argon (31.0 bar)	2.00	5.78	0.0642	2.71	9
	Nickel	56.0	1.04	1.67	0.482	9
	Nickel	56.7	1.05	1.69	0.487	9
	Titanium	41.9	1.45	1.25	0.674	9
	Titanium	43.8	1.50	1.31	0.699	9
	Dural	39.2	1.88	1.17	0.874	9
	Magnesium	31.1	2.38	0.928	1.11	9
	Magnesium	31.5	2.41	0.940	1.12	9
	Air (.24 bar)	0.022	8.21	0.000656	3.82	9
	Air (.243 bar)	0.0218	8.17	0.000650	3.80	9
	Air (.998 bar)	0.0746	7.56	0.00223	3.51	9
	Air (.999 bar)	0.0743	7.56	0.00222	3.51	9
	Air (9.05 bar)	0.53	6.53	0.0158	3.03	9
	Air (9.22 bar)	0.513	6.66	0.0153	3.10	9
	Argon (6.3 bar)	0.571	6.95	0.0170	3.23	9
	Argon (14.04 bar)	1.05	6.18	0.0313	2.87	9
	Argon (31.1 bar)	1.9	5.70	0.0567	2.65	9
	Argon (32.0 bar)	2.13	5.85	0.0636	2.72	9
	Krypton (1 bar)	2.56	5.79	0.0764	2.69	9
TNT (pressed) $\rho = 1.636$	Air (.7959)	0.0478	6.71	0.00235	3.73	10
	Air (.8091 bar)	0.0503	6.92	0.00247	3.85	10
	Air (.8091 bar)	0.0478	6.78	0.00234	3.77	10
TNT $\rho = 1.632$	Water	13.1	2.36	0.687	1.41	6
Cyclotol (77/23) $\rho = 1.752$	Air (.8021 bar)	0.0642	7.94	0.00210	3.76	10
	Air (.8014 bar)	0.0671	8.05	0.00219	3.81	10
	Air (.8013 bar)	0.0686	8.15	0.00224	3.86	10
Octol (77.6/22.4) $\rho = 1.821$	Air (.8101 bar)	0.0681	8.14	0.00205	3.79	10
	Air (.8099 bar)	0.0677	8.06	0.00204	3.75	10
	Air (.802 bar)	0.0702	8.34	0.00211	3.88	10

$$\frac{P}{P_{cj}} = a + b \left( \frac{u}{u_{cj}} \right) + c \left( \frac{u}{u_{cj}} \right)^2, \text{ or}$$

$$P = (aP_{cj}) + \left( \frac{bP_{cj}}{u_{cj}} \right) u + \left( \frac{cP_{cj}}{u_{cj}^2} \right) u^2, \quad (1)$$

where  $a = 2.412$ ,  
 $b = -1.7315$ , and  
 $c = 0.3195$ .  
(correlation coefficient = 0.987)

For reduced pressure below 0.08, the data is correlated by

$$\frac{P}{P_{cj}} = m \left( \frac{u}{u_{cj}} \right)^n, \text{ or}$$

$$P = \left( \frac{mP_{cj}}{u_{cj}^n} \right) u^n, \quad (2)$$

where  $m = 235$ , and  
 $n = -8.71$ .  
(correlation coefficient = 0.898)

For comparison purposes, the above correlations were used to estimate the Hugoniot of the detonation reaction products of TNT at  $1.64 \text{ g/cm}^3$  initial density. The CJ state used was  $P_{cj} = 19.01 \text{ GPa}$  and  $u_{cj} = 1.666 \text{ mm}/\mu\text{s}$ . Reasonable agreement is shown when the results are compared (Figure 3) to calculations made in 1961 by W. Fickett with a computer code at Los Alamos National Laboratory.<sup>13</sup>

## CONCLUSIONS

It has been shown for a representative body of experimental data for various explosives that the P-u Hugoniot of the detonation reaction products of a given explosive can be estimated by knowing only the CJ pressure and CJ particle velocity of that explosive. The data correlated spanned a range of pressure from 0.0015 to 81.8 GPa, particle velocity from 0.79 to 11.0 mm/ $\mu\text{s}$ , and initial explosive density from 1.133 to 7.47 g/cm<sup>3</sup>. The results are in reasonable agreement with results obtained from large computer codes.

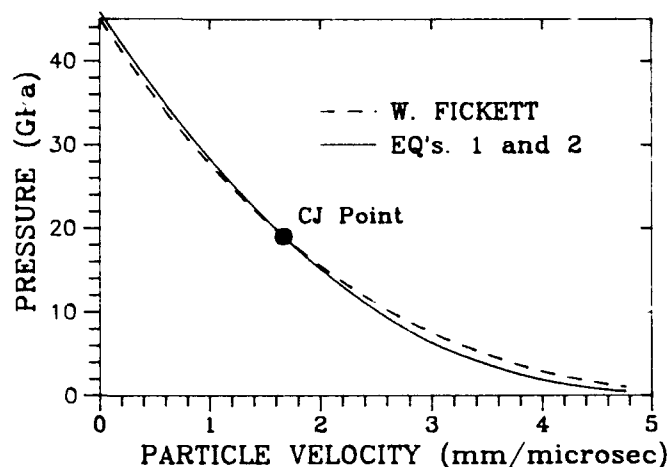


Figure 3. Comparison of TNT ( $\rho_o = 1.64$ ) Hugoniot Calculated by Reduced Parameter Method and by Computer Code<sup>13</sup>

## REFERENCES

1. Pinègree, M.; Aveillé, J.; Leroy, M.; Protat, J. C.; Chéret, R.; and Camarcat, N., "Expansion Isentropes of TATB Compositions Released into Argon," *Proceedings of the Eighth Symposium (International) on Detonation*, Albuquerque, NM, 15-19 Jul 1985, pp. 815-824.
2. Goldstein, S. and Mader, C. L., "Detonation in Tungsten-Loaded HMX," *Proceedings of the Eighth Symposium (International) on Detonation*, Albuquerque, NM, 15-19 Jul 1985, pp. 979-9814.
3. Davis, W. C. and Ramsey, J. B., "Detonation Pressures of PBX-9404, Composition B, PBX-9502, and Nitromethane," *Proceedings of the Seventh Symposium (International) on Detonation*, U.S. Naval Academy, Annapolis, MD, 16-19 Jun 1981, p. 539.
4. Burrows, K.; Chilvers, D. K.; Gyton, R.; Lambourn, B. D.; and Wallace, A. A., "Determination of Detonation Pressure Using a Manganin Wire Technique," *Proceedings of the Sixth Symposium (International) on Detonation*, Naval Surface Weapons Center, White Oak, MD, 24-27 Aug 1976, pp. 625-636.

5. Davis, W. C. and Venable, D., "Pressure Measurements for Composition B-3," *Proceedings of the Fifth Symposium (International) on Detonation*, Pasadena, CA, 18-21 Aug 1970, pp. 13-21.
6. Rigdon, J. K. and Akst, I. B., "An Analysis of the 'Aquarium Technique' as a Precision Detonation Pressure Measurement Gage," *Proceedings of the Fifth Symposium (International) on Detonation*, Pasadena, CA, 18-21 Aug 1970, pp. 59-66.
7. Roslund, L. A. and Coleburn, N. L., "Hydrodynamic Behavior and Equation of State of Detonation Products Below the Chapman-Jouguet State," *Proceedings of the Fifth Symposium (International) on Detonation*, Pasadena, CA, 18-21 Aug 1970, pp. 523-532.
8. Skidmore, I. C. and Hart, S., "The Equation of State of Detonation Products Behind Overdriven Detonation Waves in Composition B," *Proceedings of the Fourth Symposium (International) on Detonation*, U. S. Naval Ordnance Laboratory, White Oak, MD, 12-15 Oct 1965, pp. 47-51.
9. Allan, J. W. S. and Lambourn, B. D., "An Equation of State of Detonation Products at Pressures Below 30 Kilobars," *Proceedings of the Fourth Symposium (International) on Detonation*, U. S. Naval Ordnance Laboratory, White Oak, MD, 12-15 Oct 1965, pp. 52-66.
10. Deal, W. E., "Low Pressure Points on the Isentropes of Several High Explosives," *Proceedings of the Third Symposium on Detonation*, James Forrestal Research Center, Princeton University, 26-28 Sep 1960, pp. 386-395.
11. Dobratz, B. M., Ed., *LLNL Explosives Handbook* (UCRL-25997), Lawrence Livermore National Laboratory, Livermore, CA, 1985.
12. Marsh, S. P., Ed., *LASL Shock Hugoniot Data*, University of California Press, Berkeley, CA, 1980.
13. Fickett, W., Los Alamos National Laboratory, personal communication with Bass, R. C. and Chabai, A. J., Sandia National Laboratories, concerning computer generated P-u Hugoniot data for TNT, 1961.

## DISCUSSION

**WENDELL L. SEITZ**  
LANL, Los Alamos, NM

You mentioned that you had used data for metal loaded HMX. Are those data included in your scaled pressure vs. scaled particle velocity? Does the metal loaded data fit well with the data for nonmetal loaded explosives?

## REPLY

Yes, these data are included in both Table 1 and in Figure 2. The data fit well within the body of correlated data.

## DISCUSSION

**B. D. LAMBOURN**  
AWE(A), Reading RG7 4PR England

Dr. Cooper's universal pressure-particle velocity relations enable the corresponding p-v relations to be determined.

Below the CJ pressure, the detonation products expand isentropically such that

$$\partial p + p^2 c^2 \partial r = 0 \quad (1)$$

where  $\rho = 1/v$  is density and  $c$  is velocity of sound. The expansion is in the form of a simple wave, i.e. with pressure and particle velocity related by

$$dp + \rho c du = 0 \quad (2)$$

Hence, from (1) and (2)

$$\frac{1}{\rho^2 c^2} = \left( -\frac{du}{dp} \right)^2 = -\frac{\partial v}{\partial p} \Big|_s \quad (3)$$

Setting

$$P = \frac{p}{p_{cj}}, \quad U = \frac{u}{u_{cj}}, \quad V = \frac{v}{v_{cj}} \quad (4)$$

and given Dr. Cooper's relations written in the form

$$U = U(P), \quad U' = \frac{dU}{dP} \quad (5)$$

then equation (3) may be integrated to give a  $V(P)$  relationship:

$$V = 1 - \frac{1}{\gamma_{cj}} \int_1^P (U')^2 dP \quad (6)$$

where  $\gamma_{cj}$  is the adiabatic exponent at the Chapman Jouguet State and use has been made of the CJ relations.

Using Dr. Cooper's fits

$$P = a + bU + cU^2 \quad P > 0.08$$

$$P = mU^n \quad P \leq 0.08 \quad (7)$$

the 'universal' expansion adiabat is

$$V = 1 - \frac{1}{4c\gamma_{cj}} \ln \left\{ 1 - \frac{4c(1-P)}{(b+2c)^2} \right\} \quad P > 0.08$$

$$V = V_{0.08} + \frac{1}{\gamma_y m^{2/n} n^2 (1-2/n)}$$

$$\left| \frac{1}{P^{1-2/n}} - \frac{1}{(0.08)^{1-2/n}} \right| \quad P \leq 0.08 \quad (8)$$

Figure 1 shows the adiabat for  $\gamma_{cj} = 3$ . The dashed line corresponds to a 'straight-line' adiabat:  $\rho v^3 = k$ .

It is worth noting that the 'universal' adiabat first dips below the straight-line adiabat and then recrosses it as specific volume increases. Correspondingly, the adiabatic exponent must first increase and then decrease with volume, just as in the JWL EOS.

Three points emerge:

(1) There is a kink in the universal adiabat at  $P = 0.08$  corresponding to the discontinuity in  $dU/dP$  between the two fits.

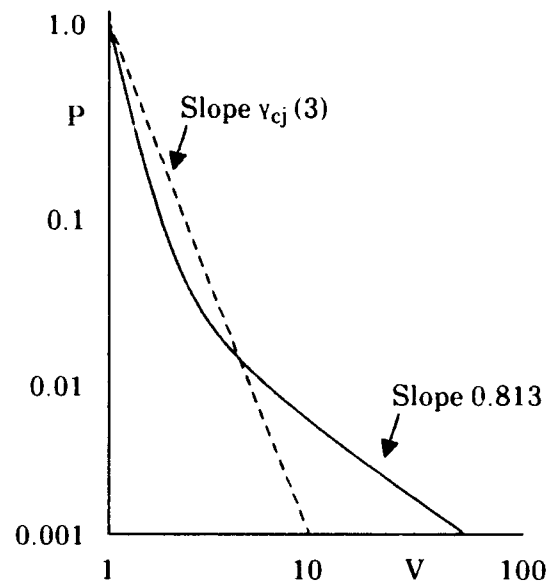


Figure 1. Universal Adiabat ( $\gamma_{cj} = 3$ )

(2) The behavior of Dr. Cooper's  $P$ - $U$  relation is incorrect at low pressures (say below  $P = 0.003$ ), for it implies that the particle velocity would be infinite at zero pressure. Correspondingly, the adiabatic exponent at low pressures ( $n/n-2$ ) is less than one and, hence is invalid. A more reasonable functional form for  $U(P)$  at low pressures would be

$$U + \frac{2\gamma}{\gamma} P^{2\gamma} = U_0$$

corresponding to a mixture of ideal gases.

(3) The initial behavior near the CJ state is of the form

$$p = \alpha + \beta \exp(-R_1 v/v_0)$$

where

$$R_1 = 4c(\gamma_{cj} + 1)$$

For a typical explosive with  $\gamma_g \sim 2.75$  and Dr. Cooper's value of 0.3195 for  $C$ , this leads to

$$R_1 \approx 4.8$$

which is a typical value that could be used as a first estimate in a JWL EOS.

In conclusion, it is noted that Dr. Cooper's Summary of available  $p$ - $u$  data and the consequential fits and deduced universal adiabatic relationships should form a useful database against which developers of new theoretical EOS can check their predictions.

lower correlation does predict infinite particle velocity at zero pressure. This can be corrected either by using a third correlation for very low pressure; or what may be useful for most applications is to limit the use of these correlations to the data range stated in the paper.

### REPLY

I am gratified to see this application made so quickly. Indeed, you are correct in that the

# ELECTRICALLY ENHANCED DETONATION AND EQUATIONS OF STATE FOR DETONATION PRODUCTS

M. Cowperthwaite  
SRI International  
Poulter Laboratory  
333 Ravenswood Avenue  
Menlo Park, California 94025

*Procedures for calculating the properties of detonation enhanced by electric current flow were based on our first-generation model for electrically enhanced detonation (EED) and our specific energy-pressure-specific volume (e-p-v) equations of state (EOS) for detonation products with a fixed composition. Our model for EED was formulated from the classical ZND model of detonation by adding a Joule heating term to the energy equation; our (e-p-v) EOS were constructed to exhibit prescribed properties of the adiabatic index ( $k$ ) similar to those determined for the detonation products of PBX9501 in TIGER code calculations. Particular (e-p-v) EOS were incorporated into our model for EED, calibrated for PBX9501, and used to calculate enhanced Chapman-Jouguet (CJ) parameters. An equivalence between EED and unsupported detonation with a higher heat of reaction was established and used to extend Kamlet's short method into the Cowperthwaite-Kamlet (CK) short method for EED.*

## INTRODUCTION

The concept of enhancement of detonation by electrical energy coupling (EEC) is based on observations<sup>1-3</sup> that a region close to a detonation front conducts electricity, whereas the unreacted explosive in front of this region and the detonation products behind it do not. The idea is to pass electric current through the conduction zone and thereby supply electrical energy externally to the detonation. The theoretical work on EEC presented here was performed to develop procedures for calculating the detonation properties of electrically enhanced detonation (EED).

A first-generation model for EED was first formulated, and then a procedure for calculating enhanced Chapman-Jouguet (CJ) parameters when the specific energy-pressure-specific volume (e-p-v) equation of state (EOS) of the detonation products is known. Different forms of the adiabatic index ( $k$ ), exhibiting properties of the detonation products of PBX9501

determined from TIGER code<sup>4</sup> calculations, were then used to construct (e-p-v) EOS for detonation products with a fixed composition. An equivalence between EED and unsupported detonation with a higher heat of reaction was established and used to extend Kamlet's short method<sup>5</sup> into the Cowperthwaite-Kamlet (CK) short method for calculating CJ parameters in EED. Particular EOS were incorporated into our model for EED, calibrated for PBX9501, and then used with the CK method to perform a series of EED calculations for PBX9501.

## MODEL FOR EED

Our first-generation model for EED was formulated as an extension of the classical ZND model for detonation.<sup>6</sup> This was done by adding a source term to the energy equation to account for the external supply of electrical energy, and by assuming that material in a stable, steady-state, conduction zone at the wavefront obeys Ohm's Law. It was also assumed that EED is not influenced by

electromagnetic effects in electric field strengths of interest.

With  $e$ ,  $p$ ,  $v$ , and  $k$  already defined, we let  $\rho$  = density,  $s$  = specific entropy,  $c$  = sound speed,  $\gamma$  = polytropic index,  $D$  = detonation velocity,  $u$  = particle velocity,  $q'_e$  = specific chemical energy release rate, and  $q''_e$  = specific electrical energy addition rate. We also let the subscript  $o$  denote the initial state;  $II$ , the shocked state; and  $u$ , the unsupported classical ZND detonation wave. The superscript,  $\wedge$ , denotes the CJ state and  $x$ , the explosive. In addition,  $\underline{E}$  denotes the electric field,  $j$  the current density, and  $\sigma$  the conductivity.

The differential equations expressing the conservation laws for the steady-state flow of an adiabatic inviscid fluid were integrated to obtain the following equations governing the steady-state zone in EED:

$$\rho(D - u) = \rho_{II}^x (D - u_{II}^x) = \rho_o^x D \quad (1)$$

$$p = \rho(D - u)u = \rho_o^x Du \quad (2)$$

$$e - e_o^x = \frac{p}{2} \left( v_o^x - v \right) + q_e \quad (3)$$

where  $q_e = \int_0^{t-t} q'_e dt$  and  $t$  denotes the time a particle enters the wave.

The equation for the specific energy addition rate  $q'_e = \underline{E} \cdot j / \rho$  and the constitutive relationship for ohmic material  $j = \sigma \underline{E}$  were used to obtain the following equation for  $q_e$ :

$$q_e = \int_0^{t-t} \frac{E_o^2 \sigma}{\rho} dt \quad (4)$$

The sonic condition at the end of the steady-state zone, where  $t - t = \hat{u}$  and  $q'_e = q'_e = 0$ , was obtained as  $D = \hat{u} + \hat{c}$  from the equation obtained by combining the differential equations governing the steady-state flow with an EOS for the mixture of explosive and its products. Equations (1) and (2), the sonic condition, and the identity relating the sound speed to the adiabatic index

$$k = - \frac{v}{p} \left( \frac{\partial p}{\partial v} \right)_s = \frac{c^2}{pv} \quad (5)$$

were then combined to show that the equations relating  $D$ ,  $\hat{u}$ ,  $\hat{c}$ ,  $\hat{v}$ ,  $\hat{k}$ , and  $\hat{p}$  can be obtained from those relating unsupported CJ parameters by setting  $D_u = D$ ,  $\hat{u}_u = \hat{u}$ ,  $\hat{c}_u = \hat{c}$ ,  $\hat{v}_u = \hat{v}$ ,  $\hat{k}_u = \hat{k}$ , and  $\hat{p}_u = \hat{p}$ . Equation (3) was written at the CJ plane as

$$\hat{e} - e_o^x = \frac{\hat{p} v_o^x}{2(\hat{k} + 1)} + \hat{q}_e \quad (6)$$

with  $\hat{q}_e$  related to the similarity parameter  $\zeta = Dt - x$ , the steady-state zone length  $\hat{L}$ , and the average conductivity  $\bar{\sigma}$ , by the equations

$$\hat{q}_e = \frac{1}{\rho_o^x} \int_0^{\hat{L}} \sigma E^2 d\zeta = \frac{E_o^2 \bar{\sigma} \hat{L}}{\rho_o^x D} \quad (7)$$

At this stage, it is clear that enhanced CJ parameters cannot be calculated unless we know an ( $e$ - $p$ - $v$ ) EOS for the detonation products. To introduce such an EOS, we consider one gram of detonation products containing  $s$  species, denote their mass fractions by  $m_i$ ,  $i = 1 \dots s$ , and their specific heats of formation by  $\Delta h_{fi}^o$ . The specific heat of formation of species  $i$  is its molar heat of formation  $\Delta H_{fi}^o$  divided by its molecular weight  $M_i$ . We formally write the equation for the specific energy of the mixture as

$$e = \sum_{i=1}^s m_i \Delta h_{fi}^o + \tilde{e}(p, v, m_1 \dots m_s) \quad (8)$$

We now assume that the products of an explosive in unsupported and EED are governed by Kamlet's  $H_2O$ - $CO_2$  arbitrary rule.<sup>5</sup> In this case, the values of  $m_1 \dots m_s$  are determined by the composition of the explosive,

$$\sum_{i=1}^s m_i \Delta h_{fi}^o$$

is constant, and Equation (8) can be used to calculate  $e$  at a given ( $p$ - $v$ ) point when the functional form of  $\tilde{e}$  is known. Our assumption of constant composition is suspect for EED because the CJ composition in EED probably depends on  $\hat{q}_e$ , but it is made here for simplicity. We now introduce the specific chemical energy liberated by the explosive,  $q_c$ , by the equation



$$q_c = - \left( \sum_{i=1}^s m_i \Delta h_{fi}^o - e_o^x \right)$$

and rewrite the (e-p-v) EOS for detonation products as  $e - e_o^x = -q_c + \tilde{e}(p, v)$ .

The Rankine-Hugoniot equations, CJ conditions, and (e-p-v) EOS for the detonation products can then be used to derive the following equations for calculating enhanced CJ parameters:

$$\hat{k} = \left( v_o^x / \hat{v} - 1 \right)^{-1} \quad (9)$$

$$\hat{p} = \frac{\rho_o^x D^2}{(\hat{k} + 1)} \quad (10)$$

$$\hat{k} = \frac{\hat{v}}{\hat{p}} \left( \frac{\hat{p} + (\partial \tilde{e} / \partial v)_p}{(\partial \tilde{e} / \partial p)_v} \right) \quad (11)$$

$$\left( 1 + \frac{E^2 \sigma \hat{I}}{\rho_o^x D q_c} \right) = \frac{\tilde{e}(\hat{p}, \hat{v})}{q_c} - \frac{\hat{p} v_o^x}{2(\hat{k} + 1) q_c} \quad (12)$$

We can now formulate our iterative procedure for calculating  $\hat{v}$ ,  $\hat{k}$ ,  $\hat{p}$ , and  $D$  when  $\rho_o^x$ ,  $q_c$ ,  $E$ ,  $\sigma$ ,  $\hat{I}$ , and  $\tilde{e}(p, v)$  are known. For a chosen value of  $\hat{v}$ , Equation (9) is used to calculate the corresponding value of  $\hat{k}$ ; then Equation (11) is used to calculate the corresponding value of  $\hat{p}$ , and Equation (10) is used to calculate the corresponding value of  $D$ . These values of  $\hat{v}$ ,  $\hat{k}$ ,  $\hat{p}$ , and  $D$  are then used to evaluate the left and right-hand sides of Equation (12). In the event that Equation (12) is satisfied, we have determined the values of the enhanced CJ parameters  $\hat{v}$ ,  $\hat{k}$ ,  $\hat{p}$ , and  $D$ . But if this is not the case, the series of calculations are carried out for other values of  $\hat{v}$  until the left and right hand sides of Equation (12) agree.

Because only the Hugoniot relation was modified when we formulated our model for EED, Equations (9) through (12) for enhanced CJ parameters obviously reduce to those for unsupported CJ parameters when we set  $E = 0$  and introduce the subscript u.

## EQUIVALENCE OF EED AND UNSUPPORTED DETONATION

Our treatment of EED as an unsupported detonation with a higher heat of reaction is based on the observation that our sets of equations for enhanced and unsupported CJ parameters differ in form only by the  $\hat{q}_e$  term, shown on the left hand side of Equation (12). We can, therefore, make these sets of equations equivalent as follows. We consider an explosive with a higher heat of formation  $(e_o^x)'$  that produces the same fixed detonation products governed by the (e-p-v) EOS,

$$e - (e_o^x)' = -\delta q_c + \tilde{e}(p, v) \quad (13)$$

with  $(e_o^x)' = e_o^x + (\delta - 1)q_c$  and  $\delta > 1$ , and set  $\delta = 1 + E^2 \sigma \hat{I} / \rho_o^x D q_c$ . This equivalence between unsupported detonation and EED will be used later to formulate the CK short method for EED.

## EQUATIONS OF STATE FOR DETONATION PRODUCTS

Our construction of (e-p-v) EOS for detonation products was based on the results of TIGER code calculations performed with the JCZ (3) EOS, which show that the adiabatic index of the detonation products for PBX9501 increases with pressure along the Hugoniot curves centered on the explosive's initial and unsupported CJ states. EOS exhibiting more realistic properties of  $k$  above the unsupported CJ state were thus constructed and incorporated into our model for EED. Use was made of the subsidiary system,<sup>7</sup>

$$\frac{dp}{kp} = - \frac{dv}{v} = \frac{d\tilde{e}}{vp} \quad (14)$$

of the following differential equation defined by the identity for  $k$ ,

$$pk \left( \frac{d\tilde{e}}{dp} \right)_v = v \left( \frac{d\tilde{e}}{dv} \right)_p = vp \quad (15)$$

We first integrated the subsidiary system defined by a prescription for  $k$  to obtain two of its independent solutions,  $\alpha_1 = f_1(\tilde{e}, p, v)$  and  $\alpha_2 = f_2(\tilde{e}, p, v)$ . We then constructed the corresponding  $(\tilde{e}, p, v)$  relationship as a general solution of Equation (15) by setting  $\alpha_2 = g(\alpha_1)$ .

with  $g(\alpha_1)$  an arbitrary function of  $\alpha_1$ . Integrations were performed with different prescriptions for  $k$  to provide a systematic treatment of this (e-p-v) construction

We first considered the simplest case of polytropic material with a constant  $k$ . Integration of the subsidiary system gives the equations,

$$pv^k = \alpha_1 \quad (16)$$

$$\tilde{e} - \frac{pv}{(k-1)} = \alpha_2 \quad (17)$$

which allows us to write the (e-p-v) EOS for polytropic material as

$$e - e_o^x = -q_c + \frac{pv}{(k-1)} + g_1(pv^k) \quad (18)$$

Here, as later, we use the  $\alpha_1$  equation to define the isentropes. We also note that Equation (18) is the general (e-p-v) EOS for polytropic material, and that the simple polytropic EOS used in many treatments of detonation<sup>6,8</sup> is obtained from Equation (18) by setting  $g_1(pv^k) = 0$ .

We next considered the case when  $k = k(v)$  and set

$$k(v) = \gamma + (\hat{k}_u - \gamma) \left( \frac{\hat{v}_u}{v} \right)^{\gamma-1} \quad (19)$$

so that  $k = \hat{k}_u$  when  $v = \hat{v}_u$ ,  $k \rightarrow \gamma$  when  $\hat{v}_u/v \rightarrow 0$ , and  $k \rightarrow \bar{k} = \gamma + (\hat{k}_u - \gamma)(\hat{v}_u/\bar{v})^{\gamma-1}$  as  $v \rightarrow \bar{v}$  and  $p_H \rightarrow \infty$  along the detonation products Hugoniot curve through the CJ point. Integrating the subsidiary system, with  $k$  prescribed by Equation (19), leads to the following EOS,

$$e - e_o^x = -q_c + \frac{pv}{(\hat{k}_u - \gamma)} \left( \frac{v}{\hat{v}_u} \right)^{\gamma-1} + g_2(\alpha_1) \quad (20)$$

with the isentropes in the (p-v) plane defined by the equation

$$pv^\gamma e^{-[(\hat{k}_u - \gamma)\gamma - 1](\hat{v}_u/v)^{\gamma-1}} = \alpha_1 \quad (21)$$

We next considered the case when  $k = k(p)$ , and set

$$k(p) = \frac{\gamma(\bar{k} - \hat{k}_u) + \bar{k}(\hat{k}_u - \gamma)(p/\hat{p}_u)^n}{(\bar{k} - \hat{k}_u) + (\hat{k}_u - \gamma)(p/\hat{p}_u)^n} \quad (22)$$

with  $n$  a positive constant so that  $k(p) \rightarrow \gamma$  as  $p \rightarrow 0$  and  $k(p) \rightarrow \bar{k}$  as  $p \rightarrow \infty$ . Performing the integrations in this case with  $n = (\gamma - 1)/\gamma$  leads to the following (e-p-v) EOS

$$e - e_o^x = -q_c + \frac{pv}{(\bar{k} - 1)} + \frac{(\bar{k} - \hat{k}_u)\gamma\hat{p}_u v}{(\hat{k}_u - \gamma)(\bar{k} - 1)} \left( \frac{p}{\hat{p}_u} \right)^{1/\gamma} + g_3(\alpha_1) \quad (23)$$

with the isentropes in the (p-v) plane defined by the equation,

$$pv^{\bar{k}} \left( \bar{k} + \gamma \frac{(\bar{k} - \hat{k}_u)}{(\hat{k}_u - \gamma)} \left( \frac{\hat{p}_u}{p} \right)^{\frac{\gamma-1}{\gamma}} \right)^{\frac{\bar{k}-\gamma}{\gamma-1}} = \alpha_1 \quad (24)$$

For the sake of tractability when  $k = k(p, v)$ , we assumed that

$$\tilde{e} = pf(v) + Bv^{-n} \quad (25)$$

where  $f(v)$  is an arbitrary function of  $v$ , and  $B$  and  $n$  are constants. We set  $f = mv^\gamma$  so that  $k \rightarrow \gamma$  as  $p \rightarrow 0$ , set  $(n+1) = \gamma$  so that we could integrate the differential equation for the isentropes, and obtained the corresponding equation for  $k(p, v)$  as

$$k(p, v) = \frac{1 + \gamma mv^{\gamma-1}}{mv^{\gamma-1}} - \frac{(\gamma-1)B}{pmv^{2\gamma-1}} \quad (26)$$

The expression for  $m$  obtained from Equation (26) evaluated at the unsupported CJ state was then used to write the (e-p-v) EOS as

$$e - e_o^x = -q_c + \frac{B}{v^{\gamma-1}} + \frac{pv}{(\hat{k}_u - \gamma)} \left( \frac{v}{\hat{v}_u} \right)^{\gamma-1} \left[ 1 - \frac{(\gamma-1)B}{\hat{p}_u(\hat{v}_u)^\gamma} \right] \quad (27)$$

## CALCULATIONS OF ENHANCED CJ PARAMETERS FOR PBX9501

Enhanced CJ calculations, with  $\hat{L} = 0.5 \text{ mm}$ ,  $\sigma = 10^3 \text{ mhom}^{-1}$  and values of  $E$  in the  $1 \times 10^7 \text{ v/m}$  to  $1.9 \times 10^7 \text{ v/m}$  range, were performed for PBX9501 ( $\rho_0 = 1.84 \text{ g/cm}^3$ ) and the following set of unsupported CJ parameters calculated from Kamlet's short method ( $D_u = 8.8 \text{ mm}/\mu\text{s}$ ,  $\hat{p}_u = 348 \text{ kbar}$ ,  $\hat{k}_u = 3.094$ ,  $q_c = 6.033 \text{ mm}/\mu\text{s}$ ).<sup>2</sup> More details of these calculations and their results will now be presented.

### Detonation Products With $k$ , A Constant, and $k = k(v)$

Because the  $g$  functions in Equations (18) and (20) were assumed to be linear in  $p$ , an EOS,  $e = e^x_0 + q_c + pf(v)$  with  $f(v)$  an arbitrary function of  $v$ , was incorporated into our model for EED and used to derive the following equation for  $D$ ,

$$D^2 = \frac{2(\hat{k} + 1)^2}{(2\rho_0^x(\hat{k} + 1)\hat{v} - 1)} [q_c + \hat{q}_c] \quad (28)$$

The facts, (1) that  $\hat{v} = \hat{v}_u$  and  $\hat{k} = \hat{k}_u = k$  for polytropic material, and (2) that the CJ condition for  $k$  written as

$$k_{CJ}(v) = (v_0^x/v - 1)^{-1}$$

can be used to show that  $\hat{v} = \hat{v}_u$  and  $\hat{k} = \hat{k}_u$  when  $k = k(v)$  and  $dk/dv < 0$ , were then combined with Equation (28) to obtain the simplest equation for  $D$ ,

$$\left( \frac{D}{D_u} \right)^2 = 1 + \frac{E^2 \sigma \hat{L}}{\rho_0^x D q_c} \quad (29)$$

We thus concluded that EOS of the form  $e = e^x_0 + q_c + pf(v)$  give the same equation for calculating enhanced detonation velocities when  $f(v)$  is chosen to satisfy the condition that  $k$  is a constant, or that  $dk/dv < 0$ . We also note that a value of  $q_c$  from Kamlet's short method can be used in the polytropic calculation when we set  $g_1(pv^k) = A_1 pv^k/(k - 1)$ . Values of enhanced CJ parameters calculated from Equation (29) are shown under EOS<sup>a</sup> in Table 1.

### Detonation Products With $k = k(p)$

The EOS obtained by setting  $g_3(a_1) = 0$  and  $g_3(a_1) = A_3 a_1$  in Equation (23) were incorporated into our model for EED, calibrated for PBX9501, and then used to calculate enhanced CJ parameters; but only the latter case is considered here because of space considerations. The equation for  $A_3$  used in this calibration was obtained as

$$\frac{(\hat{u}_u)^2/2 + q_c}{(\hat{p}\hat{v})_u} = \frac{(\bar{k} - \hat{k}_u)(\gamma - 1)}{(\bar{k} - 1)(\hat{k}_u - \gamma)} + \frac{A_3(\hat{v}_u)^{\bar{k}-1}}{[\bar{k} + \gamma(\bar{k} - \hat{k}_u)/(\hat{k}_u - \gamma)]} (\bar{k} - \gamma)/(\gamma - 1) \quad (30)$$

by combining the unsupported CJ condition  $2(\hat{e}_u - e^x_0) = (\hat{u}_u)^2$  with the EOS evaluated at the unsupported CJ point. The CJ parameters for PBX9501 and values of  $\gamma = 1.2$  and  $\bar{k} = 3.894$  were used to calculate a value of  $A_3(\hat{v}_u)^{\bar{k}-1} = 2.941 \times 10^7$  for PBX9501 ( $\rho_0 = 1.84 \text{ g/cc}$ ). The values of enhanced CJ parameters calculated with this particular EOS are shown under EOS<sup>b</sup> in Table 1.

### Detonation Products With $k = k(p, v)$

Equation (27) was incorporated into our model for EED, calibrated for PBX9501, and then used to calculate enhanced CJ parameters. The equation for  $B$  used in this calibration was obtained from Equation (27) and the unsupported CJ condition  $2(\hat{e}_u - e^x_0) = (\hat{u}_u)^2$  as

$$\frac{B}{\hat{p}_u(\hat{v}_u)^\gamma} = \frac{(\hat{k}_u - \gamma)}{(\hat{k}_u - 2\gamma + 1)} \left| \frac{(\hat{u}_u)^2/2 + q_c}{(\hat{p}\hat{v})_u} - \frac{1}{(\hat{k}_u - \gamma)} \right| \quad (31)$$

The unsupported CJ parameters for PBX9501 and a value of  $\gamma = 1.2$  were used to calculate a value of  $B/\hat{p}_u(\hat{v}_u)^\gamma = 6.230 \times 10^2$  for PBX9501. The equation for the Hugoniot curve of the detonation products of PBX9501 derived with this particular EOS showed that  $k \rightarrow k \sim 3.275$  as

$p_H \rightarrow \infty$  along this Hugoniot curve. The values of enhanced CJ parameters calculated with this particular EOS are shown under EOS<sup>c</sup> in Table 1.

### The CK Short Method for EED

The equivalence between unsupported detonation and EED, that we established earlier in this paper, was incorporated into Kamlet's short method to obtain the following equations for calculating CJ parameters in EED.

$$\Phi' = NM^{1/2} q_c^{1/2} \delta^{1/2} = \Phi \delta^{1/2} \quad (32)$$

$$D = D_u' = D_u \delta^{1/4} \quad (33)$$

$$\hat{p} = \hat{p}_u' = \hat{p}_u \delta^{1/2} \quad (34)$$

$$\delta = 1 + \frac{E^2 \hat{o} \hat{L}}{\rho_o^* D q_c} \quad (35)$$

When  $\rho_o^*$ ,  $D_u$ ,  $\hat{p}_u$ ,  $q_c$ ,  $E$ ,  $\hat{o}$ , and  $\hat{L}$  are known for a given explosive, Equations (33) and (35) can be solved to find  $\delta$  and  $D$ , and Equations (34) and (10) can then be used to calculate the corresponding values of  $\hat{p}$  and  $\hat{k}$ . The results of these calculations for PBX9501 are shown in Table 1.

## CONCLUSIONS

A first generation model for EED was formulated as an extension of the ZND model

for detonation by adding a source term to the energy equation to account for the external supply of energy from the electric field  $E$ . Material with an average conductivity  $\hat{o}$  in the steady-state conduction zone of length  $\hat{L}$  at the wavefront was also assumed to obey Ohm's Law. Specific energy-pressure-specific volume (e-p-v) EOS for detonation products, with a fixed composition and prescribed properties of the adiabatic index ( $k$ ), were constructed for the purpose of calculating electrically enhanced CJ parameters. Particular forms of these (e-p-v) EOS were incorporated into our model for EED, calibrated with the unsupported CJ parameters of PBX9501, and then used with different values of  $E$  and a constant value of  $\hat{o}\hat{L}$  to calculate values of enhanced CJ parameters in this explosive. The results of these calculations led to two conclusions about our first-generation model of EED when the composition of the detonation products is fixed. The first, that the values of  $D$  and  $\hat{p}$ , but not the values of  $\hat{k}$  and  $\hat{\gamma}$ , are sensitive to the value of  $E$  when  $\hat{o}\hat{L}$  is constant. The second, that the values of enhanced CJ parameters are not very sensitive to our (e-p-v) EOS with realistic properties of  $k$ , when  $E$  and  $\hat{o}\hat{L}$  are constant.

Examination of the equations for enhanced CJ parameters in our model for EED also led us to the following conclusions:

- In explosives with the same initial density  $\rho_o^*$ , producing detonation products with a fixed composition and

Table 1. Detonation Parameters for Electrically Enhanced Detonation in PBX9501 Calculated by Using the CK Method and Different Equations of State for the Detonation Products With a Fixed Composition

Field $E \times 10^7$ v/m	CK Method				EOS <sup>a</sup>			EOS <sup>b</sup>			EOS <sup>c</sup>		
	$\delta$	$D$ mm/ $\mu$ s	$\hat{p}$ kbar	$\hat{k}$	$D$ mm/ $\mu$ s	$\hat{p}$ kbar	$\hat{k}$	$D$ mm/ $\mu$ s	$\hat{p}$ kbar	$\hat{k}$	$D$ mm/ $\mu$ s	$\hat{p}$ kbar	$\hat{k}$
1.0	1.465	9.68	421	3.096	10.60	505	3.094	10.58	499	3.127	10.72	515	3.102
1.5	1.972	10.43	489	3.093	12.00	647	3.094	12.04	642	3.150	12.36	685	3.105
1.9	2.473	11.04	547	3.099	13.15	777	3.094	13.25	775	3.168	13.63	832	3.100

( $\rho_o^* = 1.84 \text{ g/cm}^3$ ,  $D_u = 8.8 \text{ mm}/\mu\text{s}$ ,  $q_c = 6.033 (\text{mm}/\mu\text{s})^2$ ,  $\hat{p}_u = 348 \text{ kbar}$ ,  $\hat{L} = 0.5 \text{ mm}$ ,  $\hat{o} = 10^3 \text{ mhm}^{-1}$ , (a) polytropic EOS with  $g_1(pv^k) = A_1 pv^k/k$ ,  $A_1 = 1.432 (\text{g/cm}^3)^{2/0.94}$ , and  $k = k(v)$  EOS with  $dk/dv < 0$ , (b)  $k = k(p)$  EOS with  $g_3(\alpha_1) = A_3 \alpha_1$ ,  $A_3(\hat{v})^{k-1} = 2.941 \times 10^{-7}$ ,  $\hat{k} = 3.894$ ,  $\gamma = 1.2$ , (c)  $k = k(p,v)$  EOS,  $B/\hat{p}_u(\hat{v})^{\gamma} = 6.230 \times 10^{-2}$ ,  $\gamma = 1.2$ .)

an adiabatic index satisfying the condition that either  $k$  is a constant or  $k = k(v)$  with  $dk/dv < 0$ , unsupported and electrically enhanced detonation have the same CJ volume and their propagation velocities  $D_u$  and  $D$  are related by the equation  $(D/D_u)^2 = 1 + E^2 \hat{\alpha} / \rho^x_0 D q_c$ .

- When detonation products with the same fixed composition are produced by unsupported and electrically enhanced CJ detonations, an EED propagating in an explosive with an initial density  $\rho^x_0$ , a heat of formation  $e^x_0$ , and a heat of decomposition  $q_c$ , is equivalent to an unsupported CJ detonation propagating at the same velocity in a second explosive with the same initial density, but with a higher heat of formation  $(e^x_0)'$  and a higher heat of reaction  $\delta q_c$  satisfying the equations  $(e^x_0)' = e^x_0 + E^2 \hat{\alpha} / \rho^x_0 D$  and  $(\delta - 1)q_c = E^2 \hat{\alpha} / \rho^x_0 D$ .

This equivalence between unsupported detonation and EED was used to extend Kamlet's short method into the CK short method for EED. Although the values of  $D$  and  $\hat{p}$  for PBX9501 calculated with this short method are considerably lower than the corresponding values calculated with our (e-p-v) EOS, we are in no position to account for this disparity here.

We finally conclude that the work presented in this paper has concentrated on developing more realistic EOS for detonation products with a fixed composition. Additional work to investigate the dependence of  $q_c$ ,  $\hat{\alpha}$ , and  $\delta$  on the field strength  $E$  is thus required before our first-generation model can be considered to be a working model for EED. We recommend that a CJ routine for EED based on our first-generation model with  $\hat{\alpha}$ , a constant, be incorporated into the TIGER code so that the dependence of the CJ composition and  $q_c$  on  $E$  can be investigated when the detonation products satisfy the chemical equilibrium conditions and are governed by a more realistic equation of state, such as JCZ (3).

## ACKNOWLEDGEMENT

This work was supported by the Naval Surface Warfare Center under Contract No.

N060921-86-C-0219, and was performed in conjunction with Dr. D. G. Tasker and Dr. J. W. Forbes.

## REFERENCES

1. Brish, A. A.; Tarasov, M. S.; and Tsukerman, "Electric Conductivity of the Explosion Products of Condensed Explosives," *Soviet Physics JETP*, Vol. 37, No. 10, 1960, p. 1095.
2. Hayes, B., "On Electrical Conductivity in Detonation Products," *Proceedings of the Fourth Symposium (International) on Detonation*, U.S. Naval Ordnance Laboratory, White Oak, Maryland, 12-15 Oct 1965, pp. 595-601.
3. Ershov, A. O.; Zubkov, P. I.; and Luk'yantchikov, L. A., "Measurements of the Electrical Conductivity Profile in the Detonation Front of Solid Explosives," *Explosion and Shock Waves*, Vol. 10, No. 6, 1974, pp. 776-782.
4. TIGER Computer Program, SRI Publication No. Z106, SRI International, Menlo Park, CA 94025, Poulter Laboratory, 1973.
5. Kamlet, M. J. and Jacobs, S. J., "Chemistry of Detonations, I: A Simple Method for Calculating Detonation Properties of C-H-N-O Explosives," *J. Chem. Phys.*, Vol. 48, No. 1, 1968, pp. 23-35.
6. Fickett, W. and Davis, W. C., *Detonation*, University of California Press, Berkeley, Los Angeles, London, 1979, Chapter 2.
7. Ince, E. L., *Ordinary Differential Equations*, Dover Publications, Inc., New York 14, New York, 1956, pp. 47-52.
8. Zeldovich, I. B. and Kompaneets, A. S., *Theory of Detonation*, Academic Press, New York and London, 1960, Chapter 2.

## DISCUSSION

EDWARD L. LEE, LLNL  
SRI International, Menlo Park,  
California

Since you have assured a similarity solution, why can you not simply perform a

TIGER calculation with increased heat release to derive Chapman-Jouguet (CJ) and explosion behavior? This would automatically provide the equilibrium analysis to the problem.

#### **REPLY BY M. COWPERTHWAITE**

For my present treatment of EED, I agree with Dr. E. L. Lee that there is an equivalence between an EED and an unsupported CJ detonation propagating in an explosive with a higher heat of formation when both types of detonation produce the same CJ products in chemical equilibrium and both explosives have the same initial density.

However, in using this equivalence and a code such as TIGER to estimate electrically enhanced CJ parameters inversely, one is obviously faced with the problem of calculating the values of  $E$  and  $\phi_L$  associated with the unrealistic, higher, prescribed heats of forma-

tion before the dependence of enhanced CJ parameters on the field strength can be investigated.

#### **DISCUSSION**

**HAROLD J. GRYTING**

Gryting Energetics Sciences Company  
San Antonio, Texas

Does your reference to field strength, as part of your future work, mean that you expect to consider the effects produced by electromagnetic waves (produced by the electrical applied current) as well as the effects obtained from the electric current alone?

#### **REPLY BY M. COWPERTHWAITE**

As far as I know, there are no plans to perform any more theoretical work on EED at the present time.

# THE MEASUREMENT OF ELECTRICAL CONDUCTIVITY IN DETONATING CONDENSED EXPLOSIVES

Douglas G. Tasker and Richard J. Lee  
Naval Surface Warfare Center  
10901 New Hampshire Avenue  
Silver Spring, Maryland 20903-5000

*The electrical conductivity of a range of detonating high explosives has been measured. The data have been obtained in electric fields up to  $10^7$  V/m in coaxial and linear geometries. The conductivity structure has been resolved as a function of time, with nanosecond precision, in explosive PBX-9501. These measurements are interpreted in relation to the detonation process. Conductivity data are used to study detonation stability effects and the roles of aluminum and carbon in detonation induced reactions.*

## INTRODUCTION

The time resolved measurement of electrical conductivity provides a unique means of studying detonating explosives. These measurements offer fresh insights into the physics and chemistry of detonation.

Much work has been done in an effort to understand the electrical conduction in detonating explosives that are subjected to high electric fields.<sup>1</sup> The methods that have been developed are used as tools for probing the detonation process; in particular, they can be used to study the effects of detonation wave stability and the roles of carbon and aluminum during the detonation process.

In this paper the results of a large number of experiments are summarized. The data are summarized for two types of experiment, bulk resistance and time resolved conductivity measurements, and are interpreted in the light of our existing understanding.

## DETONATION CONDUCTION MODELS

Various models have been considered during the course of these studies. The three main candidates for conduction that have been considered are: shock induced conduction in the unreacted explosive due to band gap reduction,

shock induced conduction in the reaction products, and conduction in coagulated carbon behind the reaction zone.

The first model due to Crawford<sup>2</sup> assumes that conduction occurs in the unreacted explosive in the von-Neumann spike. The unreacted explosive, at atmospheric pressure, behaves as an insulator with a relatively large energy gap  $E_g$  between the valence and conduction bands, e.g., for TNT  $E_g \approx 6.3$  eV. Estimates were made of the reduction of band gap due to pressure which suggest that TNT becomes an "organic metal" when compressed to 50% of its initial volume. This work was not pursued because the experimental data demonstrated that the conduction continued throughout the reaction zone and beyond. See the results below.

The second model due to Griem<sup>3</sup> assumes, for relative simplicity, that the reaction zone could be represented by a mixture of ionized, atomic species of carbon, hydrogen, nitrogen, and oxygen (C, H, N, and O). Here again it was assumed that the detonation pressure reduced the band gaps of the atomic species to allow ionization to occur at temperatures of 3000 to 5000°K (i.e., less than 0.5 eV). The preliminary results of this work suggested that H<sup>+</sup> ions were primarily responsible for conduction by liberating electrons that are free to move in

a conducting plasma. However, later work showed that at near solid densities H<sup>+</sup> ions may not exist. The electrons may "hop" from one H atom to the next behaving as "virtual negative ions." This preliminary study did successfully predict conductivities comparable with experimental results.

Hayes<sup>4</sup> has produced convincing evidence that the conduction may be due to carbon. He propagated a non-planar detonation wave into a divergent electric field at the end of a coaxial probe. The interpretation of the data was hampered by the divergent geometry, but this beautiful work was probably the first to demonstrate the use of conductivity measurements to probe the structure of the detonation process. Hayes showed that the peak conductivity (which is perhaps equivalent to the spike observed here) was strongly correlated to the calculated carbon content of the products.

The results of this work also suggest that conduction is due to the presence of carbon behind the shock front.

## EXPERIMENTAL METHODS

The conductivity measurements have been performed in two main classes of experiments, those that measure the bulk resistance and those that measure conductivity as a function of time and distance. A critical review of these various methods was published previously.<sup>5</sup> In this paper the results for four explosives compositions PBX 9404, PBX-9501, PBX 9502, and PBXW-115 are reported. Both sets of experiments share a common electrical circuit which is described below.

### Basic Circuit

The fundamental electrical circuit of all the conductivity experiments is shown in Figure 1. The main circuit comprises of a capacitor C, an electrical closing switch S, a transmission line inductance and resistance (L and r), and the explosive load inductance and its resistance (L<sub>x</sub> and R<sub>x</sub>). Electrical diagnostics are used to measure the current i, the rate of change of current di/dt, and the voltage V. Note that to eliminate contact resistance errors the voltage is measured using a four-probe technique.

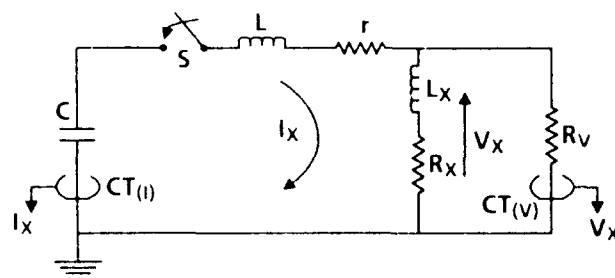


Figure 1. Basic Resistance Measurement Circuit

The choice of circuit components depends on the scale and type of the experiment. The capacitor value ranges from 50 to 1500  $\mu\text{F}$ , and it is charged to the voltage  $V_c$  (2.5 to 40 KV) prior to the start of the experiment.

There are several advantages to the use of such high voltages. First, the contact potentials that exist between the metal electrodes and the conducting explosives, which are typically only a few volts, are too small to affect the high voltage measurements. Second, the large currents that are obtained are well suited to high speed, high linearity current measurements using Rogowski coils. Finally, the conduction of certain inhomogeneous explosives, notably those that contain aluminum particles, exhibit non-linearities in low electric fields due to the complex nature of the conduction paths.

The switch is either an explosively activated closing switch, a thyatron, or a triggered spark gap. The switch protects the diagnostic circuits and explosive from prolonged exposure to the electric field. The transmission line is either an array of parallel coaxial cables or a parallel plate stripline.

The capacitor, the transmission line, and the explosive load form a classic LCR series resonance circuit. When the switch is closed, the circuit will resonate if it is not sufficiently damped or dissipative. The state of damping is expressed by the quality factor,  $q$ . If  $Z_0$  is the pulse impedance, then from classical circuit theory:

$$Z_0 = (L/C)^{1/2} \text{ and } q = Z_0 / (R_x + r)$$



If  $q > \frac{1}{2}$ , the circuit resonates; if  $q < \frac{1}{2}$ , it is over-damped. The circuit efficiency is proportional to  $1/q$ , hence more power is transferred from the capacitor to the load when  $q$  is small. Good voltage and current data depend on an efficient circuit, so it is desirable to control and minimize  $L_x$ ,  $L$ , and  $r$ . Moreover, various serious problems in high speed voltage measurement are minimized when inductances are small.<sup>6</sup>

At the time  $t = 0$ , the detonation wave, with its conduction zone, enters the electrodes and current  $i$  starts to flow. (In other experiments<sup>1</sup> it has been shown that the arrival of the detonation shock front is coincident with the start of the conduction zone within 0.5 ns.) Consequently, the explosive itself acts as the main closing switch and the voltage  $V(t)$  across the explosive becomes:

$$V(t) = V_c - L \frac{di}{dt} - r i(t) - (1/C) \int_0^t i(t) dt$$

$$= i(t) R_x + L_x \frac{di}{dt}$$

At  $t = 0$ ,  $i(0) = 0$ ,

$$\frac{di}{dt} = V_c / (L_x + L)$$

and 
$$V(0) = V_c L_x / (L_x + L).$$

Notice that at  $t = 0$  the voltage across the load is independent of  $R_x$  because  $i = 0$ . At that time all the applied voltage appears across the inductances in the circuit. The current then rises approximately sinusoidally and the voltages and currents are recorded. By plotting voltage as a function of current, with the appropriate corrections for  $L_x \frac{di}{dt}$ , the resistance of the explosive is obtained.

### Voltage Measurements

It is difficult to measure voltage accurately in explosives experiments because of the rapid changes of current, i.e.,  $(1/i) \frac{di}{dt}$  is large. These errors and their elimination are treated elsewhere.<sup>6</sup> The rapid changes are due to the short time durations of the experiments. Consequently, the stray self-inductances, in both the explosive circuits and the voltage probes,

can cause large errors. Large errors can also arise from the mutual inductances between the explosive's circuit and the voltage probes. These errors are minimized by careful design including the use of parallel striplines; mutual inductances have been reduced to  $\leq 1$  nH.

Commercial oscilloscope voltage probes are unsuitable for this work; they are poorly screened from magnetic disturbances and exhibit large errors due to the mutual inductance between the main circuit and the voltage probe circuit. Moreover, the direct connection of the ground wire of a voltage probe invariably produces large errors due to ground loop effects. Ground loops are eliminated by the indirect measurement of current, in a relatively large shunt resistor, using current transformers. The resistors used here range from 100  $\Omega$  to 10 K $\Omega$  and are made from solutions of copper sulphate ( $\text{CuSO}_4$ ) in polyethylene tubes.

### CONDUCTIVITY DISTANCE PRODUCT OBTAINED FROM BULK RESISTANCE MEASUREMENTS

These experiments are typified by either a planar or coaxial geometry where a high explosive is placed between two metal electrodes. A detonation wave is initiated at one end of the explosive outside the electrodes. The detonation wave then enters the explosive between the electrodes so that the velocity vector  $\underline{D}$  and the electric field  $\underline{E}$  are mutually perpendicular;  $\underline{D}$  is parallel to the length of the electrodes.

The electrodes are connected to a high voltage capacitor bank at a voltage in the range of 2.5 to 40 KV. The explosive acts as a good insulator with a breakdown strength of  $\approx 20$  KV/mm in its unreacted state; but when it is detonated, the reaction zone has a conductivity on the order of 100 mhos/m. The detonated explosive thus initiates current flow between the electrodes, and the subsequent electric current and voltage are monitored as functions of time. By plotting voltage as a function of current, a V-I plot, the dynamic nature of the conduction process is determined.

The resistance  $R$  of the explosive is then obtained from the slope of the  $V$ - $I$  plot. Now in these experiments we cannot measure  $\sigma(x)$  directly but rather the integral of  $\sigma(x)$  along the conduction zone. We can define a conductivity-zone width product,  $\sigma\Delta$ , where  $\Delta$  is the effective conduction zone width, as follows:

$$\sigma\Delta = \int_0^{\infty} \sigma(x).dx$$

The  $\sigma\Delta$  product is then related to  $R$  for the two geometries as follows:

**Planar**  $\sigma\Delta = h/WR$  where  $h$  is the explosive thickness and  $W$  the electrode width

**Coaxial**  $\sigma\Delta = \ln(r_1/r_2)/2\pi R$   
where  $r_1$  and  $r_2$  are the radii.

The  $V$ - $I$  plot is typically linear and the line can be extrapolated through the origin. However, recent studies have shown a small departure from the line at the time the detonation wave enters the electrodes; this curvature will be discussed later.

### Coaxial Experiments

The resistance of the conduction zone in a number of explosives was measured in a coaxial configuration similar to that reported by Demske *et al.*<sup>7</sup> The main explosives compositions are given in Table 1.

Table 1. PBX Explosives Ingredients

PBX	Ingredients (excluding binders)			
9404	94% HMX			
9501	95% HMX			
9502	95% TATB			
W-115	43% AP	12% RDX	25% Al	

Each explosive was pressed into a brass tube and a brass center electrode was inserted in the center of the explosive. The explosive

and the tube were slightly tapered (1  $\mu$ m diameter/mm length) to ensure an intimate contact between them. This avoided possible contact resistances, due to air gaps,<sup>6</sup> that can exceed the explosive's resistance. The explosives were 127 mm long and detonation was initiated at one end. Two sizes of configuration were used, see Table 2.

Table 2. Coaxial Dimensions

ID* (mm)	OD (mm)	Length (mm)	HE mass (g)
3.1	14.0	33	100
11.5	30.2	140	75
*ID and OD: Inside and outside diameters			

### Coaxial Results

The coaxial experiment results are shown in Table 3 for both the large ( $\dagger$ ) and small configurations. The PBX-9404 results show that  $\sigma\Delta$  is independent of charge size. These suggest that, provided the explosive's dimensions exceed the critical diameter, the current flow in the explosive is Ohmic. The explosive performance properties of PBX-9404 and PBX-9501 are virtually identical,<sup>8</sup> only their sensitivities differ, so they are usually treated as identical explosives. This is also true for electrical conductivity; no significant differences have been found in this study.

Table 3. Coaxial Resistance Measurements

PBX	R ( $\Omega$ )	$\sigma\Delta$ (mhos)
9404	0.12 $\dagger$	1.2
9404	0.20	1.2
9501	0.20	1.2
9502	0.02	10.2
$\dagger$ Large configuration		

## Planar Experiments

The planar experiments are essentially simplified versions of the Ershov experiments which are described later. A sheet of high explosive is placed between two flat, parallel brass electrodes, as in Figure 2. A detonation wave is initiated in the explosive sheet with a line wave generator and booster.

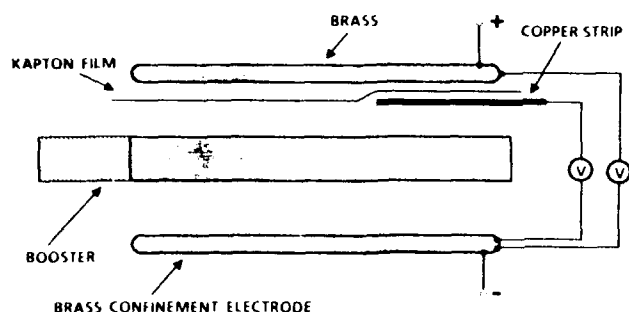


Figure 2. PBXW-115 Resistance Measurement Apparatus, Exploded View

Current and voltage data are measured while the detonation wave travels along, and parallel to, the electrodes. The electrodes were 12.7 mm wide, 12.7 mm thick, and 150 mm long. The explosives sheets ranged from 1 to 25.4 mm in thickness,  $h$ .

## Planar Results and Discussion

The conductivity data for the planar experiments are shown in Table 4; for comparison, the measured detonation velocities and the infinite diameter detonation velocities are also included. It is evident that the conductivity results for PBX's 9404 and 9501 are quite different to the coaxial results of Table 3. In the coaxial experiments the  $\sigma\Delta$  products appear to be independent of charge dimensions, but then these dimensions are much greater than their critical diameters of  $\approx 1$  mm. But in the case of the thin sheets, there is a clear thickness dependence because these sheets are close to failure. The failure thickness is expected to be half the failure diameter,<sup>9</sup> i.e.,  $\approx 0.6$  mm for PBX-s 9404 and 9501 provided that the wave can propagate 15 to 25 times the failure thickness, i.e.,  $\approx 12$  mm.

The observed dependence of the  $\sigma\Delta$  product on thickness, for explosives sheets close to failure, is clearly an important finding. These

Table 4. Planar Conductivity  $\sigma$ -Thickness  $\Delta$  Products

PBX	$h$ (mm)	$\sigma\Delta$ (mhos)	$D$ (mm/ $\mu$ s)
9404 <sup>1</sup>	1	0.20	8.3
9501 <sup>1</sup>	1	0.24	8.27
9501	2	0.54	8.52
W-115 <sup>2</sup>	12.7	0.20 - 0.4	5.27
W-115	25.4	0.04 - 0.4	5.37

<sup>1</sup> $D_\infty = 8.82$  mm/ $\mu$ s      <sup>2</sup> $D_\infty = 5.46$  mm/ $\mu$ s

effects will be returned to later in this paper when the measurement of conductivity in PBX-9501, as a function time, is reported.

As mentioned earlier, recent studies have shown small departures from the linear  $V-I$  plots at the beginning of the traces, i.e., when the detonation wave first enters the electrodes. These effects were first thought to be due to errors in voltage measurement caused by various magnetic effects. In particular, it was believed that the corrections for electrode inductance,  $L_x di/dt$ , were in error. Yet despite exhaustive tests these departures could never be completely eliminated. The true origin of these errors was not identified until time resolved conductivity measurements were made. The departure was found to be a real physical effect due to the existence of a tail in the conductivity profile, see below.

## CONDUCTIVITY OF DETONATING ALUMINIZED EXPLOSIVES

The measurement of conductivity may provide valuable clues related to the combustion of aluminum in plastic-bonded Navy explosives. The Navy's plastic-bonded explosive PBXW-115 studied here contains 25% aluminum by weight, see Table 1.

The technique for measuring resistance in aluminized explosives is essentially the same as the measurements in thin sheets of explosive discussed above. Attempts to measure the PBXW-115 conductivity structure using the Ershov experiment were unsuccessful.

cessful because of the large failure thickness of the explosive.

### Failure Thickness of PBXW-115

A series of experiments were performed to establish the failure thickness of PBXW-115 that would just sustain detonation. Square slabs of PBXW-115, 75 mm length and width, were initiated in various thickness by PBX-9501 boosters. The boosters were end-initiated by line wave generators and the configuration was similar to that of Figure 2. Ionization pins were used to monitor shock wave velocities in the PBXW-115 and steel witness blocks were used to detect detonation at the edge furthest away from the booster. The charges were confined by 12.7 mm thick brass plates. The results of the ionization pin data and the steel witness blocks showed that the explosive could be detonated in thicknesses of 12.7 mm or greater using the brass confinement. With hindsight the detonation may not have stabilized in these tests, see below.

### Attempts to Measure PBXW-115 Conductivity vs. Time

Measurements of PBXW-115 conductivity were attempted using a modified Ershov experiment. In experiments with small failure diameter explosives, e.g., PBX-9501, used in thin, flat sheets, the ratio of width  $W$  to thickness  $h$  was relatively large,  $W/h > 5$ . Consequently, errors caused by the divergent fields at the edges of the electrodes were negligible. (This had been verified in guard-rail experiments where the elimination of field divergence had no detectable effect on the measured bulk resistance of PBX-9404.)

Narrow electrodes are necessary for the Ershov experiments because of problems associated with wave curvature. But the large failure thickness of PBXW-115 causes  $W/h$  to be small. Consequently, guard-rails were used to eliminate field divergence and to provide confinement. In this experiment a center electrode, 12.7 mm square cross-section, was used to measure conductivity in a 12.7 mm thick sheet of PBXW-115. Parallel guard electrodes, 12.7 mm thick and 25.4 mm wide, provided the confinement and the elimination of fringe fields. The guard rails were insulated from the

center electrode with (polytetra-fluorethylene, PTFE) Teflon. Rogowski coils were used to monitor currents in each electrode.

It was found that the Teflon insulation was quickly destroyed by the detonation wave and the experiments were unsuccessful. Consequently, the Ershov experiments were abandoned in favor of simpler bulk resistance measurements using wide, single electrodes.

### Bulk Resistance Measurements in PBXW-115

The bulk resistance of detonating PBXW-115 was measured in the apparatus shown in Figure 2. The explosive was confined by 25.4 mm thick brass plates and initiated by the booster system described above. Prior to detonation the electric field  $E$  was applied across the explosive. Unreacted PBXW-115 conducts in electric fields exceeding  $\approx 1$  KV/mm. Consequently, it was necessary to insulate the explosive with a 25  $\mu$ m thick film of Kapton type H (polyimide) insulation. This insulation has a dielectric strength of  $\approx 3 \times 10^8$  V/m, however, it conducts readily when shock-loaded above  $\approx 5$  GPa.<sup>10</sup> The Kapton thus prevented the explosive from conducting and igniting prior to arrival of the detonation wave. When shocked to the detonation pressure,  $\approx 12$  GPa, the Kapton resistance became negligibly small, hence, the true resistance of the explosive could be measured, see Figure 2. (A second voltage probe was used to measure the potential difference across the film to verify that the Kapton's resistance was indeed negligible.)

### PBXW-115 Results and Discussion

Figure 3 shows the results of one experiment which was performed on a 25.4 mm thickness of PBXW-115. Electrodes of 75 mm width and 150 mm length were used. The voltage across the explosive was 5 KV throughout the duration of conduction.

The structure of this current waveform is unique to this explosive, it has not been observed in any other explosives. From ionization pin data the detonation wave took 26  $\mu$ s to sweep the length of the electrodes and exited the electrodes at the point marked 'End' in

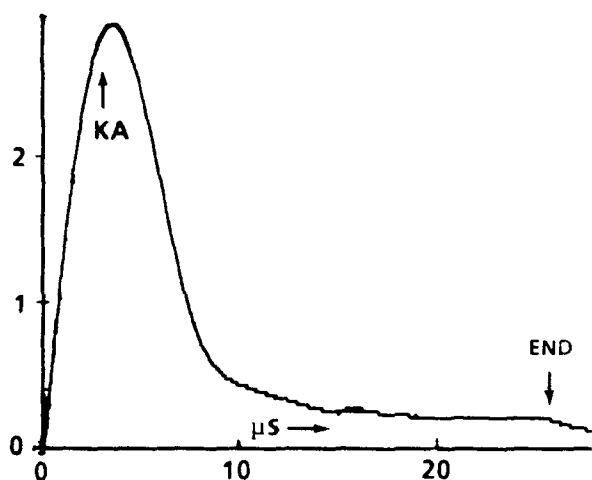


Figure 3. Current Measurements in Detonating PBXW-115

Figure 3. However, the current rose to 2.9 KA and decayed to 500 A within 8  $\mu$ s; the decay continued for the remainder of the experiment. Another apparently identical experiment gave different results, the first peak was only 1 KA followed by a similar decay and then a rapid rise after 10  $\mu$ s to 4 KA.

The results were, at first, interpreted as evidence of late reactions in the explosive. However, there are large variations from experiment to experiment which suggest that the structure is strongly affected by detonation wave instabilities. The results are probably due to a combination of wave instabilities and late reaction effects. It is certain that 25.4 mm thick sheets of PBXW-115 are close to the critical thickness. The initial current peak may therefore, be due to the over-boosting of the explosive. In light of these results, the experiments will be repeated with longer lengths of explosive to allow the detonation waves to stabilize prior to the measurements of resistance.

## TIME RESOLVED CONDUCTIVITY MEASUREMENTS

Ershov<sup>11</sup> reported an ingenious technique which can be used to measure conductivity in a plane wave geometry and in a near parallel electric field. The technique is capable of providing high time resolution data; it has been adapted to provide the measurements reported here.

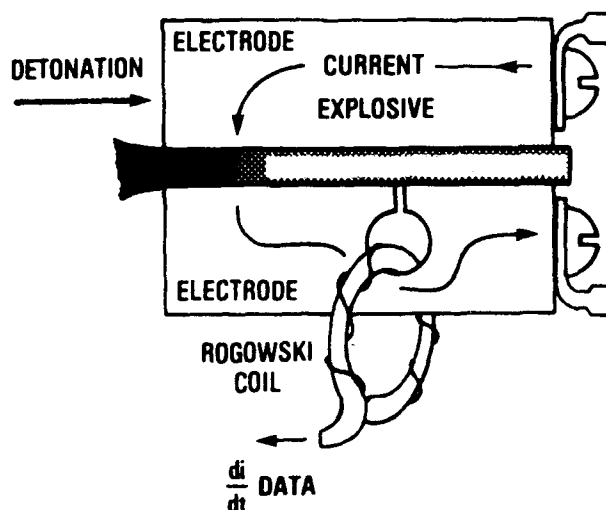


Figure 4. Time Resolved Conductivity Experiment

A sheet of high explosives is placed between two flat, parallel brass electrodes, Figure 4. A narrow insulated gap is placed against the explosive in the ground electrode and a conducting loop bridges the other end of the gap. A Rogowski coil is used to measure current on the loop. A detonation wave is initiated in the explosive sheet with a line wave generator and booster. The wave travels in a direction perpendicular to the gap so that the wave front is parallel to it.

As Ershov demonstrates, the electric field  $\underline{E}$  behind the conduction zone of conductivity  $\sigma$  is not perturbed by the current flow provided that the vectors  $\underline{E}$  and  $\underline{\text{curl}} \sigma$  are perpendicular. The current density  $\underline{j}$  and  $\sigma$  can now be expressed as functions of time  $t$  in the direction parallel to the applied field  $\underline{E}$ ,

$$\underline{j}(t) = \sigma(t) \underline{E}$$

Now  $\underline{j}(t)$  is simply the current  $i(t)$  per unit area. The area of conduction in the direction of  $\underline{E}$  is the conductor width  $W$  multiplied by the length in the  $x$  direction, so the current becomes:

$$i(t) = W \int_0^x E \sigma(x) dx \quad (1)$$

The power supply is connected to the ends of the electrodes furthest away from the detonator. The wave enters the explosive between the electrodes at  $x = 0$  and  $t = 0$  and

it arrives at the gap at  $x = x$ ,  $t = x/D$ , where  $D$  is the detonation velocity.

If the field  $E$  and the velocity  $D$  are independent of distance  $x$ , then substitution of  $x = Dt$  and  $E = V/h$ , where  $V$  is the voltage between the electrodes and  $h$  is their separation, results in:

$$i(t) = \frac{W D V}{h} \int_0^{x/D} \sigma(t) dt$$

$$di(t)/dt = \sigma(t) \{W D V / h\} \quad (2)$$

The last expression demonstrates the elegance of the Ershov technique,  $di/dt$  follows the exact profile of the required  $\sigma(t)$ . Moreover, accurate  $di/dt$  data are easy to obtain using a Rogowski coil. This coil is essentially an air-cored current transformer, the output voltage is directly proportional to the rate of change of magnetic flux  $\phi$  in the circuit. Since  $di/dt$  is directly proportional to  $d\phi/dt$ , then the output is also proportional to  $\sigma(t)$  from Equation (2).

### Experimental Details

The explosive sheets were approximately 150 mm square, 1.00 mm or 2.00 mm thick, and extended beyond the edges of the 12.70 mm wide electrodes. A 200  $\mu$ m wide gap (or slit) was cut across the width of one electrode so that it was parallel to the detonation front and interrupted current flow along the surface of the electrode. A low inductance, low resistance loop maintained current flow around the gap. The  $L di/dt$  and  $iR$  voltage differences were negligible for this experiment. The loop was formed by a 5.2 mm diameter hole drilled in the electrode at the end of the gap, see Figure 4.

The gap was insulated with Teflon film to delay breakdown across the gap. The breakdown is due to dielectric failure in the gap and mechanical gap closure by hydrodynamic flow of the metal electrodes. When breakdown occurs, the current no longer flows in the loop and the  $di/dt$  record is terminated.

The main electrical circuit is similar to that reported above for the planar experiments. The data were recorded on transient

digitizers and 1 GHz bandwidth analog oscilloscopes.

A Rogowski coil, with a time resolution of  $\leq 1$  nsec, was placed in the hole adjacent to gap to measure the rate of change of current  $di/dt$ . To test the validity of the Rogowski coil  $di/dt$  data, the record was integrated numerically and compared with independent current data from a calibrated current transformer. The data were in good agreement. For a gap of 200  $\mu$ m the time resolution, given by the detonation transit time across the gap, was 22 ns.

If the detonation front was not straight and parallel to the gap then the resultant  $di/dt$  record would be perturbed by this wave structure, i.e., the wave would take a finite time to cross the edges of the gap. Measurements of shock wave curvature using a streak camera showed a maximum uncertainty of  $\approx 10$  ns.

### Time Resolved Measurements in PBX-9501

Conductivity data are shown for 1 mm and 2 mm thick sheets of PBX-9501 in Figure 5. Typically the current and voltage at the time of conductivity measurement were 4.0 KA and 1.5 KV. The peak conductivities for both thicknesses were  $\approx 220$  mho/m and the durations of the initial conduction spikes were  $\approx 100$  ns. The initial spikes were followed by lower level, longer duration tails; these tails were markedly different for the two thicknesses.

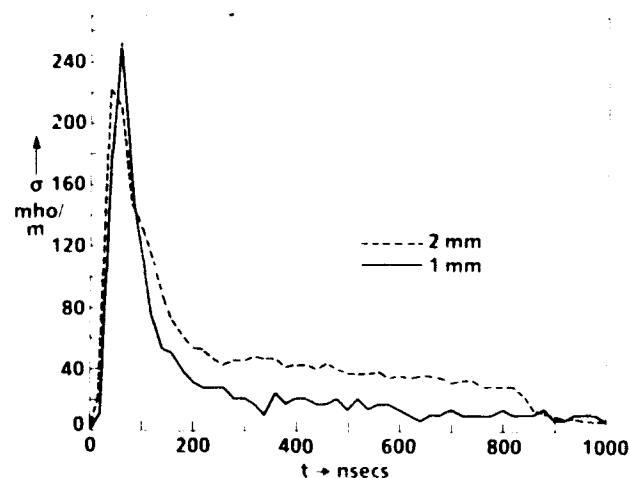


Figure 5. PBX-9501 Conductivity Structures for Thicknesses of 1 mm and 2 mm

The data shown here for the 2 mm thickness have an abrupt break at  $\approx 900$  ns which is probably due to closure of the 200  $\mu\text{m}$  gap. When the gap closes, current flows across the gap and not in the loop; such breaks are common and unavoidable. Measurements of current and voltage taken at the same time as  $di/dt$  suggest that conduction continues for an additional 1 or 2  $\mu\text{s}$  in the explosive.

## DISCUSSION

As reported in earlier work,<sup>5</sup> the peak conductivity was  $\approx 220$  mho/m. The conductivity data reported here have improved time resolution, moreover the techniques have been refined to observe longer duration structures. The new data show initial spikes of  $\approx 100$  ns duration for all experiments followed by tails that are strongly dependent on the state of detonation in the explosive. These are believed to be the first published observations of two step conductivity structures, i.e., where a short duration spike is followed by a long duration tail.

The conductivity structure of PBX-9501 is particularly interesting. It has been estimated from critical diameter measurements that the reaction zone thickness is  $\approx 100$   $\mu\text{m}$ ,<sup>8</sup> which is equivalent to a time duration of only 11 ns. Yet the data here show  $>100$  ns conduction spikes followed by  $>1$   $\mu\text{s}$  tails. Several researchers have noted that their models of detonation phenomena do not adequately match observed data unless a slow burn term for the combustion of carbon is included.<sup>12,13,14</sup> Johnson<sup>13</sup> has suggested that carbon slowly coagulates into large clusters behind the detonation front in the product gases. This coagulation provides an additional, slow energy release after the main reaction. These findings are supported by the work of Hayes<sup>4</sup> that was described in the DETONATION CONDUCTION MODELS section above.

It is estimated that the critical thickness of sheets of PBX 9501 is  $\approx 0.6$  mm, hence the propagation of detonation in these 1 mm and 2 mm thick sheets will be influenced by lateral rarefactions. This is confirmed by the measured detonation velocities (8.27 and 8.52 mm/ $\mu\text{s}$ ) which are less than published velocities, i.e., 8.83 mm/ $\mu\text{s}$ . Further studies are

planned to observe the effects of confinement and explosive thickness.

From this work it is speculated that the tails of the conduction profiles are due to the slow coagulation of carbon in the products. Moreover this coagulation appears to be strongly influenced by the thickness of the explosive sheets. In other words, the arrival of lateral rarefactions, in the wake of the reaction zone, strongly perturbs the coagulation process. The spikes are unaffected because they are too short in time. Detonation failure may therefore be due to the control of the energy release due to carbon coagulation in the tail. The measurement of conductivity may be the only way of observing these phenomena.

Similarly, the aluminized explosives data show the conductivity measurement to be a valuable tool for the analysis of combustion and wave stability during detonation. This technique should lead to the formulation of better metallized explosives.

## ACKNOWLEDGEMENTS

We are indebted to Dr. A. Roberts of the Office of Naval Research for his support under Code 123, Project 02403SB. The excellent scientific contributions by R. Granholm and P. Gustavson to these studies are acknowledged. Grateful thanks are due to R. Hay, N. Snowden, B. Snowden, H. Gillum (deceased), C. Sorrels (deceased), R. Baker, and many others for their fine experimental work. Special thanks are due to Dr. J. Forbes for many helpful discussions and encouragement.

## REFERENCES

1. Tasker, D. G., *The Properties of Condensed Explosives for Electromagnetic Energy Coupling*, NSWC TR 85-360, Oct 1985, NSWC, White Oak, MD.
2. Crawford, O. H., "Electrical Conductivity in the Reaction Zone of High Explosives," Oak Ridge National Laboratory, May 1985, private communication.
3. Griem, H. R., "Properties of Dense Plasmas Generated by Discharges Behind Shock Waves," University of Maryland, Laboratory for Plasma and Fusion

Energy Studies, College Park, MD, Final Report, 28 Jul 1986 - 28 Jul 1987.

4. Hayes, B., "On Electrical Conductivity in Detonation Products," *Proceedings of the Fourth Symposium (International) on Detonation*, Office of Naval Research, Washington, DC, Oct 1965, p. 595.
5. Tasker, D. G.; Granholm, R. H.; and Lee, R. L., "The Fast Measurement of Electrical Conductivity Structure Within the Detonation Zone of a Condensed Explosive," *Shock Waves in Condensed Matter*, Elsevier Science Publishers, B. V., 1988, p. 923.
6. Tasker, D. G. and Lee, R. J., "High Current Electrical Conduction of Pressed Condensed Detonating Explosives," *Shock Waves in Condensed Matter*, Plenum Publishing Corporation, 1986.
7. Demske, D. L.; Forbes, J. W.; and Tasker, D. G., "High Current Electrical Resistance of PBX-9404," *Shock Waves in Condensed Matter - 1983*, Elsevier Science Publishers, B. V., 1984.
8. Dobratz, B. M., *LLNL Explosives Handbook*, UCRL 52997, Lawrence Livermore National Lab, 16 Mar 1981.
9. Ramsay, J. B., "Effect of Confinement in 95 TATB/5 KEI-F," *Proceedings of the Eighth Symposium (International) on Detonation*, Albuquerque, NM, Jul 1985, p. 372.
10. Tasker, D. G., *Electrical Conductivity in Detonating Explosives*, NSWC TR 89-214, NSWC, White Oak, MD.
11. Ershov, A. P.; Zubkov, P. I.; and Luk'yanchikov, L. A., "Measurements of the Electrical Conductivity Profile in the Detonation Front of Solid Explosives," *Combustion, Explosion and Shock Waves*, Vol. 10, No. 6, 1974, p. 776.
12. Mader, C. L., *Numerical Modeling of Detonations*, Univ. California Press, 1979.
13. Johnson, J. D., "Carbon in Detonations," in *Proceedings of the 1989 APS Topical Conference in Condensed Matter*, Albuquerque, NM, 14-17 Aug 1989.

14. Tang, P. K., "A Study of Detonation Processes in Heterogeneous High Explosives," *J. Appl. Phys.*, Vol. 63, 1988, p. 1041.

## DISCUSSION

G. A. LEIPER, ICI Explosives  
NEC, Stevenston, KA20 3LN, UK

We have recently analyzed the performance of a similar highly non-ideal explosive with a slightly divergent flow code. We have found that less than 70% of the formulation reacted within the subsonic part of the flow. We have also found that even at several times the critical charge diameter, reaction was not complete before the sonic plane. Do you feel this agrees with the anomalous conductivity records you have obtained?

## REPLY BY D. G. TASKER AND R. J. LEE

Dr. Leiper's findings are certainly in keeping with our anomalous conductivity records. Many other researchers have observed, or suggested, that the detonation process in even *ideal* explosives requires relatively long distances (many charge diameters) to stabilize. Notable references to these effects include Ramsey,<sup>1</sup> Mader,<sup>2</sup> and Bdzil.<sup>3</sup> Clearly, non-ideal explosives, such as Dr. Leiper's, are likely to take even longer to stabilize. All these effects can be interpreted as evidence of late reactions behind the sonic plane.

The role of aluminum in non-ideal explosives is particularly interesting. The reaction of the aluminum is quite slow; detonation performance data suggest that it occurs in tens or hundreds of  $\mu$ s. This reaction, therefore, has little effect on the detonation velocity and pressure. Yet Akimova<sup>4</sup> has observed that the addition of aluminum to cast TNT compositions actually decreases the failure diameter and other workers, including Gimenez,<sup>5</sup> have observed the effects of aluminum reactions occurring within 10  $\mu$ s of the detonation front. We hope to have a better understanding of late carbon and aluminum reactions by the next symposium.



## REFERENCES TO REPLY

1. Ramsay, J. B., Ref. 9 cited in this paper.
2. Mader, C., "Chemistry of Build-Up of Detonation Wave," *Actes du Symposium International sur le comportement des Milieux Denses sous Hautes Pressions Dynamiques*, Commissariat a l'Energie Atomique, Paris, 1978.
3. Bdzil, J. B.; Fickett, W.; and Stewart, D. S., "Detonation Shock Dynamics: A New Approach to Modeling Multi-Dimensional Detonation Waves," Ninth Symposium (International) on Detonation, Aug 1989.
4. Akimova, L. N. and Stesik, L. N., "Detonation Capacity of Perchlorate Explosives", *Combustion, Explosion and Shock Waves*, Vol. 12, 1976, p. 247.
5. Gimenez, P. *et al.*, "F. P. I. Velocimetry Techniques Applied to Various Problems in Detonics," Ninth Symposium (International) on Detonation, Aug 1989.

# SYNTHESIS OF ULTRAFINE DIAMONDS IN DETONATION WAVES

V. M. Titov, V. F. Anisichkin, and I. Yu. Mal'kov  
Lavrentyev Institute of Hydrodynamics  
Novosibirsk, 630090, USSR

*This paper deals with the investigation of diamond-phase formation from HE (high explosives) in a detonation wave. Some explosives, such as TNT, RDX, and their-based compositions, have been considered. The experimental technique makes it possible to conserve the products of condensed detonation (soot), including ultrafine diamonds (UFDs), formed by detonation decomposition of explosives. The UFD synthesis has been shown to occur mainly in the detonation reaction zone. The size distribution curves for the UFD particles for the explosives of different composition, mass, and form have been obtained by the method of small-angle x-ray scattering. It has been proposed that, along with thermodynamic conditions, the UFD formation process can be affected by specific conditions of shock-wave compression and peculiarities of molecular structure of explosives.*

## INTRODUCTION

The formation of diamond particles by the detonation of condensed explosives has received considerable attention recently (see, for example, References 1 - 3). In this connection, the explosives, which may be decomposed with free carbon liberation, are likely to be the subject of particular interest.

The search for the experimental solution of the problem of possible diamond formation was conducted simultaneously in different countries. The first successful experiments with the explosion in a gaseous medium were made in the Soviet Union in 1982. In 1987 there appeared the work informing that such a method of synthesis had been developed.<sup>4</sup> The first results on realization of this method in the United States and West Germany were published in June 1988.<sup>5</sup> In September 1988 there appeared the work of the Soviet researchers,<sup>6</sup> where the recent basic results in this field were presented. They made it possible to develop an industrial technology of manufacturing UFDs, when about 8 to 9 percent mass of the initial explosive is synthesized into the diamond phase.

It has been reported in Reference 5 that, as in References 4 and 6, the explosive synthesis of diamond particles is provided by the experiments in explosive chambers. An inert gas contained in the chamber protects the ultrafine particles against oxidation and graphitization.

The notion of "synthesis of UFDs" incorporates the following components:

- developing a physico-chemical model of this phenomenon;
- optimization of the composition and the geometry of charges;
- determining the relation between the explosive mass, volume of chamber, and gas properties in order to conserve UFD particles;
- purification of a solid residue from carbon in non-diamond forms and other additives;
- investigating the structure and properties of UFDs; and
- other technological factors.

The objective of this paper is to investigate the main regularities of the process of

diamond synthesis, find appropriate thermodynamical parameters, and develop the qualitative models of the phenomena, which define the synthesis of UFDs.

The widespread TNT explosive has been used in the present experiments. Its detonation is attended with liberation of a significant amount of free carbon; therefore, cast TNT charges were primarily investigated from the viewpoint of their applicability for the synthesis of UFDs.<sup>5,6</sup>

## EXPERIMENTAL TECHNIQUE

The experiments used a 2 m<sup>3</sup> explosive chamber filled with inert gas, with the HE charge placed at its center. In all the experiments the explosive was initiated at the end face by a 10 g RDX-based booster. The condensed products of detonation were analyzed after each shot. The UFDs were identified as a chemical product with the use of nitric, perchloric, and other acids. In the detonation products, along with non-diamond forms of carbon, there may be found other additives, such as metallic micro-particles of the chamber walls. The correctness of soot separation was examined by chemical analysis and x-raying. When determining the synthesized ultra-diamond mass,  $M_{\text{ufd}}$ , the spread of data was not in excess of 5 percent for the explosives of one and the same type.

The features of gasdynamic processes observed in the explosive chamber were explored in Reference 7 and cannot be covered in detail here.

The UFD powder was first investigated in Reference 8. In this paper the samples to be examined by electron microscopy were prepared in an analogous manner. Figure 1 represents the photograph of diamond particles produced by detonation of RDX/TNT (50/50) cast explosives. The UFD powder consists of grains of rounded form, 2 to 20 millimicron in diameter. There exist the regions consisting of relatively small or relatively great particles only. The analysis of the powder also points to the presence of particle clusters of irregular form several microns in diameter.

The particle size distributions for several types of TNT/RDX (50/50) charges are shown in Figure 2. The data were obtained by the method of small-angle x-ray scattering.<sup>9</sup> The computer processing of the data makes it possible to determine a mean size of particles,  $d_{\text{mean}}$ .

The results obtained in the experiments with TNT/RDX and TNT/HMX cast explosives are listed in Table 1. Cylindrical charges were 33 mm in diameter and 150 mm long. The table indicates the mass of explosive,  $M_{\text{expl}}$ ; the mass of condensed carbon,  $M_{\text{cc}}$ ; the mass of isolated diamond,  $M_{\text{ufd}}$ ; relations  $m_1 = M_{\text{ufd}}/M_{\text{cc}}$ ,  $m_2 = M_{\text{ufd}}/M_{\text{expl}}$ , and  $m_3 = M_{\text{cc}}/M_{\text{expl}}$ ; as well as a mean size of particles,  $d_{\text{mean}}$ .



Figure 1. The UFD Powder

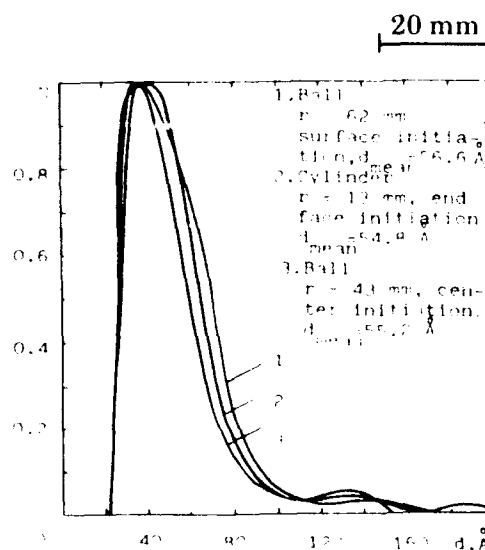


Figure 2. The UFD Particle Size Distributions in the Case of TNT/RDX (50/50)

It is evident that an absolute maximum yield of carbon is provided by the TNT charges, a maximum relative content of a diamond solid carbon phase,  $m_1$ , is observed with 40 to 50 percent of TNT in the TNT/RDX explosive, and the maximum yield of the diamond phase is provided by the use of TNT/RDX (70/30) explosive. Then it decreases with decreasing the TNT amount. For RDX,  $m_2$  is less than 1 percent.

The data listed in Table 1 show the high efficiency of this method of diamond synthesis.

## DETERMINING TIME AND PARAMETERS OF SYNTHESIS

The values of pressure and temperature for TNT in the Chapman-Jouguet plane are assumed usually to be  $p_{Ch.J} = 18-19$  GPa,  $T_{Ch.J} \approx 3.5 \times 10^3$  K.<sup>2</sup> These values correspond to the diamond phase region on the (p-T) carbon phase diagram.<sup>1,2</sup> However, the data listed in Table 1 indicate that pure TNT gives a minimum amount of the UFD relative to the solid detonation products ( $m_1$ ) and the whole of the explosive mass ( $m_2$ ). The use of more energetic compositions gives the increase of the diamond fraction. The above compositions

are characterized by high pressures and temperatures in the Chapman-Jouguet plane.

The same results may be obtained in the regime of overdriven detonation in TNT. The charge construction for realizing this regime is shown in Figure 3. The layer of high explosive (cast TNT/HMX (30/70) surrounds the TNT cylinder. Upon explosion of the charge, there appears the Mach detonation disc. The pressure jump developed behind it is higher than that in TNT in the stationary regime. The experiments show an 80 to 90 percent transformation of free carbon ( $m_1$ ), contained in TNT, into the diamond. About 16 to 18 percent of the TNT explosive mass transforms into free carbon. This is in agreement with the data

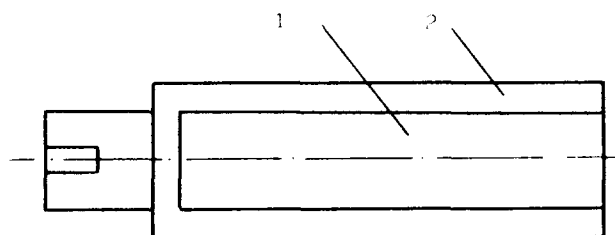


Figure 3. The Charge Construction. 1 - TNT, 2 - TNT/HMX (30/70).

Table 1. Experimental Results on the UFD Synthesis

Explosive	$M_{expl.}$ (g)	$M_{cc}$ (g)	$M_{ufd}$ (g)	$m_1$ $= M_{ufd}/M_{cc}$ (%)	$m_2$ $= M_{ufd}/M_{expl.}$ (%)	$m_3$ $= M_{cc}/M_{expl.}$ (%)	$d_{mean}$ (nm)
TNT	280	50.8	8.0	15.7	2.8	18.1	4.9
TNT/RDX (90/10)	288	42.4	11.9	28.0	4.1	14.7	
TNT/RDX (70/30)	310	38.4	25.7	66.9	8.3	12.4	5.5
TNT/RDX (60/40)	312	29.4	21.3	72.7	6.8	9.4	
TNT/RDX (50/50)	320	29.4	23.0	78.4	7.2	9.2	5.5
TNT/RDX (40/60)	320	25.3	20.4	80.7	6.4	7.9	
TNT/RDX (30/70)	310	21.7	16.9	78.0	5.4	7.0	6.0
TNT/HMX (70/30)	298	37.3	24.5	65.7	8.2	12.5	
TNT/HMX (30/70)	315	20.2	11.8	58.4	3.8	6.4	

listed in Table 1 (for TNT  $M_{cc}/M_{expl.} = 18.1$  percent). The masses of carbon and UFD synthesized from the outer layer of TNT/HMX were estimated in different experiments, when a central part of the charge was filled with an inert matter.

These results admit the assumption that the UFD synthesis mainly occurs in the chemical reaction zone, since the change of detonation regimes will primarily influence the parameters at the wave front.

The process of carbon condensation upon detonation has been studied insufficiently, and the direct experimental data on its kinetics have not been available, except for Reference 10, which appeared soon after the discovery of the UFD synthesis. The authors made an attempt to relate the measured detonation parameters with possible phase transitions. The electric conductivity of the detonation products behind the front is compared to the TNT content in the cast TNT/RDX explosive.<sup>10</sup> It is assumed that the diamond phase formation will reduce noticeably electric conductivity.

The method of measuring electric conductivity was successfully applied to estimate the completeness of transforming graphite into diamond under a shock loading.<sup>11</sup> However, it cannot provide specific results for our case, due to a very complicated structure of the medium and its variable initial content resulting from our TNT fraction variation.

Of greater interest are relative estimates of rates of conductivity change. The values of time  $t_e$ , in which a maximum electric conductivity at the front decreases by a factor of  $e$  are presented in Reference 10. They are sketched in Figure 4, along with the values of  $m_1$ ,  $m_2$  taken from Table 1. A time resolution of 0.07 mcs in Reference 10 is not high, but it is sufficient to make estimates. The separation of a significant amount of diamond phase in carbon ( $m_1$  curve) correlates with a sharp decrease in  $t_e$ . In Reference 10 it is assumed that there is a causal relationship between these facts, since the substitution of graphite by diamond in the detonation products must change the character of conductivity. The value of  $t_e$  for a maximum yield of the UFD is about several tenths of a microsecond (Figure 4). This is

comparable to the duration of a chemical reaction in the detonation wave for the cast explosive under consideration.<sup>12</sup> This is in agreement with the assumption that the UFD is formed behind the wave front during the chemical reaction.

This assumption is also confirmed by the study of the UFD particles distribution dependent on the charge size. As is known, the stationary detonation wave structure comprises the chemical reaction zone of  $t_1$  duration and pressure drop, Taylor wave, following the Chapman-Jouguet state (Figure 5). This zone, BC, is also defined by the charge geometry. As is obvious from the study of the UFD particles

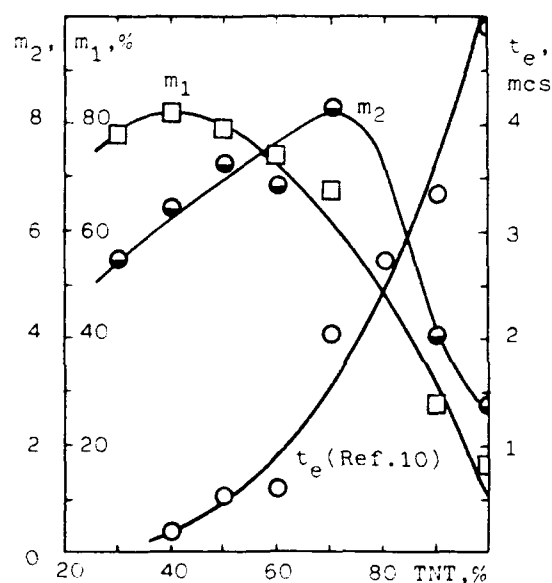


Figure 4. The Amount of the Diamond Phase and Electric Conductivity Variation Behind the Front Vs. TNT Content in the TNT/RDX Composition

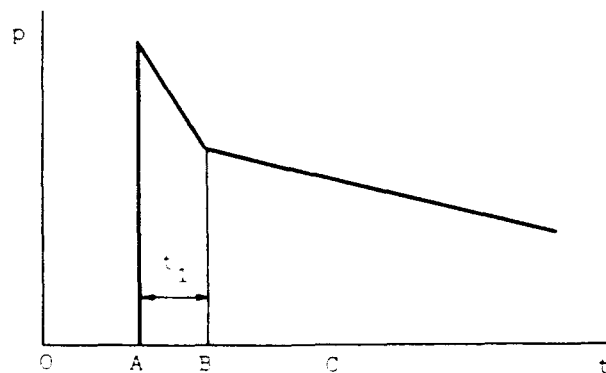


Figure 5. The Stationary Detonation Wave Structure

size distribution for the charges of different form and size (Figure 2), the curves of distribution and mean particle sizes are invariable. This is possible only when the synthesis occurs in the chemical reaction zone, whose structure is invariable for the stationary detonation wave and the above explosive compositions.

Thus, the three independent estimates of the synthesis time admit one and the same conclusion: UFD particles are formed directly at the detonation front for  $t \leq t_1$ . This defines also the pressure level upon synthesis. The data listed in Table 1 for TNT show that the synthesis occurs also at  $p \geq p_{ch-J}$  (TNT) = 18 to 19 GPa. In this case  $T \approx 3.5 \times 10^3 K$ , and for the diamond phase  $m_1 = 15.7$  percent. For the composition similar to TNT/RDX (50/50), where free carbon almost completely converts into the diamond phase (Table 1, Figure 4),  $p \geq 25$  to 30 GPa.

The above said may be related to the case of formation of individual UFD particles. The clusters of irregular form, micron or less in size, may be formed by coalescence of the produced particles in the Taylor wave.

When the particles achieve about 50 Å in size during  $t \leq 0.5 \times 10^{-6}$  s, the mean velocity of the particle radius increase is 5 mm/s. This is three orders higher than a linear velocity of diamond crystal face growth (about 0.11 to 0.15 mm/min) under the static conditions.<sup>13</sup>

## MIXING OF DETONATION PRODUCTS IN THE CHEMICAL REACTION ZONE

As mentioned above, the UFD forms directly in the chemical reaction zone of the detonation wave. Therefore, the extent to which the products of partial decomposition of different components of heterogeneous explosives are mixed is a matter of great significance for understanding the process of formation and growth of the diamond-phase particles. More particularly, this problem may be formulated as follows: May the nuclei (clusters) of the diamond (graphite) phase formed by decomposition of neighboring microvolumes of different components of the cast TNT/RDX explosive unite? It is worthy to note that the average size of the RDX particles,

being in the mixture with cast TNT, is 50 μm in our experiments.

The kinetics of the formation of condensed-carbon clusters in the detonation wave is considered in Reference 14; however, time is not taken into account. The goal of that work<sup>14</sup> was only to determine limitations imposed by diffusion on the cluster formation in order to consider them in theoretical models of detonation processes.

To estimate the diffusion layer thickness, it is appropriate to use the relation

$$l \sim \sqrt{2Dt}, \quad (1)$$

where  $D$  is the diffusion coefficient,  $t = t_1$  is the chemical reaction zone length. Let the value of about several atomic sizes, 1 nm (10 Å) be assumed the initial size of diffusing particles. Then the Einstein relation will be in the form

$$D = kT/3\eta\eta d, \quad (2)$$

where  $k$  is Boltzmann constant,  $\eta$  is the viscosity of a medium, and  $d$  is the particle diameter.

From the statistic theory of irreversible processes it follows that<sup>15</sup>

$$\eta = \frac{5}{4} (\eta mkT)^{1/2} \times \frac{1}{J},$$

where  $J$  is the mean-weighted value of the differential section of collision.

Assuming that the particles are in the form of a sphere, we have

$$\eta = \frac{5}{16} \frac{(\eta mkT)^{1/2}}{nd^2}. \quad (3)$$

Using Equations (1) through (3) and assuming  $d \approx 1$  nm,  $T \approx 3 \times 10^3 K$ ,  $t_1 \approx 0.5$  mcs, we obtain the estimate of the diffusion mixing layer thickness:

$$l \sim 0.6 \times 10^{-6} \text{ m.}$$

This value is less than the explosive grain size by two orders of magnitude. It will not change noticeably with changing  $d$  by several times. The estimate obtained is in good agreement with the value of 1 for amatol of the TNT/<sup>15</sup>NH<sub>4</sub><sup>15</sup>NO<sub>3</sub> (80/20) mixture

experimentally determined by the tracer investigations.<sup>16</sup>

Thus, the effective diffusion layer thickness is much less than a regular grain size of explosive compositions. This makes it possible to suppose that in the TNT/RDX explosive decomposition there occurs insignificant mixing of detonation products in the chemical reaction time  $t_1$ . The particles of condensed carbon (and the diamond as well) form independently without mass exchange between decomposition products of TNT and RDX.

The data of the yield of the condensed carbon (diamond and nondiamond forms) as a function of the explosive composition are listed in Table 1 ( $m_3$ ). These data may be described with a high accuracy by the unified relationship, assuming that the yield of TNT in the condensed carbon is about 17 percent, and that of RDX is about 2.5 percent. That is,

$$m_3 = 0.17a + 0.025(1-a), \quad (4)$$

where  $a$  is the TNT fraction in the explosive. As illustrated in Figure 6, the straight line determined by Equation (4) fits the experimental data of Table 1 reasonably well. These data are in good agreement with the results of some works, in which the goal of investigation was a final composition of the detonation products of TNT and RDX individually.<sup>17</sup>

Thus, the composite TNT/RDX cast explosive in the chemical reaction zone represents a heterogeneous structure, having different parameters in the microvolumes of different components. In the case of TNT/RDX (50/50), the size of such microvolumes is about 50  $\mu\text{m}$ . For these values, the propagation time of disturbances over the "cell" is  $t_0 \sim 10^{-8}\text{s}$ . The relaxation of the parameters in the whole volume is connected with the characteristic time  $t_0$ .

This peculiarity as well as a low value of 1 are the major factors responsible for a relatively weak variation of the chemical reaction zone width with changing the TNT fraction in TNT/RDX type compositions.<sup>12</sup> The RDX amount increase results in increasing pressure and accelerating TNT decomposition; however, as a whole, this component is a factor limiting a chemical reaction rate.

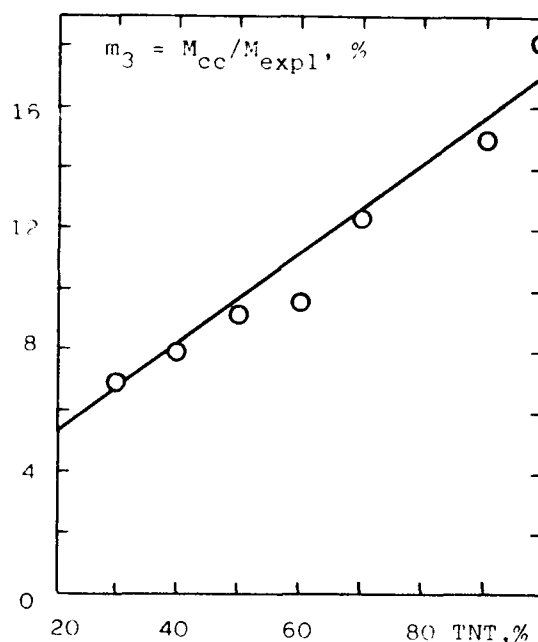


Figure 6. The Condensed Carbon Yield Vs. TNT Content in the TNT/RDX Composition

It should be noted that the models considering different temperatures in the chemical reaction zone for different components were analyzed in Reference 18 when studying transient processes occurring upon shock initiation of composite explosives.

As was mentioned above, the yield of the diamond phase upon RDX detonation is insignificant ( $m_2 < 1$  percent), and the assumption that the detonation products do not mix in the chemical reaction zone is justified. Thus, the diamond forms mainly from carbon atoms entering the molecule of TNT by the TNT/RDX composition detonation. As far as RDX is concerned, its chemical decomposition essentially provides for the increase in pressure in the reaction zone.

## NUCLEATION AND GROWTH OF UFD PARTICLES

In References 1 - 3 the pressure and temperature in the Ch-J plane are compared with the equilibrium phase diagram of carbon. If these values correspond to the state above the graphite-diamond equilibrium line, a free carbon is assumed to be condensed in the diamond phase.

At the same time, it is obvious that the kinetics of formation and growth of UFD particles is to be taken into account in order to predict correctly the appearance of them in a detonation wave. Some peculiarities may be associated also with an ultrafine structure of the phase obtained. The properties of small particles, of the order of tens angstrom in size, may essentially differ from those of macrocrystals, whose models are commonly used in considering phase diagrams and phase transformations.<sup>19</sup>

Therefore, the approaches based on the analysis of equilibrium states, cannot explain, for example, the experimental dependence of  $m_1 = M_{\text{ufd}}/M_{\text{cc}}$  on explosive power or why the average size of the UFD particles remains almost invariable (Table 1). The latter is illustrated in Figure 7, where the size distribution curves for the UFD particles formed by explosion of identical TNT (curve 1) and TNT/RDX (50/50) (curve 2) charges are presented.

The above-mentioned peculiarities may be described qualitatively within the framework of the theory of a new phase formation.<sup>20,21</sup> The expression of the critical size of the particle in a new phase has the form of the Thompson equation:

$$r_c = \frac{2va}{\Delta\mu}, \quad (5)$$

where  $v$  is the specific volume of carbon atom,  $a$  is the surface tension, and  $\Delta\mu$  is the chemical potential variation in the process of cluster formation.

A diamond phase is a stable carbon phase under high pressure; therefore, with increasing pressure and temperature the critical size of clusters in a diamond phase decreases, and their number increases, according to the theory of fluctuations.<sup>21</sup>

In the case of stationary detonation of TNT, the critical size of clusters is higher and their number is less as compared to the detonation of the TNT/RDX (50/50) explosive. As a result, the growth rate of the diamond-phase mass decreases in the first case as compared to the second one. This gives a qualitative explanation of the fact that with an insignificant difference in the distribution curves (Figure 7) and average sizes of UFD for TNT and TNT/RDX (50/50), the diamond phase yield upon the TNT decomposition is 5 times lower (Table 1).

The further growth of the nucleus is defined by the specific conditions. The two extreme mechanisms of small particle growth are available, such as:

- addition of isolated atoms,
- coalescence of the clusters available.<sup>19</sup>

For the latter mechanism, a simple statistical model is suggested, which assumes that the particles behave as liquid drops (liquid-drop coalescence).<sup>22</sup> As a result, the dependence defining a logarithmic-normal distribution was obtained:

$$f(x) = \frac{1}{(2\pi)^{1/2} \ln o} \exp \left[ -\frac{(\ln x - \ln \bar{x})^2}{2 \ln^2 o} \right] \quad (6)$$

where  $\bar{x}$  is the mean-weighted diameter,  $o$  is the standard deviation, and

$$\ln \bar{x} = \frac{\sum_i n_i \ln x_i}{\sum_i n_i} \quad \ln o = \left[ \frac{\sum_i n_i (\ln x_i - \ln \bar{x})^2}{\sum_i n_i} \right]^{1/2}$$

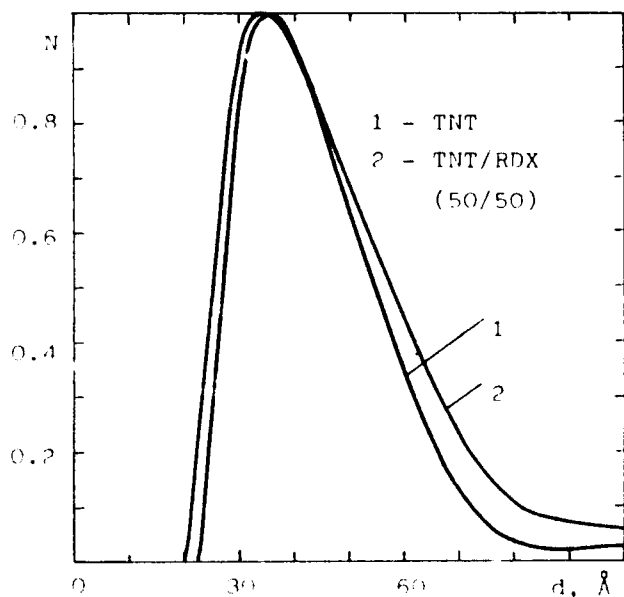


Figure 7. The UFD Particle Size Distribution Curves for the Identical Charges of TNT and TNT/RDX (50/50)



This distribution curve is characterized by a steep front and a flat fall for large-size particles.

On the contrary, if the particle growth is due to diffusion and subsequent addition of isolated atoms, the distribution curve has a flat front and steep fall.<sup>23</sup> Thus, the distribution curve form admits the conclusion as to which of the particle growth mechanisms is dominating.<sup>19</sup>

As follows from the above-mentioned considerations, a logarithmically normal form of the distribution curves obtained makes it possible to suppose that the UFD particle growth at the detonation front is due to coalescence of diamond clusters rather than diffusion of isolated atoms of carbon. In addition to thermodynamical conditions, the UFD synthesis may also be affected by specific peculiarities of shock compression which favor splitting chemical bonds in molecules.

The diamond-phase clusters, comprising several atoms of carbon, may form immediately behind the front of the initiating shock wave, i.e., prior to the beginning of chemical reactions. In this case the molecule structure peculiarities are the major factor responsible for the UFD synthesis. In the opinion of some authors,<sup>24-26</sup> the molecule destruction of aromatic compounds under a shock loading begins with the decomposition of a thermally stable aromatic ring in a carbon-carbon bond rather than in a carbon-hydrogen bond, as in the case of conventional thermal pyrolysis. This conclusion<sup>24</sup> is supported by the structural peculiarities of aromatic series compounds, coincidence of the initiation threshold of liquid TNT, and pressure at the first kink of the Hugoniot curve for benzene<sup>25</sup> and the beginning of nitrobenzene decomposition.<sup>26</sup>

What is more, a comparison of the shock wave energy and the total energy of chemical

bonds in a TNT molecule shows that the first is insufficient for a complete splitting of all the bonds. Thus, it may be supposed that the diamond clusters form the groups of carbon atoms of the aromatic ring immediately behind the shock front. This is likely to be primarily referred to the group of three atoms of carbon bound to one another and unbound to H atoms.

The search for new and direct methods of investigations is of great importance for a more fundamental understanding of the UFD synthesis. In our opinion, among them is the tracer investigation, which was used only once<sup>16</sup> (as follows from the literature available) for studying detonation processes. Now we will describe its application for studying the process of the diamond formation in the detonation wave.<sup>27</sup>

The TNT/RDX (40/60) explosive, 35 g in weight, was used in this experiment. In 58 percent of TNT molecules the  $^{12}\text{C}$  atom in the methyl radical ( $\text{CH}_3$ ) was replaced by the  $^{13}\text{C}$  atom. The tracer content in the explosive, including the booster, was 5.4 percent (the  $^{13}\text{C}/\text{C}$  ratio). The values of tracer content in the initial matters and detonation products are listed in Table 2. It should be noted that a comparative balance of the tracer prior to and after the explosive does not take place, that is confirmed by the experimental conditions.

The data listed in Table 2 allow the conclusion that approximately 80 percent of a free carbon formed by the TNT decomposition transforms into diamond. This is in agreement with all the above-stated results on the macrokinetics of the UFD synthesis.

## CONCLUSION

The main regularities of the UFD synthesis by stationary detonation have been studied using TNT and TNT/RDX compositions. Some specific experiments have shown

Table 2. Values of Tracer Content in Initial Matters and Detonation Products

	TNT	RDX	TNT/RDX (40/60)	Condensed Carbon	Diamond Phase	Nondiamond Phase	CO	CO <sub>2</sub>	CH <sub>4</sub>	C <sub>2</sub> H <sub>4</sub>
$^{13}\text{C}/\text{C} \%$	9.3	1.1	6.0	5.9	6.8	4.1	4.2	4.6	3.9	6.8

that a run-to-detonation zone covering an essential region in the charge reduces the UFD yield.

It has been established that the process of UFD synthesis mainly occurs in the chemical reaction zone. All the experimental data available nowadays are in agreement with this conclusion. This allows the synthesis time for the explosives under analysis to be determined, which is  $t_1 \approx 0.5$  mcs. Because of such low values, there can be doubt that the data of equilibrium carbon phase diagram (p-T diagram) can find a direct application for predicting the results of synthesis.

The rarefaction isentrope of the detonation products on the stationary (p-T) diagram of carbon has not been analyzed here as well, since thereby, along with the process kinetics, the ultrafine dispersion of the UFD particles must be taken into account. This problem dealing with the UFD particles conservation needs special research work.

After the fact of formation and conservation of the diamond phase in detonation waves has been established, there appeared a number of works (for example, Reference 28), where some peculiarities earlier observed upon detonation of condensed explosives are explained by the diamond transformation. In this connection, it is appropriate to consider the role of UFD particles as a peculiar "diamond label," associated with the initial region of detonation transformation.

The authors would like to thank Dr. J. Johnson, Los Alamos National Laboratory, USA, for sending information on the works by Greiner et al.<sup>5</sup> and Shaw and Johnson,<sup>14</sup> Dr. V. N. V. Kolomeichuk, Institute of Catalysis, Siberian Division of the USSR Academy of Sciences, for obtaining and processing the size distribution curves for UFD particles. The authors are also grateful to their colleagues, D. S. M. Karakhanov and Dr. S. A. Bordzilovsky for a helpful discussion of the results; A. S. Starostina for help in conducting the experiments; and T. P. Savelieva and L. V. Khoreva for their help in preparing the manuscript for publication.

## REFERENCES

1. Gubin, S. A.; Odintsov, V. V.; and Pepekin, V. I., "On the Role of Phase State of Graphite in Estimating the Detonation Parameters of Condensed Matters," *Khimicheskaya fizika*, Vol. 3, No. 1, 1984, p. 754.
2. Baute, J. and Chirat, R., "Which Equation of State for Carbon in Detonation Products?" *Proceedings of the Eighth Symposium (International) on Detonation*, NSWC MP 86-194, pp. 521-531.
3. van Thiel, M. and Ree, F. H., *Properties of Carbon Clusters in TNT Detonation Products: The Graphite Diamond Transition*, UCRL-Preprint 95839, Livermore, CA, USA, 1986.
4. *Fizika gorenii i vzryva* (Editor's article), Vol. 24, No. 5, 1987, p. 3.
5. Greiner, N. R.; Phillips, D. S.; Johnson, J. D.; and Volk, F., "Diamonds in Detonation Soot," *Nature*, Vol. 333, No. 6172, 1988, pp. 440-442.
6. Lyamkin, A. I.; Petrov, E. A.; Ershov, A. P.; Sakovich, G. V.; Staver, A. M.; and Titov, V. M., "Diamonds Manufactured from Explosives," *Dokl. Akad. Nauk SSSR*, Vol. 302, No. 3, 1988, p. 611.
7. Ershov, A. P. and Kupershtokh, A. L., "On the Temperature of Detonation Products Upon Explosion in a Chamber," *Fizika gorenii i vzryva*, Vol. 22, No. 3, 1986, p. 118.
8. Staver, A. M.; Gubareva, N. V.; et al., "Ultrafine Powders Manufactured with the Use of Explosive Energy," *Fizika gorenii i vzryva*, Vol. 20, No. 5, 1984, p. 100.
9. Vainstein, B. K., *Modern Crystallography*, Nauka Publishers, Moscow, 1979.
10. Staver, A. M.; Ershov, A. P.; Lyamkin, A. I., "Investigation of Detonation Transformations of Condensed Explosives by the Electric Conductivity Method," *Fizika*

- goreniia i vzryva*, Vol. 20, No. 3, 1984, p. 79.
11. Zhugin, Yu. N.; Krupnikov, K. K.; and Ovechkin, N. A., "Investigation of Peculiarities of Shock Compressed Graphite Transformation into Diamond on the Basis of Electric Resistance Variation," *Khimicheskaya fizika*, Vol. 6, No. 10, 1987, p. 1447.
  12. Shvedov, K. K., "On Recording Ch-J Parameters Upon Detonation of Condensed Explosives," *Fizika goreniia i vzryva*, Vol. 23, No. 4, 1987, p. 84.
  13. Novikov, N. V., "High Pressures in Science and Technology," *Book of Abstracts of 11 AIRAPT Intern. Conf.*, Kiev, USSR, 1987, p. 9.
  14. Shaw, M. S. and Johnson, J. D., "Carbon Clustering in Detonation," *J. Appl. Phys.*, Vol. 62, No. 5, 1987, pp. 2080-2085.
  15. Eisenshitz, R., *Statistical Theory of Irreversible Processes*, London, 1958.
  16. Guire, R. Mc.; Ornellas, D.; and Akst, I., *Symposium H. P. D.*, Paris, 1978.
  17. Baum, F. A.; Orlenko, L. P.; et al., *Fizika vzryva*, Nauka Publishers, Moscow, 1975, Chapter 6, p. 139.
  18. Bordzilovsky, S. A.; Karakhanov, S. M.; and Lobanov, V. F., "Transient Processes in TNT/RDX, TNT/HMX Cast Explosives," *Fizika goreniia i vzryva*, Vol. 19, No. 4, 1983, pp. 136-139.
  19. Petrov, Yu. I., *Clusters and Small Particles*, Nauka Publishers, Moscow, 1986.
  20. Fol'mer, M., *Kinetics of New Phase Formation*, Nauka Publishers, Moscow, 1986.
  21. Landau, L. D. and Lifshitz, E. M., *Statistical Physics*, Second Edition, Nauka Publishers, Moscow, 1964, p. 556.
  22. Grandvist, C. G. and Buhrman, R. A., "Ultrafine Metal Particles," *J. Appl. Phys.*, Vol. 47, 1976, pp. 2200-2219.
  23. Lifshitz, E. M. and Pitaevsky, L. P., *Physical Kinetics*, Nauka Publishers, Moscow, 1979, p. 509.
  24. Babare, L. V.; Dremine, A. N.; Pershin, S. V.; and Yakovlev, V. V., "Polimerization of Hard-to-Polimerize Organic Compounds Under Shock Compression," *Fizika goreniia i vzryva*, Vol. 5, No. 4, 1969, pp. 528-539.
  25. Yakusheva, O. B.; Yakushev, V. V.; and Dremine, A. N., "Connection Between Transparency Loss of Ca-Containing Compounds Under High Dynamic Pressures With an "Anomaly" on Shock Compressibility Curves," *Zhurnal fizicheskoi khimii*, Vol. 51, No. 7, 1977, pp. 1657-1660.
  26. Yakushev, V. V.; Dremine, A. N.; Nabatov, S. S.; and Shunin, V. M., "Physical Properties and Transformation of Nitrobenzene Under 30 GPa Dynamic Pressures," *Fizika goreniia i vzryva*, Vol. 15, No. 2, 1970, pp. 132-140.
  27. Anisichkin, V. F.; Derendyaev, B. G.; Koptug, V. A.; et al., "Investigation by the Isotope Method of Decomposition Process in a Detonation Wave," *Fizika goreniia i vzryva*, Vol. 24, No. 3, 1988, pp. 121-122.
  28. Pershin, S. V., "On Diamond Formation by Detonation of TNT," *Doklady IV Vsesoyuznogo Soveshchaniia po detonatsii*, Chernogolovka, Vol. 1, 1988, pp. 1-5.

## DISCUSSION

FRED VOLK  
Fraunhofer Institut  
7507 Pfinztal, FRG

Did you get information about the composition of the carbon soot? In our experiments we found a large concentration of N which we cannot explain.

## REPLY BY V. M. TITOV

The results of your experiments are known to us. We did not analyze the soot as a whole before the termination of the acid cleaning process, therefore, we are not able to answer your question.

# CARBON IN DETONATIONS

J. D. Johnson

Los Alamos National Laboratory  
Los Alamos, New Mexico 87545

*We review three principal results from a five-year study of carbon and its properties in detonations, and discuss the implications of these results to the behavior of explosives. We first present a new determination of the carbon melt line from release wave velocity measurements in the shocked state. We then outline a colloidal theory of carbon clustering, which from diffusion limited coagulation predicts a slow energy release rate for the carbon chemistry. Finally, we show the results from the examination of recovered soot. Here we see support for the colloid theory and find the diamond phase of carbon. The main theme of this paper is that the carbon in detonation products is in the form of a colloidal suspension of carbon clusters which grow through diffusion limited collisions. Even the final state is not bulk graphite or diamond, but is a collection of small, less than 100 Å, diamond and graphitic clusters.*

## INTRODUCTION

Other researchers<sup>1,2,3,4</sup> have noted certain problems in the modeling of the detonation process, in particular, in plate-push and interface velocity experiments with variable explosive thickness, and appealed to special properties in carbon chemistry to explain the difficulties. It is easy to convince oneself that indeed carbon is unique among detonation products, since it is the only product that can form arbitrarily large molecules in the form of pure carbon,  $C_n$ ,  $n = 1, 2, \dots, \infty$ , or the whole field of organic chemistry. This is in contrast to the nitrogen, oxygen, and hydrogen which go mainly into  $N_2$ ,  $CO_2$ , and  $H_2O$ . This picture points to carbon as a prime candidate for a slow energy release as compared to the other chemistry. It just takes time for the carbon clusters (molecules) to diffuse together and grow to a bulk solid. This prompted us to study both the thermodynamic and cluster dynamic properties of carbon in the high-temperature, high-pressure regime of detonation products.

It is helpful to have a picture that, while oversimplified in detail, contains the essence of the carbon behavior. We envision "blobs" of

carbon executing Brownian motion in the hot, dense background fluid of the other detonation products, with the carbon clusters building up through random collisions. We assume there are no back reactions and no barriers to reaction; that is, the particles always stick if they touch. This can be refined with a sticking probability. The background fluid keeps the clusters at equilibrium with respect to temperature, carrying off heat when clusters merge. We assume that newly formed clusters anneal. We consequently view the carbon clusters as fairly compact, essentially spherical objects, although a significant deviation from this shape affects our results but little. For simplicity, our initial state for the clusters at the von Neumann spike is taken to be monatomic. The annealing process may cease at some large time and cluster size, say  $10^4$ - $10^5$  atoms, and leave the infinite time state as a collection of large diamond and/or graphitic clusters. This scenario differs from past modeling of carbon in that we do not have bulk, thermodynamic graphite or diamond, even in the final state.

The remainder of this paper has four sections. The first presents the new melt line as determined from release wave velocities. As

we developed the picture outlined in the preceding paragraph, the importance of this work declined. However, we give the results here for general interest; it is a nice piece of work. Next we develop our theory of carbon coagulation and show the resulting slow energy release with some discussion of its influence on detonation behavior. We then give some experimental support for the colloidal picture from the soot recovery experiments. Here we have seen diamonds in the soot. Lastly, we very briefly discuss the slow rate in relation to hydrodynamic studies.

## CARBON MELT LINE

For some time (decades) the standard phase diagram of carbon has been qualitatively of the form shown in Figure 1. Here we are interested in the location of the melt line since even bulk carbon in the detonation regime is somewhat close to melting. If we consider that small clusters can melt at half the bulk melting temperature,<sup>5</sup> the location of the melt line becomes of even more significance. The melt line from the diamond to liquid phase is perfectly acceptable with thermodynamic considerations although the negative slope is anomalous, implying either that the liquid is denser than the diamond or that the entropy of the liquid is less than that of diamond.

To find the melting point along the Hugoniot, standard shock velocity-particle velocity measurements are not at all sensitive enough to determine the small structure in the  $u_s$ - $u_p$  curve. A much more obvious signature, a discontinuous jump as a function of shock strength, occurs in the velocity of the release wave overtaking a shock. In the solid phase this wave travels with the longitudinal elastic velocity, while it drops to a bulk velocity if the material is shocked above melting. The rarefaction velocity is determined from the dimensions of the sample, the velocity of the shockwave, and the timing of the overtake. This technique has already been used successfully for iron,<sup>6</sup> tantalum,<sup>7</sup> and aluminum.<sup>8</sup>

A series of five shots at pressures and temperatures given by the open circles in Figure 1 have been done.<sup>9</sup> All the release wave velocities are consistent with longitudinal velocities for diamond; no melt signature is seen. The higher pressure melt line must be

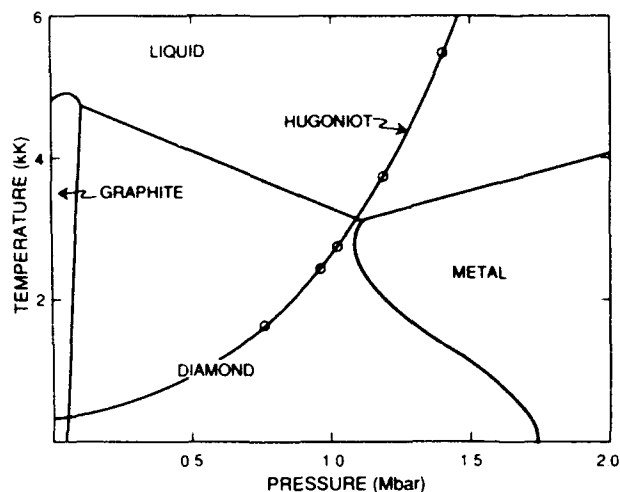


Figure 1. Phase of Diagram of Carbon. The principal Hugoniot is shown and longitudinal velocities are measured at the open circles.

moved significantly upward in temperature with the lower pressure region remaining essentially unchanged. The low pressure restriction comes from other, older experimental work.<sup>10</sup> We now have a positive slope with the melt line progressing to higher pressure above the highest data point. (As an aside, the metal region, based on theoretical work of Yin and Cohen,<sup>11</sup> is pushed out beyond 10 Mbar.)

Thus, in modeling bulk equilibrium carbon in detonation regimes, it is quite reasonable to consider only graphite and diamond. For finite clusters it is safer than with the old phase diagram to think of them as solid. Another benefit from the experiment is that one now has, from the sound velocities derivative information for equation of state determination.

## COLLOIDAL THEORY OF CARBON COAGULATION

We now turn to the picture of carbon coagulation given in the introduction. Here we will consider, for ease of discussion, a model system where at time zero we have only monatomic carbon in an inert background fluid. We assume that the background has no time dependence and has a temperature  $T$ . The carbon clusters are always spherical. Our coagulation theory comes from the classic work of Smoluchowski.<sup>12</sup>

If we denote the concentration of clusters with  $i$  atoms as  $v_i$ , the basic growth equation is

$$\frac{1}{4nDR} \frac{dv_k}{dt} = \sum_{i+j=k} K_{ij} v_i v_j - 2v_k \sum_{j=1}^{\infty} v_j K_{jk}, \quad (1)$$

$$k = 1, 2, \dots$$

The  $K_{ij}$  is a geometric factor that is a function only of the cluster radii. For our work, a very accurate approximation is to set  $K_{ij} = 1$ , independent of  $i$  and  $j$ . The combination  $D_i R_i$ , where  $D_i$  is the diffusion coefficient of an  $i$  cluster of radius  $R_i$ , is independent of  $i$ ; thus, we denote it as  $DR$ . The time is  $t$ . The interpretation of Equation (1) is that the first sum on the right represents the growth of a  $k$  cluster when  $i$  and  $j$  clusters, with  $i + j = k$ , collide to form a  $k$ . The second sum represents depletion of the  $k$  cluster population by collisions with any other cluster.

It is convenient to scale our variables to  $n_i = v_i/f_0$  and  $x = 4n DRtf_0$ , with  $f_0 = v_1$  ( $t = 0$ ). Then, with  $K_{ij} = 1$ , an exact analytic solution exists, namely,

$$n_i(x) = x^{i-1} / (1+x)^{i+1}, \quad i = 1, 2, \dots \quad (2)$$

We still require  $DR$ . We first appeal to the Stokes-Einstein relation<sup>13</sup> to relate  $DR$  to the viscosity  $\eta$  of the background fluid.

$$DR = k_B T / 6\pi\eta. \quad (3)$$

We obtain  $\eta$  from the modified Enskog theory of dense fluids. Enskog is a reasonably accurate and easily applied transport theory for dense fluids. References 14 and 15 give nice overviews of modified Enskog. This completes our rather simple theory of carbon coagulation.

We now need to apply the above to calculate the quantity of interest to detonations. This is  $\Delta E$ , the energy difference per mole of carbon between the total cluster energy at time  $t$  and the infinite time bulk carbon energy.  $\Delta E$  is given by

$$\Delta E \propto \sum_i n_i(x) \Delta E_i, \quad (4)$$

where  $\Delta E_i$  is the energy difference per mole between the  $i$  cluster energy and the bulk. This  $\Delta E_i$  we approximate by a surface term, thus  $\Delta E_i = ai^{2/3}$ . The  $a$  is obtained by fitting to

data and theory on the energies of small carbon clusters (molecules). The result is, in kcal per mole,

$$\Delta E = \frac{80}{(1+x)^2} \sum_{i=1}^{\infty} i^{\frac{2}{3}} \left( \frac{x}{1+x} \right)^{i-1}. \quad (5)$$

For large  $t$ , equivalently  $x$ , the sum in Equation (5) is well approximated by an integral and can be evaluated. Then

$$\Delta E = 80 \Gamma(5/3) x^{-\frac{1}{3}}. \quad (6)$$

This shows directly that we have a slow energy release from carbon. The chemistry of the other detonation products should release energy as  $1/t$ , a much faster rate.

Our result, Equation (6), is not sensitive to the several simplifying assumptions such as spherical clusters, monatomic initial state, etc., that we made in our modeling; i.e., if we lift these simplifications the answer will change little or none.

Still, one wants to see how the numbers work out for real explosives. We have looked at both TNT and HMX; we will discuss HMX here. Putting conservative numbers into the just present theory, that is, using estimates that always give the minimum  $\Delta E$ , we find that  $\Delta E$  at the end of the reaction zone is about 1 percent of the energy released. If, instead of conservation estimates, best guesses are made, for  $\Delta E$  again at the end of the reaction zone, we see that about 2-4 percent of the energy release is tied up in the slow rate.

This  $\Delta E$  seems very small but there is an amplifier effect. We look to simple CJ thinking to obtain a feel for how the  $\Delta E \sim 2-4$  percent will affect experiments. From this approach, we will get an effective shift in the pressure. (This is very simplified thinking. We should really look at how the slow rate changes the reaction zone and from that go to the influence on, say, plate-push and interface velocities. But we will get a handle this way.) Bdzil<sup>16,17</sup> has demonstrated that a slow release of energy of  $O(\delta^2)$  produces changes of  $O(\delta)$  in the shock state. This effect comes from the fact that the Rayleigh line is tangent to the fully reacted Hugoniot at the CJ point. See Figure 2. The dotted curve is the partially reacted Hugoniot

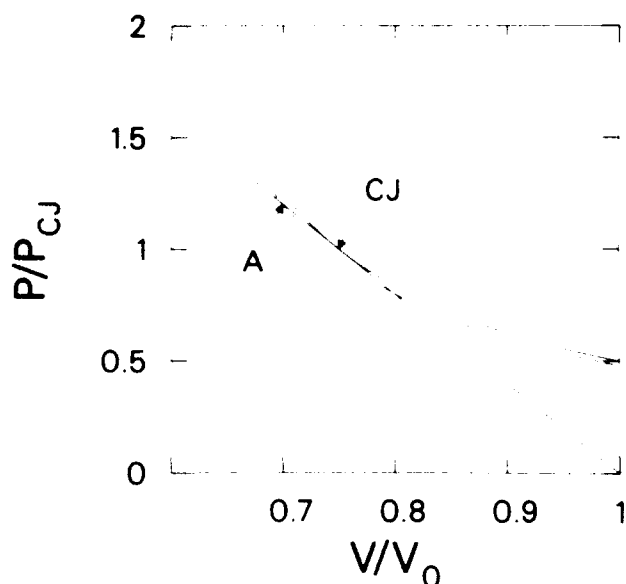


Figure 2. Influence on Pressure of Hugoniot Shift. The Rayleigh line is the solid line, the fully reacted Hugoniot is the solid curve, and the partially reacted Hugoniot is the dashed curve.

shifted  $O(\delta^2) \sim 2-4$  percent by the slow energy release. (One might worry that, besides the  $\Delta E$  from the slow rate, there is also a compensating  $\Delta P$  due to the pressure from the motion of the clusters. However, the number of moles of clusters at the end of the reaction zone is small enough to neglect such.) The  $O(\delta^2)$  shift in the Hugoniot translates to a  $O(\delta) \sim 10-20$  percent shift in pressure in going from point CJ to A. For times comparable to the slow reaction zone (the slow rate) and longer, the detonation runs at the CJ velocity for the fully reacted Hugoniot. Until times larger than the slow reaction zone, the states from A to CJ along the Rayleigh line appear to be part of the Taylor wave. Thus, we are looking at potential changes of 10-20 percent in the shock state for time scales of microseconds and distance scales of centimeters. This is about the size of effects seen experimentally. See page 106 of Reference 1 and References 3 and 4.

More details than are given in this section are presented in Reference 18.

## SOOT RECOVERY

To give some experimental support to the assumptions in the coagulation model and just

to understand better the soot from explosives, we have examined with several techniques the recovered soot from a variety of high explosives. We will discuss here only the early work on Comp B, a 50/50 mix of TNT/TATB, and a 50/50 mix of TNT/NQ. For more details than discussed here, see Reference 19. For our further investigations see the paper by Greiner and Hermes in this proceedings.<sup>20</sup>

We looked to these recovery experiments fully realizing the difficulties with such; the character of the soot most certainly changes on release from the high-pressure, high-temperature regime of interest to ambient. We mitigate this through the use of large containers, 1 cubic meter or larger, filled with argon. However, some observations at ambient can, with confidence, be related back to the explosive processes. For example, if we see diamond with specific characteristics, it is pretty certain these were not altered on release. But graphite can come from the release of diamond.

Our explosive charges range in size from 200 to 300 grams. After firing, the soot is scraped off the tank walls and dried. A number of analyses are then performed; we will talk here only about the transmission electron microscopy (TEM), TEM electron diffraction, x-ray diffraction, and Auger/ESCA analysis.

Let us first dispose of the diamonds. Under the TEM we see for all three samples roughly spherical particles, typically 50 Å diameter, but ranging in the extreme from 20 to 200 Å. See Figure 3. TEM electron diffraction on these particles identifies them as diamond clusters. See Figure 4. The "spotty ring" pattern indicates that the microcrystals are fairly clean of defects. The other morphology, the ribbons, is identified as turbostratic graphite, carbon black. The cluster sizes are in the same range as the diamond. Upon treatment of the soot in nitric and perchloric acids to remove the graphitic form, we recover a brown powder, 25 percent of the soot. X-ray diffraction on this powder verifies the diamond identification and the diffraction ring width gives a microcrystal size of  $\sim 40$  Å. Contemporaneous with us, Titov and his coworkers have found diamond clusters with very similar characteristics in explosive soots.<sup>21</sup>



Figure 3. Electron Micrograph of Comp B Sample, Scale 10 nm. T, graphitic ribbons; D, diamond spheroids.

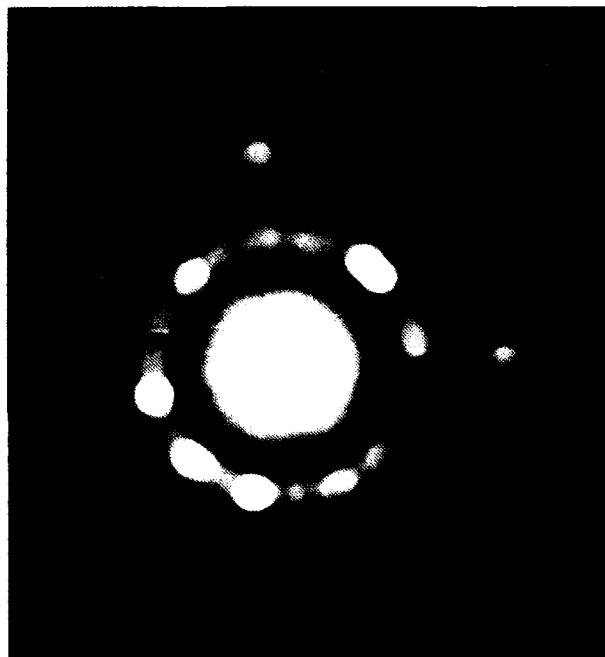


Figure 4. Electron Diffraction Pattern Showing Diamond Diffraction Rings from (111), (220), (311), (440), and (400) Weakly.

We now look at what we can learn relative to our modeling. First and most important, we see from the TEM micrographs that the soot is not bulk graphite or diamond. Even at infinite time, we have clusters with 10-20 percent of their atoms residing in the surfaces. Also, the turbostratic graphite has curved layers and the interlayer spacing is 3.5 Å, as compared to 3.35 Å for pure graphite. For early times where the carbon clusters are much smaller than our 50 Å, we cannot at all model the carbon with bulk thermodynamic thinking. For the infinite time final state, it is a good approximation, if one knows the proportion of graphitic and diamond forms, to take bulk graphite and diamond thermodynamics and correct for surface, curvature, and expansion contributions.

We have lost the use of the equilibrium phase diagram to determine whether we have graphitic or diamond phases. The surfaces shift the relative stability of the two morphologies of clusters. In fact, if one thinks of all the dangling bonds a diamond cluster will have compared to a graphitic one, one wonders why diamond forms at all. The answer must lie in the bonds being capped off by  $C \equiv N$ , or  $CO$ , or  $H$ . With Auger/ESCA analysis on the acid processed diamonds, we do see  $O$  and  $N$  atoms which disappear upon surface sputtering. Van Thiel and Ree<sup>22</sup> also use shifts in the graphite/diamond phase line to explain the detonation velocities of high carbon-content explosives. The importance and difficulty of this surface chemistry, especially for the small clusters at early time, means that simple, semi-empirical modeling is probably the best strategy.

The basic building blocks of the soot are the 50 Å "blobs." This supports our simplifying assumption of spherical clusters and the picture of annealing. We see that the larger soot structure consists of a loose collection of the "blobs," thus implying that the annealing process shuts down when the fraction of atoms in the cluster surfaces is 10-20 percent. This makes some sense if we appeal to any combination of the following mechanisms: (1) the heat from bond formation becomes too small a fraction of the total energy of a cluster; (2) the effective melting temperature for a finite cluster shifts with cluster size; (3) the kernel in



the coagulation equations<sup>18</sup> changes character as a function of cluster size; (4) the thermal fluctuations in a finite cluster are smaller on a percentage basis in larger clusters; and (5) surface tension can no longer sphericalize the clusters. Our theory from the previous section is, of course, not valid with the approximation  $K_{11} = 1$  once the annealing stops. However, this is not important for detonations because we have most of the energy out before this point.

Finally, we find that the soots contain large quantities of volatiles, say around 25 weight percent.<sup>20</sup> This makes it difficult to relate the heat of formation, as measured for the soot, to the heat of formation of pure carbon, as needed in standard modeling.

## **SLOW RATE AND HYDRODYNAMICS**

In the theory section we discussed the influence a slow carbon rate has on explosive behavior through a simple CJ model. This is a somewhat crude approach since such modeling does not really have the necessary physics to deal with the carbon chemistry. As a result, the slow rate appeared as a change in the effective CJ pressure. It is more correct to make detailed modeling of the reaction zone and look to the influence of the carbon coagulation on the reaction zone and subsequent detonation behavior.

One approach to this is to implement a slow carbon rate into the equation of state and burn models of a numerical hydrodynamic study for detonations. In particular, one should look at plate-push and interface velocity experiments. This has been done by Tang<sup>3</sup> and Tarver et al.,<sup>4</sup> independently of each other and of us. By including a slow rate, they found the agreement between experiments and calculations for TNT, HMX, and TATB nicely improved. The time scale that Tang chose for the slow reaction agrees with our estimates. We are also looking into hydrodynamic calculations to see if details beyond the zeroth order approximations done by Tang, Tarver, et al. are important. In particular, we are interested in a more physical functional form for the energy release rate.

This work of our colleagues does support our view of the place carbon occupies in

detonation behavior. The philosophies of our approaches differ; we form a microscopic picture and derive the conclusion of a slow energy release from carbon while they add an extra piece to their macroscopic hydrodynamic models and observe the consequences. The two views are complementary and supportive of each other.

## **ACKNOWLEDGMENTS**

It has been a privilege to work with the many talented people who have contributed to this research, and I thank all for allowing me to present their research in this paper. I thank especially my close colleague Sam Shaw. The other main actors are J. W. Shaner, J. M. Brown, C. A. Swenson, R. G. McQueen, J. P. Ritchie, N. R. Greiner, D. S. Phillips, F. Volk, and C. A. Vecere. I thank C. L. Mader for some of the initial push to get the project started and his continued interest and advice. We appreciate the confidence given us by L. W. Hantel and J. V. Repa. We had discussions with and work done by P. K. Tang, C. M. Tarver, B. Roof, D. Hoard, R. Lewis, D. Schiferl, R. Ryan, D. Moore, J. Erpenbeck, E. G. D. Cohen, M. H. Ernst, H. F. King, and W. S. Young. The work was sponsored by the U.S. Department of Energy and Department of the Army.

## **REFERENCES**

1. Mader, C. L., *Numerical Modeling of Detonations*, University of California Press, Berkeley, California, 1979, p. 126.
2. Green, L.; Lee, E.; Mitchell, A.; and Tarver, C., "The Supra-Compression of LX-07, LX-17, PBX-9404, and RX-26-AF and the Equations of State of the Detonation Products," *Proceedings of the Eighth Symposium (International) on Detonation*, Albuquerque Convention Center, Albuquerque, New Mexico, 15 Jul 1985, pp. 587-595.
3. Tang, P. K., "A Study of Detonation Processes in Heterogeneous High Explosives," *Journal of Applied Physics*, Vol. 63, No. 4, 1988, p. 1041.
4. Tarver, C. M.; Breithaupt, R. D.; and Kury, J. W., "Current Experimental and Theoretical Understanding of Detonation Waves in Heterogeneous Solid

- Explosives," *Proceedings of the International Symposium on Pyrotechnics and Explosives, Beijing, China, 12 Oct 1987*, pp. 692-700.
5. Ajayan, P. M. and Marks, L. D., "Quasimelting and Phases of Small Particles," *Physical Review Letters*, Vol. 60, No. 4, 1988, p. 585.
6. Brown, J. M. and McQueen, R. G., "Melting of Iron Under Core Conditions," *Geophysical Research Letters*, Vol. 7, No. 7, 1980, p. 533.
7. Brown, J. M. and Shaner, J. W., "Rarefaction Velocities in Shocked Tantalum and the High Pressure Melting Point," *Shock Waves in Condensed Matter-1983*, Santa Fe, New Mexico, 18 Jul 1983, pp. 91-94.
8. McQueen, R. G.; Fritz, J. N.; and Morris, C. E., "The Velocity of Sound Behind Strong Shock Waves in 2024 Al," *Shock Waves in Condensed Matter-1983*, Santa Fe, New Mexico, 18 Jul 1983, pp. 95-98.
9. Shaner, J. W.; Brown, J. M.; Swenson, C. A.; and McQueen, R. G., "Sound Velocity of Carbon at High Pressure," *Journal de Physique*, Vol. 45, No. 11(C8), 1984, p. 235.
10. Bundy, F. P., "Melting Point of Graphite at High Pressure: Heat of Fusion," *Science*, Vol. 137, No. 3535, 1962, p. 1056.
11. Yin, M. T. and Cohen, M. L., "Will Diamond Transform under Megabar Pressures?" *Physical Review Letters*, Vol. 50, No. 25, 1983, p. 2006.
12. Smoluchowski, M. v., "Drei Vorträge über Diffusion, Brownsche Molekularbewegung und Koagulation von Kolloidteilchen," *Physikalische Zeitschrift*, Vol. 17, No. 23, 1916, p. 585.
13. Landau, L. D. and Lifshitz, E. M., *Fluid Mechanics*, Pergamon Press Ltd., London, 1959, p. 228.
14. McQuarrie, D. A., *Statistical Mechanics*, Harper & Row, New York, 1976, pp. 440-445.
15. Hirschfelder, J. O.; Curtiss, C. F.; and Bird, R. B., *Molecular Theory of Gases and Liquids*, John Wiley & Sons, Inc., New York, 1954, pp. 634-652.
16. Bdzil, J. B., "Perturbation Methods Applied to Problems in Detonation Physics," *Proceedings of the Sixth Symposium (International) on Detonation*, Coronado, California, 24 Aug 1976, pp. 352-370.
17. Bdzil, J. B. and Davis, W. C., "Time Dependent Detonations," LA-5926-MS, Jun 1975, LASL, Los Alamos, New Mexico.
18. Shaw, M. S. and Johnson, J. D., "Carbon Clustering in Detonations," *Journal of Applied Physics*, Vol. 62, No. 5, 1987, p. 2080.
19. Greiner, N. R.; Phillips, D. S.; Johnson, J. D.; and Volk, F., "Diamonds in Detonation Soot," *Nature*, Vol. 333, No. 6172, 1988, p. 440.
20. Greiner, N. R. and Hermes, R., "Chemistry of Detonation Soot: Diamonds, Graphite, and Volatiles," *Proceedings of the Ninth Symposium (International) on Detonation*, Portland, Oregon, 28 Aug 1989.
21. Liamkin, A. I.; Petrov, E. A.; Ershov, A. P.; Sakovich, G. V.; Staver, A. M.; and Titov, V. M., "Production of Diamonds from Explosives," *Doklady Akademii Nauk USSR*, Vol. 302, No. 3, 1988, p. 611 (Russian).
22. van Thiel, M. and Ree, F. H., "Properties of Carbon Clusters in TNT Detonation Products: Graphite-Diamond Transition," *Journal of Chemical Physics*, Vol. 62, No. 5, 1987, p. 1761.

## DISCUSSION

LOUIS ZERNOW,  
Zernow Technical Services, Inc.,  
San Dimas CA

You have the information needed to provide an estimate of the average spacing of the carbon clusters in the reaction zone. It would be very informative if you could make that

estimate, even roughly, to shed light on the extent to which the carbon contributes to the conductivity in the reaction zone; even if you do it parametrically in terms of the average number of carbons in a cluster, and assume that the clusters are uniformly distributed in the reaction zone.

#### **REPLY BY J. D. JOHNSON**

Yes, we can construct a model for the conductivity in the reaction zone as a function of time using our cluster model to estimate the spacing and sizes of the carbon clusters. Some of the more difficult parts of that work would probably involve estimating the conductivity of the background fluid, computing the fraction of graphitic and diamond forms, and folding in the geometric effects of carbon spheres floating in the background fluid of other detonation products.

#### **DISCUSSION**

**FRED VOLK**, Fraunhofer Institut  
7507 Pfinztal, FRG

With regard to diamond formation, do you know how a strong confinement would work?

#### **REPLY BY J. D. JOHNSON**

We do not feel that a strong confinement would greatly influence the diamond formation. However, a big unknown in this is the influence of the containment breakup on the recovery. There would be increased turbulence and the system would not be one-dimensional.

#### **DISCUSSION**

**D. G. TASKER**, Naval Surface Warfare  
Center, Silver Spring, MD

You suggest that carbon coagulation continues for only 0.1  $\mu$ s. Our data (previous paper) could be interpreted as showing that carbon coagulation extends much further behind the detonation front ( $\sim 1$ -2  $\mu$ s). Will you comment please?

#### **REPLY BY J. D. JOHNSON**

The 0.1  $\mu$ s is the end of the reaction zone and corresponds to when we calculate that most of the energy is out of the carbon condensation. For other properties of the carbon, such as conductivity, it could be that there is still action at longer times due to the buildup of larger, fractal-like clusters with little energy release.

#### **DISCUSSION**

**B. D. LAMBOURN**, AWE(A)  
Aldermaston, England

Would more diamond be produced if detonation waves were collided head on?

#### **REPLY BY J. D. JOHNSON**

If the pressure is higher, then more diamond will be formed. This is similar to the overdriven 'TN'T' experiment described in Titov's paper. You must be careful though not to convert the diamond to graphitic forms in the recovery.

# PHASE CHANGES IN CARBON AND NITROGEN SYSTEMS: THEIR EFFECTS ON THE DETONATION PROPERTIES OF HIGH EXPLOSIVES\*

Francis H. Ree and Mat van Thiel  
Lawrence Livermore National Laboratory  
University of California, Livermore, California 94550

*The first part of this paper describes a new three-phase equation of state of condensed carbon and effective intermolecular potentials of  $N_2$ - $N_2$ ,  $N_2$ -N, and N-N pairs in fluid phase. We then examine a supercritical phase change in  $N_2$ - $H_2O$  mixtures using computer simulations and a chemical equilibrium model. The second part deals with applications to two explosives, RX-23-AB and LX-14. The calculation shows that the detonation behavior of these explosives is relatively insensitive to the dissociation of nitrogen (to 90 GPa) but sensitive to the predicted  $N_2$ - $H_2O$  phase separation. For LX-14 we predict that diamond in detonation products will melt near 70 GPa along the Hugoniot and will transform to graphite near 8.5 GPa along the Chapman-Jouguet adiabat.*

## INTRODUCTION

We are developing a theoretical model, CHEQ,<sup>1</sup> which performs a thermodynamic calculation of a multiphase, multicomponent system using the established principles of statistical mechanics, intermolecular potentials derived from shock wave experiments, *ab initio* quantum mechanical calculations and a mixture model. The main purpose for undertaking such a task is to achieve a comprehensive understanding of the behavior of explosives well enough to predict how much energy and momentum they can deliver for practical uses. This approach has been reasonably successful in calculating the Chapman-Jouguet (C-J) pressures and detonation velocities of several explosives.<sup>2,3</sup>

When we started the work on explosives reported in References 1 to 3, there was little recognition of the importance related to liquid carbon, especially of the melting line of diamond. Hence, the liquid carbon was not

included in our explosives calculations. Although the information is still scarce, more experimental<sup>4</sup> and theoretical<sup>5,6</sup> information has been collected about condensed phases of carbon now. Therefore, we decided to construct a physically reasonable equation of state (EOS) of graphite-diamond-liquid carbon using a rather elaborate Mie-Grüneisen model. The model<sup>7</sup> is now implemented in CHEQ. In this paper we will describe the model and use it in explosive calculations.

Another major detonation product of interest is nitrogen. The Livermore shock wave experiments<sup>8,9</sup> have revealed that some doubly shocked data for liquid nitrogen lie above the singly shocked data in pressure (P) - volume (V) space. In addition to this rather unusual behavior, the principal Hugoniot displays a dramatic increase in the compressibility near 30 GPa, collapsing to densities that are more typical of stiffer monatomic fluids. This unusual behavior is believed to be due to the shock induced dissociation of molecular nitrogen.<sup>10,11</sup> We have used the CHEQ code to extract specific interaction potentials for N-N,  $N_2$ -N, and  $N_2$ - $N_2$  pairs from the shock wave data of nitrogen. This analysis, for the

\*Work performed under the auspices of the U.S. Department of Energy by the Lawrence Livermore National Laboratory under contract number W-7405 ENG 48.

first time, provided the N-N interatomic potential, which is useful in interpreting overdriven Hugoniot data of high explosives.

One interesting result related to the nitrogen problem mentioned above is a CHEQ prediction<sup>2</sup> of an H<sub>2</sub>O-N<sub>2</sub> phase separation at a high temperature (T) along either the Hugoniot or the C-J adiabat. We have examined the predicted phase separation by using a Monte Carlo simulation and also by a theoretical calculation of an explosive, RX-23-AB, whose detonation products consist principally of N<sub>2</sub> and H<sub>2</sub>O. The present paper will compare theoretical Hugoniots of RX-23-AB with and without the phase separation to demonstrate the importance of this phase separation.

Next, we have made systematic CHEQ calculations for LX-14 to investigate the influence of the carbon phase changes, nitrogen dissociation, and the N<sub>2</sub>-H<sub>2</sub>O phase separation. The new data bases clearly show the shape of the boundaries at the phase changes which may be subjected to an experimental verification. Explosive calculations based on the old and new LX-14 EOS show small but noticeable differences between the two. The origins of the observed differences will be examined in order to refine the predictive power of the CHEQ code.

## CONDENSED-PHASE EOS OF CARBON

We have developed a high-T and high-P three-phase EOS model for the system, graphite-diamond-liquid carbon.<sup>7</sup> Such a model is needed, since both the graphite-diamond transition and melting affect the mixture EOS in regions important to the detonating behavior of high explosives.

The solid portion of this model describes both graphite and diamond with the Grüneisen model,

$$P(V,T) = P(V,T=0) + (\gamma/V)\delta E_n + \delta P_{el}, \quad (1)$$

where the electronic thermal correction,  $\delta P_{el}$ , is computed from the usual asymptotic form.

For diamond, the 0 K isotherm,  $P(V,T=0)$ , is given by the Birch equation (with parameters fit to first-principle's calculations),

the Grüneisen  $\gamma$  by  $\gamma_0(V/V_0)$  ( $V_0 = V$  at  $P=0$  and 0 K), and the nuclear thermal energy  $\delta E_n$  by the Einstein model, with the Einstein  $\theta$  obtained by integrating  $\gamma = -d(\ln\theta)/d\ln V$ . For graphite, we modify  $\gamma$  by

$$\gamma(V) = \gamma_0(V/V_0)\{1 + a_1[1 + \tanh((V-V_1)/b_1)] + a_2[1 + \tanh((V_2-V)/b_2)]\}. \quad (2)$$

where parameters,  $a_1$ ,  $b_1$ , and  $V_1$  are adjusted to fit experimental shock wave and atmospheric expansion data. We also modify the Birch equation (normalized to shock data) by multiplying by a factor,  $1/2[(V/V_0)^2 + (V_0/V)^2]$ , for  $V \geq V_0$ . Both modifications are necessary to explain the positive slope of the graphite low-P melting line, which implies a rapidly increasing expansion coefficient between 3000 K and the melting point at 1 atm. The Gibbs free energy is then calculated by numerically integrating  $VdP$  from Equation (1).

We fix the melting line with the Lindemann law and then extend our model to the liquid state by using the Grover scaling model.<sup>12</sup> The Grover model applies the solid EOS to the liquid phase with a modified heat capacity which is a universal function of a reduced temperature, i.e., the ratio of temperature to the melting temperature at fixed volume. The electronic correction in Equation (1) is included using the *ab initio* atom-in-cell model for the diamond-like liquid and the low-temperature heat-capacity expression for the graphite-like liquid. The liquid phase now consists of diamond- and graphite-like liquids, each with its own Gibbs free energy, i.e.,  $G_d$  for diamond-like and  $G_g$  for graphite-like liquids. The single liquid phase is constructed by treating the liquid as a solution of a binary mixture of the graphite- and diamond-like liquids with the Gibbs free energy,

$$G = xG_d + (1-x)G_g + RT[x\ln x + (1-x)\ln(1-x)] + A(P)x(1-x), \quad (3)$$

where  $x$  is the mole fraction of the diamond-like liquid. The pressure-dependent non-ideal mixing correction,  $A(P)$ , is chosen to satisfy constraints: (1) the slope  $dP_m/dT$  of the graphite-liquid melting line is negative above the midway point between the graphite-liquid-gas and graphite-liquid-diamond triple points, and (2) no artificial phase separation between

the diamond- and graphite-like liquids occurs in the liquid phase at any (P,T) value of practical interest. The diamond- and graphite-like forms are the principal structural fluctuations in the liquid. Their probabilities of occurrence are represented by the composition variable (x) that minimizes the Gibbs free energy of the single fluid phase. The shape of the graphite-diamond melting line offers the most severe constraint for this model. The resulting theoretical model fits available high-pressure and high-temperature static and dynamic data, including the phase diagram, within experimental uncertainty.

The EOS surface of carbon based on the above model is shown in Figure 1. The phase boundaries in Figure 1 fit the known information within experimental uncertainty. It also shows two Hugoniot (thick solid lines) and release adiabats (dashed lines) starting from each Hugoniot near the melting line. We note that the melting line and the adiabats almost parallel each other. The principal improvement in this work is in the melting properties and electronic correction. The negative slope of the graphite melting line (not shown in Figure 1) above 7 GPa, which is also reproduced by the present model, is due to the increasing tetrahedral character of the atomic configurations in liquid with increasing pressure.

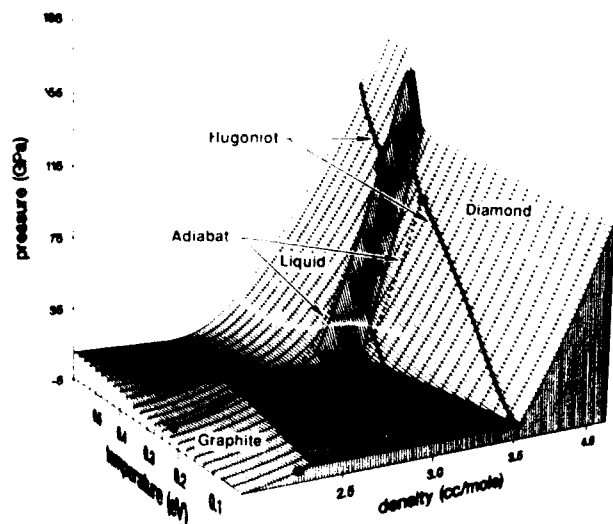


Figure 1. Three-Phase Carbon EOS Surface, Superimposed with Theoretical Hugoniots and Adiabatic Expansion Paths

## INTERACTION POTENTIALS OF NITROGEN

As mentioned earlier, the experimental shock wave data<sup>8,9</sup> of nitrogen indicate dissociation of molecular nitrogen,



Hence, the shock wave data present us with an opportunity to infer the very dissimilar N-N, N<sub>2</sub>-N<sub>2</sub>, and N<sub>2</sub>-N interaction potentials in a nonideal mixture at high pressure and temperature. We should emphasize at the outset that the pair potentials obtained in this work are effective potentials which contain average contributions of many-body forces and electronic effects.

The CHEQ calculations<sup>11</sup> evaluate the equilibrium composition of the N-N<sub>2</sub> mixture by minimizing the Gibbs free energy (G) with respect to their concentrations at fixed temperature and pressure, i.e.,

$$G(P, T, \{n_i\}) = \mu_N(P, T, \{n_i\})n_N + \mu_{\text{N}_2}(P, T, \{n_i\})n_{\text{N}_2}, \quad (5)$$

where  $\mu_i$  and  $n_i$  are the chemical potentials and molar concentrations of the monatomic and diatomic nitrogen components ( $i = \text{N}$  and  $\text{N}_2$ ). The calculation is based on Ross's free energy expression<sup>13</sup> and an improved one-fluid mixture model,<sup>14</sup> which assumes molecules to interact with exponential-6 (exp-6) potentials,

$$\phi(r) = \epsilon/(\alpha-6)[6e^{\alpha(1-r/r^*)} - \alpha(r^*/r)^6], \quad (6)$$

where parameters  $\epsilon$ ,  $r^*$ , and  $\alpha$  are the energy and distance scaling parameters and the stiffness of the repulsion, respectively.

This procedure requires a knowledge of separate interaction potentials between each of the different species. The present work uses Ross's N<sub>2</sub>-N<sub>2</sub> parameters<sup>10</sup> and the N<sub>2</sub>-N parameters given by a modified Lorentz-Berthelot combination rule,

$$\begin{aligned} r_{ij}^* &= k_{ij}(r_{ii}^* + r_{jj}^*)/2, \\ \epsilon_{ij} &= \sqrt{\epsilon_{ii}\epsilon_{jj}} \\ \alpha_{ij} &= \sqrt{\alpha_{ii}\alpha_{jj}} \end{aligned} \quad (7)$$

where parameter  $k_{ij}$  is introduced to favor one component over another in Equation (5).

In the case of the N-N parameters, we found that two sets of parameters, with different physical characteristics, can describe experimental shock wave data. The first set was obtained by fitting first-principle, quantum-mechanical data for several crystal structures of monatomic nitrogen. It is characterized by a small  $\alpha$  ( $\approx 8.92$  to  $9.75$ ) and a large  $\epsilon/k$  ( $\approx 4400$  K to  $5600$  K). This set predicts that the shock dissociation can accompany a first-order phase change. The predicted first-order phase change suggests a physical change at the atomistic level for a van der Waals-type to a metallic or semi-metallic interaction. The explosive calculations in this paper will not use this set, since we need future and more definitive shock wave experiments to either confirm or rule out this new and rather "provocative" possibility.

Instead, the present calculations will use the second set of the exp-6 parameters. This set ( $\epsilon/k = 600$  K,  $r^* = 2.39$  Å,  $\alpha = 10$ , and  $k_{ij} = 0.9$ ) was obtained by fitting the experimental P-V data of singly shocked nitrogen, and also requiring the set to approximately describe the high-P quantum-mechanical solid calculations. The second set is fundamentally different from the first, in that it has a large  $\alpha$  and a small  $\epsilon$  and produces a continuous shock dissociation without thermodynamic phase change. Having chosen the N-N parameters in this manner, we tested their suitability by making theoretical calculations on the independent experimental data, i.e., singly shocked P-T and doubly shocked P-V results. As an illustration, we show in Figure 2 a comparison between the experimental and theoretical doubly-shocked P-V data. We note that the nonreactive doubly-shocked Hugoniot agree with the experimental data (open triangle) for a low initial pressure (19.9 GPa), while the reactive results agree better with experimental data (solid triangle) for a larger initial pressure (38.6 GPa). Similar trends are also seen in the doubly shocked P vs. T plots (not shown here).

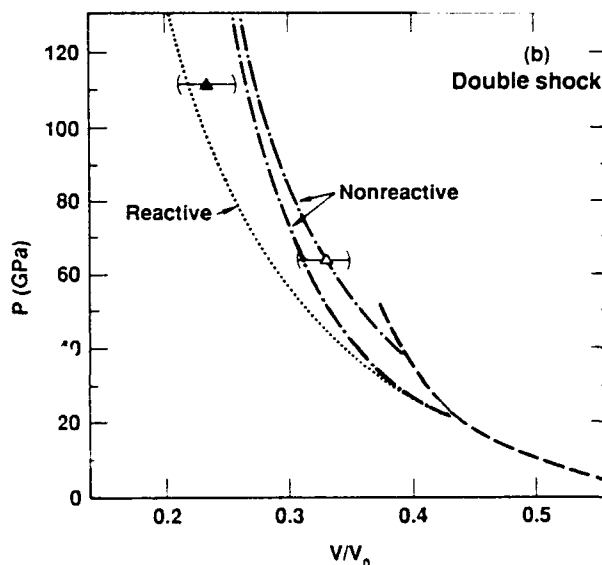


Figure 2. Doubly-Shocked Hugoniot of Nitrogen Assuming the Dissociation Reaction (Dotted Line) and No Dissociation (Dash-Dotted) Starting from the Singly-Shocked Hugoniot (Dashed Line). Solid and Open Triangles are the experimental data (Reference 8) with initial states at 38.6 and 19.9 GPa, respectively.

## GAS-GAS PHASE SEPARATION: EFFECTS ON DETONATION PROPERTIES

This section elaborates our earlier work<sup>2</sup> which indicated that the supercritical phase separation of  $N_2$ - $H_2O$  mixtures can affect the detonation properties of PBX-9404. To avoid a complexity associated with explosives products, we first carry out a simplified study of phase equilibria in  $N_2$ - $H_2O$  mixtures.

In this study an orientation-dependence in the  $H_2O$ - $H_2O$  interaction is approximated by a T-dependent attractive well-depth,

$$\epsilon(H_2O-H_2O) = \epsilon_0(1 + \lambda/T), \quad (8)$$

where parameters,  $\epsilon_0$  and  $\lambda$ , as well as other exp-6 parameters for the  $H_2O$ - $H_2O$  and  $N_2$ - $N_2$  interactions are the same as those used in Reference 2. Our recent study of hydrogen fluoride,<sup>16</sup> which has equally strong hydrogen bonds, showed that an approximation such as Equation (8) is reasonably satisfactory to describe the P-V Hugoniot above 25 GPa, but overestimates the Hugoniot pressure below 25 GPa.

The  $N_2$ - $H_2O$  parameters are determined from Equation (7) with parameter  $k_{ij} = 1.03$ . An earlier calculation of PBX-9404 with this choice of  $k_{ij}$  showed that one can place the C-J point in either the mixed or homogenous phase by a slight modification (3 percent to 3.5 percent) of the  $N_2$ - $H_2O$  parameters. In reality, all three ( $r_{ij}^*$ ,  $\epsilon_{ij}$ ,  $a_{ij}$ ) parameters should be altered. But, without knowing much about the  $N_2$ - $H_2O$  interaction in the extreme (P,T) state under consideration, we felt it sensible to modify only the  $r^*(N_2-H_2O)$ , to which detonation properties are the most sensitive. In the future, when experimental data on mixtures become available at high pressures and temperatures, this arbitrary procedure needs to be improved. In this regard, we should maintain an open mind toward all different sorts of combination rules including Equation (7) which is actually based on interactions between an isolated pair of molecules. In the case of dilute rare gases, Scoles<sup>17</sup> estimates uncertainties of about 1.5 percent and 3 percent for the unlike interaction parameters  $r_{ij}^*$  and  $\epsilon_{ij}$ .

Figure 3 shows a CHEQ isotherm (solid line) for an equimolar mixture of  $N_2$  and  $H_2O$  at 4000 K. It also shows two other isotherms, one representing a complete phase separation (dashed line; additive-volume model) and another without phase separation (dotted line), the latter based on the effective one-component parameters derived from the exp-6 parameters used in the former. The phase separation first becomes noticeable at about 14 GPa and is nearly complete at about 35 GPa. The choice of parameter  $k_{ij} = 1.03$  facilitates the phase separation. To check this prediction, we have carried out Monte Carlo (MC) simulations. The MC data<sup>18</sup> for a perfectly miscible  $N_2$ - $H_2O$  mixture is shown by open circles (the effective one-component exp-6 parameters) and the corresponding two-component simulations (which allow a possible demixing of a  $N_2$ -rich and a  $N_2$ -poor phases) by solid circles. The MC data are obtained by averaging nearly  $5 \times 10^6$  MC steps. In spite of the large computational time required in the calculations, the system-size (500 particles total) considered here is not large enough, since the computed data would be affected (probably noticeably) by surface effects present in boundaries of the phase separating mixtures. In view of this, the

reasonable agreement between theory and simulation in Figure 3 reinforces the prediction on the phase separation. Moreover, the first nearest-neighbor peak in the MC  $N_2$ - $H_2O$  pair distribution function lies distinctly below that of the like-neighbor pairs, indicating a possible structural change in phase separating mixtures.<sup>18</sup>

Since the (P,T) range in Figure 3 is relevant to detonation problems, we expect such a phase separation, if it indeed occurs, would profoundly affect the detonation behavior of many condensed explosives. The best condensed explosive to check this possibility is RX-23-AB.<sup>19</sup> Its manufacturing process involves dissolving hydrazine ( $H_4N_2$ ) in hydrazine nitrate ( $H_5N_3O_3$ ) and further dilution with water in the ratio of  $H_4N_2:H_5N_3O_3:H_2O = 0.1841:0.7364:1.3378$ . This composition will essentially produce a stoichiometric mixture of  $N_2$  and  $H_2O$  as detonation products. Experimental measurements of detonation properties of RX-23-AB are currently in various stages of development at Livermore.<sup>20</sup>

In connection with the anticipated experiments, we computed theoretical Hugoniot of R-23-AB. Figure 4 shows two Hugoniot which employ the multiplier  $k_{ij}$  for  $r^*(N_2-H_2O)$  set to 1 and 1.03, respectively, but allowing the phase separation. Comparison of the two Hugoniot shows that the shock velocities depend weakly on the interaction potentials.

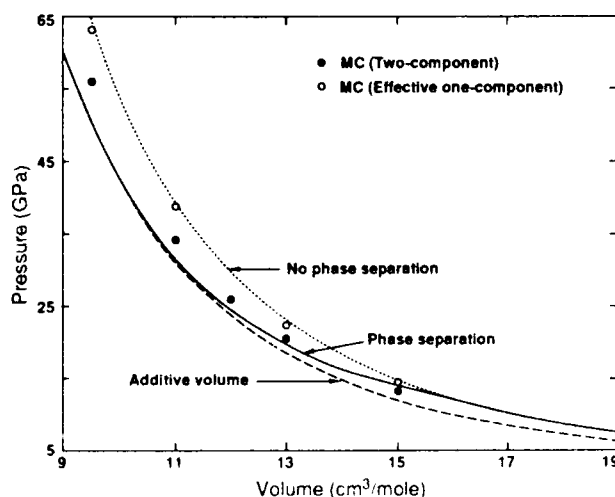


Figure 3. Isotherms of an Equimolar Mixture of an  $N_2$ - $H_2O$  Mixture at 4000 K



In comparison, if the phase separation is prohibited, the resulting shock velocities are much higher. Table 1 compares the C-J data with the experimental values in Reference 19. The relatively high detonation velocity of the single phase material seems to imply the need for the phase change. The difference in detonation velocities with and without the phase change is large and should be easily detectable in a dynamic experiment. The high experimental temperature in Table 1 has previously been questioned<sup>19</sup> and needs to be remeasured. This is also the case for the other experimental C-J data in Table 1 and Figure 4, since the samples used in the experiment

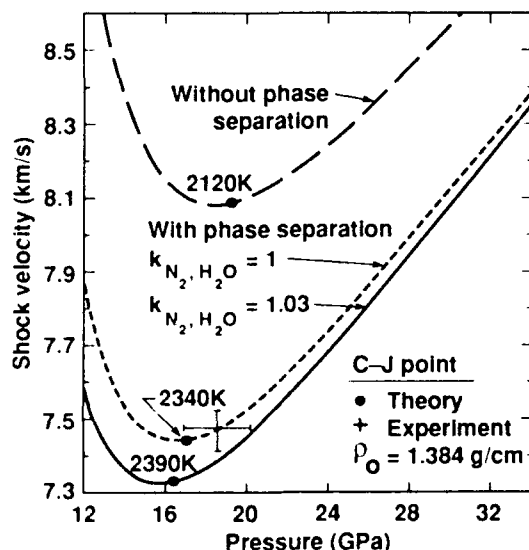


Figure 4. Hugoniot of RX-23-AB Computed With and Without the  $N_2$ - $H_2O$  Phase Separation as described in the Text. The experimental C-J data is from Reference 19.

apparently were contaminated by carbon impurities.<sup>20</sup> The presence of the impurities is significant, because differences between the two computed shock velocities (i.e.,  $k_{ij} = 1$  and 1.03 with the phase separation) in Table 1 differ by about 1 percent. The present calculations also differ from those made previously<sup>21</sup> in that additional species have been allowed to form. Near the C-J point, the number of moles of detonation products produced from 100 grams of RX-23-AB are  $H_2: O_2: H_2O: N_2: NO: NH_3: N = 2.5 \times 10^{-5}: 2.6 \times 10^{-5}: 3.546: 1.289: 3.2 \times 10^{-4}: 2.31 \times 10^{-4}: 9.7 \times 10^{-8}$ . It is clear that the additional species have little effect on the mixture. The principal difference is the result of allowing the phase change to occur. At the C-J point, 99.3 percent and 98.5 percent of  $H_2O$  and  $N_2$  are in separate phases, respectively.

## NEW EOS OF LX-14

LX-14 is a HMX-based explosive with the composition  $C:H:N:O = 1.52:2.92:2.59:2.66$  in moles per 100 g. At the Eighth Symposium on Detonation, we reported a CHEQ/EOS calculation of LX-14.<sup>22</sup> In the present work, this calculation is refined, incorporating new computational and theoretical features, some of which have been described in the previous sections.

Specifically, the new features are:

- (1) dissociation reaction:  $N_2 \rightleftharpoons 2N$
- (2) liquid carbon

Table 1. Chapman-Jouguet Data of Rx-23-AB ( $\rho_0 = 1.384 \text{ g/cm}^3$  and  $\Delta H_f = -5860 \text{ J/kg}$ ). Theoretical data are computed with and without the  $N_2$ - $H_2O$  phase separation and with  $k_{ij}$  [Equation (7)] = 1.03 and 1 for the  $N_2$ - $H_2O$  interaction.

C J	Experiment (Reference 19 & 21)	Phase Separation		No Phase Separation $k_{ij} = 1.03$
		$k_{ij} = 1.03$	$k_{ij} = 1$	
D (km/s)	7.48	7.33	7.44	8.08
P (GPa)	18.6	15.83	16.41	18.39
T (K)	4000	2390	2340	2120
$\rho$ (g/cm <sup>3</sup> )	1.82	1.76	1.76	1.74

- (3) thermal contributions ( $T > 0$ ) to the EOS of graphite and diamond
- (4) the same number of gaseous species allowed in  $N_2$ -rich and  $N_2$ -poor phases
- (5) use of  $\alpha = 13.2$  for  $N_2$ - $N_2$  exp-6 parameter<sup>10</sup> (vs. 13 for the old EOS)
- (6) speed-up of the CHEQ code.<sup>23</sup>

Item (6) deals with an approximately three-fold increase in the computational speed of CHEQ.<sup>23</sup> It was brought about by making a timing study in each subroutine and modifying a part of the code to analytically evaluate  $P$  and  $E$ . Such a speed-up significantly reduced the computation time required in items (1) to (5) above. Hence, in item (4) we were able to consider ten gaseous species ( $H_2$ ,  $CH_4$ ,  $O_2$ ,  $CO_2$ ,  $H_2O$ ,  $N_2$ ,  $CO$ ,  $N$ ,  $NO$ , and  $NH_3$ ) in both  $N_2$ -rich and  $N_2$ -poor gaseous phases. Thus, the calculations consider a total number of 23 species, i.e., 10 species each in the two gas phases and 3 condensed phases of carbon. In comparison, the old calculation was done with 13 species, including only  $N_2$  and  $H_2O$  in the  $N_2$ -rich phase.

Figure 5 shows the resulting  $P$ - $\rho$ - $T$  surface of the LX-14. The construction of the EOS surface required CHEQ calculations over 2000 ( $P, T$ ) points and took more than 20 hours of Cray XMP time. We have indicated in

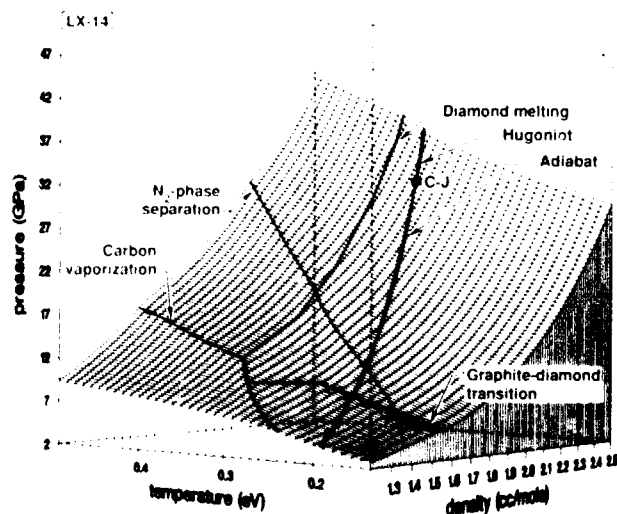


Figure 5.  $P$ - $\rho$ - $T$  EOS Surface of LX-14, Superimposed with the C-J Expansion Adiabatic and Hugoniot.

Figure 5 the boundaries of various thermodynamic phase changes described in the previous sections. Figure 5 also shows the loci of the C-J expansion adiabat and the over-driven Hugoniot.

The dissociation of nitrogen is negligible (0.02 mole percent or less in the two gaseous phases) at the C-J point. Its mole fraction in the  $N_2$ -rich phase increases to 4.4 percent at 89 GPa (5400 K) along the Hugoniot. The Hugoniot of LX-14 enters into the liquid carbon phase at  $P \approx 67$  GPa and  $T \approx 4800$  K. In our earlier work on another HMX-based explosive, PBX-9404,<sup>2</sup> we noted that its experimental shock data show a softening at pressure above 65 GPa and temperatures above 4500 K.<sup>2</sup> The present calculation suggests that the softening could be due to the melting of diamond clusters present in detonation products of PBX-9404. The softening will be further facilitated by small but non-negligible dissociation of  $N_2$  molecules, as predicted by the present calculation.

The expansion adiabat below the C-J point crosses the  $N_2$ -phase boundary at a relatively low pressure ( $\approx 11.5$  GPa or 2900 K). Another noteworthy feature in Figure 5 is that the  $N_2$ -phase separation occurs gradually over an extended pressure range. Consequently, the new EOS surface has a much smoother appearance than the one obtained in the previous work.<sup>22</sup> At  $P \approx 8.5$  GPa and  $T \approx 2700$  K, the C-J adiabat crosses the diamond-graphite phase line. With the improved accuracy of experimental Fabry-Perot velocimeter data, it may be possible to detect either the predicted  $N_2$ -phase separation boundary or the graphite-diamond phase boundary.

Table 2 shows a comparison of the experimental<sup>24</sup> and theoretical C-J data of LX-14. The new EOS gives the detonation velocity ( $D_{CJ}$ ) of 8.95 km/s, which is 1.8 percent above the experimental value. In contrast,  $D_{CJ}$  of the old EOS agreed almost exactly with the experimental  $D_{CJ}$ . It is worthwhile to note that the  $N_2$ -rich phase in the new EOS contains non-negligible amounts of  $CO_2$ ,  $CO$ , and  $H_2O$  at the C-J point. Their mole percentages are  $N_2:CO_2:CO:H_2O = 86.9\%:8.1\%:1.9\%:1.9\%$ . Such a mixture tends to produce a stiffer

Table 2. Chapman-Jouguet Data of LX-14 ( $\rho_0 = 1.835 \text{ g/cm}^3$  and  $\Delta H_f = 62.8 \text{ kJ/kg}$ ). Theoretical data are computed with Different Values of  $k_{ij}$  [Equation (7)] for the  $\text{N}_2\text{-H}_2\text{O}$  and  $\text{CO}_2\text{-H}_2\text{O}$  Interactions. The old calculation is from Reference 22.

C J	Experiment (Reference 24)	Theory	New		Old
		$k(\text{N}_2\text{-H}_2\text{O}):$ $k(\text{CO}_2\text{-H}_2\text{O}):$	1.03	1.00	1.03
			0.965	1.00	0.965
D (km/s)	8.79		8.95	9.32	8.78
P (GPa)			33.2	35.5	32.3
T (K)			3960	3860	4070
$\rho$ ( $\text{g/cm}^3$ )			2.37	2.36	2.38

Hugoniot. A slightly high  $D_{CJ}$  predicted from the new EOS is probably related to this fact. In contrast, the old EOS does not consider  $\text{CO}_2$  and  $\text{CO}$  in the  $\text{N}_2$ -rich phase. Table 2 also shows that the use of the conventional Lorentz-Berthelot rule (i.e.,  $k_{ij} = 1$  for both  $\text{N}_2\text{-H}_2\text{O}$  and  $\text{CO}_2\text{-H}_2\text{O}$  interactions) considerably overestimates the experimental  $D_{CJ}$  data. The reason lies in the use of  $k_{ij} = 1$ , which favors a miscible gaseous phase instead of the  $\text{N}_2$ -phase separation.

## CONCLUDING REMARKS

The ultimate goal of carrying out a research program, such as presented here, is to separate out what equilibrium and kinetic effects are important to dynamic phenomena behind a detonation front. The present effort is a prerequisite to this goal, i.e., to perform an unambiguous theoretical calculation that assumes thermodynamic equilibrium. Only when this becomes possible, one would expect to know whether time dependent factors influence the post detonation behavior.

Our most recent effort described here has revealed the significance of various physical changes (i.e.,  $\text{N}_2$  dissociation,  $\text{N}_2\text{-H}_2\text{O}$  phase separation, and phase transitions in carbon) to the detonation behavior of explosives. Nonetheless, we should stress the tentative nature of the predictions made here. Areas of importance for improving the predictive power of our theoretical approach are: (1) unlike pair interactions, (2) fluid fluid and fluid solid phase separation kinetics, and (3) carbon clustering mechanisms.

All these subjects require a close collaboration between theoretical and experimental efforts. On the theoretical side, we suggest detailed *ab initio* calculations of quantum mechanical  $\text{HF-HF}$ ,  $\text{HF-N}_2$ , and  $\text{HF-CO}_2$  potentials. The choice of hydrogen fluoride ( $\text{HF}$ ) for a polar component would be suitable for this purpose because of its simple shape, strong tendency to form hydrogen bonds, and occurrence in detonation products of explosives with fluorine containing binders. We also need similar knowledge on interactions in condensed phases of carbon. The resulting interaction potentials may be used in molecular dynamics simulations to investigate items (2) and (3). Related to these subjects and also to the present work are two papers presented in this Symposium, i.e., Byers Brown and Braithwaite's investigation<sup>25</sup> on polar-polar interactions and Kerley's Monte Carlo study<sup>26</sup> of  $\text{N}_2\text{-H}_2\text{O}$  mixture. Interested readers should refer to these articles. In tandem with theoretical studies, similar efforts are desired on the experimental side. We need both dynamic data (on RX-23 AB,  $\text{N}_2\text{-H}_2\text{O}$  mixtures, and liquid  $\text{HF}$ ) and static data using a heated diamond-anvil-cell (on  $\text{N}_2\text{-H}_2\text{O}$  mixtures). Some of these studies are currently in various stages of development at Livermore.

## REFERENCES

1. Ree, F. H., "A Statical Mechanical Theory of Chemically Reacting Multiphase Mixtures: Application to the Detonation Properties of PETN," *J. Chem. Phys.*, Vol. 81, 1984, pp. 1251-1263.

2. Ree, F. H., "Supercritical Fluid Phase Separations: Implications for Detonation Properties of Condensed Explosives," *J. Chem. Phys.*, Vol. 84, 1986 pp. 5845-5856.
3. Van Thiel, M. and Ree, F. H., "Properties of Carbon Clusters in TNT Detonation Products: Graphite-Diamond Transition," *J. Appl. Phys.*, Vol. 62, 1987, pp. 1761-1767.
4. Shaner, J. W.; Brown, J. M.; Swensor, C. A.; and McQueen, R. G., "Sound Velocity of Carbon at High Pressures," *J. de Phys.*, Vol. 45 (Suppl.), 1984, pp. C8-235-C8-238.
5. Fahy, S.; Louie, S. G.; and Cohen, M. L., "Pseudopotential Total-Energy Study of the Transition from Rhombohedral Graphite to Diamond," *Phys. Rev. B*, Vol. 34, 1986, pp. 1191-1199.
6. Fahy, S. and Louie, S. G., "High Pressure Structural and Electronic Properties of Carbon," *Phys. Rev. B*, Vol. 36, 1987, pp. 3373-3385.
7. Van Thiel, M. and Ree, F. H., "Theoretical Description of the Graphite, Diamond, and Liquid Phases of Carbon," *J. Thermophysics*, Vol. 10, 1989, pp. 227-236.
8. Nellis, W. J.; Holmes, N. C.; Mitchell, A. C.; and van Thiel, M., "Phase Transition in Fluid Nitrogen at High Densities and Temperatures," *Phys. Rev. Lett.*, Vol. 53, 1984, pp. 1661-1664.
9. Radousky, H. B.; Nellis, W. J.; Ross, M.; Hamilton, D. C.; and Mitchell, A. C., "Molecular Dissociation and Shock-Induced Cooling in Fluid Nitrogen at High Densities and Temperatures," *Phys. Rev. Lett.*, Vol. 57, 1986, pp. 2419-2422.
10. Ross, M., "The Dissociation of Dense Liquid Nitrogen," *J. Chem. Phys.*, Vol. 86, 1987, pp. 7110-7118.
11. Hamilton, D. C. and Ree, F. H., "Chemical Equilibrium Calculations on the Molecular to Nonmolecular Transition of Shock Compressed Liquid Nitrogen," *J. Chem. Phys.*, Vol. 90, 1989, pp. 4972-4981.
12. Grover, R., "High-Temperature Equation of State for Simple Metals," *Proceedings of Seventh Symposium on Thermophysical Properties*, Cezairliyan, Ed., Am. Soc. Mech. Eng., New York, 1977, pp. 67-74.
13. Ross, M., "A High-Density Fluid Perturbation Theory Based on an Inverse 12th-Power Reference System," *J. Chem. Phys.*, Vol. 71, 1979, pp. 1567-1571.
14. Ree, F. H., "Simple Mixing Rule for Mixtures with Exp-6 Interactions," *J. Chem. Phys.*, Vol. 78, 1983, pp. 409-415.
15. Ross, M. and Ree, F. H., "Repulsive Forces of Simple Molecules and Mixtures at High Density and Temperature," *J. Chem. Phys.*, Vol. 73, 1980, pp. 6146-6152.
16. Ree, F. H. and Calef, D. F., "Theoretical Hugoniot of Liquid Hydrogen Fluoride," to appear in *Proceedings of the Sixth APS Conference on Shock Waves in Condensed Matter*, Lawrence Livermore National Laboratory Report UCRL-101434 (1989).
17. Scoles, G., "Two-Body, Spherical, Atom-Atom, and Atom-Molecule Interaction Energies," in *Annu. Rev. Phys. Chem.*, Vol. 31, B. S. Rabinovitch, Ed., Annu. Rev. Inc., Palo Alto, 1981, pp. 81-96.
18. Ree, F. H., 1989, (to be published).
19. Finger, M.; Lee, E.; Helm, F. H.; Hayes, B.; Hornig, H.; McGuire, R.; and Kahara, M., "The Effect of Elemental Composition on the Detonation Behavior of Explosives," *Proceedings of the Sixth Symposium on Detonation*, D. J. Edwards, Ed. (Office of Naval Research, Dept. of the Navy, 1976), pp. 710-722.
20. Simpson, R. 1989, Private communication.
21. Urtiew, P., "Brightness Temperature of Detonation Wave in Liquid Explosives," *Acta Astronautica*, Vol. 3, pp. 555-566.
22. Ree, F. H. and van Thiel, M., "Detonation Behavior of LX 14 and PBX-9404: Theoretical Aspect," *Proceedings of the Eighth Symposium on Detonation*, J. M. Short, Ed., Albuquerque Convention

- Center, Albuquerque, NM, 15 Jul 1985, pp. 501-511.
23. Calef, D. F.; Nichols, A.; and Ree, F. H., Unpublished results.
24. Lee, E.; Breithaupt, D.; McMillan, C.; Parker, N.; Chau, H.; Quirk, W.; Urtiew, P.; and Walton, J., "The Motion of Thin Metal Walls and the Equation of State of Detonation Products," *Proceedings of the Eighth Symposium on Detonation*, J. M. Short, Ed., Albuquerque Convention Center, Albuquerque, NM, 15 Jul 1985, pp. 613-624.
25. Brown, W. Byers and Braithwaite, M., "Sensitivities of Adiabatic and Gruneisen Gammas to Errors in Molecular Properties of Detonation Products," *Proceedings of the Ninth Symposium (International) on Detonation*, Portland, OR, 28 Aug-1 Sep 1989.
26. Kerley, G. I., "Theoretical Model of Explosive Detonation Products: Test and Sensitivity Studies," *Proceedings of the Ninth Symposium (International) on Detonation*, Portland, OR, 28 Aug-1 Sep 1989.

# THE DETONATION PARAMETERS OF NEW POWERFUL EXPLOSIVE COMPOUNDS PREDICTED WITH A REVISED VLW EQUATION OF STATE\*

Wu Xiong, Sun Jian, and Xiao Lianjie  
Xian Modern Chemistry Research Institute  
Xian 710061, CHINA

*Some new target explosive compounds whose detonation performance significantly exceeds that of HMX have been predicted with the revised VLW equation of state, which includes up to the fifth viral term. Either of the intermolecular potential EXP-6 or Lennard-Jones 6-12 may be available. A comprehensive criterion, based on the specific kinetic energy of detonation products  $\frac{1}{2}u^2$ , is proposed to assess the detonation performance of explosives.*

## INTRODUCTION

The world is developing and science and technology is advancing. But the field of synthesis of high explosive compounds has remained mostly at a standstill. In spite of 40 years of effort and a great deal of cost an acceptable high energy explosive whose detonation performance significantly exceeds that of HMX has not been produced yet. What is the correct direction and what efforts should be emphasized in future explosive research?

In our opinion, first, the predicting ability by means of an equation of state (EOS) of detonation products should be improved. Second, a reliable method of evaluating the detonation performance especially for new powerful explosive compounds should be developed and, third, we need to develop a class of target compounds to be worth synthesizing as more powerful explosives. For these purposes, we carried out the investigations described below.

## VLW EOS

Our VLW EOS, which was presented at the Eighth Symposium on Detonation in

1985,<sup>1</sup> was based on both the viral theorem and Lennard-Jones potential. It is given by

$$\frac{PV}{RT} = 1 + B^* \left( \frac{b_0}{v} \right) + \frac{B^*}{\bar{T}^{*1/4}} \sum_{n=3}^m (n-2)^{-n} \left( \frac{b_0}{v} \right)^{(n-1)} \quad (1)$$

where

$$\bar{T}^* = \sum_{i,j} x_i x_j T_{ij}^* / \bar{X}; T_{ij}^* = (T_i^* T_j^*)^{1/2}; \bar{X} = \sum_i x_i$$

$$(b_0)_1 = \frac{2}{3} n N_0^3; T^* = \frac{KT}{\epsilon}; m = 4;$$

$$B^*(T^*) = \sum_{j=0}^{\infty} \left[ -\frac{2^{j+1/2}}{4j!} \Gamma\left(\frac{j}{2} - \frac{1}{4}\right) \right]$$

$$T^{*-(2j+1)/4}$$

In this paper, we use a modified Buckingham intermolecular potential (EXP-6), the computed results of which are in comparison with those of the Lennard-Jones potential.

\*Projects Supported by National Natural Science Foundation of China

The EXP-6 potential is expressed as

$$\Phi(r) = \frac{\epsilon}{\alpha - 6} \left\{ 6 \exp \left[ \alpha \left( 1 - \frac{r}{r_m} \right) \right] - \alpha \left( \frac{r_m}{r} \right)^6 \right\}, \quad (2)$$

where  $\phi(r)$  is the potential energy between two molecules at a separation distance  $r$ ;  $\epsilon$ , the depth of the potential minimum;  $r_m$ , the separation at the energy minimum;  $\alpha$ , the measure of steepness of the repulsive part of potential.

The EXP-6 potential is more reasonable and more flexible since it contains three parameters. In fact, it is becoming widely used in modern calculations.<sup>7,8</sup>

For an EXP-6 potential, the reduced second virial coefficient,  $B^*(T^*)$ , becomes<sup>2</sup>

$$B^*(T^*, \alpha) = - \frac{1}{T^*} \int_0^\infty r^3 \frac{d\phi^*(r^*)}{dr^*} \exp \left[ -\phi^*(r^*)/T^* \right] dr^*, \quad (3)$$

where

$$\phi^*(r^*) = \frac{\phi(r)}{\epsilon}; \quad r^* = \frac{r}{r_m}$$

To improve the accuracy, Equation (1) should include up to the fifth term. Namely, let  $m = 5$  instead of 4. In this case, Equation (1) becomes

$$\frac{P_v}{RT} = 1 + WB^* + W^2q + W^3q/2^4 + W^4q/3^5, \quad (4)$$

where

$$W = \frac{bo}{v}; \quad q = \frac{B^*}{T^{*1/4}}$$

Equation (4) is called the revised VLW EOS.

By means of thermodynamic relations, from Equation (4) we obtain

Internal energy:

$$E = \sum_i \frac{x_i}{X} \left[ (H^0 - H_r^0)_i - RT + (H_r^0)_i \right] - RTW \left( T^* \frac{\partial B^*}{\partial T^*} + \frac{Wg}{2} + \frac{W^2g}{48} + \frac{W^3g}{972} \right) \quad (5)$$

Entropy:

$$S = \sum_i \frac{x_i}{X} \left( S_i^0 - R \ln \frac{X_i RT}{V} \right) - RW \left\{ T^* \frac{\partial B^*}{\partial T^*} + B^* + \frac{W}{2} (g+q) \left[ 1 + \frac{W}{2} \left( \frac{1}{12} + \frac{W}{243} \right) \right] \right\} \quad (6)$$

Chemical Potential:

$$\mu_i = \left\{ (F^0 - H_r^0)_i + (H_r^0)_i + RT \ln \frac{x_i RT}{V} \right\} + RTB^* \left( W + \frac{bo_i}{V} \right) + RTWq \left( \frac{W}{2} + \frac{bo_i}{V} \right) + \frac{RTW^2q}{16} \left( \frac{W}{3} + \frac{bo_i}{V} \right) + \frac{RTW^3q}{243} \left( \frac{W}{4} + \frac{bo_i}{V} \right), \quad (7)$$

where

$$W = \frac{bo}{V}; \quad q = \frac{B^*(T^*, \alpha)}{T^{*1/4}};$$

$$g = T^{*-1/4} \left( T^* \frac{\partial B^*}{\partial T^*} - \frac{B^*(T^*, \alpha)}{4} \right);$$

$$T^* \frac{\partial B^*}{\partial T^*} = - \frac{1}{T^{*2}} \int_0^\infty r^3 \frac{d\phi^*(r^*)}{dr^*} \left( \phi^*(r^*) - T^* \right) \exp \left( -\phi^*(r^*)/T^* \right) dr^*$$

## CALCULATION

The detonation parameters of some new powerful explosive compounds are predicted by

using the revised VLW EOS with both the EXP-6 potential and Lennard-Jones potential in Table 1.

## DISCUSSION

From the predicted detonation properties of explosive compounds listed in Table 1, we conclude that:

(A) Although the detonation velocities  $D$  of some compounds, such as in octanitrocubane, are as high as 9700 m/s, and C-J pressure is over 40 GPa, the cylinder-test data

(E6 and E19), which give a fair indication of hydrodynamic performances of an explosive, are not yet exceeding those of HMX. The reason may be that their adiabatic exponents,  $\gamma$ , which are very sensitive to influence on the detonation energy, are too high (over 3.6). In this case, a sole reliance on detonation velocity or C-J pressure could be misleading in assessing the detonation performance of an explosive. How do we evaluate the detonation performance? And what is a reasonable criterion for doing this job? To answer these questions, we consider

Table 1. Comparison of Computed Results With Experiment Data

Explosive	Param.	Exp.	Calcn	
			EXP-6	L-J
No. 1 (HMX) 1,3,5,7 tetranitro-1,3,5,7-tetraazacyclooctane				
$\text{H}_2$	D	9100 <sup>3</sup>	9107	9107
$\text{O}_2\text{N}-\text{N}-\text{C}-\text{N}-\text{NO}_2$	P	39.3 <sup>3</sup>	40.5	39.6
$\begin{array}{c}   \quad   \\ \text{H}_2\text{C} \quad \text{C} \quad \text{H}_2 \\   \quad   \\ \text{O}_2\text{N}-\text{N}-\text{C}-\text{N}-\text{NO}_2 \end{array}$	T		4585	4840
$\gamma$			2.9	2.94
$\frac{1}{2}u^2$			2.7	2.64
$\text{H}_2$	E6	1.44 <sup>4</sup>	1.45	1.42
$\rho_0 = 1.90$	E19	1.754 <sup>4</sup>	1.80	1.78
$H_f = 11.3$				
-----				
No. 2 2,4,6,8 tetranitro-2,4,6,8-tetraazacyclooctanone 1				
$\text{H}_2$	D		9454	9335
$\text{O}_2\text{N}-\text{N}-\text{C}-\text{N}-\text{NO}_2$	P		43.4	48.8
$\begin{array}{c}   \quad   \\ \text{H}_2\text{C} \quad \text{C}=\text{O} \\   \quad   \\ \text{O}_2\text{N}-\text{N}-\text{C}-\text{N}-\text{NO}_2 \end{array}$	T		4924	5218
$\gamma$			3.07	2.53
$\frac{1}{2}u^2$			2.69	3.48
$\text{H}_2$	E6		1.5	1.89
$\rho_0 = 1.98$	E19		1.88	2.35
$\Delta H_f = +3.6$				
-----				
No. 3 1,3,3,5,7,7-hexanitro-1,5-diazacyclooctane				
$\text{NO}_2$				
$\text{H}_2\text{C}-\text{N}-\text{CH}_2$	D	8800 <sup>6</sup>	8794	8933
$\begin{array}{c}   \quad   \\ \text{(O}_2\text{N)}_2\text{C} \quad \text{C} \quad \text{(NO}_2)_2 \\   \quad   \\ \text{H}_2\text{C}-\text{N}-\text{CH}_2 \\ \text{NO}_2 \end{array}$	P		37.1	39.9
$\text{H}_2\text{C}-\text{N}-\text{CH}_2$	T		5065	5301
$\gamma$			2.91	2.75
$\frac{1}{2}u^2$			2.52	2.84
$\rho_0 = 1.875$	E6		1.35	1.50
$\Delta H_f = -6.5$	E19		1.7	1.88



Table 1. (continued)

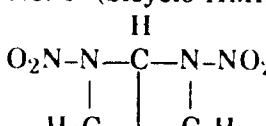
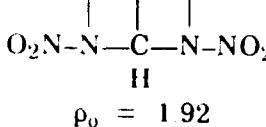
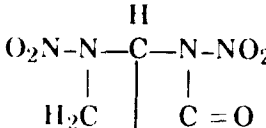
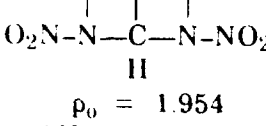
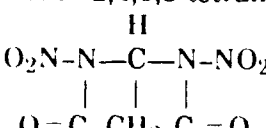
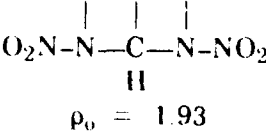
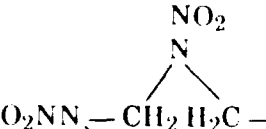
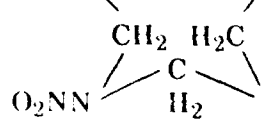
Explosive	Param.	Exp.	EXP-6	Calcn L-J
No. 4 - (bicyclo-IMX) 2,4,6,8-tetranitro-2,4,6,8-tetraazabicyclo [3,3,0]actane				
	D		9171	9134
	P		40.5	42.0
	T		4805	5064
	Y		2.98	2.81
	$\frac{1}{2}u^2$		2.65	2.87
	E6		1.27	1.55
$\rho_0 = 1.92$	E19		1.53	1.94
$\Delta H_f = 20$				
No. 5 - 2,4,6,8-tetranitro-2,4,6,8-tetrazabicyclo[3,3,0]actanone-3				
	D		9331	9257
	P		40.5	46.1
	T		5146	5385
	Y		3.2	2.62
	$\frac{1}{2}u^2$		2.47	3.26
	E6		1.38	1.76
$\rho_0 = 1.954$	E19		1.73	2.19
$\Delta H_f = +5.5$				
No. 6 - 2,4,6,8-tetranitro-2,4,6,8-tetraazabicyclo[3,3,0]actandione-(3,7)				
	D	9034*	8989	9060
	P		37.9	41.9
	T		5109	5312
	Y		3.11	2.78
	$\frac{1}{2}u^2$		2.39	2.87
	E6		1.32	1.55
$\rho_0 = 1.93$	E19		1.67	1.95
$\Delta H_f = -8.0$				
No. 7 - 1,3,5,7,9-pentanitro-1,3,5,7,9-pentaazacyclodecane				
	D		9159	9110
	P		42.2	40.9
	T		4636	4896
	Y		2.79	2.88
	$\frac{1}{2}u^2$		2.92	2.76
	E6		1.56	1.49
	E19		1.95	1.87
$\rho_0 = 1.91$				
$\Delta H_f = 22$				

Table 1. (continued)

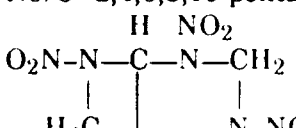
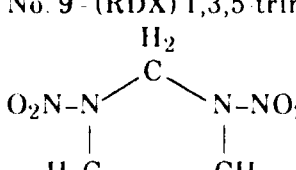
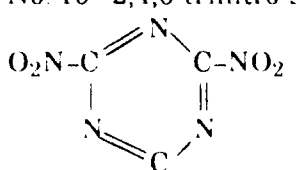
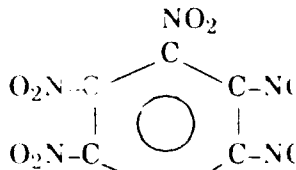
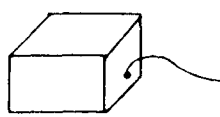
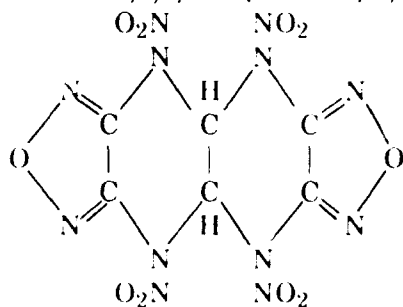
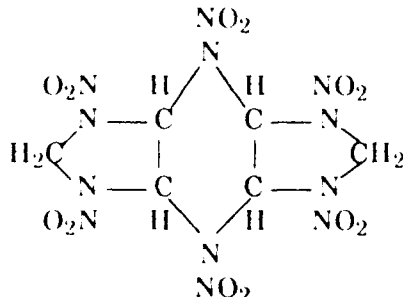
Explosive	Param.	Exp.	Calcn	
			EXP-6	L-J
No. 8 - 2,4,6,8,10-pentanitro-2,4,6,8,10-pentaazabicyclo[5,3,0]decane				
	D		9406	9331
	P		47.3	47.7
	T		4780	5049
	$\gamma$		2.71	2.62
	$\frac{1}{2}u^2$		3.2	3.31
	E6		1.76	1.81
$\rho_0 = 1.987$	E19		2.19	2.26
$\Delta H_f = 25$				
No. 9 - (RDX) 1,3,5 trinitro-1,3,5-triazacyclohexane				
	D	8754 <sup>3</sup>	8776	8764
	P	34.7 <sup>3</sup>	34.4	34.7
	T		4657	4909
	$\gamma$		3.03	2.99
	$\frac{1}{2}u^2$		2.37	2.41
	E6		1.24	1.26
$\rho_0 = 1.8$	E19	1.6 <sup>4</sup>	1.57	1.59
$\Delta H_f = 14.7$				
No. 10 - 2,4,6-trinitro-s-triazine				
	D		9530	9292
	P		37.0	36.1
	T		5331	5306
	$\gamma$		3.84	3.71
	$\frac{1}{2}u^2$		1.94	1.94
	E6		1.13	1.13
$\rho_0 = 1.973$	E19		1.43	1.43
$\Delta H_f = 18$				
No. 11 - 1,2,3,4,5,6 hexanitrobenzene				
	D	9300 <sup>3</sup>	9413	9384
	P		37.3	37.7
	T		6176	6087
	$\gamma$		3.68	3.61
	$\frac{1}{2}u^2$		2.03	1.92
	E6		1.17	1.12
$\rho_0 = 1.973$	E19		1.48	1.42
$\Delta H_f = 35$				

Table 1. (continued)

Explosive	Param.	Exp.	Calcn	
			EXP-6	L-J
No. 12 - 1,2,3,4,5,6,7,8-octanitrocubane				
 $\rho_0 = 1.92$ $\Delta H_f = 80$	D		9792	9750
	P		41.2	41.5
	T		6361	6263
	$\gamma$		3.72	3.64
	$\frac{1}{2}u^2$		2.15	2.2
	E6		1.27	1.29
E19		1.60	1.62	
No. 13 - 2,3,6,7 bis[furazan]-1,4,5,8-tetranitro-1,4,5,8-tetraazadecalin				
 $\rho_0 = 1.861$ $\Delta H_f = 185$	D	9150*	9075	9140
	P		41.2	45.0
	T		5914	6118
	$\gamma$		2.71	2.45
	$\frac{1}{2}u^2$		2.98	3.50
	E6		1.56	1.80
E19		1.95	2.23	
No. 14 - 2,3,5,6 bis[dinitroimidazoline]-1,4-dinitropiperazine				
 $\rho_0 = 1.91$ $\Delta H_f = 45$	D		9140	9134
	P		40.4	42.2
	T		4949	5024
	$\gamma$		2.94	2.75
	$\frac{1}{2}u^2$		2.68	2.96
	E6		1.45	1.58
E19		1.82	1.98	

D is the detonation velocity (m/s);

P is the C-J pressure (GPa);

T is the C-J temperature;

$\gamma$  is the adiabatic exponent;

u is the C-J particle velocity (m/s);

$\frac{1}{2}u^2$  represents the specific kinetic of detonation products of explosive (KJ/g);

$\Delta H_f$  is heat of formation (Kcal/mol); and

$\rho_0$  is density (g/cc).

E6 and E19 are the calculated cylinder-test data (KJ/g) which provide a measure of relative effective explosive energy for detonation; i.e., E6 is the specific wall kinetic energy at 6 mm wall displacement and E19 at 19 mm wall displacement.

\*Is this work.

$$E - E^{\circ} = \frac{1}{2} P (V^{\circ} - v) \quad (8)$$

$$= \frac{1}{2} \frac{PV}{\gamma} \quad (9)$$

$$= \frac{1}{2} \left( \frac{P}{\rho_0 D} \right)^2 \quad (10)$$

$$= \frac{1}{2} \left( \frac{D}{\gamma + 1} \right)^2 \quad (11)$$

$$= \frac{1}{2} u^2 \quad (12)$$

It may be said that the specific kinetic energy  $\frac{1}{2}u^2$  can be represented not only by the increase of Hugoniot energy  $E-E^{\circ}$ , but also by all the C-J parameters like  $D$ ,  $P$ , and  $\gamma$  comprehensively. So it may be regarded as the foundation in assessing the detonation performance. As a matter of fact, the cylinder-test E6 and E19 can be estimated on the basis of specific kinetic energy  $\frac{1}{2}\rho_0 u^2$ .

(B) Some nitrogen heterocycles that are expected to be promising target compounds, such as No. 8, No. 2, and No. 5, in the order listed, are significantly more powerful than the best current military explosive HMX. These nitrogen heterocycles exceed HMX's detonation energy output.

## ACKNOWLEDGEMENTS

The authors wish to thank Professors Zhang Mingnan, Li Fuping, and Jiang Chengwei, and Associate Professor Li Shengying for useful discussions during the course of this work.

## REFERENCES

1. Wu, X., "Detonation Performance of Condensed Explosive Computed with the VLW Equation of State of Detonation Products," *Proceedings of the Eighth Symposium (International) on Detonation*, Albuquerque, NM, 1985, p. 796.
2. Wu, X. and Sun, J., "Calculations of Derivative of Second Virial Coefficients

Based on EXP-6 Intermolecular Potential," *Propellants, Explosives, Pyrotechnics*, No. 2, 1988, p. 48.

3. Mader, C. L., *Numerical Modeling of Detonations*, 1979.
4. Dobratz, B. M., LLNL Explosives Handbook, *Properties of Chemical Explosives and Explosive Stimulants*, UCRL-52997, 1981.
5. Wu, X., "A Method for Evaluation of the Detonation Performance and the Metal Accelerating Ability of Explosives," *Proceedings of the International Symposium on Pyrotechnics and Explosives*, Beijing, 1987, p. 707.
6. Li-hua, X., "The Properties of 1,3,5,7,7-Hexanitro-1.5-Diazacyclopentane and its Application in Propellants," *Propellants, Explosives, Pyrotechnics*, No. 1, 1988.
7. Ree, F. H., "Supercritical Fluid Phase Separations Implications for Detonation Properties of Condensed Explosives," *J. Chem. Phys.*, Vol. 84, No. 10, 1986.
8. Chirat, R. and Pittion-Rossillon, G., "A New Equation of State for Detonation Products," *J. Chem. Phys.*, Vol. 74, No. 8, 1981.
9. McGuire, R. R. and Finger, M., "Composite Explosives for Metal Acceleration," *Proceedings of the Eighth Symposium (International) on Detonation*, Albuquerque, NM, 1985, p. 1018.

## DISCUSSION

Frances Ree, LLNL

Could you explain why the specific kinetic energy of detonation products  $\frac{1}{2}u^2$  is regarded as the foundation in assessing the detonation performance of explosives?

## REPLY BY WU XIONG

To explain this, we consider two explosives whose detonation properties are given in Table 2.

Although the density, detonation velocity and C-J pressure of the former explosive are higher than those of the latter, McGuire and

Table 2. Comparison of the Detonation Parameters of the Following Two Explosives

Explosive	$\rho_0$	$D(\text{Expl't})^9$	$P_c\text{-J}$	$\gamma c\text{-J}^9$
HMX/TATB/ BTF 1/1/0 (mole)	1.84	8300	30.3	3.17
HMX/TATB/ BTF 1/1/3 (mole)	1.838	7890	28.7	2.98

$\gamma c\text{-J}$  calculated by McGuire etc., using

BKWR-Tiger code at  $\rho_{0,2} = 1.85$ .

$P_c\text{-J}$  calculated from  $\rho_0 D^2 / (\gamma c\text{-J} + 1)$ .

Finger's cylinder test showed that the wall energy of the former was lower than that of the latter.

In addition, several years ago, our colleagues synthesized a new explosive compound. Although its experimental detonation velocity was as high as 9500 m/s, the experimental metal accelerating properties were still lower than those of HMX.

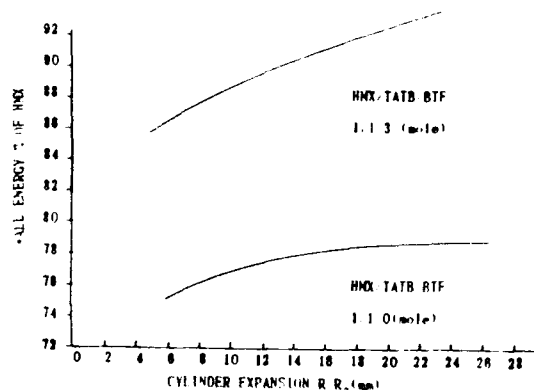


Figure 1. Cylinder Test Performance

According to the facts mentioned above and Equations (8) through (12), Wu Xiong proposed that the specific energy  $\frac{1}{2}u^2$  may be better as the foundation in assessing the detonation performance of unit mass explosives and the specific volume energy  $\frac{1}{2}\rho_0 u^2$  in assessing those of unit volume explosives.

# THEORETICAL MODEL OF EXPLOSIVE DETONATION PRODUCTS: TESTS AND SENSITIVITY STUDIES\*

G. I. Kerley  
Sandia National Laboratories  
Division 1533  
Albuquerque, New Mexico 87185-5800

*A model for calculating equations of state for reactive materials, introduced at the previous Detonation Symposium, is reviewed and applied to a broader class of problems. It is shown to give very good agreement with experimental measurements of detonation velocities, overdriven Hugoniot, and Hugoniot for nonexplosive materials that decompose when shocked. The ideal mixing approximation, one of the central features of the model, is tested and shown to give satisfactory results when compared with Monte Carlo calculations. The reaction products formic acid, liquid carbon, and atomic N, O, and H, usually neglected in other theories, are shown to be important. The parameters used for carbon and formic acid are examined in some detail.*

## INTRODUCTION

At the Eighth Detonation Symposium, we described a (nearly) *a priori* theory for calculating equations of state (EOS) for the detonation products of explosives.<sup>1</sup> Two main conclusions emerged from that work. First, we found that the ideal mixing approximation gave surprisingly accurate results. The most important advantage of ideal mixing is that it enables one to include much more realistic models for complicated chemical species than would be possible using mixture theories based upon simple intermolecular pair potentials. Second, we showed that formic acid (HCOOH), which has been overlooked in most other theoretical work, is an important reaction product for explosives having a negative oxygen balance (O.B.). Including formic acid in the calculations eliminated discrepancies with experiments that had previously required unrealistic assumptions about the carbon EOS. The existence of such discrepancies had led to speculation that nonequilibrium behavior in

the reaction products could be a significant effect, even for steady-state detonations. However, our chemical equilibrium model gave satisfactory results for all classes of explosives, obviating the need for such an explanation.

The purposes of this paper are to justify the foundations of our theory, to discuss tests and sensitivity studies of the calculations, and to present some new results and comparisons with experimental data. We begin with an overview of the model and its predictions of explosive detonation properties, overdriven Hugoniot data, and Hugoniot for nonexplosive CHNO compounds. Next, we discuss some Monte Carlo calculations of the EOS for mixtures in the pressure-temperature regime relevant to detonations. These tests show that ideal mixing is not only a reasonable approximation for such problems, but that it is also better than other available theories. We also discuss several ways to estimate EOS parameters of formic acid, for which there are very few experimental data. We show that our EOS parameters are reasonable and that EOS uncertainties do not alter the fact that HCOOH is an important reaction product. Finally, we discuss some revisions to our model for the carbon EOS and phase diagram. The

\* This work performed at Sandia National Laboratories supported by the U.S. Department of Energy under Contract No. DE AC04 76DP00789

revised carbon EOS indicates that melting is partly responsible for the change in slope of the curve of TNT detonation velocity vs. density.

## OVERVIEW OF THE MODEL

Our model for the EOS of a material undergoing chemical reactions can be divided into four parts.<sup>1</sup>

- We must identify the important chemical species that can be produced by the reactions. For CHNO compounds, most models include a minimum of ten components --  $\text{CO}_2$ ,  $\text{N}_2$ ,  $\text{H}_2\text{O}$ ,  $\text{CO}$ ,  $\text{NO}$ ,  $\text{NH}_3$ ,  $\text{CH}_4$ ,  $\text{H}_2$ ,  $\text{O}_2$ , and elemental carbon. In addition, we have included  $\text{HCOOH}$ , atomic N, O, and H, and three forms of carbon -- graphite, diamond, and the liquid phase.
- Second, the PANDA code<sup>2</sup> is used to construct a separate EOS for each of the above species, making one library of data tables that can be used for materials of all compositions. Fluid perturbation theory<sup>3</sup> is used for all species except for solid carbon. The general approach is discussed in Reference 1 and the references cited within. In the present work, we have omitted the dipole terms<sup>1</sup> that were found to be negligible. Some of the EOS are semi-empirical, in that the parameters have been chosen to match the Hugoniot and other experimental data for the pure component. However, the EOS have not been adjusted to fit the explosive data except for  $\text{HCOOH}$  and carbon. These two cases are discussed below in more detail.
- Next, the ideal mixing model is used to compute the thermodynamic properties for a mixture having an arbitrary composition of the various species. The validity of this approximation is discussed below.
- Finally, the composition of the system is determined from the assumption of chemical equilibrium, i.e., by minimizing the Helmholtz free energy at constant density and temperature. The validity of the equilibrium approximation, which is presently made in all

theoretical models of detonation properties, is not examined here; it is justified only by the success of the model in predicting experimental results.

For the present paper, the mixture-chemical equilibrium calculations and computation of the detonation and shock-wave properties were made using a new version of the PANDA code<sup>2</sup> that includes capabilities formerly available in an undocumented code called POGO.

In Reference 1, we compared our model predictions of the detonation properties of 15 CHNO explosives with experimental data. It is well-known that the greatest challenge to any theoretical model is that of predicting the behavior of carbon-rich explosives. A study of the detonation properties for three explosives, RDX, PETN, and TNT, as functions of loading density, was particularly useful in illuminating the nature of the phenomena involved. The detonation velocities are shown in Figure 1.

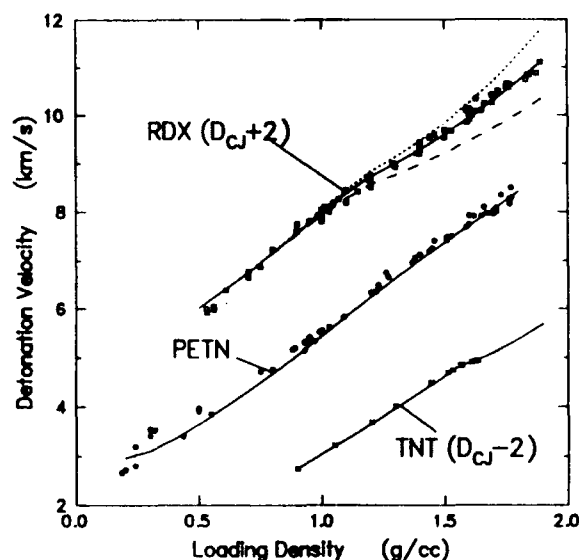


Figure 1. Detonation Velocity Vs. Loading Density for Three Explosives. Experimental data are from References 4-6; the curve labeled RDX shows data for HMX as well.<sup>4</sup> For clarity, the RDX and TNT velocities are shifted by  $\pm 2$  km/s, respectively. The solid curves were computed using the theory discussed in the text. For RDX, the dashed and dotted curves are calculations in which the density of formic acid was shifted by  $\pm 10$  percent, respectively.

For low initial densities, we find that PETN and RDX do not form either carbon or  $\text{HCOOH}$  in the reaction products. For high initial densities, PETN forms  $\text{HCOOH}$  but no carbon, while RDX forms both. These changes in chemical composition result in changes in slope that can be seen in both the data and the theoretical predictions. TNT, which has a large negative O.B., forms elemental carbon at all loading densities. In that case, the change in slope at high initial densities is related to the formation of diamond and liquid carbon, as discussed below.

In this work, the model is tested further by comparing its predictions with experimental measurements of overdriven shock Hugoniots for four explosives. The results, shown in Figure 2, are very good. The fact that good agreement is obtained without adjusting any parameters is evidence of the validity of

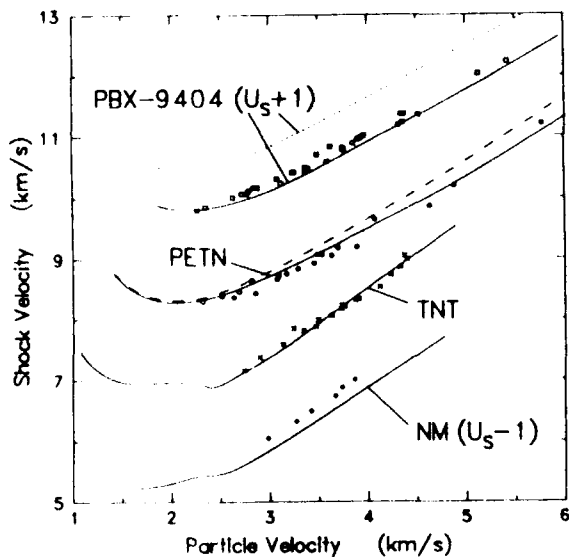
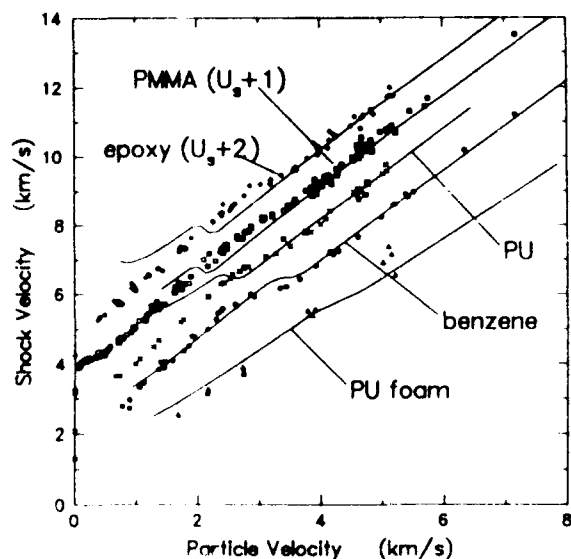


Figure 2. Overdriven Shock Hugoniots for Four Explosives. Experimental data are from References 8-12. For clarity, the PBX-9404 and NM shock velocities are shifted by  $\pm 1$  km/s, respectively. The solid curves were computed using the theory discussed in the text. The dotted curve is a calculation for PBX-9404 in which formic acid is omitted as a reaction product. The dashed curve is a calculation for PETN in which atomic N, O, and H are omitted as reaction products.

our model. In particular, we note that the formic acid and carbon EOS are found to be quite important in all of these cases. For example, the dotted line in Figure 2 shows a calculation for PBX-9404 that omits  $\text{HCOOH}$  as a reaction product; this prediction badly overestimates the shock velocity. (The small amount of elements Cl and P were neglected in the calculations for PBX-9404.) Other theoretical models either omit atomic N, O, and H or treat them in a very simplified way that ignores the effects of strong binding at high densities. The dashed curve in Figure 2 shows a calculation for PETN in which these species were omitted; the results are noticeably poorer, showing that molecular dissociation is an important effect for overdriven explosives. We do note that agreement with the data for nitromethane (NM)<sup>12</sup> is not as good as for the other explosives; the discrepancy in that case may be due to deficiencies in the liquid carbon EOS at low densities, as discussed below.

As further tests of the model, we computed Hugoniots for several reactive but non-explosive materials -- benzene ( $\text{C}_6\text{H}_6$ ), PMMA ( $\text{C}_5\text{H}_8\text{O}_2$ ), polyurethane ( $\text{C}_{200}\text{H}_{286}\text{N}_{16}\text{O}_{79}$ ), and epoxy ( $\text{C}_{46}\text{H}_{61}\text{N}_3\text{O}_8$ ). These calculations were totally *a priori*, using the same model and parameters that were developed for explosive detonation products. The results are shown in Figure 3. The chemistry of these materials is similar to that of explosives, in that they decompose under intense shock loading; the principal reaction products are  $\text{H}_2\text{O}$ ,  $\text{CH}_4$ ,  $\text{N}_2$ , and elemental carbon. Of course, the model is valid only at pressures and temperatures above which decomposition occurs. The calculations for PMMA, epoxy, and polyurethane all show very good agreement with the data above about 25-30 GPa and 2500-3000°K; at lower pressures and temperatures, the decomposition is probably incomplete. For benzene, the theory gives good agreement at even lower pressures and temperatures, including the prediction of the phase transition for a particle velocity of  $\sim 3$  km/s (20 GPa). The calculated and measured temperatures, shown in Figure 4, are also in reasonable agreement. These tests provide further evidence that our theory is valid in the range that is relevant to detonation problems.





**Figure 3. Hugoniot for Nonexplosive Materials.** Experimental data are from References 20-22. The curve marked PU is normal density polyurethane; that marked PU foam is polyurethane with a density of 0.32. For clarity, the PMMA and epoxy shock velocities are shifted by +1 and +2 km/s, respectively. Solid curves were computed using the theory discussed in the text.

## ACCURACY OF IDEAL MIXING

The general success of the model in predicting the properties of explosive detonation products and other reactive materials can be offered as a *a posteriori* justification for assuming ideal mixing. However, the results depend upon the validity of several other approximations as well, so it is desirable to evaluate this feature of the theory by independent tests. This section discusses such tests.

A quantitative discussion of the ideal solution and its relation to the statistical mechanics of mixtures is given in Reference 7. A qualitative description of the model is as follows. Starting with a heterogeneous mixture in thermal and mechanical equilibrium, allow the components to mix homogeneously at constant temperature and pressure. In ideal mixing, this step produces no change in volume or internal energy, while the change in entropy is that for complete randomness. This model completely specifies the mixture properties in

terms of the EOS for the pure components, requiring no additional parameters to describe the interactions between unlike molecules.

In recent years, there have been many studies using statistical mechanical theories that relate the properties of mixtures to intermolecular potentials. The so-called van der Waals one-fluid theory (vdW1) is probably the most popular method available because it has been found to give good results and because its simplicity is advantageous in chemical equilibrium problems that involve extensive numerical computation.<sup>13</sup> However, a limitation of these models is that they require simplifying assumptions about the intermolecular forces that are not valid for certain explosive detonation products, including liquid carbon and the high-density atomic species, N, O, and H.

Although ideal mixing is sometimes viewed as a crude and oversimplified theory, experience has shown that it usually gives very good results for the EOS of a mixture, i.e., the dependence of the total volume, energy, and entropy on pressure and temperature. In fact, the predictions of ideal mixing are often superior to those of the vdW1 model. Moreover, ideal mixing does not require any assumptions about the nature of the intermolecular forces and permits the use of realistic models for complicated mixture species.

We have compared the two mixture models with Monte Carlo calculations for fluids of spherical molecules having simple repulsive potentials and differing in diameter by a factor of three.<sup>7</sup> These studies are relevant to the detonation problem because the EOS is determined primarily by the repulsive forces at high densities and temperatures. For the inverse-12 potential, ideal mixing was found to have a maximum error of about 5 percent and to give the better results at high densities. The vdW1 model was better at very low densities but was much poorer at high densities, with an error approaching 22 percent. In addition, the vdW1 model gave the wrong sign for the volume change on mixing; this result was surprising because it was different from the hard-sphere case. For the inverse-6 potential, ideal mixing was slightly better than vdW1, with the maximum error approaching 10 percent.

The water-nitrogen mixture, in which the molecules differ both in size and in attractive energy, is an important system in detonation problems. Ree has proposed that separation into  $N_2$ -rich and  $N_2$ -poor phases occurs in the detonation products of certain explosives, markedly affecting their properties.<sup>14</sup> However, the ideal mixing approximation, which assumes that heterogeneous and homogeneous mixtures have the same pressure and energy relations, predicts that phase separation would have little effect on the detonation properties.

In order to investigate this question, we have made Monte Carlo calculations for  $H_2O$ - $N_2$  mixtures in the regime of interest, including the high pressure region obtained in overdriven detonations. We used the exp-6 potential, with parameters given by Ree for like pairs<sup>14</sup> and the Lorentz-Berthelot combination rules for unlike pairs. The results are given in Table 1. Ideal mixing underestimates the pressure and energy in the mixture, but the error is not greater than 5 percent. The vdW1 model gives somewhat poorer results, overestimating the pressure and energy by up to 7 percent; hence, vdW1 tends to exaggerate the effects of phase separation. These calculations show that the ideal mixing approximation gives reasonable results and is actually better than vdW1. Therefore, it is not likely to be a major source of error in the prediction of detonation properties. Of course, it would be desirable to include corrections to the simple model, but it is not clear that a better mixture theory exists at the present time.

Table 1. Equation of State for an Equimolar Binary Mixture at 4000°K, with Pair Potentials Representative of  $H_2O$  and  $N_2$ . Calculations were made using the Monte Carlo Method, with 216 Particles and  $10^5$  Configurations. Accuracy of results is estimated to be better than 0.5 percent.

Volume (cc/mole)	P (GPa)			E (MJ/kg·mole)		
	ideal	real	vdW1	ideal	real	vdW1
20.888	5.0	5.1412	5.3019	59.095	60.203	60.828
13.691	15.0	15.626	16.375	81.952	84.798	87.102
10.953	30.0	30.906	32.674	114.33	118.31	123.10
9.3025	50.0	52.445	55.848	154.60	162.17	170.61
8.0754	80.0	83.884	89.892	211.08	221.67	235.44

## PARAMETERS FOR FORMIC ACID

Our theory can be regarded as *a priori* in the limited sense that explosive data were not used to determine the model parameters. But one exception to this rule is that the detonation velocity data for RDX were used to adjust the EOS for  $HCOOH$ , for which there are no high-pressure measurements. Therefore, it is desirable to show that our EOS for this species is a reasonable one, not simply a "knob" used to fit the experiments.

In discussing this matter, we emphasize that formic acid is not of equal importance for all classes of explosives.  $HCOOH$  has the same chemical composition as an equimolar  $H_2O$ - $CO$  mixture. Explosives with a positive O.B. will not produce a significant amount of formic acid because most of the carbon is consumed in making  $CO_2$ . Explosives with a large negative O.B., such as TNT, will produce much less formic acid because the lack of oxygen results in free carbon rather than  $CO$  compounds. It is explosives like RDX (which has the same C-H-O ratio as formic acid) for which this species is most important.

The formic acid EOS, like that for the other compounds, consists of contributions from translational, internal vibrational, and rotational degrees of freedom. Calculation of the vibrational and rotational terms from spectroscopic data<sup>15,16</sup> is straightforward; the model gives excellent agreement with gas phase thermodynamic data that are available up to 1000°K.<sup>17</sup> The translational terms are computed from the cold curve, using fluid perturbation theory.<sup>3</sup> For detonation products, the most crucial feature of the cold curve is the compression in the pressure range 10 - 100 GPa; the binding energy is of minor importance because it is so small in comparison with the heat of formation. In fact, the details of the EOS are not crucial to demonstrating that formic acid is a reaction product; for RDX, we obtained results very similar to those given here by replacing the perturbation theory term for  $HCOOH$  with a simple BKW expression, using the  $CO_2$  covolume of 600.<sup>18</sup>

The cold curve used in the present model predicts that the atomic volume of formic acid

is approximately equal to that of CO<sub>2</sub> over the pressure range from 10 to 1000 GPa. We assert that the result is reasonable because the addition of two H atoms to the CO<sub>2</sub> molecule should cause only a small increase in volume. We made calculations using the Thomas-Fermi-Dirac model<sup>2</sup> which show that this increase is no more than 20 percent; the same conclusion is reached using geometrical estimates of the covolumes.<sup>18</sup> Moreover, a comparison of the ambient densities of the two liquids suggests that their atomic volumes are nearly equal; this fact shows that the attractive forces tend to offset the volume increase due to geometric effects (repulsive forces).

A different estimate of the intermolecular forces in formic acid can be made by treating the HCOOH molecule as consisting of H<sub>2</sub>O and CO units. The interaction potential  $\phi$  can be crudely calculated by summing the potentials between units in separate molecules, as follows:

$$\phi_{CC}(r) \approx \phi_{AA}(r) + \phi_{BB}(r) + 2\phi_{AB}(r), \quad (1)$$

where  $r$  is the intermolecular distance and A, B, and C stand for H<sub>2</sub>O, CO, and HCOOH, respectively. We used this approximation, together with two different sets of potential parameters,<sup>13,19</sup> to compute the formic acid potential and cold curve. These results predict that the atomic volume for HCOOH is about 20 percent *less* than that of CO<sub>2</sub> over the pressure range of interest.

Although extensive experimental and theoretical work will eventually be required to determine an interaction potential for formic acid, it is our contention that a cold compression curve similar to that for CO<sub>2</sub> cannot be in error by more than 10 percent in density. In order to explore the corresponding uncertainties in the model predictions, we calculated the detonation velocities for RDX using EOS in which the cold curve in our model for HCOOH was shifted by  $\pm 10$  percent in density. The results are shown in Figure 1. As expected, the lower density EOS overestimates  $D_{CJ}$ , while the higher density EOS underestimates it. Nevertheless, *all three* calculations predict that formic acid is an important species in the

detonation products. The results are very sensitive to the formic acid EOS, producing a range of uncertainty that is quite unacceptable for any application. In the absence of other data, it is necessary to use these experiments to adjust the HCOOH parameters; the model can be justified *a posteriori* by showing that it gives satisfactory predictions when tested over a wider range of applications, such as Hugoniot data shown in Figures 2 and 3. Calculations of the Hugoniot for PBX-9404 (Figure 2) show that the formation of HCOOH has a profound effect on the predictions. Our model gives very good results when this species is included as a reaction product.

## CARBON EQUATION OF STATE

In Reference 1, we described a three-phase (graphite-diamond-liquid) EOS for carbon. Our EOS for the liquid phase was constructed using fluid perturbation theory,<sup>3</sup> with a cold curve chosen to match the melting curve in the vicinity of the triple point. We also showed that the TNT detonation velocity curve shows a change in slope at high loading densities that can be explained by the transition from a graphite-like form to a diamond-like form of carbon.<sup>1</sup> To reproduce the TNT data, however, it is necessary to shift the energy of diamond relative to that of graphite, thereby raising the transition pressure. This energy increase was justified as arising from a small percentage of defects in the diamond lattice. This general idea has also been discussed by van Thiel and Ree.<sup>24</sup>

In the present work, we have improved the liquid EOS by using a cold curve that is fit to recent *a priori* band-theoretical calculations for the bc-8 structure.<sup>23</sup> The new liquid EOS also requires a slightly different energy shift for diamond in order to match the high-density TNT data. The resulting phase diagram, in which the diamond energy has been shifted by +0.9 MJ/kg, is shown in Figure 4. Also shown are the calculated pressure-temperature loci on the Hugoniots of several materials. Most of the Hugoniot data lie in the stability range of liquid carbon, which is not included in most other theoretical models. The calculated temperatures for benzene are in reasonable agreement with the experimental data.<sup>22</sup>

An interesting feature of the revised model is that the melting of carbon plays a role in determining the detonation properties of high-density TNT. As seen in Figure 4, the Hugoniot for TNT intersects and follows the graphite-liquid and diamond-liquid phase lines, passing through the triple point, before it emerges into the liquid phase. This behavior influences the nature of the broad flat region in the corresponding shock velocity curve, seen in Figure 2. The curve exhibits a double minimum;<sup>24</sup> the lower of the two values is the velocity for the stable detonation wave. Graphite formation occurs for low initial densities, and diamond formation occurs for high initial densities.

We previously noted that our liquid carbon EOS is not satisfactory at low pressures, where it fails to match the negative slope of the melting curve. An analysis of the experimental data shows that the liquid has an anomalously high compressibility as it expands. This phenomenon could be due to the formation of molecules or to changes in the electronic structure of the atoms. In any case, our EOS tends to overestimate the density of liquid carbon on expansion. As seen in Figure 4, the pressures

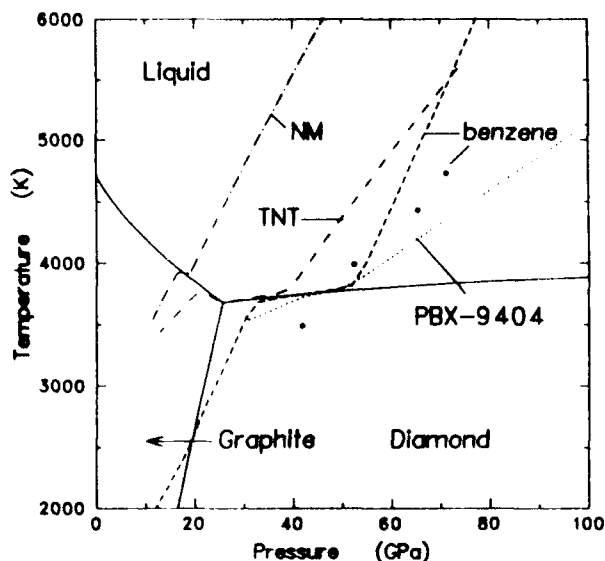


Figure 4. Carbon Phase Diagram in Which the Diamond Phase has been Shifted by 0.9 MJ/kg. Phase boundaries are shown by solid lines. The other curves are Hugoniot loci for the materials indicated. Circles are experimental data for benzene.<sup>22</sup>

on the NM Hugoniot are lower than those for the other materials, so that the corresponding carbon densities are lower. It may be that the deficiency in the expansion behavior of our liquid EOS is responsible for the discrepancy in our predictions for NM.

## CONCLUSIONS

The ability of a theoretical model to give accurate predictions for a wide variety of cases is an indication of its usefulness and also the validity of the approximations involved. In this work, we have compared our model for the detonation properties of explosives with a broader class of problems than were considered in Reference 1. We obtained very good agreement with detonation velocity data, with overdriven Hugoniots for explosives, and also with Hugoniots for several reactive but nonexplosive materials.

We have also examined specific features of the model in some detail. It was shown that the assumption of ideal mixing is very reasonable when compared with Monte Carlo calculations for various test cases and that it is often better than other mixture approximations for conditions typical of detonations. It was shown that formic acid should be expected to be an important reaction product for any reasonable set of EOS parameters and that the predictions for certain classes of explosives are strongly affected by the formation of this compound. When the parameters for formic acid are adjusted to match the detonation velocities for RDX, good results are also obtained for the other properties, and for other explosives. Finally, we have shown that liquid carbon and the atomic species N, O, and H, usually neglected in theoretical models, are also important reaction products in many problems.

## REFERENCES

1. Kerley, G. I., "Theoretical Equations of State for the Detonation Properties of Explosives," *Proceedings of the Eighth Symposium (International) on Detonation*, Naval Surface Weapons Center, White Oak, MD, 1986, pp. 540-547.

2. Kerley, G. I., *User's Manual for PANDA II: A Computer Code for Calculating Equations of State*, SAND88-2291, 1989, Sandia National Laboratories, Albuquerque, NM.
3. Kerley, G. I., "A Model for the Calculation of Thermodynamic Properties of a Fluid Using Hard-Sphere Perturbation Theory and the Zero-Kelvin Isotherm of the Solid," *Molecular Based Study of Fluids*, Haile, J. M., and Mansoori, G. A., Eds., Am. Chem. Soc., Washington, DC, 1983, pp. 107-138.
4. Steinberg, D. J., "Comparison of Experimental Data on Detonation Velocity and Chapman-Jouguet Pressure vs. Initial HE Density With Predictions from Ree's Model Equation of State," *Proceedings of the Eighth Symposium (International) on Detonation*, Naval Surface Weapons Center, White Oak, MD, 1986, pp. 513-520.
5. Hornig, H. C.; Lee, E. L.; Finger, M.; and Kurrle, J. E., "Equation of State of Detonation Products," *Proceedings of the Fifth Symposium (International) on Detonation*, Office of Naval Research, Department of the Navy, 1970, pp. 503-511.
6. Urizar, M. J.; James, E.; and Smith, L. C., "Detonation Velocity of Pressed TNT," *Phys. Fluids*, Vol. 4, 1961, p. 262.
7. Kerley, G. I., "Equations of State and Gas-Gas Phase Separation in Soft Sphere Mixtures," *J. Chem. Phys.*, Vol. 91, 1989, p. 1204.
8. Kineke, J. H., and West, C. E., "Shocked States of Four Overdriven Explosives," *Proceedings of the Fifth Symposium (International) on Detonation*, Office of Naval Research, Department of the Navy, 1970, p. 533.
9. Lee, E. L.; van Thiel, M.; Green, L. G.; and Mitchell, A., "Detonation Product EOS: The Region Above Chapman-Jouguet Pressure," *Proceedings of the APS 1983 Topical Conference on Shock Waves in Condensed Matter*, North-Holland, New York, 1984, p. 617.
10. Green, L.; Lee, E.; Metcchell, A.; and Tarver, C., "The Supra-Compression of LX-07, LX-17, PBX-9404, and RX-26-AF and the Equation of State of the Detonation Products," *Proceedings of the Eighth Symposium (International) on Detonation*, Naval Surface Weapons Center, White Oak, MD, 1986, pp. 587-595.
11. Green, L.; Holmes, N.; and Kury, J., *Shock Measurements on Explosives in the Supra-Compressive Region*, UCRL-95461, Apr 1987, Lawrence Livermore National Laboratory, Livermore, CA.
12. Sellam, M.; Presles, H. N.; Brochet, C.; and Cherét, R., "Characterization of Strong Detonation Waves in Nitromethane," *Proceedings of the Eighth Symposium (International) on Detonation*, Naval Surface Weapons Center, White Oak, MD, 1986, pp. 425-430.
13. Ree, F. H., "A Statistical Mechanical Theory of Chemically Reacting Multiphase Mixtures: Application to the Detonation Properties of PETN," *J. Chem. Phys.*, Vol. 81, 1984, p. 1251.
14. Ree, F. H., "Supercritical Fluid Phase Separations: Implications for Detonation Properties of Condensed Explosives," *J. Chem. Phys.*, Vol. 84, 1986, p. 5845.
15. Redington, R. L., "Vibrational Spectra and Normal Coordinate Analysis of Isotopically Labeled Formic Acid Monomers," *J. Mol. Spectrosc.*, Vol. 65, 1977, p. 171.
16. Davis, R. W.; Robiette, A. G.; Gerry, M. C. L.; Bjarnov, E.; and Winnewisser, G., "Microwave Spectra and Centrifugal Distortion Constants of Formic Acid Continuing  $^{13}\text{C}$  and  $^{18}\text{O}$ : Refinement of the Harmonic Force Field and the Molecular Structure," *J. Mol. Spectrosc.*, Vol. 81, 1980, p. 93.
17. Green, J. H. S., "Thermodynamic Properties of Organic Oxygen Compounds. Part III. Formic Acid," *Chem. Soc. (London)*, 1961, p. 2241.

18. Mader, C. L., Numerical Modeling of Detonations, University of California, Berkeley, 1979.
19. Chirat, R.; and Pittion-Rossillon, G., "Detonation Properties of Condensed Explosives Calculated with an Equation of State based on Intermolecular Potentials," *Proceedings of the Seventh Symposium (International) on Detonation*, Naval Surface Weapons Center, White Oak, MD, 1981, pp. 703-715.
20. Marsh, S. P., LASL Shock Hugoniot Data, University of California, Berkeley, 1980.
21. van Thiel, M., *Compendium of Shock Wave Data*, UCRL-50108, Rev. 1, Lawrence Livermore Laboratory, Livermore, CA, Jun 1977.
22. Nellis, W. J.; Ree, F. H.; Trainor, R. J.; Mitchell, A. C.; and Boslough, M. B., "Equation of State and Optical Luminosity of Benzene, Polybutene, and Polyethylene Shocked to 210 GPa (2.1 Mbar)," *J. Chem. Phys.*, Vol. 80, 1984, p. 2789.
23. Fahy, S., and Louie, S. G., "High-Pressure Structural and Electronic Properties of Carbon," *Phys. Rev. B*, Vol. 36, 1987, p. 3373.
24. van Thiel, M. and Ree, F. H., "Properties of Carbon Clusters in TNT Detonation Products: Graphite-Diamond Transition," *J. Appl. Phys.*, Vol. 62, 1987, p. 1761.

## DISCUSSION

**STEPHEN AGNEW**  
Los Alamos National Laboratory

I agree with your conclusions about ideal mixing theory being valid for molecules with similar polarities, but how can it be valid for very dissimilar molecules like  $H_2O$  and  $CH_4$ ?

### REPLY BY G. I. KERLEY

Let me replace your question with two others.

1. How important are the corrections to ideal mixing in calculating EOS for explosive detonation products?
2. How can we include these corrections in the calculations?

With regard to the first question, the Monte Carlo results in Table 1 and in Reference 7 show that the corrections are small but not completely negligible. One can expect to obtain reasonable results if they are ignored, but one would like to do better. An obvious deficiency of ideal mixing is that it cannot predict phase separation in mixtures of unlike molecules.

The second question is much more difficult. The examples that I have given show that the vdW1 model is not better than ideal mixing and can be much poorer. It is not clear that a better theory exists.

For mixtures of molecules having very different polarities, we have no data with which to compare. (The Monte Carlo calculations for the  $N_2$ - $H_2O$  mixtures treated both molecules as nonpolar.) It is indeed possible that the deviations from ideal mixing are more important in such cases. However, it is also doubtful that any existing theory would be able to predict the effects of polarity with any reliability.

## DISCUSSION

**FRED VOLK**  
Fraunhofer Institut  
FRG

In the list of reaction products mentioned you should add the components (reaction products)  $N_2O$  and  $HCN$ .  $N_2O$  is important by investigating nitroguanidine and ammonium nitrate containing HE.

### REPLY BY G. I. KERLEY

I agree with you and hope to include these components in any calculations that I make in the future.

# A NEW SIMULATION METHOD FOR THE EFFICIENT CALCULATION OF BENCHMARKS FOR DETONATION PRODUCTS EQUATIONS OF STATE

M. S. Shaw  
Group T-14, MS B214  
Los Alamos National Laboratory  
Los Alamos, New Mexico 87545

*A new variation on the Monte Carlo method is presented here in the context of its potential impact on the development of detonation products equations of state (EOS). The configurational density of states and other quantities are determined for a nonstandard reference simulation. Then the EOS for a linear combination of potentials is evaluated through a density of states transformation at arbitrary densities and temperatures in the fluid range. The computer time required for the EOS calculation (including free energies) is negligible once the reference simulation is made. The EOS over the entire fluid regime for a Lennard-Jones fluid (including the location of the gas/liquid equilibrium phase line) is calculated. Preliminary results on the extension of the method to the exponential-six potential are presented. The efficient calculation of benchmarks over the very large parameter space of relevance to detonation products EOS may now be possible.*

## INTRODUCTION

In the last two decades, a great deal of progress has been made in the area of theoretical equations of state for fluids. Of particular interest to the explosives community, has been the work of the last decade in applying these methods to the construction of physically meaningful detonation products equations of state. The goal for thermodynamic theory is to be able to take a given set of interaction potentials for an arbitrary mixture of product molecules, and calculate accurately and quickly the equilibrium EOS under the extreme conditions of pressure and temperature characteristic of detonation products. Then the potentials could be determined from quantum mechanics or normalization to data (typically the quantum calculations are qualitative, and are useful for the determination of functional forms to be used in fitting data). Until the thermodynamic theory is tied down, there will be too many free parameters to assure a predictive EOS in which all of the constants are physically meaningful.

Although much progress has been made, we are not yet at this goal for thermodynamic theory. Fast quantitative methods<sup>1</sup> are available for the EOS of single species with spherically symmetric interaction potentials. Methods exist for spherical mixtures,<sup>2</sup> but their accuracy has only been tested against a limited set of simulations in the regions of interest. An accurate method<sup>3</sup> for treating single species nonpolar, nonspherical interactions (e.g., N<sub>2</sub> and CO<sub>2</sub>) as an effective spherical interaction has been developed. The mixture problem for molecules with shape, and the problem of the large dipole moment in H<sub>2</sub>O, are largely unsolved. Of course, there are benchmark type methods, such as molecular dynamics (MD) and Monte Carlo (MC), which provide accurate thermodynamics at the cost of around 10 minutes of CRAY time per EOS point. The parameter space is too large to use these methods directly for a practical explosives EOS. They are used to test the accuracy of much faster approximate methods that are then used to model explosives.

This paper gives results for a new<sup>4</sup> variation on the Monte Carlo method that retains the accuracy of the standard MC methods, but dramatically increases the speed with which the parameter space can be mapped out. Starting from a nonstandard reference simulation, which samples essentially all of the phase space relevant to fluids, a remapping is made to determine the EOS for different values of density and temperature throughout the fluid regime. Since the reference simulation is only calculated once and the remapping is very fast, the cost per EOS point is small.

In the remainder of the paper, we will begin with a discussion of the evaluation of the configurational density of states for a reference potential using a nonstandard Monte Carlo method. Then the transformation of the reference density of states into that for a linear combination of the reference potential and other potentials is presented. Next is given the method for evaluation of thermodynamic quantities from the transformed density of states. Results for the Lennard-Jones potential are then illustrated. This is followed by a preliminary version of the treatment of the exponential-six potential fluid. Finally, the implications for the development of a predictive, accurate EOS for detonation products is discussed.

## DENSITY OF STATES FROM MONTE CARLO

The usual NVT ensemble Monte Carlo (MC) method uses importance sampling to evaluate integrals of the form

$$\langle f \rangle = \frac{\int f(r_1, \dots, r_n) \exp(-\beta U(r_1, \dots, r_n)) dr_1 \dots dr_n}{Z(\beta)} \quad (1)$$

where  $Z(\beta) = \int \exp(-\beta U(r_1, \dots, r_n)) dr_1 \dots dr_n$  is the configuration integral,  $U$  is the total potential energy, and  $\beta = 1/kT$ . The MC steps are taken with a probability density  $P_r(r_1, \dots, r_n)$ , which is proportional to  $e^{-\beta U}$ . The approximation to  $\langle f \rangle$  from the MC sample is given by

$$\langle f \rangle = \frac{\sum_{i=1}^N f_i e^{-\beta U} P_r(i)^{-1}}{\sum_{i=1}^N e^{-\beta U} P_r(i)^{-1}}$$

$$= \sum_{i=1}^N f_i / \sum_{i=1}^N 1 = N^{-1} \sum_{i=1}^N f_i, \quad (2)$$

where only ratios of integrals are evaluated, since the overall normalization is not defined by the method. Here  $i$  designates the coordinates  $r_1, \dots, r_n$  at the  $i$ th step of the simulation.

We can transform the complications of the many-body integration to that of finding the configurational density of states. Laying the foundation for a whole class of methods, McDonald and Singer<sup>5,6</sup> evaluated relative values for the configurational density of states  $\gamma(U)$  over a limited range, by reweighting the results of a standard MC simulation. That is, Equation (1) can be rewritten as

$$\langle f \rangle = \frac{\int f(U) \gamma(U) \exp(-\beta U) dU}{Z(\beta)}, \quad (3)$$

where  $Z(\beta) = \int \gamma(U) \exp(-\beta U) dU$ ,  $\gamma(U)$  is the number of configurations between  $U$  and  $U + dU$ , and  $f(U)$  is the average of  $f$  over those configurations. Then  $\gamma(U)$  is proportional to  $e^{+\beta U}$  times the number of counts in the range  $U$  to  $U + dU$ . With further reweighting, thermodynamic quantities can be evaluated for different values of density,  $\rho$ , and temperature,  $T$ , over a limited range. For example, Equation (3) can be evaluated for any value of  $\beta$ , provided  $\gamma(U)$  and  $f(U)$  are known over the range of importance to the integrals. This idea was made more efficient by Torrie and Valleau's umbrella sampling,<sup>7</sup> in which a non-Boltzmann distribution is used to cover a wider range in a single sample. A number of applications of these and related methods have been made.

In this paper, we develop a variation on the types of methods mentioned above, with the advantage of spanning a very large range in  $U$  in a straightforward manner. In addition, a reasonable number of particles can be used in the simulation (in this example  $N = 122$ ) in contrast to many of the other methods which are typically implemented with  $N = 32$ . The evaluation of thermodynamic quantities from the simulation is different from the above methods, although there is some overlap. In addition to the usual steps in configuration



space, a step in  $\ln\beta$  is made after a given number of steps in  $U$ . This combined algorithm samples with probability density  $P(\beta, r_1, \dots, r_N) = \exp(-\beta U(r_1, \dots, r_N))/Z(\beta)$  in the limit of slow motion in  $\beta$  relative to motion in  $U$ . A uniform distribution over  $\ln\beta$  could be made with random steps. For numerical convenience, however, we have chosen to make constant size steps in  $\ln\beta$ , moving alternately up and then down a given range of  $\ln\beta$ .

Consider each value of  $\beta$  to designate a separate NVT ensemble simulation. Provided the initial condition of the  $\beta$  simulation is from a configuration that is typical of a simulation at that value of  $\beta$ , then the usual equilibration part of the run can be eliminated. (Note that there is no preference inherent in the simulation for any given configuration with energy  $U$  over any other with the same  $U$ . So, a change in  $\beta$  only changes the overall probability of sampling a state with energy  $U$ , and not the relative probabilities of particular configurations with the same  $U$ .) Given 1) a small enough step in  $\beta$  to yield a small change in the distribution of  $U$ 's sampled, and 2) a long enough sub simulation at each  $\beta$  to eliminate any significant correlation in  $U$  between the initial and final state of the sub-simulation, then the neglect of the equilibration stage is valid. In addition, a repeated entry of the  $\beta$  sub-simulation at several stages in the full simulation is qualitatively the same as taking uncorrelated sub simulations from a very long NVT MC run.

Given this reference simulation, how can we evaluate  $\gamma(U)$ ? Now  $\gamma(U)$  is a very rapidly rising function and  $\exp(-\beta U)$  is a very rapidly decreasing function such that the product is sharply peaked. This peak occurs where  $d[\ln\gamma(U) - \beta U]/dU = 0$ . Because of the sharp peak, we also know that it occurs at  $U = \langle U \rangle$ . This gives a simple relation from which to determine  $\gamma(U)$ ,

$$\beta \left( \frac{d \ln \gamma(U)}{dU} \right)_{U = \langle U \rangle_\beta} = 1 \quad (4)$$

where the  $\beta$  subscript is a reminder that  $\langle U \rangle$  is a function of  $\beta$ . Then by integration,

$$\ln \gamma(U) = - \int_U^\infty \beta(U) dU. \quad (5)$$

From the reference simulation, we obtain approximate values for  $U(\beta)$  for as many values of  $\beta$  as were sampled. The scatter in this data can be reduced by fitting to a reasonable functional form. Since the reference simulation used throughout this paper is for the  $r^{-12}$  potential, we will restrict the discussion to that particular case. In Reference 4 we fit  $\ln\beta$  vs.  $\ln U$ , which is fine for a relatively large but finite range in  $U$ . For this study, however, we have extended the range of the simulation from the virial region to the melt line. By choosing a functional form consistent with the virial EOS, the range is further extended from the ideal gas regime to the melt line.

The soft sphere fluid has scaling properties that allow the "excess" or non-ideal properties to be expressed in terms of a single scaled variable,  $x = \beta^{1/4} \rho$ . (The reference simulation of the soft sphere fluid was made with parameters  $\rho = \epsilon = \sigma = 1$ .) In the virial region (i.e., ideal gas plus second virial coefficient terms only), the compressibility factor  $Z = PV/NkT$  is given by  $Z = 1 + Bx$  where  $B = n^{23/2} \Gamma(3/4)/3 = 3.62958864$  is the reduced second virial coefficient. Similarly, the excess energy is given by  $U/N = 1/4 B x^3$ . Since we have chosen  $\rho = 1$ , this expression can be inverted to give  $x = \beta^{1/4} = (4U/NB)^{1/3}$ . The simulation results are then fit to the form,

$$x = \beta^{1/4} = \sum_{i=1}^n a_i U^{-1/3}. \quad (6)$$

The fit and the simulation data are compared in Figure 1. Note that Equation (5) can now be integrated analytically for the functional form, Equation (6).

Periodic boundary conditions were used with a potential cutoff radius  $r_c$  chosen at half the box size. Corrections were made with the usual approximation that  $g(r) = 1$  outside  $r_c$ , and integrating the appropriate expressions to get the long range contribution to the quantities of interest. The initial configuration was determined by choosing each coordinate from a

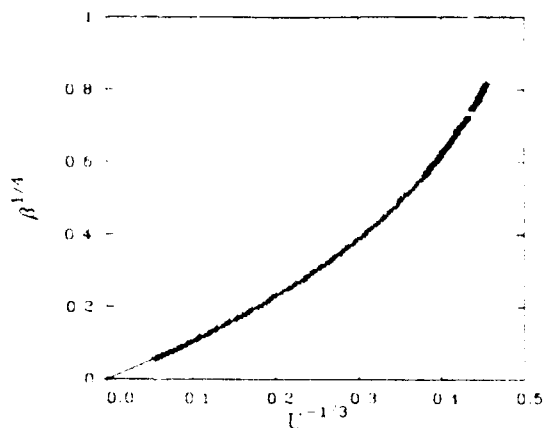


Figure 1. Comparison of Simulation Data (  $\times$  ) and Equation (6) (Line).

uniform random distribution within the box, and then ignoring steps in an equilibration period.

As a check on whether  $\delta\beta$  is small enough and the number of steps in  $U$  between steps in  $\beta_0$  is large enough, two sub-averages of  $U$  are made for each value of  $\beta$ . One average is made from segments of the simulation where  $\beta$  is increasing, and the other for  $\beta$  decreasing. The lack of a systematic difference between the two types of averages indicates that the simulation is satisfactory.

## DENSITY OF STATES TRANSFORMATION

The real advantage of the method comes from the transformation of the reference density of states, to that for an arbitrary linear combination of potentials. Then the EOS over a large parameter space may be sampled from one reference simulation, as demonstrated below.

Consider the following functional form for  $W$  the total potential energy per particle,

$$W = \sum_i a_i W_i, \quad (7)$$

where

$$W_i = \frac{1}{2N} \sum_k \sum_{l=1}^N \phi_i(r_{kl}), \quad (8)$$

$\phi_i$  is the  $i$ th pair potential for particles  $k$  and  $l$  separated by distance  $r_{kl}$ .

For a fixed reference energy  $U$ , the probability distribution of configurations with potential energy  $W$ , denoted  $P(W, U)$ , can be sampled from the reference simulation. Then the configurational density of states for the potential  $W$  is given by

$$\Gamma(W) = \int_Y(U) P(W, U) dU. \quad (9)$$

The evaluation of  $P(W, U)$  is greatly simplified because its functional form in the variable  $W$  is that of a normal distribution to a very good approximation. (This is essentially a consequence of the central limit theorem.) Then  $P(W, U)$  is determined by the evaluation of moments

$$\langle W \rangle_U = \sum_i a_i \langle W_i \rangle_U, \quad (10)$$

and

$$\sigma(U)^2 = \langle W^2 \rangle_U - (\langle W \rangle_U)^2 = \sum_i \sum_j a_i a_j (\langle W_i W_j \rangle_U - \langle W_i \rangle_U \langle W_j \rangle_U), \quad (11)$$

where  $\langle \rangle_U$  denotes the average overall configurations with the reference energy between  $U$  and  $U + dU$ . For a given value of  $U$ , the normal distribution form is

$$P(W, U) = \exp \left( -\frac{1}{2} ((W - \langle W \rangle_U)^2 / \sigma(U)^2) \right) / \sigma(U) \sqrt{2\pi}. \quad (12)$$

Note that the linear coefficients  $a_i$  enter in a trivial fashion, and Equation (12) can be evaluated for an arbitrary set of  $a_i$ 's, once the set of  $\langle W_i \rangle$ 's and  $\langle W_i W_j \rangle$ 's are sampled from the reference simulation as a function of  $U$ . In practice, the moments are sampled over bins in  $U$  and fit to algebraic functions of  $U$  over the region of  $U$  sampled by the reference simulation. Then,  $\langle W \rangle_U$  and  $\sigma(U)^2$  are evaluated using Equations (10) and (11) for the given set of  $a_i$ 's. For a given value of  $W$ , we can evaluate  $\beta(W) = \Gamma'(W)/\Gamma(W)$  (i.e., Equation (4)) from the integral

$$\Gamma'(W) = \int ((\langle W \rangle_U - W) / \sigma^2(U)) Y(U) P(W, U) dU \quad (13)$$

and Equation (9).

In order to get the pressure, we also need the average over configurations in the range  $U$

to  $U + dU$  of that part of the virial due to interparticle forces. For spherical potentials, the relevant functions are  $\{r\phi_i'(r)\}$  rather than  $\phi_i(r)$  in Equation (8). For the special case of inverse power law potentials, these two quantities only differ by a constant multiplier. It is a straightforward generalization of the derivation above to obtain an expression for pressure involving the ratio of one dimensional integrals. The Gibbs free energy can also be obtained, since the excess entropy is equal to the logarithm of the configurational density of states

A further simplification can be made, however. Again, using the sharpness of the distributions, the integral in Equation (8) can be approximated as

$$\ln \Gamma(W) \approx \ln \{Y(U)P(W,U)\}_{U @ \text{peak}} + O(N^{-1}) \quad (14)$$

The other thermodynamic averages then become the values of quantities evaluated at the peak of the sharp distribution. For example, we now have

$$\beta(W) = \Gamma'(W) / \Gamma(W) \quad (15)$$

$$= \langle W \rangle_U = W / \sigma^2(U) = (U @ \text{peak}).$$

The details are beyond the scope of the present discussion and will be presented in a subsequent paper.<sup>8</sup> The important point is that the thermodynamic quantities are evaluated from algebraic expressions

## LENNARD-JONES FLUID

We now turn to the calculation of thermodynamics for a system of interest in order to test the precision of this method. Because of its widespread use and available simulation data from other methods, we have chosen the Lennard Jones fluid as the test case with the soft sphere fluid for the reference simulation

The soft sphere pair potential is given by

$$u_{12}(r) = 4\epsilon(r/\sigma)^{-12}, \quad (16)$$

and the Lennard Jones potential is

$$u_{12}(r) = 4\epsilon[(r/\sigma)^{-12} - (r/\sigma)^{-6}], \quad (17)$$

where  $\epsilon$  is the well depth and  $\sigma$  is the point where the LJ potential crosses 0. The same parameters are used in the soft sphere potential to simplify the connection between the two, even though a single constant would be sufficient. The scaling properties of the LJ potential make it convenient to use reduced quantities with the following relations:  $T^* = kT/\epsilon$ ,  $\rho^* = \rho\sigma^3$ ,  $u^* = u/\epsilon = U^*/N$ , and  $P^* = P\sigma^3/\epsilon$ , where  $T$  is the temperature,  $\rho$  is the number density,  $u$  is the potential energy per particle  $U/N$ , and  $P$  is the pressure. The simulation was made with  $\rho = 1$  and we have chosen  $\epsilon = 1$  for convenience. Then we have  $\rho^* = \sigma^3$ ,  $a_1 = \sigma^{12}$ ,  $a_2 = -\sigma^6$ ,  $\phi_1 = 4r^{-12}$ , and  $\phi_2 = -4r^{-6}$ . With  $\rho^*$  and  $U^*$  as the independent variables,  $T^*$ ,  $P^*$ , and  $G^*$  are calculated as outlined in the previous section. In this example, the one dimensional integral forms were evaluated using a 20 point Gauss-Hermite quadrature.

In Figure 2 we show how well the simulation fits the functional form Equation (12) for several values of  $U_{12}$ . The data are scaled such that the data would then lie on a single curve, if the functional form were exact. We see that this form does fit quite well. In Figures 3 and 4, the analytic fits to scaled values of  $\langle W \rangle$  and  $\sigma^2$  are compared with those directly evaluated from the reference simulation. The results for  $P^*$  are compared with MC<sup>9,10</sup> and molecular dynamics<sup>11,12</sup> (MD) simulation values in

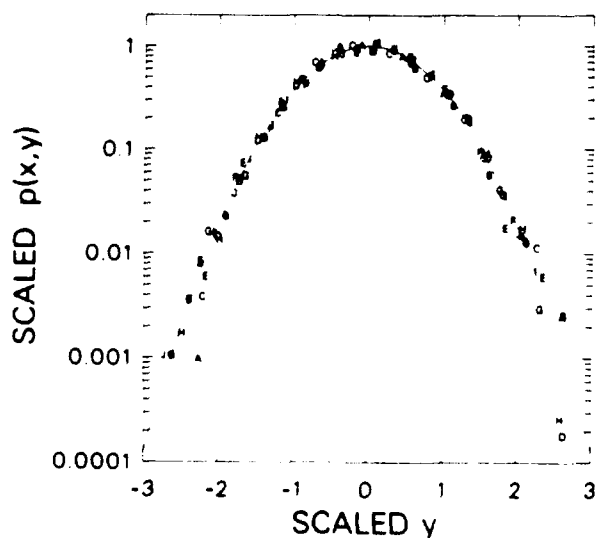


Figure 2. Comparison of the Normal Distribution (Line) and Samples of the Actual Distribution from the Simulation (Symbols)

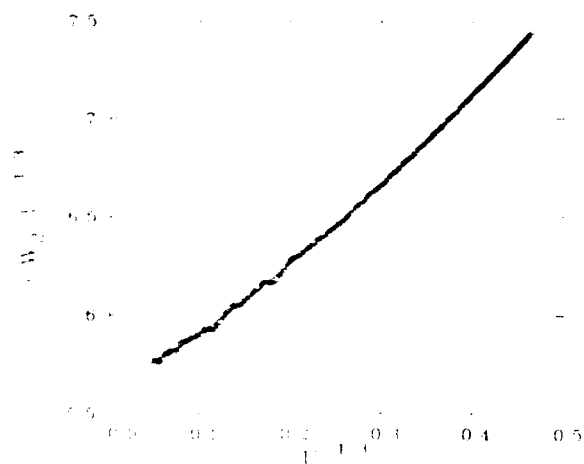


Figure 3. Comparison of the Fit to  $\langle W \rangle$  (Line) and Values from the Simulation (+). Values are scaled.

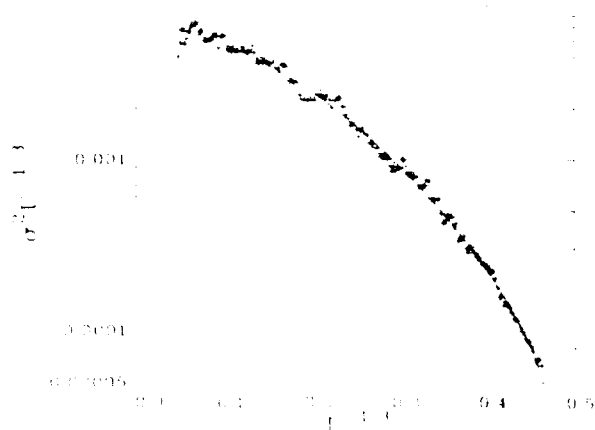


Figure 4. Comparison of the Fit to  $\sigma^2$  (Line) and Values from the Simulation (+). Values are scaled.

Figure 5. Similar comparisons for a different range of  $p^*$  and  $T^*$  are shown in Figure 6. Note that differences are smaller than the inherent scatter in the usual MD/MC methods. The gas/liquid phase equilibrium line calculation is compared with standard simulation<sup>10,13</sup> and perturbation methods<sup>14</sup> in Figure 7.

## EXPONENTIAL-SIX FLUID

The most commonly used pair potential for detonation products EOS is the exponential six form given by

$$\phi(r) = \frac{\epsilon [6 \exp(\alpha(1 - r/r^*)) - a(r/r^*)^{-6}]}{(\alpha - 6)} \quad (18)$$

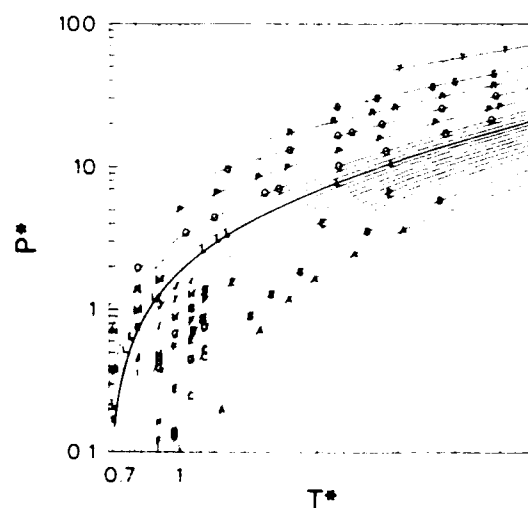


Figure 5.  $P^*$  Versus  $T^*$  for a Range of Reduced Densities from 0.6 to 1.2. MC/MD simulations (symbols), this work (line), and location of the melt line (dash).

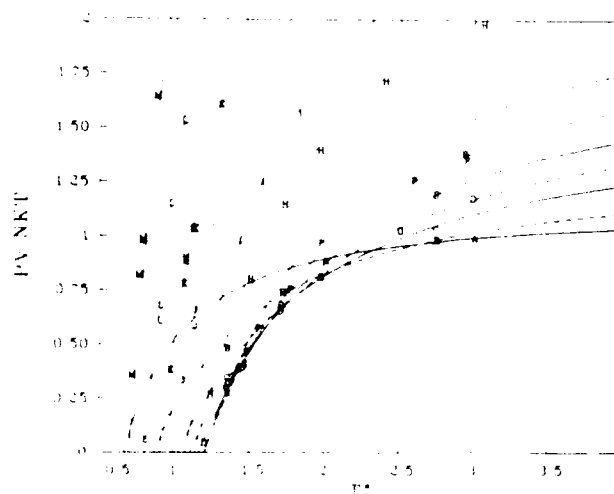


Figure 6.  $PV/NKT$  Versus  $T^*$  for a Range of Reduced Densities from 0.1 to 0.9. MC/MD simulations (symbols) and this work (line).

Preliminary results are presented here for a fit (to an accuracy of better than 1 percent) of the exp 6 as a linear combination of inverse power law potentials given by  $\phi^i = 4r^{-i}$  over a range of  $i = 6$  to 15. The  $a$ 's are chosen for a given value of  $\alpha$  with  $\epsilon = r^* = 1$ . The scaling properties in the Lennard-Jones section are the same here with the additional relation  $\sigma^6 = 2r^{*6}$ . Then the  $a_i$ 's are scaled to give results for different values of  $p^*$ . The algebraic forms for evaluation of thermodynamic quantities are used. The reference simulation needs to be run longer to

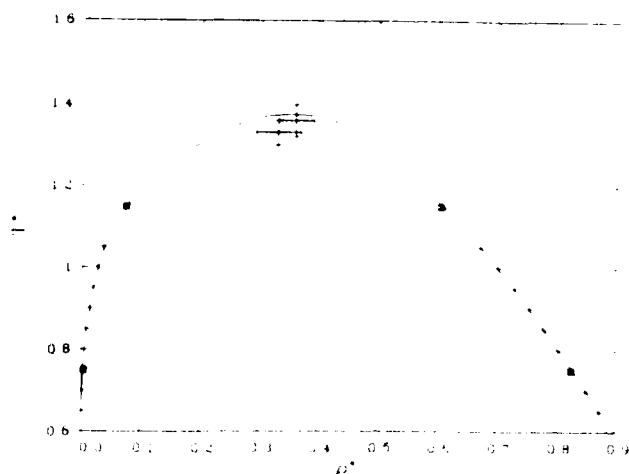


Figure 7. Gas/Liquid Equilibrium Phase Line for the Lennard-Jones Fluid. This work (line), standard MC simulation (box, +), and perturbation theory for the critical point (large +).

improve the statistics, but the preliminary results are accurate to about 2 percent in comparison with standard MC simulations<sup>15</sup> for  $\alpha = 13.5$ . The analytic representation for the moments are compared with the direct evaluation from the simulation in Figures 8, 9, and 10 for a typical case. Results for 5 values of  $\alpha$ , 30 values of  $p^*$ , and 3 values of  $T^*$  are shown in Figures 11 and 12. Since the final expressions are algebraic, as many EOS points as are desired may be generated with a negligible amount of computer time once the single long reference simulation is made.

## IMPLICATIONS

We have demonstrated a very efficient method to generate EOS simulation benchmarks for the Lennard-Jones and exponential-six potentials. Indeed, the final analytic representations could compete with perturbation theories for speed and accuracy. The extension of the method to mixtures, polar fluids, non spherical interactions, and combinations of these appears to be straightforward. For example, mixtures could be studied by choosing the  $W_i$ 's to include the interactions within and between subgroups of particles rather than all of the particles in a simulation. Then the cross potential could be varied as easily as the density. The phase segregation line could then be explored as a function of cross potential parameters, using the free energy results for pure species and mixtures.

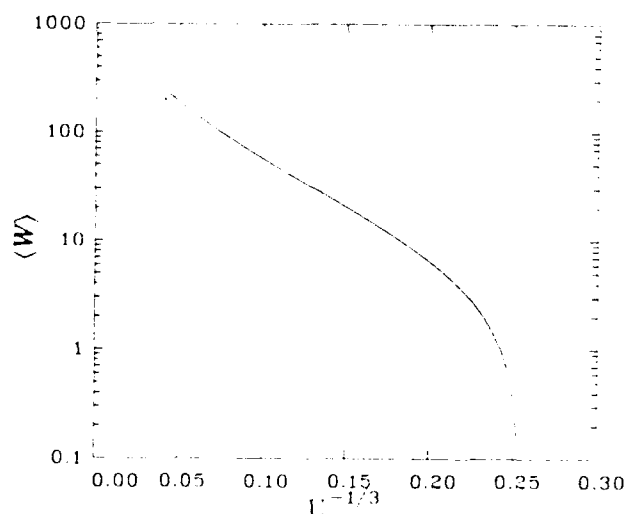


Figure 8.  $\langle W \rangle$  Versus  $U^{-1/3}$  for a Typical EXP-6 Case. Analytic fit (line) and values from the simulation (dash).

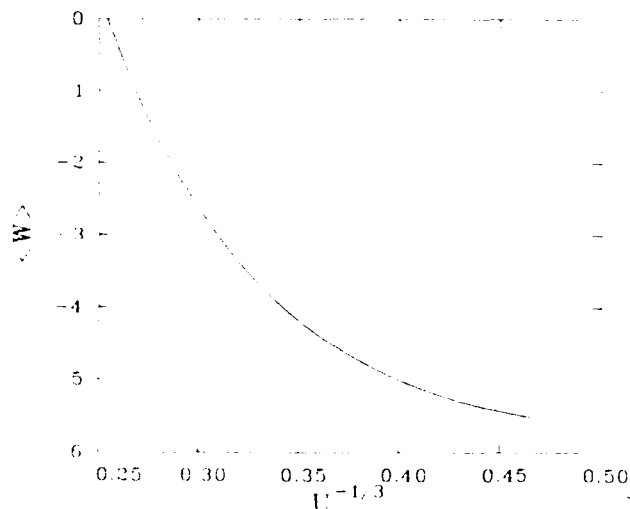


Figure 9.  $\langle W \rangle$  Versus  $U^{-1/3}$  for a Typical EXP-6 Case. Analytic fit (line) and values from the simulation (dash).

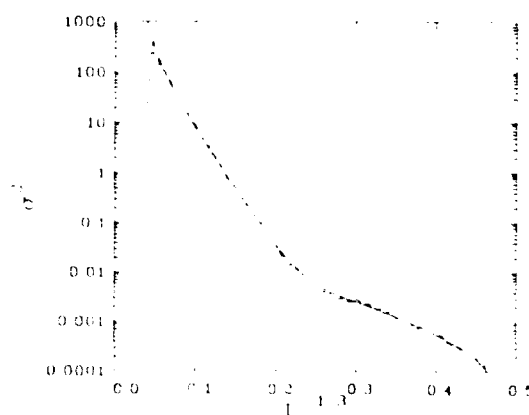


Figure 10.  $\alpha^2$  Versus  $U^{-1/3}$  for a Typical EXP-6 Case. Analytic fit (line) and values from the simulation (dash).

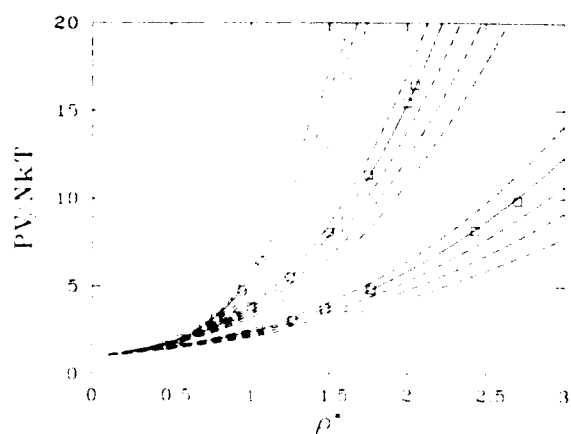


Figure 11.  $PV/NKT$  Versus  $\rho^*$  for  $a=12, 12.5, 13, 13.5$ , and  $14$ ,  $T^*=5, 20$ , and  $100$ , and  $\rho^*=0.1$  to  $3.0$ . This work  $a=13.5$  (line) and other  $a$ 's (dash), standard MC simulations for  $a=13.5$  (box).

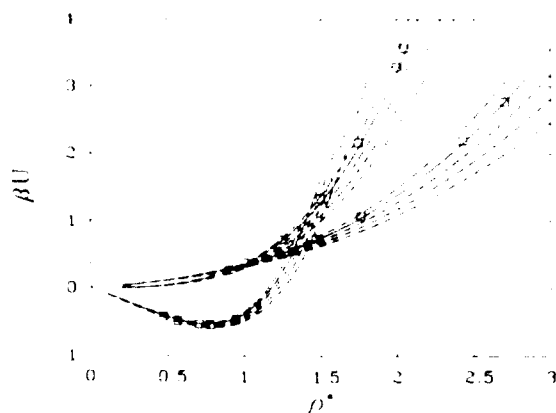


Figure 12.  $\beta U$  Versus  $\rho^*$  for  $a=12, 12.5, 13, 13.5$ , and  $14$ ,  $T^*=5, 20$ , and  $100$ , and  $\rho^*=0.1$  to  $3.0$ . This work  $a=13.5$  (line) and other  $a$ 's (dash), standard MC simulations for  $a=13.5$  (box).

These types of studies would be extremely expensive in both computer time and man time for any systematic study with standard methods. With the new method, these studies become tractable and the remaining parameter space for detonation products EOS can be explored. The net goal is to fill in the gap of missing benchmarks for the development of thermodynamic theories that will lead to a detonation products EOS that is accurate, predictive, and physically meaningful.

## REFERENCES

1. Ross, M., "A High-Density Fluid-Perturbation Theory Based on an Inverse 12th-power Hard-Sphere Reference System," *J. Chem. Phys.*, Vol. 71, No. 4, 1979, p. 1567.
2. Ree, F. H., "Simple Mixing Rule for Mixtures with EXP-6 Interactions," *J. Chem. Phys.*, Vol. 78, No. 1, 1983, p. 409.
3. Shaw, M. S.; Johnson, J. D.; and Ramshaw, J. D., "An Approximate Variational Method for Improved Thermodynamics of Molecular Fluids," *J. Chem. Phys.*, Vol. 84, No. 6, 1986, p. 3479.
4. Shaw, M. S., "A Density of States Transformation Monte Carlo Method: Thermodynamics of the Lennard-Jones Fluid," *J. Chem. Phys.*, Vol. 89, No. 4, 1988, p. 2312.
5. McDonald, I. R. and Singer, K., "Calculation of Thermodynamic Properties of Liquid Argon from Lennard-Jones Parameters by a Monte Carlo Method," *Disc. Faraday Soc.*, Vol. 43, 1967, p. 40.
6. McDonald, I. R. and Singer, K., "Examination of the Adequacy of the 12-6 Potential for Liquid Argon by Means of Monte Carlo Calculations," *J. Chem. Phys.*, Vol. 50, No. 6, 1969, p. 2308.
7. Torrie, G. M. and Valleau, J. P., "Monte Carlo Free Energy Estimates Using Non-Boltzmann Sampling: Application to the Sub-Critical Lennard-Jones Fluid," *Chem. Phys. Lett.*, Vol. 28, No. 4, 1974, p. 578; "Nonphysical Sampling Distributions in Monte Carlo Free-Energy Estimation: Umbrella Sampling," *J. Comp. Phys.*, Vol. 23, No. 2, 1977, p. 187; "Monte Carlo Study of a Phase-separating Liquid Mixture by Umbrella Sampling," *J. Chem. Phys.*, Vol. 66, No. 4, 1977, p. 1402.
8. Shaw, M. S., in preparation.
9. McDonald, I. R. and Singer, K., "An Equation of State for Simple Liquids," *Mol. Phys.*, Vol. 23, No. 1, 1972, p. 29.

10. Hansen, J. P. and Verlet, L., "Phase Transitions of the Lennard-Jones System," *Phys. Rev.*, Vol. 184, No. 1., 1969, p. 151.
11. Nicolas, J. J.; Gubbins, K. E.; Streett, W. B.; and Tildesley, D. J., "Equation of State for the Lennard-Jones Fluid," *Mol. Phys.*, Vol. 37, No. 5, 1979, p. 1429.
12. Verlet, L., "Computer 'Experiments' on Classical Fluids. I. Thermodynamical Properties of Lennard-Jones Molecules," *Phys. Rev.*, Vol. 159, No. 1., 1967, p. 98; Levesque, D., and Verlet, L., "Perturbation Theory and Equation of State for Fluids," *Phys. Rev.*, Vol. 182, No. 1., 1969, p. 307.
13. Adams, D. J., "Calculating the Low Temperature Vapour Line by Monte Carlo," *Mol. Phys.*, Vol. 32, No. 3., 1976, p. 647.
14. Verlet, L. and Levesque, D., "On the Theory of Classical Fluids VI," *Physica*, Vol. 36, 1967, p. 254.
15. Ross, M. and Alder, B. J., "Shock Compression of Argon. II. Nonadditive Repulsive Potential," *J. Chem. Phys.*, Vol. 46, No. 11, 1967, p. 4203; Fiorese, G. (unpublished work), quoted by Zerah, G. and Hansen, J. P., "Self-consistent Integral Equations for Fluid Pair Distribution Functions: Another Attempt," *J. Chem. Phys.*, Vol. 84, No. 4, 1986, p. 2336.

## DISCUSSION

F. VOLK, Fraunhofer Institut  
Pfinztal, FRG

Will you also investigate the non-spherical molecule CO<sub>2</sub>?

## DISCUSSION

W. BYERS BROWN  
University of Manchester, UK

It is possible to extend your method, which approximates an arbitrary pair potential as a sum of various inverse power potential terms, to site-site potentials for the interaction of polyatomic molecules?

## REPLY TO BOTH QUESTIONS BY M. S. SHAW

I intend to extend the method to a number of classes of systems including the non-spherical molecule CO<sub>2</sub>. Treating non-spherical potentials and polar molecules will be done using a basis set with angular, as well as radial dependence. The method should also be able to handle mixtures by sampling subsets of the distributions in which the pure species potentials and cross potentials enter as linear coefficients. If all goes well, a generalization of the method will give the EOS for arbitrary mixtures of non-spherical molecules (i.e., detonation products), including such details as phase segregation lines. Because the method is so fast, this large parameter space can be explored thoroughly as opposed to the very limited sampling that can be done with standard simulation methods.

# CALCULATIONS OF DETONATION PRESSURES FOR A HOMOLOGOUS SERIES OF POLYNITROALIPHATIC EXPLOSIVES USING A FLUID PERTURBATION EQUATION OF STATE AND A NEW CHEMICAL EQUILIBRIUM COMPUTER PROGRAM

F. J. Zerilli and H. D. Jones  
Naval Surface Warfare Center  
Silver Spring, Maryland 20903-5000

*Detonation pressures, velocities, and compositions were calculated for a homologous series of bis(2,2,2-trinitroethyl)alkanedioates,  $C(NO_2)_3CH_2-O-CO-(CH_2)_n-CO-O-C(NO_2)_3$ ,  $n = 0 - 15$ , using a fluid perturbation equation of state developed by Jones. The results are compared to previous calculations by Zerilli, Doherty, Short, McGuire, and Kamlet using the BKW and JCZ3 equations of state. A brief description of the algorithms used in the chemical equilibrium calculations is given.*

## INTRODUCTION

Kamlet<sup>1</sup> has proposed that, rather than continuing the 30 year search for agreed upon experimental detonation properties as benchmarks for equations of state, the detonations community consider whether calculations for a homologous series of organic explosives might not serve the purpose equally well or better. The argument for this is that much can be learned by studying the variation of a detonation property with the monotonic changes in heats of formation and oxygen balance, as well as the breakpoints in composition produced by the regular variation of the number of  $CH_2$  groups in the homologous series. In the series studied, bis(2,2,2-trinitroethyl)alkanedioates,  $C(NO_2)_3CH_2-O-CO-(CH_2)_n-CO-O-C(NO_2)_3$ ,  $n = 0 - 15$ , the homolog with  $n = 1$  has an oxygen balance like PETN, that with  $n = 4$  has an oxygen balance like RDX, and that with  $n = 7$  has an oxygen balance like TNT. Discontinuities occur for  $n$  between 0 and 1 where  $O_2$  is exhausted as a product and for  $n$  above 14 where  $H_2O$  is exhausted ( $H_2O$   $CO_2$  arbitrary).

The previous calculations<sup>1</sup> (at a constant density of  $1.7 \text{ gm/cm}^3$ ) showed that the BKW equation of state with BKWR parameters gives

results which agree well with the empirical Kamlet-Jacobs equation (which is a good fit for a large group of CHNO explosives) whereas STRETCH-BKW with either RDX or TNT parameters predicted detonation pressures which are almost constant as a function of oxygen balance (as determined by  $n$ , the number of  $CH_2$  groups). RUBY BKW showed the unhappy characteristic of predicting increasing detonation pressures with increasing number of  $CH_2$  groups. JCZ3 displayed a behavior similar to BKWR but with generally lower detonation pressures.

All of the previous calculations showed similar variations of detonation pressure with loading density. Also, calculations at theoretical maximum density tended to show closer agreement with the Kamlet-Jacobs equation than the calculations at constant density. The BKWR calculations with a heat of formation for solid carbon of 12 kcal/mole showed a behavior most similar to that of the Kamlet-Jacobs equation.

In the present work, detonation pressures, velocities, and compositions were calculated using a fluid perturbation equation of state developed by Jones and are compared to the previous results.



## EQUATION OF STATE

The fluid perturbation equation of state represents a departure from the equations of state cited above in that it is an attempt to provide a description of a fluid system based upon the best description of physical reality at the molecular level that is currently available. The fluid perturbation equation of state is used to describe the species in the fluid phase, while a Debye-Gruneisen model is used to describe solid carbon. Nine fluid species are currently in place: CH<sub>4</sub>, CO, CO<sub>2</sub>, H<sub>2</sub>, H<sub>2</sub>O, H<sub>3</sub>N, N<sub>2</sub>, NO, and O<sub>2</sub>. Two phases of carbon, graphite, and diamond are currently allowed.

The individual fluid species are described by a perturbation theory which is based on the assumption that the repulsive intermolecular forces provide the dominant characteristics of the material. This technique, originated by Weeks, Chandler, and Anderson,<sup>2</sup> has been shown to be applicable in both the moderate and high pressure domains.<sup>3</sup>

It is assumed that the intermolecular interaction is spherically symmetric and is taken as

$$V(r) = u_0(r) + w(r), \quad (1)$$

where  $u_0(r)$  is the reference potential with repulsive character and  $w(r)$  is the attractive perturbation. The reference potential is given by

$$u_0(r) = \begin{cases} V(r) - V(\lambda), & r \leq \lambda \\ 0, & r > \lambda \end{cases}, \quad (2)$$

and the perturbation is taken as

$$w(r) = \begin{cases} V(\lambda), & r \leq \lambda \\ V(r), & r > \lambda \end{cases}, \quad (3)$$

where

$$V(r) = \epsilon \{ (6/a) \exp[a(1 - r/r^*)] - (r^*/r)^6 / (1 - 6/a) \}. \quad (4)$$

The potential parameters denote the usual quantities. Specifically,  $\epsilon$  is the well depth,  $a$  is the steepness parameter, and  $r^*$  is the position of the minimum of the potential. In some instances the potential is divided at

the minimum;<sup>2,4</sup> however, Ree<sup>5</sup> demonstrated that the region of applicability could be extended to the high density domain by taking  $\lambda$  as a variational parameter.

Two of the important fluid constituents, H<sub>2</sub>O and NH<sub>3</sub> exhibit strong multipole interactions. Ree<sup>6</sup> has suggested the introduction of a temperature dependence in the well-depth of the intermolecular potential

$$\epsilon = \epsilon_0(1 + T^*/T) \quad (5)$$

to address this problem in a simple fashion. In the above expression,  $\epsilon_0$  and  $T^*$  are constants.

Using standard techniques,<sup>7</sup> the free energy can be written as a perturbative series in inverse temperature, which is well-suited for the shock wave domain. The result for the excess free energy per particle is

$$f = f_0 + \rho/2 \int dr w(r) g_0(r) + \dots, \quad (6)$$

where  $f_0$  and  $g_0(r)$  are the free energy per particle and radial distribution function for the reference system, respectively, and the number density is denoted by  $\rho$ . In this work, only the two leading terms in the expansion of Equation (6) are retained.

The steep, discontinuous behavior of  $u_0(r)$  is reminiscent of a hard sphere potential. Application of a functional Taylor expansion<sup>7</sup> yields the result that the free energy of the reference system is identical to second-order with that for hard spheres with a temperature and density-dependent hard sphere diameter, so that

$$f_0 = f_{Hs}, \quad (7)$$

where

$$g_0(r) = \exp(-\beta u_0(r)) y_{Hs}(r), \quad (8)$$

$$y_{Hs}(r) = \exp(-\beta V_{Hs}(r)) y_{Hs}(r). \quad (9)$$

$g_{Hs}(r)$  and  $V_{Hs}(r)$  are the radial distribution function and intermolecular potential for hard spheres, respectively, and  $\beta^{-1}$  is Boltzmann's constant times the temperature.

The hard-sphere diameter is determined from the condition

$$\int dr \{ \exp(-\beta u_0(r)) - \exp(-\beta V_{Hs}(r)) \} y_{Hs}(r) = 0 \quad (10)$$

This is the requirement that the long wavelength structure factors for the reference system and the hard-sphere system be equal.

Combination of the results of Verlet-Weis<sup>4</sup> with the Percus-Yevic description of the hard-sphere system<sup>8</sup> yields analytic results for the Helmholtz free energy aside from simple numeric integrals. The compressibility and excess internal energy per particle are obtained from derivatives of the free energy as

$$Z = \beta p / \rho = 1 + \rho (\partial f / \partial \rho)_\beta \quad (11)$$

and

$$E = (\alpha \beta f / \alpha \beta)_\rho \quad (12)$$

It was found that the compressibility defined in this manner, rather than the original analysis of Verlet-Weis compared more favorably with Monte Carlo results in the higher pressure and temperature region.

Intermolecular potential parameters for the appropriate molecular species are chosen to be consistent with Hugoniot data. Table 1 lists the fluid equation of state parameters used for the calculations performed in this work.

A Chebychev polynomial representation of the thermodynamic state variables for fluids whose molecules interact with an exp-6 potential has been given by Brown.<sup>9</sup> This is employed in the equilibrium state calculations within the appropriate region of constraints to save computer time. It should be noted that a modification must be made to the results quoted in Reference 9 to account for the temperature dependence introduced into the intermolecular potential

A semiempirical Gruneisen<sup>10</sup> equation of state which employs a Murnaghan<sup>11</sup> form for the zero degree isotherm is used to describe two of the phases of solid carbon. The required equation of state parameters are obtained by matching thermal and shock wave data

A more complete description of both the solid carbon and fluid equations of state is given in Reference 12.

Table 1. Fluid Equation of State Parameters

Species	$r^*$ (Angstrom)	$\epsilon_0/k$ (Kelvin)	$a$	$T^*$ (Kelvin)
CH <sub>4</sub>	4.15	154.1	13.0	0
CO	4.12	100	13.3	0
CO <sub>2</sub>	4.15	250	13.4	0
H <sub>2</sub>	3.46	36	11.1	0
H <sub>3</sub> N	3.50	325	12.7	200
H <sub>2</sub> O	3.20	225	13.2	500
N <sub>2</sub>	4.12	100	13.3	0
NO	3.97	112.9	13.0	0
O <sub>2</sub>	3.89	125	13.0	0

A one-fluid model suggested by Ree<sup>6</sup> is used to describe the fluid mixture. It has the advantage over similar approaches in that it removes the constraint that the steepness parameter of all the fluid constituents be the same. The free energy of the mixture can be written as that of a reference fluid characterized by averaged potential parameters given by

$$(r^*)^3 = \sum_{i,j} x_i x_j (r_{ij}^*)^3, \quad (13)$$

$$\epsilon = \sum_{i,j} x_i x_j \epsilon_{ij} (r_{ij}^*/r^*)^3, \quad (14)$$

$$a = \sum_{i,j} x_i x_j a_{ij} (\epsilon_{ij}/\epsilon) (r_{ij}^*/r^*)^3, \quad (15)$$

where the  $x_i$ 's are the mole fractions, and the interaction parameters are taken as

$$r_{ij}^* = (r_i^* + r_j^*)/2, \quad (16)$$

$$\epsilon_{ij} = (\epsilon_i \epsilon_j)^{1/2}, \quad (17)$$

$$a_{ij} = (a_i a_j)^{1/2} \quad (18)$$

It is assumed that the fluid and solid phases of the reaction products are in equilibrium at the same temperature and pressure. Therefore, the thermodynamic properties of the entire system can be obtained in the usual fashion. For example, for any molar quantity A,

$$\Lambda = x_g A_g + x_s A_s, \quad (19)$$

where  $x$  is mole fraction, and the subscripts  $g$  and  $s$  refer to the gas and solid phases, respectively.

## EQUILIBRIUM CODE DESCRIPTION

The chemical equilibrium program uses a two stage iterative process. In stage one (outer iterative loop), the chemical potential of each species in the system is calculated using the fluid and solid equations of state and the current estimate of the mole numbers for each species. Then, in stage two (inner iterative loop), a Newton-Raphson algorithm is used to find the mole numbers which make the derivatives of the Gibbs potential with respect to the mole numbers zero (the element abundance constraints having been taken into consideration). In this stage, the algorithm used assumes ideal mixing. Then, the calculation returns to stage one where a new set of (non-ideal) chemical potentials is computed and the process is repeated until the sum of the absolute values of the differences in mole numbers between two successive outer loop iterations becomes less than some pre-assigned tolerance. This process is known to converge if the dependence of the non-ideal part of the chemical potentials on the mole numbers is sufficiently weak. The sufficiency condition for convergence is hard to verify for the fluid perturbation equation of state. However, the results have been compared in several cases with the results of computations using a much slower (factor of 100), but much more robust direct minimization technique described by Levine<sup>13</sup>. The results have been found to be identical within machine round-off error. The two loop process is used because it is relatively fast but, most importantly, it obviates the need to calculate derivatives of the chemical potential with respect to the mole numbers. This would be a very expensive process with the fluid perturbation equation of state.

Hugoniot points are calculated by a straightforward technique. Given a pressure  $P$ , the temperature  $T$  which is the zero of the function

$$H(T) = E - E_0 - (P + P_0)(V - V_0)/2 \quad (20)$$

is found using Brent's algorithm.<sup>14</sup> In evaluating the function  $H(T)$  the equilibrium routine is used to find the composition and, as a by-product, the internal energy  $E$  and the specific volume  $V$  at a given pressure and temperature.

Brent's algorithm uses a combination of bisection and secant methods so that no derivatives of the thermodynamic functions are needed. This is an important feature in that it allows the use of equations of state which are not necessarily described in terms of analytic functions. Even tabular functions may be used. This contrasts with the TIGER code<sup>15</sup> which is heavily dependent upon higher than first order derivatives of the thermodynamic potentials and is, therefore, most conveniently adaptable only to equations of state representable in some relatively simple analytic form.

In keeping with the spirit of not requiring higher than first order derivatives of thermodynamic potentials, the routine to find Chapman-Jouguet states uses an algorithm which is based on the graphical method of finding the Rayleigh line which is tangent to the Hugoniot. Three Hugoniot points are computed and fit with a parabola. A simple computation then gives the point at which the Rayleigh line is tangent. This point is then made the second point of a new set of three Hugoniot points, and the old second point becomes one of the new end points. The other end point is placed on the other side of the middle point at an equal distance from the middle point and a new parabola is fit. The process is repeated until the difference between two successive tangent points is less than a pre-assigned tolerance. The procedure converges very rapidly (three to five iterations for five significant figures).

Ree<sup>16</sup> has found that certain explosives (for example, RDX) may have Chapman-Jouguet states which lie in a temperature and pressure range in which it is thermodynamically favorable for a substantial portion of the product species  $H_2O$  and  $N_2$  to exist in a second binary fluid phase. We have observed this "phase separation" in our calculations, but

the equilibrium algorithm we are currently using has severe convergence problems when more than one multispecies phase is allowed. The algorithm, however, does handle single species phases such as solid carbon without difficulty. Fortunately, the C-J states for the compounds discussed here do not seem to lie in a region where the second fluid phase is likely to be formed.

## CALCULATIONAL RESULTS FOR THE HOMOLOGOUS SERIES

Figure 1 illustrates the Chapman-Jouguet pressure as a function of  $n$ , the sequence number of the homologs where each homolog is at theoretical maximum density (TMD). Shown in the figure are the results using two forms of solid carbon—diamond and graphite. Also shown, for comparison, are predictions of the Kamlet-Jacobs equation, and TIGER calculations using the BKWR and JCZ3 equations of state. The heat of formation of solid carbon was taken to be 12 kcal/mole for the BKWR equation of state and 0 kcal/mole for the JCZ3 equation of state. The most obvious feature of the physical equations of state (fluid perturbation and JCZ3) is that they produce approximately the same results and these results are significantly lower than those produced by the empirical equations (Kamlet Jacobs and BKWR). In fact, Jones fluid perturbation equation of state with a graphite equation of state for solid carbon gives virtually identical results to those of TIGER JCZ3 with 0 kcal/mole heat of formation for carbon.

Calculations, not reproduced here, were done using Ree's fluid perturbation parameters.<sup>6</sup> Compared with the Jones parameter results, the Ree parameter results were 4 percent lower at  $n = 0$ , 5 to 7 percent lower at  $n = 16$ , and identical at  $n = 7$  with smooth variation of the difference for intermediate values of  $n$ .

Kamlet<sup>1</sup> also compared the variation of CJ pressure with  $n$ , where each homolog is initially at the constant density of  $1.7 \text{ gm/cm}^3$ . Figure 2 illustrates the results predicted by the Jones fluid perturbation equation of state, again with two different carbon phases, and again compared with Kamlet Jacobs, TIGER BKWR, and TIGER JCZ3. Again the physical

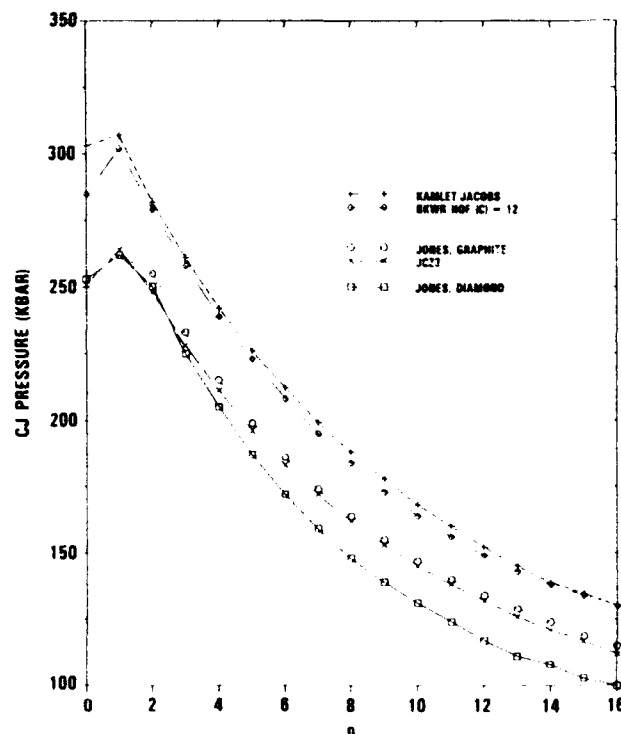


Figure 1. Chapman-Jouguet Pressure Versus Homolog Sequence Number for Homologs Initially at Theoretical Maximum Density (TMD)

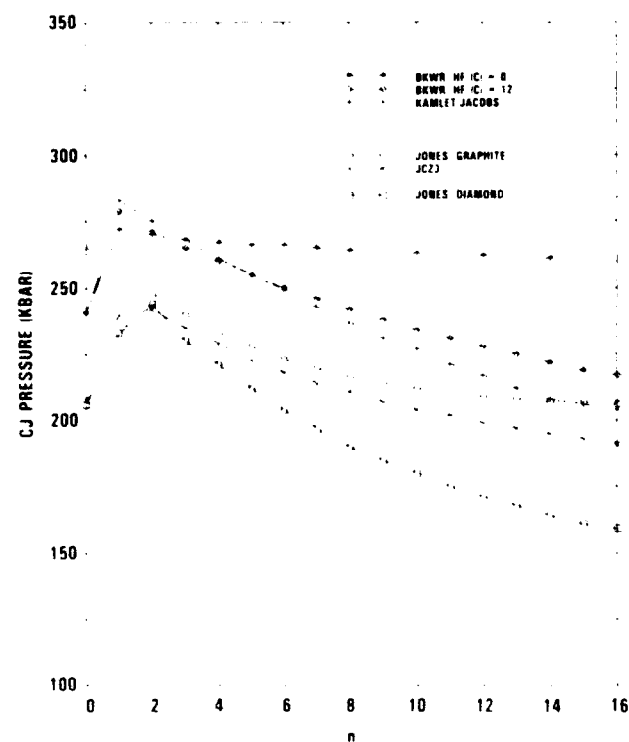


Figure 2. Chapman-Jouguet Pressure Versus Homolog Sequence Number for Homologs Initially at  $1.7 \text{ gm/cm}^3$

equations of state and the empirical equations of state give results which cluster into two separate groups with Jones Graphite giving results very similar to JCZ3.

Detonation temperatures, velocities, and mole fractions were not discussed in the article of Reference 1, however, a complete equation of state should predict all of these quantities. The Kamlet-Jacobs equation does not predict temperatures and the BKW temperatures are thought to be unreliable. Figures 3, 4, and 5 show the predictions of the Jones equation of state for mole fraction of carbon, temperature, and detonation velocity, respectively.

Both the mole fraction of carbon and the temperature are relatively independent of the initial density and of the carbon equation of state, and both vary relatively smoothly with  $n$ .

The mole fraction of carbon (Figure 3) predicted by all the equations of state is close to the value predicted by the  $H_2O-CO_2$  arbitrary (oxygen first burns hydrogen to water, then carbon to carbon dioxide). Comparing the Jones diamond result at TMD with the result at  $1.7 \text{ gm/cm}^3$  it is seen that higher initial

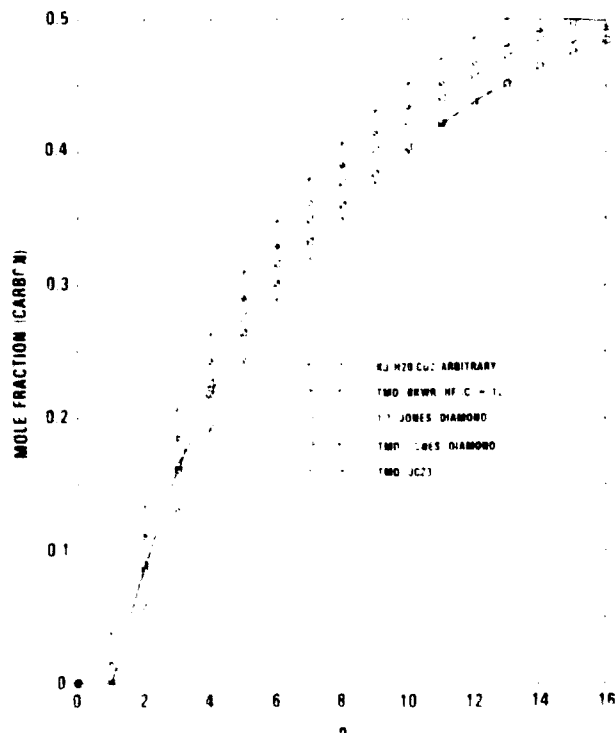


Figure 3. Chapman-Jouguet Mole Fraction of Solid Carbon Versus Homolog Sequence Number

density favors increased carbon production (to be expected from Le Chatelier's Principle). For reference, the TMD for  $n = 0$  is  $1.828 \text{ gm/cm}^3$  and varies smoothly down to  $1.359 \text{ gm/cm}^3$  for  $n = 16$ . The  $1.7 \text{ gm/cm}^3$  curves cross the TMD curves slightly beyond  $n = 2$  where the TMD is  $1.722 \text{ gm/cm}^3$ .

The CJ temperatures (Figure 4) predicted by all of the physical equations of state are in good agreement with each other. As is well known, the BKW equation predicts significantly lower temperatures. The effect of initial density upon the CJ temperature is illustrated by the BKWR curves for TMD initial density and  $1.7 \text{ gm/cm}^3$  initial density. Increasing initial density lowers the CJ temperature.

The detonation velocity (Figure 5), as expected, depends strongly on the initial density as well as upon the carbon equation of state.

## CONCLUSION

The comparison of the predictions of detonation pressures by "physical" equations of state such as those of Jones, Ree, JCZ3 with predictions by "empirical" equations such as Kamlet-Jacobs shows relative consistency within each group, but disagreement between

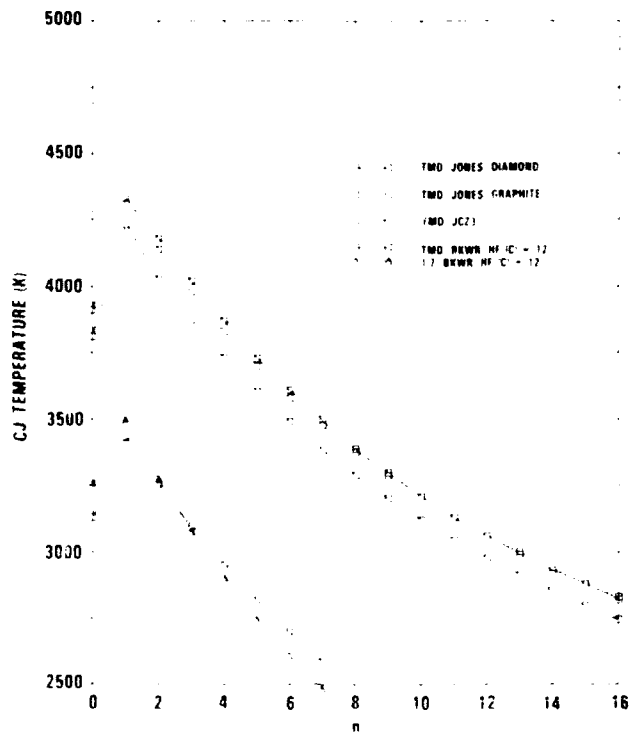


Figure 4. Chapman-Jouguet Temperature Versus Homolog Sequence Number

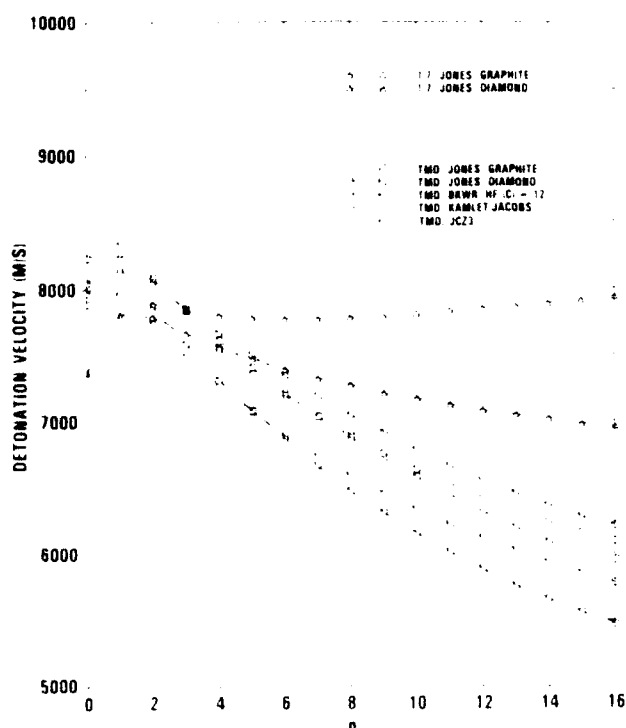


Figure 5 Detonation Velocity Versus Homolog Sequence Number

groups. The empirical equations are, of course, designed to reproduce experimental results but lack predictive capability. When the physical equations fail to reproduce experimental results the parameters cannot be changed but the assumptions must be re-examined. Ree's discovery of the importance of a second binary fluid phase to the detonation properties of RDX is an example of a phenomenon which could not be predicted by an empirical equation.

This article has presented comparative calculations based upon a hypothetical series of explosives with regularly varying properties. A comparison for the real explosives PETN, RDX, and TNT will be presented by Jones in a separate publication.

This work was supported by the NSWC Independent Research Program and the Explosives Technology Block NS3A

## REFERENCES

1. Zerilli, F. J., Doherty, R. M., Short, J. M., McGuire, R. R., and Kamlet, M. J., "A Comparison of Detonation Pressures for a

Homologous Series of Polynitroaliphatic Explosives by Different Equations of State," *Combustion and Flame*, Vol. 74, 1988, pp. 295-310.

2. Weeks, J. D., Chandler, D., and Anderson, H. C., *J. Chem. Phys.*, Vol. 54, 1971, p. 5237.
3. Jones, H. D., *J. Appl. Phys.*, Vol. 53, 1982, p. 6604.
4. Verlet, L. and Weis, J., *Phys. Rev.*, Vol. A5, 1972, p. 939.
5. Ree, F. H., *J. Chem. Phys.*, Vol. 64, 1976, p. 4601.
6. Ree, F. H., *J. Chem. Phys.*, Vol. 81, 1984, p. 1251.
7. Zwanzig, R. W., *J. Chem. Phys.*, Vol. 22, 1954, p. 1420.
8. Wertheim, M. S., *Phys. Rev. Lett.*, Vol. 10, 1963, p. E501.
9. Brown, W. B., *J. Chem. Phys.*, Vol. 87, 1987, p. 566.
10. Liebfried, G. and Ludwig, W., *Solid State Physics*, F. Seitz and D. Turnbull, Eds., Vol. 12, Academic Press, London, 1961, p. 275.
11. Murnaghan, F. D., *Proc. Nat. Acad. Sci.*, Vol. 30, 1944, p. 244.
12. Jones, H. D. and Gray, M. V., *Combustion and Flame*, Vol. 64, 1986, pp. 185-192.
13. Levine, H. B., *Final Report on the Method of Univariant Descent for Solving Problems in Heterogeneous Chemical Equilibria*, Contract No. 6334103, Lawrence Livermore National Laboratory, Livermore, CA, Jul 1982.
14. Press, W. H.; Flannery, B. P.; Teukolsky, S. A., and Vetterling, W. T., *Numerical Recipes*, Cambridge University Press, New York, 1986, pp. 251-254.
15. Cowperthwaite, M. and Zwisler, W. H., *TIGER Computer Program Documentation*, Stanford Research Institute Publication No. Z106, Stanford Research Institute, Palo Alto, CA, Oct 1984.

16. Ree, F. H., *J. Chem. Phys.*, Vol. 84, No. 10, May 15, 1986, p. 5845.

## DISCUSSION

F. VOLK  
Fraunhofer Institute  
Pfinztal, FRG

Did you calculate PETN or another HE for which we can neglect the carbon formation?

## REPLY BY FRANK ZERILLI

*The Chapman-Jouguet Shock Velocity and Pressure for Different Initial Densities of PETN from the Jones-Zerilli Code*

Initial Density (g/cc)	D (km/sec)	P (kbar)
1.77	8.21	281
1.70	7.95	261
1.60	7.63	235
1.45	7.09	177
1.23	6.19	118
0.95	5.01	66
0.48	3.53	20
0.25	2.90	8

## DISCUSSION

W. BYERS BROWN  
University of Manchester, UK

I was very interested in this paper, which appears very close in motivation to the paper by M. Braithwaite and myself presented at this symposium. I would like to ask two questions:

1. How were the intermolecular parameters quoted in Table 1 chosen?

2. Does Dr. Hermenzo Jones think it is possible to extend the treatment of polar species by the Pade-type perturbation theory of Rasiah and Stell to mixtures, so that the questionable assumption equation (5) can be replaced by a more realistic approach?

## REPLY BY HERMENZO JONES

1. The potential parameters were obtained by matching high pressure data for the individual constituents to liquid-state perturbation calculations.

2. Refinements in the treatment of multipolar interactions that you suggest are planned for future work.

**SESSIONS ON**  
**EQUATION OF STATE AND PERFORMANCE**

**Cochairmen: LeRoy Green**  
**Lawrence Livermore National Laboratory**

**Manfred Held**  
**Messerschmitt-Bölkow-Blohm GmbH**

**and**

**Gerald Kerley**  
**Sandia National Laboratories**

**Douglas Tasker**  
**Naval Surface Warfare Center**



# A DETONATION PRESSURE MEASUREMENT SYSTEM EMPLOYING HIGH RESISTANCE MANGANIN FOIL GAUGE

So-young Song and Jun Wung Lee  
Agency for Defense Development  
P. O. Box 35, Dae-jeon, 300-600  
REPUBLIC OF KOREA

*A detonation pressure measurement system consisting of a high resistance (50 ohm) manganin foil gauge, a bridge circuit, a constant voltage pulse power supply, a delay generator, a digitizer, and a personal computer has been developed to improve the previous method which requires a large number of tests with heavy charges. The system has successfully been employed for more accurate measurements of detonation pressure profiles of several explosives, from which C-J pressures and reaction times of explosives have been determined. C-J pressures of our measurements agree very well with those of the free surface velocity method within the range of our tests. Reaction times of our measurements agree quite well with those of Dremine's measurements using electromagnetic velocity gauge method. We can thus measure C-J pressure and reaction time of a test explosive by conducting only a small number of tests with light charges.*

## INTRODUCTION

Although the detonation pressure of an explosive is a fundamental quantity for predicting the explosive's performance, accurate measurement of it is very difficult. The free surface velocity method which is used most commonly measures the explosion-induced shock velocity and free surface velocity in a reference material, from which the C-J pressure in the explosive of interest can be inferred. This method incurs errors of several percent from the approximations required to solve the EOS equations and from differentiation of the time-position data and extrapolation of the results. Moreover, a total of several tens of experiments need to be conducted with large charges to determine C-J pressure and reaction time of an explosive.<sup>1,2</sup>

Some investigators have applied the manganin gauge method which has been used extensively in shockwork on inert solids for the measurement of detonation pressure profile.<sup>3,4</sup> They have used low resistance manganin wire or foil with resistance less than 0.5 ohm for their

gauge to minimize the shunting effects of any possible parallel conduction paths, one of whose origins is breakdown of insulation around the manganin by shock loading. It has not been easy to determine C-J pressure and reaction time from the detonation pressure profile obtained by analyzing the small voltage drop across the low resistance manganin gauge. It is thus natural for one to make an effort to use high resistance manganin wire or foil to produce correspondingly more accurate signals than those of the low resistance material.

A detonation pressure measurement system consisting of a high resistance (50 ohm) manganin foil gauge, a bridge circuit, a constant voltage pulse power supply, a delay generator, a digitizer, and a personal computer has been developed to improve the previous method which requires a large number of tests with large charges. The system has successfully been employed for more accurate measurements of detonation pressure profiles of several explosives, from which C-J pressures and reaction times have been determined. We

can thus measure C-J pressure and reaction time of a test explosive by conducting only a small number of tests with small charges.

## DEVELOPMENT OF THE DETONATION PRESSURE MEASUREMENT SYSTEM

A commercial manganin foil<sup>5</sup> of 50 ohm resistance is used as an active element of the detonation pressure gauge. The manganin foil is 13 microns thick and placed on a backing material of 5-micron-thick Teflon polyimide, by the manufacturer, in the form of a grid of 5.33 mm × 6.35 mm area. The detonation pressure gauge is made by placing the manganin foil between two insulating sheets and bonding them together with an epoxy resin. Air is excluded from the system between the insulating sheets and around the manganin foil by using epoxy resin out-gassed in vacuum and clamping the gauge tightly during the cure process, in order to prevent the gauge from shorting through the insulation.

The change in resistance of the gauge induced by the detonation wave is detected with the Wheatstone bridge circuit shown in Figure 1.<sup>6</sup> Simple analysis of the circuit gives the following expression for the change in resistance of the gauge,

$$\frac{\Delta R(t)}{R} = \frac{-A_1 V(t)}{E_0 + A_2 V(t)} \quad (1)$$

where  $V(t)$  is the output voltage profile of the bridge circuit and  $E_0$  is the constant voltage

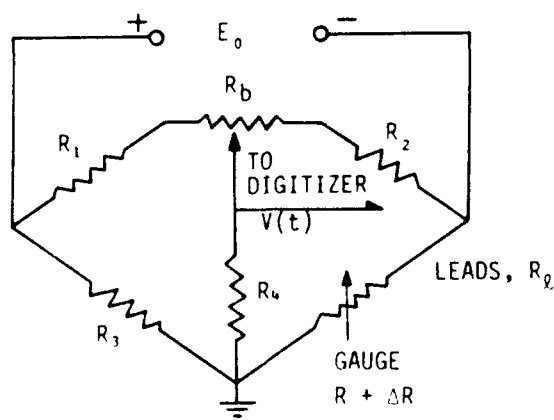


Figure 1. The Wheatstone Bridge Circuit

applied to the bridge circuit.  $A_1$  and  $A_2$  can be expressed in terms of resistances defined in Figure 1 as

$$A_1 = \frac{1}{R} \left\{ \frac{R'(R_U + R_L)}{R_4} + \frac{R_L^2}{R_3} \right\} \quad (2)$$

and

$$A_2 = \frac{1}{R_4} \left\{ \frac{R_L(R_3 + R_4)}{R_3} + \frac{R'R_U}{R_L} \right\}, \quad (3)$$

where

$$R' = R + R_\ell, \quad (4)$$

$$R_L = R_3 + R + R_\ell \quad (5)$$

and

$$R_U = R_1 + R_2 + R_b. \quad (6)$$

The resistance change is related to the pressure by a piezoresistive coefficient  $K$  that can be considered to be constant in a wide range of pressure, as

$$\frac{\Delta R(t)}{R} = KP(t). \quad (7)$$

Figure 2 is a schematic drawing of an experimental arrangement for detonation pressure measurements. The output voltage profile of the bridge circuit is recorded by a programmable digitizer with a 5 nsec sample interval, and converted to a pressure profile by

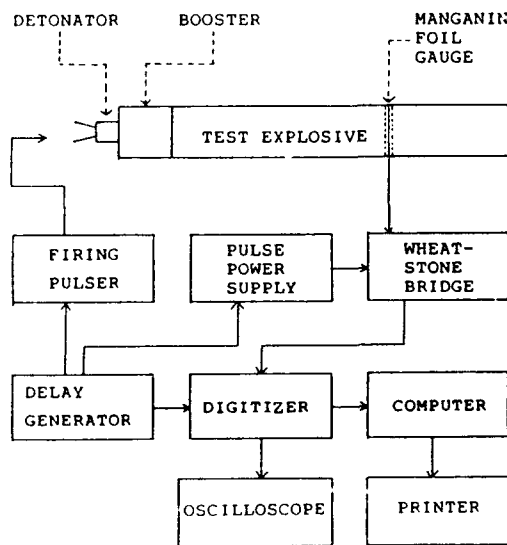


Figure 2. Schematic Drawing of Experimental Arrangement for Detonation Pressure Measurement

a personal computer, in accordance with Equations (1) - (7). The pulse power supply in the figure supplies constant voltage  $E_0$  to the bridge circuit only for a 60  $\mu$ sec time interval in order that resistivity of the manganin may not be changed by Joule heat. The delay generator supplies trigger pulses for firing pulser, pulse power supply and programmable digitizer at proper instances, respectively.

The detonation pressure gauge has been placed between the test explosive (25.4 mm diameter  $\times$  50.0 mm length) and the PTFE bar (25.4 mm diameter  $\times$  21.3 mm length) for the insulation test or detonation pressure measurement as shown in Figure 3. The PTFE bar at the rear side of the pressure gauge is placed for impedance match with high density explosives which we are interested in. We have clamped the explosive, pressure gauge and PTFE bar all together in order to prevent distortion of the pressure profile due to a rarefaction wave generated back into the gauge at the air gap between the manganin gauge and the PTFE bar. The explosive is initiated with RP87 detonator and tetryl booster (25.4 mm diameter  $\times$  21.3 mm length).

Polymer materials such as PTFE, polyethylene and Mylar have been studied as insulating sheets. Various thicknesses of polymer sheets have been tried. PTFE sheets of 0.77 mm thickness have been selected as the insulation sheet after a series of insulation tests.

Figure 4 represents the negative of the output voltage profile,  $-V(t)$ , of the bridge circuit with improper insulating sheet or bonding agent. When the shockwave arrives at the manganin foil, the profile increases due

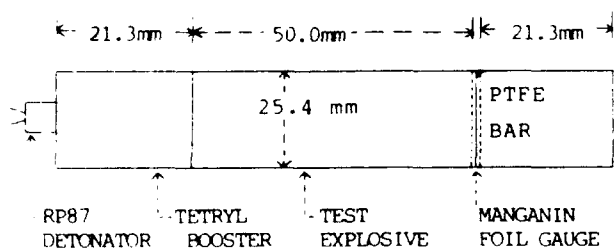


Figure 3. Details of Test Charge Assembly for Insulation Test or Detonation Pressure Measurement

to piezoresistive increase of the resistance of the manganin foil. However, the high pressure shockwave makes a shunting path through the imperfect insulators around the manganin foil before the profile reaches its maximum value, decreasing it to a negative value. It increases again due to the disconnection of the manganin foil by strain.

Figure 5 represents the negative of the output voltage profile,  $-V(t)$ , of the bridge circuit with proper use of an insulating sheet and

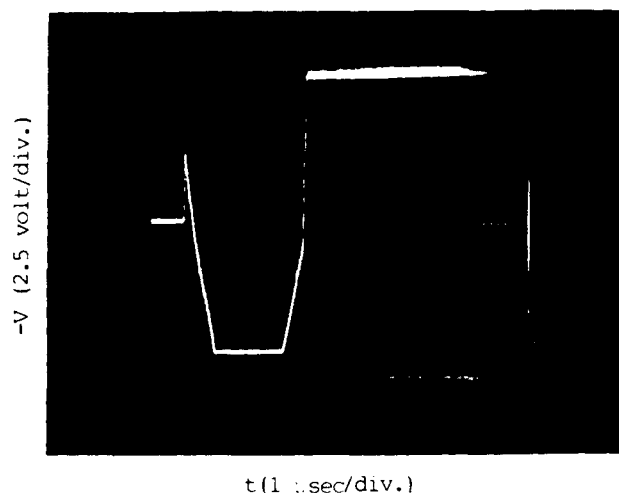


Figure 4. The Negative of the Output Voltage Profile,  $-V(t)$ , of the Bridge Circuit with Misuse of Insulation Material Around Manganin Foil

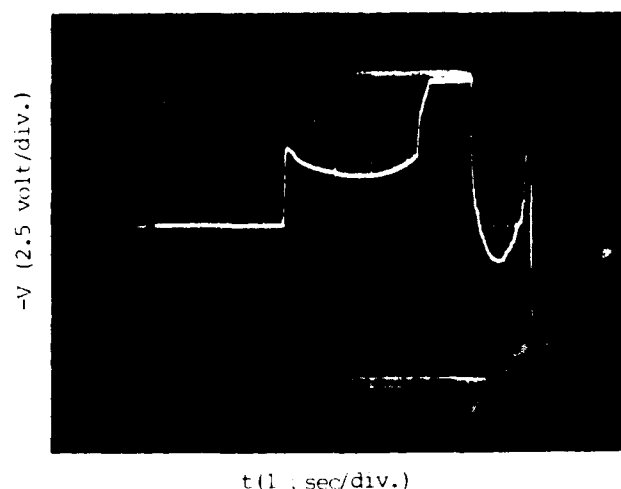


Figure 5. The Negative of the Output Voltage Profile,  $-V(t)$ , of the Bridge Circuit with Proper Use of Insulation Material Around Manganin Foil. This profile is obtained in the test with TNT explosive.

a bonding agent, which is obtained in the test with TNT explosive. The profile begins with a spike similar to the von Neumann spike in detonation pressure profile and the spike is followed by a much more gradual decay. No considerable shift of the juncture of the spike portion and gradual decay portion were observed by changing the thickness of PTFE sheet of the pressure gauge from 0.77 mm to 1.54 mm as shown in Figure 6. It can thus be decided that this juncture did not appear due to impedance mismatch between the explosion product and the PTFE sheet, and that the juncture reflects the C-J point of detonation wave. The increase of the profile about 2  $\mu$ sec after the arrival of shockfront in the Figure 5 reflects the resistance change due to the strain and disconnection of manganin foil.

Piezoresistive coefficient of the pressure gauge is determined in accordance with

$$K = \frac{(\Delta R)_{CJ}}{R} / P_{CJ} \quad (8)$$

where  $(\Delta R)_{CJ}$  is the change in resistance at the juncture of spike portion and gradual decay portion of the profile in Figure 5, and  $P_{CJ}$  is the C-J pressure of TNT which is determined by the free surface velocity method.

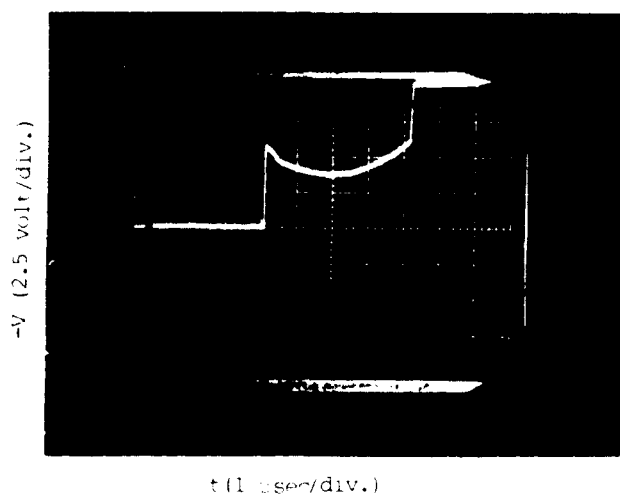


Figure 6. The Negative of the Output Voltage Profile,  $-V(t)$ , of the Bridge Circuit. Only the thickness of PTFE sheet of manganin foil gauge is changed from 0.77 mm to 1.54 mm, as compared with the test charge for Figure 5.

Since the C-J pressure of TNT explosive of 1.63 g/cm<sup>3</sup> density has been reported to be 210 kbar,<sup>7</sup> we can calculate  $P_{CJ}$  of our TNT explosive of 1.58 g/cm<sup>3</sup> density from the following empirical formulas:

$$P_{CJ} \propto \rho_0 D^2 \quad (9)$$

and

$$D(\text{km/sec}) = 6.762 + 3.187(\rho_0 - 1.534) - 25.1(\rho_0 - 1.534)^2 \quad (10)$$

which is valid in the range 1.534 g/cm<sup>3</sup> <  $\rho_0$  < 1.636 g/cm<sup>3</sup>,<sup>8,9</sup> where  $D$  and  $\rho_0$  are detonation velocity and density, respectively.

Since  $P_{CJ}$  and  $(\Delta R)_{CJ}/R$  have thus been found to be 205 kbar and 0.350, respectively, for our TNT explosive of 1.58 g/cm<sup>3</sup> density, the piezoresistive coefficient of the pressure gauge is determined to be

$$K = \frac{(\Delta R)_{CJ}}{R} / P_{CJ} = 0.00171/\text{kbar}. \quad (11)$$

## RESULTS AND ANALYSES OF DETONATION PRESSURE MEASUREMENTS

Detonation pressure profiles of some high explosives such as TNT, Tetryl, Comp B and DXD-01 have been measured with the pressure measurement system and are shown in the following figures, from Figure 7 to Figure 10

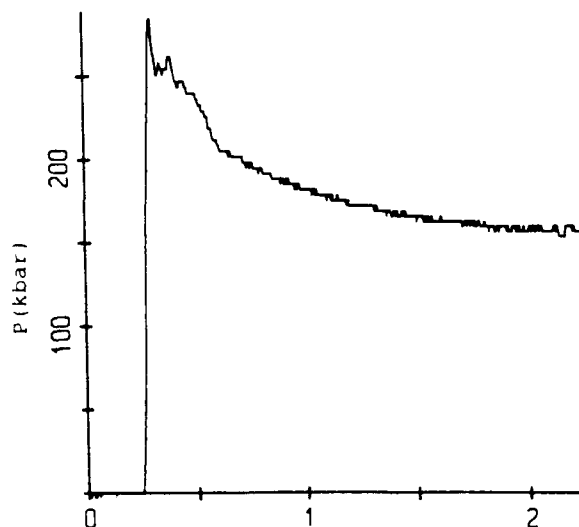


Figure 7. Detonation Pressure Profile for TNT Explosive

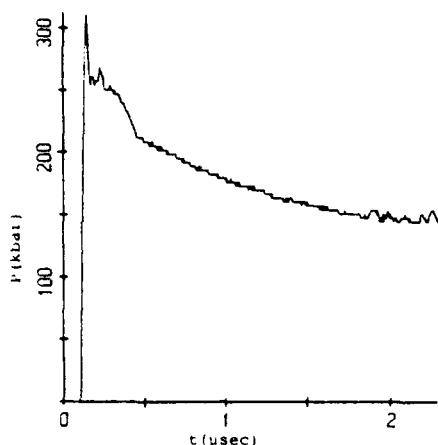


Figure 8. Detonation Pressure Profile for Tetryl Explosive

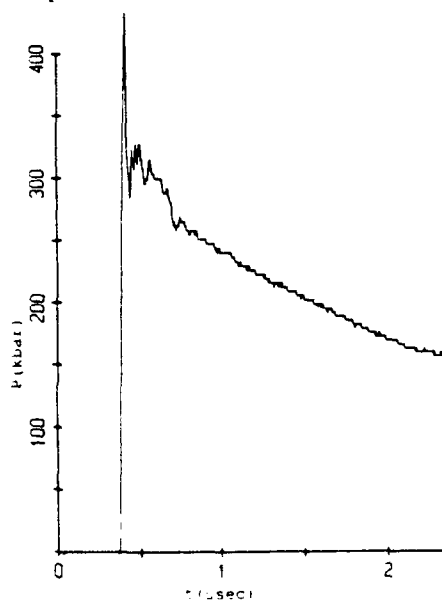


Figure 9. Detonation Pressure Profile for Comp B Explosive

respectively. C-J pressures and reaction times of the above explosives have been determined from the pressure profiles and are listed in the Table I.

The C-J pressures of this method are compared with those of the free surface velocity method which have been calculated with some empirical formulas and published data based on the free surface velocity method.

For Tetryl explosive of  $1.614 \text{ g/cm}^3$  density, the C-J pressure of 226.4 kbar has been reported.<sup>10</sup> The C-J pressure of free surface velocity method for Tetryl explosive of

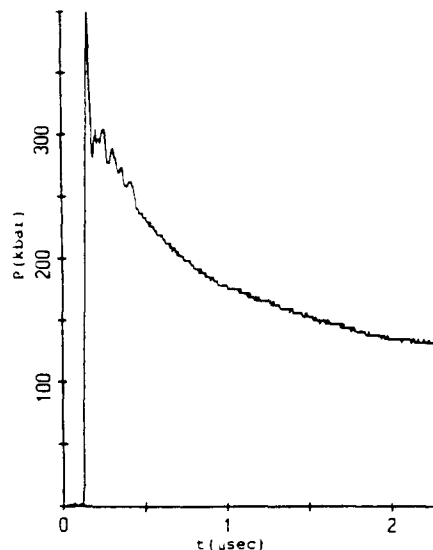


Figure 10. Detonation Pressure Profile for DXD-01 Explosive

$1.58 \text{ g/cm}^3$  density has thus been calculated to be 216 kbar, which is about two percent larger than the C-J pressure of this method, using Equation (9) and the empirical formula,<sup>11</sup>

$$D(\text{km/sec}) = 2.742 + 2.935\rho_0. \quad (12)$$

For Comp B explosive of our measurement which has  $1.67 \text{ g/cm}^3$  density and 59.5 percent RDX, the C-J pressure has been calculated to be 269 kbar, which is two percent larger than the C-J pressure of this method, using the empirical formula,<sup>10</sup>

$$P(\text{kbar}) = 295 + 1.57(\% \text{ RDX-64}) + 678.5(\rho_0 - 1.717)/\rho_0. \quad (13)$$

DXD-01 is a cast plastic-bonded explosive which has a composition of 84 percent RDX + 16 percent binder and a density of  $1.56 \text{ g/cm}^3$ . The C-J pressure of DXD-01 explosive has never been measured with the free surface velocity method.

Although the reaction times of an explosive reported in the literature differ by an order of magnitude depending on authors and measuring techniques, the reaction times of our measurements (TNT 360 nsec and Comp B 340 nsec) agree quite well with those of Dremine (TNT 300 nsec and Comp B 320 nsec) who has measured them with electromagnetic velocity (EMV) gauge method.<sup>12</sup> We cannot find any data on reaction time for Tetryl explosive or DXD-01 explosive measured with EMV gauge method.

Table 1. C-J Pressures and Reaction Times

Explosive	Density	C-J Pressure, This Method	C-J Pressure, Free Surface Velocity Method	Reaction Time, This Method
TNT (CAST)	1.58 g/cm <sup>3</sup>	205 kbar	205 kbar	360 nsec
Tetryl (Pressed)	1.58	212	216	340
Comp B (CAST)	1.67	263	269	340
DXD-01 (CAST)	1.56	237	—	350

## CONCLUSIONS

A detonation pressure measurement system consisting of a high resistance manganin foil gauge, a bridge circuit, a constant voltage pulse power supply, a delay generator, a digitizer, and a personal computer has been developed to improve the previous method which requires a large number of tests with large charges.

The system has successfully been employed for more accurate measurements of detonation pressure profiles of several explosives, from which C-J pressures and reaction times of the explosive have been determined.

We can thus measure C-J pressure and reaction time of a test explosive by conducting only a small number of tests with small charges.

## ACKNOWLEDGEMENT

The authors wish to thank Messrs K. Y. Choi, D. W. Yim, J. W. Park and J. K. Kang who executed the experiments.

## REFERENCES

- Holmes, N. C.; Hamilton, D. C.; and Radousky, H. B., *Energy and Technology Review*, edited by H. S. Cabayan and N. C. Holmes, UCRL-52000 86-3, Lawrence Livermore Laboratory, 1986.
- Jacobs, S. J., *Notes from Lectures on Detonation Physics*, edited by F. J. Zerilli, NSWC MP81-399, Naval Surface Weapons Center, 1981, pp. 169-183.
- Burrows, K.; Chilvers, D. K.; and Gyton, R., *Proceedings of the Sixth Symposium (International) on Detonation*, ONR-ACR-221, 1976, pp. 625-641.
- Erickson, L. M.; Johnson, C. B.; Vantine, H. C.; Weingart, R. C.; and Lee, R. S., *The First Symposium on Gauges and Piezoresistive Materials*, Arcachon, France, 1981.
- Wackerle, J.; Johnson, J.; and Halleck, P.; Los Alamos Scientific Laboratory Report, LA-5844, 1975.
- Dobratz, B. M., *LLNL Explosives Handbook-Properties of Chemical Explosives and Explosive Simulants*, UCRL-52997, Lawrence Livermore Laboratory, 1981, pp. 8-16.
- Gibbs, T. R. and Popolato, A., *LASL Explosive Property Data*, University of California Press, 1980, p. 179.
- Cook, M. A., *The Science of High Explosives*, Robert E. Krieger Publishing Co. Inc., Huntington, New York, 1971, p. 35.
- Dobratz, B. M., *Properties of Chemical Explosives and Explosive Simulants*, UCRL-51319 Rev. 1, 1974, p. 8-17.
- Gibbs, T. R. and Poplato, A., *LASL Explosive Property Data*, University of California Press, 1980, p. 168.
- Price, D., *Notes from Lectures on Detonation Physics*, edited by F. J. Zerilli, NSWC MP 81-399, Naval Surface Weapons Center, 1981, pp. 191-205.

## **DISCUSSION**

**LEWIS ROTHSTEIN**  
Consultant

What was the reproducibility of the measurements for each explosive and how many test runs were made for each explosive?

## **REPLY**

No reply from the authors.

## **DISCUSSION**

**J. BDZIL**  
Los Alamos National Laboratory  
Los Alamos, NM

The flow at the CJ point must be non-reactive. The following flow should be nearly similar. Did you do experiments on ID systems of varying charge lengths, and verify that the flow behind what you called the CJ point is in fact self-similar? Also to infer distances and pressures from an HE/inert interface measurement requires that you do the hydrodynamic imaging problem that occurs at the interface.

## **REPLY**

No reply from the authors.

# HEAT OF DETONATION, THE CYLINDER TEST, AND PERFORMANCE IN MUNITIONS

Irving B. Akst  
Los Alamos National Laboratory  
Los Alamos, New Mexico

*Heats of detonation of CHNO explosives correlate well with copper cylinder test expansion data. The detonation products/calorimetry data can be used to estimate performance in the cylinder test, in munitions, and for new molecules or mixtures of explosives before these are made. Confidence in the accuracy of the performance estimates is presently limited by large deviations of a few materials from the regression predictions; but these same deviations, as in the insensitive explosive DINGU and the low carbon systems, appear to be sources of information useful for detonation and explosives research. The performance correlations are functions more of the detonation products and thermochemical energy than they are of the familiar parameters of detonation pressure and velocity, and the predictions are closer to a regression line on average than are those provided by CJ calculations. The prediction computations are simple but the measurements (detonation calorimetry/products and cylinder experiments) are not.*

## INTRODUCTION

A hypothesis that heat of detonation has a primary effect on the performance of explosives and munitions is certainly neither new nor arcane. But heat of detonation is not a quantity which has been measured extensively. Heats of deflagration and explosion were measured fairly frequently in the past, but few of those data have been used or generated recently. Heat of combustion is usually measured for a new explosive, often for the determination of the heat of formation. At the same time, quite a few explosives performance measurements historically have been very direct and often narrow, as in, say, arena tests of a munition of intended application; or they have been quite indirect, as in the determination of CJ parameters. Now there is a body of data on heats and products of detonation, and a body of data on performance in a form that is more widely relatable to munitions applications. These are detonation calorimetry<sup>1</sup> and the copper cylinder test.<sup>2</sup> In

this work, these bodies of data are used to test the hypothesis, point out its importance, and derive useful information for the relationships established between the two sets of data.

One of the areas that might produce useful information has to do with the insensitive explosives. The current interest in them and the rather low performance produced by two of these (TATB and NQ)—in spite of their reasonably high calculated CJ pressure and measurements of detonation velocity and pressure—suggested that some other detonation condition or parameter is as important as CJ pressure, or more so for the performance of such explosives. Both of these explosives (or formulations very rich in them) have calculated and measured CJ parameters not too different from Comp B, which has cylinder energy 37-32 percent higher than TNT, depending on the amount of expansion ( $V/V_0$  of 2 to 11), and detonation pressure about 35 percent higher than TNT. But the TATB and NQ cylinder energies are not much



different from those of TNT: 15 to 7 percent for TATB, 12 percent to approximately 0 percent for NQ, at the same expansions (see Table 1).

Kamlet<sup>3</sup> wondered whether, for some reason, insensitive explosives were not reaching the infinite-medium steady-state condition. He also suggested that the trouble with NQ (poor performance) was the low Q (heat of detonation), and that no formulation very rich in NQ or other low-Q explosives would have high performance (of the type herein, see below).

The heat of detonation (Q, in calories or kilocalories per gram) is considered herein to be the thermochemical energy produced during detonation and usable for the work to be done by the explosive. Q or Q<sub>v</sub> (volumetric heat of detonation,  $\rho Q$ , where  $\rho$  is density) would seem from first principles--energy conservation--to be a primary parameter of an explosive, upon which all physical reaction and performance depends. Therefore, it should be useful to compare this parameter with other explosive parameters, and it seemed it would be especially useful to do so with respect to performance data relevant to munitions.

Performance is defined herein as the metal-propelling ability of an explosive, as quantified by the "standard" expanding copper cylinder test.<sup>2</sup> This test is used because

it produces information of direct use in munitions and itself resembles a number of them in form. These include shells and bombs, which are similar to the test in geometry (end-initiated internally loaded cylinders), in metal mass to explosive charge ratios, and in terms of the length of time over which the explosive energy and products are applied to the metal. The last two factors would include some shaped charges.

Thus, we considered it worthwhile to examine a range of explosives, and especially to include other apparently insensitive ones, regarding Q and performance, such as DINGU and NTO to characterize these, and try to generalize the phenomena.

## EXPERIMENTAL

The field of explosives for which both detonation calorimetry and cylinder tests have been done is rather small, with a fair number of those explosives being similar or mixtures of monomoleculars studied individually. For example, there are a number of plastic-bonded pressed explosives rich in HMX, with fluorocarbon binders. It seemed best to examine as large a range of explosives as feasible, in terms of Q and performance, but limited to comparable species, that is monomolecular ideal CHNO concentrated compounds (without additives such as aluminum

*Table 1. Detonation Pressures and Heats versus Cylinder Energy:  
Comparing Less-Sensitive Explosives with Standards*

	P (calc) GPa	Q (cyl) cal/cm <sup>3</sup>	E (V/V <sub>0</sub> = 2) (km/s) <sup>2</sup>	E (V/V <sub>0</sub> = 11) (km/s) <sup>2</sup>
TNT	21	1665	1.51	2.13
Comp B	29	2105	2.07	2.82
NQ (AFX 902)	26	1540 (calc)	1.69	2.16
TATB	29	1735	1.74	2.28
DINGU (X 0420)	32	2000 (calc)	1.69	2.25
NTO	30	1735 (calc)	1.77	2.31

or large amounts of nonexplosives). These would be likely to have as near an unfounded CJ state and as usual an adiabatic expansion coefficient ( $\gamma$ ) and detonation temperature as possible. Furthermore, there should be limited use of similar materials to have as appropriately weighted a regression as possible. The explosives for the base set were selected on that basis; there are 15 in all, with a range of power from NM to HMX. Unfortunately, in neither DINGU nor NTO has  $Q$  been measured, nor has  $NQ$  data been published; but they are important to the study, with cylinder tests having been done, and are included. Three intermoleculars—one HNO and two CNOs—were added to the base set to explore further the correlation. There is an interesting set of formulations showing effects from aluminum.

The best (and essentially the only) readily available source of a sufficient quantity of modern, accurate products and heat of detonation data is the work of Ornellas at LLNL.<sup>1</sup> However, Volk has been making products measurements recently,<sup>4</sup> and calculating heat of detonation from the products. This can yield good energy quantities, as is evident from Ornellas' work, in the usually close agreement of the energy calculated from the products and that obtained calorimetrically. Overall, the precision and accuracy of Ornellas'  $Q$  measurements are about 1 percent.

There are few other published data. Some of Volk's experiments are in the manner suggested by the author and carried out at LLNL<sup>5</sup>—that is, using a large sphere with a thin atmosphere of noble gas to slow and dilute the products, thus preventing re-equilibration through shock at the container walls, without the need for massive confinement of the explosive to carry off the energy kinetically. Los Alamos made a few measurements some time ago,<sup>6</sup> and Pantex began to make such measurements;<sup>7</sup> NSWC/WOL has made some too.<sup>8</sup>

All the thermochemical energy data listed as measured in Table 1 are taken from Reference 1. The " $\Delta H$  detonation, Experimental" values are normalized, where necessary, to the energy with water as a gas. This is

because in the cases of interest (metal-moving military munitions), that is the state which is germane; condensation to liquid is too slow and too late to influence performance. The normalization was done by subtracting 10.5 kcal/mol of water which is the difference between -68.3 and -57.8 kcal/mol—the heats of formation of liquid and gaseous water. Although DINGU has not had  $Q$  measured, the formulation X-0432 is listed as such because it has 43 percent TNT, for which  $Q$  is known, and the calculated value was used for the DINGU contribution. Calculated gravimetric heat of detonation used heats of formation in Reference 9 or, for DINGU and NTO, as reported in Reference 10, -42.3 kcal/mol and -28 kcal/mol, respectively.

The calculation for  $Q$  used the convention of burning hydrogen to water to the limit of oxygen or hydrogen, then carbon to dioxide to the limit of oxygen or carbon. Because of the thesis concerning an effect of structure on products and energy (see Results and Discussion, below), calculations were also made for DINGU and NTO in which half a mole of carbon monoxide would be produced for each carbonyl, before the dioxide.

Polymer binders were estimated to be 20 percent energetic (because most have fluorine), hydrocarbons (Comp C-4) inert, and the PBX-9404 binder 50 percent energetic, for the nitrocellulose.

Volumetric heat of detonation,  $Q_v$ , was calculated as a maximum from the measured  $Q$  (where available, calculated  $Q$  where not) and the theoretical maximum density (TMD) of the compound or mixture.  $Q_v$  was also calculated as the specific energy of the explosive in its cylinder test,  $Q_{cyl}$ , by using the density of the charge in the test rather than TMD. It is this last value,  $Q_{cyl}$ , that was used in the correlations.

For Table 2, detonation velocities and detonation pressures were calculated by the Kanilet-Jacobs short method,<sup>11</sup> because that method is suited to the sample set of "comparable species" defined above (monomolecular ideal CHNO compounds). Also, it seems to afford a rather even treatment of the samples, perhaps more so than some more

Table 2. Performance Factors

Explosive	Density TMD (g/cm <sup>3</sup> )	D, calc (km/s)	P, calc (GPa)	Q		Qv Max (cal/cm <sup>3</sup> )	Density exptl (g/cm <sup>3</sup> )	Qcyl (cal/cm <sup>3</sup> )
				Calc (cal/g)	Meas (cal/g)			
HMX	1.902	9.13	38.2	1475	1365	2595	1.894	2585
PBX-9404	1.865	9.00	36.7	1430	1325	2470	1.845	2445
RDX	1.806	8.83	34.6	1480	1340	2420	---	---
Comp C-4	1.67	7.95	25.9	1360	1235	2065	1.601	1975
Comp B	1.748	8.12	28.8	1410	1225	2140	1.717	2105
TNT	1.654	7.01	20.7	1290	1020	1685	1.630	1665
TATB	1.938	7.93	29.1	1075	935	1810	1.854	1735
PBX-9502	1.942	7.89	28.9	1030	900	2005	1.89	1695
NQ	1.775	7.90	27.5	920	---	1630	---	---
AFX-902	1.779	7.58	26.4	885	---	1570	1.742	1540
DINGU	1.982	8.49	33.8	1125	---	223	---	---
X-0420	1.93	8.31	31.9	1070	---	2065	1.874	2000
X-0432	1.826	7.78	27.1	1195	1080 <sup>a</sup>	1970	1.758	1900
NTO	1.93	8.05	30.0	950	---	1840	1.825	1735
PETN	1.78	8.73	33.5	1515	1380	2455	1.765	2435
NM	1.136	6.41	13.2	1365	1075	1220	1.136	1220
EDD	1.595	7.57	23.6	975	990	1580	1.55	1535
Octol (O)	1.845	8.63	33.4	1435	1330	2455	1.804	2400 0
HNB	2.017	9.43	42.1	1705	1665	3340	1.965	3250
H/HN	1.421	7.70	22.5	1285	1130	1605	1.421	1605
ADNT	1.63	7.82	25.5	1195	1045	1705	1.574	1645
AN/ADNT	1.67	8.15	28.2	1075	1025	1715	1.64	1680
EAR	1.678	8.16	28.3	1040	1000	1675	1.617	1615
BTF	1.901	8.50	33.1	1690	1410	2680	1.852	2615

<sup>a</sup>Measured Q of TNT + calculated Q of DINGU

complex codes with various equations of state. In Tables 3 and 4, detonation pressures were calculated from the experimental densities and detonation velocities, and an assumed constant adiabatic expansion coefficient ( $\gamma$ ) of 2.8, a value which yields, on average, pressures consistent with KSM calculations and a fair number of reported pressures.

Cylinder performance data (Table 3) are from tests done at Livermore,<sup>12</sup> Pantex,<sup>13</sup> Eglin AFB,<sup>14</sup> and Los Alamos,<sup>15</sup> in inner

diameters (i.d.) of 25.4, 50.8, or 101.6 mm—chosen to be well above unconfined failure diameter. The “standard” or usual configuration was used, that is, full copper wall thickness of 1/10 the copper tube i.d., with the sample length 6, 9, or 12 times the i.d. Initiation was by means of a plane wave lens and pad of Comp B of the HE diameter (i.d.) and thickness one-half the i.d., outboard of the tube. Detonation velocity was measured in all the tests over nearly the full sample length while the radial copper wall motion was

Table 3. Cylinder Test Performance

Explosive	Density (g/cm <sup>3</sup> )		D (km/s)	p <sup>a</sup> (GPa)	V/V <sub>0</sub> = 2		V/V <sub>0</sub> = 7		V/V <sub>0</sub> = 11	
	TMD	Expt			v (km/s)	t (μs)	v (km/s)	t (μs)	v (km/s)	t (μs)
HMX	1.902	1.894	---	---	1.70	4.30	1.90	11.47	1.95	17.23
PBX-9404	1.865	1.845	8.782	37.4	1.61	4.49	1.83	11.93	1.90	17.80
Comp C-4	1.67	1.601	8.193	28.3	1.39	5.38	1.59	13.99	1.64	20.82
Comp B	1.748	1.717	7.99	28.8	1.44	5.22	1.63	13.60	1.68	20.23
TNT	1.654	1.630	6.95	20.7	1.23	6.26	1.40	16.03	1.46	23.75
TATB	1.938	1.854	7.675	28.7	1.32	5.49	1.47	14.73	1.51	22.10
PBX-9502	1.942	1.89	7.57	28.5	1.31	5.50	1.46	14.79	1.49	22.24
AFX-902	1.779	1.742	8.344	31.9	1.30	5.58	1.42	15.04	1.47	22.69
X-0420	1.93	1.874	7.76	29.7	1.30	5.45	1.46	14.71	1.50	22.14
X-0432	1.826	1.758	7.390	25.3	1.29	5.58	1.46	14.89	1.51	22.33
NTO	1.93	1.852	8.101	31.5	1.33	5.33	1.47	14.50	1.52	21.84
PETN	1.78	1.765	8.277	31.8	1.58	4.78	1.78	12.44	1.84	18.49
NM	1.136	1.136	6.285	11.8	1.05	7.51	1.24	18.65	1.27	27.37
EDD	1.595	1.55	7.55	23.3	1.29	---	1.44	---	1.47	---
Octol	1.845	1.804	8.48	34.1	1.56	4.72	1.75	12.48	1.80	18.68
(O)										0
HNB	2.017	1.965	9.335	45.1	1.71	4.29	1.92	11.31	2.04	16.82
H/IIN	1.421	1.421	8.645	27.9	1.36	5.45	1.54	14.24	1.60	21.24
ADNT	1.63	1.574	7.868	25.6	1.30	5.68	1.49	14.80	1.53	22.05
AN/ADNT	1.67	1.64	7.890	26.9	1.37	5.29	1.53	15.14	1.57	est.---
EAR	1.678	1.617	8.17	28.4	1.36	5.32	1.51	14.20	1.56	21.36
BTF	1.901	1.852	8.485	35.1	1.59	4.61	1.80	12.05	1.88	17.93

<sup>a</sup>Calculated from experimental density, measured D, and 2.8 for  $\gamma$

Table 4. Aluminized Explosive, 50.8-mm Cylinder Tests<sup>a</sup>

	Density (g/cm <sup>3</sup> )		D (km/s)	p <sup>b</sup> (GPa)	V/V <sub>0</sub> = 2		V/V <sub>0</sub> = 7		V/V <sub>0</sub> = 11	
	TMD	Exptl			v (km/s)	t (μs)	v (km/s)	t (μs)	v (km/s)	t (μs)
80/0/20 <sup>c</sup>	1.85	1.85	8.32	33.7	1.51	4.80	1.70	12.75	1.76	19.08
76/4/20	1.883	1.868	8.28	33.7	1.51	4.83	1.74	12.73	1.80	18.97
72/8/20	1.905	1.90	8.23	33.9	1.51	4.90	1.75	12.72	1.80	18.91

<sup>a</sup>Courtesy H. G. Adolph, White Oak Laboratory, NSWC, and Group M-8, LANL

<sup>b</sup>Calculated from  $\rho$ , D, and  $\gamma = 2.8$

<sup>c</sup>Wt% HMX/aluminum/fluorinated binder

measured shadowgraphically by streak camera, with the slit about 5 or more diameters downstream from the initiated sample surface. Various analyses were used, from polynomials to power functions and splines, and derivatives thereof; all seem essentially equal, and the overall precision of the measurements is about one percent.

Data are scaled to the 25.4-mm-diameter test, that is, the radial wall distances and times have been divided by the ratio of the diameter of the test to 25.4. Typically, the wall motion could be followed accurately from at least 5 mm to 30 mm or farther (scaled to 25.4-mm diameter) radially from the static position. Scaled distances of 6, 19, and 30 mm are equivalent to internal volume expansion ratios (of the tube and products),  $V/V_0$ , of about 2, 7, and 11. These are points customarily reported, although most tests have been analyzed for each millimeter of motion. Some data on wall acceleration are also available from second derivatives of the  $r, t$  curves, but there is of course more error, and no pattern germane to the aim of this study seemed to emerge.

Both the detonation calorimetry experiments and the cylinder test principally measure energy, the former thermally and the latter kinetically. The relationships between the two should be readily quantifiable, if the experiments are reasonably precise and accurate, because both are efficient. With heats of detonation and squares of copper wall velocities as the principal variables, linear regression was carried out. The correlation coefficients and line parameters are given in Table 5.

## RESULTS AND DISCUSSION

The principal correlations to look for should be causatively correct ones to test the hypothesis that the chemical energy of the detonation reaction has the primary effect on performance in the cylinder test, and on some munitions, through energy conservation. The cylinder performance parameter is the copper wall kinetic energy. The prime correlation has the thermochemical energy  $Q_{cyl}$  as the independent variable and the square of the wall velocity at  $V/V_0 = 11$  as the dependent

variable. The expansion  $V/V_0 = 11$  is the main one used, because it is the largest one accurately measured; it represents the most efficient use of the explosive, nearest to free flight and the Gurney "final velocity" energy. The sample set best suited to test the thesis was defined above as having essentially only monomolecular ideal concentrated CHNO compounds. The hypothesis also requires a 0,0 origin. Therefore, 0,0 was added to the data to form the base set. Correlations at different expansions and with variations of the sample set—adding, deleting, or modifying data points—were also calculated to test effects, as were some using other variables such as detonation pressure.

As Table 5 shows, the correlation coefficient testing the main hypothesis is high, with  $r$  being nearly 0.98 for the base set using the principal variables as stated above. This supports the hypothesis well and suggests that one might profitably do more detonation heat tests and use the data and the correlation for predictive and other practical purposes such as designing explosives and doing research on detonation phenomena. The coefficients are over 0.97 at the lesser expansions  $V/V_0 = 7$  and 2. Also, the latter perhaps is a little surprising because one might expect velocities at such low expansion to be more responsive to detonation pressure.

The good fits also reflect well on the experimental quality, that is, the accuracy, or at least the precision, of the measurements. Noise and scatter might be expected to result from the usual experimental errors—exacerbated by those of time, place, and investigator, error generated by derivatives (wall velocity) and roundoffs (e.g., squaring a rounded-off velocity). While it is important that the data and fits are good, deviations from the regression are also important as they are the measure of uncertainty in predictions one would like to use the correlations for, and some may be sources of new information. As Table 6 shows, the deviations are reasonably small, with exceptions: the one or two data points with large deviations from the regression line decrease the correlation coefficient, but more importantly, they may indeed be sources of information. One would like to

Table 5. Correlations

Variables			Coefficients		
Sample Set	Independent	Dependent	Fit r	Slope	Y-intercept
1	Q <sub>cyl</sub> (cal/g)	v <sup>2</sup> at V/V <sub>0</sub> = 11	0.979	1.42 (km/s) <sup>2</sup> /kcal/g	-0.134 (km/s) <sup>2</sup>
1	Q <sub>cyl</sub> (cal/g)	v <sup>2</sup> at V/V <sub>0</sub> = 7	0.978	1.33	-0.122
1	Q <sub>cyl</sub> (cal/g)	v <sup>2</sup> at V/V <sub>0</sub> = 2	0.975	1.05	-0.100
2	Q <sub>cyl</sub> (cal/g)	v <sup>2</sup> at V/V <sub>0</sub> = 11	0.960	1.54	-0.367
3	Q <sub>cyl</sub> (cal/g)	v <sup>2</sup> at V/V <sub>0</sub> = 11	0.993	1.44	-0.121
4	Q <sub>cyl</sub> (cal/g)	v <sup>2</sup> at V/V <sub>0</sub> = 11	0.988	1.44	-0.143
5	Q <sub>cyl</sub> (cal/g)	v <sup>2</sup> at V/V <sub>0</sub> = 11	0.974	1.34	0.039
6	Q <sub>cyl</sub> (cal/g)	v <sup>2</sup> at V/V <sub>0</sub> = 11	0.985	1.34	-0.084
6	Q <sub>cyl</sub> (cal/g)	v <sup>2</sup> at V/V <sub>0</sub> = 2	0.963	0.95	0.097
1	Q <sub>cyl</sub> (cal/g)	P <sub>exp</sub> <sup>1</sup> (GPa)	0.909	14.2 GPa/kcal/g	1.01 GPa
5	Q <sub>cyl</sub> (cal/g)	P <sub>exp</sub> <sup>1</sup> (GPa)	0.917	13.2	3.19
1	P <sub>exp</sub> <sup>1</sup> (GPa)	v <sup>2</sup> at V/V <sub>0</sub> = 2	0.929	0.0613 (km/s) <sup>2</sup> /GPa	0.138 (km/s) <sup>2</sup>
5	P <sub>exp</sub> <sup>1</sup> (GPa)	v <sup>2</sup> at V/V <sub>0</sub> = 2	0.943	0.0626	0.117
5	P <sub>exp</sub> <sup>1</sup> (GPa)	v <sup>2</sup> at V/V <sub>0</sub> = 11	0.923	0.0858	0.134

Sample sets:

1. Base set, 15 explosives, Tables 2 and 3
2. Base set, less 0,0
3. Base set, less DINGU points
4. Base set, with DINGU points using CO calculation
5. Full set, base plus additional 6 points
6. Full set, less DINGU points

think they are not just statistical "flukes" or bad data, but that they are caused by real differences in the materials and phenomena.

The most deviant points, the only really large deviations in the original sample set, are those for the 94/6 wt percent DINGU plastic-bonded explosive (X-0420) at -18 percent in energy from the regression line, and the 57/43 wt percent DINGU/TNT mix (X-0432) at -13 percent, as may be seen in Table 6. The correlation coefficient for the base set with the DINGU points deleted is very high, above 0.99. Recall that Q has not been measured for DINGU. Therefore, its Q<sub>cyl</sub> was from calculated Q. This may be a cause of at

least part of the large deviations, because all the calculated Qs but one are higher than measured Qs by various amounts, as may be seen in Table 2.

The only other deviations of size in the base set are about -6 percent for TNT and about +6 percent for HMX and its close relative PBX-9404. A rather anomalous deviation outside of the correlation is the very large one in NM, where the measured Q is more than 20 percent below the calculated value (Table 2). There were some other interesting deviations in explosives outside of the base set; they are discussed below.

Table 6. Deviations

$$\text{Relative deviation} = \frac{100 \Delta v_{11}^2}{\text{line } v_{11}^2}, \text{ in percent,}$$

where  $\Delta v_{11}^2 = \text{exp } v_{11}^2 - \text{line } v_{11}^2$  and

where the line<sup>a</sup> is  $\Delta v_{11}^2 = 1.44 Q_{\text{cyl}} - 0.121$

and  $v_{11}$  is velocity at  $V/V_0 = 11$ .

HMX	+5.7	AFX 902	+3.2	Octol	-2.8
PBX-9404	+6.3	X-0420 (DINGU)	-18.4	HNB	-8.7
Comp C-4	-1.1	X-0432 (DINGU/TNT)	-12.7	RX-23-AA (H/HN)	+17.0
Comp B	-2.9	NTO	-2.7	ADNT	+4.3
TNT	-6.2	PETN	+0.1	AN/ADNT	+7.4
TATB	-4.0	NM	-1.2	EAR	+10.5
PBX-9502	-4.2	EDD	+3.6	BTF	-2.9

<sup>a</sup>Highest  $r$ , average slope and intercept: Sample set 3 (Table 5)

The  $Q$ s for DINGU and NTO were recalculated based on the supposition that structure has an effect on the products, and hence the energy produced. It was assumed that a carbonyl structure predisposes the set of products to contain more CO and less CO<sub>2</sub> than it otherwise would have in a system with the same elemental composition but with oxygens on nitrogen, for example. The idea that structure affects detonation characteristics is expressed well in Rothstein and Petersen's work,<sup>16</sup> in which they show high correlation of detonation velocity with composition and structure alone, without numbers for heat of formation or density (although of course those are also functions of structure) or CJ calculations. In that work, they assign oxygen use values which vary with the structure, for example, subtracting 0.4 oxygens per carbonyl available for the calculational factor  $F$ . I arbitrarily assumed, for exploratory purposes, that there would be 1/2 mol CO + 1/4 mol CO<sub>2</sub> per carbonyl oxygen, rather than 1/2 mol CO<sub>2</sub> as in the dioxide assumption. This would put energy 10.35 kcal below the dioxide assumption, for each such occurrence.

In NTO there is one carbonyl, and in DINGU there are two.

The DINGU recalculations (for X-0420 and X-0432) reduce the  $Q_{\text{cyl}}$ s to 1845 and 1810 cal/cm<sup>3</sup>. These fit the regression line better, reducing the deviations (defined below) from -18 percent and -13 percent to -13 percent and -11 percent. However, they do not raise the correlation coefficient  $r$  to the value deleting the DINGU points. The recalculated NTO does not fit the line as well as the original NTO because the deviation changed from -2.7 to +6.3 percent.

The relatively poorer correlation of detonation pressure with performance (see Tables 5 and 1) may be a reflection of the anomalous situation regarding insensitive explosives: all four (NQ, TATB, DINGU, and NTO) have cylinder test performance significantly lower than one would expect from the detonation pressures of and experience with the usual "sensitive" military explosives. In those rich in RDX or HMX, the correlation of performance with detonation pressure is good. However, much of the study and use has been

in fast-response systems, i.e., those having thin metal (low metal mass to HE charge ratios) or short flight ranges before detonation products expand greatly or escape. Those applications, where free flight occurs quickly, are no doubt more responsive to the single point (CJ) or narrow expansion range on the isentrope than is the cylinder test, which responds to much more of the area under the PV curve, as do many munitions.

The standard high-powered explosives also have high  $Q$ , however, so they too fit the correlations between  $Q$  and metal-moving performance—providing, as implied in the previous paragraph, that the metal to be moved is sufficiently massive and retentive of the explosive's detonation products and energy. Although  $P$  must be related to  $Q$  in some way, the correlation coefficient is not very high ( $r = 0.91$  to  $0.92$ ) due, no doubt, to factors other than  $Q$  and the limited accuracy or precision of the  $P$  calculations and measurements.

There are a few explosives outside the base set that widen the field, which have had both  $Q$  and cylinder performance measured. These are an HNO intermolecular (hydrazine/hydrazine nitrate, RX-23-AA), two CNOs (BTF and HNB), and two CHNO intermoleculars (EAR and AN/ADNT<sup>17</sup> along with the parent monomolecular ADNT). Adding these to the base set does not reduce the fit much, with the coefficient  $r$  still being over 0.97 at  $V/V_0 = 11$ . There are interesting deviations. HNB falls below the base set line about 9 percent in energy, the very high performance notwithstanding. BTF is almost on the line (-3 percent), but recall that HMX is +6 percent.

Also of interest are the large positive deviations, all of them in the low-carbon systems: H/HN + 17 percent, EAR + 10 percent, and AN/ADNT + 7 percent. All three are intermolecular (but seem to behave ideally), high in hydrogen, and zero or low in carbon. AN/ADNT is CO<sub>2</sub>-balanced, and EAR is nearly so. These three formulations are the only ones having that kind of elemental balance. Although it does not affect the  $Q_{cyl}$  or the present result, note that the EAR parent explosive, EDD, is the only one with a

measured  $Q$  higher than the calculated  $Q$ , indicating that the published heat of formation, -156.1 kcal/mol, may be in error.

Differences in detonation characteristics between explosives with mainly hydrogen as a fuel and those with mainly carbon as a fuel would be expected. Carbon-free and low-carbon (hydrogen) systems would produce more moles of gas per gram (or per cubic centimeter if densities are similar) at lower average molecular weight than do carbon-rich systems. Also, one would expect detonation temperatures of high-hydrogen explosives to be lower than those of high-carbon explosives, requiring less time for relaxation into translational kinetic activity. Although not necessarily relevant to the present results (because the specific energy was measured), 50 percent more energy is obtained, gravimetrically, from gaseous water as a product than from CO<sub>2</sub>: 3.21 kcal/g (57.8 kcal/mol from water as a gas, molecular weight 18) versus 2.14 kcal/g from CO<sub>2</sub> (94/44). Whether more or less energy is realized volumetrically from real materials depends of course on density, heat of formation, etc. One sees that carbon systems usually produce more net energy volumetrically than do hydrogen systems.

Some of the regressions were recalculated using the base set plus the six points just described—with and without the 0,0 point—and some without the DINGU points. This was done because the biggest deviations in the six explosives are at opposite ends of the line, and line bias by 0,0 or the different set of points might be yielding deviations higher than warranted for those materials. But that is not the case; the deviations changed little except that HNB was somewhat less deviant and HMX was somewhat more so.

The set of aluminized explosives (Table 4) indicates directly—assuming that aluminum simply adds  $Q$ —the effect of the explosive's chemical energy on cylinder energy. Replacing about 5 percent of the HMX by aluminum increases the wall energy by about 5 percent at  $V/V_0$  of 7 and larger. The CJ parameters do not seem to have been much affected, although in the nonaluminized mix the early wall velocity (hence acceleration and pressure) is



higher, as indicated by the shorter flight time to  $V/V_0 = 2$ . However, the average wall velocity in both the aluminized mixes is equal to or slightly faster than the nonaluminum mix by the time the outer copper wall diameter is a little over 2.5 times the original diameter ( $r = r_0\sqrt{7}$  at  $V/V_0 = 7$ ).

## CONCLUSIONS

Detonation calorimetry can be both pragmatically and academically useful in the study of explosives and munitions. The correlation with performance in the cylinder test and its correspondence with several kinds of munitions is of practical value, while the study of products and heats should be of academic value in research on detonation.

The large negative deviation of one insensitive explosive (DINGU, approximately 18 percent below that expected from the correlation) is noted but not explained. Large positive deviations in high-hydrogen explosives (especially the 17 percent in hydrazine/hydrazine nitrate and 10 percent in EAR) are also noted.

The detonation pressure or velocity parameters do not predict cylinder test performance as well as the thermochemical energy does.

With some refinement to improve the correlation between calculated and measured  $Q$ , performance of new explosives might be reasonably well estimated before they are made. Refinements might include the use of structure or equations of state to predict products and energy.

## GLOSSARY

ADNT	ammonium dinitrotriazole
AFX-902	95/5 NQ/Viton A
AN	ammonium nitrate
BTF	benzotrifuroxan
AN/ADNT	2/1 moles
Comp B	64/36 RDX/TNT
Comp C-4	91/9 RDX/organic binder

DINGU	dinitroglycoluril
EAR	42.5/42.5/15 EDD/AN/RDX
EDD	ethylenediamine dinitrate
H/HN	21/79 hydrazine/hydrazine nitrate
HNB	hexanitrobenzene
NM	nitromethane
NQ	nitroguanidine
NTO	nitrotriazolone
Octol	75/25 HMX/TNT
PBX-9404	94/3/3 HMX/nitocellulose/chlorethyl phosphate
PBX-9502	95/5 TATB/Kel-F 800
RX-23-AA	H/HN
TMD	theoretical maximum density
X-0420	94/5/1 DINGU/Exon/titanate
X-0432	57/43 DINGU/TNT

(All ratios are weight percent)

## REFERENCES

1. Ornellas, D. L., "Calorimetric Determination of the Heat and Products of Detonation for Explosives: October 1961 to April 1982," UCRL 52821, Lawrence Livermore Laboratory (LLNL) report, Apr 1982.
2. Kury, J. W.; Horning, H. C.; Lee, E. L.; McDonnell, J. L.; Ornellas, D. L.; Finger, M.; Strange, F. M.; and Wilkins, M. L., "Metal Acceleration by Chemical Explosives," *Fourth Symposium (International) on Detonation*, White Oak, MD, ACR-126, Office of Naval Research, Washington, DC, 12-15 Oct 1965, pp. 3-13.
3. Kamlet, M. J., in a seminar at the White Oak Laboratory, NSWC, 1987.
4. Volk, F., ICT, FRG, in talks at Los Alamos National Laboratory (LANL), 1987.

5. Akst, I., unpublished data, with calculations by H. Cheung of LLNL, 1977; test results by R. McGuire, M. Finger, D. Ornellas, et al., LLNL, 1979.
6. Urizar, M., LANL, unpublished data, 1975.
7. Mason & Hanger--Silas Mason Co., Inc., Pantex MHSM progress reports, 1972-1974.
8. Kubose, D. and Eccleston, H., White Oak Laboratory, NSWC reports, 1981 and 1982.
9. Dobratz, B. M. and Crawford, P. C., "LLNL Explosives Handbook, Properties of Chemical Explosives and Explosive Simulants," LLNL report UCRL 52997, Change 2, 31 Jan 1985.
10. Heats of formation determined by M. M. Stinecipher, LANL, for DINGU, for example.
11. Kamlet, M. J. and Jacobs, S. J., *Journal of Chemical Physics*, Vol. 48, No. 1, 1968, p. 23.
12. Cylinder performance data from Reference 9 and from personal communications, LLNL.
13. Cylinder performance data from, for example, P. E. Kramer, "TATB Performance and Sensitivity," Mason & Hanger--Silas Mason Co., Inc., Pantex report MHSMP-76-46, E1-8, 1976.
14. Akst, I. B., "Nonideal Explosives Research: Intermoleculars, Eutectics, and EAX," AFATL-TR-82-79, Air Force Armament Laboratory, Eglin AFB, Florida, 1982.
15. Cylinder performance data from Group M-8, LANL (J. W. Straight, Group Leader), Principal Investigators: A. W. Campbell, W. C. Davis, C. W. Mautz, J. R. Travis, and I. B. Akst, 1974-1988.
16. Rothstein, L. R. and Petersen, R., "Predicting High Explosive Detonation Velocities from their Composition and Structure," *Propellants and Explosives*, Vol. 4, 1979, pp. 59-60. See also Errata and (II) *Propellants and Explosives*, Vol. 6, 1981, pp. 91-93.
17. Stinecipher, M. M., "Eutectic Explosives Containing Ammonium Nitrate, 1979-1981," Los Alamos National Laboratory report LA-9973, 1984.

# THEORETICAL PREDICTION OF HIGH EXPLOSIVES EFFICIENCY: APPLICATION TO NTO

F. Bugaut, S. Bernard, and R. Chirat  
Commissariat à l'Energie Atomique  
BP n°7, 77181 Courtry, FRANCE

*We present an application of theoretical calculations of high explosive efficiency by means of the thermochemical code ETARC to the case of a new molecule: NTO, for which only a few experimental data are available. We predict all thermodynamical and chemical quantities at the Chapman-Jouguet (CJ) point and along an isentrope—for the pure molecule and for its mixtures with either a binder or other explosive molecules (HMX, TATB). Results are in good agreement with experiments.*

## INTRODUCTION

Theoretical calculations of the performances of explosives have become very common during the last 20 years and several codes have been built all over the world for that purpose. Our thermochemical code ETARC is one of them and is based on a physical equation of state for detonation products.<sup>1</sup> A lot of results were published on well-known explosives.<sup>2</sup> We present here another application of our code: the theoretical prediction of the performances of a new explosive, before experimental data are available. In this paper, we will focus on the NTO molecule,<sup>3</sup> but our goal is to provide an example of what can be done by means of theoretical methods to study a new explosive before it is manufactured.

ETARC provides an estimation of detonation properties of explosives with only three input data: the chemical composition CHON, the enthalpy of formation, and the initial density. Such a code was first designed to calculate the equation of state of detonation products, but it can be used to predict properties of new explosives. Let us consider a new molecule of given chemical composition. Before synthesis, crystal density and enthalpy of formation can be regarded as parameters and a first theoretical study can decide if the molecule is worthwhile or not. When a small

amount of molecular crystal is synthesized, density and enthalpy of formation can be measured; a theoretical study can predict properties for the pure molecule before enough material is available to perform detonation experiments. Then, before compositions are manufactured, theoretical calculations can be done for mixtures with a binder and other explosives, with percentages being regarded as parameters.

Chemists who are working in the field of new high explosives are in search of a new molecule as insensitive as TATB, but with higher energetic performances. NTO was synthesized in the United States by chemists at Los Alamos in 1985<sup>3</sup> and in France by SNPE in 1987.<sup>4</sup> In the first part, we summarize the main physical and chemical properties of NTO, together with assumptions used in the code. Then, we study the interest of this new explosive, compared to TATB and HMX, as pure molecular crystals with theoretical densities. In such a way, it is possible to avoid fluctuations due to technological parameters—such as the binder or the density actually obtained—and thus get results on the intrinsic properties of the explosive molecules. The second part is devoted to results at the CJ point; the CJ isentrope is studied in a third part. Finally, we study the use of NTO in explosive compositions with a Kelf binder.

Calculations are first done considering pure NTO with a variable percentage of binder. Then, we build an equivalence chart between NTO and HMX/TATB mixtures, and also between HMX/NTO and HMX/TATB mixtures. At last, we emphasize that sensitivity problems are out of the field of this paper, which is strictly devoted to energetic efficiency.

## SUMMARY OF DATA

### The NTO Molecule

The formula of the NTO molecule is  $C_2H_2O_3N_4$ . It can be compared to HMX and TATB in terms of chemical composition (Table 1). It is obvious that NTO does not contain a lot of carbon, but has a high percentage of nitrogen; one can guess that detonation products will be very rich in  $N_2$ , as we will show later. Theoretical estimations using quantum chemistry methods,<sup>5</sup> lead to a mean value for the enthalpy of formation of the molecular crystal of -28.0 kcal/mol. NTO is intermediate between TATB and HMX, but closer to TATB.

Experimental measurements<sup>3</sup> indicate a mean density of  $\rho = 1.91$  to  $1.93$  g/cc. We use here the lower limit of  $1.91$  g/cc and, for HMX and TATB,  $1.890$  g/cc and  $1.880$  g/cc, respectively.<sup>6</sup>

Values shown above indicate that NTO is not an exceptionally energetic molecule, which is a good point for insensitivity. On the other hand, because of a high density, one can expect high CJ properties. But, as the energetic content of the molecule is moderate, one can guess that the pressure decrease during the isentropic expansion will be quite important, compared to other explosives (HMX and TATB).

### Calculation Hypothesis

There exists now a lot of thermochemical codes designed for calculating detonation properties of explosives, such as BKW or TIGER. With our ETARC code, we can estimate all the thermodynamical quantities of detonation products ( $P$ ,  $T$ ,  $V$ , particle velocity  $U_p$ , ...), as well as their derivatives and the chemical composition of each thermodynamical state. For

Table 1. Thermochemical Data

Molecule	Formula	$\Delta H_f$ (kcal/mol)	Oxygen Balance in g of oxyg. / kg expl.
HMX	$C_4H_8O_8N_8$	+17.93	-216
TATB	$C_6H_6O_6N_6$	-36.85	-558
NTO	$C_2H_2O_3N_4$	-28.0	-246

common explosives like HMX, ETARC is known to provide results in very good agreement with experimental data.

The main physical hypothesis assumed in this code is to suppose that the different components of the molecular mixture are always in chemical equilibrium, which allows calculation of the different quantities by minimizing the Gibbs free energy. We do not have any indication of the validity of this assumption for NTO like we do for TATB. Lacking in experimental results, we can consider it reasonable. Detonation products are supposed to consist of two phases, in pressure and temperature equilibrium: a fluid phase and a solid one. For the former, we use the WCA model<sup>2</sup> which leads us to an accuracy of 5 to 10 percent in pressure and 2 to 3 percent on detonation velocity, and so as good as experimental results. We take into account the following species:  $CO_2$ ,  $H_2O$ ,  $CO$ ,  $H_2$ ,  $O_2$ ,  $N_2$ ,  $NH_3$ ,  $CH_4$ , and  $NO$ ; if fluorine exists in the binder, we also include  $F_2$ ,  $HF$ ,  $CF_4$ , and  $NF_3$ . We now know that some HCN exists in detonation products,<sup>7</sup> but it was not taken into account in our calculation. Molecular interactions are modeled by a spherical exponential-six potential, with parameters given in Table 2. For cross potentials, we use the well-known Lorentz-Berthelot rules. The solid phase is supposed to contain only crystalline carbon, as graphite (G) or diamond (D). For slightly carbonated explosives like HMX or NTO, we use the graphite assumption, because it provides the best agreement with experimental results. As for TATB, experimental data lie between theoretical results given by the two assumptions.<sup>2</sup> Actually, we know that carbon is probably not in a bulk phase<sup>8</sup> and work is in progress on this problem in several laboratories.<sup>9</sup> Even if our

Table 2. Intermolecular Potential Parameters

Molecule	$\alpha$	$\epsilon / k \text{ (K)}$	$\sigma \text{ (\AA)}$
CO <sub>2</sub>	13.0	245.6	4.17
H <sub>2</sub> O	13.5	136.0	3.37
CO	13.0	108.0	4.09
H <sub>2</sub>	13.5	30.0	3.00
O <sub>2</sub>	15.0	132.0	3.73
N <sub>2</sub>	13.5	117.0	4.11
NH <sub>3</sub>	17.0	138.0	3.50
CH <sub>4</sub>	13.5	155.8	4.198
NO	12.0	105.0	3.90
F <sub>2</sub>	13.5	200.0	3.50
HF	13.5	100.0	3.30
CF <sub>4</sub>	13.5	220.0	5.00
NF <sub>3</sub>	13.5	200.0	4.10

treatment of carbon in detonation products is not satisfactory, we can expect quite good results for NTO because of the low percentage of carbon in this molecule.

## CJ RESULTS FOR PURE NTO

We emphasize the fact that ETARC results account for a steady-state detonation with infinite diameter of the sample cartridge, made with pure NTO. They have to be decreased for small diameters. Nevertheless, comparison between the different molecules remains valid.

### Detonation Properties at Theoretical Density

Results for the Chapman-Jouguet state are presented in Table 3. Experimental data for TATB are close to TATB G for  $P_{CJ}$  and to TATB D for  $D_{CJ}$ . NTO is intermediate between TATB and HMX, and is quite similar to a 25 percent HMX/75 percent TATB mixture for CJ values. We can also consider the polytropic  $\gamma$  which is a measure of the slope for the

Table 3. ETARC Results at CJ Point

Molecule	$P_{CJ}$ kbar	$D_{CJ}$ m/s	$V_{CJ}$ cm <sup>3</sup> /g	$T_{CJ}$ K	$U_{PCJ}$ m/s	$\gamma_{CJ}$
HMX $\rho = 1.890$	405	9050	0.39066	3982	2368	2.820
TATB G $\rho = 1.880$	308	8047	0.39726	3063	2037	2.946
TATB D $\rho = 1.880$	270	7772	0.40542	2937	1848	3.203
NTO $\rho = 1.91$	327	8120	0.38760	2882	2109	2.845

isentropic expansion curve just behind the CJ point. We see in Table 3 that  $\gamma$  for NTO is quite small, as for HMX. We noticed in the first chapter that pressure strongly decreases along the isentrope; it is now possible to conclude that  $P$  is maintained just behind the CJ point and that the decrease probably occurs later in the expansion.

The CJ temperature is lower for NTO than for other molecules. In order to explain such a behavior, let us notice that the enthalpy of formation of CO<sub>2</sub> (-94.1 kcal/mol) and H<sub>2</sub>O (-57.8 kcal/mol) is lower than that of N<sub>2</sub> (0 kcal/mol). Detonation products of NTO contain a lower amount of CO<sub>2</sub> and H<sub>2</sub>O, but a large fraction of N<sub>2</sub>; to be formed, the latter needs more energy which is taken from the fluid, leading to a lower temperature.

The number of moles for the four main components of detonation products are represented in Figure 1, for 1 kg of explosive. As expected, we find a large proportion of nitrogen and a quite small amount of carbon, similar to the case of HMX.

We focus now on the problem of the enthalpy of formation of NTO. For all calculations, we choose the average value -28.0 kcal/mol. Several estimations of that enthalpy lead to a value between -30 and -26 kcal/mol. ETARC calculations indicate that a variation of 1 kcal/mol in enthalpy induces fluctuations in pressure of about 1 kbar and 11 m/s in terms of detonation

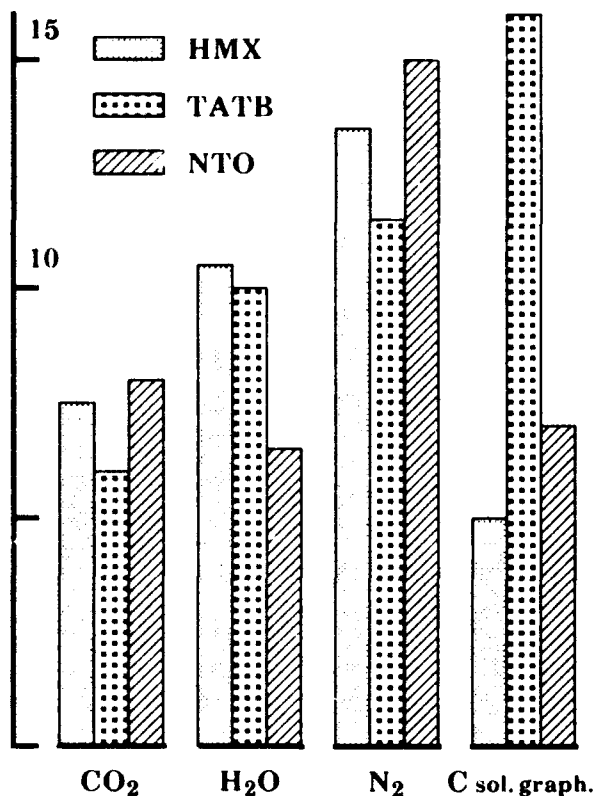


Figure 1. CJ Composition for Products

velocity. As for engineering applications, a 1 percent accuracy in pressure is required for the equation of state for detonation products. This means that the enthalpy of formation of NTO has to be measured with an accuracy better than 1 kcal/mol.

#### Evolution of CJ Results With the Density $\rho$

Initial density can be a parameter in theoretical calculations, therefore detonation properties can be determined as functions of density.  $D_{CJ}(\rho)$  is shown on Figure 2. Theoretical densities are plotted with crosses. NTO is not an intrinsically very energetic molecule (its representative curve is low), but leads to interesting CJ values because of its high density. An empirical linear fit can be done ( $D$  in m/s,  $\rho$  in g/cc):

$$\begin{aligned}
 \text{HMX} \quad D_{CJ} &= 2406 \cdot \rho + 4503 \\
 \text{TATB G} \quad D_{CJ} &= 2773 \cdot \rho + 2832 \\
 \text{TATB D} \quad D_{CJ} &= 3556 \cdot \rho + 1087 \\
 \text{NTO} \quad D_{CJ} &= 2326 \cdot \rho + 3675
 \end{aligned}$$

The slope for NTO is low, which means that a decrease in  $\rho$  leads to a moderate decrease in

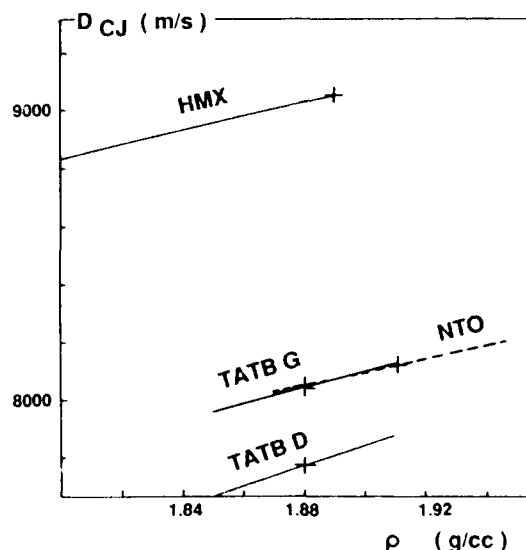


Figure 2. Detonation Velocity  $D_{CJ}(\rho)$

the detonation properties. The same figures can be drawn for other CJ quantities; for  $P_{CJ}$ , the linear fit of the results is the following ( $P$  in kbar,  $\rho$  in g/cc):

$$\begin{aligned}
 \text{HMX} \quad P_{CJ} &= 474 \cdot \rho - 491 \\
 \text{TATB G} \quad P_{CJ} &= 476 \cdot \rho - 587 \\
 \text{TATB D} \quad P_{CJ} &= 434 \cdot \rho - 545 \\
 \text{NTO} \quad P_{CJ} &= 469 \cdot \rho - 569
 \end{aligned}$$

A few experimental measurements of the CJ pressure were done for pure and pressed NTO with cartridges of several diameters.<sup>3</sup> Unfortunately, they are strongly scattered and cartridge diameters are quite small. Theoretical results seem to be in good agreement (Figure 3), but we have to wait for complementary

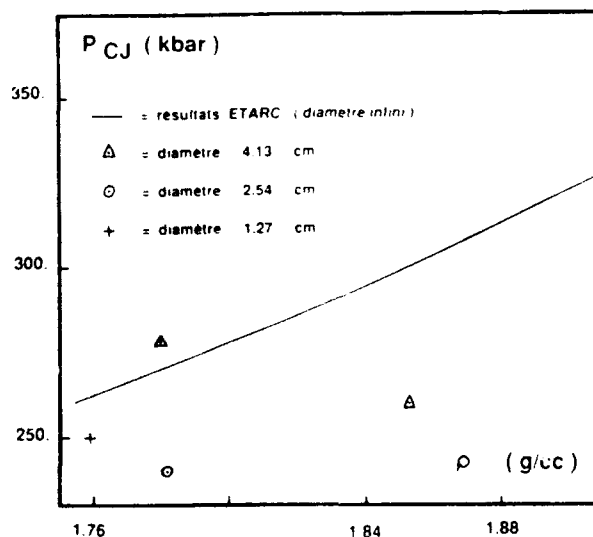


Figure 3. NTO:  $P_{CJ}(\rho)$ , Theory vs. Experiment

experimental results to decide whether the theoretical model is appropriate.

## ISENTROPIC EXPANSION FOR PURE NTO

We examine here the behavior of the different explosives during the expansion along the CJ isentrope. Comparisons are done first with TATB, with both hypothesis for carbon in detonation products (graphite or diamond); only the beginning of the isentrope of HMX is plotted on the figures, to give an order of magnitude for the thermodynamical quantities of this molecule.

Isentropes in Figure 4 show that NTO remains intermediate between TATB and HMX along the whole expansion, but closer to TATB. On this basis, we can confirm that, in a rough approximation, NTO is very similar to a (one-fourth of HMX/three-fourths of TATB) mixture.

Figure 5 indicates how the slope of the isentrope varies in (P, V) coordinates during the expansion. As predicted before, P remains high at the beginning of the expansion ( $\gamma$  is quite low from  $P_{CJ}$  to 100 kbar) and decreases after 100 kbar faster than for other explosives (higher  $\gamma$ ). NTO preferentially delivers its energy at the beginning of the expansion.

Another interesting result deals with the temperature of NTO detonation products, which remains about 300 K lower than for

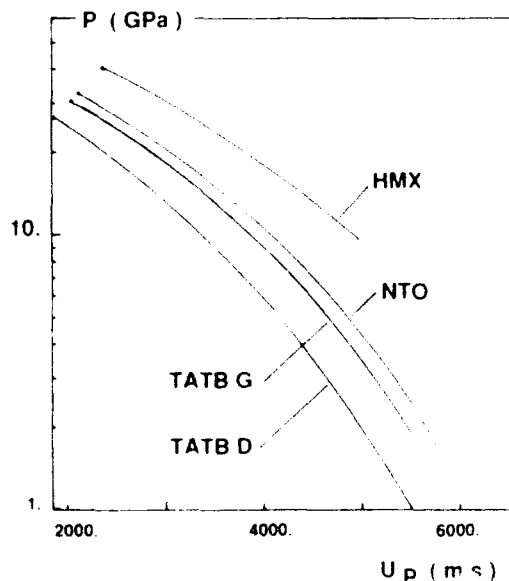


Figure 4. CJ Isentrope:  $P$  vs.  $U_p$

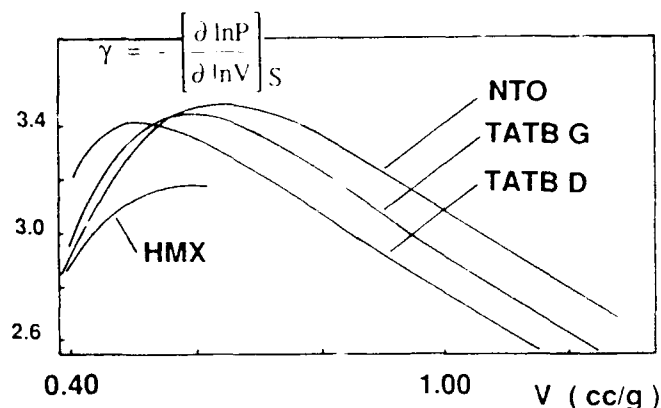


Figure 5. CJ Isentrope: Polytopic  $\gamma(V)$

TATB products (Figure 6). Temperature is of secondary importance in applications, but is theoretically very interesting, as it is very sensitive to the physical models used for the equation of state. Accurate experimental measurements of that quantity could be very important to build new theoretical models of the equation of state for the molecular mixture.

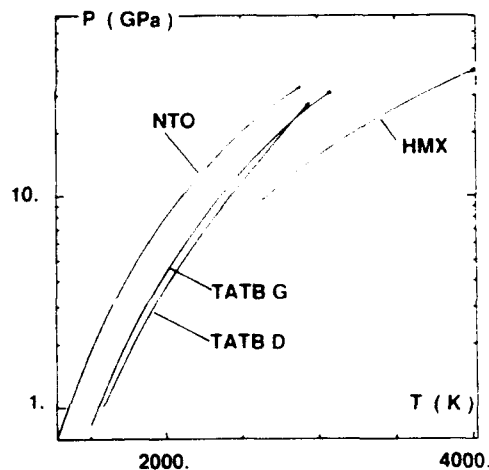


Figure 6. CJ Isentrope: Temperature

One of the most significant quantities is the energy which can be delivered by the new molecule. We calculate the total work given by detonation products during an expansion from CJ density to about 1.20 cc/g (expansion ratio  $V/V_{CJ} = 3$ ):

$$W = + \int_{V_{CJ}}^{V=1.20 \text{ cc/g}} P. dV$$

by numerical integration of the pressure.  $W$  is difficult to estimate in the case of TATB because of the two assumptions on carbon. Yet, one can approximatively estimate  $W$  to 4.5 MJ/kg for TATB and 5.3 MJ/kg for NTO; it leads to an increase of about 15 to 18 percent from TATB to NTO in terms of total work delivered by 1 kg of explosive during the expansion.

$\Gamma$  decreases continuously along the isentrope (Figure 7), which proves that simplified equations of state of the form  $P \cdot V = \Gamma(V) \cdot E + f(V)$  with a constant Grüneisen (like JWL equation of state, where  $\Gamma = 0.3 - 0.4$ ) cannot reasonably describe the actual behavior of detonation products.

In the first chapter, we examined the composition of detonation products under CJ conditions. The same thing can be done for each thermodynamic state along the isentrope. In Figures 8 and 9 (for 1 kg of explosive), we notice that the chemical equilibrium is strongly modified for pressures less than 150 kbar. Hydrogen and carbon monoxide are no more negligible. The number of moles in the fluid phase increases, as that in the carbon phase decreases; note that the solid phase has a negligible volume. The fact can be explained in terms of a classical moderation law: when pressure decreases, the system tries to maintain it by modifying the chemical composition. At high  $p$ ,  $P$  is determined by the total amount of matter in a given volume;  $P$  does not vary dramatically when the same atoms form a small number of big molecules or a great number of small ones, and composition does not change. As  $p$  decreases more and more, the ideal gas contribution to  $P$  (translation of molecules) becomes relatively more important. As big and small molecules have the same translational energy  $3/2 \cdot RT$ , the system can limit the pressure decrease by transforming bigger molecules ( $\text{CO}_2, \text{H}_2\text{O}$ ) into smaller ones ( $\text{CO}, \text{H}_2$ ), thus increasing the total number of moles in the fluid phase.

## NTO-BASED COMPOSITIONS

We now focus on the question of NTO-based compositions, i.e. NTO mixed with a binder, and eventually other explosive molecules. As for the binder, we only consider here

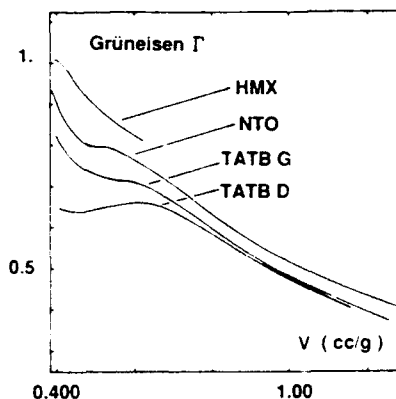


Figure 7. Gruneisen  $\Gamma$  on Isentrope

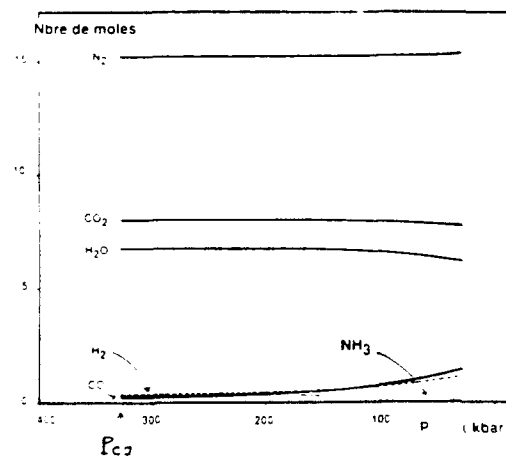


Figure 8. Products Composition

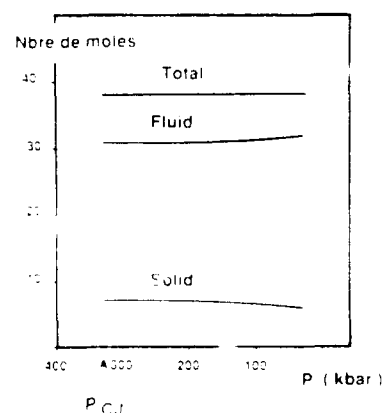


Figure 9. Total Number of Moles of Products

KelF800 (chemical formula  $\text{C}_8\text{H}_2\text{F}_{11}\text{Cl}_3$ , density  $\rho = 2.02 \text{ g/cc}$ , enthalpy of formation  $\Delta H_f = -578 \text{ kcal/mol}$ ). We do not take chlorine into account in chemical equilibrium calculations. Fractions indicated in mixtures are always weight percentages.



## Comparison of NTO vs. HMX/TATB Mixtures

We present some ETARC calculations for HMX/TATB mixtures, without binder and for the CJ state (Figure 10). The graphite assumption is relevant to describe the CJ pressure of TATB. If we choose the same CJ pressure as a criterion, we see that NTO is equivalent to a (20 percent HMX/80 percent TATB) mixture, the detonation properties of which are approximately  $P_{CJ} = 325$  kbar and  $D_{CJ} = 8000$  m/s (in terms of detonation velocity, the diamond assumption is the best to fit experimental data for TATB). For the same pressure,  $D_{CJ}$  for NTO is a bit higher than for the equivalent HMX/TATB mixture.

## NTO/KelF800 Compositions

Let us consider the fraction  $\tau$  of binder as a variable. Detonation properties are decreasing functions of  $\tau$ ; our ETARC calculations in the range 0-8 percent lead to the following linear fits ( $\tau$  in weight %):

$$\begin{aligned} P_{CJ} \text{ (kbar)} &= -2 \cdot \tau + 327 \\ D_{CJ} \text{ (m/s)} &= -13 \cdot \tau + 8120 \end{aligned}$$

The KelF800 binder contains a large fraction of fluorine. The composition of detonation products (Figure 11) shows that all fluorine atoms are included in HF molecules, which becomes a quite important component. Hydrogen is needed to form  $H_2O$ , so the percentage of water decreases and more oxygen is available to burn carbon. But, on the other hand, as the

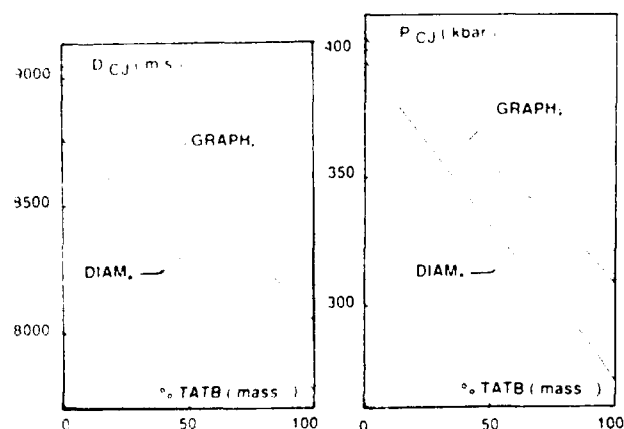


Figure 10. HMX/TATB Mixtures: CJ Results

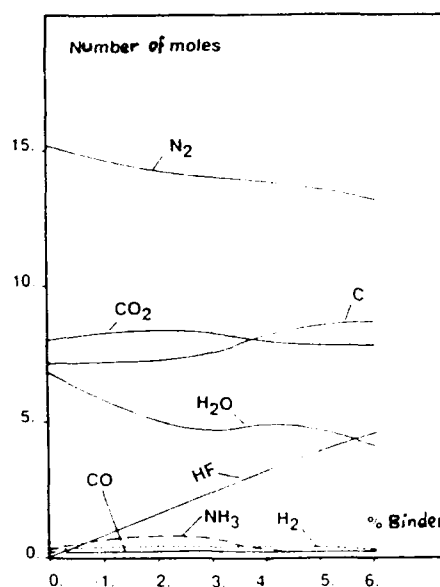


Figure 11. Products Composition vs. % of Binder

binder does not contain oxygen, the mean fraction of oxygen in the composition decreases with the percentage of binder and thus, more carbon remains unburned. Finally, the global effect is that more carbon remains unburned when binder is added and a lower energy is delivered by the explosive molecule. The binder has a negative effect not only because it is not an energetic material, but also because it strongly modifies the chemical equilibrium of detonation products in an unfavorable way.

## HMX/NTO Mixtures

We now turn to HMX/NTO mixtures, without binder. It is well-known that CJ properties of HMX/TATB mixtures are quite exactly linear functions of the fraction of components (Figure 10). Figure 12 shows that properties of HMX/NTO mixtures are higher than linear average values, of about 7 kbar on  $P_{CJ}$  and 100 m/s on  $D_{CJ}$  for a fifty-fifty mixture. Such a behavior can be explained by examining the composition of the products as a function of the fraction of NTO in the mixture; the evolution is not at all linear and the chemistry of the detonation products of the mixture is governed by that of the HMX products.

Figure 13 is a chart of equivalence between HMX/TATB mixtures and HMX/NTO

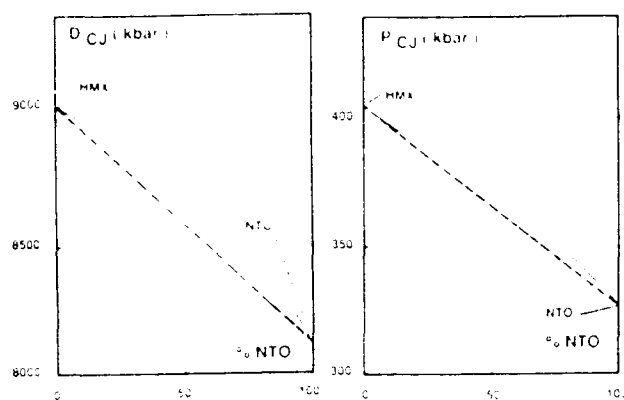


Figure 12. HMX/NTO Mixtures: CJ Results (Full Line: ETARC, Dashed line: Linear Average)

mixtures. We read for example that a fifty-fifty HMX/TATB mixture is equivalent to a (25 percent HMX/75 percent NTO) mixture (under the criterion of equal  $P_{CJ}$  pressures).

Lastly, we briefly study an HMX/NTO/KelF composition published previously,<sup>4</sup> for which a detonation velocity measurement is available. Even if that composition is not intrinsically interesting (it was a preliminary one), it is one of the rare experimental data available in literature and is important to validate our theoretical calculations. ETARC values are  $P_{CJ} = 341$  kbar and  $D_{CJ} = 8421$  m/s. The experimental value for detonation velocity is 8360 m/s, but the cartridge diameter is very

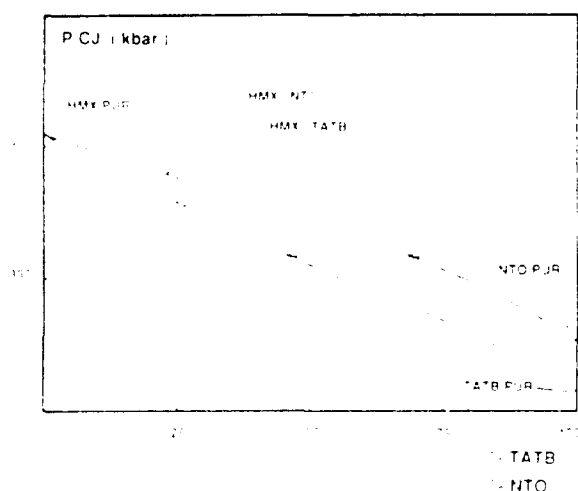


Figure 13. Equivalence Between HMX/TATB and HMX/NTO Mixtures

small (28 mm). As the ETARC results account for an infinite diameter, we can consider that the agreement is quite good.

## CONCLUSION

We predict all thermodynamic values and chemical composition of detonation products at the CJ point and along an isentrope, for the pure molecule NTO as well as for NTO-based compositions, with a good agreement with the few available experimental data.

Energetically intermediate between TATB and HMX, NTO seems to be an interesting molecule to build a new insensitive high explosive, in place of TATB. The increase in work delivered to external media is about 15-18 percent compared to TATB, for the same mass of explosive. NTO is energetically interesting first of all because of its high density, which leads to good CJ properties; the pressure of detonation products seems to decrease strongly along the isentrope below 100 kbar.

## ACKNOWLEDGEMENTS

We thank K. Y. Lee (Los Alamos National Laboratory) and M. J. Stosz (Naval Surface Warfare Center) for helpful discussions.

## REFERENCES

1. Chirat, R.; Guri, G.; and Pittion-Rossillon, G., ETARC code, CEA, CEV-M, France, 1978, unpublished work.
2. Chirat, R. and Pittion-Rossillon, G., *J. Chem. Phys.*, Vol. 74, 1981, p. 8; Chirat, R. and Pittion-Rossillon, G., *Proceedings of Seventh International Symposium on Detonation*, 1981; Chirat, R. and Pittion-Rossillon, G., *Combustion and Flame*, Vol. 45, 1982, pp. 147-159; Chirat, R. and Baute, J., *Proceedings of the Eighth Symposium (International) on Detonation*, 1985; Baute, J. and Chirat, R., *Proceedings of the Eighth Symposium (International) on Detonation*, 1985.
3. Lee, K. Y. and Coburn, M. D., LA-10302-MS, 1985; Lee, K. Y.; Chapman, L. B.; and Coburn, M. D., *J. of Ener. Materials*, Vol. 5, 1987, pp. 27-33.

4. Becuwe, A. and Delclos, A., *Proceedings of International Symposium Pyr. and Expl.*, Beijing, 1987.
5. Ritchie, J. P., accepted in *J. Org. Chem.*, 1989.
6. Dobratz, B. M., UCRL-52997, 1981.
7. Volk, F., *J. Ener. Materials*, Vol. 4, 1986, pp. 93-113.
8. Greiner, N. R.; Phillips, D. S.; Johnson, J. D.; and Volk, F., *Nature*, Vol. 333, 2 Jun 1988.
9. Van Thiel, M. and Ree, F. H., *J. Appl. Phys.*, Vol. 62, 1987, p. 5; Shaw, M. S. and Johnson, J. D., *J. Appl. Phys.*, Vol. 62, 1987, p. 5.

### DISCUSSION

LES ROSLUND, NSWC  
Silver Spring, MD

Why did you omit consideration of HCN within the decomposition products of NTO?

### REPLY

There is experimental evidence for HCN in detonation products only at the end of the expansion. Such a molecule could be taken

into account, at least as an hypothesis, but there is no proof that HCN exists at higher pressure.

### DISCUSSION

LEROY GREEN, LLNL  
Livermore, CA

What is the principal difference between ETARC and Tiger if one uses JCZ3 in the Tiger calculations?

### REPLY

ETARC is based upon a physical equation of state for the molecular mixture from statistical mechanics; there is no fit on explosives properties.

### DISCUSSION

HAROLD GRYTING, GESC  
San Antonio, TX

Have you run any cylinder expansion tests on any of your mixtures and made similar comparisons with NTO?

### REPLY

No experiment was done at CEA with NTO.

# DETERMINING JWL EQUATION OF STATE PARAMETERS USING THE GURNEY EQUATION APPROXIMATION

P. J. Miller and K. E. Alexander  
Naval Surface Warfare Center  
White Oak Laboratory  
Silver Spring, Maryland 20903-5000

*Using the assumptions implied in the Gurney formula for cylindrical case expansion, that the detonation gas products are uniform in density and composition at any fixed time in the radial expansion, we have expressed the Gurney energy in a generalized energy conservation equation. The uniformity conditions also imply a uniformity in pressure, thus a constant entropy during the radial expansion. The Gurney energy is expressed, then, in terms of the JWL relation for energy at constant entropy using the two-dimensional hydrocode result for relating relative volume of expansion to radial expansion. This Gurney-JWL energy relation is tested using reported cylinder test and JWL equation of state data on several explosives. The effect of varying the explosive-to-metal mass ratio, C/M, is also shown on the model. For volume expansion between 1.5 and 10, the model appears to fit the observed data to within the estimated experimental error. It is, then, demonstrated how "engineering quality" JWL equation of state parameters for a test explosive may be extracted directly from cylinder test data without using two-dimensional hydrocode computations.*

## INTRODUCTION

One of the most important uses of explosives is to accelerate metal in fragmentation shells and in self-forging fragment or shaped charge warheads. With the aim of saving time, money and other resources, more of these and other applications for explosives are being simulated with large computer programs which follow the hydrodynamic behavior of the complete system. The ability of a hydrocode to accurately predict the detonation performance of an explosive and the subsequent behavior of the accelerated metal depends critically upon the equation of state (EOS) introduced to describe the explosive. In general, the Jones-Wilkins-Lee (JWL) equation of state<sup>1</sup> is usually accepted as the description of the adiabatic expansion of the detonation products in warhead applications.

A variety of metal accelerating tests have been investigated for measuring the relative performance of explosives. The cylinder test was found to be the most versatile.<sup>2</sup> This test easily determines the relative performance of explosives for volume expansions between 2 and 10, which includes most applications for metal accelerating explosives. The cylinder test is also used to evaluate the 6 adjustable parameters of the JWL equation of state which are characteristic of the explosive under study. Through numerical simulation with a two-dimensional hydrocode, experimental data obtained from the radial expansion measurement of a copper cylinder accelerated by the detonation of its explosive filling are reproduced. The parameters of the JWL equation are optimized until a best fit is obtained between simulation and experiment.

This procedure is one of trial and error and can be a lengthy process.

Before the development of the computer and hydrocode computations, the Gurney formula<sup>3,4</sup> was developed and widely used to compare the relative velocities of fragments from metal-explosive systems. Among the analytical models relating metal velocity and explosive-to-metal mass ratio,  $C/M$ , the Gurney model is the best known because of its simplicity and versatility. It is still widely used today for predicting the relative performance of accelerating metal explosives. The only empirical value needed is called the Gurney energy,  $E_g$ , and this value, characteristic of each explosive, is determined experimentally usually by measuring the wall velocities in a cylinder test. The Gurney equation appears to work because, as shown previously<sup>2</sup> for volume expansions between 2 and 10, the relative volume of the detonation products in the cylinder can be simply related to the expansion of the cylinder and this relation is not sensitive to a particular explosive. Thus, one is able to obtain the relative energy delivered by explosives simply by comparing the square of cylinder wall velocities at the same expansion.

The main purposes of this report are as follows, (1) to express, within the usual Gurney approximations, the Gurney energy as a function of the cylinder expansion in terms of the JWL equation of state, and (2) to suggest, ultimately how the JWL parameters may be evaluated directly and simply from the Gurney equation approximations without the use of complex hydrocode computations. The discussions here deal only with the Cylinder Test, in which initiation of detonation is in a plane normal to the cylinder axis at one end of the charge. The Gurney analysis, of course, has also been applied to many other geometries.<sup>5</sup>

## MODEL

### Gurney Formula

The derivation of the Gurney formula<sup>3,6</sup> and a number of subsequent papers<sup>5-8</sup> on the subject have appeared in print. The derivation is summarized here for purposes of illustration. For a cylindrical system of unit axial length

and with explosive mass to metal mass,  $C/M$ , consider a cross section where the flow is entirely radial and confined to this section, so that the continuity equation can be written as

$$\partial \rho / \partial t + \rho \partial v / \partial r + v \partial \rho / \partial r + \rho v / r = 0, \quad (1)$$

where  $\rho$  is the density,  $t$  is the time,  $r$  is the radial position, and  $v$  is the radial velocity. With the assumption that gas density after detonation is uniform at any fixed time, Equation (1) can be rewritten as,

$$\partial v / \partial r + vr = -d(\ln \rho) / dt, \quad (2)$$

by letting  $\rho = \rho(t)$  and  $\partial \rho / \partial r = 0$ .

At a fixed time Equation (2) is linear with respect to  $v$  and since  $v = 0$  at  $r = 0$ , it has the solution

$$v = v(r/R), \quad (3)$$

where  $R$  is the inside radius of the cylinder with velocity  $v$ . The total energy of the system,  $E_T$ , where the metal energy is all kinetic when acceleration is complete, is

$$E_T = E_m + E_{gk} + E_{gi}, \quad (4)$$

where  $E_m$  is the kinetic energy of the metal,  $E_{gk}$  is the kinetic energy of the gas, and  $E_{gi}$  is the internal energy of the gas, all expressed as per gram of explosive. It was shown that both

$$E_{gk} = v^2/4, \quad (5)$$

$$\text{and} \quad E_m = 0.5(M/C)v^2 \quad (6)$$

can be derived from the uniform density assumption which implies that

$$m = (r^2/R^2) \text{ and } dm = (2r/R^2)dr, \quad (7)$$

the kinetic energy expression

$$E_{gk} = 1/2 \int_0^1 v^2 dm, \quad (8)$$

and Equation (3) with  $m$  being the mass between the origin and radius  $r$ , per gram of explosive. Now by combining Equations (5)

and (6), the familiar Gurney expression may be written

$$v = \{2(E_{gk} + E_m)\}^{1/2} \left( \frac{C/M}{1 + 0.5(C/M)} \right)^{1/2}, \quad (9)$$

which is more commonly expressed as

$$v = G \left( \frac{C/M}{1 + 0.5(C/M)} \right)^{1/2}, \quad (10)$$

where  $v$  is the fragment velocity and  $G$  is called the Gurney constant which is equal to the square root of twice the Gurney energy,  $\sqrt{2E_g}$ . From Equations (5) and (6), we obtain  $E_{gk} = 0.5C/M(E_m)$  and from Equation (1)

$$E_{gk} = \frac{0.5 C/M}{1 + 0.5 C/M} \frac{G^2}{2}, \quad (11)$$

The Gurney formula may be written in the more general form,

$$v = G[(M/C + A)]^{-1/2}. \quad (12)$$

It is now well known<sup>8</sup> that the quantity  $G$  is not constant, but varies with  $C/M$ . Jacobs<sup>7</sup> found, from a detailed analysis of cylinder test data, that better results are obtained by replacing the constant 0.5 with 0.3 for steel cylinders, and with 0.2 for aluminum cylinders. In addition, it is clear that the Gurney formula does not treat the explosive at the Chapman-Jouget state where the density of the explosive is compressed to about 4/3 its initial density. The assumptions that the mass and total energy in a cylindrical section remain constant while the cylinder expands, and that the gas density at any time is uniform over the entire cross section, does not account for the effects of  $C/M$  varying from small values of 0.1 to large values 4 on  $G$ , nor does it take into account effects of axial expansion on the total energy.

Defourneaux<sup>9</sup> generalized the Gurney formula,

$$v^2 = (2E_g) [M/C + n/(n+2)]^{-1} \quad (13)$$

for plane parallel motion ( $n=1$ ), axially symmetric or cylindrical motion ( $n=2$ ) and for point symmetric or spherical motion ( $n=3$ ). Jacobs<sup>7</sup> pointed out that the assumptions inherent in the Gurney assumptions imply that a uniform pressure also exists in the gas products at any instant during the case expansion due to uniform gas density. Similarly, by neglecting changes in gas composition, its entropy is considered to be constant. Thus, the gas internal energy and pressure will be only a function of volume. As a consequence, the Gurney energy can be defined as a function of case expansion,

$$E_g = E_0 - E(v), \quad (14)$$

where  $E_0$  is the initial energy per unit mass in the gas products and  $E(v)$  is the internal energy retained after expansion to specific volume  $v$ . Other investigators<sup>7,9</sup> related the case displacement to the relative specific volume,  $V = v/v_0$ , in the model by the relation,  $R^n = V$ , where  $R$  is the relative radial expansion distance ( $r/r_0$ ) from the origin to the gas/case interface; and, then, calculated the Gurney energy using a polytropic gas equation of state to obtain

$$E_g(r) = E_0 \{1 - R^{-n(\gamma-1)}\}. \quad (15)$$

This equation, however, does not reproduce the experimentally determined Gurney energy because the polytropic gas relations do not work satisfactorily for explosive gas expansion of  $V > 2$  and because the approximation used for expressing the volume of expansion to the radial expansion, also, is not satisfactory. There are several modifications that can be made to Equation (15) that perhaps can greatly improve the use of the Gurney formula to describe the relative performance of explosives used in the cylinder test. These will be described in the next section.

### Gurney Energy/JWL EOS

In this section, the Gurney energy will be expressed in terms of the JWL expression for energy at constant entropy,  $E_s$ . The resulting modified Gurney formula, then, will be applied

to the experimental results from cylinder tests that have been performed on several explosives with known JWL EOS parameters. The effects of varying C/M and expansion volume will be investigated for the model.

Wilkins<sup>10</sup> investigated the behavior of the detonation products in the cylinder test with two-dimensional hydrodynamic calculations. The results showed that the detonation products expand essentially along the CJ isentrope. He also calculated the relationship between the relative volume of the detonation products and the radial expansion of the cylinder (reproduced in Figure 1). This calculation was shown to be insensitive to the explosive used. The approximation,  $R^2 = V$ , used to derive Equation (15) is also shown in Figure 1. We have, with the reported results for  $(r-r_0)$  vs.  $V$ , fit the data to a second order polynomial to obtain the two-dimensional hydrocode relative volume as a function of case expansion. The result is

$$V = 1.0146 + 0.19174(r-r_0) + 0.006178(r-r_0)^2, \quad (16)$$

where  $(r-r_0)$ , expressed in mm units here, represents the observed radial expansion for a one inch cylinder.

In place of using the polytropic gas relations to express the Gurney energy, since they do not accurately describe an explosive gas expansion at  $V > 2$ , we use the JWL relation for energy at constant entropy. Equation (15) can then be rewritten as

$$E_g(V) = E_s(V=1) - \left( \frac{A}{R1} e^{-VR_1} + \frac{B}{R2} e^{-VR_2} + \frac{C}{\omega V^\omega} \right) \quad (17)$$

for  $V > 1$ , where  $E_s(V=1)$  (which corresponds to  $E_0$  in Equation (14)) is the internal energy in the gas available for release after expanding from the  $V_{CJ}$  point to where the case appears to first expand;  $V=1$ , evaluated by the JWL relation for energy. The terms in the parenthesis are  $E_g$  (JWL) and the constants, A,

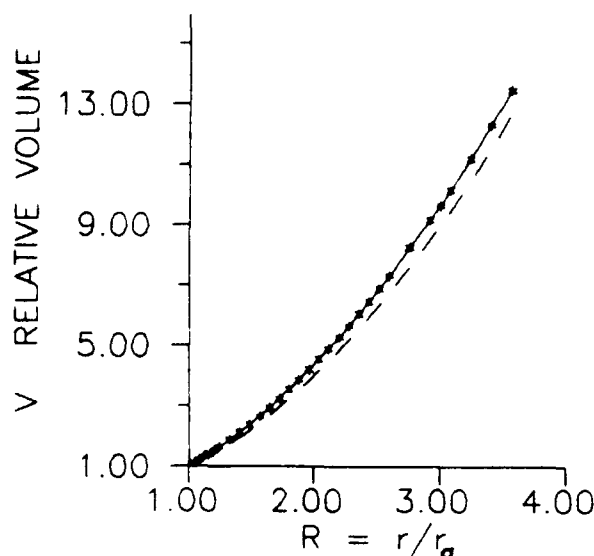


Figure 1. Relative Volume of Detonation Products as a Function of Relative Cylinder Expansion. Solid line (two-dimensional result); dashed line ( $R^2 = V$  approximation).

B, C,  $R_1$ ,  $R_2$  and  $\omega$  are the adjustable parameters of the JWL relations. The Gurney energy,  $E_g(V)$ , in Equation (17) can then be written as a function of volume expansion, then is

$$E_g(V) = E_{gk}(V) + E_M(V). \quad (18)$$

We now test the model using the reported cylinder test results<sup>1</sup> on ten explosives for which the JWL EOS parameters have been evaluated. If we insert Equations (17) and (18) into Equation (9) and rearrange the terms, we obtain

$$\frac{v}{\sqrt{2E_g(V)}} = (M/C + 1/2)^{-1/2}, \quad (19)$$

where  $v$  and  $E_g(V)$  are, respectively, the measured radial expansion velocity and the calculated Gurney energy using Equation (17) for  $V > 1$ . The case velocity as a function of volume was obtained from the measured velocity  $v(r-r_0)$  by Equation (16). In Figure 2, we plot the value of  $(M/C + 1/2)$  obtained from Equation (19) vs.  $V$  for the reported data of two explosives. The model predicts that straight lines should be obtained in the plot, where at

each value of  $V$ , the constant  $(M/C + 1/2)$  is obtained. The figure shows typical results for the ten explosives in the reported data.<sup>1</sup> The results show that for expansion volumes greater than 1.5 - 2.0, constants are obtained. They vary from the actual values of  $(M/C + 1/2)$  by a few percent at most, generally on the low side.

In Figure 3, we plot the results of this analysis for cylinder test data for PBX 9404 obtained from copper cylinder expansions using two different values of  $C/M$ ,  $\sim 0.4$  and  $\sim 2$ . Based upon these results, there does appear to be some dependency on  $C/M$  that is not taken into account by the Gurney formula, but it is not large. In addition, the results of References 1 and 7 show that the effect of increasing the yield strength of the chosen case metal (Cu, Al, steel) will cause the calculated  $(M/C + 1/2)$  to be 1 - 2 percent lower than actual values, since the Gurney formula does not take the case yield strength into account. However, the two-dimensional hydrocode calculations for the evaluated  $E_g(V)$  and  $R$  vs.  $V$  relationship that are used in our formulation for evaluating  $E_g(V)$ , can account for the case yield strength. This would, however, over complicate our rather simple approach by requiring that  $R$  vs.  $V$  be evaluated as a function of yield strength.

It appears clear that the use of the Gurney formulation with an appropriate EOS

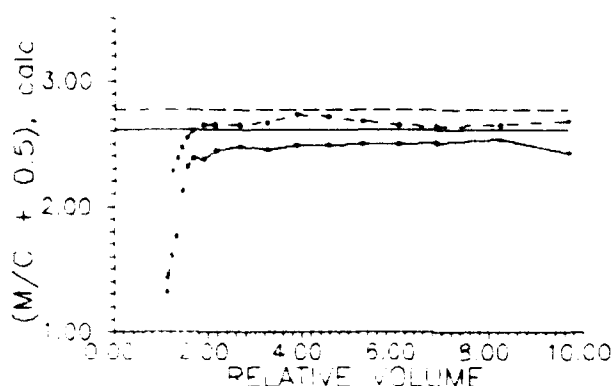


Figure 2 Comparison of the Predicted Value of  $(M/C + 1/2)$  Using Both Equation (19) and the Actual Value for (a) TNT (Solid Line) and (b) Cyclotol (Dashed Line) With  $C/M \sim 0.45$  From Cylinder Test Data

for the explosive and an appropriate relationship between volume of expansion and radial expansion does indeed describe the standard copper cylinder test (to within a 1 - 2 percent error). It also appears that the assumption of uniform entropy in the gas products behind the expanding case for  $V > 2$  is a surprisingly good approximation. Although effects of varying  $C/M$  and case yield can affect the calculated results, they are not as large as expected. We are now in a position to determine  $E_g(V)$  from cylinder test data and to relate it directly to  $E_s(V)$  from which the JWL EOS parameters for a test explosive can be approximated.

## EVALUATION OF JWL PARAMETERS

Generally, when using the Gurney formulation for analyzing cylinder test data, the velocity of the expanding case is measured at 5 mm and 19 mm radial expansion and the data is reported for comparative purposes. In this section, we show how the JWL EOS may be estimated directly from the measured wall velocities.

The Gurney energy is experimentally determined as a function of  $(r-r_0)$  from the measured wall velocity by using the following relationship

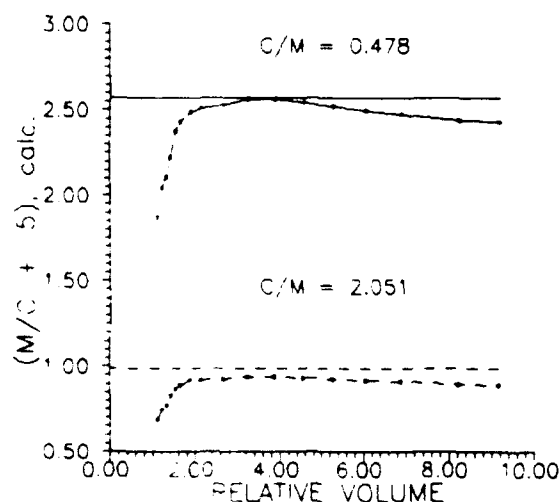


Figure 3 Comparison of the Results of Equation (19) for Cylinder Test Data From PBX 9404 Obtained From Experiments Using Thin Walled ( $C/M \sim 2$ ) and Standard Wall Thickness ( $C/M \sim 0.4$ ). The straight lines represent the actual  $(M/C + 1/2)$  values.



$$E_g = \frac{v^2}{2} (M/C + 0.5) \quad (20)$$

at each  $(r-r_0)$  measured data point. The values of  $(r-r_0)$  can be re-expressed as relative volume,  $V$ , with Equation (16). Now, by rewriting Equation (17) in terms of  $E_s$ , the internal energy of the expanding gases at constant entropy we obtain

$$E_s = E_s(V=1) - E_g(V) \quad (21)$$

for  $V > 1$ , where  $E_s$  is the experimental equation to be fit to obtain the JWL EOS parameters,

$$E_s = \frac{A}{R_1} e^{-VR_1} + \frac{B}{R^2} e^{-VR_2} + \frac{C}{\omega V^\omega} \quad (22)$$

The value for  $E_s$  at  $V=1$ , which is the total energy available for release by the expanding gases during the observations, can be estimated in different ways. It may be related to the heat of detonation,  $Q$ , that is found by using the gamma and polytropic gas relations,<sup>7</sup>

$$Q = \frac{P_{CJ}}{2(\gamma-1)} = \frac{\rho_0 D^2}{2(\gamma+1)(\gamma-1)}, \quad (23)$$

where  $Q$  (equal to  $E_s$  at  $V=1$ ) is the internal energy remaining in the gas after expanding from the CJ point with  $V_{CJ}$  and  $\rho_{CJ}$  to  $V=1$ , where  $\rho = \rho_0$ , the initial density, and  $\gamma$  is defined by  $\rho_{CJ}/\rho_0 = (\gamma+1)/\gamma$ . Also, for most of the explosives that have been examined by the JWL EOS computations,  $E_s$  at  $V=1$  is approximately equal to  $0.90 \pm 0.02$  of  $E_0$ , the total available energy in the explosive. The value of  $E_0$  is usually obtained from detonation calorimetry, or from RUBY or TIGER calculations.<sup>2</sup> For example, for Comp B where  $P_{CJ} = 286$  Kbar,  $D = 8$  mm/ $\mu$ sec,  $\gamma = 2.8$  and a measured value of  $E_0 = 0.085$  mbar cc/cc, we estimate by the two methods that  $E_s(V=1)$  equals 0.078 and 0.079.

Using the reported cylinder test data<sup>1</sup> for Comp B, we have evaluated  $E_s$  from Equation (21), using Equations (16) and (20) and  $E_s(V=1) = 0.078$ , as a function of relative volume of expansion. The results are shown in Figure 4. The curve was obtained by differentiating the reported  $(r-r_0)$  vs. time data with a cubic-spline algorithm. Also shown in

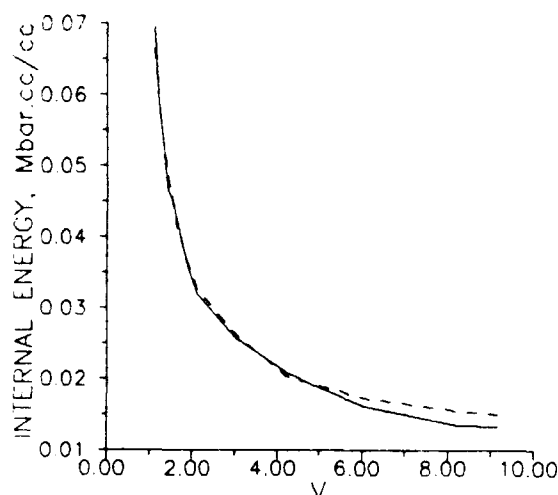


Figure 4. A Comparison for Comp B Where  $E_s$  is Obtained by the Gurney Formulation (Solid Line) and by the JWL EOS (Dashed Line)

this figure is the energy which is determined directly from the reported JWL parameters. This result is typical of the more than 15 explosives that we have thus far analyzed, where known JWL EOS parameters exist. These include: HMX, Nitromethane, PETN, TNT, Comp B, Cyclotol, PBX-9011, PBX-9404, LX-04-1, LX-07-0, PBXW-113, PBXW-114 and PBXW-115. The compositions of these explosives may be found in References 1 and 11. The values of  $E_s$  as evaluated using the Gurney formulation, generally compare quite favorably with those obtained from the two-dimensional hydrocode and JWL EOS calculation for volumes of expansion between  $V=1.5$  and  $V=7$ . The Gurney approximation, for reasons previously discussed, clearly is not useful for  $V < 1.5$ . The differences that are found for  $V > 8$  between the two techniques for obtaining  $E_s$  will be discussed later, but they are not so large as to prevent us from obtaining good estimates of JWL EOS parameters.

It is a rather simple task to fit the experimental  $E_s$  versus  $V$  curve to Equation (22) to obtain the estimated values for the JWL EOS parameters. For volumes greater than  $V=6$ , with less than 1 percent error,

$$E_s = \frac{C}{\omega V^\omega}, \quad (24)$$

therefore by choosing two points on this portion of the curve,  $C$  and  $\omega$  can be directly determined. For volumes greater than  $V=2.5$ , with less than a 3 percent error,

$$E_s = \frac{B}{R_2} e^{-VR_2} + \frac{C}{\omega V^\omega} \quad (25)$$

therefore, with any two points in the region of the curve where  $V=2$  to  $V=5$  and with the values of  $C$  and  $\omega$  evaluated from Equation (24), the parameters  $B$  and  $R_2$  may be determined. Unfortunately, due to the estimated error in the data to obtain the  $E_s$  curve, a large number of solutions can be found. We estimate that the  $x,t$  data, which was differentiated to obtain velocity, results in an error of  $\pm 1$  percent and that the energies  $E_2$  (proportional to the square of the velocity) have an error of at least  $\pm 2$  percent. It is, however, known<sup>1,2</sup> that  $\omega$  should have a value in the range of 0.2 to 0.4 and that  $R_2 \sim 1$ . Therefore, the parameters are adjusted until these conditions are met and the calculated curve for this volume region lie within the error limits of the experimental  $E_s$  curve. This is easily carried out. It was found that a small change in slope for the observed line results in large changes in these four parameters. For Comp B we used

$$R_2 = 1.29784 \text{ (1.1)}$$

$$B = 0.18898 \text{ (0.90235)}$$

$$\omega = 0.31629 \text{ (0.34)}$$

$$C = 0.01151 \text{ (0.010818)}$$

where the values in the parenthesis are the reported values<sup>1</sup> from a two-dimensional hydrocode analysis. To solve for the remaining two parameters,  $R_1$  and  $A$ , two additional experimental values are required; the detonation velocity,  $D$ , and detonation pressure,  $P_{CJ}$ . Both of these quantities, along with  $E_s$ , can be written in terms of the JWL EOS,<sup>1</sup>

$$P_s = Ae^{-VR_1} + Be^{-VR_2} + \frac{C}{V^{\omega+1}}, \quad (26)$$

$$\rho_0 D^2 = AR_1 e^{-VR_1} + BR_2 e^{-VR_2} + \frac{C(\omega+1)}{V^{\omega+2}}, \quad (27)$$

$$\text{and } E_s = \frac{A}{R_1} e^{-VR_1} + \frac{B}{R_2} e^{-VR_2} + \frac{C}{\omega V^\omega} \quad (28)$$

These equations are solved for  $A$  and  $R_1$  with the known values of  $P_{CJ}$ ,  $D$ ,  $\rho_0$ ,  $V$  and the previously determined four parameters. The experimental value for detonation velocity is usually measured and  $P_{CJ}$  may or may not be. If it is, then gamma may be determined from  $P_{CJ} = \rho_0 D^2 / (\gamma + 1)$  and  $V_{CJ}$  may be estimated from  $V_{CJ} = \gamma / (\gamma + 1)$ . Often, when  $P_{CJ}$  is not known, then  $\gamma$  is estimated to be between 2.7 and 2.9 and  $P_{CJ}$  and  $\gamma$  are determined from the above relations. For Comp B, we use  $P_{CJ} = 286$  Kbar,  $D = 8$  mm/ $\mu$ sec,  $\rho_0 = 1.7$  g/cc and  $\gamma = 2.8$  and we obtain from Equations (26) and (27)

$$A = 6.4715 \text{ (5.24229)},$$

$$R_1 = 4.7322 \text{ (4.2)},$$

where the values in the parenthesis are the reported JWL EOS parameters.<sup>1</sup>

In Figure 5, the calculated pressure adiabats are shown comparing the results for parameters determined from the Gurney analysis for  $E_s$  with the results for the parameters determined by the two-dimensional hydrocode

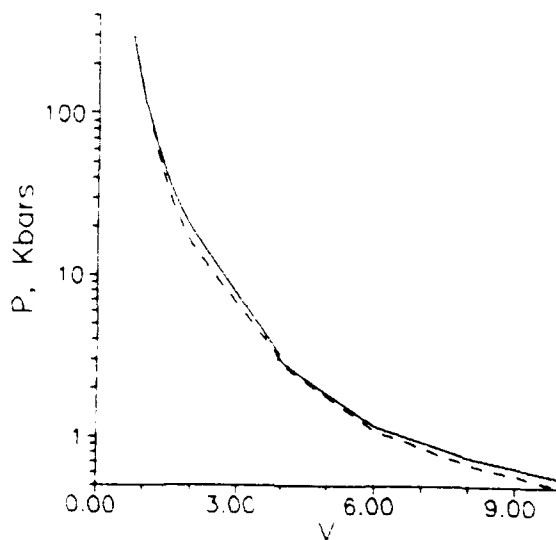


Figure 5. Comparison of Calculated Adiabats for Comp B Using JWL Parameters Determined From the Gurney Energy Analysis (Solid Line) and From the Two-Dimensional Hydrocode Analysis (Dashed Line)

analysis. Notice that now the calculated pressures for both sets of parameters are in excellent agreement for  $V < 2$ . This results from using similar CJ pressure and velocity data. The results, however, at larger values of expansion,  $V > 6$  begin to diverge. The reason for this is that the values of  $C$  and  $\omega$  that we chose for Equation (24) are extremely sensitive to the slope of  $E_s$  at  $V > 6$ . An approximate 1/2 percent deviation in the slope in this region of the  $E_s$  curve can alter the values of  $C$  and  $\omega$  such that a 5 fold difference in the calculated  $P$  at  $V = 10$  can easily occur. We must point out that the same reasoning applies to the analysis for  $\omega$  and  $C$  by the hydrocode computations and that the differences in the two adiabats at  $V > 6$  are most likely a consequence of the curve fitting procedure.

In conclusion, we have demonstrated a methodology by which the JWL EOS parameters may be extracted directly from cylinder test data, without the use of extensive two-dimensional hydrocode computations. The results indicate that the EOS's obtained are sufficient enough to make engineering calculations for explosive applications of the test explosive, but are not useful for equation of state studies. The results show that for gas expansions  $V > 2$ , the approximations which are built into the Gurney formula derivation are more than adequate to reproduce the hydrocode results to within acceptable errors for many applications.

## ACKNOWLEDGEMENT

The authors would like to thank Dr. James M. Short of the Naval Surface Warfare Center for use of NSWC's 50 pound bombproof Explosive Research Facility to perform cylinder tests and the necessary computations for this report. The authors would like to acknowledge the support of the Insensitive Munitions Advanced Development (IMAD) Program.

## REFERENCES

1. Lee, E. L.; Hornig, H. C.; and Kury, J. W., *Adiabatic Expansion of High Explosive Detonation Products*, Lawrence Radiation Laboratory Report UCRL-50422, Livermore, CA, 1968.
2. Kury, J. W.; Hornig, H. C.; Lee, E. L.; McDonnell, J. L.; Ornellas, D. L.; Finger, M.; Strange, F. M.; and Wilkins, M. L., "Metal Acceleration by Chemical Explosives," *Proceedings of the Fourth Symposium on Detonation*, Naval Ordnance Laboratory, White Oak, Silver Spring, MD, 12 Oct 1965, pp. 3-12.
3. Gurney, R. W., *The Initial Velocity of Fragments From Bombs, Shells and Grenades*, BRL Report No. 405, Sep 1943.
4. Gurney, R. W., *The Initial Velocity of Fragments From Bombs, Shells and Grenades*, BRL Report No. 635, Mar 1947.
5. Kennedy, D. R., "The Elusive  $\sqrt{2E}$ ," Presented at 21st Annual Bomb and Warhead Section Meeting, Am. Ordnance Assn., Picatinny Arsenal, 22 Apr 1969.
6. Sternberg, H. M., Unpublished Report Entitled, "Analysis of the Gurney Formulas for Cylindrical Systems," 1983, Naval Surface Weapons Center, Silver Spring, MD.
7. Jacobs, S. J., *The Gurney Formula: Variations on a Theme by Lagrange*, NOLTR 74-86, 21 Jun 1974, Naval Ordnance Laboratory, White Oak, Silver Spring, MD.
8. Kennedy, J. E., *Gurney Energy of Explosives: Estimation of the Velocity and Impulse Imparted to Driven Metal*, Research Report SC-RR-70-790, Dec 1970, Sandia Laboratories, Albuquerque, NM.
9. Defourneaux, M., "Transport of Energy in Combustion and Detonation with Confinement," *Astronautica Acta*, Vol. 17, 1972, p. 609.
10. Wilkins, M. L., *Calculation of Elastic-Plastic Flow*, UCRL-7322, 1963, Lawrence Radiation Laboratory, Livermore, CA.
11. Hall, T. N. and Holden, J. R., *Explosion Effects and Properties---Part III. Properties of Explosives and Explosive Compositions*, NSWC MP 88-116, Oct 1988, NSWC White Oak, Silver Spring, MD.

# STUDIES ABOUT THE EQUATIONS OF STATE OF THE DETONATION PRODUCTS

N. Carion, J. Aveille, P. Andriot, F. Chaisse, G. Guri, M. T. Kerihuel, and M. Leroy  
Commissariat à l'Energie Atomique  
Centre d'Etudes de Vaujours-Moronvilliers  
77181 Courtry, FRANCE

*The aim of this paper is to present the adjustment of two types of Equations of State (E.O.S.), Wilkins and Virial, on the basis of several kinds of experimental data concerning a T.A.T.B. composition.*

*When introduced in hydrodynamic computer codes the Wilkins type E.O.S. allow the simulation of several ballistic experiments with a good agreement. The Virial type E.O.S., here, is just compared to experimental data concerning the classical release isentrope issued from the Chapman-Jouget (C-J) state.*

## INTRODUCTION

The interaction of detonation waves with surrounding media is based on the explosive decomposition products expansion. The numerical simulation of such phenomena requires well adapted equations of state (E.O.S.) for the detonation products.

This determination can be performed in a theoretical way (see, for example, References 1-2), but experimental methods giving access to the parameters of these equations of state are of great interest.

In the following paper, we present complementary experimental methods which we use to determine the detonation products E.O.S. of high heterogeneous explosives. These equations are of the Wilkins-type.

With these equations of state we are able to perform the numerical simulation of several detonation/dense material interactions with a good agreement between the computational and experimental results.

The experimental methods include:

- a) The impedance matching method<sup>3</sup> (in good agreement with Doppler Laser Interferometry (DLI) measurements) in association with a first

determination of the coefficients of a Wilkins-type E.O.S.

- b) The slight modification of these coefficients to get a good agreement between measurements and numerical simulations for ballistic experiments.
- c) The validation of the E.O.S. by the numerical simulation of the following experiments:
  - cylinder expansion test,
  - the release and recompression of detonation products,
  - oblique interactions of detonation waves with dense materials.

The examples given below deal with a TATB-based heterogeneous explosive (composition T<sub>2</sub>).

On the other hand the study of chemical rates in combustion processes usually needs the knowledge of temperature T. In this case, classical E.O.S. {p(e,v)} correlating pressure to internal energy and specific volume are not well adapted. Therefore we have developed a Virial E.O.S. for detonation products which introduces a temperature scale from a theoretical point of view.<sup>2</sup>

The following hypotheses are made:

- (i) We suppose the homogeneousness of detonation products constituted by just one kind of spherical particle.
- (ii) The E.O.S. is of Virial-type set-up with a Lennard-Jones potential (6-12).

Previously, this potential has been widely used for calculation of the properties of matter in different states and the Virial coefficients, for this important model, are known in reduced form<sup>4,6</sup> up to fifth order. Of course, the two-dimensional parameters of these coefficients remain unknown.

Presently, according to the disposal of experimental results and to the fundamental impact of the C-J state properties, we prescribe the Virial E.O.S. to settle:

- ① The C-J state properties, and
- ② The experimental data associated with flow properties of detonation products along the shock and rarefaction loci originating at the C-J point in the pressure ( $p$ ) - mass velocity ( $u$ ) diagram.

The whole information concerning the detonation products properties requires a determination of the unknown parameters of the E.O.S. A numerical and specific process has been expanded, allowing the association of the parameter values to conditions ① and ② for a given high explosive (composition  $T_2$ ).<sup>2</sup>

## WILKINS-TYPE E.O.S.

### The Impedance Matching Method<sup>3</sup>

This experimental method consists in the analysis of the frontal interaction of detonation waves with several reference materials (metals, water, argon at several pressures). The velocity of the shock waves transmitted to these well known materials is measured. These measurements are completed using a streak camera. High impedance materials give access to the detonation products recompression Hugoniot starting from the Chapman Jouguet state.

Low impedance reference materials provide a determination of the release isentrope issued from the C-J state. Then, we determine the coefficients of a Wilkins, Mark (W.M.) E.O.S. type in order to fit these experimental results, and we obtain a first form of the detonation products E.O.S.

Another kind of release experiment using DLI measurements gives results in good agreement with the described matching impedance method as it can be seen in Figure 1.

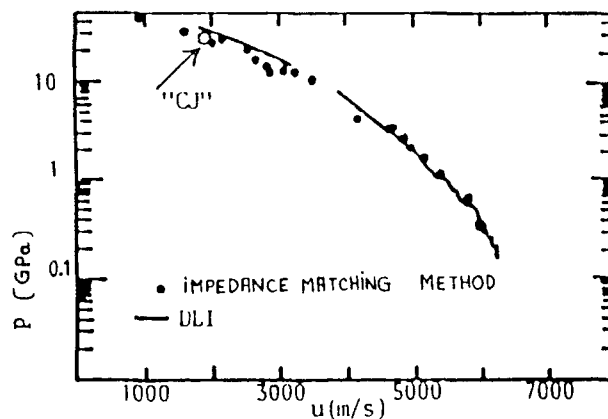


Figure 1. Comparison Between Experimental Results Issued From the Impedance Matching Method and the DLI Measurements

### Ballistic Experiments

In these experiments, the velocity of a copper plate is measured with the DLI technique as it is accelerated by the detonation of  $T_2$  composition in slab geometry.

To get a good agreement between these experimental results and numerical simulations performed with a one-dimensional hydrodynamic code, a slight modification of the coefficients of the E.O.S. previously determined is needed. This modification provides a second form of the W.M. equation still compatible with the experimental release isentrope.

### Validation

The so determined E.O.S. is validated by means of comparisons between experiments and numerical simulations of different types of

interactions between detonation products and surrounding media:

- Oblique interaction between a detonation wave and a dense material (this case is detailed in another paper submitted to the 9th Symposium Selection Committee (see Reference 7).
- Cylinder test.
- Projection of a copper plate by the detonation products partially released.

### Cylinder Tests

The material expanded by the mechanical work of the detonation products is copper.

Front waves shapes and global radial expansion measurements are performed with a streak camera while the first accelerations are measured using the DLI technique.

We use a two-dimensional hydrodynamic code to simulate this experiment. The detonation is computed using the TCD decomposition kinetic<sup>8</sup> taking into account a finite reaction zone associated with a Von Neumann-type scheme.

The elastic-plastic behavior of the copper is simulated using the Steinberg, Cochran and Guinan model.<sup>9</sup>

The calculations agree well with the experimental results (see Figure 2).

### Release and Recompression of Detonation Products

In these experiments the decomposition products are released in a vacuum delimited by

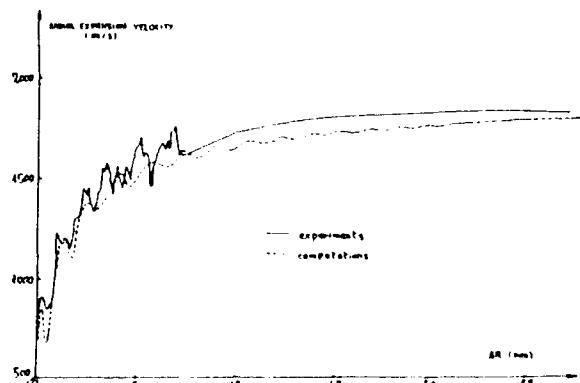


Figure 2 Cylinder Test Comparison between experiments and numerical simulations.

the detonating explosive and a metallic plate. The decomposition products are shock recompressed when they interact with the plate which is projected.

The velocity of the plate is measured using the DLI method.

The size of the vacuum  $\ell$  determines the magnitude of the release before recompression. For example, with a pressure of 20 mm Hg, the products are released down to about 1 GPa.

Numerical simulations are performed using a one-dimensional hydrodynamic code with a simulation of the elastic-plastic behavior of the plate.

On more time, the agreement between calculations and experiments confirms the validity of the determined E.O.S. (see Figure 3).

### VIRIAL-TYPE E.O.S.

Up to fifth order, the starting equations are:

$$P = \frac{N \cdot T}{v} \left[ 1 + \sum_{i=1}^4 \left( \frac{b_0}{v} \right)^i B_i (T/T_0) \right] \quad (1)$$

$$e = T \cdot \left[ C_0 - N \cdot T \cdot \left( \sum_{i=1}^4 \frac{1}{i} \left( \frac{b_0}{v} \right)^i \frac{dB_i}{dT} \right) \right]$$

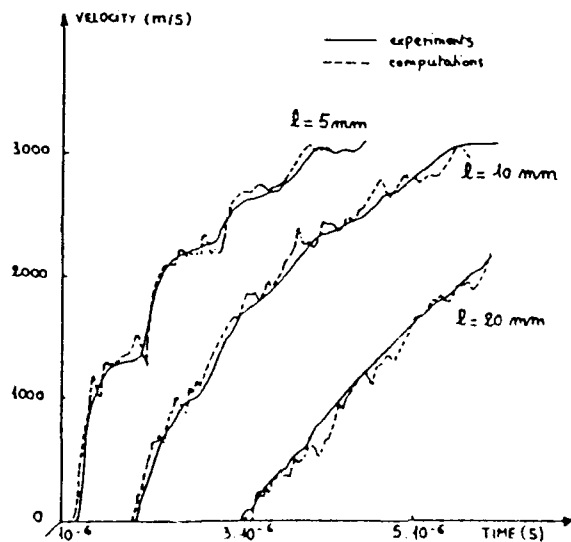


Figure 3 Release and Recompression of the Detonation Products. Comparison between experiments and numerical simulations.

where  $B_i$  are the reduced virial coefficients and  $N$ ,  $C_0$ ,  $b_0$ , and  $T_0$  are four unknown parameters. When Lennard-Jones (L.J.) (6-12) potential is written as:<sup>4</sup>

$$\phi(r) = 4\epsilon \cdot \left[ \left( \frac{\sigma}{r} \right)^{12} - \left( \frac{\sigma}{r} \right)^6 \right]$$

( $r$ : distance between particles)

the  $b_0$  and  $T_0$  coefficients are connected to  $\sigma$  and  $\epsilon$  by:

$$b_0 = \frac{2}{3} \pi \cdot \sigma^3 \cdot \frac{N}{k}$$

$$T_0 = \epsilon/k$$

( $k$ : Boltzmann constant)

The number of parameters is then reduced to 3 by use of:

$$y = T/T_0$$

$$x = b_0/v$$

According to that way Equation (1) is written:

$$\begin{aligned} p &= \frac{E_N}{b_0} \cdot x \cdot y \cdot H_1(x, y) \\ e &= y \left[ E_c - E_N \cdot H_2(x, y) \right] \end{aligned} \quad (2)$$

where  $E_N = N \cdot T_0$ ;  $E_c = C_0 \cdot T_0$ ; and  $H_1$  and  $H_2$  are two functions easily set up versus  $B_i$  and

$$\frac{dB_i}{dT}$$

The Virial E.O.S. (2) holds now only three unknown parameters:  $E_N$ ,  $E_c$ ,  $b_0$ .

For a given explosive, we have to associate the values of these parameters to conditions ① and ②. We introduce then the following notations:

$$\gamma \text{ (polytropic coefficient)} = - \left( \frac{\partial \log P}{\partial \log v} \right)_s$$

$$G \text{ (Grüneisen coefficient)} = - \left( \frac{\partial \log T}{\partial \log v} \right)_s$$

( $s$  is the entropy) and summarize the two main stages needed for their determination.

### Condition ①

Calling respectively  $D^*$  and  $u^*$  detonation and particle velocity, we use the following equation at C-J state:<sup>10</sup> [ $(^*)$  stands for values at C-J state and  $(o)$  for initial conditions].

### Jump conditions:

$$\frac{p^* - p_o}{v_o - v^*} = \left( \frac{D^*}{v_o} \right)^2 \quad (3)$$

$$e^* - e_o = \frac{1}{2} (p^* + p_o)(v_o - v^*) \quad (4)$$

$$u^* = D^* \cdot \left( 1 - \frac{v^*}{v_o} \right) \quad (5)$$

### C-J condition:

$$\left( \frac{\partial p}{\partial v} \right)_s^* = - \left( \frac{D^*}{v_o} \right)^2 \quad (6)$$

### Stanyukovich-Manson condition:

$$\left( \frac{\partial \log D^*}{\partial \log v_o} \right)_{e_o} = - \frac{\gamma^* (\gamma^* - G^* - 1)}{2 \gamma^* - G^*} \quad (7)$$

### Thermodynamical relations:

$$p^* = p(v^*, y^*, E_N, b_0) \quad (8)$$

$$e^* = e(v^*, y^*, E_N, E_c, b_0) \quad (9)$$

$$\gamma^* = \gamma(v^*, y^*, E_N, E_c, b_0) \quad (10)$$

$$G^* = G(v^*, y^*, E_N, E_c, b_0) \quad (11)$$

The C-J state physical values and the E.O.S. parameters are obtained by solving the above 9 equations where 15 quantities are introduced:

$$p_o, v_o, D^*, \left( \frac{\partial \log D^*}{\partial \log v_o} \right)_{e_o}, p^*, v^*, y^*,$$

$$e^*, e_0, u^*, v^*, G^*, E_N, E_c, b_0.$$

This can be done if we settle a set of six quantities as parameters. We have chosen two practicabilities well adapted to the jump and initial conditions:

$$- p_0, v_0, D^*, \left( \frac{\partial \text{Log } D^*}{\partial \text{Log } v_0} \right)_{e_0}, p^*, e_0$$

or

$$- p_0, v_0, D^*, G^*, p^*, e_0.$$

A specific algorithm has been developed for the solving of these nine equations [(3) - (11)].<sup>2</sup>

We get, by this way, all the other quantities versus those adopted in each set.

### Condition ③

We have to find now the right values for the set of six quantities assuming condition ②.

After the above procedure, a theoretical  $p_T(u)$  curve may be built numerically using the classical equations governing the shock and rarefaction waves originated at the C-J point ( $p^*, u^*$ ). The  $p_T(u)$  curve is compared to the  $N_p$  experimental data ( $p_i, u_i$ ). In that purpose we fix

$$p_0, v_0, D^*, \left| \frac{\partial \text{Log } D^*}{\partial \text{Log } v_0} \right|_{e_0},$$

or ( $p_0, v_0, D^*$ ) values and we look for the just quantities ( $p^*, e_0$ ) or ( $G^*, p^*, e_0$ ) of each set by minimizing the function:

$$Z(p^*, e_0)$$

$$\text{or} \quad = \frac{v_0^2}{D^{*4} \cdot N_p} \cdot \sum_{j=1}^{N_p} |p_T(u_i) - p_i(u_i)|^2$$

$$Z(G^*, p^*, e_0)$$

with a procedure based on the Nelder and Mead algorithm.<sup>5</sup>

The two algorithms are included in a numerical code which was applied to several high explosives to get the coefficients of the Virial E.O.S. for detonation products.<sup>2</sup>

### Numerical Data

A fitting of the ( $p_i, u_i$ ) experimental data is finally obtained by a  $p_T(u)$  curve with a relative uncertainty in pressure less than 10 percent in the interval  $450 \cdot 10^8 \text{ Pa} > p > 3 \cdot 10^8 \text{ Pa}$  (Figure 4). We present as an example the following results got on a TATB composition [ $T_2$ ]:<sup>3</sup>

#### Initial conditions:

$$p_0 = 10^5 \text{ Pa}$$

$$\rho_0 = \left( \frac{1}{v_0} \right) = 1855 \text{ kg} \cdot \text{m}^{-3}$$

$$D^* = 7685 \text{ m} \cdot \text{s}^{-1}$$

#### Optimized quantities:

$$p^* = 270.27 \cdot 10^8 \text{ Pa}$$

$$e_0 = 3.28 \text{ MJ} \cdot \text{kg}^{-1}$$

$$G^* = 0.884$$

$$\rho^* = \left( \frac{1^*}{v} \right) = 2462.5 \text{ kg} \cdot \text{m}^{-3}$$

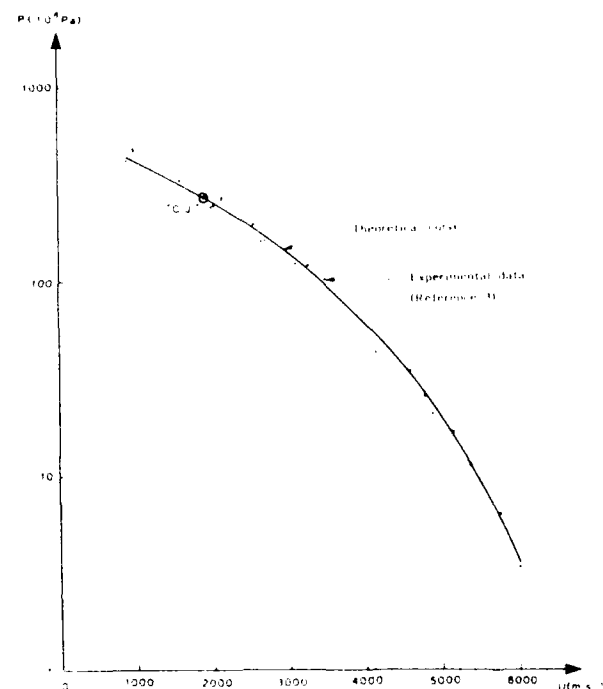


Figure 4. Pressure Versus Mass Velocity Along Shock and Rarefaction Loci Originating at the CJ Point for  $T_2$  Composition



$$e^* = 5.07 \text{ MJ.kg}^{-1}$$

$$u^* = 1895.88 \text{ m.s}^{-1}$$

$$\gamma^* = 3.053$$

$$\left( \frac{\partial \log D^*}{\partial \log v_0} \right)_{v_0} = -0.679$$

#### Parameters of Virial E.O.S.:

$$y^* = 121.24$$

$$b_0 = 0.1794 \cdot 10^{-2} \text{ m}^3 \cdot \text{kg}^{-1}$$

$$E_N = 11391.06 \text{ J.kg}^{-1}$$

$$E_c = 19316.05 \text{ J.kg}^{-1}$$

The values obtained for the E.O.S. parameters were also analyzed using some results of the WCA4 E.O.S. related to  $T_2$  composition.<sup>12</sup> We get:

$$T_0 = 39.06 \text{ K}$$

$$T^* = 4705 \text{ K}$$

$$\sigma = 3.394 \cdot 10^{-10} \text{ m}$$

$$G(v \rightarrow \infty, T) = 0.580$$

which may be considered as acceptable values in the framework of our analysis.

## REFERENCES

1. Chirat, R. and Baute, J., "An Extensive Application of WCA4 E.O.S. for Explosives," *Proceedings of the Eighth Symposium (International) on Detonation*, Albuquerque, 1985.
2. Chaisse, F.; Carion, N.; and Guri, G., "Application de la théorie du Viriel à la détermination d'une équation d'état des produits de détonation d'une substance explosive," *Sciences et Technique de l'Armement*, Vol. 62, 2ème FASC., 1988, p. 371.
3. Pinegre, M.; Aveille, J.; Leroy, M.; Protat, J. C.; and Cheret, R., "Expansion

Isentropes of TATB Compositions Released into Argon," *Proceedings of the Eighth Symposium (International) on Detonation*, Albuquerque, 1985.

4. Hirschfelder, J. O. and Curtis, C. F., *Molecular theory of gases and liquids*, J. Wiley, 1954.
5. Barker, J. A. and Monaghan, J. J., *J. Chem. Phys.*, Vol. 36, 1962, p. 2564.
6. Barker, J. A.; Leonard, J. P.; and Pompe, A., *J. Chem. Phys.*, Vol. 44, 1966, p. 4206.
7. Aveille, J.; Carion, N.; Vacellier, J.; and Plotard, J. P., "Experimental and Numerical Study of the Oblique Interaction Between a Detonation Wave and a Dense Material," (submitted to the Ninth Symposium Selection Committee).
8. Donguy, P. and Legrand, N., "Numerical Simulations of Non-Ideal Detonations of Heterogeneous Explosive with the Two-Dimensional Eulerian Code CEE," *Seventh Symposium (International) on Detonation*, Annapolis, 1981.
9. Steinberg, D. J.; Cochran, S. G.; and Guinan, N.W., *J.A.P.*, Vol. 51 (3), 1980, p. 1490.
10. Fickett, W. and Davis, W. C., *Detonation*, Los Alamos series, 1979.
11. Lootsma, F. A., *Numerical Methods for Non Linear Optimization*, Academic Press, 1972, p. 115.
12. Chirat, A. and Baute, J., Private communication, 1986.

## DISCUSSION

B. D. LAMBOURN, AWE (A)  
Aldermaston, Reading, England, UK

Is there any experimental situation where you have observed a significant difference between the modified Wilkins and Virial form of E.O.S.?

## REPLY BY AUTHORS

We have not studied experimental situations far from C-J state to observe a significant difference between the two E.O.S.

## DISCUSSION

GERALD I. KERLEY, Sandia  
National Laboratories  
Div. 1533, Albuquerque, NM

1. Would you get better agreement with the cylinder test data by adding another term to the Wilkins EOS?

2. How does your 5-term Virial EOS differ from that of Wu Xiong, et al. (Session II-C, Thursday)?

2. Starting from theoretical considerations, the reduced Virial coefficients are known up to fifth order for the Lennard-Jones potential (6-12); so we have used specific analytic form for each of them.<sup>2</sup> On the other hand, in the Wu Xiong studies, these coefficients are supposed to be similar to each other and the higher Virial coefficients are obtained from the second one.

## REPLY BY AUTHORS

1. We have not tested this solution from a numerical point of view.

# SENSITIVITIES OF ADIABATIC AND GRUNEISEN GAMMAS TO ERRORS IN MOLECULAR PROPERTIES OF DETONATION PRODUCTS

W. Byers Brown

Department of Chemistry, University of Manchester  
Manchester M13 9PL, UNITED KINGDOM

and

Martin Braithwaite

Explosives Group Technical Centre, Imperial Chemical Industries PLC  
Stevenston Works, Ayrshire KA20 3LN, UNITED KINGDOM

*Our paper concerns three related aspects of equations of state for detonation products.*

*1. The development of a new ideal detonation code is reported with the following features: (i) a fast, sophisticated, and accurate analytical equation of state based on statistical mechanics and intermolecular potentials; (ii) a new fast method of calculating chemical and phase equilibrium; (iii) a modified treatment of polar species based on the Buckingham-Keesom potential, which gives good agreement with experimental shock temperatures.*

*2. A systematic method of determining the intermolecular parameters for single species from Hugoniot data is presented.*

*3. A sensitivity analysis to calculate the errors in the calculated properties of the detonation fluid due to errors in the intra- and intermolecular parameters is extended to cover the adiabatic and Gruneisen gammas. The results for changes in inter-species parameters are dramatic.*

## INTRODUCTION

Over the last decade there have been a number of attempts to provide fundamental equations of state (EOS) for detonation fluids<sup>1,2,3</sup> and associated computer programs<sup>1,4,5</sup> to calculate ideal detonation properties. These fundamental EOS based on statistical mechanics and intermolecular forces have to be capable of reproducing both experimental shock Hugoniot and static compression results for the individual product species as well as providing ideal detonation velocities, pressures, temperatures, energies, etc., for a wide range of explosives. Results of these predictions form, along with

corrections due to detononic non-ideality, the basis of explosives design for a wide variety of applications.

Since the pioneering work of Fickett<sup>6</sup> in developing an EOS based on the Lennard-Jones and Devonshire cell model, and the very successful Jacobs-Cowperthwaite-Zwisler EOS<sup>7</sup> which modified and extended this theory, fundamental EOS developments for fluid detonation products have been based on extensions to the more recent Hard-Sphere Perturbation Theories.<sup>8,9</sup> The increasing complexity of these EOS has meant that their use in the prediction of detonation performance has been at substantial cost in terms of the

computational resources required. However, the need for large main-frame computers has recently been largely overcome by generating analytic representations of the statistical mechanical EOS which give good agreement to high density with computer simulation data for realistic intermolecular potentials.<sup>10</sup> The other heavy computational aspect of detonation calculations is the determination of chemical equilibrium between the products. We believe that the calculation of chemical and phase equilibria in the high pressure multiphase systems that constitute detonation fume can be most effectively achieved by a recent development of the method of element potentials.<sup>13</sup> This development is based on a pre-calculated EOS for equilibrium among the chemical elements (Gibbsian EOS) from which the element potentials, and therefore the chemical potentials of the products can be very easily obtained.<sup>11</sup>

In addition to the statistical mechanics, it is very important to choose the best form for the intermolecular potentials to describe experimental results at high density. Under the conditions of a condensed phase detonation, the interaction of the resultant small molecular species is mainly determined by the repulsive component of the intermolecular potential, which is best described by an exponential term. Most workers in the detonics field have, therefore, opted for a simple central Buckingham exponential- $\alpha$ :6 potential, which appears adequate for non-polar interactions, but they either ignore<sup>1</sup> or make a crude semi-empirical correction for polar species.<sup>4</sup> The three Buckingham potential parameters have been estimated using either corresponding states arguments, ab-initio calculations, or comparison of calculations with experimental shock Hugoniot measurements.<sup>4</sup> The various simplifying assumptions associated with the choice of these parameters and their incorporation in computer codes for detonation have been discussed by Ree.<sup>4</sup> The sensitivities of some of the primary detonation properties (mainly first derivatives of the calculated free energy) to global errors in the intermolecular parameters have also been discussed by one of us.<sup>12</sup> Less attention, however, has been focussed on the inadequacies of current

treatments of polar species, on the validity of interspecies mixing rules, on the lack of uniqueness and apparent correlation between the intermolecular potential parameters for single species which leads to ambiguities in fitting, or on the possible effects of high pressure on the intra-molecular contributions to the thermodynamic properties.

The object of the present paper is three-fold. First, to report the development of a new ideal detonation code incorporating the features mentioned above, namely (i) a fast, sophisticated, and accurate analytical EOS; (ii) a new fast method of calculating chemical and phase equilibrium; (iii) a new treatment of polar species based on the Buckingham-Keesom potential, which is described in detail. Second, to present a systematic method of determining the intermolecular parameters for single species and their associated errors from Hugoniot data. Third, to develop a sensitivity analysis based on the new code to calculate the errors in the calculated ideal detonation properties resulting from the known experimental errors in the single species parameters, and to discuss the consequences of the much larger uncertainties in the interspecies parameters. In particular, the errors in the two most important thermodynamic quantities occurring in the theory of detonation, the so-called adiabatic and Gruneisen 'gammas',<sup>14</sup> are examined. These thermodynamic second derivatives produce a sensitive test of a detonation fluid EOS,<sup>15</sup> as well as being of great importance in explosive engineering application.

## TREATMENT OF POLAR SPECIES

Let us first consider the treatment in detonation gases of polar species, of which water is the most important. A very good statistical perturbation theory of polar fluids exists,<sup>17</sup> but is, alas, somewhat complicated and not easy to adapt to the van der Waals one-fluid model for mixtures.

The way of treating polar molecules which is simplest and has a sound physical basis is to add a temperature-dependent

Keesom term<sup>16</sup> to a Buckingham exponential- $\alpha/6$  potential  $u_0(r)$  to give an effective potential

$$u(r) = u_0(r) - \frac{2}{3} \mu^4 / kTr^6, \quad (1)$$

where  $\mu$  is the molecular dipole moment (esu). This effective potential can be re-written as a Buckingham potential with parameters  $r_m$ ,  $\epsilon$ , and  $\alpha$  related to the non-polar ones  $r_{m0}$ ,  $\epsilon_0$ , and  $\alpha_0$  by

$$\begin{aligned} r_m &= r_{m0} (\alpha/\alpha_0), \\ \epsilon &= \epsilon_0 \left( \frac{\alpha-6}{\alpha_0-6} \right) e^{\alpha_0-\alpha}, \\ (\alpha/\alpha_0)^7 e^{\alpha_0-\alpha} &= 1 + \lambda/T, \end{aligned} \quad (2)$$

where

$$\lambda = \frac{2}{3} (\mu^2/\epsilon_0 r_{m0}^3)^2 (1 - 6/\alpha_0) \epsilon_0/k \quad (3)$$

is a polar temperature parameter. Equation (2) is easily solved iteratively for  $\alpha$ , and thence,  $\epsilon$  and  $r_m$  can be obtained. On the basis of his study of averaged pair potentials for water, instead of Equation (2) Ree<sup>4</sup> uses the relations

$$\begin{aligned} r_m &= r_{m0}, \\ \epsilon &= \epsilon_0 \left( 1 + \frac{\lambda}{T} \right), \\ \alpha &= \alpha_0. \end{aligned} \quad (4)$$

This can lead to very different results, even qualitatively, from Equation (2). For example, on Ree's theory the excess internal energy for a pure polar fluid  $U_{\text{polar}}$  is related to the corresponding non-polar quantity  $U_{\text{non-polar}}$  by

$$\begin{aligned} U_{\text{polar}} &= U_{\text{non-polar}} \\ &+ \frac{\lambda}{\lambda + T} U_{\text{non-polar}} [\text{Ree}] \end{aligned} \quad (5)$$

By contrast, the Buckingham-Keesom (B-K) potential Equation (1) leads to

$$\begin{aligned} U_{\text{polar}} &= U_{\text{non-polar}} \\ &+ \frac{\lambda}{\lambda + T} U_{\text{dispersion}} [B-K], \end{aligned} \quad (6)$$

where  $U_{\text{dispersion}}$  is the total attractive energy arising from the  $1/r^6$  dispersion term, and is always negative. Since  $U_{\text{non-polar}}$  is usually positive due to the dominance of repulsion, the two treatments can lead to quite different results. In favor of the B-K treatment is the fact that it gives better agreement with shock temperature results for water<sup>25e,f</sup> and good agreement for ammonia,<sup>26c</sup> as can be seen in Figures 1b and 2b; the intermolecular parameter values used in the theoretical calculations are given in Table 1 and are discussed in the next section.

The theory has been generalized in a straightforward way to cover mixtures of polar species (e.g., water + ammonia), and for mixtures of polar with non-polar species, dipole induced-dipole terms are added to the inter-species potentials, that is (esu),

$$\begin{aligned} u_{ij}(r) &= u_{ij}^0(r) \\ &- (\mu_i^2 \alpha_j + \mu_j^2 \alpha_i) / r^6 \quad (i \neq j) \end{aligned} \quad (7)$$

where  $\mu_i$  and  $\alpha_i$  are here the dipole and polarizability of the  $i$ th species.

## INTERMOLECULAR POTENTIAL PARAMETERS OF DETONATION FLUID PRODUCTS

For CHNO explosives the major detonation fluid product species are expected to comprise  $N_2$ ,  $H_2O$ ,  $CO_2$ ,  $CO$ ,  $CH_4$ ,  $NH_3$ ,  $NO$ ,  $O_2$ , and  $H_2$ . For the purpose of this paper, a subdivision is used based on the availability of experimental shock Hugoniot data for unreacted species. For the case of the homonuclear diatomic species and water, a number of studies have contributed to a comparative wealth of shock Hugoniot results. On the other hand, data for  $CO_2$  is limited as is that for unreacted  $CH_4$ ; data on unreacted  $CO$  and  $NO$  is unobtainable under conditions of condensed phase detonations.

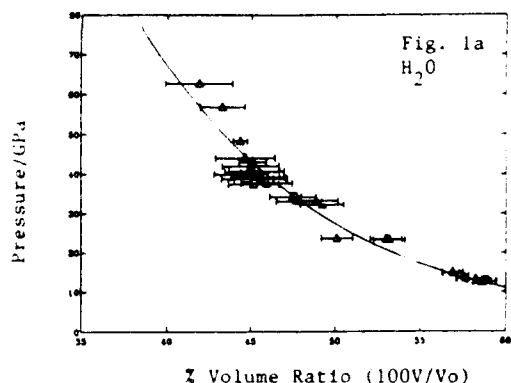


Figure 1a

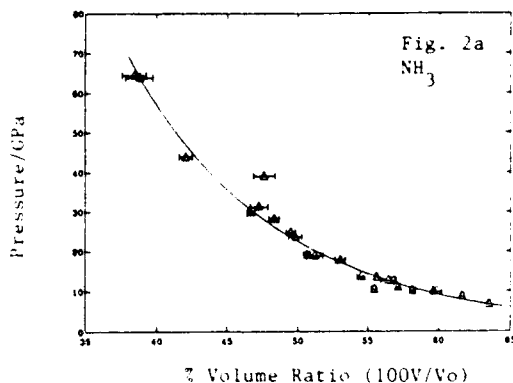


Figure 2a

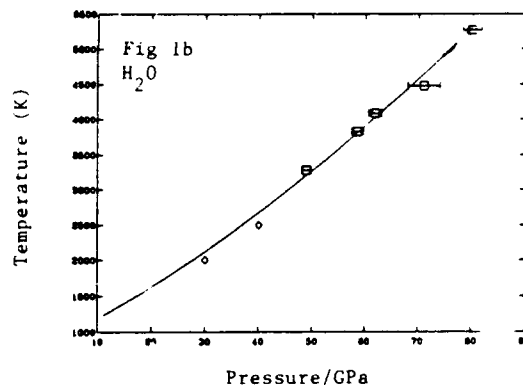


Figure 1b

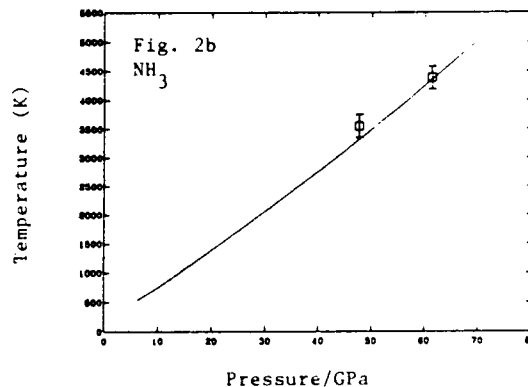


Figure 2b

Table 1. Buckingham Exponential- $\alpha$ :6 Intermolecular Potential Parameters

	$a$	$r_m$ (Å)	$\epsilon/k$ (K)	$\lambda$ (K)
Ar	$12.88 \pm .04$	$3.93 \pm .01$	$120 \pm .5$	—
N <sub>2</sub>	$13.48 \pm .04$	$4.10 \pm .02$	$101.3 \pm .4$	—
O <sub>2</sub>	$12.58 \pm .65$	$3.93 \pm .07$	$133 \pm 8.$	—
H <sub>2</sub>	$10.76 \pm .24$	$3.60 \pm .07$	$36.4 \pm .3$	—
CO <sub>2</sub>	$13.77 \pm .61$	$4.21 \pm .07$	$248.6 \pm 2.0$	—
CH <sub>4</sub>	12.17	4.39	135.8	—
H <sub>2</sub> O	$10.32 \pm .10$	$3.68 \pm .02$	$300.4 \pm 1.2$	$192.3 \pm 1.2$
NH <sub>3</sub>	$11.21 \pm .28$	$4.00 \pm .06$	200.0	$48.3 \pm .08$

Where experimental results exist,<sup>19,26</sup> an elaborate statistical fitting procedure has been carried out to find the intermolecular potential parameter values which, when incorporated in the full statistical mechanical perturbation theory for the excess thermodynamic

properties (including Buckingham-Keesom terms for polar interactions), minimize the difference between theoretical and experimental points on the shock Hugoniot. The procedure includes allowance for quoted errors in the experimental data, and leads to

standard deviation estimates of the errors in the potential parameters. In view of its simplicity and theoretical importance, and the abundance of experimental data, argon has also been included.

With regard to the theoretical calculation of thermodynamic properties for the fitting procedure, at the high temperatures attained in shocked fluids, the standard practice of using simple polynomial fits for ideal contributions to the thermodynamic properties has been found to be unsatisfactory. Instead, ideal thermodynamic data were fitted to a combination of simple rigid-rotor/harmonic-oscillator equations augmented with a small polynomial in  $T$  to take account of anharmonicity, etc.;<sup>18</sup> the results agree with the JANNAF tables over the whole range of temperatures to high accuracy.

The fitting procedure used for calculating the best parameter values from the experimental results for the mass and shock velocities,  $u$  and  $D$ , at various specific volumes will now be described in more detail. The well-known shock conservation relations may be written

$$V = V_0 (1 - u/D) \quad (\text{mass conservation}),$$

$$P = P_0 + uD/V_0 \quad (\text{momentum conservation}),$$

$$E = E_0 + 1/2 (P + P_0) (V_0 - V) \quad (\text{Rankine Hugoniot equation}),$$

where  $V$ ,  $P$ , and  $E$  denote specific volume, pressure, and specific internal energy. An objective function  $\phi$  was chosen involving for each experimental data point ( $u_i$ ,  $D_i \rightarrow P_i$ ,  $V_i$ ,  $E_i$ ) the differences

$$\Delta P_i = \tilde{P}_i - P_i \quad \text{and} \quad \Delta E_i = \tilde{E}_i - E_i,$$

where  $\tilde{P}_i = P(\tilde{T}_i, V_i)$  and  $\tilde{E}_i = E(\tilde{T}_i, V_i)$  are the theoretical EOS values of the pressure and internal energy for volume  $V_i$  and a guess  $\tilde{T}_i$  at the shock temperature for the  $i$ th data point.  $\phi$  also incorporates the standard deviations  $\sigma_u$  and  $\sigma_D$  in the experimental velocities for each data point, and is defined by

$$\phi = \sum_i \frac{(\Delta P_i)^2}{\left[ (\partial P / \partial u)_i^2 \sigma_{u_i}^2 + (\partial P / \partial D)_i^2 \sigma_{D_i}^2 \right]} + \frac{(\Delta E_i)^2}{\left[ (\partial E / \partial u)_i^2 \sigma_{u_i}^2 + (\partial E / \partial D)_i^2 \sigma_{D_i}^2 \right]}$$

This function was then minimized using a standard numerical algorithm with respect to (a) the set of shock temperatures  $\tilde{T}_i$ , and (b) the intermolecular potential parameters  $\alpha$ ,  $r_m$ ,  $\epsilon$ , and  $\lambda$  for the species in question. Note that the data used in this procedure have been restricted to experimental pressures  $< 40$  GPa, and in the case of  $\text{CH}_4$  to those  $< 23$  GPa.

The resultant parameter values are presented in Table 1, and the corresponding fits for Ar (simultaneously analyzing data on three densities),  $\text{N}_2$ ,  $\text{O}_2$ ,  $\text{H}_2$ ,  $\text{CO}_2$  (both solid and liquid initial states), and  $\text{CH}_4$  are shown in Figures 3 through 8. In addition, where experimental data are available for shock temperatures ( $\text{Ar}$ ,  $\text{N}_2$ ), comparisons with predictions based on the parameters of Table 1 and the theoretical EOS are included; some results for polar molecules ( $\text{H}_2\text{O}$ ,  $\text{NH}_3$ ) have already been mentioned in the previous section. The agreement is within the fairly large experimental uncertainties in all cases.

With regard to Table 1 the following comments should be made.

- (1) The  $\alpha$  and  $r_m$  parameters have large deviations in the context of the sensitivity of detonation velocity predictions.<sup>12</sup>
- (2) For a particular species, the values of  $\alpha$  and  $r_m$  are correlated, and the optimum fit is relatively insensitive to combinations of them.
- (3) Shock Hugoniot temperatures, where available, do not effectively discriminate between combinations of  $\alpha$  and  $r$ .
- (4) With the exception of  $\text{NH}_3$ , the well-depths  $\epsilon$  were chosen to give a best fit

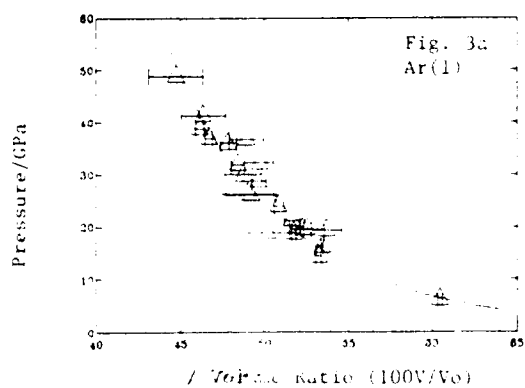


Figure 3a

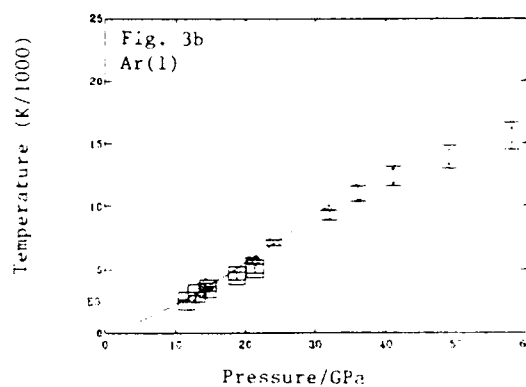


Figure 3b

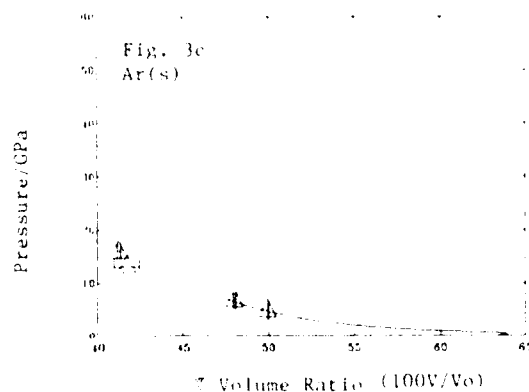


Figure 3c

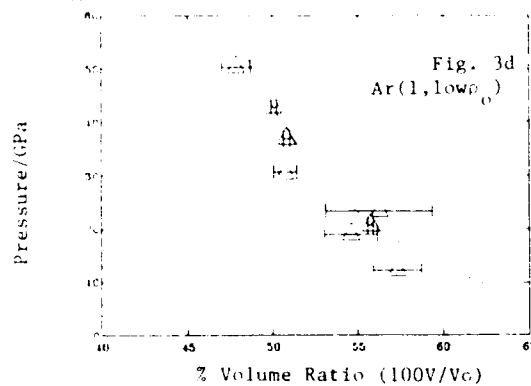


Figure 3d

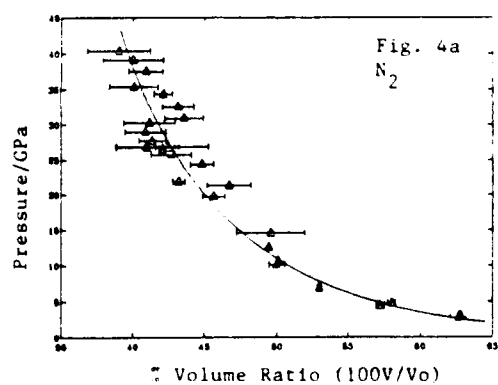


Figure 4a

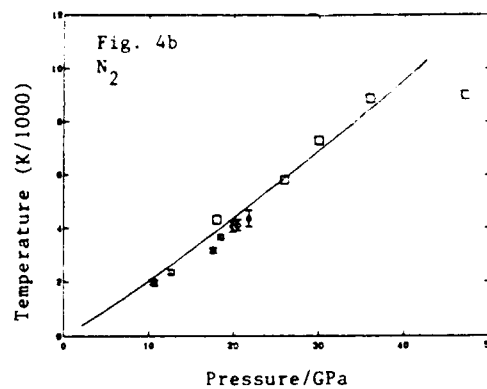


Figure 4b

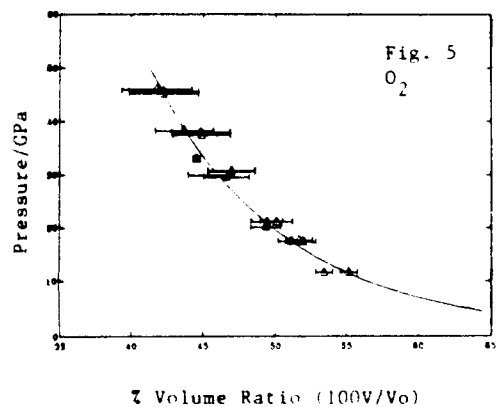


Figure 5

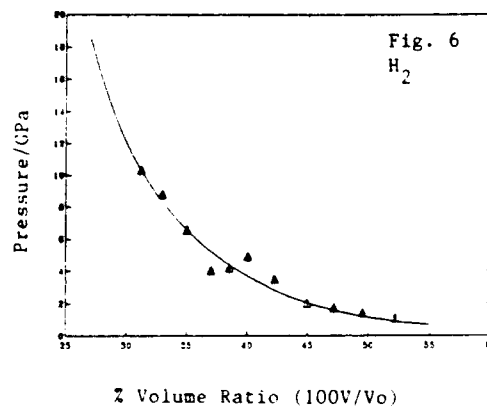


Figure 6



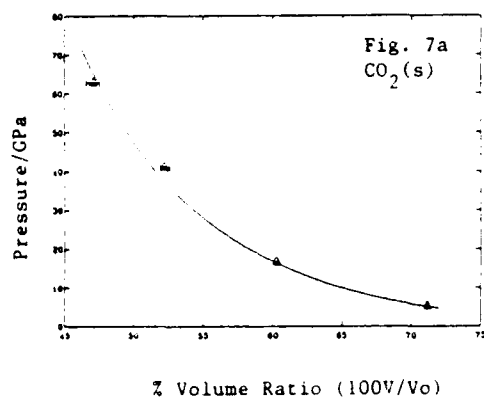


Figure 7a

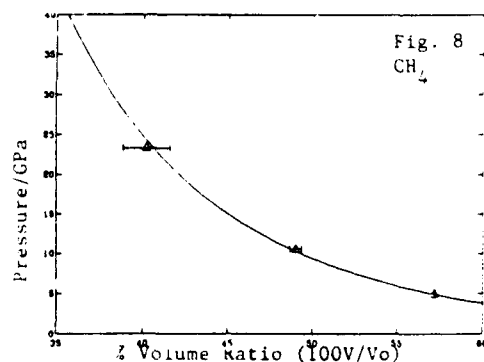


Figure 8

to the shock data. The resulting values are, however, remarkably similar to corresponding states estimates. It has previously been demonstrated<sup>12</sup> that the calculated detonation properties are relatively insensitive to the choice of  $\epsilon$ .

Given the sparsity of shock Hugoniot data for mixtures, little can be said regarding the accuracy of "combination rules" for inter-species parameters.

## PREDICTION OF IDEAL DETONATION VELOCITIES

A representative set of calculated ideal Chapman-Jouguet (CJ) detonation velocities are listed in Table 2 and compared with experiment. The calculations are subject to the following assumptions.

- (1) The allowed species are  $N_2$ ,  $O_2$ ,  $NO$ ,  $CO$ ,  $CO_2$ ,  $CH_4$ ,  $H_2$ ,  $H_2O$ ,  $NH_3$ ,  $C(\text{diamond})$ , and  $C(\text{graphite})$ .
- (2) The intramolecular properties are independent of density.

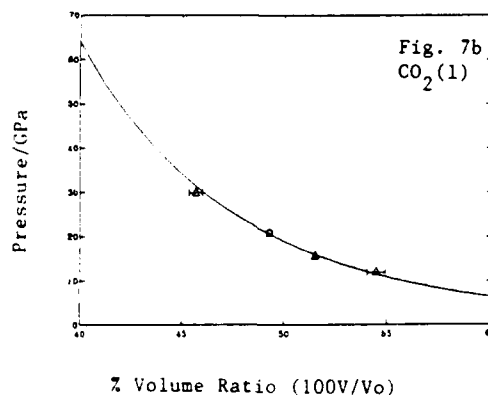


Figure 7b

- (3) There are no fluid phase separations.
- (4) The van der Waals one fluid model is adequate to describe the mixture of detonation products.
- (5) The Lorentz-Berthelot-Ree "combination rules" for the interspecies potential parameters are valid, namely

$$\epsilon_{ij} = \sqrt{\epsilon_{ii} \epsilon_{jj}}, \quad r_{mij} = \frac{1}{2} (r_{mii} + r_{mjj}),$$

$$a_{ij} = \sqrt{a_{ii} a_{jj}} \quad (8)$$

It is clear from the results in Table 2 that both the prediction of the detonation velocity and its dependence on initial density are in only moderate agreement with experiment in most cases. However, the discrepancies may be accounted for in terms of the above assumptions, and in particular (5) is discussed in the following section.

## SENSITIVITY ANALYSIS

In the previous section, estimates have been made of the errors in the intermolecular parameter values for most of the product species occurring in detonation fluid, and are given in Table 1. The question arises as to the effect of such errors on the calculated ideal detonation state properties such as detonation velocity, pressure, temperature, and density, as well as on more general quantities such as the adiabatic and Grüneisen gammas along the expansion isentrope. A preliminary analysis of such errors for both intermolecular

Table 2. Ideal Detonation State Calculations (IDEX Code) Assuming Lorentz-Bertholet-Ree Rules for Inter-Species Potential Parameters

Explosive	Density (g/cc)	Detonation Velocity (km/s)	
		Calc.	Exp.
HNB	1.97	9.50	9.30
RDX	1.80	9.46	8.75
RDX	1.00	6.10	5.98
PETN	1.77	9.06	8.30
PETN	1.23	6.64	6.37
PETN	0.48	3.62	3.60
NG	1.60	7.97	7.70
NG	0.99	5.24	5.50
HNS	1.69	7.34	7.08
HNS	1.40	6.38	6.42
TNT	1.64	7.17	6.95
TNT	1.06	5.43	5.25

and intramolecular parameters was presented at the 8th Detonation Symposium,<sup>12</sup> but the numerical results were limited (a) to the assumption of frozen chemical equilibrium, and (b) to global changes in one of the intermolecular parameters  $\epsilon$ ,  $r_m$ , or  $\alpha$  for all species and interspecies potentials. Furthermore, apart from the detonation velocity itself, the treatment was limited to thermodynamic first derivatives.

In this section, we extend the sensitivity analysis to include the Grüneisen gamma and to cover mobile chemical equilibrium. This extension is made tractable through two developments mentioned above: (1) the use of a sophisticated analytical EOS fitted accurately to statistical mechanical results, which allows first, second, and even third thermodynamic derivatives to be obtained easily; (2) the formulation of the chemical and phase equilibrium conditions in terms of element potentials. The second feature places emphasis naturally on thermodynamic derivatives for

which the elemental mole composition  $m = m_1, m_2, \dots, m_M$ , for the  $M$  elements present, is held fixed. Such derivatives will be dubbed "Gibbsian" since the concept of total equilibrium between elements was first introduced by Gibbs.<sup>13</sup> By contrast, constant species mole compositions  $n = n_1, n_2, \dots, n_N$ , for the  $N$  molecular species, implies frozen chemical equilibrium as usual.

The two most important Gibbsian derivatives for the analysis of shocks and detonations are the adiabatic gamma,

$$\Gamma_s = -(\partial \log P / \partial \log V)_{S,m}$$

and the Grüneisen gamma

$$\Gamma_G = -(\partial \log T / \partial \log V)_{S,m}$$

These occur, for example, in the well known expressions<sup>6</sup> for the Jones coefficient

$$\frac{d \log D}{d \log \rho_0} = \frac{\Gamma_s(\Gamma_s - \Gamma_G - 1)}{(2\Gamma_s - \Gamma_G)}$$

and Stanyukovich-Manson coefficient

$$\frac{DdD}{dE_0} = \frac{\Gamma_G(\Gamma_S + 1)^2}{(2\Gamma_S - \Gamma_G)}$$

The fractional sensitivity coefficient for a detonation state property  $X$  with respect to an intermolecular parameter  $\epsilon$  can be defined by<sup>12</sup>

$$\frac{\delta X/X}{\delta \epsilon/\epsilon} = \left| \frac{\partial \log X}{\partial \log \epsilon} \right|_{CJ}$$

In Table 3 we quote the fractional sensitivity coefficients for the detonation velocity and the density, pressure, and temperature of the ideal detonation state for various intermolecular parameter changes for PETN at an initial density  $\rho_0 = 1.77 \text{ g cm}^{-3}$ . Since the Lorentz-Berthelot-Ree rules are uncertain for all the interspecies parameters, the first three sets of figures show the combined effect of changing all the  $\epsilon_{ij}$ ,  $r_{mij}$ , and  $\alpha_{ij}$  by the same fraction. Unlike Table 1 of Reference 12, these results (a) do not include changes in the like-like parameters ( $i = j$ ), and (b) allow for the change in the chemical equilibrium composition when the parameter is changed. However, the signs, orders of magnitude, and relative values are very similar on the whole to those quoted in the earlier paper. Thus, changes with well depth

are small compared to the effects of size and repulsion index changes. Note that a 10 percent decrease in the  $\alpha_{ij}$  would lead to a decrease of about 8 percent in the detonation velocity (assuming linearity).

Also shown are the effect of interspecies parameter changes for  $\text{CO}_2\text{-H}_2\text{O}$ , two of the most abundant species. Again, the largest effects are due to size changes, followed by changes in  $\alpha$ . What is surprising are the magnitudes of the changes. A 10 percent decrease in  $\alpha(\text{CO}_2\text{-H}_2\text{O})$  is enough to lower the velocity of detonation by over 5 percent, whereas the expectation from the global change results would be more like 1 percent. Also shown is the effect of changing  $\alpha(\text{CH}_4\text{-H}_2\text{O})$ , which as expected is very small owing to the low concentration of methane.

Table 4 gives corresponding figures for PETN at the lower initial density  $\rho_0 = 0.48 \text{ g cm}^{-3}$ , and it can be seen that the effects of parameter changes are a good deal smaller, but that the pattern is the same.

It was noted in the previous section that the ideal detonation velocity calculations quoted in Table 2 assuming the Lorentz-Berthelot-Ree relations tended to be high at high densities. For example, in the case of PETN at  $1.77 \text{ g/cc}$ , the calculated VoD is  $9.06 \text{ km/s}$  compared with an experimental

Table 3 Fractional Sensitivity Coefficients for CJ State Properties of PETN with Initial Density  $\rho_0 = 1.77 \text{ g/cc}$

Inter Species Potential Parameter Changes	Ideal Detonation State Property			
	Velocity $D_{CJ}$	Density $\rho_{CJ}$	Pressure $P_{CJ}$	Temperature $T_{CJ}$
all $\epsilon_{ij}$	+0.16	0.10	+0.01	+0.02
all $r_{mij}$	+1.41	-0.31	+1.80	-0.37
all $\alpha_{ij}$	+0.76	0.19	+0.92	+0.22
$\epsilon(\text{CO}_2\text{-H}_2\text{O})$	+0.01	-0.02	+0.15	-0.05
$r_m(\text{CO}_2\text{-H}_2\text{O})$	+0.92	0.07	+1.60	-0.84
$\alpha(\text{CO}_2\text{-H}_2\text{O})$	+0.54	-0.10	+0.73	-0.26
$\alpha(\text{CH}_4\text{-H}_2\text{O})$	0.001	0.001	0.001	0.000

Table 4. Fractional Sensitivity Coefficients for CJ State Properties of PETN with Initial Density  $\rho_0 = 0.48$  g/cc

Inter-Species Potential Parameter Changes	Ideal Detonation State Property			
	Velocity $D_{CJ}$	Density $\rho_{CJ}$	Pressure $P_{CJ}$	Temperature $T_{CJ}$
all $\epsilon_{ij}$	+0.08	-0.03	+0.08	+0.03
all $r_{mij}$	+1.03	-0.32	+1.36	+0.08
all $\alpha_{ij}$	+0.38	-0.14	+0.46	+0.06
$\alpha(\text{CO}_2\text{-H}_2\text{O})$	+0.11	-0.04	+0.14	-0.03

Table 5. Fractional Sensitivity Coefficients for Adiabatic and Gruneisen Gammas for CJ State of PETN

Inter-Species Potential Parameter Changes	Initial density $\rho_0 = 1.77$ g/cc		Initial density $\rho_0 = 0.48$ g/cc	
	$\Gamma_S (= 3.25)$	$\Gamma_G (= 0.773)$	$\Gamma_S (= 2.07)$	$\Gamma_G (= 0.275)$
all $\epsilon_{ij}$	+0.17	-0.29	+0.12	-0.35
all $r_{mij}$	+1.24	-4.02	+0.97	+1.25
all $\alpha_{ij}$	+0.86	-0.45	+0.49	+0.50
$\alpha(\text{CO}_2\text{-H}_2\text{O})$	+0.45	+0.32	-0.09	-0.28

value of 8.30 km/s, too high by 9 percent; on the other hand, at 0.48 g/cc the values are 3.62 and 3.60, which are in good agreement. From the sensitivity results in the present section, we see that lowering either all the unlike  $\alpha$ 's or that for  $\text{CO}_2\text{-H}_2\text{O}$ , could bring the calculated and experimental results into good agreement.

It should be mentioned, however, that the ideal detonation state (IDS) calculations were made assuming a single fluid phase, and no checks were made on phase stability. If Ree<sup>4</sup> is correct, high density high explosives rich in nitrogen may have two fluid phases at the IDS, and this decreases the ideal VoD. Checks are underway on this point, and if confirmed, may mean that the IDS calculations, even assuming the Lorentz-Berthelot-Ree relations, agree with experiment.

Table 5 shows the sensitivity of the calculations of the adiabatic and Gruneisen

gammas to errors in the intermolecular potential parameters. This was the goal of the paper as indicated by the title. The results for  $\Gamma_S$  are essentially the same as those for  $\rho_{CJ}$ , but the  $\Gamma_G$  results are new, and show an unexpectedly large effect of changing  $\alpha$  for  $\text{CO}_2\text{-H}_2\text{O}$  on  $\Gamma_G$  at the higher initial density.

## CONCLUSIONS

We have shown, first, that polar species can be effectively described by the Buckingham-Keesom potential. Second, that intermolecular potential parameters for most like pairs can be derived systematically from PV shock data and that (a) the parameters agree well with corresponding states values, (b) they describe shock temperature results well, but (c) the  $r_m$  and  $\alpha$  values lack uniqueness. Third, we have shown that ideal detonation state properties, including the adiabatic and Gruneisen gammas, are

unexpectedly sensitive to unlike pair potential parameters.

## REFERENCES

1. Chirat, R. and Pittion-Rossillon, G., *Proceedings of the 7th Symposium (International) on Detonation*, 1981, p. 703.
2. Ross, M., *J. Chem. Phys.*, Vol. 71, 1979, p. 1567.
3. Kang, H. S.; Lee, C. S.; Ree, T.; and Ree, F. H., *J. Chem. Phys.*, Vol. 82, 1985, p. 414.
4. Ree, F. H., *J. Chem. Phys.*, Vol. 81, 1984, p. 1251.
5. Braithwaite, M., Imperial Chemical Industries, Internal Report, 1987.
6. Fickett, W. and Davis, W. C., "Detonation," University of California Press, 1979.
7. Cowperthwaite, M. and Zwisler, W. H., *Proceedings of the 6th Symposium (International) on Detonation*, 1976, p. 162.
8. Mansori, G. A. and Canfield, F. B., *J. Chem. Phys.*, Vol. 51, 1969, p. 4958.
9. Weeks, J. D.; Chandler, D.; and Andersen, H. C., *J. Chem. Phys.*, Vol. 59, 1971, p. 5237.
10. Brown, W. Byers, *J. Chem. Phys.*, Vol. 87, 1987, p. 566.
11. Van Zeggeren, F. and Storey, S. H., "The Computation of Chemical Equilibria," Cambridge University Press, 1970.
12. Brown, W. Byers, *Proceedings of the 8th Symposium (International) on Detonation*, 1985, p. 770.
13. Brown, W. Byers, "Gibbsian Equilibrium and Equations of State," (to be published).
14. Davis, W. C., *Proceedings of the 8th Symposium (International) on Detonation*, 1985, p. 785.
15. Shaner, J. W., *J. Chem. Phys.*, Vol. 89, 1988, p. 1616.
16. Keesom, W. H., *Phys. Z.*, Vol. 23, 1922, p. 225. See also Lennard Jones, J. E., *Proc. Phys. Soc., London*, Vol. 43, 1931, p. 461.
17. Stell, G.; Rasaiah, J. C.; and Narang, H.; *Mol. Phys.*, Vol. 23, 1972, p. 393; Vol. 27, 1974, p. 1393.
18. Robertson, S. H., *Combustion and Flame*, Vol. 77, 1989, p. 411.
19. Ar
  - (a) Van Thiel, M. and Alder, B. J., *J. Chem. Phys.*, Vol. 44, 1966, p. 1056.
  - (b) Ross, M. and Alder, B. J., *J. Chem. Phys.*, Vol. 46, 1967, p. 4203.
  - (c) Dick, R. D.; Warnes, R. H.; and Skalyo, J., *J. Chem. Phys.*, Vol. 53, 1970, p. 1648.
  - (d) Voskoboinikov, I. M.; Gogulya, M. F.; and Dolgoborodov, Y. A., *Sov. Phys. Dokl.*, No. 24, 1979, p. 375.
  - (e) Grigor'ev, F. V.; Kormer, S. B.; Mikhailova, O. L.; Mochalov, M. A.; Urlin, V. D., *Sov. Phys., JETP*, Vol. 61, 1985, p. 751.
  - (f) Nellis, W. J. and Mitchell, A. C., *J. Chem. Phys.*, Vol. 73, 1980, p. 7137.
20. N<sub>2</sub>: 19(d), 19(f) +
  - (a) Christian, R. H.; Duff, R. E.; and Yarger, F. L., *J. Chem. Phys.*, Vol. 23, 1955, p. 2045.
  - (b) Zubarev, V. N. and Telegin, G. S., *Sov. Phys. Dokl.*, Vol. 7, 1962, p. 34.
  - (c) Dick, R. D., *J. Chem. Phys.*, Vol. 52, 1970, p. 6021.
  - (d) Schott, G. L.; Shaw, M. S.; Johnson, J. D., *J. Chem. Phys.*, Vol. 82, 1985, p. 4264.
  - (e) Radousky, H. B. and Ross, M., *High Pressure Research I*, Vol. 39, 1988.
21. O<sub>2</sub>: 19(f), 20(d) +
  - (a) Wackerle, J.; Seik, W. L.; Jamieson, J. C., "Behaviour in Dense Media Under High Dynamic Pressure," Gordon & Breach, New York, 1968, p. 85.

22. H<sub>2</sub>
  - (a) Van Thiel, M. and Alder, B. J., *Mol. Phys.*, Vol. 19, 1966, p. 427.
  - (b) Dick, R. D. and Kerley, G. I., *J. Chem. Phys.*, Vol. 73, 1980, p. 5264.
  - (c) Nellis, W. J.; Mitchell, A. C.; Van Thiel, M.; Devine, G. J.; Trainor, R. J.; and Brown, N., *J. Chem. Phys.*, Vol. 79, 1983, p. 1480.
23. CO<sub>2</sub>: 20(b) +
  - (a) Schott, G. L., private communication, 1987; *Bull. Am. Phys. Soc.*, Vol. 31, 1986, p. 824.
24. CH<sub>4</sub>
  - (a) Nellis, W. J.; Ree, F. H.; Van Thiel, M.; and Mitchell, A. C., Vol. 75, 1981, p. 3055.
25. H<sub>2</sub>O
  - (a) Walsh, J. M. and Rice, M. H., *J. Chem. Phys.*, Vol. 26, 1957, p. 815.
  - (b) Al'tshuler, L. V.; Bakanova, A. A.; and Trunin, R. F., *Sov. Phys. Dokl.*, Vol. 3, 1958, p. 761.
  - (c) Skidmore, I. C. and Morris, E., "Thermodynamics of Nuclear Materials," IAEA, Vienna, 1962, p. 173.
  - (d) Mitchell, A. C. and Nellis, W. J., *J. Chem. Phys.*, Vol. 76, 1982, p. 6273.
  - (e) Lyzenga, G. A.; Ahrens, T. J.; Nellis, W. J.; and Mitchell, A. C., *J. Chem. Phys.*, Vol. 76, 1982, p. 6282.
  - (f) Kormer, S. B., *Soviet Physics Uspekhi*, Vol. 11, 1968, p. 229.
26. NH<sub>3</sub>: 22(b) +
  - (a) Kovel, M. I., Lawrence Livermore Laboratory Report UCRL - 51367, 1973.
  - (b) Dick, R. D., *J. Chem. Phys.*, Vol. 74, 1981, p. 4053.
  - (c) Radousky, H. B.; Mitchell, A. C.; Nellis, W. J.; and Ross, M., "Shock Waves in Condensed Matter," Ed. Y. M. Gupta, Plenum, NY, 1985, p. 467.

## DISCUSSION

J. P. RITCHIE

Los Alamos National Laboratory  
Los Alamos, NM

How does your well-depth for H<sub>2</sub>O agree with the known hydrogen-bond strength of 5-7 kcal/mol? Is it unrealistic to expect these quantities to be the same?

## REPLY BY W. BYERS BROWN

The well-depth implied by the Buckingham-Keesom model for the maximum static interaction of two water molecules is roughly

$$\epsilon_0 + 2\mu^2/r_{mo}^3 \approx \epsilon_0 + \sqrt{12}\lambda\epsilon_0.$$

From the figures in Table 1 this is 300 + 830 = 1130 K or 2.3 kcal/mol. It is, therefore, only about a third of the hydrogen bond energy. However, it is known that a point dipole term by itself is inadequate to describe hydrogen bonding, but may still be useful at longer range. The Buckingham-Keesom parameter  $\lambda$  is treated as a semi-empirical quantity whose value is chosen to give the best fit to the PV shock Hugoniot data for water. It is, therefore, not too surprising that its value is not consistent with the hydrogen bond energy for water.

# REACTIVE FLOW MEASUREMENTS AND CALCULATIONS FOR ZrH<sub>2</sub>-BASED COMPOSITE EXPLOSIVES\*

Michael J. Murphy, Randall L. Simpson,  
R. Don Breithaupt, and Craig M. Tarver  
Lawrence Livermore National Laboratory  
Livermore, California 94550

*Cylinder test, Fabry-Perot laser interferometric and detonation velocity-charge diameter experiments were done to determine the detonation reaction zone structures and reaction product equations of state of a family of HMX/AP/ZrH<sub>2</sub>/estane explosives. This experimental data base is used to develop ignition and growth reactive flow models of the detonation waves in these composite explosives. The experiments and calculations clearly demonstrate the Zeldovich-von Neumann-Doering (ZND) structure of the detonation reaction zones which are several millimeters long. The inferred reaction rates imply that the HMX in these formulations reacts first at rates comparable to those measured in other HMX-based explosives and propellants. The remaining components of these explosives then decompose at much slower rates. However, this decomposition is rapid enough to contribute to the propagation of the detonation wave and to the total energy delivered in metal acceleration applications.*

## INTRODUCTION

Composite or non-ideal explosives are mixtures in which the fuel (carbon and/or hydrogen rich) and oxidizer (oxygen and/or fluorine rich) are separated either partially or completely in distinct molecules and/or phases. Theoretically, if all of the oxidizer atoms are able to diffuse to and react with fuel atoms, composite explosives can liberate significantly more energy than monomolecular explosives during metal acceleration and other applications. The desire to understand and control the reaction kinetics of energy release in composite explosives has driven a long term study<sup>1-6</sup> of the effects of particle size, elemental composition, reaction zone temperature and pressure, and other initial conditions on the performance of this class of explosives.

\*Work performed under the auspices of the U.S. Department of Energy by the Lawrence Livermore National Laboratory under Contract W-7405-Eng 48.

The basic experimental tool used to measure the relative energy release of composite versus monomolecular explosives as a function of time has been the cylinder test, in which a copper wall is accelerated radially outward by the detonating explosive. The copper wall velocity is continuously recorded by streak cameras and in recent years by Fabry-Perot laser interferometric techniques. The detonation velocity and sometimes the detonation pressure are also measured. The main theoretical analysis has been to fit the wall velocity history with a Jones-Wilkins-Lee (JWL) reaction products equation of state assuming that a Chapman-Jouguet (CJ) detonation had been established. Approximate analyses, such as those recently published by Doherty et al.,<sup>7,8</sup> have also been developed for relative energy release estimations at certain volume expansions of the explosive products.

Several nanosecond time resolved experimental techniques and reactive flow computer code models are currently being

used to measure and calculate the detonation reaction zones and overall energy delivery of monomolecular and composite explosives. Embedded pressure and particle velocity gauges and VISAR and Fabry-Perot laser interferometric techniques have been widely applied to measure the reactive flows produced during shock initiation and detonation of monomolecular explosives.<sup>9-16</sup> In addition to confirming the hot spot mechanism of shock initiation and the Zeldovich-von Neumann-Doering (ZND) structure of detonation waves, these experimental records provide the quantitative information required to develop reactive flow computer models, such as the ignition and growth model,<sup>17</sup> which can then be used to predict the explosive's response in other scenarios. In this paper and a related one,<sup>18</sup> these experimental techniques and reactive flow modeling are applied to families of composite explosives and propellants to determine the detonation reaction zone structures of these multicomponent materials. In this paper composite explosives containing HMX, ammonium perchlorate (AP),  $ZrH_2$  and an estane binder are studied in cylinder tests, one-dimensional Fabry-Perot laser interferometric experiments, and detonation velocity as a function of charge diameter experiments to determine their energy release rates under several conditions for reactive flow model development.

## EXPLOSIVES AND EXPERIMENTS

The HMX/AP/ $ZrH_2$ /binder family of explosives, designated as RX-25-xx, was developed for applications requiring relatively high density, high energy and low detonation velocity explosives. Two main formulations, RX-25-BH and RX-25-BF, were used in this study. RX-25-BH contains 19 percent by weight HMX (Class A particle size), 47 percent AP (5 micron particle size), 30 percent  $ZrH_2$  (Class F particle size) and 4 percent estane binder. RX-25-BH is pressed to a density of  $2.30 \text{ g/cm}^3$  (98.3% TMD) and has a detonation velocity of  $6.01 \text{ mm}/\mu\text{sec}$ . RX-25-BF contains 38 percent by weight HMX (Class A particle size), 36 percent AP (5 micron particle size), 22 percent  $ZrH_2$  (Class F) and 4 percent estane binder. RX-25-BF is pressed to

$2.149 \text{ g/cm}^3$  (98.2% TMD) and has a detonation velocity of  $7.506 \text{ mm}/\mu\text{sec}$ . Two particle size variations of this 38 percent HMX formulation were also used in some of the experiments: RX-25-BP (LX-04 grade HMX, 8 micron AP) and RX-25-BQ (6 micron HMX, 8 micron AP). While these particle size variations affect the formulation and shock initiation properties, they do not have significant effects on the detonation experiments done in this study.

These detonation experiments include: five cylinder tests, eight Fabry-Perot laser interferometry shots and two critical diameter-detonation velocity measurements. Three standard cylinder tests with 50 mm diameter explosive charges driving 2.54 mm thick copper walls were fired using RX-25-BH, RX-25-BF and RX-25-BP. Two other cylinders were fired using 25 mm diameter RX-25-BF charges, one with a 1.27 mm thick copper wall and one with a 2.54 mm thick copper wall. The 25 mm diameter cylinder test velocity histories scaled with those obtained in the 50 mm diameter shots indicating that the 38 percent HMX formulations release their energy nearly identically at these diameters. Since two streak records are taken per cylinder test, eight wall velocity histories are available for the 38 percent HMX formulations. Fabry-Perot laser interferometry was available for the most recent cylinder test on RX-25-BP, and the two Fabry-Perot velocity histories closely agree with the streak camera records when the required corrections for copper wall angle directions are made.<sup>19</sup> The one-dimensional Fabry-Perot shots consist of: a 0.254 mm thick Mylar flyer plate accelerated to  $4.3 \text{ mm}/\mu\text{s}$  by an electric gun, a 3 mm thick LX-10 booster pellet, a 12.6 mm or 25.5 mm thick RX-25-BH, -BF, -BP or -BQ pellet, and a LiF crystal coated with 4000 Å of gold to provide a reflecting surface. The Fabry-Perot laser interferometer thus measures the particle velocity history of the explosive-LiF interface. The LX-10 boosters were added to insure RX-25 detonation, but Fabry-Perot records taken without the LX-10 booster pellet showed no effects of the shock initiation process in the RX-25 explosives. The two critical diameter-detonation velocity experiments consisted of SE-1 detonators



igniting tetryl pellets which in turn initiated LX-17 pellets (TATB was used for close CJ pressure matching to RX-25-BP) and finally either 6.4 mm diameter or 12.7 mm diameter charges of RX-25-BP. The 6.4 mm diameter RX-25-BP charge was 32 mm long and piezoelectric crystal pins were placed 6.3 mm apart to measure detonation velocity. The 12.7 mm diameter RX-25-BP charge was 63.6 mm long with shorting switches every 12.7 mm to measure detonation velocity.

This combination of three experimental tests yields one-dimensional detonation reaction zone structure and early product expansion histories, the two-dimensional effects of finite charge diameters on reaction zone structure and the two-dimensional overall energy delivery to an expanding metal wall. Although ideally one should obtain as much experimental data as possible, this amount of data is sufficient to develop a useful reactive flow computer model of these detonating explosives.

## REACTIVE FLOW MODEL DEVELOPMENT

A reactive flow hydrodynamic computer code model for a monomolecular explosive requires: an unreacted explosive equation of state, a reaction product equation of state, a reaction rate law that governs the chemical conversion of explosive molecules to reaction product molecules, and a set of mixture equations to describe the states attained as the reactions proceed. The unreacted equation of state is normalized to shock Hugoniot and von Neumann spike state detonation data. The reaction product equation of state is normalized to expansion data, such as that obtained in a cylinder test. The reaction rates are inferred from embedded gauge and/or laser interferometric measurements of pressure and/or particle velocity histories. Ideally, for multicomponent composite explosives, each component's unreacted and product equations of state and all of the possible reaction rates should be modeled, as discussed by McGuire and Finger.<sup>6</sup> Such detailed models have been implemented in the DYNA2D hydrodynamic code.<sup>20</sup> However, as is the case with these HMX/AP/ZrH<sub>2</sub>/estane explosives,

the equations of state for all of the individual components have not been measured and the experimental data has been obtained on the composite explosive formulations. Therefore the available unreacted and product equations of state are those of the explosive mixture.

The measured reaction rates are also "composites" for the whole mixtures. However, for systems whose individual components react at different rates, the reaction rate laws in the ignition and growth model have been used to describe the sequential or simultaneous decomposition of individual components. This treatment has successfully calculated experimental data on RX-26-AF,<sup>21</sup> which is half HMX and half TATB, and various HMX-based propellants.<sup>18</sup> For RX-25-BH and RX-25-BF, the reaction rates calculated for the HMX-based explosives PBX-9404 and LX-14<sup>17</sup> are used to model the initial decomposition of 19 percent in RX-25-BH and 38 percent in RX-25-BF, because the HMX in these formulations reacts first. Then, since the decomposition rates of ZrH<sub>2</sub> and AP, and the rates of any diffusion controlled reactions between reaction product molecules at these temperatures and pressures are unknown, the remainder of the energy release is modeled as a single term in the ignition and growth reaction rate law.

Table 1 contains the equation of state, reaction rate law coefficients, and detonation parameters for RX-25-BH and RX-25-BF used in this paper. The unreacted and product equations of state are both JWL (i.e., Gruneisen) forms

$$p = A e^{-R_1 V} + B e^{-R_2 V} + \frac{w C_v T}{V} - R_2 V \quad (1)$$

where  $p$  is pressure,  $V$  is relative volume,  $T$  is temperature, and  $A$ ,  $B$ ,  $R_1$ ,  $R_2$ ,  $w$  (the Gruneisen coefficient) and  $C_v$  (the average heat capacity) are constants. The ignition and growth reaction rate law is of the form:

$$\frac{\partial F}{\partial t} = I(1-F)^b(r/r_0 - 1 - a)^x + G_1(1-F)^c F^d p^y + (1-F)^e F^g p^z \quad (2)$$

Table 1. Equation of State and Reaction Rate Parameters for RX-25-BH and RX-25-BF

Explosive	RX-25-BH		RX-25-BF	
JWL Parameters	Unreacted	Products	Unreacted	Products
A(Mbars)	286.9	20.622243	286.9	53.24
B(Mbars)	-0.1453	0.2867773	-0.1453	0.5140
R <sub>1</sub>	10.0	7.0	10.0	8.0
R <sub>2</sub>	2.0	1.0	2.0	1.75
$\omega$	0.8161	0.6	0.8161	0.6
C <sub>v</sub> (Mbars/K)	$2.7298 \times 10^{-5}$	$1 \times 10^{-5}$	$2.7298 \times 10^{-5}$	$1 \times 10^{-5}$
T <sub>0</sub> (°K)	298	—	298	—
E <sub>0</sub> (Mbar-cc/ccg)	—	0.08	—	0.100
CJ State Parameters				
$\rho_0(\text{g/cm}^3)$	—	2.300	—	2.149
D(mm/ $\mu$ s)	—	6.010	—	7.506
p <sub>CJ</sub> (Mbars)	—	0.210	—	0.280
$\rho_{\text{CJ}}/\rho_0$	—	0.7472	—	0.7687
u <sub>CJ</sub> (mm/ $\mu$ s)	—	1.519	—	1.736
Reaction Rate Parameters				
I( $\mu\text{s}^{-1}$ )	$7.43 \times 10^{11}$		$7.43 \times 10^{11}$	
b	0.667		0.667	
a	0.0		0.0	
x	20.0		20.0	
G <sub>1</sub> (Mbars <sup>y</sup> $\mu\text{s}^{-1}$ )	3.1		3.1	
c	0.667		0.667	
d	0.111		0.111	
y	1.0		1.0	
G <sub>2</sub> (Mbars <sup>z</sup> $\mu\text{s}^{-1}$ )	85.0		25.0	
e	0.667		0.667	
g	0.111		0.111	
z	2.0		1.2	
Figmax	0.03		0.03	
F <sub>G1max</sub>	0.19		0.38	

where F is the fraction reacted, t is time,  $\rho_0$  is initial density,  $\rho$  is current density, p is pressure in Mbars, and I, G<sub>1</sub>, G<sub>2</sub>, b, x, a, c, d, y, e, g, and z are constants. The first rate is the hot spot ignition term and is set equal to zero when F exceeds Figmax. Since the amount of

explosive ignited by the shock front has been experimentally demonstrated to be approximately the initial void volume, Figmax is set equal to 0.03 because the RX-25-BH and RX-25-BF were pressed to 97-98 percent TMD. The second rate describes the growth of the

ignited hot spots and the HMX rates previously published<sup>17</sup> are used until  $F$  exceeds  $F_{G1max}$  (0.19 for RX-25-BH and 0.38 for RX-25-BF). The third rate models the completion of reaction for  $F_{G1max} \leq F \leq 1$ . The comparisons between the experimental records and the corresponding reactive flow calculations are shown in the next section.

## COMPARISONS OF EXPERIMENTS AND CALCULATIONS

### RX-25-BH (19 Percent HMX) Formulations

One cylinder test and two Fabry-Perot experiments using 2.55 cm lengths of RX-25-BH boosted by 0.3 cm of LX-10 were performed. Figure 1 shows the comparison of the average of the two streak camera experimental records of the copper wall velocity history with the hydrodynamic code calculations assuming a CJ detonation using the product equation of state listed in Table 1 and a ZND reactive flow detonation using all of the parameters listed in Table 1. This average experimental record agrees more closely with the ZND reactive flow calculation at early times (less than five microseconds), and then with the CJ detonation calculation at later times. The late time agreement with the ideal

CJ calculation occurs because the product JWL equation of state is fitted to the overall energy and momentum produced by the entire expansion process. Thus this product equation of state includes some of the momentum produced in the finite thickness reaction zone of RX-25-BH but delivers it to the cylinder wall at later times. When a finite thickness reaction zone is known to be present, more recent product JWL equations of state are based on lower CJ pressures and initial energies.

The presence of a high initial wall velocity produced by a high pressure reaction zone is not seen in Figure 1, which contains only the average of the two streak camera records. One of the two camera records did record initial velocities of 0.8 mm/ $\mu$ s or higher. When Fabry-Perot laser interferometry or a similar technique is used to measure the initial velocity, the von Neumann spike state is easily observed. Figure 2 compares two experimental velocity histories of the interface between detonating RX-25-BH and LiF to two hydrodynamic code calculations, one assuming an ideal CJ detonation of RX-25-BH and the other a reactive flow calculation of the shock initiation and subsequent detonation of RX-25-BH. Since the Fabry-Perot technique has a time resolution of a few nanoseconds,

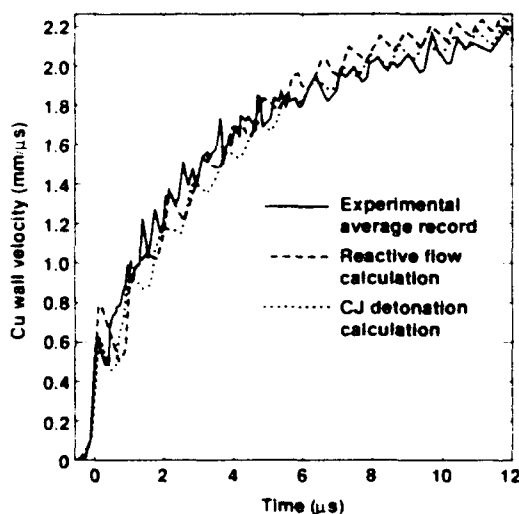


Figure 1. Comparison of Average Experimental Records and Calculations of the Copper Cylinder Wall Velocity History Produced by Detonating RX-25-BH

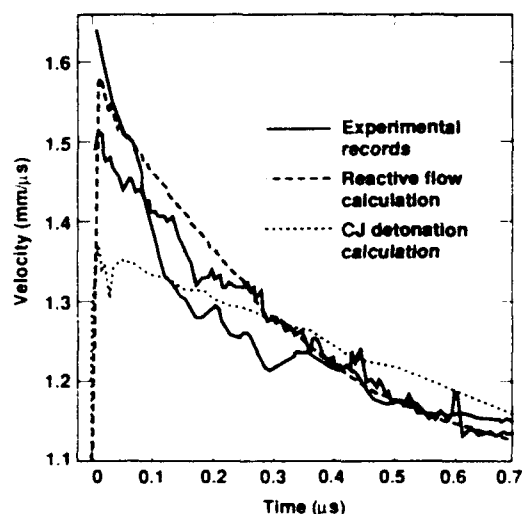


Figure 2. Explosive-LiF Window Interface Velocity Histories Produced by 2.55 cm of Detonating RX-25-BH

most of the detonation reaction zone is observed, as demonstrated by the measured initial velocities of 1.5–1.6 mm/ $\mu$ s in Figure 2 compared with the 1.37 mm/ $\mu$ s predicted by the ideal CJ calculations. The ZND reactive flow calculation agrees with the measured initial velocities in Figure 2. The predicted time for complete reaction of RX-25-BH at the LiF interface is approximately 0.4  $\mu$ s, and the reactive flow calculation agrees very closely with both experimental records from 0.4  $\mu$ s to the end of the records in Figure 2. Both the reactive flow calculation and the experimental velocities in Figure 2 are less than those predicted by an ideal CJ detonation at times greater than 0.4  $\mu$ s. This implies that the RX-25-BH detonation wave has not yet attained its final ZND structure after only 2.55 cm of propagation. This has been previously observed for explosives which exhibit detonation reaction zone lengths of several tenths of a microsecond, such as triaminotrinitrobenzene (TATB)-based explosives.<sup>22</sup> Experiments using longer charges are required to resolve this matter. However, this reactive flow model for RX-25-BH is certainly useful for estimating most of its detonation properties. The calculation predicts that the first 19 percent of reaction occurs in approximately 60 ns and its predicted particle velocity decrease in the first 60 ns agrees closely with experiment, as shown in Figure 2. This justifies the use of the HMX reaction rates for the first 19 percent of the reaction. A better understanding of the reaction rates of the remaining explosive components and the approach to a sonic or CJ-like state requires more experiments and further modeling.

#### **RX-25-BF (BP, BQ) – 38 Percent HMX Formulations**

As previously mentioned, four cylinder tests have been fired using RX-25-BF and BP. The streak camera records for these four shots (eight in all) agree quite closely. The most recent cylinder test also yielded two Fabry-Perot wall velocity histories. Figure 3 compares the average Fabry-Perot velocity history (corrected to slit velocity), the average streak camera velocity history, the reactive flow calculated wall velocity history and the CJ

detonation calculated wall velocity history. Both experimental techniques show the effect of the finite thickness reaction zone (several of the eight individual streak camera records show initial velocities as high as 1.4 mm/ $\mu$ s) and agree more closely with the reactive flow calculation than the CJ detonation calculation.

Six one-dimensional Fabry-Perot laser interferometric experiments using LiF windows were run on detonating RX-25-BF, -BP and -BQ. One experiment had a 3 mm thick LX-10 booster and only 12.6 mm of RX-25-BF. The measured explosive-LiF interface velocity is shown in Figure 4 along with the CJ detonation and reactive flow calculations. The experimental presence of a developing von Neumann spike state is clearly observed in Figure 4 because the ideal CJ calculation underestimates the momentum produced in this experiment. Five Fabry-Perot experiments were shot with 25.5 mm of RX-25-BF, -BP or -BQ with and without LX-10 boosters. The measured interface velocities are shown in Figure 5, along with the corresponding reactive flow and CJ detonation calculations. The reactive flow parameters for RX-25-BF in

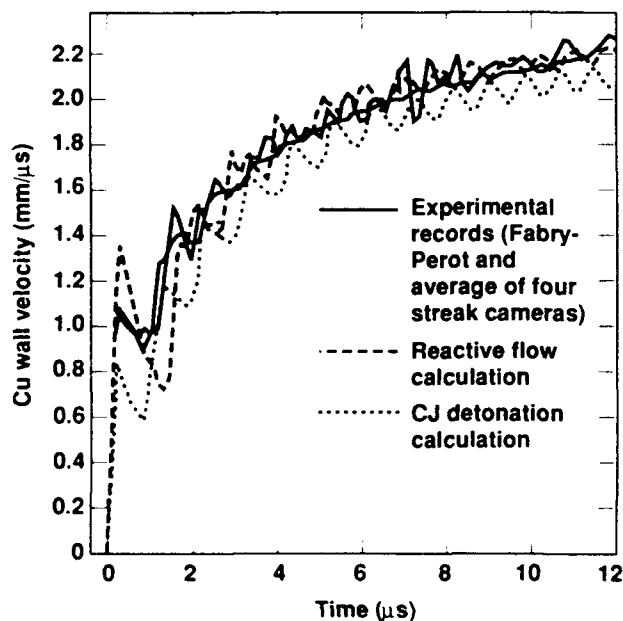


*Figure 3. Comparison of Average Experimental Records and Calculations of the Copper Cylinder Wall Velocity Produced by Detonating RX-25-BF and RX-25-BP*

Table 1 yield excellent agreement with the measured von Neumann spike and subsequent reaction time of approximately 0.3  $\mu\text{s}$  in Figure 3 and agrees with the CJ detonation calculation at times longer than 0.5  $\mu\text{s}$ . The slower decrease in particle velocity in the

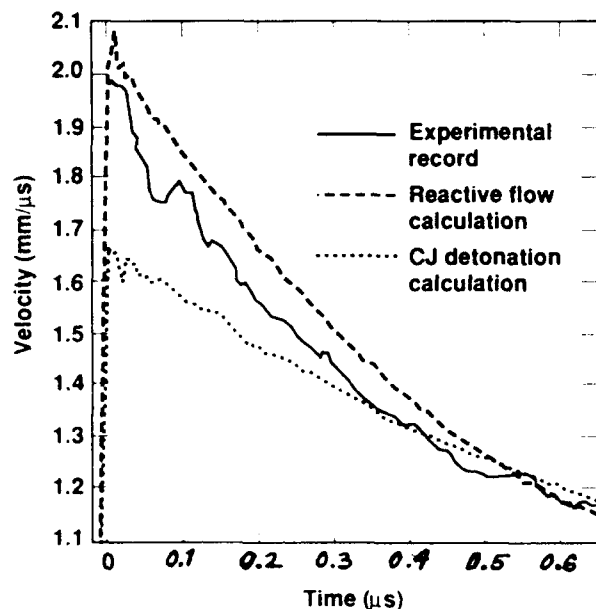


Figure 4. Explosive-LiF Window Interface Velocity Histories Produced by 1.26 cm of Detonating RX-25-BF and RX-25-BP

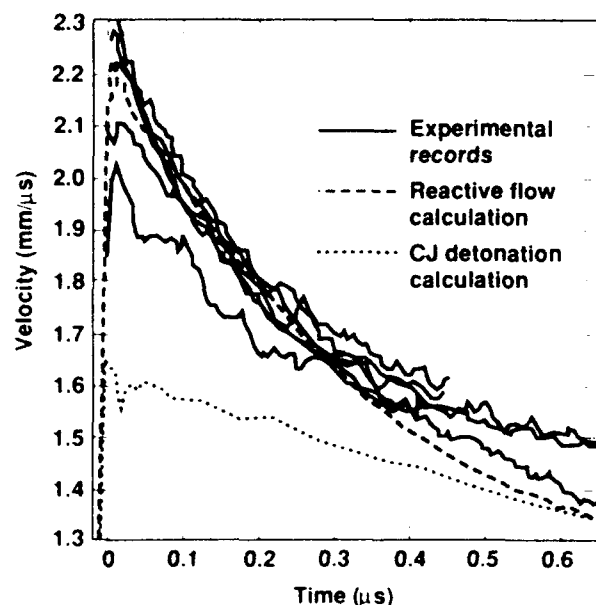


Figure 5. Explosive-LiF Window Interface Velocity Histories Produced by 2.55 cm of Detonating RX-25-BF and RX-25-BP

experimental records of Figure 5 as compared to the calculations in the 0.4-0.6  $\mu\text{s}$  region implies either that a relatively slow, weak exothermic reaction is occurring in this time frame or that the product equation of state is slightly incorrect at these pressures. Nevertheless, this ZND reactive flow model is an excellent one-dimensional representation of the fully developed detonation wave in RX-25-BF. The agreement between the experimental records and the reactive flow calculation during the first 0.1-0.15  $\mu\text{s}$  of Figure 5 also justifies the use of the HMX reaction rates for the initial 38 percent of the reaction in RX-25-BF.

The critical diameter-detonation velocity experiments described earlier measure the response of the detonation reaction rates to rarefaction waves propagating inward from the unconfined charge boundaries. They also represent good tests of the two-dimensional reactive flow model. The entire experiment is modeled in DYNA2D<sup>20</sup> with 50 zones per centimeter in the tetryl booster (CJ detonation), LX-17 booster (reactive flow<sup>13</sup>) and RX-25-BP (reactive flow). Figures 6 and 7 show the calculated pressure and fraction reacted contours for the detonating 12.7 mm diameter (6.35 mm radius) RX-25-BP charge near the end of the 6.36 cm long run distance. After an initial slight overdrive to 7.13 mm/ $\mu\text{s}$ , the detonation velocity in this RX-25-BP charge measured by the final three pins was 6.98 mm/ $\mu\text{s}$ . The calculated detonation velocity for the RX-25-BP reactive flow parameters listed in Table 1 is  $6.75 \pm 0.09$  mm/ $\mu\text{s}$ . Figure 6 shows that this calculated detonation wave front exhibits considerable curvature but its peak pressure approaches the one-dimensional CJ pressure of 28 GPa. Figure 7 shows that 90 percent of the reaction is completed within 0.2 cm (or 0.3  $\mu\text{s}$ ) of the shock front.

Figures 8 and 9 show the calculated pressure and fraction reacted contours for the detonating 6.4 mm diameter (3.2 mm radius) RX-25-BP charge at the end of the 3.20 cm long run distance. The measured detonation velocity for this experiment was 6.70 mm/ $\mu\text{s}$ , while the calculated detonation velocity was  $6.14 \pm 0.14$  mm/ $\mu\text{s}$ . Figure 8 shows a very

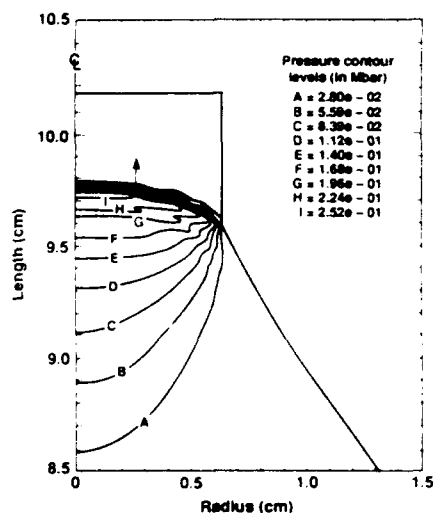


Figure 6. Calculated Pressure Contours for RX-25-BF Detonating in a 12.7 mm Diameter Cylindrical Charge

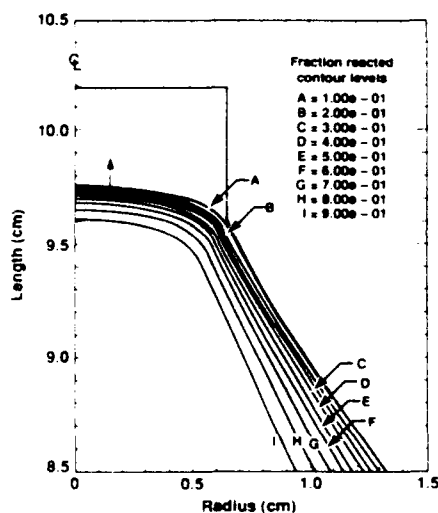


Figure 7. Calculated Fraction Reacted Contours for RX-25-BP Detonating in a 12.7 mm Diameter Cylindrical Charge

weak, curved detonation wave with a peak pressure of only 16 GPa and Figure 9 shows that the 90 percent reacted contour is approximately 0.5 cm (or 0.8  $\mu$ s) behind the shock front on the charge axis. While this reactive flow model accurately simulates the 12.7 mm diameter detonation wave of RX-25-BP, it appears to predict too great a pressure and detonation velocity deficit at 6.35 mm diameter, which is very close to the failure diameter of RX-25-BP. Additional detonation

velocity-charge diameter and embedded pressure gauge experiments in the region of reaction failure are required for further model refinement.

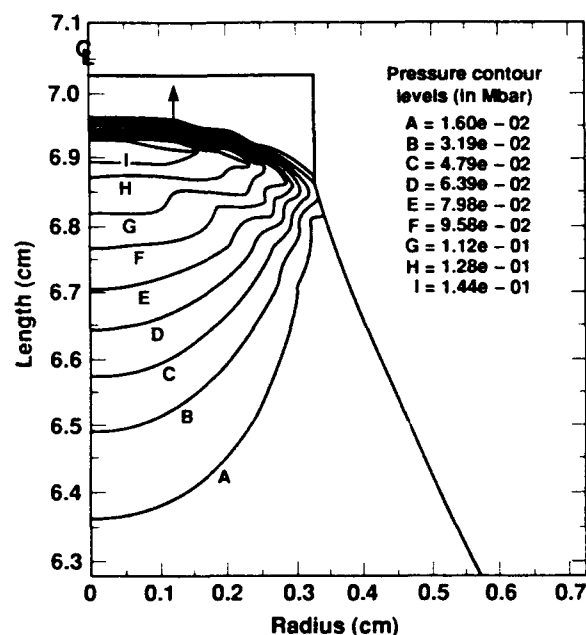


Figure 8. Calculated Pressure Contours for RX-25-BF Detonating in a 6.35 mm Diameter Cylindrical Charge

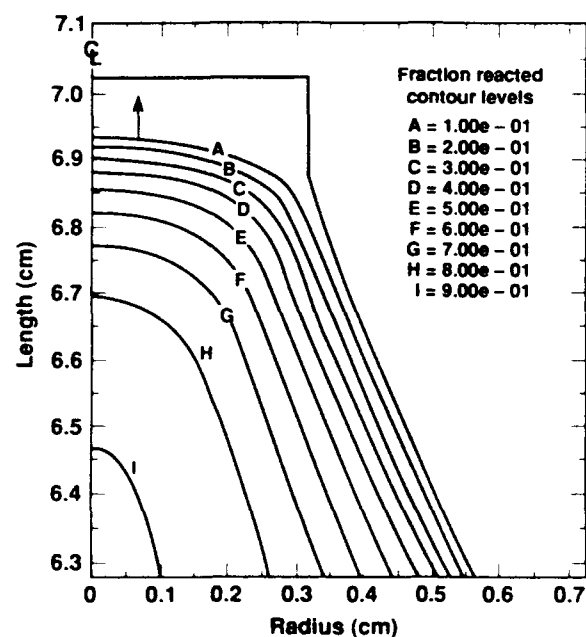


Figure 9. Calculated Fraction Reacted Contours for RX-25-BP Detonating in a 6.35 mm Diameter Cylindrical Charge

## CONCLUSIONS

One- and two-dimensional experiments and reactive flow hydrodynamic calculations for detonating RX-25-BH (19 percent HMX/47 percent AP/30 percent  $ZrH_2$ /4 percent estane) and RX-25-BF (38 percent HMX/36 percent AP/22 percent  $ZrH_2$ /4 percent estane) have yielded sufficient information to develop a computer model which can be used to evaluate these composite explosives in a wide variety of metal acceleration applications. In this model the HMX reaction rates determined for other HMX-based explosives are used for the first 19 percent (RX-25-BH) or 38 percent (RX-25-BF) of reaction. The remainder of the chemical reactions (AP and  $ZrH_2$  decomposition and any subsequent diffusion reactions between the sets of reaction products) are described by one pressure dependent term in the reaction rate equation. Further experimentation on the equations of state and decomposition rates of the individual components  $ZrH_2$  and AP and the diffusion of their reaction products is required to model more completely the complex reactive flow produced by the detonation of these and other composite explosives.

## REFERENCES

1. Kury, J. W.; Hornig, H. C.; Lee, E. L.; McDonnell, J. L.; Ornellas, D. L.; Finger, M.; Strange, F. M.; and Wilkins, M. L., *Fourth Symposium (International) on Detonation*, Office of Naval Research, ACR 126, 1965, p. 3.
2. Finger, M.; Hornig, H. C.; Lee, E. L.; and Kury, J. W., *Fifth Symposium (International) on Detonation*, Office of Naval Research, ACR 184, 1970, p. 137.
3. Finger, M.; Lee, E. L.; Helm, F. H.; Hayes, B.; Hornig, H. C.; McGuire, R.; and Kahara, M., *Sixth Symposium (International) on Detonation*, Office of Naval Research, 1976, p. 710.
4. Finger, M.; Helm, F.; Lee, E.; Boat, R.; Cheung, H.; Walton, J.; Hayes, B.; and Penn, L., *Sixth Symposium (International) on Detonation*, p. 729.
5. McGuire, R. R.; Ornellas, D. L.; Helm, F. H.; Coon, C. L.; and Finger, M., *Seventh Symposium (International) on Detonation*, Naval Surface Weapons Center, NSWC MP 82-334, 1981, p. 940.
6. McGuire, R. R. and Finger, M., *Eighth Symposium (International) on Detonation*, Naval Surface Weapons Center, NSWC MP 86-194, 1985, p. 1018.
7. Doherty, R. M.; Short, J. M.; and Kamlet, M. J., *Combustion and Flame*, Vol. 76, 1989, p. 297.
8. Doherty, R. M.; Short, J. M.; Akst, I. B.; and Kamlet, M. J., *Combustion and Flame*, Vol. 76, 1989, p. 369.
9. Lee, E. L. and Tarver, C. M., *Phys. Fluids*, Vol. 23, 1980, p. 2362.
10. Hayes B. and Tarver, C. M., *Seventh Symposium (International) on Detonation*, Naval Surface Weapons Center, NSWC MP 82-334, 1981, p. 1029.
11. Tarver, C. M.; Parker, N. L.; Palmer, H. G.; Hayes, B.; and Erickson, L. M., *J. Energetic Materials*, Vol. 1, 1983, p. 213.
12. Sheffield, S. A.; Blomquist, D. D.; and Tarver, C. M., *J. Chem. Phys.* Vol. 80, 1984, p. 3831.
13. Bahl, K.; Bloom, G.; Erickson, L.; Lee, R.; Tarver, C.; Von Holle, W.; and Weingart, R., *Eighth Symposium (International) on Detonation*, Naval Surface Weapons Center, NSWC MP 86-194, 1985, p. 1045.
14. Tarver, C. M.; Breithaupt, R. D.; and Kury, J. W., *International Symposium on Pyrotechnics and Explosives*, Beijing, China, 1987, p. 692.
15. Green, L. G.; Tarver, C. M.; and Ershine, D. J., paper presented at this Symposium.
16. Urtiew, P. A.; Erickson, L. M.; Aldis, D. F.; and Tarver, C. M., paper presented at this Symposium.
17. Tarver, C. M.; Hallquist, J. O.; and Erickson, L. M., *Eighth Symposium (International) on Detonation*, Naval

Surface Weapons Center, NSWC MP 86-194, 1985, p. 951.

18. Tarver, C. M. and Green, L. G., paper presented at this Symposium.
19. Lee, E.; Breithaupt, D.; McMillian, C.; Parker, N.; Kury, J.; Tarver, C.; Quirk, W.; and J. Walton, *Eighth Symposium (International) on Detonation*, Naval Surface Weapons Center, NSWC MP 86-194, 1985, p. 613.
20. Hallquist, J. O., *User's Manual for DYNA2D*, UCID-18756 Rev. 3, 1986, Lawrence Livermore National Laboratory, Livermore, California.
21. Tarver, C. M.; Erickson, L. M.; and Parker, N. L., *Shock Waves in Condensed Matter-1983*, edited by Asay, J. R.; Graham, R. A.; and Straub, G. K., Elsevier Science Publishers B. V., 1984, p. 609.
22. Seitz, W. L.; Stacy, H. L.; and Wackerle, J., *Eighth Symposium (International) on Detonation*, Naval Surface Weapons Center, NSWC MP 86-194, 1985, p. 123.

## DISCUSSION

DOUGLAS G. TASKER  
NSWC, Silver Spring, MD

Why did you choose  $ZrH_2$  to modify detonation behavior?

## REPLY BY C. M. TARVER

In a previous study of additives to HMX/AP to produce high density, high energy explosives without increasing the detonation velocity,  $ZrH_2$  was chosen because it is very dense and contributes some fuel to the reaction. Two series of these HMX/AP/ $ZrH_2$  formulations, one with 19 percent HMX and one with 38 percent HMX, were developed for testing.

## DISCUSSION

MATHIES VAN THIEL  
Lawrence Livermore National  
Laboratory, Livermore, CA

You did not mention the unburned EOS needed for the reactive flow calculation. Generally, it is extrapolated to the pressure of interest—can you adjust this extrapolation to improve the agreement with experiment.

## REPLY BY C. M. TARVER

The unreacted equation of state used for HMX/AP/ $ZrH_2$  is quite similar to those used for other HMX and HMX/AP formulations. It is predicted von Neumann spike detonation state agrees quite well with the Fabry-Perot records in Figures 2, 4, and 5 for both the 19 percent HMX and 38 percent HMX formulations.



**SESSIONS ON**  
**COMPOSITES AND EMULSIONS**

**Cochairmen: Ding Jing**  
**Center for Explosive Technology Research**

**Raymond McGuire**  
**Lawrence Livermore National Laboratory**

**and**

**Herbert Richter**  
**Naval Weapons Center**

**James Short**  
**Naval Surface Warfare Center**

# DETONATION CHARACTERISTICS OF GUN PROPELLANTS

Blaine W Asay, A. Wayne Campbell, Michael J. Ginsberg, and John B. Ramsay  
Los Alamos National Laboratory  
Los Alamos, New Mexico

*We have investigated various aspects of detonation of several formulations of gun propellants and show that granular propellants behave similarly to ANFO-type nonideal explosives. The detonation velocity is a strong function of diameter and confinement. Stable velocities 25 percent below the estimated infinite-diameter velocity are measured for some materials at diameters of 50-75 mm. The failure diameter is smaller at low temperatures (-40°C) than at 20°C for one material investigated. Experiments have eliminated microjets as a mechanism of propagation. Forcing the failure of the detonation by decreasing the tube diameter from greater than to less than the failure diameter shows the ionization at the wave front decreases quickly at the transition. After the step decrease in diameter, the pressure decreases, whereas no significant decrease in velocity is noted after a significant length of run. Preliminary interpretation of these data indicates the presence of some form of a wave structure that is affected by the mechanical properties of the propellant, even at the pressures involved in a detonation. Carbon resistors are being developed as pressure gauges. Preliminary work is shown.*

## INTRODUCTION

The behavior of heterogeneous gun propellants when they are impacted by shaped charge jets is of interest because the detonation\* of one charge can lead to sympathetic detonation. An understanding of the behavior is important so that steps can be taken to reduce the vulnerability of future propellant systems to this threat. This is a report of exploratory experiments on materials that are normally not studied as explosives.

Figure 1 shows a jet-propellant interaction model proposed by Gerri, Watson, and

Rocchio.<sup>1</sup> In the immediate area surrounding the jet trajectory, the pressure can be as high as a megabar or more. Thus, in the immediate vicinity of the jet, a detonation is likely to occur. However, the detonation does not necessarily propagate. It may fail promptly or slowly but will probably move through several stages delimited by pressure or velocity. Figure 2 shows another view of the same process depicted in Figure 1. Near the jet tip, a steady-state reaction occurs. As the wave moves radially, the reaction begins to weaken and eventually fails.

Even in the event of detonation failure, the deflagration reaction of these propellants, when supported by a penetrating jet or high-pressure front, can be very violent and can cause significant damage. The response may be a function of grain size, web, perforation pattern, jet diameter, propellant failure diameter, and/or composition. This seriously complicates the problem.

\* Detonation, as used in this paper, is defined as "a wave that is supersonic in the medium of interest and is at least partially supported by an exothermic chemical reaction behind the wave." It does not imply a steady-state detonation unless so stated.

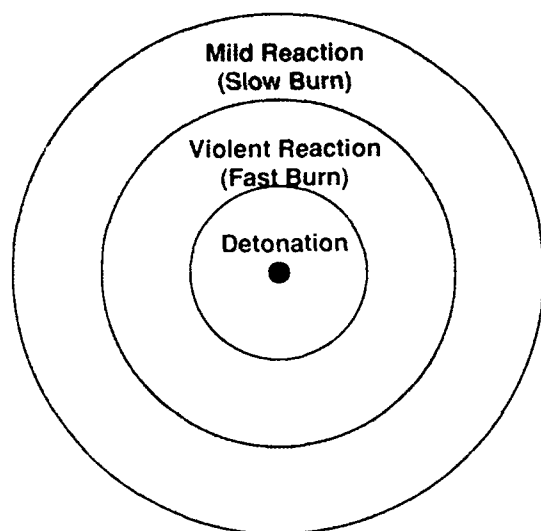


Figure 1. Idealized Schematic of Regions of Interest for the Case of Detonation Failure (Adapted from Reference 1). Jet impact point is at center.

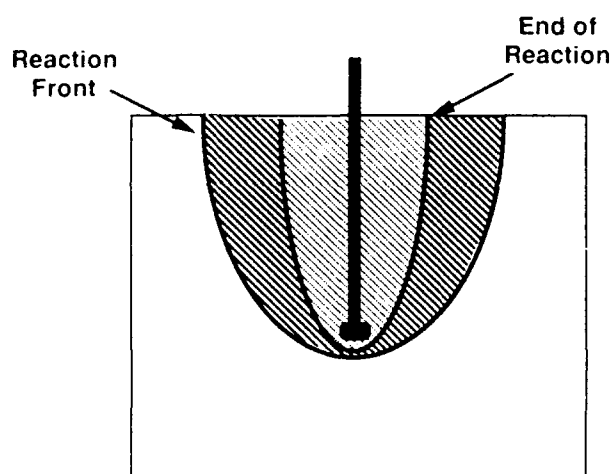


Figure 2. Idealized Schematic Showing Failing Reaction Zone During Penetration of Propellant by Shaped-Charge Jet

Many investigators have examined the effects of jet impacts on full-density explosives and have found that the response depends strongly on jet diameter and velocity (the  $v^2D$  criterion described, for example, by Held).<sup>2</sup> Chick, Bussell, and Frey<sup>3</sup> have extended these studies to include the effect of the explosive's failure diameter. Most studies of jet impact in propellant beds have involved far-field blast wave measurements and fragment characterization (for example, Majerus and Merendino),<sup>4</sup>

near-field measurements using crush gauges (Reeves and Gerri),<sup>5</sup> and instrumented blocks (Gerri, Watson, and Rocchio).<sup>1</sup> Watson<sup>6</sup> has recorded the velocity of propagation of a pressure front in a variety of propellants and has attempted to correlate violence with wave velocity.

We have compared the behaviors of a variety of gun propellants when initiated by high-explosive boosters [PBX 9501 (95 wt percent HMX/5 wt percent Estane)], as well as after impact by shaped-charge jets. Booster-initiated systems have the advantage of a known initial condition. This permits the study of the detonation front-failure interface, as will be described in the section on forced failure. These studies have permitted us to consider the propellants in the larger context of high explosives; and some classic tests used by the high-explosives community have been adapted for use here.

Tables 1 and 2 show the compositions and geometry of the propellants used in this study. Represented are a range of grain sizes, shapes, webs, and compositions.

## DETONATION VELOCITY OF PROPELLANTS

### Detonation Velocity as a Function of Charge Radius

One method of assessing the reaction zone thickness of an explosive and of gaining an understanding of its sensitivity to the thermodynamic state within the reaction front is by determining the effect of charge radius on the detonation velocity and the failure diameter. This was explored experimentally by Campbell and Engelke.<sup>7</sup> Engelke and Bdzil<sup>8</sup> used those data to show that the differences in the diameter-effect curves between heterogeneous and homogeneous ideal explosives arise from differences in mechanical energy concentrations, and the state dependence of the heat release rate is considerably less for the heterogeneous explosive than it is for the homogeneous one. By measuring the diameter effect of a propellant, we may better understand the nature of the chemical reaction at the front.

Table 1. Major Components in Propellants (wt percent)

Composition	XM39	JA2 <sup>a</sup>	M5	M2
RDX	76			
Nitrocellulose		59	82	75
Cellulose acetate butyrate (CAB)	12			
Acetyl triethyl citrate (ATEC)	8			
Nitroglycerin (NG)	15	15	20	
Diethylene glycol dinitrate (DEGDN)		25		

<sup>a</sup>Both cylindrical and hexagonal cross sectional materials were tested.

Table 2. Physical Characteristics of Propellants

	XM39	JA2	JA2 <sup>a</sup>	M5	M2
Length (in.)	0.375	0.625	0.500	0.250	0.437
Diameter (in.)	0.250	0.375	0.437	0.03135	0.187
Perforations	19	7	19	1	

<sup>a</sup>Hexagonal cross section.

The detonation velocity at infinite diameter was calculated for several explosives and propellants using the method proposed by Kamlet and Jacobs.<sup>9</sup> This method uses the elemental composition, loading density, and the heat of formation for C H N O explosives to predict the detonation pressure and velocity. Predictions for full density explosives have been fairly accurate ( $\pm 1.5$  percent).

The data for the gun propellants we have tested are compared with those for TNT<sup>10</sup> and ANFO<sup>11</sup> in Figure 3. The lines connecting experimental data points are meant only as guides. The TNT and ANFO data are for densities of 0.9 g/cm<sup>3</sup>. Confinement for the propellant tests was copper or brass tubes with nominal 1.65 mm wall thickness. Confinement in PMMA of the same diameter was found to be insufficient. The precise failure diameters for the propellants have not been determined. However, the

failure diameter will lie between the values in the box labeled "failed" and the next larger diameter at which detonation propagated.

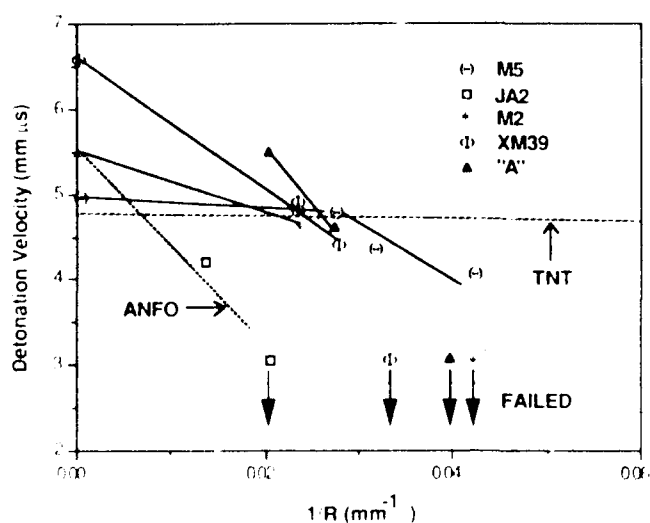


Figure 3. Diameter-Effect Curves for Selected Propellants and Explosives

Propellant "A" is a special formulation that shows promise as a low-vulnerability ammunition. A clear distinction exists between TNT and both ANFO and the propellants. The slopes of data obtained from nonideal explosives are much greater than those of TNT, and the velocity deficits before failure are also greater than that of TNT. These data demonstrate that the propellants can be considered nonideal explosives.

In the case of XM39 (76 percent RDX), this nonideal condition may be caused by the heterogeneity of the bed. Nonideal explosives are characterized by long reaction zones. Also, propagation of the detonation is not a strong function of the state at the front as it is with standard explosives. This means that a detonation, once initiated, can "coast" for many charge diameters before failing, even though the charge may be below its failure diameter. This finding may have important implications to those interested in the jet-propellant interaction in propelling charges.

#### Detonation Velocity as a Function of Temperature

The failure diameters of ideal explosives increase as the temperature decreases.<sup>12,13</sup> This fact is attributed to the temperature effect on the reaction rate. XM39 was fired at 20°C and at -40°C in 63.5 mm-o.d. Cu confinement with a 1.65-mm wall. The propellant failed to propagate a detonation at 20°C, but a detonation was sustained at -40°C with a velocity of 4.5 mm/μs. This material is below its glass transition temperature at -40°C. It would first appear that at detonation pressures, fracture behavior should not influence propagation. This behavior may be evidence that a precursor is leading the detonation front, or perhaps the front is broad enough, because of the granular (and thus dispersive) nature of the bed, that a ramp wave is being driven instead of a shock.

Propellant "A" was also tested at -40°C at two diameters that were determined to be just below the failure diameter determined at 20°C. The results of these tests are found in Figure 4. Unlike the XM39, "A" also failed at

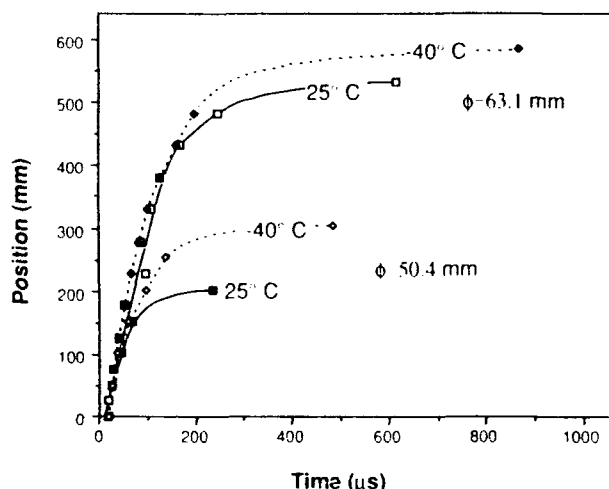


Figure 4. Data from Propellant A, which was Initiated at Two Temperatures and Two Diameters

the low temperature at both diameters, although it appeared to fail more slowly than at 20°C. The reported glass transition temperature for this propellant is below -40°C. However, the glass transition temperature is a function of frequency as well as pressure<sup>14</sup> and it is possible that, at detonation conditions, there are other physical parameters that will more easily correlate the observed behavior. Additional studies of different materials conducted at a range of temperatures and with enhanced diagnostics need to be made to understand this phenomenon.

#### MECHANISM OF DETONATION PROPAGATION

It has been suggested that microjets between grains are a primary mechanism for the propagation of detonation in heterogeneous gun propellants. Campbell<sup>15</sup> found that the insertion of thin neoprene diaphragms in beds of fine-grained (<250 μm) HMX did not disturb the propagation of an established detonation. We designed an experiment in which disks, approximately one grain thick, were fabricated with a silicone potting compound into which propellant was embedded to form a barrier. These disks were inserted midway in a tube of propellant, and the propellant was initiated with a booster. M2 and XM39 were tested separately. For each propellant the detonation propagated with the same velocity through both sections

of the tube with no indication of any interruption by the disks. Thus, interparticle jetting must not play a major role. Shock loading may be the predominant mechanism.

## FORCED FAILURE

We have developed a test that we have called "forced failure" to elucidate the transition from detonation to deflagration in propellant beds. The purpose of this test is to cause detonation failure at a precise point in space and time, thereby allowing the monitoring of the behavior of the reaction during this critical phase. The experimental arrangement is shown in Figure 5. It consists of a copper tube with a diameter larger than the failure diameter of the propellant under study. Connected to the copper tube is a PMMA tube with a slightly smaller diameter, in which a detonation cannot propagate. The propellant in the copper tube is initiated by a PBX-9501 booster. The copper tube was two diameters long to reduce the effect of the booster. This assembly was instrumented with shock pins on the outer wall, and ion pins and pressure gauges in the center of the bed.

Figure 6 shows the data from a test using XM39. Only time-of-arrival data from the pressure gauges are reported in this figure. Two ion pins and one shock pin did not respond. Because of the curvature of the detonation front, the ion pins respond first, followed by the pressure gauges, and then, at a later time, by the shock pins. Once the copper/PMMA transition is reached, the detonation begins immediately to fail, as shown by the ion pins. The shock pins stop responding after approximately 55  $\mu$ s and ~200 mm into the PMMA tube, indicating that a shock is no longer present at the tube wall. Of special interest is the fact that, although the pressure level falls dramatically after failure and after the strong reaction wave has dissipated, the velocity as measured by the pressure gauges remains relatively constant.

The picture that emerges from this test is that detonation failure in XM39 is first shown by a retarding and thickening of the reaction front, with the center of strong reaction moving farther and farther back. The

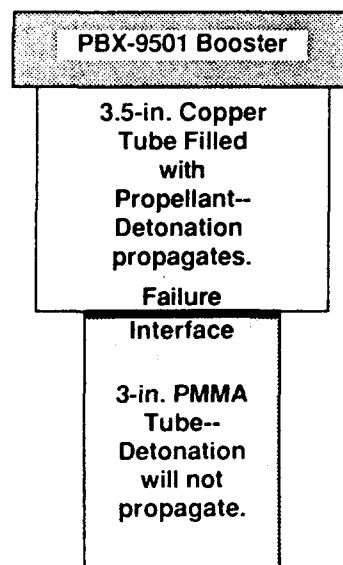


Figure 5. Schematic of Forced-Failure Shot

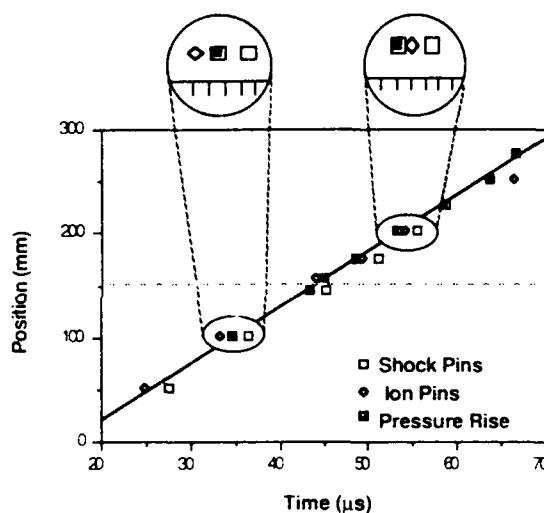


Figure 6. Pin and Stress Gauge Data from Forced-Failure Shot. The time units in the enlargements are 1  $\mu$ s. Horizontal line at 152 mm shows location of tube interface.

pressure at the front falls immediately after detonation failure, but a constant-velocity wave continues even after the weak reaction has failed. Once the test has been refined and the data more fully understood, this same configuration will be used with a jet as the stimulus.

## PRESSURE GAUGE DEVELOPMENT

We have been developing carbon resistor pressure gauges for use in beds of reacting

heterogeneous gun propellants. No conventional gauges now available are capable of surviving long enough under these severe conditions to provide the desired data. Watson<sup>16</sup> was the first to report on the use of 470-ohm, 1/8 watt resistors as pressure gauges and others (see, for example, Stankiewicz and White<sup>17</sup> and Hollenberg<sup>18</sup>) have used the gauges in water and provided calibration curves under specialized conditions. However, no one has reported their use in heterogeneous media or calibration of the gauges under well-defined one-dimensional conditions. We have undertaken a calibration program using a gas gun to provide shocks under controlled conditions. Only a brief summary of this work will be given here. A full report of the calibration tests and jet penetration studies is being prepared for publication.

Figure 7 shows the results from one calibration shot in which a polymethylmethacrylate (PMMA) target containing a carbon gauge was impacted by a PMMA flyer to give an initial shock of 10 kbar. The target was backed by foam. The release wave from the foam interface produced a step decrease to 5 kbar. The results from a 1-D code prediction as well as a coplanar manganin gauge are also shown. The resistance change for each gauge was scaled for ease of comparison and the prediction was similarly scaled. The initial response of both gauges is very similar; however, the carbon resistor gauge attains its peak value at a later time, as expected because of its large diameter (3mm). The unloading behavior of the carbon gauge is also slower than the manganin gauge. Further tests are being conducted to quantify the release behavior.

Gauges have also been placed into propellant that is being penetrated by a LAW shaped-charge jet. The gauge positions are shown in Figure 8. Thin-film manganin gauges do not survive this environment. However, the carbon gauges apparently perform well, as shown by Figure 9. Shown here is a pressure time history acquired by the carbon resistor gauge array. Figure 9a shows the radial progression and Figure 9b shows

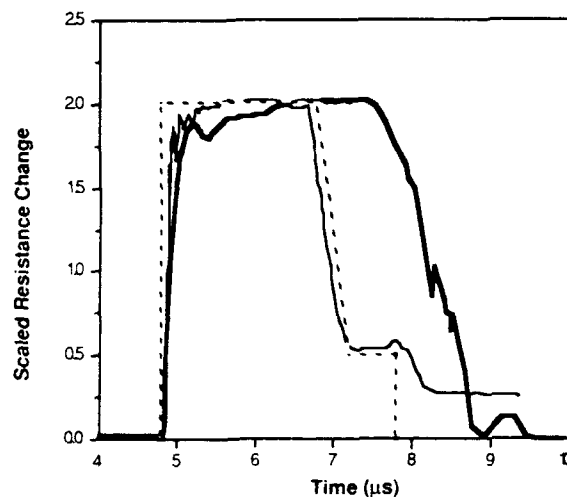


Figure 7. Comparison of Response of Thin-Film Manganin Gauge (—), Carbon Resistor Gauge (---), and Prediction of One-Dimensional Hydrodynamic Code (---). Vertical axis units are relative.

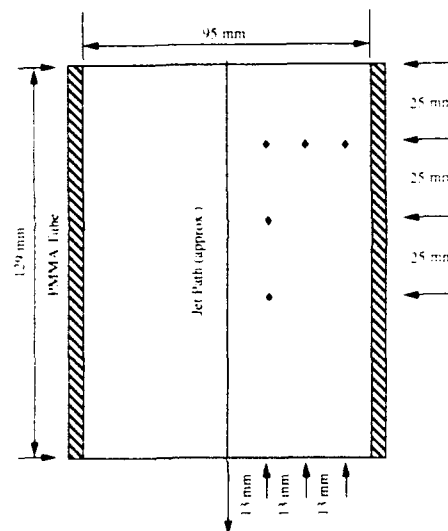


Figure 8. Schematic of Jet-Propellant Interaction Test Configuration. Dark diamonds show the positions of the carbon-resistor gauges.

the axial progression. The calibration curve of Watson<sup>16</sup> was used to obtain pressure from the change in resistance. These gauges have the potential of accurately mapping out the stress field in the vicinity of a penetrating jet. This would serve to more fully define the regions suggested by Figures 1 and 2.

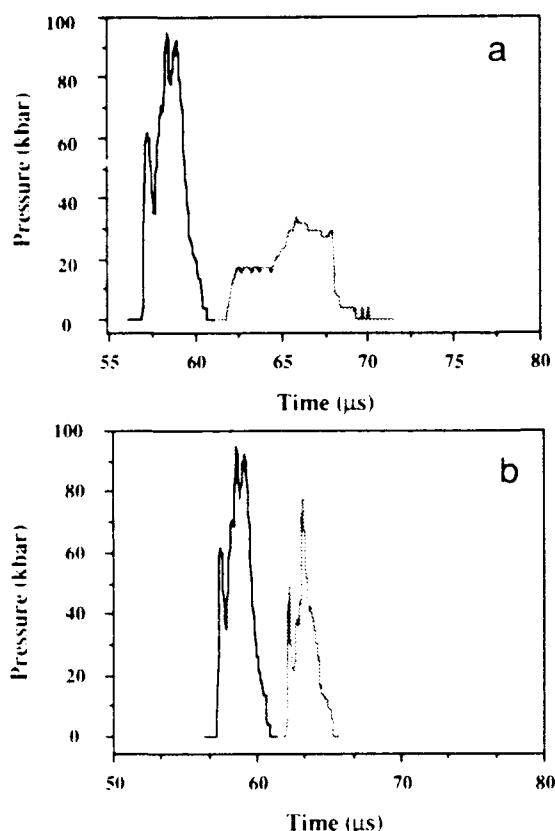


Figure 9 Data Showing the Radial (a) and Axial (b) Pressure Time History in a Propellant During Jet Penetration

## CONCLUSIONS

We have shown that these gun propellants behave as nonideal explosives. This implies a long reaction zone for them and a lack of strong dependence on the thermodynamic state at the front. Thus, detonation failure in propellants confined near their failure diameters occurs slowly and violent reactions can propagate for many charge diameters. We have also shown that the temperature dependence on failure diameter for XM39 is opposite that which has been observed for ideal explosives. Microjetting has been ruled out as a predominant mechanism for propagation, and the use of the forced-failure test has permitted us the first detailed look at a failing detonation wave in granular propellant. An interpretation of the data leads to the conclusion that the friability of the propellant formulation affects the detonation behavior.

Carbon resistor gauges are being developed that will survive in a reacting heterogeneous propellant bed. Calibration of these gauges has begun and their behavior under various conditions is being studied.

## REFERENCES

1. Gerri, N. J.; Watson, J. L.; and Rocchio, J. J., "A Laboratory Simulator for Evaluating Propellant Response to Hypervelocity Impact Initiation," *1986 Propulsion Systems Hazards Subcommittee Meeting*, Monterey, CA, Mar 1986, pp. 277-283.
2. Held, M., "Initiierung von Sprengstoffen, ein vielschichtiges Problem der Detonationsphysik," *Explosivstoffe*, Vol. 5, 1968, pp. 2-17.
3. Chick, M. C.; Bussell, T. J.; and Frey, R. B., "Mechanisms of the Jet Initiation of Solid Explosives," *Combustion and Detonation Phenomena*, 19th International Annual Conference of ICT 1988, Karlsruhe, Federal Republic of Germany, 29 Jun-3 Jul 1988, pp. 24.1-24.4.
4. Majerus, J. N. and Merendino, A. B., "Observations of Shaped-Charge Jet/M30 Propellant Reactions," ARBRL-TR-02108, U.S. Army Ballistic Research Laboratory Report, Sep 1978.
5. Reeves, H. J. and Gerri, N. J., "Propellant Responses to Shock," *1986 Propulsion Systems Hazards Subcommittee Meeting*, Monterey, CA, Mar 1986, pp. 267-275.
6. Watson, J., "Technique for Measuring the Response of Propellant Beds to Shaped-Charge Attack," *1986 Propulsion Systems Hazards Subcommittee Meeting*, Monterey, CA, Mar 1986, pp. 257-266.
7. Campbell, A. W. and Engelke, R., "The Diameter Effect in High-Density Heterogeneous Explosives," *Proceedings of the 6th Symposium (International) on Detonation*, Coronado, CA, 24-27 Aug, pp. 642-652.
8. Engelke, R. and Bdzil, J. B., "A Study of the Steady State Reaction Zone



Structure of a Homogeneous and a Heterogeneous Explosive," *Physics of Fluids*, Vol. 26, No. 5, May 1983, pp. 1210-1221.

9. Kamlet, M. J. and Jacobs, S. J., "Chemistry of Detonations. I. A Simple Method for Calculating Detonation Properties of C-H-N-O Explosives," *Journal of Chemical Physics*, Vol. 48, No. 1, Jan 1968, p. 23.
10. Urizar, M. J.; James, E. and Smith, L. C., "Detonation Velocity of Pressed TNT," *Physics of Fluids*, Vol. 4, No. 2, Feb 1961, pp. 262-274.
11. Johnson, J. N.; Mader, C. L., and Goldstein, S., "Performance Properties of Commercial Explosives," *Propellants, Explosives, and Pyrotechnics*, Vol. 8, 1983, pp. 8-18.
12. Campbell, A. W., "Diameter Effect and Failure Diameter of a TATB Based Explosive," *Propellants, Explosives, and Pyrotechnics*, Vol. 9, 1984, pp. 183-187.
13. Price, D., "Notes From Lectures on Detonation Physics," Frank Zerilli, Ed., Naval Surface Warfare Center (NSWC) Report, MP 81-399, 1981.
14. Nielsen, L. E., *Mechanical Properties of Polymers and Composites*, Marcel Dekker, Inc., 1974.
15. Campbell, A. W., "Deflagration to Detonation Transition in Granular HMX," LA-UR 80-2016, Los Alamos National Laboratory unpublished report, 1980.

## DISCUSSION

HOWARD M. SHEINFELD  
U.S. Army FSTC  
Charlottesville, VA

Are you planning to publish the results of your tests for specific propellants? If so, when?

## REPLY BY BLAINE ASAY

Our continuing progress reports to the Army will contain information about the

behavior of specific propellants. Further information regarding carbon gauge development is being prepared for publication.

## DISCUSSION

RICHARD H. GRANHOLM  
Ireco, Inc., Salt Lake City, Utah

What do you do for electrical insulation of your carbon resistor gauges?

## REPLY BY BLAINE ASAY

We insulate the resistor leads with Teflon tubing and the entire assembly with shrink tubing.

## DISCUSSION

DONNA PRICE, ATR  
Laurel, MD

I think it is misleading to conclude that the failure diameter of the propellants tested decreased with decreasing temperature. It is true that the failure diameter at temperatures below the glass point ( $t_g$ ) are smaller than those above. But I believe that a propellant at temperatures less than  $t_g$  and the same propellant at  $t > t_g$  are different explosives as, for example, are cast and pressed TNT. If so, each has its own range of detonability and should be tested for temperature effect within that range only—not from one range to another.

## REPLY BY BLAINE ASAY

We do not yet have the data to fully evaluate the behavior of these propellants above and below the glass transition temperature. It is possible that they would behave as you have proposed, although, as stated in the paper, the  $T_g$  may not be the only important mechanical property under these conditions. The data for propellant A indicate that failure is occurring more slowly at  $-40^\circ\text{C}$  than at  $25^\circ\text{C}$ , even though the propellant is above its glass transition temperature at  $-40^\circ\text{C}$ . This supports the conclusion in the paper, but your comment must be carefully considered during future work.

# DETONATION PROPERTIES OF MIXTURES OF HMX AND EMULSION EXPLOSIVES

J. D. Renick  
Air Force Weapons Laboratory  
Kirtland AFB, New Mexico 87117-6008

P. A. Persson  
Center for Explosives Technology Research  
New Mexico Institute of Mining and Technology  
Socorro, New Mexico 87801

and

J. A. Sanchez  
Los Alamos National Laboratory  
Los Alamos, New Mexico 87544

*The detonation properties of mixtures of HMX and an aqueous emulsion explosive have been determined. Cylindrical and conical charge experiments were conducted for mixtures ranging from 10 to 60 percent HMX. Sufficient data were obtained to describe the velocity-mixture-diameter relationships for mixtures containing from 20 to 50 percent HMX. A qualitative description of these relationships was determined for mixtures of less than 20 percent and more than 50 percent HMX.*

## BACKGROUND

Due to the inherent insensitivity of most aqueous emulsion explosive formulations, it is necessary to increase their initiation sensitivity by the use of additives. The additives can be either high density inert particles, energetic particles, or voids. In each case, it is believed that localized regions of very high energy density (hot spots) are produced resulting in high chemical reaction rates which lead to thermal initiation. In the case of high density particles, the increased energy density is due to shock interactions caused by the impedance mismatch between the particles and emulsion resulting in pressure induced hot spots. In the case of energetic particles, it is likely that shock interaction effects combine with the effects of particle initiation to generate initiation in the emulsion. In the case of voids, the increased

energy density is due to hydro-dynamic collapse. Johansson and Persson<sup>1</sup> provide a good review of the mechanisms believed to be involved in the hot spot model of initiation.

Considerable work has been done in recent years to characterize the detonation performance of aqueous emulsion explosives sensitized with glass microballoons. Lee<sup>2</sup> conducted an extensive investigation of the effects of microballoon size and loading on the detonation properties of emulsion explosives. His research was preceded by that of Yoshida, et al,<sup>3</sup> and Hattori, et al.<sup>4</sup> Lee found, in part, that: (1) at a given diameter, as the emulsion/microballoon density increases, the detonation velocity also increases until a maximum is reached, after which, the velocity begins to decrease until detonation failure occurs and (2) failure diameter increases as the density increases.

Lee's results for unsieved microballoons are summarized in a *qualitative* manner in Figure 1 where detonation velocity, normalized to the infinite diameter detonation velocity of the pure emulsion ( $D/D_i$ ), is plotted as a function of density, normalized to the pure emulsion density ( $\rho/\rho_0$ ). Thus, the region to the left of  $\rho/\rho_0 = 1$  is for mixtures of emulsion and microballoons. The effects of explosive density and diameter on detonation velocity and failure diameter are shown. The detonation velocity at failure for a given diameter is difficult to define experimentally, thus the failure boundary in Figure 1 should be taken as highly idealized, but nevertheless, descriptive of the qualitative behavior. The results of BKW calculations are also shown to provide an idealized prediction of detonation velocity for an infinite diameter charge. Note that the behavior shown in Figure 1 is descriptive of (1) and (2) in the previous paragraph.

If a particulate molecular explosive was added to the pure emulsion, then an extension of the results in Figure 1 could be made into the region where  $\rho/\rho_0 > 1$ , assuming that the density of the molecular explosive is greater than that of the pure emulsion. In this case, the detonation velocity at infinite diameter is expected to increase as the density of the

mixture increases with the maximum obtained when the mixture reaches the limit of 100 percent molecular explosive. If the failure diameter and velocity at failure of the molecular explosive is known, then it is possible to construct a qualitative prediction of the effects of molecular/emulsion explosive density and charge diameter on detonation velocity and failure diameter. This qualitative prediction is shown in Figure 1 where the nominal values of HMX density and detonation velocity have been assumed for the molecular explosive. Note that at a given charge diameter, the path of constant charge diameter through  $D/D_i$  vs  $\rho/\rho_0$  space is continuous only for diameters greater than the failure diameter of the pure emulsion. For diameters less than that of the failure diameter of the pure emulsion, it is observed that the lines of constant diameter are discontinuous, being "cut off" by the detonation failure boundaries. Note again, that the purpose of Figure 1 is to represent only the qualitative detonation behavior of the mixtures.

It would be a rather large task to characterize the entire three-component (emulsion/microballoons/molecular explosive) system and it is not clear that a three-component system would be of practical interest. Regardless, the microballoon/emulsion and molecular/emulsion systems are of interest and a complete characterization is warranted. Thus, it was the objective of this research program to investigate the detonation characteristics of a molecular/emulsion explosive system.

HMX was selected as the molecular explosive to be used because of its energetic properties and availability. Material availability was an important consideration because of schedule constraints.

The emulsion was prepared at the Center for Explosive Technology Research (CETR), New Mexico Institute of Mining and Technology (NM Tech). HMX/emulsion mixing was performed at the Los Alamos National Laboratory. All experimental work was performed at the CETR Eagle Site located west of the NM Tech campus.

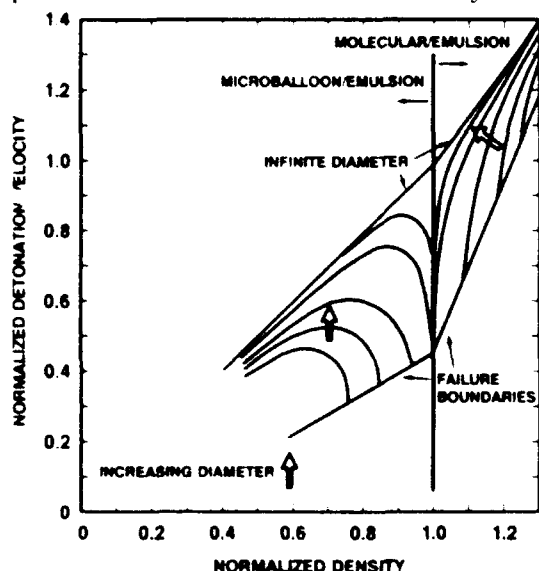


Figure 1 Detonation Velocity as a Function of Density for Emulsion/microballoon and molecular/emulsion explosive systems, normalized parameters

## EXPERIMENT DESCRIPTION

### Charge Design

Rigid high-density closed-cell urethane foam provided by General Plastics Inc., Tacoma, WA, was selected for use in fabrication of cylindrical and conical charge containers. This material is available at several densities. Densities of 0.24 g/ml and 0.08 g/ml were chosen for the cylindrical and conical charge containers, respectively. The cylindrical charge containers were machined while the conical charge containers were cast. Ionization pin, shorting pin, resistance probe, and streak camera techniques were used to measure detonation front arrival time in the experiments. The particular technique used varied depending on the type and size of the charge.

Additional cylindrical charges were prepared for plate dent experiments. These consisted of cardboard and PVC pipe containers positioned on the center of steel plates. No TOA measurements were made in the plate dent experiments.

All of the experiments in which detonation velocity was determined were conducted at charge diameters of 51.5 mm or less. A complete description of the charge containers is given in Reference 5.

### Emulsion Preparation

The emulsion formulation selected was as follows:

#### Salt Solution

Ammonium Nitrate (AN)	71.5%
Sodium Nitrate (SN)	10.0%
Distilled Water	12.0%

#### Fuel

Light Mineral Oil/Emulsifier	6.5%
------------------------------	------

The salt solution (discontinuous phase) is dispersed as tiny spherical cells of from 1- to 10  $\mu$ m diameter throughout the fuel (continuous phase). The fuel consists of 2.7 parts light mineral oil to one part emulsifier.

The fuel was prepared by adding the emulsifier components to the light mineral oil at a temperature of 80° C and stirring for 4 h.

The emulsifier components consisted of 100 parts of polyisobutenyl succinic anhydride and 5.62 parts of a 50/50 mixture of diethanolamine and monoethanolamine. This formulation was developed based on discussions with Griffith and Oxley<sup>6</sup>.

The emulsion was prepared by heating the fuel and salt solution to an initial temperature of 107° C and mixing them together in a preheated thermally insulated mixing bowl. The components were mixed at increasing shear rates for a total of 9 minutes by which time the mixture cooled to 88° C. Void-free density of the resulting emulsion was determined to be 1.43 g/ml. The nominal mass mean cell size of the emulsion was approximately 7  $\mu$ m as determined by optical microscope.

### HMX/Emulsion Mixing Operations

We originally intended to use a HMX blend composed of 35 percent fine and 65 percent coarse grades of HMX. However, initial attempts at mixing the HMX blend resulted in very stiff mixtures and we subsequently used only the coarse grade. For instance, one of the first mixes was a mixture of 40 percent HMX blend and 60 percent emulsion which had the consistency of a very smooth, nontacky putty. This particular mix is identified as 40B/60 ("B" for blend). This was the only blend mixture for which detonation data was obtained.

We were successful in preparing 10/90, 20/80, 30/70, 40/60 and 50/50 HMX/emulsion mixtures with the coarse grade HMX. We found that excessive shear applied during mixing of the HMX and emulsion could result in matrix failure. This occurred for two different batches of 50/50 mix resulting in solidification of the mixtures within 2 days after mixing. Mixtures of 60/40 and 70/30 HMX/emulsion were also prepared but competent matrices were not obtained, i.e., they tended to be noncohesive.

The results of HMX/emulsion density measurements are shown in Figure 2 where density is plotted as a function of percent HMX. The mixture equation which calculates the density,  $\rho_m$ , of a mixture of  $n$  components of

densities  $\rho_1, \rho_2, \dots, \rho_n$  and mass fractions  $x_1, x_2, \dots, x_n$  is

$$\rho_m = \frac{1}{x_1/\rho_1 + x_2/\rho_2 + \dots + x_n/\rho_n} \quad (1)$$

The curve shown in Figure 2 is a plot of Equation 1 where the emulsion density,  $\rho_1$ , has been adjusted to provide the best fit to the data. The emulsion density which gave the best fit was  $\rho_1 = 1.389$  g/ml. The standard density of 1.89 g/ml for HMX,  $\rho_2$ , was used. For a void-free emulsion density of 1.43 g/ml this implies that the preparation and mixing processes consistently introduced air into the emulsion at a volume fraction of about 3 percent, regardless of HMX content.

The density for the 60/40 mix lies slightly above the curve because it had to be packed into the container which drove out some of the entrained air. The density of the 70/30 mix lies well below the other data because a coherent mass could not be obtained by packing.

### Charge Loading

Various techniques were developed for loading of the test articles because of the range of matrix stiffnesses encountered. The smaller charge containers were loaded successfully with 10/90, 20/80, 30/70, and 40/60 mixtures using manually pressed frosting bags with a simple conical tip. For loading of the larger charge containers, a simple pressure vessel

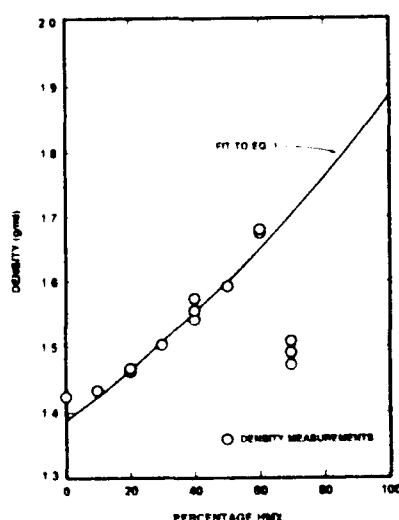


Figure 2. Variation of HMX/Emulsion Density with Percentage HMX

was constructed which forced the mixture into the containers under air pressure produced by a hand-operated bicycle pump. These loading procedures worked quite well and resulted in uniform void-free charges. Because of the very stiff nature of the 40B/60, 50/50 and 60/40 mixtures, it was necessary to load the test articles by tamping with wooden dowel rods.

## RESULTS AND DISCUSSION

### Detonation Velocity-Diameter-Mixture Analysis

The experimental results are tabulated in Table 1. Analysis of these results are presented in Figures 3-6. However, before we discuss the results, some general comments are in order.

Craig<sup>7</sup> has shown that an overshoot in the propagation of detonation along the charge axis of up to one charge diameter can occur at detonation failure. This occurs because the detonation at any given station along the axis of a conical charge is always slightly overdriven. Thus, conical charge data tend to indicate failure at a diameter that is slightly smaller than the true failure diameter. The lower bound on failure diameter determined in the conical charge experiments has been adjusted to reflect this overshoot.

An additional factor that affects all of the experimental results is that, as indicated previously, there was a relatively constant 3 percent air entrainment in the HMX/emulsion mixtures, regardless of HMX loading. Based on previous research with aqueous emulsions<sup>2,3</sup> the effects of voids (in the form of glass microballoons) is well understood. Thus, if we assume that the effects of air voids on emulsion alone can be qualitatively superimposed on the behavior of HMX/emulsion mixtures, we may conclude that for small percentages of air entrainment at a given HMX/emulsion mixture, the effect of air entrainment is to reduce detonation velocity and failure diameter. This effect would be more noticeable for small HMX loadings than for heavy HMX loadings.

Figure 3 provides a comprehensive description of the results of the cylindrical and

Table 1. Experimental Results

Shot No.	Configuration	Composition % HMX/Emul.	Diameter (mm)	Density (g/ml)	Results
BE87 110	CYL	10/90	26.10	1.426	DET FAILURE
BE87 111	CYL	20/80	26.10	1.466	DET FAILURE
BE87 112	CYL	30/70	26.10	1.510	D = 6.298 mm/ $\mu$ s
BE87 115	CON	10/90	50.80 12.70	1.426	DET FAILURE
BE87 116	CYL	50/50	26.10	1.602	D = 7.768 mm/ $\mu$ s
BE87 116	CYL	40B/60	26.10	1.554	D = 7.132 mm/ $\mu$ s
BE87 116	CYL	30/70	26.10	1.510	D = 6.132 mm/ $\mu$ s
BE87 117	CYL	50/50	12.55	1.602	D = 7.430 mm/ $\mu$ s
BE87 117	CYL	40B/60	12.55	1.554	D = 6.548 mm/ $\mu$ s
BE87 117	CYL	30/70	12.55	1.510	DET FAILURE
BE87 118	CON	20/80	50.80 12.70	1.466	df = 14.7-17.5 mm
BE87 119	CYL	30/70	51.50	1.510	D = 6.959 mm/ $\mu$ s
BE87 120	CYL	20/80	51.50	1.466	D = 5.514 mm/ $\mu$ s
BE87 122	CYL	40B/60	12.55	1.554	D = 6.740 mm/ $\mu$ s
BE87 122	CYL	30/70	12.55	1.510	DET FAILURE
BE87 238	CYL	60/40	12.55	1.652	D = 7.802 mm/ $\mu$ s
BE87 241	CYL	40/60	41.28	1.554	DENT, P = 234 kbar
BE87 242	CYL	10/90	101.60	1.426	DENT, P = 74 kbar
LE87 126	CON	50/50	12.70 3.18	1.602	df = 5.7-8.1 mm
LE87 127	CON	40B/60	25.40 6.35	1.554	df = 7.1-8.6 mm
LE87 128	CON	40B/60	12.70 3.18	1.554	df = 8.4-9.8 mm
LE87 129	CON	30/70	25.40 6.35	1.510	df = 9.8-11.9 mm
LE87 130	CYL	50/50	6.35	1.602	DET FAILURE
LE87 131	CON	50/50	12.70 3.18	1.602	df = 5.8-6.6 m
LE87 137	CON	40/60	12.70 3.18	1.554	df = 7.6-9.1 mm
LE87 138	CON	30/70	25.40 12.70	1.510	FAILURE NOT OBSERVED
LE87 139	CYL	60/40	6.35	1.652	DET FAILURE
LE87 140	CYL	60/40	3.18	1.652	DET FAILURE

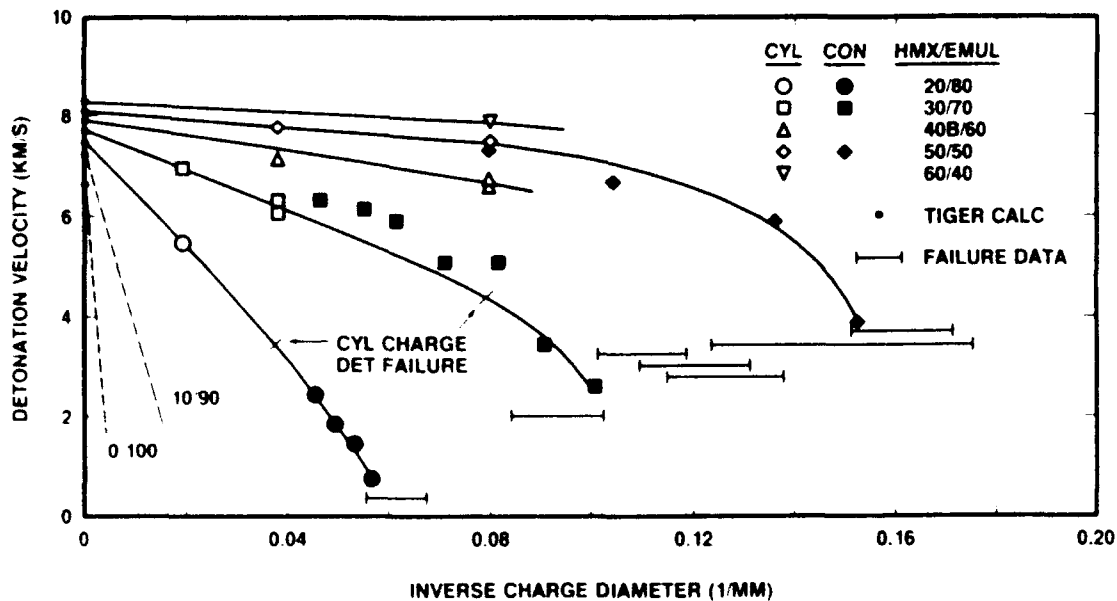


Figure 3 Detonation Velocity Versus Inverse Charge Diameter for Various Percentages of HMX

conical charge experiments. Detonation velocity is plotted as a function of inverse charge diameter for each HMX/emulsion mixture. The open symbols are data from the cylindrical charge experiments while the solid symbols are points read from streak camera film records and resistance probe data for the conical charges. The horizontal bars are estimates of failure diameter based on interpretation of the streak camera film records and resistance probe data. The results of the 40/60 experiments produced anomalously low detonation velocities relative to the other data, therefore, the results of the 40R/60 experiments were plotted in Figure 3.

Figure 3 shows that, for a given mixture, a straight line through the cylindrical charge data, extrapolated to the infinite diameter (TIGER) velocity represents the results very well. This is consistent with the behavior of numerous molecular explosives as shown by Campbell and Engelke.<sup>7</sup> It is reasonable to assume that for diameters significantly larger than failure diameter, there is a consistency, or as stated by Campbell and Engelke, a "regularity," in the relationship between slopes of constant mixture and percentage HMX. These slopes in Figure 3 were measured and the logarithm of their absolute values plotted against percentage HMX in Figure 4. A curve was fit by hand to these results, recognizing that the slope of the 100 percent HMX mixture should be very nearly zero and thus influences the

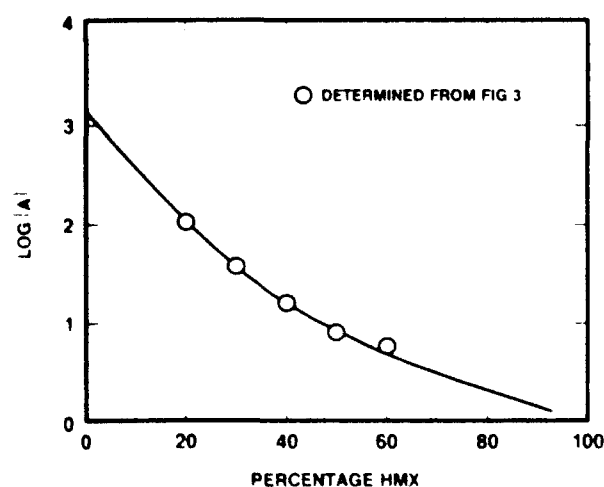


Figure 4 Plot of Logarithm of Absolute Value of  $a$  (Slope of  $D$  VS  $1/d$  at Large Diameters from Figure 3) VS Percentage HMX

behavior of the curve for mixtures greater than 60 percent in the manner shown. For mixtures of less than 20 percent HMX the curve has simply been extrapolated to the pure emulsion where the only constraint on the result is that the slope must be finite. Results in this region can only be treated as a rough guess.

The results of Figure 4 have also been used to provide an estimate of the slopes in Figure 3 for 10 percent HMX and the pure emulsion. These results are shown as dashed lines.

In principle it is possible to use the results shown in Figure 3 to determine the detonation velocity at failure for each mixture. However, due to the large negative slopes at and near failure, and, in some cases, the large uncertainties in estimates of failure diameter, it is not possible to provide a definition of the failure boundary with any degree of confidence. A general observation can be made, however, that for low percentage HMX mixtures failure occurs at large diameters at low velocities, while for high percentage HMX mixtures failure occurs at small diameters at high velocities. This result is in qualitative agreement with the behavior indicated in Figure 1.

The short lines crossing the 20/80 and 30/70 data in Figure 3 indicate that at those diameters detonation was not observed in cylindrical charge experiments. Since the results of the 20/80 and 30/70 conical charge experiments indicate detonation at smaller diameters, the adequacy of the boosters used to initiate these charges becomes suspect.

Figure 5 shows the variation of detonation velocity with percentage HMX for each charge diameter. The results of the TIGER calculations are included. As shown, charges with higher percentage HMX and larger diameters result in increased detonation velocity as well as a closer approach to the TIGER results which are assumed to be a good estimate of detonation velocity at infinite diameter. The open symbols are plots of the results from the cylindrical charge experiments. The solid symbols are plots of points determined by extrapolating results in

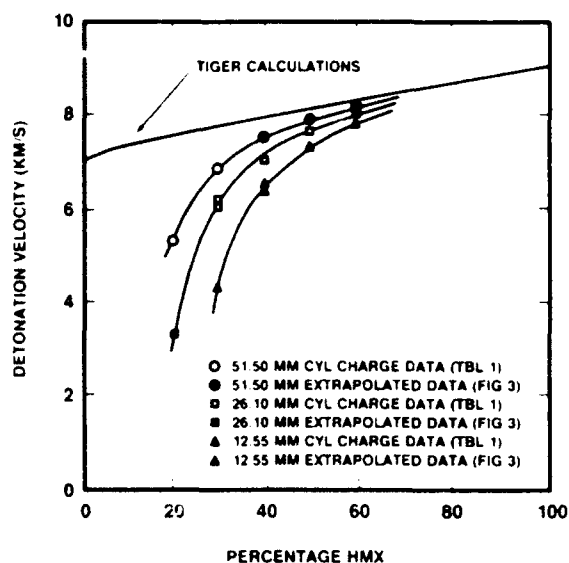


Figure 5. Detonation Velocity as a Function of Percentage HMX for Diameters of 12.55 mm, 26.10 mm, and 51.50 mm.

Figure 3. Because of the limited data and large uncertainties in velocity at failure, no attempt has been made in Figure 5 to establish the detonation failure boundary. As noted before, qualitative agreement with the behavior described in Figure 1 is demonstrated.

In Figure 6 an estimate of the detonation failure envelope was made by constructing a curve between the regions of detonation and detonation failure. The curve shown was constructed assuming that 100 percent HMX fails at less than 1-mm diameter and that this limit dominates the behavior of the curve for high-percentage HMX mixtures. The 40/60 data have been included here even though prior analysis indicated that the measured detonation velocities are anomalously low relative to the other mixtures. Preference has been given to the conical charge data over the cylindrical charge data in constructing the curve. Note that two cylindrical charge data points indicating failure lie well within the detonation region. These points were previously identified in Figure 3. It is felt that the curve in Figure 6 is reliable to within  $\pm 15$  percent for mixtures containing more than 20 percent HMX. For mixtures containing less than 20 percent HMX, the curve can be treated only as an estimate. A precise determination

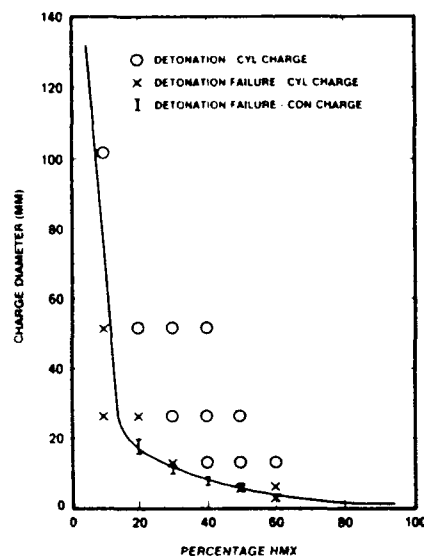


Figure 6. Definition of Detonation Failure Envelope.

of the failure diameter of pure emulsion would remove much of the uncertainty in this region.

### Diameter Effect Analysis

The diameter effect analysis of Campbell and Engelke<sup>8</sup> was applied to the 50/50 mixture data in Figure 3. Campbell and Engelke determined that the following functional form was descriptive of the behavior of a large number of heterogeneous explosives in a cylindrical geometry,

$$D = D_i [1 - A/(R - R_c)] \quad (2)$$

where  $D_i$  is the detonation velocity at infinite diameter,  $R$  is the charge radius, and  $A$  and  $R_c$  are length parameters. The 50/50 mixture was selected for this analysis because the data were sufficient to provide a reasonable definition of the downward concavity of the  $D$  vs  $1/d$  relationship near detonation failure. Four points on the  $D$  vs  $1/d$  curve from Figure 3 were selected and fit by Equation 2. The results are shown in Table 2 where the values of  $D/D_i$  calculated from the fit are compared with the experimentally determined values. As shown, a reasonable fit is achieved.

If Equation 2 is descriptive of all other HMX/emulsion mixtures, then a generalized description or model of the diameter effect for all HMX/emulsion mixtures should be achievable by defining the dependence of  $A$



Table 2. Results of Diameter Effect Analysis  
( $A = .25$ ,  $R_c = 2.8$ ,  $D_i = 8.098$  km/s)

Data			Eq. 2	Percent Error
R(mm)	D(km/s)	D/D <sub>i</sub>	D/D <sub>i</sub>	
3.27	3.877	.479	.468	-2.2
4.17	6.607	.816	.817	-
6.28	7.430	.918	.928	1.1
13.05	7.768	.959	.976	1.8

and  $R_c$  on percentage HMX. This generalized model would require additional experimental data to better define the behavior of mixtures other than 50/50 in the region of downward concavity in plots of  $D$  vs  $1/d$ .

### Plate Dent Tests

Plate dent experiments were conducted to provide an estimate of CJ pressure for 40/60 and 10/90 mixtures. A pressure of 234 kbar was determined for a 41.28 mm diameter 40/60 charge which agrees very well with the TIGER calculated pressure of 237 kbar. A test of 10/90 mixture at 101.6 mm diameter resulted in an estimated pressure of 74 kbar, well below the theoretical value of 180 kbar. It is quite likely that the behavior of the 10/90 charge was strongly influenced by diameter effects, while, as can be seen from Figure 3, the 40/60 charge would be expected to be near ideal velocity and pressure.

### SUMMARY AND CONCLUSIONS

Sufficient velocity mixture diameter data were generated to define the behavior of HMX/emulsion mixtures over the range of 20 to 50 percent HMX. A qualitative description of the behavior was predicted over the entire range of mixtures. The main conclusions of this research are summarized as follows:

- (1) At a given diameter, an increase in HMX loading results in an increase in detonation velocity. As HMX loading increases, the failure diameter decreases and the detonation velocity at failure increases. The trend in velocity at failure was evident in the data but

precise measurements of velocity at failure were not obtained. The qualitative behavior predicted in Figure 1 has been confirmed.

- (2) The diameter effect on detonation velocity for HMX/emulsion mixtures is adequately described by the Campbell-Engelke model. This was clearly demonstrated for the 50/50 mixture and the trend of downward concavity on the  $D$  vs  $1/d$  curve was observed for other mixtures.
- (3) Physical properties of the HMX/emulsion mixtures varied (soft grease, stiff paste, putty, solid), depending on the HMX loading, HMX particle size and shear history.

### REFERENCES

1. Johansson, C. H. and Persson, P. A., *Detonics of High Explosives*, Academic Press, London, England, 1970, pp. 81-156.
2. Lee, J., *The Effect of Microballoon Size on Detonation Behavior of Emulsion Explosives*, Masters Thesis, New Mexico Institute of Mining and Technology, Socorro, NM, 1987.
3. Yoshida, M.; Iida, M.; Fujiwara, S.; Kusakabe, M.; and Shiino, K., "Detonation Behavior of Emulsion Explosives Containing Microballoons," *Eighth Symposium (International) on Detonation*, Albuquerque, NM, Jul 1985, pp. 171-177.
4. Hattori, K.; Fukatsu, Y.; and Sakai, H., "Effect of the Size of Glass Microballoons on the Detonation Velocity of Emulsion Explosives," *J. Ind. Explos. Soc. Japan*, Vol. 43, 1982, pp. 295-309.
5. Renick, J. D., et al., *Detonation Characteristics of Mixtures of HMX and Emulsion Explosives*, AFWL-TR-88-106, Air Force Weapons Laboratory, Kirtland AFB, NM, Apr 1989.
6. Oxley, J. and Griffith, G., private communication, May 1987.
7. Craig, B. and Lee, J., private communication, Jul 1985.

8. Campbell, A. W. and Engelke, R., "The Diameter Effect in High Density Heterogeneous Explosives," *Sixth Symposium (International) on Detonation*, Naval Weapons Center, China Lake, California, 1976, pp. 642-652.

### DISCUSSION

G. A. LEIPER,  
ICI Explosives  
NEC, Stevenson, KA 20, 3LN, UK

The use of conical charges to estimate failure diameters, and the diameter dependence of detonation velocity, assumes that conical flow approximates that in a right cylinder and that the detonation wave instantaneously adjusts as the cone diameter alters. Can you comment on the likely errors the case of a cone technique will have on your results, in particular the failure diameter and velocities obtained?

### REPLY BY J. D. RENICK

While it was not mentioned in the presentation, all conical charge data were adjusted by the assumption that an overshoot in propagation of detonation along the charge axis of up to one charge diameter, measured at the axial position of apparent failure of detonation, could occur. This assumption was based on conversations with J. Lee (CETR) regarding information provided by B. Craig. For a cone angle of three degrees, this results in an adjustment in the apparent failure diameter of plus 2.6 percent.

### DISCUSSION

WALTER B. SUDWEEKS, Ireco Inc.  
3000 West 8600 South  
West Jordan, Utah 84088

What changes in data would you expect to see with a change in emulsion formulation such as all AN, etc., and do you have plans to repeat this work with other emulsion formulations?

### REPLY BY J. D. RENICK

I would expect that for an all-AN emulsion, we would see a noticeable increase in the detonation velocity for HMX/emulsion mixtures containing low fractions of HMX (less than 20 percent) for diameters smaller than that at which the curve describing detonation velocity vs. inverse charge diameter makes the break from linear to downward concavity. For higher fractions of HMX this effect would be less noticeable. In retrospect, it would have been preferable to use an all-AN emulsion in this research but at the time, we had not recognized the improved detonation performance of all-AN emulsions relative to emulsions containing other salts (such as CN and SN).

### DISCUSSION

I. B. MISHRA, Kanan Associates Inc.  
2925 Churchville Rd.  
Churchville, MD 21028

You use a very high shear method to form emulsion. I would like to tell you that we found a "gentle persuasion" technique and have been rather successful in making emulsions with lesser void content. The method is to use an emulsifying agent and then add a cosolvent—as is common in tertiary extraction of crude oil by microemulsion technique. Have you tried this technique?

### REPLY BY J. D. RENICK

Because of the time constraints of this research program, we had little opportunity to explore alternative processing methods. We did not investigate the "gentle persuasion" approach, but it sounds very interesting.

# THE PROSPECTS FOR COMPOSITE EXPLOSIVE

Guo Yuxian  
Gansu Research Institute of Chemical Industry  
P.O. Box 111, Lanzhou  
Gansu, CHINA

*This paper briefly reviews the research of high explosives. The author believes that the individual explosives and CHNO composite explosives have very little possibility of being used to obtain an explosive with performances better than HMX and applicable in practice. We suggest that the high energy composite explosive is an important direction of high explosive.*

## INTRODUCTION

During the past 30 years scientists have made great efforts in the region of high explosives research to find an applicable explosive with performances better than HMX. But all attempts have been unsuccessful, and many researchers have taken a pessimistic view of the prospects for finding such an explosive.

In this paper, the research in the field of high explosive development was briefly reviewed. We provide some frank views, and consider that the high energy composite explosive is a most promising direction.

## THE RESEARCH OF INDIVIDUAL EXPLOSIVES

Currently, the best explosive used in practice is HMX whose  $D = 9,100$  m/sec,  $P = 38$  Gpa,  $Q = 1.4$  Kcal/g, and  $d = 1.91$  g/cm<sup>3</sup>. Scientists have made great efforts to develop explosives with better performances and have synthesized nearly 10 compounds. Their performances reached  $D = 9,500$  m/sec,  $P = 42$  Gpa,  $Q = 1.6-1.7$  Kcal/g, and  $d = 2.0-2.1$  g/cm<sup>3</sup>. Unfortunately, their stability (thermal sensitivity, storage stability, etc.) is not satisfactory. They only possess theoretical significance.

The principal parameters determining the performances of individual explosives are their energy and density. The highest energy of CHNO explosive is about 1.7 Kcal/g, when

the OB (oxygen balance) is zero, in which the energy is highest, and its density is about 2.1 g/cm<sup>3</sup>. In comparison with these data, HMX has reached a better level. Smith<sup>2</sup> pointed out that there is little possibility in the short term of obtaining an applicable explosive with performances better than HMX. Many scientists agree with him.

In the 1960s, scientists started to investigate the explosives containing B, -NF<sub>2</sub> in molecules and have, since then, synthesized some compounds. The performances of those compounds in comparison with that of CHNO explosives are as follows. When the OB is the same, the explosion energy of the former is higher than that of the latter, and the density of the former is slightly lower than that of the latter; when both the OB and density are the same, the detonation velocity of the former is slightly lower than that of the latter.

The most important problem of the explosives containing B, -NF<sub>2</sub> is that the compounds with good OB are hardly synthesized and almost all of these compounds are less stable. Scientists have actually given up efforts to investigate such compounds as high explosives.

## THE RESEARCH OF COMPOSITE EXPLOSIVES

The research of composite explosives was also started in the 1960s. The advantage of

these explosives is that the oxidizer or compounds with positive OB can be mixed with fuel or compounds with negative OB according to the best proportion to obtain ideal performances. Because the oxidizer and fuel do not exist in the same molecule, it is possible to expect better stability.

The composite explosive is called "inter-molecular explosive." Since the particle with diameter of  $1\text{ }\mu\text{m}$  still contains about  $10^{11}$  molecules, we considered it more suitable to call this system a "composite explosive." If the mixture is uniform such as a liquid solution or a solid solution, then it can be called a "homogeneous composite explosive." If the system is a mixture of solid particles or suspended of solid particles in liquid, it can be called a "heterogeneous composite explosive."

Efforts put into the research of composite explosives are much smaller than those of

individual explosives. Only some fundamental research has been carried out. However, some significant results have been obtained.<sup>3-13</sup>

We did some research about this system in 1981-1983.<sup>10,11</sup> We developed a method for the preparation of superfine particles of explosives, studied some characteristics of composite explosives composed of superfine particles, and proposed a mechanism for their detonation reactions. In our investigations, the bis-(trinitroethyl)nitramine "(1)" was selected as a typical positive OB explosive, and was mixed with TNT, TATB, or HMX. The main results are shown in Table 1 and Figure 1. The method and reproducibility measured detonation parameters and particle size (see Reference 11).

From the results listed in Table 1, it can be seen that the detonation velocity of superfine systems is about 300 m/sec higher than

Table 1. The Performances of Composite Explosives

SYSTEM	$\bar{d}$	$D/\rho_0$	$P/\rho_0$	R%	L
(1)81.8/TNT18.2	51X5	8098/1.792	28.6/1.785	0	----
" "	0.97	8432/1.792	30.6/1.792	41.3	0.10
(1)77.0/TATB23.0	0.44	8686/1.881	40.3/1.876	41.0	0.09
(1)57.0/HMX43.0	0.73	9046/1.883	39.6/1.878	50.8	0.15

where  $\bar{d}$ ---mean diameter of particles,  $\mu\text{m}$   
 $D$ ---detonation velocity, m/sec  
 $P$ ---detonation pressure, Gpa  
 $R\%$ ---percentage of composite explosive reacted  
 $L$ ---thickness of diffusion layer,  $\mu\text{m}$   
 $\rho_0$ ---charge density,  $\text{g}/\text{cm}^3$

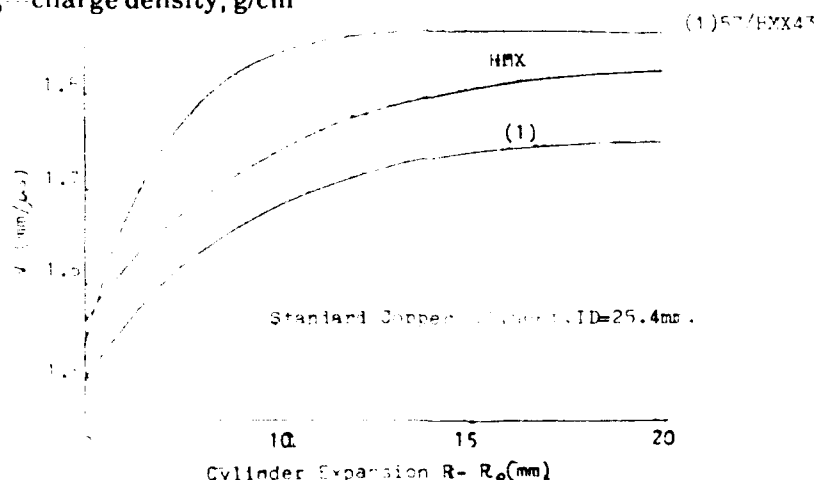


Figure 1. The Cylinder Test Results

that of coarse particle systems. The detonation pressure of the former are also higher than that of the latter. In the detonation zone, the percentage of reacted explosives in superfine systems is about 50 percent; according to the reaction mechanism of diffusion control the thicknesses of diffusion layer of superfine systems are 0.10 - 0.15  $\mu\text{m}$ , which shows that when the particle diameter is 0.20 - 0.30  $\mu\text{m}$ , the components of composite explosive will react completely in the detonation zone.

The results of cylinder tests show that at  $R - R_0 = 8, 14, 19$ , the wall energy of (1)/HMX system is about 13 percent, 8 percent, and 6 percent higher than that of HMX and about 25 percent, 17 percent, and 14 percent higher than that of (1), respectively.

The key to obtain a composite explosive with excellent performance is that the components must possess high density and high energy. For example, if HMX was mixed with hexanitroethane and their superfine system was prepared, the detonation velocity would be 9,400 m/sec, and wall energy of cylinder test would be as high as 130 percent of that of HMX.

The above results are encouraging but, unfortunately, the stability of bis(trinitroethyl)nitramine(1) and hexanitroethane are not satisfactory for practical application. According to the opinion of chemists, the high energy positive OB explosives have no possibility to possess the satisfactory stability for application. Therefore, the prospects are not good for obtaining some CHNO composite explosives with excellent performances for practical application.

## THE PROSPECTS OF HIGH ENERGY COMPOSITE EXPLOSIVES

Earlier, high explosives research was concentrated on improving the detonation parameters. Neither the individual explosive nor the composite explosive were successful. Later, scientists turned to the high energy systems and expected to make a breakthrough in this field. As discussed above, the individual explosive with high energy actually was not successful. However, the prospects of the

high energy composite explosive still needs to be confirmed.

The highest energy of energetic materials are estimated and are listed in Table 2.

Table 2. Highest Energy of Energetic Materials

SYSTEM	Q Kcal/g
(CH)-NO <sub>2</sub>	1.7
(Al)-NO <sub>2</sub>	3.2
(B)-NO <sub>2</sub>	2.7
(Be)-NO <sub>2</sub>	4.6
(CH)-NF <sub>2</sub>	1.7
(Al)-NF <sub>2</sub>	2.2
(B)-NF <sub>2</sub>	3.4
(Be)-NF <sub>2</sub>	4.7

The systems listed in Table 2 all are zero OB. Among these systems, the (CH)-NO<sub>2</sub> system has been obtained in individual and composite explosives whose energy had reached the highest energy. As described above, in other systems it is difficult to obtain an individual explosive with energy near the highest level. But composite explosives with high energy can be prepared.

One of the cruxes of the matter is the effects of energy of explosives to accelerate metal, especially for heterogeneous composite explosives whose energy is partially delivered outside of the detonation zone. We designed some experiments to investigate this problem.<sup>14</sup>

## The Effects of Energy

The experiments and results made by our laboratory are as follows:

(1) was dissolved in CCl<sub>4</sub>, and the solution was slowly added to petrol containing suspending Al powder. (1) was separated out and mixed with Al powder. Then the mixture was filtrated and dried to remove the liquid. By this process, the composite explosives with different proportions of (1) and Al were prepared. The particle size of (1) is about 20  $\mu\text{m}$ , and that of Al is about 10  $\mu\text{m}$ .

Those composite explosives were used as the charge to load shaped charge which was used for penetrating the petroleum wall. The

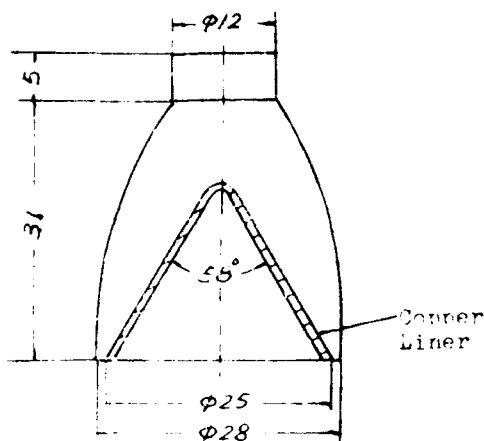


Figure 2. Schematic Diagram of Shaped Charge

Table 3. Explosion Heat of Explosives

Explosives	Q Kcal/g	
	Exp.	Cal.
(1)	1.21	1.16
(1)86.1/Al13.9	2.06	2.06
(1)81.9/Al18.1	2.17	2.19
(1)71.4/Al28.6	2.41	2.42

Q cal. method.<sup>14</sup>

shaped charge is shown in Figure 2 and the performances of explosives and deepness penetrated steel plate are shown in Tables 3 and 4.

These results showed that the penetration deepness of (1)88/Al12 was largest, was much deeper than that of the charge without Al, and exceeded that of PB-HMX. As is known, the penetration deepness of a shaped charge strongly depends on the detonation parameters of the explosive. The detonation parameters of charges with Al were lower than that of the charges without Al. But the explosion heat of the former is higher than that of the latter. The increase of penetration deepness illustrated that the energy has effects on the penetration.

McGuire<sup>12</sup> published results of cylinder tests in which the charges loaded were TNM, TNM + C, and TNM + C + Al. Partial results are listed in Figure 3. Particle sizes used were C - < 40  $\mu$ m, Al - 5  $\mu$ m.

From McGuire's results it can be seen that the wall energy of cylinder tests with TNM + C and TNM + C + Al were higher than those of TNM. We think that the increase of wall energy is due to the fact that the energy of the former is higher than that of the latter, and the energy was contributed to accelerate metal.

The particle size of charges loaded in shaped charge and cylinder were much larger than that of superfine systems listed in Table 1. Consequently, it is evident that the quantity of energy delivered by the reaction between oxidizer and Al in the detonation zone was very small. Most of the energy was delivered outside the detonation zone. Increase of penetration deepness and wall energy illustrated the effects of energy delivered outside

Table 4. Deepness of Steel Plate Penetration

Explosive	g/cm <sup>3</sup>	TMD%	D m/sec	P Gpa	Q Kcal/g	Deep mm
(1)	1.85	93.6	8402	32.5	1.16	101
(1)88/Al12	1.89	91.8	8396	32.2	1.89	109
PB RDX*	1.77	98.1	8302	32.7	1.31	98
PB HMX**	1.83	96.1	8646	35.8	1.46	105

$\rho_0$ , D, P Exp Q Cal

\*96.5% RDX, Q Exp

\*\*97.0% HMX, Q Exp.

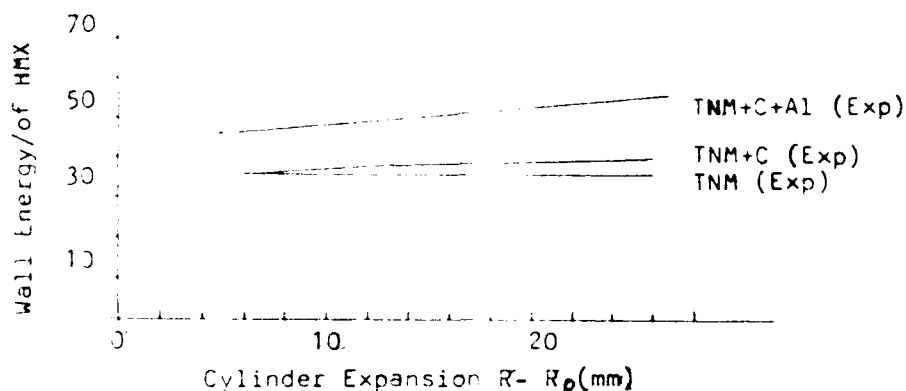


Figure 3. McGuire's Results<sup>12</sup>

the detonation zone. These results merit attention.

It is not very clear whether or not the energy is completely delivered in the duration of driving metal. It is possible, because the particle size of explosives in the above experiments were so large, that the energy cannot be delivered completely during the duration of driving metal; therefore, we can suppose that the ability to drive metal will be increased with the decrease of particle size of explosives.

### The Oxidizer of Composite Explosives

Another key issue is whether the stability of the oxidizers used in high energy composite explosives could be satisfactory for use.

The positive OB explosives or oxidizers used in CHNO composite explosives must have high density and high energy, otherwise the high ability of driving metal cannot be realized. It is well known that the energy of chemical reaction is decided by the difference of formation heat of products and reactants. The lower the formation heat of reactants, the higher the reaction heat.

There are many factors deciding the stability of a compound, one of them is the high heat of formation. For example,  $\text{NH}_4\text{NO}_3$  and  $\text{NH}_4\text{ClO}_4$  have high formation heat, so their stability is satisfactory, and they have been used as explosives for many years. They are

often used in mixtures with fuel or negative OB explosives and the compositions are adjusted to reach the  $\text{CO}_2$  balance. Their explosion heat is only 1.00 - 1.20 kcal/g, corresponding to 60-70 percent of the highest energy of CHNO explosives. The ability of both of them to drive metal and detonation parameters is low. It is due to the fact that the formation heats of  $\text{NH}_4\text{NO}_3$  and  $\text{NH}_4\text{ClO}_4$  compose a rather large proportion of their explosion heat. In high energy composite explosives, the formation heat of reactants is not significant in the total energy, so the positive OB explosives or oxidizers with fairly high formation heat can be used. The demands on their density and energy are lower and the range of their selection is wider than that of CHNO composite explosives. Therefore, it is possible to obtain some compounds with satisfactory stability to the demands of application.

### The Research Direction of High Explosives

Table 2 shows that the energy of high systems are about 2 to 3 times higher than that of CHNO explosives. Therefore, it is very promising to obtain high ability of metal driving with high energy composite explosives.

From the above experimental results and discussion, we suggest that the high energy composite explosive is a promising direction of high explosive development. It can be expected

that in the near future an applicable composite explosive with performance better than CHNO explosive can be obtained and used in practice.

There are some technical problems to be resolved in the research of composite explosives. To obtain a suitable oxidizer is always a significant task. Chemists can do much work to push forward the research of high explosives.

## SUMMARY

Reviewing the research of high explosives, we suggest that CHNO individual explosives, high energy individual explosives, and CHNO composite explosives have very little possibility of obtaining an applicable explosive with performances better than HMX. The experimental data obtained from the research of composite explosives composed of positive OB explosives and Al powder showed that the energy delivered outside the detonation zone can be used by the reflected waves for increasing the ability of driving metal. It is estimated that the highest energy of energetic materials composed of the fuels, such as Al, B, Be, and the oxidizers with  $\text{-NO}_2$   $\text{-NF}_2$ , are 2 to 3 times as high as that of CHNO explosives. The positive OB explosives or oxidizers used in high energy composite explosives are discussed. We considered that the stable positive OB explosive or oxidizer could be expected, because they could be selected in a wider range. So we concluded that the high energy composite explosive is a promising direction for research of high explosives. It could provide a possibility of obtaining explosives with higher ability of driving metal than that of CHNO explosives, and it could be applied in practice.

## ACKNOWLEDGEMENT

The author wishes to thank Professor Xu Kang for his help in preparing this paper

## REFERENCES

1. Zhou Faqi, "Synthetic Chemistry of Explosives," National Defense Industry Publishing House, Beijing, China, 1984
2. Smith, L. C., UCRL 52396, 1977, 11
3. Price, D.; Clairmont, Jr., A. R.; Erkman, J. O.; and Edwards, D. J., "Ideal Detonation Velocity of Ammonium Perchlorate and Its Mixture with H.E.," NOLTR 68-132, AD 683298.
4. Apin, A. Ya.; Voskoboinikov, I. M.; and Sonova, G. S., *PMTF*, No. 5, 1963, p. 115.
5. Price, D.; Clairmont, Jr., A. R.; and Erkman, J. O., *Combustion and Flame*, Vol. 20, 1973, p. 389.
6. Finger, M.; Hornig, H. C.; Lee, E. L.; and Kutty, J. W., *Proceedings of the Fifth Symposium (International) on Detonation*, 1970, p. 137.
7. Moulard, H.; Fauguignon, C.; Lichtenberger, M.; and Lomard, J. M., *H.D.P. Symposium on Behavior of Dense at High Dynamic Pressure*, Paris, UCRL-Trans 11405, 1978, pp. 27-31.
8. McGuire, R. R. and Ornellas, D. L., *Propellants and Explosives*, Vol. 4, No. 2, 1979, p. 23.
9. Stinecipher, M. M., *Proceedings of the Seventh Symposium (International) on Detonation*, 1981, p. 733.
10. Guo Yuxian, Peng Guoshu, Song Jialiang, Zou Quanqing, Wang Aiqin, Xu Laibin, and Zeng Min, "The Experimental Study of Heterogeneous Composite Explosives," Oct 1983 (Unpublished).
11. Guo Yuxian, Peng Guoshu, Wang Aiqin, Song Jialiang, Zou Quanqing, and Xu Laibin, "The Detonation Reaction of Heterogeneous Composite Explosive," *Proceedings of the Eighth Symposium (International) on Detonation*, 1985, p. 1011.
12. McGuire, R. R. and Finger, M., "Composite Explosives Metal Acceleration. The Effect of Detonation Temperature," *Ibid*, p. 1018.
13. Akst, I. B., "Intermolecular Explosives," *Ibid*, p. 1001
14. Guo Yuxian, "The Research of Formation Theory of Jet Produced by Shaped Charge," *The Scientific Conference of Chinese Ammunition Society*, Chong Qing, China, Oct 1981



# DETONATION VELOCITY AND PRESSURE OF THE NON-IDEAL EXPLOSIVE AMMONIUM NITRATE

A. Miyake  
Department of Safety Engineering  
Yokohama National University  
156 Tokiwadai, Hodogaya-ku  
Yokohama, JAPAN

and

A. C. van der Steen and H. H. Kodde  
Prins Maurits Laboratory TNO  
P.O. Box 45  
2280 AA Rijswijk  
THE NETHERLANDS

*The detonation velocity and pressure of low density prilled ammonium nitrate were measured in steel tubes with different diameters and wall thicknesses. It was found that the tube diameter has a much larger influence on the non-ideal behavior of the detonation velocity and pressure than the confinement. For a diameter of 300 mm, the detonation velocity and pressure are  $D=3.95$  km/s and  $P=3.4$  GPa, which values coincide with the ideal detonation parameters for ammonium nitrate, as predicted by the TIGER code.*

## INTRODUCTION

Ammonium nitrate (AN) is an explosive known for its non-ideal detonation behavior. This is shown, for example, by the detonation velocity, which does not easily reach theoretically predicted values. Explosives behave non-ideally between the critical diameter ( $d_c$ ), below which a steady state detonation wave cannot be sustained, and the minimum diameter ( $d_m$ ), above which the detonation is ideal. AN is a typical "non-ideal" explosive because it has a large value for  $d_m$  and a relatively small value for  $d_c$ . For most practical conditions, it will never reach the ideal behavior as predicted by thermo hydrodynamic theory.

Generally, the non ideal detonation behavior is explained by the relatively low decomposition rate of AN, which causes a wide reaction zone, in combination with lateral heat

losses and rarefaction waves, which extinguish the decomposition reactions.<sup>1</sup>

It is the purpose of these investigations to obtain a better understanding of the non-ideal detonation behavior of AN. A series of experiments were carried out to study the influence of the diameter and the confinement of the explosive charge on the detonation properties in the non-ideal region. In a previous paper, the detonation velocity was considered, and the results will be repeated here shortly.<sup>2</sup>

A readily available, highly porous type of AN (ANFO quality prills) with well-defined properties and the additional advantage that, due to the high sensitivity, the dimensions of the experiments could be kept within reasonable limits was used in these investigations. It consists of low density prills with a diameter between 1.0 and 2.8 mm. The purity is about 99 percent (the sample is treated with

0.8 percent of anticaking agent). The loading density is about  $850 \text{ kg/m}^3$ .

First, the detonation velocities of AN measured in steel tubes are presented. Next, the results for the detonation pressure measurements are given. The results are compared to predictions made with the thermohydrodynamic TIGER code.<sup>3</sup>

The ideal detonation velocity of AN has been calculated by the thermohydrodynamic theory describing the state attained behind the detonation front. We used the TIGER code in combination with the JCZ3 equation of state to calculate the ideal detonation velocity and Chapman-Jouguet pressure. The results for a density of  $850 \text{ kg/m}^3$  are:  $D = 4.0 \text{ km/s}$ , and  $P_{CJ} = 3.5 \text{ GPa}$ . More detailed information about these calculations can be found in Reference 2.

## DETONATION VELOCITY

### Experimental

In all experiments, the AN was confined in steel tubes. The inner diameters varied between 50 and 300 mm, and the wall thicknesses between 5 and 30 mm. The length of the tube was 1 m, except for the large diameter experiments (60 cm). The AN was initiated by a booster over the whole cross section of the tube. The booster had a thickness of about 50 mm and was made of a plastic explosive (PETN/oil, 88/12,  $\rho = 1550 \text{ kg/m}^3$ ) with a detonation velocity of about  $7.5 \text{ km/s}$ . For the small diameter tubes (50-100 mm), a 10 g pellet of pressed tetryl was used to initiate the booster. To obtain a more or less flat detonation wave for the larger diameters, multi-point initiation techniques using detonation cords were used to initiate the booster.

The shock/detonation velocities were measured with a continuous velocity probe consisting of resistance wire (271 ohm/m) with a skip wound nylon insulation inserted in a thin walled stainless steel tube (i.d. = 1.0 mm, o.d. = 1.2 mm). The probe is mounted in the center of the tube, and a constant current (100 mA) is fed through the probe leading to a voltage drop over the resistance wire proportional to its length. When a shock wave

passes alongside the probe, the current will be short circuited and, from the voltage change as a function of time, the shock velocity can be calculated. The accuracy of the velocities is about 2 percent.

### Results

Two series of steel tube tests were carried out with the AN prills. The results are summarized in Figure 1.

In the first series, the effect of confinement on the detonation velocity was investigated. Steel tubes with a constant inner diameter of 100 mm and wall thicknesses between 5 and 29 mm were used. In all tests, an incoming shock wave with a velocity of about  $4.5 \text{ km/s}$ , the effect of the booster, was observed. This shock wave velocity decreases to a constant value in about 30 cm. A constant detonation velocity was measured for the last 70 cm for all wall thicknesses, except for a thickness of 5 mm. Several experiments were carried out at this wall thickness: in some cases a constant velocity was observed over the last 30 to 40 cm ( $1.7 \text{ km/s}$ ), while in other experiments, the shock wave decayed to a velocity close to the sound velocity of AN. Probably, a 5 mm wall thickness is close to the critical condition to sustain a detonation wave in a 100 mm tube. Between 8 and 20 mm, the detonation velocity increases from 2.2 to  $3.1 \text{ km/s}$ . However, at wall thicknesses above 20 mm, the detonation velocities converge to a constant value of about  $3.1 \text{ km/s}$ . This value is still far below the theoretically predicted values at a density of  $850 \text{ kg/m}^3$ , which is  $4.0 \text{ km/s}$ .

In the second series of experiments, the diameter of the steel tube was varied between 49 and 303 mm, while the wall thickness was kept constant at 10 mm. Although AN could not sustain a detonation wave in a tube, of 49 mm diameter, no AN was recovered after the experiment. The tube did not fragment over the total length, but was fragmented like a peeled banana. Between 100 and 303 mm, all tests showed a steady state detonation wave, the velocity increasing from 2.6 to  $3.95 \text{ km/s}$ .

In Figure 1, the dashed line indicates the ideal detonation velocity ( $4.0 \text{ km/s}$ ) as calculated with the TIGER code, using the

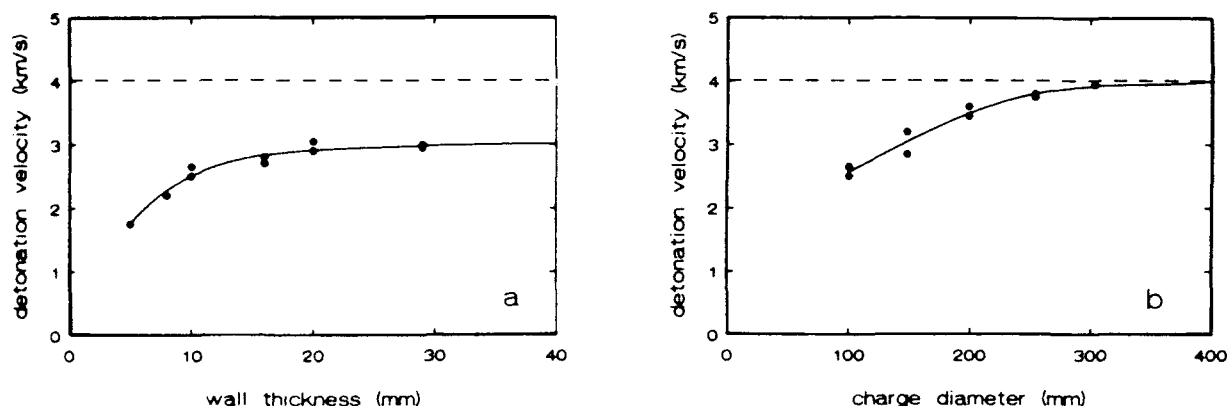


Figure 1. Detonation Velocity as a Function of a) Wall Thickness (Charge Diameter is 100 mm), and b) Charge Diameter (Wall Thickness is 10 mm). The dotted line indicates the value for an ideal detonation.

JCZ3 EOS. Although a slight increase is still observed between 254 and 303 mm, it appears that a nearly ideal detonation for AN has been reached. In fact, 3.95 km/s is the highest detonation velocity measured for AN up to now.

Additional experiments were performed with a tube diameter of 200 mm and a wall thickness of 20 mm. The detonation velocity was about the same (3.6 km/s) as found for the 100 mm wall thickness. It seems that each diameter has an upper limit in the detonation velocity that could be attained (3.0 km/s for 100 mm and 3.6 km/s for 200 mm). This upper limit is also reached for weaker confinements at higher diameters.

## DETONATION PRESSURE

### Experimental

From preliminary tests, we learned that it was not possible to use manganin pressure gauges in the AN directly. To minimize the effect of short-circuiting, we used a gap of 20 mm PMMA between the AN and the gauge. In these investigations, 50 Ohm, commercially available gauges were used. The piezoresistive coefficient was taken  $K = 2.92 \times 10^{-2}$  GPa<sup>-1</sup>.<sup>4</sup>

The dimensions of the steel tubes were the same as those used for the detonation velocity measurements. Using tubes with different lengths, we found that at least 750 mm was needed to obtain a steady detonation. At

shorter distances, the effect of the booster, a slowly decreasing pressure, is observed (e.g. for i.d. = 100 mm, o.d. = 140 mm, the pressure is 3.0 GPa after 350 mm and 2.5 GPa after 600 mm). This transition point to a stable detonation lies further away from the booster than would be expected from the detonation velocity experiments.

### Results

The results of the pressure measurements for different tube diameters and different confinements are summarized in Table 1 and presented in Figure 2.

To correlate the pressures observed in the PMMA to the detonation pressures in the AN, we had to know the attenuation of the shock wave in the PMMA. Due to experimental limitations only at the smallest tube diameter a shock wave through the plexiglas and generated by detonating AN (tube and PMMA diameter are 100 mm) could be recorded with a

Table 1. Detonation Pressures for Low Density Prilled AN as a Function of the Inner and Outer Diameter of the Tube

i.d. (mm)	o.d. (mm)	P (PMMA) (GPa)	P (AN) (GPa)
100	120	2.7	2.0
100	140	3.2	2.5
150	170	3.3	2.6
254	274	4.1	3.4

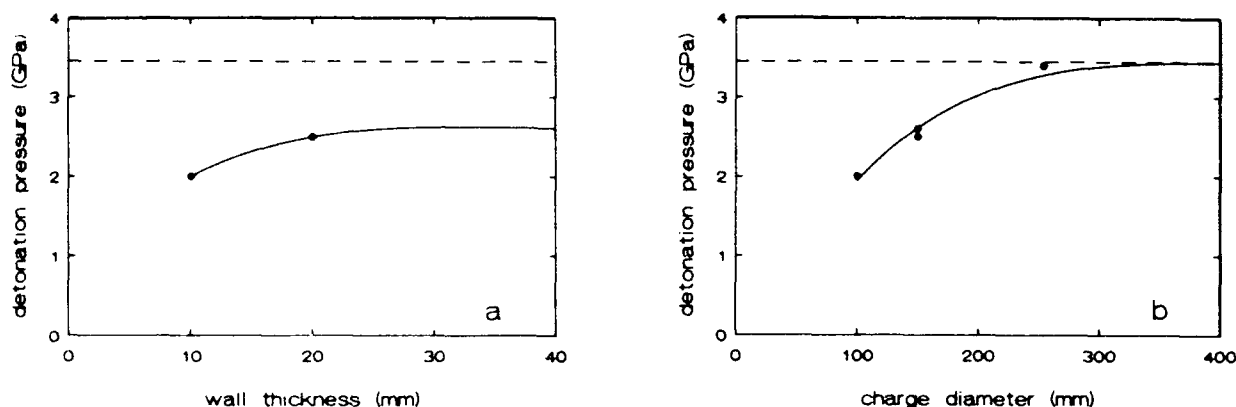


Figure 2. Detonation Pressure as a Function of a) Wall Thickness (Charge Diameter is 100 mm), and b) Charge Diameter (Wall Thickness is 10 mm). The dotted line indicates the value for an ideal detonation.

streak camera. These experiments revealed that there is hardly any attenuation of the shock wave velocity in the first 20 mm of plexiglas. Also, the results from the manganin pressure measurements at this diameter coincide with the pressure in the plexiglas as calculated from the shock velocity.

For this reason it is assumed that the gauge pressure after 20 mm PMMA are the same as at the PMMA/AN interface. The detonation pressures are obtained using a relation derived by Duff et al. using the impedance-mismatch technique and the acoustic approximation for the detonation gases.<sup>5</sup>

$$\frac{P_{AN}}{P_P} = \frac{1}{2} \left( \frac{\rho_0 D}{\rho_P U_P} + 1 \right)$$

Here  $\rho_0$  and  $\rho_P$  are the initial densities of the AN, and the plexiglas,  $D$  ( $P_{AN}$ ) is the measured detonation velocity (pressure) of AN under the given conditions, and  $U_P$  ( $P_P$ ) is the (constant) shock velocity (pressure) in the PMMA.

In the tubes with an inner diameter of 100 mm, the peak pressures increase from 2.0 to 2.7 GPa with an increase of the wall thickness from 10 to 20 mm. As the wall thickness is kept constant at 10 mm, the peak pressures increase from 2.0 to 3.4 GPa with increasing diameter of the tube. The dashed line indicates the ideal detonation pressure

calculated with the TIGER code and the JCZ3 EOS, which is 3.5 GPa.

## DISCUSSION

These experiments with low density AN prills show that the ideal detonation conditions could be attained if the diameter of the AN charge is large enough. For this type of AN, a diameter of about 250 mm is needed to reach these conditions. The results also show that the TIGER code, in combination with the JCZ3 EOS, gives very accurate and reliable predictions of the ideal detonation conditions of AN.

In Figure 3, the non-ideal detonation pressures are given as a function of the non-ideal detonation velocities. A linear relation exists between these two parameters. A linear relation is certainly not found as only ideal detonation conditions, for different densities, are compared. The cross in Figure 3 denotes the conditions for a density of 850 kg/m<sup>3</sup>, and an extrapolation of the non-ideal experimental results nearly coincides with this point.

Hopefully these investigations could help to give a more accurate theoretical description of non-ideal detonations in the future.

It is important to note that the results presented in this paper are obtained for one type of AN. It is well-known that the detonation properties of different kinds of AN can vary considerably. For example, we could

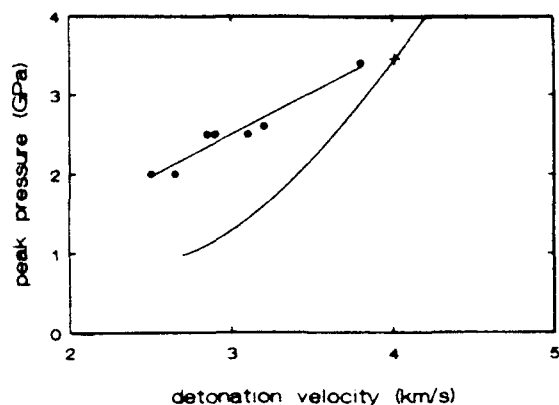


Figure 3. Relation Between the Non-Ideal Detonation Velocity and Pressure (for a Constant Density) and Between the Ideal Detonation Velocity and Pressure (Varying Density)

not detonate high density prills or a crystal type of AN in tubes with a diameter of 100 mm and a wall thickness of 10 mm. However, the general trends are certainly applicable to other "non-ideal" explosives.

## ACKNOWLEDGEMENTS

The authors wish to express their thanks to the people of MSS (Mineur en Sappeur School of The Netherlands) for their help and permission to use their explosion facilities.

## REFERENCES

1. Cook, M. A., "The Science of High Explosives," Rheinhold, 1958.
2. Miyake, A.; van der Steen, A. C.; and Kodde, H. H., "Detonation Velocities of the Non-Ideal Explosive Ammonium Nitrate," *Proceedings of the 19th International Conference of ICT on Combustion and Detonation Phenomena*, Karlsruhe, BRD, 1988; also to be published in *Propellants, Explosives, Pyrotechnics*, 1990.
3. Cowperthwaite, M. and Zwisler, W. H., "TIGER Computer Program Documentation," SRI Publ. No. Z106, Stanford Research Institute, 1973.
4. Graham, R. A. and Asay, J. R., "Measurement of Wave Profiles in Shock

Loading Solids," *High Temperatures-High Pressures*, Vol. 10, 1978, p. 355.

5. Duff, R. E. and Houston, E., *J. Chem. Phys.*, Vol. 23, 1955, p. 1268.

## DISCUSSION

DR. J. ROTH, Consultant,  
Portola Valley, CA

There appears to be some inconsistency in your calculation of ideal detonation parameters. From  $k+1 = \rho_0 \cdot D^2 / P_{CJ}$  and your calculations  $k \approx 2.9$ . However, for ANFO (and other explosives in this density range)  $k \approx 2.1$ , of course as  $\rho_0 \rightarrow 0$ ,  $k \rightarrow 1.2$  or  $C_p/C_v$  gas are ideal gas.

## REPLY BY A. MIYAKE

The value of  $\gamma$  ( $k$  in the question) depends not only on the initial density but also on the ideality of the detonation behavior. For example, a high  $\gamma$  value was obtained ( $\gamma = 2.5$ ) in our experiments for a nearly ideal detonation. However, values as small as 1.9 were found for non-ideal detonation of AN at smaller diameters. Figure 4 (Figure 5) shows the relationship between the detonation velocity (the charge diameter) and the  $\gamma$  value calculated from the measured detonation velocity and pressure. Also, the  $\gamma$  values for the ideal detonation of AN calculated with the TIGER code with different EOSs are in the range of 2.8 to 3.1 at a density of  $850 \text{ kg/m}^3$ .

## COMMENT

PROF. P-A. PERSSON,  
CETR/New Mexico Tech, Socorro, NM

The  $\gamma$  ( $=2.9$ ) may be high because the internal energy of pure AN at the CJ state is much lower than that of normal explosives at the CJ state. AN (without fuel added) has a low explosion energy and, consequently, a low internal energy at the CJ point. A recent publication (By K-H Oh and P-A. Persson, "Full Range Hugoniot Equation of State for Porous Materials," APS Topical Conference on Shock Waves, Albuquerque, Aug 1989) shows that  $\gamma$  is strongly dependent on (internal) energy, and it generally increases with decreasing energy (except at very low

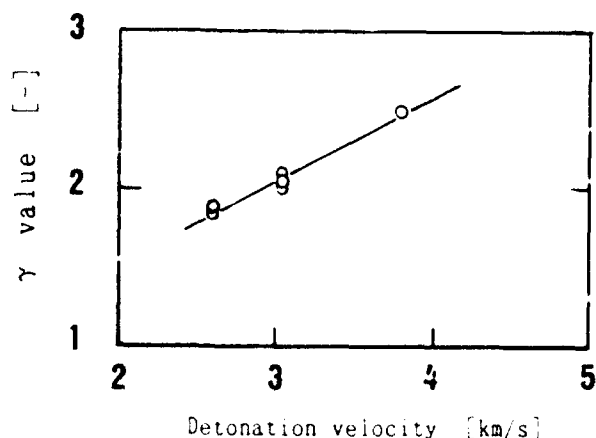


Figure 4 Relationship Between Detonation Velocity and  $\gamma$  of AN

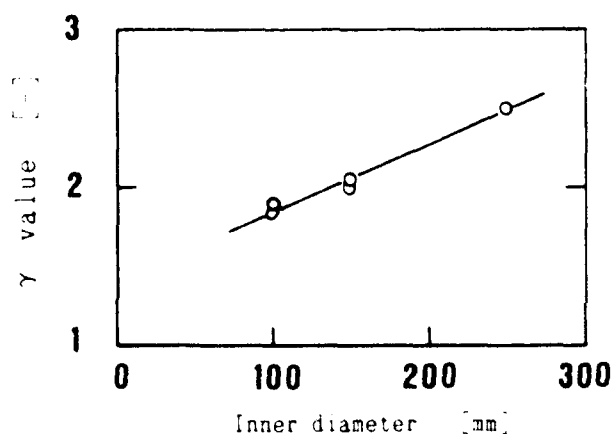


Figure 5 Relationship Between Inner Diameter and  $\gamma$  of AN

energies).  $\gamma$  should be higher at the CJ state for pure AN than ANFO, and  $\gamma_{CJ} = 2.9$  for AN does not appear an unlikely value

## DISCUSSION

DR. M. HELD, MBB-8898  
Schrobenhausen, West Germany

The streak record, which was shown (not in the Proceedings), of the shock wave of the detonating charge has a structure of a weaker shock in the beginning, which is then overtaken by a stronger shock wave after about 10 mm run distance in the plexiglass block. What causes this structure?

## REPLY BY A. MIYAKE

We are not sure the trace is related to the typical characteristics of a non-ideal detonation. At the moment, we think that the weaving trace is caused by the uneven structure of the detonation front.

## DISCUSSION

DR. R. SARRACINO, AECI,  
Modderfontein 1645, South Africa

Did you obtain velocity-time traces, and if so, what did they look like—specifically, for the 300 mm trail?

## REPLY BY A. MIYAKE

The velocity-time traces were obtained with resistance wire probes mounted in the center and along the total length of the steel tubes. First the overdriven shock wave of the booster is observed and changes its form to a straight line from which the detonation velocity is calculated. For large diameters (300 mm) the shock wave generated by the booster is almost the same as the detonation velocity, and a constant velocity over the total length of the tube is measured.

# SHOCK SENSITIVITIES OF ENERGETICALLY SUBSTITUTED BENZOFUROXANS

May L. Chan and C. D. Lind  
Naval Weapons Center  
Code 3891  
China Lake, California 93555

and

Peter Politzer  
Department of Chemistry,  
University of New Orleans  
New Orleans, Louisiana 70148-1614

*The shock sensitivities of 7-amino-4,6-dinitrobenzofuroxan (ADNBF) and 4,6-dinitrobenzofuroxan (DNBF) were evaluated in both pressed and castable compositions at the same volume percent of solid loading (53 V percent). These test results were compared with the shock sensitivity data obtained from comparable compositions containing HMX as the solid filler. The test configuration, sample preparation, and chemical structure and sensitivity property relationships were studied.*

## INTRODUCTION

Ingredients presently used in the explosive or propellant of conventional weapons systems have some performance or hazard-sensitivity deficiencies. New energetic ingredients offer the opportunity to improve the chemical energy while reducing hazardous properties. In the past, minimum effort has been devoted to the evaluation of new ingredients early in the development cycle.

High performance propellants and explosives constitute a class of energetic composite materials that contain various energetic solid and binder ingredients. The vulnerability properties of energetic propellants and explosives are determined by many factors. Of these factors, the very important macroscopic and microscopic properties of the composites have been the focus of continuing study. However, inherent sensitivity properties of individual ingredients also play a determining role in the overall vulnerability characteristics of these materials. Shock sensitivity is an important property of energetic materials; reduced shock sensitivity

generally lessens the processing hazards in production and minimizes vulnerability to accidental initiation in transportation, storage, and use. Desensitization through the use of elastomeric binder material is effective in improving resistance toward mechanical damage, but provides only limited success in the area of reducing shock sensitivity. The overall shock sensitivity of an energetic composition is determined mainly by the inherent shock sensitivity of the energetic solid that is present in the formulation.

Current efforts in new energetic solids were to uncover promising ingredients for energetic composites that will satisfy both the performance and in vulnerability goals of future energetic propellants and explosives.

## EXPERIMENTAL RESULTS

Energetic organic solids used for conventional propellants contain mostly nitro(-C-NO<sub>2</sub>), nitramine (-N-NO<sub>2</sub>) or nitrate (-C-ONO<sub>2</sub>) groups as the energetic functionalities. However, other functional groups, such

as the unique furoxan ring structure can also provide large amounts of chemical energy and high performance. ADNBF and DNBf are recently synthesized, energetic, substituted benzofuroxans.<sup>1,2</sup> These compounds were scaled up in multi-pound quantities at the Naval Weapons Center. Energetic compositions containing either ADNBF or DNBf were prepared to compare their shock sensitivity with that of comparable samples containing conventional high-explosive solid cyclotetramethylenetetranitramine (HMX).

### Physical and Chemical Properties

The physical and chemical properties of ADNBF and DNBf are listed in Tables 1 and 2. ADNBF is a thermally stable ( $E_{act} =$

69 kcal/mol), high-density energetic solid ( $1.9 \text{ g/cm}^3$ ) with a measured heat of formation of +36 kcal/mol. ADNBF showed higher calculated performance<sup>3</sup> ( $P_{CJ} = 310 \text{ Kbar}$ ) as neat explosive than did DNBf ( $P_C = 260 \text{ Kbar}$ ). DNBf is less thermally stable ( $E_{act} = 36.79 \text{ kcal/mol}$ ) and less dense ( $1.75 \text{ g/cm}^3$ ) than ADNBF. However, DNBf has slightly higher oxygen balance ( $OB_{100} = -0.88$ ) than ADNBF ( $OB_{100} = -1.24$ ). Where  $OB_{100}$  is defined as the number of equivalents of oxidant per hundred grams of the solid required to burn all hydrogen to water and all carbon to carbon monoxide. Thus, DNBf showed higher calculated specific impulse ( $I_{sp} = 240 \text{ seconds}$ ) as monopropellant than did ADNBF ( $I_{sp} = 230 \text{ seconds}$ ). The safety property data (Table 3) indicated that DNBf

Table 1. Physical and Chemical Properties of ADNBF and DNBf

Properties	ADNBF	DNBF
Molecular formula	$C_6H_3O_6N_5$	$C_6H_2O_6N_4$
Density, $\text{g/cm}^3$	1.902	1.752
Melting point $^\circ\text{C}$	270 (decomposition)	174
Phase change ( $-100^\circ\text{C}$ to $+100^\circ\text{C}$ )	None	None
Heat of formation, kcal/mol	36.79	48.8
Oxygen balance, $OB_{100}^a$	-1.24	-0.88
Specific impulse, $I_{sp}^b$	230	240
Detonation pressure ( $P_{CJ}$ ) <sup>c</sup> , Kbar	310	260

<sup>a</sup> $OB_{100} = 100(2N_O N_H - 2N_C - 2N_{COO})/\text{mol. wt.}$  where  $N_O$ ,  $N_H$ , and  $N_C$  represent the number of atoms of each element in the molecule.  $N_{COO}$  represents the carboxyl group.

<sup>b</sup>Calculated performance as monopropellant.

<sup>c</sup>Calculated performance as neat explosive.

Table 2. Thermal Properties of ADNBF and DNBf

Sample	TGA onset $^\circ\text{C}$	TGA 1% wt loss $^\circ\text{C}$	Number of exotherm	DSC onset $^\circ\text{C}$	Peak exotherm $^\circ\text{C}$	$E_{act}$ kcal/mol	Log A $\text{sec}^{-1}$
ADNBF	253	263	3	264 273 278	269	69.0	23.9
DNBF	190	196	1	222	274	37.0	11.7



is more impact sensitive than ADNBF and that both are less impact sensitive than HMX.

### Small-Scale Shock Sensitivity Test

Because the quantities of recently synthesized energetic materials were limited, a small-scale test was needed to measure shock sensitivity. Therefore, a new, Small Scale Intermediate Gap Test,<sup>4</sup> developed at the Naval Surface Warfare Center was adapted to evaluate the shock sensitivities of experimental compositions containing new energetic solid material. The test configuration is illustrated in Figure 1. The shock stimulus is generated from the donor system (two 2 inch OD pressed pentolite donors). One 1/2 inch diameter by 2 inch long sample is confined in a steel tube with an 1/8 inch thick wall. A set of 20-25 samples was tested with varying thicknesses of

the attenuator, polymethyl methacrylate (PMMA), to find the 50 percent threshold shock strength for initiation. This is a direct scaledown of the NOL Large Scale Gap Test (LSGT).<sup>5</sup> Test results from the Small Scale Intermediate Gap Test and the LSGT were compared for a number of conventional materials, as shown in Table 4. A good correlation of test results was obtained in these two configurations.

Two sets of model compositions were prepared for evaluation. The first set of samples (see Table 5) used a castable binder system to simulate castable service propellants; the samples contained 53 percent (by volume) ADNBF (18-19  $\mu$ m), DNBf (18-19  $\mu$ m), and HMX (19-20  $\mu$ m) in dioctyladipate (DOA) plasticized hydroxyl-terminated polybutadiene (HTBP) binder. The only variable was the type of energetic solid used. The results indicated that ADNBF based

*Table 3. Safety Properties of ADNBF and DNBf*

	Impact, cm <sup>a</sup> (50%, 2.5 kg)	Friction ABL	Electrostatic (0.25 J)
ADNBF	28-33 cm	10/10 NF (at 794 lbs)	10/10 NF
DNBF	16-19 cm	10/10 NF (at 1000 lbs)	10/10 NF

<sup>a</sup>By comparison, HMX = 14 cm.

*Table 4. Comparison of Small Scale Intermediate Gap Test and NOL Large Scale Gap Test*

	Density g/cm <sup>3</sup>	% TMD	Small Scale Intermediate Gap Test	NOL Large Scale Gap Test <sup>a</sup>
TNT <sup>b</sup>	1.58	94.9	1.92 in (20.5 kbar) <sup>c</sup>	1.95 in (21.5 kbar)
TNT	1.62	98.1	1.807 in (25 kbar)	1.80 in (25 kbar)
TATB <sup>b</sup>	1.82	94.5	0.92 in (60 kbar)	0.78 in (65 kbar)

<sup>a</sup>Data obtained from Reference 4.

<sup>b</sup>Data obtained from Reference 3.

<sup>c</sup>Pressure in PMMA.

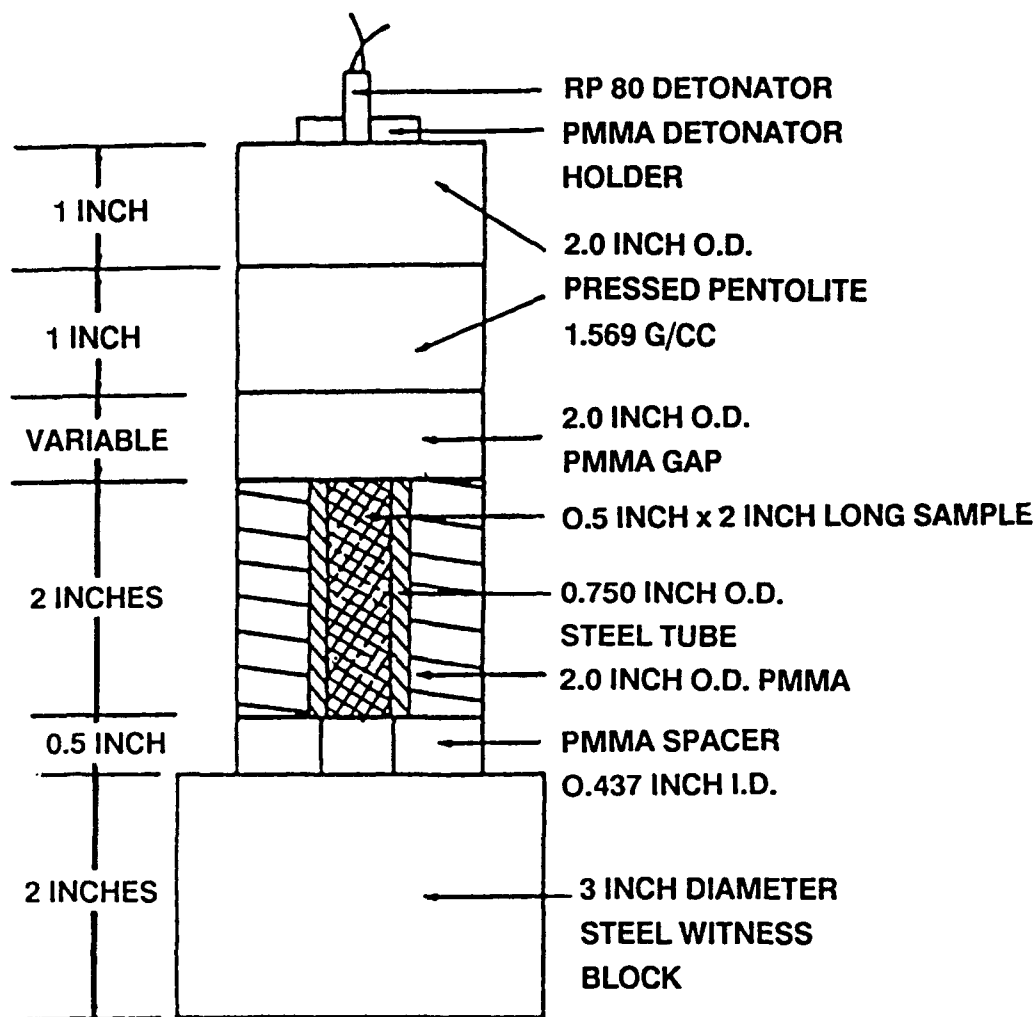


Figure 1. Small Scale Intermediate Gap Test Configuration

Table 5. A Comparison of Shock Sensitivity of Various Solid-Filled Compositions

Sample	Vol. % solid	Gap, in (50% point)	Pressure into sample (kbar) <sup>a</sup>	Density g/cm <sup>3</sup>	%TMD
HTPB/HMX	53	1.435 ± 0.009	42.58	1.43	99.9
HTPB/ADNBF	53	1.303 ± 0.020	46.96	1.44	99.9
HTPB/DNBF	53	1.430 ± 0.009	42.76	1.36	99.9

<sup>a</sup>Estimated pressure in the PMMA (attenuator).

samples were less shock sensitive than the shock sensitivity of DNBF or HMX-filled material at the same volume percent loading, solid particle size (19-20  $\mu$ m) and high (99.99 percent) theoretical maximum density (TMD). A 50 percent shock initiation pressure of 43 kbar would initiate

the shock-to-detonation reaction in the DNBF or HMX-filled material, but would not initiate an ADNBF based composition.

The second set of samples (see Table 6) used pressed materials to simulate pressed service explosives. The samples contained

Table 6. A Comparison of Shock Sensitivity of Various Pressed Compositions

Sample	Wt. % solid	Vol. % solid	Gap, in (50% point)	Pressure into sample (kbar) <sup>a</sup>	Density g/cm <sup>3</sup>	%TMD
EVA/HMX	97	93.55	1.866 ± 0.018	23.9	1.74	94.2
EVA/ADNBF	97	93.45	1.862 ± 0.007	24.0	1.72	93.2
EVA/DNBF	97	94.60	2.343 ± 0.003	14.8	1.63	94.5

<sup>a</sup>Estimated pressure in the PMMA (attenuator).

97 weight percent ADNBF, DNBF and HMX, and 3 weight percent ethylene vinyl acetate. All samples were pressed to 94% TMD. The 50 percent initiation shock pressure was reduced from 43-47 kbar in the cast samples to 15-24 kbar in the pressed samples. The reduction is largely due to the presence of voids in the pressed materials. The introduction of voids into the sample during the pressing process significantly degraded the resistance to shock of the DNBF samples as compared to HMX- or ADNBF-filled materials.

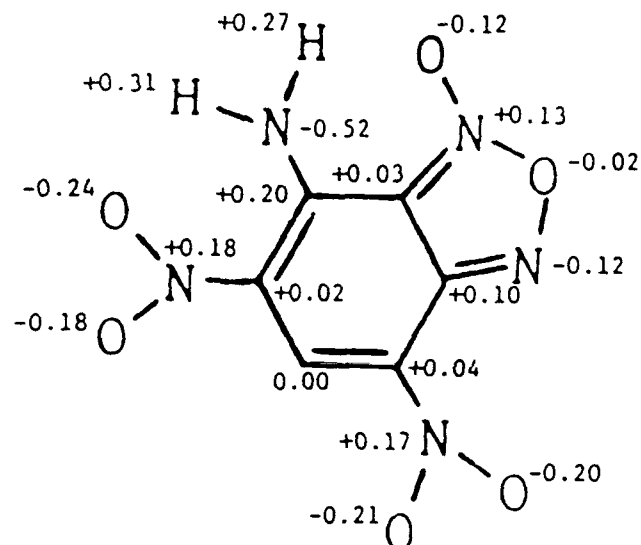
## THEORETICAL CALCULATIONS

The new energetic solids, ADNBF and DNBF, were subjected to abinitio self-consistent-field (SCF) molecular orbital calculations by using the Gaussian 82 program at the STO-3G level.<sup>6,7</sup> These calculations coupled with X-ray crystallographic structures of these compounds<sup>8,9,10</sup> allows one to calculate the atomic charges on each of the atoms in the molecule (as shown in Figure 2) and the electrostatic potential at the C-NO<sub>2</sub> bond midpoint, computed using the formula:

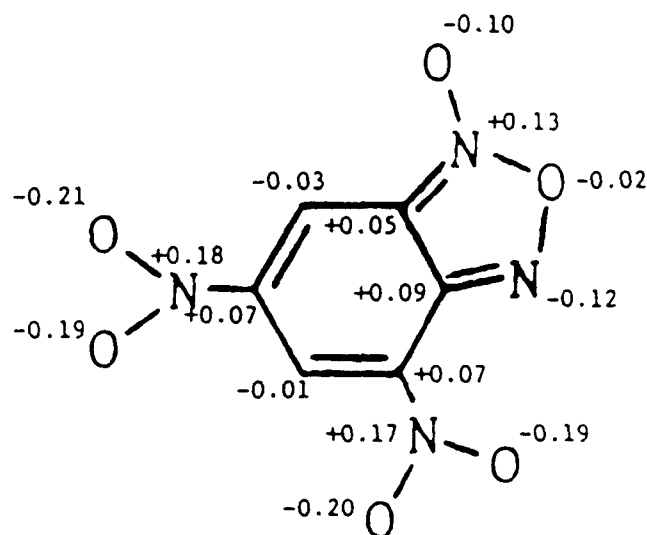
$$V_{\text{mid}} = Q_c/0.5 R + Q_n/0.5 R$$

where  $Q_c$  and  $Q_n$  are the calculated charges on the carbon and nitrogen and  $R$  is the bond length.  $V_{\text{mid}}$  is given in atomic units (1 au = 27.21 eV).

It has been shown that, in a group of nitroaromatics, the  $V_{\text{mids}}$  of the trigger linkages (-C-NO<sub>2</sub>) can be directly related to the measured impact and shock sensitivity.<sup>11</sup> When these techniques were applied



ADNBF



DNBF

Figure 2. Atomic Charges of ADNBF and DNBF

to DNBf and ADNBF, the results showed that the  $V_{mid}$  values are 0.172 and 0.175 for DNBf and 0.143 and 0.155 for ADNBF (each molecule has two C-NO<sub>2</sub> substitutions). The  $V_{mid}$  is a measure of bond lability toward breakage, which is believed to be a critical step in decomposition of energetic compounds. These decompositions are the governing chemical reactions for the initiation of impact and shock-to-detonation reactions. The difference between ADNBF and DNBf is the presence of the -NH<sub>2</sub> group in the ADNBF molecule, but not in DNBf. The -NH<sub>2</sub> group stabilizes the aromatic ring through electron donating and reducing the  $V_{mid}$  of C-NO<sub>2</sub> bonds (decreased positive charges of carbon and nitrogen atoms). It is this difference that made these bonds in ADNBF more resistant to breakage in thermal or other chemical decomposition. This could be the reason that ADNBF is less impact and shock sensitive and more thermally stable than DNBf, as indicated by the experimental results.

## CONCLUSIONS

The new Small Scale Intermediate Gap Test provided a good tool for ranking the shock sensitivity of energetic compositions containing new solids. ADNBF and DNBf were chosen as examples of new solids. They were used to determine the formulation strategy (i.e., sample preparation) and test methodology. The test results showed that DNBf or HMX are more impact and shock sensitive than ADNBF. This finding was supported by the calculated electrostatic potentials at the midpoint of C-NO<sub>2</sub> bonds in these compounds as the measure of relative bond stability toward breakage.

These efforts will be continued to screen for other new, less shock-sensitive energetic ingredients for future propellant and explosive formulations and to develop the necessary technology base for chemical structure/energy versus sensitivity properties of energetic solid ingredients.

## ACKNOWLEDGEMENT

The authors wish to express appreciation to Dr. M. Kramer for providing ADNBF

material for evaluation and Mr. S. Martin for shock sensitivity testing and Mr. A. Turner and Mr. Will Carey, Jr., for sample preparation.

## REFERENCES

1. Norris, W. P., *7-Amino-4,6-Dinitrobenzofuroxan and Insensitive High Explosive*, NWC TP 6522, NWC, China Lake, CA, Jun 1984.
2. Norris, W. P., *Improved Synthesis of 7 - Amino - 4, 6 -Dinitrobenzofuroxan (ADNBF)*, NWC TP 6724, NWC, China Lake, CA, May 1986.
3. Kamlet, M. J. and Jacobs, S. J., "Simple Method of Calculating Detonation Properties of C-H-N-O Explosives," *Journal of Chemical Physics*, Vol. 48, 1968, p. 23.
4. Forbes, J. W.; Bloom, G. H.; Von Holle, W. G.; Adolph, H. G.; and Spivak, J. L., "Detonation Thresholds of Unusual Explosives," *Bulletin of American Physics Society*, Vol. 33, No. 3, Mar 1988, p. 537.
5. Price, D.; Clairmont, A. R., Jr.; and Erkman, J. O., *NOL Large-Scale Gap Test. III Compilation of Unclassified Data and Supplementary Information for Interpretation of Results*, NOLTR 74-40, White Oak, Silver Spring, MD, 8 Mar 1974.
6. Politzer, P.; Abrahmsen, L.; and Sjoberg, P., "Effects of Amino and Nitro Substituents Upon the Electrostatic Potential of an Aromatic Ring," *Journal of the American Chemical Society*, Vol. 106, 1984, pp. 855-860.
7. Politzer, P.; Laurence, P. R.; Abrahmsen, L.; Zilles, B. A.; and Sjoberg, P., "The Aromatic C-NO<sub>2</sub> Bond as a Site for Nucleophilic Attack," *Chemical Physics Letters*, Vol. III, No. 1, 2, Oct 1984, pp. 75-78.
8. Ammon, H. L. and Dechun Zhang, "Structure of 4-Amino-5,7-dinitrobenz [1,2-C][1,2,5]oxadiazole 3-oxide," *Acta Cryst.*, C42, 1986, pp. 724-727.

9. Prout, C. K.; Hodder, O. J. R.; and Viterbo, D.; "The Crystal and Molecular Structure of 4,6-dinitrobenzofuroxan," *Acta Cryst.*, B28, 1972, pp. 1523-1526.
10. Ammon, H. L. and Bhattacharjee, S. K., "Crystallographic Studies of High-Density Organic Compounds: 4-Amino-5-nitrobenzo [1,2-c:3,4-c'] bis [1,2,5] oxadiazole 3,8-Dioxide," *Acta Cryst.*, B38, 1982, p. 2498.
11. Owens, F. J.; Jajasuriya, K.; Abrahmsen, L.; and Politzer, P., "Computational Analysis of Some Properties Associated With the Nitro Groups in Polynitroaromatic Molecules," *Chemical Physics Letters*, Vol. 116, No. 5, 1985.

### DISCUSSION

I. B MISHRA, Kanan Associates, Inc.  
Churchville, MD 21028

Your shock sensitivity increases a great deal for non-recrystallized ADNBF as compared with crystallized ADNBF. You ascribe that to "perhaps" presence of glacial acetic acid, consequent "uncured" sample. The difference is too great to be due to the nature of the cure.

Have you considered the formation and trapping of  $\text{NO}_x$  in the crystal, giving rise to more sensitive material? What specific tests did you do to eliminate the second possibility ( $\text{NO}_x$ ) and also to establish the so-called voids that you said may be there?

### REPLY BY MAY L. CHAN

I agree with your comments to the effect that the recrystallization process for ADNBF removed or greatly reduced the amount of physical defects (internal voids, fissures) and chemical impurities (acetic acid or water) or entrapped gases ( $\text{N}_2$ ,  $\text{NO}_x$ , etc.) that are present in the crude ADNBF material. These physical defects were known to be blamed for initiation sites upon shock loading. This could be the reason that the compositions contain the recrystallized ADNBF shown to be less shock sensitive than the ones containing unrecrystallized material. The other source of the problem was that the acetic acid and water could interfere with the urethane cure reaction in the castable binder system, and these side reactions could also produce voids in the sample.

# DETONATION AND SHOCK INITIATION PROPERTIES OF EMULSION EXPLOSIVES

J. Lee, F. W. Sandstrom, B. G. Craig, and P. -A. Persson

Center for Explosives Technology Research/

Research Center for Energetic Materials

New Mexico Institute of Mining and Technology

Socorro, New Mexico 87801

*The detonation and shock initiation properties of water-based emulsion explosives are described. The failure diameter and the detonation velocity were measured as a function of initial density. The detonation velocity as a function of density showed a markedly different behavior from those of high energy monomolecular explosives. The failure diameter increased exponentially with increasing density. At the matrix density,  $1.353 \text{ g/cm}^3$ , the failure diameter was found to be larger than 378 mm. Diameter effect curves were similar in trend to, but much steeper in slope than, those of mono-molecular explosives. The distance of run to detonation and the shock Hugoniot of the unreacted explosive, at density  $1.248 \text{ g/cm}^3$ , were measured in wedge experiments. From this, the unreacted Hugoniots for the emulsion matrix were determined using the Mie-Grüneisen equation of state. The Pop plot showed that the emulsion explosive at density  $1.248 \text{ g/cm}^3$  was less sensitive than cast TNT.*

## INTRODUCTION

Emulsion explosives<sup>1,2</sup> are widely used in the blasting industry. They are composite explosives in which intimacy between oxidizer and fuel is achieved by high-shear mixing a hot aqueous solution of the oxidizer with a liquid or molten hydrocarbon fuel including an emulsifying agent. A typical oxidizer is ammonium nitrate (AN), and typical fuels are mineral oils or waxes. By high-shear mixing, the concentrated solution of the nitrate salt in water is dispersed into  $\mu\text{m}$ -sized supercooled liquid droplets, surrounded by a continuous phase of fuel. The final product, a water-in-oil emulsion, is surprisingly water-resistant. In most applications the emulsion matrix can be sensitized by adding hollow microballoons, typically  $100 \mu\text{m}$  or less in diameter, rather than by explosive materials. A wide range of properties, including initiating sensitivity, can be obtained by simply changing the weight percentage of microballoons. Emulsion

explosives have replaced most other types of cartridged or pumpable explosives and blasting agents in the blasting industry. About a quarter of a billion kg of emulsion explosives and blasting agents are consumed yearly in the US alone.

Since each microballoon acts as a hot spot from which the chemical reactions start, the size and the number of microballoons have a profound effect on the detonation properties of emulsion explosives. Hattori et al.<sup>3</sup> reported that the detonation velocity of emulsion explosives increased linearly with decreasing microballoon size in unconfined charges while it was nearly independent of microballoon size in confined charges.

The steady-state detonation and failure phenomena of monomolecular explosives have been studied extensively, but not much work has been reported on emulsified composite explosives. Yoshida et al.<sup>4</sup> studied the detonation and failure behavior of ammonium

nitrate/sodium nitrate-based (AN/SN) emulsion explosives with a critical thickness of about 1 mm at density 1.1 g/cm<sup>3</sup>. Lee and Persson<sup>5</sup> used ammonium nitrate/calcium nitrate-based (AN/CN) emulsion explosives, where the failure diameter was about 11 mm at density 1.1 g/cm<sup>3</sup>, to study the detonation characteristics and the effect of microballoon size.

The detonation velocity predicted theoretically using the BKW equation of state<sup>6</sup> for the reaction products has been used in many applications. The predictions generally agree well with experimental data of monomolecular high explosives. The predictions have been reported to be considerably higher than the ideal detonation velocities of most explosives containing ammonium nitrate.<sup>7</sup>

The effect of charge diameter on the detonation velocity stems from the reaction zone structure. For most explosives, the diameter effect curves are downward concave. These downward concave curves were reproduced theoretically by Bdzil.<sup>8</sup> Campbell and Engelke<sup>9</sup> showed that the diameter effect can be expressed as

$$D = D_i \left( 1 - \frac{A}{d - d_c} \right) \quad (1)$$

where  $D$  and  $D_i$  are detonation velocities at a given diameter  $d$  and at infinite diameter, and  $A$  and  $d_c$  are fitting constants.

The wedge test<sup>10</sup> has been widely used to study the shock to detonation transition phenomena. It provides information needed for calibrating global kinetics models such as Forest Fire,<sup>11</sup> which are needed for future calculations, as well as information on the mechanism, shock sensitivity, and detonation velocity. Bauer et al.<sup>12</sup> have reported wedge test results for several industrial type emulsion and slurry explosives of proprietary compositions.

## EXPERIMENTAL PROCEDURES

### Preparation of Emulsion Explosives

The formulation of the emulsion matrix used in this study was 77 AN/16 water/6 oil/1

emulsifier (weight percentage). The cell size was from 1 to 5  $\mu$ m. The density was  $1.353 \pm 0.003$  g/cm<sup>3</sup> at 20°C. The emulsion matrix was sensitized by adding microballoons, and the density of the resulting explosive was controlled by the weight percentage of microballoons. The microballoons were type C15/250, manufactured by 3M Coporation. Their true density was about 0.15 g/cm<sup>3</sup>, with an average diameter of 70  $\mu$ m. The weight percentage of microballoons,  $x$ , is related to the resulting explosive density by

$$x = \frac{100\rho_{mb}(\rho_e - \rho_o)}{\rho_o(\rho_e - \rho_{mb})}, \quad (2)$$

where  $\rho_o$ ,  $\rho_e$ , and  $\rho_{mb}$  are densities of the resulting explosive, the emulsion matrix and microballoons, respectively.

## DETONATION VELOCITY AND FAILURE DIAMETER MEASUREMENTS

All experiments were done with cylindrical charges of emulsion explosives, with or without microballoons. For unconfined small diameter charges with diameters ranging from 21 to 102 mm, emulsion explosives containing small amounts of microballoons were tested in US standard schedule 40 PVC pipes. The experimental setup is shown in Figure 1a.

For "unconfined" large diameter charges with diameters ranging from 203 to 378 mm, the emulsion matrix without microballoons was tested in PVC pipes with from 4 to 7 mm wall thicknesses. An emulsion plane wave generator (PWG) and a 13 to 25 mm thick PBX-9501 booster were used to assure detonation for all charges above the critical diameter. For confined charges with diameters ranging from 126 to 255 mm, the emulsion matrix without microballoons was tested in mild steel pipes with wall thicknesses ranging from 7 to 14 mm. An emulsion PWG and a 52 mm thick composition C-3 booster were used together as an initiator. For both confined and unconfined charges, the experimental configuration is shown in Figure 1b. The physical dimensions and initiator systems of all the charges are listed in Table 1.

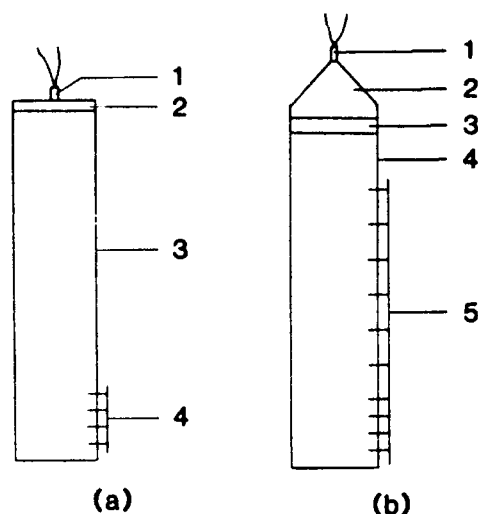


Figure 1. Experimental Setups for Detonation Velocity Measurements. (a) Configuration for charges with diameters less than 102 mm: 1-detonator; 2-booster; 3-PVC pipe; 4-ionization pin assembly. (b) Configuration for charges with diameters greater than 102 mm: 1-detonation; 2-emulsion plane wave lens; 3-booster; 4-PVC or mild steel pipe; 5-ionization pin assembly.

Table 1. Dimensions of Charges (mm)

diameter	wall thickness	length	casing	driver system
20.9	2.9	305	PVC	1
26.6	3.4	381	PVC	1
52.5	3.9	610	PVC	1
77.9	5.5	914	PVC	1
102.3	6.0	1219	PVC	1
202.7	7.1	914	PVC	2
315.9	4.0	914	PVC	3
378.0	4.0	1016	PVC	3
125.7	14.0	915	steel	4
146.0	11.4	991	steel	4
205.0	7.0	1626	steel	4
255.0	9.3	1524	steel	5

1 - 8 mm thick Detasheet

2 - 203 mm PWG and 13 mm thick PBX 9501

3 - 316 mm PWG and 26 mm thick PBX 9501

4 - 203 mm PWG and 51 mm thick comp. C-3

5 - 316 mm PWG and 51 mm thick comp. C-3

## Wedge Tests

The unreacted Hugoniot and the shock to detonation transition data for the 1.248 g/cm<sup>3</sup> emulsion were obtained using two different wedge test configurations. The first of these, a buried self-lighting (BSL) technique, uses a relatively thin plexiglas plate set on edge to form the wedge (actually a prism) profile, and to define arrival time flashers for both initial shock arrival and attenuator free-surface velocity across a known gap. The wedge angle was 30°, and wedge heights of 19 and 30 mm were used. The slant portion or wedge face of the plate was coated with microballoons to indicate shock arrival times along the wedge face. The upper edge of the plexiglas plate was polished to give a window for viewing the wedge and flasher surfaces with a streak camera. After the plate was cemented to the attenuator, a length of PVC pipe was used to surround the plate forming a containment tank for the emulsion (Figure 2a). The emulsion was carefully loaded into the tank in a manner to ensure contact with the bottoms of the wedge shaped window and tank, and to minimize air bubbles. A typical streak camera record is shown in Figure 3a.

In the second wedge test configuration, the explosive wedge or prism was formed by a plexiglas box cemented to the attenuator, resulting in a 22.5° wedge angle, 30 mm height, and 60 mm width. While the sides, back, and top flat portion of the wedge were enclosed, the wedge face was left open. A shock proceeding through the wedge compresses the gas trapped in the microballoons in the emulsion, which in turn luminesce upon shock arrival at the wedge face. Consequently, we call this the open face self lighting (OFSL) technique. Initial shock arrival times and attenuator free-surface velocity across a known gap were again obtained using an arrival time flasher block mounted adjacent to the wedge toe (Figure 2b). The emulsion was carefully loaded into the box just prior to shooting. A uniform wedge face and well-defined toe were obtained by removing excess material with a straight edge. During loading and firing the entire plane wave lens/booster/attenuator/wedge assembly was oriented so that the



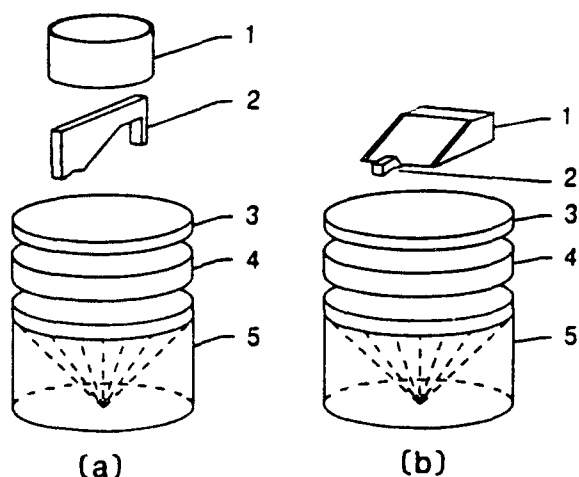


**Figure 2. Wedge Test Configurations.** (a) BSL: 1-containment tank; 2-Plexiglas wedge/flasher; 3-attenuator; 4-explosive booster; 5-200 mm explosive plane wave generator. (b) OFSL: 1-wedge form container; 2-flasher block; 3-attenuator; 4-explosive booster; 5-200 mm explosive plane wave generator.

wedge face remained horizontal. A typical streak camera record is shown in Figure 3b.

The OFSL technique was adopted to address concerns about shock interactions between the emulsion and the plexiglas window used in the BSL technique, and also to investigate the effect of a 30° wedge angle vs a 22.5° wedge angle. Shots with identical driver systems, using each of the two configurations, yielded the same nominal data. Additionally, since the light emitted from the wedge face is not quenched as in the BSL test, it was hoped that this technique would better define where transition-to-detonation takes place. Unfortunately, the light generated by the shock microballoons is so intense that it does not distinguish between shocks and detonations at practical camera exposure.

The shock driver systems used in each test, consisted of a 200 mm diameter plane wave generator developed and manufactured at New Mexico Tech/CETR, a booster explosive at least 25  $\mu$ m thick, and a 6 to 18 mm thick plexiglas attenuator. Prior to performing the wedge tests, several of the driver systems

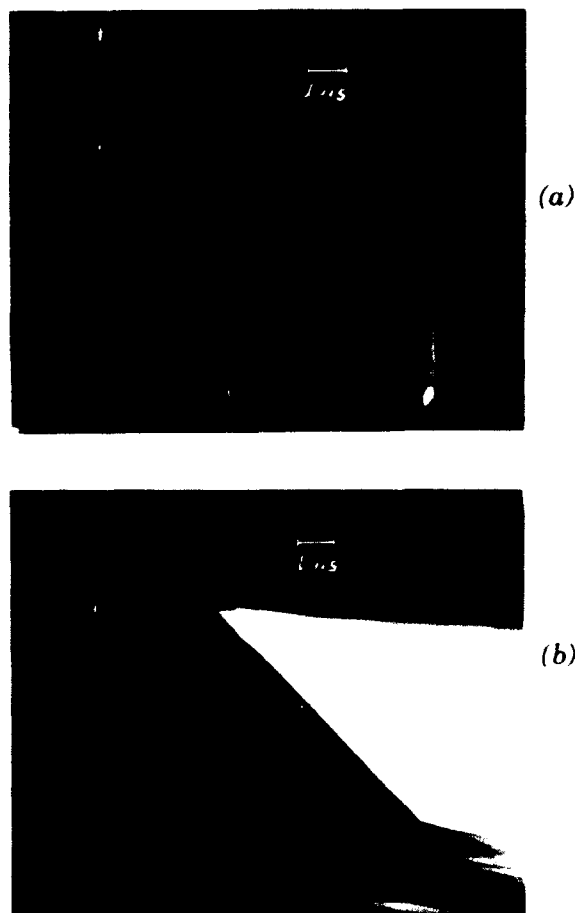


**Figure 3. Typical Streak Camera Records.** Time increases to the right. (a) BSL; (b) OFSL.

were characterized for wave planarity and pressure uniformity at the attenuator output surface. For the central 120-140 mm diameter of a typical driver system, the wave simultaneity was within 100 ns; and pressure uniformity, determined from free surface velocity measurements, varied smoothly and from shot to shot by no more than 10 percent of the nominal pressure.

## RESULTS AND DISCUSSIONS

### Detonation Velocity Data and Analysis

The detonation velocity, as a function of initial density for emulsion explosives at various diameters, is shown in Figure 4. These curves showed a marked difference from those of monomolecular explosives. As the initial density increased, the detonation velocity increased to its maximum far below the

theoretical maximum density, rapidly decreased, and then failed. The failure diameter increased with increasing density. The density at which the maximum detonation velocity was attained increased with increasing diameter. The difference between the detonation velocity extrapolated to infinite diameter and that at a finite diameter increased with increasing density.

The detonation velocities at infinite diameter with respect to initial density fitted well to the linear relationship:

$$D_{\infty} = -0.152 + 5.383\rho, \quad (3)$$

where  $D_{\infty}$  is the detonation velocity at infinite diameter in mm/ $\mu$ s and  $\rho$  is the initial density in g/cm<sup>3</sup>. The reason for the negative intercept and the very large value of slope in Equation (3) is due to the increasing weight percentage of microballoons with decreasing density. For most monomolecular explosives, the  $D_{\infty}$  vs  $\rho$  curve shows a linear relationship, but the intercept at  $\rho=0$  is in a range from 1.5 to 2.0, and the slope is about 3.5.

The detonation velocity calculated by the BKW code using the BKW equation of state with the RDX parameter set is compared with the ideal detonation velocity extrapolated to

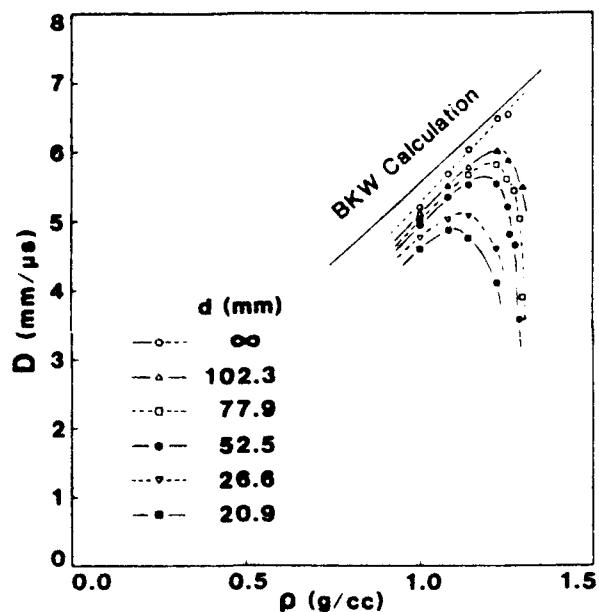


Figure 4. Detonation Velocity as a Function of Initial Density of the AN Emulsion Explosive

infinite diameter with fixed diameter curves in Figure 4. The calculated detonation velocity was slightly higher than the velocity at infinite diameter, but within the tested range of density. The difference was less than 0.35 mm/ $\mu$ s and decreased with increasing density. Thus, at large charge diameter, the emulsion explosives used in this study can be considered to detonate close to ideal.

Lee and Persson<sup>5</sup> for AN/CN emulsion explosives and Yosida et al.<sup>13</sup> for AN/SN explosives reported that the velocity at infinite diameter was considerably lower than the BKW code calculations. The relative performance of the three types of emulsion explosives mentioned above is compared in Figure 5. The major differences between the AN emulsion explosive used in this study and the AN/CN and AN/SN ones were in the composition of the oxidizing salt system and in the oxygen-balance. The AN emulsion explosives were slightly carbon-rich and the others were oxygen-balanced. One possible explanation for the non-ideal behavior of both AN/CN and AN/SN explosives is that the metallic salts (CN and SN) decompose endothermically and with solid reaction products. Possibly this leads to a more sluggish decomposition of the CN and SN salts, and consequently they may behave as inert. Miron et al.<sup>14</sup> reported recovery of 60 to 100 wt percent of the original SN, and significant portions of intermediate products of original CN for a variety of granular, gelatinous, and water gel formulations.

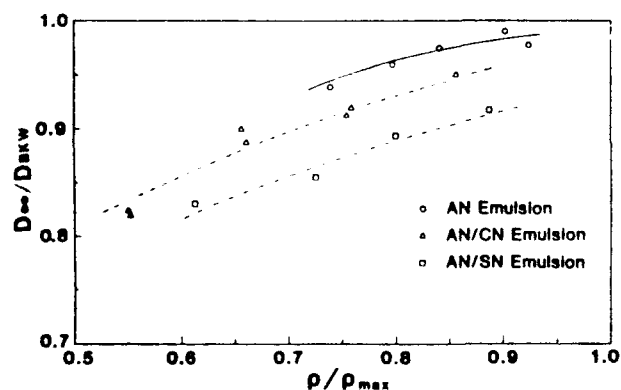


Figure 5. Relative Performance of Three Types of Emulsion Explosives Compared to BKW Calculations

The diameter effect curves of the AN emulsion explosive at various densities are shown in Figure 6. The curve at 1.288 g/cm<sup>3</sup> density was downward concave, while the other curves for densities lower than 1.288 g/cm<sup>3</sup> were straight. The straight curves are expected to become downward concave at diameters near failure. The downward concavity is common in heterogeneous explosives and it has also been seen for AN/CN emulsion explosives.<sup>5</sup> The downward concavity may be due to a hot spot mechanism,<sup>9,15-17</sup> or when a two-dimensional steady-state solution is no longer possible.<sup>8</sup> The straight diameter effect curves were fitted into Equation (1) with  $d_c = 0$ , which is identical to the diameter effect equation proposed by Eyring et al.<sup>18</sup> Fitting constants,  $D_i$  and  $A$ , are listed in Table 2.

Even though the shape of diameter effect curves of the emulsion explosives were similar to those of monomolecular explosives, the detonation velocity observed near failure was as much as 50 percent lower than the ideal velocity; for monomolecular explosives, such as HMX and RDX, the failure velocity is generally no more than 15 percent less than the ideal velocity.

The failure diameters of the emulsion explosives at various densities were measured in PVC pipes (US standard schedule 40), and are given in Figure 7. The failure diameter rapidly increased with increasing density. The failure diameter data are fitted by the equation:

$$d_f = 14.1 + 4.35 \times 10^{-15} \exp(28.47\rho), \quad (4)$$

where  $d_f$  is the failure diameter at a density  $\rho$ . Equation (4) predicts the failure diameter of the emulsion matrix without microballoons ( $\rho = 1.35$  g/cm<sup>3</sup>) as 227 mm. Tests of the emulsion matrix were subsequently made in a 378 mm diameter, 4 mm wall thickness PVC pipe; and a 255 mm diameter, 9.3 mm wall thickness mild steel pipe. In both tests, ionization pin records showed that the detonation was decaying, with a velocity of about 2.1 mm/ $\mu$ s at the end of the charge. Thus, the failure diameter of the matrix could not be estimated by Equation (4) from emulsion explosives containing a large number of microballoons.

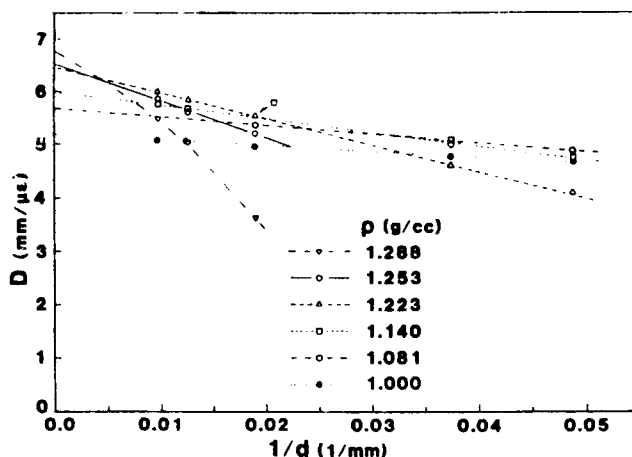


Figure 6. Charge Diameter Effect Curves of the AN Emulsion Explosive

Table 2. Fitting Constants for Diameter Effect Curves

density (g/cm <sup>3</sup> )	$D_i$ (mm/ $\mu$ s)	$A$ (mm)
1.000	5.202	11.306
1.081	5.681	16.922
1.140	6.025	26.155
1.223	6.478	49.788
1.253	6.530	69.956

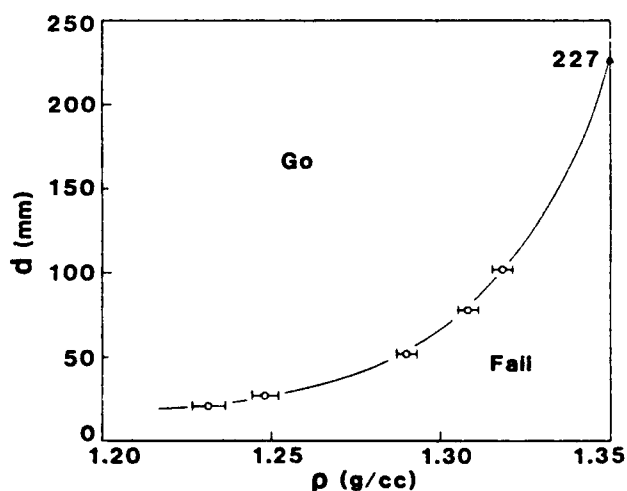


Figure 7. Failure Diameter of the AN Emulsion Explosive as a Function of Initial Density

Equation (4) fails near the matrix density because an emulsion matrix can be considered as a homogeneous explosive; accordingly, a different mechanism dominates if a steady detonation is even possible. As discussed by Campbell et al.,<sup>15,16</sup> in a homogeneous explosive, such as nitromethane or liquid TNT, the chemical reaction is triggered by the bulk heating caused by the shock compression. In a heterogeneous explosive containing a large number of density discontinuities, the chemical reaction is triggered by hot spots created by the interaction of the shock wave and the density discontinuities. Evidently, hot spots are important in detonation, as well as in initiation, corner turning, and failure diameter.

Another feature of the emulsion matrix, is that the predicted Chapman-Jouguet temperature is low--less than 1300 K. The unreacted shock temperature of the emulsion matrix, when driven by Comp C-3, is estimated to be 960 K by the Walsh and Christian Method.<sup>19</sup> This low value for the shock temperature of the emulsion matrix also points towards long reaction times, shock insensitivity, and a very large failure diameter for high order detonation at ambient temperature.

### Wedge Test Data and Analysis

The initial shock pressures, unreacted Hugoniot points, distance of run to detonation, final detonation velocities, and type of wedge test configuration used for seven wedge shots on the 1.248 g/cm<sup>3</sup> emulsion are listed in Table 3. The space (x) and time (t) data obtained from streak camera records of the wedge shots were reduced using the methods described for Technique 4 in Reference 10. It is noted that the final or detonation velocities are consistently below the steady-state velocity expected from Equation (3) (6.57 mm/ $\mu$ s).

While the initial shock pressure data are accurate to better than 5 percent, the transition points given are subject to a greater percentage of error. This is due largely to a lack of a well-defined transition point on the film records; the initial shock amplitudes required to obtain a transition within the wedge height are quite close to the final or detonation state, thus, the initial shock

velocity is close to the final velocity. The small change between initial and final velocity results in increased significance of typical non-uniformities inherent in explosive plane wave generators. These can be tolerated with more sensitive or higher energy materials. This would also explain, to some extent, the lack of constancy or a systematic variation in final detonation velocity with increasing initial shock pressure.

The initial shock pressure and distance of run to detonation data for the 1.248 g/cc emulsion, along with the Pop plots for several other explosives, are illustrated in Figure 8. The points with arrows on the right of the plot are shots that did not transit to detonation within the 30 mm wedge height. It is interesting to note that a linear fit to the data (solid line in Figure 8) fails to accommodate the two points where transition was not observed. For this reason, a curved fit to the data (dashed line in Figure 8) is hypothesized to account for the two outlying points, which in turn implies a high threshold pressure and extremely long runs to detonation near that pressure. In any case, both the linear and curved fits to the data indicate that the shock sensitivity of the emulsion is less than that of cast TNT, which is supported by our observation of a larger failure diameter for the emulsion than for the cast TNT. The general trend of the Pop plot for the 1.248 g/cm<sup>3</sup> emulsion contrasts sharply to the Pop plot for Emulsion "C" reported by Bauer et al.<sup>12</sup> Emulsion "C" is described as a large failure diameter, non-cap sensitive product containing glass microballoons; the 1.248 g/cm<sup>3</sup> emulsion described here is also non-cap sensitive. Similarly, the Pop plot for a cap sensitive 1.06 g/cm<sup>3</sup> AN/CN emulsion containing approximately 5 weight percent microballoons reported by Anthony,<sup>20</sup> contrast sharply with the Pop plots reported by Bauer et al. for Emulsions "A" and "B". These materials are described as cap sensitive products, containing glass microballoons, and 3 and 5 percent aluminum, respectively. Bauer et al. do not give any further information as to compositions or densities of their emulsions, nor is any data provided on unreacted Hugoniot or detonation performance.

Table 3. Wedge Test Data for the 1.248 g/cm<sup>3</sup> Emulsion Explosive Containing 1 Wt Percent Microballoons

Shot	Technique	Attenuator	Initial Shock Parameters			Coordinates for Detonation		Final Velocity
		$U_{fs}$ (mm/ $\mu$ s)	$P_o$ (GPa)	$u_{po}$ (mm/ $\mu$ s)	$U_{so}$ (mm/ $\mu$ s)	$x^*$ (mm/ $\mu$ s)	$t^*$ ( $\mu$ s)	D (mm/ $\mu$ s)
88LE-036	OFSL 30	3.10	9.38	1.48	5.07	>30	>5.8	—
88LE-037	OFSL 30	3.37	10.48	1.66	5.05	>30	>5.6	—
88LE-031	BSL 30	3.45@	11.03	1.68@	5.26	22.8	4.2	6.26
88LE-038	OFSL 30	3.55	11.58	1.72	5.38	13.4	2.4	5.94
88LE-032	BSL 30	3.56	11.59	1.72	5.39	13.6	2.5	5.86
88LE-027	BSL19	3.83	13.00	1.85	5.64	9.7	1.7	5.89
88LE-029	BSL 19	4.27	15.60	2.05	6.09	7.8	1.3	6.19

@ Values based on ratio of attenuator thickness to booster explosive thickness and type. The measured value of attenuator  $u_{fs}$  was 3.80 mm/ $\mu$ s, which results in a  $u_{po}$  of 1.89 mm/ $\mu$ s and  $P_o$  of 12.4 GPa.

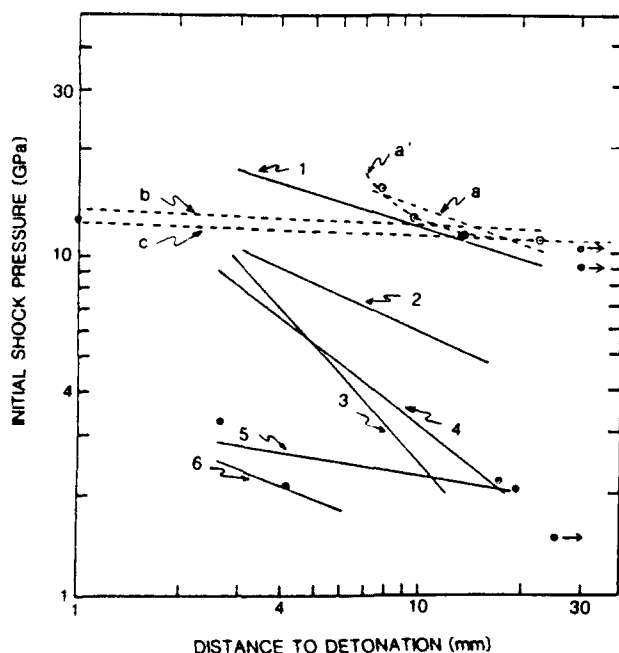


Figure 8. Pop-plot Data Points for 1.248 g/cc Emulsion With Linear Fit (Solid Line) and Hypothetical Curved Fit (Dashed Line); Pop-plots for Cast TNT,<sup>10</sup> Emulsions A, B, and C, AN/CN Emulsion, and PETN<sup>10</sup>

We feel, from a hazards point of view, that the concave upward or the flatter Pop plots (i.e., large changes in distance of run with small changes in initial shock pressure) for the 1.248 and 1.06 g/cm<sup>3</sup> emulsions are more representative of the shock initiation characteristics of these materials. The good safety record achieved by industry in using these materials would support this conclusion. On the other hand, Bauer et al. were able to simulate the go/no go response of their emulsions when subjected to impact by 13 mm diameter x 13 mm long brass projectiles with a two-dimensional reactive hydrocode incorporating Forest Fire reaction kinetics. While the results of their simulations agreed quite well with the experiments, the criteria for a go response was whether or not the material being impacted decomposed.

The experimentally determined  $U_s - u_p$  points for the unreacted Hugoniot of the 1.248 g/cm<sup>3</sup> emulsion are illustrated in Figure 9a. A linear least squares fit of the data is expressed by

$$U_s = 2.04 + 1.92u_p \quad (5)$$

for  $5.05 \leq U_s \leq 6.09$  mm/ $\mu$ s. The unreacted Hugoniot of the emulsion matrix at density

1.353 g/cm<sup>3</sup>,<sup>3</sup> was obtained from the above  $U_s$  -  $u_p$  points by using the Mie-Grüneisen equation of state, with the Grüneisen gamma formulated by Oh and Persson.<sup>21</sup> The  $U_s$  vs  $u_p$  relationship of the emulsion matrix was assumed to be straight line. The shock Hugoniot of the emulsion matrix is expressed by

$$U_s = 2.55 + 2.01u_p \quad (6)$$

From the unreacted Hugoniot of the matrix, the unreacted Hugoniots of emulsion explosives at densities 1.248 and 0.945 g/cm<sup>3</sup> were calculated. The unreacted Hugoniots are shown in Figure 9; 9a for  $U_s$  vs  $u_p$  Hugoniot and 9b for  $p$  vs  $v$  Hugoniot. In Figure 9b, the Hugoniot and the isentrope of the reaction products of the emulsion explosive at density 1.248 g/cm<sup>3</sup>, calculated by the BKW code, are also presented. On the unreacted Hugoniot the pressure at the von Neumann spike was calculated to be 19 GPa.

## CONCLUSIONS

The detonation behavior of the water-in-oil emulsion explosive studied is markedly different from that of monomolecular explosives: the behavior becomes more nonideal, and the failure diameter increases, as the initial density increases. The extrapolated ideal velocities are in good agreement with the theoretical calculations using the BKW code, especially at high densities. Hot spots are important in detonation, as well as the initiation, of this explosive.

The Pop plot of the emulsion explosive showed that the emulsion explosive is less sensitive than cast TNT, and the plot may be concave upward, which implies a relatively high threshold pressure for shock initiation. Regardless, the runs to detonation are predicted to be very long for pressures below 8 GPa. Considerations of the reaction zone and initial shock temperature, and limited experiments suggest that the matrix material will not detonate at charge diameters below 378 mm without a sensitizer, hot spot source, or elevated temperature.

It is very difficult to find useful and reproducible experimental data for industrial type explosives. In this paper, we have presented

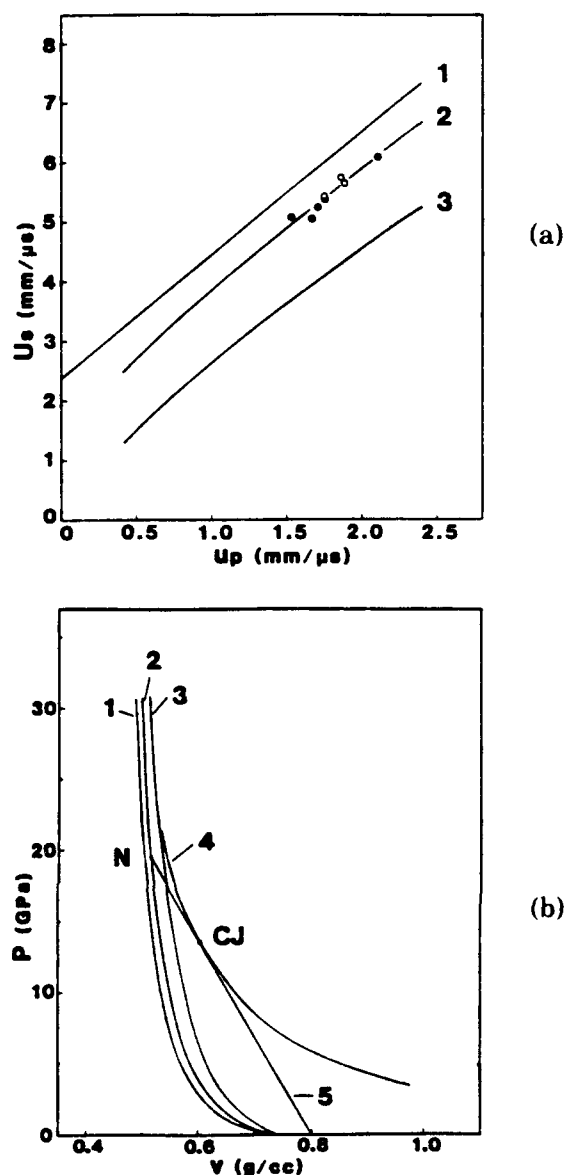


Figure 9. Hugoniots of AN Emulsion Explosives. (a) Unreacted Hugoniots in the  $U_s$  vs  $u_p$  plane; 1-for 1.353 g/cm<sup>3</sup> emulsion matrix; 2-for 1.248 g/cm<sup>3</sup> emulsion explosive including data points; 3-for 0.945 g/cm<sup>3</sup> emulsion explosives. (b) Unreacted Hugoniots in the  $P$  vs  $v$ ; 1-for 1.353 g/cm<sup>3</sup> emulsion matrix; 2-for 1.248 g/cm<sup>3</sup> emulsion explosive; for 0.945 g/cm<sup>3</sup> emulsion explosive; 4-Hugoniot and isentrope of the reacted products of the emulsion explosive at density 1.248 g/cm<sup>3</sup>, calculated by the BKW code; 5-Rayleigh line for detonation velocity of 6.66 mm/μs; N-von Neumann spike; CJ-Chapman-Jouguet point.

data that has been obtained over the last few years. However, considerable work still needs to be done to fully characterize the behavior of many industrial explosives in use today.

## ACKNOWLEDGMENTS

The work presented was supported by the Center for Explosives Technology Research (CETR) and the Research Center for Energetic Materials (RCEM). Authors are grateful to CETR and RCER for permission to publish this work. The authors express thanks to the firing crew at the CETR Eagle Facilities, P. D. Anthony.; T. E. Gould.; J. E. LaBerge.; and J. M. Reed. The authors also thank Nelson Brothers, Inc. for making the emulsion matrix, and 3M Corporation for providing microballoons for this work

## REFERENCES

1. Gehrig, N. E., "Aqueous Emulsified Ammonium Nitrate Blasting Compositions Containing Nitric Acid," U.S. Patent No. 3164503, 1965.
2. Bluhm, H. F., "Ammonium Nitrate Emulsion Blasting Agent and Method of Preparing Same," U.S. Patent No. 3447978, 1969.
3. Hattori, K.; Fukatsu, Y.; and Sakai, H., "The Effect of the Size of Glass Microballoons on the Detonation Velocity of Emulsion Explosives," *Journal of Industrial Explosives Society of Japan*, Vol. 43, 1982, p. 295.
4. Yoshida, M.; Iida, M.; Fujiwara, S.; Kusakabe, M.; and Shiino, K., "Detonation Behavior of Emulsion Explosives Containing Microballoons," *Proceedings of the Eighth Symposium (International) on Detonation*, NSWC MP 86-194, Naval Surface Weapons Center, Albuquerque, NM, Jul 15-19, 1985, pp. 993-1000.
5. Lee, J. and Persson, P.-A., "Detonation Behavior of Emulsion Explosives," submitted to *Propellant, Explosives, Pyrotechnics*.
6. Mader, C. L., *Fortran BKW: A Code for the Detonation Properties of Explosives*, LA-3704, Los Alamos National Lab., Los Alamos, NM, Jul 1967.
7. Mader, C. L., *Numerical Modeling of Detonation*, University of California Press, Berkeley, CA, 1979, pp. 88-100.
8. Bdzil, J. B., "Steady-State Two-Dimensional Detonation," *Journal of Fluid Mechanics*, Vol. 108, 1981, p. 195.
9. Campbell, A. W. and Engelke, R., "The Diameter Effect in High Density Heterogeneous Explosives," *Proceedings of the Sixth Symposium (International) on Detonation*, ACR-221, Office of Naval Research, Coronado, CA, Aug 24-27, 1976, pp. 642-652.
10. Gibbs, T. R. and Popolato, A., Eds., *LASL Explosives Property Data*, University of California Press, Berkeley, CA, 1980, pp. 293-296, 315, 340.
11. Forest, C., *Burning and Detonation*, LA-7245, Jul 1978, Los Alamos National Lab., Los Alamos, NM.
12. Bauer, A.; Katsabanis, P.; Moroz, J. W.; Feng, K. K.; and Vandebeek, R., "High Velocity Impact Sensitivity of Commercial Slurry and Emulsion Explosives," *Minutes of the Twenty Second Explosives Safety Seminar*, Department of Defense Explosives Safety Board, Anaheim, CA, Vol. 1, Aug 26-28, 1986, pp. 381-416.
13. Yoshida, et al.; *ibid.* For comparison with other types of emulsion explosives, the ideal velocity data were recalculated by the BKW code.
14. Miron, Y.; Watson, R. W.; and Hay, J. E., "Nonideal Detonation Behavior of Suspended Explosives as Observed from Unreacted Residues," *Proceedings of the International Symposium on the Analysis and Detection of Explosives*, FBI Academy, Mar 1984, pp. 79-89.
15. Campbell, A. W.; Davis, W. C.; and Travis, J. R., "Shock Initiation of Detonation in Liquid Explosives," *Physics of Fluids*, Vol. 4, 1961, p. 498.
16. Campbell, A. W.; Davis, W. C.; Ramsay, J. B.; and Travis, J. R., "Shock Initiation

of Solid Explosives," *Physics of Fluids*, Vol. 4, 1961, p. 511.

17. Engelke, R., "Effect of a Physical Inhomogeneity on Steady-State Detonation Velocity," *Physics of Fluids*, Vol. 22, 1979, p. 1623.
18. Eyring, H.; Powell, R. E.; Duffey, G. H.; and Parlin, R. B., "The Stability of Detonation," *Chemical Review*, Vol. 45, 1949, p. 69.
19. Walsh, J. M. and Christian, R. H., "Equation of State of Metals from Shock Wave Measurements," *Physics Review*, Vol. 97, 1955, p. 1554.
20. Anthony, P. D., *Annual Report 1986-1987*, RCEM Report A-02-87, Jul 1987, Research Center for Energetic Materials, New Mexico Institute of Mining and Technology, Socorro, NM, pp. 32-38.
21. Oh, K.-H. and Persson, P.-A., "Universal Features of the Effective Grüneisen Function Derived from Experimental High Pressure Data," to be published.

## DISCUSSION

J. B. RAMSAY, Los Alamos National Laboratory, Los Alamos, NM

The low-pressure limit for initiation has been proposed in most discussions of shock initiation, but there are only limited data to support this idea. It would be a real contribution to confirm the idea, even for one explosive.

## REPLY BY B. G. CRAIG AND F. W. SANDSTROM

Measurement of a threshold pressure for initiation would be desirable as well as a challenge. We point out that our failed efforts to establish a detonation in large charges of unsensitized emulsion at ambient temperature strongly suggest that the threshold for this material exceeds the calculated von Neumann spike pressure. That is, it appears the base emulsion will not propagate detonation at ambient temperature unless strongly overdriven. Additional effort on this interesting facet of the emulsion is planned.

For the case of initiation of sensitized emulsions, the determination of a threshold is even more difficult. The Pop-plot, assuming it can be determined for these materials, cannot be extrapolated to infinite run distances. An alternative method used by Craig presents wedge test data in the form

$$P_0 = P_t + B(1/x^*)$$

and can be used to provide a measure of threshold pressure when  $x^* = \text{infinity}$  for the initiation mechanism dominating the typical wedge test. However, the limited low pressure wedge experiments we have performed deviate from the fit, which suggests a change in the dominant mechanism. Such a change is consistent with available threshold data and Frey's model for shock initiation.

## DISCUSSION

D. KENNEDY, ICI Australia  
Ascot Vale 3032 Australia

I have two comments:

(1) Our experience would indicate that the walls of the PVC tubes used for detonation velocity measurements are too thick. The failure diameters in Figure 7 will be too low by about 10 to 20 percent. The detonation velocities for small diameters in Figure 6 will be too high, leading to extrapolated  $D_\infty$  values that are too low.

(2) I have used a reactive flow model (see G. A. Leiper and D. L. Kennedy, 4th Symp. on High Dynamic Pressures, La Grande Motte, France, Jun 1989) in the hydrocode DYNA2D to examine the behavior of this type of emulsion in the wedge test. The simulations reproduce the experimental observations of a lack of a definite transition point in the shock front location versus distance or time.

There is a smooth and gradual buildup to detonation. Inspection of the pressure and extent of reaction profiles, and of the location of the sonic plane, all failed to give an unambiguous criterion that could be used to determine when detonation was reached.

The success of initiation experiments such as the wedge test, and of failure experiments such as the cone test, depends on there



being a strong dependence of the reaction rate upon the local pressure or temperature. This is true for "ideal" explosives. However, for composite "nonideal" explosives, mass diffusion is more important, and the reaction rate no longer shows the same degree of acceleration with increasing pressure or temperature.

Experiments designed for ideal explosives are not always appropriate for nonideal explosives.

**REPLY BY J. LEE,  
F. W. SANDSTROM, AND  
P.-A. PERSSON**

The failure diameter is strongly affected by confinements. The failure diameter of an unconfined charge will be larger than that measured in a PVC tube. The purpose of our experiments was to estimate the failure diameter of the unsensitized emulsion matrix, which is difficult to measure experimentally, by extrapolation from experimental values at lower densities to the matrix density. The detonation velocity in a PVC tube will be higher than that of an unconfined charge. The diameter effect curve, detonation velocity ( $D$ ) as a function of charge diameter ( $d$ ) in the  $D$  vs.  $d^1$  plane, for charges in PVC tubes will also have a different slope from that for unconfined charges. However, the extrapolation of the diameter effect curve to infinite diameter will

lead to the same value for either case. For most explosives, the diameter effect curves are quadratic theoretically,<sup>1</sup> but it can be approximated very well by a straight line at relatively large diameters. We have not found any experimental evidence to contradict that behavior in the emulsion explosives we investigated. The extrapolated ideal velocity agrees well with the theoretical calculated value by the BKW code: 5.23 mm/ $\mu$ s extrapolated value compared to 5.55 mm/ $\mu$ s for the BKW calculation at a density of 1.000 g/cm<sup>3</sup> and 6.59 mm/ $\mu$ s extrapolated value compared to 6.68 mm/ $\mu$ s at 1.253 g/cm<sup>3</sup>.

We agree with your comments on initiation behavior of a composite nonideal explosive. The emulsion explosive which we investigated required very high initial shock pressure and showed a smooth and gradual transition to detonation. The detonation velocity estimated from the streak camera record was much lower than that extrapolated from a number of rate stick experiments, suggesting that the steady-state may not have reached in the wedge shots.

**REFERENCE TO REPLY**

1. Bdzil, J. B., "Steady-State Two-Dimensional Detonation," *Journal of Fluid Mechanics*, Vol. 108, 1981, p. 195.

# EFFECT OF PRESSURE ON SHOCK SENSITIVITY OF EMULSION EXPLOSIVES

G. Om Reddy  
INBRI, Division of IDL Chemicals Limited  
P.O. Box No. 397, 18th Cross, Sankey Road  
Malleswaram, Bangalore-560 003  
INDIA

and

Frank P. Beitel, Jr.  
Research Supervisor, Pittsburgh Research  
Center, U.S. Bureau of Mines  
Pittsburgh, Pennsylvania 15236 USA

*Effect of static pressure on emulsion explosives (EE) containing glass microballoons (GMB) was studied. The shock sensitivity of EE after they were subjected to pressure was determined by cap sensitivity experiments. The pressure effect on detonation velocity was measured using continuous rate probe. The stability of emulsion was judged by Differential Scanning Calorimetry (DSC). An optical microscope was used to study the effect of pressure on the emulsion matrix. Cap sensitivity experiments indicate that pressure above 700 psi makes EE insensitive to cap. A decrease in detonation velocity was observed in pressurized explosives. DSC thermograms of normal emulsion did not show freezing of water above -40°C, whereas explosive pressurized above 500 psi showed freezing point of water at -33°C. Thermograms of pressurized sample showed peaks corresponding to ammonium nitrate phase transitions, which were absent in normal sample. Optical microscopic study clearly indicated that the detonation failure in pressurized emulsion was due to emulsion breakage, and not to breakage of GMB.*

## INTRODUCTION

Explosives lose their detonation sensitivity for various reasons like storage conditions; storage time; temperature; and pressure,<sup>1</sup> which in turn affect the detonation velocity, burning properties, and performance of an explosive. Studies on pressure desensitization of water-based explosives<sup>2-4</sup> indicate that the applied pressure brings only temporary changes in gel structure, whereas emulsion explosives (EEs) undergo permanent density change due to compression, and they become insensitive to shock. There are two types of

applied pressure: dynamic and static. The main causes for desensitization are:

1. During delay blasting, the pressure resulting from the detonation of an explosive charge in one borehole can affect the adjacent undetonated explosive charge.
2. If the initiation energy for propagation is not sufficient, the explosive may undergo dynamic compression from the initiating charge.
3. Because of bad drilling or very fragile rock medium, the adjacent borehole may collapse and thereby pressurize the charge.

4. The stemming as well as the natural hydrostatic pressure can also create pressure on the bottom charge.

The hazards associated with pressure desensitization (dynamic or static) are many. In the case of EEs applied pressure reduces initiation sensitivity. The pressurized charge either fails to undergo detonation, or shows a low detonation reaction. The low detonation may result in a dangerous phenomenon "deflagration" which is a serious problem in coal mining operations. On the other hand, the unreacted explosive can remain in the muck pile, which might later lead to accidental explosion, and create a safety problem for mining personnel.

Recently, work was done at the Bureau of Mines on dynamic pressure desensitization.<sup>5</sup> It was found that water-in-oil (W/O) EEs undergo desensitization far more rapidly than water gels under transient shock pressure. Previous researchers assumed that the pressure desensitization may be due to the breakage of glass microballoons (GMB) present in emulsion matrix, but a detailed study is not available on the mechanism of desensitization. In this context, more detailed study is warranted on understanding the causes for shock insensitivity of pressurized EEs.

In the present study, pressure desensitization experiments were carried out on aged (3-9 months) EEs. The shock sensitivity was determined by cap sensitivity experiments. The detonation velocity was measured using a continuous rate probe. Optical microscope, differential scanning calorimetry (DSC), and conductometry were applied to judge the emulsion stability.

## EXPERIMENTAL

### Material

The composition of emulsion matrix is shown in Table 1.

### Equipment

**Pressurization.** The whole cartridge was placed in a suitable steel bomb and pressurized with compressed air. The pressure was released after some time, and the cartridges

Table 1. Material Composition of Emulsion Matrix

Material	Wt. %
Ammonium nitrate	65.0
Sodium nitrate	15.0
Water	11.0
Sobitan monooleate	2.0
Elfacos ST-37	1.0
Paraffin	4.0
Glass Microballoons	2.0

were taken out and stored in magazines at ambient temperature for 24 hours for further experiments.

**Detonation velocity.** One normal cartridge (donor) was used in conjunction with a pressurized cartridge (acceptor), and both were wrapped in thick brown paper. A 13-inch long continuous rate probe was fixed on the surface of the explosive, and the donor cartridge was initiated by a No. 6 cap. A Nicolet oscilloscope No. 97 was used to determine the detonation velocity. The arrangement is shown in Figure 1.

**Cap Sensitivity.** The pressurized cartridges were stored at room temperature for 24 hours before firing with the No. 6 cap. In the case of complete detonation, none of the cartridge was left, whereas part of the cartridge was left unreacted in the case of incomplete detonation.

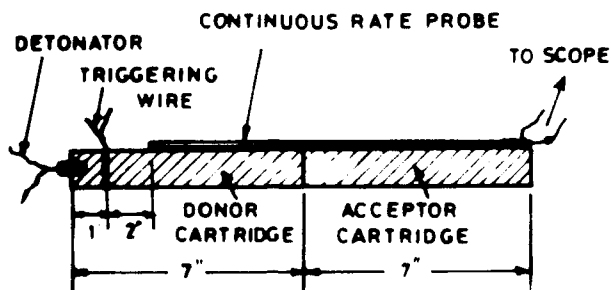


Figure 1. Arrangement of Cartridges for Detonation Velocity Measurement

**DSC.** A Perkin-Elmer DSC-4 was used. Aluminum cups (P.E. Part No. 0219-0041) and high pressure gold-plated cups (P.E. Part No. 0419-0205) were used. Intracooler-I was used for the low temperature study. Analysis was carried out under nitrogen atmosphere.

**Optical Microscope.** A E-Leitz orthoplan microscope with a phase contrast facility was used. A Polaroid camera was used for taking photographs.

**Conductivity Measurement.** Fisher conductivity meter model-152 was used for measuring the electrical conductivity of EEs before and after pressurization. Two hundred g's of deionized and double distilled water was weighed accurately and poured into a clean, dry 250 ml glass beaker, and 0.5 g of explosive was weighed accurately, added to the beaker, and stirred well for 2 minutes using a magnetic stirrer. A conductivity measurement of the aqueous layer was taken after 10 minutes.

## RESULTS AND DISCUSSION

### Detonation Velocity Measurement

Pressurized cartridges were stored for 24 hours at room temperature before shooting. The detonation velocity of the pressurized explosive was compared to unpressurized explosive. The oscilloscope traces of time versus voltage are shown in Figure 2. The normal EEs showed a velocity of  $5000 \pm 100$  m/s before it was pressurized. The same explosive, when pressurized at 125, 250, 500, 650, 750, and 850 psi for 5 minutes, showed detonation velocities of 5000, 5000, 4650, 3800, 3400, and

1200 m/s, respectively. A gradual decrease in the velocity was observed as the pressure was increased. A decrease in the velocity within the cartridge was also noticed (see Figure 2). In the case of explosives pressurized at 1000 and 1250 psi, an incomplete detonation was observed and a portion of the cartridge was unreacted. It appears that the explosive undergoes a drastic change when the applied pressure is above 500 psi. It is presumed that if one cartridge, pressurized (above 500 psi) by some means, was filled along with normal cartridges in a borehole, it might pose a problem of incomplete detonation.

**Cap Sensitivity.** Cap sensitivity experiments were carried out on pressurized EEs using the No. 6 cap. The results are presented in Table 2. These results show that pressure above 500 psi desensitizes the charge. About a 4- to 5-inch cartridge was left unreacted when the explosive was pressurized at 750 and 1000 psi. It was stated earlier that a complete detonation was observed up to a pressure of 850 psi, although there was a considerable decrease in detonation velocity. This difference may be due to different firing conditions. In detonation velocity measurements the pressurized cartridge was preceded by a normal cartridge, whereas in cap sensitivity experiments only the No. 6 cap was used for initiation.

### Thermal Analysis

**Thermal Sensitivity and Decomposition Energy.** The objective of the study was to see the effect of pressure on thermal sensitivity. DSC thermograms were recorded

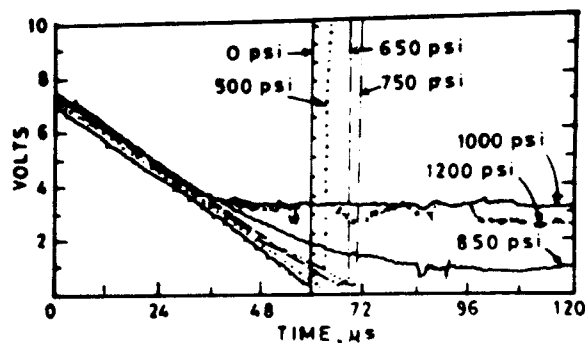


Figure 2. Oscilloscope Traces of Time Vs. Volts for the Determination of Detonation Velocity of Pressurized EE

Table 2. The Cap Sensitivity Results on Pressurized EE

Pressurized for 5 min (psi)	Firing Results
125	Complete detonation
250	Complete detonation
500	50% Pass
750	Incomplete Detonation
1000	Incomplete detonation

on pressurized samples and compared with unpressurized samples. Slow heating rates and open aluminum cups provided little information regarding decomposition temperature and energy. Good thermograms were obtained with gold-plated high pressure cups. The results appear in Table 3. It is apparent from the inception temperature that the thermal sensitivity decreases with applied pressure. The areas under the curves were measured with a planimeter, and the decomposition energy ( $\Delta H$ ) was estimated after calibrating the instrument with high purity Indium. The results show that the applied pressure decreases the decomposition energy. The peak heights, which are proportional to the reaction rates, decreased as applied pressure increased. The decrease in reaction rate, thermal sensitivity, and decomposition energy indicates that the fine bubble structure of dispersed phase in W/O EEs is affected by applied pressure.

**Low Temperature Study.** A good EE shows very low freezing temperature of water present in the matrix. This is mainly due to the very fine particle size of dispersed aqueous phase. A low temperature study on pressurized explosive was carried out using DSC to see the pressure effect on the emulsion stability. About 30.0 mg sample weighed into an aluminum cup was cooled from  $+20^{\circ}\text{C}$  to  $-45^{\circ}\text{C}$  at a  $5^{\circ}\text{min}^{-1}$  heating rate. Unpressurized samples, samples pressurized at 125, 250, and 500 psi, did not show freezing of water before

$-45^{\circ}\text{C}$ ; whereas samples pressurized at 750 and 1000 psi, and a sample left over during cap sensitivity experiments showed a freezing point of water at  $-34^{\circ}\text{C}$ ,  $-33^{\circ}\text{C}$ , and  $-32^{\circ}\text{C}$ , respectively. This explains that the applied pressure has a noticeable effect on the freezing point of water in EEs. The samples pressurized at 125, 250, and 500 psi did show freezing of water when they were kept isothermal at  $-45^{\circ}\text{C}$ . All the samples heated from  $-45^{\circ}\text{C}$  to  $0^{\circ}\text{C}$  at a  $5^{\circ}\text{min}^{-1}$  rate, gave a melting point of water at  $-30^{\circ}\text{C}$ . This indicates that once the water freezes, the emulsion matrix is affected, irrespective of applied pressure.

**High Temperature Study.** Pure ammonium nitrate (AN) shows phase transition temperatures<sup>6</sup> at  $-16.9$ ,  $32.3$ ,  $84.2$ , and  $125.2^{\circ}\text{C}$ . In EEs, AN will be in a liquid or semisolid state with no definite crystal structure. Good emulsion when heated from  $30^{\circ}\text{C}$  to  $150^{\circ}\text{C}$  does not show AN phase transitions. The effect of pressure on the emulsion stability was studied by recording DSC thermograms between 30 and  $150^{\circ}\text{C}$  with  $10^{\circ}\text{min}^{-1}$  rate. The heating thermograms of a sample pressurized at 750

Table 3. Thermal Characteristics of EEs

Sample	Inception Temperature ( $^{\circ}\text{K}$ )	$\Delta H$ (J/g)
1. Normal	530.5	452.5
2. Pressurized at 125 psi	538.0	386.3
3. Pressurized at 250 psi	545.5	253.5
4. Pressurized at 500 psi	557.5	242.0
5. Pressurized at 1000 psi	553.0	237.7

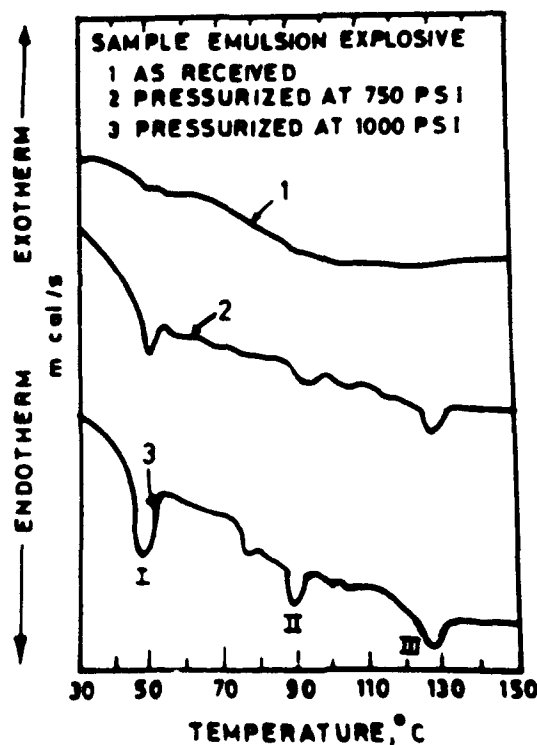


Figure 3. Heating Thermograms of Normal and Pressurized EEs

and 1000 psi were recorded and compared with an unpressurized sample. The thermograms are shown in Figure 3. The cooling thermograms are shown in Figure 4. Cooling curves showed more resolved peaks compared to heating curves. Pressurized samples showed peaks corresponding to AN (peaks I, II, and III) which were absent in unpressurized samples. In addition to ammonium nitrate phase transition peaks, other small peaks in EEs may be due to hydrocarbons. This study establishes the criteria to distinguish bad and good emulsions by monitoring their breakage during pressurization, followed by the crystallization of AN and other salts present in the system.

**Optical Microscopic Study.** An optical microscope was used to monitor the physical changes that occurred during pressurization. Two sets of experiments were carried out. In one set of experiments pressure was varied from 0 to 1250 psi, keeping the time constant. In another set of experiments, pressure was kept constant and time was varied from 15 to 240 seconds. The samples examined were pressurized at 125, 250, 400, 500, 600,

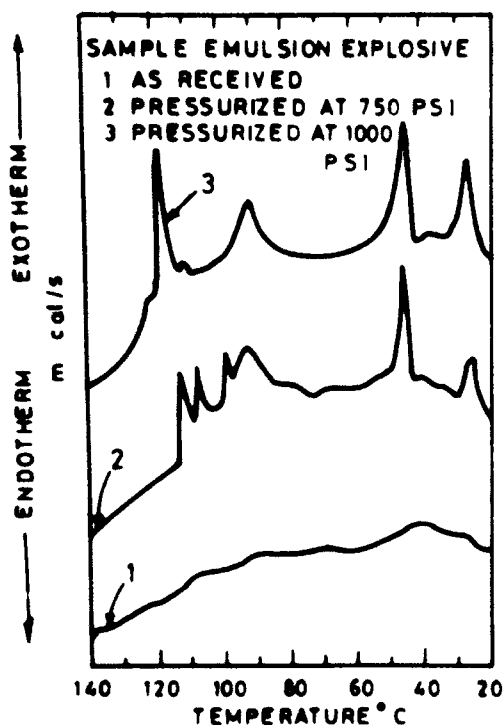


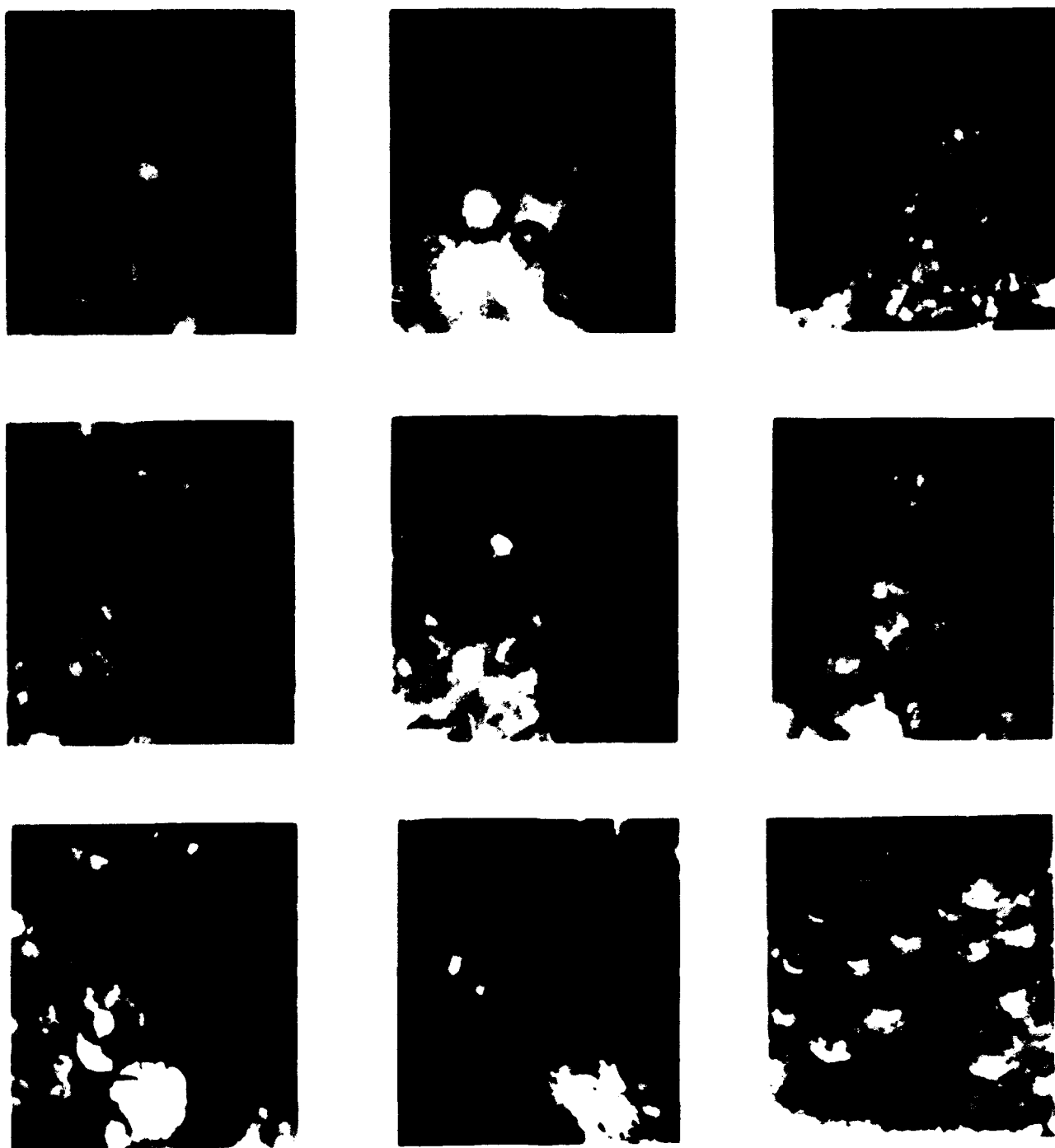
Figure 4. Cooling Thermograms of Normal and Pressurized EEs

800, 900, 1100, and 1250 psi for 5 min. Figure 5 shows the photomicrographs of: (a) unpressurized sample, (b) sample pressurized at 125 psi, (c) sample pressurized at 250 psi, (d) sample pressurized at 500 psi, (e) sample pressurized at 750 psi, and (f) sample pressurized at 1000 psi.

The photomicrographs of emulsion: (a) desensitized by shock wave (underwater test), (b) failed to undergo detonation due to bad quality, and (c) GMB separated from pressurized (1250 psi) sample are shown in Figure 5(g), 5(h), and 5(i), respectively. The unpressurized sample showed a homogeneous background with scattered GMB. As the pressure increased from 125 to 1250 psi, the background became globular. The size of the bubble increased up to 600 psi, and emulsion breaks when the pressure is above 600 psi. In the second type of experiment with pressure at 1000 psi and varying time, it is clear from the photographs that the changes taking place during pressurization are very fast, and complete breakage occurs even in 15 seconds. This suggests that dynamic pressure coming from an adjacent borehole during delay blasting may damage the EEs. The photomicrographs of shock desensitized explosive and bad quality emulsion which failed to undergo detonation are comparable with the sample pressurized at 1000 psi.

Photomicrographs of pressurized and desensitized EEs show very few GMB. Initially, it was thought GMB were broken during pressurization. To check this argument, GMB were isolated from pressurized samples and examined under a microscope. Surprisingly, no broken GMB were seen in the pressurized sample. Since the emulsion was broken and the oil phase was not continuous, the GMBs were not seen clearly. This study enabled us to understand the reasons for desensitization during pressurization. Detonation failure is due to the breakage of emulsion and the crystallization of AN, but not to the breakage of GMB.

**Conductivity Measurement.** Conductivity increases rapidly up to 900 psi and remains almost constant above that pressure (Figure 6). When emulsion breaks, its solubility and conductivity in water increases



*Photomicrographs of EEs: (a) Unpressurized Sample, (b) Pressurized at 125 psi, (c) Pressurized at 250 psi, (d) Pressurized at 500 psi, (e) Pressurized at 750 psi, (f) Pressurized at 1000 psi, (g) Desensitized by Shock Wave, (h) Bad Quality Emulsion (Broken), and (i) GMB Separated from Pressurized (1250 psi)—Sample Magnification: x 160*

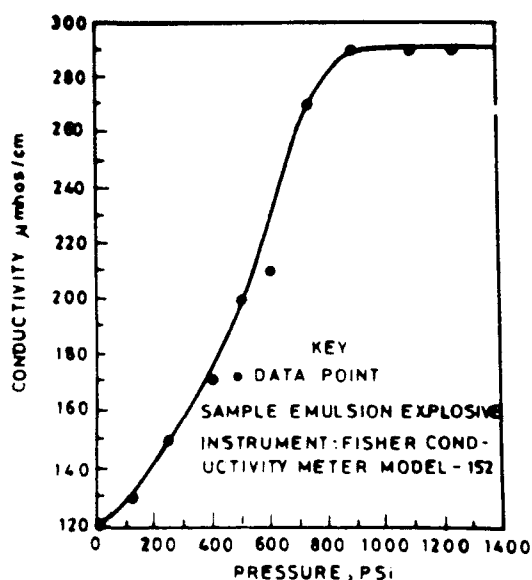


Figure 6. Conductivity of Pressurized EEs

as more ions (ammonium, nitrate, etc.) are released into the water. This data also supports our argument that the applied pressure breaks the emulsion and the explosive becomes shock insensitive.

## CONCLUSIONS

Detonation velocity and shock sensitivity of EEs decreases with increased pressure.

Thermal sensitivity and thermal decomposition energy of EEs decreases with increased pressure.

Detonation failure in pressurized EEs is due to the breakage of emulsion, but not due to the breakage of GMB.

## ACKNOWLEDGEMENTS

The authors thank M/S IDL Chemicals Limited, India, and the U.S. Bureau of Mines, Pittsburgh, PA, USA for giving them the opportunity to do this work under the Joint Research Program, and for permission to publish this work. We wish to thank Messrs. Tom Ruhe and Don Voigt, and their colleagues for their cooperation and help. One of the authors, G. Om Reddy, thanks the management of IDL Chemicals, Hyderabad, India, for providing this opportunity, and the U S. Bureau of Mines, Pittsburgh, PA,

USA for providing the facilities. He also thanks Dr. V. Krishna Mohan and Dr. P. L. Hariharan for useful discussions.

## REFERENCES

1. Sandus, O., "Concept of Ideal and Non-Ideal Explosives," Technical Report ARLCD-TR 81042, 1981.
2. Ahmed, A. and Hay, J. E., "Possibilities of Pressure Desensitization of Water Based Permissibles During Multiple Delay Blasting," U.S. Bureau of Mines, Internal Report, 1982.
3. Miron, Y. and Ruhe, T., "The Effect of Applied Pressure on the Sensitivity of Explosives," U.S. Bureau of Mines, Internal Report, 1981.
4. Mukherjee, A. K., "Research on Hazard Characteristics of Water Based Explosive Systems," U.S. Bureau of Mines, Internal Report, 1983.
5. Weiland, M., "Nozzled Pipe Fixtures for Studying Dynamic Pressure Desensitization," U.S. Bureau of Mines, Internal Report, 1984.
6. Dellien, I., "Thermochimica Acta," Vol. 55, 1982, pp. 181-191.

## DISCUSSION

WALTER B. SUDWEEKS, Ireco Incorporated, West Jordan, Utah

Is there a difference between static and dynamic pressure on emulsion desensitization?

REPLY BY G. OM REDDY  
AND F. P. BEITEL, JR.

We have not seen any difference between static and dynamic pressure on emulsion desensitization.

## DISCUSSION

WALTER B. SUDWEEKS, Ireco Incorporated, West Jordan, Utah

What strength glass micro balloons were used on this study?



Would higher strength change the results? (The presenter indicated more recent data since this work showed that desensitization could be delayed for several hundred psi if higher strength microballoons were used.)

**REPLY BY G. OM REDDY  
AND F. P. BEITEL, JR.**

The strength of glass microballoons could not be revealed because the information is proprietary. It was proven that desensitization is not due to the breakage of glass microballoons, but due to the breakage of emulsion. Even weaker glass microballoons were not broken under the pressure employed.

**DISCUSSION**

**PER-ANDERS PERSSON,**  
CETR/New Mexico Tech.  
Socorro, New Mexico

What is the mechanism of breakdown of an emulsion due to pressure?

**REPLY BY G. OM REDDY**

We assume that during pressurization a very thin continuous oil phase (since W/O F<sub>2</sub>

is a high internal phase emulsion) is ruptured, and thereby facilitating the union of a small oxidizer particle into a big particle, and eventually emulsion breaks. These sequential changes are shown in series of photomicrographs. Once emulsion is broken, crystallization of oxidizer salt takes place.

**DISCUSSION**

**HAROLD GRYTING,** Gryting  
Energetics Sciences Company, San  
Antonio, Texas

What storage life would you predict for these EEs under ambient conditions of temperature and humidity?

**REPLY BY G. OM REDDY  
AND F. P. BEITEL, JR.**

Under normal conditions of storage, a good EE can be stored for one and half to two years without losing cap sensitivity. It is a known fact that emulsion stability decreases with increased storage time. Aged samples showed desensitization at very low pressures compared to fresh samples.

# DEVELOPMENT OF A MODEL OF REACTION RATES IN SHOCKED MULTICOMPONENT EXPLOSIVES

Kibong Kim  
Naval Surface Warfare Center  
Detonation Physics Branch  
Silver Spring, Maryland 20903-5000

*An earlier model<sup>1-3</sup> which describes microscopic hot spot generation and subsequent chemical reaction growth from these hot spots is improved in this paper to explain shock-to-detonation transition (SDT) in multicomponent explosives. The improved model, once completed by empirical determination of a small number of constants, can predict SDT in "similar" explosives. The term "similar" means: (a) made of same materials (component explosive and binder), (b) of different particle sizes, (c) of different initial porosities, (d) of different initial temperatures, and/or (e) of different initial mass distributions between the component explosive and the binder.*

## INTRODUCTION

In recent years, reaction rate models which describe shock-to-detonation transition in explosives have been developed. Forest Fire<sup>4,5</sup> has been calibrated for reaction rates of many explosives using Pop plot data<sup>4</sup> from wedge test experiments. The model was proven to be effective for numerical simulation of SDT, but it says little about the basic physics and chemistry of the reaction process. Therefore, the model lacks flexibility in describing non-straight-line Pop-plot data, as observed in aluminized explosives. Also, it cannot predict SDT in "similar" composite explosives, with the exception of variation of initial porosity. The term "similar" is used as follows. It is assumed that a multicomponent explosive is made of a component explosive and a binder material. If two multicomponent explosives are made of same materials, but of different particle sizes, of different initial temperatures, of different densities, and/or of different mass distributions between the component explosive and the binder, then they are called similar.

The Ignition and Growth model<sup>6,7</sup> provides insight into the basic physics. Indeed, the basic concept offered by the model,

separate descriptions of ignition and growth, has been used as one of the main features in the present model. While the Ignition and Growth model has greatly increased our understanding of the physics of SDT, it still is a phenomenological model in the sense that (a) the derivation of the ignition term is not firmly based on physics, and (b) SDT of similar explosives cannot be predicted.

Tang's model<sup>8-12</sup> also simulates SDT. The model is capable of reproducing the effects of changes in both density and grain size by varying some of the constants in the model until good fit with experimental data is obtained. In this empirical model, however, no attempt is made to explicitly model any of the physical mechanisms leading to hot spot formation. Instead, time constants are defined for each of the significant SDT processes: (a) hot spot excitation, (b) transport of energy, and (c) decomposition in the bulk explosive. These and some other constants are empirically fitted to experimental data.

Anderson et al.<sup>13</sup> proposed the DAGMAR model to describe initiation of PBX-9404 and porous TATB. Karakatoa model<sup>14</sup> describes

the ignition process while successfully reproducing experimental Pop plot data.

Some models describe the microscopic hot spot formation during the ignition process. Cochran and Tarver<sup>15</sup> proposed a shock initiation model which statistically described effects of particle size distribution, initial temperature and initial density on hot spot formation and subsequent reaction. Hot spots are areas in explosives which have a higher temperature than the rest of the explosive such that chemical reactions start here. Hayes,<sup>16</sup> Pastine, and Frankel<sup>17</sup> assumed that plastic work generated around a pore in an explosive is converted into heat in the solid near the pore whose volume is equal to the original pore volume. The temperature is assumed high and uniform in space in the solid volume. Nunziato, Baer, and Kipp<sup>18-20</sup> also developed a constant temperature hot spot model based on a two- or three-phase mixture theory. Figure 1<sup>21</sup> shows their assumption. On the right,

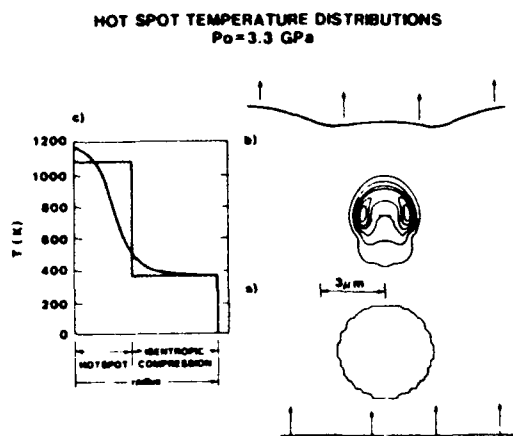


Figure 1. Shock Induced Collapse of a Single Pore and the Corresponding Temperature Profile in the Vicinity of a Hot Spot

a hydrocode simulation of pore collapse during a passage of a shock is shown. A spherical hole at the bottom of the figure awaits a shock coming from below. At the top, the pore deformation after passage of the shock is shown. On the left, the corresponding temperature profile is presented as a monotonically decreasing function of the radial coordinate from the center of the pore. Also shown in the same plot is the constant temperature hot spot approximation. This type of approach has two major

difficulties: (a) The extent of hot spots cannot be accurately determined, and (b) since the chemical reaction rate is a sensitive function of the temperature, it is impractical to describe the chemical reaction rate with such a simple constant-temperature model.

Another shortcoming of most of the above models is that the models were developed based on observations from sharp shocks applied to explosives, and therefore show difficulty in handling compression waves with finite rise times or multiple shocks. As an example, most of these models will not show the desensitization effect of ramp waves properly. Since there are many real situations where such compression waves or multiple shocks are encountered, this is a serious problem.

In order to remedy the above shortcomings, a reaction rate model must be developed which is based on microscopic hot spot concepts. Several people, Kim,<sup>1-3</sup> Khasainov et al.,<sup>22</sup> Kooker and Anderson,<sup>23</sup> Partom,<sup>24</sup> Wackerle et al.,<sup>25</sup> Frey,<sup>26</sup> and Nutt<sup>27</sup> attempted to solve the problem of determining microscopic hot spot temperature distribution. They all used the hollow sphere collapse model developed by Carroll and Holt<sup>28</sup> for compaction of inert materials and later applied to hot spots in explosives by Taylor.<sup>29</sup> This paper describes an extension of Kim's model.

## CONCEPTUAL INTERPRETATION OF SDT PROCESS

Construction of the model is explained in the following. The essential feature in shock compression of composite explosives is the formation of hot spots. The formation of hot spots depends on defect structures (porosity, pore size, impurities, grain size, etc.) in the explosives. Dependence on the complex defect structure often results in confusion and disagreement regarding quantitative determination of operating mechanisms in the formation of hot spots. However, it appears to be firmly established<sup>4</sup> that the concept of the hot spots adjacent to each pore is a necessary ingredient in any theory or in any analysis of shock initiation of chemical reaction.

Figure 2 shows a typical pore in a multicomponent explosive. The hot spots are created by many different forms of mechanical deformation: hydrodynamic deformation,<sup>29</sup> jetting,<sup>30</sup> shear banding, crack propagation, shock wave reflections, dislocation pileup and others. The elevated temperature in hot spots is not uniform in space and time, and the concept of the "size" of hot spots is rather ill-defined. Most likely, there will be a peak or peaks of temperature around pores or discontinuities in the explosives surrounded by regions of steep but continuous decay of temperature to relatively cold surroundings. Below some critical temperature in these hot spots, chemical reaction can be ignored and the temperature in the hot spot region will increase with time due to mechanical deformation and will be moderated by heat conduction to the surroundings.

If the temperature (nonuniform in space and time) further increases beyond the critical value, the region of the highest temperature will undergo temperature-dependent chemical reaction processes (such as thermal explosion or a deflagration). The chemical reaction (being exothermic) will further increase the temperature in that region of highest temperature, thus rendering the temperature

gradient in space steeper. This causes an increase in the heat conduction rate to the surrounding material.

At the same time, the product gas of the chemical reaction fills the pore. The gas in the pore before any chemical reaction is originally cold and of low pressure, but as the chemical reaction continues, the density, the pressure, and the temperature of the gas will increase continuously. The high gas pressure will compress the binder material as well as the component explosive.

As the gas pressure in the pore continuously increases, at some point in time the mechanical deformation (creating hot spots) ceases because there will be less difference between the applied stress on the solid by the initial shock wave and the deformation-resisting gas pressure from within the explosive. The solid by this time is losing heat to the direction into the solid by heat conduction and losing (solid) material to the direction toward the pore by vigorous chemical reaction.

At this point, the overall chemical reaction around the pore is similar to the classical surface burning form: heat conduction from hot, high pressure gas to solid,

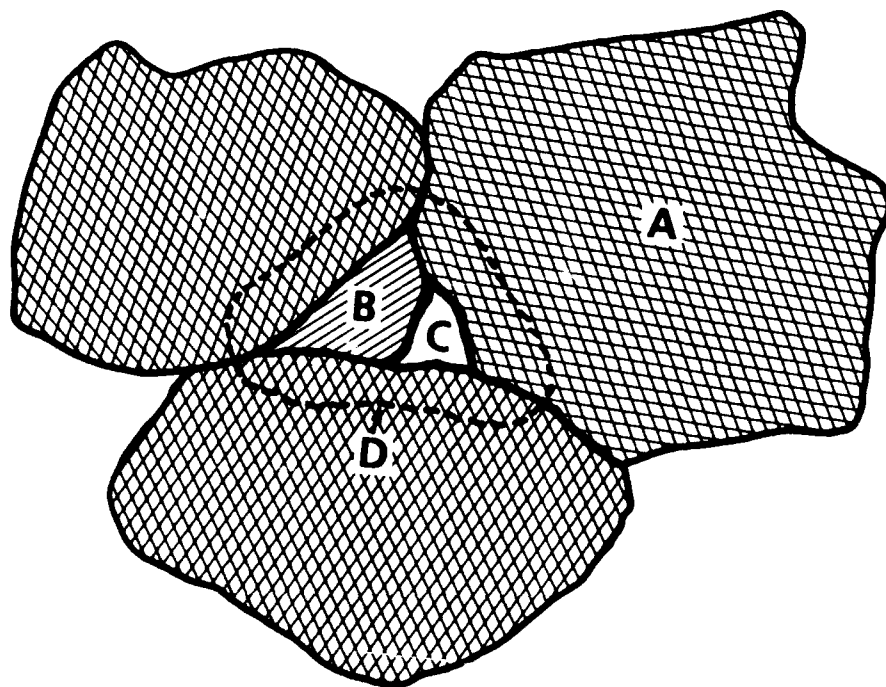


Figure 2. A Typical Pore in Multicomponent Explosives. A: component explosive, B: binder, C: void (pore), D: areas of high mechanical deformation (hot spots).

steep temperature gradient within thermal layer of solid, heat conduction into solid, chemical reaction and phase transition (from solid to gas) at and near solid surface. The reaction will grow continuously.

In the following the reaction rate model is developed based on the above description in two phases: the ignition phase and the reaction growth phase.

## IGNITION PHASE

A practical requirement of a model describing shock-induced reaction in explosives is that it be simple enough to use in hydrodynamic codes without unacceptably increasing the computation time. Also, as proposed in the Introduction, the model should be general and explicitly describe the physical phenomena described in the previous section. Such a model, one hopes, will have at least a qualitative predictive capability on explosives of various porosities and various grain sizes.

For a model to be useful in hydrocodes simulating explosives under shock loading conditions, one wishes to have a local reaction rate expressed as a function of the space coordinate,  $x$ , and time,  $t$ :  $\lambda(x, t)$ . If one examines a small finite volume of the explosive at a location,  $x$ , there are a large number of pores of various shapes and sizes, not to mention boundaries between grains and imperfections around which much of mechanical deformation is observed. It is possible that regions around some pores may start chemical reaction earlier than other regions. Thus, the situation is very complicated. An exact study of the formation of hot spots around these pores (or several pores) which combines them into a general model is very difficult.

If one simplifies his method of observation of the hot spots, then findings from such observation can be described in a simple and generic fashion without loss of the basic characteristics of the hot spots. Such characteristics will be investigated here. If the porosity of the explosive is of the order of a few percent, then the volume of a pore is much smaller than that of the component explosive material which surrounds the pore. When the explosive is shocked, there will be peaks of

temperature around the pores generated by shear banding, friction, microjets, etc., with a steep temperature decay to the neighboring explosive material such as shown in Figure 1. These peaks will be more closely packed together near the pore edges than far from the edges.

If one looks at the temperature distributions near and around many pores through a "hazy" glass and overlaps the resulting visions together, he might say there is one peak temperature around the pores with a monotonically decreasing temperature toward outside. This "view through a hazy glass" process is necessary for masking details and showing a global representation of a system.

Using these observations, the approach taken for a simple model is as follows. Disregard the details (but do not deny the physics) of shear banding, friction, jet impingements, or other mechanical deformation, and assume that near the pore there is a global mechanical deformation in progress and that the material behavior is such that the stress is dependent on strain and strain rate (elastic-viscoplastic). Assume that a hot spot around a pore is similar to all other hot spots in the vicinity and, therefore, the study of one hot spot represents all hot spots in the vicinity. This model has a peak temperature which monotonically decreases away from the pore. Since the description of the hot spot should be simple (therefore, a one-dimensional description would be needed), one adopts a hollow sphere pore collapse model. The hollow sphere model can represent all of the features described above. The model is represented in Figure 3.

Figure 3 shows a typical space arrangement of the component explosive, the binder material and a pore in a given composite explosive. The component explosive material (of volume  $V_E$ ) surrounds both the binder material (of volume  $V_B$ ) and the pore (of volume  $V_P$ ). The outer radius,  $r_o$ , is determined such that (1) it is same as the typical particle radius, and (2) the volume within it is the total of  $V_E$ ,  $V_B$ , and  $V_P$ .

$$V_o \equiv \frac{4}{3} \pi r_o^3 = V_E + V_B + V_P \quad (1)$$

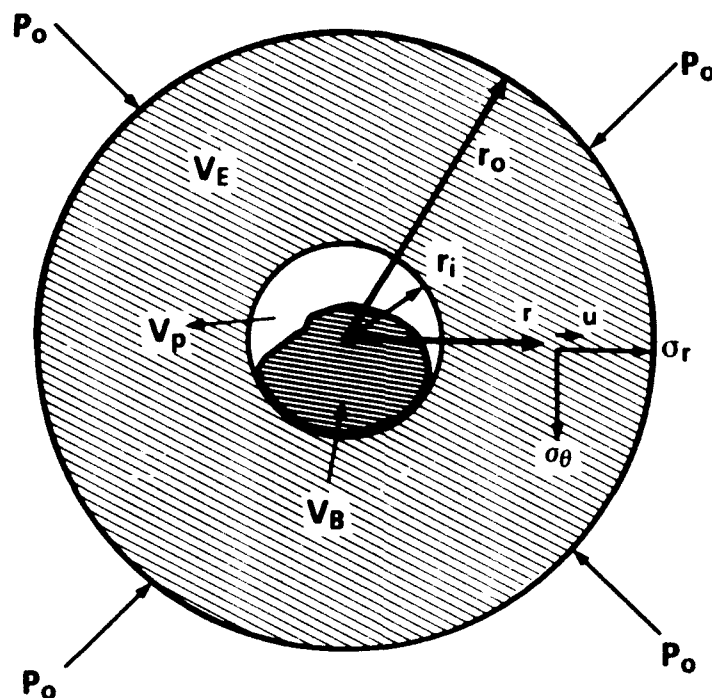


Figure 3. Hollow Sphere Model.  $r_o$  is the outer radius of the hollow sphere,  $r_i$  is the inner radius,  $V_E$  is the volume of explosive,  $V_B$  is the volume of binder (or other slow reacting materials),  $V_P$  is the pore volume,  $r$  is the space coordinate,  $u$  is the displacement,  $\sigma_r$  and  $\sigma_\theta$  are radial and tangential stresses and  $P_o$  is the applied stress.

The inner radius,  $r_i$ , is determined such that the ratio of the volume inside ( $V_B + V_P$ ) to  $V_o$  is same as that of the multicomponent explosive under investigation. Similarly,  $V_B$  is determined.

If the binder material is softer than the explosive material, one can develop the following picture of hot spot formation. As a stress,  $P_o$ , is applied from outside, the explosive material undergoes a one-dimensional (spherical) shear deformation around the pore. Bulk compression of the explosive and the binder material may occur. As the temperature of the hot spot (in the component explosive material near the pore) increases, chemical reaction may take place and its product gas may fill the pore. The increased gas pressure in the pore may further compress the explosive and the binder material. A mathematical description of this process will result in a reaction rate term during the hot-spot-induced ignition stage.

Even when there is no apparent initial porosity, ( $V_P \sim 0$ ), the above figure is able to

represent the hot spot formation process as long as volume changes in both the explosive and binder materials are accounted for such that the gas pressure in the pore,  $P_g$ , is properly calculated.

A somewhat different situation is presented when the binder material is harder than the explosive material, because the hot spot formation is probably due more to the explosive material moving relative to the binder material than due to its own shear deformation. Even in this case, however, if one once again utilizes the "hazy glass," the description given in Figure 3 may still be adequate in depicting hot spot behaviors.

The above description of the hot spot formation process allows exactly the same mathematical formalism introduced in References 2 and 3 to be also applicable here. The only change comes in the ratio between inner and outer radii of the hollow sphere and in calculation of the gas pressure in the pore which takes the existence of binder in the pore into consideration.

The overall reaction rate  $\lambda(x,t)$  is obtained as follows.<sup>2,3</sup>

$$\frac{d\lambda(x,t)}{dt} = \int_{r_i}^{r_o} \frac{\frac{d\Lambda}{dt}(r,x,t) 4\pi r^2}{\frac{4}{3}\pi(r_o^3 - r_i^3)} dr$$

$$\frac{d\Lambda}{dt} = (1 - \Lambda) Z \exp\left(-\frac{T^*}{T(r,x,t)}\right)$$

$$T = T_0(r,x,t) + \int_0^t \frac{dT}{dt}(r,x,t) dt \quad (2)$$

$$\frac{dT}{dt} = \frac{2.25 \gamma (p_o - p_g - 2\sqrt{3} k \ln(r_o/r_i))^2}{\rho C_p (r_i^{-3} - r_o^{-3})^2 r^6}$$

$$+ \frac{1}{\rho C_p} \frac{1}{r^2} \frac{1}{\partial r} (r^2 k^* \frac{\partial T}{\partial r}) + \frac{Q}{\rho C_p} \frac{d\Lambda}{dt}$$

where  $\Lambda(r,x,t)$  is the local degree of reaction,  $k$  is shear yield strength,  $Z$  is the pre-exponential factor in Arrhenius kinetics,  $T^*$  is the activation temperature,  $T_0$  is the initial temperature,  $\rho$  is the density,  $k^*$  is the thermal conductivity,  $C_p$  is the heat capacity, and  $Q$  is the heat of reaction of the explosive.

Equation (2) completely describes the ignition process with all material properties available from the literature except the constant  $\gamma$  which has not been defined yet.  $\gamma$  can be roughly estimated through use of experimental data as follows.

As an example, the case of PBX-9404 is considered. Parameters used in the derivation of the constant  $\gamma$  of the model are shown in Table 1, based on the values obtainable from the literature of HMX.

The initial volume fraction of HMX is assumed to be 94 percent, the initial binder volume fraction to be 5 percent, and the initial pore volume fraction to be 1 percent. The initial HMX particle size is assumed to be 100  $\mu\text{m}$ . A simple description for the bulk compressibility for the binder is used (not described here).

Table 1. PBX-9404 Parameters Used in the Derivation of the Constants of the Model

Z	$5 \times 10^{13}$	$\mu\text{s}^{-1}$
$T^*$	26500	$^{\circ}\text{K}$
$T_0$	300	$^{\circ}\text{K}$
$\rho$	1.844	$\text{g/cm}^3$
$C_p$	$1.4 \times 10^{-5}$	$\text{cm}^2/\mu\text{s}^2/^{\circ}\text{K}$
$k$	$8 \times 10^{-5}$	Mbar
Q	$5.439 \times 10^{-2}$	$\text{cm}^2/\mu\text{s}^2$
$k^*$	$8 \times 10^{-14}$	$\text{cm}/\mu\text{s}/^{\circ}\text{K}$
$r_i$	0.0039	cm
$r_o$	0.01	cm

When a shock of magnitude of 25 kbar is suddenly applied onto this hollow sphere, the mechanical deformation, the resulting temperature increase, and the change in the degree of reaction can be calculated if a value for  $\gamma$  is given. Since we did not know this value yet, a parametric study was performed with various values of  $\gamma$ . Figure 4 shows the result.

Three observations can be made. First, the reaction shows an exponential growth at the beginning. After it reaches a value of, say, 0.01, it grows more slowly for all values of  $\gamma$ . The earlier exponential growth before this value is reached is due mainly to the mechanical deformation, and the later slower reaction is strongly influenced by the thermal conduction and the Arrhenius chemical kinetics. In other words, the later reaction mimics the surface burn type behavior. For all values of  $\gamma$  tested, the value of  $\lambda_{hs}$ —to be called the degree of hot spot reaction—is nearly constant for a given set of parameters such as shown in Table 1.

The second observation is that the time when  $\lambda_{hs}$  is reached is a direct function of  $\gamma$ . In other words, the value of  $\gamma$  is only important in determining how fast or how slow  $\lambda_{hs}$  is obtained, but it is not important in determination of  $\lambda_{hs}$  itself.

The third observation from the calculation is that  $\lambda_{hs}$  is obtained well before the pore is completely collapsed. While the pore is collapsing, the temperature within the hot spot region becomes sufficiently high that the

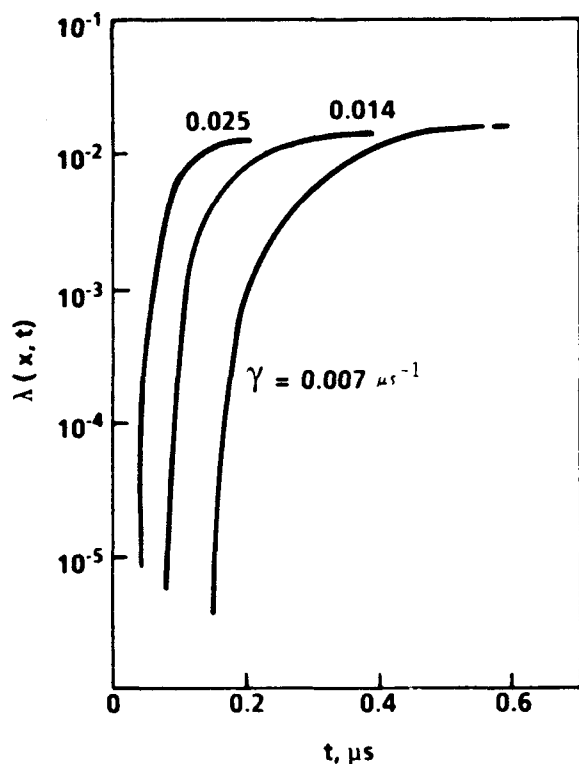


Figure 4. Growth of Degree of Reaction for Three Values of  $\gamma$

subsequent Arrhenius chemical reaction generates hot product gas into the pore. Even after  $\lambda_{hs}$  is reached, the pore still collapses until later time when the gas pressure in the pore becomes large enough to resist further collapse of the pore.

From these observations, the following conclusion can be made. After  $\lambda_{hs}$  is obtained, the reaction is more like a surface burn. Therefore, the model becomes simpler by switching to a form of the surface burning. The surface burning will be discussed in the next section.

The value of  $\gamma$  can also be estimated from the above observations. Setchell's<sup>31</sup> ramp wave experimental data showed that the reaction rate depended on the rise times of the ramp waves in PBX-9404. If the time when  $\lambda_{hs}$  is obtained,  $t_{hs}$ , is longer than the rise times of the experiment (0.2–0.8  $\mu$ s), then there would have been no observation of chemical reaction as shown in the experiment. On the other hand, if  $t_{hs}$  is much smaller than the experimental rise times, then Figure 6 indicates that even the smallest pressure would generate the

hot spot reaction,  $\lambda^{hs}$ , immediately. This would not then show the slowdown of reaction in ramp waves as clearly observed in the experiment. Therefore, the value of  $t_{hs}$  must be of the order of 0.1  $\mu$ s (which is the scale of experimental rise time) and was arbitrarily chosen as 0.05  $\mu$ s. The corresponding  $\gamma$  value is 0.025. Once again, it is fortunate that the choice of the value of  $\gamma$  is not important in any aspects other than  $t_{hs}$ , and since  $t_{hs}$  is very small compared to the overall time scale of most of the experiments ( $\sim$  a few  $\mu$ s) it does not critically affect the usefulness of the model.

With the determination of the value of  $\gamma$ , the description of the hot spot reaction model up to  $\lambda_{hs}$  is complete. The model describes the hot spot behavior, with a help of minimum amount of experimental data (Reference 31 was qualitatively used), explaining the effects of properties of the component explosive material, initial particle size, initial porosity, initial binder volume fraction, initial temperature, and the applied stress. The next section describes terms associated with surface burn reactions after  $\lambda_{hs}$  is reached.

## GROWTH OF REACTION PHASE

Tarver et al.<sup>6,7</sup> postulated that the growth of reaction can be modeled by a surface burn type formalism. Wackerle and Anderson,<sup>32</sup> and Kim<sup>3</sup> investigated this concept further. The following is the improvement of their model.

Tarver et al.<sup>7</sup> introduced two terms to describe the growth of reaction. The first term represented a slow burning at low pressures at the beginning stage of the reaction, and the second term represented fast reaction at high pressure near the end of the reaction. In this paper, the same concept was used in the development of the reaction growth term. However, their actual form was modified as follows. This follows from References 3 and 32.

At the early stage of chemical reaction just after hot spots are created, it is assumed that the reaction progresses outward from the inner surface of the hollow sphere in a surface burning mode. If the initial porosity is ignored, the volume reaction rate can be expressed as follows.



$$\frac{d\lambda}{dt} = - \frac{\dot{V}}{V} = \frac{4\pi r^2 \dot{r}}{4\pi r_o^3/3} = \frac{3 \lambda^{2/3}}{r_o} \dot{r} \quad (3)$$

where  $\dot{r}$  is the surface burning rate of the explosive. Equation (3) contains no unknown constants as  $\dot{r}$  is expressed as

$$\dot{r} = a P_g^n \quad (4)$$

However, Equation (3) does not account for the initial porosity and, when  $\lambda$  is small (of the order of  $\lambda_{hs}$ ), it underestimates the available surface area for burning. Therefore, a geometrical constant which is larger than one has to be multiplied to the above equation at the beginning. At the same time, as  $\lambda$  increases (or the gas pressure,  $p_g$ , increases) this factor should become close to one. As a result, a geometrical factor

$$\alpha p_g^\beta (\beta < 0)$$

is multiplied to Equation (3).

After the reaction has progressed to a significant degree, it is possible to consider that the burning in the pores has generated high enough gas pressure such that the hot product gas has penetrated into all crevices between the particles, and the burning at this stage occurs all around the particle surfaces. Then the reaction takes the form of inward burning of individual particles. Assuming that, once again for simplicity, the particles are spherical (not-hollow), the following volume reaction rate can be obtained.

$$\frac{d\lambda}{dt} = - \frac{\dot{V}}{V} = \frac{3(1-\lambda)^{2/3}}{r_o} \dot{r} \quad (5)$$

Once again a geometrical factor has to be multiplied to Equation (5). This is because, as the pressure increases to higher and higher level, some brittle solid materials, such as HMX, are expected to break into smaller pieces and generate more available surface area for burning. Therefore the factor

$$\delta p_g^\zeta (\zeta > 0)$$

is multiplied to Equation (5).

Equations (3) and (5) contain four unknown constants ( $\alpha$ ,  $\beta$ ,  $\delta$ , and  $\zeta$ ) and their values can be obtained by parametrically searching for the right values through comparison against experimental data such as pressure-time histories obtained from embedded pressure gages. The best set of these values have been obtained for PBX-9404 as shown in Figure 5. Here the pressure-time histories obtained from pressure gages embedded at  $x=2, 5$ , and 8 mm into the PBX-9404, which is subjected to a flat shock of 25 kbar, are shown as solid lines. Dotted lines are results of the calculated pressure curves with the values of the constants as given in the figure. The search for the four constants is not very difficult because the second term expressed by Equation (5) does not play an important role at the beginning and the constants  $\alpha$  and  $\beta$  in Equation (2) are easily obtained by examining the lower pressure portions of the curves. Then the remaining constant  $\delta$  and  $\zeta$  in Equation (5) are obtained through the examination of the higher pressure portions of the curves. The two terms Equations (3) and (5), are added together in expressing the reaction growth behavior of PBX-9404.

Indeed, in the process of obtaining values for the constants, all three curves in Figure 5 are not needed. The first curve, for  $x=2$  mm, is sufficient to give a fairly accurate estimate of the values of the constants. The fact that the model, with the constants obtained only with the first curve, predicts very closely the second ( $x=5$  mm) and the third ( $x=8$  mm) curves is significant. The model does not predict very high pressure portions of the curves accurately, though. The value of  $\zeta$  may not be as large when particles stop breaking after they reach a certain size.

The pre-exponential constant  $a$  in Equation (4) can be expressed as a function of initial solid temperature<sup>32,33</sup>

$$a = a_o \exp \left( - \frac{T_o}{T_i} \right) \quad (6)$$

where  $a_o$  is a reference constant,  $T_o$  is a reference temperature, and  $T_i$  is the initial solid temperature.

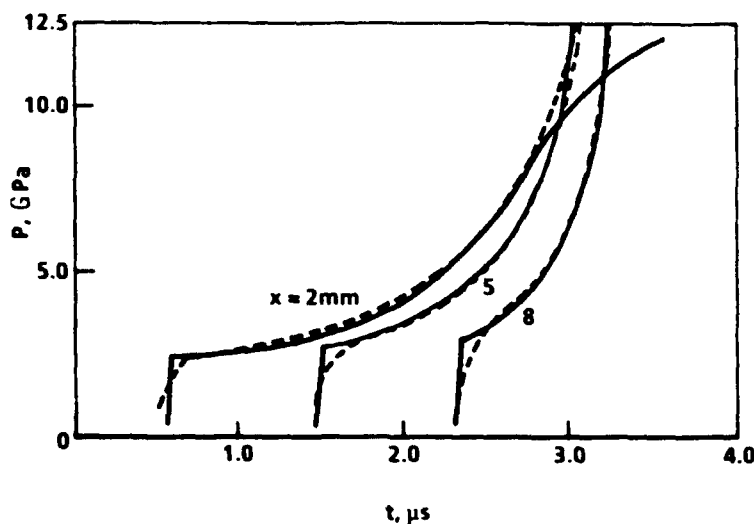


Figure 5. Experimental and Calculated Pressure Time Histories at Three Different Locations of  $X=2, 5$  and  $8$  mm. Values of constants in Table 1 were used for the calculation.  $\alpha = 1.2$ ,  $\beta = -0.4$ ,  $\delta = 32500$ , and  $\zeta = 2.5$ .

Equations (3)-(6), with appropriate values for constants, give a complete description of the reaction rate of PBX-9404 as a function of the applied pressure, the initial particle size, the initial porosity, and the initial temperature in the explosive. Parametric studies can be performed with these data. One example is shown below for the case of a different initial temperature (Figure 6).

## CONCLUSIONS

A comprehensive reaction rate model which describes behaviors of composite explo-

sives under shock has been developed. This model describes the ignition phase as a function of many physical parameters, including the applied pressure, the composition of the explosive, the particle size, the porosity, the shear yield stress, etc. The model shows that there is a very clear transition from the ignition to the growth of reaction marked by  $\lambda_{hs}$ . After that transition, the growth of reaction is expressed in terms of surface burning mechanism as a function of particle sizes and the initial temperature. The model was tested for PBX-9404. The model lends itself easily, because of analytical expressions of all terms,

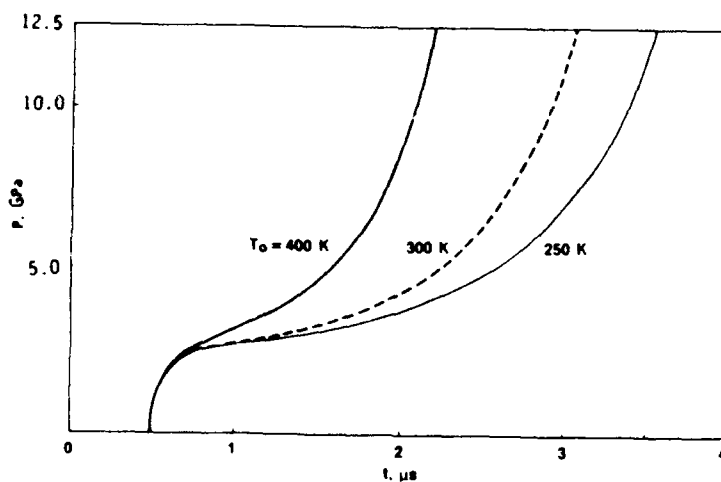


Figure 6. Growth of Reaction Shown for Three Different Initial Temperature of Composite Explosives at  $x = 2$  mm Location Under 25 kbar Pressure

to improvements such as inclusion of the effect of shear stresses applied to explosives. This can be useful in the study of explosive behaviors under moderate velocity fragment impact.

## ACKNOWLEDGEMENT

This work was supported by Navy 6.2 Explosive Block Program managed by L. Roslund.

## REFERENCES

1. Kim, K. and Sohn, C. H., "Modeling of Reaction Buildup Processes in Shocked Porous Explosives," *Proceedings of Eighth Symposium (International) on Detonation*, Albuquerque, NM, 1985, pp. 926-933.
2. Kim, K., "An Approach to Build a Reaction Rate Model in Shocked Heterogeneous Explosives," *Proc. of 1986 JANNAF PSHS*, 1986, pp. 513-521.
3. Kim, K., "Particle-size-dependent Reaction Rate in Shocked Explosives," *Shock Waves in Condensed Matter-1987*, Monterey, CA, 1987, pp. 531-534.
4. Madril, J. L., *Numerical Modeling of Detonations*, University of California Press, Los Alamos Series in Basic and Applied Sciences, 1979.
5. Forest, C. A., "Burning and Detonation," *Proceedings of Seventh Symposium (International) on Detonation*, Annapolis, MD, 1981, pp. 234-243.
6. Lee, E. L. and Tarver, C. M., "Phenomenological Model of Shock Initiation in Heterogeneous Explosives," *Phys. Fluids*, 23, 1980, pp. 2362-2372.
7. Tarver, C. M.; Hallquist, J. O.; and Erickson, L. M., "Modeling Short Pulse Duration Shock Initiation of Solid Explosives," *Proceedings of Eighth Symposium (International) on Detonation*, Albuquerque, NM, 1985, pp. 951-961.
8. Johnson, J. N.; Tang, P. K.; and Forest, C. A., "Shock-Wave Initiation of Heterogeneous Reactive Solids," *J. Appl. Phys.*, 57, pp. 4323-4334.
9. Tang, P. K.; Johnson, J. N.; and Forest, C. A., "Modeling Heterogeneous High Explosive Burn with an Explicit Hot-spot Process," *Proceedings of Eighth Symposium (International) on Detonation*, Albuquerque, NM, 1985, pp. 52-61.
10. Tang, P. K.; Forest, C. A.; Johnson, J. N.; and Seitz, W. L., "Effects of Physical Properties on the Initiation Behaviors of Heterogeneous High Explosives," *Proceedings of the International Symposium on Intense Dynamic Loading and its Effects*, Science Press, Beijing, China, 1986, pp. 207-212.
11. Tang, P. K., "A Numerical Investigation of High-Explosive Grain Size Effects on the Performance of Boosters," *Combustion and Flame*, Vol. 70, 1987, pp. 61-64.
12. Tang, P. K., "Initiation and Detonation of Heterogeneous High Explosive: A Unified Model," LA-11352-MS, Los Alamos National Laboratory, 1988.
13. Anderson, A. B.; Ginsberg, M. J.; Seitz, W. L.; and Wackerle, J., "Shock Initiation of Porous TATB," *Proceedings of Seventh Symposium (International) on Detonation*, Annapolis, MD, 1981, pp. 385-393; and Wackerle, J.; Rabie, R. L.; Ginsberg, M. J.; and Anderson, A. B., "Shock Initiation Study of PBX-9404," *Proceedings of the Symposium on High Dynamic Pressures*, Paris, France, 1978, p. 127.
14. Damamme, G. and Missonier, M., "Simulation of the Reaction Zone of Heterogeneous Explosives," *Proceedings of Seventh Symposium (International) on Detonation*, Annapolis, MD, 1981, pp. 641-645.
15. Cochran, S. G. and Tarver, C. M., "Modeling Particle Size and Initial Temperature Effects on Shock Initiation of TATB-Based Explosives," *Shock Waves in Condensed Matter - 1983*, Elsevier, 1984.
16. Hayes, D. B., "Shock Induced Hot Spot Formation and Subsequent Decomposition in Granular, Porous, Hexanitrostilbene Explosive," *Proc. Eighth Int'l.*

*Collo. on Gasdynamics of Explosions and Reactive Systems*, 1981.

17. Frankel, M. J. and Pastine, D. J., "Hot Spot and Bulk Temperature Induction in Shock Compressed Explosives," *Proceedings of the Seventh Symposium (International) on Detonation*, 1981, pp. 523-528.
18. Kipp, M. E.; Nunziato, J. W.; Setchell, R. E.; and Walsh, E. K., "Hot-spot Initiation of Heterogeneous Explosives," *Proceedings of the Seventh Symposium (International) on Detonation*, Annapolis, MD, 1981, pp. 394-406.
19. Baer, M. R. and Nunziato, J. W., *Intl. J. Multiphase Flows*, Vol. 12, 1986, p. 861.
20. Nunziato, J. W. and Baer, M. R., "A Macroscopic Approach to the Initiation and Detonation of Condensed-Phase Energetic Mixtures," *Journal de Physique*, Colloque C4, Supplement au No. 9, Tome 48, Sep 1987.
21. Taylor, P. A., "The Effects of Material Microstructure on the Shock Sensitivity of Porous Granular Explosions," *Proceedings of the Eighth Symposium (International) on Detonation*, Albuquerque, NM, 1985, pp. 26-34.
22. Khasainov, B. A.; Borisov, A. A.; Ermolaev, B. S.; and Kotrov, A. I., "Two-Phase Visco-Plastic Model of Shock Initiation of Detonation in High Density Pressed Explosives," *Proceedings of the Seventh Symposium (International) on Detonation*, 1981, pp. 435-447.
23. Kooker, D. E. and Anderson, R. D., "A Mechanism for the Burning Rate of High Density, Porous, Energetic Materials," *Proceedings of the Seventh Symposium (International) on Detonation*, 1981, pp. 198-215.
24. Partom, Y., "A Void Collapse Model for Shock Initiation," *Proceedings of the Seventh Symposium (International) on Detonation*, 1981, pp. 506-516.
25. Wackerle, J.; Johnson, J. O.; and Halleck, P. M., "Reactive Shock-Wave Buildup in Porous PETN," LAUR-75-1912, Los Alamos National Lab., 1975.
26. Frey, R. B., "Cavity Collapse in Energetic Materials," *Proceedings of the Eighth Symposium (International) on Detonation*, Albuquerque, NM, 1985, pp. 68-80.
27. Nutt, G. L., "A Reactive Flow Model for Monomolecular High Explosive," *J. Appl. Phys.*, Vol. 64, 1988, pp. 1816-1826.
28. Carroll, M. M. and Holt, A. C., "Static and Dynamic Pore-Collapse Relations for Ductile Porous Materials," *J. Appl. Phys.*, Vol. 43, No. 4, 1972.
29. Taylor, J., Private Communications, 1977.
30. Bowden, F. P. and McOnie, M. P., "Formation of Cavities and Microjets in Liquids and Their Role in Initiation and Growth of Explosion," *Proc. Roy. Soc. London*, A 298, 1967, pp. 38-50.
31. Setchell, R., *Combustion and Flame*, Vol. 43, 1981, p. 255.
32. Wackerle, J. and Anderson, A., "Burning Topology in the Shock-Induced Reaction of Heterogeneous Explosives," *Shock Waves in Condensed Matter*, North-Holland, 1984, pp. 601-604.
33. Price, C., Private Communications, 1988.

## DISCUSSION

HAROLD GRYPING

Gryting Energetics Sciences Co.  
San Antonio, Texas

Please explain how this model applies to particle size or particle size distribution in a composition. It seems it would be difficult to predict beyond an individual particle.

## REPLY BY KIBONG KIM

The model in the paper applies to explosive compositions with uniform size particles. We are currently expanding the model to explosive compositions with bimodal particle distributions.

# A MODEL FOR THE INITIATION OF HETEROGENEOUS HIGH EXPLOSIVES SUBJECT TO GENERAL COMPRESSIVE LOADING

John Starkenberg  
U.S. Army Ballistic Research Laboratory  
Aberdeen Proving Ground, Maryland 21005-5066

*The state of the explosive initiation modeling art does not provide an accurate predictive capability for problems of practical interest. Initiation modeling efforts at the Ballistics Research Laboratory have been conducted with the objective of providing a more broadly applicable treatment for the initiation of explosives. The basic elements of this model include a description of the reacting mixture, the continuum mechanics model, boundary conditions, and the reaction model. These are all tied together by an appropriate numerical treatment. The model is consistent with a reaction phenomenology characterized by simultaneous hot spot generation, extinction, and reaction followed by reaction propagation. The hot spot generation function is generally applicable to all forms of compressive loading, and reaction propagation is assumed to occur by surface burning. While a complete model has been formulated, only a limiting form has been implemented. It is assumed that very rapid hot spot reaction prevents extinction from occurring in a shock wave while extinction dominates in the downstream flow. The model is calibrated such that only a small level of reaction occurs in the shock wave and transition to inward grain burning occurs relatively early. Even this simplified form of the model gives a quite adequate representation of the response of PBX-9404 to both sustained and short-duration shock wave loading.*

## INTRODUCTION

The explosives/munitions community has a long-range requirement for predictive capabilities for explosive initiation in complex environments in order to treat hazard scenarios. These involve such problems as sympathetic detonation of munitions and initiation of cased explosive by impact of arbitrarily shaped projectiles or fragments. A number of investigators have developed models applicable to initiation of explosives subject to shock loading. These include the Forest Fire model,<sup>1,4</sup> the Johnson Tang-Forest (JTF) model,<sup>5,6</sup> and the ignition and growth model<sup>7,9</sup> among others. Although considerable success has been achieved using these models,<sup>10,11</sup> many difficulties persist which render the state of the art inadequate in providing an accurate predictive capability for problems of practical

interest. The two most significant difficulties are the complex waveforms loading the explosive and the presence of ignition mechanisms other than those associated with shock waves.

Detonation in heterogeneous solid high explosives is generally initiated by means of shock or rapid compression waves. The compressive loading may be generated directly, by the impact of materials external to the explosive charge, or indirectly, by a burning reaction induced in a portion of the explosive charge. In these explosives, the waves act-by various mechanisms associated with the presence of discrete grains and voids--to generate small regions of heated material (referred to as "hot spots") which serve as ignition sites. Subsequently, reaction propagates throughout the explosive

apparently (but not necessarily) by means of surface burning which begins at the hot spots. Interest in the study of shock initiation stems from a desire to design reliable initiating systems while preventing accidental initiation of explosive charges in a variety of hostile environments. In order to model these phenomena, descriptions of wave propagation and flow in the reacting mixture of gas-phase products and solid-phase reactants are required. In addition, a model describing the dependence of the rate of reaction on the local state and loading history of the mixture is needed.

Development of a reaction model is facilitated by consideration of the physical phenomena involved in the burning of a volume of explosive small enough to be described by a single set of state variables but large enough to contain many hot spots. Generally, such a particle may be conceived as subject to a series of rate processes leading to complete reaction. The first of these steps is the activation of the hot spots. This is followed by hot spot burning and finally by the reaction of the remainder of the explosive. A model may incorporate some or all of these steps and may describe each step based on any desired phenomenology and at any desired level of detail. The number of steps described by rate processes in a model may be reduced by considering certain limits (such as very rapid hot spot reaction) or increased by incorporating substeps (such as rapid reaction completion) into the treatment of any reaction process. Assumptions governing all of the steps are strongly influenced by the answers to several key questions: How much material is involved in the hot spots? How rapidly do hot spots react? What is responsible for the delay before significant reaction is observed following the passage of a shock wave? What is responsible for the apparent increase in the order of the pressure dependence of the reaction rate observed at high pressure?

The success of such a model is measured by its ability to predict a number of relationships characterizing the behavior of explosives. These include a) the distance of run to detonation as a function of initial shock pressure ("Pop plot") for long duration pulses

delivered to explosive samples; b) the relationship between pressure and pulse duration producing incipient detonation ("p<sup>n</sup>t-relation") for short-duration pulses; c) desensitization of explosive samples due to multiple shocking and finite-rate compression (although data on these are scarce); and d) detonation failure in multidimensional corner-turning experiments and associated wave forms in all of these cases where gauge data giving pressure and particle velocity as functions of Lagrangian position are available.

While excellent agreement with the Lagrange pressure records from individual experiments have, in some cases, been demonstrated, the level of agreement with pressure-pulse duration initiation threshold data achieved does not inspire confidence in the broad applicability of these models. Treatment of the distribution of energy between the reactants and products has not always been carried out in a realistic fashion. Hot spots have been assumed to always provide initiation sites. Mechanisms which allow the creation of hot spots during finite-rate compressions have not been included. The mechanism of propagation as reflected by the dependence of fraction reacted has often been treated in an unrealistic form. The treatment of reactive shock waves by the method of artificial viscosity has not been properly resolved with the application of reaction rate laws. Finally, existing approaches are complicated and their development for the treatment of a wider range of problems has further increased their complexity.

Initiation modeling efforts at the Ballistics Research Laboratory have been conducted with the objective of providing a more broadly applicable treatment for the initiation of explosives by achieving improved representations of the short-duration and complex-loading responses. This is accomplished by drawing on the best features of existing models, using more realistic equilibrium assumptions, a simple general law describing hot spot generation for all forms of compressive loading (while providing for the extinction of activated hot spots), and employing a surface burning model for reaction propagation. Wherever possible, phenomenological detail

has been sacrificed in favor of simplicity in order to limit the number of unknown constants and facilitate the calibration of the model. While the complete model has been formulated, only a limiting form has been implemented

## MODELING ISSUES

### Equilibrium Assumptions

In most models, the phases have been assumed to have equal values of pressure and particle velocity at any point. The assumption of mechanical equilibrium is appropriate when characteristic times of the processes of interest are long compared with wave propagation times. For example, a simple shock wave might not be expected to immediately produce equal pressures in each phase. However, if the phases are well mixed such that their spatial dimensions are small, the pressures can be expected to equilibrate quite rapidly. The assumption of mechanical equilibrium seems reasonable. The assumption of equal particle velocities is applicable at least during the early portion of reaction progress (when the products are imbedded in a reactant matrix) and during the late portions (when high drag forces rapidly accelerate small unreacted particles). Many models also rely on the assumption of thermal equilibrium. Since equilibration of the phase temperatures is relatively slow, this assumption appears incorrect. The alternative assumption is adiabatic reaction, in which all chemical energy released heats the product phase only. Both Johnson, Tang, and Forest<sup>5</sup> and Wackerle and Anderson<sup>12</sup> report that the assumption selected has little or no effect on the computed results when the HOM equation of state is used.

### Hot Spot Extinction

In existing models, hot spots have been assumed to always provide initiation sites. Consideration has not been given to the possibility that some low temperature hot spots may extinguish without burning. This depletion of possible ignition sites may account for desensitization to multiple shocks and finite-rate compressions. Mechanisms which

allow the creation of hot spots during finite-rate compressions have not been included.

### Reactive Shock Waves

The Forest Fire and ignition and growth models make use of reactive shock waves in different senses. The approach used in Forest Fire is more widely applicable since it does not assume that only hot spot reaction may be associated with the shock. The ignition and growth approach is only applicable when hot spot reaction occurs much more rapidly than reaction propagation. In most experiments, very little shock acceleration is observed until just before transition to detonation. A reactive shock analysis for PBX-9404 shows that as little as two percent reaction produces a ten percent increase in shock velocity.<sup>13</sup> This indicates that either the mass fraction of the hot spots is quite small or that they burn too slowly to influence the shock velocity.

The approaches employed for the numerical implementation of shock initiation models usually rely on the use of the method of artificial viscosity to describe shock waves and often on integration of an empirical or phenomenological ignition rate law through the distorted time scales of these viscous shocks. In this case, parameters in the rate law must reflect the level of viscosity and the spacing of the computational mesh and cannot be regarded as purely explosive properties. This renders the approach less general than it might otherwise have been since results will be sensitive to the mesh size and subject to inaccuracy when meshes differing from those in the calibration problems are used.

### Propagation Topology

Reactions characterized by first order kinetics have their maximum rates (with respect to fraction reacted) at the beginning of reaction. In contrast, reactions modeled as spherical hot spots transitioning to surface burning have vanishing reaction rates at the beginning and end of reaction. The choice of the form of dependence on reacted mass fraction affects the mechanism implied for the observed delay in the onset of significant reaction following the passage of a shock wave. It may have far reaching influence on other

modeling choices regarding the amount of explosive which should be included in the hot spots and the rate at which they react. The original ignition and growth model, which relies (initially) on spherical outward (or hole) burning, incorporates only a very small fraction of explosive into the hot spots and allows them to burn very rapidly. The JTF model, which uses first order kinetics, includes considerably more explosive in the hot spots, requires them to burn more slowly and does not initiate propagation of reaction until a specified portion of the hot spots have reacted.

Several investigators have analyzed reactive flows in shocked explosives, using pressure and particle velocity measurements to deduce mass fraction and phase states as a function of position and time.<sup>14-16</sup> Wackerle and Anderson<sup>12</sup> have used this approach to investigate the burning topology associated with the shock initiation of PBX-9501. It is notable that their analysis indicates that the hole burning assumption implies a surface regression rate that is initially very high and decreases with increasing pressure, while the grain burning assumption is more consistent with the expected pressure dependence. These investigators acknowledge, however, that this result is difficult to reconcile with the most plausible initiation phenomenology and is inconsistent with the success achieved in representing measured pressure and particle velocity histories using this model.

Johnson, Tang, and Forest<sup>5</sup> have interpreted these observations as invalidating hole burning and justifying the use of slowly reacting hot spots and first order kinetics for reaction propagation in their model. This implies that the bulk of the explosive is universally and immediately influenced by the hot spots. Actually, only surface hole burning is brought into question by the Wackerle and Anderson observations. Clearly, if initial reaction propagation occurs by a bulk thermal mechanism limited to regions near the hot spots, application of a surface burn representation will yield very high regression rates. This mechanism is still consistent with vanishing reaction rates at small reacted mass fractions. Transition from the hot spot burning

mechanism to any surface burning mechanism thus occurs gradually rather than abruptly. At the same time, preferential spreading of reaction along crystal boundaries may lead to quick transition to grain burning and it is possible that no hole burning phase strictly characterized by surface reaction exists. However, reaction rates which vanish at the beginning and end of reaction and are maximum at some intermediate value are still appropriate.

### Rapid Reaction Completion

It is widely agreed that rapid completion of the reaction accounts for the abrupt transition to detonation observed in the wedge test. A number of different approaches to this have been reported in the literature. Forest Fire accounts for this empirically. The Forest Fire reaction rate for PBX-9404, for example, begins to increase rapidly for pressures greater than about 10 GPa. In addition, reaction is forced to completion when the mass fraction exceeds a specified value. Tarver proposed a generalized phenomenology to account for rapid reaction completion.<sup>9</sup> He assumed that it is due to surface area generation which occurs at high pressure and offered a new pressure dependent reaction rate, in addition to that associated with surface burning, to account for this. While this approach may be adequate as long as the explosive is being compressed, the pressure dependence is reversible and it quenches the reaction too strongly during rarefactions. Mechanisms which allow the creation of hot spots during finite-rate compressions can produce the desired increase in surface area during the later portions of explosive reaction in an irreversible fashion and account for the apparent increase in the order of pressure dependence. Rapid thermal completion of reaction may also contribute to this phenomenon when the dimensions of the remaining unreacted material are small enough to cause the breakdown of the surface burning assumption. However, this may not be significant due to the small amount of unreacted explosive remaining when the mechanism dominates. It can probably be neglected with little consequence.



## Model Calibration

Any practical explosive initiation model requires calibration through adjustment of a (sometimes large) number of unknown constants. In most cases, these constants are associated with the various assumed rate processes. This introduces a certain level of ambiguity into the model. That is, there may be more than one set of values for the calibration constants which yields agreement with the available experimental data. This results in more than one interpretation of the physical phenomenon implied. The ambiguity persists because it is not generally possible to experimentally isolate the physical phenomena associated with the steps in the reaction in order to independently adjust the constants associated with each process. The ambiguity increases with the complexity of the model.

## MODELING ELEMENTS

The basic elements of this, or any, model include a description of the reacting mixture, the continuum mechanics model, boundary conditions which define any specific problem, and the reaction model. These are all tied together by an appropriate numerical treatment. The existing approaches provide a menu of alternatives for the modeler. Should the reacting mixture be modeled as two phases, or more? Should thermal equilibrium, adiabatic reaction, or neither be assumed? Should some of the reaction be incorporated into the shock wave or should all reaction be assumed to occur in the downstream region? If reaction is incorporated into the shock, should only hot spot contributions be considered? How much material should be incorporated into the hot spots? Should first order kinetics, surface burning, or some other phenomenology be used to represent reaction propagation? How is rapid reaction completion to be obtained?

## MATERIAL/MIXTURE MODELING

The reacting explosive is assumed to be a two-phase mixture of reactants and products. The mixture is assumed to be saturated such that the total volume is the sum of the phase volumes, giving

$$\frac{1}{\rho} = \frac{1-y}{\rho_r} + \frac{y}{\rho_p}$$

where  $y$  is the mass fraction reacted and the subscripts  $r$  and  $p$ , respectively, refer to reactants and products.

The assumption of mechanical equilibrium is used. For materials which support stress deviators under conditions of uniaxial strain, this condition may be written as follows:

$$\sigma = -p_r(\rho_r, e_r) + s_r(\rho) = -p_p(\rho_p, e_p) + s_p(\rho).$$

Expressing equilibrium in terms of the normal stress, rather than the pressure, simplifies the characteristic structure of the equations of motion. The stress deviators are negligible at high pressures and generally vanish for the products.

In order to determine the equation of state of the reacting mixture, equations of state for each of the two coexisting phases must be known in a form giving pressure as a function of density and internal energy. The foregoing equations comprise a system of three equations in seven variables. Thus, three dependent and four independent variables may be identified as follows:

$$\sigma = \sigma(\rho, e_r, e_p, y)$$

$$\rho_r = \rho_r(\rho, e_r, e_p, y)$$

$$\rho_p = \rho_p(\rho, e_r, e_p, y).$$

## CONTINUUM MECHANICS MODEL

At this point, the assumption that the phase particle velocities at any point are equal is introduced. This assumption greatly simplifies the mathematical formulation of the problem. Conservation of mass for the mixture is written in one-dimensional form as

$$\frac{\partial \rho}{\partial t} + u \frac{\partial \rho}{\partial x} = -\rho \frac{\partial u}{\partial x}.$$

The reaction equation arises as a consequence of phase mass conservation.

$$\frac{\partial y}{\partial t} + u \frac{\partial y}{\partial x} = \dot{y}$$

where  $\dot{y}$  is the reaction rate.

Conservation of momentum is required for the mixture only.

$$\frac{\partial u}{\partial t} + u \frac{\partial u}{\partial x} = \frac{1}{\rho} \frac{\partial \sigma}{\partial x}$$

The adiabatic reaction assumption is reflected in the following energy conservation equations:

$$\frac{\partial e_r}{\partial t} + u \frac{\partial e_r}{\partial x} = \frac{\sigma}{\rho_r} \frac{\partial u}{\partial x}$$

$$\frac{\partial e_p}{\partial t} + u \frac{\partial e_p}{\partial x} = \frac{\sigma}{\rho_p} \frac{\partial u}{\partial x} + (e_r + \Delta h - e_p) \frac{\dot{y}}{y}$$

## REACTION MODELING

### Reaction Phenomenology

The reaction model is based on a fundamental phenomenology. Compression of the explosive is assumed to generate hot spots which may subsequently react or simply cool. The processes of hot spot generation, extinction, and reaction generally occur simultaneously and result in a population of activated hot spots. The competition between extinction and burning is such that extinction dominates for cool hot spots while burning dominates for hot ones. This is similar to the approach of Tang, Johnson, and Forest<sup>6</sup> except that the extinction concept has been added. Following hot spot reaction, propagation of reaction to the bulk of the explosive may proceed. Here a surface burning model is used. This is similar to the treatment of Lee and Tarver<sup>7</sup> but incorporates explicit dependence on the density of reacted hot spots. This latter dependence can account for the rapid completion of reaction. As a result of this, the order of the local pressure dependence may be lowered.

### Hot Spot Activation

Hot spots are assumed to be generated by an irreversible process associated with the compression of the unreacted explosive, extinguished by a diffusive process and consumed by chemical reaction such that the

following equation for the rate of change of the density of activated hot spots may be written.

$$\dot{n}_a = \left( \frac{Dn_a}{Dt} \right)_g + \left( \frac{Dn_a}{Dt} \right)_e + \left( \frac{Dn_a}{Dt} \right)_b$$

Here,  $n_a$  represents a number density of activated hot spots and has an arbitrary scale.

The hot spot generation function is intended to apply to compressive loading both in the shock and finite-rate form. The generation rate is a function of the local pressure, the pressurization rate, and the mass fraction reacted. The following expression provides a generation rate which has a conservative form, influences the hot spot density only during compression (providing irreversibility), and is proportional to the fraction of unreacted explosive remaining.

$$\left( \frac{Dn_a}{Dt} \right)_g = \begin{cases} a_g (1-y) \left( \frac{p_r}{p_n} \right)^{a_g-1} \frac{D}{Dt} \left( \frac{p_r}{p_n} \right) \frac{Dp_r}{Dt} > 0 \\ 0 & \frac{Dp_r}{Dt} \leq 0 \end{cases}$$

where the pressure has been normalized with respect to a reference value. Since  $n_a$  is of arbitrary scale, the constant of proportionality in the generation rate expression is arbitrary. Its value has been chosen to facilitate integration of the generation rate.

This model differs most significantly from that of Johnson, Tang, and Forest by the inclusion of the hot spot extinction term, which represents the decay of ignition sites at cool hot spots produced at low pressure. It is assumed to be proportional to the density of activated hot spots and to depend, in an as yet unspecified manner, on some measure of the energy of the hot spot which shall be referred to as the hot spot thermal parameter

$$\left( \frac{Dn_a}{Dt} \right)_e = -n_a E(\theta_a)$$

Similarly, the rate at which reacted hot spots are created is proportional to the density of activated hot spots and depends on the hot spot thermal parameter

$$\left( \frac{Dn_a}{Dt} \right)_b = - \frac{Dn_b}{Dt} = -n_a B(0_a)$$

where  $n_b$  is the number density of burned hot spots. These models have not yet been implemented. Therefore, a discussion of their details has been relegated to the appendix.

The relationship between the arbitrary hot spot density and the reacted mass fraction is given by

$$\dot{y}_b = a_g \left( \frac{Dn_b}{Dt} \right)$$

where  $a_g$  is a calibration parameter which is proportional to the mass per hot spot and is referred to as the hot spot size.

The generation rate law depends on reactant pressure and pressurization rate in a form that is conservative. Thus, the activation rate can be integrated explicitly for application to shock waves, where the extinction and burn rates make no contribution. The resulting expression gives the activated hot spot density on the downstream side of the shock as a function of the downstream pressure

$$\begin{aligned} n_{ad} - n_{au} &= \int_{p_u}^{p_d} \frac{Dn_a}{Dt} dt \\ &= (1 - y_u) \left| \left( \frac{p_{rd}}{p_n} \right)^{a_g} - \left( \frac{p_{ru}}{p_n} \right)^{a_g} \right| \end{aligned}$$

It is equal to unity when the upstream reacted mass fraction is zero, the upstream pressure is negligible (as it generally is), and the downstream pressure is equal to the reference value,  $p_n$ . This form can be used for shock waves described either as explicit discontinuities or by artificial viscosity.

The hot spot activation formulation involves only two calibration parameters. Additional parameters may be introduced in the hot spot extinction and reaction models.

## Reaction Propagation

Reaction propagation by surface burning is assumed to be the dominant contributor to the overall reaction rate. This rate is

proportional to the reacted hot spot density, surface area per hot spot and surface regression rate.

$$\dot{y}_s = a_s n_b a_r \dot{r}_s$$

The constant of proportionality is a calibration parameter.

Each hot spot is initially assumed to be a reacted sphere of explosive which is burning in an outward direction. At some point the burning topology must change to spherically inward. There is some question as to when this occurs. If the spheres continue to burn outward and are of uniform size and spacing, they will coalesce and begin to burn inward at a reacted volume fraction of about one half. If the explosive burns preferentially along grain boundaries, transition to inward grain burning will occur at a lower value of volume fraction. On the other hand, if the outward burning spheres are not of uniform size, coalescence may not occur until a higher value of volume fraction has been reached. The surface area per hot spot is given by

$$a_r(p_r, p_p, y) = \begin{cases} \left( \frac{v_p}{v_t} \right)^{\frac{2}{3}} & v_p \leq v_t \quad v_p = y\rho/p_p \\ \left( \frac{v_r}{1-v_t} \right)^{\frac{2}{3}} & v_r \geq v_t \quad v_r = (1-y)\rho/p_r \end{cases}$$

This form is consistent with transition from outward to inward spherical burning at a transition volume fraction,  $v_t$ . This is a calibration parameter which can be used to adjust the point of transition to inward burning to an early or late point in the reaction. The maximum surface area is assumed to occur at the transition point. Its value is included in the proportionality constant,  $a_s$ . Although the surface burning assumption may be inconsistent with the actual phenomenology for the early portions of reaction, it yields a mass fraction dependence which has the appropriate general form. The surface regression rate depends on the reactant pressure in the usual empirical form.

$$\dot{r}_s(p_r) = \left( \frac{p_r}{p_n} \right)^{a_s}$$

The surface regression exponent is the final calibration parameter. Thus, the propagation formulation involves three such parameters.

### Reaction Rate

The overall reaction rate is given by

$$\dot{y} = \dot{y}_b + \dot{y}_s$$

with the propagation rate generally dominating.

### The Ignition Limit

A number of assumptions which simplify the model while restricting its applicability may be made. When it is assumed that hot spot reaction takes place very rapidly, no hot spot extinction may occur and the hot spot ignition rate may be identified with the generation rate.

$$\left( \frac{Dn_b}{Dt} \right) = \begin{cases} a_g (1-y) \left( \frac{p_r}{p_n} \right)^{a_g-1} \frac{D}{Dt} \left( \frac{p_r}{p_n} \right) & \frac{Dp_r}{Dt} > 0 \\ 0 & \frac{Dp_r}{Dt} \leq 0 \end{cases}$$

This is most applicable to the high temperature hot spots generated by a shock wave and the integrated form of the above equations gives

$$n_{bd} - n_{bu} = (1 - y_u) \left[ \left( \frac{p_{rd}}{p_n} \right)^{a_g} - \left( \frac{p_{ru}}{p_n} \right)^{a_g} \right]$$

for the density of reacted hot spots on the downstream side of a shock.

Further, if it is assumed that hot spot reaction takes place very slowly in the downstream region, the extinction term will deplete all activated hot spots and no additional reacted hot spots will be produced. This is applicable to the low temperature hot spots produced in the unreacted explosive by compression of the reacting mixture until, approaching detonation, the compression rate becomes very high. The propagation rate in the region downstream of a strong shock wave propagating into unreacted explosive is then a

function of both local and shock pressure as follows:

$$\dot{y}_s = a_s a_r (\rho_r, \rho_p, y) \left( \frac{p_{rd}}{p_n} \right)^{a_g} \left( \frac{p_r}{p_n} \right)^{a_s}$$

These simplifying assumptions are useful in reducing the ambiguity of the formulation and allowing calibration of a smaller number of unknown constants using data appropriate to the assumptions. The resulting model is not applicable to multiple shock and finite-rate compression problems. Since the rapid completion of reaction at high pressure is not represented in this limit, and the predicted distance of run to detonation is expected to be longer than the experimentally determined values. However, the slope of the Pop plot should be properly represented. Accurate modeling of short-duration shock response may require a higher order of local pressure dependence than would be required by the full model.

### NUMERICAL IMPLEMENTATION

A one-dimensional Eulerian finite-difference computer code has been written for the implementation of this model. Following Moretti,<sup>17-20</sup> this code treats shock waves and gradient discontinuities as well as pistons and contact surfaces as explicit boundaries separating analytical regions of the flow field. Boundary computations are facilitated by characteristic compatibility conditions and shock jump conditions. Interior regions are stretched between these boundaries and integrated by means of MacCormack's predictor/corrector scheme.<sup>21</sup> Because of the discontinuous shock wave treatment, the code is referred to as the One-Dimensional Explicit Shock (ODES) code.

### CALIBRATION

Calibration of the five parameters associated with the model in the ignition limit is facilitated by recognition of their relations to the predicted Pop plot and Lagrange pressure histories.

Consider the case in which each explosive particle is subjected to shock loading followed by compression due to reaction as occurs in

wedge test experiments. Further assume that the local pressure can be approximated as

$$p_r = p_{rd}f(y)$$

The propagation rate can then be written as

$$\dot{y}_s = a_s a_r (\rho_r, \rho_p, y) f(y) \left( \frac{p_{rd}}{p_n} \right)^{a_g + a_s}$$

This suggests that the order of the shock pressure dependence of the reaction rate, and hence the slope of the Pop plot, is determined by the sum of the generation and surface regression exponents. The Pop-plot intercept depends on the propagation being proportionately constant and, to a lesser extent, on the hot spot size. The inflection point observed in Lagrange gauge pressure data is related to the transition volume fraction. These relations have all been computationally verified. The best specific values determined so far are

$$\begin{aligned} a_g &= 0.8 & a_s &= 1.4 \\ a_g &= 0.015 & a_s &= 4.0 \times 10^7 \text{ s}^{-1} \\ v_t &= 0.2 \end{aligned}$$

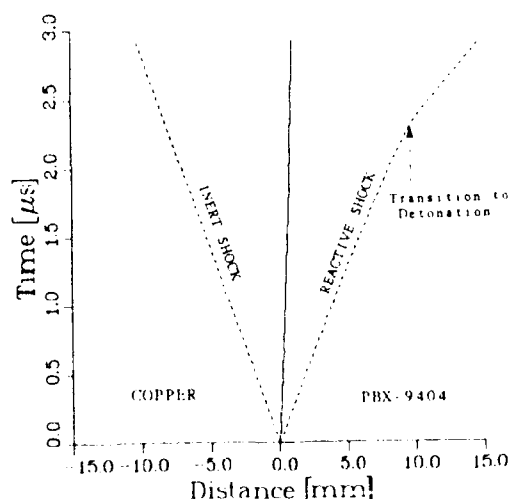
The hot spot size is chosen such that the amount of reaction in the shock wave always remains small. Even in the ignition limit, the order of the local pressure dependence of the reaction rate as given by the surface regression exponent is lower than that implied by other models. The value of 0.2 for the transition volume fraction is consistent with relatively early transition to inward grain burning. It is reasonable to assume that an even earlier transition would be required for the complete model in which reaction rates may increase rapidly due to continued hot spot activation downstream of the initial shock.

## RESULTS

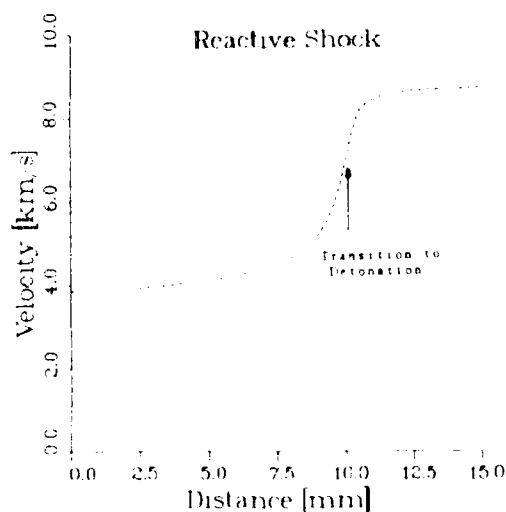
### Sustained Shock Response of PBX-9404

Figure 1 illustrates the shock motion in PBX 9404 impacted by a thick copper flyer at 550 m/s corresponding to an experiment reported by Wackerle and his coworkers.<sup>22</sup> The explicit shock treatment allows tracking of the reactive and inert shock trajectories (Figure 1a) as well as the reactive shock velocity

(Figure 1b). Transition to detonation is evidenced by the change in slope of the reactive shock wave and the rapid increase in the reactive shock velocity. The point of transition to detonation is identified as the point of maximum rate of change in the shock velocity. The computed run is slightly longer than the experimental run consistent with the assumptions of the ignition limit. Lagrange gauge pressure data are available in this case. The computed and measured pressure histories at four Lagrange stations are compared in Figure 2. The agreement is quite satisfactory, although no attempt to model the gauge itself was made. A comparison with the Pop plot data for PBX-9404 is shown in Figure 3. The



(a) Shock Trajectories



(b) Reactive Shock Velocity

Figure 1. Impact of a Thick Copper Flyer on PBX-9404 at 550 m/s

computed distances of run to detonation are just slightly longer than the experimentally determined values. Again, this is consistent with expectations for the model in the ignition limit.

### Short-Duration Shock Response of PBX-9404

In another experiment by Wackerle, a thin copper flyer was fired at a PBX-9404 sample.<sup>22</sup> The shock and rarefaction wave

trajectories from the corresponding computation are shown in Figure 4a. This indicates that the impact of the thin plate generates a reactive shock followed by numerous rarefactions propagating into the explosive. Again, transition to detonation is indicated by the change in slope of the reactive shock wave (Figure 4b). The rarefactions cause the shock velocity to decrease slightly before building to detonation. A favorable comparison with the Lagrange pressure histories is also achieved in this case as shown in Figure 5.

A number of experiments in which thin mylar flyers were thrown against PBX-9404 samples were conducted by Weingart and his coworkers at Livermore.<sup>23</sup> In these experiments, the initiation threshold velocity was determined as a function of flyer thickness. As shown in Figure 6, the results are fit very well by a straight line in a log-log plot of threshold velocity versus flyer thickness. Predictions from the ignition limit model are in close agreement with the experimental results although a slightly steeper slope is predicted. It should be noted that a somewhat more stringent initiation criterion than that used for the experiments was applied to the computations. This could account for the difference in slope. A computed transition to detonation within 20 mm of run was required while in the experiments pressures of only 20 GPa at the free surface signaled initiation. If desired, the slope can be altered

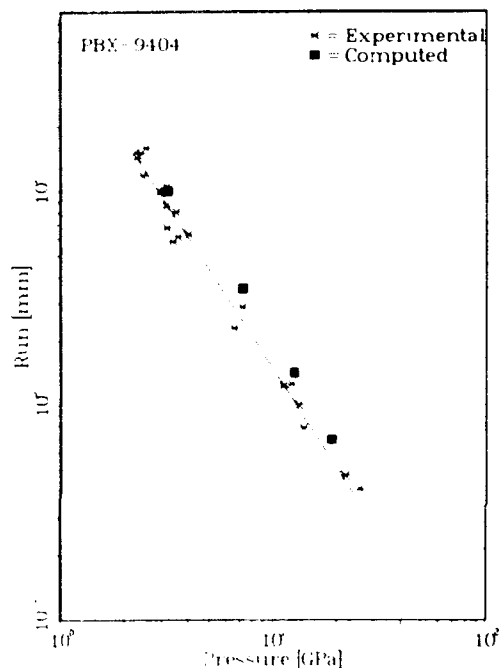


Figure 3. Comparison of Experimental and Computed Plog Plot for PBX-9404

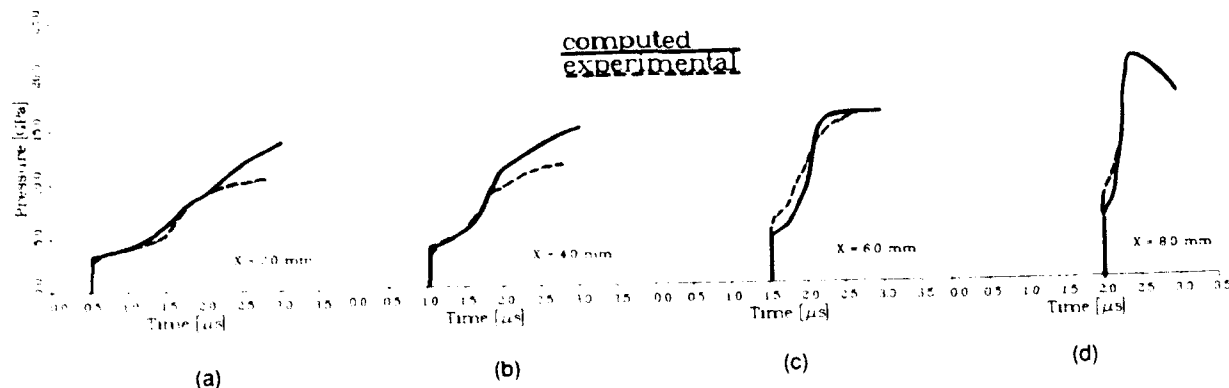
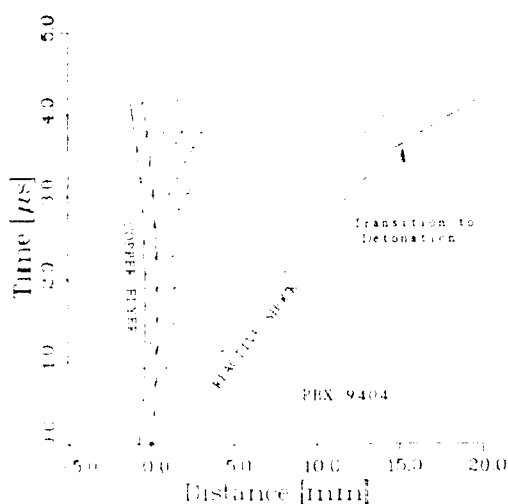
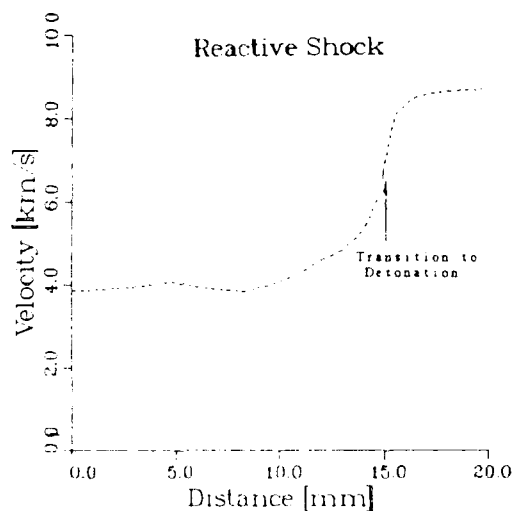


Figure 2. Comparison of Computed and Measured Pressure Histories at Four Lagrange Stations for Impact of a Thick Copper Flyer or PBX-9404 at 550 m/s



(a) Wave Trajectories



(b) Reactive Shock Velocity

Figure 4. Impact of a 0.76 mm Thick Copper Flyer on PBX-9404 at 550 m/s

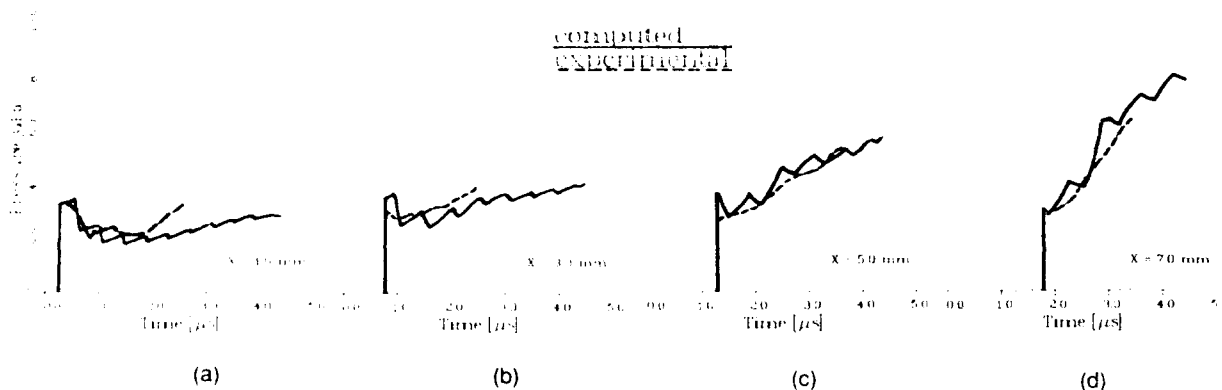


Figure 5. Comparison of Computed and Measured Pressure Histories at Four Lagrange Stations for Impact of a 0.76 mm Thick Copper Flyer on PBX-9404 at 550 m/s

by adjusting the generation and surface regression exponents subject to the condition on their sum which determines the Pop plot slope. This should have minimal impact on the Lagrange pressure comparisons for either sustained or short duration shock waves. Our results may be compared with Tarver's for the same simulation. The latter show a transition in the slope of the threshold curve. The correct slope is achieved only at lower pressures.

## SUMMARY

A more general explosive initiation model consistent with the assumptions of two phase

flow in mechanical equilibrium with adiabatic reaction has been developed. The model is consistent with a reaction phenomenology characterized by simultaneous hot spot generation, extinction, and reaction followed by reaction propagation. The hot spot generation function is generally applicable to all forms of compressive loading and reaction propagation is assumed to occur by surface burning.

The model has been implemented in the ignition limit. This is a relatively simple form involving only five calibration parameters. It is assumed that very rapid hot spot reaction prevents extinction from occurring in a shock

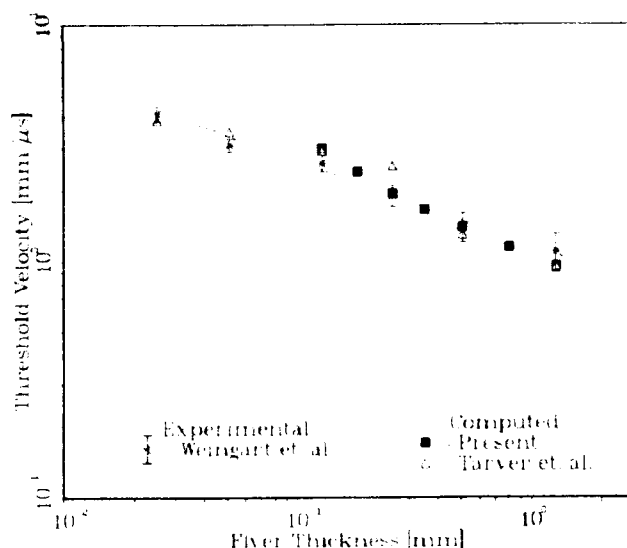


Figure 6 Comparison of Experimental and Computed Initiation Thresholds for Thin Mylar Flyer Impact

wave while extinction dominates in the downstream flow. The model is calibrated to reflect only a small level of reaction in the shock wave and transition to inward grain burning occurring relatively early in the reaction. Even this simplified form of the model gives a quite adequate representation of the response of PBX-9404 to both sustained and short duration shock wave loading.

Future plans for this work include finalization of the ignition limit calibration, implementation of the hot spot extinction and reaction models and, ultimately, the development of a shear ignition model.

## APPENDIX: HOT SPOT EXTINCTION AND BURN RATES

The extinction and reaction models for hot spots have not yet been implemented. Hot spot extinction and burning are assumed to depend on the hot spot thermal parameter, theta. This may be thought of as, but is not necessarily, the hot spot temperature. The form of the expression being considered gives this parameter for newly generated hot spots as a monotonic increasing function of both pressure and pressurization rate

and introduces two additional calibration parameters.

$$\theta_g = a_h p_r \tanh\left(\frac{u_h}{p_n} \frac{Dp_r}{Dt}\right)$$

The hyperbolic tangent is used to provide a finite limiting value as the pressurization rate becomes arbitrarily large, corresponding to a shock wave. Thus,

$$\theta_{gd} = \lim_{\frac{Dp}{Dt} \rightarrow \infty} \theta_g = a_h p_{rd}$$

The thermal parameter of the generated hot spots must be averaged with that of existing hot spots in accordance with the following equation.

$$\begin{aligned} \frac{D\theta_a}{Dt} = \frac{1}{n_a} & \left\{ \left( \theta_g - \theta_a \right) \left( \frac{Dn_a}{Dt} \right)_g \right. \\ & \left. + 2\theta_a \left| \left( \frac{Dn_a}{Dt} \right)_e + \left( \frac{Dn_a}{Dt} \right)_b \right| \right\} \end{aligned}$$

The average value is then used to compute the extinction and burn rates.

$$E(\theta_a) = a_e \theta_a^{a_e}$$

$$B(\theta_a) = a_b \theta_a^{a_b}$$

Each of these expressions also introduces two additional calibration parameters for a total of six. Thus, the number of calibration parameters is more than doubled to a total of eleven. This is still fewer than the fifteen parameters reported by Tarver.

## LIST OF SYMBOLS

a	proportionality calibration constant
e	specific internal energy
f	unspecified function
n	hot spot density
p	pressure
s	normal stress deviator



t	time
u	particle velocity
x	spatial coordinate
y	mass fraction reacted
$\alpha$	calibration exponent
$\Delta h$	heat of reaction
$\rho$	density
$\theta$	hot spot thermal parameter
$\sigma$	normal stress
$\tau$	time constant

### Subscripts

a	hot spot activation
b	hot spot burn
d	downstream
e	hot spot extinction
g	hot spot generation
h	thermal
n	reference
p	products
r	reactants
s	surface burn
u	upstream

### REFERENCES

1. Mader, C. L., "An Empirical Model of Heterogeneous Shock Initiation of 9404," Los Alamos Scientific Laboratory Report LA-4475, 1970.
2. Mader, C. L. and Forest, C. A., "Two Dimensional Homogeneous and Heterogeneous Detonation Wave Propagation," Los Alamos Scientific Laboratory Report LA-6259, 1976.
3. Mader, C. L., *Numerical Modeling of Detonation*, University of California Press, Berkeley, 1979.
4. Lundstrom, E. A., "Evaluation of Forest Fire Burn Model of Reaction Kinetics of Heterogeneous Explosives," Naval Weapons Center Technical Publication 6898, May 1988.
5. Johnson, J. N.; Tang, P. K.; and Forest, C. A., "Shock Wave Initiation of Heterogeneous Reactive Solids," *Journal of Applied Physics*, Vol. 57, No. 9, May 1985.
6. Tang, P. K.; Johnson, J. N.; and Forest, C. A., "Modeling Heterogeneous High Explosive Burn with an Explicit Hot-Spot Process," *Proceedings of the Eighth Symposium (International) on Detonation*, Jul 1985, pp. 52-61.
7. Lee, E. L. and Tarver, C. M., "Phenomenological Model of Shock Initiation in Heterogeneous Explosives," *Physics of Fluids*, Vol. 23, No. 12, Dec 1980, pp. 2362-2372.
8. Tarver, C. M. and Hallquist, J. O., "Modeling Two-Dimensional Shock Initiation and Detonation Wave Phenomena in PBX-9404 and LX-17," *Proceedings of the Seventh Symposium (International) on Detonation*, Jun 1981, pp. 488-497.
9. Tarver, C. M.; Hallquist, J. O.; and Erickson, L. M., "Modeling Short Pulse Duration Shock Initiation of Solid Explosives," *Proceedings of the Eighth Symposium (International) on Detonation*, Jul 1985, pp. 951-961.
10. Bowman, A. L.; Forest, C. A.; Kershner, J. D.; Mader, C. L.; and Pimbley, G. H., "Numerical Modeling of Shock Sensitivity Experiments," *Proceedings of the Seventh Symposium (International) on Detonation*, June 1981.
11. Starkenberg, J.; Huang, Y. K.; and Arbuckle, A., "Numerical Modeling of Projectile Impact Shock Initiation of Bare and Covered Composition B," Ballistic Research Laboratory Technical Report ARBRL-TR-02576, Aug 1984.
12. Wackerle, J. and Anderson, A. B., "Burning Topology in the Shock Induced Reaction of Heterogeneous Explosives," *Proceedings of the American Physical Society Topical Conference on Shock*

- Waves in Condensed Matter*, Jul 1983, pp. 601-604.
13. Starkenberg, J., "A Model for the Initiation of Heterogeneous High Explosives Subject to General Compressive Loading," Forthcoming BRL Report.
  14. Vantine, H. C.; Rainsberger, R. B.; Curtis, W. D.; Lee, R. S.; Cowperthwaite, M.; and Rosenberg, J. T., "The Accuracy of Reaction Rates Inferred from Lagrange Analysis and In-situ Gauge Measurements," *Proceedings of the Seventh Symposium (International) on Detonation*, Aug 1976, pp. 466-478.
  15. Nutt, G. L. and Erickson, L. M., "Reactive Flow Lagrange Analysis in Plastic Bonded Explosives," *Journal of Energetic Materials*, Vol. 2, 1984, pp. 263-292.
  16. Vorthman, J.; Andrews, G.; and Wackerle, J., "Reaction Rates from Electromagnetic Gauge Data," *Proceedings of the Eighth Symposium (International) on Detonation*, Jul 1985, pp. 99-110.
  17. Moretti, G., "The Choice of a Time-Dependent Technique in Gas Dynamics," Polytechnic Institute of Brooklyn, PIBAL Report No. 69-26, Jul 1969.
  18. Moretti, G., "Thoughts and Afterthoughts about Shock Computations," Polytechnic Institute of Brooklyn, PIBAL Report No. 72-37, Dec 1972.
  19. Moretti, G., "Experiments in Multi-Dimensional Floating Shock-Fitting," Polytechnic Institute of Brooklyn, PIBAL Report No. 73-18, Aug 1973.
  20. Moretti, G., "A Pragmatical Analysis of Discretization Procedures for Initial- and Boundary-Value Problems in Gas Dynamics and Their Influence on Accuracy, or Look Ma, No Wiggles!" Polytechnic Institute of New York, POLY-AE/AM Report No. 74-15, Sep 1974.
  21. MacCormack, R. W., "The Effect of Viscosity in Hypervelocity Impact Cratering," AIAA 7th Aerospace Sciences Meeting, Paper No. 69-354, 1969.
  22. Wackerle, J.; Rabie, R. L.; Ginsberg, M. J.; and Anderson, A. B., "A Shock Initiation Study of PBX-9404," *Symposium on High Dynamic Pressures*, Paris, Aug 1978.
  23. Weingart, R. C.; Jackson, R. K.; Honodel, C. A.; and Lee, R. S., "Shock Initiation of PBX-9404 by Electrically Driven Flyer Plates," *Propellants and Explosives*, Vol. 5, 1980, pp. 158-162.

**SESSION ON**  
**COMPOSITES AND EMULSIONS/  
UNDERWATER EXPLOSIVES**

**Cochairmen: Leslie Roslund**  
**Naval Surface Warfare Center**

**Algot Persson**  
**Swedish Detonic Research Foundation**

# CALCULATION OF DETONATION PROPERTIES OF EMULSION EXPLOSIVES

K. Tanaka, M. Iida, Y. Nakayama, N. Ishiokawa, M. Yoshida,  
and S. Fujiwara

National Chemical Laboratory for Industry,  
Tsukuba, Ibaraki 305 JAPAN

*Detonation properties of a recent popular commercial explosive, emulsion explosive, was studied by underwater detonation and blast wave measurements. Results of these tests were compared with calculations of detonation properties and incorporated into a hydrodynamic study.*

## INTRODUCTION

Explosives containing a large amount of ammonium nitrate (AN) are generally non-ideal explosives which are defined as having detonation properties significantly different from those predicted from C-J theory based on an equation of state (EOS) under conditions of high pressure and temperature. The emulsion explosive (EE) which contains about 70 percent AN is considered to be a kind of intermolecular explosive. In EE, an aqueous solution of AN and other salts with oil are emulsified by a surface active agent and mixed with fine glass microballoons. EE gives a detonation velocity for infinite charge diameter of about 6 km/s for an initial density of 1.2 g/cc. For EE, impact tests by drop hammer show insensitive results, while shock initiation tests show that critical shock pressure is on the order of several kbar. Detonation energy of EE is generally 60 to 80 percent TNT. Because EE is a relatively new explosive, it is important to study the detonation properties and sensitivity for both practical and safe use of the explosive.

## CALCULATION

The detonation properties of EE have been studied by Kihara - Hikita - Tanaka (KHT),<sup>1</sup> Becker - Kistiakowskii - Wilson (BKW),<sup>2</sup> Lennard - Jones - Devonshire (LJD),<sup>3</sup> Exponential 6 (Exp-6),<sup>4</sup> and virial expansion using LJ intermolecular potential (VLW).<sup>5</sup> Some thermodynamic data given by Gordon and McBride<sup>6</sup> are used for detonation proper-

ties calculation by these EOS. Parameters for Exp-6 given by Ree<sup>4</sup> are used. Exp-6 equations are solved by a method given by Fickett.<sup>3</sup> Assumed solid detonation products are  $\text{Na}_2\text{O}$ ,  $\text{SiO}_2$ , and solid carbon.

Detonation velocities measured by Yoshida, et al.,<sup>7</sup> for EE KE-1 with various initial densities, are compared with calculated results by using these EOS. Predictions of detonation properties of explosives using these EOS generally agree with experimental detonation velocity and pressure. However, these EOS predict different detonation properties for explosives with relatively low detonation temperature such as AN or hydrazine nitrate explosives which are mostly nonideal.

Experimental detonation velocities for KE-1 are compared with theoretical calculations in Figure 1; BKW predicts the highest detonation velocity and VLW predicts the lowest detonation velocity. However, these results indicate that EE behaves as an ideal explosive.

Detonation temperatures are given in Figure 2.

Both pressure and energy isentrope are basic data for the calculation of underwater detonations and blast waves. Higher energy release rate gives higher energy to surroundings near the explosive and makes peak-overpressures higher for underwater detonations and blast waves. As EE performance is not higher than commercial dynamite explosives, energy release rate is an important estimation for

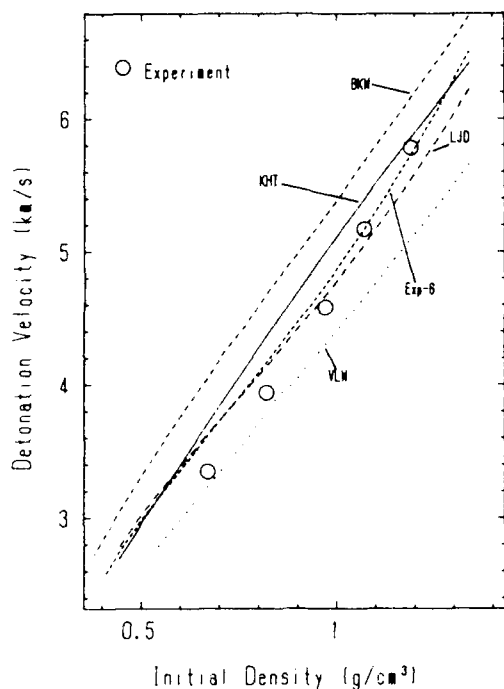


Figure 1. Calculated and Experimental (7) Detonation Velocity at infinite charge diameter for Emulsion Explosive (KE-1)

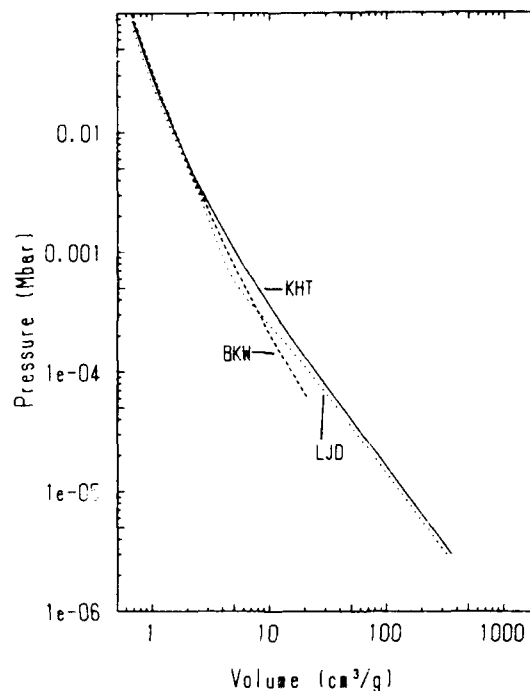


Figure 3. Calculated Pressure vs. Volume Isentropes for Emulsion Explosive (KE-1,  $\rho_0 = 1.08 \text{ g/cm}^3$ )

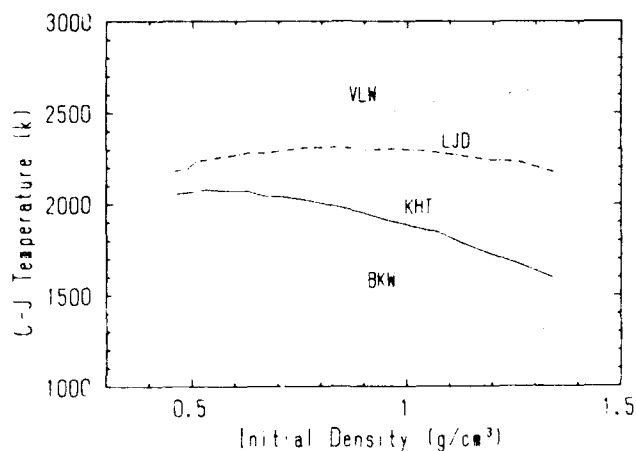


Figure 2. Calculated Detonation Temperature for Emulsion Explosive (KE-1)

practical use, especially for hard rock blasting. C-J isentropes of KHT, BKW, and LJD for KE-1 are shown in Figures 3 and 4. BKW gives a higher energy release rate.

## UNDERWATER DETONATION

Underwater detonation tests using a maximum charge weight of 1 kg were performed to measure the explosive energy. The

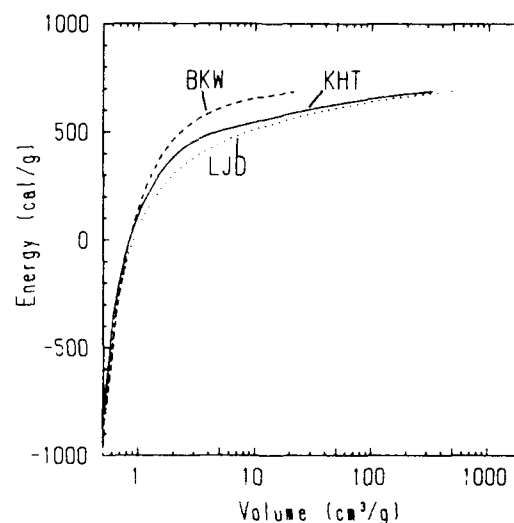


Figure 4. Calculated Energy vs Volume Isentropes for emulsion explosive (KE-1,  $\rho_0 = 1.08 \text{ g/cm}^3$ )

experimental results were compared with hydrodynamic computations. The hydrodynamic computations for underwater detonation for KE-1, using KHT and LJD C-J isentrope, show favorable agreement as shown in Figure 5. (The LJD result is not shown due to the difficulty of separating the plotted curve.)

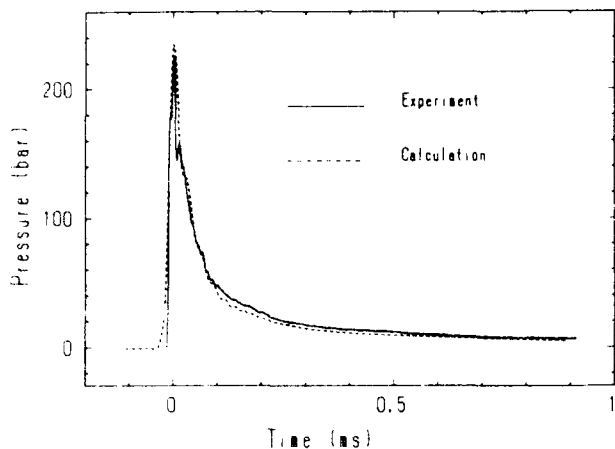


Figure 5. Calculated and Experimental Pressure for Underwater Detonation of EE (KE-1) of 200 g at a depth Of 2 m measured at 1 m from an explosive charge.

BKW isentropes were not available for the calculation of KE-1 detonation because BKW gives a temperature of less than 300K at about 60 bars. However, differences of peak pressures are not significant at a distance of 1 to 2 m from an explosive source. Bubble pulse was calculated by the Rayleigh equation, using the calculated expansion velocity at gas/water boundary when the relative radius of the gas bubble was 10. LJD and KHT gave bubble energies of 463 cal/g and 460 cal/g, respectively, while experimental data was 420 to 460 cal/g.

## BLAST WAVE

A blast wave field experiment was conducted by MITI on a 500 kg commercial EE. The explosive charge was placed above the ground at a height of 857 mm. Profiles of the blast wave measured by piezoelectric transducers are shown in Figure 6. Results calculated by a one-dimensional Lagrangian hydrodynamic code using a KHT isentrope where the hemispherical shock wave was assumed are shown in Figure 7. Air was assumed to be ideal gas. Experimental results show lower than calculated peak overpressures, possibly due to the energy loss resulting from cratering at the explosion point. A comparison with the experimental results obtained from 508 kg of TNT at the same place corresponded to a TNT equivalence of 60 to 80 percent which contrasts

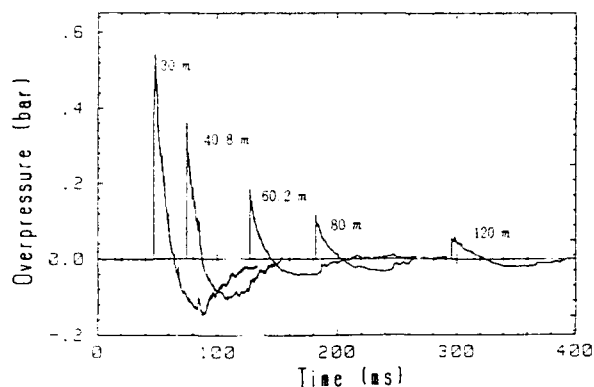


Figure 6. Experimental Blast Wave Profile for a Commercial Emulsion Explosive on a Surface Burst. Explosive charge of 500 g was initiated by 10 kg of dynamite.

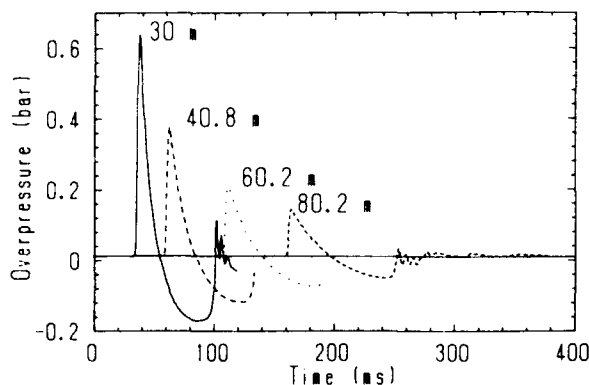


Figure 7. Calculated Blast Wave Profile corresponding to Figure 6.

with 66 percent from a KHT calculation for the commercial EE used.

## EFFECT OF VOID

It is well known that voids in water gels play an important role in detonation initiation and propagation. The effect of voids in water was studied numerically by a two-dimensional Eulerian hydrodynamic code based on the donor-acceptor method. Air was assumed to be ideal gas. The EOS used for water was a linear relationship between shock velocity  $U_s$  and particle velocity  $u_p$ .

$$U_s = 1.483 + 2.0 u_p \text{ (km/s).}$$

At a shock pressure lower than 10 kbar, the temperature rise in water due to the

impact of the water jet is not high due to precompression. (See Figure 8.) Calculated results suggest that a jet generated in a void for pressure shock waves lower than about 10 kbar is not enough to initiate EE, because it is precompressed by shock wave propagation through the emulsion around the void before jet impact. At a shock pressure higher than 10 kbar, a jet generated in a void impacts water prior to the arrival of the shock wave propagating through water around the void. (See Figure 9.) There the temperature rise near the water-void interface is much higher. Suggesting that a shock wave with pressure higher than 10 kbar is able to initiate EE. Results of hydrodynamic calculations for shock wave propagation in water with voids seem to be consistent with both behaviors for shock initiation and impact sensitivity of EE.

## CONCLUSION

Prediction of detonation properties may be possible for water gels. Detonation properties calculated by KHT, LJD, and Exp-6 predict well the detonation properties of emulsion explosives. Detonation of emulsion explosives is mainly initiated by jets in voids in which the size of the void is an effective parameter for the length of the reaction zone.

## ACKNOWLEDGMENTS

The authors thank Drs. K. Aoki, Y. Kakudate, S. Usuba, S. Oinuma, T. Matsunaga, and many others who helped in our studies.

## REFERENCES

1. Tanaka, K., "Detonation Properties of High Explosives Calculated by Revised Kihara-Hikita Equation of State," *Proceedings of Eighth Symposium (International) on Detonation*, NSWC MP 86-194, 1985, p. 548.
2. Cowan, R. and Fickett, W., *J. Chem. Phys.*, Vol. 24, No. 932, 1956.
3. Fickett, W., *Detonation Properties of Condensed Explosives Calculated with an Equation Based on Intermolecular Potentials*, Los Alamos Scientific Laboratory Report LA-2712, 1962.
4. Ree, F., *J. Chem. Phys.*, Vol. 81, No. 1251, 1984.
5. Wu Xiong, "Detonation Properties of Condensed Explosives Computed with the VLW Equation of State," *Eighth Symposium (International) on Detonation*, NSWC MP 86-194, 1985, p. 796.
6. Gordon S. and McBride, B. J., "Computer Program for Calculation of Complex Chemical Equilibrium Compositions, Rocket Performance, Incident and Reflected Shocks and Chapman-Jouguet Detonations," NASA SP-273, 1971.
7. Yoshida, M.; Iida, M.; Tanaka, K.; Fujiwara, S.; Kusakabe, M.; and Shiino, K., "Detonation Behavior of Emulsion Explosives Containing Glass Microballoons," *Eighth Symposium (International) on Detonation*, NSWC MP 86-194, 1985, p. 993.

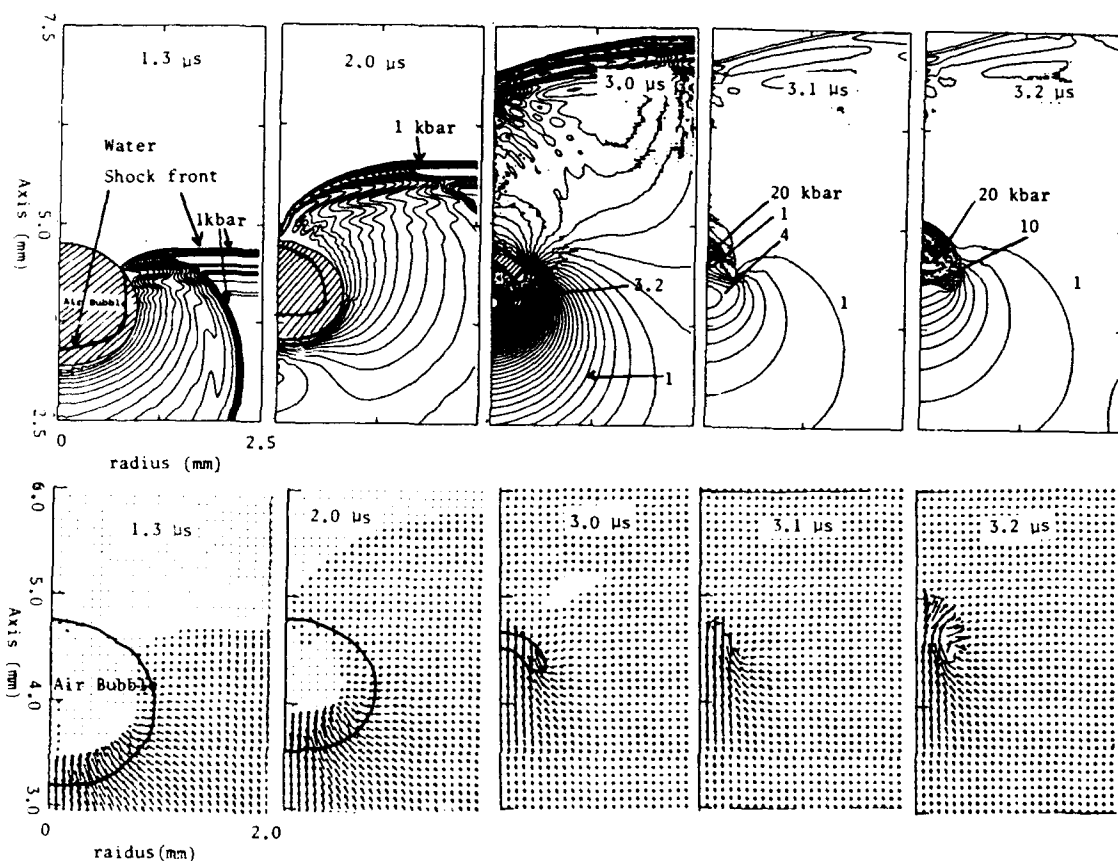


Figure 8. Shock Wave Propagation of Incident Pressure Of 10 kbar in Water with a Bubble of 1 mm in Radius. Upper for Isobars and Lower for velocity vector.

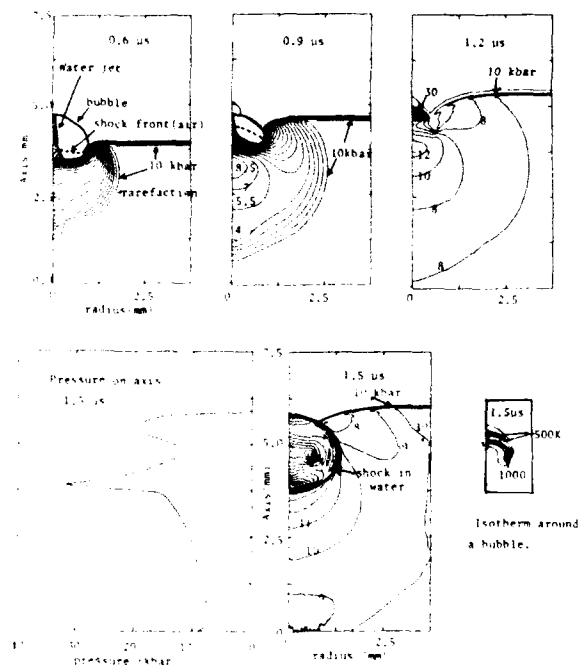


Figure 9. Shock Wave Propagation of Incident Pressure of 10 kbar in Water with a Bubble 1 mm in Radius



# CHEMISTRY OF UNDERWATER EXPLOSIVE DETONATIONS

D. Carlson, R. Doherty, V. Ringbloom, J. Deiter, and G. Wilmot  
Naval Surface Warfare Center  
10901 New Hampshire Avenue, Silver Spring, Maryland 20903-5000

*Five grams of pressed high explosive were detonated underwater, and chemical products were captured for analysis. Product mixtures were analyzed by spectroscopic and chromatographic chemical analysis methods. The method used to confine the reaction products from an underwater explosion is called the "balloon test." A charge was mounted inside a large rubber balloon filled with water. The balloon was itself surrounded and supported by water. When detonated, the balloon appeared to be transparent to the shock wave. The balloon oscillated with the explosion bubble, but did not rupture. All gaseous, dissolved, and solid products of the explosion were trapped inside the balloon. Chemical analysis of the product gases formed by PETN detonation underwater showed agreement with experimental recoveries of PETN detonations in vacuum or inert atmosphere. Some significant differences, however, were detected.*

## INTRODUCTION

When an explosion is detonated underwater, the chemistry of the detonation and afterburning can be affected in several ways:

(1) The explosive is confined by a large mass of water with no structural strength but with a large amount of inertia. The explosion transfers shock, kinetic, thermal and PV energy to the surrounding water. The amount of shock versus non-shock energy transferred, and the time scale in which these transfers occur, determine the effectiveness of the explosive. Especially for non-ideal and under-oxidized high explosives, the degree of confinement of a charge has a significant effect on the observed product distribution following detonation.<sup>1</sup> Even the confinement caused by less than one atmosphere of argon yields measurably different product ratios from the same charge fired in vacuum.<sup>2,3</sup> The effect of confinement by water is much larger, and the effects of water confinement with or without additional charge confinement on the chemical outcome of the detonation are not well understood.

(2) The explosive is detonated in a different chemical environment than that found in air or inert-gas media. Many non-ideal explosives exhibit enhanced performance when detonated in an oxidizing atmosphere, due to afterburning of the detonation products.<sup>4</sup>

This paper reports on progress in obtaining experimental data on the detonation of explosives underwater in a test called the "balloon test"<sup>5</sup> which is designed to closely simulate free-field underwater detonation. The purpose of the balloon test was to generate experimental chemical data on a system which, as closely as possible, mimics the end-use underwater detonation of metallized explosives. The test mimics both the physical and chemical environment of a free-field underwater detonation.

This close modeling, however, requires a compromise: the samples studied in the balloon test must be small. This is a shortcoming because the experimental firing now represents a system further removed from the actual large-scale event which the research seeks to model, and also because the test in its present form is limited to explosive charges

with small critical diameters. Despite this shortcoming, the balloon test has the marked advantage that it yields direct experimental data on the chemistry of underwater detonations in a constant-pressure environment.

## EXPERIMENTAL

Figure 1 shows a schematic diagram of the balloon test configuration. To perform the test, a five-gram pressed charge was mounted inside a large flexible rubber balloon filled with water. The balloon itself was surrounded and supported by water in an open-topped firing tank filled with 50,000 liters of water. The explosive was detonated underwater and chemical products were captured for analysis. Product mixtures were analyzed by gas and liquid chromatography, mass spectroscopy, energy dispersive x-ray spectrometry and x-ray photoelectron spectroscopy. When detonated, the balloon appeared to be transparent to the shock wave. The balloon oscillated with the explosion bubble but did not rupture. All gaseous, dissolved and solid products of the explosion were trapped inside the balloon.

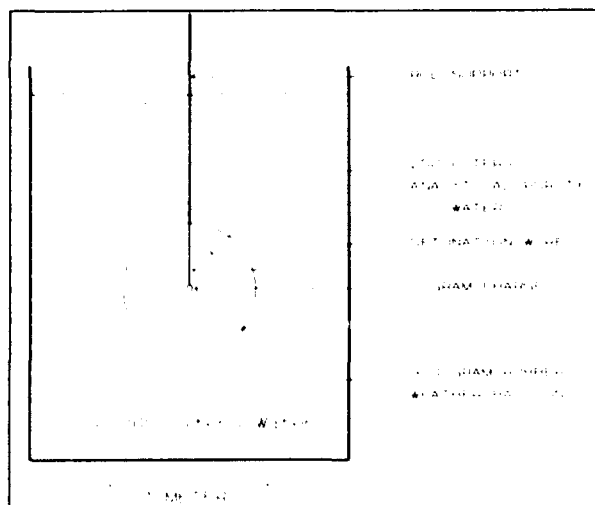


Figure 1. Balloon Test Setup

### Charges

The ultimate purpose of the balloon test was to generate data on detonation of metallized explosives. To establish an experimental baseline, the initial tests have all been performed using well characterized non-metallized high explosives. PETN was chosen because it detonates cleanly, because degree of

confinement has relatively little effect on observed detonation products, and because PETN and its products are not expected to react chemically with external water. The charges fired were unconfined pressed cylinders of PETN with diameter 12 mm and weight 4.9 grams. One charge of 2.6 grams of pento-lite lightly confined in a thin-walled copper tube was also detonated. Detonators used were custom-made RP-80s containing 80 milligrams PETN as the only explosive. The charges were cemented to the detonators using about 3 milligrams of cyanoacrylate adhesive. The detonator wires were used to support the charge inside the balloon and keep it in position. The only materials present in the test other than PETN were (inert) copper, the plastic header on the detonator, the plastic insulation on the detonator wires and the small amount of adhesive. These plastic contaminants which could not be avoided were, for the most part, recovered broken but undecomposed when recovered.

### Balloons

The explosive charge was suspended within a weather balloon weighing about 300 grams. The balloons used were commercially available or slightly modified 300-gram weather balloons designed to inflate to 17 feet before bursting.\* A smaller balloon would trap the products in less water, making analysis easier, but it was found that balloons much smaller than 300 grams frequently ruptured upon charge detonation. The commercial balloons were washed in 10 percent aqueous hydrofluoric acid to remove the layer of talc from one surface of the balloon; the specially modified balloons were manufactured using a silicone release agent instead of talc in the formation process (if not removed talc interfered seriously with the solid product filtering and analysis).

### Water

The balloon was held at the surface of the firing tank filled with 50,000 liters of tap

\*Custom and off-the-shelf weather balloons were obtained from Kaysam Corp., Patterson, NJ.

water. The balloon was filled with analysis-grade water purified by reverse osmosis, followed by deionization through ion-exchange columns. The balloon was filled until it maintained its spherical shape, but the rubber was not yet stretched. About 250 liters were required. The filled balloon was about 80 centimeters in diameter. The balloon could not support the weight of the water it contained unless it was suspended in water at all times. The charge was placed in the approximate center of the water balloon and the balloon was purged of any bubbles and stoppered. (It was important to remove all air from the balloon, because bubbles in direct contact with the balloon rubber might damage it during sympathetic oscillation with the detonation gas globe.<sup>6</sup>)

The balloon and charge assembly were then lowered 2 meters below the water surface. To ensure that the balloon had a slight negative buoyancy and would indeed sink into the tank, the temperature of the tank was maintained at 20°C, while the temperature of the pure water used to fill the balloon was held at 5°C.

### Sampling

The test charge was initiated by normal experimental methods. Following the explosion, the buoyancy of the trapped gas quickly carried the balloon to the surface. The thicker rubber at the neck of the balloon was punctured with a hypodermic needle, and the entire gas bubble was bled off into an evacuated glass bulb within two minutes of the explosion. (Rapid gas sampling was necessary to minimize loss of the gas bubble by dissolution into the water in the balloon.) It was found that if the point of entry of the needle was not held underwater, leakage of air into the gas sample was invariably observed.

In the same manner, a sample of the liquid was bled into another evacuated bulb, this time for dissolved gas analysis. The remainder of the water in the balloon was pumped through a 0.45-micron cellulose acetate filter into a holding tank from which liquid samples were taken for dissolved product analysis. Analyses were performed on the solids trapped by the filter and on the

water in the holding tank. Larger solids (mostly fragments of copper and plastic from the detonator) were picked by hand from the empty balloon.

### Gas Analysis

Product gases were analyzed by gas chromatography and independently by Fourier-transform infrared spectroscopy. Four replicate PETN charges were fired and the gases analyzed. Table 1 shows the analytical conditions used to perform the analyses.

*Table 1. Conditions for Gas Chromatographic Analysis*

ALL GASES EXCEPT HYDROGEN:	
Stationary phase:	8m x 1/8" packed 50/80m Porapak-Q
Carrier gas:	Helium
Temperature program:	-30° - +200°C
Detector:	thermal conductivity
HYDROGEN ANALYSIS:	
Stationary phase:	Chrompack 25m x .32mm capillary Molsieve 7A
Carrier gas:	Argon 100kPa
Temperature program:	+35° - +120°C
Detector:	thermal conductivity $\mu$ -cell

In all samples significant amounts of oxygen were detected. The amount detected was too great to be attributed to pickup of dissolved oxygen from the balloon water, and was attributed to leaks to the atmosphere introduced during the drawing off of the gases. (This finding prompted the change in gas sampling procedure requiring the point of sample draw-off be held underwater.) For these analyses, the amount of air leakage was calculated from the assumption that all oxygen present came from atmospheric contamination, and the concentrations of all gaseous components were corrected accordingly.

A large sample-to-sample variation in the assay of the detonation product gases was observed, probably due in part to the air leakage problem which was encountered, and in part to modifications made in the setup and sampling procedures during the time period over which the tests were performed. Figure 2 shows graphically the variation in data for the

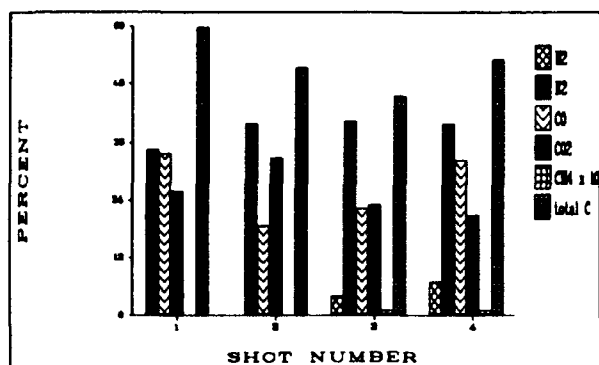


Figure 2. Variation in Measured Gases from Balloon Test PETN Detonations

four PETN shots that have been performed. Hydrogen and methane were not assayed during the first two shots fired

Table 2. Analysis of PETN Product Gases

Gas	Environment of Detonation				
	H <sub>2</sub> O <sup>a</sup>	Vac <sup>b</sup>	Arc <sup>c</sup>	Air <sup>d</sup>	Hee
H <sub>2</sub>	5.2	6.7	5.6	6.0	5.7
N <sub>2</sub>	38.6	26.3	15.1	43.4	26.8
CO	26.7	20.5	16.9	18.3	22.1
CO <sub>2</sub>	25.6	46.1	29.2	31.6	45.5
CH <sub>4</sub>	0.1	0	0.1	0.3	0

Volume percent excluding water vapor. Gases NH<sub>3</sub>, NO<sub>2</sub> not reported or not detected. Gas NO less than 0.02% when reported.

<sup>a</sup>Experimental results in this paper.

<sup>b</sup>Bomb calorimeter under vacuum.<sup>1</sup>

<sup>c</sup>Detonation chamber, 100% Argon.<sup>7</sup>

<sup>d</sup>Detonation chamber, 4% Air/96% Argon.<sup>7</sup>

<sup>e</sup>Burned under Helium; not detonated.<sup>8</sup>

Table 2 shows the results of the analysis of product gases from PETN underwater detonation, along with analysis results culled from the literature on PETN detonation and combustion in other environments. Experimental results from the balloon test were consistently higher in N<sub>2</sub> and CO, and lower in CO<sub>2</sub>, than most literature results for PETN firings in the absence of water. This was indicative of more extensive dissolution of

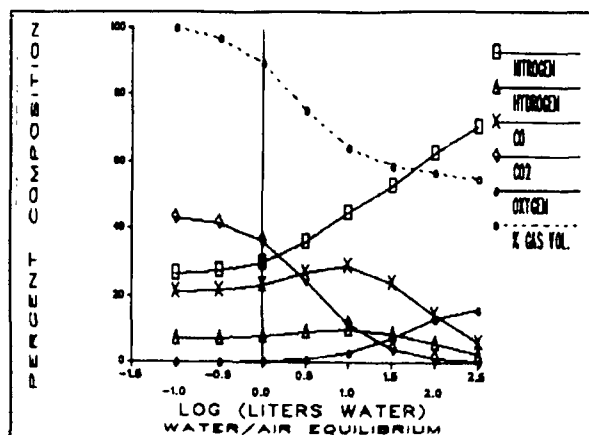


Figure 3. Calculated Gas Bubble Composition in Equilibrium with Water

gases into the balloon water than anticipated from gas diffusion rate constants.<sup>9,10</sup>

Gas dissolution into water can be greatly accelerated by turbulence and entrainment, such as occurs during an underwater explosion. The dissolution of product gases from underwater PETN explosion was modeled by assuming the gas bubble produced to be in solution equilibrium with some fraction of the water within the balloon. In this model, the volume of water in equilibrium with the gas bubble was unspecified in advance, but assumed to increase monotonically as a function of time. For any given amount of water, the composition of dissolved and free gases can be calculated using Henry's Law.<sup>11</sup>

Figure 3 shows the expected composition of the PETN product gas bubble when the gases equilibrate with water. The X axis represents the logarithm of the number of liters of water in equilibrium with the gas bubble. The water was taken to be initially in complete equilibrium with air. The initial gas composition was taken from experimental results obtained under vacuum in a water-free bomb calorimeter by Ornellas.<sup>1</sup>

Figure 3 shows that when the gas bubble had equilibrated with about 3 liters of water, the composition of CO<sub>2</sub> in the bubble was about half of its initial amount, and the compositions of less water-soluble gases such as N<sub>2</sub>, H<sub>2</sub>, and CO had increased. As shown graphically in Figure 4, assuming the initial product gas

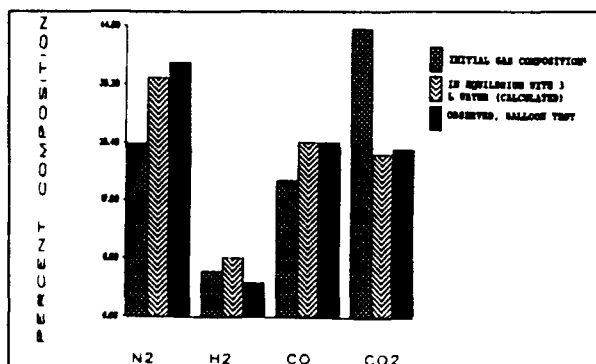


Figure 4 Comparison of Calculated and Observed Gas Bubble Composition

distribution reported by Ornellas, the calculated gas bubble after equilibration with about 3 liters of water agreed with the composition observed in the balloon test, within experimental error.

### Dissolved Product Analysis

Inorganic ionic detonation products dissolved in the water were analyzed by ion chromatography ("IC"). Table 3 shows the conditions used for the IC. Table 4 shows the observed amounts of dissolved ammonia, nitrite and nitrate ion found. Nitrite and nitrate ion are both products of the reactions of nitrogen oxides with water.

Dissolved CO<sub>2</sub> was expected to be a significant component of the water collected. It was analyzed by gas chromatography using the methods described in Table 2. No significant concentration of CO<sub>2</sub> was observed. We believe CO<sub>2</sub> to be dissolved in the balloon water in easily measurable amounts; it is suspected that the rapid liquid sampling method used did not provide a homogeneous water sample.

### Solid Product Analysis

When detonated, PETN gave too little solid residue to analyze. To practice the types of solid residue analysis which will be used on other charges, a sample of pentolite was detonated. This produced a black residue which was found to decompose in the presence of light (as TNT and some of its decomposition products do). The solid residues were examined

Table 3. Conditions for IC Analysis of Dissolved PETN Detonation Products

<b>CONDITIONS</b>	
Injection volume:	200 $\mu$ L
Aqueous sample preparation:	none
Cation analysis:	
Columns:	Dionex CG-1 guard, CS-1 separator, fiber suppressor
Mobile phase:	2.5mL/min 0.005M HCl
Suppressor eluent:	0.040N KOH
Detector:	conductivity
Anion analysis:	
Columns:	Dionex CG-1 guard, CS-1 separator, fiber suppressor
Mobile phase:	2.3mL/min 0.0030M NaHCO <sub>3</sub> /0.0024M Na <sub>2</sub> CO <sub>3</sub>
Suppressor eluent:	0.025N H <sub>2</sub> SO <sub>4</sub>
Detector:	UV absorbance (206nm) or conductivity

Table 4. Analysis of Dissolved Ions from PETN Detonation

Ion	Dissolved Concentration <sup>a</sup>	Fraction of N Recovered as Ion <sup>b</sup>
NH <sub>3</sub> <sup>+</sup>	3 x 10 <sup>-7</sup> M	1.2 x 10 <sup>-3</sup>
NO <sub>2</sub> <sup>-</sup>	3 x 10 <sup>-7</sup> M	1.2 x 10 <sup>-3</sup>
NO <sub>3</sub> <sup>-</sup>	9 x 10 <sup>-7</sup> M	4 x 10 <sup>-3</sup>

Estimate error:  $\pm 20\%$  relative.

<sup>a</sup>Total volume of water in balloon: 260L.  
<sup>b</sup>Based on 4.9gm PETN = 1.55x10<sup>-2</sup>mole PETN = 6.2x10<sup>-2</sup>mole Nitrogen

by Nuclear Magnetic Resonance (NMR), Scanning Electron Microscopy (SEM), X-ray Photoelectron Spectroscopy (XPS), and Mass Spectrometry (MS)

SEM data indicated that the pentolite residue was composed of irregularly shaped and agglomerated 0.1- to 0.2- $\mu$ m particles, mixed with silica particles with an average diameter of 0.7  $\mu$ m. The backscatter image was used to differentiate the residue particles, which were composed of C, N, and O, from the balloon impurity particles which contained silicon, copper, and lead.

A broad XPS scan of the residue found the following elements: C, O, N, Si, Cu, S, and Pb. The Cu, S, and Pb contaminants were present in concentrations of less than one percent; Si was present at about the 2 percent level. The source of the silica was probably incomplete washing out of the talc originally in the balloon. The lead and sulfur probably came from additives to the balloon rubber.

High resolution XPS of the nitrogen (1s) region was performed to determine the oxidation state of nitrogen present. This provides an indication of any remaining energetic organic compound. Two peaks were found in the N(1s) spectrum at 401.6eV (30 percent of total intensity) and at 399.95eV (70 percent). The anticipated N(1s) binding energies for the nitrogen moieties in pentolite would be approximately 406eV for the nitro group in TNT and approximately 408eV for the nitrate ester group in PETN. The observed spectrum indicates no unreacted TNT or PETN in the pentolite residue.

The water insoluble solid residue was also extracted with acetone-d<sub>6</sub> and the solution was analyzed by NMR. Both TNT and PETN are soluble in acetone and would appear in characteristic NMR patterns if present. No such patterns were found, confirming the total consumption of both PETN and TNT in the detonation.

## SUMMARY

Capture and analysis of detonation products by the use of a flexible balloon was accomplished successfully. The balloon test method generates detonation chemistry data in a constant pressure underwater environment.

Assay of the gaseous products of PETN detonation from several replicate shots showed a wide variability. This may have been due to air contamination allowed by a flawed gas sampling procedure used for most of the firings.

Experimental product ratios for the gas bubble agreed fairly well with results obtained by other experimental configurations. The results were high in CO and N<sub>2</sub>, and low in CO<sub>2</sub>. The difference between balloon test results and results generated by others in

closed bomb tests can be explained by partial equilibration of the product gases with the balloon water.

Solid analysis from the firing of the single sample of pentolite yielded results that would normally be expected. Analysis of more complex residues from metallized explosives will be attempted in future work.

## REFERENCES

1. Ornellas, D. L., "Calorimetric Determinations of the Heat and Products of Detonation for Explosives: October 1961 to April 1982," UCRL-52821, Lawrence Livermore Laboratory, 5 Apr 1982.
2. Volk, F., "Detonation Gases and Residues of Composite Explosives," *Journal of Energetic Materials*, Vol. 4, 1986, pp. 93-113.
3. Volk, F. and Schedlbauer, F., "Detonation Products of Less Sensitive High Explosives Formed Under Different Pressures of Argon and in Vacuum," *Ninth Symposium (International) on Detonation*, Aug 1989.
4. Matle, C. C., "The Contribution of Afterburning to the Airblast from Aluminized Explosives," NOLTR 61-178, 22 Jun 1967.
5. Fye, P. M.; Arsove, S.; Cottell, R.; and Curtis, W., "A Study of the Chemical Products of an Underwater Explosion," NAVORD Report 412, Underwater Explosives Research Laboratory, Woods Hole Oceanographic Institution, Sep 1947.
6. Goertner, J. F., "Dynamical Model for Explosion Injury to Fish," NSW TR 76-155, 18 Dec 1978.
7. Volk, F., "Investigation of the Detonation Reaction Products of Different Explosives," *Propellants and Explosives*, Vol. 3, 1978, pp. 9-13.
8. Bernecker, R. and Smith, L. C., "On the Products Formed in the Combustion of Explosives. Freeze-out of the Water-Gas Reaction," *Journal of Physical Chemistry*, Vol. 71, 1967, pp. 2381-2390.

9. Hartman, B. and Hammond, D. E., "Gas Exchange Rates Across the Sediment Water and Air-Water Interfaces in South San Francisco Bay," *Journal of Geophysical Research*, Vol. 89(C3), 1984, pp. 3593-3603.
10. Liss, P. S.; Balls, P. W.; Martinelli, F. N.; and Coantic, M., "The Effect of Evaporation and Condensation on Gas Transfer Across an Air-Water Interface," *Oceanologica Acta* 4(2), 1981, pp. 129-138.
11. *CRC Handbook of Chemistry and Physics*, 44th Edition, pp. 1706-1709.

### DISCUSSION

**H. GRYTING**

Gryting Energetics Sciences Company

What happened to the 8 pound minimum rule for valid underwater explosion data? The products could be considerably different from such small samples.

### REPLY BY D. CARLSON

That's true -- our results could be quite different. Even worse, many of the explosives of most interest to the underwater community will not detonate at all using these small sample sizes. This is a major limitation of the balloon test in its present form. We're looking into ways of scaling up.

### DISCUSSION

**I. B. MISHRA**

Kanan Associates, Inc.

You have considered the reaction between hot Al and water at 110°C. Should

you not consider the reaction between very hot  $\text{Al}_2\text{O}_3$  as it comes in contact with water during bubble formation?

### REPLY BY D. CARLSON

We considered the Al-water system at moderate temperatures to satisfy ourselves that significant reaction between metallic Al and water would not take place in the minutes which elapse between detonation and product sampling. The actual reactions occurring during the detonation are very complex. The balloon test can at best give us limits of reaction extent, and suggest mechanisms.

### DISCUSSION

**J. W. ENIG**

Enig Associates, Inc.

I think your unique balloon measurement technique can be extended to shed light for the first time on the reaction of aluminized explosives with the surrounding water during an underwater detonation. If some fraction of the water in the balloon contained oxygen of a different isotope, the concentration of the isotope in the  $\text{Al}_2\text{O}_3$  products would suggest the degree of reaction with the external water.

### REPLY BY D. CARLSON

I agree. The main purpose of the test was to answer questions about how aluminum reacts in an underwater explosive. If our initial experiments continue to yield encouraging results, we may try an isotopic labelling experiment.

# ESTIMATION OF PERFORMANCE OF UNDERWATER EXPLOSIVES

D. A. Cichra and R. M. Doherty  
Naval Surface Warfare Center

Code R11, White Oak, Silver Spring, Maryland 20903-5000

*A collection of 175 underwater compositions, for which shockwave energy and bubble energy were measured, has been compiled from the literature. The heat of detonation ( $Q$ , cal/cm<sup>3</sup>), number of moles of product gases ( $N$ , mol/100 cm<sup>3</sup>), and the average molecular weight of the product gases ( $M$ , g/mol) have been calculated for these compositions using a number of different arbitrary decomposition mechanisms. These parameters were used in regression analyses of the performance parameters to arrive at equations for the equivalent volume for shockwave energy (relative to pentolite) and the relative bubble energy (relative to pentolite). The equations had correlation coefficients ( $R$ ) of 0.97.*

## INTRODUCTION

When an explosive is detonated under water, the energy liberated is partitioned between the shockwave that goes out in the water and the residual energy in the hot explosion products or bubble.<sup>1</sup> In order to compare the performance of explosives under water, two figures of merit have been employed. They relate the energies in the shockwave and in the bubble of an explosive to those of a reference material. The most commonly used figures of merit are the equivalent weight for shockwave energy (SWE) and the relative bubble energy (RBE).<sup>2</sup> SWE is an average over some distance range of the mass of reference explosive (typically taken as pentolite) required to give the same energy in the shockwave as unit mass of the explosive being tested. RBE is the ratio of the energy in the gas bubble produced by the detonation of the explosive being tested to the energy in the gas bubble produced by an equal mass of reference explosive, usually pentolite. For both SWE and RBE, a larger value corresponds to better performance. Although both of these ratios are used to compare equal or equivalent masses of materials, they can be converted to expressions based on volume if the densities of the reference and test explosives are known. In some instances, a comparison on the basis of volume rather than mass is more

meaningful. In this work we describe how explosive composition can be related to SWE and RBE.

The use of arbitrary decomposition pathways, or arbitraries, to predict the products of a detonation, and from those products certain detonation properties, was pioneered by S. J. Jacobs and the late Mortimer Kamlet.<sup>3</sup> They assumed that for CHNO explosives oxygen is used first to form H<sub>2</sub>O, then CO<sub>2</sub>, and that the nitrogen appears in the products as N<sub>2</sub>. This assumption was referred to as the H<sub>2</sub>O-CO<sub>2</sub> arbitrary. From this assumed distribution of products, they calculated the heat of detonation ( $Q$ ), the number of moles of product gases ( $N$ ), and the average molecular weight of the product gases ( $M$ ). The values of  $Q$ ,  $N$ , and  $M$  were used in combination with the density to estimate detonation velocities and detonation pressures. Kamlet and Ablard noted that the results did not differ markedly if the H<sub>2</sub>O-CO-CO<sub>2</sub> or CO-H<sub>2</sub>O-CO<sub>2</sub> arbitrary was used instead.<sup>4</sup>

Since this method tacitly assumes instantaneous decomposition of the explosives, it does not give accurate predictions of detonation pressure and detonation velocity for non-ideal explosives, particularly metallized compositions. However, in the underwater



environment, the time allowed for reactions to contribute to explosive effects is much longer, of the order of tens to hundreds of milliseconds, as compared to a fraction of a millisecond for metal acceleration by an explosive.<sup>5</sup> Following the lead of Kamlet and Jacobs, we have studied the relationship between Q, N, and M for ten arbitraries, and the performance of a set of explosive compositions that range from ideal to very heavily metallized.

The three variables Q, N, and M have been used here to characterize the composition of explosives. These variables have been calculated for 175 explosive formulations for which both SWE and RBE have been measured. The values of Q, N, and M were computed from the masses and the heats of formation of the ingredients for each formulation for each of the arbitraries considered. They were then used, together with the measured densities of the compositions, in multiple linear regression analyses. The result is a set of equations from which one can estimate the shockwave and bubble performance of a new formulation from its composition.

## RESULTS AND DISCUSSION

From the underwater explosive literature, performance data on 175 compositions, some differing only in density, were accumulated. For this work, no effort was made to evaluate the data as to charge size, method of preparation, or other such variables that might affect performance, although no data were included for compositions that showed an effect of booster size. If more than one result were available for a given composition at a given density, the results were averaged. The equivalent volume for shockwave energy relative to pentolite for these compositions ranged from 0.13 to 1.82, while the bubble energies relative to an equal volume of pentolite ranged from 0.18 to 3.27. These values were obtained from the performance data expressed on a weight basis by multiplying the weight data by the density of the composition and dividing by 1.65 (the density of pentolite). The types of compositions represented in the data set are shown in Table 1.

*Table 1. Composition of Assembled Formulations*

Group	Ingredients*	Number of Data Points
1	Organic HE, Al	57
2	AP, Al, PNC binder	40
3	Organic HE	18
4	AP, Al, Zr, PNC binder	15
5	Oxidizer, Zr, PNC binder	15
6	Organic HE, AP, Al	9
7	HN, AN	5
8	Organic HE, AN, Al	4
9	Organic HE, AN, or AP	4
10	HN, Al	3

\*AN = ammonium nitrate

AP = ammonium perchlorate

HE = high explosive

HN = hydrazine mononitrate

PNC = plastisol nitrocellulose

*Table 2. Arbitraries Used in the Correlations*

No.	Assumed Order of Products
1	MO, CO, CO <sub>2</sub> , H <sub>2</sub> O
2	MO, CO, H <sub>2</sub> O, CO <sub>2</sub>
3	MO, H <sub>2</sub> O, CO, CO <sub>2</sub>
4	MO, MN, H <sub>2</sub> O, CO, CO <sub>2</sub>
5	MO, MN, CO, H <sub>2</sub> O, CO <sub>2</sub>
6	MO, MN, CO, CO <sub>2</sub> , H <sub>2</sub> O
7	CO, MO, CO <sub>2</sub> , H <sub>2</sub> O
8	CO, MO, H <sub>2</sub> O, CO <sub>2</sub>
9	CO, MO, MN, H <sub>2</sub> O, CO <sub>2</sub>
10	CO, MO, MN, CO <sub>2</sub> , H <sub>2</sub> O

The values of Q, N, and M were then calculated for a number of arbitraries. The arbitraries that were examined are listed in Table 2. In all the arbitraries, chlorine, if present, was assumed to form HCl. The two major families of arbitraries were the family in which oxygen was assumed to react first with metal to form metal oxide (MO, such as  $\text{Al}_2\text{O}_3$  or  $\text{ZrO}_2$ ), and the family in which oxygen was assumed to react first with carbon to form carbon monoxide and then with metal to form metal oxide. In five of the arbitraries, nitrogen is assumed to be available to oxidize metal if necessary. In all cases, any hydrogen that is not oxidized is assumed to form  $\text{H}_2$ , nitrogen forms  $\text{N}_2$ , and unoxidized carbon forms solid C with  $H_f = 0$ .

The calculated values of Q, N, and M, along with the experimental density, were used as parameters in multiple linear regression analyses. All compositions were treated alike, regardless of their ingredients. This assumption ignores factors such as differences in detonation temperatures and pressures, and differences in reaction rates that may result in different reaction products, thereby affecting performance.

The initial correlations were of the form of Equation (1), where the values of a, b, c, e, and f were determined by a least squares fit of the data.

$$\log(\text{RBE or SWE}) = a \log Q + b \log N + c \log M + e \log d + f \quad (1)$$

The results of these correlations were used to determine which of the terms to retain. Terms that were judged to be significant at the 95 percent confidence level by the Student's t test were retained. The second step in the procedure was to revert to the linear form of the equation in RBE or SWE, as in Equation (2).

$$\text{SWE or RBE} = mQ^{a'}N^{b'}M^{c'}d^{e'} + s \quad (2)$$

The values of  $a'$ ,  $b'$ ,  $c'$ , and  $e'$  were fixed by rounding the values of a, b, c, and e to the nearest value of  $1/2^n$  (i.e.,  $1/8$ ,  $1/4$ , etc.). With the values of  $a'$ ,  $b'$ ,  $c'$ , and  $e'$  fixed, a second regression for each arbitrary of the appropriate product  $Q^{a'}N^{b'}M^{c'}d^{e'}$  against RBE or SWE was conducted.

All the parameters were used on a volume basis. The analyses were done on subsets based on the amount of metal, carbon, and oxidizing species present. The subsets were: (1) those compositions with no more metal than can react with the oxygen remaining after all carbon has been oxidized to CO (88 compositions); (2) those with no more metal than can react with all the oxygen present to form metal oxide (133 compositions); (3) those with no more metal than can react to form metal oxide with the oxygen remaining after all carbon has been oxidized to CO, and with nitrogen to form metal nitride (150 compositions); and (4) all the compositions (175 compositions). The goodness of fit for the various subsets guided changes in the arbitrary used.

It is generally recognized that the heat of detonation is a reasonably good predictor of shockwave and bubble performance under water. The shockwave energy for the 88 compositions in subset 1 correlates well with Q alone (i.e.,  $a' = 1$ ,  $b' = c' = e' = 0$ ) for any of the arbitraries in which metal oxide and CO are the first two products ( $r > 0.92$ ). The correlation is not as good when all the compositions are included. When all the points are included, the correlation coefficient between Q and SWE is  $> 0.88$  for arbitraries 7 and 8, but  $< 0.7$  for arbitraries 1 and 2.

There are several series of aluminized compositions for which both the shockwave and bubble energy have been measured. Figure 1 is a plot of observed  $\text{SWE}_v$  versus (mol O)/(3/2 mol Al + mol C), which is a measure of oxidant balance, for a series of TNETB/Al formulations.<sup>8</sup> As the amount of aluminum in the formulation increases, this ratio decreases. The shockwave energy reaches a maximum when there is enough metal to react with all the oxygen except that needed to convert C to CO. Additional metal degrades SWE. The superior correlation with arbitraries using CO as the preferred oxygen-containing product supports the contention that CO must be considered.

When parameters other than Q are included in the correlation, the difference between the MO, CO and CO, MO arbitraries

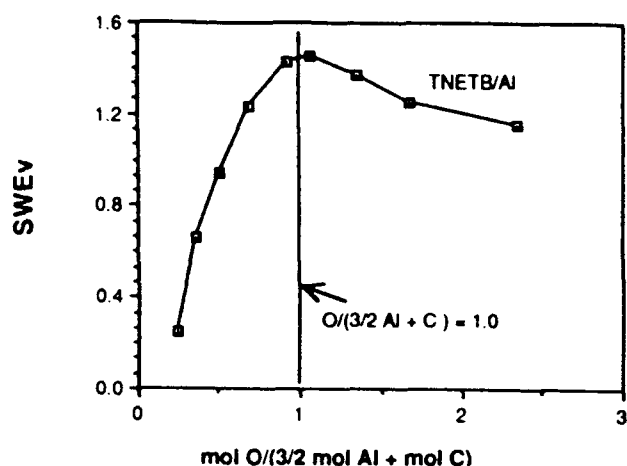


Figure 1 Dependence of  $SWE_v$  on Elemental Composition for TNETB/Al

disappears. The best result for the MO, CO arbitraries involves  $(Q^3M^2Nd)^{1/4}$ . The best fit for the CO, MO arbitraries uses  $(Q^3N^2d)^{1/4}$ , but it gives a standard error (se) and correlation coefficient (R) equivalent to the MO, CO equation. The CO, MO, MN arbitraries, which were added to help correlate the bubble results, also give correlations with approximately the same goodness of fit. As Kamlet and Ablard observed earlier,<sup>4</sup> the correlations may be very insensitive to the arbitrary chosen.

Good correlations can be obtained using only Q and N in the form  $Q^{3/4}N^{1/2}$  ( $R > 0.95$ ). It can be improved slightly by adding M and d (or just d in the case of the CO, MO arbitraries). This implies that the most important factors affecting the shockwave energy are the heat of detonation and the number of moles of gases formed. Unfortunately, N and M are correlated ( $r = 0.73$ ) for the MO, CO arbitraries, which affects the interpretation of the results.

The best predictive equation for  $SWE_v$  is Equation (3), using Q, N, and M from the MO, CO,  $H_2O$  arbitrary.

$$SWE_v = 5.73 \times 10^4 (Q^3N^2Md)^{1/4} + 0.04 \quad (3)$$

$$R = 0.971 \quad se = 0.084$$

The average values of  $SWE_v$  and root mean square (rms) deviations for the groups listed in Table 1, are given in Table 3. Changing the arbitrary does little to change the values of the slope and intercept in the equation. This being the case, it is possible to use Equation (3) with

Table 3. Agreement Between Calculated and Observed  $SWE_v$

Group	No. of Points	Average obs $SWE_v$	rms dev.
1	57	1.02	0.10
2	40	1.52	0.07
3	18	0.95	0.09
4	15	1.50	0.09
5	15	1.51	0.10
6	9	1.24	0.17
7	5	0.41	0.28
8	4	1.06	0.08
9	4	1.00	0.12
10	3	0.82	0.12

the values of Q, N, and M from the CO, MO, MN,  $H_2O$  arbitrary, which is used to predict RBE to obtain good estimates of the shock-wave energy.

The poor agreement between observed and calculated  $SWE_v$  for group 7 is probably attributable to incomplete reaction of the AN in the formulation.<sup>6</sup> The deviations between calculated and observed  $SWE_v$  increase with increasing percentage of AN, and the observed performance is always lower than predicted. The same trend is observed with the RBE<sub>v</sub> for this group, although the deviations are not as large.

It has been observed that the dissipated energy due to shock heating of water by the shockwave decreases as the detonation pressure of an explosive decreases.<sup>7</sup> The methodology described here does not take this into account explicitly. The inclusion of density as a factor in Equation (3) may be a reflection of the fact that incorporating a metal such as aluminum or zirconium, which increases the density of the formulation, lowers the detonation pressure.

The fact that the correlations are about the same for the various arbitraries is probably not due to an insufficient number of compositions that have Q, N, and M that differ depending on the arbitrary used. There are 94 of the 175 compositions for which Q, N, and M for the

MO, CO (CO<sub>2</sub> or H<sub>2</sub>O), arbitrary are the same as those for the CO, MO (CO<sub>2</sub> or H<sub>2</sub>O), arbitrary. Similarly, there are 96 compositions for which Q, N, and M for the MO, CO, CO<sub>2</sub> arbitrary are the same as those for the MO, CO, H<sub>2</sub>O arbitrary. These same 96 compositions also have values for the CO, MO (CO<sub>2</sub> or H<sub>2</sub>O), and CO, MO, MN (CO<sub>2</sub> or H<sub>2</sub>O) arbitraries that are independent of the order of formation of CO<sub>2</sub> and H<sub>2</sub>O. It should be noted that compositions for which Q differs depending on whether H<sub>2</sub>O or CO<sub>2</sub> is assumed to be formed first may still have identical values of N and M for those two cases. The values for Q, N, and M for the CO, MO (CO<sub>2</sub> or H<sub>2</sub>O) arbitraries are the same as those for the CO, MO, MN (CO<sub>2</sub> or H<sub>2</sub>O) arbitraries only for those 88 compositions with no more than enough metal to react with all the oxygen remaining after C has been converted to CO.

The lack of distinction between the CO, MO, and the MO, CO arbitraries can be explained by looking at a series of compositions with increasing metal content. As metal is added to a given composition in increasing amounts, Q for the MO, CO arbitraries keeps increasing until there is enough metal to react with all the oxygen. At this point it starts to decrease since the metal is no longer reacting to release energy. The number of moles of gas (N) initially decreases slightly as the amount of metal is increased, since the amount of explosive present decreases. However, at the point at which there is enough metal to react with all the oxygen except that needed to oxidize C to CO, N begins to decrease faster since gaseous CO is converted to solid C.

For the CO, MO arbitraries, however, Q increases only to the point where there is enough metal to react with all the oxygen remaining after all C is oxidized to CO. At this point, increasing the metal leads to a decrease in Q since the extra metal no longer reacts to release energy. N decreases uniformly over the whole range of metal content due to the decrease in the amount of explosive present as the amount of metal is increased.

For the CO, MO, MN arbitraries, Q increases as metal is added until there is enough to react with all the oxygen remaining after the C has been oxidized to CO. Then Q

continues to increase but at a lower rate as the metal reacts with nitrogen present. When the metal has reacted with all the nitrogen, Q begins to decrease. Meanwhile, N decreases due to the decrease in the amount of explosive present until that point at which the metal begins to react with the nitrogen. Here N starts to decrease more rapidly, since gaseous nitrogen is being converted to solid metal nitride.

Interesting results were also obtained for the relative bubble energy on a volume basis (RBE<sub>v</sub>). Useful insights were gained by treating various subsets of the data.

Using the CO, MO arbitraries, it was found that the correlation with Q alone is much worse for subset 3 than for subset 1. This seemed to indicate that a further reaction might be occurring as more metal is added. One possibility was reaction with nitrogen. This did not seem unreasonable, since AlN has been identified in the products of an underwater detonation of Torpex.<sup>9</sup> It was found that the CO, MO, MN arbitraries did have better correlations with Q alone for subset 3 than the arbitraries that neglected formation of metal nitride (se = 0.20 vs. se = 0.25 - 0.32). However, the correlation still drops off when all the compositions are included. Attempts to fit the very highly metallized compositions by adding another reaction (such as with the CO or HCl, if it is present) to the arbitrary have not been successful. Since the predictions are generally lower than the observed RBE<sub>v</sub> for the most highly metallized systems, the prospect of participation by ambient water seems reasonable.

It was found that the fit for subset 3, i.e., the less highly metallized compositions, could be improved by including other parameters in addition to Q. The best fit was obtained with  $Q(M^{-1}d)^{1/4}$  using the CO, MO, MN arbitraries. It was again not possible to distinguish between the two arbitraries. Equation (5) was obtained using the Q and M from the CO, MO, MN, H<sub>2</sub>O arbitrary, but gives equally good results with the Q and M values from the CO, MO, MN, CO<sub>2</sub> arbitrary.

$$\begin{aligned} \text{RBE}_v &= 1.10 \times 10^{-3} Q(M^{-1}d)^{1/4} + 0.10 \quad (5) \\ R &= 0.971, \text{ se} = 0.17 \end{aligned}$$

These equations are not suitable for use with over-metallized compositions. [Compositions are considered to be over-metallized when they contain excess metal over that which can react with the residual oxygen and nitrogen after all C has been oxidized to CO.] In general, formulations that are over-metallized are undercalculated by Equation (5). For example, a formulation consisting of 38 percent Al, 36 percent AP, and 26 percent TNT was determined to have an  $RBE_v$  of 3.05. The value calculated by Equation (5) is 2.43. The rms deviations and average observed  $RBE_v$  values for the groups listed in Table 1 are given in Table 4. Only those formulations to which the equation is applicable are included in the averages.

Table 4. Agreement Between Calculated and Observed  $RBE_v$

Group	No. of Points	Average obs $RBE_v$	rms dev.
1	36	1.90	0.17
2	40	2.51	0.15
3	18	0.98	0.17
4	15	2.69	0.16
5	14	2.62	0.14
6	7	2.52	0.24
7	5	0.50	0.19
8	4	1.99	0.22
9	4	1.13	0.10
10	3	1.63	0.31

The largest deviations between observed and calculated values of  $RBE_v$  were in group 10, the HN-Al compositions. This group and group 7 differ from the other composition, since they have no carbon. In general, the standard deviation in the measured  $RBE$  is about 5 to 10 percent. For pentolite, which is very reproducible and for which a large amount of data is available, the standard deviation is about 4 percent. Thus, the agreement between calculated and observed  $RBE_v$  is quite good for most of the subsets of the data.

One of the surprising results from the correlations, was that the number of moles of

gas, N, was not significant in any of the correlations with  $RBE_v$ . Intuitively, it seems that, all other things being equal, the compositions with the larger number of moles of gas should produce a larger bubble. Based on the arbitraries used here, this is not the case. The dependence of  $RBE_v$  on the reciprocal of the square root of the molecular weight, has an analogy in the computation of specific impulse in rocket propulsion problems. Lower molecular weight gases lead to larger values of specific impulse, and here they appear to enhance bubble performance.

## CONCLUSION

A method has been presented by which estimates may be made of the shockwave energy and bubble energy, both relative to pentolite, for explosives fired under water. The equations presented may be used to estimate the performance of an explosive from its composition and the heat of formation of its ingredients.

## REFERENCES

1. Cole, R. H., *Underwater Explosions*, Princeton University Press, Princeton, NJ, 1948.
2. Swisdak, M. M., *Explosion Effects and Properties: Part II - Explosion Effects in Water*, NSWC/NCI, TR 76-116, NSWC, Silver Spring, MD, Feb 1978.
3. Kamlet, M. J. and Jacobs, S. J., "Chemistry of Detonations. I. A Simple Method for Calculating Detonation Properties of C-H-N-O Explosives," *J. Chem. Phys.*, Vol. 48, 1982, p. 23.
4. Kamlet, M. J. and Ablard, J. E., "Chemistry of Detonations. II. Buffered Equilibria," *J. Chem. Phys.*, Vol. 48, p. 36.
5. Finger, M. et al., "Metal Acceleration by Composite Explosives," The Fifth Symposium (International) on Detonation, ONR ACR-184, 1970, p. 138.
6. Thiel, M. A., *Comparison of the Underwater Power of Explosives in Small Charges*, NAVORD Rept. 6859, NOL, Silver Spring, MD, Apr 1960.

7. Sternberg, H. M. and Hurwitz, H., "Calculated Spherical Shock Waves Produced by Condensed Explosives in Air and Water," *Sixth Symposium (International) on Detonation*, ONR ACR-221, 1976, p. 528.
8. Christian, E. A., *The Contribution of Aluminum to the Effectiveness of an Explosion. I. Underwater Performance of One-Pound Charges*, NAVORD Rept. 3760, NOL, Silver Spring, MD, Aug 1954.

### DISCUSSION

J. ROTH, Consultant  
Portola Valley, CA

Does your correlation for highly metallized explosives improve if you assume that some of the metal does not react?

### REPLY BY D. A. CICHRA AND R. M. DOHERTY

The highly metallized compositions are, in general, undercalculated by our method using the equation for RBE, presumably because there is unreacted metal present using the CO, MO, MN arbitrary. That is, once there is enough metal to react with the oxygen (except that used to form CO) and with all the nitrogen, any additional metal remains unreacted. Attempts to include some further reaction, such as reaction with the CO in the CO, MO, MN arbitraries, did not improve the fit when all the compositions were included. Likewise, using arbitraries that result in the formation of less CO and, therefore, more MO, did not improve the fit, although all the simpler possibilities have not yet been looked at.

### DISCUSSION

M. COWPERTHWAIT, SRI  
International, Menlo Park, CA

I have modified Kamlet's method with the assumptions that all the Al reacts and that the

rest of the composition obeys his  $\text{CO}_2\text{-H}_2\text{O}$  arbitrary rule, and have obtained no agreement between the calculated values and the experimental values given in the literature.

### REPLY BY D. A. CICHRA AND R. M. DOHERTY

It is not surprising that an arbitrary that assumes all the aluminum reacts does not fit the cylinder test results because of the time frame involved in that test. It would be interesting to see if a fit could be obtained using an arbitrary like the CO, MO ones used in our work -- or some other arbitrary that, in essence, has the aluminum reacting with only some of the oxygen present.

### DISCUSSION

G. O. BJARNHOLT, Swedish Defence  
Research Establishment  
Stockholm, Sweden

The detonation pressure influences the energy partitioning between shock and bubble energy. If a rough estimate of the detonation pressure of an explosive can be made and the heat of detonation is known, the shock and bubble energies could probably be predicted with good accuracy. If you include an estimated detonation pressure as a parameter in your regression analyses, the correlation coefficients of the equations should improve considerably.

### REPLY BY D. A. CICHRA AND R. M. DOHERTY

Including the detonation pressure would probably improve the fit, however, there is no method of estimating the detonation pressure for the metallized composition, especially the highly metallized ones.

# **UNDERWATER EXPLOSION OF EMULSION EXPLOSIVES**

**K. Hattori, Y. Kato, K. Tokita, Y. Fukatsu, N. Mori, and A. Torii**  
**Chemicals and Explosives Laboratory**  
**Taketoyo, Aichi, Japan**

This paper was presented at the Ninth Symposium (International) on Detonation. However, it is not published here because it

was not submitted to the editor in sufficient time to be published.

# THE FUNDAMENTALS OF METAL COMBUSTION IN COMPOSITE EXPLOSIVES REVEALED BY HIGH SPEED MICROPHOTOGRAPHY\*

William C. Tao, Alan M. Frank, and Rochelle E. Clements  
Lawrence Livermore National Laboratory  
Livermore, California 94550

and

Joseph E. Shepherd  
Department of Mechanical Engineering  
Rensselaer Polytechnic Institute  
Troy, New York 12180

*High-speed and high resolution microphotography has been used to examine the ignition and combustion of small 25-76- $\mu\text{m}$  diameter and 23-mm long aluminum wires in water, rapidly heated by a capacitor discharge system. Streak photographs were obtained over periods of 30-500  $\mu\text{s}$  with a spatial resolution of 2  $\mu\text{m}$ . The wire temperature was determined as a function of time by integrating the circuit equation together with the energy equation for an adiabatic wire and known aluminum electrical resistivity and temperature functions of energy density. We discovered a transition in the ignition and combustion of the aluminum from mild to rapid sustained chemical reaction with the water when the wire is heated above a critical temperature within 1  $\mu\text{s}$ . The triggering mechanism for this rapid reaction appears to be the collapse of a vapor blanket during its first oscillation.*

## INTRODUCTION

The combustion of metals, such as aluminum (Al), in the presence of gaseous and liquid oxidizers is relevant to many disciplines.<sup>1-3</sup> These range from nuclear reactor safety and industrial manufacturing to propellant and composite explosives applications. In the first two areas of interest, the temperature encountered by the metal is not much higher than the melting point, and the interaction with water results in the explosive production of steam due to the rapid heat transfer from the molten metal to the water. In explosive applications such as air blast, cratering, and fragmentation,

metallic additives chemically react with the oxidizer and are used to tailor the rate of energy delivery by the expansion gas. Mass and thermal transport limitations determine the rates of reaction between the Al, intermediate oxidizing species, and detonation products. The formation of aluminum oxide ( $\text{Al}_2\text{O}_3$ ), an extremely exothermic reaction ( $\Delta H^\circ_{f,298} = -1675.7 \text{ kJ/mole}$ ), increases the temperature of the expansion gas, and directly influences the equilibrium product distribution. As the product gas expands, the increase in thermal energy is partitioned between the rotational and vibrational states of the detonation products. This stored energy is recovered from the deactivation of the excited states and transformed into translational kinetic energy in the expansion push at later times (10's of  $\mu\text{s}$ ). In underwater applications in which prompt delivery of the available

\*Work performed under the auspices of the U.S. Department of Energy by the Lawrence Livermore National Laboratory under contract No. W-7405-ENG-48.



energy in the bubble expansion is not a requirement, the aluminum content in typical explosive formulations can be as high as 30-35 weight percent.<sup>4</sup>

In all applications, the major issues are the coupled processes of chemical reaction between the aluminum and the oxidizing medium, the role of energy (heat) transfer, and fluid dynamics. Although the specific mechanism for sustained chemical reaction remains in question, it is generally accepted that fragmentation of the molten particle and disruption of the oxide layer is a necessity. It has been shown that physical mixing or even steam explosion does not trigger any appreciable chemical reaction unless the melt temperature is above the melting point of its oxide.<sup>5,6</sup> The two are obviously related in the time sequence of events from boiling to explosion. Using composite explosives as an illustration, the diffusion of oxidizing species through the oxide layer to react with superheated aluminum is dependent on the local temperature, which in turn is dependent on the rate of  $\text{Al}_2\text{O}_3$  formation, and the exposure of new surfaces for the reaction. It is beneficial to briefly review the concepts of fragmentation.

According to Harlow et al.,<sup>7</sup> the existence of a triggering pressure pulse impacting the molten metal surface, whether internally induced or externally provided, is crucial for fine fragmentation to occur. Usynin et al.<sup>8</sup> classified this pressure perturbation into two regimes where thermal and hydrodynamic effects dominate. Hydrodynamic breakup, or Taylor instability, occurs when the inertial forces acting on the molten mass exceed the surface energy. This mechanism requires an initiating shock pulse that can cause a steam film to collapse into the molten metal-oxide mass. Anderson<sup>9</sup> found that an exploding wire is the critical factor triggering the vapor explosion of molten Al injected into water. Similarly, Nelson<sup>10</sup> attempted, and in certain cases succeeded, in triggering a vapor explosion by firing a bridgewire at critical intervals to disturb the oxide layer. The cushioning effect of the noncondensable hydrogen gas can be overcome by increasing the trigger pressure. In the case where no hydrodynamic

forces exist, the key factors governing the film layer are heat flux and boiling. In this case, intense collapse and formation of steam bubbles can take place and the pressure fluctuations that develop near the molten surface can lead to breakup of the droplet. A change in the surface oxide strength, with Li additives, can accelerate the fragmentation process.

Recent interest in exploiting the large amount of energy available from the formation of  $\text{Al}_2\text{O}_3$  involves the explosive dispersal of shock-heated Al particles into water. This novel coupling between fuel and oxidizer is useful only if in addition to the vapor explosion, the contact between the fluids can also result in rapid chemical conversion. Presently, however, there is little understanding<sup>11-13</sup> of the reactions, kinetics, or energetics involved in the rapid oxidation of Al at high temperatures and pressures. A major difficulty in studying Al combustion arises from the lack of proper experimental tools. The ideal case is the instantaneous placement of an inertially confined, super-heated Al particle in a mean field of water, and monitor the subsequent heat transfer and chemical reaction between the Al and the oxidizing medium. Upon understanding the combustion in water, we can extend the techniques to investigate other oxidizing mediums at different temperatures and pressures.

The objectives of this study are to probe the initial reaction of molten Al with water, without a pre-existing vapor blanket, and monitor the subsequent heat transfer and chemical reaction between the two fluids. Of special interest is the mode of interaction between the molten mass and water. Previous work on metal combustion in water used a capacitor discharge to ignite and burst large metallic wires in water followed by chemical analysis of the product gas. Baker et al.<sup>1,2</sup> observed the ignition of zirconium wires in water, 0.75 - 1.5 mm in diameter, several ms after the initial heatup from a condenser discharge. The extent of chemical conversion was measured by chemical analysis. Similar types of experiments were performed by Lee et al.,<sup>14</sup> in which 0.57 mm diameter Al wires are exploded underwater. Using an inductive

energy storage coupled with a crowbar switch current interrupter, they effect the Al heatup over periods of 75 to 125  $\mu$ s. After the experiment, the amount of hydrogen gas liberated from the formation of  $\text{Al}_2\text{O}_3$  is analyzed.

With the exploding wire technique, however, it is difficult to examine the conditions that initiate the explosions since the electrical energy not only raises the metal wire temperature but also acts as the dispersive force to drive out the molten metal into water. Therefore, any secondary type of explosions, either physical or chemical, could be buried under the primary electrically-triggered explosion. We effect the rapid heating of the aluminum up to vaporization within 1  $\mu$ s with a capacitor-discharge fireset, and observe the interfacial reaction between the fluids with an ultrafast laser microphotography setup. The latter provides spatial and temporal imaging with resolutions of 1  $\mu$ m and 1 nsec, respectively. Data obtained will be used to develop a physical picture and numerical model to analyze the coupled transient processes of particle heatup, heat transfer, vaporization, and chemical reaction.

## EXPERIMENTAL SETUP AND PROCEDURES

The ultrafast laser microphotography setup, illustrated in Figure 1, is built in a modular fashion for easy reconfiguration according to experimental needs. The

illuminator module consists of an ND:Yag, CW argon, and dye lasers to provide both short-pulse and continuous laser illumination for frontlit, backlit, and Schlieren type imaging. Small test chambers provide a controlled environment from  $10^{-6}$  torr to 10 atm or liquid immersion, and can sustain detonation of up to 1 g of high explosives. The imaging module consists of electronic framing and streaking cameras, with or without the inclusion of a spectrograph. For any one experiment, we can record any combination of two of the dimensions of space, time, and spectrum.

We used 99.5 percent pure Al wires with diameters of 25, 38, 51, and 76  $\mu$ m in the study. A constant length of wire, 23 mm, is mounted on an electrically insulated jig and pulled taut over a pair of frets. Both ends of the wire are attached to a modified Reynolds high voltage connector via tiny screw bolts. The extended frets allow the wire to be totally immersed in water. The jig, in the form of a port cover, is then inserted into a test chamber with four-way optical access, and rotated such that the wire is orthogonal to the streak plane. We then fill the chamber with deionized water, and take special care to eliminate any bubbles attached to the surface of the wire.

The electrical streak camera consists of a Thompson CSF 509 housing with an RCA tube. A 40-mm microchannel plate (MCP) serves as an intensifier for the streak shots. All streak images are recorded on both Polaroid film for setup and T-Max 400 for shot analysis. By pushing the film, the sensitivity of the imaging system is about  $10^{-3}$  and  $10^{-6}$  erg/cm<sup>2</sup>, without and with the intensifier, respectively. Resolution of 5 to 8 lp/mm is readily obtained for all devices when operating at minimum gating or maximum streak speeds.

The fireset is of commercial design, modified with a 0.491 microfarad capacitor bank and a Krytron firegap. Excess resistance within the circuit, not including the additional contact resistance between the Al and high voltage caps, is about 230 milliohms. Charging voltages used range from .65 to 3 kv. We monitor the voltage with a standard voltage divider circuit and the current with a current-viewing resistor. The voltage and current temporal profiles during the discharge are

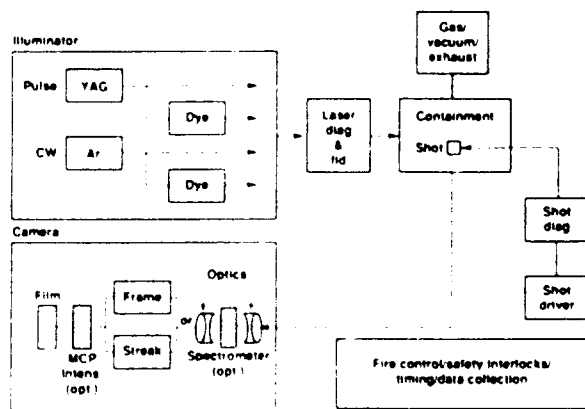


Figure 1. Schematic of the Modular High-Speed Laser Microphotography Apparatus

recorded separately on raster oscilloscopes. A typical scope trace for 1.5 kv charging voltage discharging into 51  $\mu\text{m}$  diameter Al wire is illustrated in Figure 2. It is seen that over 85 percent of the energy in the fireset is dumped into the wire within the first  $\mu\text{s}$ .

Illumination over the duration of the streak is provided by an argon laser gated to full power (2W). An electronic timing generator provides the fiducials for streak speeds above 2  $\mu\text{s}$ , and an optical delay train from the pulse laser provides submicrosecond timing. A typical experimental run consists of assembling the shot, selecting a charge voltage for the fireset, adjusting the timing for illumination and streak, firing from a one-shot coincidental unit, and recovering the film for analysis.

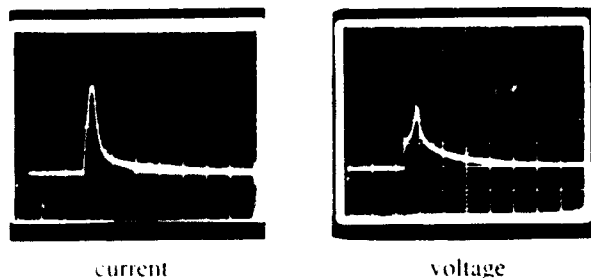


Figure 2. Current (10X Attenuation) and Voltage (500X Attenuation) Scope Traces for 1.5 kv Charging Voltage Discharging into 51  $\mu\text{m}$  Aluminum Wire

## EXPERIMENTAL RESULTS

Prior to firing, we open the image slit in front of the streak camera to align and focus onto a cross section of the Al wire between the two frets. The slit width is then decreased to 200  $\mu\text{m}$  for the image. Streak images of the combustion of 51 and 76  $\mu\text{m}$  Al in water are presented in Figures 3(A)-(H) and Figures 4(A)-(F), respectively. The streak time in each of the images is 100  $\mu\text{s}$  with the timing fiducials, a  $\mu\text{s}$  apart, located along the edge. Current to the laser diodes in the timing generator is diminished every 30  $\mu\text{s}$  leaving a marker in the fiducial train. The trigger for the fireset is delayed by 2 and 5  $\mu\text{s}$  with respect to the fiducial generator and camera triggers, respectively.

For charging voltages below 0.9 kv, the 51  $\mu\text{m}$  Al wire remained intact after the experiment. At 0.90 kv, Figure 3(A), an oscillatory disturbance, interpreted as a vapor layer, occurs along the surface of the wire, with a period of about 12  $\mu\text{s}$  and a peak amplitude of 11  $\mu\text{m}$ . It is important to note that in a shadowgraph, we cannot distinguish whether the vapor layer is generated in front or in back of the wire. The extent of the vapor layer along the wire is not known since we are only imaging a 200  $\mu\text{m}$  cross section. As the charging voltage is increased to 1.05 kv, Figure 3(B), the period of the vapor oscillation lengthens to 16  $\mu\text{s}$ , and the peak amplitude increases to 17  $\mu\text{m}$ . Further voltage increase to 1.2 kv results in a steady vapor oscillation with a 20  $\mu\text{s}$  period. At 1.35 kv, Figure 3(D), the peak amplitude increases dramatically to 80  $\mu\text{m}$  and the period is over 50  $\mu\text{s}$ . A luminous region is observed within the vapor blanket located spatially over the original wire position. It is suspected that the vapor blanket is acting as a cylindrical lens refracting part of the back illumination. Figure 3(E) illustrates the phenomenon at 1.5 kv. After the first oscillatory period, the size of the vapor blanket increases suddenly. There is evidence of a diffuse illumination, resembling that of self-lighting from the wire, extending from the time of fireset discharge to the moment of sudden expansion. These observations are better illustrated in Figure 3(F) with the voltage reaching 1.75 kv. A measure of the tangential velocity at the point of abrupt expansion indicates the expansion rate of the vapor blanket is about 12 m/sec, resembling rates of rapid combustion. Further increases in voltage results in more self-lighting and higher expansion velocity.

A quick review of Figures 4(A) to 4(F) yields a similar sequence of events for the 76  $\mu\text{m}$  Al wire. The transition from an oscillatory disturbance to an abrupt expansion occurs at a higher charging voltage, between 2.25 to 2.5 kv. A diffuse self-lighting is observed in Figure 4(F), with initial dimension similar to that of the wire. In each case, the energetic expansion seems to occur after the first period of oscillation. Figures 5(A)-5(F) present streak images for the 38  $\mu\text{m}$  diameter Al wire, with charging voltages centered around the abrupt

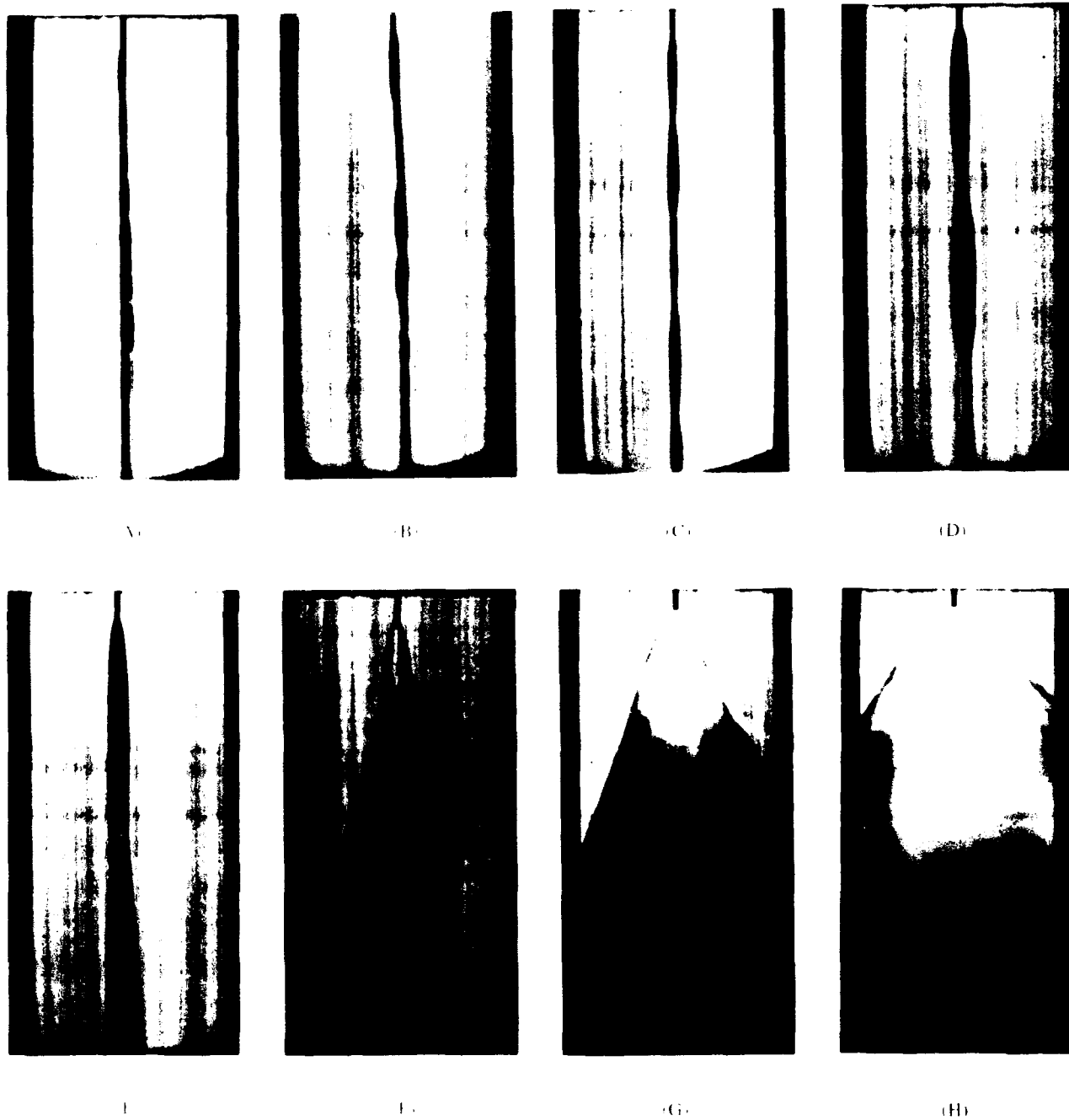
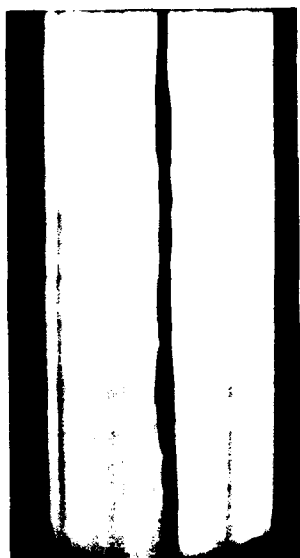
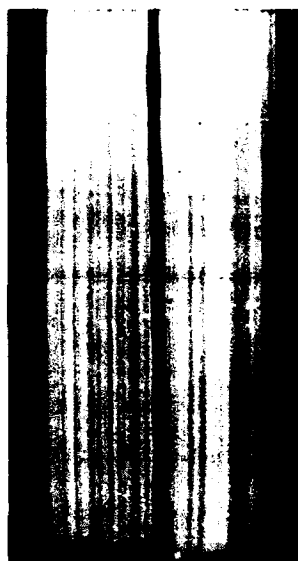


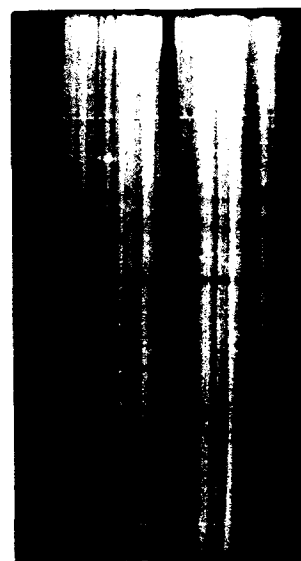
*Figure 3 Streak Images (100  $\mu$ s Sweep) of the Combustion of 51  $\mu$ m Aluminum Wire in Water. The fireset charging voltages are (A) 0.90 kv, (B) 1.05 kv, (C) 1.20 kv, (D) 1.35 kv, (E) 1.50 kv, (F) 1.75 kv, (G) 2.00 kv, and (H) 2.50 kv.*



A



B



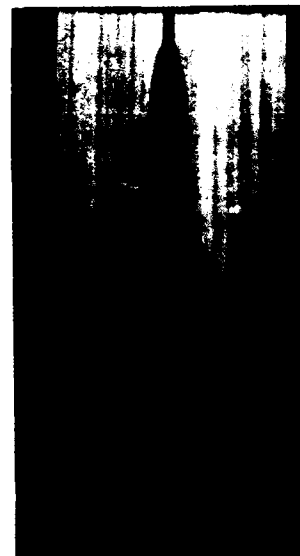
C



D

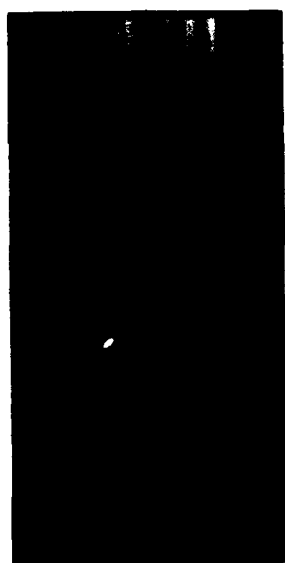


E



F

*Figure 4. Streak Images (100  $\mu$ s Sweep) of the Combustion of 76  $\mu$ m Aluminum Wire in Water. The fireset charging voltages are (A) 1.00 kv, (B) 1.50 kv, (C) 1.75 kv, (D) 2.00 kv, (E) 2.25 kv, and (F) 2.50 kv*



(A)



(B)



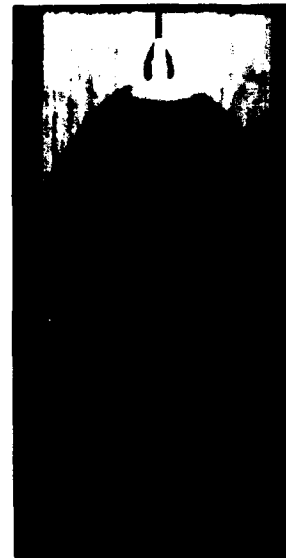
(C)



(D)



(E)



(F)

*Figure 5. Streak Images, Near the Transition Region, of the Combustion of 38  $\mu$ m Aluminum Wire in Water. The fireset charging voltages are (A) 1.00 kv, (B) 1.05 kv, (C) 1.10 kv, (D) 1.15 kv, (E) 1.20 kv.*

transition. The surface of the expanding vapor layer appears to be very rough. Table 1 summarizes the pertinent observations.

*Table 1. Period and Amplitude of Vapor Oscillation*

$V_0$ (kv)	Period ( $\mu$ s)	Amplitude ( $\mu$ m)
38 $\mu$ m Diameter Wire		
1.00	14	22.8
1.05	18	29.2
1.10	22	34.2
1.15	14	41.8
1.20	7	43.1
1.50	5	50.6
51 $\mu$ m Diameter Wire		
0.90	12	11.0
1.05	16	25.5
1.20	21	25.5
1.35	50	80.2
1.50	70	135.4
1.75	40	237.5
2.00	-	-
2.50	-	-
76 $\mu$ m Diameter Wire		
1.00	16	22.8
1.50	22	40.5
1.75	25	53.2
2.00	45	60.8
2.25	90	160.4
2.50	30	130.6

## WIRE HEATING COMPUTATIONS

Interpretation of the streak photographs requires an understanding of the physical state of the wire resulting from the electrical heating process during the capacitor discharge. A

model of the electrical circuit and wire heating process was developed to predict the wire temperature as a function of time. In the simple model used here, energy losses to the water were neglected since computations indicate that only the first several  $\mu$ s of the discharge are significant in determining the final wire temperature. Energy lost to the water in that time, due to conduction and evaporation, was estimated and found to be a small fraction of the total energy deposited.

The combination of the fireset and the wire are analyzed as an electrical circuit composed of resistance (R), inductance (L), and capacitance (C) elements in series. Initially the capacitor is charged to a voltage  $V_0$  and the circuit is open. At time zero, when the Krytron in the fireset is triggered, the circuit is completed and the capacitor begins to discharge. The current  $I$  in the circuit is determined by the circuit equation

$$L(dI/dt) + RI + (1/C) \int I dt = 0, \quad (1)$$

where the inductance and capacitance have fixed values and the resistance is composed of a fixed  $R_r$  and a variable  $R_w$  portion

$$R = R_r + R_w. \quad (2)$$

The fixed resistance  $R_r$  is determined by the fireset and cables, and also the contact resistance between the heated wire and the rest of the circuit. The wire resistance  $R_w$  increases as the wire heats up and is computed from the electrical resistivity of the wire  $\rho_e$ , the wire cross sectional area  $A = \pi d^2/4$ , and the wire length  $l$

$$R_w = \rho_e(l/A). \quad (3)$$

Electrical resistivity is considered to be a function of the wire internal energy  $e$  and is computed using the data and methodology of Tucker and Toth.<sup>15</sup> Aluminum electrical resistivity as a function of energy density and temperature is given in Table 2 and also in Figure 6.

Characteristic thermal conduction time scales within the wire are mere nanoseconds, therefore the temperature within the wire can be considered spatially uniform during the heating process. In that case, the equation for

Table 2. Aluminum Resistivity, Energy Density, and Temperature

$\rho_e$ (ohm-m)	$e-e_{300}$ (MJ/kg)	T (K)	Comments
$2.82 \times 10^{-8}$	0	300	room temperature
$9.90 \times 10^{-8}$	0.623	933	melting begins
$23.11 \times 10^{-8}$	1.021	933	melting ends
$41.52 \times 10^{-8}$	2.981	2793	evaporation begins
$393.1 \times 10^{-8}$	9.782	2793	evaporation ends

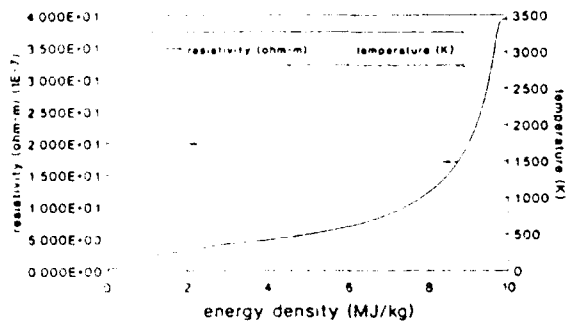


Figure 6. Electrical Resistivity and Temperature as a Function of Energy Density in Aluminum Based on Data of Tucker and Roth<sup>15</sup> and the Simple Thermodynamic Model Described in the Text

the energy density  $e$  within an adiabatic wire heated by an electrical discharge is

$$\rho_m C_v (de/dt) = I^2 R_w(e) \quad (4)$$

where  $\rho_m$  is the mass density and  $C_v$  is the specific heat. This equation is simultaneously solved together with the circuit Equation (1) to obtain current and voltage as a function of time during the capacitor discharge. A simple fourth order Runge Kutta method was used to obtain the solution to the system of equations. Temperatures were computed from energy densities by using a simple thermal equation of state for aluminum. The specific heats of solid and liquid aluminum were assumed to be constant ( $C_{v,s} = 0.984$  kJ/kg,  $C_{v,l} = 1.054$  kJ/kg).

the heat of fusion value used was 398 kJ/kg, and the heat of vaporization value was 6801 kJ/kg. The resulting temperature-energy relationship is shown in Figure 6.

The capacitance value used was the measured capacity of the fireset capacitor, 0.491  $\mu$ F. Circuit inductance was determined by discharging the fireset into a resistive short-circuit and fitting the measured current waveforms (over a range of charging voltages between 0.60 and 1.60 kv) to the analytic solution for an underdamped RLC circuit. A value of  $L = 0.3538$   $\mu$ H was obtained. The fixed circuit resistance  $R_r$  was found from both the resistive short circuit discharge tests and fitting actual wire test current waveforms. The actual fixed resistance varied with the wire size due to the significant contact resistance of the connections to the wire; for 25  $\mu$ m wire,  $R_r = 1.5$  ohm; for 51  $\mu$ m wire,  $R_r = 0.85$  ohm; for 76  $\mu$ m wire,  $R_r = 0.65$  ohm.

Measured and computed wire currents agree quantitatively within 5 percent during the first 2 or 3  $\mu$ s. At later times, the effects of heat transfer and the nonideal behavior of the Krytron switch during current reversal result in greater errors in the predictions. Figures 7(A) and 7(B) show the predicted current and wire temperature corresponding to the data for the test shown in Figure 2. Results of the voltage calculation are not shown since it is difficult to properly simulate the phase-shifting behavior of the measuring circuit. One interesting feature of the results is that for smaller wires (25-38  $\mu$ m diameter), the resistance increases so much during the discharge that the circuit characteristic changes from underdamped to overdamped. This produces a long "tail" on the current waveform and results in a longer energy deposition time for small wires than for large.

Note that the peak current occurs between 0.2 and 0.6  $\mu$ s in all cases and that 95-99 percent of the energy is deposited in the wire by 2  $\mu$ s. Final wire temperatures and wire energy densities have been computed for all cases shown in Figures 3, 4, and 5; the results are given in Table 3. Under the range of conditions in the present experiments, energy sufficient to vaporize the entire wire occurs only at the extremes of the charging



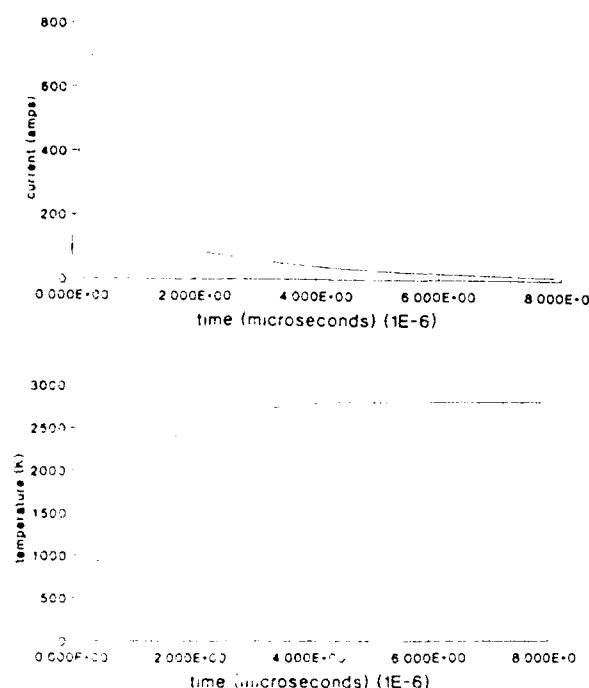


Figure 7. Computed Heating of a 51  $\mu\text{m}$  Wire with a Capacitor Charging Voltage of 1.50 kv. (A) Current in circuit. (B) Wire temperature.

voltage range. In most cases, the final state of the wire is a liquid. Even in those cases where the wire is completely vaporized, it requires several  $\mu\text{s}$  to accomplish that. Therefore, the present experiments are very different than the typical exploding wire experiment, in which the wire is vaporized in less than 50 ns.

## DISCUSSION

Four principle types of behavior are revealed in the streak photographs on a time scale of 100  $\mu\text{s}$ . These behaviors are observed at all wire diameters examined, but at different charging voltages. A common basis for these observations can be obtained by correlating the behavior with the final energy density of the wire, or equivalently the final temperature. Our behavior classification and corresponding wire physical state are given in Table 4.

The first regime occurs at the lowest charging voltages and is illustrated by the photographs of Figures 3(A), 3(B), 3(C), 4(A), 4(B), 4(C), and 5(A). The wire appears to be

Table 3. Final Energy Density and Temperature

$V_0$ (kv)	$T_f$ (K)	$ef-e_{300}$ (MJ/kg)
38 $\mu\text{m}$ Diameter Wire		
1.00	2311	2.47
1.05	2597	2.78
1.10	2793	3.09
1.15	2793	3.42
1.20	2793	3.77
1.50	2793	6.07
51 $\mu\text{m}$ Diameter Wire		
0.90	933	0.74
1.05	1068	1.16
1.20	1575	1.70
1.35	2171	2.33
1.50	2793	3.05
1.75	2793	4.45
2.00	2793	6.08
2.50	2794	9.41
76 $\mu\text{m}$ Diameter Wire		
1.00	516	0.21
1.50	933	0.63
1.75	933	1.01
2.00	1453	1.57
2.25	2098	2.25
2.50	2793	3.05

intact and only small asymmetric disturbances of amplitude less than twice the original wire diameter appear. These disturbances have a lifetime of 10-20  $\mu\text{s}$  and are apparently random bubbles created by the spontaneous nucleation of a thin layer of superheated water next to the wire. Preliminary framing camera photographs of the entire wire clearly show such bubbles distributed randomly along the wire. No chemical reaction appears to take place and our observations are very similar to

Table 4. Classification of Experimental Results

Reg.	Description	Temp. Range (K)
1.	random nucleation	300-2000
2.	oscillating vapor blanket slow chemical reaction	2000-2600
3.	vigorous chemical rxn. vapor blanket collapse	2600-2793
4.	prompt chemical rxn.	>2793

Skipov's,<sup>16</sup> obtained with inert wires (platinum) and at much lower wire temperatures (600 K). This regime occurs up to a temperature of 2000 K.

The second regime occurs over a narrow range of voltages and is illustrated in Figures 3(D), 3(E), 4(D), 4(E), and 5(B). A symmetric vapor blanket forms about the wire, grows to a maximum of 2-3 original wire diameters in about 10-20  $\mu$ s, collapses, then rebounds. This vapor blanket appears to be a cylindrical bubble centered about the wire. The bubble continues to oscillate with increasing amplitude and period. This regime occurs between temperatures of 2000 and 2600 K. No flashes of light are observed and the bubble surface appears to be smooth. We interpret this as indicating that slow chemical reaction is taking place and the bubble consists of steam and hydrogen. This would be consistent with Baker's<sup>14</sup> observations of an ignition temperature between 1700-2000 K for aluminum in water and also with observations in air, that aluminum will ignite if the temperature is above the oxide melting temperature, 2300 K.

The third regime is a transition between the rather innocuous behavior described above and the rapid expansion and vigorous chemical reaction observed when the wire is rapidly (less than 1  $\mu$ s) vaporized or actually exploded. This regime is illustrated by the photographs in Figures 3(F), 3(G), 4(F), 5(C), 5(D), 5(E), 5(F), and schematically in Figure 8. In this transition regime, which occurs when the wire temperature is between 2600 K and the boiling

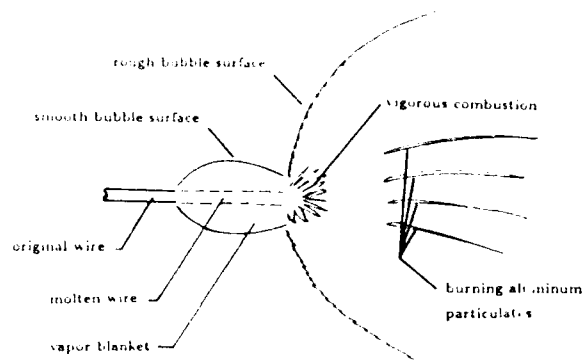


Figure 8. Schematic Representation of the Transition Region Where Rapid Chemical Reaction Takes Place

point 2793 K, a single smooth bubble forms initially, as in regime two. As the initial bubble collapses, a flash of light is produced and the bubble, now with a rough surface, is driven out with a much higher velocity, 50-100 m/s initially vs. 5-10 m/s for the first bubble. Streaks of luminosity are visible within the bubble after the initial flash.

We speculate that the collapse of the bubble results in a Rayleigh-Taylor instability near the minimum (just as in spherical bubble oscillations) and the molten aluminum and water are rapidly driven together and mixed, resulting in the vigorous chemical reaction that must have produced the observed flash of light. The streaks visible after the flash are burning aluminum fragments that were created during the breakup of the wire resulting from the vigorous interaction at the first bubble collapse. Previous investigations on the steam explosion phenomenon have also emphasized the importance of vapor blanket collapse and fragmentation for enhancing heat transfer and evaporation rates. The present observations on collapse initiating chemical reaction appear to be unique.

The fourth regime occurs at the highest charging voltages and is illustrated in Figure 3(H). A luminous and rapidly expanding (100-300 m/s) bubble with a rough surface is promptly produced without any smooth precursor bubble. This occurs when the stored electrical energy is greater than several times the energy required to vaporize the wire

completely (9850 kJ/kg) and the wire is vaporized within 1  $\mu$ s of the start of the discharge process. As the electrical energy is increased the expansion velocity increases, but is still at a relatively low magnitude ( $\leq 300$  m/s) so that only weak acoustic disturbances are produced in the water and no shock waves are visible. Ignition appears to take place promptly and the bubble composition is probably a mixture of Al vapor, hydrogen, steam, and aluminum oxide particulates.

## SUMMARY

High-speed and high resolution photography has been used to examine the ignition and combustion of small 25-76- $\mu$ m diameter and 23-mm long aluminum wires rapidly heated by a capacitor discharge system. Streak photographs were obtained over periods of 30-500  $\mu$ s with a spatial resolution of 2  $\mu$ m. The wire temperature was determined as a function of time by integrating the circuit equation together with the energy equation for an adiabatic wire and known aluminum electrical resistivity and temperature functions of energy density. The wire reaches its maximum temperature within 2  $\mu$ s.

The most significant result of the present experiment is the discovery of a transition in the ignition and combustion behavior of the system when the wire is heated above a critical temperature. Below a threshold temperature of about 2000 K, very little appears to happen in the water surrounding the wire. Between 2000-2500 K, a slow chemical reaction apparently occurs, resulting in an asymmetric vapor blanket or bubble which oscillates and slowly grows. At temperatures between 2600-2793 K (the boiling point of aluminum), an initial bubble is formed and upon collapse a vigorous ignition and combustion event occurs. At still higher temperatures, ignition and combustion begin promptly without any vapor blanket being created. The triggering of chemical reaction by the vapor blanket collapse is a new observation which has great potential significance to understanding metal-water interactions in deliberate and accidental explosions.

The present results are preliminary and will be extended to higher initial pressures

and temperatures, and also to other oxidizing atmospheres such as CO, CO<sub>2</sub>. Another goal is the direct observation of chemical species by emission and Raman spectroscopy. The wire heating model development is continuing. Conduction heat transfer, fluid motion, evaporation, and chemical reaction are being added to the existing adiabatic computation.

Our ultimate goals are to obtain measurements of reaction rates and evidence of reaction mechanisms at high temperatures and pressures. These measurements would be eventually used to develop numerical models for the reaction zones in detonating composite explosives.

## ACKNOWLEDGEMENT

The authors would like to acknowledge Mr. Ralph Hodgins of LLNL for his support of the experimental facility, and Dr. Woodrow Lee of NSWC, White Oak, for his valuable discussions.

## REFERENCES

1. Baker, Jr., L.; Warchal, R.; Vogel, R.; and Kilpatrick, M., "Studies of Metal-Water Reactions at High Temperatures (I)," *AEC R&D Report, ANL-6257*, Argonne National Laboratory, 1961.
2. Baker, Jr., L. and Just L., "Studies of Metal-Water Reactions at High Temperatures (III)," *AEC R&D Report, ANL-6748*, Argonne National Laboratory, 1962.
3. Baker, Jr., L. and Liimatainen, R., "Chemical Reactions," *The Technology of Nuclear Reactor Safety*, T. Thompson and J. Beckerley, Eds., The MIT Press, Vol. 2, Chapter 17.
4. Finger, M.; Helm, F.; Lee, E.; Boat, R.; and Cheung, H., "Characterization of Commercial Composite Explosives," *Sixth Detonation Symposium, ACR-221*, 1976, p. 729.
5. Frolov, Yu.; Pokhil, P.; and Logachev, V., "Ignition and Combustion of Powdered Aluminum in a High Temperature Gaseous Media," *Fiz. Goreniya i Vzryva*, 8, 2, 1972, pp. 212-236.

6. Belyayev, A.; Frolov, Yu.; and Korotkov, A., "Combustion and Ignition of Particles of Finely Dispersed Aluminum," *Fiz. Goreniya i Vzryva*, 4, 3, 1968, pp. 323-329.
7. Harlow, F. and Ruppel, H. "Propagation of a Liquid-Liquid Explosion," Los Alamos National Laboratory Report LA-8971 MS, Aug 1981.
8. Usynin, G. and Khramov, N., "Breakup of Molten Material Interacting with a Cold Liquid," *Fiz. Goreniya i Vzryva*, Vol. 21, 1985, pp. 117.
9. Anderson, R. and Armstrong, D., "Experimental Study of Small Scale Explosions in an Aluminum-Water System," *ASME Proc.*, Washington, D.C., Nov 1981.
10. Nelson, L. "Steam Explosion Studies with Single Drops of Molten Reactory Materials," *ANS Topical Meeting on Thermal Reactor Safety*, Knoxville, TN, Apr 1980.
11. Price, E. "Combustion of Metalized Propellants," *Fundamentals of Solid-Propellant Combustion*, K. Kuo and M. Summerfield, Eds., AIAA Press, Vol. 90, Chapter 9, 1984.
12. Lee, W., "Fast Reactions of Aluminum—A Literature Review (II)," NSWC Report, NSWC-TR 86-76, Dec 1986.
13. Rozner A. and Holden, J., "Fast Reactions of Aluminum—A Literature Review," NSWC Report, NSWC/WOL-TR-77-163, Dec 1977.
14. Lee, W. and Ford, R., "Reactivity of Al-2.5 Pct Li Alloy with Water as Studied by the Exploding Wire Technique," *Metallurgical Trans. B*, Vol. 19B, 1988, p. 255.
15. Tucker, T. and Toth, R., "EBWI: A Computer Code for the Prediction of the Behavior of Electrical Circuits Containing Exploding Wire Elements," Sandia National Laboratory Report, SAND75-0041, 1975.
16. Skripov, V., *Metastable Liquids*, John Wiley and Sons, New York, Chapter 6, 1967.

## DISCUSSION

**MANFRED HELD**  
Messerschmitt-Bolkow-Blohm  
WEST GERMANY

Can you explain the high frequency of the "bubble" in the voltage range of 1000-1500V?

## REPLY BY W. C. TAO

The bubble oscillatory periods measured in these experiments are quite similar to those observed by Skripov, Nelson, and Lee. Depending on the diameter of the aluminum wire, a voltage discharge between 1.0 to 1.5 kv will correspond to a temperature between 1000 K to 2800 K. At these temperatures, the layer of water immediately adjacent to the aluminum wire surface undergoes film boiling, vaporization, and eventually superheating. From this reactive flow, a vapor layer is driven radially outward with a maximum amplitude equal to several wire diameters. In the absence of a sustained driving force, such as that from additional chemical reaction between the aluminum and water, the inertial mass of the displaced water collapses the vapor layer.

## DISCUSSION

**DOUGLAS G. TASKER**  
Naval Surface Warfare Center  
Silver Spring, MD

Have you considered the skin effect in calculation of the temperature and resistance?

Calculations of current are extremely sensitive to resistance in LCR circuits. A more critical measurement is that of high speed voltage measurement; we have considerable experience that would help here.

Have you considered using flash X-ray photography?

## REPLY BY W. C. TAO

We have performed heat transfer calculations within the aluminum wire during its heatup period. In these calculations, we consider the change in the thermal resistivity

of the aluminum, the heat loss to the surrounding water, and account for the phase change in the vapor layer. The results from the thermal profile calculations indicate that for our largest diameter wire, 76 microns, the time required for the center of the wire to reach 80 percent of the surface temperature is about 1.2 microseconds. Therefore, within the approximations made in this study, we can neglect any "skin effect" during the transient heating.

Your comment on the sensitivity of current calculations due to the resistance in the LCR circuit is noted. We appreciate any suggestion on the techniques involved in high speed voltage measurements.

We have not considered using flash X-ray photography for these experiments primarily because of the small scale of the aluminum samples and the difficulties in the logistics of incorporating X-ray diagnostics. The technique, however, can provide valuable information on the dynamics of oxide breakup and molten aluminum fragmentation.

## DISCUSSION

**KIBONG KIM**

Naval Surface Warfare Center  
Silver Spring, MD

Is there any way of measuring particle size after the  $\text{Al}_2\text{O}_3$  layer breaks and the inner molten Al breaks into particles?

## REPLY BY W. C. TAO

Due to the initial small size of the aluminum particles, it is difficult to apply recovery techniques to measure particle size of the molten aluminum after fragmentation and reaction. Future diagnostics development toward this end must rely on in-situ probes such as X-ray or scattering techniques. Recently, colleagues at ISL have made advances in the field of micro-holography and applied it to the study of jet and bubble breakup in combustion processes. Perhaps these diagnostic techniques could be used for studying molten particle breakup.

**SESSION ON  
REACTION ZONE**

**Cochairmen: William Davis  
Los Alamos National Laboratory**

**Joseph Foster  
Air Force Armament Laboratory**

# DETONATION REACTION-ZONE STRUCTURE OF PBX 9502\*

W. L. Seitz, H. L. Stacy, Ray Engelke, P. K. Tang, and Jerry Wackerle  
Los Alamos National Laboratory  
Los Alamos, New Mexico 87545

*We present the results of interface-velocimetry experiments and numerical modeling of the detonation reaction-zone structure for PBX 9502 (95 wt percent TATB/5 wt percent Kel-F 800). This work extends and refines the experimental data for PBX 9502 presented in the Eighth Detonation Symposium. A dual Fabry-Perot velocimeter was used to observe interface-velocity histories between detonating explosive and various windows. The dual instrument allows improved resolution of the detonation wave structure by operating one velocimeter with enhanced velocity resolution with some sacrifice in time resolution, and the other velocimeter with this trade-off reversed. Further, experimental refinements include using submicron, vapor-deposited, reflective coatings on the windows. Attempts are made to better define the reaction zone by using sustained-shock and short-duration-shock driving systems, a steady two-dimensional configuration (rate sticks), and by observations of the following flow. Numerical hydrodynamic modeling, using a three-stage reaction-rate model, is performed to assess the heat release in the detonation reaction zone of PBX 9502.*

## INTRODUCTION

Global chemical reaction rates, detonation pressures, and the structure of the flow in the detonation reaction zone in condensed explosives have been the subject of many research studies. Numerous theoretical and experimental approaches have been employed. In this paper we present the results of interface-velocimetry experiments and numerical modeling of the detonation reaction zone structure for PBX 9502 (95 wt percent TATB/5 wt percent Kel F 800). This work extends and refines our experimental data for PBX 9502 presented in the Eighth Detonation Symposium.<sup>1</sup>

A dual Fabry-Perot velocimeter was used to observe interface-velocity histories between the detonating explosive and various windows. By operating the two interferometers of the dual instrument with different fringe factors the uncertainty in the number of fringes

jumped at the time of shock arrival is eliminated. Another advantage is that one velocimeter can be operated with a total recording time necessary for the complete experiment and the other with a shorter recording time to give improved time resolution of the early flow. Further experimental refinements include using submicron, vapor-deposited, reflective coatings on the windows rather than the 13  $\mu$ m aluminum foils previously employed. In addition to these refinements, additional window materials were used. The four window materials of LiF, KBr, KCl, and PMMA (that had been previously calibrated for index of refraction changes under shock loading) were chosen.<sup>2</sup> LiF is a strong overmatch, KBr a relatively good match, KCl a slight undermatch, and PMMA a strong undermatch into PBX 9502. Problems occurred with KBr that prevented it from being useful for measuring interface velocities (see below).

In addition to the one-dimensional (1D) sustained-shock configuration used in the previous study, 1D short-shock and steady

\*Work performed under the auspices of the U.S. Department of Energy.

two-dimensional (2D) divergent flow (rate stick) configurations were studied.

Measured interface-velocity histories show: (1) higher peak velocities, (2) initial decelerations an order of magnitude larger than we previously observed, and (3) that long runs of the detonation are needed to reach a steady flow in PBX 9502.

Numerical modeling of the interface-velocity histories shows that a three-stage reaction model gives results consistent with the experimental data. In this model, 85 percent of the reaction occurs very rapidly (25 ns) after the shock passes. The remaining reaction occurs much more slowly (in a time of 300 ns).

Details of the shot configuration, materials used, and assembly procedures are given under EXPERIMENTAL. Measured velocity histories and plots that show the unsteady character of the flow are given in EXPERIMENTAL RESULTS. The reaction-rate model and details of the numerical modeling are given under CALCULATIONS. In the section INTERPRETATION OF EXPERIMENTAL AND CALCULATIONAL RESULTS, the reproducibility of the measurements is discussed, a method for obtaining the *steady* PBX 9502/LiF interface particle-velocity history is given, and a comparison between calculated and measured particle-velocity histories is made (for the 1D sustained shock experiments). Finally, in the DISCUSSION AND CONCLUSIONS section, we attempt to extract and examine the salient features of the results obtained.

## EXPERIMENTAL

A dual Fabry Perot velocimeter was used to measure interface velocity histories between detonating PBX 9502 and various transparent windows. The window face next to the explosive was vapor coated with less than  $1\text{ }\mu\text{m}$  of aluminum to provide a reflective surface. Experiments were performed with windows of LiF, KBr, KCl, and PMMA for the 1D shots and with LiF windows for the 2D configurations. We found that the KBr windows became opaque at the pressures introduced by the detonating PBX 9502, however, by increasing the laser intensity relatively dim velocimeter

traces were obtained. These dim traces were found to be the result of reflection from the shock front in the KBr window. Therefore, shock velocity histories were consistently obtained but no interface velocities were recorded for this window. Explosive charge lengths were 13, 25, and 50 mm for the 1D experiments. For the KCl window, charge lengths of 2, 3, and 5 mm were also used.

The shot configuration for the sustained-shock experiments consisted of a P-40 plane-wave lens, 25.4 mm of Composition B, 10 mm of aluminum, the sample of PBX 9502, and the window -- as shown in Figure 1. For the short-shock experiments, the 25.4 mm of Composition B was replaced with 25.4 mm of Baratol, and the 10 mm of aluminum was replaced with a sandwich of 10 mm of PMMA, 0.13 mm of stainless steel, and a 3 mm vacuum gap. The PBX 9502 sample was located immediately after the vacuum gap. The vacuum chamber was pumped to about  $100\text{ }\mu\text{m}$  Hg and flushed with helium. The pumping and flushing cycle was performed 10 to 13 times. The final vacuum was typically  $80\text{ }\mu\text{m}$  Hg. Both driving systems were designed to give relatively prompt initiation of detonation (distance to detonation of about 1 mm) without overdriving the detonation wave.<sup>3</sup> Planarity of the sustained- and short-shock driving systems was within 40 ns over a diameter of 90 and 60 mm, respectively. A diameter to length ratio of the PBX 9502 samples was held to 2 or greater. Thus, edge effects were avoided for the sustained-shock experiments, but the short-shock configuration could have been marginally 2D for the longest charge thickness of 50 mm.

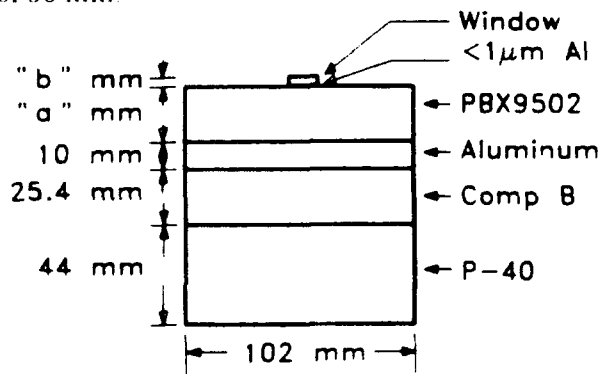


Figure 1. Schema of the Explosive Charge Assembly for the Sustained-Shock Experiments



PMMA windows were constructed from Rohm and Haas type II UVA Plexiglas with a density of  $1.186 \pm 0.001 \text{ g/cm}^3$ . Windows of LiF, KBr, and KCl were single crystals in the [100] orientation. Previous experiments performed with PBX 9502 and PMMA windows over a 75°C initial temperature range showed no measurable initial temperature effect on the interface velocity history and thus the 1D experiments were fired at ambient temperatures.

All PBX 9502 samples, except the 50 mm rate-stick charges, were machined from isotastically pressed parallelepiped billets with dimensions 114 x 114 x 368 mm. All samples were machined from the billets with their cylindrical axis parallel to the long axis of the stock charge. PBX 9502 densities were  $1.895 \text{ g/cm}^3$  with a standard deviation of  $0.001 \text{ g/cm}^3$  and a range of 1.893 to  $1.897 \text{ g/cm}^3$ . The complete designator for this material at LANL is PBX 9502 19; H0185F000E 136. This material is nominally 95/5 wt percent TATB/Kel-F 800; its measured composition is 95.24/4.76 TATB/Kel F 800. The TATB contained 0.35 wt percent chlorine. The BET<sup>4</sup> specific surface for the TATB was  $14,280 \text{ cm}^2/\text{g}$ .

Windows were attached to the PBX 9502 samples for the 1D shots with Aralhex adhesive, except for PMMA. For the PMMA windows and rate stick configurations, Devcon epoxy (Stock No. 142501) was used. All windows were carefully installed by placing a small drop of the adhesive on the window and pressing and moving the window with a small circular motion until a slight scratching of the aluminum vapor coating was observed to result from the high explosive contacting the vapor coating. Windows were then weighted until the adhesive dried. Adhesive layer thicknesses with this technique were found to be less than our measurement resolution of about 8  $\mu\text{m}$ .

Experiments were also done with the flow in the explosive's reaction zone being steady (as viewed from the shock), but 2D. The charge geometry for these experiments was that of a rate stick (see Reference 5) -- i.e., the charges were fabricated from a number of small right circular cylinders into a long right circular cylinder. The variable changed from

experiment to experiment was the diameter; decreasing the cylinder diameter increases the 2D effects. All the sticks were fired unconfined (in air). Sticks were fired with 10.0, 14.0, 25.0, and 50.0 mm diameters; two sticks were fired at each diameter, except for the 14 mm case. The 25.0 and 50.0 mm diameter rate sticks were ten diameters long, while the 10.0 and 14.0 mm diameter ones were at least sixteen diameters long. Sticks of this length assure that the detonation-wave speed is steady by the time the detonation wave has traversed half the stick length. The precision of the detonation-velocity measurement over the last half of such a stick is about  $\pm 1 \text{ m/s}$ . The rate-stick shots were all temperature controlled and were fired at  $24 \pm 2^\circ\text{C}$ . All the sticks were strongly over-boosted by high-density PBX 9404. Shockwave passage was recorded by the closure of 50  $\mu\text{m}$  insulated-copper-wire pin switches (see Reference 5). In most cases, the LiF windows with their associated mirrors were constructed and glued to the terminal pieces of the rate sticks in the same manner as described above. No pins were placed within two diameters of the window interface to minimize flow perturbations caused by the presence of the pin wires. A grid on the vapor-coated mirror allowed centering of the laser beam within about 0.5 mm of the rate-stick axis.

A schema of the dual Fabry Perot velocimeter is shown in Figure 2. The laser was a 12-watt (all lines) Spectra-Physics Model 171-07 argon-ion, which was operated single frequency at 514.5 nm with an output power of about 3 watts. The laser beam, at shot time, was directed to the target by triggering the acousto-optical modulator (IntraAction Corp., Model AOM-403) to the on position for about 30  $\mu\text{s}$ . This modulator was necessary to minimize the time that the laser beam was incident on the target to prevent damage to the thin vapor coating of aluminum. Reflected light from the target was collected and collimated with lens L5 and directed to the beam splitter B2. The beam splitter was of the cube type with 70 percent reflected and 30 percent transmitted characteristics. Thus, 70 percent of the light was incident on the first interferometer and 30 percent on the second. For each leg of the system a cylindrical lens

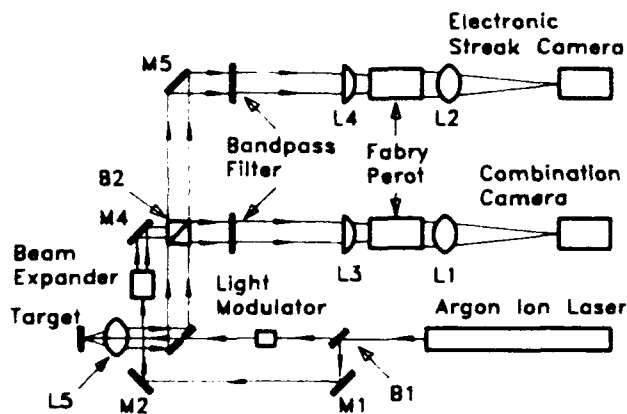


Figure 2. Schema of the Dual Leg Fabry-Perot Velocimeter Used to Obtain the Interface Particle-Velocity Histories

converged the collimated beam, in one plane, onto the Fabry Perot. Focal lengths of the cylindrical lenses were chosen to produce the desired 4 to 5 fringe pairs. High quality lenses focused the fringes onto streak camera slits. An image intensified rotating mirror streak camera (combination camera), described by Winslow and Davis,<sup>6</sup> was used to record the fringes on the first leg of the system, and an Imacon 500 electronic streak camera was used for the second leg. Both Fabry-Perot interferometers were Burleigh Model RC-110 with 50.8 mm diameter mirrors that were flat to  $1/200$ th of a wavelength and had 93 percent reflectivity. Mirror separation was normally 25.70 mm for the Fabry Perot in the first leg and 19.90 mm for the second, but for some shots these spacings were reversed.

A portion of the beam from the laser was picked off (by B1) and mixed with the return beam at the beam splitter (B2). This unshifted laser beam was brought into the beam splitter at  $90^\circ$  to the return beam from the target, as shown in Figure 2, and, therefore, 70 percent of the unshifted light went to the second leg and 30 percent to the first. With 70 percent of the unshifted beam going to the electronic streak camera, static fringes were produced across the entire record. These static fringes were used to minimize the effect of distortion in the electronic streak camera. Normally, no continuing static fringes were visible on the combination camera.

The combination camera was operated with a writing speed of about 15.6 mm/ $\mu$ s, and the electronic streak camera at about 56 mm/ $\mu$ s. Slit widths were 0.10 and 0.05 mm for the combination and electronic cameras, respectively. Streak records were recorded on T-Max film that was developed for five minutes in x-ray developer and fixed with rapid fix for five minutes.

We estimate time resolution for the velocimeter system with the electronic streak camera to be about 2 to 4 ns and that for the combination camera system to be about 4 to 9 ns.

A Spectra-Physics laser power meter (Model 404) and an NRC (Model 900) spatial filter mount with a 5  $\mu$ m pinhole were used to measure the laser beam diameter at the target. The diameter at the  $1/e^2$  intensity level was found to be 65  $\mu$ m.

A Doppler shift in wavelength of the reflected laser light resulting from target motion, beginning at shock arrival time, produced a corresponding shift in fringe spacing. Typical streak records of fringes are shown in Figure 3. Streak records were digitized with an Optical Gauging Products, Model XL-14C, optical comparator. Digital readout of the comparator was good to 2  $\mu$ m. The digital film data were transformed to velocity histories using the known camera writing speeds and a least-squares velocity analysis method superior to that used previously.<sup>1</sup> Data points were typically read such that velocities were obtained at 5 ns intervals for the first 50 ns and at 20 ns intervals for the remainder of the record.

## EXPERIMENTAL RESULTS

Results are presented for three types of experiments: (1) 1D sustained shock, (2) 1D short shock, and (3) 2D steady wave (rate stick). The 1D experiments with the two different driver systems were designed to study the reaction-zone region with two rather different types of support for the following flow. The sustained shock configuration provides prompt initiation of detonation with a relatively flat top shock and good support,

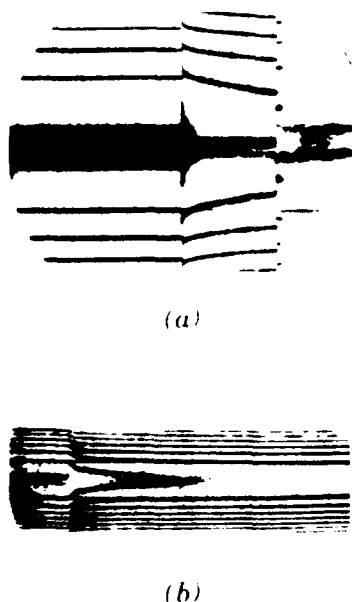


Figure 3. Experimental Fabry-Perot Particle-Velocity Records from a PBX 9502/LiF Window Interface. Figure (a) is the record obtained from the image-intensified rotating-mirror-camera leg of the velocimeter; this camera was writing at 15.6 mm/ $\mu$ s and the fringe factor was 1.500 mm/ $\mu$ s/fringe. Figure (b) is the analogous record from the electronic-streak-camera leg; this camera was writing at 56. mm/ $\mu$ s and the fringe factor was 1.928 mm/ $\mu$ s/fringe.

whereas the short shock configuration gives prompt initiation with a strong relief wave.

The rationale for studying PBX 9502 samples with the following flow supported in the two rather different ways was an attempt to better define a possible end of a reaction zone, or CJ state. Realizing from our previous work<sup>1</sup> and that of others<sup>7</sup> that PBX 9502 detonation does not reach a steady flow in the 13 to 50 mm thick charges (with normal planewave boosting systems), the thought was that by adjusting the support of the following flow a quasi-steady region would possibly be observed, i.e., the following flows from shot to shot would show some common point of connection.

The rate stick geometry was used because we knew that a steady, but 2D flow, in the detonating PBX 9502 could be established.<sup>5</sup> By an extrapolation procedure, to be described

below, we then hoped to obtain the 1D (steady) limit from the 2D results. In addition, there was a possibility that the sonic locus (the end of the reaction zone) in the rate-stick configuration would be followed (for some distance) by a constant state. Such a flow *would* show a qualitative feature, that would be indicative of the end of the reaction zone. We note, however, that the rate-stick experimental results do not support this idea over the range of experimental variables examined.

Measured interface-velocity histories are shown in Figures 4(a) through 4(g). All velocity histories shown in Figure 4 were obtained from the higher quality combination camera streak records with the electronic streak camera records being used to corroborate the peak velocity and early deceleration values for many of the shots. The curves in Figures 4(a) through 4(f) are for 13, 25, and 50 mm PBX 9502 charge thicknesses; note that 0, 2, 3, and 5 mm charge thicknesses are also included in Figure 4(b). Another point of interest is that LiF reflects a shock into the detonating PBX 9502, where KCl and PMMA reflect rarefactions. These distinct types of reflected waves could have different effects on the chemical-heat-release rate in the PBX 9502 following flow.

Comparison of velocity histories for corresponding experiments that used the sustained- and short-shock driving systems show nominally the same peak velocity and initial deceleration. However, the flow from about 10 to 20 ns to the remainder of the record shows more deceleration for the short-shock experiments, as would be expected with the strong relief wave from the rear. However, no demarcation is observed that would indicate the end of a reaction zone for either type experiment.

The measured interface-particle-velocity histories for the rate sticks are shown in Figure 4(g). The entries on this figure are the result of two experiments at each diameter, except for the 14 mm diameter case. Note that the rate-stick particle-velocity histories do not look markedly different from the LiF sustained shock and LiF short-shock measurements. That is, the measured peak particle velocities are quite similar (also see Table 1), as are the

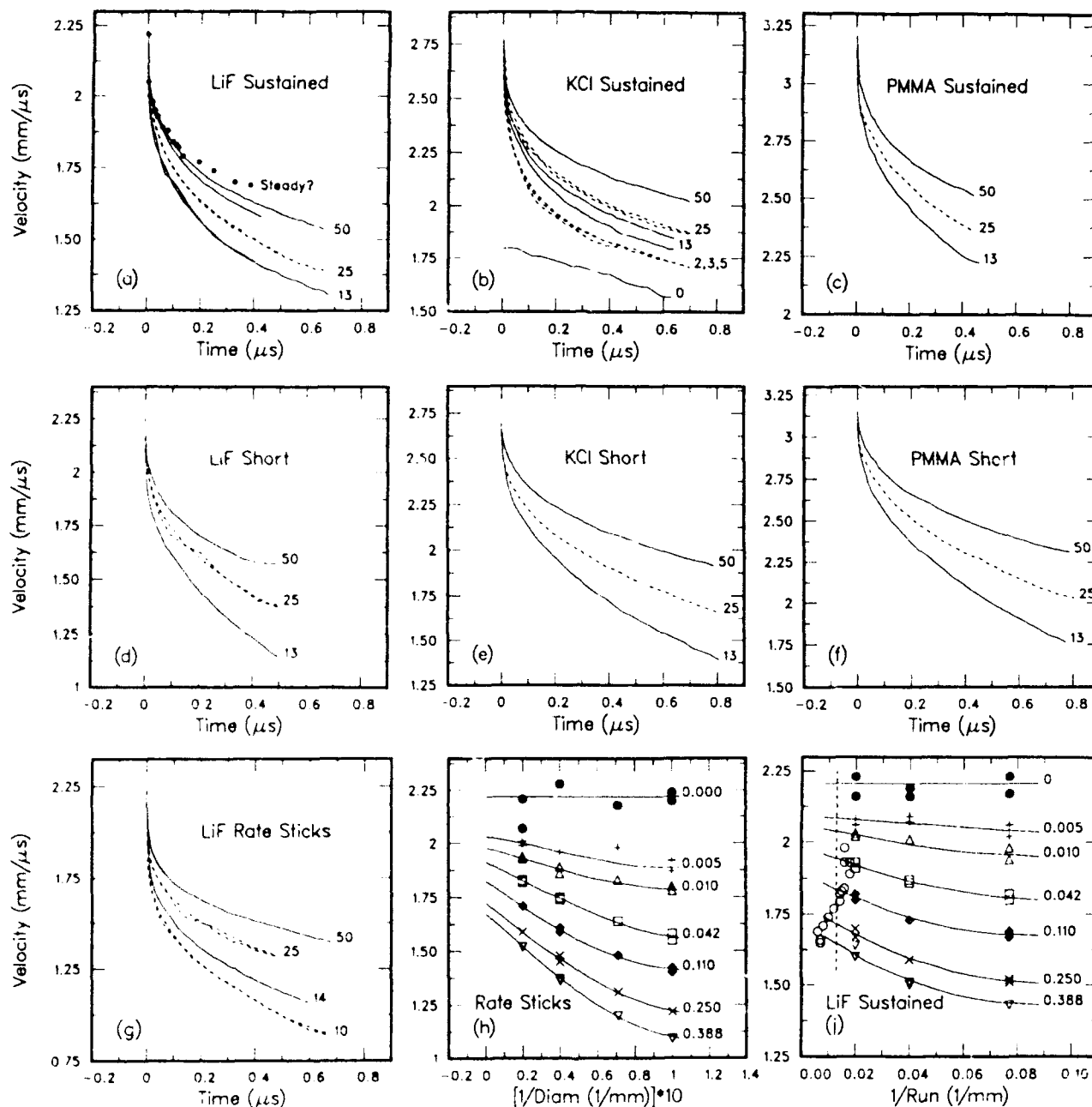


Figure 4. Experimental Interface-Velocity Histories Recorded by the Fabry-Perot Instrument, and Results of the 1D Sustained and Short-Shock Experiments. The various entries in this figure are referred to by the small letters in parentheses in their lower left-hand corners. Figures (a) through (g) are the experimental interface-velocity histories recorded by the Fabry-Perot Instrument. Figures (a) through (f) are results of the 1D sustained and short-shock experiments, respectively. As one moves to the right across the page on these figures, one moves to lower shock impedance windows. The curves on Figures (a) through (g) are made distinct from one another by plotting every other run (or diameter) as dashed. The data labeled "Steady?" on Figure (a) are discussed in the "INTERPRETATION OF EXPERIMENTAL AND CALCULATIONAL RESULTS" section. Figure (g) gives the interface-velocity histories obtained from the rate sticks. Figures (h) and (i) are plots whose purpose is to obtain information on the 1D steady-wave profile in PBX 9502. The origin of these plots is discussed in the "INTERPRETATION OF EXPERIMENTAL AND CALCULATIONAL RESULTS" section.

general shapes of the curves. One difference between the 1D and 2D experiments is that the pressure relief at the charge edges for the 10 and 14 mm diameter sticks results in significantly lower interface-particle-velocity histories after about 10 to 15 ns, than observed for even the 1D short shock case. However, the velocity history for the 50 mm rate-stick experiment closely matches that for the 25 mm charge thickness with the 1D sustained-shock configuration. The two histories differ by only about 4 percent at 5 to 10 ns times and less than 2 percent over the remainder of the flow.

High precision detonation-velocity measurements ( $\pm 1$  m/s) were also made on all the rate sticks. We estimate, by extrapolation to infinite diameter in the velocity versus  $1/\text{diam}$  plane, that the CJ detonation velocity for our material at  $\rho_0 = 1.893 \text{ g/cm}^3$  and  $T = 24 \pm 2^\circ\text{C}$  is  $7.792 \text{ mm}/\mu\text{s}$ .

## CALCULATIONS

The details of the high explosive (HE) numerical reaction model used here have been documented elsewhere<sup>8</sup> and this model has been used in some applications.<sup>9</sup> The form of this model is motivated by the following facts. Most heterogeneous explosives consist of a granulated secondary explosive (or explosives) held together by a binder; such materials usually contain voids. Adiabatic compression of such a material (e.g., by a shockwave) increases the internal energy and the temperature throughout the explosive's volume. However, at the explosive grain surfaces (which form the void boundaries), there are fluid mechanical processes present (e.g., jetting and flow stagnation) that are very effective in converting the mechanical energy delivered by the shock into high temperature and pressure. These locally extreme conditions can initiate chemical decomposition quickly and thus such a region is called a "hot spot." In view of this observation, our chemical heat-release function contains a quantity called the hot-spot mass fraction; it represents the part of the HE directly susceptible to shock action. It is (probably) related to the void surface area present and, therefore, to the degree of compaction and the density. We treat this mass fraction as an empirical parameter ( $\eta$ )

that is small. The corresponding progress variable is called  $\lambda_h$ .

The region exclusive of the hot-spot region is called the balance of the explosive. Chemical reaction in the hot-spot region of the explosive causes chemical reaction in the balance of the explosive through some form of energy transfer. The major part of the exothermic chemistry is controlled by this mechanism. It is represented in the reaction model by a mass fraction  $(1-\eta-\psi)$  and a progress variable  $\lambda_f$ . Here,  $\psi$  is defined below and the subscript "f" stands for fast.

Finally, we recognize the possibility of exothermic reactions that are slow relative to the rates of the  $\lambda_h$  and  $\lambda_f$  reactions (e.g., one possible such reaction is solid carbon coagulation<sup>10</sup>). The mass fraction and progress variable associated with this rate process(es) are called  $\psi$  and  $\lambda_s$ , respectively -- the subscript on  $\lambda_s$  denotes slow.

This model, therefore, consists of three rate equations that govern the heat released in the hot spot, propagation, and slow reaction regimes that are assumed to be present in the initiation and detonation of heterogeneous HEs. Each of these three regimes is characterized by a process time scale for that particular stage.

The total reaction (or product) fraction  $\lambda$  is given by

$$\lambda = \eta\lambda_h + (1-\eta-\psi)\lambda_f + \psi\lambda_s, \quad (1)$$

where  $\eta$  and  $\psi$  are constants. The hot-spot reaction fraction is determined by

$$\frac{d\lambda_h}{dt} = \frac{1}{\tau_h} (1 - \lambda_h), \quad (2)$$

with  $\tau_h$  being the hot-spot process time. The fast reaction  $\lambda_f$  is controlled by the energy transfer between the hot spot products and the remaining reactants; its rate is

$$\frac{d\lambda_f}{dt} = \frac{1}{\tau_f} (1 - \lambda_f) \frac{(\lambda_h - f_0/\eta)}{(1 - f_0/\eta)}, \quad (3)$$

In Equation (3),  $f_0$  determines the threshold condition that the hot-spot fraction  $\lambda_h$  must exceed in order to support reaction propagation. Finally, the rate of the slow process is

$$\frac{d\lambda_s}{dt} = \frac{1}{\tau_s} (\lambda_f - \lambda_s), \quad (4)$$

where  $\tau_s$  is the slow process time.

We note that the hot-spot process time ( $\tau_h$ ) is related to the shock state and the chemical kinetic parameters of the HE.<sup>8</sup> The slow process time ( $\tau_s$ ) is taken as a constant, since it is thought to be insensitive to the thermodynamic state. The fast process time ( $\tau_f$ ) can be written as

$$\tau_f = \tau_e / \eta, \quad (5)$$

which defines a relationship between  $\tau_f$  and an energy transfer time  $\tau_e$ ;  $\tau_e$  is a function of pressure.<sup>8</sup> At the high pressures corresponding to short run distances to detonation and to detonation itself, the weak dependence of the reaction time on pressure<sup>11</sup> means that at sufficiently high pressures,  $\tau_f$  can be treated as a constant. Therefore, the following treatment is proposed

$$\tau_f = \max(\tau_b, \tau_e / \eta), \quad (6)$$

where  $\tau_b$  is a constant representing the limiting process of decomposition.  $\tau_f$  defines the fast reaction zone width. The relation expressed by Equation (6) is similar to the original treatment of the slow process.<sup>12</sup>

In the detonation regime, the hot-spot process can be considered to be instantaneous. In this case Equations (1) through (4) reduce to

$$\lambda = \eta + (1 - \eta - \psi)\lambda_f + \psi\lambda_s; \quad (7)$$

with

$$\frac{d\lambda_f}{dt} = \frac{1}{\tau_f} (1 - \lambda_f); \quad (8)$$

and

$$\frac{d\lambda_s}{dt} = \frac{1}{\tau_s} (\lambda_f - \lambda_s). \quad (9)$$

$\tau_f$  is typically at least 10 times smaller than  $\tau_s$ . For the calculations to be discussed below, the coupled set of Equations (1) through (6) were used. We note, however, that Equations (7) through (9) are useful for interpreting the

qualitative features of the numerical results for the thermodynamic states characteristic of our experiments. Provided  $\tau_f = \text{constant}$ , the simplified rate Equations (8) and (9) can be integrated analytically. Their solutions, with the initial conditions  $\lambda_f = \lambda_s = 0$  at  $t = 0$  are

$$\lambda_f = (1 - e^{-t/\tau_f}), \quad (10)$$

and

$$\lambda_s = \lambda_f - \frac{\tau_s}{\tau_s - \tau_f} (e^{-t/\tau_s} - e^{-t/\tau_f}). \quad (11)$$

Note from these relationships that *neither* the fast *nor* the slow rate process goes to completion ( $\lambda = 1$ ) in a finite time; therefore, the steady reaction-zone length for this model is infinitely long.

The rate parameters used to model PBX 9502 were:  $\eta = 3 \times 10^{-3}$ ,  $\psi = 0.15$ ,  $f_0 = 3 \times 10^{-5}$ ,  $\tau_b = 5$  ns, and  $\tau_s = 75$  ns.  $\tau_h$  is a variable dependent on the thermodynamic state: its value is much shorter than 5 ns. The HOM equation of state was used in all of the calculations.<sup>13</sup>

## INTERPRETATION OF EXPERIMENTAL AND CALCULATIONAL RESULTS

Numerical hydrodynamic calculations with the reaction-rate model described above reproduced the experimental velocity histories quite well for the various charge thicknesses and window configurations for both the 1D sustained- and short-shock experiments. No attempts were made to model the 2D experiments. Comparisons are shown in Figures 5(a) through 5(c) between the numerical and experimental interface-velocity data for the sustained-shock configuration. Data are given in each frame of the figure according to charge thickness of the PBX 9502 sample for each of the windows.

To give a frame of reference from which to view the discussion to follow, it is worthwhile to give an indication of what we think the steady reaction-zone length in PBX 9502 is. The numerical modeling gives evidence that there is an exothermic chemical process in

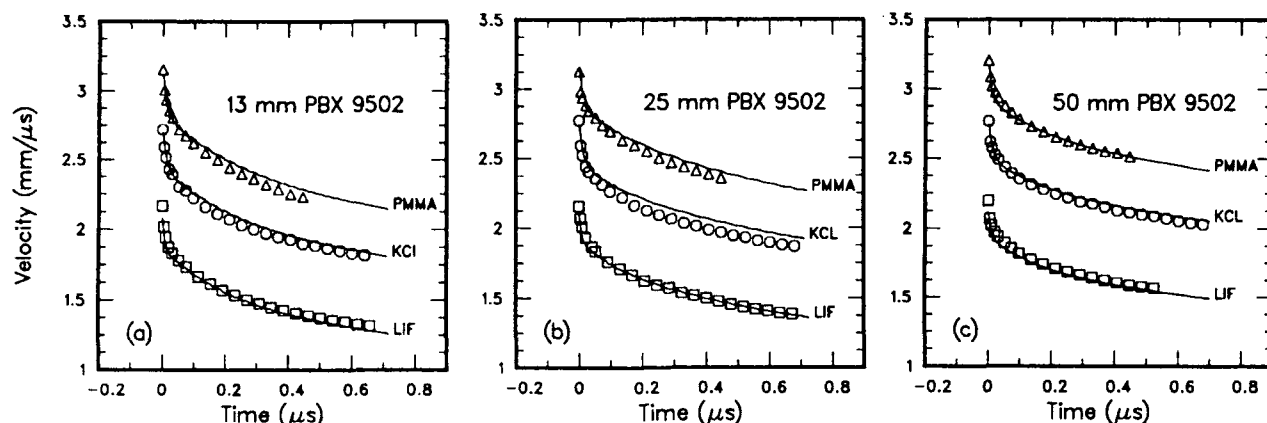


Figure 5. Comparison of Experimental (Symbols) Interface-Velocity Histories (Using Various Window Materials) with Ones Calculated (Solid Curves) from the Model Discussed in "CALCULATIONS." As one moves to the right across the page, one moves to longer runs in the PBX 9502.

PBX 9502 that requires  $\approx 300$  ns to occur (this is the time for the reaction progress variable to reach 98 percent of its final value). The reaction-zone thickness associated with such a time is  $\approx 2$  mm. This rough estimate is not dissimilar to reaction-zone lengths estimated by completely different methods.<sup>5</sup>

The nonsteady character of the following flow indicated by the increases in interface-velocity histories with run (or diameter) lead us to believe that peak velocities should also show an upward trend with increased run (or diameter). This is not observed experimentally; however, the numerical modeling shows an increase of 1.7 percent in peak velocity from the 13 to the 50 mm run. We believe the lack of an observed trend results from: (1) the limitations of our experimental resolution of the peak velocities and (2) the rapidity of the major part of the exothermic heat release.

Measured peak interface velocities for experiments that used LiF windows are given in Table 1. Standard deviations calculated from these measured peak velocities for each type of experiment (where various runs (or diameters) are combined) range from about 2 to 3 percent. We estimate this to be the error for peak velocities. Experiments performed with the two other windows gave similar results. All velocities other than the peak velocities are found, typically, to have standard deviations of less than 1 percent (see below for detailed comparisons).

Table 1. Peak Velocities for LiF Windows

Shot Number	Experiment Type	Charge Dimension (mm)	Peak Velocity (mm/μs)
8-306	Sustained	13	2.17
8-353		13	2.23
8-305		25	2.16
8-355		25	2.19
8-303		50	2.16
8-354		50	2.23
Average Velocity 2.19 mm/μs Standard Deviation 0.03 mm/μs			
8-328	Short	13	2.12
8-340		25	2.17
8-372		25	2.26
8-347		50	2.26
Average Velocity 2.18 mm/μs Standard Deviation 0.06 mm/μs			
8-339	Rate Stick	10	2.24
8-358		10	2.20
8-346		14	2.18
8-348		25	1.95*
8-359		25	2.28
8-321		50	2.21
8-322		50	2.07
Average Peak Velocity 2.20 mm/μs Standard Deviation 0.07 mm/μs			

\* See "INTERPRETATION OF EXPERIMENTAL AND CALCULATIONAL RESULTS" section.

Several reproducibility experiments were performed and are shown in Figure 4. Two velocity histories are given for 13, 25, and 50 mm charge thicknesses with LiF windows for the sustained-shock configuration. The 13 and 25 mm experiments reproduced so well that one can hardly discern that two velocity histories are given. More difference is observed for the 50 mm run. Here at 0.400  $\mu$ s, after shock arrival, the two traces differ by 2.4 percent. Two velocity histories are also shown for the 13 and 25 mm runs with KCl windows for the sustained-shock driver. The 25 mm experiment reproduced to better than 1.0 percent over the entire record. The 13 mm run experiment differs by 2.4 percent at 0.200  $\mu$ s and 3.0 percent at 0.600  $\mu$ s. Only one short-shock reproducibility experiment was performed and is given for a 25 mm run with a LiF window. Good agreement is also seen for these two experiments with one showing more structure than the other, but with both agreeing to within 2.0 percent. The structure on the one record was determined to occur from a broadening of the velocimeter traces at specific times, which is probably the result of laser fluctuations or changes in light levels reflected from the target.

Reproducibility of the 10.0, 25.0, and 50.0 mm diameter rate sticks was very good (only one 14.0 mm rate-stick experiment was performed). Again, one can hardly discern that two velocity histories are given in Figure 4(g) for the 10.0 and 50.0 mm diameter shots. One of the 25.0 mm diameter experiments shows more structure, but both records agree very closely, with a maximum difference of 2.8 percent occurring at about 0.140  $\mu$ s. We note that the measured peak particle velocity for the stick that showed the structure is anomalously low (see Table 1). In this experiment, the LiF crystal was glued to the PBX 9502 with Eastman 910 cement rather than with Devcon epoxy. We found that Aralhex and Devcon gave uniform adhesive layers, whereas Eastman 910 spread nonuniformly leaving voids. The voids possibly cause problems in measuring the peak velocity. This observation indicates that the method of gluing is an important part of the assembly procedure and must be done carefully with an adhesive that spreads uniformly.

Experiments with KCl windows were performed with very short run distances of 2, 3, and 5 mm. These records are shown in Figure 4(b) along with a record labeled 0. The 0 record is for a shot with the KCl window attached directly to the aluminum plate shown in Figure 1. The 2, 3, and 5 mm records show peak velocities in agreement with the longer runs of 13, 25, and 50 mm within the one standard deviation of 1.8 percent. Our booster system produces an initial particle velocity of about 1.8 mm/ $\mu$ s in PBX 9502; Figure 4(b) shows that this velocity has grown to 2.72 mm/ $\mu$ s in a run distance of 2 mm. This very rapid growth of the spike indicates an early fast reaction in the PBX 9502.

One of the reasons for doing the experiments described above was to attempt to obtain the wave profile, at a PBX 9502/window interface, produced by a 1D steady detonation wave from PBX 9502. It is clear from Figures 4(a) through 4(f) that with runs in PBX 9502 of up to 50 mm (in the 1D configurations), one cannot conclude that a steady-wave profile has been achieved in any of the experiments. For the rate sticks (Figure 4(g)), one never reaches the 1D steady wave profile, as stick diameter is increased, because of the finite lateral dimension of the charge. Thus, it is not clear, for example, how close the 50 mm diameter rate-stick wave profile (shown on Figure 4(g)) is to the steady 1D profile.

However, since we have a progression of data (as a function of charge thickness (run) and stick diameter) in the 1D and 2D experiments, it should be possible to utilize these data to estimate the interface velocity that would be produced by the steady 1D wave from PBX 9502.

We did this estimate as follows. Suppose we make a table of the measured interface velocity vs. time for each rate-stick diameter. Using these tables, Figure 4(h) can be constructed. We work in the reciprocal diameter plane in Figure 4(h) because we wish to eventually extrapolate the experimental data to infinite stick diameter (i.e., 1D flow). The extrapolations to  $1/\text{diam} \rightarrow 0$  were done by use of the following algorithm. The data in the range  $0.00 \leq 1/\text{diam} \leq 0.10 \text{ mm}^{-1}$  on Figure 4(h)



were averaged and smoothed at each value of the time with a French curve. We then assumed we could expand the interface velocity ( $\equiv u_p$ ) vs.  $1/\text{diam}$  function about the  $0.04 \text{ mm}^{-1}$  ( $\text{diam} = 25 \text{ mm}$ ) point in a Taylor series, and we truncated this Taylor series after three terms. The  $du_p/d(1/\text{diam})$  (i.e., slope) term in this series was approximated by its finite difference approximation, using the  $1/\text{diam} = 0.02$  and  $0.04 \text{ mm}^{-1}$  data points. The  $d^2u_p/d(1/\text{diam})^2$  (i.e., concavity) term was approximated by its finite difference approximation using the  $1/\text{diam} = 0.02, 0.04$ , and  $0.07 \text{ mm}^{-1}$  data points. The desired  $u_p$  value at infinite charge size was then obtained by setting  $1/\text{diam} = 0$  in this approximation to the Taylor series; note that there is a different Taylor series (and extrapolated value) for each value of the time. After this process, we had in hand a particle-velocity history, at the PBX 9502/LiF window interface, that we thought was characteristic of the steady 1D detonation wave profile in PBX 9502. This is the wave profile plotted on Figure 4(a) and labeled "Steady?". Note that a magnification factor would be required to obtain the actual profile in the PBX 9502.

Now consider Figure 4(i) in which the 1D sustained-shock/LiF window data are plotted in the interface-particle velocity vs.  $1/\text{run}$  plane. Surely, the  $1/\text{run} \rightarrow 0$  intercept ( $\text{run} \rightarrow \infty$ ) in this plane will yield the interface-velocity history characteristics of the 1D steady detonation wave in PBX 9502. But can one obtain the steady profile by an extrapolation to  $1/\text{run} \rightarrow 0$  similar to that used for the data in Figure 4(h)? The answer to this question is no, because the 1D flow does not require an infinitely long run to become steady. Suppose we did 1D experiments with longer and longer runs and then plotted the results on Figure 4(i). One would eventually reach a run distance at which further extension of run would not produce any further change in the recorded profile (at least, for that part of the flow produced by the steady reaction zone). That is, somewhere between  $1/\text{run} = 0.02$  (50 mm run) and  $1/\text{run} = 0.0$  (infinite run), the plotted curves would become parallel to the  $1/\text{run}$  axis. Therefore, one does not know how to (or cannot) obtain a steady wave profile from the 1D data of Figure 4(i).

However, combining the steady profile obtained from the rate-stick data with the data on Figure 4(i) allows us to estimate at what run distance the 1D system would become steady. This is done as follows: (1) first choose a time, (2) then go to Figure 4(h) and find the extrapolated steady 1D value of  $u_p$  for this time, (3) plot this value of  $u_p$  on the appropriate time curve of Figure 4(i), and (4) find the  $1/\text{run}$  value that corresponds to the plotted point. This is how the open circles that are plotted on the left side of Figure 4(i) were obtained; these circles are an indication of where the 1D flow would become steady. On Figure 4(i) more times were used to obtain the 14 open circles than there are plotted smooth curves; open circle points were only obtained for times longer than 21 ns because of the difficulty in accurately determining the steady wave profiles at earlier times. If we average the 14 values of the "run to steadiness" shown on Figure 4(i), it is found that  $1/\text{run} (\text{steady}) = 0.013 \pm 0.004 \text{ mm}^{-1}$  or  $\text{run} (\text{steady}) = 77 \pm 26 \text{ mm}$ . This value is denoted by the vertical dashed line on Figure 4(i). We conclude, that a 1D experiment (with our sustained-shock boosting system), in which the run distance is about 100 mm, should produce a reaction-zone detonation wave profile that is steady.

An estimated Hugoniot point using the measured peak velocities for the various windows, an assumed detonation velocity of  $7.70 \text{ mm}/\mu\text{s}$ , a Mie-Gruneisen equation of state, and the shock impedance-matching technique gives a point in good agreement with the extrapolation of the Hugoniot given by Dick, et al.<sup>14</sup>

## DISCUSSION AND CONCLUSIONS

The improved dual Fabry-Perot system gives improved resolution of peak velocities and of the initial deceleration for interface-velocity histories between detonating PBX 9502 and various windows. Measured peak velocities with this improved system are about 5 and 10 percent higher than we previously measured for PMMA and LiF windows, respectively.<sup>1</sup> Initial decelerations are an order of magnitude higher (20 to 30 compared to 2 or

3 mm/ $\mu\text{s}^2$ ) than we previously observed. Good agreement for the remainder of the velocity histories is observed between the present and previous work with the present measurements showing slightly lower ( $\approx 2$  percent) values at later times. The lower values are likely the result of a lower density slow component explosive being used in the present P-40 planewave lenses.

Initial attempts to model the measured interface-velocity histories using a single-stage rate form with simple depletion showed the rate to be initially too slow and later too fast. Even though this rate form was abandoned for the three-stage rate model used in this work, this does not mean that a single-stage rate form with other types of depletion could not be devised to give good results.

No indication of a classical CJ state (i.e., the end of the reaction zone) has been observed. Both the 1D and 2D measurements discussed above (and synopsized in Figures 4(h) and 4(i)) show that in none of the experiments performed have we definitely observed the steady reaction-zone detonation-wave profile of PBX 9502. The fact that the values of  $du_p/dx$  (where  $x \equiv 1/\text{diam}$  or  $1/\text{run}$ ) in Figures 4(h) and 4(i) are not equal to zero is a manifestation of this.

This observation carries over to the short-shock experiments also. Thus, some more subtle tailoring of the booster wave profile -- than is achieved by throwing a plate across a vacuum -- is required to obtain the steady detonation regime in PBX 9502 promptly.

The experimental results support the view that there is a region of the flow near the detonation shock (i.e., within about 10 to 15 ns) where the structure quickly becomes essentially steady -- for example, within the 250 ns required for the detonation wave to cross the 2 mm thick charge experiment shown in Figure 4(b). This is followed by a region of the flow that approaches steadiness very slowly (i.e., on a time scale of 1000s of ns). For example, it takes about 3000 ns for a detonation to traverse 25 mm of PBX 9502 and about 6000 ns to traverse 50 mm. Yet, if one examines any of Figures 4(a) through 4(f), it is evident that the detonation wave shape has evolved further in the time required to traverse the second 25 mm

of the 50 mm thick PBX 9502 charges (as observed in the velocity histories for times as early as 10 to 15 ns after shock passage).

It is interesting that the calculational model used (with its longest time scale being  $\tau_s = 75$  ns) can reproduce the experimental interface-particle-velocity histories. As can be seen from Equations (10) and (11), in this model essentially all the chemical reaction (98 percent as measured by the progress variable ( $\lambda$ ) value) is released within  $4\tau_s$  (300 ns). However, note that as the  $\lambda$  of Equation (7) approaches 1, the chemical heat release to the flow must  $\rightarrow 0$ . In the steady case, a point where  $\lambda = 1$  must also be a sonic point in the flow. Regions in a flow that are nearly sonic require long periods of time to adjust to flow perturbations.<sup>15</sup> The 1000 ns time scales observed in the experiments are no doubt related to this fact.

In spite of this, the analyses (in "INTERPRETATION OF EXPERIMENTAL AND CALCULATIONAL RESULTS") associated with Figures 4(h) and 4(i) indicate that (with the sustained-shock booster system being used) it should be possible to reach the steady situation with a (reasonable) further extension of the charge thickness in the sustained-shock configuration (i.e., by use of about a 100 mm thick charge).

## ACKNOWLEDGEMENTS

We greatly appreciate the technical assistance of P. J. Ulibari in digitizing all of the experimental records. We thank M. C. Whitehead for measuring the laser spot size. We also thank J. B. Bdzil, C. A. Forest, A. B. Anderson, S. A. Sheffield, and R. L. Rabie for valuable discussions and suggestions.

## REFERENCES

1. Seitz, W. L.; Stacy, H. L.; and Wackerle, J., "Detonation Reaction-Zone Studies on TATB Explosive," *Proceedings of the Eighth Symposium (International) on Detonation*, Albuquerque, NM, 15-19 Jul 1985, pp. 123-132.
2. Wackerle, J.; Stacy, H. L.; and Dallman, J. C., "Refractive Index Effects for Shocked

- Windows in Interface Velocimetry," *Proceedings of SPIE*, San Diego, CA, 17-19 Aug 1987, pp. 72-82.
3. Seitz, W. L., "Short-Duration Shock Initiation of TATB," *Proceedings of the APS Topical Conference*, Santa Fe, NM, 18-21 Jul 1983, pp. 531-534.
  4. Brunauer, S.; Emmett, P. H.; and Teller, E., *Journal of the American Chemical Society*, Vol. 60, 1938, p. 309.
  5. Campbell, A. W. and Engelke, R., "The Diameter Effect in High-Density Heterogeneous Explosives," *Proceedings of the Sixth Symposium (International) on Detonation*, Coronado, CA, 24-27 Aug 1976, pp. 642-652.
  6. Winslow, O. G. and Davis, W. C., "Rotating Mirror Streak Camera with an Optional Image Intensifier Camera Back," *Proceedings of SPIE*, San Diego, CA, 17-19 Aug 1987, pp. 96-100.
  7. Davis, W. C., "Magnetic Probe Measurements of Particle Velocity Profiles," *Proceedings of the Sixth Symposium (International) on Detonation*, Coronado, CA, 24-27 Aug 1976, pp. 637-641.
  8. Tang, P. K., "Initiation and Detonation of Heterogeneous High Explosives: A Unified Model," LA-11352-MS, LANL, Los Alamos, NM, 1988.
  9. Tang, P. K., "High Explosives Reaction Model and Its Application to Booster Performance," *Third International Symposium on High Dynamic Pressures*, La Grande Motte, France, 5-9 Jun 1989.
  10. Shaw, M. S. and Johnson, J. D., "Carbon Clustering in Detonations," *Journal of Applied Physics*, Vol. 62, 1987, pp. 2080-2085.
  11. Dremin, A. N., "On the Physical Model of Condensed Explosives Detonation Wave," *International Symposium on Pyrotechnics and Explosives*, Beijing, China, 12-15 October 1987.
  12. Tang, P. K., "A Study of Detonation Processes in Heterogeneous High Explosives," *Journal of Applied Physics*, Vol. 63, 1988, pp. 1041-1045.
  13. Mader, C. L., *Numerical Modeling of Detonation*, University of California Press, Berkeley, CA, 1979, pp. 324-326.
  14. Dick, J. J.; Forest, C. A.; Ramsay, J. B.; and Seitz, W. L., "The Hugoniot and Shock Sensitivity of a Plastic-Bonded TATB Explosive PBX 9502," *Journal of Applied Physics*, Vol. 63, 1988, pp. 4881-4888.
  15. Bdzil, J. B. and Davis, W. C., "Time-Dependent Detonations," LA-5926-MS, LANL, Los Alamos, NM, 1975.

# REACTION ZONE STRUCTURE IN SUPRACOMPRESSED DETONATING EXPLOSIVES\*

L. G. Green, C. M. Tarver, and D. J. Erskine  
Lawrence Livermore National Laboratory  
Livermore, California 94550

*Nanosecond time resolved particle velocity histories of supracompressed detonation waves in TNT-, TATB-, and HMX-based explosives are measured using a VISAR laser velocimeter, and calculated using the ignition and growth reactive flow hydrodynamic computer code model. The Zeldovich-von Neumann-Doering (ZND) detonation wave structure is observed at pressures more than twice the self-sustaining detonation wave pressure. TNT and TATB exhibited a fast reaction which liberates approximately 80 percent of the total available exothermicity within 50 ns, followed by a slower reaction which lasts another 100-200 ns. These reaction rates are not strongly dependent on the initial shock pressure. The slower reaction is attributed to diffusion controlled solid carbon coagulation. The ignition and growth model, using a ZND type model with a fast reaction preceding a slower reaction to the fully reacted product state, accurately calculates the VISAR experimental data for TNT, LX-17, PBX 9404, and RX-26-AF.*

## INTRODUCTION

In recent years it has become possible to supracompress (overdrive) detonating solid explosives to pressures exceeding their self-sustaining Chapman-Jouguet (CJ) pressures by impacting them with gas-gun accelerated flyer plates at velocities of several millimeters per microsecond. In previous studies,<sup>1-4</sup> sub-nanosecond time response pins were used to measure shock transit times (shock velocities) in the samples. From the flyer shock Hugoniot and measured velocity, the particle velocity in the supracompressed wave could also be determined. Pressure-volume and shock velocity-particle velocity relationships were determined for several explosives at pressures from just exceeding CJ pressure to approximately 110 GPa. Hydrodynamic computer code calculations showed that the Jones-Wilkins-Lee (JWL) equations of state which accurately

calculate product states below the CJ state do not, in general, agree with the supracompression data. Tarver<sup>5</sup> suggested that this discrepancy is due to relatively slow exothermic reactions, such as diffusion controlled solid carbon coagulation into complex structures (graphite, diamond, etc.) which can directly affect the shock front velocity in piston supported waves, but only gradually affect the propagation of self-sustaining detonation waves. Supracompression and detonation experiments on PETN, which produces little or no solid carbon in its detonation products, have shown that one JWL equation of state can accurately calculate all of the available data up to 80 GPa.<sup>2,3</sup> A great deal of theoretical and experimental research on the amounts and states of solid carbon produced by detonating underoxidized solid explosives has recently been reported.<sup>6-9</sup> Reactive flow hydrodynamic computer models of the ZND structure of detonation waves, in which a fast exothermic reaction is followed by a slower one to the Chapman-Jouguet (CJ) state, have accurately simulated a great deal of Fabry-Perot laser

\*Work performed under the auspices of the U.S. Department of Energy by the Lawrence Livermore National Laboratory under Contract W7405-ENG-48.

interferometric particle velocity history data on detonating HMX-, TATB-, and TNT-based explosives.<sup>10</sup> These calculations also resulted in detonation reaction zone structures similar to those predicted theoretically by Fickett<sup>11</sup> for multireaction sequences.

Although slow carbon condensation reactions appear to explain the shock and particle velocities measured in supracompression experiments, the structures of the reaction zones in these waves could theoretically be quite complex, as illustrated in Figure 1 of the pressure-specific volume plane. Curve X in Figure 1 represents the unreacted explosive Hugoniot, curve P1 the incompletely equilibrated reaction product Hugoniot, and curve P2 the completely equilibrated reaction product Hugoniot. Curve P2 is drawn to the right of curve P1 to represent an exothermic process, such as  $C_1$ ,  $C_2$ ,  $C_3$ , etc., coagulating into long chains of  $C_{60}$  or greater. For a CJ self-sustaining detonation wave, the chemical reaction proceeds from the von Neumann spike state S in Figure 1 along Rayleigh line D to state CJ, where the relatively fast exothermic chain reactions which produce vibrationally excited diatomic and triatomic fluid molecules ( $N_2$ ,  $H_2O$ ,  $CO_2$ ,  $CO$ , etc.) are completed.<sup>12</sup> Slow exothermic reactions cause the end state of the

reaction zone to eventually reach the lower pressure complete equilibration state CJ in Figure 1. The approach to a steady state CJ detonation for this type of energy release has been discussed by Fickett.<sup>13</sup> Rayleigh lines 1, 2, and 3 in Figure 1 represent supracompressed waves supported by pistons at velocities and pressures exceeding the self-sustaining CJ values. Since the entire reaction zone is subsonic at these velocities, the effects of the slow reaction can modify the leading shock front. States along curve P2 should be reached from spike states  $S_1$ ,  $S_2$ , and  $S_3$ . As long as the unreacted Hugoniot curve X lies to the left of curves P1 and P2, the measured reaction zone structure will show decreasing particle velocities and pressures, such as from state  $S_1$  through curve P1 to curve P2 on Rayleigh line 1 in Figure 1. Should the unreacted Hugoniot be less compressible than the product Hugoniot at very high pressures, measured reaction zone structures may show the effects crossing (or merging) Hugoniot for states such as  $S_2$  and  $S_3$  in Figure 1.

The main purposes of this paper are to measure and hydrodynamically model the reaction zones of supracompressed detonation waves in solid explosives containing TNT, TATB, and HMX. The experiments and the reactive flow computer models are briefly described, and then the comparison of results is presented.

## EXPERIMENTS

The reaction zone structures of supracompressed detonation waves were measured by the laser interferometric techniques VISAR and Fabry-Perot. The VISAR technique was used for most experiments because it currently has a greater time resolution (approximately 2 ns) and velocity resolution (10-15 m/s) than Fabry-Perot. Plane shock waves were sent through thin explosive samples by accelerating 3 mm thick aluminum plates in the LLNL two-stage light gas gun. The explosive samples were 25 mm in diameter and 2 or 3 mm thick. A 5 mm thick LiF window was attached to the rear of the explosive sample with a 4000 Å gold layer evaporated onto the LiF to provide a specularly reflective surface for the laser interferometer at the explosive/LiF interface.

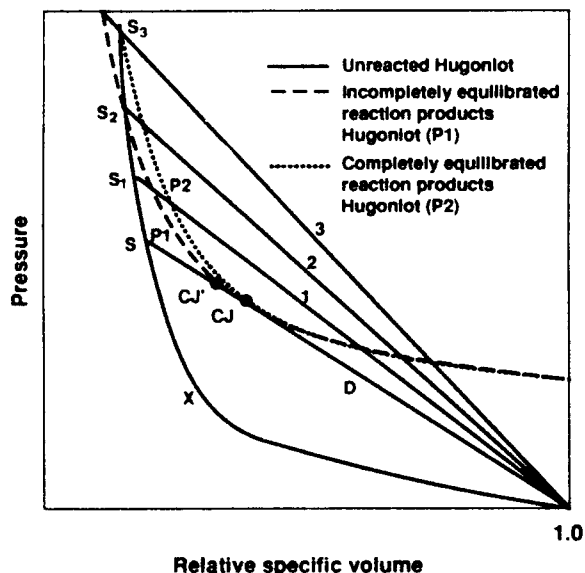


Figure 1. Pressure-Specific Volume Relationships for Supracompressed Detonation Waves

In some experiments, a 0.5 mm thick buffer plate of magnesium alloy AZ31B was placed between the explosive and the LiF window to protect the reflective interface from the three-dimensional irregularities of the leading shock front.<sup>12</sup> Thus, the average interface velocity histories between the explosive and LiF or the magnesium and LiF were measured for approximately 500 ns. Table 1 lists the 14 shots [13 using VISAR and one (BG01) using Fabry-Perot] fired at various flyer plate velocities into TNT, LX-17 (92.5 percent TATB, 7.5 percent Kelf), PBX 9404, and RX-26-AF (essentially half TATB and half HMX in an estane binder). The details of the experimental techniques (VISAR, pins, fiber optics, data recording, data analysis, etc.) were recently reported in a companion paper.<sup>14</sup>

## REACTIVE FLOW MODELING

A reactive flow hydrodynamic computer code model consists of: an unreacted explosive equation of state, a reaction product equation of state, a reaction rate law that governs the chemical conversion of explosive molecules to reaction product molecules, and a set of mixture equations to describe the states attained as the reactions proceed. The unreacted equation of state is normalized to shock

Hugoniot and von Neumann spike state detonation data. The reaction product equation of state is normalized to expansion data, such as that obtained in a cylinder test. The reaction rates are inferred from embedded gauge and/or laser interferometric measurements of pressure and/or particle velocity histories. The ignition and growth reactive flow model has been normalized to a great deal of one- and two-dimensional shock initiation and self-sustaining detonation data.<sup>15-20</sup> In this reactive flow formulation, the unreacted and product equations of state are both JWL (i.e., Gruneisen) forms:

$$p = Ae^{-R_1 V} + Be^{-R_2 V} + \frac{\omega C_v T}{V} \quad (1)$$

where  $p$  is pressure;  $V$  is relative volume;  $T$  is temperature; and  $A$ ,  $B$ ,  $R_1$ ,  $R_2$ ,  $\omega$  (the Gruneisen coefficient); and  $C_v$  (the average heat capacity) are constants. The ignition and growth reaction rate law is of the form:

$$\frac{\partial F}{\partial t} = I(1-F)^b (\rho/\rho_0 - 1 - a)^x + G_1(1-F)^c F^d p^y + G_2(1-F)^e F^g p^z \quad (2)$$

Table 1. Two-Stage Gun Supracompression Experiments

Al Impact		Explosive		Mg (AZ31B)	LiF
Shot	Velocity (km/s)	Explosive	Thickness (mm)	Thickness (mm)	Thickness (mm)
EG06	2.849	TNT (1.645 g/cc)	3	0	5
BG01	2.429 (steel)	TNT	6	0	12.8
EG07	4.167	TNT	3	0	5
EG04	4.455	TNT	3	0	5
EG09	4.725	TNT	2	0.5	5
EG08	6.084	TNT	2	0	5
EG19	3.573	LX-17 (1.903 g/cc)	2	0	5
EG13	3.685	LX-17	2	0.5	5
EG05	4.249	LX-17	2	0	5
EG12	6.191	LX-17	2	0	5
EG14	4.154	PBX 9404 (1.843 g/cc)	2	0.5	5
EG15	5.782	PBX 9404	2	0.5	5
EG16	3.910	RX-26-AF (1.836 g/cc)	2	0.5	5
EG17	6.241	RX-26-AF	2	0.5	5

where  $F$  is the fraction reacted;  $t$  is time;  $p_0$  is initial density;  $p$  is current density;  $p$  is pressure in Mbars; and  $I, G_1, G_2, b, x, a, c, d, y, e, g,$  and  $z$  are constants. The first term in Equation (2) controls the initial rate of reaction ignited during shock compression and is limited to fraction reacted  $F \leq F_{\text{igmax}}$ . The second term in Equation (2) is used to simulate the relatively slow growth of hot spot reactions during low pressure shock initiation calculations, and the third term is used to rapidly complete the shock to detonation transition in those calculations.<sup>15</sup> However, detonation is a fundamentally different process from shock initiation and, thus, must be modeled differently. Recent Fabry-Perot experiments and reactive flow calculations<sup>10</sup> have demonstrated the previously mentioned fast exothermic reaction followed by a slower exothermic reaction. Therefore, for detonation modeling, the second term in Equation (2) represents the fast reaction following ignition up to its limiting value  $F \leq F_{\text{GIMAX}}$ . The third term is then used to simulate the slow (carbon coagulation) reaction. Table 2 contains the equations of state and reaction rate parameters used for the four explosives studied in this paper. Numbers in parentheses in Table 2 are alternatives used to study the effects of equation of state or reaction rate changes on the simulation of an experiment.

Since the entire supracompression experiment must be accurately modeled with fine zoning (usually 100 or 200 zones per millimeter in the explosive) to obtain nanosecond resolution, the equations of state used for the inert materials are also extremely important. Table 3 lists the Gruneisen form and parameters used for aluminum, steel, magnesium (AZ31B), and LiF in the calculations.

## COMPARISON OF EXPERIMENTS AND CALCULATIONS

### Supracompressed Detonating TNT

Six experiments (five VISAR and one Fabry-Perot) were done using TNT impacted at various velocities ranging from 2.849 km/s, which results in a pressure just above CJ, to 6.084 km/s, which results in a pressure more than twice CJ. The ignition and growth

reactive flow model parameters for TNT in Table 2 provide good simulations of Fabry-Perot<sup>10</sup> and ORVIS<sup>18</sup> particle velocity histories measured for self-sustaining detonation waves. The reaction product equation of state for TNT in Table 2 has a lower CJ pressure (18 GPa) than is normally used (19-21 GPa) so that the overall cylinder test energy plus the previously measured supracompression states<sup>21</sup> can be accurately calculated. Figure 2 shows the experimental VISAR record for the lowest velocity shot EG06 plus the ignition and growth reactive flow calculation. The measured peak velocity is simulated by the reactive flow calculation which assumes that only 3 percent of the reaction occurs promptly during shock compression ( $F_{\text{igmax}} = 0.03$  in Table 2) to the state predicted by the unreacted Hugoniot based on  $R_1 = 9.8$  and  $R_2 = 0.98$  that was normalized to von Neumann spike states for self-sustaining detonation waves. Figure 2 clearly demonstrates that approximately 80 percent of the chemical energy is released in the first 60 - 70 ns while the remaining 20 percent of the energy is released over the next 70 - 80 ns or more. The reaction rates listed for TNT in Table 2 simulate this experiment very closely, although the reaction product equation of state predicts a final

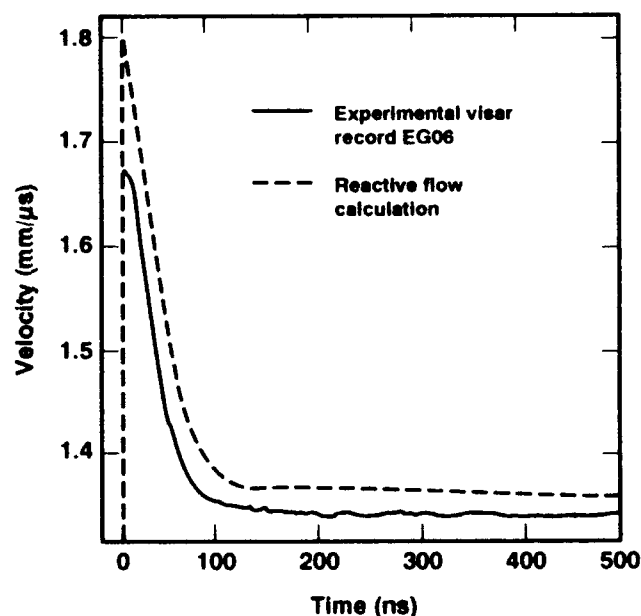


Figure 2. TNT Supracompressed Experiment EG06 Aluminum Flyer Impact Velocity = 2.849 km/s

Table 2. Parameters for Ignition and Growth Calculations

Explosive	TNT	LX-17	PBX 9404	RX-26-AF
Unreacted Equations of State				
$\rho_0$ (g/cc <sup>3</sup> )	1.645	1.903	1.843	1.836
A (Mbars)	171.01 (82.57)	778.1 (469.76)	9522.	2011.
B (Mbars)	-0.03745 (-0.03609)	-0.05031 (-0.0385)	-0.05944	-0.05204
$R_1$	9.8 (9.0)	11.3	14.1	12.4
$R_2$	0.98 (0.9)	1.3	1.41	1.24
w	0.5647 (0.5533)	0.8938	0.8867	0.9451
$C_v$ (Mbars/K)	$2.7172 \times 10^{-5}$	$2.48709 \times 10^{-5}$	$2.781 \times 10^{-5}$	$2.4063 \times 10^{-5}$
$T_0$ (K)	298	298	298	298
Reaction Product Equations of State				
D (mm/ $\mu$ s)	6.930	7.596	8.800	8.239
$P_{CJ}$ (Mbars)	0.180	0.250	0.370 (0.340)	0.325 (0.300)
A (Mbars)	33.94889	43.42773	8.524 (41.8548)	8.018 (31.34582)
B (Mbars)	0.821662	1.94564	0.1802 (1.2553)	0.5264 (1.11739)
$R_1$	8.3	8.5	4.6 (7.7)	5.0 (7.5)
$R_2$	2.8	3.28	1.3 (2.4)	2.1 (2.4)
$\omega$	0.6	0.6	0.38 (0.38)	0.34 (0.34)
$C_v$ (Mbars/K)	$1 \times 10^{-5}$	$1 \times 10^{-5}$	$1 \times 10^{-5}$	$1 \times 10^{-5}$
$E_0$ (Mbar-cc/ccg)	0.058	0.07	0.102	0.085
Reaction Rate Parameters				
$I$ ( $\mu$ s <sup>-1</sup> )	50.0	$4.0 \times 10^6$	$7.43 \times 10^{11}$	14.0
b	0.667	0.667	0.667	0.667
a	0.0	0.22	0.0	0.0
x	4.0	7.0	20.0	4.0
$G_1$ (Mbars <sup>y</sup> $\mu$ s <sup>-1</sup> )	360.0	48.0	3.1	488.0
c	1.00	0.111	0.667	0.667
d	0.667	0.111	0.111	0.333
y	1.2	1.0	1.0	2.0
$G_2$ (Mbars <sup>z</sup> $\mu$ s <sup>-1</sup> )	—	500.0	400.0	500.0
e	—	1.0	0.333	0.222
g	—	1.0	1.0	0.667
z	—	3.0	2.0	3.0
F <sub>igmax</sub>	0.03	0.0232 (0.5)	0.3	0.05
F <sub>GI</sub> MAX	1.0	0.85	0.5	0.5

particle velocity that is 1.5 percent higher than experiment. Other product JWL equations of state (particularly those with 19 - 20 GPa CJ pressures) predict this final velocity exactly, but do not calculate correct final velocities at higher pressures. The product JWL in Table 2 is the best overall fit to all of the available detonation and supracompression final particle velocity data for TNT.

Figure 3 shows the Fabry-Perot record from shot BG01 which lasted approximately 1800 ns. Also shown in Figure 3 is the reactive flow calculation which closely agrees with the measured initial velocity and reaction zone structure and then lies near the lowest velocities of the noisy Fabry-Perot record for times of 100 - 1300 ns. The calculated arrival time of the reflected shock from the steel flyer



Table 3. Gruneisen Equations of State for Inert Materials

$p = \rho_0 c^2 \mu [1 + (1 - \gamma_0 / 2) \mu - a/2 \mu^2] / [a - (S - 1) \mu] + (\gamma_0 + a \mu) E$					
where $p$ is pressure, $\rho_0$ is density, $c$ is the intercept of the shock velocity-particle velocity curve, $S$ is the slope of the shock velocity-particle velocity curve, $\gamma_0$ is the Gruneisen coefficient, $a$ is the first order volume correction to $\gamma_0$ , and $\mu$ is the relative compression.					
Material	$\rho_0$ (g/cm <sup>3</sup> )	$c$ (mm/ $\mu$ s)	$S$	$\gamma_0$	$a$
Aluminum	2.713	5.24	1.400	1.97	0.48
Steel	7.90	4.57	1.490	1.93	0.5
Magnesium (AZ31B)	1.78	4.52	1.242	1.54	0.33
LiF	2.638	5.15	1.350	1.69	0.34

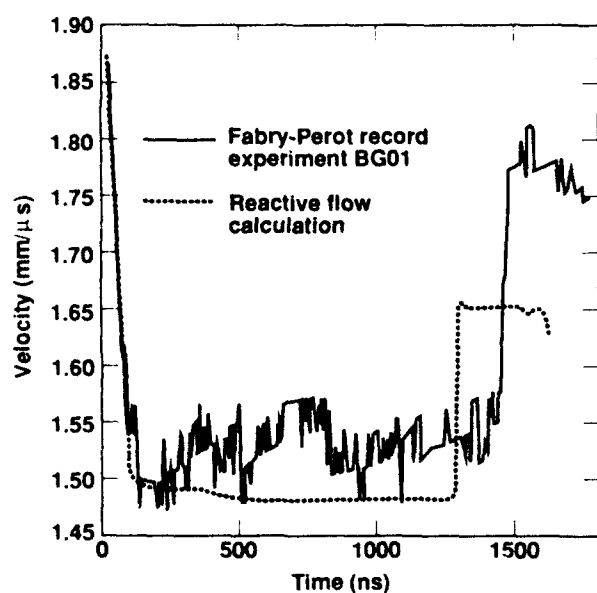


Figure 3. TNT Supracompression Experiment BG01 (Fabry-Perot) Steel Flyer Impact Velocity = 2.429 km/s

plate-explosive products interface at  $\sim 1300$  ns  $\sim 150$  ns earlier than the measured arrival at 1450 ns. This experimental arrival time can, in principle, be used to determine the average sound velocity in the supracompressed products. Figures 2 and 3 also demonstrate the agreement between the VISAR and Fabry-Perot techniques, and the usefulness of VISAR for accuracy over the first 500 ns and of Fabry-Perot for obtaining longer records.

Figure 4 contains the VISAR record from shot EG07 in which the aluminum impacted

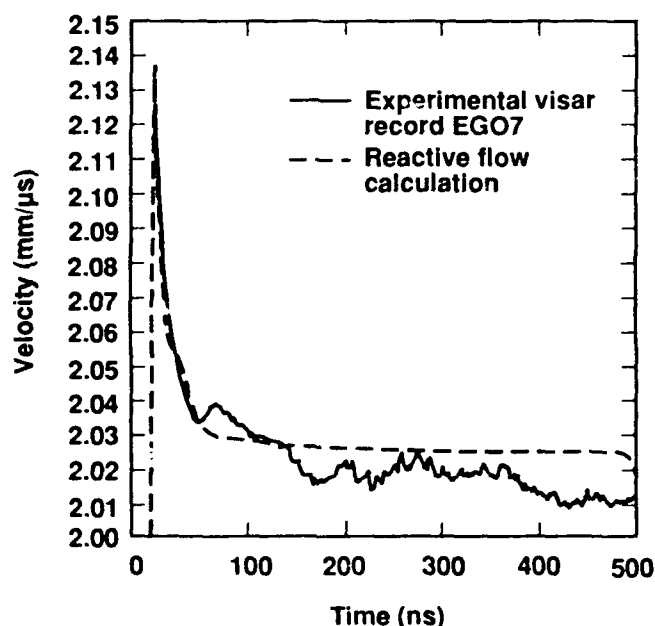


Figure 4. TNT Supracompression Experiment EG07 Aluminum Flyer Impact Velocity = 4.167 km/s

TNT at 4.167 km/s and the corresponding reactive flow calculation. The spike state and reaction zone profile to 140 ns are accurately simulated. For this case, the calculated final particle velocity is high by less than 1 percent. Figure 5 shows the VISAR record and calculation for shot EG04, which had a slightly higher flyer velocity than shot EG07. This experimental record lasted only 200 ns and contained an unusual increase in particle velocity from 60 to 140 ns. The calculated spike velocity and final product velocity agree

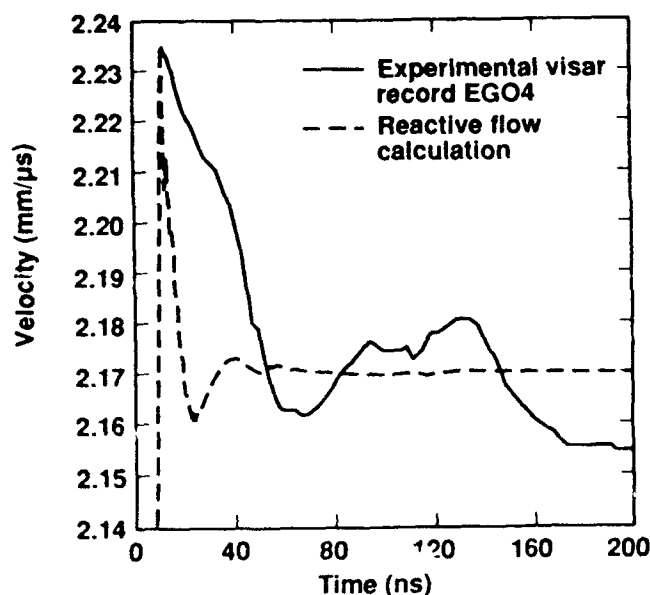


Figure 5. TNT Supracompression Experiment EG04 Aluminum Flyer Impact Velocity = 4.455 km/s

excellently with experiment, but the calculated reaction zone width appears to be too narrow.

The TNT VISAR records imply that the overall reaction zone length in TNT does not decrease with increasing pressure, while the reactive flow model does predict faster reactions at higher pressures by using an exponent of 1.2 in the pressure dependent second term in Equation (2).

Figure 6 contains the VISAR record for shot EG09, which included 0.5 mm of magnesium alloy between the TNT and LiF. Also shown in Figure 6 are two reactive flow calculations: one used the normal  $R_1 = 9.8$ ,  $R_2 = 0.98$  unreacted Hugoniot and the other used a more compressible  $R_1 = 9.0$ ,  $R_2 = 0.9$  unreacted Hugoniot which results in a higher spike velocity. The normal  $R_1 = 9.8$ ,  $R_2 = 0.98$  unreacted Hugoniot agrees more closely with the experimental record and the product equation of state agrees very closely. However, the arrival times of signals from the TNT/Mg/LiF interfaces do not agree.

Figure 7 shows the VISAR record for the highest pressure TNT experiment and two reactive flow calculations with the  $R_1 = 9.8$  and  $R_1 = 9.0$  unreacted equations of state listed in Table 2. Although this VISAR record lasts only 80 ns, it does show a maximum in

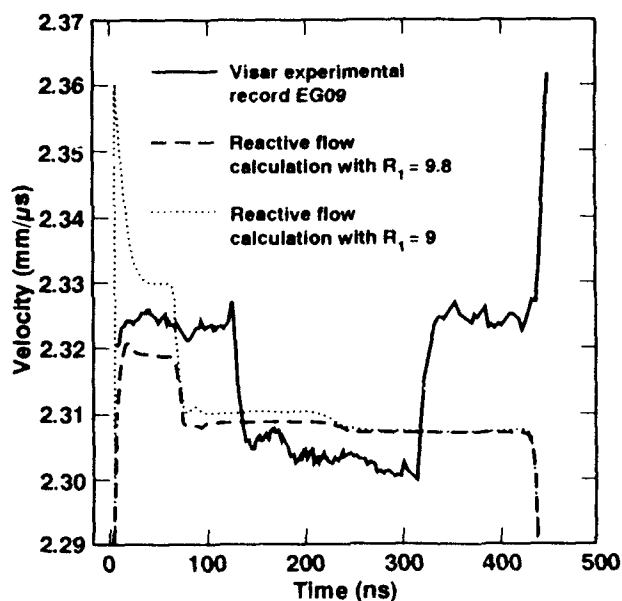


Figure 6. TNT Supracompression Experiment EG09 Aluminum Flyer Impact Velocity = 4.725 km/s

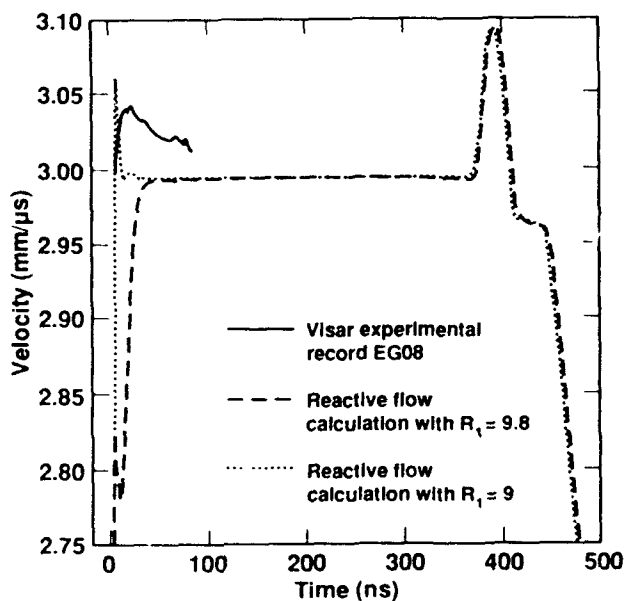


Figure 7. TNT Supracompression Experiment EG08 Aluminum Flyer Impact Velocity = 6.084 km/s

particle velocity, not at the shock front, but 20 ns later. This VISAR record is very similar to state S3 of Figure 1 in which the unreacted Hugoniot X and complete equilibrium Hugoniot P2 lie to the right of the partially reacted Hugoniot P1. The  $R_1 = 9.8$  unreacted equation of state spike state is quite low at these extremely high pressures, and the more

compressible  $R_1 = 9.0$  unreacted equation of state spike state is slightly high. The predicted time for complete reaction of 50 ns is too fast, but the product equation of state predicts the final particle velocity to within 1 percent.

An overall comparison of the six experiments and the various reactive flow calculations for TNT yields the results that the unreacted equation of state from detonation experiments is not compressible enough at very high pressures, the experimental reaction rates are less dependent upon pressure than the model assumes, and that the product equation of state, while not perfect, agrees on the average with the experimentally determined final particle velocities.

### Supracompressed Detonating LX-17

As for TNT, the reaction product equation of state listed for LX-17 in Table 2 has a lower CJ pressure (25 GPa) than is normally used (27.5 - 30 GPa) to match the available supracompression data<sup>1</sup> plus the cylinder test energy. Both the TNT and LX-17 product equation of state use higher values of  $R_1$ ,  $R_2$ , and  $\omega$  than older JWL cylinder test fits to provide better descriptions of the high pressure (>10 GPa) regime while still matching the overall energy delivered in the cylinder test. The unreacted LX-17 equation of state and reaction rate parameters in Table 2 yield good agreement with self-sustaining detonation reaction zone measurements.<sup>10</sup> Figure 8 contains the VISAR record from shot EG19, the lowest impact velocity experiment on LX-17, and the corresponding reactive flow calculation. The calculated spike and reaction rate agree closely with the VISAR record and, as in TNT, approximately 75 percent of the reaction occurs in the first 50 - 60 ns, while the remainder takes at least 200 additional ns. The product equation of state underestimates the final velocity by less than 1 percent and correctly calculates the arrival of the shock reflected from the aluminum piston-LX-17 interface back at the LX-17-LiF interface. Figure 9 shows the VISAR experimental record from shot EG13, which had a slightly higher impact velocity and a 0.5 mm magnesium alloy buffer, plus the corresponding calculation. The magnesium buffer again adds a great deal of

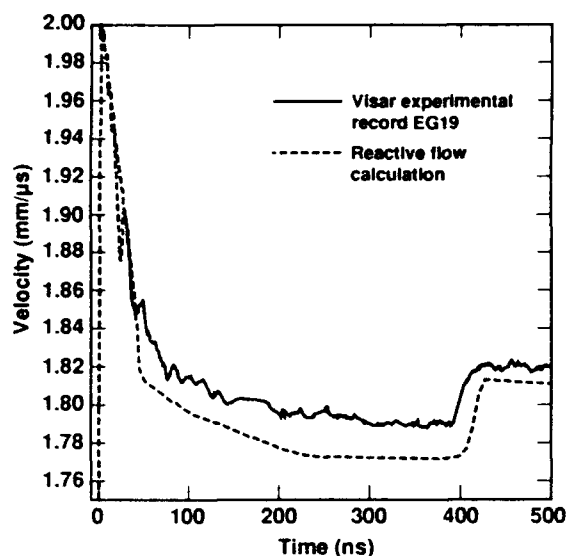


Figure 8. LX-17 Supracompression Experiment EG19 Aluminum Flyer Impact Velocity = 3.573 km/s

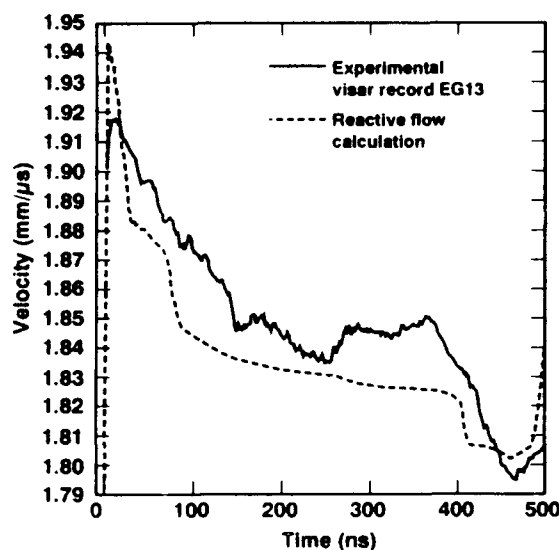


Figure 9. LX-17 Supracompression Experiment EG13 Aluminum Flyer Impact Velocity = 3.685 km/s

structure to the experimental record that is not yet totally understood. The calculated peak pressure is high and the velocity history for the first 100 ns has a different shape than the VISAR record, but the calculation is generally less than 1 percent low from 40 to 400 ns.

At higher impact pressures, the calculated LX-17 reaction rates are faster than the

VISAR records imply, as shown in Figure 10 for shot EG05. The calculated spike agrees with the VISAR record and the final velocity from the product equation of state is 1.5 percent higher than the experimental record when it ends at 360 ns. Figure 11 includes a reactive flow calculation using a more compressible unreacted equation of state, which in this case was obtained by decreasing A and increasing B in Equation (1), while leaving  $R_1$  and  $R_2$  unchanged for shot EG12, the highest impact velocity experiment on LX-17. The normal reactive flow calculation results in an initial velocity that is well below the experimental VISAR record. It then predicts a reaction zone of increasing velocity of approximately 60 ns to a final product velocity that is less than 1 percent lower than the VISAR record. The product equation of state also accurately predicts the reflected shock arrival at 270 ns and the subsequent rarefaction processes. Two other reactive calculations of shot EG12 are also shown in Figure 11 to illustrate how the initial velocity can be raised. One calculation, similar to the ones shown in Figures 6 and 7, uses a more compressible unreacted Hugoniot (by lowering A and raising B) and still allowing only 2.32 percent of the LX-17 to react during shock compression. In this particular calculation, the reaction rates and mixture algorithm create a minimum in particle velocity at approximately 15 ns, although the spike and final product states are close to the VISAR record, which is essentially flat or slightly increasing for 270 ns. The other calculation allows 50 percent of the LX-17 to react during shock compression, which raises the initial velocity approximately halfway to the reaction product equation of state. It is not yet known how much chemical reaction can actually occur within 2 ns (the VISAR time resolution) of the passage of the multi-dimensional leading shock front as a function of impact pressure. Obviously, if all of the LX-17 had reacted in less than 2 ns in shot EG12, the VISAR record would be flat. However, this is considered unlikely since the three other supracompressed LX-17 VISAR records exhibit reaction times not much shorter than those measured at detonation (250-300 ns) and since the nonequilibrium ZND model for condensed explosives<sup>12</sup> predicts finite reaction

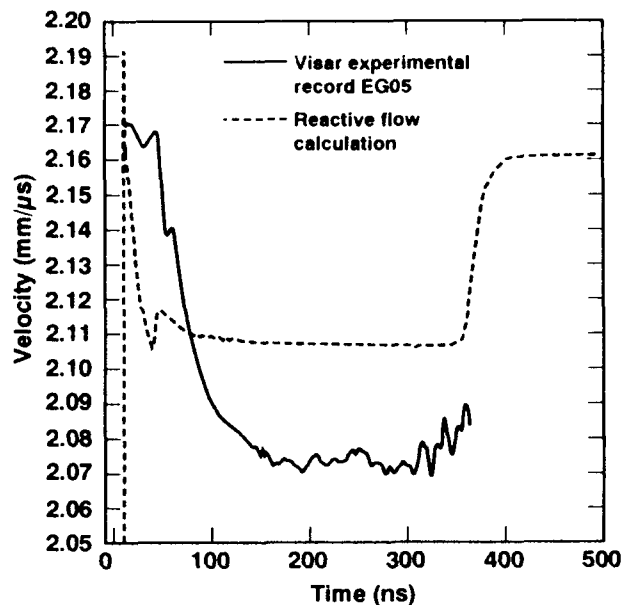


Figure 10. LX-17 Supracompression Experiment EG05 Aluminum Flyer Impact Velocity = 4.249 km/s

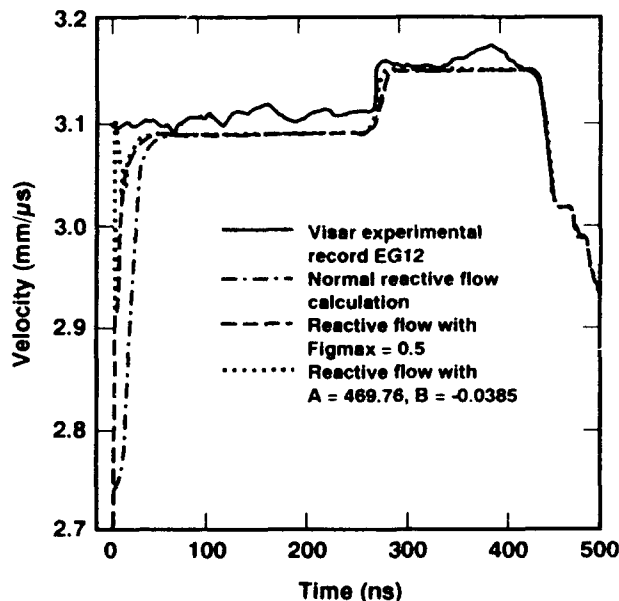


Figure 11. LX-17 Supracompression Experiment EG12 Aluminum Flyer Impact Velocity = 6.191 km/s

times even at these extreme shock pressures and temperatures.

### Supracompressed Detonating PBX 9404

Two shots were fired using PBX 9404, shot EG14 being slightly above the CJ pressure and shot EG15 at a much higher velocity. Due to the complex three-dimensional structure of the HMX detonation wave front, 0.5 mm of

magnesium had to be used to protect the LiF crystal. Thus, the main reaction zone structure, which is only 20 - 30 ns for detonating PBX 9404,<sup>10</sup> is obscured in these experiments. Figure 12 shows the VISAR record from shot EG14 and two reactive flow calculations, one using the standard 37 GPa CJ pressure JWL product equation of state, and another using the 34 GPa CJ pressure JWL product equation of state that accurately calculates the shock velocity—particle velocity supracompression data.<sup>1,4</sup> The 34 GPa equation of state was expected to more closely simulate the reaction product state and appears to in Figure 12, although the difference between the two calculations is less than 0.5 percent. The initial calculated velocities agree with the VISAR record in Figure 12, but the magnesium plate again seems to create a great deal of noise and/or reflected wave structure in the VISAR record. Figure 13 shows the higher velocity shot EG15 and the two reactive flow calculations. Again, the calculated initial velocities seem accurate, but the 34 GPa product equation of state agrees more closely with the VISAR record than the 37 GPa calculation, except perhaps in the timing of rarefaction waves and reflected shock waves. More experiments at intermediate pressures are required to understand PBX 9404.

## Supracompressed Detonating RX-26-AF

Two shots, one just above CJ conditions and one at very high velocity, were also fired for RX-26-AF, which had previously been modeled<sup>20</sup> using HMX reaction rates for the first 50 percent reacted and TATB reaction rates for the last 50 percent reacted. The original JWL product equation of state in Table 2 has a CJ pressure of 32.5 GPa, while the alternate equation of state listed in parentheses in Table 2 has a CJ pressure of 30 GPa, and more closely agrees with previous supracompression shock velocity data.<sup>1</sup> Figure 14 shows the VISAR record for shot EG16 and two reactive flow calculations, one using the 32.5 GPa CJ pressure equation of state, and one using the 30 GPa CJ pressure equation of state. The calculated spike is approximately 3 percent high, but the RX-26-AF unreacted equation of state is not normalized to as much Fabry-Perot data for self-sustaining detonations as are the other unreacted equations of state. The 30 GPa product equation of state appears to agree slightly better with most of the VISAR record than the 32.5 GPa equation of state. At the higher pressures of shot EG17 in Figure 15, the same trend holds with the 30 GPa CJ pressure equation being closer to experiment, except in the timing of the reflected shock arrival. More

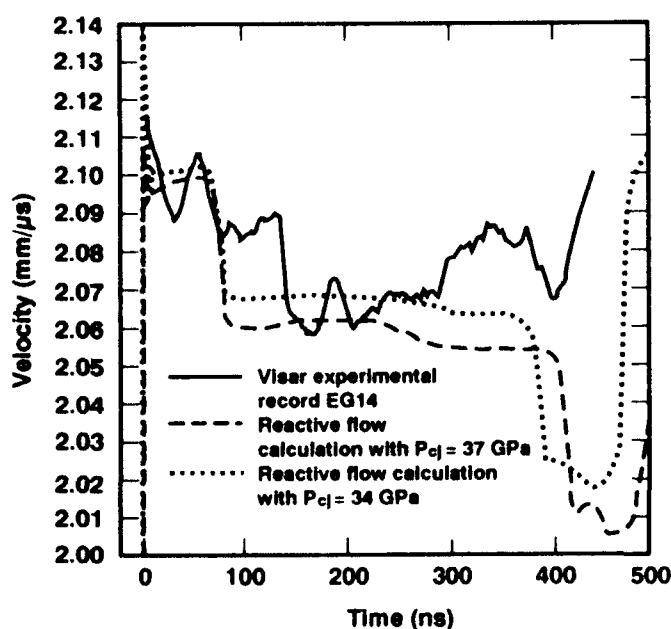


Figure 12. PBX 9404 Supracompression Experiment EG14 Aluminum Flyer Impact Velocity = 4.154 km/s

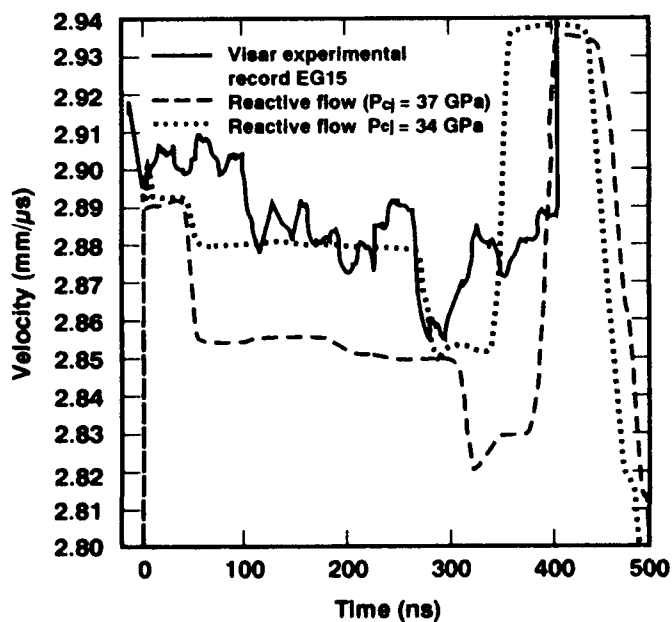


Figure 13. PBX 9404 Supracompression Experiment EG15 Aluminum Flyer Impact Velocity = 5.782 km/s

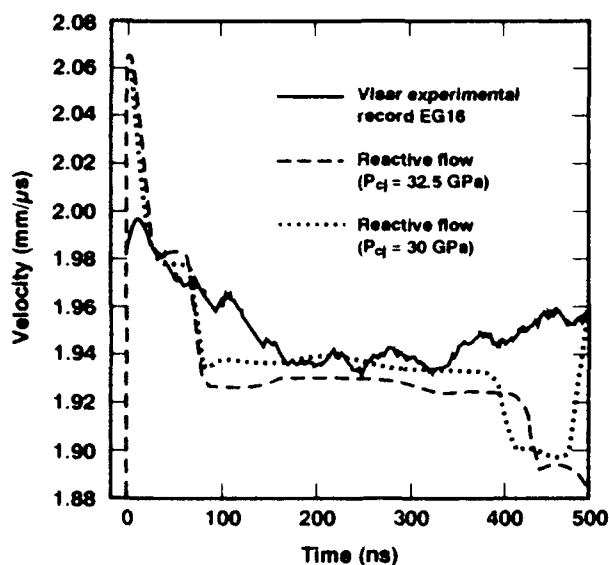


Figure 14. RX-26-AF Supracompression Experiment EG16 Aluminum Flyer Impact Velocity = 3.910 km/s

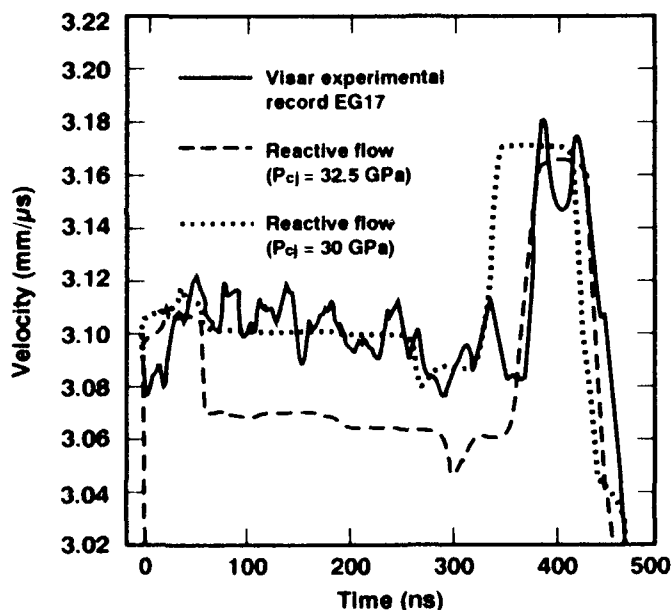


Figure 15. RX-26-AF Supracompression Experiment EG17 Aluminum Flyer Impact Velocity = 6.241 km/s

experiments at intermediate pressures are also required for understanding supracompressed detonating RX-26-AF.

## CONCLUSIONS

The supracompression VISAR experiments and reactive flow calculations presented in this paper have resolved the reaction zone

structure of detonating TNT, HMX, and TATB explosives at several pressures above their normal CJ states. Obviously, additional VISAR experiments are required to fully study these structures as functions of shock pressure and temperature. The "unreacted" explosive equation of state appears to be more compressible at very high pressures than predicted by the JWL equations of state fitted to low pressure Hugoniot and self-sustaining detonation von Neumann spike data. This problem may be solvable if a more complex equation of state form (perhaps,  $U_S = a + bu_p + cu_p^2 + \dots$ ) is used to describe the unreacted explosive. However, this issue is complicated by the lack of knowledge of the fraction of the explosive that reacts within the first 2 ns after shock arrival as a function of input pressure. The greater the fraction reacted, the further the initial velocity measurement will be from the true unreacted Hugoniot.

Extrapolation of the self-sustaining detonation reaction rates to these supracompressed states was successful to first order, but the measured reaction rates were less sensitive to pressure than the rates calculated by the pressure dependent ignition and growth model. This is most likely because the supracompressed shock temperatures, which actually control the initial fast reactions, are not much higher than the temperatures reached in various regions of the complex, three-dimensional multishock interaction process that controls self-sustaining detonation. Additionally, the rate of the relatively slow diffusion controlled carbon coagulation process is unlikely to be a strong function of pressure or temperature. More supracompression experiments, plus a nanosecond time resolution technique for measuring shock temperatures under these conditions, are required for more complete understanding of these global reaction rates.

As demonstrated by the experimental-calculational comparisons, the supracompressed wave structures can be calculated to within 1 percent in velocity with the current rate laws and equations of state. The reaction product equation of state can also be improved by comparison with more supracompression data and with thermodynamic chemical equilibrium code predictions of these high

pressure states. Like the unreacted equation of state, the reaction product equation of state may have to be more complicated than the JWL form currently used. The ability to use nanosecond time resolution techniques, such as VISAR, in the supracompression regime certainly opens many avenues to the understanding of ultra high pressure and temperature reaction rates, and equations of state.

## REFERENCES

1. Green, L.; Lee, E.; Mitchell, A.; and Tarver, C., *Eighth Symposium (International) on Detonation*, Naval Surface Weapons Center, NSWC MP 86-194, 1985, p. 587.
2. Green, L.; Holmes, N.; and King, J., *International Symposium on Pyrotechnics and Explosives*, Beijing, China, 1987, p. 518.
3. Green, L. G.; Lee, E. L.; Breithaupt, D.; and Walton, J., *Shock Waves in Condensed Matter -- 1987*, S. C. Schmidt and N. C. Holmes, Eds., Elsevier Science Publishers B. V., 1988, p. 507.
4. Lee, E. L.; Van Thiel, M.; Green, L. G.; and Mitchell, A., *Shock Waves in Condensed Matter -- 1983*, J. R. Asay, R. A. Graham, and G. K. Straub, Eds., Elsevier Science Publishers B. V., 1984, p. 617.
5. Tarver, C. M., *On the Difference Between Self-Sustaining Converging Detonation Waves and Piston-Supported Overdriven Detonation Waves*, UCRL-90714, Lawrence Livermore National Laboratory, Livermore, CA, Mar 1984.
6. Johnson, J. D., "Carbon in Detonations," *Proceedings of the Ninth Symposium (International) on Detonation*, Portland, OR, Aug 1989.
7. Ree, F. H. and Van Thiel, M., "Dissociation of Nitrogen and EOS of Condensed Carbon: Their Effect on the Detonation Properties of High Explosives," *Proceedings of the Ninth Symposium (International) on Detonation*, Portland, OR, Aug 1989.
8. Greiner, N. R., "Chemistry of Detonation Soot: Diamonds, Graphite and Volatiles," *Proceedings of the Ninth Symposium (International) on Detonation*, Portland, OR, Aug 1989.
9. Volk, F. and Schedlbauer, F., "Detonation Products of Less Sensitive High Explosives Formed Under Different Pressures of Argon and in Vacuum," *Proceedings of the Ninth Symposium (International) on Detonation*, Portland, OR, Aug 1989.
10. Tarver, C. M.; Breithaupt, R. D.; and Kury, J. W., *International Symposium on Pyrotechnics and Explosives*, Beijing, China, 1987, p. 692.
11. Fickett, W. and Davis, W. C., *Detonation*, University of California Press, Berkeley, 1979, Chapter 5.
12. Tarver, C. M., *Combustion and Flame*, Vol. 46, 1982, p. 157.
13. Fickett, W., *Phys. Fluids A*, Vol. 1, 1989, p. 371.
14. Erskine, D. J.; Green, L.; and Tarver, C., "VISAR Wave Profile Measurements of Supracompressed HE," paper presented at the *APS Topical Conference on Shock Waves in Condensed Matter*, Albuquerque, NM, Aug 1989.
15. Tarver, C. M.; Hallquist, J. O.; and Erickson, L. M., *Eighth Symposium (International) on Detonation*, Naval Surface Weapons Center, NSWC MP 86-194, 1985, p. 951.
16. Hayes, B. and Tarver, C. M., *Seventh Symposium (International) on Detonation*, Naval Surface Weapons Center, NSWC MP 82-334, 1981, p. 1029.
17. Tarver, C. M.; Parker, N. L.; Palmer, H. G.; Hayes, B.; and Erickson, L. M., *J. Energetic Materials*, Vol. 1, 1983, p. 213.
18. Sheffield, S. A.; Blomquist, D. D.; and Tarver, C. M., *J. Chem. Phys.*, Vol. 80, 1984, p. 3831.
19. Bahl, K.; Bloom, G.; Erickson, L.; Lee, R.; Tarver, C.; Von Holle, W.; and Weingart, R., *Eighth Symposium (International) on Detonation*, Naval Surface Weapons Center, NSWC MP 86-194, 1985, p. 1045.

20. Tarver, C. M.; Erickson, L. M.; and Parker, N. L., *Shock Waves in Condensed Matter -- 1983*, J. R. Asay, R. A. Graham, and G. K. Straub, Eds., Elsevier Science Publishers B. V., 1984, p. 609.
21. Kineke, J. H. and West, C. E., *Fifth Symposium (International) on Detonation*, Office of Naval Research, ACR-184, 1970, p. 533.



# LAGRANGIAN ANALYSIS OF MIV GAUGE EXPERIMENTS ON PBX 9502 USING THE MASS-DISPLACEMENT MOMENT FUNCTION\*

C. A. Forest, J. Wackerle, J. J. Dick,  
S. A. Sheffield, and D. R. Pettit  
Los Alamos National Laboratory  
Los Alamos, New Mexico 87545

*Magnetic Impulse-Velocity (MIV) gauges were used to measure the impulse and particle-velocity fields at discrete Lagrangian positions in two samples of the TATB explosive PBX 9502. Each sample was shock driven by a 6.4 mm layer of reacting superfine TATB ( $\rho_0 = 1.80 \text{ g/cm}^3$ ), which was itself shocked by a gas-driven projectile. The gauge histories of particle velocity and impulse, and the derived displacement history were simultaneously fit to the partial derivatives of the mass-displacement moment function employing a single set of parameters. (The function also gives volume, energy, pressure, and their time derivatives.) With an assumed mixture equation of state, the reaction extent and reaction rate were calculated. The two experiments were compared and rate correlations were examined.*

## INTRODUCTION

Lagrangian analysis<sup>1-6</sup> is the application of the conservation laws of mass and momentum to flow data obtained from gauges embedded in a material. The gauges are designed to disturb the flow as little as possible, and in the Lagrangian analysis are assumed to be massless and moving with the flow. The analysis uses the measured variables (such as particle velocity, stress, and impulse) and the conservation laws to form surfaces over the Lagrangian ( $h, t$ ) domain of the measured variables and of derived variables (such as volume, stress, and energy). Generally, the surfaces are not fluid-dynamic solutions because certain essential information (such as the equation of state, constitutive relation, or reaction rate) needed to construct the solution is unknown and is itself the object of the experiment. Rather, approximating surfaces are formed that fit the data in some optimum way and that have a subset of the physical properties of a solution. The analysis for reaction

rate is completed by the assumption of a reactant product equation of state  $P = P(V, e, w)$ , and its time derivative  $P_t = -(\rho c)^2 V_t + P_w w_t$ , where  $w$  = mass fraction of undecomposed reactant,  $e$  = specific energy, and  $V$  = specific volume.

The data set may comprise data from several experiments or a single experiment with multiple gauges, such as the MIV assembly described here.

Magnetic impulse and velocity (MIV) gauge assemblies<sup>6</sup> are used to record a material's response to shock waves, and in particular, to record an explosive's reactive response to such stimuli. The record consists of simultaneous histories of the impulse ( $I$ ) and particle velocity ( $u$ ) at a number (typically five) of distinct Lagrangian distance ( $h$ ) positions.

The impulse gauge is an integrating velocity gauge and

$$I(h, t) = \int_h^{h_s(t)} u(h', t) \rho_0 dh',$$

\*Work performed under the auspices of the U.S. Department of Energy.

and also then by momentum conservation,

$$I(h, u) = \int_{t_s(h)}^t \left[ P(h, t') - P_0 \right] dt'$$

where

$h_s(t)$  = position of the shock,

$t_s(h)$  = arrival time of the shock,

and

$P$  = the pressure

These data, along with shock front data, form the basis for a Lagrangian analysis in which approximations to  $I$ ,  $u$ , and other flow and state variables are constructed.

Commonly the method for constructing the surface  $u$  and  $I$  is the Path-Line Method<sup>3</sup> in which a family of lines (roughly parallel to the shock line) are chosen so that each line cuts each of the gauge histories. Then a one-dimensional fit is made of  $u$  and  $I$  on each line using as data the values of  $u$  and  $I$  at the

intersections of the path line with the history lines.

This paper, however, constructs the surface by using a mass-displacement moment function  $a(h, t)$  for which  $u$  and  $I$  are partial derivatives. The value of  $a$  is unimportant; the importance of  $a$  is that it induces the proper relationship between the variables  $\Delta x$  (displacement),  $I$  (impulse),  $\eta$  (compression),  $u$  (particle velocity), and  $P$  (pressure), and that all the data are fitted simultaneously with one parameter set.

## EXPERIMENT

The explosive PBX 9502 (TATB 95 percent/Kel-F 5 percent) at density  $\rho_0 = 1.89 \text{ g/cm}^3$  is quite insensitive and its prompt shock initiation is beyond the capabilities of our current gas gun. Thus, each of the samples of PBX 9502 was boosted by a reacting, but not detonating, layer of superfine TATB of density  $\rho_0 = 1.80 \text{ g/cm}^3$ . The superfine TATB was shocked by the gas-gun projectile as shown in Figure 1. Of course,

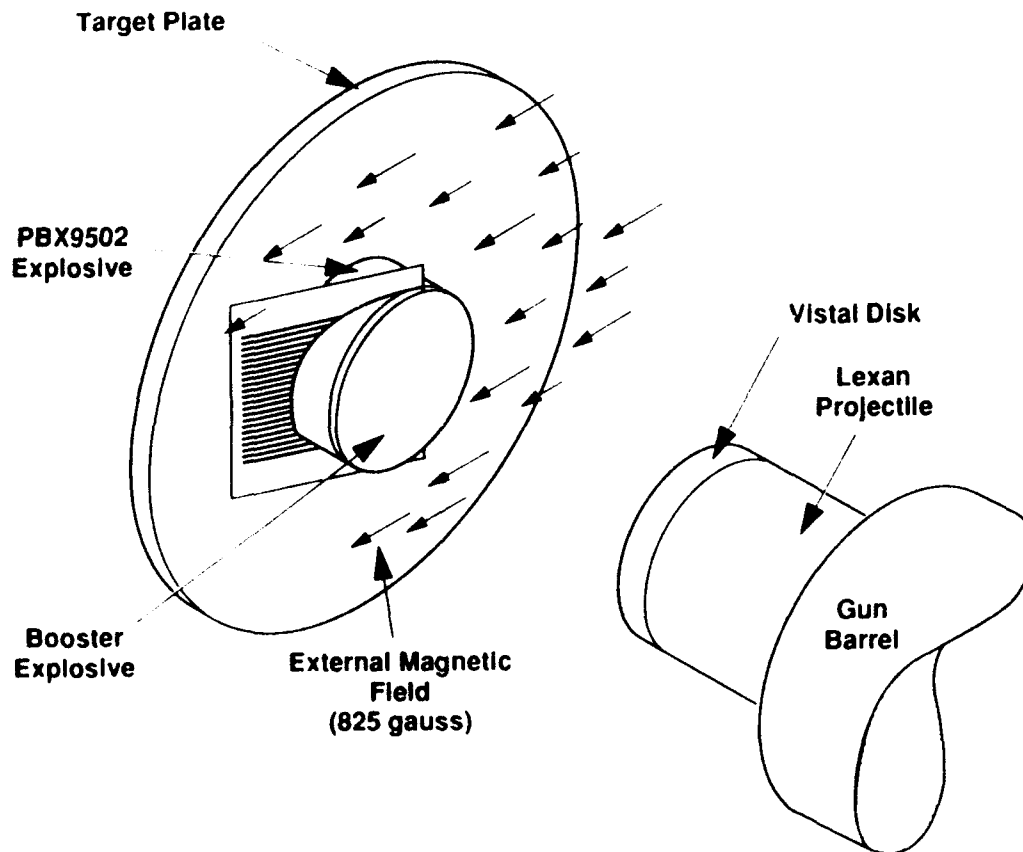


Figure 1 MIV Gauge Experimental Assembly

the magnitude and profile of the shock entering the PBX 9502 depends upon the projectile velocity and the superfine booster thickness. Accordingly, three preliminary experiments were done to find an appropriate booster thickness. The last of these, the 6.4-mm thick superfine TATB booster, was a composite double wedge in which the shock track of each wedge fact was recorded. The two MIV experiments were both made with a 6.4-mm superfine booster. The projectile velocities, however, were slightly different.

For the composite double wedge (Shot G684), the shock trajectories of both faces were simultaneously recorded by a single streak camera. The TATB booster was impact shocked by a 11-mm VISTAL impactor ( $\rho_0 = 3.959$ ) mounted on a gas-gun projectile with velocity of 1.112 mm/ $\mu$ s. The shock trajectories were each fit by a nonparametric data smoother TFIS that allowed a discontinuous derivative (shock velocity) at the TATB-PBX 9502 interface. The shock velocities are shown in Figure 2. The shock velocity of one side is higher throughout than that of the other side, which may have resulted from wave tilt. A portion of the initial shock trajectory was lost from each.

Similarly, in the MIV gauge experiments (Shots G705 and G717), the TATB boosters

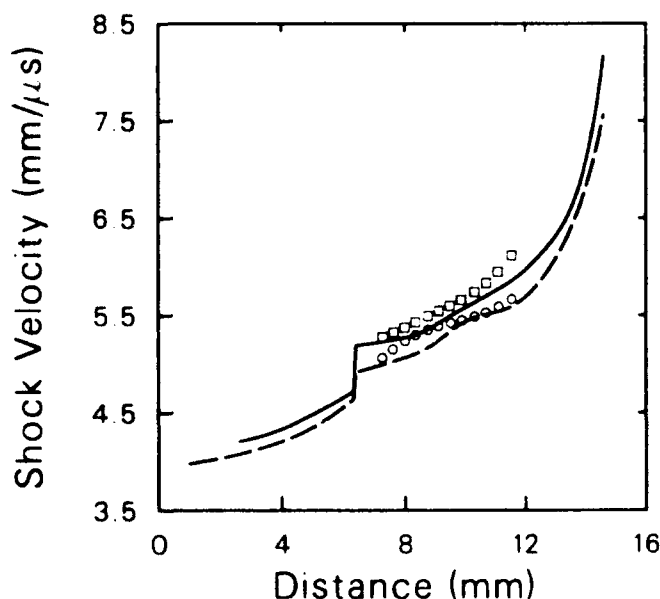


Figure 2 Shock Trajectory Velocities for Double Wedge Shot G684 (Lines), MIV Shot G705 (Circles), and MIV Shot G717 (Squares)

were shocked by VISTAL-faced gas-gun projectiles of velocities 1.116 and 1.134 mm/ $\mu$ s. The MIV gauge assemblies were placed at an angle of 30° relative to the charge face in the two-inch diameter PBX 9502 charges. Nominally, the impulse and particle-velocity gauges are located 1, 2, 3, 4, and 5-mm deep into the PBX 9502 and are isolated from two-dimensional effects for the duration of the experimental record. The shock-trajectory data are the shock arrival times at the particle-velocity gauges and the shock velocities inferred from the Hugoniot ( $U_s = 2.773 + 1.899 u_p$ ) and the shock-jump particle velocities. The shock arrival time is taken at the midrise of the particle-velocity gauge. The shock particle velocity is the extrapolated value of the particle-velocity history at the shock arrival time. The shock velocities from a simultaneous least-squares fit of shock position and velocity are shown in Figure 2.

## ANALYSIS

The method is centered on a simultaneous constrained least-squares fit to the function, partial derivatives, and shock-path derivatives of the mass-displacement moment function,<sup>7</sup>

$$\alpha(h, t) = \int_{t_s(h)}^t dt' \int_h^{h_s(t')} u(h', t') \rho_0 dh'.$$

Note that

$$\alpha(h, t) = \int_{t_s(h)}^t I(h, t') dt',$$

the impulse time integral, and that by reversing the order of integration

$$\alpha(h, t) = \int_h^{h_s(t)} \left[ X(h', t) - X_s(h') \right] \rho_0 dh',$$

the displacement moment, where  $X(h, t)$  is the Euclidean space position and  $X_s(h)$  is the Euclidean space position at shock arrival. Partial derivatives of  $\alpha$  are the functions associated with mass and momentum conservation; only energy need be integrated separately. Figure 3 shows the partial derivatives of  $\alpha$ ; moving in the table diagonally downward left indicates differentiation in Lagrangian

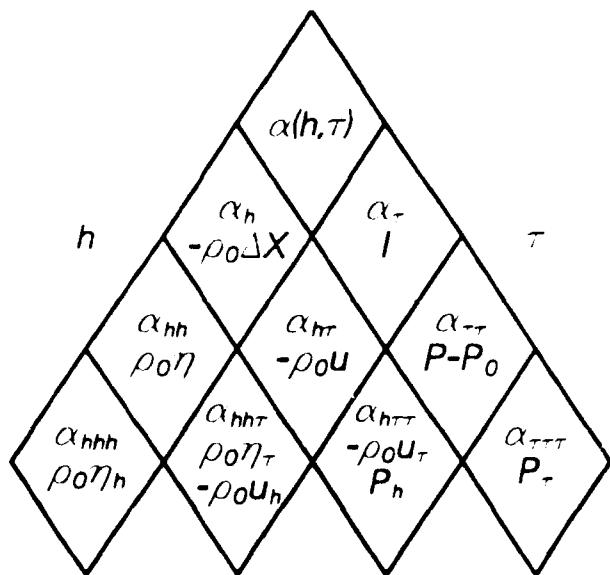


Figure 3. The Function  $\alpha$  and its Partial Derivatives

distance  $h$  and diagonally right indicates differentiation in time  $\tau$ . For example then,  $\partial^2 \alpha / \partial h^2 = \rho_0 \eta$ ,  $\partial^2 \alpha / \partial \tau^2 = P - P_0$ , and  $\partial^2 \alpha / \partial h \partial \tau = -\rho_0 u$ , where  $\eta = 1 - V/V_0$  is the volume strain. On the shock line  $\alpha(h, \tau_s(h)) = 0$ ,  $\partial \alpha / \partial \tau = I = 0$ , and  $\partial \alpha / \partial h = -\rho_0 \Delta X = 0$ , where  $\Delta X = X - X_s$ . Furthermore, first derivatives of  $I$  and  $-\rho_0 \Delta X$  along the shock path yield the Rankine-Hugoniot shock-jump relations, and second derivatives are the kinematic shock-change equations. In practice  $\alpha$  is represented as a function of time after shock arrival, thus  $\alpha(h, \tau) = \beta(h, \tau - \tau_s(h))$  and properties of  $\alpha$  are applied to  $\beta$ . Note that derivatives of  $\alpha$  and  $\beta$  satisfy

$$\begin{aligned} \alpha_h &= \beta_1 - \tau'_s \beta_2, \quad \alpha_\tau = \beta_2, \\ \alpha_{hh} &= \beta_{11} - 2\tau'_s \beta_{12} + (\tau'_s)^2 \beta_{22} - \tau''_s \beta_2 \\ \alpha_{\tau\tau} &= \beta_{22} \text{ and} \\ \alpha_{h\tau} &= \beta_{21} - \tau'_s \beta_{22}. \end{aligned}$$

Subscripts of 1 and 2 denote partial differentiation of  $\beta$  with respect to first and second arguments. The shock line is thus placed on the abscissa axis of the function  $\beta$ . Thus  $\beta_{22}(h, 0)$  is the pressure on the shock line and the shock-line conditions applied to  $\beta$  give  $\beta(h, 0) = 0$  and  $(\partial \beta / \partial \tau)(h, 0) = 0$ , which reduces the number of parameters necessary for the least square fit. The function may be expanded piecewise with each sub area being bounded by a time line

similar to  $\tau_s(h)$  and with appropriate continuity conditions applied.

For the least-squares fit of  $\alpha$ , particle velocity and impulse data are entered as the partial derivatives  $\alpha_{h\tau} = -\rho_0 u$  and  $\alpha_\tau = I$ . Particle-velocity histories are also individually smoothed and integrated to give displacement data  $\alpha_h = -\rho_0 \Delta X$ . The shock-trajectory pressure is determined by an independent least-squares fit (as described above) and is used as a constraint. The function  $\beta_{22}(h, 0)$  is the shock pressure and is completely determined by the shock trajectory. Smoothing terms of  $(\eta_{hh})^2$ ,  $(u_{\tau\tau})^2$ , and  $(P_{\tau\tau})^2$  are added to the least-squares merit function. The smoothing is necessary to dampen the untoward effects on the volume strain  $\eta$  and other subsequently derived variables of energy, reaction extent and reaction rate caused by the gauge to gauge calibration uncertainty in particle velocity and impulse.

The streak-camera trace and the individual MIV gauge histories were fit by a new nonparametric least-square method Tabular Function Least Squares (TFLS). In this method the least-square function is represented as a table  $\{z_i, f_i\}$ ,  $i = 1, NF$  with an associated interpolation function  $G$ , where  $G(\{z, f\}, x) =$  interpolated value at  $x$ . The table  $\{z\}$  is uniformly spaced over the domain of the fit. (The current choices for  $G$  are linear or cubic interpolation on a central interval.) Smoothness is induced upon the table by adding to the merit function the sum of the squares of the  $N$ th order forward-difference operator over the interior tabular points. Thus given data  $\{(x_i, y_i)\}$ , the merit function

$$\begin{aligned} E(\{f\}) &= \sum_{i=1}^{ND} \left[ G(\{z, f\}, x_i) - y_i \right]^2 \\ &+ wt \cdot \sum_{i=1}^{NF-N} (\Delta^N f_i)^2 \end{aligned}$$

is minimized with respect to the table  $\{f_i\}$ , where  $ND$  = number of data points,  $NF$  = number of tabular points, and  $N$  = order of the difference operator.

Following the determination of the function  $\alpha(h, \tau)$  by least squares fitting, the

reactant mass fraction  $w$  is found by solution of  $P = P(V, e, w)$ , an assumed solid and product mixture equation of state. The reactant (solid) EOS was taken to be a Mie-Grüneisen form with a first shock Hugoniot reference line. The parameters are  $U_s = 2.773 + 1.899u_p$ ,  $\Gamma_0 = 1.50$ ,  $\rho_0 = 1.893$ . The product EOS was also a Mie-Grüneisen form with a BKW calculated detonation isentrope reference line.<sup>8</sup> Two mixture rules were applied. The first is temperature and pressure equilibrium. The second is pressure equilibrium with an isentropic solid in which solid isentrope for each mass point passes through its first shock  $(V, e, P)$  point

## RESULTS

Comparisons of the data,  $\alpha$  surface lines, and derived reaction graphs for shots G705 and G717 are shown in Figures 4 through 13 with shot G705 appearing on the left. In Figure 4 and 5, the impulse and particle velocity data histories and  $\alpha$  partial-derivative lines are shown. The particle-velocity graphs show that shot G717 was subject to higher initial shock pressure. The impulse histories are similar but those of G717 are steeper, which is reflected in the pressure graphs of Figure 6. Constant-time profiles (snapshots) are shown in Figures 7, 8,

and 9 at times of 0.2, 0.4, 0.6, 0.8, 1.0, and 1.2  $\mu s$ . The snapshots verify that the  $\alpha$  surface is well-behaved between the gauge positions.

With the mixture equation of state, the mass fraction of reactant histories are calculated for Lagrangian positions of 2.0, 2.5, 3.0, 3.5, and 4.0 mm; points well interior to the Lagrangian domain. Figure 10 shows the mass-fraction histories; no exponential first order reaction tail is seen, although such a feature may be lost in the least-squares fitting.

The time derivative of  $-\ln(w)$  is graphed versus pressure in Figure 11, which shows that the reaction rate is not a simple function of pressure. The reaction rate is graphed versus equilibrium temperature in Figure 12 and versus isentropic solid temperature in Figure 13. The isentropic solid temperature is dependent only on the initial shock and the subsequent solid compression history and therefore cannot be expected to closely reflect reaction. The solved reaction histories for the two equation of state mixture rules were indistinguishable.

Each of the reaction or reaction-rate graphs does show that the reaction rate is initially slow following the shock and increases in time thereafter, indicating some induction process.

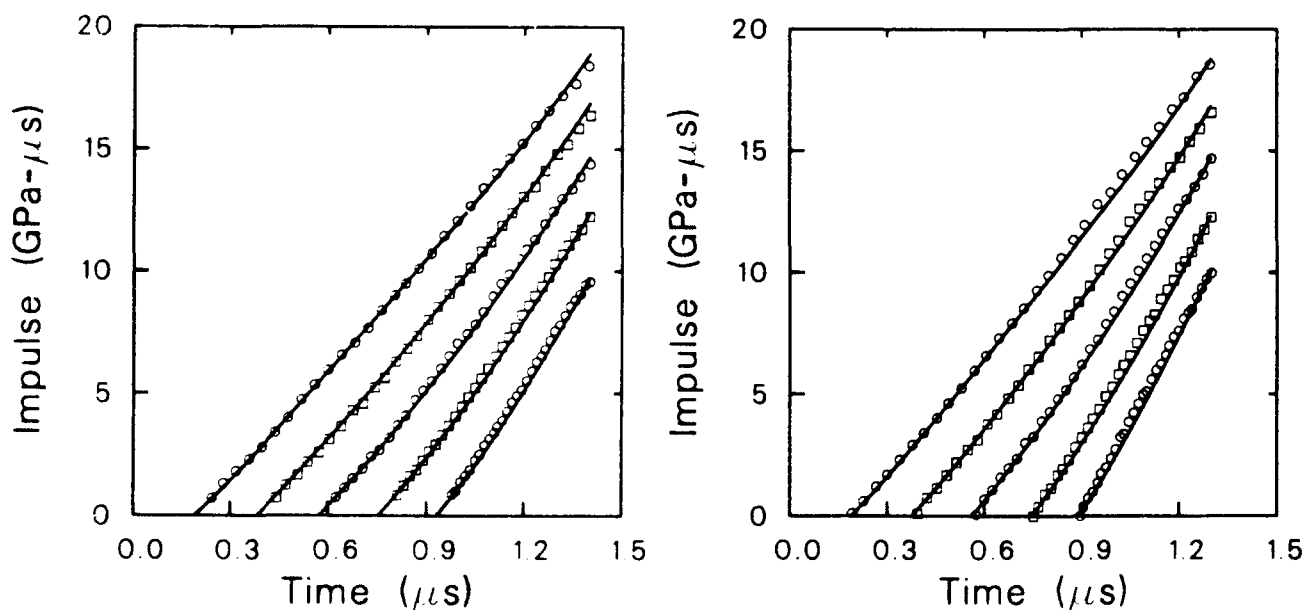


Figure 4 Impulse Gauge Data and  $\alpha_i$  Fit Lines for Shots G705 (Left) and G717 (Right)

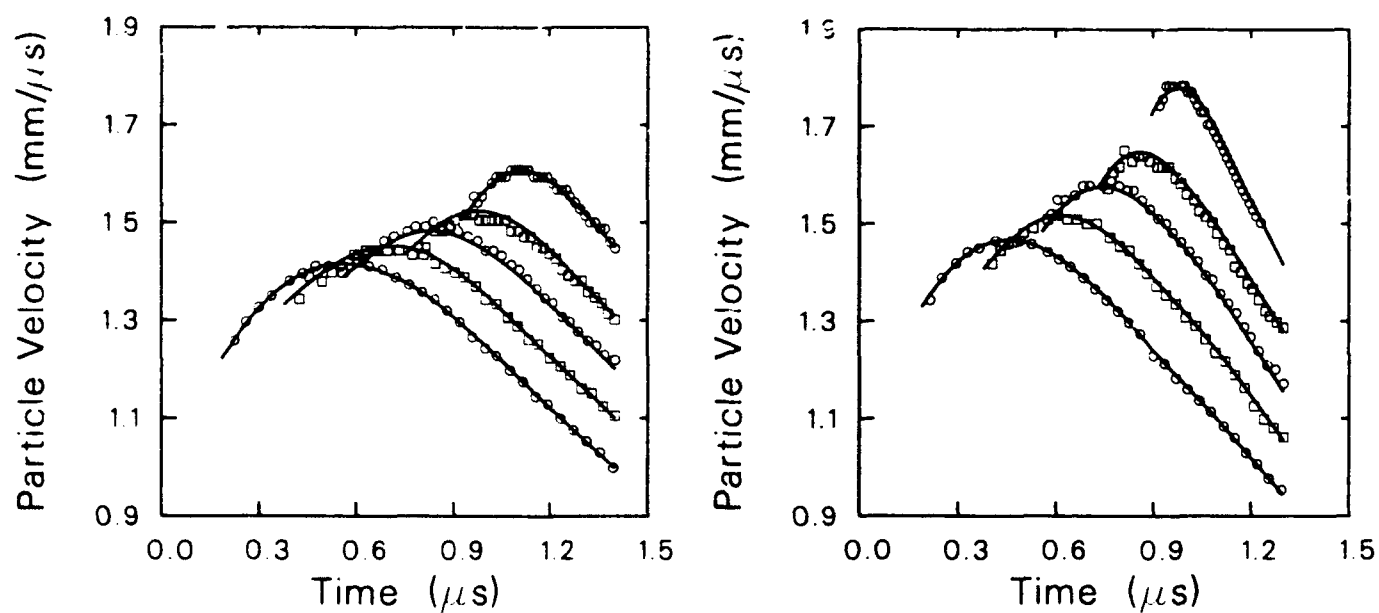


Figure 5 Particle Velocity Gauge Data and  $-V_0 a_{h,i}$  Lines for Shots G705 (Left) and G717 (Right)

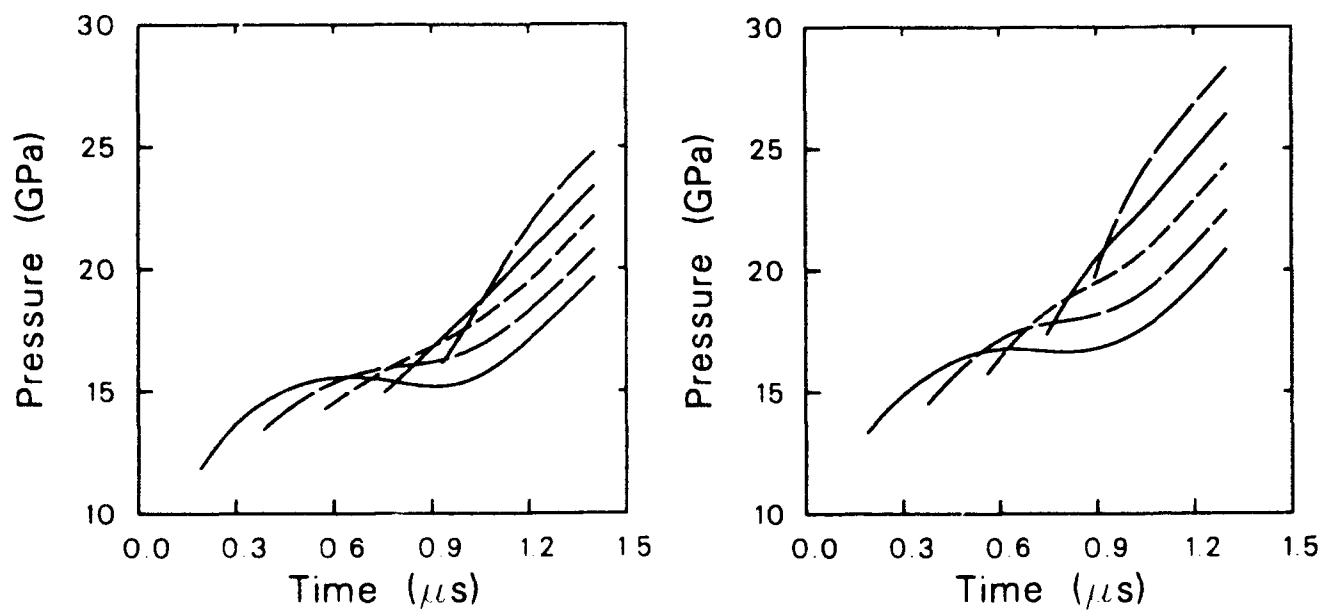


Figure 6. Pressure at the Gauges ( $a_{h,i}$ ) for Shots G705 (Left) and G717 (Right)

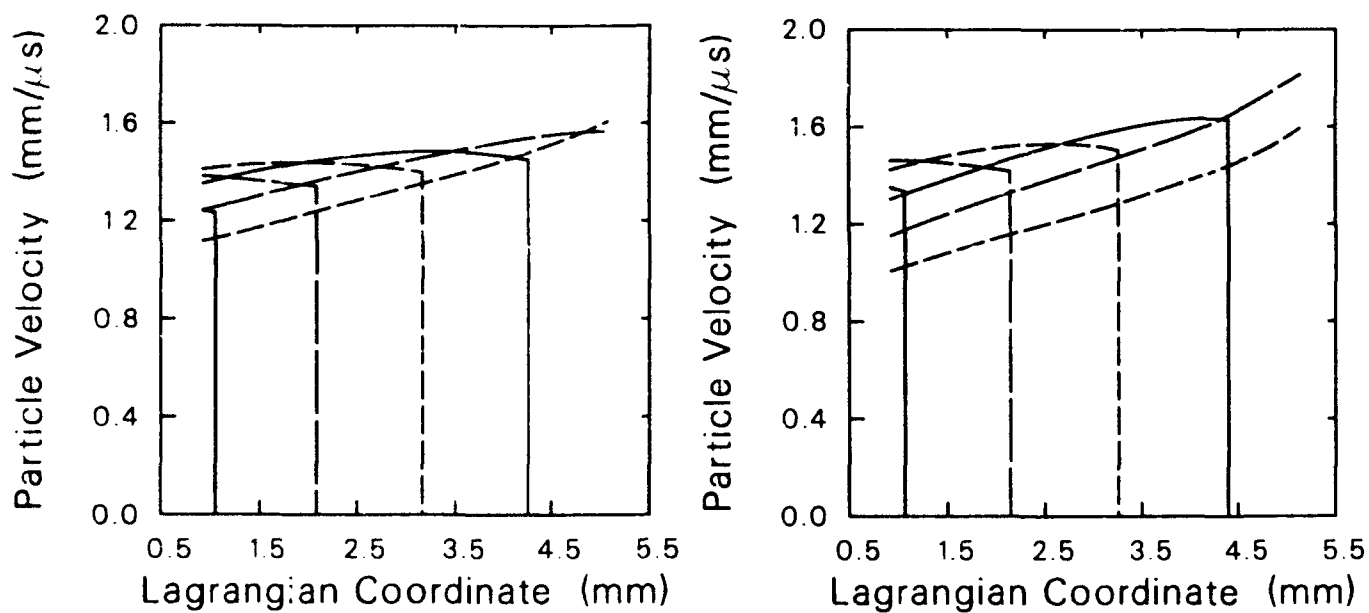


Figure 7 Particle Velocity Snapshot Profiles at Six Times ( $t = 0.2, 0.4, \dots, 1.2$ ) for Shots G705 (Left) and G717 (Right)

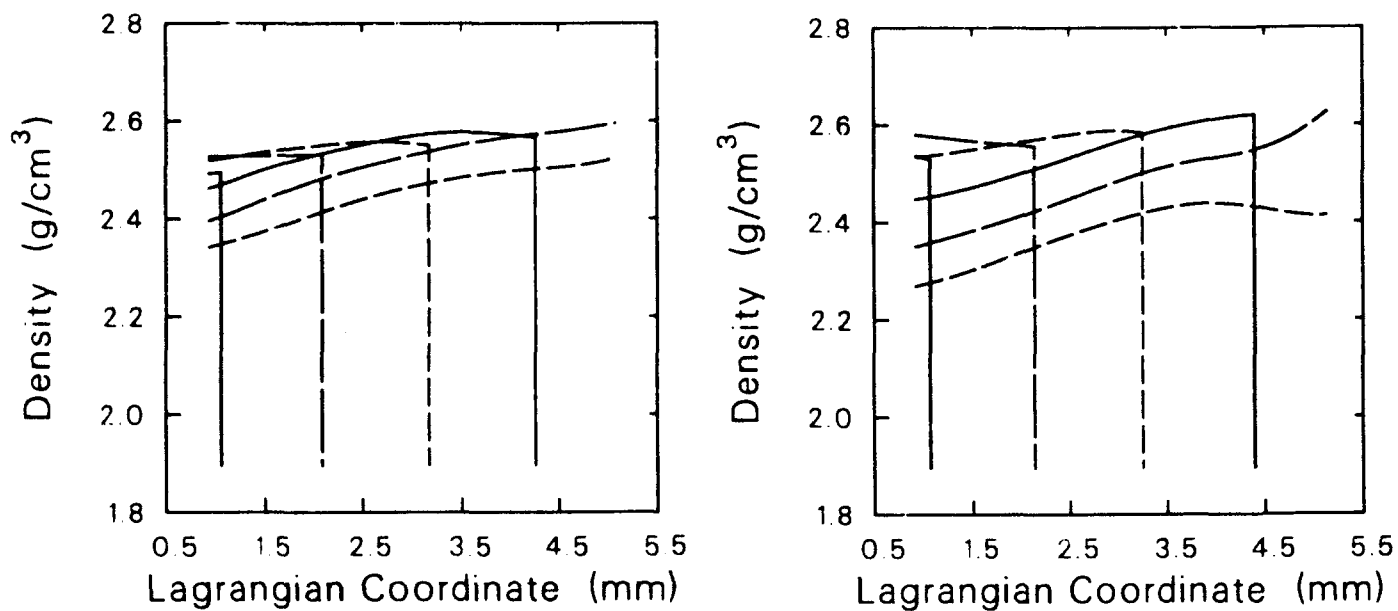


Figure 8 Density Snapshot Profiles at Six Times ( $t = 0.2, 0.4, \dots, 1.2$ ) for Shots G705 (Left) and G717 (Right)

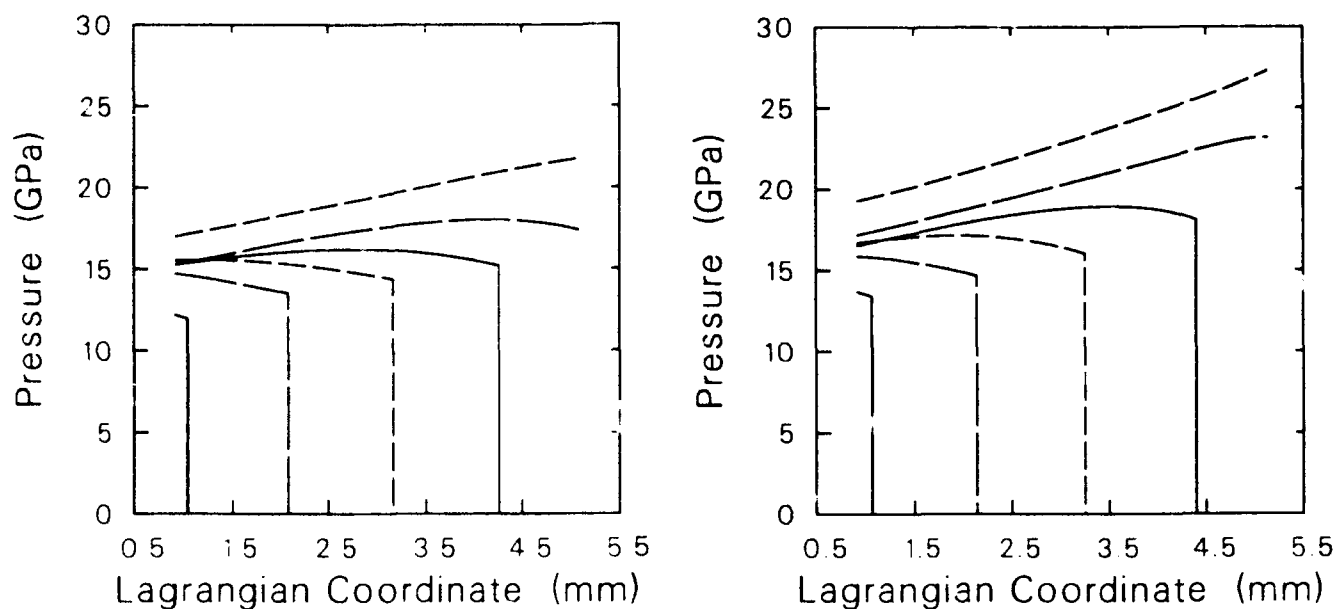


Figure 9. Pressure Snapshot Profiles at Six Times ( $t = 0.2, 0.4, \dots, 1.2$ ) for Shots G705 (Left) and G717 (Right)

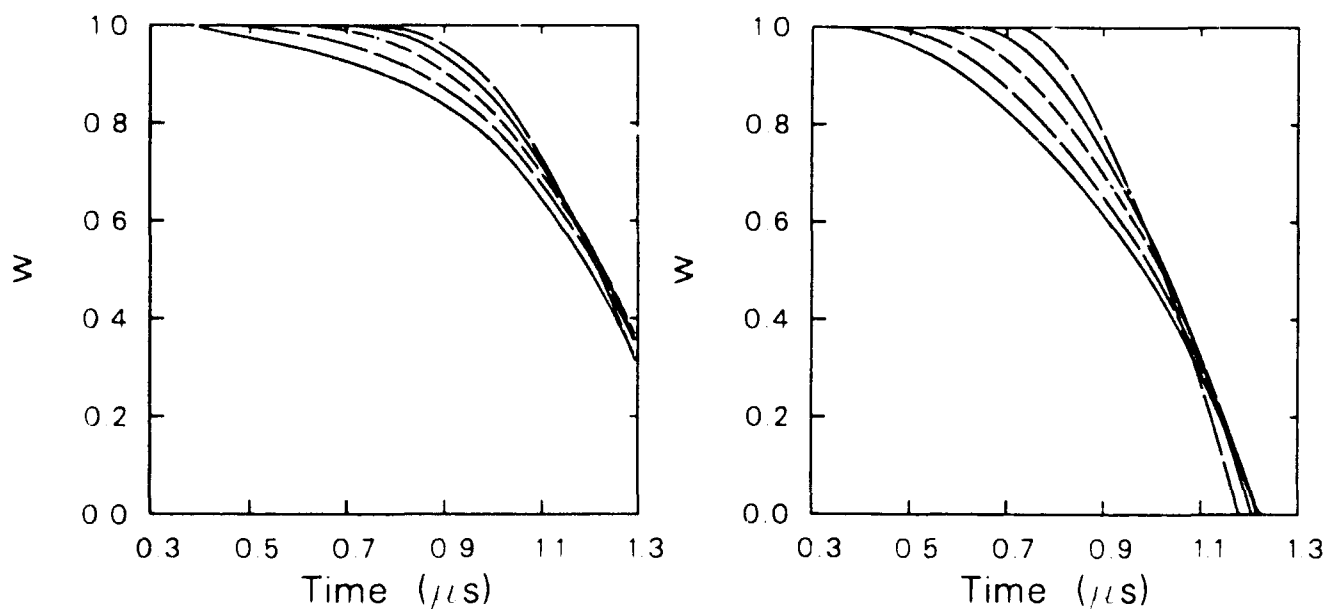


Figure 10. Mass Fraction of Reactant Histories at  $h = 2.0, 2.5, 3.0, 3.5$ , and  $4.0$  for Shots G705 (Left) and G717 (Right)



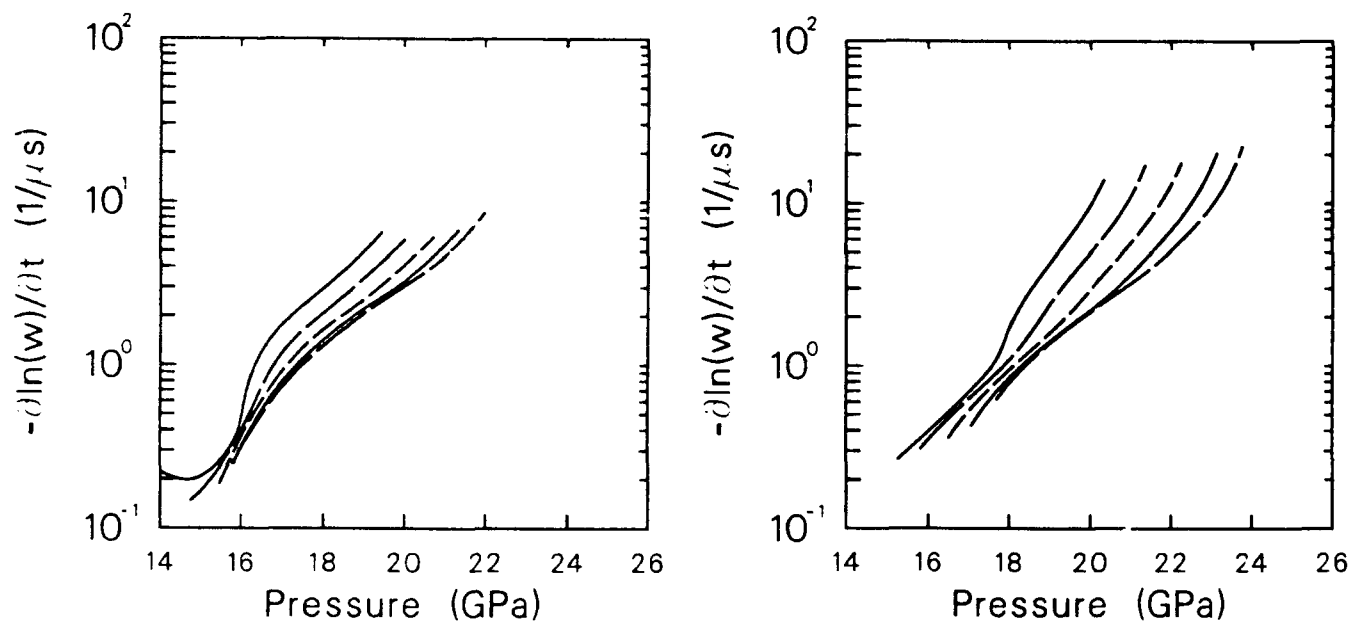


Figure 11. Time Derivative of  $-\ln(w)$  Histories at  $h = 2.0, 2.5, 3.0, 3.5$ , and  $4.0$  for Shots G705 (Left) and G717 (Right)

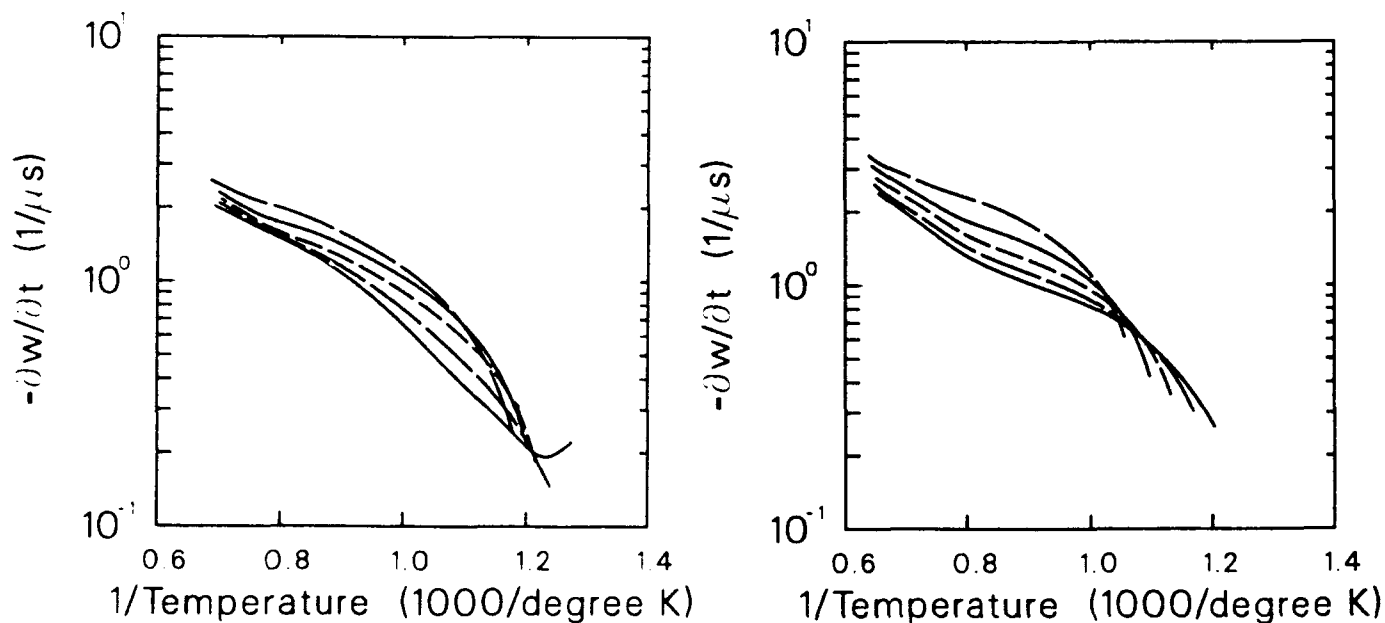


Figure 12. Reaction Rate Histories Versus Equilibrium Temperature at  $h = 2.0, 2.5, 3.0, 3.5$ , and  $4.0$  for Shots G705 (Left) and G717 (Right)

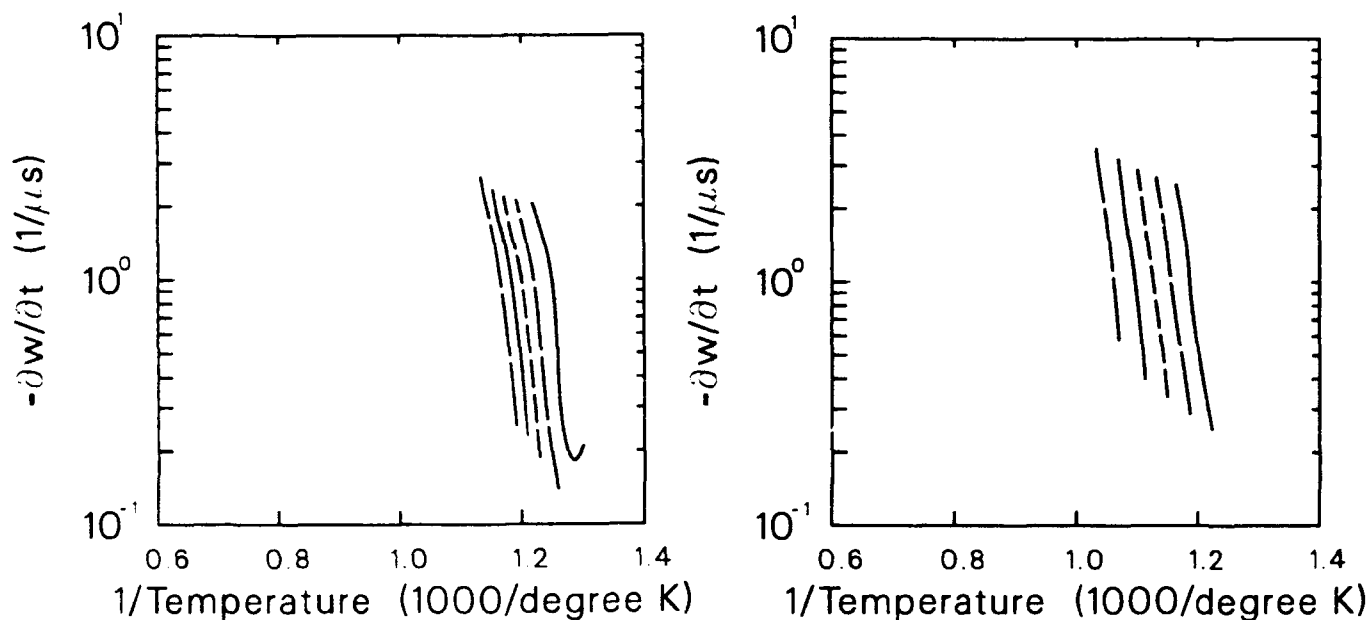


Figure 13. Reaction Rate Histories Versus Isentropic Solid Temperature at  $h = 2.0, 2.5, 3.0, 3.5$ , and  $4.0$  for Shots G705 (Left) and G717 (Right)

Unfortunately, the reaction-rate function or system is not obvious from the common graphs and will require further study of rate forms for its deduction. A possible method to examine a reaction-rate function (or system) is to integrate the rate form by using the derived state histories and compare the integrated reactant histories to the derived reactant histories in the context of a nonlinear least-squares optimization.

## REFERENCES

1. Fowles, R. and Williams, R. F., "Plane Stress Wave Propagation in Solids," *J. App. Phys.*, Vol. 41, Jan 1970, p. 360.
2. Cowperthwaite, M. and Williams, R. F., "Determination of Constitutive Relationships with Multiple Gauges in Nondivergent Waves," *J. App. Phys.*, Vol. 42, No. 1, Jan 1971, p. 456.
3. Grady, D. E., "Experimental Analysis of Spherical Wave Propagation," *J. of Geophysical Research*, Vol. 78, No. 8, Mar 10, 1973, p. 1299.
4. Seamon, L., "Lagrangian Analysis for Multiple Stress or Velocity Gauges in Attenuating Waves," *J. Appl. Phys.*, Vol. 45, No. 10, Oct 1974, p. 4303.
5. Vantine, H. C.; Rainberger, R. B.; Curtis, W. D.; Lee, R. S.; Cowperthwaite, M.; and Rosenberg, J. T., "The Accuracy of Reaction Rates Inferred from Lagrangian Analysis and In-Situ Gauge Measurements," *Proceedings of the Seventh Symposium (International) on Detonation*, NSWC MP 82-334, Annapolis, MD, Jun 1981, p. 466.
6. Vorthman, J.; Andrews, G.; and Wackerle, J., "Reaction Rates from Electromagnetic Gauge Data," *Proceedings Eighth Symposium (International) on Detonation*, NSWC MP 86-194, Albuquerque, NM, Jul 1985, p. 99.
7. Forest, C. A., "Impulse Time-Integral Function and Lagrangian Analysis," *Proceedings of the American Physical Society 1989 Topical Conference on Shock Compression of Condensed Matter*, Eds. Schmidt, S. C.; Johnson, J. N.; and Davison, L. W., Albuquerque, NM, Aug 1989.
8. Mader, C. L., *Numerical Modeling of Detonations*, University of California Press, Berkeley, 1979, p. 412.

# THE HETEROGENEOUS EXPLOSIVE REACTION ZONE

Charles L. Mader and James D. Kershner  
Los Alamos National Laboratory  
Los Alamos, New Mexico 87545

*The calculated reaction zone of PBX-9404 using solid HMX Arrhenius kinetics is stable to perturbations. The calculated reaction zone von Neumann spike pressure agrees with the experimental observations within experimental uncertainty associated with different experimental techniques. The calculated homogeneous explosive reaction zone thickness is larger than observed for the heterogeneous explosive. The effect of two volume percent air holes on the reaction zone was modeled using the three-dimensional Eulerian reactive hydrodynamic code, 3DE. The air holes perturb the reaction zone. A complicated, time-dependent, multidimensional reaction region proceeds through the heterogeneous explosive. The experimentally observed reaction zone characteristic of heterogeneous explosives are mean values of an irregular, three-dimensional reaction region.*

## INTRODUCTION

The hydrodynamic stability of one-dimensional detonations in an ideal gas was studied analytically by Erpenbeck,<sup>1</sup> and numerically by Fickett and Wood;<sup>2</sup> Fickett, Jacobson, and Schott;<sup>3</sup> and Mader.<sup>4</sup> The hydrodynamic stability of two-dimensional detonations in gases was studied by Mader,<sup>4</sup> by Taki and Fujiwara,<sup>5</sup> and by Markov.<sup>6</sup> Mader also studied the stability of detonations in the homogeneous explosives nitromethane and liquid TNT. Detonations of the condensed homogeneous explosives nitromethane and liquid TNT were found to exhibit unstable periodic behavior. The steady-state Chapman-Jouguet theory of the detonation process will not properly describe the homogeneous explosives that exhibit such unstable behavior. Most experimental studies of reaction zone characteristics of explosives have been performed using heterogeneous explosives, rather than liquids or single crystals. Heterogeneous explosives are explosives containing density discontinuities, such as voids or air holes. The shock interactions that occur when shocks interact with voids or air holes, result in local high temperature and pressure regions called "hot spots." These "hot spots" decompose and

add their energy to the flow, and result in the process of heterogeneous shock initiation. The process has been modeled numerically, and is described in detail by the hydrodynamic hot spot model.<sup>7,8,9,10</sup> The success of the three-dimensional numerical models in describing the interaction of shock waves with density discontinuities and of a detonation wave interacting with a matrix of tungsten particles in HMX,<sup>11</sup> encourages us to numerically examine the interaction of a resolved reactive zone in HMX with a two volume percent matrix of air holes.<sup>12</sup> An objective of the study was to determine the nature of the flow being examined in experimental studies of reaction zones of heterogeneous explosives.

## EXPERIMENTAL OBSERVATIONS

The heterogeneous explosive reaction zone that has been the most studied is PBX-9404 (94/3/3HMX/Nitrocellulose/Tris- $\beta$ -Chloroethyl phosphate). A summary of the estimated reaction zone thickness and von Neumann spike pressure is given in Table 1, along with the calculated reaction zone parameters using the solid Arrhenius HMX constants of 34.8 kcal/mole for activation

energy, and  $3 \times 10^4 \mu\text{s}^{-1}$  for frequency factor described in Reference 9.

The metal free-surface measurements of B. G. Craig used the technique described in Reference 13.

The infrared radiometry measurements of W. von Holle used the technique described in Reference 14.

Table 1 PBX-9404 Reaction Zone

Experimental Technique	Reaction Zone Thickness (cm)	$P_{VN \text{ Spike}}$ (kbar)	$P_{C-J}$ (kbar)
Bromoform	0.02	485	
Interferometer	<0.01		
Infrared Radiometry	0.02-0.03		
Metal Free Surface	0.01	550	365
Calculated	0.07	560	365

The interferometer measurements were performed by W. Seitz. The application of this method to reaction zone measurements is described in Reference 15.

The bromoform measurements were made by R. McQueen and J. Fritz, using the technique described in Reference 16.

The calculated reaction zone for "homogeneous" PBX-9404 is larger than the observed reaction zone for heterogeneous PBX-9404; although within the uncertainties associated with experimental interpretation and with the solid Arrhenius constants. We undertook an investigation of the effect of heterogeneities on reaction zone structure, to determine if they might result in a reaction zone whose effective thickness was different than the ideal steady-state reaction zone length.

The calculated steady-state reaction zone for the homogeneous explosive liquid TNT is 0.001 cm; in good agreement with the Hayes

conductivity thickness of 0.0013 cm, and consistent with the Craig upper limit free surface reaction zone thickness of 0.01 cm reported in Reference 7. The observed reaction zone thickness is probably a mean of a periodic flow, since Hayes observed a 1000 megacycle ( $10^{-3} \mu\text{s}/\text{cycle}$ ) oscillation in liquid TNT and we calculate a period of  $5 \times 10^{-2} \mu\text{s}$ .

## NUMERICAL MODELING

The steady-state reaction zone for PBX-9404 was calculated using the one-dimensional reactive hydrodynamic code, *SIN*, the HOM equation-of-state constants described in Reference 7, and the Arrhenius constants for solid HMX described in Reference 9.

The calculated PBX-9404 reaction zone profile is shown in Figure 1.

The time-dependent behavior of the flow in the reaction zone of detonating PBX-9404, was investigated using one-dimensional Lagrangian and three-dimensional Eulerian numerical hydrodynamics. The steady-state solution was stable and perturbations were found to decay. This is in contrast to the time-dependent, unstable, and periodic reaction zones reported for liquid TNT and nitromethane in References 4 and 7.

The stable steady-state reaction zone of PBX-9404 permits us to study the effect of heterogeneities on the reaction zone profile, without the complication associated with a time-dependent reaction zone.

To examine the effect of heterogeneities on the reaction zone, we used the three-dimensional Eulerian reactive hydrodynamic code, *3DE*.<sup>17</sup> It uses the techniques identical to those described in detail in Reference 7, and used successfully for describing two-dimensional Eulerian flow with mixed cells and multicomponent equations of state, and for modeling reactive flow including reaction zone stability.<sup>4</sup>

The three-dimensional computational grid contained 30 cells in the x direction, 28 cells in the y direction, and 57 cells in the z direction; each 0.004 cm on a side. The time increment was  $8 \times 10^{-4} \mu\text{s}$ . At the bottom of the grid was a reaction zone piston, as described in

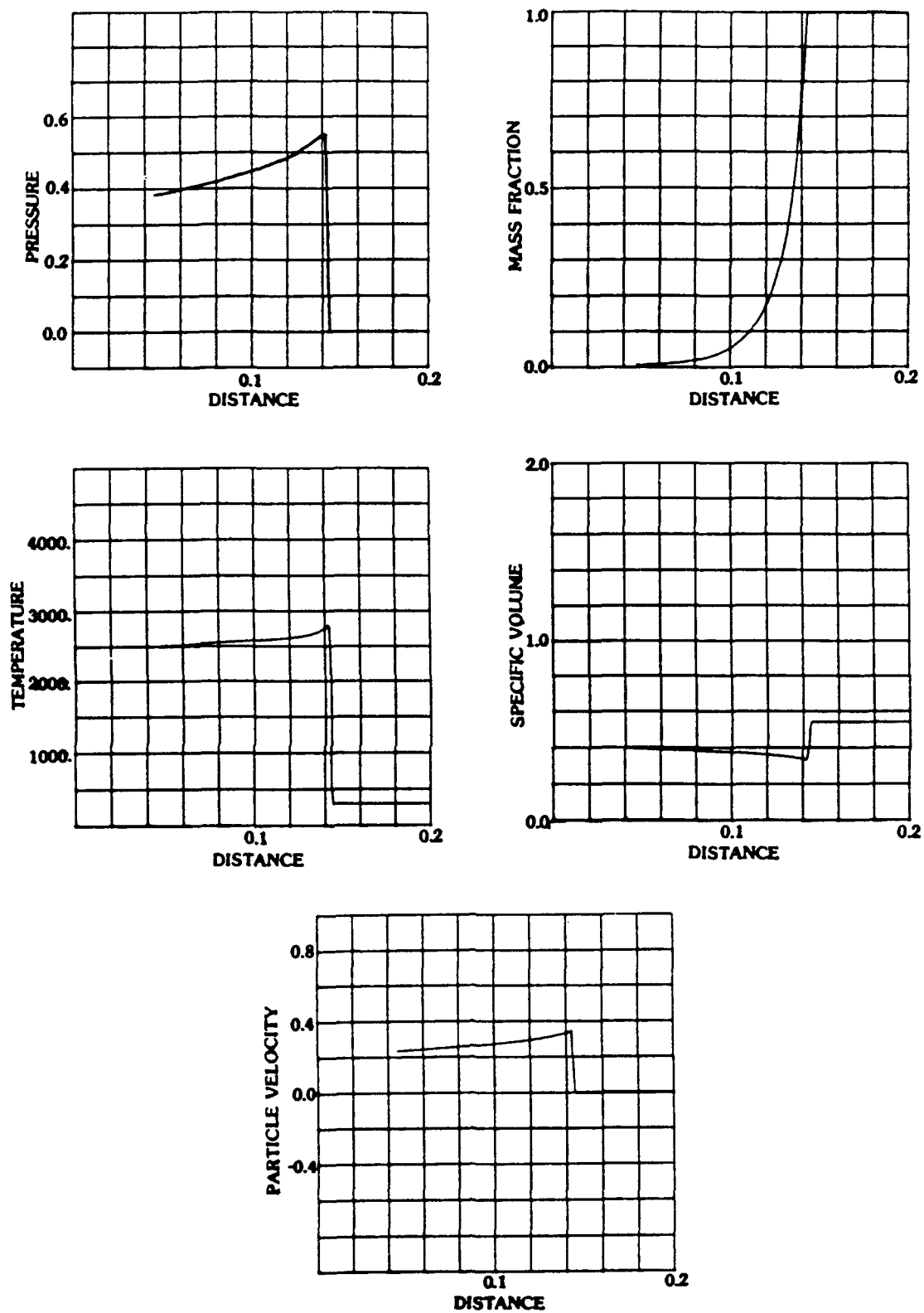


Figure 1. The High Resolution One-Dimensional Reaction Zone Profile of PBX-9404 Calculated Using the SIN Code

References 4 and 7, which was programmed to initialize the flow with a steady-state reaction zone. After the steady-state reaction zone had traveled one reaction zone length in solid PBX-9404, it interacted with a two percent by volume HCP (hexagonal close packed) matrix of air holes.

Thirty-four spherical air holes, each with a diameter of 0.012 cm, occupy a region in the middle of the mesh about 25 cells high. Partial air spheres occur on the boundaries as necessary. The air hole size was chosen to be representative of the actual hole size present in pressed PBX-9404.

Numerical tests with two to six cells per air sphere diameter, showed the results were independent of grid size for 3 or more cells per sphere diameter.

Figure 2 shows the initial configuration of spherical air holes in PBX-9404.

The low resolution necessary for the three-dimensional calculation, results in a less resolved reaction zone than described earlier using the one-dimensional SIN code. The reaction zone burn fraction, as a function of distance, is shown in Figure 3 for the SIN one-dimensional calculation and the 3DE calculation for two viscosity coefficients. The viscosity coefficient shifts the location of the start of the burn. The profile is not significantly changed by variations in the viscosity.

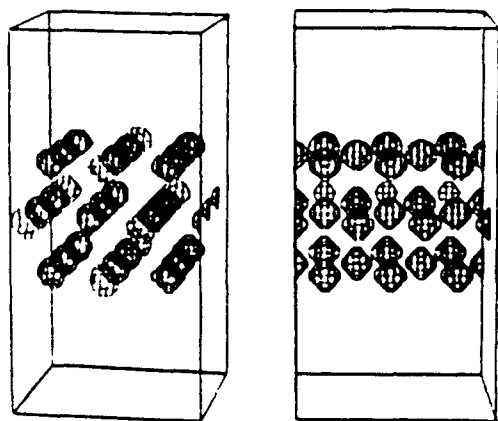


Figure 2. The Initial Configuration of Air Spheres in a Cube of Solid PBX-9404

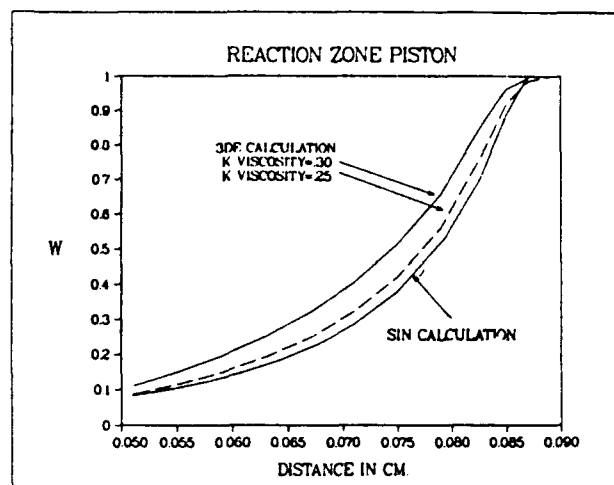


Figure 3. The Reaction Zone Mass Fraction as a Function of Distance for the High Resolution SIN Calculation and Low Resolution 3DE Calculation

The 3DE reaction zone profile for pressure, temperature, particle velocity, and mass fraction, as a function of distance, are shown in Figure 4.

The burn fraction surfaces of a PBX-9404 reaction zone, after it has interacted with the region of two volume percent air spheres, is shown in Figure 5. The heterogenities perturb the reaction zone. A complicated reaction region develops, and is maintained by the reactive flow.

Cross sectional plots of pressure and burn fraction through the 15th cell in the x direction ( $I=15$ ) are shown in Figure 6. A complicated time-dependent, multi-dimensional reaction region proceeds through the heterogeneous explosive.

## CONCLUSIONS

The calculated reaction zone of PBX-9404, using solid HMX Arrhenius kinetics, is stable to perturbations, and a steady-state reaction zone profile is maintained. This is in contrast to the time-dependent, periodic reaction zone calculated for nitromethane and liquid TNT, as described in References 4 and 7.

The effect of two volume percent spherical air holes on the reaction zone, was modeled

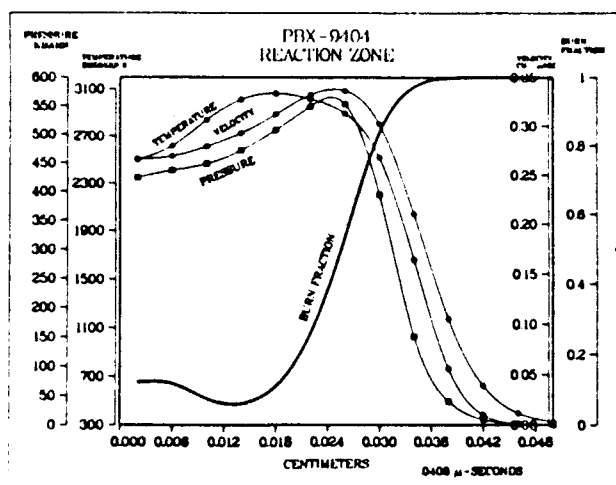


Figure 4 The Reaction Zone Profiles in the 3DE Calculation

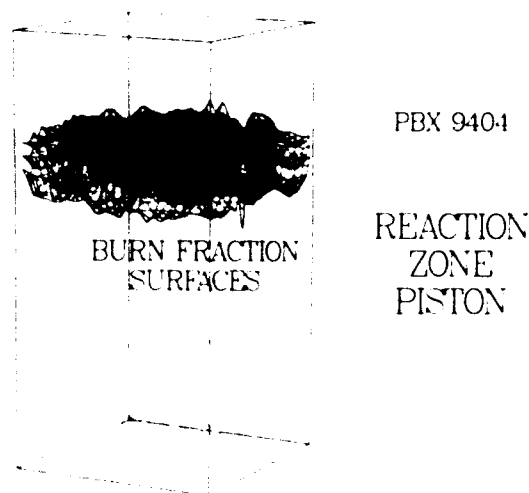


Figure 5 Burn Fraction Surface Profiles After Reaction Zone Interacts with Heterogeneities in PBX-9404

using the three-dimensional Eulerian hydrodynamic code, 3DE. The air holes perturb the reaction zone flow. A complicated reaction region develops, and is maintained by the reactive fluid dynamics.

Thus, any experimental study of a reaction region in a heterogeneous explosive is actually measuring some mean value of an irregular, complicated multidimensional flow. It is not surprising that different experimental techniques may give quite different reaction zone "thicknesses," von Neumann spike pressures, and profiles.

As shown in Table 2 for PBX-9502 and Table 3 for Composition B, the measured reaction zone parameters for heterogeneous explosives vary considerably with the experimental technique. The reported reaction zone thickness for PBX-9502 (95/5TATB/Kel F,  $\rho = 1.894$ ), varies by a factor of 8 between the metal free-surface measurement of Craig<sup>13</sup> and the foil/water measurement reported by Sheffield.<sup>18</sup> The reaction zone lengths for several TATB formulations, reported by Campbell and Engelke,<sup>19</sup> vary from 0.5 to 0.014 cm or by a factor of 35. Some of this variation is probably a result of the different binders and densities of the TATB formulations, and the indirect estimation methods used to obtain some of the reaction zone thickness. As shown in Table 3, the reaction zone thickness of Composition B (64/36 RDX/TNT,  $\rho = 1.713$ ), varies by a factor of 4 between the bromoform measurement and the conductivity measurement of Hayes.<sup>20</sup>

The measured von Neumann spike pressure can also vary with the experimental technique, as shown in Table 3 where the reported Composition B von Neumann spike pressure varies from 374 to 420 kilobars, and in Table 1 where it varies from 485 to 550 kilobars for PBX-9404.

The reaction region in heterogeneous explosives is complicated, time-dependent, and multi-dimensional (nonlaminar).

The reactive region has bounds which approach a steady-state condition, but the flow inside those bounds is multi-dimensional and time-dependent.

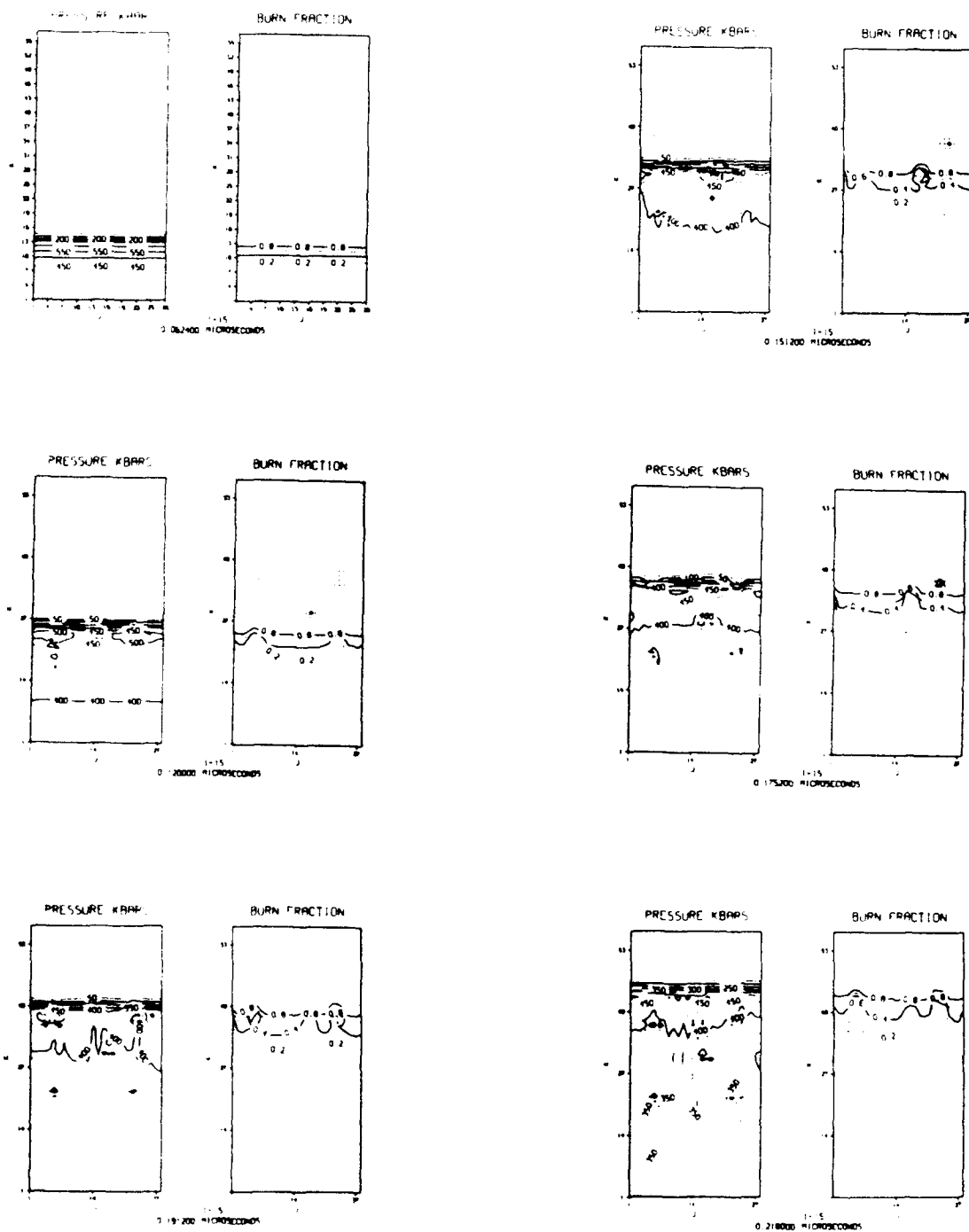


Figure 6 Cross Sectional Plots Through  $I=15$  of Pressure and Burn Fraction Showing the Heterogeneous PBX-9404 Reaction Region



Table 2. PBX-9502 Reaction Zone

Experimental Technique	Reaction Zone Thickness (cm)	$P_{VN\ Spike}$ (kbar)	$P_{C-J}$ (kbar)
Interferometer	0.08-0.16	376	290
Infrared Radiometry	0.08		
Metal Free Surface	0.03		
Foil/Water	0.21	375	
Calculated		377	290

Table 3. Composition B Reaction Zone

Experimental Technique	Reaction Zone Thickness (cm)	$P_{VN\ Spike}$ (kbar)	$P_{C-J}$ (kbar)
Bromoform	0.04	395	285
Interferometer	0.02	420	
Metal Free Surface	0.014	374	
Conductivity	0.013		
Calculated		437	285

## REFERENCES

- Erpenbeck, J. J., "Stability of Idealized One-Reaction Detonations," *The Physics of Fluids*, Vol. 7, 1964, pp. 684-696; Vol. 8, 1965, p. 1192; Vol. 9, 1966, p. 1293.
- Fickett, W. and Wood, W. W., "Flow Calculations for Pulsating One-Dimensional Detonations," *The Physics of Fluids*, Vol. 9, 1966, pp. 903-916.
- Fickett, W.; Jacobson, J. D.; and Schott, G. L., "Calculated Pulsating One-Dimensional Detonations with Induction-Zone Kinetics," *A.I.A.A. Journal*, Vol. 10, 1972, pp. 514-516.
- Mader, C. L., "One- and Two-Dimensional Flow Calculations of the Reaction Zones of Ideal Gas, Nitromethane and Liquid TNT Detonations," *Twelfth Symposium (International) on Combustion*, 1969, pp. 701-710.
- Taki, S. and Fujiwara, T. F., "Numerical Analysis of Two-Dimensional Nonsteady Detonations," *A.I.A.A. Journal*, Vol. 16, 1978, pp. 73-77.
- Markov, V. V., "Numerical Modeling of the Formation of Many-Front Structure of a Detonation Wave," *Doklady Akademii Nauk S.S.S.R.*, Vol. 258, No. 2, 1981, pp. 314-317.
- Mader, C. L., *Numerical Modeling of Detonations*, University of California Press, Berkeley, CA, 1979.
- Mader, C. L. and Kershner, J. D., "Three-Dimensional Modeling of Shock Initiation of Heterogeneous Explosives," *Nineteenth Symposium (International) on Combustion*, 1982, pp. 685-690.
- Mader, C. L. and Kershner, J. D., "Three-Dimensional Modeling of Explosive Desensitization by Preshocking," *Journal of Energetic Materials*, Vol. 3, 1985, pp. 35-47.
- Mader, C. L. and Kershner, J. D., "The Three-Dimensional Hydrodynamic Hot Spot," *Eighth Symposium (International), on Detonation*, 1985, pp. 42-51.
- Mader, C. L.; Kershner, J. D.; and Pimbley, George H., "Three-Dimensional Modeling of Inert Metal-Loaded Explosives," *Journal of Energetic Materials*, Vol. 1, 1983, pp. 293-324.
- Mader, C. L. and Kershner, J. D., "Numerical Modeling-of-the-Reaction Zone in Heterogeneous Explosives," *Journal of Energetic Materials*, Vol. 5, 1987, pp. 143-155.
- Craig, B. G., "Measurements of the Detonation-Front Structure in Condensed-Phase Explosives," *Tenth Symposium (International) on Combustion*, 1965, pp. 863-867.
- von Holle, W. G. and McWilliams, R. A., "Application of Fast Infrared Detectors to

Detonation Science," *S.P.I.E. Proceedings*, Vol. 366, 1983, pp. 19-26.

15. Seitz, W. L.; Stacy, H. L.; and Wackerle, J., "Detonation Reaction Zone Studies on TATB Explosives," *Eighth Symposium (International) on Detonation*, 1986, pp. 99-110.
16. McQueen, R. G. and Fritz, J. N., "The Reaction Zone of High Explosives," Los Alamos National Laboratory Report M-6-530, 1983.
17. Mader, C. L. and Kershner, J. D., "Three-Dimensional Modeling of Triple Wave Initiation of Insensitive Explosives," Los Alamos Scientific Laboratory Report LA-8206, 1980.
18. Sheffield, C. A.; Bloomquist, D. D.; and Tarver, C. M., "Subnanosecond Measurements of Detonation Fronts in Solid High Explosives," *Journal of Chemical Physics*, Vol. 80, 1984, pp. 3831-3844.
19. Campbell, A. W. and Engelke, R., "The Diameter Effect in High-Density Heterogeneous Explosives," *Sixth Symposium (International) on Detonations*, 1976, pp. 642-652.
20. Hayes, B., "Electrical Measurements in Reaction Zones of High Explosives," *Tenth Symposium (International) on Combustion*, 1965, pp. 869-874.

## DISCUSSION

JOHN BDZIL  
Los Alamos National Laboratory  
Los Alamos, NM

Your BD simulations show the voids in the unshocked and presumably unreacted material seem to be undergoing changes before the arrival of the shock. Does this indicate a possible precursor wave traveling ahead of the main shock?

## REPLY BY CHARLES L. MADER

The main shock is three cells thick which results in the effect you observed in the computer film showing the pressure and mass fraction contours. It is not a result of a precursor wave. The shock smear and numerical resolution were shown to be independent of the important conclusions of this paper. The reactive region in heterogeneous explosives is complicated, time-dependent, multi-dimensional, and has bounds which approach a steady condition, but the flow inside those bounds is far from steady-state.

# USING SMALL SCALE TESTS TO ESTIMATE THE FAILURE DIAMETER OF A PROPELLANT\*

C. M. Tarver and L. G. Green  
Lawrence Livermore National Laboratory  
Livermore, California 94550

*Electric gun and gas gun shock initiation experiments using embedded manganin pressure gauges were employed to determine high pressure reaction rates of propellants. This reaction rate data was used to develop ignition and growth reactive flow computer models, which then predict the unconfined failure diameter of these propellants. Two ammonium perchlorate/binder/aluminum propellants were studied: one containing no HMX and one containing 12 percent HMX. The propellant containing no HMX exhibited no reaction in any of the experiments. In the short pulse duration electric gun and the lower pressure gas gun experiments, the HMX-containing propellant exhibited partial reactions indicating that only the 12 percent HMX reacted. At 20 GPa input pressures, the rest of the propellant mixture reacted and the reaction rates were quantitatively measured and calculated. Using these reaction rates, the unconfined failure diameter of the 12 percent HMX propellant was calculated to be between 2.5 and 3 inches.*

## INTRODUCTION

When a propellant passes a large-scale card gap test for a class 1.3 (nondetonable) classification, it may still be detonable with fewer cards or in larger dimensions than those used in the test. Failure to detonate with zero cards can generally be related to the scale of the gap test and the failure diameter of the test propellant or explosive. Since these propellants are used in motors that can be several feet in diameter, full-scale failure diameter tests for all applications may not be feasible. In this study, smaller scale shock initiation tests which use embedded manganin pressure gauges to determine propellant reaction rates at pressures approaching detonation are developed to furnish reactive flow data for a two-dimensional computer code model. This model

is then used to predict the unconfined failure diameter of the propellant and also other large-scale hazard scenarios of the reacting propellant with and without confinement.

Two propellant formations were chosen for experimentation and modeling. One (Propellant A) contained no HMX, just ammonium perchlorate (AP), binder, and aluminum. The second (Propellant B) contained 12 percent HMX along with the other materials. Both propellants were tested in a series of electric gun flyer plate impact experiments to determine shock initiation thresholds in the 20-45 GPa impact pressure, 28-130 ns pulse duration regime. Then the propellants were tested in sustained pulse experiments using a 4-inch gas gun and embedded multiple manganin pressure gauges for measuring pressure increases due to reaction at 13, 16, and 20 GPa. Using this data, together with unreacted and reaction product equation of state data in the ignition and growth reactive flow model,<sup>1</sup> reactive flow models were developed to calculate these tests and then used to calculate

\*Work performed under the auspices of the U.S. Department of Energy by the Lawrence Livermore National Laboratory under contract number W-7405-Eng-48.

the unconfined failure diameter of the propellant. A final configuration test of the failure diameter calculation using a variable diameter configuration and embedded gauges to measure radial pressure histories and detonation wave front curvature is also discussed.

## ELECTRIC GUN EXPERIMENTS AND CALCULATIONS

Eighteen electric gun experiments were fired on the two propellants. Table 1 lists the nine experiments on propellant A: the initial pressure, pulse duration, target thickness, average measured shock velocity, and the calculated shock velocity assuming no reaction and an unreacted Gruneisen equation of state  $U_s = 2.3 + 2.1 u_p$ , where  $U_s$  is shock velocity and  $u_p$  is particle velocity. The close agreement between the measured velocities and these calculations implies that no reaction occurs in these experiments on propellant A, which contains no HMX.

Table 2 lists the nine similar shots on Propellant B, which contains 12 percent HMX. The shock velocities calculated assuming no reaction are much lower than the measured shock velocities, implying that some reaction did occur. The reactive flow calculations listed in Table 1 assume that 1.5 percent of the propellant reacts during shock compression and

then the 12 percent HMX reacts at the rates previously determined for other HMX-based explosives, PBX-9404, LX-14, RX-26-AF, and RX-25-xx.<sup>1-4</sup> In these short pulse duration experiments in which the leading shock velocity and pressure decay as the rear rarefaction wave overtakes the front, not all of the 12 percent HMX reacts even at the impact face. The reactive flow calculated shock velocities agree closely with the experimental measurements implying that the fractions of HMX reacted are correct as functions of pressure and pulse duration. No evidence of reaction in the other materials in these propellants can be inferred from the shock velocity experiments.

## EMBEDDED GAUGE EXPERIMENTS AND CALCULATIONS

To determine whether the non-HMX Propellant A could be driven to react in high pressure sustained pulse experiments, it was impacted with shock pressures of 13, 16, and 19 GPa. No evidence of reaction was apparent in any of the embedded manganin gauge records from these three experiments. Apparently HMX is required as a "match" to ignite the AP, binder, and aluminum reactions. To determine whether the AP in Propellant B could be initiated by the 12 percent HMX, similar embedded gauge experiments were fired using Propellant B. Figure 1 shows that

Table 1. Propellant A Electric Gun Shots

Initial Pressure (GPa)	Pulse Duration (ns)	Target Thickness (mm)	Average Shock Vel. (mm/ $\mu$ s)	Calculated Shock Vel. (mm/ $\mu$ s)
21	114	6.35	4.59	4.85
21	114	12.70	4.03	4.19
21	64	6.35	4.08	4.24
21	32	6.35	3.75	3.75
33	53	6.35	4.62	4.64
33	53	12.70	4.00	3.96
33	26	6.35	4.01	3.98
43	23	6.35	4.28	4.19
43	23	12.70	3.78	3.62

EOS:  $U_s = 2.3 \text{ mm}/\mu\text{s} + 2.1 u_p$ ;  $\rho_0 = 1.743 \text{ g/cm}^3$ .

Table 2. Propellant B Electric Gun Shots

Target Thickness (mm)	Measured Shock Vel. (mm/μs)	Calculated (No Reaction) (mm/μs)	Calculated (Reactive Flow) (mm/μs)
6.35	5.17	4.98	5.35
12.70	4.79	4.30	4.76
6.35	4.75	4.39	4.77
6.35	3.71	3.85	4.18
6.35	5.14	4.78	5.15
12.70	4.74	4.11	4.70
6.35	4.52	4.12	4.46
6.35	5.02	4.31	4.66
12.70	4.22	3.77	4.29

the experimental and calculated pressure histories for Propellant B shocked to 13 GPa at the interface (0 mm) and 13 mm deep positions. The 13-mm gauge shows an increased shock pressure plus a maximum pressure peak closer to the front than the 0 mm gauge in Figure 1, indicating faster HMX rates at higher pressures. At 13 and 16 GPa, the HMX-containing propellant showed slow small pressure increases which were accurately calculated by assuming that the HMX component of Propellant B reacted completely and that no

additional reactions were initiated in the other components. Table 3 contains the equation of state, reaction rate law coefficients, and detonation parameters for Propellant B used in this paper. The unreacted and product equations of state are both JWL (i.e., Gruneisen) forms

$$p = Ae^{-R_1 V} + Be^{-R_2 V} + \frac{\omega C_v T}{V} \quad (1)$$

where  $p$  is pressure;  $V$  is relative volume;  $T$  is temperature; and  $A, B, R_1, R_2, \omega$  (the Gruneisen coefficient), and  $C_v$  (the average heat capacity) are constants. The ignition and growth reaction rate law is of the form:

$$\frac{\partial F}{\partial t} = I(1-F)^b(\rho/\rho_0 - 1 - a)^x + G_1(1-F)^c F^d p^y + G_2(1-F)^e F^g p^z \quad (2)$$

where  $F$  is the fraction reacted;  $t$  is time;  $p_0$  is initial density;  $\rho$  is current density;  $p$  is pressure in Mbars; and  $I, G_1, G_2, b, x, a, c, d, y, e, g,$  and  $z$  are constants. The first rate is the hot spot ignition term and is set equal to zero when  $F$  exceeds  $F_{\text{igmax}}$ , which is 0.015 for this propellant. The second term describes the growth rate of ignited hot spots and previously published HMX rates are used until  $F$  exceeds 0.12 or  $F_{G1\text{max}}$  in Table 3. The third term describes the global reaction for the rest of the propellant (AP/binder/Al).

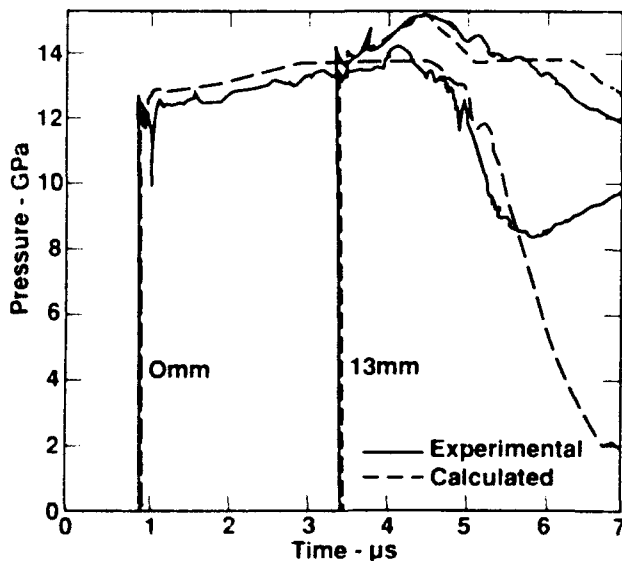


Figure 1. Experimental and Calculated Pressure Histories for Propellant 13 GPa

Table 3. Equation of State and Reaction Rate Coefficients for Propellant B (12 Percent HMX)

JWL Parameters	Unreacted	Products	Reaction Rate Parameters	
$\rho_0$ (g/cm <sup>3</sup> )	1.848	-	$I$ ( $\mu$ s) <sup>-1</sup>	40.0
A (Mbars)	40.66	7.737	b	0.667
B (Mbars)	-1.339	0.1155	a	0.0
R <sub>1</sub>	7.2	4.8	x	4.0
R <sub>2</sub>	3.6	1.2	$G_1$ (Mbars <sup>-y</sup> $\mu$ s <sup>-1</sup> )	3.1
$\omega$	0.8351	0.24	c	0.667
$C_v$ (Mbars/K)	$2.5035 \times 10^{-5}$	$1.0 \times 10^{-5}$	d	0.111
T <sub>0</sub> (K)	298	-	y	1.0
E <sub>0</sub> (Mbars-cc/cc-g)	-	0.120	$G_2$ (Mbars <sup>-z</sup> $\mu$ s <sup>-1</sup> )	18.0
			e	1.0
			g	0.111
			z	2.0
			Figmax	0.015
			F <sub>G1max</sub>	0.12

The two 19 GPa shots on Propellant B employed a relatively new manganin gauge technique<sup>5</sup> in which a series of gauges is placed along an explosive wedge so that each gauge is not perturbed by wave interactions produced by previous gauges. In these experiments the gauges were placed 2 mm apart in the flow direction. Figure 2 shows some of the experimental gauge records for a 19 GPa, 1  $\mu$ s shock pulse into Propellant B and the corresponding reactive flow calculations. In this case, some of the AP and/or binder material did react because the initial shock grows to a detonation-type wave of approximately 25 GPa peak pressure at approximately 19 mm. The reactive flow calculation uses the regular HMX rates for the first 12 percent reaction, and then the second growth term in the ignition and growth rate law is used to globally calculate the AP/binder/aluminum energy release. Figure 3 shows the calculated fraction reacted histories at the four reported gauge positions 0, 11, 15, and 19 mm.

A second high pressure experiment is shown in Figure 4 which contains the embedded gauge pressure histories for propellant shocked to 20 GPa for 0.7  $\mu$ s at the 0, 10, 14, and 18 mm positions. In this experiment, the shock pressure grows to 25 GPa at 10 mm but

the transition to detonation does not quite occur, as evidenced by lower peak pressures at 14 and 18 mm in Figure 4. The reactive flow calculations also predict this pressure buildup without detonation formation. Figure 5 shows the calculated fraction reacted histories at the

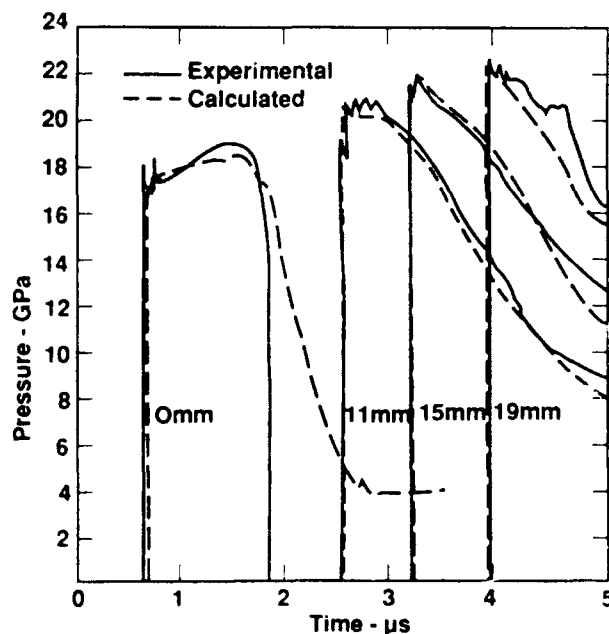


Figure 2. Experimental and Calculated Pressure Histories for Propellant B Shocked to 19 GPa for 1  $\mu$ s

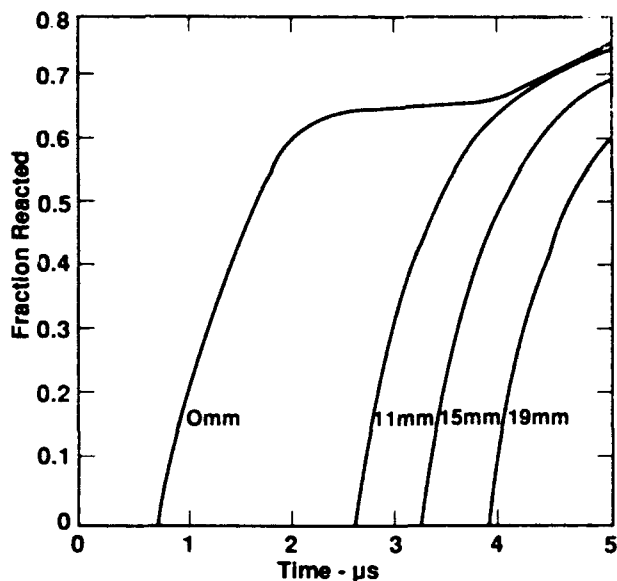


Figure 3. Calculated Fraction Reacted Histories for Propellant B Shocked to 19 GPa for 1  $\mu$ s

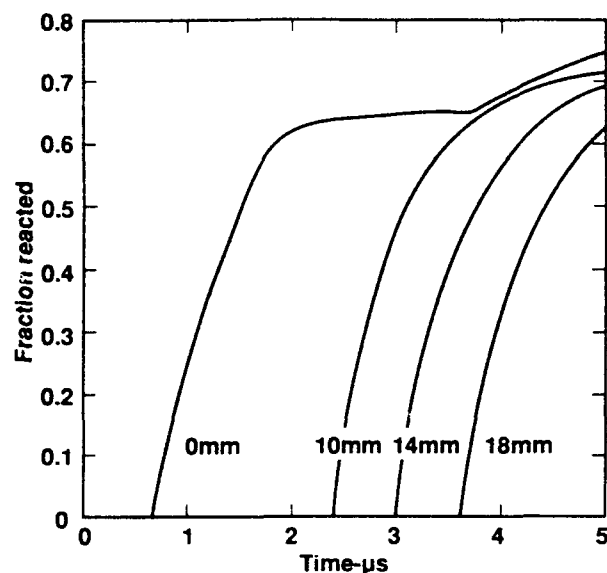


Figure 5. Calculated Fraction Reacted Histories for Propellant B Shocked to 20 GPa for 0.7  $\mu$ s

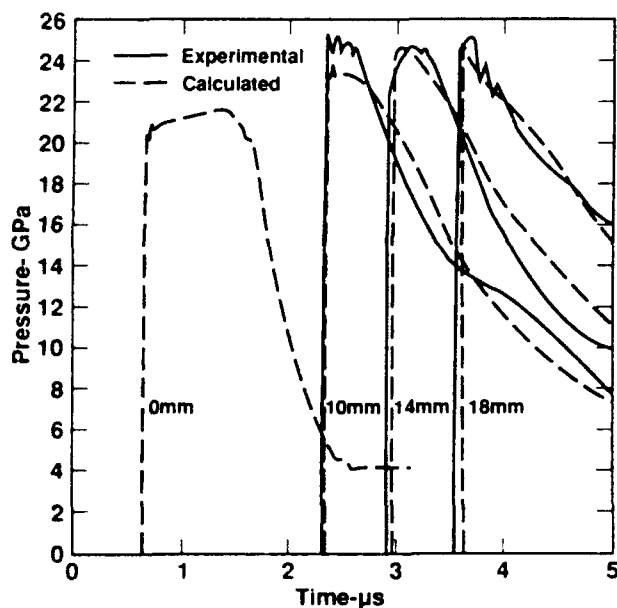


Figure 4. Experimental and Calculated Pressure Histories for Propellant B Shocked to 20 GPa for 0.7  $\mu$ s

0, 10, 14, and 18 mm positions. As compared to Figure 3, these fraction reacted histories start out at the 0 mm position reacting more quickly due to the higher initial shock pressure. However, since the pulse duration is shorter in this experiment, the growth of reaction is slightly slower at the deeper gauge positions as the rarefaction wave overtakes the high pressure region. Generally, such

marginal high pressure shock initiation calculations are the toughest test for reactive flow models so the accurate calculation in Figure 4 implies that this reaction rate is reliable in this relatively narrow pressure regime which approaches detonation conditions. Therefore, the use of the reaction rates in Table 3 for Propellant B are applied to the unconfined failure diameter estimation in the next section.

## FAILURE DIAMETER ESTIMATIONS

The reactive flow model for Propellant B was used in the DYNA2D hydrodynamic code<sup>6</sup> to estimate the unconfined charge diameter above which self-sustaining detonation continues to propagate and below which the initial detonation wave from a donor explosive charge decays in velocity and pressure, and eventually fails to propagate. Failure diameter modeling just consists of donor and acceptor charges of adequate lengths and of various diameters. Formulations similar to Propellant B generally have failure diameters of a few inches so the modeling began with calculations of 2-, 4-, 6-, and 8-inch diameter charges. Both Composition B and TNT were used in donor charges of various lengths. In the preliminary calculations, the 2 inch diameter charge failed to detonate, while 4 inch and larger diameters

detonated. Detailed calculations using 10 zones per centimeter were then run with 5 cm long Composition B donors and 20 cm long Propellant B acceptors at diameters of 2.5 inches (6.35 cm), 3 inches (7.62 cm), and 3.5 inches (8.89 cm). Figures 6 and 7 show the calculated pressure and fraction reacted contours, respectively, for the 3.5 inch (8.89 cm) diameter failure diameter calculation near the end of the 20-cm charge length. After an initial transient from the booster charge, a detonation wave with constant pressure, velocity, and curvature developed in Propellant B. The maximum pressure was 28.6 GPa, as shown in Figure 6, and approximately 78 percent of the reaction occurred within 0.9 cm of the shock front and 88 percent within 1.7 cm of the shock front, as shown in Figure 7. Figures 8 and 9 show similar contours for the 3-inch (7.62 cm) failure diameter calculation. In this case, a detonation wave was established which slowly approached a constant pressure and curvature near the end of the charge. As shown in Figure 8, the maximum pressure was 24.6 GPa and the detonation took approximately 1  $\mu$ s longer to reach the end of the charge than did

the 3.5-inch diameter calculation. Figure 9 shows that the 77 percent fraction reacted contour is approximately 1.4 cm behind the shock front and the 87 percent contour is 3 cm back. Figures 10 and 11 contain similar contours for the 2.5-inch (6.35 cm) calculation, which resulted in a continuously decreasing pressure and velocity wave whose peak pressure decayed to 17.7 GPa after 20 cm. Figure 10 shows the pressure contours at the same position as Figures 6 and 8. An additional run time of 2  $\mu$ s was required to reach that position, as compared to the 3 inch calculation in Figure 8. Figure 11 shows the fraction reacted contours for the 2.5-inch diameter calculation. The 65 percent reacted contour is 2.7 cm behind the shock front on the charge axis and the 75 percent reacted contour is over 7 cm back. Longer charge lengths of 2.5-inch diameter Propellant B were run to insure that this failing wave does completely die out eventually.

Therefore, the calculated failure diameter of Propellant B is between 2.5 inches (6.35 cm) and 3 inches (7.62 cm). Obviously, additional calculations could determine the failure diameter as precisely as required. As a check on this method of predicting failure diameters from embedded gauge data, a "proof of principle" experiment has been assembled and will be

Time=34  $\mu$ s Contours of Pressure  
Max=28.6GPa

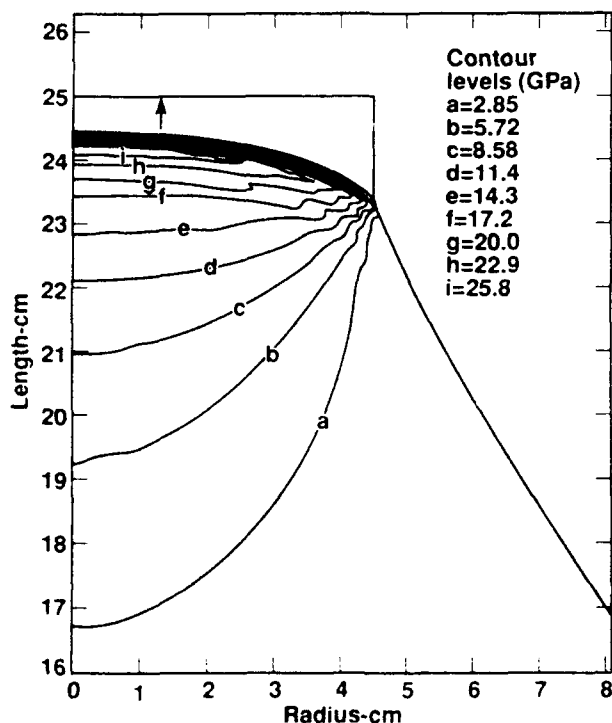


Figure 6. Pressure Contours for Detonating Propellant B (3.5-Inch Diameter)

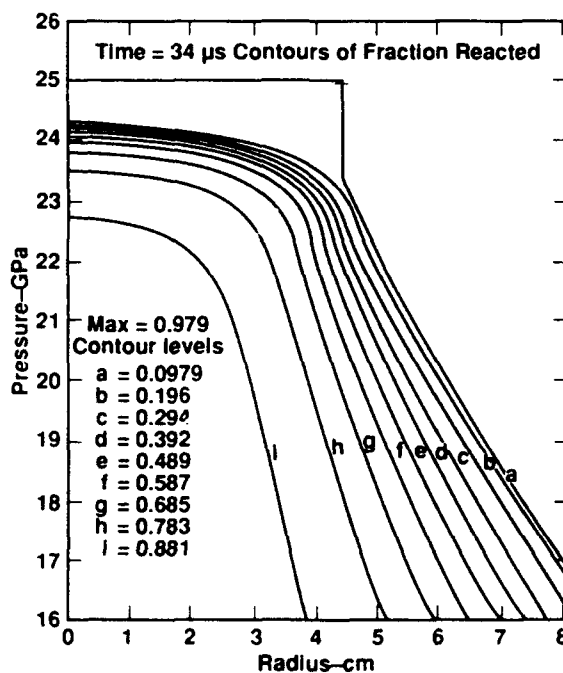


Figure 7. Fraction Reacted Contours for Detonating Propellant B (3.5 Inch Diameter)



Time=35  $\mu$ s contours of pressure  
Max=24.6GPa

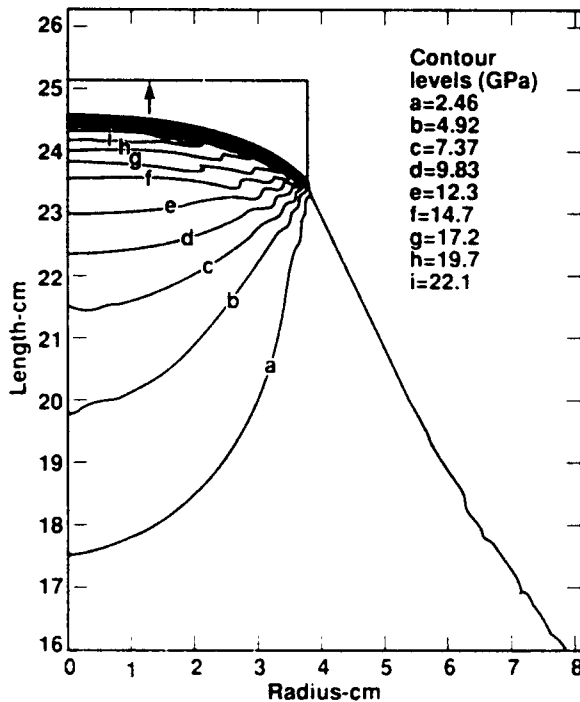


Figure 8. Pressure Contours for Detonating Propellant B (3-Inch Diameter)

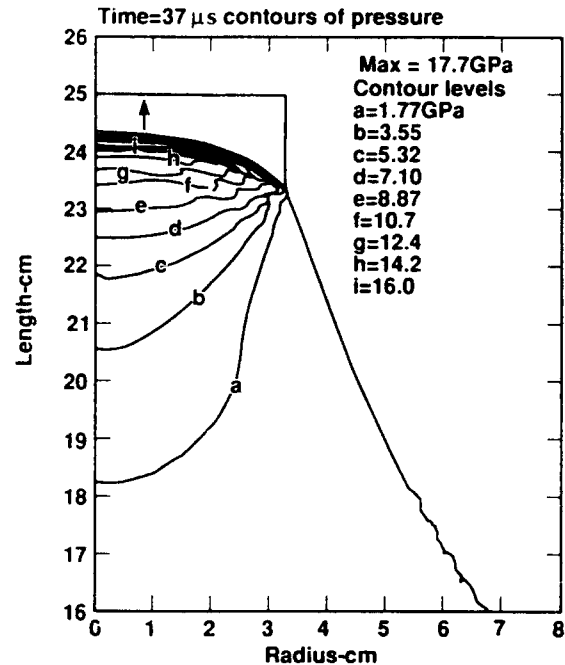


Figure 10. Pressure Contours for Failing Propellant B (2.5-Inch Diameter)

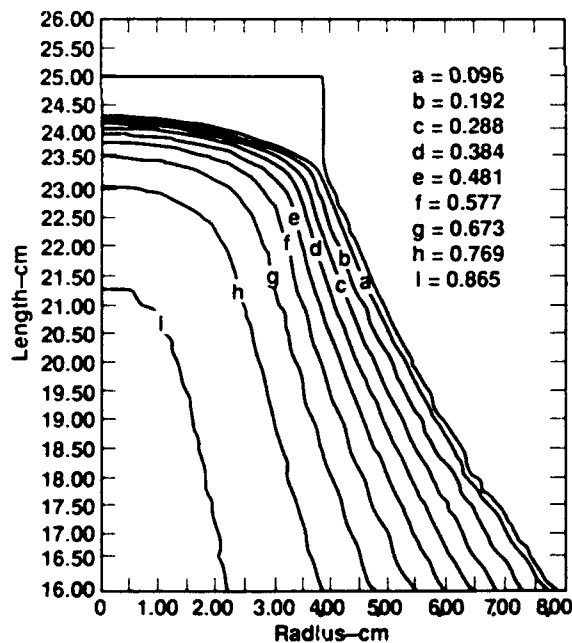


Figure 9. Fraction Reacted Contours for Detonating Propellant B (3-Inch Diameter)

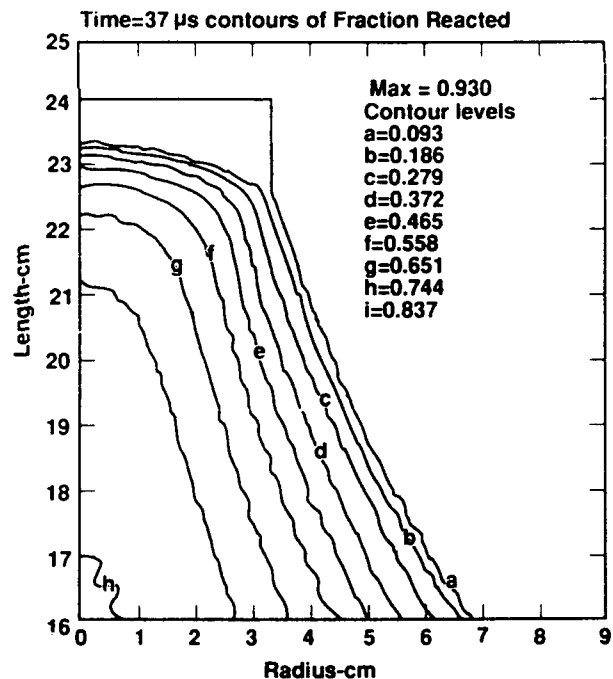


Figure 11. Fraction Reacted Contours for Failing Propellant B (2.5-Inch Diameter)

fired soon. Figure 12 shows the dimensions of the four explosive sections: a 3.5-inch diameter by 7-inch long Composition B booster

initiated by an SE-1 detonator and a disk of PBX-9407; a 3.5-inch diameter by 10-inch long charge of Propellant B; a 3-inch diameter by

9.75-inch long charge of Propellant B; and a 2.5-inch diameter by 8.625-inch charge of Propellant B. This test will be heavily instrumented with time of arrival switches for velocity measurements *plus* arrays of embedded manganin gauges near the ends of the 3.5-inch diameter and the 2.5-inch diameter sections of Propellant B. These gauges will furnish pressure histories at several positions across the curved detonation wave at 3.5-inch diameter and the decaying shock front at 2.5-inch diameter. Such pressure measurements will be an essential check on the radial dependence of shock front pressure and reaction zone shape. Detailed calculations of this variable diameter test have shown very similar peak pressures, velocities, and curvatures to the individual failure diameter calculations in Figures 6 through 11. Figures 13 and 14 show the calculated pressure contours for the 3.5-inch diameter and 2.5-inch diameter sections, respectively, at the embedded gauge positions (approximately four centimeters from the ends of the sections). Such time resolved data will be the key element in normalizing reactive flow models and eventually in determining how much reaction must be eliminated by rarefaction waves to cause detonation wave failure.

## CONCLUSIONS

Electric gun and four-inch gun shock initiation experiments to determine the pressure and time conditions for and the extent of reaction were run to two propellants, one without HMX and one with HMX. Propellant

A with no HMX did not react in any of the experiments and, therefore, is considered highly unlikely to detonate even in charges several feet in diameter. It is very likely that HMX or another reactive material is required as an ignition source to start rapid decomposition. In the electric gun and lower pressure gas gun experiments, only some or all of the 12 percent HMX in Propellant B reacted. However, at 19 GPa input pressure, the AP/binder/Al partially reacted. The measured pressure histories may be the first quantitative measurements of AP reacting under these shock conditions. These gauge records also served as

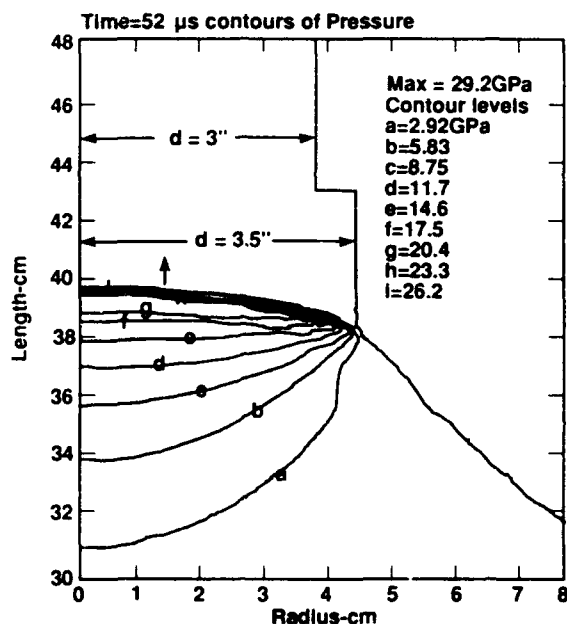


Figure 13. Pressure Contours in the 3.5-Inch Diameter Section of the Failure Diameter Test

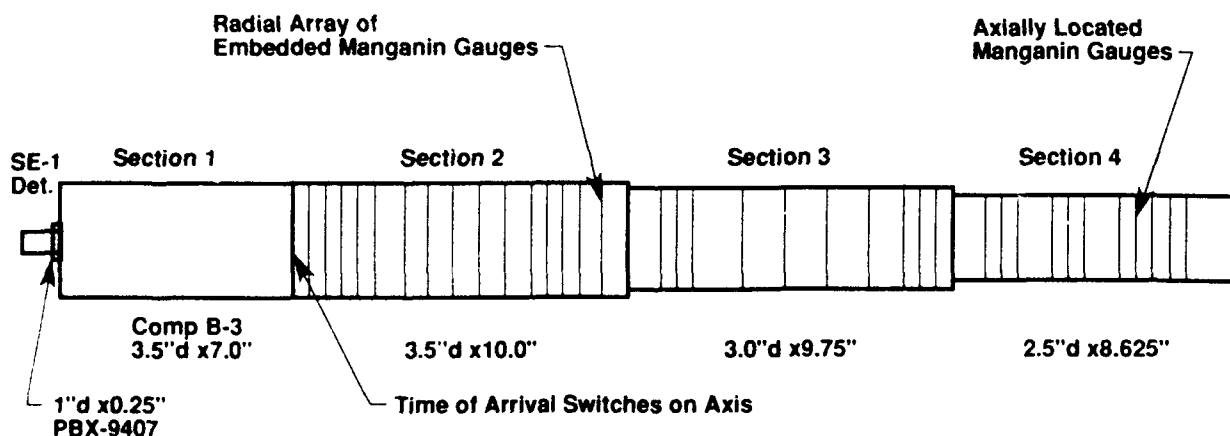


Figure 12. Failure Diameter Test Assembly

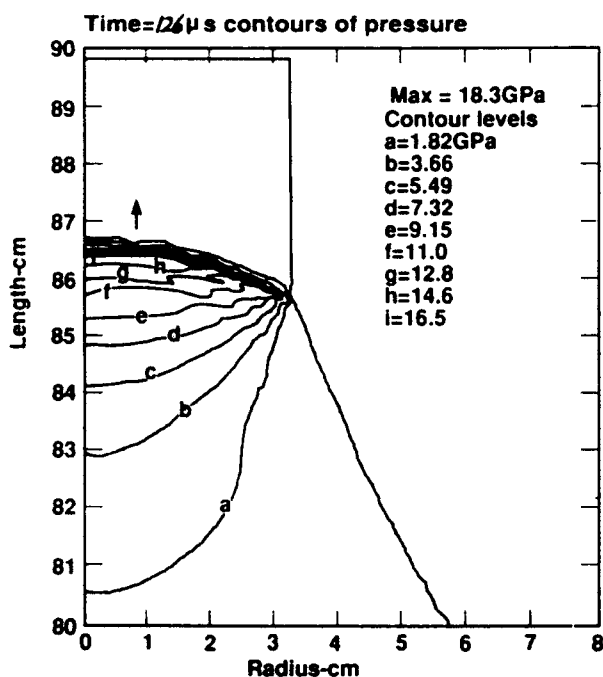


Figure 14. Pressure Contours in the 2.5-Inch Diameter Section of the Failure Diameter Test

the basis for developing a global reaction rate for the AP/binder/Al portion of Propellant B.

The reactive flow parameters predicted a failure diameter of between 2.5 and 3 inches. Such a propellant would be considered as a class 1.3 material, but could detonate in charge diameters slightly larger than the 2-inch diameter large scale gap test. This failure diameter estimation will be tested experimentally in a large scale variable diameter test on Propellant B.

To be considered useful and trustworthy, the procedure for estimating failure diameter developed in this study must be tested on other types of propellants or explosives whose failure diameters are known or can be measured.

## REFERENCES

1. Tarver, C. M.; Hallquist, J. O.; and Erickson, L. M., *Eighth Symposium (International) on Detonation*, Naval Surface Weapons Center, NSWC MP 86-194, 1985, p. 951.
2. Tarver, C. M.; Erickson, L. M.; and Parker, N. L., *Shock Waves in Condensed*

*Matter* -- 1983, J. R. Asay, R. A. Graham, and G. K. Straub, eds., Elsevier Science Publishers B. V., 1984, p. 609.

3. Lee, E.; Breithaupt, D.; McMillian, C.; Parker, N.; Kury, J.; Tarver, C.; Quirk, W.; and Walton, J., *Eighth Symposium (International) on Detonation*, Naval Surface Weapons Center, NSWC MP 86-194, 1985, p. 613.
4. Murphy, M. J.; Simpson, R. L.; Breithaupt, R. D.; and Tarver, C. M., "Reactive Flow Measurements and Calculations for ZrH<sub>2</sub>-Based Composite Explosives," *Ninth Symposium (International) on Detonation*, Portland, OR, Aug 1989.
5. Urtiew, P. A.; Erickson, L. M.; Aldis, D. F.; and Tarver, C. M., "Effects of Initial Temperature on Shock Initiation of LX-17," *Ninth Symposium (International) on Detonation*, Portland, OR, Aug 1989.
6. Hallquist, J. O., "User's Manual for DYNA2D," UCID-18756 Rev. 3, Lawrence Livermore National Laboratory, Livermore, CA, 1986.

## DISCUSSION

KIBONG KIM  
 Naval Surface Warfare Center  
 Silver Spring, MD

You use thin plate flyer (high pressure) initiation and reaction observation where the second term in IAG dominates and the first ignition term is unimportant. Isn't it difficult to apply this information to estimation of failure diameters where the ignition term may be important?

## REPLY BY C. M. TARVER

The electric gun flying plate experiments (very high pressure, very short pulse duration) were used to study the ignition of the two propellants. The embedded gauge experiments at 13 and 16 GPa measured the HMX reaction rates in Propellant B. The embedded gauge experiments at 20 GPa measured the global reaction rate of the rest of Propellant B. In failure diameter tests, a donor explosive is detonated in contact with the material being

tested. In this situation, the HMX in Propellant B would certainly ignite and then react completely. The rest of Propellant B (AP, Al, and binder) would then begin to react and the reaction rates of these components will determine whether the detonation wave in

Propellant B fails or continues to propagate. Therefore, in the ignition and growth calculations for failure diameter of Propellant B, it is the second growth term in Equation (2) which controls the failure or propagation of detonation at all charge diameters.

---

**SESSIONS ON**  
**DETONATION WAVE PROPAGATION**

**Cochairmen: Roger Cheret**  
**Commissariat a l'Energie Atomique**

**Michael Cowperthwaite**  
**SRI International**

**and**

**Craig Tarver**  
**Lawrence Livermore National Laboratory**

**Patrick Gimenez**  
**Ministere de la Defense**  
**Centre d'Etudes de Gramat**

**and**

**Jerry Forbes**  
**Naval Surface Warfare Center**

**James Kennedy**  
**Los Alamos National Laboratory**

---

# MOLECULAR DYNAMICS SIMULATION OF THE EFFECT OF MOLECULAR DISSOCIATION AND ENERGY ABSORPTION ON DETONATION STRUCTURE IN ENERGETIC SOLIDS

S. G. Lambrakos, M. Peyrard, and E. S. Oran  
Laboratory for Computational Physics and Fluid Dynamics  
Naval Research Laboratory  
Washington, D.C. 20375

*Molecular dynamics simulations are used to study the influence of microscopic processes on the structure of detonations in solids. The physical model consists of a three-dimensional lattice in which intermolecular interactions are given by Lennard-Jones potentials. The intermolecular dynamics are resolved in the computation, whereas the intramolecular behavior and the interaction between intramolecular and intermolecular degrees of freedom are modeled phenomenologically using adaptive constraints. One feature of this general approach is that it allows modeling of molecular dissociation on a timescale that is more realistic than in previous simulations. Another feature of this method is that it allows the modeling of complex intramolecular processes for calculations carried out at the characteristic timescale intermolecular interactions. Here we describe two models of the coupling between intermolecular and intramolecular modes and the results of calculations using these models.*

## INTRODUCTION

Many of the dominant structures of detonations in solids have widths that are extremely small compared with the dominant structures of detonations in gases and liquids. These observations suggest that the region behind the shock, extending over a distance of many unit cells, is not in thermal equilibrium. Karo et al.,<sup>1</sup> who were the first to use molecular dynamics to study detonations in solids, investigated a two dimensional monatomic crystal consisting of atoms bound to each other by a predissociative exothermic potential. They found that the widths of the induction zone and of the shock front may be of the order of a few unit cells. In another investigation, Karo et al. showed that a narrow shock front can transmit substantial amounts of energy from intermolecular motions to intramolecular modes. Recent studies of shock-induced detonations in solids have been carried out by Tsai and Trevino<sup>2,3</sup> and Peyrard et al.<sup>4,5</sup> Tsai and Trevino<sup>2,3</sup> showed that the region behind the

shock front is not in thermal equilibrium. However, their model consists of a highly symmetric solid made of one type of atom and one type of bond that is maintained by a predissociative potential.

Peyrard et al.<sup>4,5</sup> used a more sophisticated lattice model to study how detonation properties depend on the structural characteristics of solids. They modeled an energetic solid that consisted of an array of two-component molecules corresponding to an approximate representation of solid-phase nitromethane. The model consists of three types of intermolecular bonds and a predissociative intramolecular bond, all represented by Morse or Lennard-Jones potentials. Peyrard et al. showed that there are conditions on both the geometry of the solid and on the intramolecular and intermolecular potentials that must be met in order to sustain a detonation. In particular, these simulations showed that the energy released from an exothermic chemical reaction is transferred to the shock front through coherent

excitation of the crystal lattice; that the reaction front, i.e., the front defined by the onset of molecular dissociation, propagates only if the potentially dissociative bonds link two inequivalent sublattices; and that the energy transfer between longitudinal and transverse motions plays an important role in determining the structure of the detonations.

Recently Lambrakos et al.<sup>6,7</sup> used a three-dimensional lattice model to study the structure of detonations in solids. This model is similar to the two-dimensional lattice model used by Peyrard et al.<sup>4,5</sup> except that the chemistry of the dissociation is modeled using an adaptive constraint algorithm. Although this model is fundamentally different in many ways from the models used in other studies, the results support those of the previous studies.<sup>1-5</sup> By separating intramolecular states from intermolecular motions, it is possible to investigate the effect of the delay time for molecular dissociation and energy-release on the detonation structure. Lambrakos et al. determined that the qualitative structure of the detonation is preserved when the energy-release delay for dissociation increases by more than one order of magnitude. However, changes in the delay time affect the detonation by changing its velocity and by increasing the size of the induction zone. This effect has a macroscopic analog in detonation structures in liquids or gases where the rates of chemical reaction affect the size of the induction zone.

## BACKGROUND

An important contribution of previous molecular dynamics studies<sup>1,2,3</sup> to the understanding of macroscopic detonation structure in solids is the observation that local and stable detonation structures can exist in solids under a variety of different conditions. In other words, a self-sustaining detonation structure is possible at the microscale. However, a limitation of the models for the detonation process used in previous studies is that the characteristic time delay for molecular dissociation and subsequent energy release is too small compared to the time delay that is typical of real physical systems.

One approach to modeling molecular dissociation on a more realistic timescale and

to modeling complicated intramolecular degrees of freedom is to use timestep splitting approaches to separate the calculation into intramolecular and intermolecular processes, model the intramolecular processes phenomenologically, and couple this to a resolved calculation of the intermolecular processes. We have implemented this by using constraints that are a function of intermolecular forces. In particular, this adaptive-constraints method provides a general framework for using molecular dynamics to investigate the general properties of microscale detonations when molecular dissociation and subsequent energy-release occur on a timescale that is long (greater than  $10^{-13}$ s) with respect to intermolecular interactions and how energy transfer between intramolecular and intermolecular degrees of freedom affect detonation structure when energy release occurs over a relatively long time.

In our previous study in which we introduced the adaptive-constraints method, we described a model for molecular dissociation and energy release that takes explicit account of the minimum time  $t_{\min}$  for energy release that can occur in the calculation following molecular dissociation. The purpose of that model, subsequently referred to as model I, was to investigate the qualitative character of microscopic detonation structure as a function of  $t_{\min}$ . In that model, energy transfer between intramolecular and intermolecular degrees of freedom was effected using highly qualitative or approximate procedures. In this study, we describe a phenomenological model for energy transfer between intramolecular and intermolecular degrees of freedom, subsequently referred to as model II, that is more realistic and permits a more quantitative analysis of the effects of energy transfer on detonation structures.

## PHENOMENOLOGICAL MODELS FOR ENERGY TRANSFER

The basic idea of model I is to use a constraint force to maintain intramolecular bonds and to represent the internal state of the molecule through a state function  $S$ . The function  $S$  is continuous and represents an average of many changes in the intramolecular state as

viewed on an intermolecular timescale. It is closely related to the constraint force between the parts of the molecules.<sup>6</sup>  $S$  is a function of the impulse along the line joining the two interaction centers. This impulse provides a direct measure of the level of interaction of the molecule with its environment and of the level of stress that is internal to the molecule and that could pull it apart. At a *threshold* value  $S_T$ , some type of transition occurs. For example, when the threshold is passed, the molecule could dissociate or some other bound state could be assumed. The form of the state function and of the force function that is "switched on" when  $S(t) = S_T$  is problem dependent. The energy transfer process is modeled using simple procedures that either increase or decrease the kinetic energy of each molecular group according to the value of a state function  $S$ . This gives a qualitative representation of the energy transfer between intermolecular and intramolecular modes.

Model II employs a more sophisticated procedure for modeling energy transfer between large molecules. This procedure conserves momentum and energy, is more computationally efficient, and also permits a physically realistic representation of large molecules with many internal degrees of freedom. In model II, a large molecule is represented by two interaction centers,  $i$  and  $j$ , and a potential energy surface that can change continuously according to the internal state of the molecule. These changes in the potential energy surface are associated with the inelastic response of one large molecule interacting with another. A dissociative potential is switched on when the molecule absorbs a specified amount of energy  $E_T$ .

In model II, the total external force  $F_i^n$  on a given particle  $i$  is given by

$$F_i^n = \sum_{k=1}^{N_k} (1 + \alpha) F_{ik}^n \quad (1)$$

where the energy-transfer function  $\alpha$  satisfies the condition  $0 < \alpha \leq 1$ . The force  $F_{ik}$  represents the interaction between force centers  $i$  and  $k$ , where  $k = 1, \dots, N_k$  indexes force centers associated with the neighbors of

molecule  $ij$  that are within the interaction range. The total energy  $E_{ij}^n$  absorbed by molecule  $ij$  at timestep  $n$  is given by

$$E_{ij}^n = E_{ij}^{n-1} + \Delta E_i^n + \Delta E_j^n \quad (2)$$

where

$$\Delta E_i^n = \frac{[G_i^n \cdot G_i^n - F_i^n \cdot F_i^n](\delta t)^2}{2m_i} \quad (3)$$

and

$$G_i^n = \sum_{k=1}^{N_k} F_{ik}^n \quad (4)$$

It is necessary to specify two types of functions: the force-function  $F_{ik}$  and the energy-transfer function  $\alpha$ . In model I we defined a state function  $S$  whose value increases linearly with time when the stress on the molecule due to external forces is above a given threshold value. Using a similar prescription for  $S$ , we define  $\alpha$  as a linear function of the intramolecular stress,

$$\alpha(S_i, S_k) = \gamma \frac{\max(S_i(t), S_k(t))}{S_T} \quad (5)$$

where the quantity  $S_k^n$  is the value of the state function  $S$  associated with the molecule in which force center  $k$  is located, and  $\gamma$  is a scaling parameter satisfying the condition  $0 < \gamma < 1$  and  $S_k$  is such that  $0 < S_k \leq S_T$ . The *max* operator assures symmetry in computing inelastic interactions between any two force centers.

The procedure defined by Equations (1) through (5) can be explained with the help of the set of potential energy curves shown in Figure 1. Because both  $\alpha$  and  $S$  are continuous functions, we interpret the separation between these curves as a representation of a finite-difference (or quasicontinuous) approximation of a continuous function of two variables, the inter-particle separation and the state function  $S$ . First, assuming that  $\alpha$  varies linearly with  $S$  (which takes on discrete values), we observe that the difference in energy between two curves increases with decreasing inter-particle



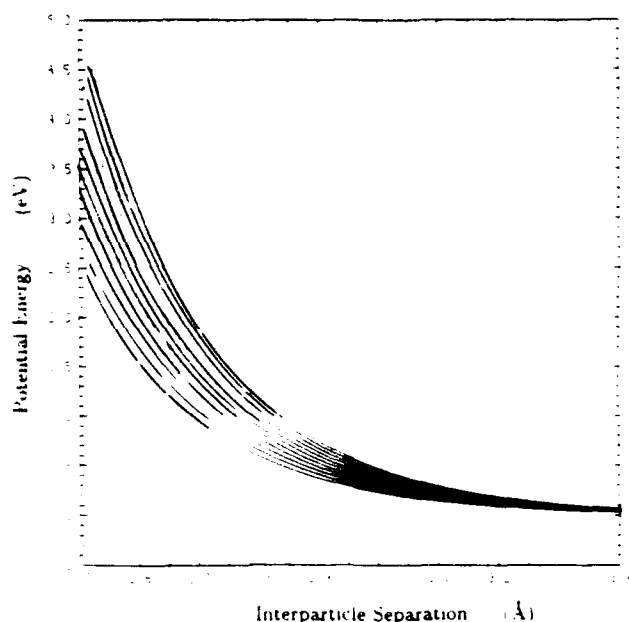


Figure 1. Schematic Description of Potential Energy as a Function of Separation and Energy-Transfer Function  $\alpha$  Defined in Equation (1)

separation. As a result, when the internal stress of the molecule is above a given threshold, the rate of energy transfer increases with an increase in the strength of the interaction. Second, the energy transfer, although phenomenological, is reversible prior to molecular dissociation. However, energy transfer into or out of each molecular system is not spontaneous. Each individual molecule must interact with another molecule in order for any energy transfer to occur. In addition, the strength of the interaction will be a function of the relative orientation of two interacting systems. These properties are consistent with the general character of an inelastic interaction between two large molecules. Finally, the strength of the coupling between a molecule and its neighbors as well as the associated rate of energy transfer depends on the relative orientation and separation of the neighbors in a manner that is consistent with real physical systems.

Note that there is flexibility in selecting the form of the function  $\alpha$ . The criteria for selecting  $\alpha$  are: a specified amount of energy is absorbed before dissociation; a specified average rate of energy transfer can occur; and energy transfer between intramolecular and

intermolecular modes results from smooth changes in the intermolecular force function.

## A BRIEF CRITIQUE OF MODEL I AND MODEL II

In a previous study,<sup>6</sup> we constructed a model system which can be used to simulate a self-sustaining front moving through a crystal lattice. In order to model a detonation process consisting of energy transfer into a solid from a passing shock wave, molecular dissociation, and then energy release, it was necessary to adopt a relatively simple model of an energetic solid. This model, model I, represents the combined effect of energy absorption prior to molecular dissociation, molecular dissociation, and energy release from subsequent exothermic chemical reactions. The significant physical parameters in model I are the strength of coupling between intermolecular and intramolecular degrees of freedom and the minimum time delay before energy is transferred irreversibly to intermolecular degrees of freedom.

Although model I neglects details of the coupling between intermolecular and intramolecular degrees of freedom, it provides a method for investigating the response of various types of lattice configurations to a stable self-sustaining pulse of energy. For example, the energy transferred along directions transverse to a front propagating through a particular lattice structure can be calculated using model I. It would then be possible, in principle, to calculate an integrated average rate of energy loss due to coupling of the detonation front to transverse lattice modes. Similarly, model I can be used to determine the dependence of the distribution of energy on the details of a particular crystal structure. However, one limitation is that the characteristic lengths associated with many of the highly localized peaks in energy (i.e., energy peaks on the order of several unit cells) that are calculated can be artifacts due to the level of approximation assumed by this model. Further, the process defining model I may actually impose a length scale on the structures that are calculated.

The physical motivation for model II is to establish a molecular-dynamics model of energy transfer in energetic solids that can be used to simulate microscopic structures which

are statistically significant on the characteristic length and time scales of macroscopic detonations in solids. The purpose of model II is to simulate properties of energy transfer in solids that are associated with the coupling between intramolecular and intermolecular degrees of freedom and with the breakdown of lattice structure resulting from molecular dissociation or phase transition. Model II represents only the effect of intramolecular processes which occur prior to molecular dissociation and does not include chemical reactions following dissociation. The conditions defining model II are sufficient for a relatively detailed investigation of properties associated with the induction zone in a detonation. A detailed investigation of the induction zone is important for the following reasons:

1. In a molecular-dynamics model, it is unclear how to include the information associated with the relatively large set of chemical reactions that follow dissociation of molecules in an energetic solid. However, it is possible to specify the physical parameters for modeling a crystal in the unreacted solid phase even for lattice structures containing impurities and defects. Therefore, the molecular-dynamics method is very well-posed for determining properties of the induction zone in real explosive solids.
2. The structure of the induction zone is that part of the detonation that is most strongly related to the solid-phase properties of an energetic solid. There are results that support the idea that molecular dissociation in the solid is due to mechanical scission rather than energy absorption through interaction among intramolecular and intermolecular degrees of freedom. However, both of these mechanisms for dissociation are, in principle, likely to occur in the solid phase.
3. No matter what the details of the chemistry, it is likely that the characteristics of the induction zone define the rate-limiting step for energy release and energy transfer due to chemical reactions occurring after dissociation. In fact, it is probable that the dissociation efficiency

of the induction zone determines the stability of a solid explosive.

We describe below a series of simulations investigating effects of molecular dissociation in the induction zone.

### The Crystal Model

The crystal model used in the simulations described here is the type 2 lattice described in Reference 1. This is a three-dimensional lattice that is in a stable minimum-energy state and is composed of two-component molecules. The components of each molecule are designated N and C, and are each meant to represent a complicated group of atoms. Each component is bound to the other through a rigid constraint. We do not associate this rigid constraint physically with any intramolecular bond; its purpose is to provide a physically realistic orientational dependence for any type of coupling between intramolecular and intermolecular degrees of freedom. For example, two colliding molecules will tend to absorb more energy from intermolecular modes if their relative motion is parallel to their longest dimensions. The energy transfer between lattice modes and intramolecular modes is modeled using model II. The masses of the N and C groups are 47 and 15 atomic mass units.

The underlying physical assumptions defining the boundary and initial conditions for our present model are different from those in our previous study,<sup>6</sup> where, in order to simulate the shock initiation process, an impulse of specified strength was applied to the left most plane of cells of the crystal. The purpose of this impulse was to start a self-sustaining process analogous to macroscopic detonation processes. Consequently, the parameters defining the coupling between intramolecular and intermolecular degrees of freedom were limited to a range of values that would permit microscopic self-sustaining detonation structures *within* the solid. Although these simulations demonstrate that localized detonation-type structures can exist, there is still an assumption about the nature of the chemical reactions occurring after molecular dissociation that is implicit in the process associated with model I.

In our present model, an impulse of specified strength is applied to the left boundary of the system and the energy transfer through the crystal lattice is monitored. Here, we associate this impulse with either some type of initiation process or momentum transfer due to energy release from one or more exothermic chemical reactions. However, the parameters associated with model II are not limited to a range of values that would permit only self-sustaining detonation structures within the solid, but rather a range of values that would permit realistic levels of energy absorption. Our goal in this study is to investigate effects associated with the absorption of energy by molecules and molecular dissociation resulting from shocks traveling through a solid. We consider these effects as uncoupled from the details of any particular chemical reaction.

## RESULTS

### Effect of Highly Localized Structures

In many of our simulations, especially those where the unshocked lattice is at a low temperature, we observe structures that are extremely sharp on the atomic scale, i.e., structures whose width is on the order of 2 or 3 unit cells. An example of such structures is shown in Figure 2 for a constant-velocity front moving through the crystal at near zero temperature. The results shown in Figure 2 were obtained using model I, for which there is no energy transfer between intramolecular and intermolecular modes and the minimum time delay  $t_{\min}$  is  $2.0 \times 10^{-13}$  s. In these calculations, the only mechanism for molecular dissociation is the stress tending to pull a molecule apart. For this system, any localized increase in energy is only associated with energy transfer between intermolecular degrees of freedom. We have found that the presence of these localized peaks does not affect the average velocity of the front moving through our model lattice. Although they locally increase the level of molecular dissociation, they are statistically insignificant in that they do not affect the average width of the induction zone or the average distribution of energy and momentum in the induction zone. These localized structures are highly unstable and tend to vanish when the temperature of the crystal lattice is above very low values.

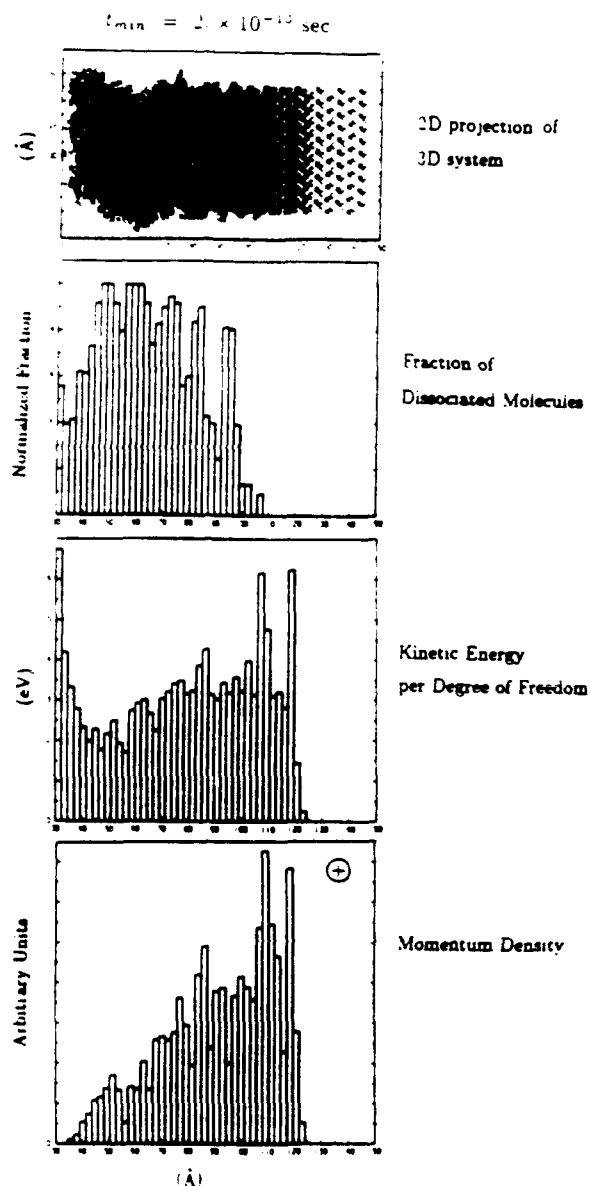


Figure 2. Constant-Velocity Front Moving Through Crystal Lattice at Near Zero Temperature

The structures shown in Figure 3 are for the same calculation as Figure 2, but at a later time. In this case, the front moves through an undissociated crystal at finite temperature. As is seen in Figure 3, there are no longer any sharp structures present.

### Effect of Energy-Transfer Rate on Molecular Dissociation

A series of simulations were conducted to investigate the dependence of the molecular dissociation level on the rate at which energy

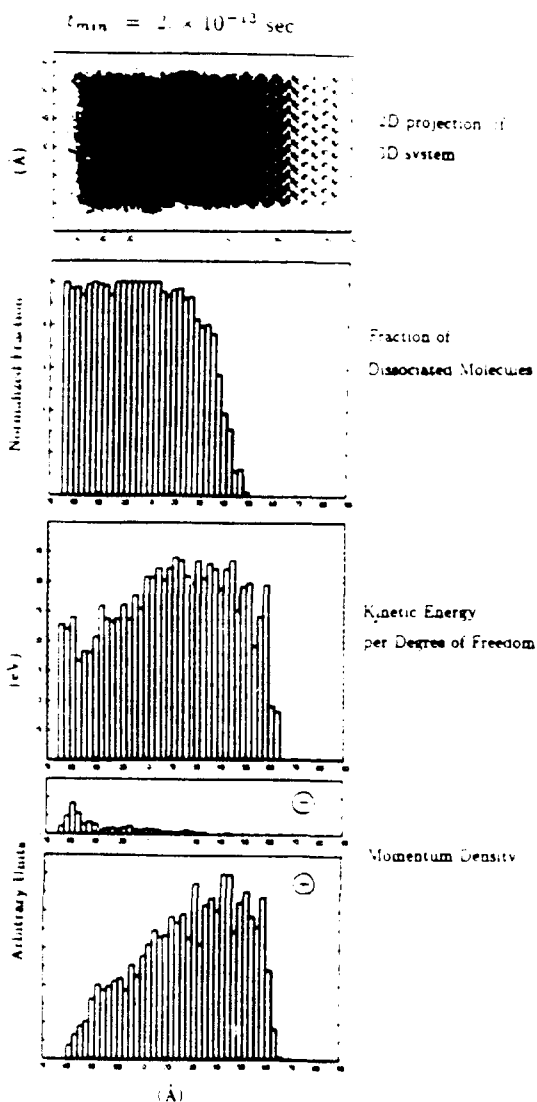


Figure 3. Constant-Velocity Front Moving Through Crystal Lattice at Finite Temperature

is transferred to the crystal lattice. As discussed earlier, we associate the initial impulse at the boundary of our model system with either momentum transfer resulting from exothermic reactions occurring behind the front or some type of initiation process. We found that for the range of parameters considered here, the amount of molecular dissociation increases with the rate of energy transfer into the undisturbed lattice. This result supports the idea that the lattice must remain intact in order for there to be a coherent transfer of energy through the lattice and into intramolecular modes. The inelastic component resulting

from lattice disruption tends to decrease the energy of the longitudinal modes which define the propagating shock. Some results of our calculations are shown in Figure 4. Figure 4 compares the evolution of two shocks moving through the crystal. The two shocks are caused by impulses with energy-transfer rates that differ from each other by a factor of three. The total energy transferred to the undisturbed lattice is the same for both impulses. Note that the shock front caused by the impulse of shorter duration (higher energy-transfer rate) has traveled further through the crystal at time  $6 \times 10^{-13}$  s. Further, note that for the front caused by the faster pulse, the distribution of positive momentum (i.e., the component momentum along the direction of the front) tends to be skewed toward the leading edge of the front. In this case, the crystal response is sufficiently *elastic* to allow efficient transfer of energy to the front before lattice disruption or *plasticity*.

The faster pulse increases the level of molecular dissociation and still produces a shock speed that is faster than that caused by the weaker pulse even though the total energy transferred is the same in each case. These results support the idea that if the rate of energy transfer into the undisturbed lattice is small, kinetic energy will be given to only a relatively small number of lattice sites before lattice disrupts due to either phase changes or dissociation of molecules making up the unit cells. As the rate of energy transfer increases, kinetic energy can be given to more molecules before disruption of the lattice.

### Effect of Energy Absorption and Molecular Dissociation

A series of simulations were conducted to investigate the influence of energy absorption and molecular dissociation on the structure of fronts propagating through our model crystal. We found that for the range of parameters considered here, the shock velocity over a local region (on the order of 100 unit cells) is relatively insensitive to intramolecular processes and is mostly influenced by the strength of the impulse applied to the undisturbed lattice. This result supports the idea that there is weak coupling between relatively slow and

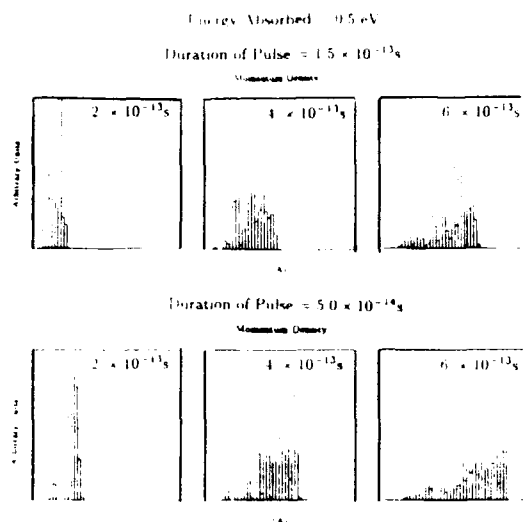


**Figure 4a.** Comparison of the Evolution of the Momentum-Density Distribution of Two Shocks Caused by Impulses with Energy-Transfer Rates that Differ from Each Other by a Factor of Three

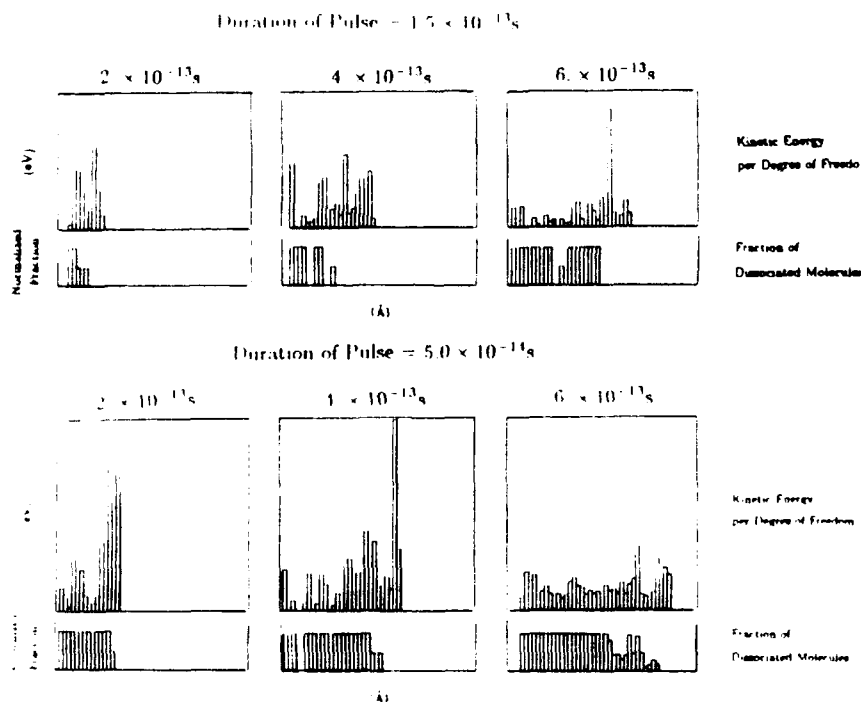


**Figure 4b.** Comparison of the Evolution of the Kinetic Energy Distribution of Two Shocks and Fraction of Dissociated Molecules Caused by Impulses with Energy-Transfer Rates that Differ from Each Other by a Factor of Three

nonexothermic processes occurring behind the front and excited modes of the undisrupted lattice. Some results of our calculations are shown in Figure 5. Figure 5 compares the state at the same time of two fronts moving through our model crystal after an impulse is applied to

the undisrupted lattice. In both cases the rate of energy transfer and the total energy transferred is the same. However, the total energy required per molecule for dissociation in one case differs from the other by a factor of 4. We observe that in both cases the leading edge of

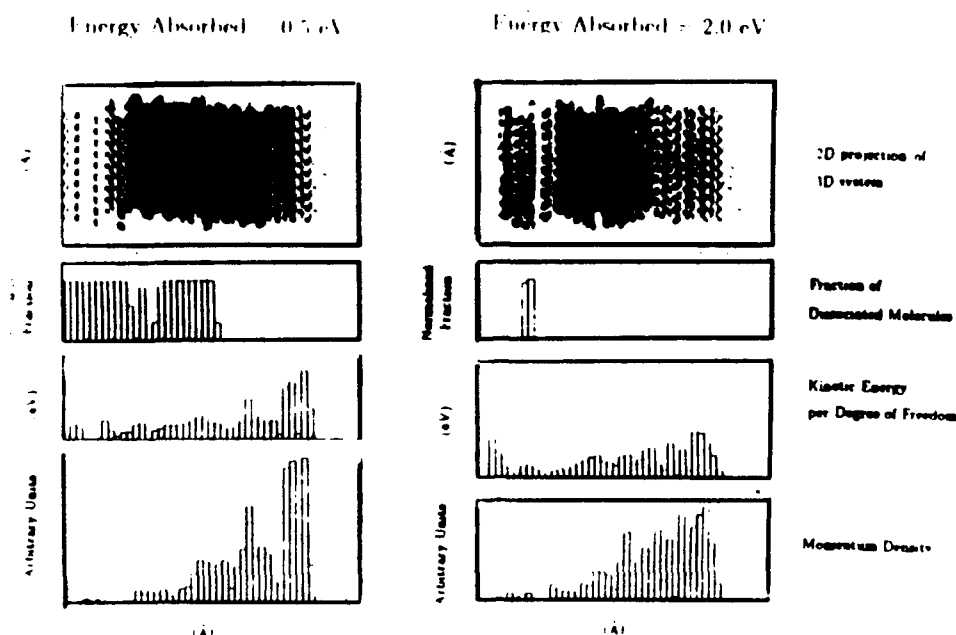


Figure 5. Comparison of the State at the Same Time of Two Fronts. The total energy required per molecule for dissociation in one case differs from the other by a factor of 4.

the front is at the same position in the solid. However, the general shape and composition of the two fronts are dissimilar. Referring to Figure 4, note that the system requiring a large amount of energy absorption prior to dissociation shows almost no dissociated species. In addition, note that in the case of the larger absorption, (compare the  $z$ -momentum density) we observe that there is less energy available for longitudinal lattice modes close to the front.

## DISCUSSION AND CONCLUSIONS

In this paper we have introduced an approach for modeling energy transfer between intramolecular and intermolecular degrees of freedom prior to molecular dissociation in molecular dynamics simulations of shocks and detonations in crystal lattices. This model, model II, is based on the adaptive-constraints algorithm introduced previously and defines a coupling between degrees of freedom that is more realistic than our previous model, model I. We use model II to investigate how energy transfer between intermolecular and intramolecular degrees of

freedom influences molecular dissociation in the solid. The present calculations support the following conclusions:

1. The spatial distribution of kinetic energy in the propagating wave depends mostly on the lattice modes and is relatively insensitive to intramolecular modes. The spatial distributions of the kinetic energy calculated using model II are very similar qualitatively to those calculated using model I. As in previous results from model I, the shock front is sharp on the atomic scale. This is the case even with relatively large amounts of energy absorption per molecule, e.g., 0.5 eV and greater.
2. In our present calculations with model II, we observe structures within the shock with a width of two unit cells. These structures preserve their shape as the front propagates through the solid. However, these structures are unstable to temperature perturbations and are uncorrelated with the average width of the shock. That is, the existence of these structures does not seem to affect the

average properties of the propagating shock front, e.g., velocity and average level of molecular dissociation.

3. The level of molecular dissociation tends to increase with the rate of energy transfer into the undisrupted lattice. That is, for a given total amount of energy transferred into the unexcited lattice, the level of dissociation depends on how fast the energy is transferred. In addition, the velocity of the leading edge of the shock tends to be locally insensitive to the level of dissociation and depends on the energy transfer rate into the undisrupted solid. This means that the local velocity of a propagating front is a characteristic of the local rate of chemical energy release from behind the front into the undisrupted lattice and depends mostly on the overall coupling between these exothermic processes and lattice modes of the undisrupted crystal. Lattice disruption and molecular dissociation is a required precursor to subsequent exothermic reactions and determines this coupling. However, highly localized structures associated with these processes do not influence the local velocity. These results help to explain results obtained previously<sup>6</sup> using model I. In a previous study, we observed that the detonation speed decreased as the minimum delay for molecular dissociation  $t_{\min}$  increased. This effect follows since a relatively large  $t_{\min}$  is equivalent to a relatively small rate of energy transfer into the undisrupted solid.
4. For realistic energy absorption levels prior to molecular dissociation, i.e., 2 eV and larger, a relatively high rate of energy transfer to the undisrupted solid is required in order to produce significant levels of molecular dissociation. A relatively high rate of energy transfer results in a propagating pulse that is insensitive to microstructures associated with intramolecular processes but sensitive to undisrupted-lattice modes.

Our results, based on the models we have chosen, suggest a reasonable estimate of the characteristic width of small scale structures

that can be *directly* related to macroscopic properties. We find that this width is between 40 to 100 Å for the perfect crystal systems considered in our studies.

## ACKNOWLEDGEMENTS

This work was supported by the Physics Division of the Office of Naval Research and by the Naval Research Laboratory. The authors would like to acknowledge the continued support of Dr. Don Liebenberg and the encouragement of Dr. Simone Odier.

## REFERENCES

1. Karo, A. M.; Hardy, J. R.; and Walker, F. E., *Acta Astronaut*, Vol. 5, 1978, p.1041.
2. Tsai, D. H. and Trevino, S. F., *J. Chem. Phys.*, Vol. 81, 1984, p. 5636.
3. Trevino, S. F. and Tsai, D. H., *Proceedings of the Eight Symposium (International) on Detonation*, Albuquerque, NM, 1985.
4. Peyrard, M.; Odier, S.; Oran, E.; Boris, J.; and Schnur, J., *Phys. Rev.*, Vol. B 33, 1986, p. 2350.
5. Peyrard, M.; Odier S.; and Blain, M., *J. de Chim. Phys.*, to be published.
6. Lambrakos, S. G.; Peyrard, M.; Oran E. S.; and Boris, J. P., *Phys. Rev.*, Vol. B, 1989.
7. Lambrakos, S. G.; Oran, E. S.; Boris, J. P.; and Guirguis, R. H., *Proceedings of the APS Conference on Shock Waves in Condensed Matter*, Elsevier Science Publishers B. V., 1988.
8. Lambrakos, S. G.; Peyrard, M.; and Oran, E. S., *J. Comp. Phys.* (in preparation).

## DISCUSSION

ROGER CHERET

Commissariat a l'Energie Atomique  
France

The manuscript reports a very nice work of computational physics. But it is still questionable whether it bears any relation with detonation.

## REPLY BY S. G. LAMBRAKOS

Formalisms based on the Navier-Stokes or Euler equations cannot be used to model extremely short time or length scale processes. In recent years, the molecular dynamics method has experienced significant advances with respect to the complexity of systems to which it may be applied. In particular, methods are being developed for calculating noncentral and adaptive potential energy functions that are constructed to represent, either directly or phenomenologically, changes in local energy associated with chemical transformations. These methods represent a tractable approach to modeling short time and length scale processes such as those that occur in detonations.

## DISCUSSION

C. O. LEIBER  
BICT  
Swisttal, FRG

Is it possible to use your method for the calculation of the elastic properties of single crystals?

## REPLY BY S. G. LAMBRAKOS

Yes. That is an easier problem to solve.



# MULTIPROCESS DETONATION MODEL

A. N. Dremin, V. Yu. Klimenko, O. N. Davidova,  
and T. A. Zoludeva

Institute of Chemical Physics (Branch)  
USSR Academy of Sciences, Moscow region,  
Chernogolovka, 142432, USSR

*The physical model of detonation is presented. The hot spots mechanism developed earlier in detail as well as the homogeneous mechanism of explosive decomposition are involved in the model. The homogeneous mechanism consists of two stages. The first stage (inside front) is conditioned by thermodynamical nonequilibrium processes taking place inside the detonation wave shock front. The second stage (after front) is characterized by some reactions of neutral explosive molecules with active particles originated during the first stage. The hot spots decomposition mechanism dominates at low pressure regions and the homogeneous mechanism dominates at high pressure regions.*

## INTRODUCTION

The problem of a detailed mechanism of detonation is still a central point in the explosion science. To describe sufficiently enough various detonation processes some models of condensed explosives detonation are used. The models are based on different explosive shock decomposition mechanisms. Common shortcomings of the models are the fact that each of them uses the same mechanism to describe explosive response to the shock effect within a wide region of pressure from units up to tens of GPa. It is in this way that the hot spots decomposition mechanism in its various versions is used most widely at present. However, some experimental data are available which demonstrate that shock decomposition processes at low and high pressures proceed qualitatively differently. For instance, detonation decomposition of any explosive proceeds equally in both liquid and solid states at pressures larger than some certain value  $P^*$  characteristic of each explosive.<sup>1</sup> ( $P^*$  is smaller than Chapman-Jouguet detonation pressure.) This means that the hot spots mechanism governed by the solid explosive's initial heterogeneous state does not work at high pressures. It works at low pressures ( $P < P^*$ , region I). In high pressure regions ( $P > P^*$ , region II) explosive

decomposition is not influenced by the initial state; it is governed by some processes inside the explosive particles. The following experimental data testify in favor of this conclusion.<sup>2</sup> It has been found out that detonation reaction times of pressed TNT with various liquid fillers in pores, as well as in the case of absence of any fillers, lie on one the same curve of the times dependence on pressure. The fillers do not effect the explosive detonation decomposition time because it is governed by the processes inside the explosive particles. Thus, it is not correct to describe any explosive shock decomposition in wide pressure regions by only one mechanism. On the other hand, it is also incorrect to develop individual models for different pressures because the transition from the first pressure region to the second one often takes place at some detonation process progress. For instance, it occurs at the most frequently modeling process of detonation initiation by shocks of various intensity and time. Hence, one needs some joint model comprising explosive decomposition features characteristic of each pressure region.

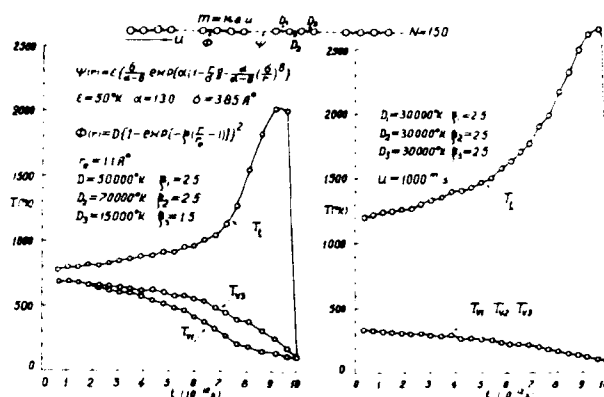
In order to develop a detonation computation model with great predictive power, it is required that the physical model include all physical and chemical processes in explosives

under the shock effect. A model of this kind is proposed in the paper. The model includes some explosive shock decomposition mechanisms which work in parallel simultaneously. But the mechanisms contribution to the explosive decomposition process within various pressure regions is different. The model is termed the multiprocess detonation model.

There are some well-developed hot spots models for the first pressure region (see, for example, References 3-7). What mechanism works in the second pressure region? Two stages can be distinguished in the second region. The first stage is some explosive portion decomposition inside the shock wave front during  $\sim 10^{-10}$ s time. The second one is the decomposition down behind the shock front during  $\sim 10^{-6}$ s time. Let us consider each stage in detail. Some of our previous papers have been devoted to the explosives decomposition process inside the front.<sup>7-9</sup> The so-called accumulation mechanism has been introduced for polyatomic molecules. According to the mechanism the translational temperature overheat appears at the beginning and is followed by the overexcitation of certain bonds. The overheat term is the higher temperature level, not the equilibrium one behind the front. The model is phenomenological. Therefore it should be verified by direct calculations. In particular, both the translational temperature overheat and the overexcitation of some certain bonds should be tested. With this aim the direct simulation of the polyatomic molecule excitation process inside the shock front has been performed by the nonequilibrium molecular dynamic method.<sup>10,11</sup> The shock wave passage along the one-dimensional system consisting of four-atomic molecules has been calculated. There were 150 molecules in the system (see figure). Morse potential has been used to describe the atoms interaction inside the molecules

$$\phi(r) = D \left\{ 1 - \exp \left[ - \left( \frac{r}{r_e} - 1 \right) \right] \right\}^2$$

The potential parameters have been varied to change the characteristic frequencies of the corresponding bonds. The calculation results shown in the figure have been obtained



with the parameters values presented in the figure. The potential (exp-6)

$$\psi(r) = \epsilon \left\{ \frac{6}{a-6} \exp \left[ a \left( 1 - \frac{r}{\sigma} \right) \right] - \frac{a}{a-6} \left( \frac{\sigma}{r} \right)^6 \right\}$$

has been used to describe the interaction of various molecules atoms. The "shock wave" has been generated by forced motion of the left boundary molecule with 1000 m/s velocity. The motion, in essence, is the shock wave particle velocity. The translational temperature T<sub>t</sub> profile, as well as the profiles of the vibrational temperatures T<sub>v1</sub>, T<sub>v2</sub>, and T<sub>v3</sub> of three bonds in the molecule, are shown in the figure. The profiles are average results of  $\sim 100$  separate systems calculations. In the right side of the figure the profiles are presented for the case in which all three bonds of the molecule have the same high vibration frequency. One can see that the translational-vibrational (T-V) relaxation proceeds extremely slowly. Obviously it is due to the tremendous difference between the high intramolecular frequencies ( $\sim 10^{14} \text{ s}^{-1}$ ) and the frequencies characteristic of the molecule translation motion ( $\sim 10^{13} \text{ s}^{-1}$ ). The left side of the figure represents the case in which one of the molecules bonds has a low vibration frequency. As a result, in this case the T-V relaxation proceeds considerably faster. As to the overheat of the fast-excited mode, it has not been observed in this numerical experiment. It is quite probable that the one-dimensional model is responsible for the result. However the result does not exclude the phenomenon for the other composite molecules.

So the translational temperature overheat (which was predicted as far back as 1980<sup>8</sup>) takes place in both cases. This fact is of great significance for understanding the complex molecule shock compression mechanism. The conclusion follows from the evidence that the translational temperature overheat for molecules consisting of tens of atoms is to be one order higher than the shock compression equilibrium temperature (behind the shock front). It means that the translational temperature overheat can reach ten thousand degrees for 10 GPa shock wave intensity. In this case the process of electron excitation (activation energy  $E = 2 \div 5 \text{ eV}$ <sup>12</sup>) and even the thermal ionization process ( $E = 6 \div 10 \text{ eV}$ <sup>13</sup>) become possible inside the translational temperature overheat zone.

Thus, the polyatomic molecules decomposition inside the shock wave front can proceed in three ways: the first way is the overexcited bonds decomposition (accumulation mechanism), the second one is decomposition through electron excitation, and the third one is decomposition through thermal ionization. The accumulation mechanism has been developed before.<sup>8,9</sup> The decomposition mechanism through thermal ionization is not discussed in the paper since it has not been investigated so far. Let us discuss in detail the decomposition mechanism through electron excitation. There are some experimental data indicative of the mechanism. For example, it has been found that hexogen shock decomposition products differ from those of the thermal decomposition and are identical to those of the photochemical decomposition.<sup>14</sup> The data testify in favor of the electron excitation decomposition under the shock, because it is well known that the photochemical decomposition proceeds through the electron excitation. Besides that, to explain the experimentally observed correlation between the molecule electron structure and the detonation ability, some preliminary molecule electron excitation has been assumed.<sup>15</sup> However, it should be mentioned that no reliable and convincing explanation of the excitation has been given. But from the results obtained it does follow that the high-energy molecule collisions inside the translational temperature overheat zone are responsible for

the excitation. Moreover, some benzene nitro-compound electron state changes at their compression in condensed state have been investigated.<sup>16</sup> The CNDO/S quantum-chemical method<sup>17</sup> has been used for the investigation. It has been revealed that the energy of the transition from basic electron state to the excited one decreases at the process of molecule approach and compression.

Thus, generally speaking, one may advance a certain hypothesis: the highest detonation ability corresponds to the electron structure of the explosive changes at compression in such a way that it favors the explosive molecule electron excitation. However, the problem needs some further investigation.

The explosive detonation homogeneous decomposition second stage proceeds behind the shock front at the substance thermodynamic equilibrium state when the translational temperature overheats and the overexcitation of some certain bonds disappear. The explosive molecules interaction with active particles (radicals, ions) originated during the first stage (inside the front) is the main process of the stage. As a rule, the interaction activation energy value is low ( $5 \div 15 \text{ kcal/mole}$ ).<sup>18</sup> Due to the activation energy's low value, the decomposition proceeds extremely fast and it is almost independent of the temperature change.

The nontrivial experimental results<sup>19</sup> can be explained in terms of the two-stage mechanism. The result is the following. It has been discovered that TNT detonation wave chemical spike width varies from  $\sim 1.5$  to  $\sim 0.2 \mu\text{s}$  at the pressure change from  $\sim 5$  up to  $\sim 20 \text{ GPa}$ . The chemical spike width change is very weak, although, according to the classical thermodecomposition regularity prediction, the explosive decomposition rate increase of  $5 \div 10$  orders of value should be expected at the pressure interval mentioned. According to the two-stage decomposition mechanism the temperature high level inside the detonation wave shock front and the decomposition process low activation energy value behind the front are responsible for the explosive decomposition rate's weak dependence on detonation pressure

The homogeneous mechanism obviously works at any shock pressure in both pressure regions. But its share in the explosive decomposition process at low pressures is small; the main portion of the explosive decomposes through the hot spots mechanism. The homogeneous mechanism decomposition rate increases with pressure increase considerably faster in comparison with that of the hot spots mechanism. At some definite pressure ( $P^*$ ) the homogeneous mechanism becomes dominant. It is going from the aforesaid that the hot spots and the homogeneous mechanisms of the explosive detonation decomposition work in parallel, and at the shock process pressure change their share in the explosive decomposition alters continuously. This is the gist of the multiprocess detonation model. The model calibration is presented in Reference 20.

## DISCUSSION AND CONCLUSION

The physical nature of the detonation process has been developed in the paper. Taking into account this development, it might be realized that the computation models which are based on the hot spots explosive decomposition mechanism as well as the computation models based on some formal kinetics are both imperfect and unreliable (as regards to the prediction opportunity). Indeed, as a rule, these models are calibrated for some certain gasdynamic motion conditions. But when the conditions are appreciably altered, they work inadequately. This fact was intuitively evident earlier, however now it is easy to explain. Let us consider the gasdynamic motion parameter. The hot spots and homogeneous mechanisms work in parallel at detonation, the homogeneous mechanism characteristic work time  $\tau_h$  being essentially smaller than that of the hot spots mechanism  $\tau_{hs}$ . The  $\tau_{hs}$  term denotes some necessary time to decompose a sufficient explosive quantity through the hot spots mechanism to affect the gasdynamic process. It is obvious that at some certain pressure ( $P < P^*$ ) the explosive shares, decomposed through the hot spots and homogeneous mechanisms, will strongly depend on the shock wave characteristic time  $\tau_s$ . The homogeneous mechanism is dominant irrespective of pressure at  $\tau_s < \tau_{hs}$ , but if  $\tau_s \geq \tau_{hs}$  the whole process will depend on pressure.

Therefore it is of great importance in what region of  $\tau_s$  time ( $\tau_s < \tau_{hs}$  or  $\tau_s \geq \tau_{hs}$ ) the calibration is performed, since the computation model calibrated in one region cannot be employed in the other region. The conclusion is valid for both the models applying some formal kinetics and for the hot spots models.

It should be mentioned that the hot spots computation models are no better than those which are based on the formal kinetics despite the fact that the exact physical mechanism of the hot spots origin and progress are used in the models. Usually the hot spots models parameters are calibrated for some certain shock wave (one-dimensional, some time duration). As a matter of fact, the parameters are not true and are unable to represent adequately the hot spots model. They are formal and only describe, in essence, some complex (as it has been shown) process. These formal parameters reflect the shock wave process inadequately if the gasdynamic motion changes (for example, two-dimensional and with the other time duration). This is especially observed at the pressure at which the hot spots and homogeneous mechanisms shares are comparable ( $P \sim P^*$ ). However, if the physical model used is perfect, the calibration parameters are true and they work adequately irrespective of the motion picture. So, it might be said that this is the very advantage of the proposed multiprocess detonation model.

## ACKNOWLEDGEMENTS

The authors wish to acknowledge the work discussions and support of E. S. Stepanov and V. P. Kobelev.

## REFERENCES

1. Dremin, A. N. and Schvedov, K. K. "On Shock Wave Explosive Decomposition," *Sixth Symposium (International) on Detonation*, ACR-221, 1976, pp. 29-35.
2. Dremin, A. N.; Savrov, S. D.; Trofimov, V. S.; and Schvedov, K. K., *Detonation Waves in Condensed Explosives*, Nauka, Moscow, 1970, pp. 171-172.
3. Lee, E. L. and Tarver, E. M., "Phenomenological Model of Shock Initiation in

- Heterogeneous Explosives," *Physics of Fluids*, Vol. 23, 1980, pp. 2362-2372.
4. Lobanov, V. F., "Modeling of Detonation Waves in Heterogeneous Explosives," *Fizika Gorenija i Vzryva*, Vol. 16, No. 6, 1980, pp. 113-116.
5. Cochran, S. G. and Tarver, C. M., "Modeling Particle Size and Initial Temperature Effects on Shock Initiation of TATB-based Explosives," *Shock Waves in Condensed Matter*, 1983, North-Holland, *Physics Publishing Amsterdam*, 1984, pp. 593-596.
6. Tang, P. K.; Johnson, J. N.; and Forest, C. A., "Modeling Heterogeneous High Explosive Burn with an Explicit Hot-Spot Progress," *Eighth Symposium (International) on Detonation*, Albuquerque, NM, 1985, pp. 52-61.
7. Dremin, A. N.; Klimenko, V. Yu.; and Kosireva, J. Yu., "On the Mechanism of the Reaction "Hot-Spots" Origin at Liquid Explosives Detonation," *Eighth Symposium (International) on Detonation*, Albuquerque, NM, 1985, pp. 678-687.
8. Klimenko, V. Yu. and Dremin, A. N., "On the Decomposition Reaction Kinetics in the Shock Wave Front," *Detonation, Chemical Physics of Combustion and Explosion Processes*, Chernogolovka, USSR, 1980, pp. 69-73 (English translation in Sandia National Laboratories Report RS 3140(81/38, Feb 1981).
9. Dremin, A. N.; Klimenko, V. Yu.; Mikhailijuk, K. M.; and Trofimov, V. S., "On Decomposition Reaction Kinetics in Shock Wave Front," *Seventh Symposium (International) on Detonation*, NSWCP MP 82-334, 1981, pp. 789-794.
10. Klimenko, V. Yu. and Dremin, A. N., "The Structure of the Shock Waves Front in Liquids," *Detonation, Critical Phenomena, Physico-Chemical Transformation in Shock Waves*, Ed. by O. N. Breusov, Chernogolovka, USSR, 1978, pp. 79-84.
11. Dremin, A. N. and Klimenko, V. Yu., "On the Effect of Shock Wave Front on the Reaction Origin," *Progress in Astro-nautics and Aeronautics*, Vol. 75, 1981, pp. 253-268.
12. Barltrop, J. A. and Coyle, J. D., *Excited States in Organic Chemistry*, John Wiley, London, 1975.
13. *The Energies of the Chemical Bond Dissociation, the Ionisation Potentials and the Electron Affinity*, Ed. by V. N. Kondratiev, Nauka, Moscow, 1974.
14. Owens, F. J. and Sharma, J., "X-ray Photoelectron Spectroscopy and Paramagnetic Resonance Evidence for Shock-Induced Intramolecular Bond Breaking in Some Energetic Solids," *Journal of Applied Physics*, Vol. 51, 1980, pp. 1496-1500.
15. Odiet, S.; Peyrard, M.; Schnur, J.; and Oran, E., "Molecular Theory and Cooperative Mechanism of Shock Wave-Induced Detonation in Energetic Molecular Crystals," *International Journal of Quantum Chemistry*, Vol. 29, No. 5, 1986, pp. 1625-1634.
16. Klimenko, V. Yu., unpublished.
17. Delbene, J. and Jaffe, H. H., "The Use of the CNDO Method in Spectroscopy," *Journal of Chemical Physics*, Vol. 48, 1968, pp. 1807-1812.
18. Kondratiev, V. N., *Gas-Phase Reactions Rate Constants*, Nauka, Moscow, 1971.
19. Schvedov, K. K. and Koldunov, S. A., "On the Influence of the Physical State and Structure of TNT Charge on the Detonation Wave Decomposition Time," *Gorenje i Vzriv*, Nauka, Moscow, 1972, pp. 439.
20. Klimenko, V. Yu.; Davidova, O. N.; Yakovtsev, M. A.; and Dremin, A. N., "Multiprocess Detonation Model for Heterogeneous Explosives," *Journal of Chemical Physics (USSR)*, to be published.

## DISCUSSION

PER-ANDERS PERSSON  
CETR/New Mexico Tech  
Socorro, NM 87801

Could you please amplify your two regions of detonation with two specific explosives detonating in the steady state: (a) liquid NM and (b) single crystal PETN.

## REPLY

No reply from the authors.

## DISCUSSION

I. B. MISHRA  
Kanan Associates Inc.  
Churchville, MD 21028

1. We have designed experiments where we vibrationally freeze the molecules and only have transl. motion, but often find the process does not occur as in nature. EDM is rarely reached (see paper in this Proceedings by Kolodney, et al.).

2. The measurement of data by electroconductivity would not tell us what happened in picosecond time frame. It will tell us when equilibrium is reached--in my opinion. How do you think in your work you are able to get any data when system is not in equilibrium?

## REPLY

No reply from the authors.

## DISCUSSION

PIER K. TANG  
Los Alamos National Laboratory  
Los Alamos, NM 87545

I have formulated a model with both heterogeneous and homogeneous processes in parallel and found the same changeover behavior. However, for the homogeneous process to be effective at moderate shock level, the activation temperature appeared in the Arrhenius kinetics must be much lower than the normal thermal decomposition value. Since only the ratio of the activation temperature to the high explosive temperature enters into the kinetics, the low activation temperature requirement is actually equivalent to the overheat condition. This overheat must have an excitation phase and then a relaxation phase. Can you comment on my observation?

## REPLY

No reply from the authors.

# DETONATION SHOCK DYNAMICS: A NEW APPROACH TO MODELING MULTI-DIMENSIONAL DETONATION WAVES\*

J. B. Bdzil and Wildon Fickett  
Los Alamos National Laboratory  
Los Alamos, New Mexico 87545

and

D. S. Stewart  
University of Illinois  
Urbana, Illinois 61801

*One of the principal questions in computational two-dimensional (2D) detonation hydrodynamics concerns the development of an efficient numerical method that yields high-resolution results in both the thin reaction zone and in the broad products expansion region. When the radius of curvature of the detonation shock is large compared to the reaction-zone length, we show how the 2D problem can be reduced to a one-dimensional evolution equation for the shock. We call this method Detonation Shock Dynamics (DSD). We have implemented the DSD method as a Fortran subroutine. It can solve detonation wave spreading problems in complex explosive geometries. Calculations done with this code take only a few minutes: a small fraction of the tens of hours needed to do a full numerical simulation.*

## INTRODUCTION

Most applications of explosives utilize pieces with complex three-dimensional (3D) shapes. At times, these applications require precise knowledge of the time of detonation arrival at specified locations in the explosive. In such situations, the designer needs to be able to accurately predict the evolving multi-dimensional detonation pressure and shock shape. In this paper we show that our Detonation Shock Dynamics<sup>1</sup> (DSD) method can be used to efficiently calculate the wave-spreading problem, including the effects accompanying the finite length of the reaction zone. We begin by describing the basic problem that concerns us.

As a high-order detonation consumes a piece of explosive, the evolving 3D detonation-shock surface (shock) mirrors in its complexity the shape of the undetonated explosive. That is, geometric effects (herein called **kinematics**), such as the shapes of the explosives' boundaries and the shock in the booster region, dominate the shock evolution problem. The hydrodynamic effects (herein called **dynamics**), which determine the response of the shock-normal speed ( $D_n$ ) to the flow, play a secondary role. In the extreme limit that  $D_n$  is the constant Chapman-Jouguet (CJ) speed ( $D_{CJ}$ ), the problem becomes a purely geometrical one, the Huygens construction of geometrical optics. This simple model has for years been the workhorse used to propagate detonation in two-dimensional (2D) numerical hydrodynamic computer codes. The advantage of the model is that all of the computational resources can be dedicated to the working fluid: the large-scale expansion wave that the

\*Work performed under the auspices of the U. S. Department of Energy.

detonation products undergo. Although this is an idealization, it is a reasonable one when sensitive explosives are used. With the advent of insensitive high-explosives, this simple model is no longer adequate, however. To understand why this is so, we need to discuss how the reaction zone and  $D_n$  are influenced by multi-dimensional diverging flows.

Two observations need to be made. The first is a simple scaling law. Let us say that the explosive piece's representative dimension is  $L_1$ , and its reaction-zone length is  $L_2$ . Then, all other things being equal, the shock evolution depends only on the dimensionless ratio,  $P = L_2/L_1$ . The second is an observation made of steady 2D detonation in the liquid explosive nitromethane and its interpretation via steady-state theory.<sup>2</sup> The measured shock shape and the inferred reaction-zone length are shown in Figure 1. If the reaction zone were infinitesimally thin, the shock would be flat and the Huygens model would apply. Instead one observes that compared to its length, the reaction zone has a disproportionately large effect on the shock. The shock is broadly curved over a distance of many tens of reaction-zone lengths, while  $L_1 \sim 1000 - 10,000L_2$ . In this configuration, the shock-normal speed ( $D_n$ ), is

$$D_n = D_o \cos(\phi), \quad (1)$$

where  $D_o$  is the steady wave phase velocity, and  $\phi$  is the angle between the shock normal and the axial direction. It is thus clear that the

physically important wave speed,  $D_n$ , is lower than  $D_{CJ}$  (i.e.,  $D_n < D_{CJ}$ ) over a distance from the edge of  $\approx 100L_2$ . Concomitantly, in this region the pressures, etc. are reduced, which affects both the reaction rates and ultimately the entropy on the products release isentrope. When these observations are combined, one sees that for  $P \ll 1/1000$  only a few percent of the explosive experiences a reduced detonation state.

Returning to the question concerning the suitability of the Huygens construction, when  $P \ll 1/1000$  the non-Huygens region represents one percent of the explosive; this is a tolerable error. When  $P \geq 1/1000$ , the non-Huygens region is ten percent; this is an unacceptable level.

The typical engineered explosive piece is  $O(100 \text{ mm})$ , and the reaction-zone length for the nominal sensitive explosive PBX 9404 is  $O(.01 \text{ mm})^3$ , which makes  $P \sim 1/10,000$ . The Huygens method would provide a tolerable description for such a system. By contrast, the reaction-zone length for the nominal insensitive TATB-based explosives is  $O(1 \text{ mm})^4$ , which makes  $P \sim 1/100$ . For such a system the errors resulting from the Huygens model are intolerably widespread. Reversing this argument, we adopt the following convention for sensitivity under the conditions of high-order detonation:

- sensitive:  $P < 1/1000$
- insensitive:  $P > 1/1000$ .

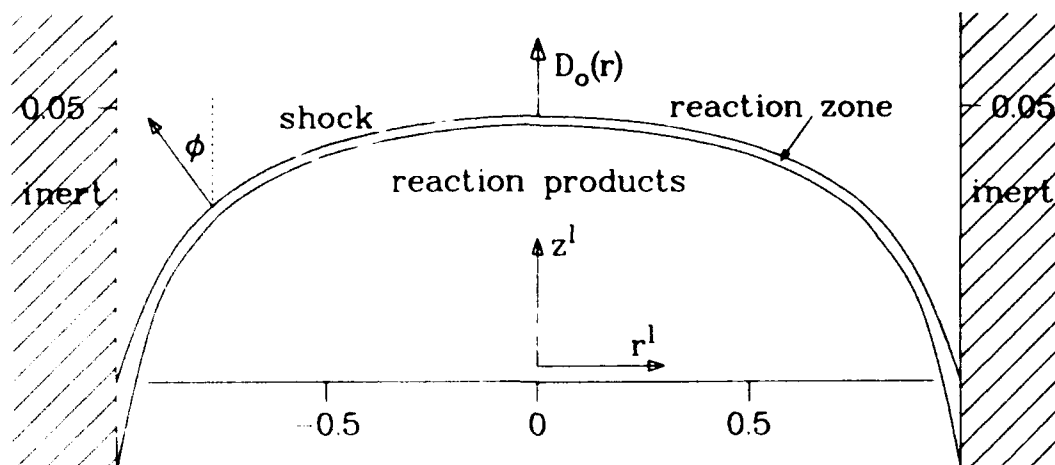


Figure 1. Snapshot of a Detonation Propagating Steadily in a Right-Circular Cylinder (Axis Pointing Upwards) in Liquid Nitromethane Explosive. The shock is experimentally measured and the reaction-zone length is calculated. Three length scales are apparent. The detonation state (i.e., pressure, etc.) is reduced near the edges. Note that the vertical scale is expanded.



The size of the explosive piece defines its sensitivity. In order to adequately be able to predict wave spreading when  $P \geq 1/1000$ , one needs to model the reaction-zone dynamics.

The standard approach to this problem is to model both the thin reaction zone and broad products regions with a uniform grid 2D numerical simulation. This requires that we have a compatible equation of state (EOS) and rate law ( $R$ ) set calibrated to the detonation regime. To get a quite modest level of resolution in the reaction zone (i.e.,  $O(20)$  cells) in the streamwise direction) necessitates using many tens of thousands of computational zones in the full problem. With today's generation of supercomputers, the computation times for a typical problem are tens of hours.

Some years ago (see Reference 5), we suggested an alternative approach: we referred to it as a "reactive-Huygens" construction. The calculations reported in Reference 5 deal with a fully time-dependent, 2D detonation reaction zone, and consider how a rarefaction from the explosive's lateral edge penetrates into the reaction zone and deforms the shock. The significant conclusions of that calculation are:

- (i) after a short, small shock-deformation phase, the flow in the reaction zone becomes quasisteady. The reaction zone interacts with the shock, which is broadly curved, only parametrically, and
- (ii) the surface kinematics carry the time dependence.

Importantly, not only is the flow quasisteady, but it is also quasi one-dimensional (1D) in the shock-normal direction. Even though the net shock deflection is large, the local radius of curvature of the shock ( $R$ ) is much greater than the reaction-zone length. When taken together, the result is the flow pictorial shown in Figure 2: (i)  $L_2/R \ll 1$ , and (ii) in adjacent weakly interacting streamtubes the reaction zone flow is of a 1D nozzle type.

Drawing on these conclusions, and inspired by Whitham's<sup>6</sup> 2D theory for inert shock propagation called Geometrical Shock Dynamics, we have developed a "reactive-Huygens" theory. We call it Detonation Shock Dynamics (DSD). It applies to problems where

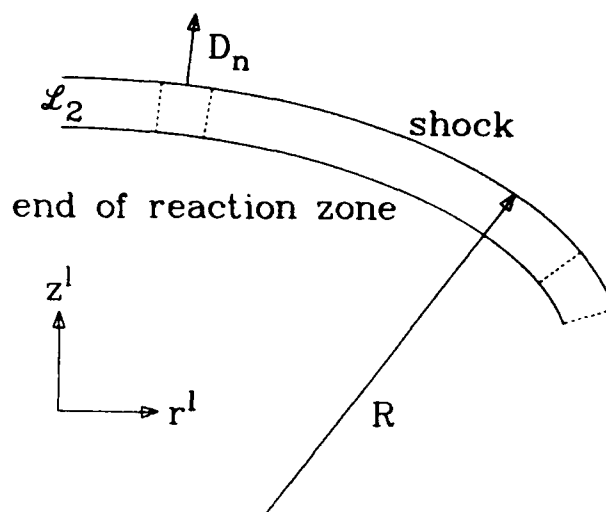


Figure 2. A Schema of a Large Radius of Curvature ( $R$ ) Shock and the Following Quasi One-Dimensional Reaction-Zone Streamtubes. The reaction-zone length ( $L_2$ ) and the laboratory ( $z^1, r^1$ )-coordinates are shown.

the radius of curvature of the shock is large compared to the reaction-zone length (i.e.,  $R/L_2 \gg 1$ ), the typical situation in many explosive applications. A key element in the development of the theory is the transformation of the 2DEuler equations and kinematics into a problem conforming, intrinsic coordinate frame.<sup>1</sup> When  $R/L_2 \gg 1$ , the 2D time-dependent equations in this frame are reduced to a sequence of 1D problems. We have recently completed work on a Fortran 77 subroutine that uses this method to solve wave-spreading problems for any 2D, multi-boundary explosive geometry. In the last sections of this paper we display and discuss some calculations done on prototypical explosive geometries.

We note that Lambourn<sup>7</sup> has recently developed a method similar to ours. He uses a different coordinate representation of the equations. Also Bukiet and Menikoff<sup>8</sup> have studied the 1D spherically expanding wave problem by assuming quasisteady reaction zone dynamics. These results can be found in these proceedings.

This paper is subdivided into seven sections. In the section entitled Kinematics and Boundaries, we present our coordinate representation of the surface kinematics and describe how we treat multiple boundaries and

the boundary conditions. In the section entitled Reaction-Zone Dynamics, we discuss the intrinsic coordinate form of the 2D Euler equations in terms of the master equation and outline how we find the reaction-zone dynamics. In the section entitled Results for the Analog, we employ a generalization of Fickett's analog model<sup>9</sup> to 1D cylindrical flow to briefly review the dependence of the dynamics on the shock curvature and the rate. Some analytical results for the steady 2D rate-stick geometry and the DSD code solution of the time-dependent problem are given in the section entitled 2D Rate Stick. In the section entitled DSD Examples, we present and briefly describe some DSD calculations of detonation in prototypical explosive geometries. We conclude with a summary.

## KINEMATICS AND BOUNDARIES

A key ingredient of our theory is the geometric compatibility condition for a moving surface: commonly referred to as the eikonal. Since we wish to describe wave spreading in explosives with complex boundaries where flow conditions may need to be applied, we adopt arc-length ( $\xi$ ) along the shock and time ( $t$ ) as the independent variables and the angle ( $\phi$ ) that the shock normal makes with the cartesian  $z$ -axis as the dependent variable. The zero of arclength is the shock and local left explosive edge intersection locus. See Figure 3 for details. The laboratory coordinates are returned by

$$\begin{aligned} z_o^l &= z_{e1} - \int_0^\xi \sin(\phi) d\xi ; \\ r_o^l &= r_{e1} + \int_0^\xi \cos(\phi) d\xi , \end{aligned} \quad (2)$$

where  $z_{e1}(t)$  and  $r_{e1}(t)$  are the coordinates of the left edge.

### Kinematics

In our coordinates, the 2D shock geometric compatibility condition is a 1D Burgers equation:<sup>1</sup>  $B$  is the "wave" velocity and  $D_{n,\xi}$  is the transport term

$$\phi_{,\xi} + B\phi_{,\xi} = -D_{n,\xi} , \quad (3)$$

where the subscript  $_{,x}$  indicates a partial derivative with respect to  $x$ . The local shock curvature is  $\kappa \equiv \phi_{,\xi}$  and  $B$  is the change in arclength with time along a constant- $\beta$  ray

$$B = \int_0^\xi \phi_{,\xi} D_n d\xi + D_{n1} \tan(\phi_1 - \phi_{e1}) , \quad (4)$$

where the integral is taken at constant time and subscript 1 indicates the current left-edge value. The cartesian coordinates of the left edge are

$$r_{e1}(t) = r_{e*} + \int_0^t \frac{D_{n1} \sin(\phi_{e1})}{\cos(\phi_1 - \phi_{e1})} dt \quad (5a)$$

$$z_{e1}(t) = z_{e*} + \int_0^t \frac{D_{n1} \cos(\phi_{e1})}{\cos(\phi_1 - \phi_{e1})} dt , \quad (5b)$$

where  $(r_{e*}, z_{e*})$  are initial values. See Reference 1 for more details.

As a general rule, the space into which the shock spreads is either expanding or contracting. Thus, the shock's total arclength from the left to the right boundary must also vary. The instantaneous rate of change of its total length is

$$\frac{d\xi_2}{dt} = B_2 - D_{n2} \tan(\phi_2 - \phi_{e2}) , \quad (6)$$

where  $B_2$  is obtained from Equation (4), the next term measures the rate at which a constant- $\beta$  ray intercepts the right edge and subscript 2 refers to the right boundary. The total arc-length is obtained by integrating Equation (6) with respect to time along the shock/right edge intersection locus.

Taken together, Equations (3), (4), and (6) provide the complete kinematic description of the shock in our variable width  $\xi$ -space. Significantly, this geometry conforming intrinsic representation remains uniformly valid for all realizable explosive geometries. As a counter example, the cartesian coordinates used in Reference 14 are suitable for detonation propagating in the  $z_o^l$ -direction, but not for detonation in the  $r_o^l$ -direction.

Two more issues need to be addressed to complete the problem: (i) a rule for  $D_n$  and (ii) the edge boundary conditions. The discussion

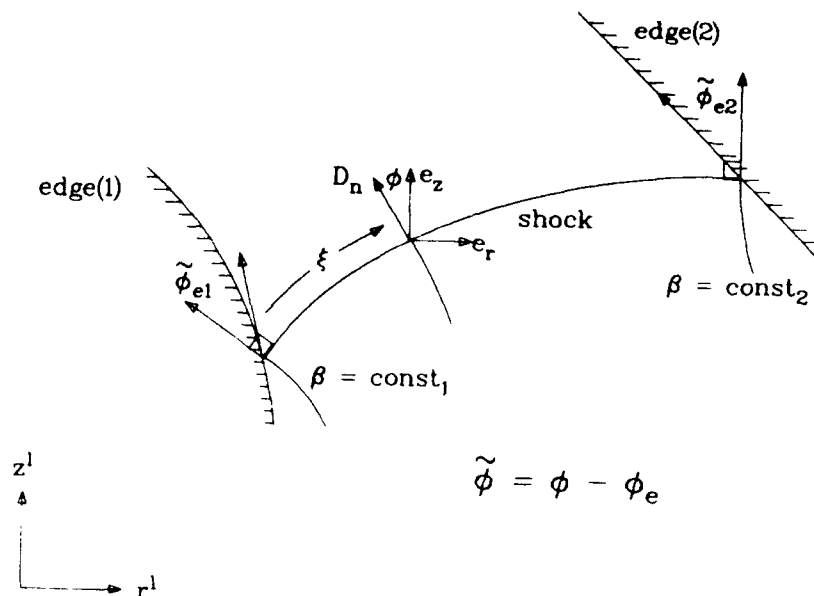


Figure 3. The Intrinsic Coordinate Representation of the Shock. The shock-normal angle is  $\phi$  (measured as positive in the clockwise direction from  $e_z$ ),  $D_n$  is the speed of the shock normal to itself and  $\phi_e$  is the direction of the tangent to the edge. The curves  $\beta = \text{constant}$  are normal to the shock and are Whitham's shock generators.<sup>6</sup>

of (i) is presented in the section entitled Reaction-Zone Dynamics. Here we remark only that for the simple Huygens wave (e.g., say with  $D_n = 1$ ), Equations (3), (4), and (6) are a closed system. We now turn to (ii).

### Boundary Conditions

For a more complete discussion of the boundary conditions consult References 1, 3, 5, and 10. Here we simply state the proper conditions for a free edge (i.e., an explosive/vacuum interface).

The control function for the boundary condition is the sonic parameter,  $S$ , evaluated at the shock/interface locus and defined by

$$S \equiv C^2 - |\tilde{U}|^2 \quad (7)$$

In Equation (7)  $C$  is the sound speed and  $\tilde{U}$  is the vector particle velocity measured relative to an observer riding with the shock/interface intersection locus, which at the left edge is

$$\tilde{U} \equiv U_1^1 - n_1 D_{n1} + t_1 D_{n1} \tan(\phi_1 - \phi_{e1}) \quad (8)$$

where  $n_1$  and  $t_1$  are the shock's normal and tangent vectors at the edge. When the state

ahead of the shock is quiescent, Equation (7) reduces to

$$S_1 = C_1^2 - (U_{n1}^1 - D_{n1})^2 - D_{n1}^2 \tan^2(\phi_1 - \phi_{e1}) \quad (9)$$

Depending on the detonation model we assume, we need an unreacted and/or reacted EOS to evaluate  $C^2$ .

The boundary condition is summarized by the following rule: monitor  $S(D_{n1}, \phi_1 - \phi_{e1})$  at the edges. If  $S_1 < 0$ , the flow is supersonic and no condition is applied. When  $S_1 \geq 0$ , then  $D_{n1}$  and  $(\phi_1 - \phi_{e1})$  are adjusted to satisfy  $S(D_{n1}, \phi_1 - \phi_{e1}) = 0$ . This rule is applied at both edges of the shock.

This sonic boundary condition also applies when the explosive is confined with materials of sufficiently low shock impedance. For a discussion of this problem and the conditions for strong confinement, the reader is referred to References 2, 3, 10, and 14.

### REACTION-ZONE DYNAMICS

To get a rule for  $D_n$ , we need to solve the time-dependent 2D Euler equations. We express them in terms of the same shock-based intrinsic frame already discussed, and

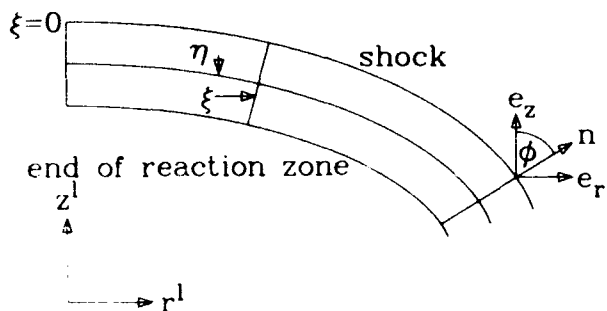


Figure 4. The Spatial Coordinates Used for the Euler Equations

introduce the variable  $\eta$  to measure distance behind the shock (measured along the extension of the local shock normal). These coordinates are shown in Figure 4. They are related to the laboratory cartesian frame by

$$z^1 = z_o^1 - \eta \cos \phi; \quad r^1 = r_o^1 - \eta \sin \phi, \quad (10)$$

where  $(z_o^1, r_o^1)$  are given by Equation (2). The four Euler equations of mass, two components of momentum and energy are transformed to these coordinates. Here we do not record them in their native form, but instead give one derived equation that highlights their hydrodynamically significant features: the master equation

$$\begin{aligned} & [C^2 - (D_n - U_\eta)^2] (D_n - U_\eta)_{,\eta} + (E_\lambda / \rho E_p) R = \\ & - C^2 (1 - \eta \kappa)^{-1} (\kappa U_\eta + U_{\xi,\xi}) \\ & - (D_n - U_\eta) J\{U_\eta\} - \rho^{-1} J\{P\} \\ & - U_\xi (D_n - U_\eta) (1 - \eta \kappa)^{-1} (D_{n,\xi} - \kappa U_\xi). \end{aligned} \quad (11)$$

The new variables appearing in Equation (11) are the  $\eta$  and  $\xi$ -components of the particle velocity;  $U_\eta$  and  $U_\xi$ , the specific internal energy EOS;  $E(P, \rho, \lambda)$ , the pressure, density, rate and degree of reaction ( $P, \rho, R, \lambda$  with  $\lambda = 1$  indicating complete reaction); and the operator

$$J\{\} \equiv \{\}_{,\eta} + B\{\}_{,\xi} + \quad (12)$$

$$(1 - \eta \kappa)^{-1} (U_\xi - \eta D_{n,\xi}) \{\}_{,\xi}.$$

The native equations are given in Reference 1. In this frame, the shock conditions are simply the standard 1D Hugoniot conditions. At the shock (i.e.,  $\eta = 0$ ), the transverse velocity  $U_\xi = 0$  and Equation (11) is called in the literature the 2D shock-change equation.

Equation (11) does not provide a self-contained description of the flow. However, it focuses our attention on all of the important physical balances that determine the reaction-zone dynamics. We will now examine these balances, beginning with the familiar one, and ending with the one relevant for our application.

- (i) The basic steady detonation balance is obtained with the right side of Equation (11) set to zero: acoustics (i.e., the flow gradient) balances the heat-release rate. Both terms are  $O(1)$  near the shock, but simultaneously go to zero as  $\lambda \rightarrow 1$  (i.e.,  $R \rightarrow 0$  as the local sonic parameter  $[C^2 - (D_n - U_\eta)^2] \rightarrow 0$ ).
- (ii) When the flow is 1D (i.e., cylindrically symmetric with  $U_\xi = 0$  and  $\{\}_{,\xi} = 0$ ) and the shock is broadly curved (i.e., the curvature  $\kappa = \phi_{,\xi} = O(\epsilon)$  with  $0 < \epsilon < 1$ ), then the flow near the shock acts like (i) plus a small correction that is related to  $\kappa$ . However, this (i)-like balance is disrupted as  $\lambda \rightarrow 1$ , since  $R$ ,  $[C^2 - (D_n - U_\eta)^2]$  and  $\kappa$  are all small there. In Reference 5 we showed that for a fully 2D broadly curved detonation driven by a state-independent  $R$ , both  $U_\xi$  and  $J\{\}$  are negligible near  $\lambda \rightarrow 1$ . From these results it follows that:
- (iii) the basic balance for a broadly curved 2D detonation is given by

$$\begin{aligned} & [C^2 - (D_n - U_\eta)^2] (D_n - U_\eta)_{,\eta} \\ & + (E_\lambda / \rho E_p) R = -\kappa C^2 U_\eta + \dots, \end{aligned} \quad (13)$$

where the ellipses denote higher-order terms. This basic balance is

locally 1D (i.e., in the  $\eta$ -direction) and quasisteady; it is a nozzle flow.

At this level of approximation, the 2D Euler equations also yield a Bernoulli law

$$E + P/\rho + \frac{1}{2}(D_n - U_\eta)^2 = E_0 + \frac{1}{2}D_n^2, \quad (14)$$

and the nozzle equation

$$\rho(D_n - U_\eta) = \rho_0 D_n - \kappa \rho_0 D_n \int_0^\lambda \frac{U_\eta}{R} d\lambda, \quad (15)$$

where the subscript zero denotes the unshocked state and the integral is evaluated using the ZND expressions for  $U_\eta$  and  $R$ . Together with Equation (13) and the 1D Hugoniot relations, this is simply the detonation eigenvalue problem considered in Fickett and Davis.<sup>11</sup> The only acceptable solution for a diverging detonation has the rate ( $R$ ) and divergence ( $\kappa$ ) terms balance where  $[C^2 - (D_n - U_\eta)^2] = 0$ . This functionally constrains  $D_n$  and  $\kappa$

$$D_n(\kappa) \quad (16)$$

Equation (16) describes the reaction-zone dynamics for a diverging system. It is strikingly simple and universal, in the sense that it is independent of initial/boundary data. Taken together with the kinematic and edge conditions discussed earlier, it provides a complete method for including reaction zone effects in the shock propagation problem.

In the next section we solve this eigenvalue problem for a variety of rate-law forms,  $R$ . The vehicle we use for our presentation is Fickett's analog.<sup>9</sup>

## RESULTS FOR THE ANALOG

The generalization of Fickett's reactive analog to nozzle flows is described in Reference 12. The solution of the reaction-zone dynamics problem that concerns us is presented there in detail. Here we just briefly sketch the solution.

The analog equivalent of Equation (13) is

$$-2D_n(\rho - D_n)\rho_{,x} - R = -\kappa D_n, \quad (17)$$

where  $\rho$  is the analog variable (not to be confused with the physical density of the last section) and  $x$  is distance behind the shock.

The relation of Equation (17) to Equation (13) is clear. The shock condition for this model is  $\rho = 2D_n$  at  $x = 0$ . We study rates of arbitrary order,  $v$

$$D_n \lambda_{,x} \equiv R = (1 - \lambda)^v \quad (18)$$

In the  $(\rho, \lambda)$ -plane, Equations (17) and (18) yield

$$2(\rho - D_n)\rho_{,x} = -1 + \kappa D_n(1 - \lambda)^{-v}, \quad (19)$$

which is easily integrated to get

$$(\rho - D_n)^2 = D_n^2 - \lambda + (1 - v)^{-1} \kappa D_n [1 - (1 - \lambda)^{1-v}], \quad (20)$$

after the shock condition is applied. Insisting that the solution be real valued for  $0 \leq \lambda \leq 1$ , gives the eigenvalue condition

$$\rho - D_n = 0 \quad \text{when} \quad \kappa D_n(1 - \lambda)^{-v} - 1 = 0. \quad (21)$$

The simultaneous solution of Equations (21) yields an implicit relation for  $D_n(\kappa)$

$$D_n^2 = 1 - (1 - v)^{-1} \kappa D_n + v(1 - v)^{-1} (\kappa D_n)^{1/v}, \quad (22)$$

which for  $\kappa \ll 1$  has the leading order dependencies shown

$$\begin{aligned} 0 \leq v \leq \frac{1}{2} & \quad D_n = 1 - \frac{1}{2}(1 - v)^{-1} \kappa + O(\kappa^2) \\ \frac{1}{2} < v < 1 & \quad D_n = 1 - \frac{1}{2}(1 - v)^{-1} \kappa + O(\kappa^{1/v}) \\ v = 1 & \quad D_n = 1 + \frac{1}{2} \kappa \ln \kappa - \frac{1}{2} \kappa + O((\kappa \ln \kappa)^2) \\ 2 \geq v > 1 & \quad D_n = 1 + \frac{1}{2} v(1 - v)^{-1} \kappa^{1/v} + O(\kappa) \\ v > 2 & \quad D_n = 1 + \frac{1}{2} v(1 - v)^{-1} \kappa^{1/v} + O(\kappa^{2/v}). \end{aligned}$$

The higher-order terms indicated by the  $O$ -symbol have recently been calculated for the physical system by Klein.<sup>13</sup> For results on the physical problem, the reader is referred to References (14), (13), and (8). We note that Wood and Kirkwood<sup>15</sup> have been widely credited with showing that  $D_n$  is a linear function of  $\kappa$ . They considered cases where  $v \geq 1$ . Our results on both the physical system<sup>14</sup> and

the analog<sup>12</sup> show that their result is flawed. The source of the error can be traced to their improper treatment of the solution layer near  $\lambda = 1$ . Terms like  $\kappa \ln \kappa$  arise in that layer.

The flow profile (i.e., the analog variable  $\rho$  vs.  $\lambda$ ) through the reaction zone is given by Equation (20). The results for  $\rho$  vs.  $x$  are plotted in Figure 5 for  $v = 1$  and three values of  $\kappa$ . The most striking feature is the large influence that  $\kappa$  has on the flow near the end of the reaction zone. This is a consequence of the transonic character of the flow there. We note that calculations done with the physical equations (i.e., Equation (13), etc.) closely mirror all of these results.

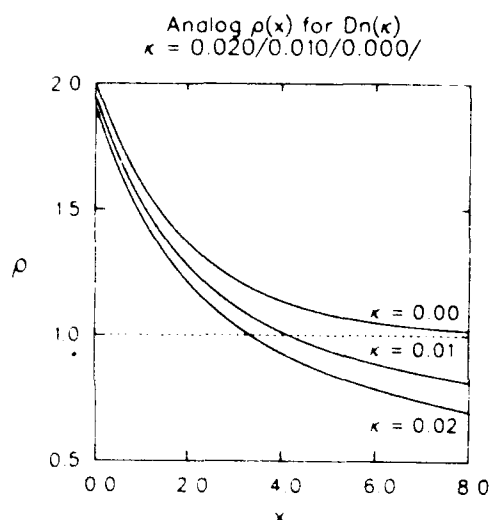


Figure 5. The Reaction Zone Flow for the Analog<sup>9</sup> When  $\kappa = 0.00/0.01/0.02$ . Note that the greatest departure from a planar 1D flow is near the end of the reaction zone.

In the remaining sections, we turn our attention to applying the DSD method to calculating detonation evolution in some typical 2D explosive geometries.

## 2D RATE STICK

The prototypical 2D explosive geometry is that of the detonation-rate stick. For the calculations we report here, we consider 2D explosive slabs rather than the axisymmetric cylindrical geometry. Qualitatively, the results are the same for these two cases.<sup>3</sup>

## Steady State

We begin by giving some new results for steady-state detonation. In the following calculations, we assume a scaling where  $D_{CJ} = 1$ , a strong-shock approximation and a polytropic EOS, with  $\gamma$  the polytropic exponent. Then for an unconfined explosive edge, Equation (9) gives the boundary condition

$$\tan^2(\phi_1 - \phi_{e1}) = \frac{\gamma - 1}{\gamma + 1} \quad (24)$$

We assume detonation in the positive  $z^1$ -direction and that the edges of the explosive are planes of constant  $r^1$  (i.e.,  $\phi_{e1} = 0$ ) separated by a distance  $2r$ . For this problem, the kinematics reduce to Equation (1).

$$D_n = D_o(r) \cos(\phi) \quad (25)$$

where  $D_o(r)$  is the measured steady  $z^1$ -direction phase velocity of the wave (improperly called the detonation velocity). The inverse function,  $\kappa(D_n)$  is assumed to exist.

We can generate a differential equation for the steady shock angle,  $\phi(r_o^1)$  by equating  $\kappa(D_n)$  to  $\phi_{,\xi}$  and then using Equation (2) to change independent variables (i.e.,  $dr_o^1 = \cos(\phi)d\xi$ ). Integrating the resulting equation, we get an expression for  $r_o^1(\phi)$ ,

$$r_o^1(\phi) = \int_{\phi_e}^{\phi} \frac{\cos(\phi)d\phi}{\kappa(D_o \cos \phi)} \quad (26)$$

where the left explosive edge is at  $r_o^1 = 0$ . By symmetry, it follows that

$$r = \int_{\phi_e}^0 \frac{\cos(\phi)d\phi}{\kappa(D_o \cos \phi)} \quad (27)$$

When  $D_n(\kappa)$  is known, Equation (27) defines the diameter effect,  $D_o(r)$ . We can also think of Equation (27) as defining an inverse problem: determine  $\kappa(D_n)$  given  $r(D_o)$ . Viewed in this way, it gives us a way to use the large body of phase velocity data to get at least a crude calibration for the  $D_n(\kappa)$  function that we need for DSD. We demonstrate how this might be done by showing that in the limit  $D_n \rightarrow 1$  Equation (27) is an Abel integral equation.

Under the transformation  $y \equiv (D_0 \cos \phi)^2$ , Equation (27) becomes

$$\int_{D \cos^2 \phi}^D \frac{dy}{\kappa(\sqrt{y})\sqrt{D-y}} = 2 \cdot r(D_0) \cdot D_0 \equiv f(D), \quad (29)$$

where  $D \equiv D_0^2$ . As  $D_0 \rightarrow 1$  and  $r(D_0) \rightarrow \infty$ , we can approximate Equation (29) by taking the lower limit to zero (see Reference 12 for details). In this limit, the solution of the resulting Abel integral equation is

$$\lim_{D_0 \rightarrow 1} \frac{1}{\kappa(D_0)} = \frac{1}{\pi} \int_0^D \frac{f'(s)ds}{\sqrt{D-s}} + \dots \quad (30)$$

Equation (30) gives us some insights into how  $D_n(\kappa)$  is mapped into  $D_0(r)$ . In turn, when these are combined with the results of the previous section, we can get some hints about explosive heat-release rates. As an example, we consider that as  $D_0 \rightarrow 1$ ,  $D_0(r)$  is given by

$$D_0 = 1 - (a/r)^m + \dots, \quad (31)$$

where  $a$  and  $m$  are constants with  $m \geq 1$ . Performing the quadrature in Equation (30) and then simplifying the result consistent with  $D_0 \rightarrow 1$ , we find

$$D_n = 1 - \left[ \frac{a m \Gamma\left(\frac{m+1}{2}\right) \Gamma\left(\frac{1}{2}\right)}{\sqrt{2} \pi \Gamma\left(\frac{m+2}{2}\right)} \kappa \right]^{\frac{2}{m+1}} + \dots, \quad (32)$$

where  $\Gamma()$  is the gamma function (e.g.,  $\Gamma(5) = 4!$ ). The combined results of this section and the section entitled Results for the Analog are summarized in Table 1.

The important lessons that we learn are: simultaneous linear fits for  $D_0$  vs  $r^{-1}$  and  $D_n$  vs  $\kappa$  are incompatible, and upward concavity in  $D_0$  vs  $r^{-1}$  implies that the explosives' heat-release rate has a long tail. In the next subsection, we solve the DSD equations for a time-dependent rate stick problem.

Table 1.  $D_0(r)$  Mappings

$D_0 = 1 - (a/r)^n$	$D_n = 1 - (\alpha\kappa)^\mu$	$(1 - \lambda)^\nu$
$n$	$\mu$	$\nu$
2	1	$0 \leq \nu < 1$
1	2/3	3/2
2/3	1/2	2

### Time Dependent

We have written a Fortran 77 subroutine that uses DSD to solve 2D detonation wave spreading problems.<sup>16</sup> A partial list of its features includes:

- (i) a variable arclength shock, intrinsic coordinate formulation with a uniform arclength density computational mesh,
- (ii) the ability to treat explosives with two edges and independent boundary conditions at each edge,
- (iii) general  $D_n(\kappa)$  reaction-zone dynamics,
- (iv) a variety of boundary conditions,
- (v) arbitrary initial shock data,
- (vi) conventional Huygens reference shocks, and
- (vii) wave tracking for disturbances moving along the shock (e.g., delineating the regions of the shock that have been affected by edge rarefactions).

More details are given in a Los Alamos Report<sup>16</sup> entitled "DSD Technology: A Detonation Reactive-Huygens Code." We demonstrate some of its capabilities with a few examples. Importantly, a high-resolution calculation on any of our examples takes only a few minutes of supercomputer time.

The symmetric 2D-slab geometry detonation-rate stick serves as a useful test problem since it has an analytical steady-state solution. For all the remaining examples we select a linear  $D_n(\kappa)$  (i.e.,  $D_n = 1 - \alpha\kappa$ ; with  $\alpha = 0.05$ ) for the dynamics, a polytropic EOS with  $\gamma = 3$ , no confinement, and a flat shock as

initial data. Figure 6 shows snapshots of the cartesian representation of the shock locus after a travel of roughly 1, 2, 3, and 4 explosive "radii." At  $t = 0$  the shocks are drawn to scale, at later times they are magnified vertically. The track along the shock of the edge rarefaction wave head is denoted by circles.

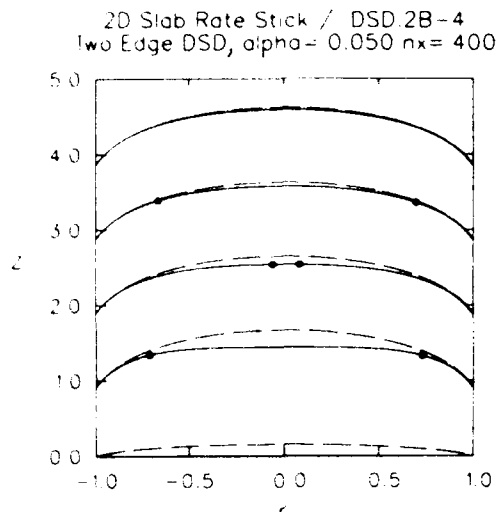


Figure 6. DSD Calculated Shock Shapes for the Rate Stick Explosive Geometry. The exact steady-state solution (i.e., — · — · —) is shown for comparison. The parameter values are:  $DCJ = 1$ ,  $\alpha = 0.05$  and  $\gamma = 3$ . At  $t = 0$  the shocks are unscaled: at later times they are magnified.

The chain-dot curve is the edge-justified steady-state shock locus. Noteworthy features of this calculation include: (i) the shock travels roughly one "diameter" before the edge rarefaction reaches the centerline, and (ii) based on a comparison with the steady solution, the wave is steady after running two "diameters." The flow is always sonic (i.e., Equation (9) is zero) at the edge.

A considerable phase-velocity database exists for detonation in this geometry that could be used to help calibrate DSD.<sup>1</sup> However, this simple geometry is hardly typical of the complex explosive pieces encountered by the engineer. In the next section, we consider some of these other geometries.

## DSD EXAMPLES

The popularity of the rate stick as a probe is attributable largely to matters of convenience; it is simple to fabricate, it supports a

steady wave whose phase velocity is easy to measure, and it has a sharp wave-extinction point called the failure diameter. However, this experiment, which does probe the interaction of the two edge rarefactions, does not test the full spectrum of 2D stimuli that detonation can experience. The important practical problem of wave spreading, either by divergence or diffraction (i.e., corner turning), is barely probed in this geometry.

All of these phenomena are kinematical in nature. We can appreciate what some of the differences are between them by examining Equation (3) in more detail

$$\phi_{,t} + B\phi_{,\xi} = -D_{n,\xi} \quad ,$$

edge

where

$$\left(\frac{d\xi}{dt}\right)_\beta \equiv B = \int_0^\xi \phi_{,\xi} D_n d\xi + D_{n1} \tan(\phi_1 - \phi_{e1}) .$$

divergence      diffraction

The role of each term is labeled. In the rate stick geometry, the diffusion-like or edge term is the most important. It carries the edge rarefaction. The flow is only weakly expansive and the total shock arclength is nearly constant. On the other hand, the simple cylindrically diverging detonation is governed by the B term alone;  $D_{n,\xi}$  is zero for this problem. The shock expansion, which is driven by an  $O(1)$  B term, is a consequence of the integral part of B. The shock arclength grows. In the corner turning problem, the detonation is diffracting. It is an expanding flow that is driven by the changes in the B term arising from the growth of  $\phi_{e1}$  in the tangent term. This last flow is the most complex type, since the divergence and edge terms also play important roles. We now examine two geometries in which the divergence and diffraction terms play important roles.

## Onionskin

The onionskin experiment is used to measure a detonation's ability to propagate from hemispherical initial data supplied by a booster (see Reference 17 for experimental



particulars). This test probes a combination of the wave spreading produced by the divergence term in B and the edge effect. Unlike the rate stick, here the two edge rarefactions do not interact.

The DSD calculation for unsymmetric initial data in a 2D-slab geometry is shown in Figure 7. The edge rarefaction wave track and the Huygens wave are displayed in addition to the DSD calculation: (— · — · —) corresponds to a  $D_n = D_{CJ} = 1$  Huygens wave and (-----) is the wave track. The initial data for this unsteady flow are given by the union of a quarter circle with a square. At the edges the flow begins and remains sonic.

There are qualitative differences between the DSD and Huygens waves, particularly near the edge. Using the Huygens method, with the time reversed, to infer the initial data given the outermost wave shape would produce a false picture of the spreading. The Huygens wave is distorted even in the edge-rarefaction free central right-half sector where only divergence acts. We note that even though the rarefaction has propagated far into the flow, strong perturbations to the wave are confined to a 30° pie-shaped region.

### Arc Experiment

The arc is more typical of the geometries that arise in explosive applications than are the previous examples. It also has the richest

mix of 2D effects: edge effect, divergence, and also diffraction. The initial data for this unsteady flow are taken to be a flat CJ detonation. The results of our calculation are shown in Figure 8, where the parameters and legends are the same as before. From the outset, the diffraction (i.e., corner turning) that occurs at the inner explosive edge dominates the flow. With the passage of time, the displacement between the DSD and Huygens waves becomes large. This implies that  $D_n$ , the pressure and particle velocity are all substantially reduced from the CJ values near this edge. After a short initial transient, all these quantities achieve steady values that are a function of the inner edge radius.

Initially, the outer edge also experiences an edge rarefaction. The influence of the edge rarefaction is soon lost to the developing supersonic flow there (i.e.,  $S(D_{n2}, \phi_2 - \phi_{e2}) < 0$ ). After the track of the leading disturbance from the outer edge rarefaction reaches the inner edge, the flow there becomes steady as well. The entire shock is then steady as viewed in a system of polar coordinates that rotate with a fixed angular velocity. The shape of this steady shock is independent of the value of the outer radius. Its shape is determined by the interaction of the rarefactions coming from the inner edge and diffraction. The value that the sonic parameter has at the outer edge,  $S_2$ , is a function of the outer radius; reducing the outer radius moves  $S_2$  towards zero. While  $S_2$

### asymmetrical onion skin

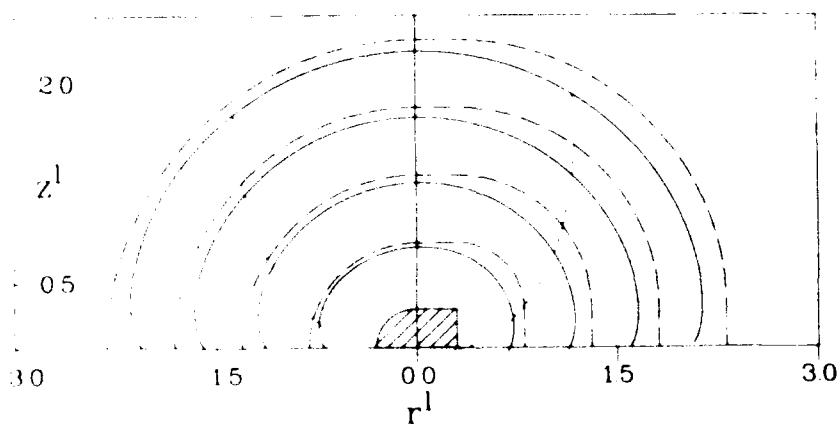


Figure 7. DSD Calculated Shock Spreading for the Onionskin Experiment. The initial data is asymmetrical. The Huygens wave is shown for comparison (— · — · —), and the dashed curve is the track of the edge rarefaction.

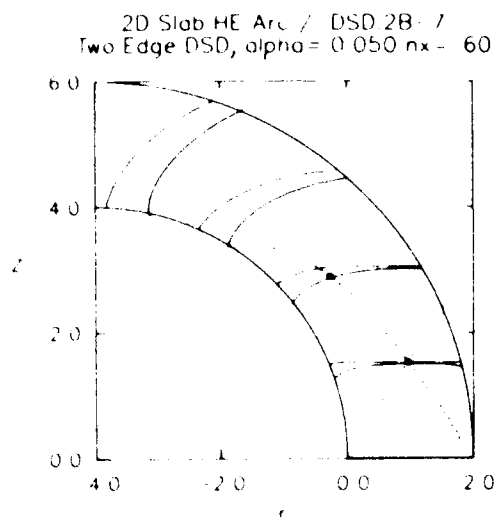


Figure 8. DSD Calculated Shock Evolution in the Arc Explosive Geometry. The flow is dominated by the inner edge-driven wave diffraction. The Huygens wave is shown for comparison (---).

$< 0$ , the steady shock shape and phase velocity that develop are not a function of the outer radius. At the value of the outer radius at which  $S_2$  just becomes zero, the independence of the steady solution on the value of the outer radius is lost. This defines a critical arc width below which the flow is determined by the interaction of two edge rarefactions and diffraction.

The richness of interactions that can occur in this geometry make it a valuable one to study. Importantly, since this geometry can support a steady wave, it is a useful one for experimentation and DSD calibration. It also probes explosive physics more relevant to the design engineer than do the other geometries we have considered.

## SUMMARY

The DSD theory that we have developed and the code that implements it represent both a major improvement over the Huygens construction and a desirable alternative to full numerical simulation of the detonation reaction zone. The theory is the rational consequence of doing an asymptotic analysis on the 2D time dependent Euler equations in the limit that the radius of curvature of the

detonation shock is large compared to the reaction-zone length. It is a fully nonlinear large amplitude theory.

The explosives design engineer is aware of the serious shortcomings of the Huygens construction for predicting wave spreading for insensitive explosives (i.e., when  $P > 1/1000$ ). Numerical simulations that resolve the reaction zone take many tens of hours for a single design iteration: this makes them impractical for routine use. When DSD technology is used to propagate high-order detonation, the same calculations can be done in minutes.

We are currently doing DSD calibration experiments to determine the reaction-zone dynamics for the explosive PBX 9502. The rate-stick and arc geometries are being used in this work.

## ACKNOWLEDGEMENTS

We thank William C. Davis and James R. Travis for their suggestions, help, and unwavering strong support of our work.

## REFERENCES

1. Bdzil, J. B. and Stewart, D. S., *Phys. Fluids A*, Vol. 1, No. 7, 1989, pp. 1261-1267.
2. Engelke, R. and Bdzil, J. B., *Phys. Fluids*, Vol. 26, No. 5, 1983, pp. 1210-1221.
3. Bdzil, J. B., *J. Fluid Mech.*, Vol. 108, 1981, pp. 195-226.
4. Seitz, W. L.; Stacy, H. L.; and Wackerle, J., "Detonation Reaction Zone Studies on TATB Explosive," *Proceedings of the Eighth Symposium (International) on Detonation*, Albuquerque, NM, 15-19 Jul 1985, pp. 123-132.
5. Bdzil, J. B. and Stewart, D. S., *J. Fluid Mech.*, Vol. 171, 1986, pp. 1-26.
6. Whitham, G. B., *Linear and Nonlinear Waves*, Wiley-Interscience, NY, 1974, pp. 263-311.
7. Lambourn, B. D., "Application of Whitham's Shock Dynamics Theory to the Propagation of Divergent Detonation Waves," *Proceedings of the Ninth*

*Symposium (International) on Detonation*, Portland, OR, 28 Aug - 1 Sep 1989.

8. Bukiet, B. G., "Computation of a Diverging Comp B Detonation," *Proceedings of the Ninth Symposium (International) on Detonation*, Portland, OR, 28 Aug - 1 Sep 1989.
9. Fickett, Wildon, *Introduction to Detonation Theory*, University of California, Berkeley, 1985.
10. Bdzil, J. B., "Perturbation Methods Applied to Problems in Detonation Physics," *Proceedings of the Sixth Symposium (International) on Detonation*, Coronado, CA, 24-27 Aug 1976, pp. 352-370.
11. Fickett, W. and Davis, W. C., *Detonation*, University of California, Berkeley, CA, 1979, Chapter 5.
12. Bdzil, J. B. and Fickett, W., "A Simplified Theory of the Steady 2D Detonation," *Phys. Fluids A*, to be submitted, 1989.
13. Klein, R., "Stable Curved Detonations," *Combustion Flame*, to be submitted, 1989.
14. Stewart, D. S. and Bdzil, J. B., *Combustion Flame*, Vol. 72, 1988, pp. 311-323.
15. Wood, W. W. and Kirkwood, J. G., *J. Chem. Phys.*, Vol. 22, 1954, pp. 1920-1924.
16. Fickett W. and Bdzil, J. B., "DSD Technology: A Detonation Reactive-Huygens Code," *Los Alamos Report* (to be published), 1989.
17. Bahl, K.; Bloom, G.; Erickson, R.; Lee, R.; Tarver, C.; Von Holle, W.; and Weingart, R., "Initiation Studies on LX-17 Explosive," *Proceedings of the Eighth Symposium (International) on Detonation*, Albuquerque, NM, 15-19 Jul 1985, pp. 1045-1056.

## DISCUSSION

MANFRED HELD

MRB

Schrobenhauser, West Germany

In corner effects we have high pressure in the initiation direction (head-on) and low pressure in the radial direction (side-on). This gives different reaction zone lengths. Is this taken into account in your model?

## REPLY BY J. B. BDZIL

The response of a detonation to the flow divergence associated with phenomenon such as the detonation corner effect is dependent on the ratio of two lengths; (1) the characteristic length scale of the two-dimensional flow and (2) the explosive's reaction-zone length. The DSD theory accounts for these effects through the function  $D_n(\kappa)$ . One example of a system where the detonation corner effect is important is the high-explosive arc experiment. Figure 8 shows DSD computed shock shapes for this problem. The initial configuration of the shock is the segment  $0 \leq r \leq 2$  and  $z = 0$  of the  $r$ -axis. In response to the presence of the circular left edge, the detonation shock (solid line) moves upwards more slowly here than elsewhere. This causes it to lag well behind the ideal Huygens wave (chain-dot line) near this edge. In turn, the amount by which the detonation velocity and pressure are reduced near this boundary (side-on-detonation) is a function of the product of the local shock curvature and a proportionality factor that is related to the reduced pressure "reaction-zone length." The experimentally calibrated function  $D_n(\kappa)$  (i.e., Equation 16)) accounts for all these effects.

# NONEQUILIBRIUM EFFECTS OF SLOW DIFFUSION CONTROLLED REACTIONS ON THE PROPERTIES OF EXPLOSIVES\*

M. van Thiel and F. H. Ree  
Lawrence Livermore National Laboratory  
Livermore, California 94550

*We describe the effect of the growth of several phases on the calculated equilibrium properties of explosive product mixtures. Calculations made with a statistical-mechanical multi-phase chemical-equilibrium (CHEQ) code are compared with experiment. Such comparisons show that the EOS of two condensed carbon phases deviate from equilibrium, and indicate the appearance of a nitrogen rich phase at high pressure. A cluster structure is discussed in terms of recent theory and experiment, and preliminary calculations, replacing diamond with an estimated cluster EOS indicate small but, for some design work, significant changes of 0.3 percent in density and 2 percent in energy at constant  $P$  and  $T$ .*

## INTRODUCTION

Solid carbon formed in detonation waves can exist in a graphitic form, below-, or a diamond-like form, above the transition pressure. Equilibrium calculations of TNT detonation products predict the formation of the diamond-like phase<sup>1</sup> well below that indicated by experiment. Previous analysis of shock compressed unsaturated hydrocarbons<sup>2</sup> also showed that the equilibrium prediction is considerably below the transition observed in experiment. A hint of this nonequilibrium behavior of carbon has been available, in conductivity measurements of explosive products,<sup>3</sup> since 1965. The conductivity of pure TNT products is 10 times that of Composition-B, a 36/64 weight percentage mixture of TNT and RDX with a higher detonation pressure than pure TNT. This high conductivity is largely due to the presence of graphitic carbon in TNT at 20 GPa, well above the equilibrium transition pressure of about 10 GPa. However,

the nonequilibrium character of this observation could only be considered later, with the advent of accurate chemical equilibrium calculations.<sup>4</sup> Such calculations on PBX-9404 uncovered another high pressure nitrogen phase,<sup>5</sup> which is subject to such nonequilibrium effects. We will briefly discuss the nature of these phase separations, consider possible scale sizes for the separation-growth process, and give an estimate of the effect carbon clusters have on the  $P$ ,  $V$ ,  $T$  properties of the detonating mixture.

## NITROGEN

The computed detonation velocity of PBX-9404 is considerably higher (9.3 km/s) than measured (8.80 km/s) if the separation of a nitrogen-rich phase occurs above the peak pressure of the detonation wave.<sup>6</sup> A similar observation was made for another HMX formulation, LX-14. The computed phase line is quite sensitive to small changes in the position of the potential minimum of the  $N_2$ - $H_2O$  interaction potential.

These calculations are made with a statistical-mechanical chemical-equilibrium model,<sup>4</sup> that allows for the existence of several phases. The model uses effective spherical pair

\*Work performed under the auspices of the U. S. Department of Energy by the Lawrence Livermore National Laboratory under contract number W-7405-ENG 48.

potentials for the gas phase molecules that are of the exp-6 form with the three adjustable constants  $\epsilon/k$ ,  $r^*$ , and  $\alpha$ : the well depth, the molecular separation at the potential minimum, and the exponential stiffness coefficient, respectively. The potentials for a series of molecules have been obtained with the help of the principle of corresponding states. This also correctly determines their shock Hugoniot.<sup>7</sup> The strong intermolecular binding of polar molecules, like water and ammonia, precludes corresponding states scaling and requires a modification of the exponential potential ( $\phi$ ) to  $(1 + \lambda/T)\phi$ .

Here we must also consider a key feature of the model, the Lorenz-Berthelot combination rules:

$$\begin{aligned} r_{ij}^* &= k_{ij}(r_{ii}^* + r_{jj}^*) \\ \epsilon_{ij} &= (\epsilon_{ii}\epsilon_{jj})^{1/2} \\ \alpha_{ij} &= (\alpha_{ii}\alpha_{jj})^{1/2} \end{aligned} \quad (1)$$

The constant  $k_{ij}$  is generally taken as 1. The above rules have been shown to work well for  $H_2$ -He mixtures.<sup>8</sup> The thermodynamic properties of the mixture are computed with an effective van der Waals one-fluid (vdW1f) model. The vdW1f potential parameters are given by:

$$\begin{aligned} (r^*)^3 &= \sum x_i x_j (r_{ij}^*)^3 \\ \epsilon &= \sum x_i x_j \epsilon_{ij} (r_{ij}^*/r^*)^3 \\ \alpha &= \sum x_i x_j \alpha_{ij} \epsilon_{ij} (r_{ij}^*/r^*)^3 \end{aligned} \quad (2)$$

where  $x$  is the atom fraction of the specie.

With  $k_{ij} = 1$  in Equation (1), the  $N_2$ -phase separation occurred above the detonation pressure, resulting in a high detonation velocity. But modifying  $k(H_2O-CO_2)$  and  $k(H_2O-N_2)$  to 0.965 and 1.03, respectively, shifts this transition below the CJ pressure and removes the disagreement with experiment. Currently available data does not allow us to confirm

these  $k_{ij}$  values, and the behavior of HMX must be the guide for the nonideality of these hydrophylic and hydrophobic interactions.

## CARBON

### Condensation Effects

The properties of condensed carbon also turn out to be important to the detonation properties of HMX explosives. Cylinder expansion data from LX-14 filled metal cylinders were represented by a JWL fit<sup>9</sup> and compared to the equilibrium theoretical (CHEQ) data. The energy imparted to the cylinder in computer simulations tends to be about 2 to 3 percent lower than the empirical data require. Comparison of the empirical and theoretical isentropes shows that the transition from graphitic carbon to a diamond-like solid reduces the volume sufficiently to produce such an energy discrepancy.

The composition and stable phases in our model calculations, are determined by minimizing the Gibbs free energy,  $G(P,T)$ . We use the heat capacity at one atmosphere,

$$C_p^0 = R \sum_{-3}^3 b_i (T/1000)^i \quad (3)$$

and integrate from their standard state to any required temperature, to obtain the enthalpy and entropy at 1 atmosphere. These are then used to obtain the 1 atmosphere Gibbs free energy,  $G^0(T)$ , and

$$G(P,T) = G^0(T) + \int_1^P V_T(P) dP \quad (4)$$

of the various species.

Increasing the enthalpy of formation of the diamond phase relative to that of graphite, increases its free energy and the pressure at which the transition to diamond occurs. This increases the PdV work done by expansion of the mixture due to the larger specific volume of graphite and reduces the discrepancy observed above. The increased heat of formation implies a small carbon cluster size, rather than the macroscopic crystal (100 nm radius or more) size of equilibrium thermodynamics.

A similar conclusion may be drawn from analysis<sup>1</sup> of porous TNT detonation velocities.<sup>10</sup> The experimental data show a sharp break in the detonation velocity vs. density curve at a density of 1.54 g/cm<sup>3</sup>. The equilibrium TNT calculation shows a similar break at  $\rho_0 = 1.0$  g/cm<sup>3</sup>. These data provide an estimate of the heat of formation of diamond-like clusters between 0.067 and 0.103 eV. Such heats of formation are needed to match the data.

### Cluster Formation Characteristics

The turbulent diffusion range available on the time scale of a detonation process limits the amount of mixing. Isotope tracer experiments<sup>11</sup> show that the scale for turbulent diffusion mixing during the full cycle of detonation and gas expansion, that covers a number of shock reverberations, is about 1,000 nm. This scale is large compared to the diffusion range behind the shock front, but it is small compared to the nominal 20,000 to 40,000 nm grain size of the explosive formulations generally used. A lower limit of the diffusion range might be 20 to 40 nm, the TNT volume producing ten times the number of atoms in a cluster. This argument shows that mixing between grains of explosive is negligible, and clusters are formed exclusively from atoms within the grain.

Several papers have recently been published that bear on the size of diamond clusters produced in detonations. Greiner et al.<sup>12</sup> recovered 7 nm diameter diamond clusters from TNT-RDX mixtures, and 4 nm spherical diamond clusters from TNT-TATB and TNT-NIGU mixtures. Such cluster dimensions are confirmed by Oinuma et al.<sup>13</sup> The work of Titov Anisichkin and Mal'kov<sup>14</sup> show a distribution of particle sizes from 2 nm to 12 nm, with a peak at 4 and an average of 5 nm. These particles were recovered from the soot produced by TNT-RDX, TNT-HMX, and explosive-benzene mixtures. The size distribution was determined by small angle x-ray scattering.

The prepared electron microscope samples showed groups of large and small clusters, apparently consistent with the narrow distribution in Reference 12. The reason for the

relatively larger (7nm) particles in the above mentioned RDX-TNT samples of Reference 12 may be due to a reduced evaporation and regraphitization time of the smaller charge used here during decompression. This 200 gm sample size is 2/3 of the other charges ( $\approx 300$  g) used by References 12 and 14.

Some limits may be computed for the time scale to grow the observed particles. The work of Shaw and Johnson<sup>15</sup> offers one such value. Their particle size distribution from their Smoluchowski model yields a time for the cluster size containing the maximum amount of solid carbon. This yields about  $10^{-7}$  s, using a viscosity of 0.01 poise, to grow a cluster of 10,000 atoms or  $\sim 4.5$  nm. Recognizing the rate enhancement of turbulence, a lower bound on time may be obtained if one considers the mean radius ( $r_m$ ) of the diffusion sphere of a particle undergoing Brownian motion with a probability distribution.<sup>16</sup>

$$\rho(r,t) = \left[ 4\pi(Dt)^3 \right]^{-1/2} \exp \left[ -r^2/(4Dt) \right]. \quad (5)$$

This allows the determination of  $r_m (= [6Dt]^{1/2})$  by integrating  $r^2$  over the distribution. The diffusion constant ( $D$ ) is then obtained from the Einstein equation for a sphere in a medium with viscosity  $\eta$ ,

$$D = kT / (6\pi\eta R_n), \quad (6)$$

where  $R_n$  is the radius of the cluster containing  $n$  carbon atoms. Recognizing that the volume swept out by the diffusing sphere is greatly enlarged by turbulence, we may define a dimerization time

$$t(R_n) = \ell_n^2 / 6D$$

for clusters of size  $R_n$ , with  $\ell_n$  equal to half the average cluster separation. Assuming a narrow distribution around sizes of  $n_i$  and  $n_{i+1}$ , we compute  $t = \sum t(R_n)$ , for  $n_i = 2^i n_0$ , where  $n_0$  is the initial cluster size of 2 or 3 atoms and  $i = 1, 2, 3 \dots k \dots$ . This procedure gives a minimum of  $4 \times 10^{-9}$  s to grow the above cluster, using the same viscosity used in Reference 15.

The growth rate and details of the cluster formation process pose some interesting questions. The process is, by the nature of the

sample heterogeneity, a diffusion process that is enhanced by turbulent mixing and punctuated by annealing cycles of the coalescing particles. Diamond clusters can grow from a pair of coalescing graphitic clusters that make the resulting cluster of sufficient size that the diamond form is stable, from the collision of a graphitic and a diamond cluster, or from the coalescence and annealing of two diamond clusters. Annealing is enhanced by a large surface energy since the rate is a function of the activation energy for surface diffusion (the average temperature of the medium) and the surface energy density. The surface energy density is significant for small clusters, but not for large ones. The annealing process may not be significant for large diamond cluster pairs on detonation time scales. The other two processes could account for much of the growth.

Measurements of annealing rate were made at a static pressure of 9 GPa, between 600 and 4000 centigrade, on amorphous carbon samples.<sup>17</sup> The rate of formation of graphite and diamond was determined by x-ray diffraction. An analysis of the rate process has been made.<sup>18</sup> While the time for graphite formation (annealing) was about  $10^{-8}$  s at 4000 C, the rate for diamond formation was quite slow at that pressure and appeared to require graphite particles of sufficient size before diamond would grow. But a significant yield was obtained in dynamic experiments above 50 GPa, with an activation energy of  $\approx 3000$  Kelvin, that appeared to be independent of pressure.<sup>19</sup>

First principles calculations,<sup>20</sup> however, indicate that diamond nucleation does get easier as the energy barrier to nucleation decreases with pressure, and goes to 0 at 90 GPa for rhombohedral graphite. The principal difference between the nucleation of a diamond particle in pure carbon and in a post-detonation mixture, is the presence of active molecular fragments that can share any unpaired electrons that tend to result from the bending (that occurs in the compression process) of the graphite bonds on the cluster surface, thereby reducing the barrier to transformation. The constant activation energy observed in Reference 19 may be due to our lack of information on diamond to graphite conversion rates on unloading.

## CLUSTER EOS

The EOS of such small clusters can be significantly different from that of bulk carbon, thereby changing the detonation properties. We have made preliminary calculations of the heats of formation and the EOS of a cluster to assess the effect on the PVT properties of explosive product mixtures.

The surface of the diamond cluster has a high probability to be the 111 plane of the cubic crystal, since other surfaces would increase the surface energy. Experiments also have indicated that this is the surface of choice.<sup>21</sup> Figure 1 shows a portion of the surface of a diamond cluster with some H and OH groups bound to the surface. The surface is covered with other molecules to pair the electrons around the surface carbons. The surface could, in general, be covered by CN, OH, H, and CO radicals. These are all reactive molecules that can pair with free electrons on the surface. They are either a part of the original explosive (CN) or components of the equilibrium gas phase (CO, H<sub>2</sub>O and CO<sub>2</sub>). The relative amounts of such particles depend on the heats of reaction with the surface. We may estimate such heats of reaction from those measured with small molecules,<sup>22</sup> in so far as the bond strengths do not differ greatly from those on the surface of large clusters.

Table 1 shows several reaction processes and the associated enthalpies ( $E + PV$ ) for the process occurring at 1 atm and 298 K. Note that for the sake of simplicity we write the symbol of the carbon core of the cluster  $C_n$  and only those surface molecules of interest in their reaction, e.g.,  $C_n(CN)_2$ , in reality there are, of course, many more surface groups. In the first part of the table, we show simple bond breaking reactions. It may be noted, that breaking the C-CN bond between the cluster and the radical takes about 5.5 eV. The gain in forming a 9.8 eV N-N bond makes the reverse reaction from  $N-N + C_{n+2}$  to  $C_n(CN)_2$  unfavorable. This may be seen by comparing the heats of reaction of the first and second line, in the second section of the table. The result is that the reaction removing water from the surface requires more net energy than removing N<sub>2</sub>. Note that such reaction should

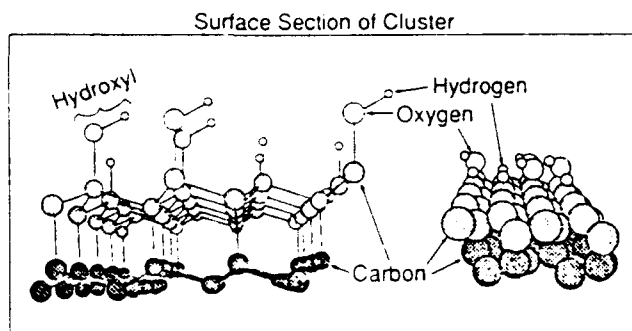


Figure 1. Surface Layers of a Diamond Cluster with H and OH Radicals

Table 1. Heats of Reaction

Bond breaking		$\Delta H$	eV
$C_nOH$	$\rightarrow C_n + OH$	4.54	
$C_nH$	$\rightarrow C_n + H$	$3.98 \pm .02$	
$C_nCN$	$\rightarrow C_n + CN$	5.46	
$C_nCO$	$\rightarrow C_n + CO$	$0.85 \pm .03$	
$C_nCO^*$	$\rightarrow C_n + CO$	3.1 max	
Complete removal process			
$C_nOH, H$	$\rightarrow C_n + OH_2$	$3.36 \pm .02$	
$C_n(CN)_2$	$\rightarrow C_{n+2} + N_2$	1.91	
$C_n(CO)_2$	$\rightarrow C_{n+1} + CO_2$	$-0.96 \pm .06$	
$C_n(CO)_2^*$	$\rightarrow C_{n+1} + CO_2$	4.4 max	
Cluster surface formation (2 surface sites)			
$C_n + H_2 + .5O_2$	$\rightarrow C_nOH, H$	$1.80 \pm .30$	
$C_n + N_2$	$\rightarrow C_{n+2}(CN)_2$	5.46	

\*Marks strained species covering two active surface sites: e.g., with low probability.

be considered as a diffusion of surface radicals followed by a surface reaction to form  $N_2$  and an increase of  $C_n$  by 2 atoms of carbon.

The CO radical is bound fairly loosely to the surface of the cluster and easily removed. A highly strained pair of bonds may be formed between CO and two neighboring surface sites. The table shows a maximum heat of dissociation for the unstrained case, not realizable in the real system. That reaction may, therefore, be equally unlikely, especially since the need for two neighboring sites reduces the probability of reaction. Uncertainties in the table are

due to variations in apparent bond strengths between different molecules containing the same bond. More detailed cluster calculations are required to remove such uncertainties.

The most likely surface coverage, therefore, is water after all the original CN has been removed from the cluster. This will be true if the reacting mixture is sufficiently hot. In what follows, we have assumed that only H and OH particles cover the surface. The heats of reaction to cover two active surface sites, is shown for the reaction with water and  $N_2$  in Table 1.

We may now compute the heat of formation of the cluster assuming a strain free core. The total specific energy is then represented by

$$H_f^0 = \sum H_{si} n_{si} / 2n, \quad (7)$$

where  $n_{si}$  is the number of surface sites covered by radical  $i$  of the cluster of size  $n$ , and  $H_{si}$  is the two site heat of formation per surface radical pair. The result for a pure water covered surface is shown in Figure 2. The high surface energy for small clusters will aid the annealing process as heat is released in the growth process. The large clusters have a smaller specific energy and will, therefore, anneal more slowly. The heat of formation at high temperatures requires a knowledge of the heat capacity.

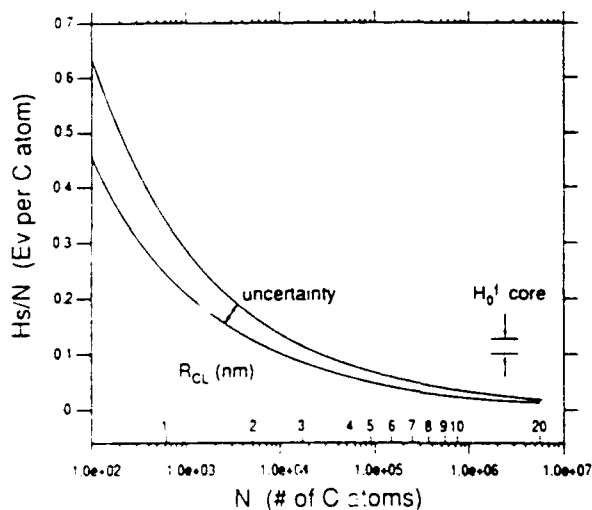


Figure 2. Heat of Formation of Diamond Clusters



The heat capacity of the cluster may be estimated using the Einstein heat capacity of the diamond core ( $C_{v,c}$ ) and adding that due to the surface molecules ( $C_{v,s}$ ). We then obtain for the most general surface coverage,

$$C_v = C_{v,c} + C_{v,s}$$

$$C_{v,c} = 3R \left( \frac{\theta_E}{T} \right)^2 \frac{n}{n_{Av}} \frac{\exp(\theta_E/T)}{[\exp(\theta_E/T) - 1]^2} \quad (8)$$

$$C_{v,s} = R \sum \left( \frac{h\nu_{ij}}{kT} \right)^2 \frac{n_{sj}}{n_{Av}} \frac{1}{i} \frac{\exp(h\nu_{ij}/kT)}{[\exp(h\nu_{ij}/kT) - 1]^2}$$

where  $n_{Av}$  is Avogadro's number and  $\theta_E$ ,  $n$ ,  $n_{sj}$ , and  $\nu_{ij}$  are the Einstein temperature of the core of the carbon cluster, the number of C atoms in the cluster, the number of surface radicals of type  $j$ , and the vibrational frequency of the  $i$ th mode of the surface radical  $j$ , respectively. Here again, the vibrational frequencies must be estimated from those of small molecules. Both the entropy and the enthalpy of the cluster at 1 atmosphere may now be computed as a function of  $T$  by integrating Equation 8.

The compressibility for clusters of this size is significantly different from that of diamond. The envelope of H and OH groups forms a significant fraction of the volume. We write

$$R_{c1}(P, T=0) = R_{cc}(P) = \delta 1 + \delta 2 + \delta 3 \quad (9)$$

where subscript  $cc$  refers to the radius of the diamond core and  $\delta 1$ ,  $\delta 2$ , and  $\delta 3$  are half the diamond interatomic distance, the average of the C-O and C-H bond lengths, and the average of the OH and H dispersion force radii. We may use the EOS of water and methane to estimate these. We use the Wigner-Seitz (WS) radius of these molecules and write

$$\delta 3(P) = 0.5 [R_{ws}(\text{CH}_4) + r_{cH} + R_{ws}(\text{H}_2\text{O})] \quad (10)$$

The correction terms  $\delta 1$ ,  $\delta 2$ , and  $r_{cH}$  are relatively incompressible and may, to first order, be considered to change like the diamond interatomic distance with pressure. The important terms that change the modulus

from that of diamond are the two WS radii. Using the theoretical EOS for methane and water we obtain an approximate bulk modulus and its pressure derivative of 2.78 Mbar and 3.65, and an initial density of 3.0 g/cc. These are then used in the Birch equation to describe the 0 K curve. We have retained the diamond thermal pressure terms.

Preliminary results show that the reduction in the gas-phase water content causes small shifts in the gas-phase equilibrium composition, with a net 1 percent decrease of the gas phase. The larger compressibility, heat of formation, and initial volume of the cluster, compared to diamond, reduces the density by 0.3 percent and increases the energy by 2 percent near the CJ temperature and pressure of LX-14. Such small changes do have a measurable effect on the detonation velocity and can significantly affect the performance of some designs. A more accurate description of the surface layer will require detailed first principles calculations to check the estimates derived from small molecules made here.

## REFERENCES

1. van Thiel, M. and Ree, F.H., "Properties of Carbon Clusters in TNT Detonation Products: Graphite-Diamond Transition," *J. Appl. Phys.* Vol. 63, No. 5, 1987, p. 1761.
2. Ree, F. H., "Systematics of High-Pressure and High Temperature Behaviour of Hydrocarbons," *J. Chem. Phys.*, Vol. 70, No. 2, 1979, p. 974.
3. Hayes, B., "On Electrical Conductivity in Detonation Products," *Proceedings of the Fourth Symposium (International) on Detonation*, U. S. Naval Ordnance Laboratory, White Oak, MD, 12 Oct 1965, pp. 595-601.
4. Ree, F. H., "A Statistical Mechanical Theory of Chemically Reacting Multi-phase Mixtures: Application to the Detonation Properties of PETN," *J. Chem. Phys.*, Vol. 81, No. 3, 1984, p. 1251.
5. Ree, F. H. and van Thiel, M., "Detonation Behavior of LX-14 and PBX-9404," *Proceedings of the Eighth Symposium*

- (*International*) on Detonation, Convention Center, Albuquerque, NM, Jul 1985, pp. 501-512.
6. Ree, F. H., "Supercritical Fluid Phase Separations: Implications for Detonation Properties of Condensed Explosives," *J. Chem Phys.*, Vol. 84, No. 10, 1986, p. 5845.
  7. Ree, F. H., "Postdetonation Behavior of Condensed High Explosives by Modern Methods of Statistical Mechanics," *Proceedings of the Seventh Symposium (International) on Detonation*, U.S. Naval Academy, Annapolis, MD, 16 Jun 1981, pp. 646-660.
  8. Ree, F. H., "Simple Mixing Rule for Mixtures with Exp-6 Interactions," *J. Chem. Phys.*, Vol. 78, 1983, p. 2846.
  9. W. J. Quirk, Private Communication, Lawrence Livermore National Laboratory, Livermore, CA, concerning LX-14 cylinder test analysis, 1985.
  10. Urizar, M. J.; James, E., Jr.; and Smith L. C., "Detonation Velocity of Pressed TNT," *Phys. Fluids*, Vol. 4, No. 2, 1960, p. 262.
  11. McGuire, R. R.; Ornellas, D.; and Akst, I., *Symposium H. P. D.*, Paris, 1978.
  12. Greiner, N. R.; Phillips, D. S.; Johnson, J. D.; and Volk, F., "Diamonds in Detonation Soot," *Nature*, Vol. 333, 1988, p. 440.
  13. Oinuma, S.; Tanka, K.; Iida, M.; Nakayama, Y.; and Natsonaga, T., "Diamonds Recovered from Detonation Products," *Shock Waves in Condensed Matter*, 1989, Ed. Schmidt, S.C. Elsevier Science Publ., NY, to be published.
  14. Anisichkin, V. F. and Mal'kov, T. Yu., *Doklady Akademii Nauk SSSR*, Vol. 303, 1988, p. 625. (Rus), also Titov, V. M.; Anisichkin, V. F.; and Mal'kov, T. Yu., "Synthesis of Ultrafine Diamonds in Detonation Waves," *Proceedings of the Ninth Symposium (International) on Detonation*, Red Lion Inn, Portland, OR, 28 Aug 1989.
  15. Shaw, M. S. and Johnson, J. D., "Carbon Clustering in Detonations," *J. Appl. Phys.*, Vol. 62, No. 5, 1987, p. 2080.
  16. Landau, L. D. and Lifschitz, E. M., *Fluid Mechanics* Pergamon Press, NY, 1959, p. 227.
  17. Hirano, S.; Shimono, K.; and Naka, S., *J. Materials Science*, Vol. 17, 1982, p. 1856.
  18. Ree, F. H.; van Thiel, M.; and Calef, D., "Stability of Graphite and Diamond Clusters and Their Transformation Rates Under High Pressure and High Temperature," *Bull. Am Phys. Soc.*, NY, 16 Mar 1987.
  19. Yosida, N.; Aoka, K.; Kakodate, Y.; Usuba, S.; and Fujiwara, S., "Shock Induced Phase Transition from Graphite to Diamond," *Shock Waves in Condensed Matter*, 1989, Ed. Schmidt, S. C., Elsevier Science Publ., NY, to be published.
  20. Fahy, S.; Louie, S. G.; and Cohen, M. L., "Pseudopotential Total Energy Study of the Transition from Rhombohedral Graphite to Diamond," *Phys. Rev.*, Vol. 34, No. 2, 1986, p. 1191.
  21. Weathers, M. S. and Basset, W. A., "Melting of Carbon at 50 to 300 Kbar," *Phys. Chem. Minerals*, Vol. 15, 1987, p. 105.
  22. Weast, R. C., Ed., *CRC Handbook of Chemistry and Physics, 65th Edition*, CRC Press Inc., Boca Raton, FL, 1985.

## DISCUSSION

FRED VOLK,  
Fraunhofer-Institute, Pfinztal, FRG

What is the heat of formation of the diamond clusters in cal/g? Can you take into account that within the clusters will be elements other than carbon?

## REPLY BY M. VAN THIEL

Our Figure 2 gives a curve for the heat of formation in units of eV/C atom versus cluster size, assuming that the surface is covered with hydroxyl and hydrogen. This

converts to Kcal/mole of C by multiplying by 23.06 Kcal/mole/eV/C atom. Then dividing by the molecular weight of carbon to get the per gram of carbon value. This then yields: for 2.0, 4.0, and 6.0 nm diameter clusters  $\Delta H_0^f = 547.$ , 274., and 182 cal/g respectively.

The purity of the cluster depends, of course, on the annealing rate of the agglomerating clusters. We have not pursued this problem theoretically. The data of Greiner et al. (this conference) indicates that the recovered diamond particles are remarkably free of impurities. We may speculate that at the roughly 4000 K temperature of the explosive the particles may be sufficiently

close to the melting point ( $\sim 5000$  K)<sup>1c</sup> that the heat produced in the annealing process yields a high annealing rate. Virgin diamond clusters that grow from a graphitic cluster may be pure because the growth process keeps the impurities ahead of the growing surface. Sufficiently large, poorly annealed agglomerates will, of course, contain impurities.

## REFERENCES TO REPLY

- 1c. van Thiel, M. and Ree, F. H. "Theoretical Description of the Graphite, Diamond, and Liquid Phases of Carbon," *Int. J. of Thermophys.*, Vol. 10, No. 1, 1989, pp. 227-236.

# COMPUTATION OF A DIVERGING COMP-B DETONATION

Bruce G. Bukiet\*  
Los Alamos National Laboratory  
Los Alamos, New Mexico 87545

*Recent advances have been made in understanding the effect of curvature on expanding detonation waves. These results are implemented in a Random Choice Method hydrodynamics code to model a spherically diverging detonation of the explosive Comp-B. The effect of varying the order of reaction as well as the rate law parameters is studied. Finally, the application of the theory of diverging detonation waves to the two-dimensional Front Tracking Method is discussed.*

## INTRODUCTION

The expansion which occurs in diverging detonations weakens the wave and yields pressures and densities below those occurring in planar geometry. Recent advances in understanding the relationship between the form of the reaction rate law and the form of the correction to wave speed (and other state variables) due to the curvature of the detonation front have been made by Jones<sup>1</sup> and Stewart and Bdzil.<sup>2</sup> In this paper, we apply these advances in the context of a Random Choice Method hydrodynamics code. We study the problem of a spherically expanding detonation of Comp-B. The effect of varying the order of reaction as well as the rate law parameters (using an Arrhenius burn model) is also studied. The implementation of curvature corrections for general two-dimensional detonation waves using the method of Front Tracking is discussed.

## CURVATURE CORRECTIONS

Asymptotic analysis of the equations of reactive gas dynamics with finite reaction rate<sup>3</sup> in a symmetric geometry shows that the form of the curvature correction depends on the order of the chemical reaction,  $\delta$ .<sup>1,2</sup>

$$\text{For } \delta < 1 \quad D = D_{CJ} - a_1 \kappa$$

+ higher order terms.

$$\text{For } \delta = 1 \quad D = D_{CJ} - a_2 \kappa - a_3 \kappa \ln \kappa$$

+ higher order terms. (1)

$$\text{For } \delta > 1 \quad D = D_{CJ} - a_4 \kappa^{1/\delta}$$

+ higher order terms.

The parameter  $\delta$  can be thought of as the number of molecules reacting in the rate determining step of the chemical decomposition process. Thus, for example, for the one-step unimolecular reaction  $A \rightarrow B$ ,  $\delta = 1$ . Here,  $D$  is the detonation wave speed at the particular radius of curvature,  $D_{CJ}$  is the wave speed in the planar (CJ) case, and  $\kappa$  is the inverse radius of curvature. The  $a$ 's are constants which may be calculated by numerically solving a set of ordinary differential equations using an iterative technique. The leading order corrections to pressure, velocity, and density have the same form (at the shock which initiates the detonation and at the sonic point).

We use the Arrhenius rate law:

$$R(\lambda, T) = \begin{cases} k(1-\lambda)^\delta \exp\left(-\frac{E_a}{T}\right), & T \geq T_c \\ 0, & T < T_c \end{cases} \quad (2)$$

\*Currently employed at New Jersey Institute of Technology, Newark, NJ

where  $k$  is called the pre-exponential factor,  $E_a$  is the activation energy and  $\delta$  is the order of reaction.  $T_c$  is the critical temperature below which the reaction rate is taken to be identically zero. The method described in this paper can easily incorporate other reaction rate laws as well. (For example, the Forest Fire rate law has been applied in Reference 4.) This leading order theory neglects transients and assumes that the reaction zone is much smaller than the radius of curvature.

## THE RANDOM CHOICE METHOD

The Random Choice Method (RCM)<sup>5,6,7</sup> is a one-dimensional numerical scheme for solving systems of partial differential equations which are in conservation form. When there are also source terms, as in our case, operator splitting may be employed.<sup>8</sup> The Front Tracking Method<sup>9-12</sup> is a two-dimensional numerical scheme in which sharp waves such as detonations are represented by curves superimposed on a rectangular grid. The most important feature of these methods in their application to detonation problems is that they keep wave fronts perfectly sharp. This enables us to find the location of the detonation front at each time step without having to deal with the smearing that occurs using finite difference schemes. Also, the (hydrodynamic) waves are resolved at each time step. We can thus calculate wave speeds without taking numerical derivatives.

To apply the analysis described above, we must obtain the coefficients in Equations (1). That is, we must find the curvature correction coefficients for each of the state variables (pressure, particle velocity, and density), as well as the correction coefficient for the detonation wave speed. If we are given an equation of state and reaction rate law, we can numerically solve a set of ordinary differential equations<sup>4</sup> (in which the reaction zone is resolved) for various values of curvature and fit to the form of Equations (1) for the coefficients. If experimental values are available (at a number of radii of curvature) for pressure, density, and velocity at the end of the reaction zone, as well as the detonation wave

speed, one need not know the equation of state of the explosive or the rate law, in the reaction zone. Rather, one needs only to fit these values to the form of Equations (1). In this paper we take the first approach. It may be possible to combine the two approaches if some experimental data is available.

In whichever manner the coefficients are obtained, they are then supplied as input into the hydrodynamics code. This code needs to know only the coefficients in Equations (1) and  $\delta$  but not the reaction rate parameters  $k$  and  $E_a$ . From the knowledge of the local radius of curvature (which is available since the fronts are sharp) and these coefficients, the state behind the detonation (we use the state at the sonic point) is computed. Since the flow is sonic at that point, we neglect any effects coming from behind the wave. If we were modeling a strong detonation, where the flow is always subsonic, effects emanating from the flow behind the detonation wave would have to be taken into account. The reaction zone is assumed to be small compared to the grid spacing. Thus, we jump from the ahead state to the sonic state in one grid block using Equations (1) to set the state behind the wave. This eliminates the need to resolve the reaction zone at each time step in the RCM and Front Tracking codes. Rather than requiring us to use many points in the reaction zone and, thus, many points in the one-dimensional (equi-spaced) computation, the implementation of the recent theoretical advances allows us to use only one point in the reaction zone (the sonic point) and, thus, enables us to coarsen the entire mesh. An important goal of this work is to compute detonation behavior without having to resolve reactions on fine grids thus yielding great savings in computational effort.

Behind the sonic point, the reaction is modeled as a polytropic gas which does not undergo further burning. In this region, the standard random choice algorithm is employed. That is, the laws of conservation of mass, momentum, and energy are applied between each pair of adjacent (piecewise constant state) grid blocks. The shock, rarefaction, and contact waves emanating from the interactions at the grid cell boundaries are

resolved and one of the physical states a short time later is randomly chosen to be each cell's piecewise constant state at the next time step. In cylindrical and spherical geometry source terms arise. These are handled separately by the technique of operator splitting.<sup>8</sup> This entails solving a simple ordinary differential equation in time at each cell using the randomly chosen piecewise constant state from the solution to the conservation laws as initial data.

## MODELING A SPHERICALLY EXPANDING COMP-B DETONATION

We use the method described above to numerically model a spherically symmetric detonation in Comp-B. The experimental data to which we compare our numerical results was obtained by Venable at the Los Alamos PHERMEX Facility in the form of a radiograph of a spherically diverging detonation wave in Comp-B. This experiment has been modelled by Mader<sup>13</sup> using the CJ-Volume Burn technique. That is, no reaction rate was used. We use the same equation of state as Mader in the reaction zone (see Appendix). Behind the sonic point, we use a polytropic equation of state (since we neglect combustion there) with  $\gamma = 2.672$ . The rate law is of the form of Equation (2) where the activation energy is 34.8 kcal/mole. Although this activation energy describes solid HMX initiation data, we assume it is about correct for solid RDX. A more detailed description of solid HMX Arrhenius kinetics results is found in Reference 14. The activation energy found for solid HMX did not vary greatly in experiments by several researchers.<sup>14</sup> We varied the pre-exponential factor,  $k$ , such that the value of density we obtain at the sonic point at a radius of 6.4 cm matches the maximum value of density recorded in the PHERMEX radiograph. (That is, we are assuming that the experiment is capturing the sonic point). The units of  $k$  are  $\mu\text{sec}^{-1}$ . We performed this numerical experiment for several values of  $\delta$ . The results of these calculations are presented in Figure 1.

In Figure 1, several density profiles are plotted. Spherical runs were performed for

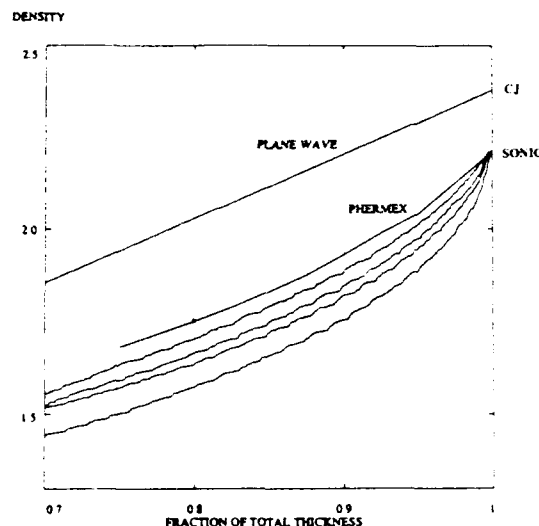


Figure 1. Calculated and Experimental Taylor Wave Density Profiles for the Explosive Comp-B. The uppermost curve is the calculated plane wave profile. This is followed by curves representing a spherically expanding Comp-B explosion at a radius of approximately 6.4 cm. The lowest curve is the calculated profile where  $\delta = 1/2$  followed by profiles in which  $\delta = 1$ ,  $\delta = 2$ , and  $\delta = 4$ , respectively. The curve labelled PHERMEX is the experimental result.

$\delta = 1/2$ , 1, 2, and 4 using RCM. The computed planar result is also shown. The planar run was initialized at radius zero. The spherical runs were initialized at radius 1 or 2 cm since the curvature corrections could give negative pressures and densities if the radius is too close to zero. The initial radius is important only insofar as the run needs to proceed far enough for transients to settle down. The results are insensitive to variations in the initial conditions. We see that as  $\delta$  varies from  $\delta = 1/2$  to  $\delta = 4$ , the shape of the density profile more closely approximates the radiographic data. For  $\delta > 4$ , there was no perceptible change in the density profile. The difference between the right side of the profile for the spherical computations and that for the planar computation is the curvature correction from the CJ point (which is a sonic point) to the spherical sonic point. The planar computation does not depend on the rate law used. Another effect of increasing  $\delta$  is that the fraction of

explosive remaining unreacted at the sonic point also increases. When the leading order corrections to  $\lambda$  are computed at the radius of our experiment, we find that for  $\delta = 2$  more than 30 percent of the explosive has not yet reacted at the sonic point. When  $\delta = 4$  this figure rises to over 40 percent.

A study was also performed to ascertain the sensitivity of the density profiles to changes in  $k$  and  $E_a$  (for fixed  $\delta$ ) where these parameters were varied such that the density drop from CJ to the sonic point remained fixed. An example is presented in Figure 2. The two density profiles at radius approximately 6.4 cm have values of the pre-exponential factor,  $k$ , which vary by a factor of 8. Here,  $\delta = 1/2$ . The curves are virtually identical. Based on this result (and similar results found for other values of  $\delta$ ), we conclude that the profiles are not sensitive to changes in  $k$  and  $E_a$  when these changes keep the density drop from CJ fixed. The same result holds for pressure and velocity corrections to CJ.

In Figures 3a-c the variations of the density profiles are presented where  $\delta$  and  $E_a$

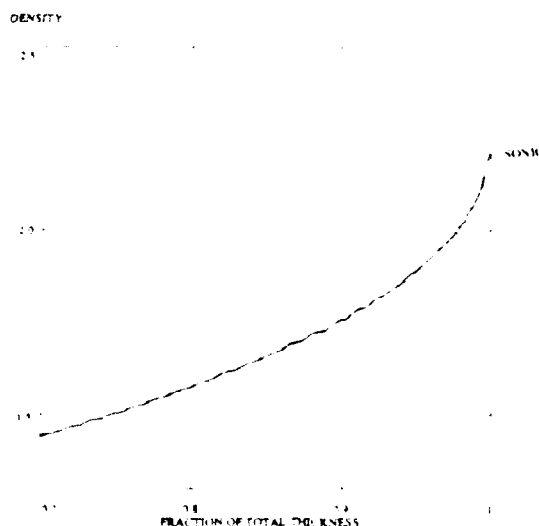


Figure 2 Density Profiles for  $\delta = 1/2$  for 2 Cases in Which Activation Energy  $E_a$  and  $k$  Vary but Yield the Same CJ to Sonic Point Density Drop. The small differences in the profiles are caused by small oscillations inherent in the random choice method. One curve has  $k = 1500 \mu\text{sec}$  and  $E_a = 34.8 \text{ kcal/mole}$ . The other has  $k = 12,000 \mu\text{sec}$  and  $E_a = 46.6 \text{ kcal/mole}$ .

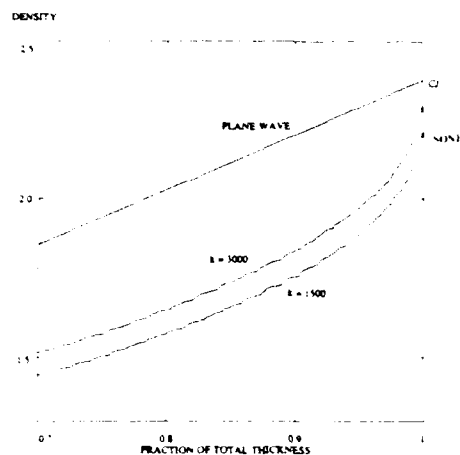


Figure 3a. Calculated Taylor Wave Density Profiles for  $\delta = 1/2$ . To halve the drop from the planar CJ density to the sonic density, sonic (in diverging geometry), the pre-exponential factor,  $k$ , must be doubled.

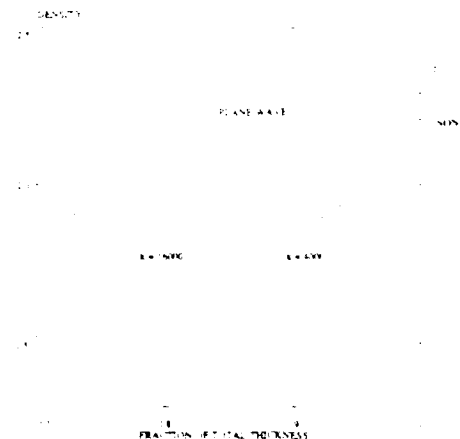


Figure 3b. Calculated Taylor Wave Density Profiles for  $\delta = 2$ . To halve the density drop from CJ to the sonic point, sonic (in diverging geometry),  $k$  must be quadrupled.

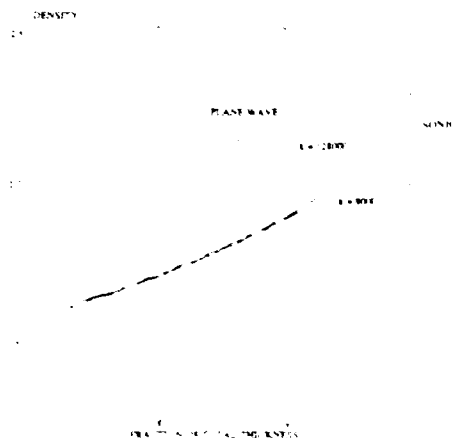


Figure 3c. Calculated Taylor Wave Density Profiles for  $\delta = 4$ . When  $k$  is increased by a factor of 16, the density drop from CJ to sonic is halved.

are held fixed and the frequency factor  $k$  is varied. In Figure 3a, density profiles are plotted for two values of  $k$ , for spherically expanding detonations where  $\delta = 1/2$ . We see that doubling  $k$  (from  $k = 1500/\mu\text{sec}$  to  $k = 3000/\mu\text{sec}$ ) halves the density drop from CJ to the sonic point. When  $\delta = 2$ ,  $k$  must be quadrupled to achieve the same effect at the sonic point. For  $\delta = 4$ , one must multiply  $k$  by 16 to halve the sonic point density drop from CJ. It is interesting to note that as  $\delta$  increases and  $k$  is increased to get halving of the density drop at the sonic point, the density profiles get closer together. That is, as  $\delta$  increases, the effect of variations in the frequency factor on the density profiles lessens. In Figures 3a-c, the profiles were plotted when the detonation front reached a radius of approximately 6.4 cm. The equation of state data and activation energy were the same as in Figure 1.

## CONCLUSIONS

The form of corrections to detonation wave speed, as well as pressure, velocity, and density due to the curvature of a detonation front has been applied in the context of a Random Choice Method hydrodynamics code to model an expanding detonation wave in Comp B. The same idea may be applied in the two-dimensional framework of the Front Tracking Method. Here, a one-dimensional interface representing the reaction zone and detonation wave is super-imposed on a rectangular mesh. Finite difference equations solve the conservation relations in the smooth regions ahead of and behind the detonation wave. The detonation wave motion and the state immediately behind the wave may be found using Equations (1) after calculating the local curvature at each point along the front. Although the case considered in this paper of a spherically symmetric detonation of Comp B can be modelled by a one dimensional method, (e.g., RCM) more general two dimensional problems can be modelled using Front Tracking. We plan to incorporate curvature corrections in a Front Tracking code in the near future.

## REFERENCES

1. Jones, J., *An Asymptotic Analysis of an Expanding Detonation*, Ph.D. Dissertation, New York University, 1986.
2. Stewart, S. and Bdzil, J., "The Shock Dynamics of Stable Multidimensional Detonation," *Combustion and Flame*, Vol. 72, No. 3, 1988, pp. 311-324.
3. Fickett, W. and Davis, W., *Detonation*, University of California Press, Berkeley, 1979.
4. Bukiet, B., "The Effect of Curvature on Detonation Speed," *SIAM J. on Appl. Math*, Vol. 49, No. 5, 1989, pp. 1433-1446.
5. Glimm, J., "Solutions in the Large for Nonlinear Hyperbolic Systems of Equations," *Comm. Pure Appl. Math.*, Vol. 18, No. 4, 1965, pp. 695-715.
6. Chorin, A., "Random Choice Solution of Hyperbolic Systems," *J. Comp. Phys.*, Vol. 22, No. 4, 1976, pp. 517-533.
7. Moler, C. and Smoller, J., "Elementary Interactions in Quasilinear Hyperbolic Systems," *Arch. Rat. Mech. Anal.*, Vol. 37, No. 2, 1970, pp. 309-322.
8. Sod, G., "A Numerical Study of a Converging Cylindrical Shock," *J. Fluid Mech.*, Vol. 83, No. 4, 1977, pp. 785-794.
9. Glimm, J., Klingenberg, C., McBryan, O., Plohr, B., Sharp, D., and Yaniv, S., "Front Tracking and Two-Dimensional Riemann Problems," *Adv. Appl. Math.*, Vol. 6, No. 3, 1985, pp. 259-290.
10. Glimm, J., Isaacson, E., Marchesin, D., and McBryan, O., "Front Tracking for Hyperbolic Systems," *Adv. Appl. Math.*, Vol. 2, No. 1, 1981, pp. 91-119.
11. Ewing, R., Ed., *The Mathematics of Reservoir Simulation*, SIAM, Philadelphia, 1983, pp. 137-160.
12. Glimm, J., McBryan, O., Menikoff, R., and Sharp, D., "Front Tracking Applied to Rayleigh Taylor Instability," *SIAM J.*



*Sci. Stat. Comp.*, Vol. 7, No. 1, 1986, pp. 230-251.

13. Mader, C., *Numerical Modeling of Detonations*, University of California Press, Berkeley, 1979.
14. Mader, C. and Kershner, J., "Numerical Modeling of the Reaction Zone in Heterogeneous Explosives," *J. Energetic Materials*, Vol. 5, No. 2, 1987, pp. 143-155.

N	=	0.00231769800713
O	=	0.000021168400127
Q	=	7.50817729081
R	=	-0.459258992057
S	=	0.0586701406641
T	=	0.0214354608379
U	=	-0.00706308896779
C <sub>v</sub>	=	0.5

## APPENDIX

### HOM Solid EOS

C	=	0.231
S	=	1.83
F <sub>s</sub>	=	-8.64822676597
G <sub>s</sub>	=	76.4979489714
H <sub>s</sub>	=	148.807985901
I <sub>s</sub>	=	122.606878623
J <sub>s</sub>	=	34.1390458579
C <sub>v</sub>	=	0.3
Γ <sub>s</sub>	=	2.0 (Gruneisen)

### HOM Gas EOS

A	=	3.51800663591
B	=	2.672
C	=	0.0
D	=	0.0
E	=	0.0
K	=	1.5571312936
L	=	0.517893826309
M	=	0.0619664002969

## DISCUSSION

B. D. LAMBOURN

AWE(A), Aldermaston  
Reading RG74PR, England

Simple Taylor theory suggests that the density contour has infinite gradient behind the detonation wave. The gradient may not be infinite but is likely to be very steep. If so, it would almost certainly not have been resolved radiographically. A better fit to the experimental data would have been obtained by letting the experimentally measured 'density' at the detonation wave float.

## REPLY BY BRUCE G. BUKIET

I would like to thank Dr. Lambourn for his insightful remarks. Initially, it was hoped that this research would give us some insight into the physical value of the order of reaction,  $\delta$ , for the explosive. However, due to the lack of resolution of the radiograph near the sonic point (where the gradient is very steep) this was not possible. As Dr. Lambourn suggests, one could let the location of the sonic point (in the radiograph) float and attempt to match the flow behind it with particular values of experimental parameters such as  $\delta$ . This would be a worthwhile issue to pursue.

# A THEORETICAL ANALYSIS OF THE SONIC POINT PROPERTIES IN A PLANE DETONATION WAVE

L. Brun and F. Chaisse  
Commissariat à l'Energie Atomique  
Centre D'etudes de Vaujours-Moronvilliers  
B. P. N° 7 - 77181 Courtry, FRANCE

*Most of the theoretical discussion of this paper is devoted to the physical properties of the flow variables in the vicinity of the sonic point in a plane detonation wave. Only one dissipative process is supposed to contribute to entropy production. The influence of the reaction rate on the gradients at the sonic point is discussed independently of the precise functional forms of the E.O.S. and reaction rate. It is proved unambiguously that, whenever the coefficient of thermicity is nonzero, the reaction rate must vanish there; and further that, if the kinetics obey the thermodynamics of irreversible processes, the effective order of reaction is to be 1/2.*

## INTRODUCTION

The behavior of the space-derivatives is among the questions raised by the numerous studies which have been devoted to the plane structure of the detonation wave within the frame of the Z.N.D. model. For example, it is asserted in Reference 1 that "to avoid singularities in space derivatives," the local flow equations require "an additional condition at the end of the steady zone" and in Reference 2, that "[the thermicity] must also become zero if the derivatives of the flow variables are to remain finite." At variance with the former statements, allowance is made in Reference 3 for infinite derivatives. Such infinite derivatives happen to occur only along a so-called *sonic line*.

The status and especially the relationship to kinetics of the sonic line thus clearly call for further clarification. We therefore propose a theoretical approach to this subject along a line of reasoning extending the work of Reference 4 in order to answer what we consider to be the main question: *what are the general features displayed by a reactive flow in the vicinity of a sonic line?*

But first, what is a sonic line? The proposed definition which will prove meaningful in the context of any planar, cylindrical or spherical flow is the following: *a sonic line is an envelope of characteristic lines.*

We specifically assume that the exothermic reactions are driven by one scalar  $\lambda$ . The constitutive relations associated with the classical flow equations consist of both the equation of state (E.O.S.) and the reaction rate; for example:

$$e = e(p, v, \lambda)$$

$$\hat{r} = \hat{r}(p, v, \lambda),$$

where  $p$ ,  $v$ ,  $e$  stand for the pressure, the specific volume and the specific internal energy. No precise form for  $e$  and  $\hat{r}$  will be needed.

The first section throws some light on the main problem in the general one-dimensional context ( $N = 0, 1, 2$ ). The following sections concentrate on the plane permanent detonation.

# Index of notations:

$\rho$  : density

$v$  : specific volume ( $\rho \cdot v = 1$ )

$\lambda$  : progress variable ( $0 \leq \lambda \leq 1$ )

$\hat{r}$  : rate of reaction

$n$  : (effective) reaction order

$m$  : thermodynamical reaction order

$T$  : temperature

$s$  : specific entropy

$c$  : frozen sound speed ( $c^2 = -v^2 \left[ \frac{\partial p}{\partial v} \right]_{s,\lambda}$ )  
(Reference 2)

$\sigma$  : thermicity coefficient ( $\rho c^2 \sigma = \left[ \frac{\partial p}{\partial v} \right]_{e,v}$ )  
(Reference 2)

$\sigma \hat{r}$  : thermicity (Reference 2)

$N$  : geometrical index equal to 0, 1 or 2

$\frac{\Delta F}{T}$  : affinity of the chemical reaction  
(Reference 2)

$u$  : particle velocity

$w$  : particle velocity in the frame of the steady flow

$*$  : appends a physical quantity at the sonic point

$t$  : time

$x$  : space coordinate

## CONNECTING THE REACTION RATE AND THE TOPOGRAPHY OF THE $\xi^+$ LINES

When neglecting transport properties of the fluid, the equations of motion turn out to be of hyperbolic type. Since we are to study the behavior of the flow variables in the vicinity of a sonic point supposed to exist, the very concept of a sonic line calls for the writing down of the Euler equations along the characteristic directions

In characteristic form,<sup>2</sup> the flow equations at point  $M(x, t)$  read:

$$\text{along } \xi^+ : \frac{dx}{dt} = u + c$$

$$D^+ u + \frac{1}{\rho c} D^+ p + N \frac{uc}{x} - c \sigma \hat{r} = 0 \quad (1)$$

$$\text{along } \xi^- : \frac{dx}{dt} = u - c$$

$$D^- u - \frac{1}{\rho c} D^- p - N \frac{uc}{x} + c \sigma \hat{r} = 0 \quad (2)$$

$$\text{along } \xi^\circ : \frac{dx}{dt} = u$$

$$D^\circ p - c^2 D^\circ \rho - \rho c^2 \sigma \hat{r} = 0 \quad (3)$$

$$D^\circ \lambda = \hat{r} \quad (4)$$

The  $D$  symbols stand for the operators:

$$D^\pm = \frac{\partial}{\partial t} + (u \pm c) \frac{\partial}{\partial x}$$

$$D^\circ = \frac{\partial}{\partial t} + u \frac{\partial}{\partial x}$$

We introduce the sonic line  $L^*$  with slope  $dx^*/dt = W$ . By hypothesis, we have  $W = u^* + c^*$ . Let point  $M$  move towards  $L^*$ . We have, in the limit, for the  $\xi^+$  line passing through  $M$ :

$$\lim D^+ u + \left[ \frac{1}{\rho c} \right]^* \lim D^+ p + N \frac{u^* c^*}{x^*} - c^* (\sigma \hat{r})^* = 0 \quad (5)$$

Care is to be taken in interpreting Equation (5) since, as shown in Reference 4, situations occur where the operations of limits and derivations may be non-commutable. Specifically, setting

$$\Lambda^* = \frac{du^*}{dt} + \left[ \frac{1}{\rho c} \right]^* \frac{dp^*}{dt} + N \frac{u^* c^*}{x^*} - c^* (\sigma \hat{r})^*, \quad (6)$$

with  $d/dt$  the derivative along  $L^*$ , it was shown that  $\Lambda^*$  may be nonzero and that:

$$\Lambda^* \neq 0 \rightarrow \lim D^+ \neq \left[ \frac{d}{dt} \right]^* \quad (7)$$

From its very definition, parameter  $\Lambda^*$  is related among others to the thermicity of. It proves to be related, as well, to a concept of relative acceleration which we are going to make precise.

Call  $x$  and  $x^*$  the coordinates at time  $t$  of points  $M$  and  $M^*$ , respectively fastened to a  $\xi^+$  line and to  $L^*$ , and

$$e = x - x^* \quad (8)$$

their mutual algebraic distance. Following Reference 4, we have:

$$\frac{de}{dt} = (u + c)_{\xi^+} - (u^* + c^*) \quad (9)$$

$$\frac{d^2e}{dt^2} = (D^+ u - \frac{du^*}{dt}) + (D^+ c - \frac{dc^*}{dt}) \quad (10)$$

Equation (10) is the *relative acceleration* along the  $\xi^+$  line with respect to the sonic point.

Now, using  $p$ ,  $s$ , and  $\lambda$  as state variables,  $D^+ c$  and  $dc^*/dt$  are expressed as:

$$D^+ c = \left[ \frac{\partial c}{\partial p} \right]_{s,\lambda} D^+ p + \left[ \frac{\partial c}{\partial s} \right]_{p,\lambda} D^+ s + \left[ \frac{\partial c}{\partial \lambda} \right]_{p,s} D^+ \lambda \quad (11)$$

$$\frac{dc^*}{dt} = \left[ \frac{\partial c}{\partial p} \right]_{s,\lambda}^* \frac{dp^*}{dt} + \left[ \frac{\partial c}{\partial s} \right]_{p,\lambda}^* \frac{ds^*}{dt} + \left[ \frac{\partial c}{\partial \lambda} \right]_{p,s}^* \frac{d\lambda^*}{dt}$$

The adiabaticity of the flow and the finite character of  $\dot{r}$  imply:

$$\lim D^+ s = \frac{ds^*}{dt} \quad (12)$$

$$\lim D^+ \lambda = \frac{d\lambda^*}{dt}$$

Resorting now to the analysis in Reference 4 of the properties along the sonic line, we should distinguish between the limits of  $D^\pm u$  and  $D^\pm p$ , obtaining as a result:

$$\begin{aligned} \lim D^+ u &= -\frac{\Lambda^*}{2} + \frac{du^*}{dt} \\ \lim D^+ p &= -(\rho c)^* \frac{\Lambda^*}{2} + \frac{dp^*}{dt} \end{aligned} \quad (13)$$

$$\lim D^- u, \lim D^- p \rightarrow \infty (\Lambda^* \neq 0)$$

$$\begin{aligned} \lim D^- u, \lim D^- p \\ \text{indeterminate } (\Lambda^* = 0) \end{aligned}$$

Combining Equations (9) through (13), as  $e \rightarrow 0$  we get:

$$\lim \frac{de}{dt} = 0 \quad (14)$$

$$\lim \frac{d^2e}{dt^2} = -\frac{\Lambda^*}{2} \left( 1 + (\rho c)^* \left[ \frac{\partial c}{\partial p} \right]_{s,\lambda}^* \right) \quad (15)$$

Equation (14) reflects the definition of a sonic line given in the introduction: an envelope of characteristic lines.

Equation (15), with  $\Lambda^*$  defined by Equation (6), emerges as the key result of this section. It establishes a connection between the reaction rate, the underlying state of motion along the sonic line and the topography of the  $\xi^+$  family of characteristic curves in the neighborhood of  $L^*$ .

To make use of this result in the present reactive context, one observation is in order:

we should distinguish between *two* limiting relative accelerations, one for each side of  $L^*$ , since the sonic line is supposed to exist *within* the domain of continuity of the physical fields. Recalling Equation (8), we infer from Figure 1 that for any of the two possible patterns of the  $\xi^+$  lines "on the right" of  $L^*$ , the left-hand member of Equation (15) is  $\geq 0$ , and  $\leq 0$  on the left. Consequently,

$$\Lambda^* = 0. \quad (16)$$

Precisely stated:

**Theorem:** *a sonic line  $L^*$  within any one-dimensional continuous flow is necessarily a characteristic line.*

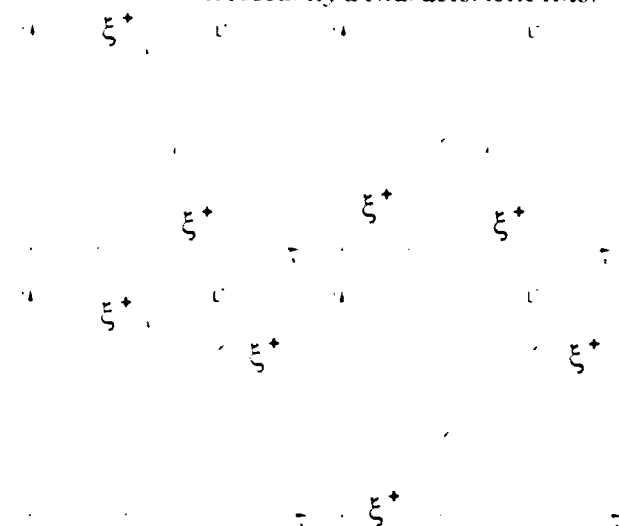


Figure 1. The Four Possible Patterns of Incoming or Outgoing  $\xi^+$  Lines on Both Sides of a Sonic Line

Since  $L^*$  should be an envelope of characteristic lines as well, we conclude that the presence of a sonic line is associated with the property of two characteristic curves passing through the same point. Since this is known to be impossible in a nonreactive flow, one should address reactive flows for possible examples of sonic lines *within* a continuous domain of the flow. The simplest example of reactive flow we know of is the steady state one dimensional detonation. Despite some of its nongeneric features, it will suffice to render the foregoing analysis meaningful. We henceforth focus on this situation.

**Remark 1:** The Chapman-Jouguet scheme of a detonation allows of a sonic line  $L^*$  on the downstream side of the totally reactive shock front, which is nonreactive. As already emphasized in Reference 4,  $\Lambda^*$  is nonzero along  $L^*$ . The apparent conflict with Equation (16) and the theorem is cleared up at once observing that  $L^*$  is bordered on one side only by a continuous flow and does not coincide with a characteristic line.

## APPLICATION TO THE STEADY PLANE SELF-SUSTAINED DETONATION WAVE

When the flow is steady in a frame moving with the sonic point, we get on the sonic line:

$$\frac{du^*}{dt} = \frac{dp^*}{dt} = 0, N = 0, \text{ so that } (\sigma\bar{r})^* = 0.$$

In the case of one progress variable, we are led to the following corollary:

**Corollary:** - *In a steady one-dimensional detonation, the sonic state is equivalently a state of zero thermicity.*  
- *Whenever the thermicity coefficient is nonzero, a sonic state is a state of chemical equilibrium.*

**Remark 2:** When a progress variables are present, the sonic state should satisfy the condition:

$$\sum_{i=1}^n (\sigma_i \cdot r_i)^* = 0.$$

We admit that both conditions of sonicity and zero thermicity determine a unique flow, and proceed to consider this particular flow.

## Flow Variables Versus Degree of Advancement ( $\sigma^* \neq 0$ )

We intend here to specify the behavior of the physical variables in the vicinity of the sonic point. In a slab geometry,  $v$  and  $p$  are expressed as functions of  $w$  alone using mass and momentum conservation equations:

$$\begin{cases} p - p^* = -\frac{w^*}{v^*} (w - w^*), \\ v - v^* = \frac{v^*}{w^*} (w - w^*) \end{cases} \quad (17)$$

To set up first the connection between  $w$  and  $\lambda$ , we work in a frame moving with the sonic line, where we write for  $M \neq 1$  (Reference 2):

$$\frac{dw}{d\lambda} = \frac{\sigma c^2 w}{c^2 - w^2} \quad (18)$$

We deduce therefrom:

$$\lim_{\lambda \rightarrow 1} \frac{dw}{d\lambda} \rightarrow \infty \quad (19)$$

As usual, we set  $\lambda^* = 1$  for convenience.

Near the sonic point, a first order estimate of  $w(\lambda)$  may be derived. To this end, we use the integrated form of the flow equations and prove [see Appendix] that, in the reactive part of the flow, the function  $w(\lambda)$  behaves as:

$$w^* - w \propto \frac{c^*}{v^*} \left[ \frac{-2 \left| \frac{\partial \Delta F}{\partial v} \right|_{s,\lambda}}{\left| \frac{\partial^2 p}{\partial v^2} \right|_{s,\lambda}} \right]^{1/2} (1 - \lambda)^{1/2} \quad (20)$$

$$\text{with } - \left| \frac{\partial \Delta F}{\partial v} \right|_{s,\lambda} = (pc^2 \sigma)^*.$$

Equation (20) indicates that we should have:

$$\sigma^* \left| \frac{\partial^2 p}{\partial v^2} \right|_{s,\lambda} > 0 \quad (21)$$

for the flow to exist.

The role of the E.O.S. is thus clearly identified and we remark that the approximation in Equation (20) extends to a general

E.O.S. a result known only for a polytropic gas. Elsewhere in Reference 3, it is assumed that:

$$\frac{d\lambda}{du} \propto (u - u^*)^k \quad (22)$$

and subsequently that  $k = 1$  for a  $\gamma$ -law gas. Equation (20) indicates that this result holds independently of the functional form of the E.O.S., a property which apparently the author of Reference 3 was not aware of.

Call  $X$  a physical quantity of the reactive flow. When  $X(p, v, \lambda)$  is expanded as a Taylor's series, we get, according to Equations (17) and (20), the useful estimate:

$$X - X^* \propto (1 - \lambda)^{1/2} \quad (23)$$

*Remark 3:* When  $\sigma^* = 0$ , Equation (18) is indeterminate. The removal of this indetermination yields:

$$w - w^* \propto (1 - \lambda) \text{ and consequently}$$

$$X - X^* \propto (1 - \lambda).$$

### Reactivity Versus Degree of Advancement

Let us introduce the concept of reaction order  $n$  (understood in the vicinity of the sonic point of the flow) via the following definition:

$$\sigma \hat{r} \propto (1 - \lambda)^n \quad (24)$$

We also assume a power-law dependance for  $\hat{r}$ :

$$\hat{r} \propto -\text{sgn } \Delta F \left| \Delta F \right|^m \quad (m \geq 0) \quad (25)$$

Inserting Equation (23) into  $\Delta F$ , we deduce from Equation (25):

$$\hat{r} \propto (1 - \lambda)^{m/2}, \quad (26)$$

and get:

$$n = m/2. \quad (27)$$

The effective reaction order is thus always half the thermodynamic reaction order.

The sonic point is at a finite distance whenever  $n \in [0, 1]$ . On the other hand, the case  $m = 1$  ( $n = 1/2$ ) corresponds to the classical linear relation developed in the framework of the thermodynamics of irreversible processes (T.I.P.). In this case we write:

$$\hat{r} = -B^*(s^*, v^*) \Delta F,$$

where  $B^*$  is a so-called phenomenological coefficient.

This situation we call the *generic* case.

At the approximation of the T.I.P., the effective reaction order is necessarily  $1/2$ .

The choice  $m = 1/2$  made by Fickett and Rivard<sup>5</sup> thus proves to be consistent with the thermodynamics of irreversible processes. If  $\sigma^* = 0$ , following Remark 3, we get  $n = 1$ .

### Gradients at the Sonic Point

When  $\sigma^* \neq 0$ , the results obtained allow one to remove the indetermination due to the fact that  $\Lambda^* = 0$  [i.e.: Equation (13)]. To this end,  $dw/dx$  is expressed as:

$$\frac{dw}{dx} = \frac{dw}{d\lambda} \cdot \frac{d\lambda}{dx} \quad (28)$$

On account of Equations (20), (4), and (24), we deduce the estimate:

$$\frac{dw}{dx} \propto (1 - \lambda)^{n - 1/2} \quad (29)$$

The uncertainty concerning the flow gradients is removed. We get for  $\lambda \rightarrow 1$  Table 1.

For  $\sigma^* = 0$ , the gradient  $dw/dx$  is finite (cf.: Remark 3 and  $\hat{r}^* \neq 0$ ) at the sonic point.

Table 1. For  $\sigma^* \neq 0$ ,  $\left| \frac{dw^*}{dx} \right|$  versus the effective order of reaction [ $g^* = \sigma^{*2} c^{*4} B^* / (v^{*3} \left| \frac{\partial^2 p}{\partial v^2} \right|_{s, \lambda})$ ]

n	0+	1/2	1-
$\left[ \frac{dw^*}{dx} \right]$	$\infty$	$g^*$	0

For  $\sigma^* \neq 0$ , as the sonic point is approached from the reactive side, the gradients of the flow variables become infinite for  $0 < n < 1/2$ , whatever the E.O.S. Thus, contrary to common belief (References 1-2), the solution may involve infinite gradients according to the value of  $n$ . The results obtained in Reference 3 may be arranged as in Table 1, with  $1/2$  replaced by  $k/k + 1$ . Our results imply that, in a proper thermodynamical setting,  $k$  should be taken equal to one and not only for the  $\gamma$ -law gas, as already observed after Equation (22).

The fundamental effect of the reaction rate on the evolution of the flow variables in the vicinity of the sonic point is thus demonstrated.

### Topology of the $\xi^+$ Lines ( $\sigma^* \neq 0$ )

We go on studying the conformation of the  $\xi^+$  curves in the steady case near the sonic line on the reactive side for a nonzero  $\sigma^*$ . The  $\xi^+$  characteristics are a one parameter family of integral curves of the equation:

$$\frac{dx}{dt} = u(x) + c(x). \quad (30)$$

The integration of Equation (30) requires the knowledge of  $u(x)$  and  $c(x)$ . By use of Equations (4) and (24) we get:

$$1 - \lambda \propto (x - x^*)^{\frac{1}{1-n}} \quad (31)$$

As already shown, the gradients behave as  $(1 - \lambda)^{n - 1/2}$ , so we obtain the gradient of  $u + c$  in the following form:

$$\frac{d(u + c)}{dx} \propto (x - x^*)^{\frac{2n-1}{2(1-n)}} \quad (32)$$

A first integration gives:

$$(u + c) - (u + c)^* \propto \beta^* (x - x^*)^{\frac{1}{2(1-n)}}, \quad (33)$$

with  $\beta^*$  a computable thermodynamic coefficient, which, from the definition of the  $\xi^+$  lines, may be rewritten as:

$$\frac{d(x - x^*)}{dt} \propto \beta^* (x - x^*)^{\frac{1}{2(1-n)}} \quad (34)$$

A second integration determines the graph of the  $\xi^+$  line through point  $M_1 (x_1, t_1)$  near  $L^*$ .

Two circumstances should be distinguished:

First, when  $n \neq 1/2$

$$x(t) - x^*(t) \propto \left| \beta^* q (t - t_1) + [x_1 - x^*(t_1)]^q \right|^{1/q} \quad (35)$$

$$\text{with } q = \frac{1 - 2n}{2(1 - n)},$$

Second, when  $n = 1/2$

$$x(t) - x^*(t) \propto [x_1 - x^*(t_1)] \exp |\beta^* (t - t_1)|. \quad (36)$$

Equations (35) and (36) specify the behavior of a  $\xi^+$  line near the sonic point.

For  $0 < n < 1/2$  (infinite gradients) coefficient  $q$  is positive. Each of the  $\xi^+$  is initially tangent to the  $L^*$  line: the  $L^*$  line is an envelope to the  $\xi^+$  and a characteristic line as well (see Figure 2). This is an example of two characteristics of the same family passing through the same point.

In agreement with Equations (15) and (16), the initial relative acceleration  $\ddot{e}^*$  is seen to be zero. The contact of the  $\xi^+$  lines with their envelope is higher than second order.

For  $1/2 \leq n < 1$  (finite gradients) the  $L^*$  line is an asymptote to the  $\xi^+$  curves and a characteristic as well (see Figure 3).

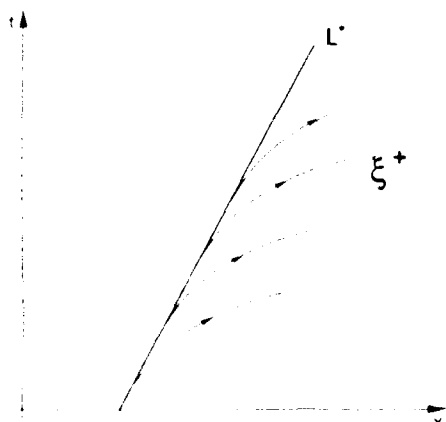


Figure 2. The  $\xi^+$  Lines on the Steady Side of  $L^*$  ( $0 < n < 1/2$ ),  $\sigma^* \neq 0$ .

Note the exponential departure in the generic case ( $n = 1/2$ ). These results were obtained independently of a specific E.O.S. and, above all, without recourse to a global study of the flow.

Figure 4 displays a typical array of the  $\xi^+$  lines within the classical Z.N.D. model, which requires an inert shock ahead.

N.B.: The schematic graph of Figure 4 presupposes the existence of a solution to the stationary problem with a non-pathological sonic point within the flow. It may be seen that, for such a solution to exist, it is at least necessary that, at the "frozen CJ point" of the equilibrium Hugoniot curve  $H_e$  as defined on p. 143 of Reference 2, a condition on  $(dp/d\lambda)_{H_e}$  be fulfilled.

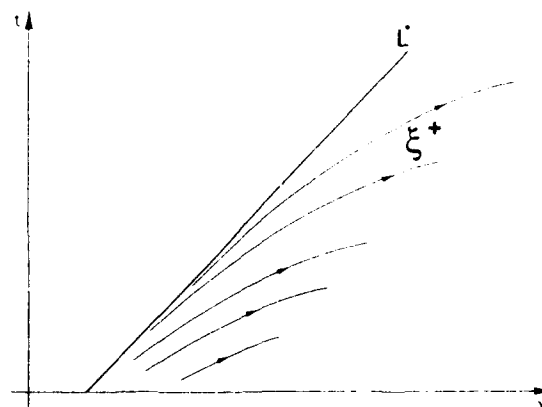


Figure 3. The  $\xi^+$  Lines on the Steady Side of  $L^*$  ( $1/2 \leq n < 1$ ),  $\sigma^* \neq 0$

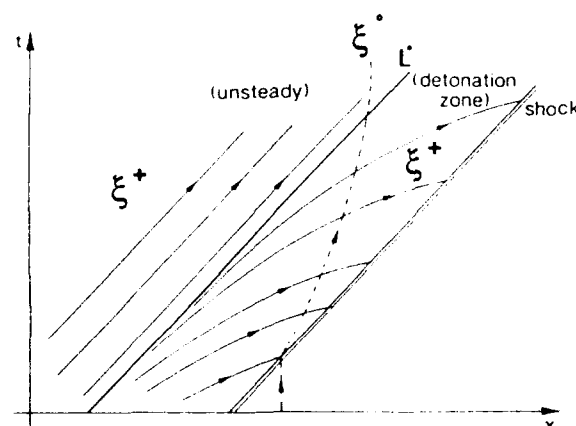


Figure 4. Characteristic Diagram for  $1/2 \leq n < 1$  in the Case  $\sigma^* \neq 0$



## CONCLUSION

Starting from the assumption that the distinctive features of the *non-supported* one-dimensional detonation should be ascribed to the existence of a sonic line  $L^*$ , an envelope to one family of characteristic lines, we endeavoured to make clear the status of  $L^*$  in the unrestricted one-dimensional context without appealing to the kinetics, a mere local problem. The main result is that, if it is to exist within a reactive domain of the flow,  $L^*$  must be a characteristic line as well. In the workable situation of the steady one-dimensional detonation front, this amounts to the condition of zero thermicity at the sonic point. There, the gradients of the physical variables on the *stationary* side prove to be finite whenever the state is either one of equilibrium and the kinetics conform to T.I.P., or a pathological state. Otherwise they are infinite or zero.

## REFERENCES

1. Kirkwood, J. G. and Wood, W. W., *Journal of Chemical Physics*, Vol. 22, 1954, p. 1915.
2. Fickett, W. and Davis, W. C., *Detonation*, University of California Press, 1979.
3. Sternberg, H. M., *Astronautica Acta*, Vol. 15, 1970, p. 359.
4. Brun, L., *Journal de Mécanique théorique et appliquée*, Vol. 1, n° 4, 1982, p. 623.
5. Fickett, W. and Rivard, W. C., *Test Problems for Hydrocodes*, LASL Report LA 5479, 1979.

## APPENDIX

We start from Equation 2:

$$\frac{dw}{d\lambda} = \frac{\sigma c^2 w}{c^2 - w^2} \quad (1)$$

In the steady frame, the mechanical equations are integrated to give:<sup>2</sup>

$$\frac{w}{v} = a_1$$

$$a_1 w + p = a_2 \quad (2)$$

$$e + pv + \frac{1}{2} w^2 = a_3,$$

where the  $a_i$  are a set of arbitrary constants.

Let us first establish an apparently unnoticed expression for  $\sigma$ , which will prove both simple and suggestive.

We start from the definition of  $\sigma$  (Reference 2):

$$\rho c^2 \sigma = \left[ \frac{\partial p}{\partial \lambda} \right]_{e,v} \quad (3)$$

The right-hand member is transformed to:

$$\left[ \frac{\partial p}{\partial \lambda} \right]_{e,v} = \left[ \frac{\partial p}{\partial \lambda} \right]_{v,s} + \left[ \frac{\partial p}{\partial s} \right]_{v,\lambda} \left[ \frac{\partial s}{\partial \lambda} \right]_{e,v} \quad (4)$$

From the thermodynamic differential relation for the internal energy  $de = Tds - pdv + \Delta F d\lambda$ , we derive successively:

$$\left[ \frac{\partial p}{\partial \lambda} \right]_{v,s} = - \left[ \frac{\partial \Delta F}{\partial v} \right]_{s,\lambda}, \quad \left[ \frac{\partial p}{\partial s} \right]_{v,\lambda} = - \left[ \frac{\partial T}{\partial v} \right]_{s,\lambda}$$

$$\text{and} \quad \left[ \frac{\partial s}{\partial \lambda} \right]_{e,v} = - \frac{\Delta F}{T}$$

Inserting first into Equation (4) and then into Equation (3), we obtain:

$$\rho c^2 \sigma = - T \frac{\partial}{\partial v} \left[ \frac{\Delta F}{T} \right]_{s,\lambda} \quad (5)$$

This last relation brings out the general connection between the chemical affinity and the thermicity coefficient. When specialized to the sonic point, which is a point of chemical equilibrium in this study ( $\sigma^* \neq 0$ ;  $\dot{r}^* = \Delta F^* = 0$ ), we get:

$$(c^2 \sigma)^* = - v^* \left[ \frac{\partial \Delta F}{\partial v} \right]_{s,\lambda}^* \quad (6)$$

The quantity  $c^2 - w^2$  is then expanded in a Taylor's series in the vicinity of the sonic point ( $\Delta v = v - v^*$ ,  $\Delta s = s - s^*$ ,  $\Delta \lambda = \lambda - 1$ ,  $\Delta w = w - w^*$ ).

Noting that the order of partial differentiations does not affect the results, we write:

$$\left| \frac{\partial c^2}{\partial \lambda} \right|_{v,s} = v^2 \left| \frac{\partial^2 \Delta F}{\partial v^2} \right|_{s,\lambda}; \quad \left| \frac{\partial c^2}{\partial s} \right|_{v,\lambda} = v^2 \left| \frac{\partial^2 T}{\partial v^2} \right|_{s,\lambda} \quad (7)$$

In the absence of transport we also have:

$de = -p dv$  and consequently:

$$ds = - \frac{\Delta F}{T} d\lambda. \quad (8)$$

Finally, using Equations (2), (7), and (8) combined with  $\Delta F^* = 0$ , we obtain after some algebra:

$$c^2 - w^2 = -v^{*2} \left| \frac{\partial^2 p}{\partial v^2} \right|_{s,\lambda}^* \Delta v + \left( v^2 \left| \frac{\partial^2 \Delta F}{\partial v^2} \right|_{s,\lambda} - 2v \left| \frac{\partial \Delta F}{\partial v} \right|_{s,\lambda} \right)^* \Delta \lambda \quad (9)$$

On account of the relation  $\Delta v = v^*/w^* \Delta w$ , Equation (1) is expressed to first order in the form:

$$\frac{dw}{d\lambda} = \frac{N^*}{A^*(w - w^*) + B^*(\lambda - 1)} \quad (10)$$

$$A^* = - \frac{v^{*3}}{c^*} \left| \frac{\partial^2 p}{\partial v^2} \right|_{s,\lambda}^* \neq 0$$

$$B^* = \left( v^2 \left| \frac{\partial^2 \Delta F}{\partial v^2} \right|_{s,\lambda} - 2v \left| \frac{\partial \Delta F}{\partial v} \right|_{s,\lambda} \right)^* \neq 0$$

$$N^* = (\sigma c^3)^* = -c^* v^* \left| \frac{\partial \Delta F}{\partial v} \right|_{s,\lambda}^* \neq 0.$$

The integration of Equation (10) gives the solution:

$$\lambda - 1 = \frac{A^* N^*}{B^{*2}} \left| \exp \frac{B^*}{N^*} (w - w^*) - 1 \right| - \frac{A^*}{B^*} (w - w^*),$$

which is now expanded as:

$$\lambda - 1 = \frac{A^*}{2N^*} (w - w^*)^2 + 0 (w - w^*)^3.$$

To finish with, the next estimate on the reactive side of the sonic line is obtained ( $w < w^*$ ;  $\lambda < 1$ ):

$$w^* - w \propto \frac{c^*}{v^*} \frac{-2 \left| \frac{\partial \Delta F}{\partial v} \right|_{s,\lambda}^*}{\left| \frac{\partial^2 p}{\partial v^2} \right|_{s,\lambda}^*}^{1/2} (1 - \lambda)^{1/2}.$$

# INVESTIGATIONS OF THE INFLUENCE OF POLYMORPHOUS TRANSFORMATION ON THE PROCESS OF DETONATION OF MIXTURES CONTAINING HE AND SUBSTANCES UNDERGOING TRANSFORMATION

E. Włodarczyk, R. Trebinski, W. Trzcinski, and W. Witkowski  
Technical Military Academy  
00-908 Warsaw  
POLAND

*The analysis is made of the detonation process of mixtures containing high explosives and materials such as graphite, boron nitride, and silicon that undergo polymorphous transformation in the reaction zone of the detonation wave. It is shown that the detonation velocity in such mixtures depends on the kinetics of both chemical and polymorphous transformations. The possibility of the realization of a weak detonation is concluded.*

## FACTS

Investigations of the detonation process of mixtures of high explosives with substances undergoing polymorphous transformation under high pressure (graphite, hexagonal boron nitride, silicon)<sup>1,2,3,4,5</sup> revealed interesting features of the process. It was established that the polymorphous transformation, taking place in the detonation wave, influences the character of the dependence of the detonation velocity  $D$  on the density of explosive  $\rho_0$ . In Figures 1 and 2  $D(\rho_0)$  curves, plotted on the basis of data published in References 1, 3, and 4 are presented. Instead of the usual linear diagrams, we have to make do with discontinuity points (throws) of the function  $D(\rho_0)$ , as well as discontinuity points of its first derivative (bends). In the bends the slope of the  $D(\rho_0)$  function decreases or increases. In throws the value of  $D$  always increases. It was noticed that the location and the character of peculiarities of  $D(\rho_0)$  curves depend on the size of granules of material undergoing transformation. In particular, no throws were observed for the mixture of RDX and silicon with the granules size of  $200 - 250 \mu\text{m}^4$ .

Another interesting feature of the process under consideration is a character of mass

velocity changes in the reaction zone of the detonation wave. In Figure 3 oscillograms of mass velocity, obtained by the use of the electromagnetic method, are presented. Behind the von Neumann spike a rapid decrease (a throw) of the velocity  $u$  appears. It corresponds to a  $300 - 600 \text{ m/s}$  velocity decrease. A small increase in the velocity comes after the throw, followed in some cases by a plateau. Only at a distance from the throw does a decrease in velocity occur; this can be attributed to a Taylor wave. In the case of a pressure excess in the initiation of detonation, a small jump of the mass velocity is observed that can be attributed to a shock traveling in the same direction as detonation. Mass velocity profiles of the type presented in Figure 3 were observed at densities  $\rho_0$ , corresponding to the throws on the  $D(\rho_0)$  curves. At densities corresponding to the bends, mass velocity profiles without throws were obtained.

Additional information, useful for the experimental facts interpretation, was obtained in the way of theoretical estimation of detonation parameters. In Figure 4 detonation adiabates of RDX/graphite 75/25 mixture are

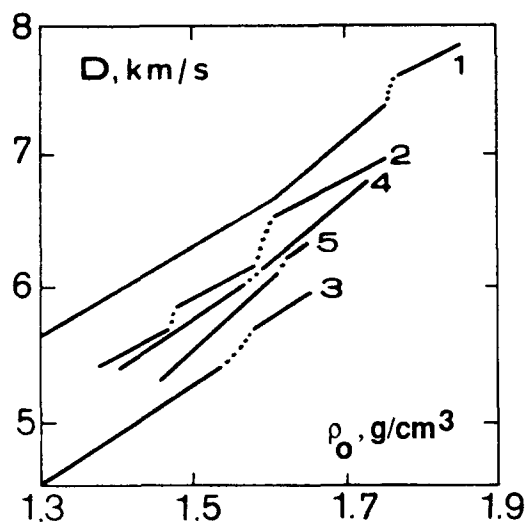


Figure 1. Detonation Velocity-Density Diagrams for: 1-RDX/C 75/25, 2-TNT/RDX/BN 18.75/56.25/25, 3-TNT/RDX/BN 15/45/40 4-TNT/RDX/Si 18.75/56.25/25 (125 – 250  $\mu\text{m}$ ), 5-TNT/RDX/Si 18.75/56.25/25 (< 40  $\mu\text{m}$ )

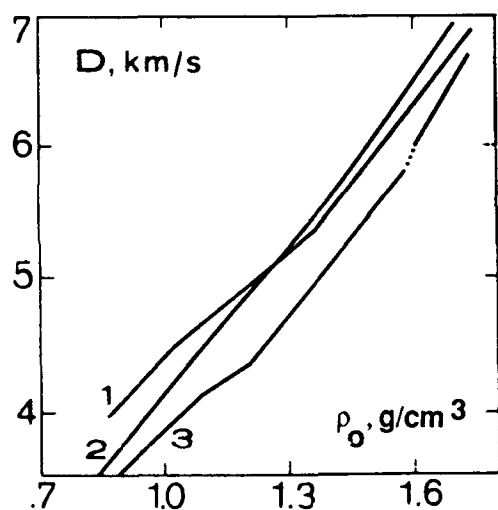


Figure 2. Detonation Velocity-Density Diagrams for: 1-TNT/RDX/BN 18.75/56.25/25, 2-TNT/RDX/Si 18.75/56.25/25 (200 – 250  $\mu\text{m}$ ), 3-TNT/RDX/Si 18.75/56.25/25 (40 – 50  $\mu\text{m}$ )

presented. They were calculated by the method described in Reference 6.  $H_D$  and  $H_G$  adiabates were obtained when estimating the compressibility of the addition on the base of the lower and upper branches of the shock adiabat of graphite, respectively. The influence of thermal effects was assessed; these were assumed, in Reference 3, to be the reason for the peculiarities of the  $D(\rho_0)$  function

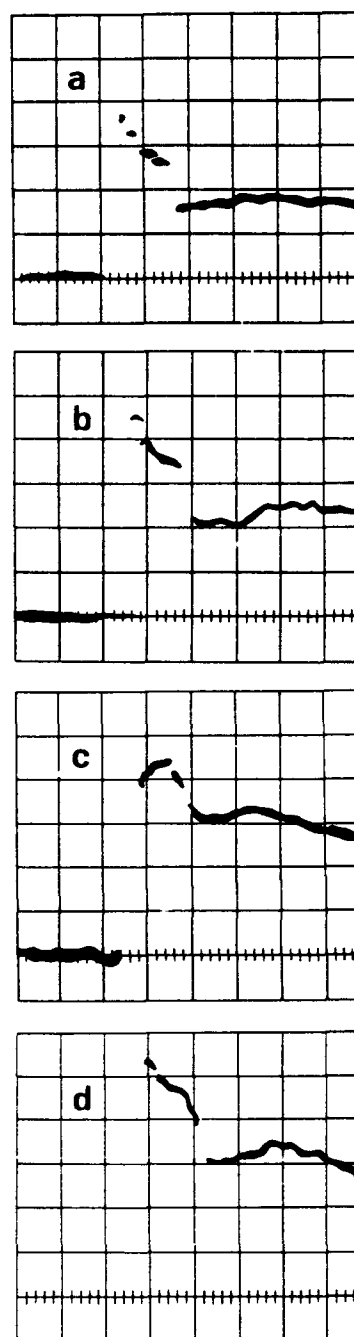


Figure 3. Experimental Oscillograms of the Mass Velocity, Recorded by the Use of Lorentz Type Electromagnetic Gauges Made of 20  $\mu\text{m}$  Aluminum Foil;  $u = 500 \text{ m/s/div}$ ,  $t = 100 \text{ ns/div}$ . Oscillogram (a) corresponds to the detonation of TNT/RDX/BN 18.75/56.25/25 mixture, (b) – (d) to the detonation of RDX/C 90/10 mixture.

(adiabate  $H_{DC}$ ). The heat of the polymorphous transformation was appraised, by setting it to be equal to the potential barrier of rhombohedral graphite to diamond transformation<sup>7</sup> -- 32 kJ/mole. The difference between heats absorbed by graphite and diamond was appraised by calculating the difference between heats absorbed by these materials by heating them from 300 to 3500 K -- 2.6 kJ/mole. Mutual location of the adiabates proves that the transformation causes a decrease in the slope of the Rayleigh line, that means a drop in the detonation velocity.

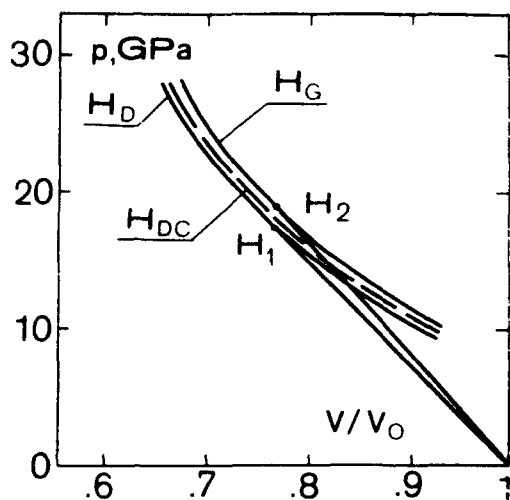


Figure 4. Detonation Adiabates for RDX/C 75/25 Mixture with Density 1.6 g/cm<sup>3</sup>

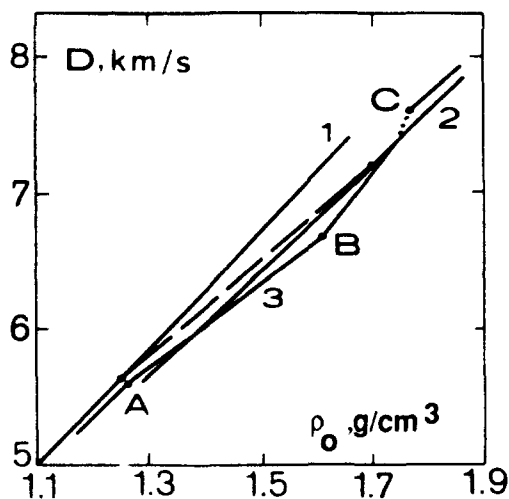


Figure 5. Theoretical (1 and 2) and Experimental (3) Detonation Velocity-Density Diagrams for RDX/C 75/25 Mixture

Theoretical calculations gave values of  $D$  differing by 100 - 400 m/s from the results of measurements. However, it was established that the comparison of slopes of experimental and theoretical  $D(\rho_0)$  curves is very informative. In Figure 5 exemplary  $D(\rho_0)$  curves are presented. Graph 1 corresponds to the lack of transformation, 2 to the full transformation, and 3 is plotted on the basis of experimental results. Below the lower bend A, graphs 1 and 3 are parallel. Above that point the experimental diagram has a distinctly lower slope than the two others. Joining points lying on graphs 1 and 2, in which von Neumann spike pressure is equal to the pressure in the lower and the upper cusps on shock adiabates (12 and 21 GPa for BN, 20 and 37 GPa for graphite), a line segment is obtained roughly parallel to the appropriate segment of the experimental line. Above the bend B the experimental curve has a considerably higher slope than both theoretical diagrams. The slope increases when approaching the throw C. Above the throw the slope of graph 3 decreases. Described regularities refer not only to diagrams shown in Figure 5, but also to other accessible data.

Estimated values of the pressure  $p_n$  in lower bends are concurrent with pressures in lower cusps on shock adiabates  $p_{sA}$ . Pressures corresponding to upper bends B are significantly lower than pressures in upper cusps  $p_{sB}$ . Considerably better concurrence takes place when comparing values of  $p_{sB}$  and  $p_n$  for upper edges of the throws.

## INTERPRETATION

Let us consider a transition along the Rayleigh line between two adiabates of intermediate composition -- Figure 6. The progress of the reaction is characterized by a quantity,  $n$ , and the progress of the transformation by a quantity,  $l$ . If the transformation was frozen, the state would change from the point I on the adiabat ( $n, l$ ) to the point J on the adiabat ( $n + \Delta n, l$ ). The transformation causes the state changing to the point K<sub>1</sub> on the adiabat ( $n + \Delta n, l + \Delta l_1$ ). The location of the adiabat ( $n + \Delta n, l + \Delta l_1$ ) between ( $n, l$ ) and ( $n + \Delta n, l$ ) depends on the relation between  $\Delta n$  and  $\Delta l_1$ , i.e., it depends on the relation between

the rate of the reaction  $dn/dt$  and the rate of the transformation  $dl/dt$ .

In the case when  $dl/dt \gg dn/dt$ , a shift of the adiabat  $(n + \Delta n, l + \Delta l_2)$  to the left of the adiabat  $(n, l)$  is possible. The transition to the point  $K_2$  is accompanied by a pressure increase. If the point  $I$  lay on the weak branch of the  $(n, l)$  adiabat, a drop in the pressure would correspond to this situation ( $I_3 - K_3$  transition).

The dependence of state changes on the reaction and the transformation kinetics makes us look for the explanation of the  $D(p_0)$  function peculiarities in the relation between rates of both processes. For the analysis of this relation information is necessary concerning the order of magnitude of  $dn/dt$  and  $dl/dt$ , their dependence on the pressure and the character of their changes in time. In Reference 7 the order of magnitude of  $dn/dt$  at the beginning and at the end of the reaction zone was estimated on the basis of experimental data. The following values were obtained: 60 and  $8 \mu s^{-1}$  for TNT and 80 and  $2 \mu s^{-1}$  for PBX 9505. These data prove, that the reaction starts with a very high rate, after that its rate decreases by more than one order of magnitude. The results of reaction time measurements<sup>8,4</sup> showed that the change of the pressure  $p_N$  from 10 to 30 GPa is accompanied by the increase in the rate by 4 to 5 times. For  $p_N > 30$  GPa the reaction time is almost constant.

Measurements of changes in time of pressure and electrical resistance<sup>10</sup> of shocked graphite and BN samples provided a reason for the assessment that, at pressures approximate to  $p_{SA}$ , the rate of transformation does not exceed  $1 \mu s^{-1}$ . At pressures lower than  $p_{SA}$   $dl/dt$  rapidly decreases with pressure drop. Little scatter in experimental  $p_{SA}$  values can be explained by this fact. When the upper cusp of the shock adiabates is approaching, the rate grows to the order of  $100 \mu s^{-1}$ . It stems from this data that the change in pressure from 12 to 21 GPa for BN and from 20 to 37 GPa for graphite is accompanied by the increase of  $dl/dt$  by two orders of magnitude.

The initial rate of the transformation is relatively low. There is a distinct induction period of the transformation at pressures considerably exceeding  $p_{SA}$ . The induction period is followed by the fast phase of the transformation. A little part of the material undergoes transformation in the third, relatively slow phase.

The following conclusions stem from the above information. First, the value of  $dl/dt$  becomes comparable with the  $dn/dt$  value at the end of the reaction zone for pressure approximate to  $p_{SA}$ . It explains the concurrence between  $p_{SA}$  and  $p_{NA}$  values. Second, the dependence of the transformation rate on pressure is much stronger than that of the reaction rate. Therefore, the influence of the

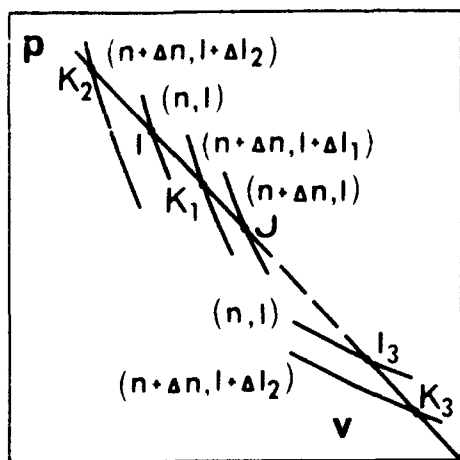


Figure 6 Possible Transitions Between Adiabates of Intermediate Composition

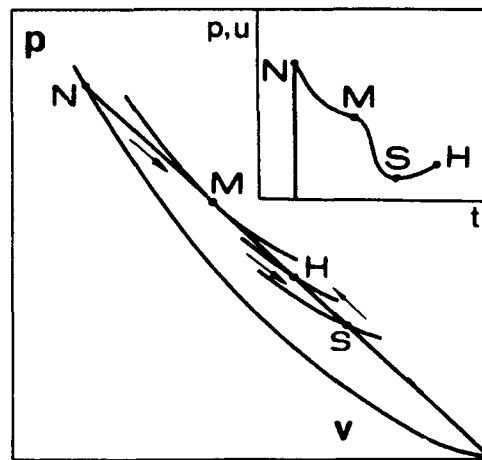


Figure 7. The  $p$ - $v$  Diagram for Detonation with High Rate of the Transformation

transformation on the detonation process becomes stronger with pressure increase. At pressures considerably exceeding  $p_{SA}$ , the relation  $dl/dt \gg dn/dt$  may be fulfilled. The character of changes in time of  $dn/dt$  and  $dl/dt$  suggests, that at first this relation is fulfilled at the end of the reaction zone. Third, the presence of an induction period of transformation causes the influence of the reaction to always prevail at the front of the detonation wave.

Based on the above conclusions, the interpretation of the course of the  $D(p_0)$  function can be performed. The lower bend appears, when the transformation rate approaches the value of the same order of magnitude as  $dn/dt$  at the end of the reaction zone. For  $dl/dt$  growing faster with pressure than  $dn/dt$ , the degree of the transformation in the reaction zone increases when  $p_0$  increases. This is the reason for the decreasing of the slope of  $D(p_0)$  curves. For a value of  $p_0$ , the influence of the reaction and the transformation balance each other at the end of the reaction zone. At higher values of  $p_0$  in a part of the zone the influence of the transformation prevails. As it was established before, this fact has consequences for the character of state changes inside the zone. The analysis of various possibilities proved,<sup>11</sup> that the case corresponding to Figure 7 takes place in reality. The Rayleigh line is tangent to an adiabat, for which the influences of both processes are balanced. At the change of state from the point N to M, the influence of the reaction prevails. When state changes from point M to S, the influence of the transformation is stronger. After the point S has been reached, the reaction starts to prevail. The balance between the influence of the transformation and the reaction means that  $dv/dt = 0$  and  $dp/dt = 0$ . It follows from the equations governing the flow in the reaction zone, that also  $du/dt = 0$ . Moreover, the equality  $d^2v/dt^2 = 0$  is fulfilled in the point M, and also  $d^2u/dt^2 = 0$ . It means, that the function  $u(t)$  has an inflexion. There is a qualitative agreement between the character of the  $u(t)$  function followed from the above considerations and experimental records shown in Figure 3.

The point H lies on the weak branch of the detonation adiabat. It means that the weak detonation regime is realized. This fact explains the occurrence of a plateau of mass velocity behind the reaction zone and the propagation of the initiation pressure excess in the form of a shock at a distance from the detonation wave. Because the velocity of a weak detonation is higher than the velocity of the normal detonation, an increase in the  $D$  value should occur. This increase manifests itself in the form of an increase of the slope of the  $D(p_0)$  function above the point B. The point B corresponds to the situation, when both processes are in the equilibrium at the end of the reaction zone. Measurements have shown that for 40 mm charges, used in investigations reported in References 1-5, the velocity of detonation deviates from its ideal value by 200-300 m/s. Therefore, the appearance of the supersonic flow domain inside the reaction zone may cause an additional increase in the slope of  $D(p_0)$  by weakening the lateral rarefaction influence.

At pressures approaching  $p_{SB}$  the polymorphous transformation considerably accelerates.<sup>10</sup> Its acceleration gives rise to an increase in the detonation velocity which manifests itself as a throw in the  $D(p_0)$  diagram. The upper edge of the throw corresponds to the situation in which almost the whole material undergoes transformation in a very short time, preceded by an induction period comparable with the reaction time. Calculated values of  $p_N$  for the upper edge of throws are close to the location of the upper cusps on shock adiabates.

An increase of  $p_N$  above  $p_{SB}$  gets the induction time of the transformation to shorten, and the sonic point M to move toward the front of the detonation wave. It gives rise to the diminishing of the reaction progress,  $n$ , corresponding to the adiabat which the point M lies on. For that reason, the detonation velocity increment is less than it would be if a constant value of  $n$  corresponded to the point M. It explains the decrease of the slope of the  $D(p_0)$  curves above the point C (see Figure 5).

The process of thermal relaxation, consisting in heat exchange between detonation

products and addition, can have considerable influence on detonation parameters. This is the reason for observed dependence of the location and the character of peculiarities of the  $D(p_0)$  function on the granules' size of the addition undergoing transformation. Non-homogeneous distribution of the temperature inside large granules gives rise to the induction period of the transformation varying significantly inside those granules. In macroscopic scale, this effect reveals as a decrease of the maximum rate of the transformation. For that reason, the effect of an accelerated growth of  $D$ , manifesting itself as a throw, may not appear. The thermal relaxation process can influence the slope of  $D(p_0)$  diagrams, by decreasing the quantity of heat absorbed by the addition as the reaction time diminishes with increasing  $p_0$ .

## CONCLUSIONS

1. The segments of the  $D(p_0)$  curves between the lower and the upper bends correspond to the increasing degree of the polymorphous transformation. In the whole reaction zone the influence of the reaction prevails, i.e.,  $dv/dt > 0$ .
2. The appearance of the upper bend can be attributed to the balance between the influences of the reaction and the transformation. At the end of the reaction zone  $dv/dt = 0$ .
3. The segments of the  $D(p_0)$  curves above upper bends correspond to the situation in which, in a part of the zone, the influence of the transformation prevails. It gives rise to a weak detonation.
4. The appearance of the throws on the  $D(p_0)$  curves can be connected with the fast rise of the  $dl/dt$  value, when pressure approaches the  $p_{SH}$  value.
5. The segments of the  $D(p_0)$  curves above throws correspond to the movement of the sonic point  $M$  toward the front of the detonation wave. It causes diminishing of the  $D(p_0)$  slope.
6. The throws, observed in the mass velocity oscillograms, are connected with the fast phase of the polymorphous transformation. A delay of their appearance can be interpreted as the occurrence of the transformation induction period.
7. When interpreting the character of  $D(p_0)$  curves, the thermal relaxation process should be taken into account.

## REFERENCES

1. Pyaternev, S. V.; Pershin, S. V.; Dremine, A. N.; and Aniskin, A. I., "Influence of Carbon and Boron Nitride Additions on the Detonation of Explosives," *Fizika Goreniya i Vzryva*, Vol. 22, No. 3, 1986, p. 99.
2. Pyaternev, S. V.; Pershin, S. V.; Dremine, A. N.; and Anankin, A. V., "On a Peculiarity of Mass Velocity Profile of Detonation Wave in Explosives, Containing Addition, Undergoing Polimorphous Transformation," *Fizika Goreniya i Vzryva*, Vol. 22, No. 3, 1986, p. 136.
3. Pershin, S. V.; Dremine, A. N.; Pyaternev, S. V.; and Tsaplin, D. N., "On the Appearance of the Polimorphous Transformation of Addition in Measurements of Wave and Mass Velocities of Detonation of Explosives," *Fizika Goreniya i Vzryva*, Vol. 23, No. 1, 1987, p. 74.
4. Dremine, A. N.; Pershin, S. V.; Pyaternev, S. V.; Tsaplin, D. N.; and Shcherbakova, N. P., "Polimorphous Transformations of Boron Nitride and Silicon in the Detonation Wave," *Proceedings of the Seventh Symposium (International) on the Use of Explosion*, Pardubice, 25-27 Oct 1988, p. 350.
5. Wlodarczyk, E.; Maranda, A.; Trebinski, R.; and Witkowski, W., "Investigations of the Polimorphous Transformation in the Detonation Wave in Explosives Containing Various Types of Graphite by the Electromagnetic Method," *Proceedings of the Seventh Symposium (International) on the Use of Explosion*, Pardubice, 25-27 Oct 1988, p. 344.
6. Trebinski, R.; Trzcinski, W.; and Wlodarczyk, E., "A Method of Determining Detonation Adiabates of Explosives



- with Admixture of Inert Additions," *J. Tech. Phys.* (to be published).
7. Fahy, S.; Louie, S.G.; and Cohen, M. L., "Pseudopotential Total-Energy Study of the Transition from Rhombohedral Graphite to Diamond," *Phys. Rev. B*, Vol. 34, No. 2, 1986, p. 1191.
  8. Sheffield, S. A.; Bloomquist, D. D.; and Tarver, C. M., "Subnanosecond Measurements of Detonation Fronts in Solid High Explosives," *J. Chem. Phys.*, Vol. 80, No 8, 1984, p. 3831.
  9. Anankin, A. V.; Dremin, A. N.; Kanel, G. I.; and Pershin, S. V., "Investigation of Shock Waves Structures in Boron Nitride and Graphite in the Range of Polimorphous Transformations," *Prikl. Mech. Tech. Phys.*, No. 3, 1978, p. 112.
  10. Jugin, Yu. N.; Krupnikov, K. K.; and Ovechkin, N. A., "Investigation of Peculiarities of Transformation of Shocked Graphite into Diamond on the Base of Resistance Measurements," *Khimicheskaya Fizika*, Vol. 6, No. 10, 1987, p. 1447.
  11. Trebinski, R.; Trzcinski, W.; and Wlodarczyk, E., "Analysis of the Influence of Polimorphous Transformations on the Process of Detonation of Mixtures of High Explosives with Substances Undergoing Transformation," *J. Tech. Phys.* (to be published).

# EXAMPLES OF DETONATION SHOCK DYNAMICS FOR DETONATION WAVE SPREAD APPLICATIONS

D. Scott Stewart

Department of Theoretical and Applied Mechanics  
University of Illinois  
Urbana, Illinois 61801

and

John B. Bdzil

Los Alamos National Laboratory  
Los Alamos, New Mexico 87545

*This paper gives some examples of the method of detonation shock dynamics applied to simple geometries suitable for experiment. In particular we consider the rate stick geometry (which involves cartesian coordinates), and cylindrical and spherical geometry. With an assumed form for the normal detonation shock velocity - curvature relation, we calculate characteristic relaxation to steady state dynamics which can be observed in experiment. This paper is a companion of a paper by Bdzil, Fickett, and Stewart appearing in these proceedings.*

## INTRODUCTION

Many explosives engineering problems involve the prediction of a fully developed, high order detonation spreading through explosive that has a complex two- or three-dimensional shape. The prediction of the time of arrival of the detonation at a chosen point is a necessary ingredient in the design of the explosive element in a system. The most common rule used in design assumes that the detonation shock advances along the local normal to the shock at the one-dimensional, Chapman-Jouguet (CJ) velocity. This is equivalent to the Huygens construction of geometrical optics. Recent theoretical work in the hydrodynamic theory of time-dependent, multidimensional detonation<sup>1,2</sup> has shown that when the detonation reaction zone is short compared to the radius of curvature of the diverging detonation shock (which is comparable to the dimensions of the device), the normal detonation shock velocity is the CJ value minus a correction which is a function of the local curvature. This is represented as

$$D_n = D_{CJ} - a(\kappa). \quad (1)$$

We call this relation the  $D_n$ - $\kappa$  relation.

This discovery has led us to suggest the method of "Detonation Shock Dynamics" (DSD) as a simple way to calculate the dynamics of the leading detonation shock. Since our theoretical calculations have shown that the functional form of the  $D_n$ - $\kappa$  relation depends on the equation of state (EOS) and the form of the energy release, which are properties of the explosive, we have postulated that such a relation exists and can be measured directly by experiment in systems with smoothly evolving detonation shocks.<sup>3,4</sup> Once the  $D_n$ - $\kappa$  relation is determined, it implies a partial differential equation for the location of the shock surface for multidimensional geometry and an ordinary differential equation in one-dimensional geometry for the shock location.

The surface construction for the shock implied by this method is a modification of the CJ-Huygens construction. The  $D_n$ - $\kappa$  relation

implicitly includes and predicts the non-ideal behavior due to finite length reaction zone effects.

In what follows, we will solve the initiation transient for a rate stick, which is a multidimensional problem. Cartesian (or cylindrical) coordinates are the natural ones to use, with the  $z$ -axis aligned in the direction of the propagating detonation. The DSD solution to this problem involves a partial differential equation (PDE) for the shock position. The solution of the PDE requires a discussion of the boundary conditions to be applied at the edge of the stick. We then analyze the expanding cylindrical and spherical DSD detonation and show how experiments in simple geometry could be used to discover the  $D_n$ - $\kappa$  relation intrinsic to the explosive.

## RATE STICK EXAMPLE AND SOME REPRESENTATIVE DYNAMICS

For the case of a rate stick, we represent the equation of the surface of the shock by

$$S = z - (z_s(r,t) + D_{CJ}t) = 0. \quad (2)$$

Note that Equation (2) reflects that the velocity of the shock is  $D_{CJ}$  to a first approximation. A schematic of the rate stick and coordinate system is shown in Figure 1.

In order to illustrate the partial differential equation implied by Equation (1), we need expressions for  $D_n$  and  $\kappa$  in terms of  $r$  and  $t$ . Note that  $\kappa$  is the total curvature of the surface and is defined by the surface relation

$$\kappa = \nabla \cdot \hat{n}, \quad (3)$$

where  $\hat{n}$  is the local unit normal to the detonation shock. With the surface representation given by Equation (2)  $\hat{n}$  is simply

$$\hat{n} = \frac{\hat{e}_z}{\sqrt{1+z_s'^2}} - \frac{z_s' \hat{e}_r}{\sqrt{1+z_s'^2}}, \text{ where } z_s' \equiv \frac{\partial z_s}{\partial r}. \quad (4)$$

In plane and axisymmetric cylindrical coordinates,  $\kappa$  is given by

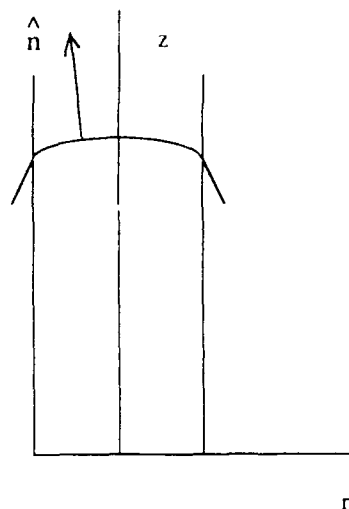


Figure 1. Rate Stick Geometry

$$\kappa = \nabla \cdot \hat{n} = \frac{\partial}{\partial r} \left( \frac{n_r}{r} \right) + \frac{1}{r} \frac{\partial}{\partial r} \left( r n_r \right), \quad (5)$$

respectively. Substitution of  $n_r$  into the left-hand side of Equation (5) shows

$$\kappa = \frac{-z_s''}{3\sqrt{1+z_s'^2}}, \text{ for plane and}$$

$$\kappa = - \left[ \frac{z_s'}{r\sqrt{1+z_s'^2}} + \frac{z_s''}{3\sqrt{1+z_s'^2}} \right],$$

for  $r \neq 0$  and

$$= -[2 z_s''],$$

for  $r = 0$ , for cylindrical geometry. (6)

The definition of the normal velocity of the shock surface is defined in terms of  $S$  by

$$D_n = \frac{-\frac{\partial S}{\partial t}}{|\nabla S|} \equiv \frac{\dot{z}_s + D_{CJ}}{\sqrt{1+z_s'^2}}, \text{ where } \dot{z}_s \equiv \frac{\partial z_s}{\partial t}. \quad (7)$$

If  $c(\kappa)$  is known explicitly, then the following PDE is derived for  $z_s$  from Equation (1),

$$\dot{z}_s = \sqrt{1 + z_s'^2} (D_{CJ} - \alpha(\kappa)) - D_{CJ}, \quad (8)$$

where  $\kappa$  is shown in Equation (6).

To discuss the results, we choose length, velocity, and time scales appropriate to the experiment; the velocity scale is  $D_{CJ}$ ; the length scale is the diameter of the stick,  $d$ ; and the time scale is  $d/D_{CJ}$ . Thus we replace  $\bar{z}_s$  by  $\tilde{d}z_s$  and so on, where the tilde superscript now refers to dimensional quantities and plain variables like  $z_s$ , etc., now refer to the dimensionless, scaled variables. For example, the scaled Equation (1) now reads

$$D_n = 1 - \alpha(\kappa), \text{ where } \alpha(\kappa) \equiv \tilde{a}(\tilde{\kappa})/\tilde{D}_{CJ}. \quad (9)$$

One of the fundamental hypotheses of DSD is that the correction to the normal detonation velocity is small. This requires that

$$\alpha(\kappa) = \tilde{a}/\tilde{D}_{CJ} \ll 1. \quad (10)$$

For illustration, we assume that the  $D_n$ - $\kappa$  relation is linear. (A linear relation was derived in Equation (2) for a particular EOS and energy release law.) Thus we write

$$\tilde{a}(\tilde{\kappa}) = \tilde{b} \tilde{\kappa}. \quad (11)$$

Since the shock curvature  $\kappa$ , measured on the scale of the stick diameter is not necessarily small, consistency with the requirement Equation (10) implies that

$$b \equiv \tilde{b}/(\tilde{d}\tilde{D}_{CJ}) \ll 1. \quad (12)$$

Equation (8) (for plane geometry) now reads

$$\dot{z}_s = (\sqrt{1 + z_s'^2} - 1) + \frac{bz_s''}{(1 + z_s'^2)} \quad (13)$$

Suppose that the shock slope is very small, compared to one, so that  $z_s'^2$  can be neglected. Then the first term of the right-hand side of Equation (13) vanishes and the denominator of the second term is replaced by unity. The heat equation results for  $z_s$ , with  $b$  acting as the diffusion coefficient. Indeed, Equation (13) is a nonlinear heat equation; DSD calculations show the diffusive behavior of parabolic evolution equations.

If an equation like Equation (13) governs the behavior of the detonation shock in a finite domain, then boundary conditions must be applied at the end of the domain, i.e., at the cylindrical surface of the rate stick.

## Boundary Conditions

The boundary condition is applied at the interface between the explosive shock and the confinement: the curve generated by the intersection of the explosive shock and the cylindrical surface of the stick. Immediately behind the shock the pressure is near the CJ value. When the explosive is unconfined, the pressure just outside the explosive is at or near the undisturbed value (zero). In order for the flow to execute such a transition, an expansion fan must be embedded in the flow at the intersection of the shock and the edge. If the flow evolves quasi-steadily at the edge, then it is a two-dimensional, steady, supersonic flow with an imbedded fan.

The effects are different for strong confinement provided by a (metal) tube wall or by adjoining explosive than when no confinement is provided and the explosive products expand freely into a vacuum. Bdzil showed,<sup>5</sup> for a reasonable EOS and for a finite thickness inert tube, that the matching problem described above determines the shock attachment angle, relative to the wall. If there is no confinement, then one can derive the edge condition by noticing that if the flow is quasi-steady, it must be either a sonic or a supersonic flow in a frame where the observer is moving along the edge at the shock/edge intersection speed (which is different from the local detonation speed). In either case, the shock/edge intersection angle is determined.

Thus a very simple and theoretically consistent boundary condition for Equation (13) is

$$\dot{z}_s = \pm a \text{ at } r = \mp \frac{1}{2}, \text{ for } a \geq 0. \quad (14)$$

Note that  $a$  is zero when the confinement is perfect and provided by adjacent explosive. The slope  $a$  probably takes on a value no bigger than one for most explosives when the flow is unconfined.

## Typical Detonation Shock Dynamics

A multidimensional DSD calculation requires that the initial detonation shock location be given in the explosive. In addition, the confinement must be specified, i.e., a given. To illustrate typical detonation shock dynamics, we consider the problem of a plane detonation that is initially plane and CJ. Thus we solve Equation (13) (for plane geometry) with the boundary condition Equation (14) and the initial data that

$$z = z_s = 0 \text{ for } -\frac{1}{2} < r < \frac{1}{2} \text{ at } t = 0. \quad (15)$$

Once  $z_s$  is found, the shock location is

$$z = t + z_s(r, t). \quad (16)$$

The PDE, with boundary and initial conditions, can be solved numerically, easily, and quickly with a standard PDE package that is suitable for the heat equation. In this case, we chose the IMSL routine DPDES. A copy of the Fortran code, suitable for plane geometry is found in the appendix.

Figure 2 shows the results of solving the initial, boundary value problem with  $a = 1.0$ ,  $b = .1$  and with the final calculated time,  $t_{\text{final}} = 1.0$ . The wave fronts are plotted at 10 equal time increments. If the wave were plane then it would travel exactly one unit in  $z$ . Notice that the final wave location is retarded from its plane value due to the slight decrement in the wave velocity. The initial transient clearly shows that the wave is initially flat and then distorts into its steady shape due

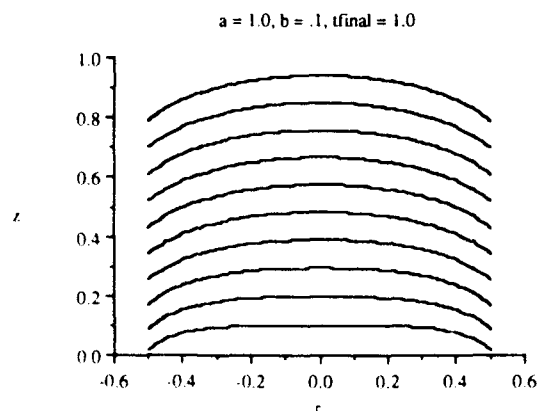


Figure 2. Evolution in a Rate Stick

to the disturbance (rarefactions) caused by the confining edges.

An important experimental question is: How long does it take to get a steady wave? This question has implications for the sizing of the experimental apparatus. In this instance we can answer the question by first computing long enough to achieve the steady wave velocity (which will be slightly below the CJ value), and then comparing that to the transient velocities in the stick. Not surprisingly, one finds that the decay to steady state is different depending on  $r$ , the distance from the centerline of the stick. Figure 3 shows the transient of  $z_s$  (which is the velocity decrement from the CJ value along the axis of the stick), as a function of time. The figure shows that the edge initially lags far behind the center, but eventually achieves the steady velocity of the final detonation shock.

Another, similar comparison is shown in Figure 4, where the velocity was monitored along the edge and centerline. The steady velocity decrement (the difference between the steady wave velocity and CJ) and the time required to achieve 99 percent of the steady decrement was recorded. Then  $a$  was varied to show the effect of confinement.

Note that the time for 99 percent of the steady velocity to be achieved for the centerline is consistently smaller than at the edge; this is consistent with the edge flow being more unsteady. Also, notice that the limit  $a = 0$  corresponds to an infinitesimal disturbance applied to the detonation shock by the wall. In

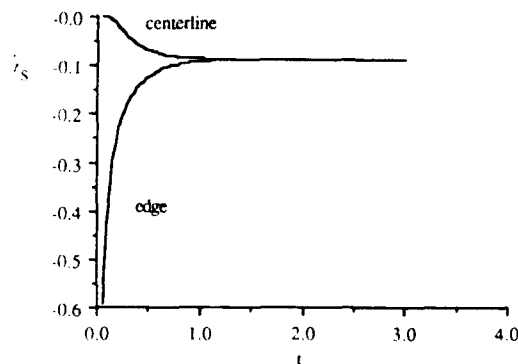


Figure 3. Decay to Steady State at Edge and Centerline for  $a = 1$ ,  $b = .1$

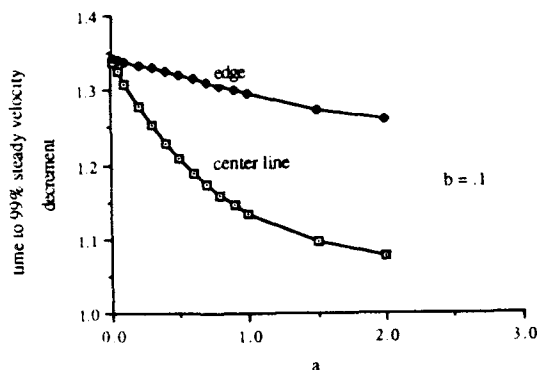


Figure 4. Time to 99 Percent Steady Velocity Decrement Shown for the Edge and Centerline

the small disturbance limit, Equation (13) reduces to the heat equation, which has a finite relaxation time for a small disturbance to decay.

An immediate conclusion is that there is a finite relaxation time for even a small disturbance to decay on the surface of the detonation shock in explosives. If the DSD hypothesis holds, this characteristic relaxation time should be measurable by experiment.

As  $a$  is increased, the disturbance to the detonation shock from the wall increases in magnitude corresponding to the behavior shown in the figure.

Finally, Figure 5 shows the diameter effect curve, which is easily calculated for this example. Note that the dimensional diameter  $\bar{d}$  appears in the denominator in the definition of  $b$  in Equation (12). Consequently, varying  $b$  is equivalent to varying the inverse stick diameter,  $1/\bar{d}$ .

## EXAMPLES OF EXPANDING CYLINDRICAL AND SPHERICAL DETONATION

When spherical and cylindrical detonation are considered, the expressions for the curvature and the normal detonation velocity are simply related to the detonation radius,  $\bar{r}$ . The problem of DSD in this instance reduces to solving a first order, separable differential equation. (Note that the cylindrical detonation considered here differs from the rate stick in that the detonation propagates only radially as

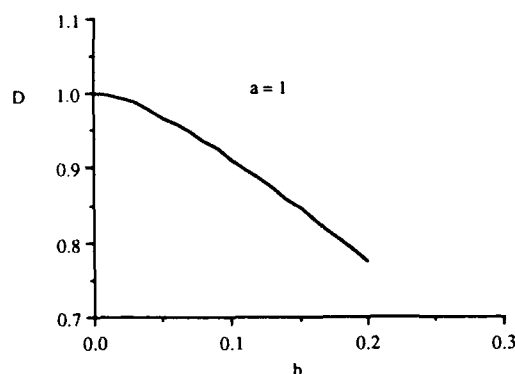


Figure 5. The Diameter Effect Curve

opposed to along the axis for the rate stick.) In particular

$$\bar{\kappa} = j/\bar{r}, \text{ where } j = 1 \text{ for cylindrical detonation and } j = 2 \text{ for spherical detonation.} \quad (17)$$

Also

$$\bar{D}_n = d\bar{r}/d\bar{t} \quad (18)$$

Again, it is useful to identify characteristic scales for an experiment. The velocity scale is again chosen as  $\bar{D}_{CJ}$ , the length scale is chosen as the initial detonation radius  $\bar{R}$ , and the time scale is chosen as  $\bar{R}/\bar{D}_{CJ}$ . The scaled version of Equation (1) now reads

$$\bar{r} = 1 - \alpha(j/r), \text{ where } \alpha(j/r) = \bar{\alpha}(j/\bar{r})/\bar{D}_{CJ}. \quad (19)$$

Equation (19) is a separable first order differential equation that can be solved directly by integration.

To illustrate the relaxation dynamics of cylindrical and spherical waves, we consider two cases with different functional forms for the  $D_n$ - $\kappa$  relation. We consider the cases where the dependence on the curvature is linear and varies as a square root, i.e.,

$$\begin{aligned} \text{linear, } \bar{\alpha}(\bar{\kappa}) &= \bar{b}\bar{\kappa}, \\ \text{square root, } \bar{\alpha}(\bar{\kappa}) &= \bar{b}\bar{\kappa}^{1/2}. \end{aligned} \quad (20)$$

Note that the constant  $\bar{b}$  has different dimensions in the two cases.

The requirement that the normal detonation velocity is corrected by a small amount

for these cases leads to a restriction on  $b$ , namely

$$\begin{aligned} \text{linear, } b &\equiv \bar{b}/(\bar{R}\bar{D}_{CJ}) < < 1, \text{ and} \\ \text{square root, } b &\equiv \bar{b}/(\bar{R}\bar{D}_{CJ})^{\frac{1}{2}} < < 1. \end{aligned} \quad (21)$$

For these examples Equation (19) now reads

$$\begin{aligned} \text{linear, } \dot{r} &= 1 - bj/r, \text{ and} \\ \text{square root, } \dot{r} &= 1 - bj^{\frac{1}{2}}/r^{\frac{1}{2}}, \end{aligned} \quad (22)$$

subject to the initial condition

$$r = 1 \text{ at } t = 0. \quad (23)$$

The solutions to Equation (22) with Equation (23) are found analytically by integration to obtain

$$\begin{aligned} \text{linear, } r - 1 + bj \ln\left(\frac{r - bj}{1 - bj}\right) &= t, \text{ and} \\ \text{square root, } r - 1 + 2bj^{\frac{1}{2}} \ln\left(\frac{r^{\frac{1}{2}} - bj^{\frac{1}{2}}}{1 - bj^{\frac{1}{2}}}\right) &= t. \end{aligned} \quad (24)$$

The decay to steady-state is a function of  $b$ , which contains in its definition the properties of the explosive.

Suppose we ask: at what time does the detonation achieve 99 percent of its final velocity from a given initial radius,  $r$ ? Then for the linear case we find from Equation (22) that

$$\dot{r} = .99 \text{ and } bj/r = .01, \quad (25)$$

and substitution into Equation (24) gives

$$t_{99\%} = 100bj - 1 + bj \ln\left(\frac{99bj}{1 - bj}\right). \quad (26)$$

A similar calculation for the square root case shows

$$t_{99\%} = b^2 j (100)^2 - 1 + 2bj^{\frac{1}{2}} \ln\left(\frac{99bj^{\frac{1}{2}}}{1 - bj^{\frac{1}{2}}}\right). \quad (27)$$

The time  $t_{99\%}$  is plotted versus  $b$  in Figure 6 for the cylindrical and spherical geometries.

These results show clearly that the decay to the steady state is strongly affected by the

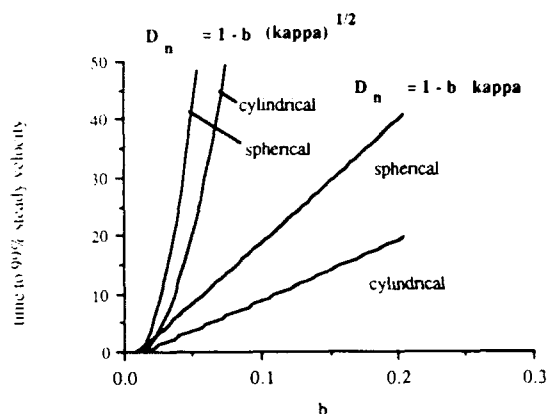


Figure 6. Decay to  $D_{CJ}$  for Cylindrical and Spherical Geometries for Different  $D_n$ - $\kappa$  Relations

curvature: both by the influence of the geometry and through  $\alpha(\kappa)$ . For example, Figure 6 shows that independent of the explosive's intrinsic dependence on curvature, a cylindrical detonation decays to CJ more quickly than a spherical detonation. This is a geometric effect, since for a given radius, the curvature of the spherical detonation is twice that of a cylindrical detonation. The figure also shows that the square root case decays (relatively) much more slowly to the steady state than the linear case due to the larger velocity decrement effect of square root curvature.

Finally, these simple geometries offer the possibility of determining portions of the  $D_n$ - $\kappa$  relation directly from experiment. For example, consider a cylindrical or a spherical shot in which the radius, time, and velocity of the detonation shock is recorded by a pin method. Once the expanding wave has approached a velocity within 10 percent of the CJ velocity, one plots the data of velocity versus radius. A hypothetical example is shown in Figure 7.

In this figure the radius is scaled with respect to its initial value and the velocity is scaled with the CJ velocity. Since in these simple geometries  $\kappa = j/r$  and  $\dot{r} = D_n$ , the data shown in Figure 7 can be converted pointwise into the experimentally measured  $D_n$ - $\kappa$  relation, which is shown in Figure 8.

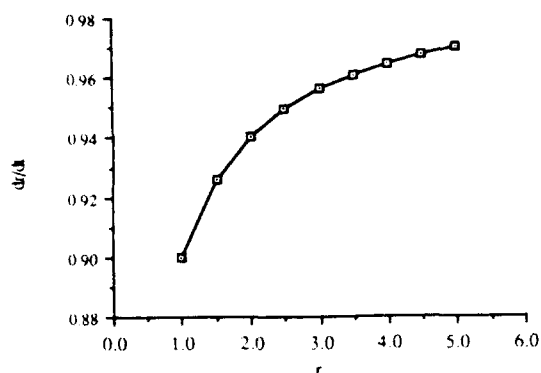


Figure 7. Hypothetical Velocity - Radius Data from a Cylindrical Shot

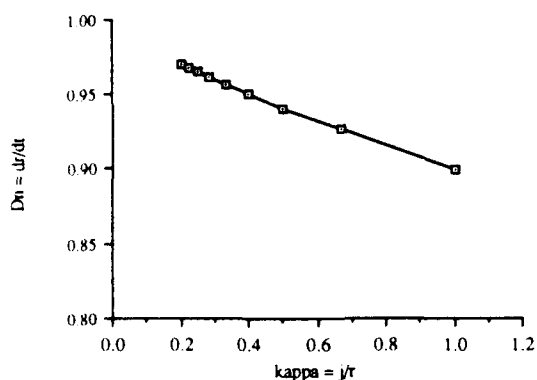


Figure 8. Conversion to the  $D_n$ - $\kappa$  Relation Corresponding to Figure 7

## ACKNOWLEDGEMENTS

D. S. Stewart acknowledges support from Los Alamos National Laboratory, DOE-LANL-9XG8-3931-P1. This work was supported by the U. S. Department of Energy.

## REFERENCES

1. Bdzil, J. B. and Stewart, D. S., "Time-Dependent Two-Dimensional Detonation: The Interaction of Edge Rarefactions with Finite Length Reaction Zones," *J. Fluid Mech.*, Vol. 171, 1986, pp. 1-26.
2. Stewart, D. S. and Bdzil, J. B., "The Shock Dynamics of Stable Multidimensional Detonation," *Combust. and Flame*, Vol. 72, 1986, pp. 311-323.
3. Stewart, D. S. and Bdzil, J. B., "A Lecture on Detonation Shock Dynamics," *Lecture*

*Notes in Physics*, Buckmaster, J. D. and Takeno, T. eds., Springer-Verlag, Pub., Vol. 299, 1988, pp. 17-30.

4. Bdzil, J. B. and Stewart, D. S., "Modeling Two-Dimensional Detonations with Detonation Shock Dynamics," *Phys. Fluids*, Vols. 1, 7, 1989, pp. 1261-1267.
5. Bdzil, J. B., "Steady-State Two-Dimensional Detonation," *J. Fluid Mech.*, Vol. 108, 1981, pp. 195-226.

## APPENDIX

```

program rtstk
parameter(npdes = 1,nx = 101,iy = npdes)
dimension wk(68*nx + 5), x(nx),
&y(npdes,2,nx)
external fcn,bndry
common/dcj/dcj,a,b
open(unit = 6,status = 'new',file = 'rsout')
open(unit = 7,status = 'old',file = 'rsin')
open(unit = 8,status = 'new',file = 'edge')

c
c x(i) plays the role of r and y(1,1,i) plays the
c role of z-shock in the paper
c
c input data, dcj, shock confinement angle
c
c   read(7,*)dcj,a,b,tfinal,nstep
c   dcj = 1
c   a = 1.0
c   b = .1
c   tfinal = 1.0
c   nstep = 10
c
c initial data corresponds to a flat shock
c
c   xx = -.5
c   nxm1 = nx-1
c   dx = 1.0/nxm1
c   do 10 i = 1,nx
c     x(i) = xx
c     y(1,1,i) = 0.0
c     y(1,2,i) = 0.0
c     if(i.eq.1)y(1,2,i) = a
c     if(i.eq.nx)y(1,2,i) = -a
c     xx = xx + dx
10 continue
c
c starting parameters for dpdes
c

```



```

ye = 0.0
ycl = 0.0
tol = 1.e-6
h = 1.0e-5
t = 0.0
dt = tfinal/nstep
index = 1
c
c solve the equation implied by the
c Dn-kappa relation to determine shock
c locus relative to the steady Dcj frame.
c
  do 20j = 1, nstep
  tend = t + dt
  call dpdes(npdes,fcn,bndry,t,h,&tend,x,y,
  iy,nx,tol,index,wk,ier)
c
c evaluate lab frame shock location and
c write to output
c also evaluate the shock velocity along the
c shock and centerline and write to output
c
  do 30 i = 1,nx
  z = y(1,1,i) + dcj*t
  write(6,*)x(i),z
30 continue
  nxh = nxm1/2 + 1
  ve = (y(1,1,1) - ye)/dt
  vc1 = (y(1,1,nxh) - ycl)/dt
  write(8,25)t,ve,vc1
25 format(e12.6,2x,e12.6,2x,e12.6)
  ye = y(1,1,1)
  ycl = y(1,1,nxh)
20 continue
end
c
c this subroutine evaluates the pde implied
c by the Dn-kappa relation
c
  subroutine fcn(npdes,x,t,u,ux,uxx,ut)
  dimension u(1),ux(1),uxx(1),ut(1)
  common/dcj/dcj,a,b
  crv = -uxx(1)/(sqrt(1+ux(1)**2))**3
  cal dkappa(crv,alph)
  dn = dcj - alph
  ut(1) = dn*sqrt(1+ux(1)**2)-dcj
  return
  end
c
c this subroutine evaluates the constant
c slope boundary condition according to

```

```

c imsl dpdes
c
  subroutine bndry (npdes,x,
  &t,alpha,beta,gamp)
  dimension alpha(2),beta(2),gamp(2)
  if(x.lt.0.0)then
    alpha(1) = 0.0
    beta(1) = 1.0
    gamp(1) = 0.0
  else
    alpha(1) = 0.0
    beta(1) = 1.0
    gamp(1) = 0.0
  endif
  return
end
c
c this subroutine defines the Dn-kappa
c relation
c
  subroutine dkappa (crv,alph)
  common/dcj/dcj,a,b
  alpha = b*crv
  return
end

```

## DISCUSSION

**M. COWPERTHWAIT**  
SRI International  
Menlo Park, CA

Have you considered the possibility of a reactive Prandtl-Meyer fan when the flow at the edge of the charge is sonic?

**M. COWPERTHWAIT**  
SRI International  
Menlo Park, CA

It would seem to me that the shock polar analysis for determining the angle of the shock at the charge-boundary interface is only valid if the boundary is thick. Do you know what thick means in terms of the charge radius to wall thickness ratio?

**JOSEPH C. FOSTER JR.**  
Air Force Armament Lab.  
Eglin AFB, FL

Can you comment on the range of edge boundary conditions validity without accounting for impedance mismatch and possible mach

stem formation at the edge which could result in propagation of triple point toward the center of the rate stick problem with metal confinement.

## REPLY BY J. B. BDZIL

Because there were a number of questions/comments (including the three above) related to the nature of the edge boundary condition, I will reply to all of them below.

As input, the DSD theory only needs a boundary condition relating the shape and velocity of the shock at the explosive's edge. To get such a condition, the details of the flow through the reaction zone and the interaction with the confining inert material need to be considered. Although, many of the important problems in this area are unsolved, something is known about strictly steady two-dimensional edge flows in large diameter rate sticks. I will give a brief overview of the possible boundary conditions for such flows. The reference frame for our discussion moves at constant speed,  $D$ , with the intersection of the shock and the edge, upwards along the edge (see Figure 9). The nature of the boundary condition is dependent on the sonic character of the flow as measured in this reference frame. When the detonation propagates near its full strength Chapman-Jouguet speed, the angle,  $\omega$ , between the incident shock and the edge is

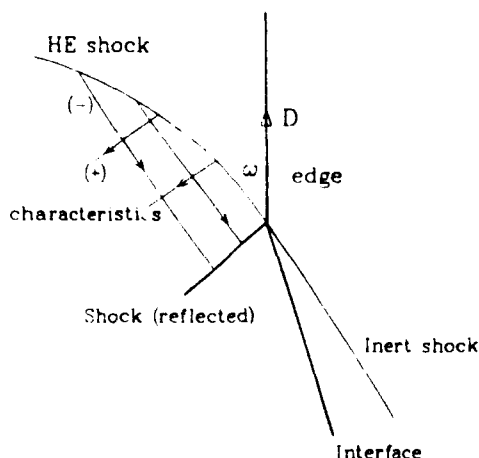


**Figure 9.** The Interaction of a Detonation with a Boundary. The case of supersonic flow behind the shock. The high-explosive (HE) shock is not perturbed by the edge.

the variable that determines the sonic character. We use this angle as the control parameter to produce supersonic, sonic, and subsonic flows in the reaction zone.

The flow type shown in Figure 9 is supersonic. For this flow, both families of characteristics carry information away from the HE shock. A reflected wave is generated by the interaction of the incident shock with the edge. Depending on the equations of state of the HE and the inert, this wave can be either a reflected shock (single or Mach wave) or an expansion centered at the interaction point. When the pressure induced into the inert is less than that behind the incident shock in the HE, the reflected wave is expansive. Since all the information flow is away from the HE shock for this case, the edge does not influence either the shock or the supporting reaction zone. The detonation is unaffected by the edge in this limit. This configuration is inappropriate for a rate stick boundary. It is the desirable edge condition for a wedge test.

As the angle,  $\omega$ , that the incident shock makes with the edge is increased, there comes a point when the flow behind the shock is just sonic. When the pressure induced in the inert is below that behind the incident detonation, the flow configuration resembles that depicted in Figure 10. The flow behind the detonation shock is either sonic or subsonic: the sonic

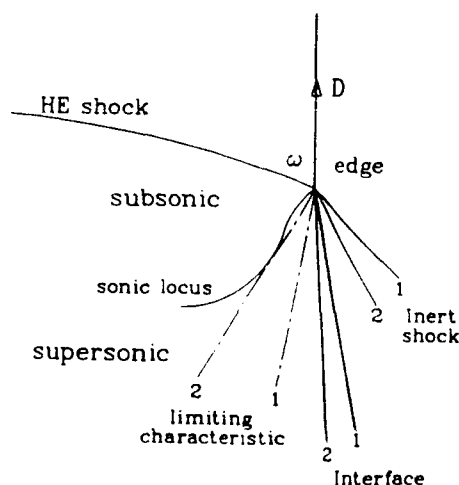


**Figure 10.** The Case of Exactly Sonic Flow at the Edge. Two cases of weak confinement are shown: weak (2) and weaker (1). The detonation propagates as it would were it totally unconfined.

locus is internal to the reaction zone and intersects the shock at the edge. Below the sonic locus the flow is supersonic with both families of characteristics in the explosive being downward going. A Prandtl-Meyer singularity is located in the supersonic flow at the shock/edge intersection point. It allows the pressure at the intersection to be reduced discontinuously from the explosive to the inert value. Its structure dominates the flow in the vicinity of the edge. In this supersonic region, the right-going characteristics (not shown) carry information from the region below the detonation sonic locus to the inert. The left-going characteristics emanating from the singularity (dashed lines) and the interface carry information about the confinement back to the detonating explosive. These characteristics are actually curved lines for this resolved reaction zone problem (see Appendix C in Reference 5).

Two cases of weak confinement are shown in Figure 10. They are labeled as weak (2) and weaker (1). The two left-going characteristics shown separate the flow into regions that are uninfluenced (to the left) and influenced (to the right) by confinement. For case (1), the confinement does not influence the structure of the detonation shock: the structure is the same as that for an unconfined detonation. For case (2), the limiting characteristic just contacts the detonation sonic locus.

Information about the confinement now can influence the structure of the detonation shock and in turn the "detonation" velocity. As the strength of the confinement is further increased, the sonic locus detaches from the shock and the flow looks like that shown in Figure 11. With this change we leave the case of a pressure drop in going from the explosive to the inert. For the typical condensed phase explosive, an inert such as polymethyl methacrylate (PMMA) is below yet near this critical amount of confinement.

When the pressure induced in the inert is either *at* or *above* the pressure behind the incident detonation shock, the shock angle,  $\omega$ , increases so as to equilibrate the explosive and inert pressures. The flow is now subsonic behind the detonation shock all the way out to the confining inert (in contrast to the situation

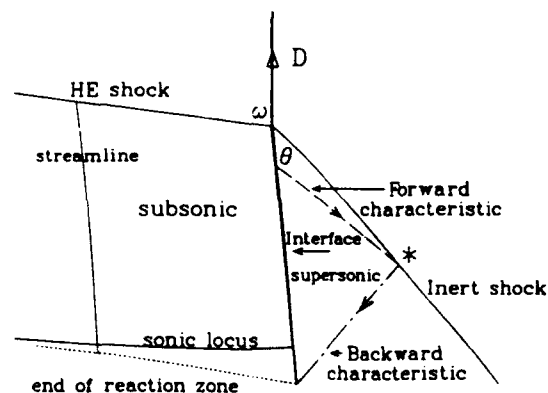


Figure 11. The Case of Subsonic Flow at the Edge. The confinement is strong. The critical inert confinement thickness is marked with an asterisk.

in Figures 9 and 10). Owing to the reactivity, a steady smooth flow can exist in the reaction zone (i.e., free of internal reflected shocks or Mach waves). The flow configuration shown in Figure 11 is the result of a calculation for the case of a high-order PBX 9502 detonation confined by copper. Such a steady wave is an *admissible* solution.

The stability of this flow to Mach wave formation is a complex issue. Mach waves can form spontaneously anywhere in the reaction zone. They are believed to be a consequence of the hydrodynamic instabilities that can arise when the state-dependence of the detonation heat-release rate is strong. Importantly, Mach waves are not the only possibility. The smooth flow discussed in the previous section is also a solution.

We now focus our attention on the flow in the confining material. The issue that concerns us is the critical thickness of the inert confining layer shown in Figure 11. We examine the question: What thickness of inert is essentially infinite as far as confinement is concerned? Three hydrodynamically distinct cases can arise: (1) the sound speed in the inert is faster than  $D_{CJ}$ , (2) the shock speed in the inert is slower than  $D_{CJ}$  and the flow is subsonic in the earlier defined shock fixed

reference, and (3) the shock speed is slower than  $D_{CJ}$  and the flow is supersonic. Here we consider only the most typical and most easily analyzed situation, case (3). The ease of analysis of case (3) is a consequence of the relatively small values of  $\theta$  and the very limited zones of hydrodynamic influence that are properties of supersonic flow. For case (2), the values of  $\theta$  are larger (although  $\theta < \pi/2$ ). The subsonic flow makes it possible for the post reaction zone flow in the explosive to drive energy up the inert and thereby influence both the reaction zone and the inert shock. Case (1) is the most nonlocal. A disturbance moves up the inert faster than the detonation velocity. This case does not even admit a steady solution.

A calculated example of case (3) behavior is shown in Figure 11. Because the inert flow is supersonic, both families of characteristics are downward going. The adjacent regions of the detonation reaction zone that drive the inert send information down the inert forward characteristics (see Figure 11). Information

about the inert (e.g., the inert equation of state, shock, and its right edge) is sent back to the explosive along the backward characteristics. The last backward characteristic to influence the reaction zone is the one shown. Since the flow in the explosive behind the reaction zone is supersonic, this backward characteristic bounds from below the region of the inert flow that can influence the reaction zone. Thus, if the inert thickness is greater than the value indicated by the asterisk on the inert shock, then its influence on the detonation reaction zone is equivalent to that of an infinitely thick inert. For the example shown, the critical inert thickness is roughly one-half a reaction-zone length.

In addition to addressing most of the issues raised by the questions, this discussion should serve to clarify most of the important features of the explosive boundary problem. It is noteworthy that the flow considered was steady. Much remains to be done on the time-dependent boundary problem.

# APPLICATION OF WHITHAM'S SHOCK DYNAMICS THEORY TO THE PROPAGATION OF DIVERGENT DETONATION WAVES\*

B. D. Lambourn and D. C. Swift  
AWE(A), Aldermaston  
Reading RG7 4PR, UNITED KINGDOM

*To allow for multidimensional HE effects simply in hydrocodes, Whitham's Shock Dynamics theory has been developed to apply to the propagation of divergent detonation waves. Two assumptions have been made: that detonation velocity is a function only of the wavefront curvature and that there is a maximum limiting angle between the wavefront and the HE boundary. A numerical method for integrating the equations is described. Parameters for four explosives have been determined by measuring waveshapes at the end of long sticks and slabs. Features of the model, including the development of dead zones, are illustrated.*

## INTRODUCTION

The propagation of a detonation wave in any finite explosive charge is initially modified by, and eventually dominated by, the effects of the charge boundaries. Waves propagate from the boundaries into the reaction zone and change the rate of reaction, and hence the local detonation velocity. As a result, the detonation wave changes shape with time.

In fact, the natural shape of a detonation wave is curved, and more often than not the detonation wave is divergent. For example, even though a rod of explosive, such as in a cylinder test, may be initiated at one end with a plane wave lens, the detonation wave becomes a steady curved wave after it has travelled only a few charge diameters.

When a detonation wave has become curved, the shock wave propagated into an adjacent material is modified and so is the flow behind the detonation wave. Hence, the way in which adjacent materials are driven by the detonation products will be different from a model which assumes simple Chapman-Jouget theory.

Most hydrocodes used for calculating the motion of metal shells and plates driven by

explosive apply a simple programmed burn model with the detonation wave shape calculated by Huygen's construction using a constant plane wave detonation velocity. The effects of the charge boundaries are ignored. A model of a resolved reaction zone can be incorporated into a hydrocode, but the meshing of the reaction zone has to be impractically small to calculate metal driving geometries on a regular basis.

The purpose of this paper is to describe an improved Huygen's construction method for divergent detonation waves using an adaptation of Whitham's Shock Dynamics theory,<sup>1</sup> and two assumptions,

- (a) detonation velocity is a function only of curvature, and
- (b) there is a maximum limiting angle that a detonation wavefront can make with an explosive boundary, which depends on the shock properties of the material adjacent to the boundary--the higher the impedance of the boundary, the greater the maximum angle.

The detonation velocity-curvature relationship and the maximum angle are determined by experiment.

\* Copyright © Controller HMSO, London, 1989.

Assumption (a) is not sufficient on its own, e.g., a plane detonation wave would continue to propagate undisturbed by the boundaries. Assumption (b) is the equivalent of a drag on the wave at the boundary which propagates as curvature along the wavefront and, hence, slows it down.

The origin of the two assumptions can be traced back at least to Eyring et al.,<sup>2</sup> but in their theoretical treatment of two-dimensional waves, Bdzil,<sup>3</sup> and Stewart and Bdzil<sup>4</sup> have shown that both assumptions are very good approximations for charges which are large compared with the reaction zone thickness. Bdzil and Engelke<sup>5</sup> have confirmed experimentally that the boundary angle of the wave is constant for different charge diameters. Bdzil and Stewart<sup>6</sup> have also integrated Whitham's equations for two-dimensional detonation waves in a somewhat different form from that given below, deriving the  $D \propto \kappa$  relationships from various assumed reaction rates.

## WHITHAM'S SHOCK DYNAMICS

The basic assumptions in Whitham's theory of Shock Dynamics are that the wave velocity is purely a function of the geometry of the wavefront and of the rays which are orthogonal to the wavefront, and is independent of signals catching up from behind the wave. The latter assumption is particularly appropriate to diverging detonation waves for which there is a sonic, or near sonic, state near the end of the reaction zone.

The problem is to find the waveshape (and ray trajectories) as a function of time, starting with an initial wavefront shape at time  $t_0$ . For detonation waves, the objective is to define burn time in each mesh in an HE region in a hydrocode calculation; the method being to integrate Whitham's partial differential equations for Shock Dynamics using the two additional assumptions given in the introduction.

### Whitham's Partial Difference Equations

Consider the trace of the wavefronts and rays in the  $z$ - $r$  plane. In Figure 1, let ABC, DEF, GHJ be three successive wavefronts and ADG, BEH, and CFJ be three adjacent rays which are locally orthogonal to each wavefront.

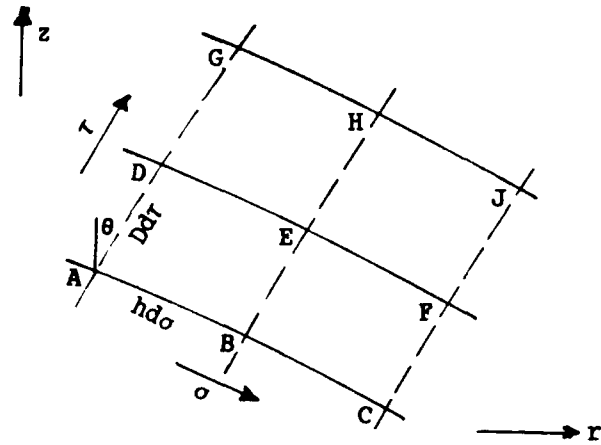


Figure 1. Wavefronts and Rays

A parameter  $\sigma$  is associated with each ray and a time  $t$  with each wavefront. Both the angle  $\theta$  that a ray makes with the  $z$  axis, and the local detonation velocity  $D$ , vary with  $\sigma$  and  $t$ .

The distance along a ray between two successive wavefronts is  $Ddt$ . The corresponding arc length between two adjacent rays along a wavefront is defined as  $hdo$ , where the ray expansion ratio  $h$  is another function of  $\sigma$  and  $t$ .

If at time zero,  $h$  is set to be 1 uniformly along the wavefront, then  $do$  is the increment of arc length  $ds_0$  along the initial wavefront. The ray parameter  $\sigma$  is like a Lagrangian coordinate propagating through  $z$ ,  $r$  space. On a ray

$$\frac{\partial z}{\partial t} = D \cos \theta; \quad \frac{\partial r}{\partial t} = D \sin \theta \quad (1)$$

so that by integration, the ray trajectories and the wavefront shapes can be determined once  $D(\sigma, t)$  and  $\theta(\sigma, t)$  have been found.

The wavefronts and rays form a set of orthogonal curvilinear coordinates, and Whitham's partial differential equations relating  $D(\sigma, t)$  and  $\theta(\sigma, t)$  are geometrical relations effectively equating two different formulae for the local curvature  $\kappa_T$  of the trace of the wavefront and the local curvature  $\rho_T$  of the trace of the rays.

If  $O$  is the center of curvature of the incremental arc  $AB$  on the trace of the wavefront (Figure 2a) and  $\kappa_T$  its local curvature, then

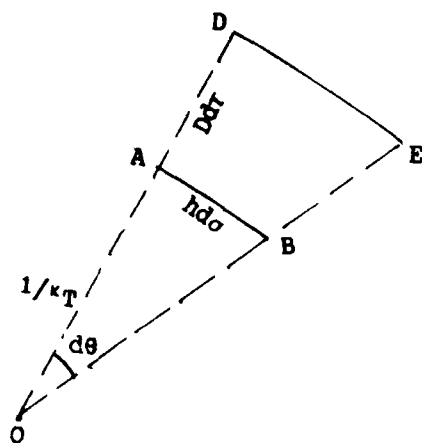


Figure 2a. Wavefront Curvature

$$AB = \frac{d\theta}{\kappa_T} = h d\sigma$$

so that

$$\kappa_T = \left( \frac{1}{h} \frac{\partial \theta}{\partial \sigma} \right)_t \quad (2)$$

In addition, by similar triangles OAB and ODE,

$$\frac{\left( h + \frac{\partial h}{\partial t} dt \right) d\sigma}{1/\kappa_T + D dt} = \frac{h d\sigma}{1/\kappa_T}$$

Hence, the alternative formula for  $\kappa_T$  is

$$\kappa_T = \left( \frac{1}{h} \frac{1}{D} \frac{\partial h}{\partial t} \right)_o = \left( \frac{1}{D} \frac{\partial \ln h}{\partial t} \right)_o \quad (3)$$

Equating (2) and (3) gives the first of Whitham's Shock Dynamics equations

$$\kappa_T = \left( \frac{1}{h} \frac{\partial \theta}{\partial \sigma} \right)_t = \left( \frac{1}{hD} \frac{\partial h}{\partial t} \right)_o \quad (4)$$

By similar arguments, using Figure 2b, if  $P$  is the center of curvature of the trace of the ray  $AD$  and  $\rho_T$  its curvature, then the second Shock Dynamics equation is

$$\rho_T = - \left( \frac{1}{D} \frac{\partial \theta}{\partial t} \right)_o = \left( \frac{1}{Dh} \frac{\partial D}{\partial \sigma} \right)_t \quad (5)$$

Equations (4) and (5) form a pair of first order partial differential equations in the independent variables  $\sigma$  and  $t$ , to which must be added boundary conditions and a

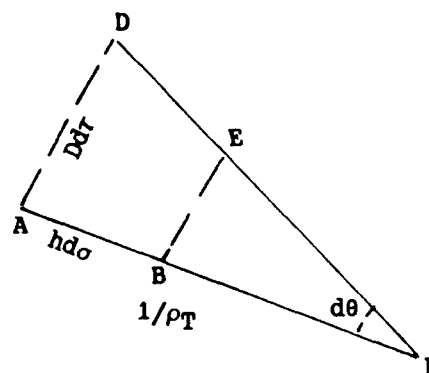


Figure 2b. Ray Curvature

relationship between two of the dependent variables  $\theta$ ,  $D$ , and  $h$ . They are applicable in plane and axisymmetric geometry and are solved by a finite difference technique to give the development of the detonation waveshape with time.

### Whitham's Analysis<sup>1</sup> for Shock Waves

The basic assumption in Whitham's analysis for shock waves of constant initial strength moving into a diverging or converging region is that the shock velocity is purely a function of the width ratio  $h$  along a 'tube' formed between adjacent rays, i.e.,

$$h = h(D)$$

where

$$h' = \frac{dh}{dD} < 0$$

Equations (4) and (5) are then hyperbolic, with analogies to the equations of one-dimensional compressible fluid flow, but with the 'wave' velocity along the wavefront given by

$$\frac{d\sigma}{dt} = \pm \left( \frac{D}{-hh'} \right)^{\frac{1}{2}}$$

The boundary condition assumed by Whitham was that the shock wavefront remained normal to the wall. He successfully used his "shock dynamics" theory to explain the diffraction of shock waves around spheres, cylinders and bends and corners in walls, and by developing the concept of "shock shocks," to

the growth of Mach Stems. All were in good agreement with experiment.

In another application, one of the authors<sup>7</sup> applied Whitham's Shock Dynamics theory to the growth of Mach Stems for interacting detonation waves by developing the  $h$ - $D$  relationship for overdriven detonation waves. Again, the results were in reasonable agreement with experiment.

### Diverging Detonation Waves

Whereas for a shock wave, the wave velocity decreases as the rays diverge, the opposite is true for a detonation wave. The detonation velocity increases as a detonation wave expands, i.e.,  $h'$  is positive. Clearly Whitham's theory cannot be applied directly. Rather it is necessary to make another assumption.

We make the assumption that detonation velocity is purely a function of the curvature of the wavefront. For plane geometry this can be written

$$\kappa_T = \kappa_T(D) \quad (6)$$

where

$$\kappa_T' = \frac{d\kappa_T}{dD} < 0$$

Equations (4), (5), and (6) now form a parabolic set. For differentiating the LHS of Equation (4) with respect to  $\sigma$  and combining with Equation (5) gives a diffusion equation for  $\theta$

$$\frac{d\theta}{dt} = - \frac{1}{\kappa_T'} \frac{1}{h} \frac{\partial}{\partial \sigma} \left( \frac{1}{h} \frac{d\theta}{d\sigma} \right) \quad (7)$$

The rate at which effects diffuse along the wavefront from the boundary of the charge is proportional to the inverse gradient  $(-\kappa_T')^{-1}$  of the detonation velocity curvature relationship. Thus, for the linear  $D$ - $\kappa$  relationship,

$$D = D_{c_j} (1 - a\kappa) \quad (8)$$

the rate of diffusion  $aD_{c_j}$  increases with the parameter  $a$ , which is proportional to reaction zone thickness

### Curvature

This paper is concerned with detonation waves in plane and axisymmetric geometries. Experimentally, detonation velocity will be related to the mean curvature for spherically diverging or axisymmetric waves.

The appropriate mean curvature to use in  $(z, r)$  geometry is

$$\kappa = \frac{1}{2} \left( \kappa_T + \frac{a \sin \theta}{r} \right) \quad (9)$$

where  $a = 0$  for plane geometry and  $a = 1$  for axisymmetric geometry.

To show this for  $a = 1$ , note that curvature  $\kappa$  of a spherical wavefront can be found from the incremental expansion  $dA$  of an element of area  $A$  on the wavefront surface for a small change  $dR$  in the radius of the sphere by

$$\kappa = \frac{1}{2} \frac{1}{A} \frac{dA}{dR} \quad (10)$$

For an axisymmetric wavefront surface an element of area is proportional to  $rR$ , where  $R$  is the radius of curvature of the trace of the wavefront. Hence, by analogy with Equation (10), noting that for an increment  $dR$  along a ray

$$\frac{dr}{dR} = \sin \theta,$$

the mean curvature of the wavefront is

$$\kappa = \frac{1}{2} \left( \frac{1}{R} + \frac{\sin \theta}{r} \right) = \frac{1}{2} \left( \frac{1}{h} \frac{d\theta}{d\sigma} + \frac{\sin \theta}{r} \right) \quad (11)$$

which is the formula given by Equation (9) with  $a = 1$ .

The effective curvature in plane geometry is found by letting  $r$  tend to infinity in Equation (9), so that the second term tends to zero. The relevant effective curvature is

$$\kappa \Big|_{a=0} = \frac{1}{2} \frac{1}{h} \frac{d\theta}{d\sigma} = \frac{1}{2} \kappa_T \quad (12)$$



## Relationship Between Detonation Velocity and Curvature

Whereas Bdzil and Stewart<sup>6</sup> deduce the detonation velocity-curvature relationship from the form of the reaction rate in the reaction zone, in this paper it is assumed that there is an experimentally determined relationship between  $D$  and  $\kappa$ , i.e.,

$$D = D(\kappa) \text{ or } \kappa = \kappa(D)$$

Examples are the linear  $D$ - $\kappa$  relation, Equation (8) and Bdzil's relation<sup>3</sup> for the variation of  $D$  with  $\kappa$  along the central axis of a rod of explosive

$$\kappa = \frac{\ell^{1+m}(1-\ell^2)}{b} \quad (13)$$

where

$$\ell = D/D_{cj} \quad (14)$$

$m$  is a parameter for the explosive and  $b$  is proportional to the 1D reaction zone thickness for the particular form of reaction rate chosen. For Equation (12), detonation failure occurs when  $d\kappa/d\ell$  is zero, i.e.

$$\ell_f^2 = \frac{1+m}{3+m}; \quad \kappa_f = \frac{2\ell_f^{1+m}}{(3+m)b} \quad (15)$$

## Boundary Conditions

A detonation wavefront can only propagate normally to a wall if the wall is rigid. Energy is lost from the reaction zone through real walls, slowing the detonation wave beside the wall.

Clearly for a steady state wave in a long rod or slab of explosive, the angles that the detonation wave make with the wall material become a constant value, which depends on the wall material. The stable angle increases with the shock impedance of the adjacent material.

For materials of mid to high impedance, Bdzil<sup>3</sup> has related the critical wall angle to the solution of the interaction of the oblique von Neumann Shock with the wall, such that there is no reflected wave into the reaction zone. For materials of low impedance and void outside the explosive, Bdzil's critical wall angle is such that the flow behind the oblique

von Neumann shock is just sonic, so that there can be a Prandtl Meyer rarefaction propagating through the reaction zone near the wall.

Following Bdzil, it is assumed that there is a limiting maximum angle  $\phi_c$  between the wavefront and the boundary where  $\phi_c$  depends on the particular combination of explosive and boundary material. Correspondingly, there is a limiting minimum angle  $\theta_c$  between the outward ray and the explosive boundary.

$$\theta_c = \pi/2 - \phi_c \quad (16)$$

Because in this paper no reaction zone model is being assumed,  $\theta_c$  will be determined experimentally, using Bdzil's theory as a guide to interpolate for other materials.

Since the rays make angle  $\theta_c$  to the boundary, it follows that a boundary cuts across lines of constant  $\sigma$ . In general, if in  $r, z$  space the boundary is defined by  $r_b(z)$  such that the angle  $\eta$  between the boundary and the  $z$  axis is given by

$$\tan \eta = \frac{dr_b}{dz} \quad (17)$$

then the boundary trajectory in  $\sigma, \tau$  space is

$$\frac{d\sigma}{d\tau} = -\frac{D}{h} \tan(\theta_0 - \eta) \quad (18)$$

where  $\theta_0 = \theta_c + \eta$  is the angle the outward ray makes with the  $z$  axis.

Further comments on the application of the boundary condition will be given in the section "Examples."

## Numerical Scheme

In order to obtain second order accuracy, a two-step technique is used to integrate Equations (4) and (5), written in finite differences form.

For convenience, it is desirable to replace  $\theta$  as a variable on the wavefront by  $\underline{y}$ , the unit normal to the front, in order to more easily cover the transition from  $\theta = -\pi$  to  $\theta = +\pi$ .

Given that  $\theta^n$  is known at one point on the wavefront, say at one end, then values at the  $(j+1)$ th mesh junction at time  $\tau^n$  can be found successively from

$$\theta_{j+1}^n = \theta_j^n + \sin^{-1}(\underline{v}_j^n \wedge \underline{v}_{j+1}^n) \quad (19)$$

All variables are assumed known at time  $t^n$ . For as near natural centering as possible, the parameters  $\sigma$ ,  $\underline{v}$ ,  $z$ , and  $r$  are defined at the mesh junctions and  $h$ ,  $\kappa$ , and  $D$  at the mid points in the meshes. The 'predictor' step evaluates parameters at time  $t^{n+\frac{1}{2}}$  using forward time differences. The "corrector" step evaluates values at  $t^{n+1}$  using central differences. The equations used for the corrector step are as follows:

$$\begin{aligned} h_{j+\frac{1}{2}}^{n+1} &= h_{j+\frac{1}{2}}^n + \delta t \tilde{h}_{j+\frac{1}{2}} \tilde{D}_{j+\frac{1}{2}} \tilde{\kappa}_{Tj+\frac{1}{2}} \\ \theta_j^{n+1} &= \theta_j^n - \frac{4\delta t}{(\tilde{h}_{j-\frac{1}{2}} + \tilde{h}_{j+\frac{1}{2}})} \left( \frac{\tilde{D}_{j+\frac{1}{2}} - \tilde{D}_{j-\frac{1}{2}}}{\sigma_{j+1} - \sigma_{j-1}} \right) \\ \kappa_{Tj+\frac{1}{2}}^{n+1} &= \frac{2}{h_{j+\frac{1}{2}}^{n+1}} \left( \frac{\theta_{j+1}^{n+1} - \theta_j^{n+1}}{\sigma_{j+1} - \sigma_j} \right) \\ r_j^{n+1} &= r_j^n + \delta t \left( \frac{(\sigma_j - \sigma_{j-1}) \tilde{D}_{j-\frac{1}{2}} + (\sigma_{j+1} - \sigma_j) \tilde{D}_{j+\frac{1}{2}}}{\sigma_{j-1} + \sigma_{j+1}} \right) \underline{v}_j \\ \kappa_{j+\frac{1}{2}}^{n+1} &= \frac{1}{2} \left[ \kappa_{Tj+\frac{1}{2}}^{n+1} + \alpha \frac{\sin \theta_j^{n+1} + \sin \theta_{j+1}^{n+1}}{r_j^{n+1} + r_{j+1}^{n+1}} \right] \\ D_{j+\frac{1}{2}}^{n+1} &= D(\kappa_{j+\frac{1}{2}}^{n+1}) \\ \underline{v}_j^{n+1} &= M(\delta \theta_j) \underline{v}_j^n \end{aligned} \quad (20)$$

where the tilde values are determined at the halftime interval in the predictor step,

$$\delta t = t^{n+1} - t^n$$

$$\delta \theta_j = \theta_j^{n+1} - \theta_j^n$$

and  $M$  is the two-dimensional rotation matrix

$$M(\delta \theta_j) = \begin{bmatrix} \cos \delta \theta_j & -\sin \delta \theta_j \\ \sin \delta \theta_j & \cos \delta \theta_j \end{bmatrix}$$

The initial condition for the integration is the initial shape of the detonation wave at its emergence from, for example, a detonator or plane wave lens.

A stability criterion is used to limit the size of the timestep  $\delta t$  according to the minimum separation  $do_{\min}$  between mesh points

$$\delta t_{\max} = f \cdot \frac{(do_{\min})^2}{-\kappa'}$$

where  $f$  is a safety factor usually taken as 0.8, and  $\kappa'$  is given by Equation (8) or (12).

Fortran programs have been written to run on both a PC (maximum number of points on a wavefront  $\sim 100$ ) and on CRAY.

## STEADY STATE WAVESHAPES IN RODS AND SLABS

There are various methods for determining the detonation velocity-curvature relationship experimentally, e.g., Aveillé et al.<sup>8</sup> have used a charge geometry called a Logosphere to measure the  $D$ - $\kappa$  relationship for three explosives. They found in each case that the relationship is linear for  $\kappa$  between 0.004 and 0.014 mm<sup>-1</sup>.

The method adopted in this paper is to analyze the steady state waveshapes in rods and slabs of explosive with various wall materials, so that the critical wavefront angle can be determined at the same time.

In this section, the theoretical steady wavefront shape is determined for the two assumed forms of  $D$ - $\kappa$  relationships, Equations (8) and (12), together with the relationship between the detonation velocity and the diameter or thickness of the rod or slab.

### Slab Geometry

Suppose that the steady wave velocity in a slab of half thickness  $r_0$  is  $D_0$ . Then, at any point on the wavefront where the angle between the ray and the  $z$  axis is  $\theta$ , the detonation velocity  $D$  of an element of the wave along the ray normal to the wavefront is given by

$$D = D_0 \cos \theta \quad (21)$$

which may also be deduced from the steady state limit of Whitham's equations.

Defining an arc length  $s$  along the wavefront, with origin at the  $z$  axis, the steady state waveshape may be found parametrically from

$$\frac{1}{2} \frac{d\theta}{ds} = \kappa(D); \quad \frac{dr}{ds} = \cos\theta; \quad \frac{dz}{ds} = -\sin\theta. \quad (22)$$

For the linear  $\kappa$ - $D$  relationship (8), the wavefront shape can be found by integration of Equations (21) and (22).

$$r = R(\theta) = \frac{a}{2\ell_0} \left| \frac{2}{\sqrt{1-\ell_0^2}} \tan^{-1} \left\{ \left( \frac{1+\ell_0}{1-\ell_0} \right)^{\frac{1}{2}} \cdot \tan \frac{\theta}{2} \right\} - \theta \right| \quad (23)$$

$$z = Z(\theta) = \frac{a}{2\ell_0} \ln \left\{ \frac{1-\ell_0 \cos\theta}{1-\ell_0} \right\} \quad (24)$$

where  $\ell_0 = D_0/D_{cj}$ .

In particular, taking the boundary condition as  $\theta = \theta_c$  at  $r = r_0$ , Equation (23) becomes an implicit equation for the variation of  $\ell_0$ , the steady wave velocity ratio, with slab half thickness  $r_0$

$$r_0 = \frac{a}{2\ell_0} \left| \frac{2}{\sqrt{1-\ell_0^2}} \tan^{-1} \left\{ \left( \frac{1+\ell_0}{1-\ell_0} \right)^{\frac{1}{2}} \cdot \tan \frac{\theta_c}{2} \right\} - \theta_c \right|. \quad (25)$$

Figure 3 shows the variation of  $\ell_0$  with  $a/r_0$  for various values of  $\theta_c$ .  $D_0$  is nearly linear with  $a/r_0$  except close to zero curvature, where, as Bdzil<sup>3</sup> showed, the slope  $dD_0/d(a/r_0)$  becomes zero. As expected,  $D_0$  varies more quickly with  $a/r_0$  for a larger  $\theta_c$ , i.e., for less confinement to the charge.

Figure 4 shows the steady state waveshapes for  $\theta_c = 0.25$ ,  $\ell_0 = 0.999$ , and  $\ell_0 = 0.8$ , both normalized to unit slab half width. For

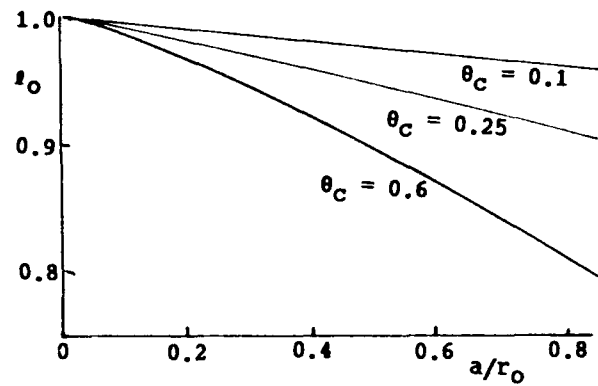


Figure 3. Variation of  $D_0$  with Charge Half Thickness  $r_0$  (Plane, Linear  $\kappa$ - $D$ )

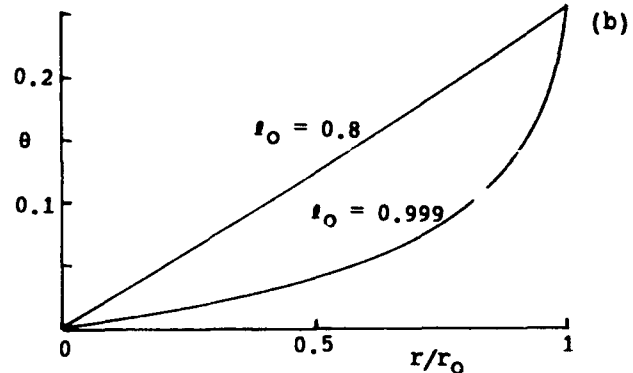
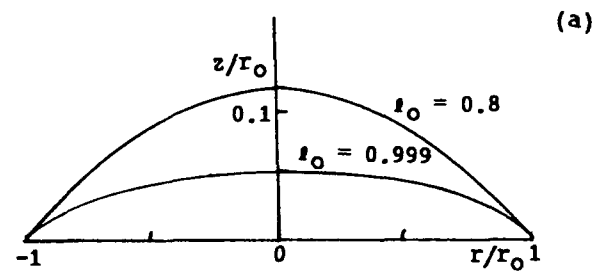


Figure 4. Waveshape, Plane Geometry ( $\theta_c = 0.25$ )

the higher detonation velocity, the curvature is concentrated at the charge edge. For the lower detonation velocity, the wavefront is almost a circular arc.

For Bdzil's central streamline curvature  $D$ - $\kappa$  relationship Equation (12), the wavefront shapes can be integrated analytically for integer values of the parameter  $m$ . For example, for  $m = 2$

$$r = \frac{b}{2\ell_0 \sqrt{1-\ell_0^2}} \left[ \tan^{-1} \left\{ \left( \frac{1+\ell_0}{1-\ell_0} \right)^{\frac{1}{2}} \tan \frac{\theta}{2} \right\} + \tan^{-1} \left\{ \left( \frac{1-\ell_0}{1+\ell_0} \right)^{\frac{1}{2}} \tan \frac{\theta}{2} \right\} \right] + \frac{b}{2\ell_0^3} \tan \theta$$

$$z = \frac{b}{2\ell_0} \left[ \ell_n \left\{ \frac{1-\ell_0^2 \cos^2 \theta}{1-\ell_0^2} \right\}^{\frac{1}{2}} - \ell_n \cos \theta \right] - \frac{b}{4\ell_0^3} (\sec^2 \theta - 1) \quad (26)$$

where the relation between charge half thickness  $r_0$  and  $D_0$  can be found by setting  $\theta = \theta_c$  into the first of Equation (26).

Figure 5 shows the variation of  $\ell_0$  with  $b/r_0$  for  $m = 0$  and 2. Failure is clearly apparent for  $\theta_c = 0.25$ ,  $m = 2$ . As Bdzil showed, the failure diameter occurs when the curvature at the edge of the charge reaches the failure criterion Equation (14), i.e., when

$$\ell_0 \cos \theta_c = \left( \frac{1+m}{3+m} \right)^{\frac{1}{2}} \quad (27)$$

For  $\theta_c = 0.25$ ,  $m = 2$ , failure occurs when  $\ell_0 = 0.778$ .

### Axisymmetric Geometry

No exact analytic solution has been found for the steady state shape of a detonation wave in a rod of explosive. However, a solution can be found using an approximation similar to that made by Bdzil.

If the wavefront is written in the form

$$z = Z(r) \quad (28)$$

$$\text{then } \frac{dZ}{dr} = Z' = \tan(\pi - \theta) = -\tan \theta \quad (29)$$

and, hence,

$$\cos \theta = \frac{1}{\sqrt{1+Z'^2}}; \sin \theta = \frac{-Z'}{\sqrt{1+Z'^2}} \quad (30)$$

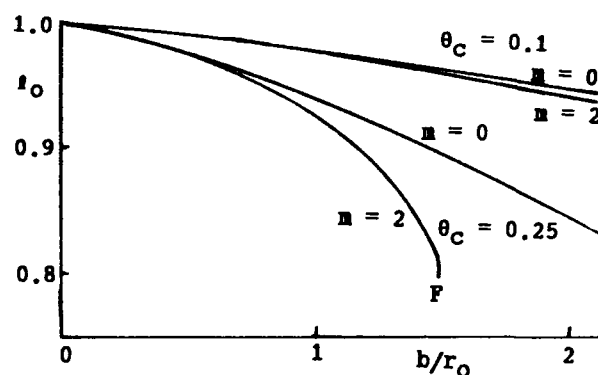


Figure 5. Variation of  $D_0$  with Charge Half Thickness (Plane, Bdzil  $\kappa$ -D)

Then using Equation (9), the differential equation for  $Z(r)$  is

$$-\frac{1}{2} \left\{ \frac{Z''}{(1+Z'^2)^{3/2}} + \frac{a}{r} \frac{Z'}{(1+Z'^2)^{1/2}} \right\} = \kappa(D) \quad (31)$$

where

$$D = D_0 \cos \theta = D_0 (1+Z'^2)^{-\frac{1}{2}} \quad (32)$$

The approximation made by Bdzil is to neglect terms  $O(Z'^3)$ . Then, for example, for the linear  $\kappa$ -D relationship, Equation (31) becomes

$$Z'' + \frac{aZ'}{r} = -\frac{2}{a}(1-\ell_0) - \frac{3-2\ell_0}{a} Z'^2 \quad (33)$$

and for Bdzil's central streamline curvature  $\kappa$ -D relationship

$$Z'' + \frac{aZ'}{r} = -\frac{2\ell_0^{1+m}}{b} \left[ 1 - \ell_0^2 + \left\{ 1 - \frac{m}{2} (1 - \ell_0^2) \right\} Z'^2 \right] \quad (34)$$

Equations (33) and (34) are both of the same form as Bdzil's equation.<sup>3</sup> If a substitution of the form

$$Z' = A c \frac{f'(cr)}{f(cr)}$$

is made, Bdzil's equation reduces to Bessel's equation for  $J_0(cr)$ .

Hence the solution to Bdzil's equation is

$$Z' = -Ac \frac{J_1(cr)}{J_0(cr)} \quad (35)$$

$$Z = A \ln \left( \frac{J_0(cr)}{J_0(cr_0)} \right) \quad (36)$$

where  $r_0$  is the charge radius.

For the linear  $\kappa$ -D relationship

$$A = \frac{a}{3-2\ell_0} ; c = \frac{\sqrt{(2(1-\ell_0)(3-2\ell_0))}}{a} \quad (37)$$

and for Bdzil's central streamline  $\kappa$ -D relationship

$$A = \frac{b}{2\ell_0^{1+m} \left\{ 1 - \frac{m}{2} (1 - \ell_0^2) \right\}} ;$$

$$c = \frac{2\ell_0^{1+m} \sqrt{(1 - \ell_0^2) \left\{ 1 - \frac{m}{2} (1 - \ell_0^2) \right\}}}{b} \quad (38)$$

In either case the variation of detonation velocity with charge radius is given by the non-linear Equation (35), with  $r = r_0$  and  $Z' = -\tan\theta_c$ , i.e.,

$$\tan\theta_c = Ac \left( \frac{J_1(cr_0)}{J_0(cr_0)} \right) \quad (39)$$

where the product  $Ac$  is purely a function of  $\ell_0$ .

Using the approximation of neglecting  $Z'^3$  in the plane case leads to the  $D - r_0$  relationship

$$\tan\theta_c = A \tan(cr_0) \quad (40)$$

and the waveshape

$$Z(r) = A \ln \left( \frac{\cos cr}{\cos cr_0} \right) \quad (41)$$

where  $A$  and  $c$  are again given by Equations (37) and (38).

Figure 6 compares the variation of  $\ell_0$  with  $a/r_0$  for  $\theta_c = 0.6$  for the linear  $\kappa$ -D relationship

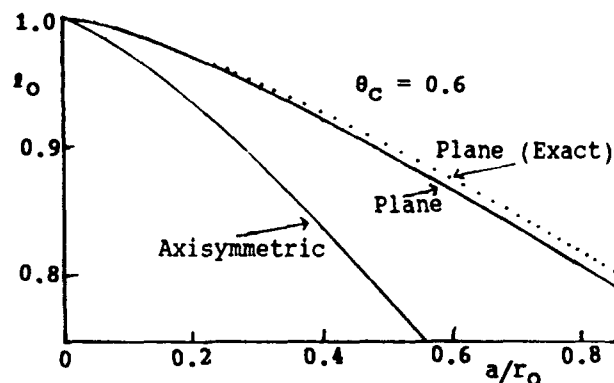


Figure 6. Variation of  $D_0$  with  $r_0$  (Plane vs. Axisymmetric, Linear  $\kappa$ -D)

in both axisymmetric and plane geometry. As observed by Bdzil,  $\ell_0$  falls off roughly twice as fast with  $a/r_0$  for the axisymmetric case as for the plane case. The dotted line in Figure 6 is the exact plane geometry solution, Equation (25), and shows that Equation (40) is quite accurate.

### Relaxation to a Stable Waveshape

In order to derive parameters for the model from the experimental waveshape at the end of rods or slabs of explosive, it is necessary to know how long the explosive must be before the waveshape has become steady. This can be determined from the new code using Whitham's method, but it is desirable to have a simple means of predicting a relaxation time. From the diffusion Equation (7) for the propagation of a detonation wave in a slab, if  $hds$  is written as arc length  $ds$ , and the linear detonation velocity-curvature relationship is used, Equation (7) becomes

$$\frac{\partial\theta}{\partial t} = \frac{aD_{cj}}{2} \frac{\partial^2\theta}{\partial s^2} \quad (42)$$

For the slab problem with  $\theta = 0$  initially, boundary conditions  $\pm\theta_c$  and assuming  $\partial s/\partial t$  is small, standard separation of variable techniques and Fourier analysis can be used to solve Equation (42), leading to terms of the form

$$A_i \exp \left\{ - \frac{aD_{cj}}{2} \left( \frac{i\pi}{d} \right)^2 t \right\} \sin \frac{i\pi s}{d}$$

where  $d$  is slab thickness. Clearly the time dependent effects decay with a time constant proportional to  $d^2/a$ , so that the larger the charge thickness, the greater the time constant.

The program outlined in the "Numerical Scheme" section can be used to determine the relaxation from different starting conditions. Figure 7 illustrates the approach of a detonation wave towards a stable shape in axisymmetric geometry for various charge diameters, for the EDC29 experiments described in the "Experimental Results" section. The ordinate is the scaled maximum "height" of the waveshape (i.e., axial  $Z$  minus edge  $Z$  value, divided by  $d$ ) as a function of scaled time ( $D_{cj}/d$ ). The 20 mm and 40 mm charges have clearly not reached a stable shape when the detonation wave has travelled six charge diameters, as used in the experiments.

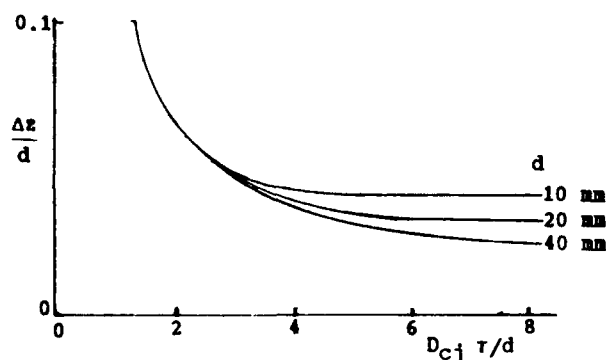


Figure 7. Relaxation of Wavefront Shape to a Steady State

## EXPERIMENTAL RESULTS

So far, experiments have concentrated on determining the basic parameters for various explosives using simple slab and rod geometries. Later, the theory will be tested in other geometries.

Experiments have been carried out on four explosives: EDC29, EDC32, EDC35, and UK Baratol (see Table 1), by G Eden, W. A. Bailey, A. M. Collyer, R. A. Belcher, and M. I. Andrew.<sup>9</sup> In some experiments, the explosive charges were bare. In others, copper, brass or PMMA walls were used. Rod charges were initiated by

either plane wave lenses or single detonators. Slab charges were initiated at the mid plane of one edge by a line initiator.

Table 1. Explosive Compositions Used

Explosive	Composition	Density
EDC29	95/5 HMX/Polyurethane	1.78
EDC32	85/15 HMX/Viton	1.87
EDC35	95/5 TATB/Kel-F	1.905
UK Baratol	70/30 TNT/Barium Nitrate	2.50

The waveshape was monitored at the end of the charges by mounting a glass block and using Eden and Wright's total internal reflection technique<sup>10</sup> to observe the waveshape with a streak camera. Detonation velocity was measured by probes along the edges of the charge.

Figure 8a shows the analysis of a typical waveshape for a bare 10 mm diameter x 60 mm long EDC29 cylinder of explosive initiated by a single detonator at one end. The estimated angle  $\theta_c$  at the edge of the charge is 0.2 radians ( $11\frac{1}{2}^\circ$ ). Assuming the waveshape is steady, the best fit to the data is also shown in Figure 8a using the parameters given in Table 2.

Experiments with 20 mm diameter x 120 mm long and 40 mm diameter x 240 mm long bare EDC29 cylinders have also been carried out. The shock dynamics calculations (Figure 7) show that the waveshapes would not have reached steady states. However, Figures 8b and 8c show that, using the parameters obtained from the 10 mm diameter experiment, acceptable fits were obtained to the experimental waveshapes, by shock dynamics calculations.

A linear  $\kappa$ -D relation has also been deduced from a best fit to the waveshapes for the other explosives.

Values of  $\theta_c$  for various combinations of explosive and wall material are given in Table 3, and are compared with theoretical estimates based on Bdzil's theory.

It is apparent that there is a fairly significant disagreement between Bdzil's theory and

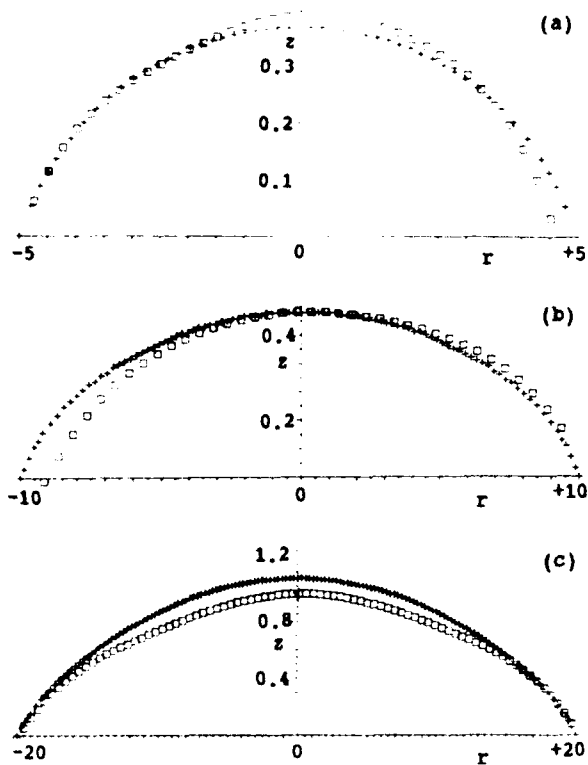


Figure 8. Comparison of Calculated (+ +) and Experimental ([]) Waveshapes for EDC29 Rods of Length  $\times$  Diameter (a) 10 mm  $\times$  60 mm, (b) 20 mm  $\times$  120 mm, and (c) 40 mm  $\times$  240 mm

Table 2. Linear  $\kappa$ -D Parameters

	$D_{c1}$ (mm/ $\mu$ s)	$a$ (mm)
EDC29	8 785	0.34
EDC32	8 475	0.30
EDC35	7 77	0.79
UK Baratol	5 06	2.27

Table 3. Comparison of Experimental and Theoretical  $\theta_c$  Values

	Wall	$\theta_c$ (expt)	$\theta_c$ (theorl)
EDC29	Air	$11\frac{1}{2}^\circ$	$34.2^\circ$
EDC32	Cu	$6^\circ$	$7.3^\circ$
EDC35	Brass	$11\frac{1}{2}^\circ$	$7.1^\circ$
UK Baratol	Air	$34^\circ$	$34.7^\circ$
	PMMA	$25\frac{1}{2}^\circ$	—
	Brass	$16^\circ$	$1.7^\circ$

experiment in most cases. Experiment suggests that  $\theta_c$  increases with the reaction zone length parameter 'a' for both air and brass, though there is some uncertainty in  $\theta_c$  for bare charges, where it is difficult to assess the edge conditions exactly.

The low theoretical value of  $\theta_c$  for UK Baratol with Brass follows because the shock velocity in brass at the von Neumann spike pressure in UK Baratol (320 kbar) is close to detonation velocity. The shock velocity in PMMA at 100 kbar is equal to detonation velocity, so there is no theoretical solution for UK Baratol with a PMMA wall. However, there is no evidence that the shock in the PMMA is running ahead of the detonation wave and dragging the point of intersection forward, as Eden and Belcher<sup>11</sup> found with EDC35 and Beryllium.

Further experiments are being carried out to test the theory and to determine wall angles for various wall materials. Some development of the theory is also clearly required.

## AN EXAMPLE

To illustrate some of the features of the model and some difficulties that have arisen, an artificial problem has been set up called the christmas tree problem. The geometry consists of a fine cone of base diameter 40 mm, and length 90 mm with a short cylindrical trunk of length 10 mm and diameter 20 mm. The edges of the trunk and cone are assumed to have critical ray angle  $\theta_c = 0.6$  radians.

The explosive has a linear detonation velocity-curvature relationship with  $D_{c1} = 8.875$  mm/ $\mu$ s and  $a = 0.5$  mm.

Figure 9a shows the development of the wavefronts from an initial hemispherical wavefront of radius 2.5 mm. Because of lagging of the wavefronts on the base of the trunk and, after diffraction, on the exposed base of the cone, breakout of the detonation would first occur on the side faces of the trunk and cone, respectively.

However, two problems are immediately obvious. Both at the intersection of the initial wavefront with the base of the trunk and at the

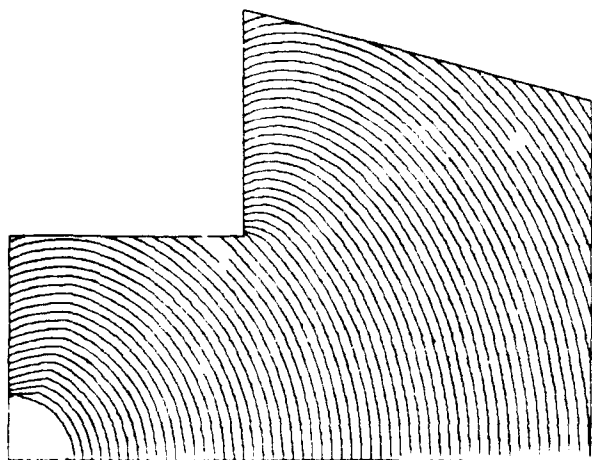


Figure 9a Wavefronts from Hemispherical Initiation ( $\kappa_F = 20 \text{ mm}^{-1}$ )

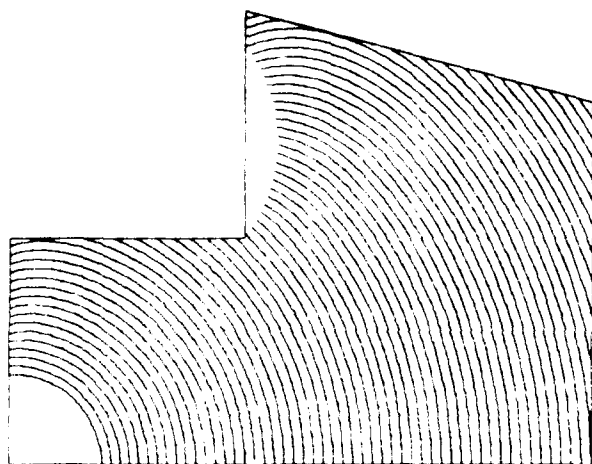


Figure 9b Wavefronts from Hemispherical Initiation ( $\kappa_F = 2 \text{ mm}^{-1}$ )

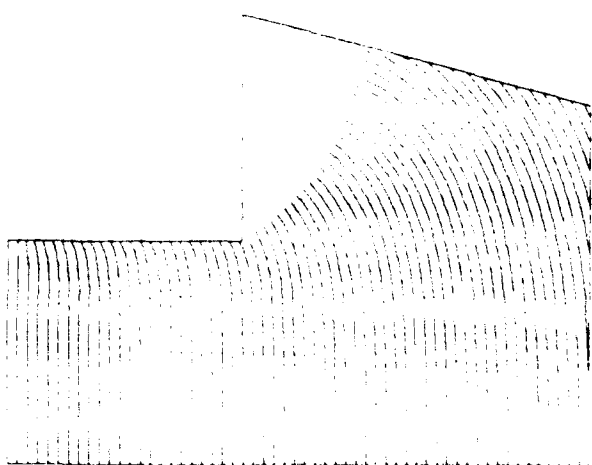


Figure 9c Wavefronts from Plane Initiation ( $\kappa_F = 2 \text{ mm}^{-1}$ )

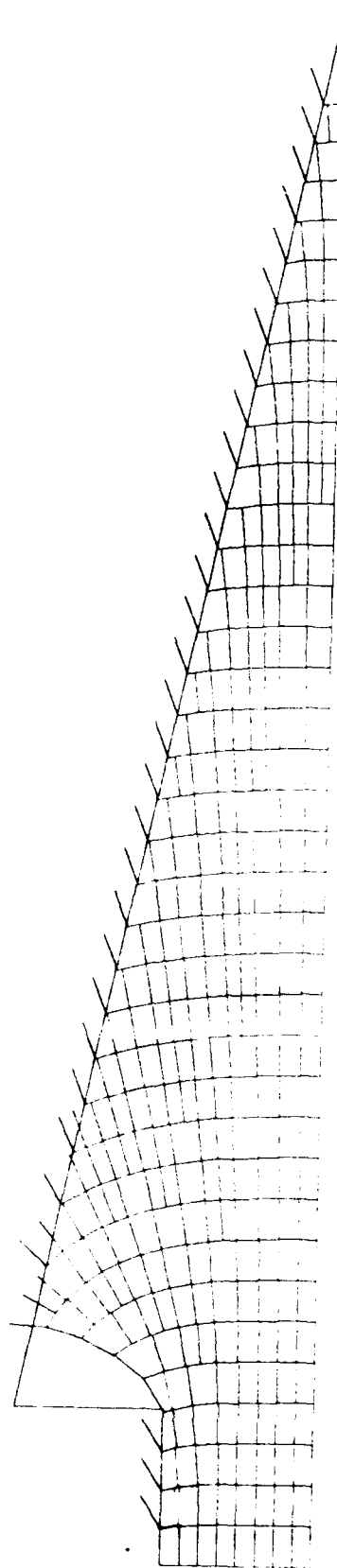


Figure 9d Wavefronts and Rays from Plane Initiation ( $\kappa_F = 2 \text{ mm}^{-1}$ )



corner turning, the normal to the wavefront is beyond the critical angle and instantaneously has to be rotated. This leads to the curvature at the wall being very large and hence the detonation velocity being very small.

Whereas detonation failure may well occur on corner turning, it should not occur when the wave starts to propagate from the initial wavefront.

Three ways of overcoming this difficulty have been considered and tried:

- (i) to relax the bounding ray angle towards  $\theta_c$  with a time constant  $T$  corresponding to a few reverberations of the reaction zone;
- (ii) to allow the bounding ray to rotate at a maximum rate  $\theta_b$ , another material constant;
- (iii) in each time step, to allow the bounding ray to rotate so that the curvature of the wavefront never exceeds the failure curvature  $\kappa_f$ .

In each case, explosive outside the bounding ray is declared to have failed to detonate.

Figure 9b shows the calculated wavefronts using the third option. The propagation of the initial wavefront up the base of the trunk now looks more plausible, and the model has predicted that detonation would fail after corner turning. The curvature of the wavefronts on the ray at the edge of the region of failure all have the failure curvature.

Figure 9c shows the same problem, but calculated with plane wave initiation of the base of the charge. Here the angle through which the wavefront has to turn at the corner is much greater, so the region of undetonated HE now extends to the conical face of the charge.

Finally, Figure 9d shows the whole cone, with detonation failing also near the tip of the cone because the diameter has become so small. Also shown are some ray trajectories. As rays move across the charge boundary, new rays are generated on the wavefront.

## CONCLUSIONS

A method of determining the time development of a divergent detonation wave shape has been described, based on Whitham's Shock

Dynamics geometrical equations, but making the simple assumptions that the detonation velocity is purely a function of the waveshape curvature, and that when the wavefront interacts with a boundary, there is a maximum limiting angle that the wavefront can make with the boundary. The Shock Dynamics equations are integrated by a 2nd order finite difference scheme.

The model requires three parameters for the  $D$ - $\kappa$  relationship, e.g., for a linear relationship the parameters are  $D_{cj}$ , the infinite charge detonation velocity;  $a$ , a length parameter proportional to reaction zone thickness; and  $\kappa_f$ , a failure curvature. These parameters are being determined experimentally by fitting the waveshapes measured at the end of long charges to theoretical steady state waveshapes determined from the basic assumptions.

The critical angles are also being determined experimentally. Experiment suggests that the limiting boundary angle increases with the reaction zone length parameter, and for a given explosive confirm that the angle increases as the impedance of the adjacent material decreases, though not agreeing in magnitude with Bdzil's theoretical estimate.

In the theory, the rays are like Lagrangian coordinates which are generated on the initial wavefront and eventually cross the HE boundary. As is illustrated in Figure 9d, the final waveshape, therefore, derives from a very short length of the initial waveshape.

The model requires slight modification when the initial wavefront angle exceeds the critical angle. By ensuring that the ray at the end of a wavefront turns only just enough to ensure that the curvature never exceeds the failure curvature, it is possible to predict 'dead-zones' -- regions of detonation failure.

The next stages of the work include building the model into a hydrocode and further experiments to calibrate the parameters and demonstrate the 'dead zones.'

## ACKNOWLEDGEMENTS

The authors gratefully acknowledge the contributions of G. Eden, W. A. Bailey, A. M. Collyer, M. I. Andrew, and R. A. Belcher for

carrying out the experiments and their analysis, and for many helpful discussions.

## REFERENCES

1. Whitham, G. B., *Linear and Non Linear Waves*, Wiley-Interscience, Ch. 8, 1974, pp. 263-311.
2. Eyring, H.; Powell, R. E.; Duffey, G. H.; and Parlin, R. B., *Chem Rev.*, 45, 1949, p. 69.
3. Bdzil, J. B., *J. Fluid Mech.*, 108, 1981, pp. 195-226.
4. Stewart, D. S. and Bdzil, J. B., *Combustion and Flame*, 72, 1988, pp. 311-323.
5. Engelke, R. and Bdzil, J. B., *Phys. Fluids*, 26, 1983, pp. 1210-1221.
6. Bdzil, J. B. and Stewart, D. S., *Sixth ARO Conference on Applied Maths*, University of Colorado, Jun 1988.
7. Lambourn, B. D. and Wright, P. W., *Fourth Symposium (International) on Detonation*, 1965, pp. 142-152.
8. Aveillé, J.; Baconin, J.; Carion, N.; and Zoé, J., *Eighth Symposium (International) on Detonation*, 1985, pp. 151-156.
9. Eden, G.; Bailey, W. A.; Collyer, A. M.; Belcher, R. A.; and Andrew, M. I., private communication.
10. Eden, G. and Wright, P. W., *Fourth Symposium (International) on Detonation*, 1965, pp. 573-583.
11. Eden, G. and Belcher, R. A., *Ninth Symposium (International) on Detonation*, 1989.

# PROPAGATION OF DETONATION WAVES FROM AN IMPACT REGION\*

R. S. Lee, W. C. Tao, and L. D. Crouch  
Lawrence Livermore National Laboratory  
Livermore, CA 94550

*We have developed an experimental system for studying the propagation of a detonation wave away from a region that is initiated by the impact of a thin flyer plate. We have studied the propagation of detonation waves away from this region in pressed pellets of TATB and in RX-26-AF, a TATB/HMX formulation. The system permits measurements at elevated, ambient, and low temperatures. We measured the distance-time trajectory and arrival time of the detonation front at the downstream face of the explosive pellets for pellets with thicknesses of 1-16 mm over the temperature range -80°C to +80°C.*

## INTRODUCTION

The function time of an initiation train is always longer than the transit time of a detonation wave traveling through the train at ideal detonation velocity. The excess transit time is an indication of the robustness of the initiation, with long excess transit times indicating marginal initiation. Excess transit time may arise from a number of causes. There may be a short run-up to detonation after the initial stimulus, detonation velocity may be lower when the wave is propagating with a small radius of curvature or at low temperature, and delays may be introduced by small gaps between charges.

One can study a detonation wave as it propagates away from an initiation region by performing cutback experiments, where the same initiation stimulus is applied to successively thinner samples and the detonation breakout time is measured across the face and

along the sides of the samples. Such experiments were done by Jackson and co-workers in initiation studies on TATB explosives<sup>1</sup> and more recently by Kleinhanss and Zöllner<sup>2,3</sup> on a number of other explosives.

The motivation for our study was to develop an experimental system which would allow us to conveniently perform cutback experiments to study propagation of detonation waves at low and elevated temperatures. Because of the lengthy thermal equilibration times required for such experiments, we developed a system which permits simultaneous measurements on three samples of different thickness. This reduces the number of shots required for a study by a factor of 2/3.

Temperature effects are most pronounced in insensitive explosives, so we chose to study two relatively insensitive explosives: TATB pressed to a density of 1.60 g/cm<sup>3</sup> and RX-26-AF (46.6/49.3/4.1% TATB/HMX/Estane) pressed to a density of 1.84 g/cm<sup>3</sup>. These two materials have roughly the same shock initiation threshold.

The experiments consisted of streak camera measurements of detonation breakout on the downstream face of explosive pellets of different thicknesses after impact by 4 mm diameter, thin flyer plates. From the streak records one can extract the distance-time curve for the

\*Work performed under the auspices of the U.S. Department of Energy by the Lawrence Livermore National Laboratory under contract number W-7405-ENG-48. Partial support was also provided by the Air Force Armament Laboratory, Fuzes and Guns Branch, under Project ATL 8 205.

detonation front, as well as the detonation front curvatures after various distances of travel. Experiments were performed over the temperature range  $+80^{\circ}\text{C}$  to  $-80^{\circ}\text{C}$ . We observed no significant temperature effects in the experiments on the pure TATB, but observed a significant temperature effect in the RX-26-AF material at low temperatures.

## EXPERIMENTAL PROCEDURE

### Explosive Sample Preparation

Samples of TATB and RX-26-AF were pressed to respective densities of  $1.60\text{ g/cm}^3$  and  $1.84\text{ g/cm}^3$ . Sample densities were approximately 83 percent of theoretical maximum density (TMD) for the TATB and 99 percent for the RX-26-AF. Sample diameters were 12.7 mm, and sample thicknesses were approximately 1, 2, 3, 4, 5, 8, 10, 13, and 16 mm.

The TATB was a grade known as "ultrafine" with an arithmetic mean particle size of about 10 micrometers and a specific surface area of about  $4.5\text{ m}^2/\text{g}$ . Thresholds for shock initiation have been measured for both materials using thin, electrically driven flyer plates. At  $1.60\text{ g/cm}^3$ , ultrafine TATB requires a flyer kinetic energy of about  $762\text{ kJ/m}^2$  at room temperature and the initiation threshold velocity is constant down to 3 mm flyer diameter.<sup>4</sup> RX-26-AF requires a flyer kinetic energy of about  $784\text{ kJ/m}^2$  at room temperature, but the initiation threshold begins to rise for flyer diameters less than 5 mm.<sup>5</sup>

### Electric Gun Laminate

The LLNL electric gun has been described at length in the literature, and we will not discuss details of operation. Briefly, a fast capacitor bank is discharged into a circuit which has a thin metal foil as its most resistive element. Energy is delivered to the foil by Joule heating faster than it can escape thermally, so the energy density and pressure build up until the foil explodes violently. If a thin plastic sheet (typically 0.02-3 mm Mylar or Kapton) is placed on top of the exploding foil, it will be driven to velocities of several km/s and the subsequent impact of the plastic sheet can produce an intense shock wave in an inert target or a prompt detonation in an explosive

target. In its larger versions we call such a device an electric gun, and in its miniaturized form it is called a slapper detonator.

We have used a 40 kV, 56  $\mu\text{F}$ , 50 nH capacitor bank to explode seven copper bridgefoils in parallel. The bridgefoils were 4 mm square and 0.033 mm thick and they drove seven, 0.127 mm thick, Kapton flyer plates down 3 mm long, 4 mm diameter barrels. The bridgefoils and flyer plate material were part of a disposable laminate that was clamped into the flat transmission line from the capacitor bank. In the experiments described here, the laminate was fired at a bank charging voltage of 25 kV, and Figure 1 shows the velocity-distance record of one of the flyer plates as determined using a Fabry-Perot laser velocimeter. The flyer plates, traveling down a 3 mm barrel, struck the explosive targets at about 5.4 km/s. The flyer kinetic energy is approximately  $2592\text{ kJ/m}^2$ , more than adequate to promptly initiate both the TATB and RX-26-AF samples.

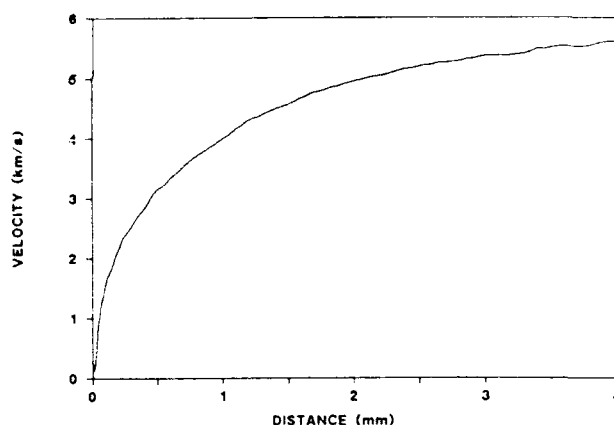


Figure 1. Velocity-Distance Curve for a Flyer Plate Fired at 25 kV

### Sample Holder and Shot Assembly

Three of the seven flyer plates thrown by the laminate were allowed to strike three high explosive pellets. The other four flyer plates struck the transparent Plexiglas sample holder on either side of the explosive pellets, and the flashes produced at impact served as impact time fiducials. Simultaneity of the flyer impacts was quite good. Over the course of 24 shots, we observed a standard deviation in

flyer impact times of about 10 ns. Impact time usually varied monotonically from one side of the sample holder to the other. The uncertainty in impact time on an explosive pellet was further reduced by taking it to be the average of the impact times on either side of the pellet. A diagram of the shot assembly is shown in Figure 2.

The temperature of the shot was controlled by placing the shot assembly in an insulated box. The temperature inside the box was monitored with a thermocouple and the desired temperature was attained by either cooling with cold nitrogen gas or by heating with heating tape. The signal from the thermocouple was fed back to a temperature controller, so the desired temperature could be maintained. A second thermocouple mounted in the center of a 2.54 cm square block of epoxy was mounted in close proximity to the shot assembly, and when the second thermocouple reached the desired temperature, the shot was fired.

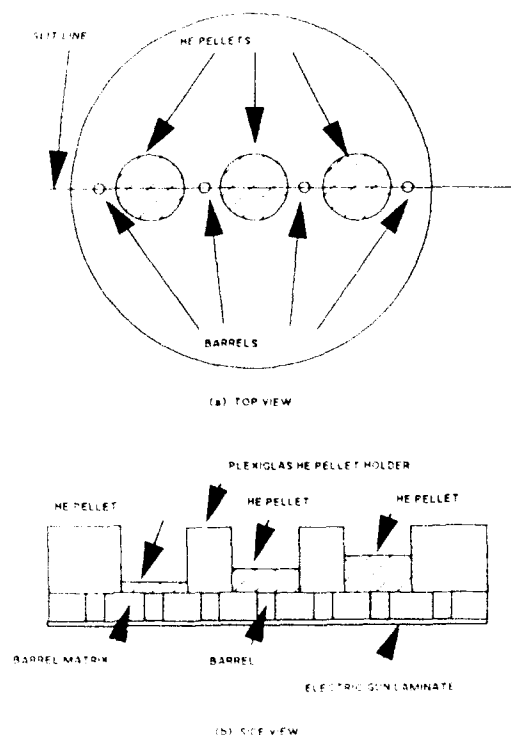


Figure 2. Sample Holder

## Data Recording and Analysis

A rotating mirror streak camera, run at a streaking rate of 15 km/s, was used to record the impact flashes and the detonation break-outs on the downstream faces of the pellets. Figure 3 shows a typical experimental record from a shot using RX-26-AF. Experimental records were analyzed by digitizing the streak records to determine the time intervals between impact and first breakout and the time variation of the detonation breakout across the face of the pellet. We estimate the digitization to be accurate to about 5 ns.

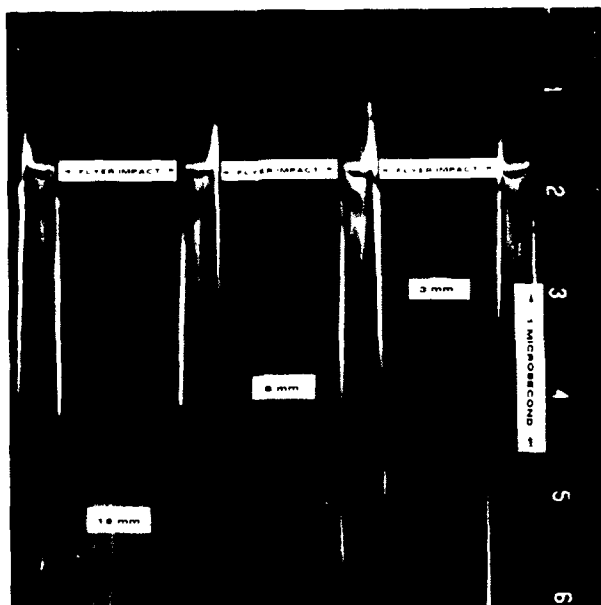


Figure 3. A Typical Experimental Record. Time is increasing downward. The four flashes at the top are flyer impacts on the plexiglas. The streak rate is 15 mm/ $\mu$ s.

## RESULTS AND DISCUSSION

### HMX Results

A preliminary experiment using the laminates and experimental procedures described above was performed on HMX pellets pressed to a density of 1.84 g/cm<sup>3</sup>. Figure 4 shows a distance-time plot for detonations traversing pellets of 3.2, 6.4, and 12.9 mm thickness. The line through the points was obtained by linear regression analysis, which gives a detonation velocity of 8.83 km/s, in excellent agreement with the published value of 8.85 km/s.<sup>6</sup>

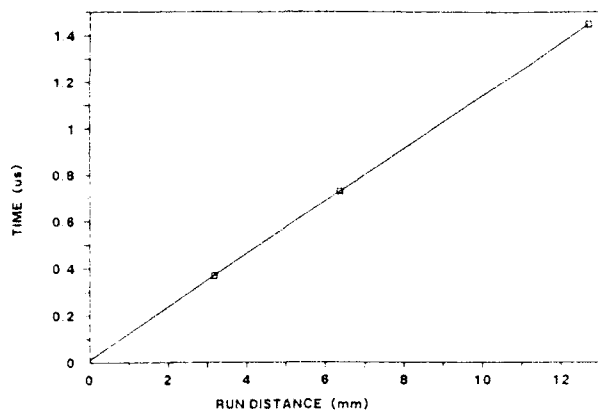


Figure 4. Detonation Front Arrival Time Versus Distance of Run for HMX Pressed to  $1.84 \text{ g/cm}^3$

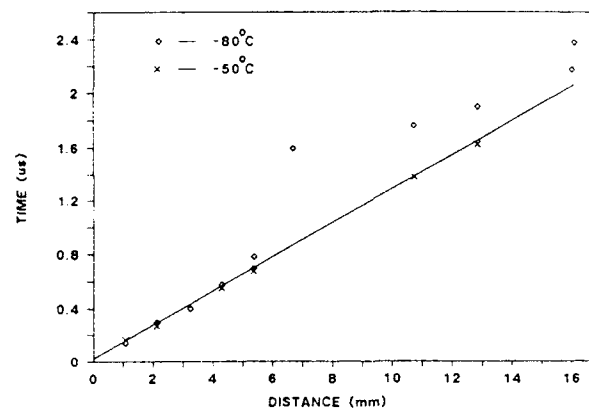


Figure 6. Detonation Front Arrival Time Versus Distance of Run for RX-26-AF Over Range  $-50$  to  $-80^\circ\text{C}$

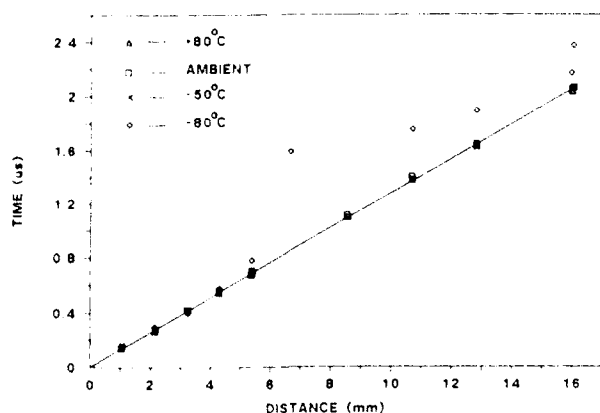


Figure 5. Detonation Front Arrival Time Versus Distance of Run for RX-26-AF Over Range  $-80$  to  $+80^\circ\text{C}$

### RX-26-AF Results

Figure 5 shows the distance-time trajectory for the detonation front induced in the RX-26-AF pellets by the impact of the 4 mm diameter flyer plates. The room temperature data and the data obtained at  $+80$  and  $-50^\circ\text{C}$  all fall on the same regression line, corresponding to a detonation velocity of  $7.80 \text{ km/s}$ . The data obtained at  $-80^\circ\text{C}$  also fall on this line out to about 5 mm of run, but then depart significantly from the other data. The room temperature detonation velocity obtained in these experiments is about 6 percent below the detonation velocity for RX-26-AF measured in a number of cylinder tests.<sup>7</sup> Figure 6 shows in more detail the departure of the  $-80^\circ\text{C}$  data from the data obtained at  $-50^\circ\text{C}$ .

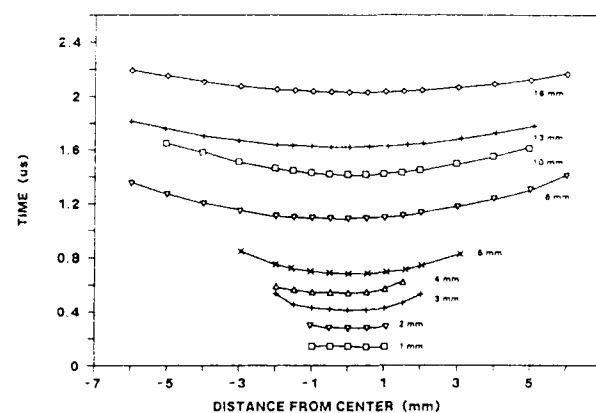


Figure 7. Arrival Time of Detonation Front at Downstream Surface of RX-26-AF Pellets

When we started the study, we expected to be able to relate the curvature of the detonation front to the detonation velocity as the detonation wave progressed through the explosive samples. Figure 7 shows the arrival time of the detonation front at the downstream surface of RX-26-AF pellets of thickness 1, 2, 3, 4, 5, 8, 11, 13, and 16 mm thickness, as determined in room temperature measurements. One can estimate, at a given distance from the axis, how the arrival time of the detonation wave varies with distance along the axis. By interpolation, one can then reconstruct the detonation wave at the time it just reached the downstream face of the various pellets. The results are shown in Figure 8. There is no discernible variation in front curvature near

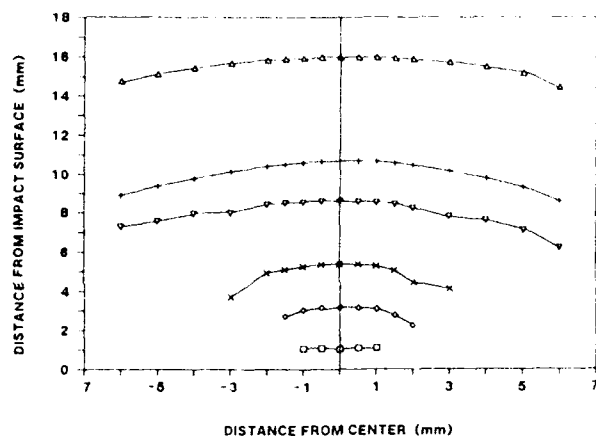


Figure 8. Detonation Front Reconstructions in RX-26-AF

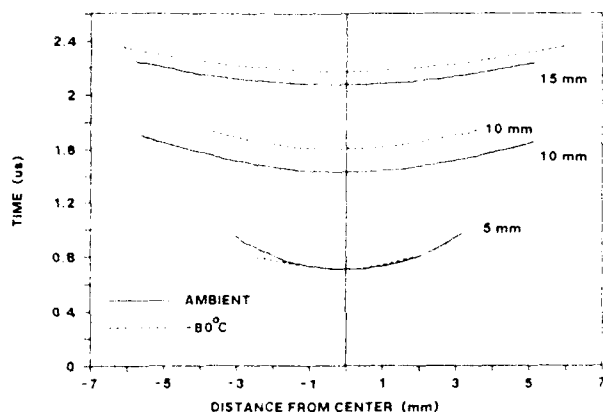


Figure 9. Wavefront Arrival Times in RX-26-AF at Ambient and -80°C

the axis, consistent with our observation of constant detonation velocity.

More surprisingly, we observed no difference in curvature near the axis between the room temperature and -80° data, even though the detonation front had slowed significantly. This is seen in Figure 9 where wavefront arrival times at 5, 10, and 16 mm are compared at ambient temperature and at -80°C.

#### TATB Results

Figure 10 shows the distance-time curve for the detonation induced in the TATB pellets by the impact of the 4 mm diameter flyer plates. We observed no change in the trajectory of the detonation front with temperature.

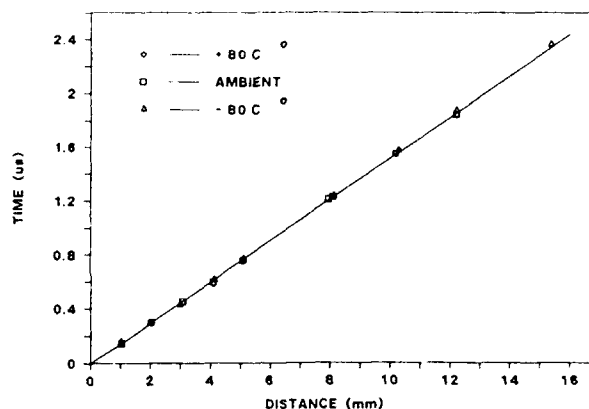


Figure 10. Detonation Front Arrival Time Versus Distance of Run for TATB Over the Range -80 to +80°C

The data taken at +80°C and -80°C all fall very close to the room temperature regression line, giving a detonation velocity of 6.50 km/s. The measured detonation velocity is only about 2% lower than the value of 6.65 km/s obtained using the density-velocity relationship listed in the LLNL High Explosives Handbook.<sup>8</sup> Within the uncertainties in the density-velocity formula, this is quite a reasonable agreement.

#### DISCUSSION

The experimental system proved to be very useful in studying the initial propagation of a detonation wave. We demonstrated that detonation velocity measurements could be made with good accuracy and acceleration or deceleration of the detonation wave can be easily observed. The ability to detonate three pellets at once proved to be a great advantage. One of the disadvantages of cutback experiments is the large number of shots which must be fired, and our experimental system greatly reduced the cost and the time for performing the experiments.

The temperature effect we observed in RX-26-AF at 20° was very interesting. The detonation wave at -80° appeared to be marginal, rather than clearly dying, because it did diverge in the thicker pellets and appears to be speeding up as well. It is very close to going out, however, because one of the shots with an

8 mm pellet failed to detonate at  $-80^{\circ}\text{C}$ . It has been recognized for some time that the critical initiation diameter, below which the initiation threshold begins to rise, depends on temperature, but the data of Figure 6 give insight into the mechanism by which temperature affects detonation wave propagation. The abrupt slowing down of the detonation wave after a run of 4-5 mm must clearly be due to the arrival of lateral rarefaction waves on the charge axis.

Most of the current high explosive burn models postulate a two-stage, reaction and growth model, where the first stage is dominated by the formation of hot, reacting regions formed during the passage of the shock front and the second stage involves the burning and subsequent coalescence of the hot regions. Arrival of lateral rarefactions would affect the growth stage of the reaction through the pressure dependence of the reaction rate, but one would expect this effect to be relatively independent of the initial temperature. There are mechanisms, however, which could give the initiation of the reaction a significant temperature dependence.

At low temperatures, one would expect the critical size, below which a hot spot cannot grow, to be larger due to greater thermal losses to surrounding material. Thus, fewer viable hot spots would be produced at low temperature. The cooling produced by the arrival of lateral rarefaction waves will reduce even further the number of hot spots capable of growth. To sustain the reaction, the hot spots produced by the passage of the shock front must be able to grow to a sufficient size before the arrival of the lateral rarefactions.

The low detonation velocity observed for the RX-26-AF is also interesting. It suggests that the detonation wave we are observing has not yet reached its steady state. Nutt and Erickson<sup>9</sup> observed a two stage reaction in RX-26-AF and suggested that the latter stage might be associated with the slower reaction of the TATB component. Incomplete reaction of the TATB could account for the low detonation velocity observed in our experiments. It would be interesting to formulate some RX-26-AF with ultrafine or crash-precipitated TATB to see if a smaller TATB particle size would bring

the detonation velocity up to a value consistent with the cylinder test data.

No temperature effect was observed in the TATB, even though TATB is known to be a very insensitive material. With its lower density and small mean particle size, a very large number of hot spots is produced in the TATB by the passage of the shock front. If the number of hot spots is sufficiently large, the quantity of material reacted before the arrival of the lateral rarefactions is sufficient to sustain the detonation.

In contrast, the RX-26-AF is pressed to near maximum density and while the HMX may react faster than TATB, the number of hot spots is marginal for producing a diverging detonation at low temperature. The arithmetic mean particle size of both the HMX and TATB in the RX-26-AF is about 40 micrometers, considerably larger than for the ultrafine TATB. One might expect that RX-26-AF formulated with ultrafine or crash-precipitated TATB would show less temperature dependence.

## SUMMARY AND CONCLUSIONS

We have described an experimental system for studying the initial stages of propagation of a detonation wave at various temperatures. The initial stages of detonation propagation are of great importance in the performance of detonators and boosters, and it seems clear that there is much to learn from studying the first few millimeters of run.

We observed no temperature effect in TATB at a density of  $1.6\text{ g/cm}^3$  over the temperature range  $-80$  to  $+80^{\circ}\text{C}$ . We observed a significant slowing down of the detonation wave in RX-26-AF after 5 mm of run at  $-80^{\circ}\text{C}$ . We attribute the slowing down of the wave to quenching of hot spots due to greater thermal losses at low temperatures. We attribute the lack of a temperature effect in the TATB to a much greater density of hot spots due to its lower density and fine particle size.

We also observed a detonation velocity in RX-26-AF that was lower than the steady state velocity observed in large charges, while the measured detonation velocity in pure HMX and TATB agreed with published values at the



appropriate density. The low value observed in the RX-26-AF may be due to incomplete reaction of the TATB.

We expected to see changes in detonation velocity reflected in changes in detonation front curvature, but did not observe such an effect. Curvatures of detonation fronts at ambient and cold temperatures appeared to be the same, even though the velocities were significantly different.

The results we report here suggest many possibilities for future investigation. Important experimental parameters which can be varied include density and particle size distribution in the explosive samples, diameter and thickness of the flyer plate, impact velocity of the flyer plate, and the temperature range.

It would be extremely interesting, for example, to perform experiments on ultrafine TATB to see if a slowing down of the detonation front at  $-80^{\circ}$  is observed at some higher density. It would also be interesting to vary the particle size while holding the density constant, to investigate the role of hot spot size in temperature effects.

The dependence of detonation velocity on density is interesting in its own right, and although the detonations we are studying probably do not represent steady detonation states, it might be possible to observe changes in detonation velocity with density that are predicted by postulated carbon coagulation in the reaction zone.<sup>6</sup>

Detonation velocity measurements where the explosive density is varied can be done quickly and require small amounts of material. The technique could possibly be used for preliminary evaluation of the equation of state of new materials, where only a small amount of explosive is available.

Another interesting line of investigation would be to reduce the flyer plate diameter and see if an analogous effect is observed at room temperature in RX-26-AF as was observed at low temperature with larger flyer plates.

## ACKNOWLEDGEMENTS

It is a pleasure to acknowledge the assistance of Henry Chau for his velocimeter

measurements, the work of George Elliott for fabricating the early laminate designs, and the work of Herb Massey for firing some of the early shots.

## DISCLAIMER

This document was prepared as an account of work sponsored by an agency of the United States Government. Neither the United States Government nor the University of California nor any of their employees, makes any warranty, express or implied, or assumes any legal liability or responsibility for the accuracy, completeness or usefulness of any information, apparatus, product, or process disclosed, or represents that its use would not infringe privately owned rights. Reference herein to any specific commercial products, process, or service by trade name, trademark, manufacturer, or otherwise, does not necessarily constitute or imply its endorsement, recommendation, or favoring by the United States Government or the University of California. The views and opinions of authors expressed herein do not necessarily state or reflect those of the United States Government thereof, and shall not be used for advertising or product endorsement purposes.

## REFERENCES

1. Jackson, R. K.; Green, L. G.; Barlett, R. H.; Hofer, W. W.; Kramer, P. E.; Lee, R. S.; Nidick, E. J., Jr.; Shaw, L. L.; and Weingart, R. C., "Initiation and Detonation Characteristics of TATB," *Proceedings of the Sixth Symposium (International) on Detonation*, Office of Naval Research, ACR-221, 1976.
2. Kleinhanss, H. R. and Zöllner, H., "The Role of Impact Area by the Initiation of High Explosives with Flyer Plates," *Proceedings of the International Symposium on Pyrotechnics and Explosives*, Beijing, China, 1987.
3. Kleinhanss, H. R. and Zöllner, H., "Experimentelle Untersuchungen zur Detonationsentwicklung bei Initiierung mit Elektrisch Beschleunigten Folien," *13th International Annual Conference of ICT*, Fraunhofer-Institut, Karlsruhe, Federal Republic of Germany, 1988.

4. Lee, R.; Bloom, G.; Von Holle, W.; Weingart, R.; Erickson, L.; Sanders, S.; Slettevold, C.; and McGuire, R., "The Relationship Between the Shock Sensitivity and the Solid Pore Sizes of TATB Powders Pressed to Various Densities," *Proceedings of the Sixth Symposium (International) on Detonation*, Naval Surface Weapons Center, NSWC MP 86-194, White Oak, Silver Spring, MD, 1985.
5. Weingart, R. C., LLNL, private communication.
6. Steinberg, D. J., "Comparison of Experimental Data on Detonation Velocity and Chapman-Jouget Pressure vs Initial HE Density with Predictions from Ree's Model Equation of State," *Proceedings of the Sixth Symposium (International) on Detonation*, Naval Surface Weapons Center, NSWC MP 86-194, White Oak, Silver Spring, MD, 1985.
7. Green, L., LLNL, private communication.
8. Dobratz, B. M., *LLNL Explosives Handbook*, UCRL 52997, Lawrence Livermore National Laboratory, 1981.
9. Nutt, G. M. and Erickson, L. M., "Reactive Flow Analysis in RX-26-AF," *Shock Waves in Condensed Matter - 1983*, Asay, J. R.; Graham, R. A.; and Straub, G. K., Eds., North Holland, 1983.

### DISCUSSION

**J. BOILEAU, SNPE**  
Paris, France

What is the glass transition temperature of Estane (probably not far from  $-30^{\circ}\text{C}$ )? I suggest to do the same experiments at  $-80^{\circ}\text{C}$ , but with the same proportion of:

1. HTPB polyurethane with  $T_g < -80^{\circ}\text{C}$
2. Polysiloxane with  $T_g < -80^{\circ}\text{C}$

They have a different Urizar coefficient.

See de Longueville et al., *Seventh Detonation Symposium*, Annapolis, 1981; C. Gaudirs or Roche, Int. Symposium, Karlsruhe in 1980 (?)

### REPLY BY R. S. LEE, W. C. TAO, AND L. D. CROUCH

The glass transition temperature of Estane is  $-31^{\circ}\text{C}$ , as you estimated. I strongly agree with your suggestion that it would be interesting to investigate binder systems with lower glass transition temperatures.

### DISCUSSION

**J. C. FOSTER, JR., Air Force**  
**Armament Lab., Eglin AFB, Florida**

How do you account for the relief from downstream end of specimen in cut back experimental approach? This effect would appear to be most pronounced for the lower end of L/D specimens; i.e., the 3 mm long specimens in the data presented.

### REPLY BY R. S. LEE, W. C. TAO, AND L. D. CROUCH

If the sample thickness were less than the run to detonation, relief from the downstream end of the samples would have a big effect on the experimental results. In our experiments, however, the run to detonation is very short, probably the order of the thickness of the flyer plate. Under these conditions, it is not necessary to worry about relief from the downstream face.

# DETONATION WAVE PROPAGATION IN PBXW-115

J. W. Forbes, E. R. Lemar, and R. N. Baker  
Naval Surface Warfare Center  
10901 New Hampshire Avenue  
Silver Spring, Maryland 20903-5000

*This study was undertaken to develop a data base on PBXW-115 and to improve our understanding of its sensitivity and performance. A high speed streak camera was used to measure detonation velocity, failure diameter, wave front curvature, effects of confinement on wave propagation and wave front curvature, and corner turning ability of PBXW-115.*

## INTRODUCTION

PBXW-115 is a cast cured explosive with a nominal composition of 20 percent cyclotrimethylene trinitramine (RDX), 43 percent ammonium perchlorate (AP), 25 percent aluminum (Al) and 12 percent hydroxy terminated binder (HTPB). Its composition is similar to that of some propellants<sup>1,2</sup> except that it contains RDX instead of cyclotetramethylene tetranitrimine (HMX). PBXW-115 cylinders are found to have failure diameters of a few centimeters and curved wave fronts. PBXW-115 generates a large amount of gas within the reaction products. This contributes to its usefulness as an underwater explosive. In order to avoid batch to batch differences in composition, all the charges used in detonation velocity, failure diameter and wave curvature tests were cast at the same time. The charges used in the corner turning experiments were cast a few months later.

The detonation velocity and wave front curvature data were used to calculate reaction zone lengths from the Wood-Kirkwood theory.<sup>3</sup> The calculated reaction zone lengths are a few millimeters and are consistent with previously published calculations on ammonium perchlorate<sup>4</sup> and two plastic-bonded 2,4,6-trinitro-1,3,5-benzene-triamine (TATB) explosives.<sup>5,6</sup>

## DETONATION VELOCITY OF UNCONFINED CHARGES

Three lighting methods commonly used in experiments to observe the detonation wave on a single cylindrical explosive charge are depicted in Figure 1.

In the first lighting method, a line is scribed on the surface of the plane wave booster (PWB) and then covered with clear tape, creating an air gap. When the detonation wave strikes this gap, the shocked air in the gap flashes. The advantage of this method is that no external light source is needed. However, this method was not suitable for use with PBXW-115. It was found that the detonation wave in PBXW-115 was not strong enough to produce adequate light to be recorded by a rotating mirror streak camera.

In the second lighting method, a piece of aluminized mylar is glued to the surface of the charge. The light from an exploding wire<sup>7</sup> is specularly reflected off the mylar and into the streak camera. This method requires precise alignment of light source, specularly reflective surface and camera. When the detonation wave strikes the mylar, the aluminized surface becomes less reflective and the alignment is destroyed, resulting in a tremendous decrease in the amount of light reaching the film.

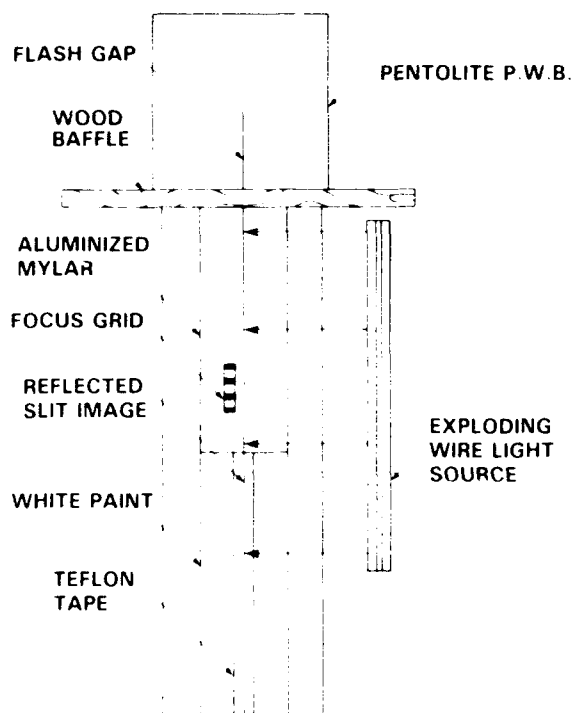


*Figure 1. Schematic of Detonation Velocity Experiment Testing Three Different Lighting Methods*

In the third lighting method, developed by A. R. Clairmont of NSWC, a piece of diffusely reflecting teflon tape is glued to the white painted surface of the charge. The background white paint increased the initial reflectivity of the surface. The reflectivity of the teflon tape greatly decreases when the detonation wave strikes it. An exploding wire is used as the light source in this method, but it does not have to be precisely aligned. It is worth noting that this third technique can easily be used to observe a shock wave arriving on a curved surface.

Figure 2 shows a streak camera record of the experiment testing the three lighting techniques depicted in Figure 1. This record shows that the flash gap technique works on the PWB and that both the reflective mylar and diffuse reflector techniques give adequate records. However, the diffuse reflector technique using teflon tape produces the clearest and easiest to read record. Therefore, this diffuse reflector technique was used to measure the detonation velocities of the unconfined charges.

The unconfined charges were 153 mm long and, except for two described later, were



*Figure 2. Streak Camera Film Record of Experiment 5*

boosted by 50.8 mm diameter by 50.8 mm long pentolite (1.56 g/cm<sup>3</sup>) PWB's. It should be noted that a wood baffle was placed at the end of the PWB to keep its detonation products from obscuring the camera's view of the test charge.

Pentolite PWB's, wood baffles, and light reflectors (behind the exploding wire light source) were used on all streak camera shots discussed in this paper, although they are not shown in all figures.

Two experiments were conducted to ensure that boosting of the PBXW-115 charges was adequate. These experiments were performed because unreacted AP, RDX and aluminum were found in the test chamber following earlier experiments. It was speculated that boosting provided by a pentolite PWB allowed a long run distance to detonation in PBXW-115, resulting in the unburned AP, RDX and aluminum. In the first experiment, a 49.7 mm diameter charge was boosted by a pentolite PWB with an additional 50.8 mm diameter by 25.4 mm long pentolite pellet. This increased the shock pulse width (impulse time) from the booster but kept the peak pressure the same. In the second experiment, a 49.6 mm diameter charge was boosted by a pentolite PWB and a 50.8 mm diameter by 12.7 mm long Comp B-3 pellet with a density of 1.71 g/cm<sup>3</sup>. This increased both impulse time and peak pressure over that of a pentolite PWB. The booster system with longer impulse time did not affect the detonation velocity. However, the booster with longer impulse time and larger peak pressure increased the detonation velocity by about

2 percent. This small increase in velocity was near experimental uncertainty and, therefore, did not warrant further investigation of the booster system. Boosting by all systems was interpreted as adequate for PBXW-115.

None of the booster system caused all of the AP, RDX, and aluminum to react. Small amounts of explosive were recovered in the debris from all unconfined experiments. Chemical analyses were performed by E. Kayser of NSWC on the debris of four experiments. The results of the analyses are presented in Table 1. Small amounts of AP, RDX and aluminum were found in these chemical analyses. It should be noted that a few micron thick cylindrical outer ring of any charge will not detonate due to the relief wave originating at that surface. However, it is an unusual experience to discover the steel-walled test chamber coated with unreacted explosive powder following detonation of a charge. Since this occurred with PBXW-115, it appears that explosives with large wave front curvatures and long reaction zone lengths allow a small (tenths of a mm thick) ring of explosive at the surface to go unreacted.

## DISCUSSION OF DETONATION VELOCITY RESULTS FOR UNCONFINED CHARGES

Detonation velocities were measured for 153 mm long unconfined charges with diameters ranging from 35.5 to 69.1 mm. It was found that the booster system needs to be at least as large as the test charge or the streak record appears very curved near the booster as occurred for the 69.1 mm diameter charge. The detonation wave velocities near the non-booster ends of the charges (the last 30-40 mm) were steady within the measurement error of  $\pm 1.5$  percent. These results are presented in Table 2. The detonation velocity data was least squares fitted to a function of the form

$$D = D^{\circ} * (1 - A/d) \quad (1)$$

where  $D$  is the detonation velocity in mm/ $\mu$ s, and  $d$  is the charge diameter in mm.  $D^{\circ}$  and  $A$  are parameters whose values 6.195 mm/ $\mu$ s and 6.870 mm, respectively, were determined by the fit. The data and fit are presented in Figure 3.

Table 1. Recovered Explosive After Detonation of PBXW-115

SHOT NO	CHARGE			RECOVERED MATERIAL*				CALC **
	LENGTH (mm)	DIA (mm)	WT (g)	AP (g)	RDX (g)	AL (g)	THICK (mm)	
1	152	50.4	542	2.09	0.03	0.03	PRESENT	0.1
2	153	50.3	542	4.17	0.03	0.03	PRESENT	0.2
5	152	50.8	529	12.53	1.3	1.2	NOT FOUND	0.7
7	152	50.8	529	14.60	0.6	0.6	PRESENT	0.8

\*AP PRESENCE DETERMINED BY ION CHROMATOGRAPHY. RDX PRESENCE DETERMINED BY HIGH PERFORMANCE LIQUID CHROMATOGRAPHY. AL PRESENCE DETERMINED BY REACTION WITH HYDROGEN CHLORIDE

\*\* ASSUMED A TUBE OF UNREACTED HE AT OUTER DIAMETER OF CHARGE

Table 2. Detonation Velocity of Unconfined PBXW-115 as a Function of Diameter

EXPERIMENT NO.	DENSITY (g/cm <sup>3</sup> )	CHARGE DIAMETER (mm)	DETONATION VELOCITY (mm/ $\mu$ s)
3	1.788	69.1	5.540
4	1.790	49.9	5.315
5	1.791	49.7	5.331
6	1.792	49.6	5.365
7	1.796	49.6	5.421
8	(1.790)**	44.5	5.228
9	1.794	41.1	5.190
10	-	38.7	5.036
11	1.786	35.5	FAILED

\*ALL CHARGES WERE 153 mm IN LENGTH

\*\* THIS VALUE IS LESS CERTAIN THAN THE OTHERS

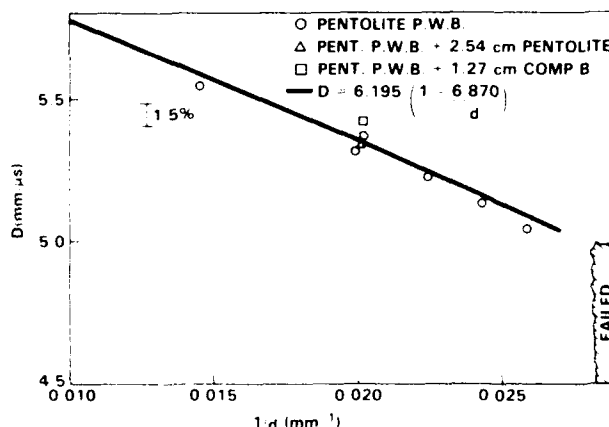


Figure 3. Detonation Velocity of an Unconfined Cylindrical Charge as a Function of Reciprocal Diameter

A failure diameter of  $37.1 \pm 1.6$  mm was measured for unconfined PBXW-115. The failure diameter was determined from the data in Table 2 by taking the diameter midway between the largest diameter charge to fail and the smallest diameter charge to detonate. This critical diameter is large compared to explosives such as cast Comp B5 (4.3 mm) but comparable to AP composites<sup>8</sup> such as PBXN-103 (27-29 mm) and PBXN-105 (60-90 mm).

## FAILURE DIAMETER OF CONFINED CHARGES

Experiments were performed to determine the effect of confinement on the failure diameter. Each combination of charge diameter and confinement was tested twice to ensure accurate results. In this work 303 mm long cylindrical charges were boosted by 50.8 mm diameter pentolite PWB's. The PBXW-115 charges were machined to slip fit into brass tubes with either 2.5 mm or 5 mm thick walls. A streak camera was used to measure shock velocity along the last 150 mm of the brass tube by recording reflected diffuse light from a strip of teflon tape attached to the brass tube as depicted in Figure 4. This lighting technique was described earlier. Since the brass cases were thin, it was assumed that shock waves in the brass were attached to the detonation wave in the explosive and traveling at the detonation velocity.

These charges were made 303 mm long to ensure that nearly steady wave propagation conditions could exist. This length should allow detection of a marginally detonating charge by giving the detonation wave enough run distance to fail. Incomplete consumption of the charge, observation of decaying wave velocity and lack of deformation of the brass tube near the far end of the charge were used to determine if the wave failed.

## DISCUSSION OF FAILURE DIAMETER RESULTS FOR CONFINED CHARGES

The results from the experiments on confined 303 mm long charges are presented in Table 3. For charges confined by brass tubes

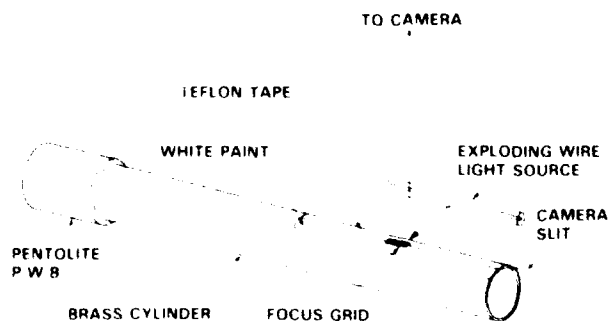


Figure 4. Detonation Velocity Test Schematic of a Brass Confined Cylindrical Charge

Table 3. The Effect of Brass Confinement on PBXW-115's Failure Diameter

EXPERIMENT NO	BRASS THICKNESS (mm)	CHARGE DIAMETER (mm)	DETONATION VELOCITY (mm/ $\mu$ s)
12	2.5	25.4	5.12
13	2.5	25.4	5.13
14	2.5	22.2	5.06
15	2.5	22.2	5.14
16	2.5	19.0	FAILED
17	2.5	19.0	FAILED
18	5.1	25.4	5.12
19	5.0	25.4	4.96**
20	5.1	19.0	4.86
21	5.0	19.1	4.84
22	5.0	15.8	FAILED
23	5.0	15.9	FAILED

\*ALL CHARGES WERE 303 mm IN LENGTH

\*\*THIS VELOCITY IS OVER RANGE OF 183 mm  $\times$   $\gamma$  251 mm THE VELOCITY SLOWED TO 4.796 mm/ $\mu$ s OVER LAST 47 mm OF CHARGE

with 2.5 mm thick walls, 25.4 and 22.2 mm diameter charges detonated while the 19 mm diameter charges failed. For charges confined by brass tubes with 5 mm thick walls, 25.4 and 19.0 mm diameter charges detonated while the 15.8 mm diameter charges failed. The failure diameter for 5 mm thick brass confined charges is about one half that of the unconfined failure diameter. Since the difference between the failure diameters of 2.5 and 5 mm brass confined charges was small, only slightly smaller failure diameters would be obtained if brass confinement greater than 5 mm thickness was used.

## DETONATION WAVE ARRIVAL AT END OF CHARGE

A streak camera was used to record the detonation wave arrival at the ends of confined and unconfined cylindrical PBXW-115 charges. The experimental setup used to obtain this breakout data is shown in Figure 5. Aluminized mylar was affixed to the end of the charge. The camera and exploding wire light source were aligned such that, when the shock arrived at the foil, the alignment would be destroyed reducing the amount of light reaching the film.

Streak camera breakout records were obtained on three different 305 mm long unconfined charges with diameters of 41, 48 and 68 mm. These streak camera film records show that the detonation wave arrives at the center about 1  $\mu$ s before arriving at the edges. These results clearly show that the detonation

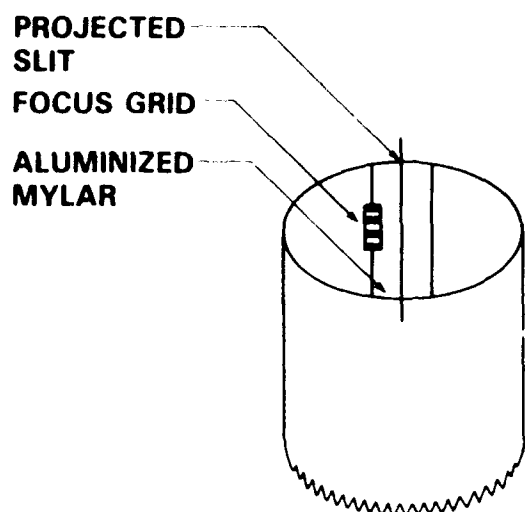


Figure 5. Schematic of Detonation Wave Breakout Experiment

waves have very curved fronts. As would be expected, the larger diameter charges have less wave front curvature than the smaller diameter charges.

Breakout experiments were also conducted on 305 mm long brass confined charges with diameters of 68 and 48 mm. For the 48 mm diameter charge, brass confinement of a 17 mm thick wall did reduce the wave front curvature. For the 68 mm diameter charge, brass confinement of 7 mm thickness had no effect on the wave front curvature relative to the unconfined charge's wave front curvature.

## DETONATION WAVE CURVATURE RESULTS OF UNCONFINED CHARGES

To obtain the wave front shape inside the unconfined explosive, the detonation wave was assumed steady. This assumption appears justifiable since the measured velocities were constant for at least the last 30-40 mm of the cylinders.

In the following discussion, the Z axis is taken to be along the axis of the cylindrical charge and the X axis is taken to be along a charge diameter. For any X value, the Z position of the wave front at the instant the wave breaks out at the center is obtained from

$$Z = D * (T_0 - T_x) \quad (2)$$

where  $T_x$  is the breakout time at the position X,  $T_0$  is the time the wave breaks out at the center and D is the detonation velocity. In the experiment with a charge diameter of 41.1 mm, both the wave arrival and detonation velocity were measured in the same experiment. The measured detonation velocity was within 0.6 percent of the value given by the fit to Equation (1). The calculated wave front curvature did not differ, within experimental error, using either the measured velocity or the velocity obtained from Equation (1). For consistency, the values of D used in Equation (2) were obtained from Equation (1).

Wave front shape data for each experiment were least squares fitted to circles of the form

$$(X - a)^2 + (Z - b)^2 = R^2 \quad (3)$$

where R is the radius of curvature and the point  $(X = a, Z = b)$  is the center of the circle. It should be noted that the value of "a" will be zero if the position of the Z axis is chosen exactly at the center of the wave front. The inclusion of "a" in the fit means that the position of the Z axis is determined by the fit.

## DISCUSSION OF WAVE FRONT CURVATURE

Wave front curvature measurements<sup>4</sup> on porous RDX and Tetryl explosives have shown that length to diameter ratios of these materials need to be greater than five before constant curvature is attained. Since sufficient data on wave curvature in PBXW-115 as a function of diameter does not exist, the assumption of steady state is based solely on the observed constant detonation velocity.

The wave fronts were not spherical over the whole diameter of the cylindrical PBXW-115 charges. This is particularly true near the edge of the cylinders. As a result, the best fit for the radius depends on how much of the data across the diameter of the charge is used. In this work the data was fit over the center 50 percent of the charge diameter. Figure 6 shows a typical fit of curvature data for a 41.05 mm diameter charge. The radii of curvature as a function of charge diameter for the

unconfined breakout experiments are given in Table 4. The results have large scatter but the trend is that the larger diameter charges have larger radii of curvature, consistent with the findings of Campbell et al.<sup>5</sup>

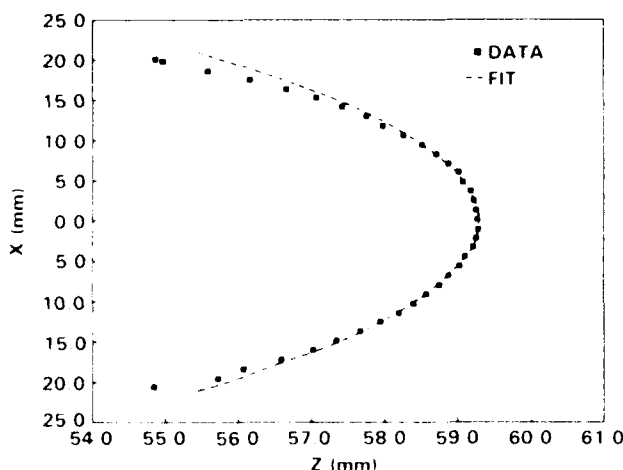


Figure 6. Detonation Wave Curvature for a 41.05 mm Diameter PBXW-115 Charge

Table 4. Wave Front Curvature and Detonation Zone Length for PBXW-115

SHOT NO	CHARGE DIAMETER (mm)	DETONATION VELOCITY* (mm/μs)	RADIUS OF CURV (mm)	ACTUAL % OF FIT**	ZONE LENGTH (mm)
24	68.25	5.571	144.3	49	4.2
25	48.02	5.309	60.4	49	2.5
9	41.05	5.158	60.9	48	2.9

\* DETONATION VELOCITY WAS CALCULATED FROM EQUATION (1).

\*\* RADIUS OF CURVATURE WAS DETERMINED BY FITTING THIS CENTER PERCENTAGE OF CHARGE DIAMETER

## WOOD-KIRKWOOD REACTION ZONE LENGTH

Calculations for the length of the detonation zone in PBXW-115 were performed for the three unconfined charges of different diameters for which wave curvatures were measured. These calculations are based on the Wood-Kirkwood radius of curvature theory<sup>3</sup> which is given by

$$\frac{D^0 - D}{D^0} = \frac{C * Z}{R} \quad (4)$$

where  $D$  is the measured detonation velocity,  $D^0$  is the infinite diameter detonation velocity,  $Z$  is the reaction zone length at the center of

the charge,  $C$  is a constant dependent on the equation of state of the material and  $R$  is the radius of curvature of the wave front. A recent review<sup>8</sup> of selected measurements and calculations of detonation zone lengths indicates that the Wood-Kirkwood theory predicts the correct order of magnitude.

The Wood-Kirkwood paper<sup>3</sup> used the properties of a liquid explosive to calculate a value of 3.5 for  $C$ . We used this value for  $C$  in our calculations. Effort is ongoing to refine the value of  $C$  for PBXW-115. Table 4 gives charge diameters, radii of curvature of the detonation waves and calculated detonation zone lengths. The detonation zone is slightly smaller for smaller diameter charges. The large scatter in this limited data set is to be expected because of experimental uncertainty in determining  $R$ .

## CORNER TURNING

Two corner turning experiments have been performed on PBXW-115. Figure 7 is a schematic of the experimental setup. The acceptor charge was in the shape of a solid bowl. The bowl-shaped charge was boosted by a 50.8 mm diameter, 152.5 mm long cylinder of PBXW-115. In one experiment this booster was unconfined and in the other experiment it was confined by a brass tube with a 16.5 mm thick wall. The curved surface of the PBXW-115 bowl was machined with a radius of curvature of 50.8 mm, measured from the edge of the booster charge. The arrival of the detonation (or shock wave) was observed on the curved surface and bottom of the bowl by a streak camera recording reflected light from an attached teflon tape. The amount of light being reflected changes significantly when the shock wave enters the teflon tape. Note that if a detonation wave with a perfectly flat front entered the bowl shaped charge and turned the corner without any delay, the detonation wave would breakout simultaneously along the entire curved surface and the bottom. The result would be a vertical line on the film record as depicted in Figure 8. For a wave that turns the corner with some delay (non-ideal corner turning), then a curved line on the film record would be expected.

The streak record for the experiment with a 16.5 mm thick brass tube surrounding the



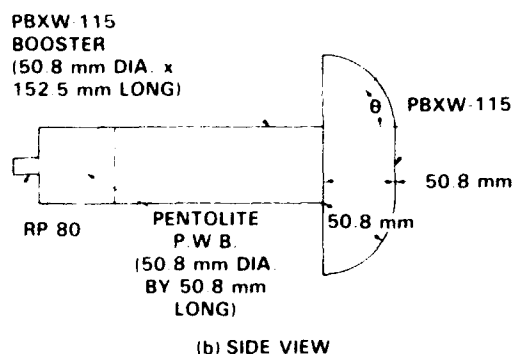
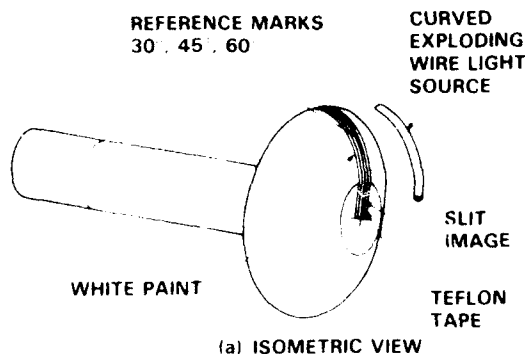


Figure 7. Corner Turning Experiment

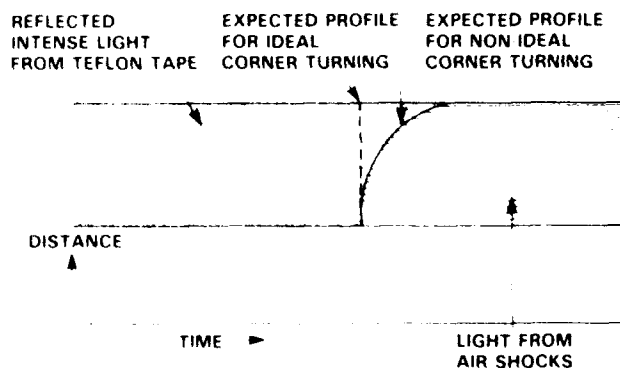


Figure 8. Schematic of Expected Streak Camera Film Record for Ideal Corner Turning

booster is shown in Figure 9. The detonation wave arrived at the flat bottom a few microseconds before it arrived at the curved surface. The experiment was designed to obtain a film record when the wave arrived at the teflon tape. The slit of the camera covered more of the charge than was covered with teflon tape. This allowed recording of the wave arrival beyond the bottom center of the charge where the tape ended, because an air shock was created at the surface when the wave arrived. This air shock provided adequate light for the camera.

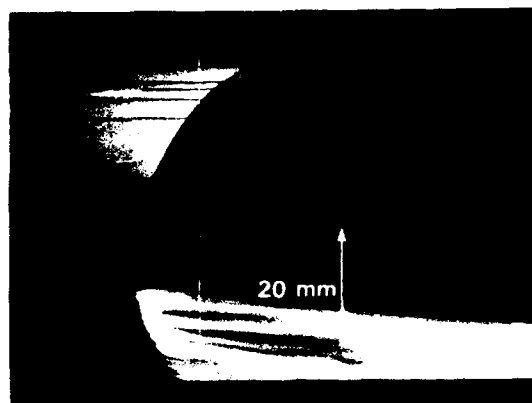


Figure 9. Streak Camera Film Record of the Corner Turning Experiment with a Brass Confined PBXW-115 Booster

Table 5 gives the times of arrival of the wave as a function of angle  $\theta$  for both unconfined and brass confined PBXW-115 booster experiments. Note that  $\theta$  is  $0^\circ$  where the wave arrives at the flat part of the bowl directly under the edge of the booster charge as shown in Figure 7. The wave arrived at the same locations on the curved surface of the bowl a few microseconds sooner for the confined booster arrangement than for the unconfined booster arrangement. A large part of the difference in arrival times can be attributed to the flatter wave front (i.e., a larger radius of curvature) in the confined booster.

Table 5. Times of Wave Arrival for Corner Turning Experiments

$\theta$ 's FOR UNCONFINED CHARGE					$\theta$ 's FOR CONFINED CHARGE					
0°	29°	45°	60°		0°	30°	39°	45°	49°	60°
0.7	3.5	5.5	7.4		0.6	2.4	3.1	3.6	4.0	5.0

\*ZERO TIME IS WHEN WAVE ARRIVES AT CENTER OF CHARGE

## SUMMARY OF RESULTS

The detonation velocity for unconfined PBXW-115 ranged from 5.04 to 5.54 mm/ $\mu$ s for charges with diameters of 35.5 to 69.1 mm, respectively. The increase in detonation velocity as the diameter increases is quite gradual. The failure of propagation of the detonation wave occurs without a sharp drop in detonation velocity as the charge diameter is

decreased to the failure diameter. The measured failure diameter for unconfined PBXW-115 charges was 37.1 mm. This failure diameter is moderately higher than that of most high explosives<sup>5</sup> but still much smaller than that of many propellants.<sup>10</sup>

It has been known for a long time that the failure diameter of an explosive charge decreases with confinement. This effect is most striking for materials of large failure diameter. Even thin layers of low impedance material have a dramatic effect on failure diameter of AP and AN charges.<sup>11,12</sup> This effect has been explained as the confinement delaying expansion of the detonation products. This increases the time available for reaction at high temperature and pressures before a rarefaction reaches the reaction zone. Hence confinement increases the "effective diameter" of the explosive. A large confinement effect on failure diameter for PBXW-115 was measured in the present study. A 2.5 mm thick brass wall reduced the failure diameter to about 21 mm while a 5mm thick brass wall reduced it to about 17 mm.

Recent improvements in the time resolution of reaction zone length measurements<sup>6</sup> have provided data accurate enough to distinguish between various analytical failure diameter theories. D. Price<sup>9</sup> has pointed out that the zone length is calculated reasonably well by the Wood-Kirkwood curved front theory. The detonation zone length of PBXW-115 calculated using the Wood-Kirkwood theory resulted in a zone length of 2-4 mm. These calculated zone lengths are consistent with similar calculations<sup>8,9</sup> on AP explosives. A larger experimental data base of accurately determined zone lengths of explosives is needed.

It should be noted that caution has to be exercised in interpreting zone lengths in composite explosives. The whole question of what comprises the reaction zone length in a non-ideal explosive needs more experimental and theoretical treatment. In the case of PBXW-115, we believe that reaction is likely to be occurring beyond the CJ plane and well into the Taylor expansion wave.

The ability of a detonation wave to turn a corner is a complicated function of shape of the wave arriving at the corner, stress induced into the explosive at the corner and ability of the explosive to initiate the lateral material. Even though this process is complicated, understanding it is of great practical importance for the design of many explosive devices.

Corner turning experiments on TATB compositions using flash X-ray techniques have shown that substantial amounts of material at corners go unreacted.<sup>14,15</sup> Experiments using streak photography have also shown substantial unreacted TATB.<sup>16</sup> In addition, studies of wave arrivals<sup>17,18</sup> at surfaces have shown that the wave does not follow simple spherical expansion from the corner. The present limited results on PBXW-115 suggest that detonation wave turning ability should be experimentally verified for situations where the wave is required to turn a corner.

Obtaining a more comprehensive understanding of these various wave propagation results requires two-dimensional code calculations with an accurate initiation model and a reactive flow constitutive relationship. In particular, initiation lateral to the direction of the input shock needs to be better understood to model divergence or corner turning of the detonation wave. Hydrodynamic code calculations and initiation modeling will accompany the future corner turning experimental efforts on PBXW-115.

## ACKNOWLEDGEMENTS

The authors wish to acknowledge many useful discussions on the contents of this paper with R. Bernecker, S. Jacobs, and D. Price. In addition, V. Ringbloom made the curved capillaries used to make the curved light sources for the corner turning experiments.

## REFERENCES

1. Dick, J. J., "Detonation Initiation Behavior of Some HMX/AP/Al Propellants," *Comb. and Flame*, Vol. 37, 1980, pp. 95-99.

2. Price, D. and Clairmont, Jr., A. R., "Explosive Behavior of Simplified Propellant Models," *Comb. and Flame*, Vol. 29, 1977, pp. 87-93.
3. Wood, W. W. and Kirkwood, J. G., "Diameter Effect in Condensed Explosives. The Relation Between Velocity and Radius of Curvature of the Detonation Wave," *J. Chem. Phys.*, Vol. 22, Nov 1954, pp. 1920-1924.
4. Erkman, J. O. and Price, D., "Comparison of Curvature of Detonation Front in AP with that Found in Some Conventional Explosives," NOLTR 69-235, May 1970.
5. Campbell, A. W. and Engelke, R., "The Diameter Effect in High-Density Heterogeneous Explosives," *Proc. Sixth Symposium (International) on Detonation*, Coronado, CA, 24-27 Aug 1976, pp. 642-652.
6. Sheffield, S. A.; Bloomquist, D. D.; and Tarver, C. M., "Subnanosecond Measurements of Detonation Fronts in Solid High Explosives," *J. Chem. Phys.*, Vol. 80, 1984, pp. 3831-3844.
7. Liddiard, T. P. and Forbes, J. W., "A Summary Report of the Modified Gap Test and the Underwater Sensitivity Test," NSWC TR 86-350, Appendix A, 12 Mar 1987.
8. Hall, T. N. and Holden, J. R., "Navy Explosives Handbook: Explosion Effects and Properties - Part III. Properties of Explosives and Explosive Compositions," NSWC MP 88-116, Oct 1988.
9. Price, D., "Review of Information on Composite Explosives. I. General Background," Final Progress Report, ATR 88-0046, Nov 1988.
10. Kapeles, J. A. and Graham, K. J., "Literature Survey on Critical Diameter of Solid Rocket Propellants," NWC TP 6835, Oct 1987.
11. Gor'kov, V. A. and Kurbangalina, R. Kh., "Some Data Concerning the Detonation Ability of Ammonium Perchlorate," *Comb., Expl., and Shock Waves*, Vol. 2., No. 2, 1966, p. 12.
12. Kurbangalina, R. Kh. and Patronova, L. I., "Effect of a Steel Sheath on the Critical Detonation Diameter of Condensed Explosives," *Comb., Expl., and Shock Waves*, Vol. 12, No. 4, 1976, pp. 587-590.
13. Price, D., "Critical Parameters for Detonation Propagation and Initiation of Solid Explosives," NSWC TR 80-339, 10 Sep 1981.
14. Dick, R., "Pulsed High Energy Radiography Machine Emitting X-rays (PHERMEX): Applications to Study High Pressure Flow and Detonation Waves," *Proc. First European Conf. on Cineradiography on Photons and Particles*, Paris, France, 1981, Pub. by SPIE, Vol. 312, 1983, pp. 66-81.
15. Mader, C., *LASL PHERMEX Data*, Vol. III, University of California Press, Berkeley, 1980.
16. Cox, M. and Campbell, A. W., "Corner-Turning in TATB," *Proc. Seventh Symposium (International) on Detonation*, Annapolis, MD, 16-19 Jun 1981, pp. 624-633.
17. Boggs, E. M.; Messerly, G. H.; and Strecker, H. A., "Initiation Studies on Solid Explosives," OSRD 5617, 14 Dec 1945.
18. Jackson, R. K.; Green, L. G.; Barlett, R. H.; Hofer, W. W.; Kramer, P. E.; Lee, R. S.; Nidick, Jr., E. J.; Shaw, L. L.; and Weingart, R. C., "Initiation and Detonation Characteristics of TATB," *Proc. Sixth Symposium (International) on Detonation*, Coronado, CA, 24-27 Aug 1976, pp. 755-765.

## DISCUSSION

**K. J. GRAHAM**, Atlantic Research Corporation, Gainesville, VA

Regarding the use of Teflon tape to follow progress of detonation wave: I have used this technique successfully in the NWC Small-Scale Aquarium Gap Test, using a simple flash tube for illumination while recording the wave

progress with a streak camera. This technique was reported in several JANNAF Propulsion System Hazards Subcommittee Proceedings. The advantages include ease of application and no requirement for precise lighting alignment.

#### **REPLY BY J. W. FORBES**

The authors are grateful to learn that the use of Teflon tape as a diffuse reflector has worked successfully in other explosive experiments.

# NON-STEADY FLOW IN A DETONATOR

Jia Quansheng, Chen Fumei, and Wang Tinzheng

Department of Mechanical Engineering

Beijing Institute of Technology, P. O. Box 327, Beijing, CHINA

*The non-steady flow in a detonator, loaded with explosives DDNP, RDX, and TNT, is measured by EMV particle-velocity gauge. Some characterized signals corresponding to retonation, growth, and decay of explosive detonation are observed—where the negative pulse indicates the retonation and the slope of signal indicates the degree of violence of chemical reaction in shocked explosive. In some environments Lagrangian analysis may be used to study the non-steady flow in a detonator. As an example, two groups of particle velocity curves of detonators with PMMA shell and paper shell are measured by Lagrangian gauge. Other parameters of flow field are calculated by Lagrangian analysis. In addition, two-dimensional flow in a detonator with PMMA shell is measured by a two-dimensional composite manganin-constantan ring gauge. The experimental data are compared with computed results using both a two-dimensional Lagrangian numerical calculation code and a Lagrangian analysis code.*

## INTRODUCTION

Studying the SDT process in a detonator can be used to understand the action of each layer of explosive in it. Because the size of a detonator is so small, quantitative study of the flow field in the detonator is difficult. This paper measures the SDT process in a detonator with a special EMV gauge

Fowles, Williams and Cowperthwaite<sup>1</sup> introduced the Lagrangian analysis. It is a one-dimensional numerical method based on experimental data measured by Lagrangian gauge. It is used to study flow field of explosion and demarcate a reaction rate equation of explosive.<sup>2,3</sup> In a limited environment, the method may be used to study non-steady flow in a detonator. As an example, the SDT process of detonators with PMMA shell and paper shell are calculated by the Lagrangian analysis.

Two-dimensional Lagrangian gauges have been studied in recent years.<sup>4,5</sup> In order to measure in the two-dimensional flow field in a detonator, we improved a two-dimensional composite manganin-constantan designed by

Huan Shi.<sup>6</sup> Then the two-dimensional experimental data were compared with computational results using a two-dimensional Lagrangian numerical calculation code<sup>7</sup> and Lagrangian analysis.

## EMV EXPERIMENT AND LAGRANGIAN ANALYSIS

The experimental system is shown in Figure 1. The EMV experimental results are shown in Figures 2, 3 and 4 separately. The  $u(t)$  profiles indicate the character of chemical decomposition of the explosives. The slope of  $u(t)$  indicates the degree of violence of chemical reaction in shocked explosives.

Figure 2 is a group of  $u(t)$  profiles of a detonator with paper shell (ID = 6.44 mm, OD = 8.14 mm) at A(0.00 mm), B(3.88 mm), C(7.72 mm), and D(11.85 mm). At position A the  $u(t)$  profile appears convex which indicates the acceleration of decomposition of the explosive. From position A to B, the strength of the shock wave is increased progressively. At position B the profile becomes a triangle.

The slope of the profile is increased, which indicates chemical decomposition acceleration further. It is interesting that negative pulses appear after the shock front has passed as shown in the second profile in Figure 2. Several shots repeat the phenomenon. One of the explanations could be that the negative pulse is a result of boundary conditions behind the gauge; that is, the detonator header may have blown out backward due to energy release at position C, and driven the gas backward at position B. Another explanation is retonation. Because position B is the only place where there appears negative pulse among A, B, C, and D—four positions in Figure 2—and there was also not a negative tail in the traces in Figures 3 and 4; so we hold that retonation is the only reason to explain the negative pulse. At this position there is still a significant part of the explosive energy remaining until retonation occurs when the shock wave front has passed. At position C, sensitivity of TNT is low, the strength of shock is not strong enough, and  $u(t)$  profile appears rectangular. At the D position, the profile appears triangular again, but the slope is less than that at the B position.

Figure 3 is a group of profiles for a detonator with PMMA shell (ID 6 mm), (OD 13.9 mm) at A(0.00 mm), B(4.32 mm), C(8.64 mm) and D(13.87 mm), where TNT ( $\rho = 1.692$ ) is replaced by RDX with the same density. A growth of explosive detonation is observed. Retonation has not been found at position B of the detonator with PMMA shell, where most energy has been released in a neighbor region of the shock wave front.

Figure 4 is a group of decays of explosions in a detonator with paper shell, in which reaction dampens. Peaks of a particle velocity are decreased progressively. The profile is a rectangle completely at C position, where the explosive appears inert. Retonation has not been found, due to decay of explosion.

From the above experiments we come to the conclusion that shapes of the  $u(t)$  profile depend on the kind of shell and the shocked strength of the explosive.

Flow field of explosion in a detonator under different conditions can be calculated

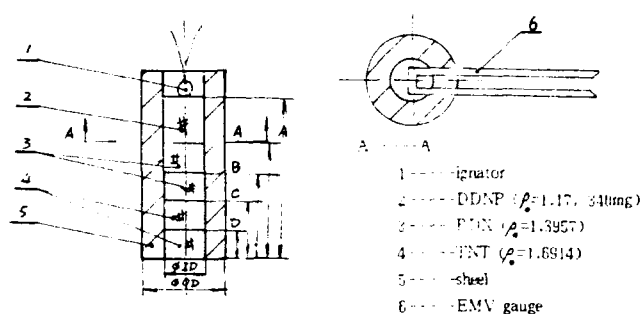


Figure 1. Scheme of an Experimental Arrangement for a Detonator

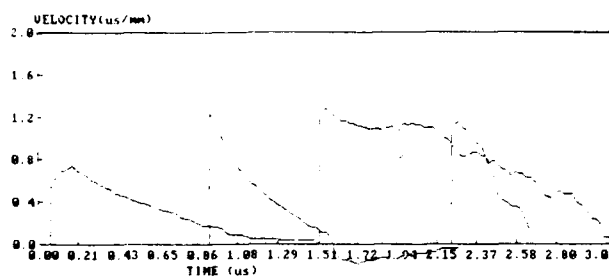


Figure 2. The Experimental  $u(t)$  Profiles of  $H = 0.00, 3.88, 7.72, 11.85$  mm for a Detonator with Paper Shell

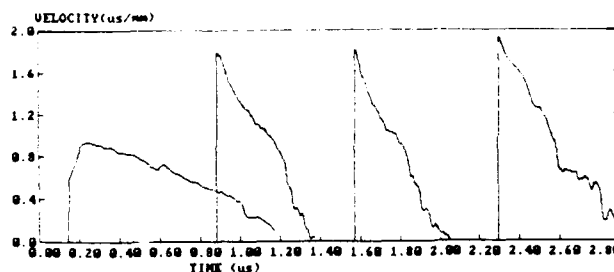


Figure 3. The Experimental  $u(t)$  Profiles of  $H = 0.00, 4.32, 8.64, 13.87$  mm for Detonator with PMMA Shell

quantitatively by Lagrangian analysis based on the above  $u(t)$  profiles. The calculated results are shown in Figures 5 and 6. From calculated  $P(t)$ ,  $p(t)$  and  $e(t)$  profiles, the process of decay, retonation, and growth of detonation that occur in a detonator can be observed more clearly. In Figure 5 retonation corresponds to the second pressure peak, as shown in the second profile in Figure 5.

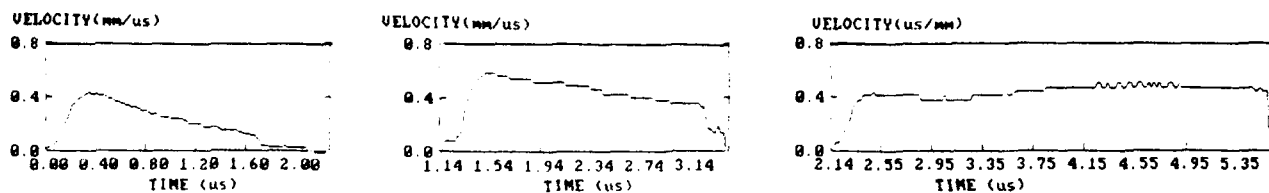


Figure 4. The Experimental  $u(t)$  Profiles of  $H = 0.0, 3.88, 7.72$  mm for a Detonator with Paper Shell (Decay of Detonation)

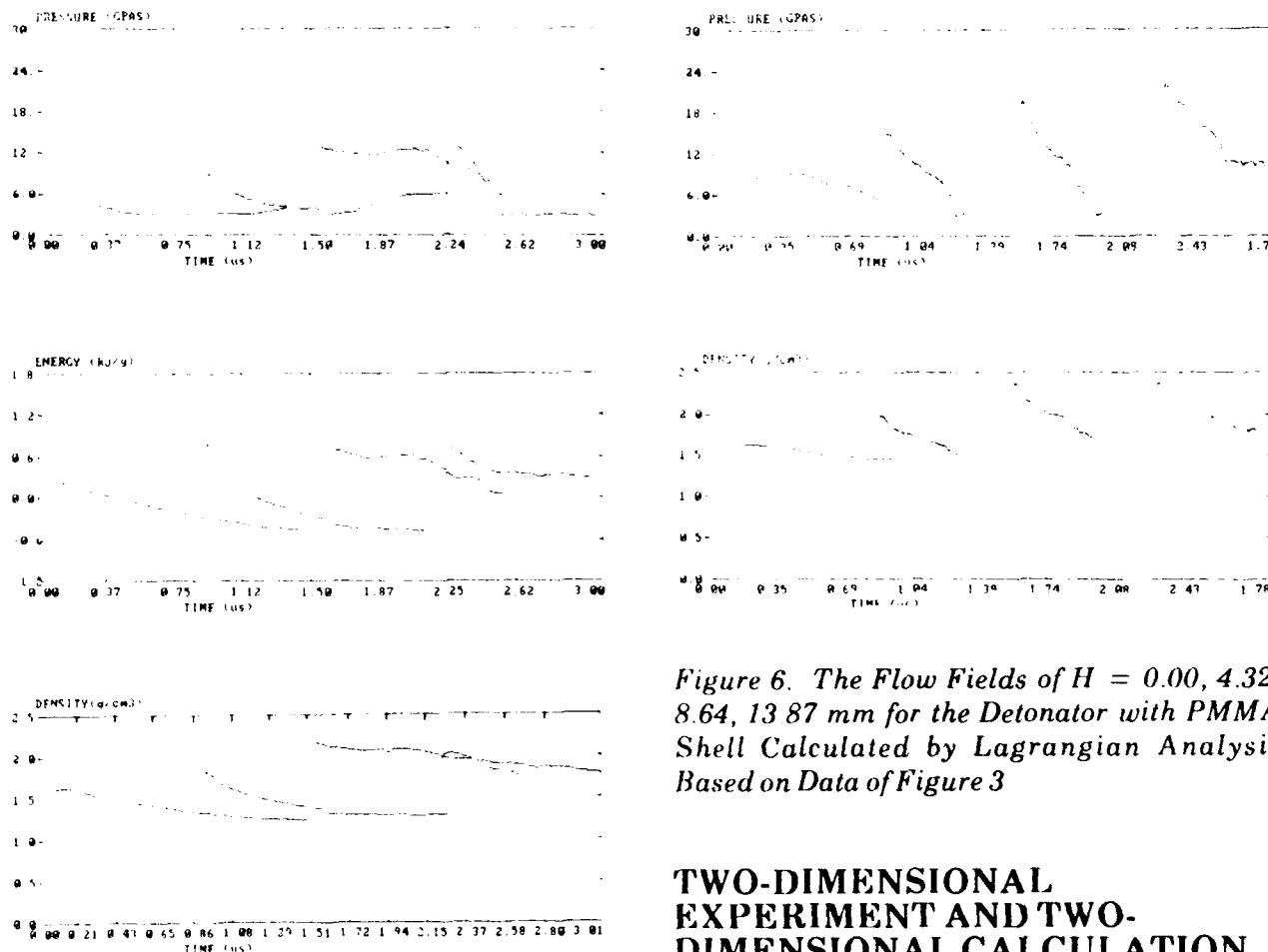


Figure 5. The Flow Fields of  $H = 0.00, 3.88, 7.72, 11.85$  mm for the Detonator with Paper Shell Calculated by Lagrangian Analysis Based on Data in Figure 2

Figure 6 shows the flow fields of  $h = 0.00, 4.32, 8.64, 13.87$  mm for the detonator with PMMA shell calculated by Lagrangian analysis based on data in Figure 3.

Figure 6. The Flow Fields of  $H = 0.00, 4.32, 8.64, 13.87$  mm for the Detonator with PMMA Shell Calculated by Lagrangian Analysis Based on Data of Figure 3

## TWO-DIMENSIONAL EXPERIMENT AND TWO-DIMENSIONAL CALCULATION

In order to measure a two-dimensional flow field in a detonator, we improved a two-dimensional composite manganin-constantan ring gauge. The gauge is shown in Figure 7. Pressure and radial displacement of a particle in a cylindrical geometry flow field of detonation can be measured by using the gauge. Sensitive parts of the gauge are composed of circles with different radii and the width of these circles is 0.2 mm. In experiment, the sensitive parts to be used are retained. Other sensitive



Figure 7. A Two-Dimensional Composite Manganin-Constantan Ring Gauge. Thickness of manganin gauge is 20  $\mu\text{m}$ , and that of constantan is 15  $\mu\text{m}$ .

parts are cut. Pressure and radial displacement of a particle in a two-dimensional flow field are calculated according to Equation 1.

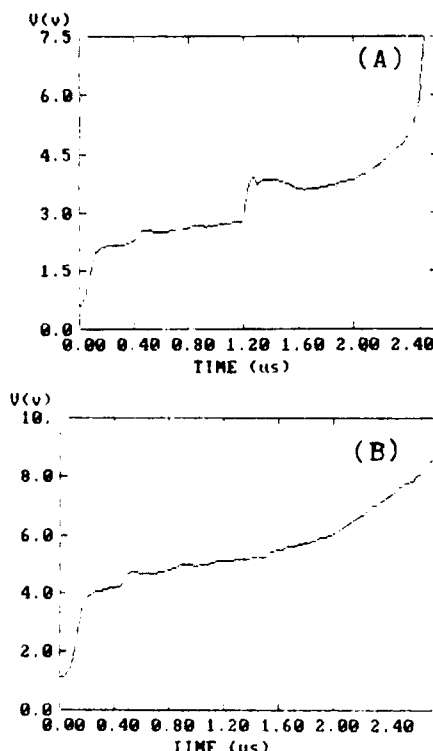
$$P = \alpha((\Delta R/R_0)_m - K_m/K_c (\Delta R/R_0)_c)$$

$$r = r_0 (1 + 1/K_c (\Delta R/R_0)_c) \quad (1)$$

where  $(\Delta R/R_0)_m$  and  $(\Delta R/R_0)_c$  are relative change of resistor of manganin gauge and constantan,  $r_0$  is initial radius of sensitive part,  $\alpha$  is dynamic piezoresistance of manganin.  $K_m$  and  $K_c$  are strain coefficients for manganin and constantan.

Pressure near the axis ( $r_0 = 1.22$  mm) at D position in a detonator with PMMA shell is measured by the ring gauge. The experimental data are shown in Figure 8.

Profile of pressure at D position ( $r_0 = 1.22$  mm) calculated using Equation 1 is shown in Figure 9(a). The result is compared with that computed by two-dimensional numerical calculation code and Lagrangian analysis code separately. The comparisons are shown in Figures 9(b) and 9(c). Figure 9 shows a very good agreement between the results of the two-dimensional experiment and those computed by two-dimensional Lagrangian numerical calculation code and Lagrangian analysis. From these, the reliabilities of the two-dimensional Lagrangian ring gauge and our two-dimensional code for studying two-dimensional propagation of the detonation wave are checked against each other. To observe the flow field in a detonator in detail, Figure 10



Note: Curves A and B are relative changes of resistor for manganin ring gauge and constantan ring gauge, respectively. In experiment, a constant current source is used, so  $R/R_0 = V/V_0$ .

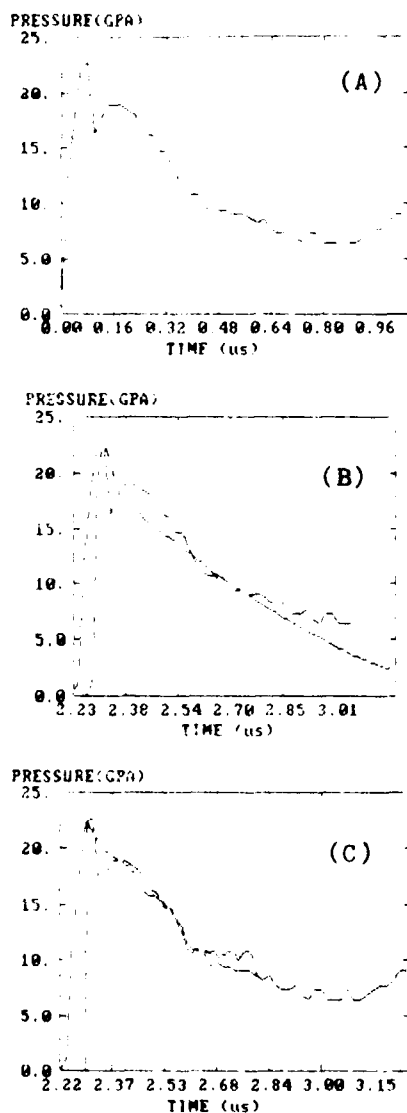
Figure 8. Relative Changes of Resistor of Manganin Gauge and Constantan when Propagation of Detonation Wave at Position D ( $r_0 = 1.22$  mm) in a Detonator with PMMA shell

shows a two-dimensional propagation of the detonation wave in a detonator with a PMMA shell at 0.95  $\mu\text{s}$ , 1.45  $\mu\text{s}$ , and 1.87  $\mu\text{s}$  modeled numerically using the Forest Fire rate and HOM state equation in our two-dimensional reactive hydrodynamics 2DLE. Figure 10 shows little curvature in the explosive and much curvature in the PMMA shell with propagation of the detonation wave along the detonator.

## CONCLUSIONS

1. EMV gauge can be used to study the SDT process in a detonator with non-metal shell. The slope of  $u(t)$  profiles indicate the degree of violence of chemical reaction in shocked explosives.





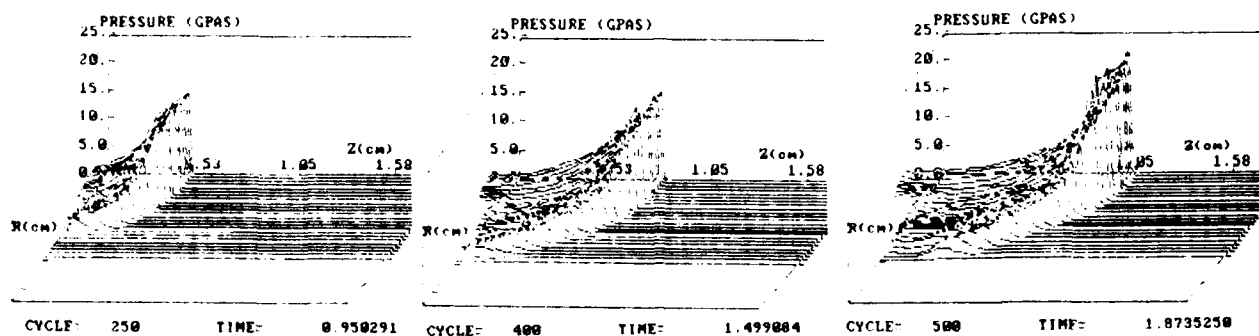
Note: Curves A is measured by the two-dimensional gauge. Curve B is a comparison between two-dimensional experimental data and results of two-dimensional code. Curve C is a comparison between two-dimensional experimental data and results of the Lagrangian analysis.

Figure 9. Comparison Between Two-Dimensional Experimental Data and Results of Two-Dimensional Code and Lagrangian analysis

2. In limited environments the Lagrangian analysis may be used to quantitatively study the non-steady flow in a detonator.
3. The agreement between results of the two-dimensional experiment and those of the two-dimensional code and Lagrangian analysis is good.
4. The improved two-dimensional Lagrangian gauge is reliable for studying two-dimensional flow field.
5. The two-dimensional code successfully models the two-dimensional propagation of detonation wave in a detonator with PMMA shell.

## REFERENCES

1. Fowles, G. R. and Williams, R. F., "Plane Stress Wave Propagation in Solids," *J.A.P.*, No. 41, 1970, p. 360.
2. Grady, D. E., "Experimental Analysis of Spherical Wave Propagation," *J.G.R.*, No. 78, 1973, p. 1299.
3. Jia Quansheng and Chen Fumei, "Generalized One-Dimensional Lagrangian Analysis for Wave Propagation," *Int. Syn.p. on Explosive and Pyrotechnics*, 1987, p. 544.
4. Rosenberg, G; Yaziv, D.; and Mayseless, M., *Shock Waves in Condensed Matter*, 1981, p. 495.
5. Rosenberg, Z.; Mayseless, M.; and Rosenberg, G.; *Shock Waves in Condensed Matter*, 1983, p. 247.
6. Huan Shi and Ding Jing, *Shock Waves in Condensed Matter*, 1987, p. 593.
7. Jia Quansheng and Chen Fumei, "FORTRAN 2DLE: A Lagrangian and Eulerian Finite-Difference Code for Reactive Media," *China 3rd Symp. on Pyrotechnics and Explosives*, 1988.



*Figure 10. Two-dimensional Wave Propagation in a Detonation with PMMA Shell Modeled Numerically by Two-dimensional Code*

# POLYSULFONE SIP GAGE FOR FLYING PLATE EXPLOSIVE COMPONENTS\*

Truman W. Warren  
Mason & Hanger - Silas Mason Co., Inc.  
P.O. Box 30020  
Amarillo, Texas 79177

and

Reuben R. Weinmaster  
Sandia National Laboratories  
P.O. Box 5800  
Albuquerque, New Mexico 87185

*A simple, inexpensive polymeric gauge has been devised for measuring the output shock parameters of selected small flying plate components. The gauge consists of a thin polysulfone (PSF) film with sputtered copper electrodes in a guardring configuration. PSF exhibits strong shock-induced polarization (SIP) in its natural, isotropic state. When impacted at a pressure level above its polarization threshold, the polymer generates an electrical current with a risetime (to peak) equal to shock transit time through the film. Precise measurement of risetime and film thickness with knowledge of the Hugoniot equation-of-state of flyer and gage materials yields a good first order approximation of the sought impact parameters: shock velocity, particle velocity, pressure and flyer velocity.*

*Experimental firing data from several types of flying plate detonators are presented.*

## INTRODUCTION

Self-generated electrical polarization signals from shock-loaded polymers have been known to exist for many years.<sup>1,2</sup> Recent work<sup>3</sup> described a technique using the polarization effects of polymethylmethacrylate (PMMA) as a pressure transducer. Graham<sup>4</sup> measured the shock-induced polarization in polysulfone (PSF) and reported the largest magnitude for any polymer tested. The higher output current from PSF provided the impetus for its use here.

Substituting PSF for the weakly polarized PMMA in the contact type pressure

transducer described in Reference 3, should provide a better signal-to-noise ratio for instrumenting the transducer. However, the objective of this work is to devise a gauge for measuring flyer velocity at prescribed standoff distances from flying plate explosive components. This would offer an alternative to the more complex laser interferometry techniques, such as VISAR and Fabry-Perot, currently used for the task.

## DISCUSSION

A variety of gauge designs were tested initially to optimize the electrode pattern. Best results were obtained when the active area, circumscribed by a guardring, conformed closely to the impact area.

\* This work was supported by the U.S. Department of Energy.

The typical electrode configuration shown in Figure 1 was designed to accommodate 4.0 mm diameter flyers. A guardring surrounds the rear electrode to minimize the polarization area and reduce lateral shock effects. Electrically, the guardring is connected in common with the front (impact) electrode and instrument ground, as shown in Figure 2.

The copper electrode circuits were sputtered onto Udel P-1700 PSF film<sup>5</sup> to a coating thickness of 200 nm per side. Surface profilometer measurements were made after each sputtering run, and the standard deviation of coating thickness was typically less than 5 nm. In some cases, the final electrode pattern was then photoetched. Twisted lead wires 10 cm long were soldered

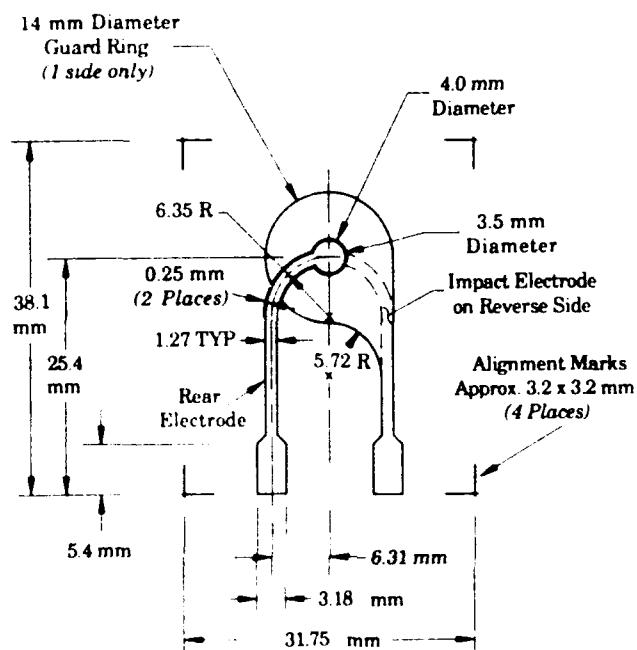


Figure 1. SIP Gauge Pattern

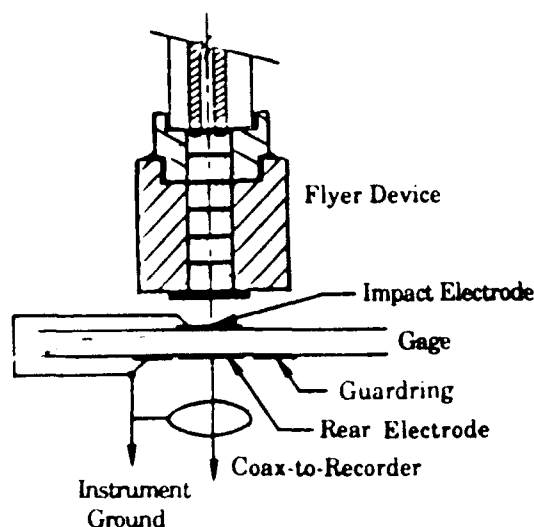


Figure 2. PSF SIP Gauge Connections

to the electrodes. (In the experiments, the leads were cut as short as possible before connecting to low loss coaxial cable.) All of the gauges were fabricated to our specifications by the Piezo Film Division of Pennwalt Corporation<sup>a</sup>.

Thickness of the active area of each gauge was measured to the nearest tenth of a micrometer at a controlled temperature of  $20 \pm 0.3^\circ\text{C}$ . The combined thickness of copper cladding (400 nm) was subtracted from each reading.

Several substrate materials were tested with PSF gauges. Qualitatively, the best results

were achieved using either PSF or PMMA substrates.

Flying plate detonator tests were assembled in PMMA fixtures, as depicted in Figure 3. No adhesive was used in assembly. Several types of detonators were fired, containing various loading densities of 2-(5-cyanotetrazolato) pentaamminecobalt (III) perchlorate (CP) and pentaerythritol tetranitrate (PETN). An initial standoff distance between the flyer and PSF gauge was set for all tests. Flyers were 127- $\mu\text{m}$  thick steel.

A wide bandwidth recording instrument capable of sub-nanosecond time resolution was

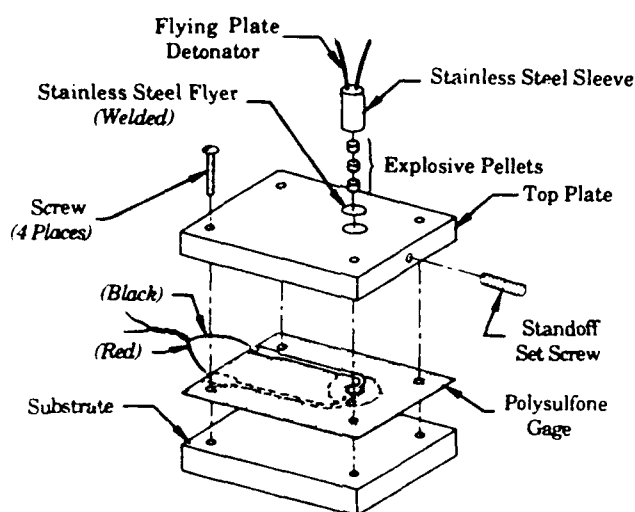


Figure 3. Test-Fire Assembly

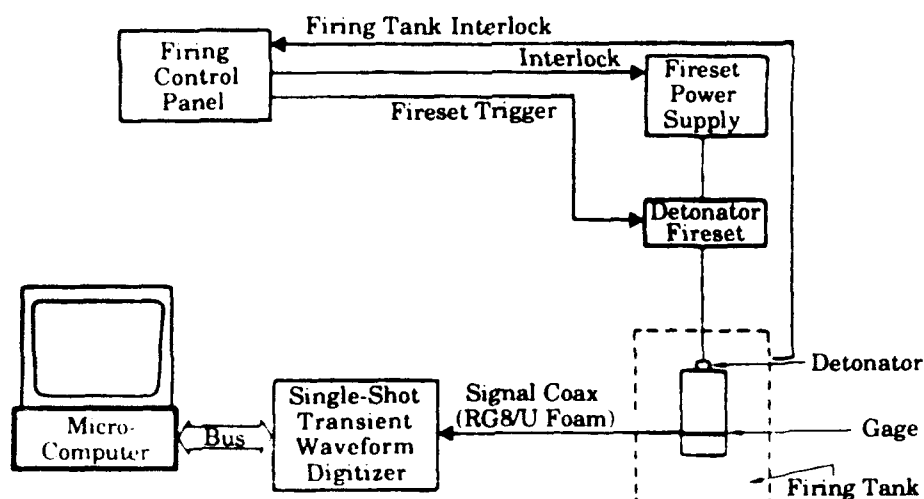


Figure 4. PSF Gauge Instrumentation Block Diagram

<sup>a</sup>Pennwalt Corporation, P. O. Box 799, Valley Forge, PA 19482

required to monitor the risetime of the polarization current pulse. Transient waveform digitizers, with a sample interval of 0.39 nanoseconds, were utilized here. A block diagram of the instrumentation system is shown in Figure 4, and a typical PSF gauge record is shown in Figure 5.

Gauge records were analyzed by computing shock velocity in the PSF, then solving for other impact parameters by applying

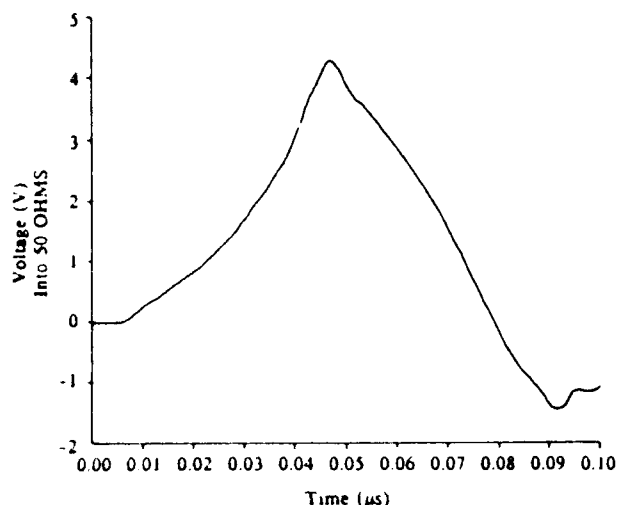


Figure 5. Typical PSF SIP Gauge Record 1.425 g/cm<sup>3</sup> PETN Driver; 0.127 x 3.81-mm Diameter Steel Flyer; 256-μm Thick PSF Gauge at 1.0-mm Standoff

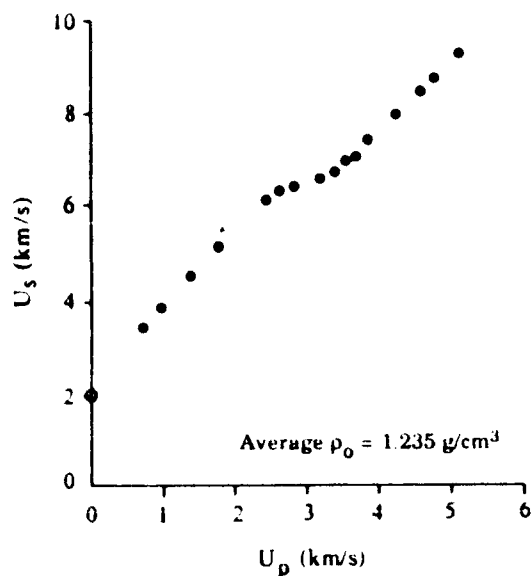


Figure 6. Polysulfone Hugoniot (Reference 7)

the Rankine-Hugoniot relations for conservation of momentum. Published Hugoniot equation-of-state data was obtained for Type 304 steel<sup>6</sup> and PSF.<sup>7</sup> The usable range of PSF gauges is limited by a polarization threshold at 1.8 GPa,<sup>8</sup> and a cusp in the  $U_s$ - $U_p$  Hugoniot at about 24 GPa ( $U_s = 6.64$ ,  $U_p = 2.93$ ), shown in Figure 6.

A least-squares fit of the PSF Hugoniot data below the cusp, in the form

$$U_s = C_0 + SU_p + QU_p^2,$$

was used in gauge analysis. The Hugoniot intercept term,  $C_0$ , was modified to accommodate temperature firings in the range of -54 to 74°C. Longitudinal and shear wave velocities in PSF were measured over this range<sup>9</sup> to derive bulk sound velocity as a function of temperature yielding the following  $U_s$ - $U_p$  relationship:

$$U_s = 2.042 + 2.066 U_p - 0.1651 U_p^2 - 0.00152T \quad (1)$$

where

$U_s$  = shock velocity (mm/μs),

$U_p$  = particle velocity (mm/μs), and

$T$  = firing temperature (°C).

Initial densities and thicknesses of the impacting materials were also corrected for firing temperature. Calculations were made as follows where subscripts zero, one, and two denote initial states, conditions in the flyer, and conditions in the gauge, respectively:

$$\chi = \chi_0 [1 + \alpha(T - T_0)] \quad (2)$$

where,

$\chi$  = thickness (mm), and

$\alpha$  = linear coefficient of thermal expansion (mm/mm-°C)

$\alpha_1 = 17.3 \times 10^{-6}$  (Type 304 Steel),

$\alpha_2 = 55.8 \times 10^{-6}$  (PSF)

$$\rho = \rho_0 [1 + \alpha(T - T_0)]^{-3} \quad (3)$$

where,

$\rho$  = density (g/cm<sup>3</sup>)

$\rho_{01}$  = 7.896 (Type 304 Steel),

$\rho_{02}$  = 1.235 (PSF)

$$U_{s_2} = X_2/t \quad (4)$$

where,

$U_{s_2}$  = shock velocity in PSF (mm/ $\mu$ s),

$X_2$  = corrected gage thickness (mm), and

$t$  = risetime to peak current ( $\mu$ s).

$$U_{p_2} = 6.257 - 51.523 - 0.0092T - 6.058 U_{s_2} \quad (5)$$

where

$U_{p_2}$  = impact particle velocity (mm/ $\mu$ s).

$$P = \rho_2 U_{s_2} U_{p_2} \quad (6)$$

where

$P$  = impact pressure (GPa), and

$\rho_2$  = corrected PSF density (g/cm<sup>3</sup>)

For flyer materials having a linear  $U_s$ - $U_p$  relationship of the form  $U_s = C_0 + S U_p$ , conditions in the flyer are obtained from:

$$P = \rho_1 U_{p_1} (C_{01} + S_1 U_{p_1}) \quad (7)$$

giving

$$U_{p_1} = \frac{-\rho_1 C_{01} + \rho_1^2 C_{01}^2 + 4\rho_1 S_1 P}{2\rho_1 S_1} \quad (8)$$

and,

$$U_{s_1} = \frac{1}{2} \left( C_{01} + \frac{\rho_1^2 C_{01}^2 + 4\rho_1 S_1 P}{\rho_1} \right) \quad (9)$$

The Hugoniot equation-of-state for Type 304 stainless steel from Reference 6 gives:

$$U_{s_1} = 4.569 + 1.49 U_{p_1} \quad (10)$$

where

$U_{s_1}$  = shock velocity in steel (mm/ $\mu$ s), and

$U_{p_1}$  = net particle velocity in steel (mm/ $\mu$ s).

$$\tau = 2X_1 / U_{s_1} \quad (11)$$

where,

$\tau$  = pressure pulse width ( $\mu$ s), and

$X_1$  = corrected flyer thickness (mm)

$$V_f = U_{p_2} \left( \frac{\rho_2 U_{s_2}}{\rho_1 U_{s_1}} + 1 \right) = U_{p_1} + U_{p_2} \quad (12)$$

where

$V_f$  = flyer velocity (mm/ $\mu$ s).

Samples of each type of detonator tested were also fired separately with dual-leg VISAR instrumentation to measure flyer velocity. A comparison of the VISAR and PSF gauge data is given in Table 1. Location of these data in the  $P$ - $U_p$  Hugoniot plane is shown in Figure 7 with the usable range for steel flyers indicated.

The lower limit for producing reliable PSF gauge records is actually about three times the pressure value given for onset of polarization in Reference 8, or approximately 6 GPa. A plot of the usable range for PSF gauges in the  $P$ - $U_s$  plane is shown in Figure 8.

For thin flyer applications, optimum gauge thickness is dependent on the expected pressure pulse width. The shock transit time through the gauge should be equal to or less than the pressure pulse width; i.e., the material in a gauge of optimum thickness stays "shocked up" at the flyer interface until the transmitted shockwave reaches the back surface of the gauge. Neglecting attenuation in thin impactors, the ratio of gauge-to-flyer thicknesses is given by:

$$\frac{X_2}{X_1} = \frac{2U_{s_2}}{U_{s_1}} \quad (13)$$

A plot of optimum PSF gauge thicknesses for several types of flyers is shown in Figure 9.

Table 1. Comparison of VISAR and PSF Gauge Data<sup>a</sup>

Flyer Driver Type (127- $\mu$ m Steel Flyers)	VISAR $V_f$ (mm/ $\mu$ s $\pm$ o)	PSF Gage $V_f$ (MM/ $\mu$ s $\pm$ o)
SNLA CP Det (Type 7)	1.455	Below Threshold
SNLA CP Det (Type 2)	2.018	2.086 $\pm$ 0.095
SNLA CP Det (Type 3)	2.592	2.637 $\pm$ 0.025
SNLA CP Det (Type 5)	2.751	2.913 $\pm$ 0.038
Mound CP Det	2.484 $\pm$ 0.027	2.572 $\pm$ 0.131 <sup>b</sup>
1.258 g/cm <sup>3</sup> PETN Det	2.777 $\pm$ 0.108	2.744 $\pm$ 0.053
1.425 g/cm <sup>3</sup> PETN Det	3.036 $\pm$ 0.049	3.004 $\pm$ 0.056
1.565 g/cm <sup>3</sup> PETN Det	3.225 $\pm$ 0.093	3.225 $\pm$ 0.079
1.685 g/cm <sup>3</sup> PETN Det	3.475 $\pm$ 0.036	3.393 $\pm$ 0.038

<sup>a</sup> Flyer velocity ( $V_f$ ) values were measured at 1-mm flight distance. Standard deviation is shown for mean of four or more data points. All tests were fired at room temperature ( $22 \pm 2^\circ\text{C}$ ). PSF gauges were nominally 254  $\mu$ m thick.

<sup>b</sup> Fired at Mound Plant, Miamisburg, OH

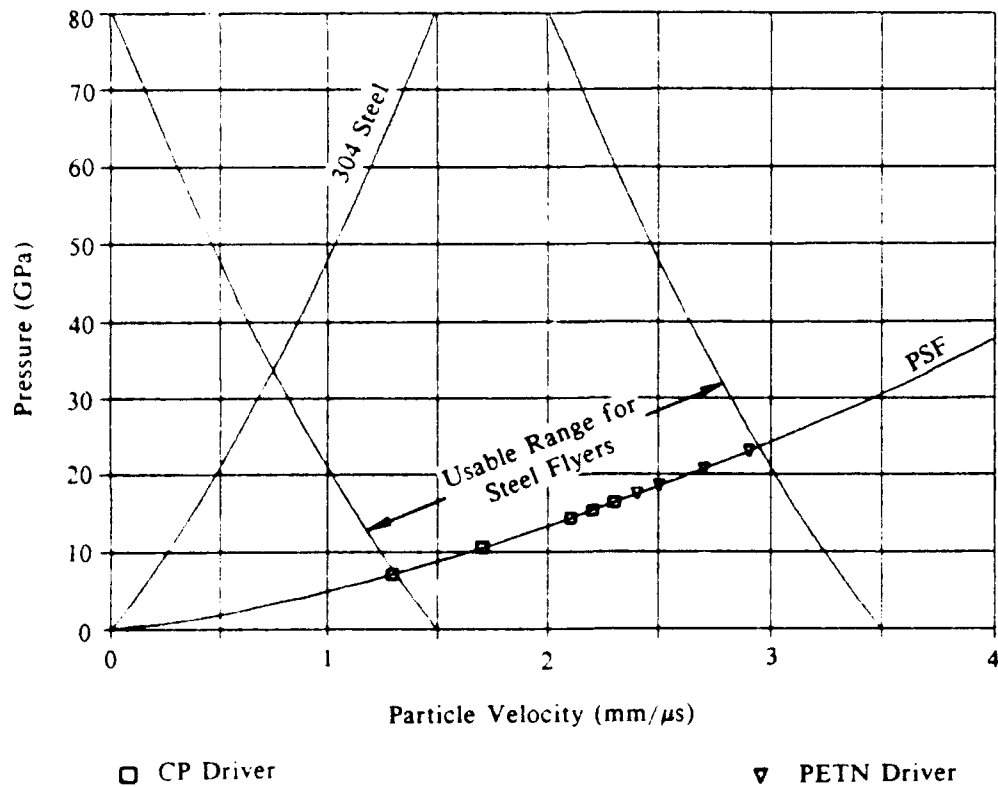


Figure 7. PSF Hugoniot (Flyer Impact)



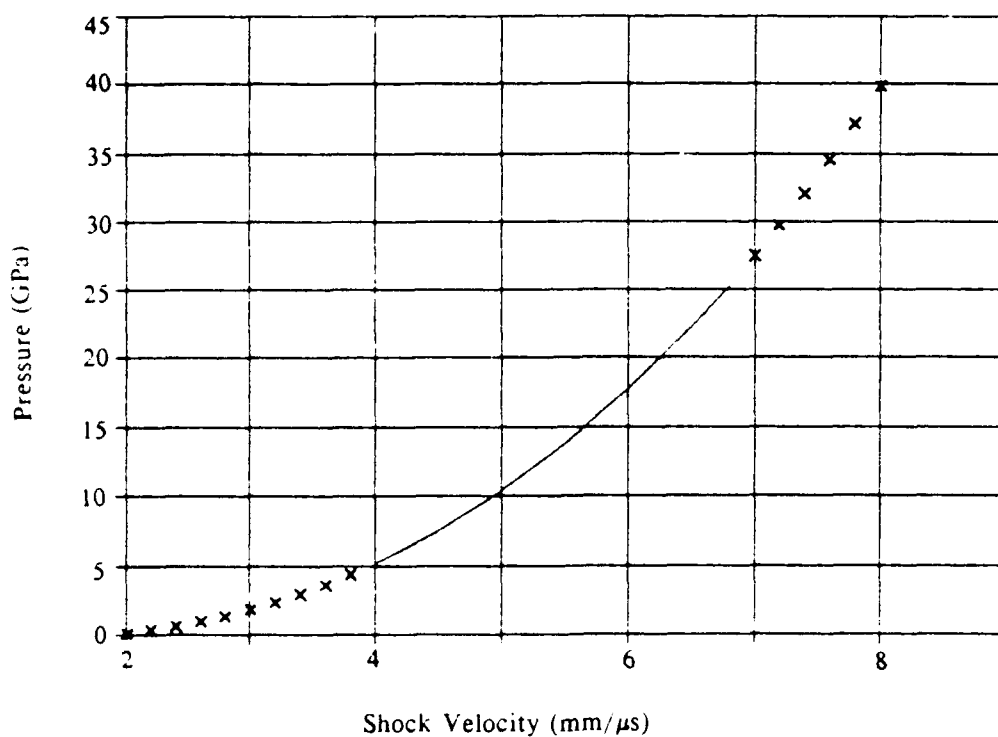


Figure 8. Usable Range for PSF SIP Gauges

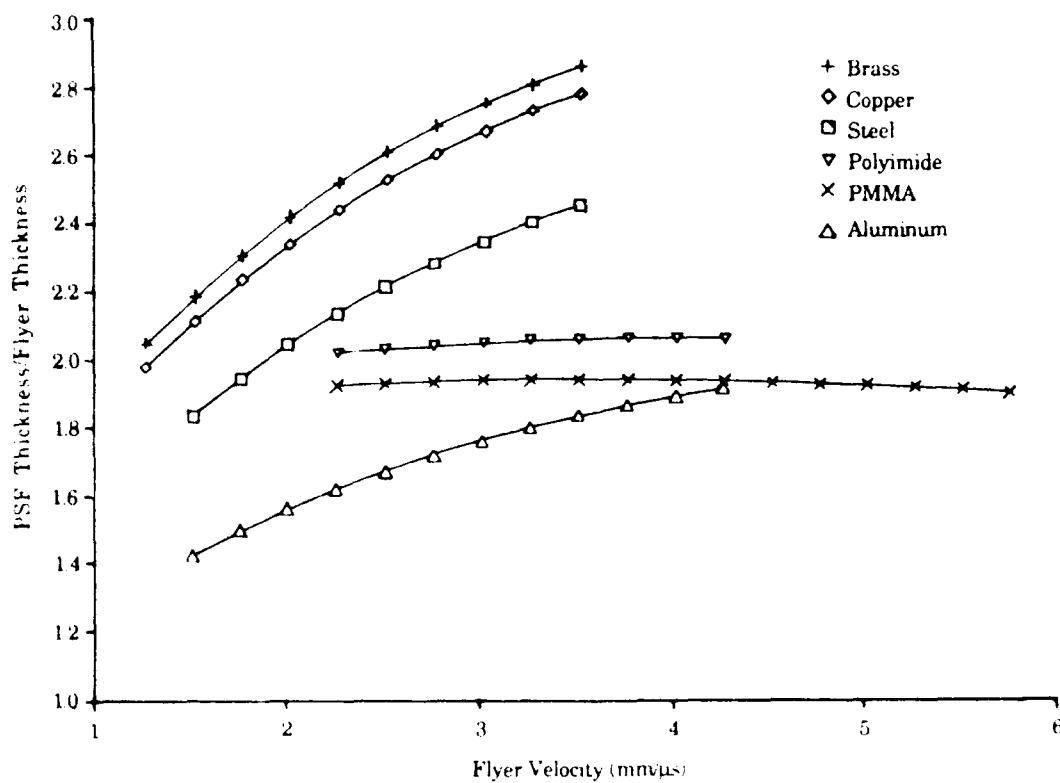


Figure 9. Optimum PSF Gauge Thickness for 100 Percent Pressure Pulse Width

A series of PSF gauges were fired at temperatures ranging from -54 to 74°C. CP and PETN drivers were used to provide flyer velocities in the range of 2.0 to 3.5 mm/μs. The gauges functioned normally, with only a slight decrease in polarization current at the extreme temperatures.

## CONCLUSIONS

Due to its favorable operating region, the PSF SIP gauge is a good candidate for testing explosive components producing flyers in the following ranges:

Flyer Material	Velocity Range (mm/μs)
Steel, copper, or brass	1.5 - 3.5
Aluminum	1.8 - 4.2
Polymer	2.7 - 6.0

Two-dimensional shock effects tend to round off the otherwise sharp features of polarization current waveforms. Therefore, for specific applications, the gauge electrode geometry should be tailored closely to flyer dimensions. Close tolerances are achieved by photoetching or laser etching after the metalization process. Optimum gauge thickness is determined by matching the shock transit time in PSF with the pressure pulse width expected. The substrate should be a material which provides a reasonably good shock impedance match to avoid reflections in the gauge.

A numerical root-solving method may be used to find flyer shock parameters, when the  $U_s - U_p$  relationship of the flyer material is nonlinear.

## ACKNOWLEDGEMENT

The authors gratefully acknowledge the assistance of R. M. Meighan of Pennwalt Corporation; W. K. Cline, T. O. Meyer, R. W. Ashcraft, and A. V. Lucero of Mason & Hanger-Silas Mason Co., Inc.; and R. A. Graham and J. H. Gieske of Sandia National

Laboratories. The diligent efforts of firing technicians at the Pantex and Mound DOE Facilities are also appreciated.

## REFERENCES

1. Eichelberger, R. J. and Hauver, G. E., "Les Ondes De Detonation," Editions du Centre National de la Recherche Scientifique, 15 Quai Anatole France, Paris VII, 1962, p. 363.
2. Hauver, G. E., J. Appl. Phys., Vol 36, 1965, p. 2113.
3. Ijsselstein, R. R., "A Simple Shock Pressure Transducer for Measuring the Performance of Explosives and Explosive Devices," Proc. 12th Symp. Explos. Pyrotech., 1984, p. 3-89.
4. Graham, R. A., "The Electrical-To-Chemical Connection," *Shock Waves in Condensed Matter*, American Institute of Physics, NY, 1982, p. 52.
5. Union Carbide Engineering Polymers, Technical Bulletin No. F-42072H, Udel™ Polysulfone Product Data, Union Carbide Corporation, 270 Park Avenue, NY, 1980.
6. "High Velocity Impact Phenomena," Edited by R. Kinslow (Academic, NY, 1970), Appendix E, p. 530.
7. LASL Shock Hugoniot Data, Edited by S. P. Marsh, University of California Press, Berkeley, CA, 1980.
8. S. A. Sheffield and D. D. Bloomquist, "Low Pressure Hugoniot Cusp in Polymeric Materials," *Shock Waves in Condensed Matter*, American Institute of Physics, NY, 1982, p. 57.
9. Gieske, J. H., "Longitudinal and Shear Velocity Measurements in Udel 1700 Polysulfone Plastic as a Function of Temperature," *Nondestructive Test Report*, Sandia National Laboratories, Albuquerque, NM, 1988.

## DISCUSSION

**FRANK DAVIES**

General Research Corp.

1. What is the inaccuracy associated with the assumption that the average shock velocity equals the shock velocity at the impact face?
2. Have the wave propagation characteristics of the polymers at low impact stresses been defined?
3. Are there any elastic/plastic, drain rate, or dispersion effects that modify the shape of the propagated stress wave?

### REPLY BY K. K. KUHRITS

The method used to analyze the SIP records is derived from the Rankine-Hugoniot jump equations and is, therefore, subject to the inaccuracies associated with those equations. I am not aware of any studies done to examine the details of shock wave propagation in the polysulfone gage material.

## DISCUSSION

**A. van der STEEN**, Prins Maurits Lab.  
Rijswijk, The Netherlands

1. Did you try to decrease the diameter of the gauge and what is the effect on the signal?

2. Did you try to measure detonation pressures in explosives with the gauge?

### REPLY BY K. K. KUHRITS

Decreasing the gage diameter can lead to problems with lateral shock propagation in the gage material. Preliminary testing indicates that the Polysulfone SIP gage will be suitable for use in direct contact with explosives.

## DISCUSSION

**BARRY NEYER**, EG&G Mound  
Applied Technologies

1. How could you distinguish between a curved fast flyer and a slower planar flyer? Both would show a slightly longer transit time than a flat fast flyer.
2. How reproducible is the voltage output?

### REPLY BY K. K. KUHRITS

We are currently performing testing to quantitatively evaluate the effect of flyer planarity on the obtained SIP gage record. Due to the small thickness of the polysulfone gage material compared to the curvature of a standard flyer, we do not expect the planarity of the flyer to have a significant effect on the shock velocity in the gage material.

The maximum output voltage obtained is generally reproducible to a 10 percent range.

# THE EFFECTS OF INERT WALLS ON THE VELOCITY OF DETONATION IN EDC35, AN INSENSITIVE HIGH EXPLOSIVE

G. Eden and R. A. Belcher  
MOD (PE), Atomic Weapons Establishment  
Aldermaston, Reading RG7 4PR  
Berkshire, ENGLAND

*Experiments at ambient temperature are reported which quantify the effect on detonation velocity in EDC35, due to an adjacent wall of (a) brass and (b) beryllium.*

*A streak camera monitored arrival times of shock and detonation waves at the end of a 25 mm thick slab of explosive sandwiched between walls of the two inerts. The lengths of beryllium were varied between 20 mm and 100 mm, keeping the EDC35 and brass lengths constant. The streak record shows that in the beryllium, the shock advances ahead of the detonation front, and apparently induces a higher detonation velocity along that wall. The shock velocity in the brass is slower than the detonation wave, and the local detonation velocity is apparently retarded. The effects are quantified by measurement of the absolute velocity along the brass/EDC35 interface using a line of coaxial electric probes, and the relative velocities were deduced from relative arrival times at the end of the charge assembly.*

## INTRODUCTION

When a detonation wave in explosive runs along an adjacent wall of inert material, the shock velocity ( $U$ ) generated in the wall is generally lower than the detonation velocity ( $D$ ), and the shock trails behind the detonation front at an angle to the interface of  $\sin^{-1}(U/D)$ . With certain combinations of explosive and inert,  $U$  can be chosen to exceed  $D$ , and there is a small amount of evidence suggesting that in this case the wall transmits a disturbance back into the undetonated explosive just ahead of the detonation front, and that this disturbance affects the local velocity of detonation (References 1, 2).

The experiments reported here were designed to show the extent of this effect on the detonation velocity in EDC35 when adjacent to beryllium.

<u>Materials</u>	<u>Density</u>
EDC35	
TATB/Kel F 95/5	1.90 gcm <sup>-3</sup>

## Materials

Composition B  
- RDX/TNT 60/40

Beryllium S65-

Brass -

## Density

1.66 gcm<sup>-3</sup>

1.844/1.846 gcm<sup>-3</sup>

8.32 gcm<sup>-3</sup>

## EXPERIMENTAL ASSEMBLY

Figure 1 shows the assembly which consists of a 25 mm thick EDC35 charge (A) sandwiched between a 9.3 mm thick beryllium S65 plate (B) and a 10 mm thick brass plate (C). The charge was initiated by a 76.2 mm line initiator, with a 12.7 mm square cross section Composition B/perspex smoothing system (D), followed by a 25 mm square cross section Composition B booster (E). A brass plate (F) was used with the beryllium to balance the length of the sandwich. Coaxial pin probes were fitted through the brass plate at 10 mm intervals on the center line, in contact with the explosive, to measure the detonation velocity.

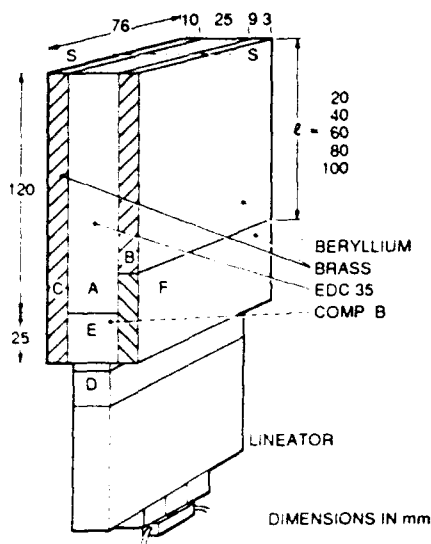


Figure 1. Experimental Assembly

## EXPERIMENTAL METHOD

The basic method used is as described in Reference 1. The slit of an S4 rotating mirror streak camera was focussed on the line marked S in Figures 1 and 2 to record the frustration of total reflection of light at the base of the glass block on the end of the charge assembly.

To follow the development of wave shapes and separations, the length of beryllium, 1, was varied between experiments keeping the length of explosive constant.

A 360 mm lens was used at an aperture of f5.5; the camera speed was approximately 3200 cycles/s, giving a writing speed on the film of the order of 20 mm/ $\mu$ s. The slit width in the camera was 0.051 mm. The film used was either HP5 developed in Microphen fine grain developer or XP1 developed in the XP1 or C41 color process. All experiments were fired at ambient temperature (15 to 20°C).

## EXPERIMENTAL RESULTS

Figure 3 shows diagrammatically the interpretation of the streak camera record reproduced in Figures 4 to 8, and Table 1 lists relative times of the various features on each trace.

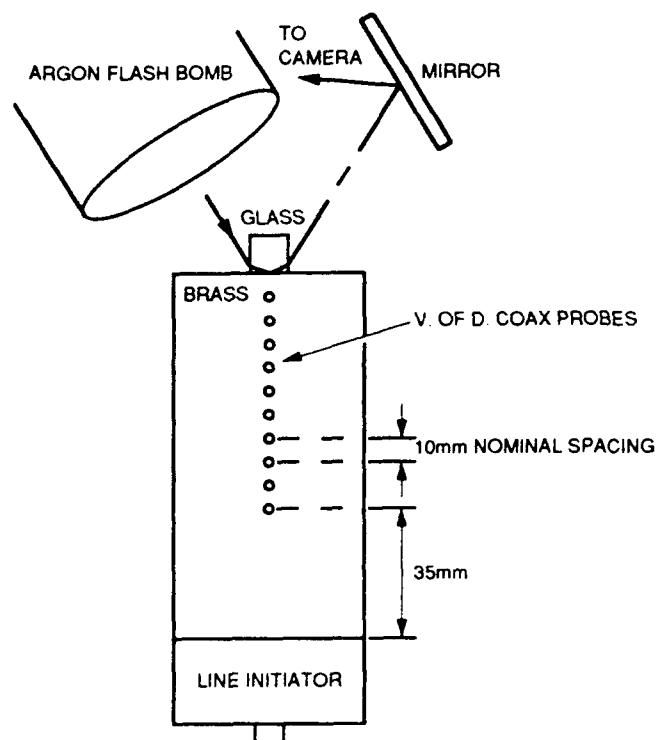


Figure 2. Side Elevation

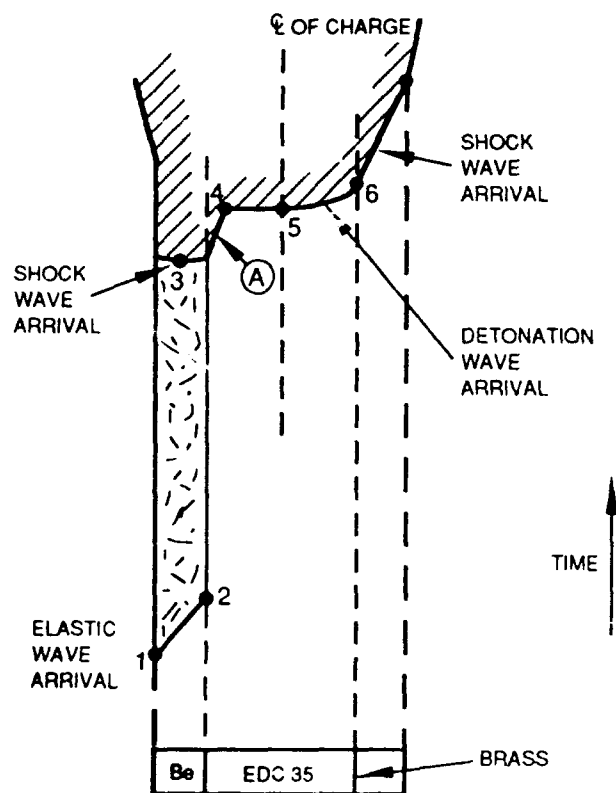


Figure 3. Interpretation of S4 Records

Table 1

Shot Number	$\ell$ mm	FEATURE NUMBER					
		1	2	3	4	5	6
		Beryllium Elastic	Beryllium Elastic	Beryllium Shock	Detonation (Beryllium Wall)	Detonation on Center Line	Detonation (Brass Wall)
3	100	-4.603	3.847	-0.568	-0.071	0	0.149
4						0	0.152
7	80	3.082	3.435	-0.603	0.035	0	0.180
9						0	0.145
8	60	-2.198	1.756	-0.395	-0.023	0	0.163
10						0	0.162
5	40	-1.047	0.976	-0.274	+0.028	0	0.170
6						0	0.150
11	20	*	*	-0.040	+0.085	0	0.144
12						0	0.137
		Mean 0.156 s.d. 0.013					

\* Indistinguishable from Feature 3

Times  $t \pm 0.002$  in Microseconds of Arrival of Features Numbered as in Figure 3, Relative to Detonation on Center Line of Charge (Feature 5)



Figure 4. S11

20mm Beryllium

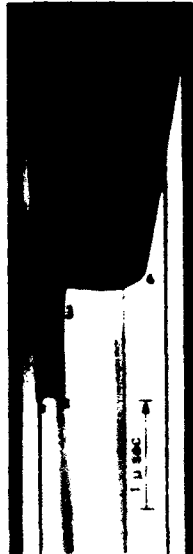


Figure 5. S5

40mm Beryllium

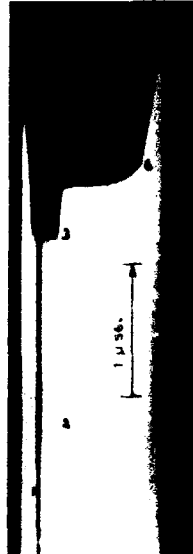


Figure 6. S8

60mm Beryllium



Figure 7. S7

80mm Beryllium



Figure 8. S3

100mm Beryllium

Generally, the elastic wave in the beryllium can be seen as an early partial change in reflectivity, followed by the plastic wave in beryllium which extinguishes the partial reflection. The shape of the detonation wave is clearly affected by the material adjacent to the EDC35 and is, consequently, not symmetric about its center line. The latest wave to arrive is the shock, which sweeps across the surface of the brass.

### Shock in EDC35

On most of the shots, an effect marked A in Figure 3 can be seen, which indicates some deformation caused by the advanced shock in the beryllium. The shocked beryllium must tend to expand laterally, but whether this trace is caused by the edge of the metal expanding into the explosive or is the shock front moving through the EDC35 cannot be judged from the appearance of the trace alone. However, the velocities derived for the disturbance, 2.8 to 3.1 mm  $\mu\text{s}^{-1}$ , in Appendix A strongly indicate that the trace represents the velocity of a 16 to 23 Kb compression wave in EDC35. (No unreacted shock data exists for EDC35, so this pressure has been estimated from extrapolation of data given in Reference 3 for PBX-9502 of initial density 1.8915 gcm<sup>3</sup>.) If the trace were actually the velocity of the beryllium plate edge, it would be overdriving the EDC35 to a pressure above even its Chapman-Jouguet pressure, and also representing an unrealistically high pressure of shock in the beryllium.

### Velocity of Detonation Along EDC35/Brass Interface

Velocities of detonation ( $D_{Br}$ ) adjacent to the brass wall were obtained from least squares fits to  $s$ ;  $t$  data where  $s$  is the distance of the probe from the line initiator (see Figure 9), and  $t$ , its time of operation. Results for all rounds are shown in Table 2.

Mean velocity of detonation along EDC35/brass interface

$$D_{Br} = 7.66 \pm 0.03 \text{ mm } \mu\text{s}^{-1}$$

This value (for a cylindrically divergent wave) may be compared with the velocity derived from the Cylinder Test (a plane wave

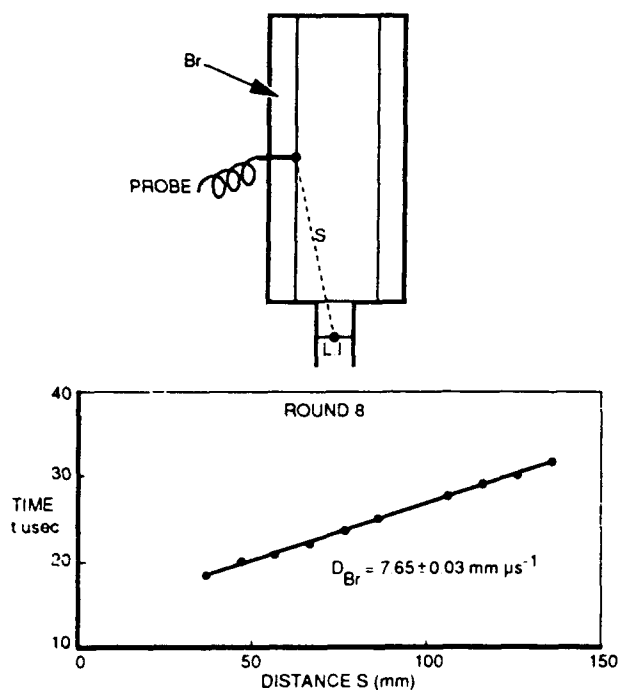


Figure 9. Velocity of Detonation  $D_{Br}$

Table 2. Detonation Velocity Along EDC35/Brass Interface

Round Number	Detonation Velocity mm $\mu\text{s}^{-1}$	s.d. mm $\mu\text{s}^{-1}$	Weighted Mean mm $\mu\text{s}^{-1}$	s.d. mm $\mu\text{s}^{-1}$
3	7.69	0.04		
4	7.67	0.02		
5	7.64	0.02		
6	7.60	0.02		
			7.66	0.03
8	7.65	0.03		
9	7.71	0.02		
10	7.65	0.02		
11	7.66	0.03		
12	7.66	0.02		

initiated stick, 25.4 mm diameter),  $7.70 \pm 0.02$  mm  $\mu\text{s}^{-1}$ .

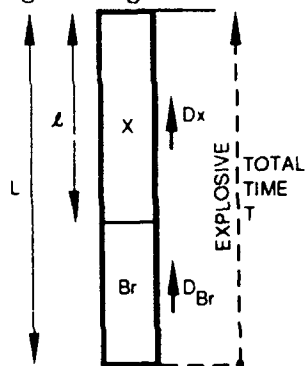
### Velocity of Detonation Along EDC35/Beryllium Interface

From Table 1, we have plotted in Figure 10 the time  $t$  by which the detonation along

the inert walls (Features 4 and 6), lags behind or is ahead of the detonation at the center of the charge (Feature 5). Even a perfect Huygens construction from the initiator would lag a little (0.064  $\mu\text{s}$ ) at the edge of the charge, because the line initiator did not completely cover the base area of the Composition B charge.

Considering the scatter on the data, the following simple analysis method was adopted:

The composite wall of fixed length  $L$  consists of a length  $\ell$  of material X, the remaining length being brass.



If the local velocity of detonation in the explosive adjacent to the brass is  $D_{Br}$  and adjacent to material X is  $D_X$ , then the time for the detonation to move along the whole length of the wall

$$T = \frac{L - \ell}{D_{Br}} + \frac{\ell}{D_X}$$

When  $\ell = 0$ ,

$$T_0 = \frac{L}{D_{Br}}$$

Defining  $\delta T = T_0 - T$

$$= \frac{\ell}{D_{Br}} - \frac{\ell}{D_X}$$

then

$$D_X = \left( \frac{\ell}{\ell - D_{Br} \cdot \delta T} \right) D_{Br} \quad (1)$$

where  $\delta T$  is the interval of time between the detonation arrival along the composite wall and the detonation arrival along the brass wall. Values of  $\delta T$  are shown by the right-

hand ordinate scale in Figure 10 whose origin is set at the mean of the ten results at  $\ell = 0$ , and is, therefore, subject to a standard deviation of 0.013  $\mu\text{s}$  (see Table 1, Feature 6).

Reading from the eye-fitted curve in Figure 10, after 100 mm travel along beryllium, the EDC35 detonation wave arrives  $0.23 \pm 0.01 \mu\text{s}$  (i.e.,  $\delta T$ ) earlier than a wave along a brass wall.

From Equation (1),

$$D_{Be} = 7.80 \pm 0.03 \text{ mm } \mu\text{s}^{-1}$$

Because the curve appears to be nonlinear, a slightly higher result is obtained for lower values of  $\ell$ , e.g.,  $7.84 \text{ mm } \mu\text{s}^{-1}$  for  $\ell = 50 \text{ mm}$ , indicating a decreasing effect on velocity of detonation with distance of travel.

### The Huygens Velocity of Detonation

The time interval,  $t$  in Figure 10, between detonation arrival at the center of the top face of the charge and the edge of the charge in contact with the brass, is denoted by the points plotted at  $\ell = 0$ . This interval is considerably greater than that to be expected if the detonation wave developed according to Huygens propagation from the PETN pellets in the line initiator. Assuming a detonation velocity of  $\approx 7.7 \text{ mm } \mu\text{s}^{-1}$ , a Huygens construction would result in a time difference

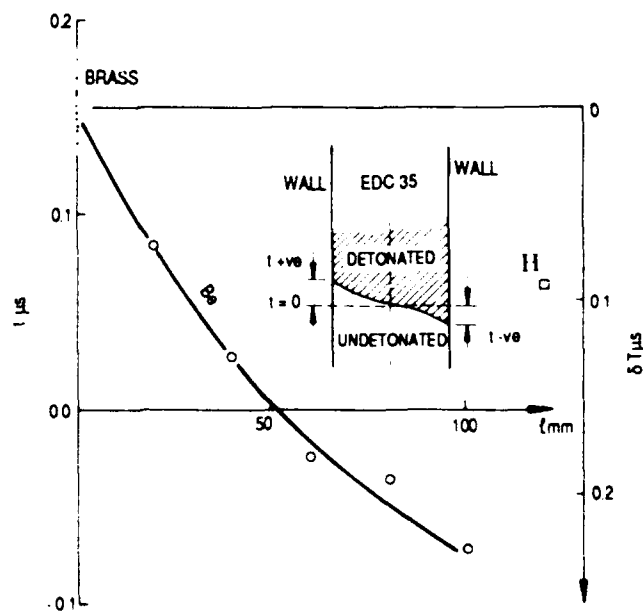


Figure 10. Time  $t$  of Detonation Wave Arrival Adjacent to Inert Wall Length  $\ell$



of  $t = 0.064 \mu\text{s}$ . The length of EDC35 is 120 mm, and this point is plotted as (H), the Huygens point, in Figure 10.

As before, we can now use Equation (1) to obtain a Huygens velocity of detonation,  $D_H$ , which is the velocity of propagation down the center plane of the charge because, after travelling  $\ell = 120$  mm along the EDC35 brass interface, the Huygens wave would arrive  $\delta T = 0.092 (\pm 0.01) \mu\text{s}$  earlier than the observed wave.

Hence,

$$D_H = \left( \frac{120}{120 - D_{Br} \cdot \delta T} \right) D_{Br} = 7.71 \pm 0.03 \text{ mm } \mu\text{s}^{-1}.$$

### Observed Detonation Velocities Compared with Huygens $D_H$

Instead of comparing the numerical values of the above velocities of detonation, whose absolute values are subject to the spread of results at  $\ell=0$ , a more sensitive ratio is obtained by rearranging Equation (1) to

$$\frac{D_X}{D_{Br}} = \frac{\ell_X}{\ell_X - D_{Br} \cdot \delta T_X} \quad (2)$$

and combining it with the special case of the previous section,

$$\frac{D_H}{D_{Br}} = \frac{\ell_H}{\ell_H - D_{Br} \cdot \delta T_H} \quad (3)$$

to give

$$\frac{D_X}{D_H} = \frac{\ell_X}{\ell_H} \cdot \frac{\ell_H - D_{Br} \cdot \delta T_H}{\ell_X - D_{Br} \cdot \delta T_X} \quad (4)$$

Where

$$\ell_H = 120 \text{ mm}$$

$$\delta T_H = 0.092 \pm 0.01 \mu\text{s}$$

$$D_{Br} = 7.66 \pm 0.03 \text{ mm } \mu\text{s}^{-1}$$

$$D_H = 7.71 \pm 0.03 \text{ mm } \mu\text{s}^{-1}$$

thus

$$D_{Br} = 101.2 \pm 0.1\% D_H$$

$$D_{Br} = 99.4 \pm 0.1\% D_H$$

### The Elastic Wave in Beryllium

In Appendix B, the time  $T(\ell)$  taken for a disturbance to traverse the length  $\ell$  of the beryllium is expressed in terms of

- (a) the geometry of the experiment,
- (b) the time of arrival of the disturbance relative to the center line detonation, and
- (c) the detonation velocity  $D_{Br}$ :

$$T(\ell) = \frac{L - k \cdot x(\ell)}{k D_{Br}} - \{t(5) - t(B)\} \quad (5)$$

where  $k = D_H/D_{Br} = 1.006$  from the previous section and  $t(B)$  = arrival time of Feature B.

Taking a mean arrival time of the elastic wave as  $t(B) = \frac{1}{2}(t(1) + t(2))$  from Table 1, values of  $T(\ell)$  are shown in Table 3.

Corresponding values of  $\ell$  and  $T(\ell)$  are plotted in Figure 11, and a weighted linear least squares fit through them gives

$$T(\ell) = a + b \cdot \ell \mu\text{s} \quad (6)$$

where

$$a = 0.826 \pm 0.006 \mu\text{s}$$

$$b = 0.0777 \pm 0.0003 \mu\text{s mm}^{-1}$$

i.e., the velocity of the observed earliest disturbance is

$$c = b^{-1} = 12.87 \pm 0.06 \text{ mm } \mu\text{s}^{-1}.$$

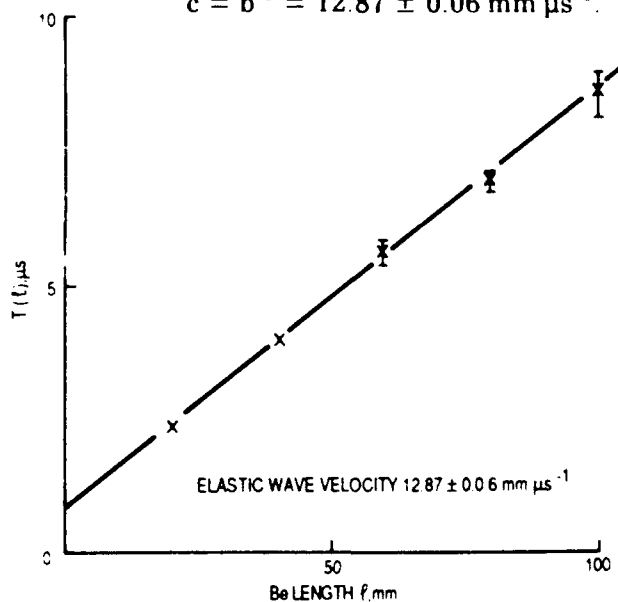


Figure 11 Length of Beryllium  $\ell$  Versus Elastic Wave Transit Time  $T(\ell)$

Table 3. Elastic Wave in Beryllium

$\ell$ mm	$x(\ell)$ mm	$t(1)$ $\mu s$	$t(2)$ $\mu s$	$t(B)$ $= (t(1) + t(2))/2$	$t(5)$ $\mu s$	$T(\ell)$ $\mu s$
100	59.08	-4.60	-3.85	$-4.23 \pm 0.37$	0	$8.52 \pm 0.42$
80	78.73	-3.08	-3.44	$-3.26 \pm 0.18$	0	$6.93 \pm 0.21$
60	98.52	-2.20	-1.76	$-1.98 \pm 0.22$	0	$5.62 \pm 0.24$
40	118.38	-1.50	-0.98	$-1.02 \pm 0.03$	0	$3.99 \pm 0.05$
20	138.284	-0.04	-0.04	-0.04	0	$2.37 \pm 0.01$

This slope is in accord with previously reported values (Reference 4) for  $C_L$ , the plane wave longitudinal sound velocity in Table 4, in which  $U_{FS}$  is the corresponding free surface velocity.

Reference 4 used explosively generated plane waves. The materials were hot pressed sintered powders, as are the materials used in these experiments.

The elastic waves generated in the experiments reported here are unlikely to be plane, and it may be more appropriate to compare them with the thin rod velocity,

$$C_R = \left( \frac{E}{\rho_0} \right)^{1/2}$$

where  $E$  = Young's modulus. But since the plane sound velocity,

$$C_L = \left( \frac{E}{\rho_0} \cdot \frac{(1-\sigma)}{(1+\sigma)(1-2\sigma)} \right)^{1/2}$$

we see that the difference between them is governed by the magnitude of Poisson's ratio,  $\sigma$ , which is between 0.05 and 0.06 which, at most, would give a difference of only 0.4 percent between  $C_L$  and  $C_R$ .

We propose the following explanation of the intercept "a" on the  $T(1)$  axis of Figure 11. Although the surface finish on the beryllium face in contact with the glass was controlled at 0.5  $\mu m$  in all samples, two flat surfaces in normal mechanical contact can be separated by a small distance because of point contacts.

Taking the value of free surface velocity generated by the elastic wave from Table 4 as  $0.033 \pm 0.007 \text{ mm } \mu s^{-1}$ , the time interval (from Equation (6))  $a = 0.083 \mu s$  would be fully accounted for if there had been a gap of 0.027 mm (0.001 in) between the beryllium and glass. This is consistent with the difference between the initial mechanical contact of the two surfaces (say 0.02 to 0.05 mm separation) and the optical contact (say a wavelength of light separation) at which the total reflection of light is frustrated. Similarly, we may account for the non-reproducible shape of the elastic wave arrival contours on the streak camera traces by assuming that the contact gap between glass and beryllium could have been very slightly nonparallel.

The arrival times of the elastic wave in beryllium from Table 3 are plotted in Figure 12, and are compared with the full spread of  $C_L$  values quoted in Table 4 from other alloys of Be plus a conceivable spread of contact gaps from 0.02 to 0.05 mm, which would give intercepts on the  $T(1)$  axis of 0.6 and 1.5  $\mu s$ , respectively.

Since the elastic and shock waves in the beryllium are continuously drawing ahead of the detonation wave and losing energy laterally in the process, the system is not in equilibrium, and this may produce non-linear effects in longer specimens.

The elastic wave is generated by a shock wave, so we assume that its initial amplitude is the

Table 4. Sound Velocity and Associated Free Surface Velocity in Beryllium

Material	Density $\rho_0 \text{ g cm}^{-3}$	Experiment Type	$C_L$ $\text{mm } \mu\text{s}^{-1}$	$U_{FS}$ $\text{mm } \mu\text{s}^{-1}$	Reference
S200D	1.845	EPW	13.80	$0.031 \pm 0.004$	5
			$13.79 \pm 0.1$		
1400	1.856	EPW	$13.35 \pm 0.1$	$0.036 \pm 0.004$	5

Table 5. Shock in Beryllium

$\ell$ mm	$x(\ell)$ mm	$t(B) =$ $t(3) \mu\text{s}$	$t(5)$ $\mu\text{s}$	$T(\ell)$ $\mu\text{s}$
100	59.08	-0.57	0	12.18
80	78.73	-0.60	0	9.59
60	98.52	-0.40	0	7.20
40	118.38	-0.27	0	4.74
20	138.28	-0.04	0	2.37
0*	157.7	$+0.16 \pm 0.01^*$	0	0.02/0.05

\* For  $\ell = 0$ , the mean time of arrival of Feature 6 was taken from Table 1, i.e.,  $t(B) = t(6)$  in Equation (3)

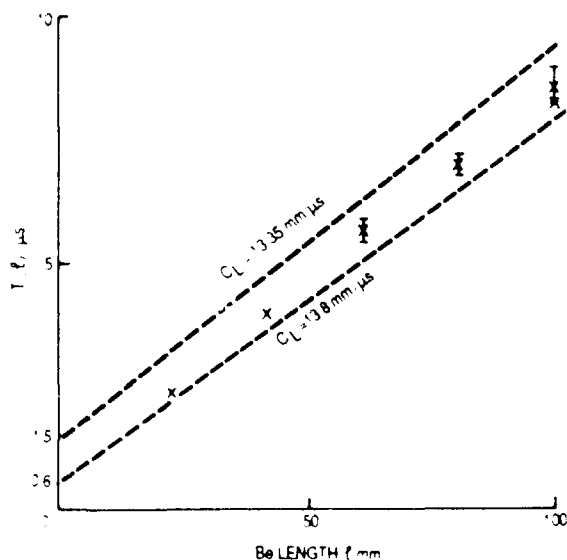


Figure 12 Elastic Wave Arrival Times Compared With Spread of Reference 4 Values Plus Conceivable Contact Gaps 0.02 to 0.05 mm

magnitude of the Hugoniot Elastic Limit (HEL), 3.8 Kb (Reference 4).

### The Shock Wave in Beryllium

Using Equation (3) from Appendix B and substituting values from Feature 3, Table 1 for  $t(B)$ , the values for  $T(\ell)$  are given in Table 5.

Corresponding values of  $\ell$  and  $T(\ell)$  are plotted in Figure 13 from which a linear least squares fit minimizing T errors, gives:

Shock velocity in beryllium =  $8.22(5) \pm 0.03 \text{ mm } \mu\text{s}^{-1}$ .

An estimate of the shock pressure using the linear relationship between shock and particle velocity quoted in Reference 6 for beryllium

$$U_S = 8.056 + 1.145 U_p \text{ mm } \mu\text{s}^{-1}$$

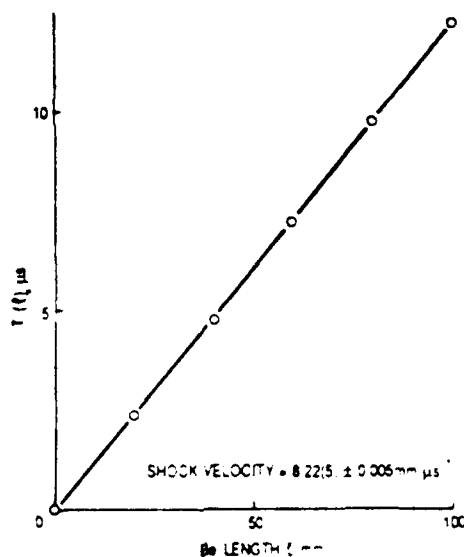


Figure 13. Length of Beryllium  $\ell$  Versus Shock Transit Time  $T(\ell)$

gives:

Shock pressure = 22 Kb above HEL

The error bar on this value is probably large since the pressure lies outside the range of the Reference 6 data

## CONCLUSIONS

The detonation velocity along an EDC35 inert interface is affected by the choice of inert material. For brass against a 25 mm thick charge, the velocity of detonation ( $V$  of  $D$ ) is reduced by  $0.6 \pm 0.1$  percent. For beryllium the  $V$  of  $D$  is increased by  $1.2 \pm 0.1$  percent.

The enhancement of  $V$  of  $D$  with beryllium is associated with a thin layer of undetonated EDC35, which is preshocked by the advance beryllium shock just before the detonation front reaches it.

The amplitude of the beryllium shock estimated from its velocity,  $8.22(5) \pm 0.03$  mm  $\mu$ s $^{-1}$ , is  $22 \pm 6$  Kb above the HEL of 3.8 Kb

The amplitude of the preshock in the EDC35 estimated from its velocity  $(2.9(5) \pm 0.15(5))$  mm  $\mu$ s $^{-1}$  is  $15 \pm 5$  Kb

The low amplitude of the beryllium shock allows a two wave structure to develop,

and an elastic wave precedes it at a velocity of about 12.9 mm  $\mu$ s $^{-1}$ . Although this must be presumed to start at the HEL and is clearly measurable up to at least 30 mm ahead of the detonation front, it has no visible effect on the EDC35, probably because Poisson's ratio for the beryllium is near zero making the transverse expansion very small.

## ACKNOWLEDGEMENTS

The authors gratefully acknowledge the support received from P. W. J. Moore and B. D. Lambourn, and they thank G. G. Dale and G. Reece for their invaluable assistance with the experiments.

## REFERENCES

1. Eden, G. and Wright, P. W., "A Technique for the Precise Measurement of the Motion of a Plane Free Surface," *Proceedings of Fourth Symposium (International) on Detonation*, US Naval Ordnance Laboratory, White Oak, MD, ACR 126, 12-15 Oct 1965, pp. 573-583.
2. Neal, T. R., "Perpendicular Explosive Drive and Oblique Shocks," *Proceedings of Sixth Symposium (International) on Detonation*, Coronado, CA, ACR 221, 24-27 Aug 1976, pp. 602-611.
3. Dick, J. J.; Forest, C. A.; Ramsay, J. B.; and Seitz, W. L., "The Hugoniot and Shock Sensitivity of a Plastic-Bonded TATB Explosive PBX 9502," *Journal of Applied Physics*, Vol. 63, No. 10, 1988, p. 4881.
4. Eden, G. and Smith, C. P. M., "Elastic-Plastic Behaviour of Porous Beryllium," *Proceedings of Fifth Symposium (International) on Detonation*, Pasadena, CA, ACR 184, 18-21 Aug 1970, pp. 467-475.
5. Reference 4, Figure 6.
6. Van Thiel, M., Editor, *Compendium of Shock Wave Data*, UCRL-50108, Vol. 1, Sec A 1

Copyright © Controller HMSO, London, 1989.

Table A-1

Experiment	Beryllium Length (mm)	$\theta^\circ$	$\omega$ (mm $\mu\text{s}^{-1}$ )	M	V (mm $\mu\text{s}^{-1}$ )
3	100	$5\frac{1}{2}/6$	32.19	$\frac{40.6}{38.02}$	2.90/3.17
7	80	4	48.76	$\frac{45.4}{38.02}$	2.86
8	60	$5\frac{1}{2}/6$	48.40	$\frac{45.0}{38.02}$	3.94/4.30
5	40	$4\frac{1}{2}/5$	31.79	$\frac{37.3}{38.02}$	2.55/2.84
11	20	$4\frac{1}{2}$	47.97	$\frac{51.5}{38.02}$	2.79

## APPENDIX A

$$v = \omega \tan \theta \quad (1)$$

### Feature A

Measurement of Feature A was made by measuring angle  $\theta$  on magnified transparency prints of the original S4 traces.

It moves a distance  $y$  in time  $t$

$$\text{where } y = v \cdot t \quad (2)$$

$$\text{and } t = \frac{x}{\omega} \quad (3)$$

If the magnification of the print,

$$M = \frac{\text{print dimension}}{\text{true dimension on object}}, \text{ then the}$$

effect moves across the object a true distance  $Y$ , in time  $t$ , where

$$Y = \frac{y}{M} \quad (4)$$

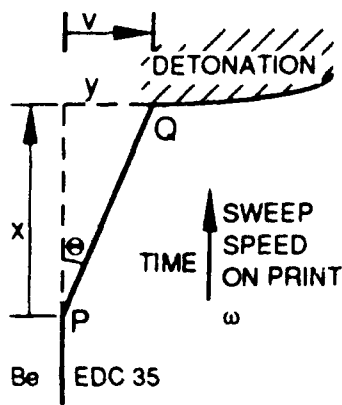
The effect causes a displacement from P on the beryllium/EDC35 interface, to Q where the detonation obscures further observations.

If  $x$  and  $y$  are distances measured on the print and  $\omega$  is the sweep speed on the print, then the velocity of the effect across the print perpendicular to the sweep direction is

Thus, from (1) to (4), the true velocity of the effect "A" laterally across the object is,

$$V_{\text{TRUE}} = \frac{\omega \tan \theta}{M}$$

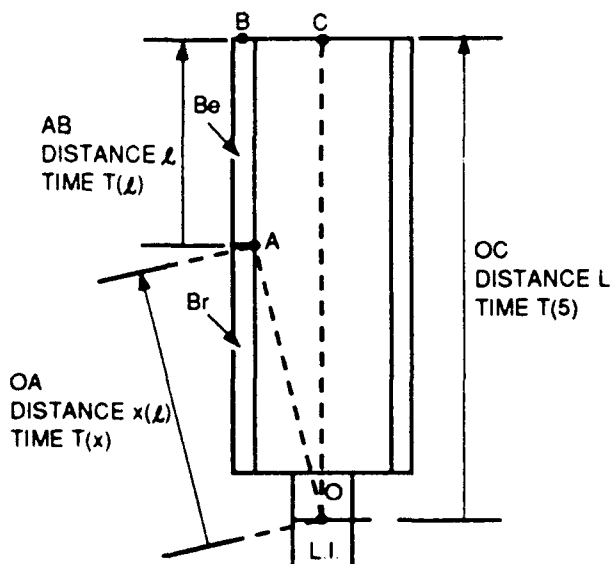
$$\begin{aligned} \text{Mean } V &= 2.84 \text{ (omitting 8)} \\ \text{or Mean } V &= 3.10 \text{ (including 8)} \end{aligned}$$



## APPENDIX B

## Progress of a Disturbance in the Beryllium

The event at C is designated as Feature 5 in Table 1, so the time from 0 to C is labelled T(5). Let the time of events at B and C relative to an arbitrary time datum be



$t(B)$  and  $t(5)$  respectively, so that values of  $t(B)$  and  $t(5)$  can be taken directly from Table 1. Then

$$t(5) - t(3) = T(5) - \{\Gamma(x) + T(\ell)\} \quad (1)$$

where

$$T(5) = \frac{L}{D_H} \text{ by definition of } D_H$$

(from the section, The Huygens Velocity of Detonation),

$$T(x) = \frac{x(\ell)}{D_{Br}} \text{ by definition of } D_{Br}.$$

(from the section, Velocity of Detonation  
Along EDC35/Brass Interface)

Hence,

$$T(\ell) = \frac{L}{D_H} - \frac{x(\ell)}{D_{Br}} - \{t(5) - t(B)\} \quad (2)$$

Putting  $D_H = k \cdot D_{Br}$ 

$$T(\ell) = \frac{L - k \cdot x(\ell)}{k \cdot D_{Br}} - \{t(5) - t(B)\} \quad (3)$$

in which the value of  $k$  has been determined in the section, The Elastic Wave in Beryllium, and

$$x(\ell) = \{(L - \ell)^2 + W^2\}^{\frac{1}{2}}.$$

## DISCUSSION

**MICHAEL J. GEORGE**  
Los Alamos National Laboratory  
Los Alamos, NM

In 1975, in some early IIE tests, we observed similar effects regarding leading waves in beryllium, including elastic wave, plastic wave, and apparent leading detonation wave at the boundary. The geometry and diagnostics were quite different. Results without beryllium were also different with no leading waves.

## REPLY BY G. EDEN AND R. A. BELCHER

Thank you for your comments, and we are gratified to learn that the effects we have quantified here have been observed using different diagnostics. Using different materials but similar diagnostics in 1965, Eden and Wright (Reference 1) reported similar enhancement of detonation velocity of baratol adjacent to aluminium and of Comp B adjacent to beryllium. At that time, we attributed "effect A" to motion of the HE/metal boundary but we adhere now to the explanation given in the section, Shock in EDC35.

# EXPERIMENTAL AND NUMERICAL STUDY OF OBLIQUE INTERACTIONS OF DETONATION WAVES WITH EXPLOSIVE/SOLID MATERIAL INTERFACES

J. Aveillé, N. Carion, J. Vacellier, and J. M. Servas  
Commissariat à l'Energie Atomique  
Centre d'Etudes de Vaujours  
BP n°7 - 77181 Courtry, FRANCE

*This paper presents the results of experimental and numerical studies on oblique interactions of a detonation wave with an explosive/solid material interface for several incidence angles. We describe an experimental method which allows us to analyze the plane two-dimensional flow in oblique interaction.*

*In Section I of the Results, we study the interaction TATB/Copper; experimental results show a continuous set of solutions. Outside the regular refraction zone a large discrepancy appears with the results provided by the hydrodynamic theory as well as with those obtained with Lagrangian 2D-Code. Best results are obtained when the detonation front is treated with a burn model.*

*In Section II of the Results, the interaction of a detonation wave with an elastic-plastic material (alumina) is investigated. Two heterogeneous high explosives are used (TATB- and HMX-based compositions). The experimental results show that the adjacent medium affects the detonation front.*

## INTRODUCTION

The study of plane two-dimensional flows at the heterogeneous explosive solid medium interface shows some particular solutions depending both on the characteristics of the explosives and the material properties. Our purpose in this paper is the experimental and numerical analysis of the interaction appearing in a medium which is subjected to an oblique detonation wave.

In order to study the zones of the regular or irregular refractions given by hydrodynamic theory, we have used an experimental set-up which allows us to study this flow for different angles between the detonation front and the interface: from  $20^\circ$  to  $90^\circ$ .

We have studied two cases:

- a TATB-based explosive together with a dense material—copper.

- TATB- and HMX-based explosives together with a material (Alumina) which has a high longitudinal sound speed ( $C_L$ ).

The experimental study is connected on the one hand to a theoretical study where the flow is assumed to be plane, steady in the assumption of compressible fluid; and on the other hand to two-dimensional lagrangian numerical simulations.

## THEORETICAL ASPECTS OF OBLIQUE INTERACTIONS

Let us recall some considerations on the theoretical problem of oblique interaction of a detonation wave with a solid sample. Let us consider a solid specimen in contact with a detonating high explosive. A plane detonation front (D) is assumed to be inclined at an angle  $\eta$  to the undisturbed interface (Figure 1).

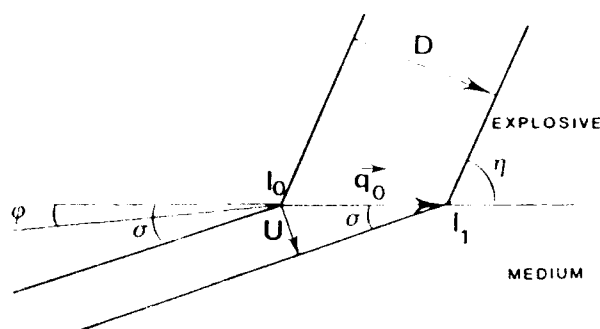


Figure 1. Oblique Interaction Explosive/Solid Medium

Dimensionally the inert specimen is assumed to be semi-infinite, while the assembly is infinite in the direction perpendicular to the drawing. Hence, no reflections occur within the specimen, and the flow in the detonation products and in the specimen is two-dimensional and steady in time.

The shock induced in the specimen due to the high pressure of the gases produced by detonation deflects the streamline in the specimen.  $U$  is the shock velocity inclined at angle  $\sigma$  to the interface. If a frame of reference is attached to the incidence point  $I$ , the flow speed,  $q_0$ , behind detonation front is defined as:

$$q_0 = \frac{D}{\sin \eta} = \frac{U}{\sin \sigma}$$

In the hydrodynamic theory [1-2-3-4] two different types of configurations may occur in the detonation products: when regular refraction exists, the flow corresponds to a reflected shock (Figure 2a), the other flow consists of Prandtl-Meyer rarefaction waves starting from Point  $I$  (Figure 2b).

For the case when the flow is everywhere supersonic, a solution may be obtained by applying hydrodynamic theory. With a known equation of state of explosive, for each incidence angle  $\eta$ , it is possible to define the angle  $\phi_G$  of streamline deflection across the detonation front and the pressure  $P_G$  at the interface. The locus of all states attainable behind the detonation front ( $P_G$ ,  $\phi_G$ ) is the shock polar curve  $\pi_G$  for detonation products. In the specimen, shock wave theory is used to calculate the shock pressure  $P_m$  and the

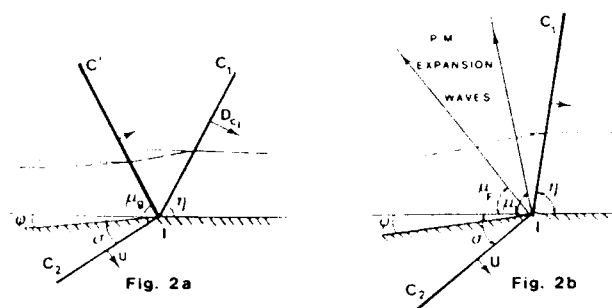


Figure 2. Schematic Illustration of a Regular Refraction

streamline angle  $\phi_m$  behind the shock front, the locus of all states ( $P_m$ ,  $\phi_m$ ) is the shock polar curve  $\pi_m$  for specimen.

The solutions of regular refraction are coupled by the requirements that the pressure is continuous across the gas sample interface, and that adjacent streamline in the two media be parallel. The intersection of the two shock-polars,  $\pi_G$  and  $\pi_m$ , then provide us a solution of the regular refraction. Other parameters for shocks are easily calculated from the jump conditions and assumed metal equation of state.

Two particular cases are taken into account:

- 1) Dense Materials. The solutions given by the intersection of shock-polars  $\pi_m$  and  $\pi_G$  are steady if the flow is supersonic in the two media (Figure 3a). For dense materials, incidence angles exist  $\eta \in [\eta_1, \eta_2]$  for which the flow in detonation products is subsonic, and supersonic in solid sample. (Point  $S$  is the sonic point in detonation products or in medium.) Another type, the shock-polar  $\pi_G$  and  $\pi_m$  does not intersect for incidence angles  $\eta \in (\eta'_1, \eta'_2)$  (Figure 3b).
- 2) Elastic-Plastic Materials. The second particular case about refraction deals with the elastic-plastic materials. The first assumption allowing solution of the refraction problem is that the material has hydrodynamical behavior. There is a critical incidence angle ( $\eta = \eta^*_{CR}$ ) for which the material velocity behind the



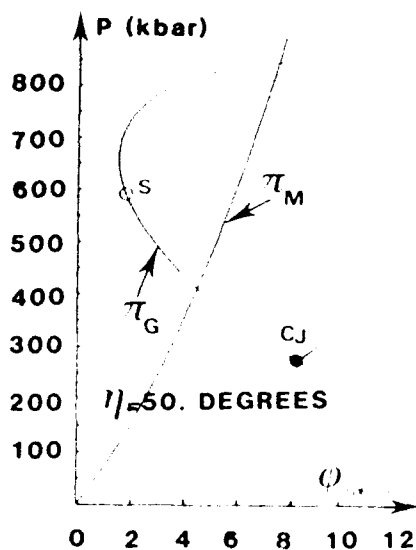


Figure 3a. Regular Refraction

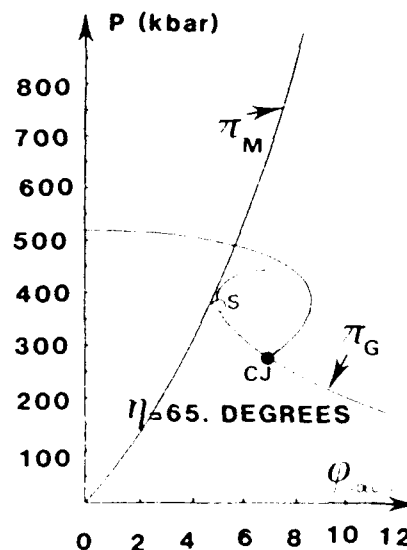


Figure 3b. Irregular Refraction

shock front equals the hydrodynamic sound speed in the material. A second configuration appears beyond a particular value of the incidence angle for which the shock polars  $\pi_G$  and  $\pi_m$  do not intersect. A particular case is obtained when the bulk velocity  $C_B$  of the material is greater than the detonation velocity of the explosive. Then the shock-polar  $\pi_m$  does not exist.

To illustrate these different cases, we have collected (Figure 4) the different position of the shock polars  $\pi_G$  (detonation products) and  $\pi_m$  (Alumina) in the  $(P, \phi)$  plane versus the incidence angle  $\eta$  between the detonation and the interface.

Two explosive compositions are considered: HMX based (X1) and TATB-based (T2). Their detonation properties are listed in Table 1.

Then, according to the hydrodynamic assumption, the set of theoretical solutions obtained by shock polar intersection is shown in Figure 5: the pressure  $P$  versus incidence angle  $\eta$  corresponding to the two explosives X1 and T2.

For alumina, elastic plastic properties are listed in Table 2.



Figure 4. Shock Polar Configurations Explosive/Alumina

Table 1. Explosives Parameters X1 and T2

	$\rho_e$ g/cm <sup>3</sup>	$D_{CJ}$ m/s	$P_{CJ}$ C <sup>2</sup> /a	$\gamma$
Comp. X1	1.822	8778	34.2	3.10
Comp. T2	1.855	7700	29.0	2.79

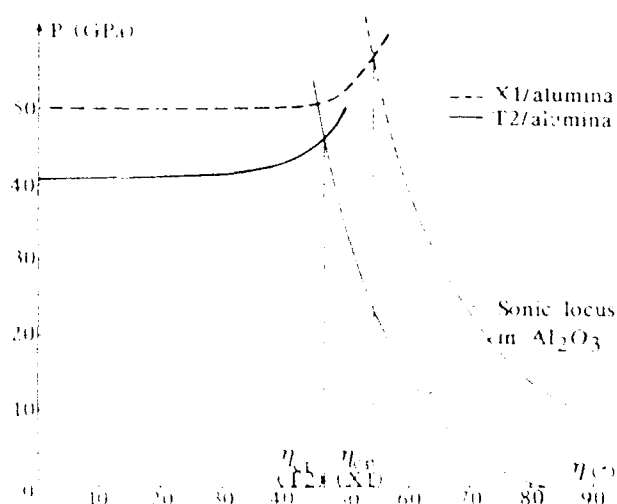


Figure 5. Explosive/Alumina -  $P(\eta)$  Shock Polars Solution in Hydrodynamic Hypothesis

Table 2. Elastic Plastic Parameters in Alumina

	$\rho_0$ g/cm <sup>3</sup>	$C_L$ m/s	$C_T$ m/s	$C_B$ m/s	$\sigma_{HEL}$ GPa
Alumina	3.92	10774	6324	7922	8.00

We can see that the critical incidence angle  $\eta_{CR}$  is close to  $\eta^*_{CR}$  for which the flow speed equals the longitudinal sound speed  $C_L$ .

The critical incident angles corresponding to  $q_0 = C_L$  are respectively  $\eta^*_{CR} \approx 46^\circ$  for T2 and  $\eta^*_{CR} \approx 55^\circ$  for X1.

Beyond  $\eta_{CR}$ , the interaction results from the propagation of an elastic precursor wave in the adjacent medium. With alumina, this phenomenon is important since the Hugoniot Elastic Limit (H.E.L.) is particularly high (H.E.L. = 8 GPa) and the behavior of the material cannot be described only by the hydrodynamic pressure, but requires the different components of the stress. Then the interaction must be studied with the elastic plastic assumption.

## EXPERIMENTAL STUDY

The aim of the experiments was to study the waves near the interface for different incidence angles ( $\eta$ ) of the detonation (20° to 90°).

The explosive prismatic slabs (Figure 6) are machined at angle  $\eta$ ; the angle of copper or iron confinement is chosen to provide a plane detonation wave. So built, the experimental device provides plane steady two-dimensional flow. The explosive slab is initiated by a plane-wave lens with booster.

We have studied the T2/Copper configurations. In that case, the hydrodynamic theory shows that the flow is sonic in the detonation products for incidence angles  $\eta_1 \approx 61-62^\circ$  and  $\eta_2 \approx 76^\circ$ . The behavior is the same as that for all dense metals, such as iron, uranium, and tantalum together with the explosive T2.

The copper samples (OFHC) are machined and polished with the angle  $\sigma_0$ .

We have chosen an optical method with a streak camera which allows us to see the ionization as soon as the detonation front arrives at the explosive surface; and simultaneously the emergence of the shock wave on the free surface of copper sample. So it is possible to measure the shock angle ( $\sigma_{exp}$ ) between the shock wave and interface in the copper.

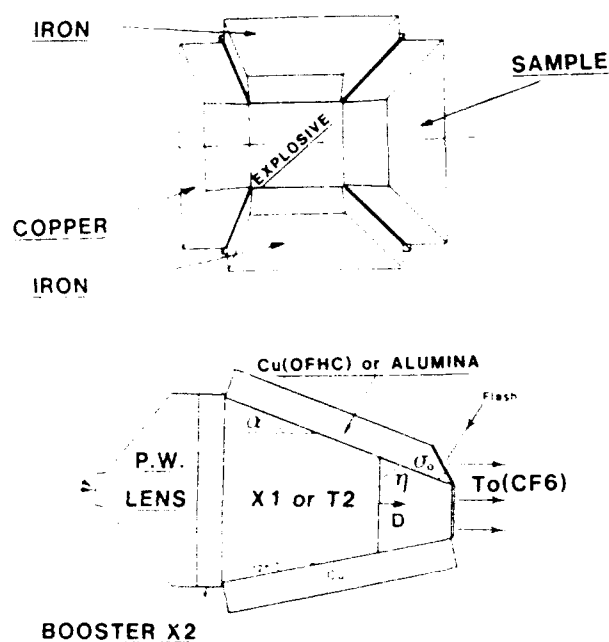


Figure 6. Typical Experimental Device Configuration

With alumina, the critical angle  $\eta_{CR}$  is respectively  $\eta_{CR} \approx 46^\circ$  for T2 and  $\eta_{CR} \approx 55^\circ$  for X1; we have carried out several experiments below and beyond these values in the range of  $40^\circ$  to  $90^\circ$ .

The alumina slabs are machined with the angle  $\sigma_0 = \eta$ .

## RESULTS

### 1 - T2 on Copper

Several records are shown on Figure 7.

#### 1-1 - Analysis of the Detonation Front.

The analysis of the shape of the detonation front shows that the detonation is synchronous and the experimental set-up determines its tilt when the refraction is regular ( $20^\circ \leq \eta \leq 60^\circ$ ). For incidence angles corresponding to no solution zone ( $\eta = 67^\circ/70^\circ/73^\circ$ ), experiments show no advance of the detonation corresponding to a Mach wave as is predicted in the Sternberg-Piacesi model;<sup>2</sup> on the other hand, the detonation is modified near the T2/Cu interface.

The detonation is curved and delayed for  $78^\circ < \eta < \eta^*$ . In that case, the hydrodynamic assumption leads to solutions with reflected waves in the detonation products. The experimental shapes of the detonation front ( $\Delta T_{ns}$ ,  $x_{mm}$ ) are plotted in Figure 8 and show that the

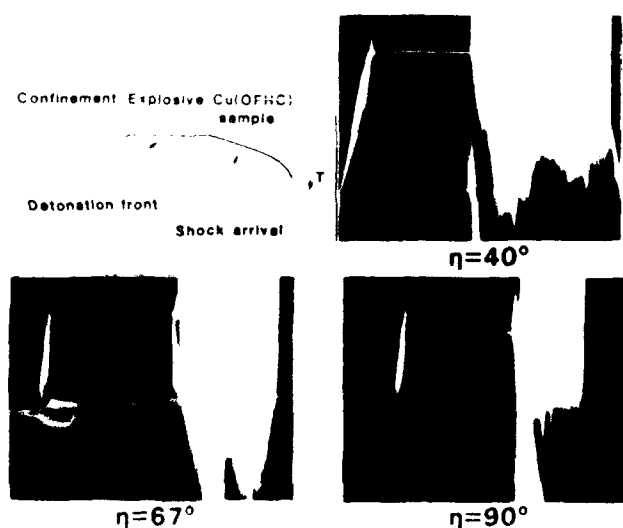


Figure 7. T2 on Copper

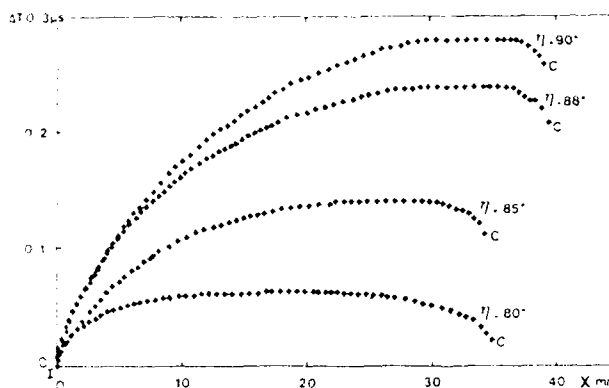


Figure 8. T2/Copper Space Time Profiles of Detonation Front

curvature (or delay  $\Delta T$ ) increases continuously until glancing detonation ( $\eta = 90^\circ$ ).

#### 1-2 - Transmitted Shock in Copper.

From experimental angles ( $\sigma_{exp}$ ) measured near the interface in copper, we calculate the shock velocity  $U'$  in the copper by:

$$U' = \sin \sigma_{exp}(\eta) \cdot \frac{D}{\sin \eta}$$

and the pressure  $P'$  behind the shock is estimated from momentum equation relation:

$$P' = \rho_0 \cdot U' \cdot u'$$

$U'$  is the shock velocity,  $u'$  is the particle velocity; the Hugoniot relationship used for copper is linear in the shock velocity-particle velocity representation.

$U' = 3940 + 1.49 u'$  m/s for the OFHC Copper  $\rho_0 = 8.955$ . The experimental values ( $\sigma_{exp}$ ) and shock pressure data  $P'$  are plotted in Figure 9 and Figure 10.

We have also plotted shock polar calculations and those obtained theoretically from the Sternberg-Piacesi model with a Mach stem.

For these calculations, the explosive has been described by a CJ (Chapman Jouguet) detonation and a  $\gamma$  law equation of state:

$$P = P_{CJ} (V_{CJ}/V)^\gamma$$

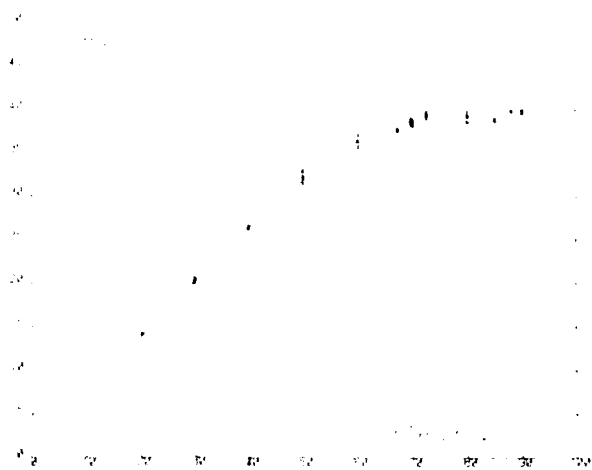


Figure 9.  $\sigma[\eta]$  Shock Polar and Experimental Results

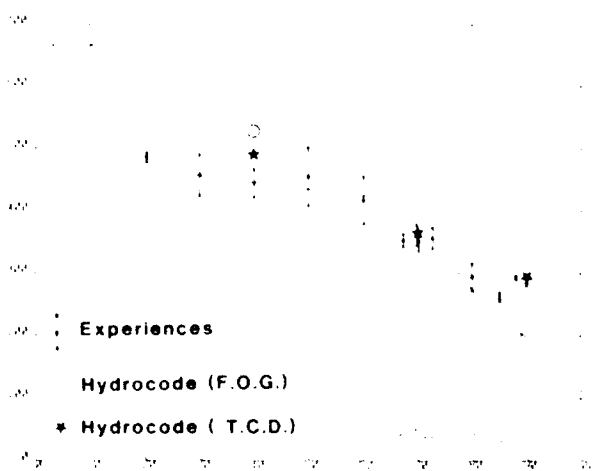


Figure 10.  $P[\eta]$  Shock Polar, Experimental, and Hydrocode Results for T2/Cu

The comparison of these results shows:

1. When  $\eta \in (20^\circ-60^\circ)$ , the values of angle  $\sigma_{\text{exp}}$  are in quite good agreement with the shock polar solutions.

2. When  $\eta \in (67^\circ-73^\circ)$  on the one hand, the values of  $\sigma_{\text{exp}}$  are below the Mach stem model results ( $\sigma$ ); on the other hand, the pressure values  $P'$  are well below the theoretical curve; the relative variation  $(P'-P)/P$  decreases as  $\eta$  increases: [(20 percent) for  $\eta = 67^\circ$ , (-19 percent) for  $\eta = 70^\circ$ , and (-8 percent) for  $\eta = 73^\circ$ ].

3. For  $\eta \geq 80^\circ$ , the discrepancy exists, but in the opposite direction:  $\sigma_{\text{exp}} > \sigma$  and  $P' > P$ ,

the relative variation  $(P'-P)/P$  equals (+ 5, 6 percent) for  $\eta = 80^\circ$  and near (+ 45 percent) for  $\eta = 90^\circ$ .

R. Chéret<sup>5</sup> propounds a model to resolve the refraction problem at incidence angles greater than transition angles at which the regular reflection is not possible. For this, with considerations on the detonation front in the vicinity of interface explosive/specimen, he supposes a reflected shock near the detonation front followed by a relative sonic flow and an unsustained shock in copper followed by a Prandtl-Meyer rarefaction wave. This solution applies up to glancing detonation ( $\eta = 90^\circ$ ). These assumptions allow us to explain in the aggregate the important problem of flow deflection by an oblique detonation from head-on incidence to glancing detonation.

**I-3 - Numerical Simulations.** We have carried out a numerical study with a Lagrangian two-dimensional code for three particular incidence angles of detonation waves corresponding to:

- $\eta = 40^\circ$  • Regular Refraction
- $\eta = 70^\circ$  • No shock-polar solution zone.
- $\eta = 90^\circ$  • Regular Refraction with reflected rarefaction wave.

The copper is treated hydrodynamically with a multi-phase E.O.S. The explosive is treated with a modified Wilkins formulation E.O.S. To obtain good accuracy in calculations, we used a fine enough zoning into the two blocks: 2 mm thickness near the T2/Cu interface (rectangular mesh cells  $0.2 \times 0.1$  mm). In the other part in each block, the mesh cell thickness steadily increases and reaches 1 mm for explosive and 0.4 mm near free surface of copper.

In first case calculations, the detonation wave propagation is calculated geometrically with the ideal Chapman-Jouguet Model (F.O.G.); in the second case, the detonation wave propagation is treated with the shock to detonation transition burning Model (T.C.D.)<sup>7</sup> associated with the Von Neumann scheme and a finite thickness of the reaction zone. Figure 11 shows propagation contours in explosive and copper for three incidence angles.

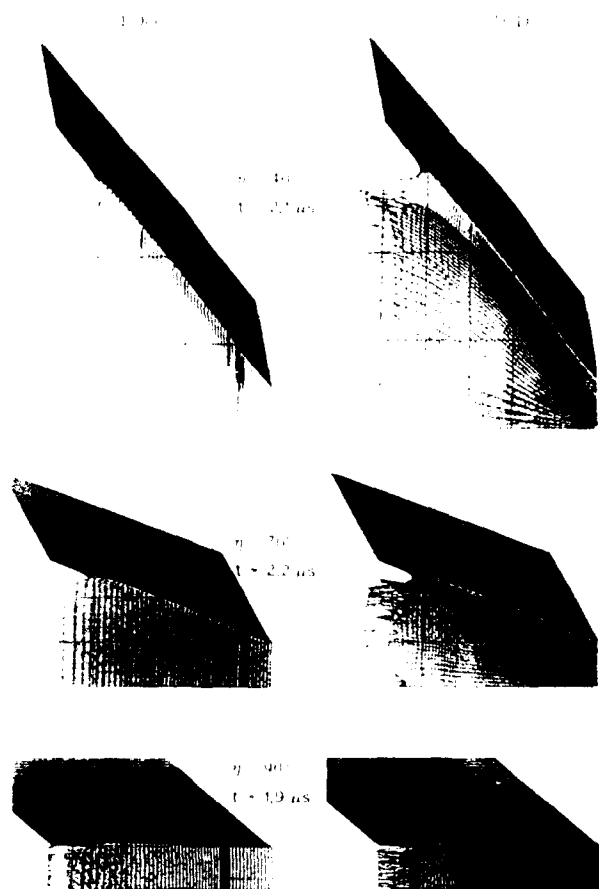


Figure 11. Numerical Simulations T2/Copper

The T.C.D. computations indicate a modification of the detonation wave near the interface explosive/copper for all tested incidence angles. Numerically the detonation front is in advance for incidence angles  $\eta = 40^\circ$  and  $70^\circ$ , which has not been proved by the experiments. On the opposite side for glancing detonation ( $\eta = 90^\circ$ ), the remote curve is equivalent to that one carried out experimentally. An attempt to keep close together experimental results (shock angle  $\sigma$ —Pressure  $P$  in copper) and numerical results obtained with a Mach wave model has failed because of discrepancies.

For  $\eta = 90^\circ$ , the computations with the T.C.D. kinetic method agree with experiments, however, classical theory and the F.O.G. method lead to lower values. The same results are obtained for  $\eta = 70^\circ$ . However in the regular refraction zone ( $\eta = 40^\circ$ ) the two numerical treatments give values higher than experimental ones and also those coming from the

classical theory; values got by numerical model from T.C.D. treatment are the most accurate.

Recently, J. M. Walsh<sup>6</sup> has been led to the same conclusions connected with experimental results completed on both PBX-9501/Uranium and Comp B/Uranium.

## II - Interactions X2/Alumina and T1/Alumina

**II-1 - Results.** First, we have decided to choose an optical process as in Reference 8 based on the extinction of total internal reflection from a transparent prism. This experiment has detected an elastic-precursor in alumina which appears for  $\eta \geq \eta_{CR}$ . Nevertheless, we have noticed a decay in the signal suggesting an early alteration (boost or inhibition) in the detonation front. An attempt with an X-Ray device has disagreed with this last hypothesis by bringing on the detonation wave continuity and on the local modification near confinement. The defect on optical signals was due to the alumina precursor effect on the glass prism. That conclusions make us adopt the same method as in the T2/Copper case, which means the use of ionization for explosive and light deflection at free surface sample. Figure 12

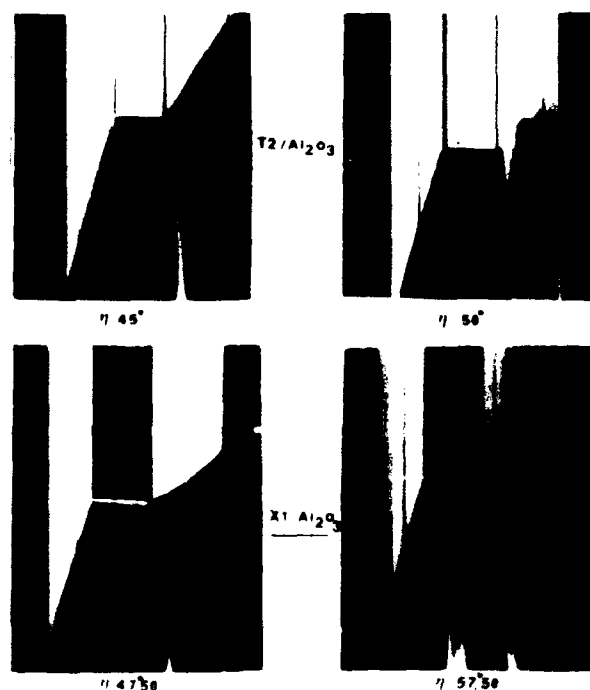


Figure 12. Streak Camera Records - Explosive/Alumina

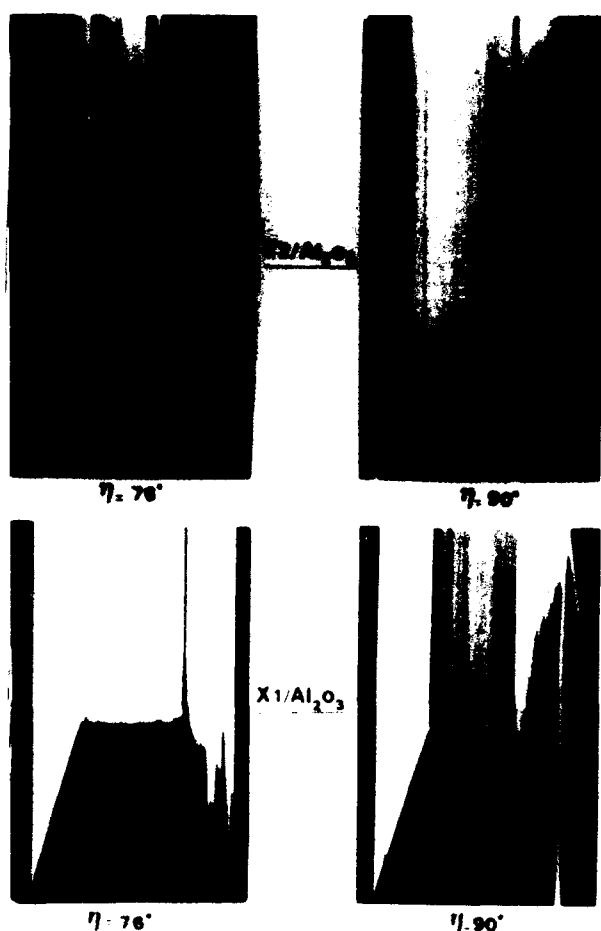


Figure 13. Streak Camera Records T2 and X1/Alumina

gives the records that show all waves in explosive slab and in alumina.

While  $\eta < \eta_{CR}$ , we detect an elastic wave and a plastic shock linked to the detonation wave by the point I. For  $\eta > \eta_{CR}$ , the elastic precursor escapes from the detonation wave while the plastic shock keeps linked to it. The angle between the elastic precursor and the interface is generally close to  $90^\circ$ , whatever the initial incidence. However, we notice a modification of the detonation wave shape near the interface. This phenomenon (advance or delay) depends on the nature of the explosive and also of the incidence angle, it increases when  $\eta$  increases. A comparison can be made by analysis of experimental records obtained on two compositions and for two incidence angles,  $\eta = 76^\circ$  and  $\eta = 90^\circ$  (Figure 13).

For  $\eta = 76^\circ$ , a curved front appears for whatever explosive is used. If  $\eta$  reaches the

vicinity of  $90^\circ$ , the influence of alumina on X1 or T2 detonation becomes different. For X1 the detonation wave shows a local advance near the interface, and on the other side T2 shows a delayed curvature as has already been found in the T2/Copper case. Additional experiments carried out with each explosive composition and different explosive slab heights (from 75 to 150 mm) have shown the same wave configuration. It has been proven that the flow is quasi-steady near the detonation wave located at the explosive/Alumina interface. The local advance (or delay) taken by the detonation wave does not change after a distance of 100 mm. I.D.L. records contain information about the precursor in alumina; for example, its magnitude is practically constant at the plastic wave bottom. The longitudinal elastic velocity  $C_L$ , defined from those experiments does not seem to depend on the incidence angle  $\eta$  nor on the explosive composition: its value is near  $C_L = 10600 \pm 150$  m/s. The elastic precursor intensity in the detonation propagation way is about 7.3 GPa.

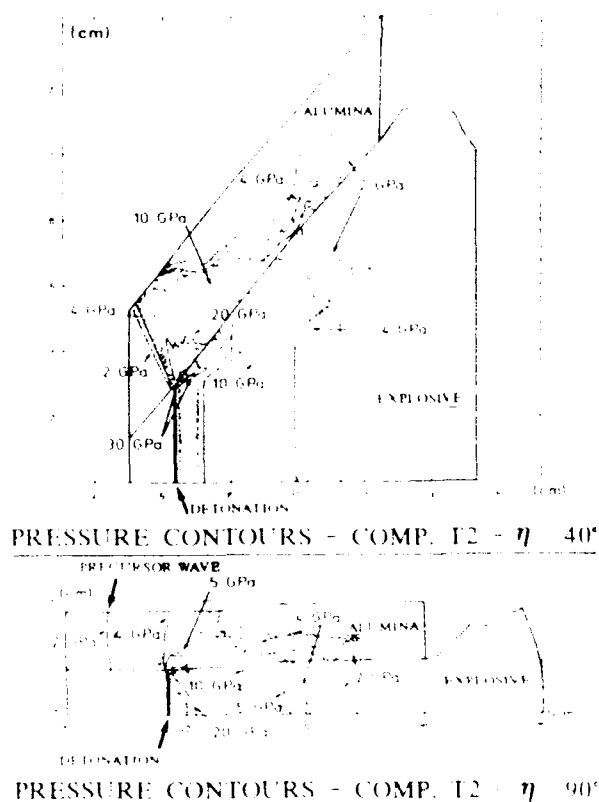


Figure 14. T2/Alumina Numerical Pressure Contours

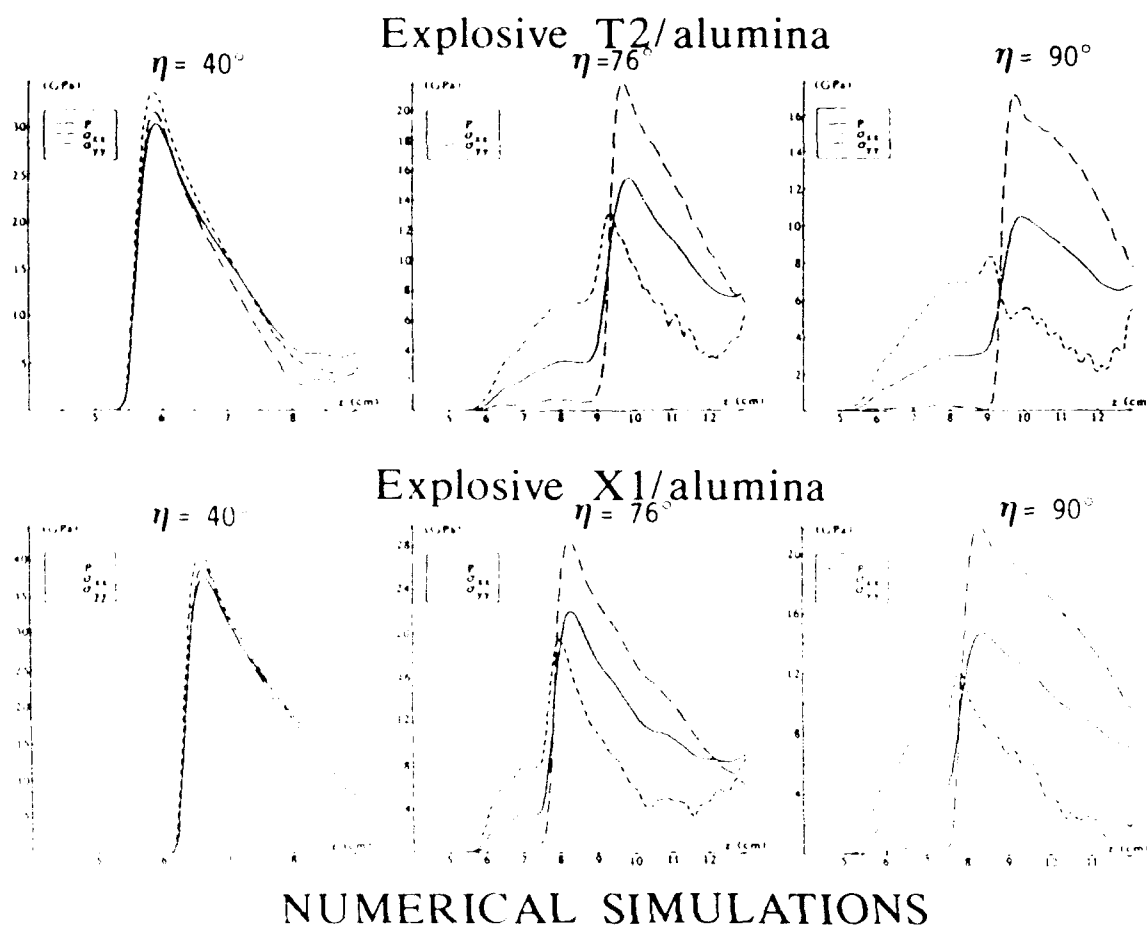


Figure 15 Stress Tensor at the Interface

**II-2 - Numerical Simulations.** We have computed a numerical simulation with a bidimensional Lagrangian Code on three experimental devices  $\eta = 40^\circ$ ,  $76^\circ$ , and  $90^\circ$ . The explosive is treated with a Modified Wilkins (W.M.) formulation E.O.S.; the detonation front is calculated with the F.O.G. method; the alumina elastic plastic behavior has been simulated by Steinberg-Cochran-Guinan (S.C.G.) model.<sup>9</sup>

These results compared to experiments give:

- good agreement in time between the different waves.
- similar phenomenology if we consider the pressure contours given by computations.

From stress tensor  $\sigma_{xx}$  and  $\sigma_{yy}$  in the alumina (Figure 15), we can notice a quasi hydrodynamical behavior for  $\eta < \eta_{cr}$  ( $\sigma_{xx} \approx \sigma_{yy} \approx P$ ). For  $\eta > \eta_{cr}$ , an elastic plastic behavior becomes more outstanding when  $\eta$  increases.

Along the T2/Alumina interface for  $\eta = 90^\circ$ , the longitudinal component  $\sigma_{xx}$  is about 7.0 GPa and the transverse component  $\sigma_{yy}$  remains at a less important level of several kbar.

The numerical simulations are unable to show the experimentally noticed modification on the detonation front unless a more sophisticated chemical kinetic model is used, the model taken for our computations is inadequate for weak shock in the inert explosive.

## CONCLUSION

These experimental and numerical results have improved our understanding of oblique detonation wave interaction between a solid explosive and an inert material.

In the explosive/dense medium interaction such as T2/Copper, we have shown good agreement between experimental data and shock-polar theory results inside the Regular Refraction zone from 20° to 60°. For higher incidence angles, a large discrepancy appears between experimental and model results.

Several experiments carried out with the elastic-plastic material alumina show that other new experiments are needed to improve the understanding of the precursor effect (weak shock) on the reactivity of explosives.

The computational study has shown the importance of the method picked to calculate the detonation front, and it showed that a more complete kinetic model is needed, in particular to describe the effect of multiple shocks (precursor wave) in solid explosive.

## REFERENCES

1. Courant, R. and Friedrichs, K. O., *Supersonic Flow and Shock Waves*, Wiley, NY, 1948.
2. Sternberg, H. M. and Piacesi, D., "Interaction of Oblique Detonation Waves with the Iron," *Phys. Fluids*, Vol. 9, No. 7, Jul 1966, pp. 1307-1351.
3. Walsh, J. M., "Oblique Interactions of Detonation Waves with Explosive/Metal Interfaces," *LANL LA 9612 MS*, Dec 1982.
4. Neal, T., "Perpendicular Explosive Drive and Oblique Shocks," *Proceedings of the Sixth Symposium (International) on Detonation*, Office of Naval Research Publication, A.C.R. 221, 1976, pp. 602-610.
5. Chéret, R., Aveillé, J., and Carion, N., "Emergence d'une Détonation quasi C.J. sur le bord libre d'un Domaine Explosif," *C.R. Acad. Sc. Paris*, t 303, Série II, n°1, 1986.
6. Walsh, J. M., "On the Problem of the Oblique Interactions of a Detonation

Wave with an Explosive Metal Interface," *Shock Waves in Condensed Matter*, 1987, 3-10, S. C. Schmidt, N. C. Holmes (Editors), 1988.

7. Donguy, P. and Legrand, N., "Numerical Simulation of Non Ideal Detonation of Heterogeneous Explosive with the Two-Dimensional Eulerian Code CEE," *Proceedings of the Seventh Symposium (International) on Detonation*, Annapolis, 1981.
8. Eden, G. and Wright, P. W., "A Technique for the Precise Measurement of the Motion of a Plane Free Surface," *Preprints Fourth Symposium on Detonation*, U.S. Naval Ordnance Lab, 12/15 Oct 1965.
9. Steinberg, D. J.; Cochran, S. C.; and Guinan, M. W., *J. Appl. Phys.*, 51 (3) pp. 1498-198.

## DISCUSSION

J. BDZIL  
LANL/GROUP M-9

TATB-based explosives have a long reaction zone length. Thus, the sample Mach stem theory that you showed for your comparison is not relevant. That theory assumes that the problem has no length scales.

## REPLY BY J. AVEILLÉ

Yes, TATB-based explosives have a long reaction zone length. It is clearly shown in our publication that for TATB/copper, better results are obtained with consideration of the reaction zone in flow than without it.

## DISCUSSION

B. D. LAMBOURN  
AWE(A), Aldermaston, Reading, UK

(1) The Sternberg-Piacasi Mach stem solution is discontinuous with the regular reflection solutions, because it makes the assumption that the Mach stem does not grow. A theory which allowed the Mach stem to grow would be more continuous between the low angle and high angle regular solutions.



(2) Isn't the interaction pressure constant for  $\alpha > 76^\circ$  because the detonation wave cannot sustain an interaction angle greater than  $76^\circ$ ?

### REPLY BY J. AVEILLÉ

We have checked a theory which allowed the Mach stem to grow (as those published by Walsh). We obtained also less discontinuity

between the low angle and high angle regular solutions.

Yes, from  $\eta = 76^\circ$  to  $90^\circ$  (incidence angle) the detonation wave keeps close conditions at boundary explosive/sample because the large reaction zone in TATB is perturbed by P. Meyer rarefaction waves. In the copper sample, the transmitted pressure is constant.

# **EXPERIMENTAL AND NUMERICAL STUDY OF CORNER-TURNING DETONATION**

**A. W. Gibb  
Defence Research Establishment  
Ralston, Alberta, Canada**

This paper was presented at the Ninth  
Symposium (International) on Detonation.  
However, it is not published here because it

was not submitted to the editor in sufficient  
time to be published.

## AUTHOR INDEX\*

Agnew, S. F.	1019	Boyer, L. R.	1295
Alcon, R. R.	39	Boyle, V. M.	3, 897, 1460
Akst, I. B.	478	Braithwaite, M.	513
Aldis, D. F.	112, 280	Brazell, N.	1131
Alexander, K. E.	498	Breithaupt, R. D.	133, 525, 1378
Anderson, C. J.	1364	Brill, T. B.	228
Andrew, M. I.	1253	Brun, L.	757
Andriot, P.	506	Brush, P. J.	228
Anisichkin, V. F.	407	Bugaut, F.	489
Arbuckle, A. L.	1489	Bukiet, B. G.	751
Armstrong, R. W.	1260	Buntain, G. A.	1037
Asay, B. W.	265, 537	Russell, T. J.	1404
Atwood, A. I.	363	Butler, P. B.	906
Aubert, S. A.	1284	Byers Brown, W.	513
Austing, J. L.	972		
Aveill�, J.	506, 842	Campbell, A. W.	265, 537
		Campos, J.	925
Baer, M. R.	293, 906	Capellos, C.	1084
Bahl, K. L.	133	Carion, N.	506, 842
Bai Chunhua	879	Carlson, D. W.	626, 1260
Bainville, D.	1070	Castille, C.	1070
Baker, D. E.	972	Chaisse, F.	506, 757
Baker, R. N.	806	Chan, M. L.	566
Bardo, R. D.	235	Chapman, L. B.	1001
Baudin, G.	1371	Chaudhri, M. M.	857
Bauer, P.	925, 933	Chen Fumei	816
Bdzil, J. B.	730, 773	Chen Peiqi	142
Beard, B. C.	897	Cheret, R.	246
Becuwe, A.	1008	Cherin, H.	1271
Bedoch, J. P.	1371	Chick, M.	1404
Beitel, F. P., Jr.	585	Chiles, W. C.	1335
B�langer, C.	1480	Chirat, R.	489
Belcher, R. A.	831, 1253	Cichra, D. A.	633
Belmas, R.	1070	Clements, R. E.	641
Benjamin, K. J.	1460, 1489	Coffey, C. S.	58, 897, 1243
Bernard, S.	489	Cook, M. D.	1027, 1441
Bernecker, R. R.	354	Cooper, J.	197
Bhasu, V. C. Jyothi	1276	Cooper, P. W.	379
Bines, A.	1404	Costantino, M. S.	1310
Blais, N.	953	Cowperthwaite, M.	89, 388
Blake, O.	3	Craig, B. G.	573
Boggs, T. L.	363	Crane, S. L.	1543
Boslough, M. B.	1199	Crawford, P. C.	25
Bourne, N. K.	869	Crouch, L. D.	798

\*Pages 1 through 854 appear in Volume I and pages 855 through 1646 appear in Volume II.

## AUTHOR INDEX (Cont.)\*

Davidova, O. N.	724	Gimenez, P.	1371
Davis, W. C.	1335	Ginsberg, M. J.	537
Deal, W. E.	1543	Glancy, B. C.	341, 1260
Deiter, J. S.	626	Glenn, J. G.	1284
Delclos, A.	1008	Gohar, P.	1271
Delpuech, A. E.	172	Graham, K. J.	1295
Demske, D.	1131	Graham, R. A.	1529
DeVost, D. F.	1243	Green, L. G.	670, 701
Dick, J. J.	683	Green, N. J. B.	1193
Dickson, P. M.	1100	Greiner, N. R.	953, 1170
Dimas, P.	1076	Groux, J.	1217
Ding-Jing	77, 252, 879	Guo Yuxian	554
Doherty, R. M.	626, 633	Guri, G.	506
Dold, J. W.	219		
Dong Haishan	995	Han Chengbang	947
Dorsey, T. M.	1489	Hannaford, C. E.	1076
Dremin, A. N.	724	Haskins, P. J.	1027, 1441
Dufort, S.	1271	Hattori, K.	640
Dunand, M.	933	Held, M.	1416
		Helm, F. H.	25
Eden, G.	831, 1253	Hermes, R.	1170
Elban, W. L.	1260	Heuzé, O.	925, 933
Engelke, R.	39, 657	Hikita, T.	939
Erickson, K. L.	1140	Ho, S. Y.	1052
Erickson, L. M.	112	Holmes, N. C.	190
Erskine, D. J.	670	Hrdina, D. J.	972
		Hsieh, T.	329
Fanget, A.	1047	Huan Shi	77, 252
Farley, W. E.	1131	Huang Lihong	947
Ferm, E. N.	1427	Hubbard, P. J.	1322
Fickett, W.	730	Huntley, J. M.	886
Field, J. E.	869, 886, 1100, 1276	Hutchinson, C. D.	123
Foan, G. C. W.	123		
Forbes, J. W.	806, 897, 1235	Iida, M.	621
Forest, C. A.	683	Ishiokawa, N.	621
Fortov, V. E.	50	Iwata, L.	1084
Fortova, T. N.	50		
Frank, A. M.	641	James, H. R.	1441
Frey, R. B.	3, 1404	Jia Quansheng	816
Fu Xinghai	1360	Johnson, J. D.	417
Fujiwara, S.	621	Jones, A. G.	123
Fukatsu, Y.	640	Jones, H. D.	461
		Jungst, R. G.	1510
Gibb, A. W.	853, 1364		

\*Pages 1 through 854 appear in Volume I and pages 855 through 1646 appear in Volume II.

# AUTHOR INDEX (Cont.)\*

Kanel, G. I.	50	Lyman, O. R.	1460
Kang, J.	906	Mader, C. L.	693
Kang Shufang	947	Mal'kov, I. Yu.	407
Kapila, A. K.	219	Malyrenko, S. I.	50
Kato, Y.	640, 939	Marlow, W. R.	1253
Kennedy, D. L.	1224	McAfee, J. M.	265
Kennedy, M.	1351	McCandless, P.	190
Kenney, I.	1019	McFadden, D. L.	1460
Kenney, J.	1019	McKinney, T. L.	1037
Kerihuel, M. T.	506	Meulenbrugge, J. J.	83
Kerley, G. I.	443	Miller, P. J.	341, 498
Kerr, I. D.	1351	Miller, S.	1131
Kershner, J. D.	693	Mishra, I. B.	1084
Kim, K.	329, 593	Miyake, A.	560
Kinney, J. H.	868	Moen, I. O.	1364
Kipp, M. E.	209, 1510	Mohan, V. Krishna	1276
Kleinhanß, H. R.	66	Moore, D. S.	180
Klimenko, V. Yu.	724	Moore, L. M.	1529
Kober, E. M.	1185	Mori, N.	640, 939
Kodde, H. H.	560	Moulard, H.	18
Kolodney, K.	1084	Murphy, M. J.	525
Kooker, D. E.	306		
Kornhauser, M.	1451	Nakayama, Y.	621
Krall, A. D.	341	Nanut, V.	98
Kury, J. W.	25, 1378	Nilsson, H.	162, 1151
		Nunziato, J. W.	293
Lambourn, B. D.	784		
Lambrakos, S. G.	713	Oran, E. S.	713
Lanzerotti, M. Y. D.	918	Ornellas, D. L.	1162, 1310
Larson, T. E.	1076	Östmark, H.	162, 1151
Lawn, H. R.	123	Otani, G.	190
Lee, E. L.	280	Ouyang Denghuan	142
Lee, J.	573		
Lee, J. W.	471	Pace, M. D.	987
Lee, L. M.	1529	Paisley, D. L.	1110
Lee, R. J.	396	Palmer, S. J. P.	886
Lee, R. S.	798	Parry, M. A.	886, 1100
Leiper, G. A.	197, 1224	Parsons, G. H.	1284
Lemar, E. R.	806	Persson, P. A.	545, 573
Lepie, A. H.	1295	Pettit, D. R.	683
Leroy, M.	506	Peyrard, M.	713
Liddiard, T. P.	1235	Pilarski, D. L.	1460
Lind, C. D.	566	Pilling, M. J.	1193
de Longueville, Y.	1371	Pinto, J. J.	918
Loupas, C.	1047	Politzer, P.	566
Lungenstraß, F.	66		

\*Pages 1 through 854 appear in Volume I and pages 855 through 1646 appear in Volume II.

## AUTHOR INDEX (Cont.)\*

Powers, P. S.	1084	Song, S. Y.	471
Presles, H. N.	925, 933	Spear, R. J.	98
Price, C. F.	363	Stacy, H. L.	657
Price, D.	1235	Stanton, P. L.	1118
		Starkenberg, J.	604, 1460, 1489
Quidot, M.	1217	Steele, R. D.	1014
		Stewart, D. S.	730, 773
Ramsay, J. B.	265, 537, 1427, 1543	Stretz, L. A.	1014
Reddy, G. Om	585	Sumida, W. K.	972
Ree, F. H.	425, 743	Sun Chengwei	142
Reed, R. P.	1529	Sun Jian	435
Reisler, H.	1084	Swanson, B. I.	1019
Renick, J. D.	545	Swift, D. C.	784
Renlund, A. M.	153, 1118		
Reynier, P.	1070	Takala, B. E.	1543
Rice, S. F.	190	Taliancich, A. G.	89
Richter, H. P.	1295	Tanaka, K.	621
Ringbloom, V.	626	Tang, P. K.	657
Ritchie, J. P.	1185	Tao, W. C.	641, 798, 868, 1310
Rivera, T.	1014, 1037	Tarver, C. M.	112, 133, 525, 670, 701
Robertson, S. H.	1193	Tasker, D. G.	396
Rosenberg, J. T.	89	Taylor, G. W.	1014, 1037
		Thoreen, J. L.	1284
Saint-Martin, C.	1371	Titov, V. M.	407
Sakai, H.	939	Tokita, K.	640
Sakurai, T.	939	Tomlinson, R.	1322
Samirant, M.	259	Torii, A.	640
Sanchez, J. A.	545	Trebinski, R.	766
Sandstrom, F. W.	573	Trofimov, V. S.	250
Sandusky, H. W.	341, 1260	Trott, W. M.	153, 1118
Schedlbauer, F.	962	Trzcinski, W.	766
Schmidt, S. C.	180	Tulis, A. J.	972
Schott, G. L.	1335		
Seitz, W. L.	657	Utkin, A. V.	50
Servas, J. M.	842	Urtiew, P. A.	112
Setchell, R. E.	209		
Sharma, J.	897	Vacellier, J.	842
Shaw, M. S.	452	van der Steen, A. C.	83, 320, 560
Sheffield, S. A.	39, 683	van Thiel, M.	425, 743
Shepherd, J. E.	641	Verbeek, H. J.	83, 320
Shi Buisheng	947	Vigil, M. G.	1385
Simpson, R. L.	25, 280, 525	Volk, F.	962
Sitzmann, M. E.	1162	Von Holle, W. G.	133
Skocypec, R. D.	1140		

\*Pages 1 through 854 appear in Volume I and pages 855 through 1646 appear in Volume II.

## AUTHOR INDEX (Cont.)\*

Von Rosen, K.	1364	Woody, D. L.	1243
Wackerle, J.	657, 683	Wu Xiong	435
Wang Tinzheng	816	Xiao Lianjie	435
Warnes, R.	1131	Yoshida, M.	621
Warren, T. W.	822	Yu Jun	1360
Weinmaster, R. R.	822	Zhao Feng	142
Weirick, L. J.	1060	Zerilli, F. J.	461
Weston, A. M.	280	Zhang Guanren	1360
Wilmot, G. B.	626	Zöllner, H.	66
Witkowski, W.	766	Zoludeva, T. A.	724
Wittig, C.	1084	Zwierzchowski, N. G.	1295
Wlodarczyk, E.	766		
Wolfe, A.	918		

\*Pages 1 through 854 appear in Volume I and pages 855 through 1646 appear in Volume II.

REPORT DOCUMENTATION PAGE			Form Approved OMB No. 0704-0188	
Public reporting burden for this collection of information is estimated to average 1 hour per response, including the time for reviewing instructions, searching existing data sources, gathering and maintaining the data needed, and completing and reviewing the collection of information. Send comments regarding this burden estimate or any other aspect of this collection of information, including suggestions for reducing this burden, to Washington Headquarters Services, Directorate for Information Operations and Reports, 1215 Jefferson Davis Highway, Suite 1204, Arlington, VA 22202-4302, and to the Office of Management and Budget, Paperwork Reduction Project (0704-0188), Washington, DC 20503.				
1. AGENCY USE ONLY (Leave blank)		2. REPORT DATE Aug 28 through Sep 1, 1989		3. REPORT TYPE AND DATES COVERED Proceedings, 8/28-9/1/89
4. TITLE AND SUBTITLE Proceedings of the Ninth Symposium (International) on Detonation, Volume I			5. FUNDING NUMBERS	
6. AUTHOR(S) Wanda J. Morat, editor				
7. PERFORMING ORGANIZATION NAME(S) AND ADDRESS(ES) Naval Surface Warfare Center 10901 New Hampshire Avenue Silver Spring, MD 20903-5000			8. PERFORMING ORGANIZATION REPORT NUMBER	
9. SPONSORING/MONITORING AGENCY NAME(S) AND ADDRESS(ES) Office of Naval Research 800 North Quincy Street Arlington, VA 22217-5000			10. SPONSORING/MONITORING AGENCY REPORT NUMBER  OCNR-113291-7	
11. SUPPLEMENTARY NOTES				
12a. DISTRIBUTION/AVAILABILITY STATEMENT  Approved for public release; distribution is unlimited.			12b. DISTRIBUTION CODE	
13. ABSTRACT (Maximum 200 words)  This book is the first of two volumes that document the proceedings of the Ninth Symposium (International) on Detonation which was held August 28 through September 1, 1989, at the Red Lion Inn, Portland, Oregon. Papers presented in this publication cover special problems in the field of energetic materials, particularly detonation phenomena in solids and liquids. General subject areas include shock-to-detonation transition, time resolved chemistry, initiation modeling, deflagration-to-detonation transition, equation of state and equation of state and performance, composites and emulsions, and composites and emulsions/underwater explosives, reaction zone, detonation wave propagation, hot spots, detonation products, chemistry and compositions, and special initiation.				
14. SUBJECT TERMS Detonation Energetic materials Time resolved chemistry			15. NUMBER OF PAGES 884	
Explosives Composites and emulsions Special initiation			16. PRICE CODE	
Shock-to-detonation transition Hot spots				
17. SECURITY CLASSIFICATION OF REPORT UNCLASSIFIED	18. SECURITY CLASSIFICATION OF THIS PAGE UNCLASSIFIED	19. SECURITY CLASSIFICATION OF ABSTRACT SAR	20. LIMITATION OF ABSTRACT SAR	



### GENERAL INSTRUCTIONS FOR COMPLETING SF 298

The Report Documentation Page (RDP) is used in announcing and cataloging reports. It is important that this information be consistent with the rest of the report, particularly the cover and its title page. Instructions for filling in each block of the form follow. It is important to *stay within the lines* to meet optical scanning requirements.

**Block 1. Agency Use Only (Leave blank).**

**Block 2. Report Date.** Full publication date including day, month, and year, if available (e.g. 1 Jan 88). Must cite at least the year.

**Block 3. Type of Report and Dates Covered.** State whether report is interim, final, etc. If applicable, enter inclusive report dates (e.g. 10 Jun 87 - 30 Jun 88).

**Block 4. Title and Subtitle.** A title is taken from the part of the report that provides the most meaningful and complete information. When a report is prepared in more than one volume, repeat the primary title, add volume number, and include subtitle for the specific volume. On classified documents enter the title classification in parentheses.

**Block 5. Funding Numbers.** To include contract and grant numbers; may include program element number(s), project number(s), task number(s), and work unit number(s). Use the following labels:

C - Contract	PR - Project
G - Grant	TA - Task
PE - Program Element	WU - Work Unit Accession No.

**BLOCK 6. Author(s).** Name(s) of person(s) responsible for writing the report, performing the research, or credited with the content of the report. If editor or compiler, this should follow the name(s).

**Block 7. Performing Organization Name(s) and Address(es).** Self-explanatory.

**Block 8. Performing Organization Report Number.** Enter the unique alphanumeric report number(s) assigned by the organization performing the report.

**Block 9. Sponsoring/Monitoring Agency Name(s) and Address(es).** Self-explanatory.

**Block 10. Sponsoring/Monitoring Agency Report Number. (If Known)**

**Block 11. Supplementary Notes.** Enter information not included elsewhere such as: Prepared in cooperation with...; Trans. of...; To be published in... When a report is revised, include a statement whether the new report supersedes or supplements the older report.

**Block 12a. Distribution/Availability Statement.** Denotes public availability or limitations. Cite any availability to the public. Enter additional limitations or special markings in all capitals (e.g. NOFORN, REL, ITAR).

DOD - See DoDD 5230.24, "Distribution Statements on Technical Documents."  
DOE - See authorities.  
NASA - See Handbook NHB 2200.2  
NTIS - Leave blank.

**Block 12b. Distribution Code.**

DOD - Leave blank.  
DOE - Enter DOE distribution categories from the Standard Distribution for Unclassified Scientific and Technical Reports.  
NASA - Leave blank.  
NTIS - Leave blank.

**Block 13. Abstract.** Include a brief (*Maximum 200 words*) factual summary of the most significant information contained in the report.

**Block 14. Subject Terms.** Keywords or phrases identifying major subjects in the report.

**Block 15. Number of Pages.** Enter the total number of pages.

**Block 16. Price Code.** Enter appropriate price code (*NTIS only*)

**Blocks 17.-19. Security Classifications.** Self-explanatory. Enter U.S. Security Classification in accordance with U.S. Security Regulations (i.e., UNCLASSIFIED). If form contains classified information, stamp classification on the top and bottom of the page.

**Block 20. Limitation of Abstract.** This block must be completed to assign a limitation to the abstract. Enter either UL (unlimited) or SAR (same as report). An entry in this block is necessary if the abstract is to be limited. If blank, the abstract is assumed to be unlimited.